Study of the environment of Titan : the stratosphere and the surface of the satellite, future mission experiments & educational activities

Georgios Bampasidis

OBSERVATOIRE DE PARIS
NATIONAL & KAPODISTRIAN UNIVERSITY OF ATHENS

ECOLE DOCTORALE
ASTRONOMIE ET ASTROPHYSIQUE D' ILE-DE-FRANCE

Doctorat en co-tutelle
ASTRONOMIE ET ASTROPHYSIQUE

Georgios Bampasidis

STUDY OF THE ENVIRONMENT OF TITAN

The stratosphere and the surface of the satellite, future mission experiments & educational activities

Thesis Supervisors: Athena COUSTENIS
Xenophon MOUSSAS
Panagiota PREKA-PAPADEMA

Date of Defence: 30 October 2012

Jury :

President : Christos S. ZEREFOS
Rapporteurs : Ioannis DANDOURAS
Panagiotis NASTOS
Examiners : Olivier MOUSIS
Olivier GRASSET

OBSERVATOIRE DE PARIS
NATIONAL & KAPODISTRIAN UNIVERSITY OF ATHENS

ECOLE DOCTORALE
ASTRONOMIE ET ASTROPHYSIQUE D' ILE-DE-FRANCE

Doctorat en co-tutelle
ASTRONOMIE ET ASTROPHYSIQUE

Georgios Bampasidis

STUDY OF THE ENVIRONMENT OF TITAN

The stratosphere and the surface of the satellite, future mission experiments & educational activities

Thesis Supervisors: Athena COUSTENIS
Xenophon MOUSSAS
Panagiota PREKA-PAPADEMA

Date of Defence: 30 October 2012

Jury :

President : Christos S. ZEREFOS
Rapporteurs : Ioannis DANDOURAS
Panagiotis NASTOS
Examiners : Olivier MOUSIS
Olivier GRASSET

This PhD Thesis is a joint supervision Doctorate (co-tutelle) between, the Paris Doctoral School of Astronomy (Ecole Doctorale d'Astronomie et Astrophysique d'Ile-De-France), Paris Observatory and the National & Kapodistrian University of Athens, School of Sciences, Faculty of Physics.

The specialty of the Thesis is Astronomy and Astrophysics (Paris Observatory) and Astrophysics, Astronomy and Mechanics (Faculty of Physics, National & Kapodistrian University of Athens).

The author's student IDs:

- Og5egj00055 (Paris Observatory)
- 2007509 (Faculty of Physics, National & Kapodistrian University of Athens)

The Jury Composition:

Thesis supervisors:

- Dr. Athena Coustenis, Research Directror, CNRS, LESIA, Observatoire de Paris, France
- Prof. Xenophon Moussas, Professor, Faculty of Physics, National & Kapodistrian University of Athens
- Prof. Panagiota Preka-Papadema, Assistant Professor, Faculty of Physics, National & Kapodistrian University of Athens

President of the Jury:

- Prof. Christos S. Zerefos, Professor, National Academy of Athens, Greece
- Dr. Ioannis Dandouras, Research Director, CNRS, IRAP (ex-CESR), Institut de Recherche en Astrophysique et Planétologie, Toulouse, France
- Dr. Panagiotis Nastos, Assistant Professor, Faculty of Geology and Geoenvironment, National & Kapodistrian University of Athens
- Prof. Olivier Mousis, Professor, Université de Franche-Comté, France
- Prof. Olivier Grasset, Professor, Université de Nantes, France

ACKNOWLEDGEMENTS

For the completion of this work I am indebted to my supervisors Dr. Athena Coustenis, Prof. Xenophon Moussas and As. Prof. Panayota Preka-Papadema not only for their invaluable guidance and insight but also for their constant encouragement over the last years.

I am grateful to the Goddard Team (R. Achterberg, D. Jennings, C. Nixon, R. Carlson, E. Guandique, M. Segrura) for the support they offered in data retrieval. Without them this work would have never existed.

I would also like to thank S. Vinatier and M. Hirtzig from Paris Observatory for their help in scientific interpretation, G. Kollias and S. Stamogiorgos for helping in software, D. Couritis and T. Hadzistergos for helping in future missions chapter, as well as R. Kirk for the fruitful discussions on RADAR image processing.

It is also a great pleasure to acknowledge E. Bratsolis for his guidance in despeckle filtering technique and A. Hayes for providing RADAR data and interpretations of software.

I owe particular thanks to my friends and colleagues A. Solomonidou for her valuable help during my Thesis and E. Mitsakou for her tolerance with my last minute planning.

Deserving of special mention are I. Dandouras and P. Nastos for reviewing my thesis and improving significantly the manuscript with comments and suggestions.

Last, but by no means least, I would like to record a special note of thanks to my wife, my parents and sister whose patience, understanding and support, I have so heavily drawn upon. There are no words enough to thank them for all they have offered.

Abstract

This study concerns Titan's environment from the analysis of spatial data acquired by the Cassini orbiter. On one hand, the temperature and the chemical composition of Titan's stratosphere is determined by the exploitation of spectra recorded by the instrument CIRS of Cassini. The thesis describes a complete work on the data since their extraction, their calibration and up to their analysis by a radiative transfer code. The results permitted to highlight the presence of variations in latitude but also in time, due to the seasons of the satellite. The study also contains contributions to the determination of the abundance of the water vapor and in the variations between hemispheres in the gaseous and aerosol content. Furthermore, a search for new molecules was initiated from large CIRS spectra. A second part deals with the surface of the satellite and its liquid components, the lakes of methane, from Cassini/RADAR data and brings information on the geology and on the cycle of the methane which links the atmosphere with the surface and the interior. The astrobiological implications of this work are discussed within the framework of the quest for habitable environments in our solar system among the icy satellites of the giant planets. All these studies have an impact on the preparation of future space missions to Titan, Saturn and the system of Jupiter and possible instrumentation is proposed. Finally, the context for education and outreach possibilities is discussed.

Résumé

Cette étude porte sur l'environnement de Titan à partir de l'analyse de données spatiales enregistrées par la sonde Cassini. D'une part, la température et la composition chimique de la stratosphère de Titan sont déterminées par l'exploitation des spectres fournis par l'instrument CIRS de Cassini. La thèse décrit un travail complet sur les données depuis leur extraction, leur calibration et jusqu'à leur analyse par un code de transfert radiatif. Les résultats ont permis de mettre en évidence la présence de variations en latitude mais aussi avec le temps, dues aux saisons du satellite. L'étude comporte aussi des contributions à la détermination de l'abondance de la vapeur d'eau et aux variations entre hémisphères des gaz et de la brume sur Titan. De plus, une recherche de nouvelles molécules a été initiée à partir de larges spectres CIRS. Un second volet traite de la surface du satellite et de ses composantes liquides, les lacs de méthane, à partir des données Cassini/RADAR et apporte des informations sur la géologie et sur le cycle du méthane qui relie l'atmosphère à la surface et à l'intérieur. Les implications astrobiologiques de ces recherches sont discutées dans le cadre de la quête pour des habitats dans notre système solaire parmi les satellites de glace des planètes géantes. Tous ces travaux ont un impact sur la préparation de futures missions spatiales vers Titan, Saturne et le système de Jupiter et des instruments possibles sont proposés. Enfin, le contexte pédagogiques et les retombées dans l'éducation et l'information du grand public sont discutés à la fin du manuscrit.

Περίληψη

Η παρούσα μελέτη αφορά στο περιβάλλον του Τιτάνα με βάση την ανάλυση δεδομένων από το διαστημόπλοιο Cassini. Αρχικά, καθορίζεται η θερμοκρασία και χημική σύσταση της στρατόσφαιρας του Τιτάνα μέσω της αξιοποίησης των φασμάτων του οργάνου CIRS του διαστημοπλοίου Cassini. Η διατριβή αποτελεί μια ολοκληρωμένη επεξεργασία των δεδομένων, από τη στιγμή της καταγραφής, της βαθμονόμησης και της ανάλυσής τους με τη χρήση ενός λογισμικού επίλυσης της εξίσωσης διάδοσης της ενέργειας με ακτινοβολία. Τα αποτελέσματα τονίζουν την παρουσία διαβαθμίσεων στη θερμοκρασία και τη σύσταση της στρατόσφαιρας, είτε σε γεωγραφική κατά πλάτος κατανομή, είτε χρονικά, λόγω των εποχών στο δορυφόρο. Η μελέτη επίσης συνεισφέρει στον καθορισμό της περιεκτικότητας των υδρατμών, καθώς και στις διαβαθμίσεις που παρατηρήθηκαν στα ατμοσφαιρικά αέρια και στα αερολύματα ανάμεσα στα δύο ημισφαίρια. Επιπλέον, επιχειρείται αναζήτηση για νέα μόρια με τη χρήση μεσοσταθμισμένων φασμάτων του οργάνου CIRS από την έναρξη έως και το τέλος του πρώτου μέρους της αποστολής. Το δεύτερο μέρος πραγματεύεται την επιφάνεια του δορυφόρου, εστιάζοντας στις λίμνες υδρογονανθράκων και στον περιβάλλοντα χώρο, με την αξιοποίηση των εικόνων RADAR από το Cassini. Δίνονται πληροφορίες για τη γεωλογία και για τον κύκλο του μεθανίου, που αποτελεί συνδετικό κρίκο μεταξύ της ατμόσφαιρας, της επιφάνειας και του εσωτερικού. Επίσης, αναλύονται οι παράμετροι αναζήτησης περιοχών που μπορούν να φιλοξενήσουν βιολογικά μόρια στους δορυφόρους των γιγάντιων πλανητών του ηλιακού μας συστήματος. Οι μελέτες αυτές συνεισφέρουν στην προετοιμασία μελλοντικών αποστολών στον Τιτάνα, στον Κρόνο και στο σύστημα του Δία και προτείνονται σχετικά πειράματα. Τέλος, περιγράφονται εκπαιδευτικές πτυχές και εκλαϊκευτικές εφαρμογές της έρευνας.

Contents

Chapter 1

Introduction

1.1 History of Titan's exploration

1.1.1 Titan before the space era

The story of Titan begins on the night of March 25, 1655, when the young Dutch astronomer Christiaan Huygens (1629-1695), with his brother Constantijn, turned their own designed and constructed 4 m long telescope to Saturn. As he described it in his report entitled "*De Saturni luna observatio nova*", which was published a year later in the Hague, Huygens wanted to understand the strange protrusions referred to as *ansae* or handles appearing at both sides of the giant planet.

Huygens not only observed these odd extends of Saturn but also by using his telescope with a magnification of 50 he noticed the existence of a bright star – as he initially thought- which he eventually realized that it was a satellite. Huygens gathered all his observations in *Systema Saturnium* which was published in 1659[1]. Based on his observations, Huygens calculated the orbital period of Titan at 15 days, 23 hours, 13 minutes not far from the modern value of 15 days, 22 hours, 41 minutes and 24.35 seconds. Except for the discovery of Titan, Huygens explained that Saturn's strange extends were in fact its rings.

Huygens did not name Titan with its contemporary name but he called it *Luna Saturni*. In 1847, Sir John Frederick William Herschel in his publication *Results of Astronomical Observations made at the Cape of Good Hope* proposed to give the names of legendary Titans to Saturn's satellites, inspired from the Greek Mythology. Following Herschel's suggestion, the biggest moon of the Saturnian system is now known as Titan.

Catalan astronomer José Comas Solà assumed the existence of a strongly absorbing atmosphere surrounding Titan, when he claimed he observed limb darkening in his observations in 1907 (Comas Solá, 1908). Sir James Jeans included Titan (Jeans, 1925) in the 4th edition of his theoretical work of escaping atmospheric processes, perhaps being influenced by Solà's observations but he did not refer Solà in his sources list (p. 348).

---

[1] A digital online copy of Christiaan Huygens' book Systema Saturnium can be found in: http://www.sil.si.edu/DigitalCollections/HST/Huygens/huygens-introduction.htm

Moreover, Solà claimed that he had observed limb darkening on Titan. However, it is doubtful that Solà did actually observe the darkening edges on Titan taking into account his scientific equipment and Titan's position during the observation (Lorenz, 1997).

Gerard Peter Kuiper, based on the University of Chicago, not only proved the existence of Titan's atmosphere but also identified one of its constituents when he recorded in 1943-44 methane absorption bands at 6190 and 7250 A in Titan's spectrum (Kuiper, 1944). This observation also revealed the uniqueness of Titan in the Saturnian system, since no other neighboring satellite has similar characteristics (Kuiper, 1952).

The dense cloud nature of Titan's atmosphere was finally confirmed in 1973 (Lewis & Prinn, 1973; Pollack, 1973) and Sagan discusses already the significance of the greenhouse effect on Titan (Sagan, 1973). Several years after Kuiper's work, Lawrence Trafton (Trafton, 1974) from the University of Texas observed in Titan's spectrum the $v3v_3$ band of methane, while Lutz et al. (1976) concluded that methane was a minor constituent of Titan's atmosphere.

The complexity of Titan's atmosphere was soon revealed, when the dissociation of methane was studied at higher altitudes by merely the solar UV radiation, producing more complex hydrocarbons. Gillett (Gillett, 1975) discovered other hydrocarbons in addition to methane, such as ethane at 12.2 μm, monodeuterated methane at 9.39 μm, ethylene at 10.5 μm and acetylene at 13.7 μm. Molecular hydrogen was added to Titan's gaseous inventory in 1975 (Trafton, 1975).

Two models had tried to explain these observations of Titan. One, advocated by (Danielson et al., 1973; Caldwell, 1977), suggested a cold surface at 86 K and 20 mbars under a methane-riched atmosphere where the aerosols capture the solar energy. The other model (Lewis, 1971; Hunten, 1977), assumed an atmosphere of hydrogen, nitrogen and methane, with a surface temperature close to 200 K and high pressure at 20 bars, hosting liquid methane. According to the latter model, nitrogen is a product of ammonia dissociation and contributes to a global greenhouse effect.

Although the pre-Voyager knowledge has advanced our view of Titan, the orange satellite of Saturn remained a mystery. The need for in situ exploration of the Saturnian system, the ringed planet, its rings and the satellites was obvious. Only by space missions Titan's veil can be unveiled since its atmosphere is opaque for ground-based observers.

1.1.2 Space missions: Pioneer 11 and Voyagers 1 and 2

Titan's uniqueness is evident at close scrutiny. It is the largest of the 62 known to date Saturnian natural satellites[2], the second moon in size of the Solar System, after Jupiter's Ganymede and larger than the planet Mercury. Titan orbits around Saturn within almost 16 days, performing a non-synchronous rotation of a 0.36° or $3.3\text{x}10^{-4}$ faster than the synchronous spin rate per year as inferred from RADAR measurements (Lorenz et al., 2008c; Stiles et al., 2008; 2010). The biggest Saturnian satellite is gravitationally locked in its orbit around the gas giant. Along with Venus, Titan is the only slowly rotating body with a substantial atmosphere in the Solar System.

Titan orbits around Saturn within 16 Earth-days almost synchronously. Instead, due to strong zonal winds (Bird et al., 2005; Lorenz et al., 2008c), its atmosphere is in a super-rotation state. Due to Titan's distance from the Sun of about 9.5 astronomical units (AU), the satellite receives slightly more than 1% of the solar flux that the Earth registers at the top of its atmosphere at 1 AU. Additionally, Titan revolves far enough from Saturn, at about 20 Saturnian radii, thus avoiding any critical interactions with its rings.

Pioneer 11 (Fig. 1.1) was the first space mission, which reached the Saturnian system on September 1st, 1979. However, its closest approach to Titan was limited at the distance of 363,000 km, quite far to obtain any measurements or observations.

[2] A list of the Saturnian satellites with their facts can be found in:
http://nssdc.gsfc.nasa.gov/planetary/factsheet/saturniansatfact.html

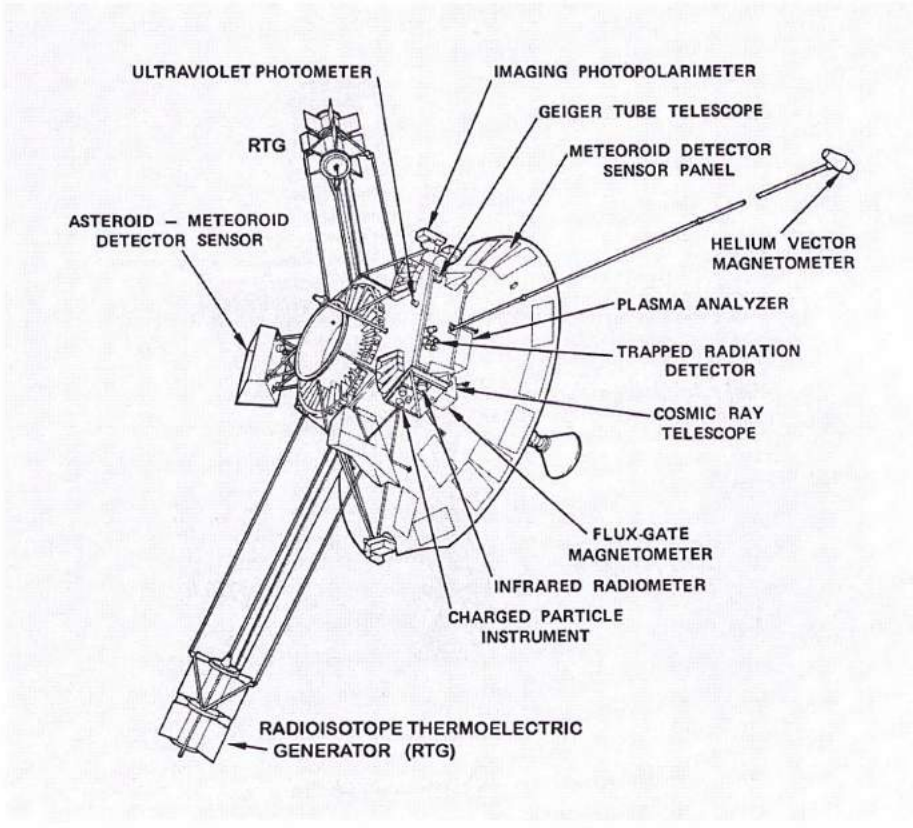

Figure 1. 1 - The Pioneer 11 structure (credit: NASA).

Pioneer's follow-ups were the legendary Voyager 1 and 2 both launched in 1977 (Fig. 1.2). The Voyager twins were the first large scale missions to the outer planets of the Solar system. Both spacecraft took advantage of the rare planetary alignment occurring every 176 years and reached the Saturnian system only few years later. In fact, the Voyager 1 encountered Saturn on November 12th, 1980, while Voyager 2 met the ringed planet on August 25th, 1981. They both observed Titan, but Voyager 2 was too far away to be able to make detailed measurements as Voyager 1. On November 12th, 1980, Voyager 1 flew by Titan at a distance of 6969 km from the centre of the satellite.

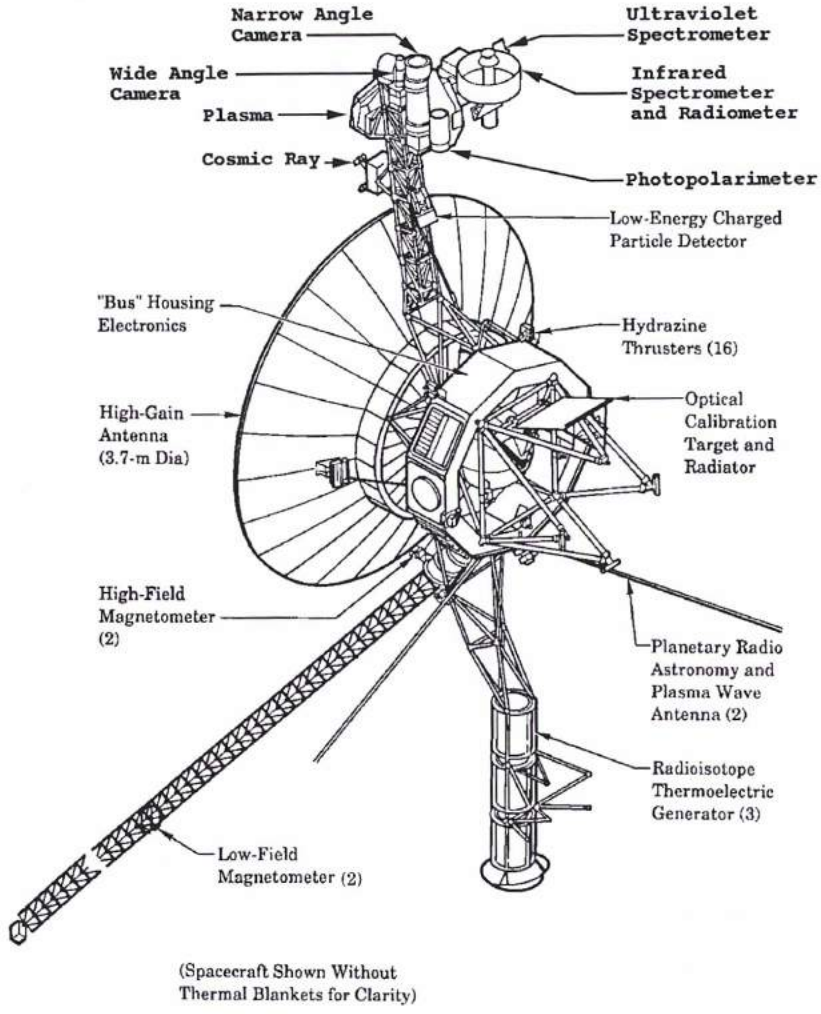

Figure 1. 2 - The Voyager sketch with its main instumentation (source: http://pds-rings.seti.org/voyager/spacecraft/sc_cartoon.gif).

The scientific importance of the Voyager missions' measurements is enormous, as they have visited all the giant planets in the Solar System returning to the Earth a wealth of data and images, which have greatly enhanced our understanding of the Solar System. Apart from the Voyagers no other human device has visited Uranus and Neptune or travelled so far away from our planet. Both spacecraft are still in operation at the edge of the Solar System.

Nowadays, Voyager 1 and 2 crossed the termination shock of the Heliosphere in December 2004 and in August 2007 respectively, where the velocities of the plasma significantly decrease due to the interaction with the interstellar medium and they are now exploring the Heliosheath. They will enter into the interstellar space possibly before 2020. The spacecraft are still detectable through the Deep Space Network (DSN).

1.1.3 The Voyagers encounters of Titan

Voyager 1 and 2 are identical twin spacecraft, the sophisticated instrumentation of which is briefly listed below (Space Science Reviews, Special Voyager instrumentation issue, vol. 21(2): 75-232, 1977):

a) the *Imaging Science System* (ISS), the spacecraft's two-camera system

b) the *Radio Science System* (RSS), the telecommunications system of Voyagers used to investigate physical data of planetary objects

c) the *Infrared Interferometer Spectrometer* (IRIS), dedicated to atmospheric composition exploration

d) the *Ultraviolet Spectrometer* (UVS), used to investigate atmospheric properties

e) the *Triaxial Fluxgate Magnetometer* (MAG), which measured the magnetic fields, the solar wind coupling of the planetary magnetospheres

f) the *Plasma Spectrometer* (PLS), which measured plasma ions and electrons from 5eV to 6 keV

h) the *Low Energy Charged Particle instrument* (LECP), which investigated energetic particles, their differential energy fluxes and angular distributions

i) the *Cosmic Ray Sys*tem (CRS), which studied the interstellar cosmic rays in the interplanetary and trapped in the planetary energetic particle environment

g) the *Planetary Radio Astronomy Investigation* (PRA), which studied the radio emissions from giant planets

k) the *Photopolarimeter System* (PPS), observed the surfaces of giants and Saturn rings

l) the *Plasma Wave System* (PWS), which measured electron-density profiles and electromagnetic waves.

From the above payload, the UVS, the MAG, the LECP, the CRS and the PWS are still in operation after 35 years.

Voyager 1 encountered Titan from north to south, having an orbital angle at 8.7° in respect to Titan's orbital plane with a relative speed of 17.3 km/s (Coustenis, 1989). Both Voyagers flew by Titan close to its northern spring equinox at solar longitude Ls=9°. The Voyagers' encounters of Titan gave a wealth of data for the nature of the biggest Kronian satellite. Their observations confirmed the presence of Titan's optically thick scattering haze and determined an optical depth larger than 5 with a peak haze brightness at 240 km above its surface (Smith et al., 1981).

The haze, which covered the southern hemisphere, was significantly brighter compared to the northern one. The northern polar regions in particular showed darker haze colors, this was called the northern polar hood. This North-South asymmetry was explained by variations in density, particle size and composition due to different solar heating. Indeed, the northern hemisphere was 10 K colder than the southern one at the V1 era (Flasar et al., 1981).

The other feature that Voyager missions recorded was the detached haze layer which was discovered at 100 km above the peak of the main haze (Smith et al., 1981; 1982). A global distribution of the detached haze with a latitudinal variation southern of 45°N at altitudes 300-350 km was reported from Voyager 2 recordings (Rages & Pollack, 1983). Above 60°N, the detached haze merged with the main haze.

The Voyager 1 remote data determined the bulk composition and the vertical temperature profile of Titan's atmosphere. Both V1/RSS and V1/IRIS estimated the mean mass ratio to be within the range of 27.8 and 29.3 amu (Lindal et al., 1983; Lellouch et al., 1989). In combination with the V1/UVS observations (Broadfoot et al., 1981; Strobel & Shemansky, 1982) and solar occultation data (Smith et al., 1982) it was then determined that nitrogen is the dominant species in Titan's atmosphere, while methane is a minor constituent. Additionally, only upper limits were estimated for argon (Strobel et al., 1993). V1 data also detected hydrogen but failed to detect ammonia (Hanel et al., 1981). As far as the methane stratospheric abundance is concerned, Lellouch et al. (1989) gave a methane mixing ratio up to 3.4% assuming that it is not supersaturated in the stratosphere.

During the radio occultation experiment, the satellite occulted the spacecraft. The phase shift as well as the attenuation of the V1 radio signal derived two vertical profiles (Smith et al., 1982). The V1/RSS also indicated the Earth-like thermal structure of the atmosphere. It estimated the surface temperature at 94±0.7K at 1496 ±0.02 mbar and a radius of 2575±0.5 km. The tropopause was located at 42 km (71.4±0.5K, 130 mbar) while the stratopause at about 200 km (0.75 mbar) with a highest value at 170K. The exact altitude and the temperature of the stratopause were not determined. V1/UVS gave also constraints for the upper atmosphere (186±20K at 1265 km) (Smith et al., 1982) and the interval was calculated by interpolation techniques. However, recent reanalysis of Voyager data showed the location of homopause higher than 1000 km (Vervack et al., 2004), while Smith et al. (1982) showed it at 925 km.

V1/IRIS spectra confirmed the existence of a rich organic environment in Titan's atmosphere. Indeed, the emissions of acetylene (C_2H_2), ethane (C_2H_6), ethylene (C_2H_4),

propane (C_3H_8), methylacetylene (CH_3C_2H), diacetylene (C_4H_2), hydrogen cyanide (HCN), cyanoacetylene (HC_3N), cyanogen (C_2N_2) and carbon dioxide (CO_2) have been recorded by IRIS in the stratospheric layers (Kunde et al., 1981; Maguire et al., 1981; Samuelson et al., 1981; Samuelson, 1983; Coustenis et al., 1989a;1989b).

The V1 encounters probed Titan's atmosphere in several latitudes (70°N, 50°N, 30°N, 9°N, 8°N, 5°N, 7°S, 30°S and 53°S) and a latitudinal distribution of trace gases abundances was constructed (Fig. 1.3) while the longitudinal variation was not significant (Coustenis & Bezard, 1995). Except for CO_2 and ethane, all the trace constituents showed an enhancement in the high northern latitudes.

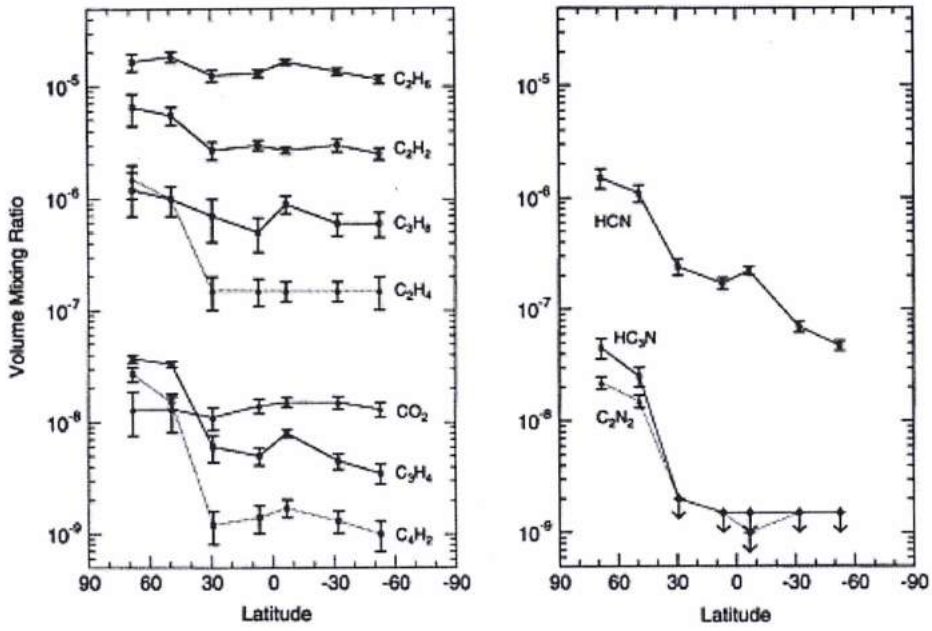

Fig. 1.3: The latitudinal distribution of trace gaseous mixing ratios. The panel (a) shows the hydrocarbons and CO_2, while the panel (b) shows the nitriles. The error bars depict the 3σ uncertainities for HC_3N and C_2N_2 at the probed latitudes below 50°N (Coustenis & Bezard, 1995).

Moreover, IRIS limb data indicate that the mixing ratios of most of the species increase with altitude above their condensation level (Coustenis et al., 1991). V2/IRIS observations, which probed Titan few months later, derived the same results (Letourneur & Coustenis, 1993). The D/H ratio in Titan's atmosphere was determined to be 3-12 times higher than the protosolar value (Kim & Caldwell, 1982; Coustenis et al., 1989b).

1.1.4 Ground-based and space-borne Titan observations

A full Titan revolution of the Sun takes about 30 years and therefore long-term observations are needed to have a complete picture of its temporal atmospheric evolution. Taking as the initial point of our temporal studies the V1 encounter in 1980, the mid-2009 stands as an important time spot in Titan's atmospheric science.

Unfortunately, due to the hazy nature of its atmosphere, distant direct observations of its lower atmosphere and of its surface are impeached. Methane bands strongly absorb the outgoing radiation and it is impossible to see through them except only through narrow methane spectral "windows" (regions of weak absorption) in the near infrared (NIR). These windows are centered at 0.83, 0.94, 1.07, 1.28, 1.58, 2.0, 2.9 and 5.0 μm and the observations are limited.

Several ground-based and space-borne observations have been performed in the time interval between the Voyager encounter of Titan (1980) and the arrival of the Cassini-Huygens mission (2004). The advent of adaptive optics and the space-borne telescopes (Hubble Space Telescope -HST, Infrared Space Observatory -ISO) made the surface and the lower atmosphere of Titan reachable from the Earth.

The adaptive optics technique returns a more accurate image of the object through the atmosphere by correcting the aberrations of the light sources. Aberrations mainly originated from atmospheric turbulence, thermal blooming and other non-atmospheric sources (Tyson, 2011). This technique allows resolving Titan's disk and obtaining some spatial resolution on the surface of Titan by using both spectroscopy and imaging. Distant observations of Titan can be performed by radio telescopes as well. Developments in signal processing by using heterodyne receivers amplify the echoes from Titan providing high resolution spectroscopy (Coustenis & Taylor, 2008).

Finally, information about Titan's atmosphere can be provided by stellar occultations of Saturn and Titan when they pass in front of a star. Six such events have been recorded so far: one on 3 July 1989, one on 21 August 1995, two on December 2001 and two on 14 November 2003 (see Coustenis et al. (2009b) and references therein).

Both Earth- and space-based observations have revealed the heterogeneous nature of the surface and showed that dark and bright regions, consisting of different ice, dominate it. Such observations came from the HST in 1994 (Smith et al., 1996) and 1997-1998 (Meier et al., 2000), the speckle interferometry from Keck Telescope within 1996-1998 (Gibbard et al., 1999; Gibbard et al., 2004) and adaptive optics from Canada–France–Hawaii Telescope

(CFHT) in 1998 (Coustenis et al., 2001), from Very Large Telescope in Chile (VLT) in 2002 (Gendron et al., 2004), from combination of CFHT and VLT data during 2001-2004 (Coustenis et al., 2005) and from W.M. Keck II telescope within 2001-2003 (Roe et al., 2004a).

As far as the composition of the surface is concerned, observations from the Infrared Telescope Facility (IRTF) on Mauna Kea, Hawaii, in 1989 showed that the surface consists of dirty ice bedrock (Griffith et al., 1991) full of organics and tholins[3], a laboratory analogue to Titan's surface material (Sagan, 1974; Sagan & Khare, 1979; Sagan et al., 1984). A mixture of water ice and tholins, which covered parts of the surface, was also discovered by albedo observations taken by the CFHT from 1991 to 1996 (Negrao et al., 2006). Additionally, observations from the VLT in 2000 also assumed also ammonia ice on Titan's surface (Lellouch et al., 2003).

More recent observations in 2005 assumed the presence of methane ice mixed with water and tholins ice by the use of the VLT measurements (Hirtzig et al., 2007; Negrao et al., 2007), while VLT measurements in 2004 also gave firm limits of carbon dioxide ice (Hartung et al., 2006). However, higher resolution observations needed to distinguish and identify surface features.

Ground-based RADAR observations also contributed significantly to the study of the surface of Titan. After the Voyager encounters, the existence of a global ocean was suggested to cover the surface (Flasar, 1983; Lunine et al., 1983). However, earth-based RADAR echoes recorded at Very Large Array in New Mexico indicated that Titan's surface possesses a very high RADAR cross section and latitudinal variation, which is inconsistent with the global ocean hypothesis (Muhleman et al., 1990). Lemmon et al. using data from Steward Observatory and the Multiple Mirror Telescope in 1992 also showed the spatial heterogeneity of Titan (Lemmon et al., 1993), while Cambell et al. noted RADAR observation areas of specular reflections, similar to small lake-like features from Arecibo echoes in 2001 and 2002 (Campbell et al., 2003).

Carbon monoxide was detected in Titan's atmosphere at 1.57 μm (Lutz et al., 1983), while its existence was established by several measurements at 5 μm, determining that CO is not uniformly mixed in the atmosphere (Coustenis et al., 2009b) (and references therein). Using IRAM-30 data taken between April 1996 and December 1999, acetonitrile (CH_3CN) was firstly detected (Bezard et al., 1993; Marten et al., 2002). These measurements provided

[3] Tholins are named after the greek word "θωλός" (=mud) by Carl Sagan.

compositional studies of the atmosphere and the first vertical profiles of nitriles, which increased with altitude in the stratosphere, outside the polar region. Moreover, these IRAM-30 recordings gave a strongly enhanced ratio of $^{15}N/^{14}N$ by a factor of 4 in HCN. The vertical stratospheric HCN profile in Titan was reported from earlier IRAM-30 observations on September 1986 and May 1987 (Tanguy et al., 1990) as well as in May 1995 (Hidayat et al., 1997).

By using heterodyne spectroscopy at the NASA Infrared Telescope Facility (IRTF) in August 1993, October 1995 and September 1996, the abundance of ethane was retrieved (Kostiuk et al., 1997; Livengood et al., 2002).

The higher resolution of echelle technique applied in IRTF (TEXES) compared to Voyager, allowed for the first time the separation of propane ν_{26} band at 748 cm^{-1} in December 2002, which was blended with the acetylene P-wing in the V1/IRIS spectra (Roe et al., 2003). Observations taken during the 1999-2002 with W.M. Keck I telescope showed seasonal variation of ethylene mixing ratio in the atmosphere at 8-13 μm (Roe et al., 2004b). Keck II/NIRSPEC observations in November 2001 provided abundances for HCN, C_2H_2, CH_4 and CH_3D at 3 μm (Geballe et al., 2003; Kim et al., 2005). Ground based measurements were available during the Huygens descent in January 2005 being obtained at National Astronomical Observatory (NAO) providing ethane abundances (Livengood et al., 2006).

IRTF/IRHS data mentioned above, were used for detecting winds in Titan's atmosphere by studying ethane in two limb positions along with December 2003 measurements at NAO and January 2005 recordings at NAO/HIPWAC, noting an equatorial wind (Kostiuk et al., 2005; Kostiuk et al., 2006; 2010). Similarly, European Southern Observatory Very Large Telescope with UVES measured global circulation wind velocities at various altitudes at the time of the Huygens landing in January 2005 (Luz et al., 2005).

ISO focused on Titan for 20 h in 1997. By viewing Titan only as a small disk, it performed disk-averaged recordings. Having much higher resolution than the V1/IRIS, it reported the same organic inventory as IRIS did (Coustenis et al., 2003; Coustenis & Taylor, 2008). Additionally, ISO detected water vapor for the first time in the atmosphere (Coustenis et al., 1998). It also detected benzene for the first time at 674 cm^{-1} (Coustenis et al., 2003), whose presence on Titan was later confirmed in Cassini/CIRS observations.

The stellar occultation of Saturn and Titan by the star 28 Sagitarii allowed retrieving information about Titan's stratosphere within a range of 250 to 500 km. During this event, two haze layers were detected, having a reverse asymmetry comparing to the Voyager 1 observations (Sicardy et al., 1990).

1.2 The Cassini-Huygens Mission

1.2.1 Mission development

The need for a space mission focused on the Saturnian system, its rings, its satellites and its magnetosphere, led scientists to propose the Cassini-Huygens mission, an ambitious program of scientific *in situ* observations. Without doubt, the Cassini-Huygens mission is one of the largest, heaviest and most complex interplanetary spacecraft ever built in a cooperative effort between National Aeronautics and Space Administration (NASA), European Space Agency (ESA) and the Agenzia Spaziale Italiana (ASI). The formal beginning of the Cassini mission was with the mission proposal in 1982 to ESA and in 1983 to NASA. After its approval by both space agencies, the mission was developed between 1987 and 1996 (Matson et al., 2002). It launched in 1997 and arrived in the Saturnian system in July 2004.

The mission concept consists of two spacecraft: the Cassini orbiter and the Huygens probe, named after Giovanni Domenico Cassini (1625-1712) and Christiaan Huygens (1629-1695) respectively, honoring them for their contribution in the early stages of astronomical observation of the Saturnian system.

1.2.2 The Cassini orbiter

The Cassini orbiter is 6.8 m high and 4 m at its widest in diameter. It functions as an artificial satellite of Saturn and was the carrier of the Huygens probe which was successfully delivered to Titan. It also operated as the link between the Huygens capsule and the Earth during the Huygens mission phase in 2005.

The orbiter's scientific objectives are to deeply investigate Saturn's atmosphere, its rings, its icy satellites, the radiation belts and its magnetosphere. Because of Saturn's distance from the Sun, at circa 10 AU, Cassini cannot rely on solar panels as power sources and is equipped with three Radioisotope Thermoelectric Generators (RTG), using the heat from the natural decay of plutonium to generate direct current electricity powers.

Cassini is a state of the art spacecraft hosting on-board science instrumentation capable of performing both remote and *in situ* observations (Fig. 1.4). The orbiter's science instruments are separated in two different platforms: the Remote Sensing Pallet and the Fields and Particles Pallet.

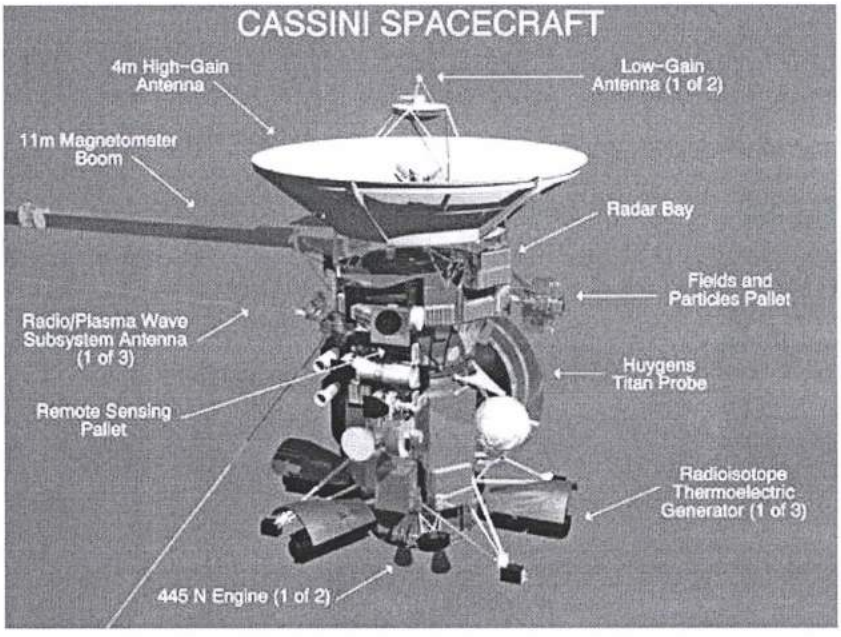

Figure 1.4: The Cassini spacecraft. The main parts of the instrumentation is shown as well as the Huygens probe and its energy sources (Henry, 2002).

Orbiter *in situ* investigations

The Fields and Particles pallet (Fig. 1.5) supports the *Cassini Plasma Spectrometer* (CAPS), the *Ion and Neutral Mass Spectrometer* (INMS) and the *Magnetosphere Imaging Instrument* (MIMI) sensors *Charge-Energy-Mass-Spectrometer* (CHEMS) and the *Low Energy Measurements System* (LEMMS). The Dual Technique Magnetometer (MAG) is placed on the orbiter's boom 11 m antenna. The *Radio and Plasma Wave Spectrometer* (RPWS) and the Cosmic Dust Analyzer (CDA) are located in the main body of the orbiter as well as MIMI's Ion and Neutral Camera (INCA).

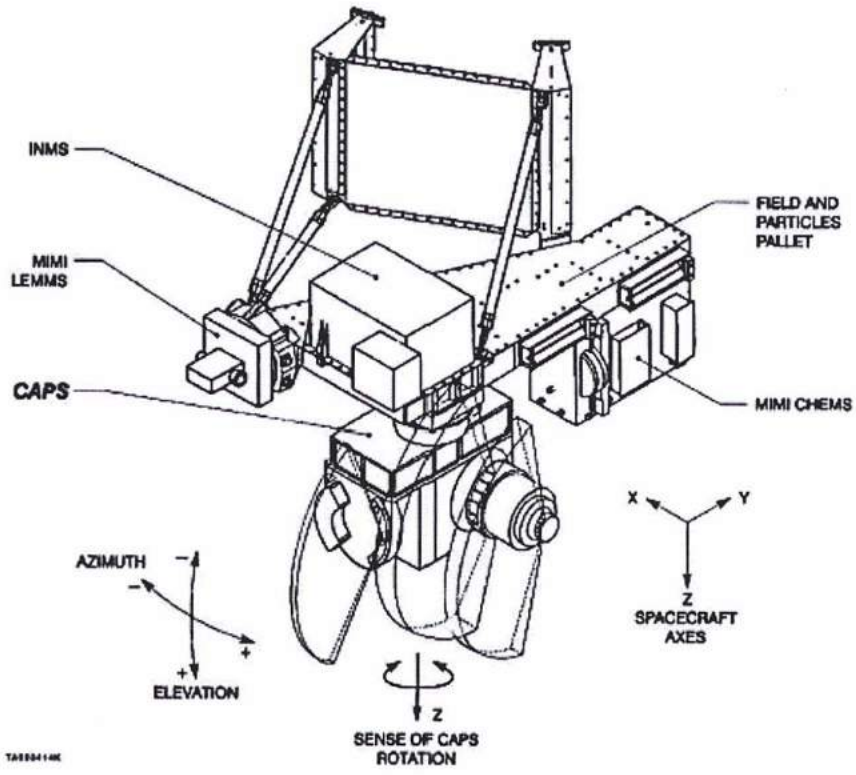

Figure 1.5: Cassini's Fields and Particles pallet where the instruments for *in situ* investigations are located (Young et al., 2004).

1. The Cassini Plasma Spectrometer (CAPS) explores the nature of the Saturnian plasma within and near Saturn's magnetic field. CAPS help us understand the complexity of the Saturnian magnetosphere and its interaction with its satellites, the rings and the solar wind. It is consisted of Electron Spectrometer (ELS), the Ion Beam Spectrometer (IBS) and the Ion Mass Spectrometer (IMS). The ELS measures electron velocity distribution ranging from 0.6 eV to 28,250 eV, while the IBS records distributions of ion velocities within the range of .1 eV to 49,800 eV. IMS measures the composition of the hot, diffuse plasma from the Saturnian magnetosphere and low concentration ion species from 1 eV to 50,280 eV (Young et al., 2004).

2. The Ion and Neutral Mass Spectrometer (INMS) detects the neutral and charged particles located near Titan, Saturn and the other moons to learn more about their extended atmospheres and ionospheres. Thus, the INMS focuses on the upper part of Titan's atmosphere, between the altitudes of 900 and 1000 km, where the complex photochemistry of nitrogen and methane begin to build more complex organic

molecules, which descend towards its surface. Moreover, INMS also studies the interaction of Titan's atmosphere with Saturn's magnetospheric plasma. It consists of two ion sources, one closed and one open. The former operates with the non-reactive neutrals, the nitrogen and methane, while the latter functions for reactive neutrals like the atomic nitrogen and for positive ions with energies less than 100 eV. The instrument is able to detect heavier hydrocarbon molecules such as benzene and determine their molecular mass (Waite et al., 2004).

3. The Magnetosphere Imaging Instrument (MIMI) images Saturn's magnetosphere, studies its dynamics and measures the interactions between the magnetosphere and the solar wind and the magnetosphere with Saturn's atmosphere, Titan and the other icy moons. It performs both *in situ* and remote measurements. It senses remotely the magnetospheric ion plasma with energies greater than 7 keV through the detection of energetic neutrals produced through charge-exchange interactions of energetic ions with cold neutrals. It also measures in 3-dimensions the ion composition and charge states for ion energies between 3 keV/e and 220 keV/e. MIMI consists of 3 sensors the Ion and Neutral Camera (INCA), the Charge-Energy-Mass-Spectrometer (CHEMS) and the Low Energy Measuremens System (LEMMS) which detects energetic electrons (>15 keV) and energetic ions with cold neutrals. During each Titan flyby, INCA studies the interaction of Titan's exosphere with the Saturnian magnetosphere every 90 s (Krimigis et al., 2004).

4. The Dual Technique Magnetometer (MAG) studies Saturn's internal magnetic field and its interactions with the solar wind, the rings and the moons of Saturn. MAG also maps the magnetic state of Titan and its atmosphere as well as Saturn's ring and dust interactions with the electromagnetic environment. MAG investigates the structure of the magnetotail and the dynamic processes therein. It consists of a fluxgate magnetometer and a vector/scalar helium magnetometer mounted both on the spacecraft's boom (see Fig. 1.4). Hence, MAG senses small changes in fields spanning four orders of magnitude with high sensitivity, recording the strength and direction of the magnetic fields (Dougherty et al., 2004).

5. The Radio and Plasma Wave Spectrometer (RPWS) studies radio emissions plasma waves, thermal plasma and dust. It consists of three orthogonal electric field antennas

which focus on the detection of electric fields ranging from 1 Hz to 16 MHz, and three orthogonal search coil magnetic antennas to detect magnetic fields in the range within 1 Hz to 12 MHz. A Langmuir probe is used for measuring the electron density and temperature. The electric antennas, the search coils and the Langmuir probe are mounted on the orbiter's main body. RPWS measures the electron density and temperature in Titan's ionosphere and study the escape thermal plasma from Titan's wake region (Gurnett et al., 2004).

6. The Cosmic Dust Analyzer (CDA) measures the ice and dust grains in and near the Saturn system with masses ranging from 10^{-19} and 10^{-9} kg. CDA studies the physical properties of the ice and dust grains and their chemical composition, as well as their interaction with the magnetosphere of Saturn, its rings and satellites (Srama et al., 2004).

Orbiter remote investigations:

Four instruments are mounted on the Cassini's Optical Remote Sensing Palette (RSP) (Fig. 1.6): the Composite Infrared Spectrometer (CIRS), the Imaging Science Subsystem (ISS), the Ultraviolet Imaging Spectrograph (UVIS) and the Visual and Infrared Mapping Spectrometer (VIMS).

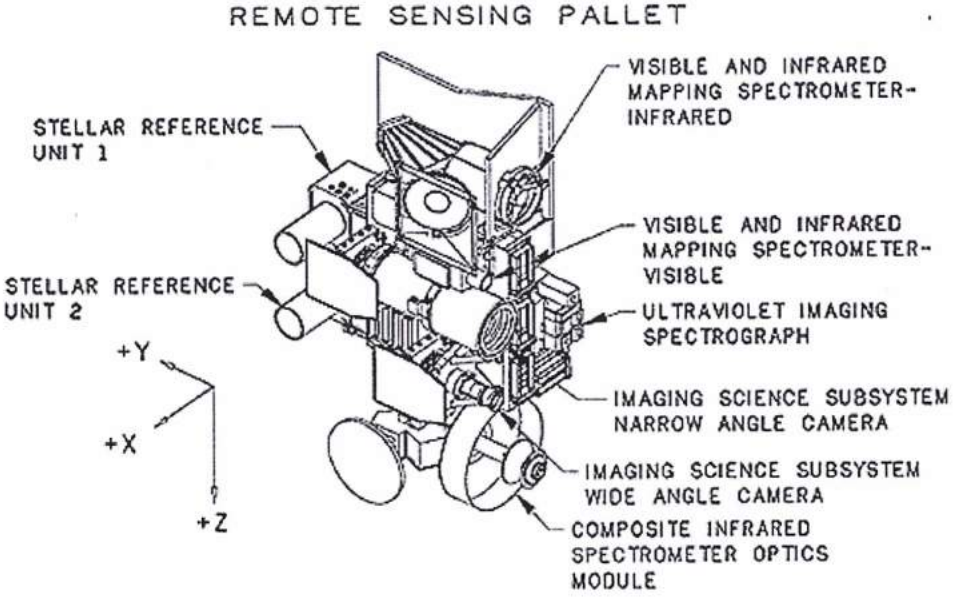

Figure 1.6: The Remote Sensing Palette on board Cassini (credits: NASA).

1. The Radio Science Subsystem (RSS) searches for gravitational waves in the Universe, studies the atmosphere, rings and gravity fields of Saturn and its moons by measuring telltale changes in radio waves sent from the spacecraft. It consists of a Ka-band traveling wave tube amplifier, a translator, an exciter, a S-band transmitter and various microwave components. It determines the temperature and composition profiles within Saturn's and Titan's atmospheres as well as the temperatures and electron densities within Saturn's and Titan's ionospheres (Kliore et al., 2004).

2. The Cassini RADAR (RADAR) mapper probes the surface of Titan using RADAR imaging and measures its topography as well. The RADAR is a multimode Ku-band instrument (13.8 GHz, λ2.17 cm) having four operational modes: Synthetic Aperture RADAR (SAR) imaging, altimetry, scatterometry and radiometry. The RADAR also observes other targets in the Saturnian system such as its icy moons and the giant planet (Elachi et al., 2004).

3. The *Visible and Infrared Mapping Spectrometer* (VIMS) searches for the chemical compositions of the surfaces, atmospheres and rings of Saturn and its moons by measuring colors of visible light and infrared energy emitted or reflected within the wavelength range 0.3 and 5.1 microns. Especially, VIMS probes the surface properties of Titan and maps them in a global scale. VIMS measurements are crucial for understanding Titan's geology and identifying any volcanic activity. It is consistent of two imagers, one in the visual part, the VIMS-VIS, and the other in infrared part of the spectrum, the VIMS-IR (Brown et al., 2004).

4. The *Composite Infrared Spectrometer* (CIRS) (Flasar et al., 2004) measures infrared radiation emitted from the surfaces, atmospheres and rings of Saturn and its moons to study their temperature and compositions. A detailed description of the instrument and its operational modes can be found in the following Chapter 2.

5. The Ultraviolet Imaging Spectrograph (UVIS) measures ultraviolet emission from atmospheres and rings to study their structure, chemistry and composition. UVIS determines the constituents' abundances in Titan's atmosphere, the aerosols in order to infer about the atmospheric circulation patterns. It also studies the UV emission from the upper atmosphere of Titan and its relation to the Saturnian magnetosphere as well.

It hosts two moderate resolution telescope-spectrographs, providing images ranging from 56 to 118 nm (EUV) and from 110 to 190 nm (FUV) respectively (Esposito et al., 2004).

6. The Imaging Science Subsystem (ISS), a high-resolution two-dimensional optical device, takes pictures in visible, near-ultraviolet and near-infrared light of the objects within the Saturnian system. It consists of two cameras, a narrow angle reflecting telescope and a wide-angle refractor. Both cameras operate at a spectral range from 1100 to 200 nm. ISS is also the optical navigation guide of the Cassini spacecraft (Porco et al., 2004).

1.2.3 The Huygens probe

The Huygens probe is the first man-made vehicle, which has performed a successful landing in such a distant place from the Earth. After a couple initial orbits of Saturn, the orbiter has released the probe on a trajectory directed towards Titan. The Huygens mission can be divided into 3 phases: the Entry, the Descent and the Landing phase. It landed in Titan's equatorial region called Adiri at 10.3° S, 192.3°W. During its descent phase as well as after touchdown, the capsule revealed a solid surface under the thick haze. The Huygens descent lasted for 2 h 27 mins 50 s (Lebreton et al., 2009).

The orbiter then passed below the probe's horizon, breaking the established link between Huygens and the Earth (Lebreton et al., 2005). However, the Very Long Baseline Interferometry (VLBI) network, consisting of 17 large radio telescopes, recovered the Huygens signal (Witasse et al., 2006) and thus Huygens continued to send back to Earth more measurements. Eventually, before Huygens' five batteries ran out of energy, it had already submitted data of 2.5 h during its descent and 3 h and 14 min after its touchdown on the ground (Lebreton et al., 2009).

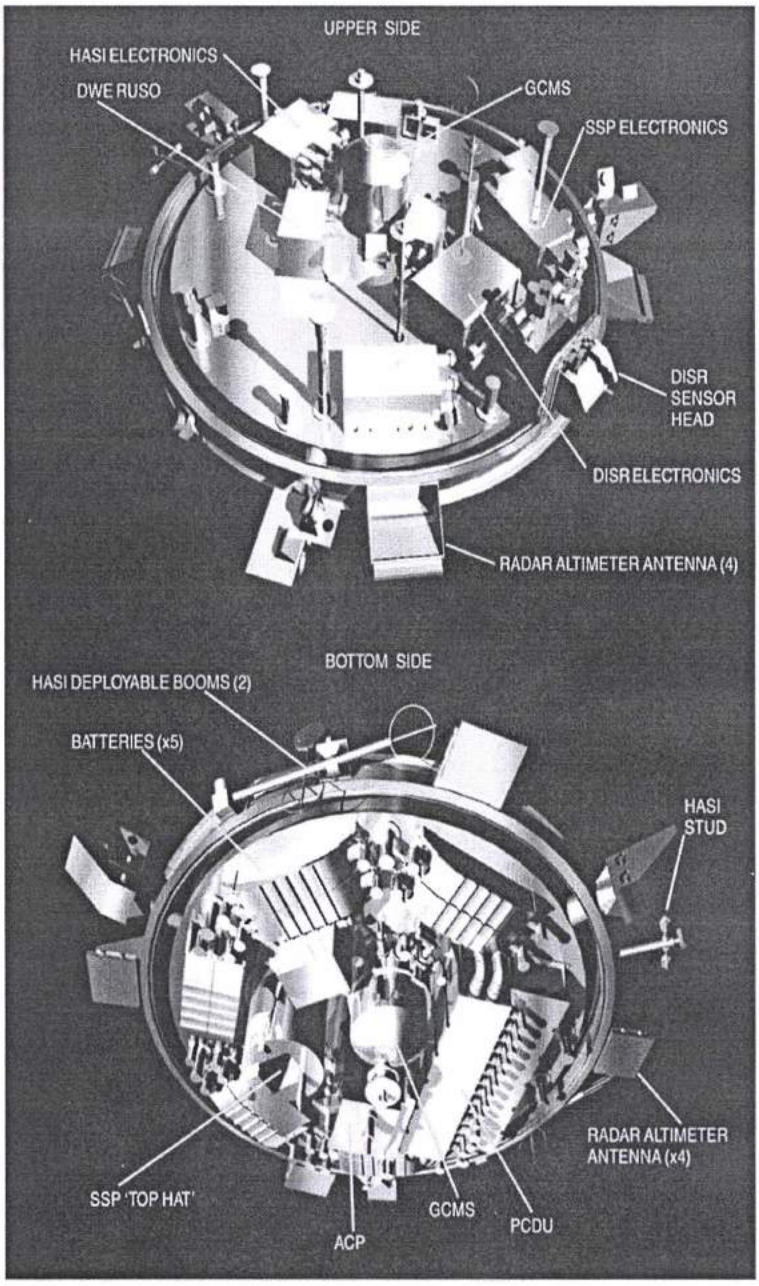

Figure 1.7: Huygens probe instrumentation, the upper and the bottom side of the vehicle (http://nssdc.gsfc.nasa.gov/image/spacecraft/huygens_cutaway.jpg).

The Huygens payload consists of six scientific instruments placed as shown in Fig. 1.7. This instrumentation has performed direct atmospheric and surface measurements of the environment of Titan during the descent and after the touchdown. The data collected is not only valuable for Titan's science, but also for reference for future missions. The six Huygens instruments are briefly described below.

1. The *Gas Chromatograph and Mass Spectrometer* (GCMS) measured the composition of the atmosphere of Titan, isotopic ratios and trace species, from the parachute release time to the surface. It consisted of ion sources, mass analyzer and ion detectors. The GCMS sampling system also analyzed samples sampled by the Aerosol Collector and Pyrolyzer (ACP) in an ACP-devoted feed tube. It has three parallel gas chromatograph columns, a quadrupole mass filter and five electron impact sources (Niemann et al., 2002). The mass spectrometer operated in the range of 2 to 141 Dalton. It began its operation after the protection shield release at the altitude of 160 km during the descent phase (Niemann et al., 2005).

2. *The Aerosol Collector and Pyrolyzer* (ACP) has sampled aerosols during the descent in two stages: (a) from the top of the atmosphere to 40 km and from 23 km to 17 km altitude. Except for the sampling system it hosts an oven where pyrolysis was performed and a transfer system of the samples. Then, it prepared the material for further analysis and it sent the samples to the GCMS for deriving their chemical composition (Israel et al., 2002; 2005).

3. The *Descent Imager/Spectral Radiometer* (DISR) is the optical remote sensing instrument in the range of 0.3 to 1.7 microns (Tomasko et al., 2002). The DISR acquired spectra and high-resolution images of Titan's atmosphere while also measuring the solar radiation in the atmosphere. Except for the imagers, a visible spectrometer, an IR spectrometer, a solar aureole camera, violet photometers, and a sun sensor are parts of the instrument. DISR also had a 20 W lamp (surface science lamp), which switched on during the last stages of the probe's descent (at 700 m altitude) in order to enlighten the surface beneath it. It also revealed traces of hydrocarbon liquids on its surface through complex drainage systems and sent back to the Earth the first images of Titan's surface (Tomasko et al., 2005).

4. The *Huygens Atmosphere Structure Instrument* (HASI) consists of a 3-axis accelerometer, a set of a coarse and a fine temperature sensors, a multi-pressure sensor, a microphone and an electric field sensor array (Fulchignoni et al., 2002). HASI studied the atmospheric structure of Titan, gave a detailed temperature vertical profile and recorded the surface pressure and temperature ($1{,}467 \pm 1$ mbar and 93.65 ± 0.25 K, respectively). HASI temperature and pressure sensors probed the

atmosphere directly for the first time from an altitude of 1400 km in altitude down to the surface. Indeed, the P, T sensors were deployed after the shield release and sampled the local atmosphere. These parameters help to calibrate measurements from other instruments both on the probe and from the orbiter. The derived HASI temperature vertical profile is used for instance as a reference when adopting inverse methods to retrieve the temperature and abundance from CIRS data. Huygens studied the winds and the turbulence of the atmosphere, as well as its conductivity and searched for lightning (Fulchignoni et al., 2005).

5. The *Doppler Wind Experiment* (DWE) used one of the two redundant chains (Transmitter A) of the probe-orbiter radio link and it is mainly based on both probe and orbiter (Bird et al., 2002). The DWE data was transmitted to Cassini through Channel A, which due to a command error, was lost. Fortunately, the Earth-based large radio telescope network recorded the signal directly (Bird et al., 2005). DWE determined the direction and the magnitude of Titan's zonal winds and confirmed the super-rotation of Titan's atmosphere (Bird et al., 2005; Lebreton et al., 2009).

6. The *Surface Science Package* (SSP) is a nine sensors suite which determined the properties of the lower atmosphere, the surface at the landing site and the subsurface. The sensors are accelerometers, internal and external, penetrometers, sonar-velocimeter and density, permittivity, refractive, thermal properties index sensors as well as a tiltmeter (Zarnecki et al., 2002). They showed a smooth surface but not flat, resembling wet clay, packed snow or sand (Zarnecki et al., 2005).

1.2.4 Mission Overview

The Cassini-Huygens mission, launched in October 1997 from Cape Canaveral, used the gravity fields of the Earth, Venus, the Sun and Jupiter, to finally enter the Saturnian System seven years later on July 1, 2004. Cassini carried the Huygens probe released in December 25, 2004 from the mother spacecraft towards Titan. After a successful enter, descent and landing (EDL) procedure, the probe touched down on the surface of Titan in January 14, 2005. The major phases of this seven-year space journey are depicted in Fig. 1.8.

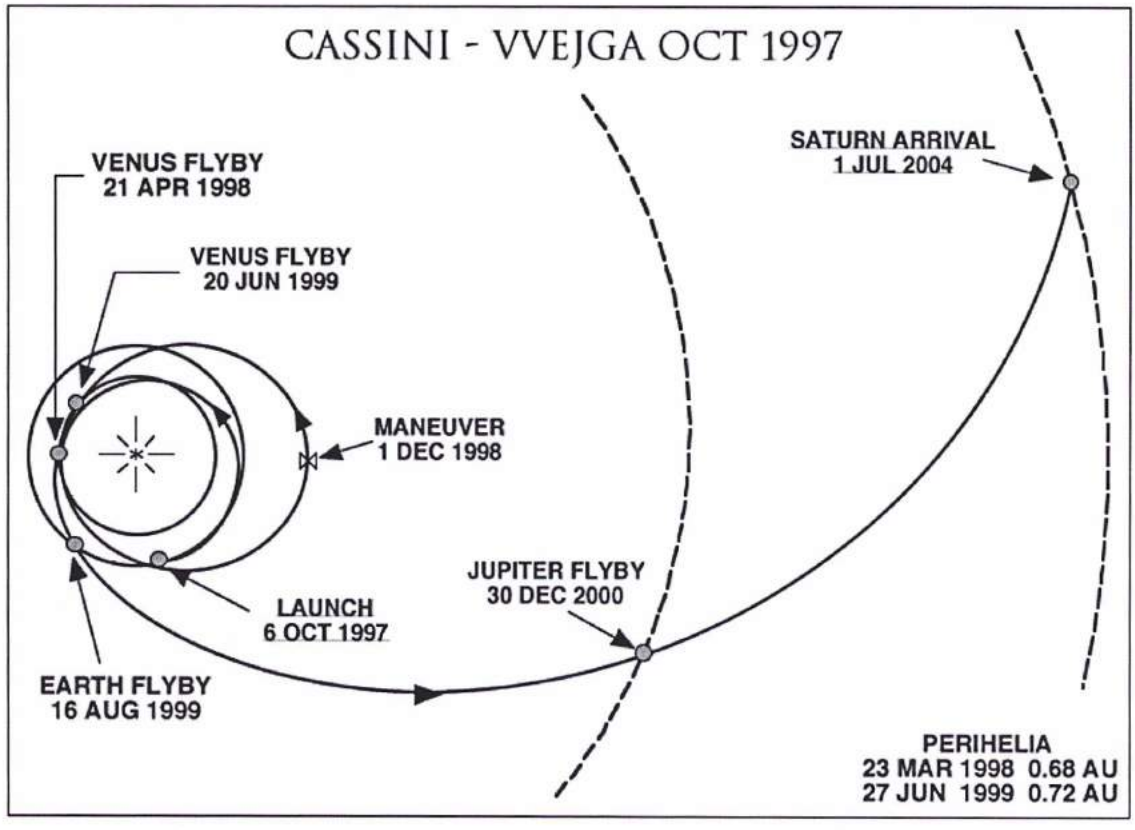

Figure 1.8: The space journey of the Cassini-Huygens mission. The spacecraft took advantage of the gravitational fields of the Earth, Venus, Sun and Jupiter in order to reach the Saturnian system. (NASA)

Since its arrival at Saturn, and after the Saturn Orbit Insertion (SOI), Cassini performs continuous revolutions around the giant planet and frequently encounters its moons (flybys). Table 1.1 below lists the phases of the Cassini/Huygens mission from its nominal stage to the second extension (Nixon et al., 2010).

Table 1. 1 - The Cassini/Huygens mission phases (Nixon et al., 2010).

Mission Phase	Start Time	End Time	Saturn Orbits	Titan Flybys	Comments
Prime Mission (PM)	1 July 2004	30 June 2008	75	45	
Equinox Mission (XM or EM)	1 July 2008	30 September 2010	63	26	Saturnian northern spring equinox in August 2009
Solstice Mission (XXM or SM)	1 October 2010	16 September 2017	155	56	Saturnian northern summer solstice in May 2017
Total			293	127	

1.3 The major achievements of the Cassini-Huygens mission about Titan

The Cassini-Huygens mission is a landmark in Planetary Exploration. Technologically, the Cassini orbiter has executed more than one hundred close flyby manoeuvers of planetary bodies, while orbiting Saturn, more than the flybys, which have ever been performed in the entire planetary program. The successful entry, descent and landing (EDL) of the Huygens probe on the surface of Titan stands for another technologically remarkable point.

Scientifically, the Cassini-Huygens mission has significantly advanced our knowledge about Saturn, its moons, its rings and its magnetosphere. Titan, one of the prime targets of the mission, has been thoroughly studied remotely by the advanced Cassini orbiter's instrumentation, during numerous flybys, and *in situ* by the Huygens probe.

The Cassini magnetometer measurements (Backes et al., 2005; Neubauer et al., 2006) confirmed Voyager 1 observations (Ness et al., 1982) that Titan has no detectable large-scale global magnetic field and showed that Titan is strongly influenced by the Saturnian dynamic magnetodisk (Arridge et al., 2008; Bertucci et al., 2008; Dandouras et al., 2009; Simon et al., 2010). Indeed, Titan orbits at an average of 20.2 R_S (1 R_S = Saturnian radius = 60,330 km), while the Saturnian magnetopause standoff distance follows a bimodal distribution with means at 21 R_S and 27 R_S, mainly controlled by the solar wind (Achilleos et al., 2008). This means that Titan is mostly located inside the Saturnian magnetosphere, close to the Saturnian magnetopause. Only during the T32 and T42 Cassini flybys, Titan was spotted in the shocked solar wind, inside the Kronian magnetosheath (Bertucci et al., 2008; Garnier et al., 2009; Rymer et al., 2009; Wei et al., 2011). The Charge-Energy-Mass-Spectrometer (CHEMS/MIMI) measurements showed that although Titan can be considered as a source of the Saturnian magnetospheric plasma, the relative low concentration of N^+ and N_2^+ in the outer magnetosphere suggests low nitrogen escape ratio of Titan (Krimigis et al., 2005),

contrary to previous believes (Eviatar & Podolak, 1983; Richardson, 1998).

Titan's atmosphere interacts directly with the corotating Saturnian magnetoplasma, generating a flow-induced magnetosphere. This interaction consists of coupling between charged particles escaping Titan and the external plasma. Therefore, the plasma variations with respect to the local time together with the changing solar wind conditions affect significantly the local plasma environment (Wolf & Neubauer, 1982). Indeed, Cassini data showed horizontal variations, observed in the upper atmosphere, originating from the magnetic plasma variability, when Titan passes through different magnetospheric regions (Bell et al., 2011; Westlake et al., 2011).

Cassini findings have put constraints on our understanding of Titan's atmospheric escape mechanisms and upgraded our knowledge of its exosphere and its interaction with the Saturnian magnetosphere (Garnier et al., 2007; Dandouras et al., 2009). The exosphere is the outermost region of a planetary atmosphere, where collisions between atmospheric particles cease to be important and the particles can escape and drift into the space (Chamberlain, 1963).

Since Titan lacks a protective intrinsic magnetic field, energetic particles originating from the Saturnian magnetosphere directly bombard its upper neutral atmosphere, undergoing charge-exchange collisions with cold neutral atoms and producing energetic neutral atoms (ENAs). The Ion and Neutral Camera (INCA) of the Cassini Magnetosphere Imaging Instrument (MIMI) measured the ENAs flux and modeled Titan's exosphere following the Chamberlain formalism in combination with Ion and Neutral Mass Spectrometer (INMS) measurements (Garnier et al., 2007), confirming pre-Cassini predictions (Dandouras & Amsif, 1999). The exospheric molecules included in this thermal model are CH_4, N_2, N, H_2 and H, while the exobase, the lower boundary above the thermosphere, is located at 1425 km with a temperature of 149K (Waite et al., 2005; De La Haye et al., 2007). However, Titan's upper atmosphere is not in thermal equilibrium and INMS data led to the model of a non-thermal exosphere, using kappa distribution functions to fit the species distributions (De La Haye et al., 2007). ENA images variability is either related to the magnetospheric variability or to their distance from Titan. Strong asymmetries have been observed to the stable ENA halo around Titan mainly caused by the finite gyroradii effects of the parent ions (Garnier et al., 2010). INCA also detected Titan's exosphere outer extent at an altitude of 50,000 km (Brandt et al., 2012) close to the Hill sphere radius, the limit of the gravitational influence.

Between the altitudes of 1500 km, close to the exobase, and 1000 km, ENAs can suffer multiple collisions, but they can still be detected. Below 1000 km, ENAs can be

considered as absorbed (Dandouras et al., 2009). At the same altitude, the keV to tens of keV O^+ ions and energetic H^+ ions (E > 50 keV) from the Saturnian magnetosphere can penetrate across field lines and deposit their energy into Titan's atmosphere (Cravens et al., 2008) resulting in heating and escape of suprathermal nitrogen and methane atoms and molecules from Titan's upper atmosphere (Michael & Johnson, 2005).

The Cassini/INMS detected very heavy negatively charged particles (most likely aerosols) above the homopause level (800-850 km) (Coates et al., 2007; Waite et al., 2007). Hence, the process of aerosol formation appears to start at more than 1000 km above the surface through complex ion and neutral chemical reactions in the atmosphere. These reactions are initiated by energetic photons and particles from the Saturnian magnetosphere. Extrapolation of Cassini INMS (with a mass limit up to 100 daltons) and Plasma Spectrometer (CAPS) data, suggests that up to several thousands daltons, high-molecular-weight species may exist in the ionosphere, including polymers of high molecular weight — up to and certainly beyond — C_7 hydrocarbons. These results show that ionospheric chemistry plays an important role in the formation of complex hydrocarbons in Titan's environment (Waite et al., 2007). Fig. 1.9 illustrates the pattern of tholin formation in the upper atmosphere as resulted from INMS (Waite et al., 2006).

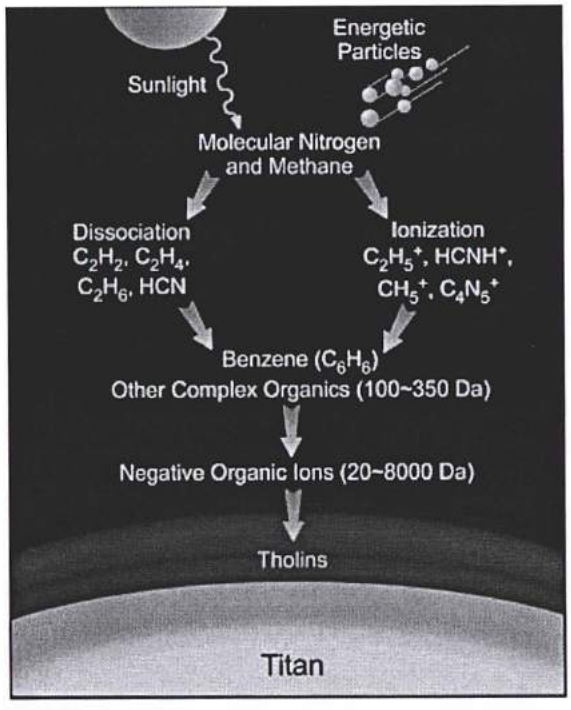

Figure 1.9: Tholin production in Titan's upper atmosphere according INMS findings (adapted from Waite et al. 2006).

The INMS data analysis showed that Titan possesses the most compositionally complex ionosphere in the Solar System. Modeling of INMS data (Vuitton et al., 2007) detected polyynes (C_4H_2, C_6H_2, C_8H_2) and cyanopolyynes (HC_3N, HC_5N) with densities higher than photochemical models' predictions (Yung et al., 1984; Toublanc et al., 1995; Wilson & Atreya, 2004). Moreover, the model also probably detected methylcyanopolyynes (CH_3C_3N, CH_3C_5N) and methylpolyynes (CH_3C_4H, CH_3C_6H) for the first time on Titan. Finally, the model indicates the existence of ammonia (NH_3), methanimine (CH_2NH), other nitriles (C_2H_3CN, C_2H_5CN) and two unidentified N containing species (C_5H_5N, C_6H_7N). INMS also detected the neutral mode of benzene (C_6H_6) in the ionosphere (Waite et al., 2007; Vuitton et al., 2008). These hydrocarbons and nitrile species form a complex layering of organic aerosols (tholins) that diffuse through the atmosphere and accumulate on the surface (Coustenis et al., 2007; Tomasko et al., 2008b) (Fig 1.9).

Titan atmospheric region from 500 to 950 km was observed by the Cassini Ultraviolet Imaging Spectrometer (UVIS), which monitored the occultation of two stars by Titan during the second Titan flyby (Shemansky et al., 2005). A mesopause was inferred at 615 km with a temperature minimum of 114 K. Methane, acetylene, ethylene, ethane, diacetylene, and hydrogen cyanide were identified at altitude ranges from 450 to 1600 km. The higher order hydrocarbons and hydrogen cyanide peak sharply in abundance and are undetectable below altitudes ranging from 600 to 750 km, leaving methane as the only identifiable carbonaceous molecule below 600 km in this experiment. Cassini instrumentation cannot probe at this altitude and this region is called agnostosphere (Coustenis et al., 2010c) or ignorosphere (Strobel et al., 2009).

The Cassini Composite Infrared Spectrometer (CIRS) instrument provides a complete pole-to-pole global coverage of Titan's stratosphere since the beginning of the mission. It can operate in nadir and limb viewing modes and provide the most spatially resolved maps of constituent species to date. Nadir sequences provide global mapping of atmospheric temperature and composition, while the limb ones provide information on the vertical profiles. CIRS has detected organics, probing the atmosphere within the range of 150 and 450 km (Flasar et al., 2005; Coustenis et al., 2007; 2010a; Vinatier et al., 2007a; 2010b; Teanby et al., 2008; 2009a) and confirmed the results of V1/IRIS and ISO. CIRS has also confirmed the benzene detection at 674 cm^{-1} (Coustenis et al. 2007) by ISO observations (Coustenis et al. 2003). The retrieved mixing ratios show no longitudinal variation. Temperatures are mostly zonally symmetric with almost no variation with the longitude as well (Achterberg et al., 2008).

In general, all the nitriles and several hydrocarbons such as C_3H_4, C_4H_2, C_6H_6 and C_2H_6 show enhanced concentrations at northern latitudes in spring, implying the existence of a global-scale Handley cell. The trace gases abundance at 55°S has decreased during the mission, which is consistent with upwelling in the South (Teanby et al., 2009b). Cassini/CIRS also indicate that very strong zonal winds occur in the stratosphere of Titan in winter northern latitudes, while in the summer the stratospheric winds are weaker (Achterberg et al., 2008), supporting the presence of a North Polar vortex (Flasar et al. 2005). When the Cassini mission has entered to its solstice phase (Table 1.1) Titan fulfilled a complete revolution of the Sun from the V1 encounter (in mid-2010) and seasonal studies can be conducted (Teanby et al., 2010).

The organics from Titan's atmosphere form the haze particles located at 80-100 km and finally, they accumulate on the surface. Cassini ISS images and RADAR echoes have recorded several earth-like features on Titan's surface such as mountains (Radebaugh et al., 2007; Lopes et al., 2010), ridges (Soderblom et al., 2007b), faults (Radebaugh et al., 2011), rectangular drainage patterns and cryovolcanic structures, which are controlled most likely, at least partially, by tectonic activity (Burr et al., 2009). Additionally, stable liquid lakes were spotted by both ISS and RADAR, located mainly at the polar regions (Fig. 1.10) (Mitri et al., 2007; Stofan et al., 2007; Hayes et al., 2008) and recently at the equatorial latitudes (Griffith et al., 2012).

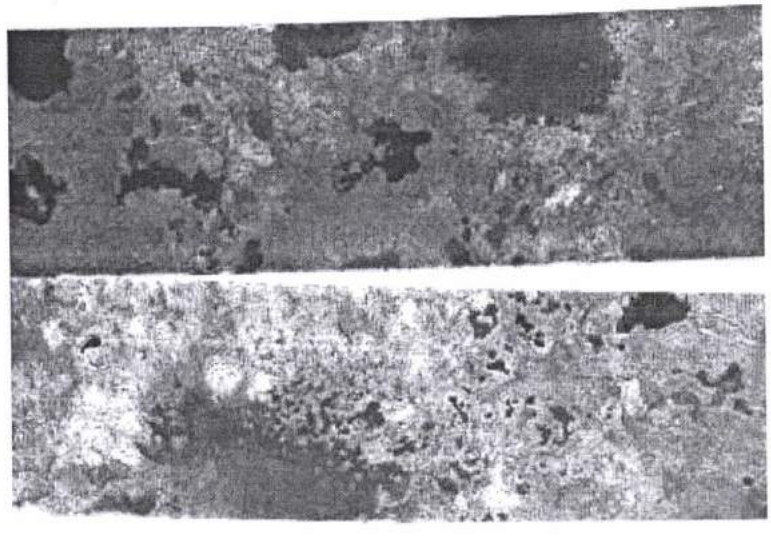

Figure 1.10: Titan lakes as discoverer by the Cassini RADAR located in the North polar region taken during the T16 flyby of Titan on 22 July 2006. The smallest is at about 1 km wide, while the biggest are more than 30 km wide (credit: NASA).

Seasonal changes have been recorded during the Cassini flybys when the shorelines of the southern large lake Ontario retreated during the Cassini mission time period (Turtle et al., 2011). Titan's organic inventory has been estimated to exceed the terrestrial one by a factor of magnitude (Lorenz et al., 2008b).

Remote sensing data from Cassini indicate that Titan's interior is partially differentiated. Indeed, the variations of its degree 2 coefficient gravitational potential provided by the Cassini Radio Science Subsystem (RSS) support internal density variations (Rappaport et al., 2008). Additionally, the Cassini Synthetic Aperture RADAR data suggest non-synchronous spin rate (Lorenz et al., 2008c), and the Permittivity, Waves and Altimetry (PWA) sensor on the Huygens Atmosphere Structure Instrument (HASI) with the Cassini Radio and Plasma Wave Science (RPWS) recorded Schumann resonance (Beghin et al., 2009b), giving evidence for internal ocean.

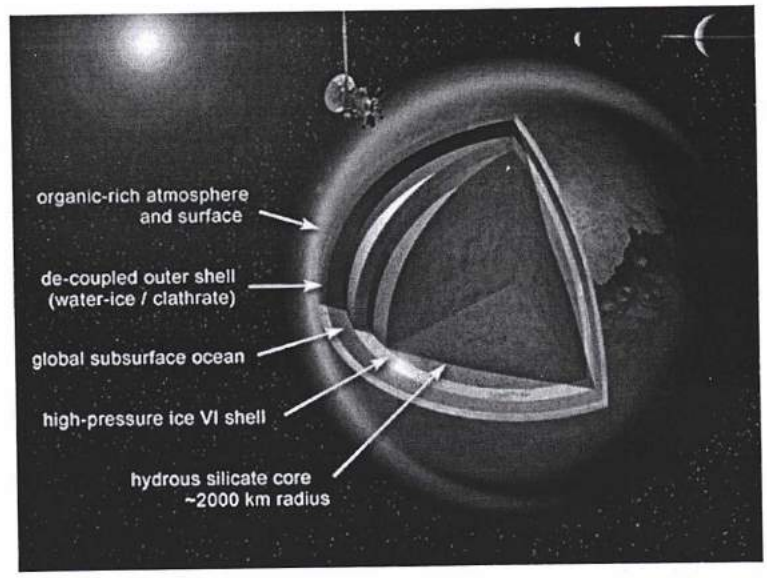

Figure 1.11: Model of the interior of Titan (credit NASA, http://scitechdaily.com/saturns-largest-moon-titan-seen-in-unprecedented-detail/).

Recent acceleration measurements of the Cassini orbiter from during flybys from 2006 to 2011 show that Saturn creates large solid tides to Titan at about 10 m in height. These observations indicate the existence of internal ocean of liquid water assuming a depth of 100 km beneath the surface. If the interior was not deformable (Fig. 1.11), such solid tides would be only at 1 m in height (Iess et al., 2012).

The Huygens probe was released from the Cassini orbiter on 25 December 2004. On 14 January 2005, the probe reached Titan's upper atmosphere and after a descent procedure, which lasted for almost 2.5 hours, it landed. Cassini collected data from the Huygens probe for 1h and 12 min after the landing before disappearing below the horizon (Lebreton et al., 2005). The probe was still in operation and its signal was monitored by a global network of 17 ground-based radio telescopes (Witasse et al., 2006). For more than three hours after the touchdown, the probe operated normally, continuing its surface experiments (Lebreton et al., 2009).

The orbiter and the probe had two radio link channels, A and B, the transmitters of which were installed on board the probe, while the receivers on board the orbiter. Both transmitters and receivers were equipped with a temperature controlled crystal oscillators (TCXO) for providing sufficient frequency stability for telemetry. Channel A was additionally equipped with ultra-stable oscillators (USO) necessary for the Doppler Wind Experiment (DWE). The performance of USOs was satisfactory during the mission's journey to the Saturnian system and it was then decided to be used instead of TCXOs. However, the command to power the USO of Channel A on the receiver (aboard the orbiter) was omitted and the receiver did not have a reference oscillator to lock on the signal of the probe. DWE frequency measurements together with the non-redundant telemetry data from Channel A were lost. The signal of Channel A from the probe's USO was received from 15 Earth-based radio telescopes (Lebreton et al., 2005).

The Huygens/HASI provided a continuous density, temperature and pressure vertical profile from the level of the exobase at 1380 km to the surface (Fulchignoni et al., 2005). Probe's trajectory remained stable at the same latitude of 10.3°S during its descent and therefore the derived profiles can be considered as representatives of the vertical structure of the atmosphere and as global average. From the entry level down to the heat shield release at 155 km, the probe measured the density indirectly from the acceleration data and then, by assuming hydrostatic equilibrium, the relative pressure (Harri et al., 2006). The corresponding temperature is derived by assuming that the atmosphere is an ideal gas, which is valid above 40 km. Below the altitude of 155 km, HASI measured directly the pressure and the temperature. The HASI profile is illustrated in Fig. 1.12 below.

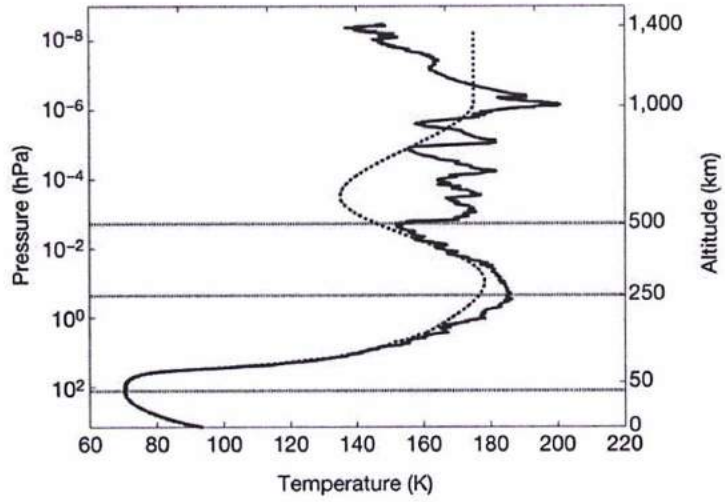

Figure 1.12: HASI temperature profile (solid line). The dashed line shows the engineering model (Yelle et al., 1997). The mesopause is located at 490 km with a temperature of 152 K, the stratopause at 250 km (186 K) and the tropopause at 44 km (70.43 K) (adapted from Fulchignioni et al., 2005).

Inversion layers, gravity waves, gravitational tides or large wind shear, which creates Kelvin-Helmholtz instability, may have caused the recorded temperature variations in the upper atmosphere (Fig. 1.12). In this region HASI provided temperatures higher compared to the one of the engineering model. The temperature oscillations above the stratopause indicates that the atmosphere is not dominated by radiative processes and is strongly influenced by the wave activity (Fulchignoni et al., 2005). However, HASI and CIRS measurements do not agree with the altitude of the stratopause. CIRS data set it higher at 312 km (183 K) (Vinatier et al., 2007b), while at this altitude HASI temperature is 185 K. Additionally, the calculation of the infrared radiance of HASI is inconsistent in relation to the observed CIRS radiance at methane 7.7 μm band (Lebreton et al., 2009). Finally, HASI measured the surface pressure and temperature at 1,467 ± 1 mbar and 93.65 ± 0.25 K, respectively (Fulchignoni et al., 2005).

The HASI's Permittivity Wave and Altimetry (PWA) sensors measured the electrical properties of Titan's atmosphere. PWA revealed a small conductivity and electron density from 80 to 140 km and a high-density electron layer with a peak at 63 km (Grard et al., 2006; Hamelin et al., 2007). As discussed above, the recorded Schumann resonance by PWA supported the existence of internal liquid ocean (Beghin et al., 2009b).

The Huygens/DWE was planned to measure the wind profile during the probe's descent, but due to the problem with Channel A in the communication link between the probe and the orbiter, DWE recordings were lost (Lebreton et al., 2005). However, the weak signal of Huygens was monitored by several large radio telescopes, which measured the signal

frequency during the whole descent and saved the experiment. The detected signal allowed an estimate of its frequency and yielded data for the probe's motion during the descent phase from the associated Doppler shift. With these measurements, the wind profile of Titan was retrieved. For the lowest part of the atmosphere, from 5 km and down to the surface, the winds are very weak with velocities less than 1 m/s. Above 10 km, winds are prograde (eastward, westerly) and above 32 km super-rotation occurs with a velocity of 11.74 m/s. From 60 to 100 km, the wind velocity reached almost zero. DWE confirmed the super-rotation of Titan's atmosphere (Bird et al., 2005).

The Huygens/ACP provided the first *in situ* measurements of Titan's aerosols (Israel et al., 2005). The collected samples show homogenous composition and the presence of N_2, CH_4, NH_3 and HCN after the pyrolysis procedure. It seems that the aerosols are made of refractory organic nucleus, covered with condensed volatile compounds and they release NH_3 and HCN during the pyrolysis. The latter assumption needs to be confirmed by laboratory work. However, these preliminary findings support the tholin hypothesis (Sagan & Khare, 1979).

The Huygens/DISR took hundreds of images of the surface during the descent, which have revealed a terrestrial-like surface, with drainage networks and rounded pebbles, made probably by water ice. DISR also measured the haze density particles during the descent phase and indicated a thin haze layer at 21 km. Additionally, DIRS recorded the continuous reflectance spectra of the surface using a lamp for a few hundred meters before the touchdown. Water ice was identified, but no tholins (Tomasko et al., 2005).

About the composition of the atmosphere, Huygens/GCMS data analysis provided a mixing ratio of methane at 1.48%±0.09 and hydrogen at 1.010.16 x 10^{-3} (Niemann et al., 2010). The CIRS value of methane at 0.016±0.005 (Flasar et al., 2005) is consistent with the GCMS one. GCMS measured a 40% increase of the methane concentration after the landing, perhaps due to thermal conductivity (Lorenz et al., 2006a). GCMS also identified organics in the surface such as ethane and cyanogen, carbon dioxide and benzene (Niemann et al., 2005).

The Huygens/SSP detected a relatively smooth, but not flat surface (Zarnecki et al., 2005). According to SSP results, the fracture of the landing surface is like the terrestrial wet sand, wet clay or packed snow.

What precedes is a short summary of a great wealth of data that the Cassini-Huygens mission provided, considerably enhancing our knowledge of Titan. In the rest of the

manuscript, I will come back to some of these results in more detail as they are connected to my research work.

Although Titan's atmosphere is much colder than the Earth's, it presents many direct similarities with our planet at different levels that have been pointed out since the Voyager days. Both atmospheres are dominated by the same main constituent, dinitrogen, albeit Titan's atmosphere extends much higher than the Earth's. A similar vertical structure from the troposphere to the ionosphere is also present, as well as a surface pressure of just 40% larger than on Earth (Fulchignoni et al., 2005). This is the only case of an extraterrestrial planetary atmospheric pressure with several similarities to that of the early atmosphere of the Earth. Furthermore, a very exciting and complex organic chemistry takes place in Titan's atmosphere. Table 1.2 summarizes the basic parameters for Titan.

Table 1. 2 - Titan basic parameters (Source: NASA, ESA[4] (Zebker et al., 2009))

Titan (SVI)	
Mass (10^{20}kg)	1345.5 (1/45 that of Earth)
Radius (km)	2575
Mean density (kg/m^3)	1880
Visual geometric albedo	0.22
Semimajor axis (10^3 km)	1221.83
Semimajor axis (Saturnian Radii)	20.273
Orbital Period (days)	15.945421
Spin rate (°/day)	22.58
Rotation Period (days)	Synchronous rotation
Inclination (degrees)	0.33
Eccentricity	0.0292
Obliquity	O.3°
Distance from Sun (10^9 km)	1,427 (9.54 AU)
Mean orbital velocity (km/s)	5.58
Rotational velocity at the equator (m/s)	11.7 – westwards
Escape velocity (km/s)	2.65
Gravity (m/s)	1.35

Without doubt, the Cassini/Huygens mission has revolutionized our perspective of the Saturn system and in particular of Titan, revealing a unique world with many similarities to our home planet, while at the same time pointing to significant differences. The purpose of this Thesis is to contribute to the study of Titan's environment by investigating its complex stratosphere and searching for relations and exchanges between the atmosphere and the surface below. In Chapter 2, I describe the CIRS instrument and its data, which I used for my research. Additionally, I present my contribution to the evaluation of CIRS database inferences and

[4] http://nssdc.gsfc.nasa.gov/planetary/factsheet/saturniansatfact.html
http://www.esa.int/esaMI/Cassini-Huygens/SEMMF2HHZTD_0.html

how the data processing was improved, when a new calibration algorithm was applied to them. The fundamentals of the theory of radiative transfer and the atmospheric model of Titan that I use for interpreting CIRS data are defined in Chapter 3. I also describe the upgrade of the radiative transfer code I have performed by adapting recent spectroscopic datasets, implementing new haze model and advancing some programmatic aspects from the previous versions.

The results of my research are presented in Chapters 4 and 5. Chapter 4 describes the meridional and temporal variations in the temperature and composition of Titan's stratosphere, as retrieved by CIRS data. The abundances' variations of the major trace gases of Titan's stratosphere are presented since the beginning of the mission up to early 2012, focusing on 5 latitudinal bins (50°N, 30°N, 0°, 30°S, 50°S). Constraints for photochemistry and dynamics are also given. Additionally, I present my contribution to water vapor retrievals from CIRS/FP1 spectra and the comparison with other radiative transfer codes' outcomes. Furthermore, I present the obtained vertical distributions of benzene from the surface of Titan to the upper atmosphere by applying the 1-D photochemical model of Lavvas et al. (2008a; 2008b). By subtracting the observations and the model, I also show spectral regions of unidentified emissions and propose new molecules for future work.

In Chapter 5, I study the connection between Titan's lakes and its atmosphere and the lakes' contribution to Titan's methane cycle. I focus on Mayda Insula in Kraken Mare, the biggest lake of Titan, and study its surroundings using geomorphological techniques. I also describe the application of a new despeckle filtering technique for obtaining restored RADAR images.

In Chapter 6, I discuss the Astrobiological potential of Titan and other icy moons of the Solar System, since the recent results from the Cassini-Huygens missions show that the habitability zone should be extended. However, although the Cassini data helps us change our perspective of the Saturnian System, several questions still remain unanswered and only a new mission will certainly shed light on them. In Chapter 7, I describe my contribution to the design of experiments to be included in such missions. I propose two experiments to be included as payload in future missions to icy moons and especially Titan. One is focused on studying the interior of a lake on Titan by using micro-electro-mechanical devices (MEMS), while the other studies a seismograph. Finally, Cassini-Huygens results have raised the public interest for Saturn and its moon. I report the outreach activities I have organized/participated of bringing Cassini-Huygens mission's accomplishments closer to the layman public in Chapter 8.

Chapter 2

Observations and CIRS data

2.1 The Cassini Composite Infrared Spectrometer (CIRS)

2.1.1 CIRS heritage and purpose

The Composite InfraRed Spectrometer (CIRS) (Flasar et al., 2004) on board the Cassini orbiter is an improved version of Voyager Infrared Interferometric Spectrometer (IRIS) (Hanel et al., 1980). CIRS high resolution (0.5 cm^{-1}) measurements are ten times higher than the IRIS ones, with an extended spectral range from 7 to 1000 μm (10-1400 cm^{-1}). The IRIS 4.3 mrad field of view (FOV) has been decreased to 0.27 mrad for the 600 to 1400 cm^{-1} region (Kunde et al., 1996).

CIRS probes both Saturn and Titan's atmospheres from deep in their troposphere to high in their mesosphere. It mainly consists of two interferometers, which share the same scanning mechanism, one in the far infrared and the other in the mid infrared. By taking advantage of the dual interferometer concept, scientists achieve the maximum advantage of optics and detectors. For this reason, Cassini's CIRS was called "Composite".

CIRS sounds both in nadir and limb viewing mode. Due to its advanced spectral resolution compared to IRIS, it is able to identify new trace constituents and its isotopologues, the spectral signatures of which are very weak to be identified by previously used instrumentation. The CIRS high spectral resolution permits also to separate some of the spectral bands, which were blended in IRIS spectra, for species such as C_3H_4 and C_4H_2 at 630 cm^{-1}.

CIRS is one of the four instruments mounted on the Cassini's Optical Remote Sensing Palette (RSP, Fig. 1.6) along with the Imaging Science Subsystem (ISS), the Ultraviolet Imaging Spectrograph (UVIS) and the Visual and Infrared Mapping Spectrometer (VIMS).

2.1.2 Description of the CIRS Instrument

The Composite InfraRed Spectrometer (CIRS) is a Fourier Transform Spectrometer (FTS) which senses the thermal radiation emitted from the objects in the Saturnian System in the thermal range of 55 to 200K and from 10 to 1400 cm^{-1} with an apodized spectral resolution varying from 0.5 to 15.5 cm^{-1} (Flasar et al., 2004) (Fig 2.1). The conceptual layout of CIRS (Fig. 2.2) consists of a telescope, the relay optics, two interferometers, a reference interferometer, a scan mechanism, the detectors, electronics assembly and a passive radiative cooler. The instrument's specifications are listed in Table 2.1 below.

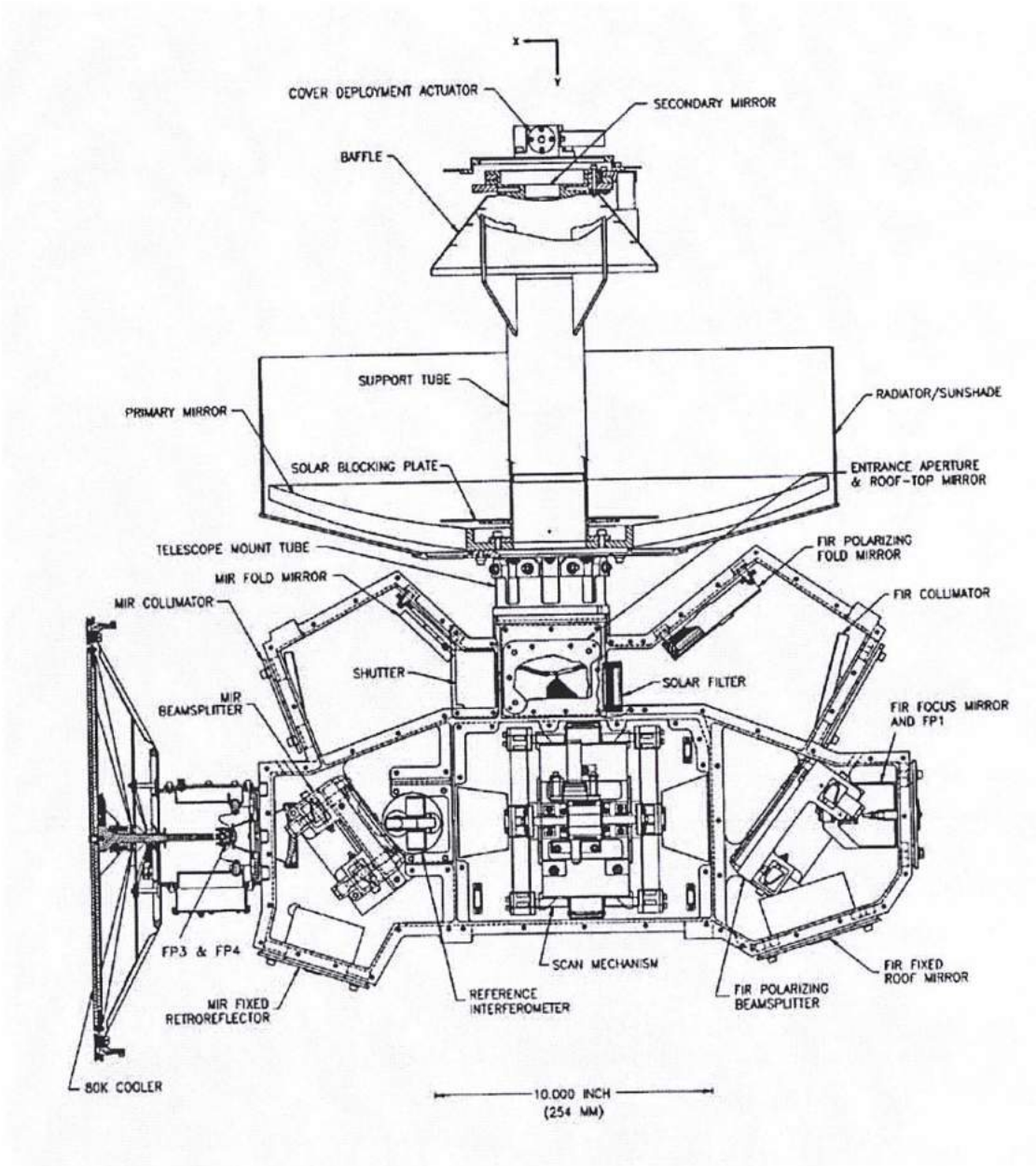

Figure 2.1: CIRS mechanical configuration. All the parts of the instrument are depicted. The scale is printed below of the instrument in both inches and mm (Kunde et al., 1996).

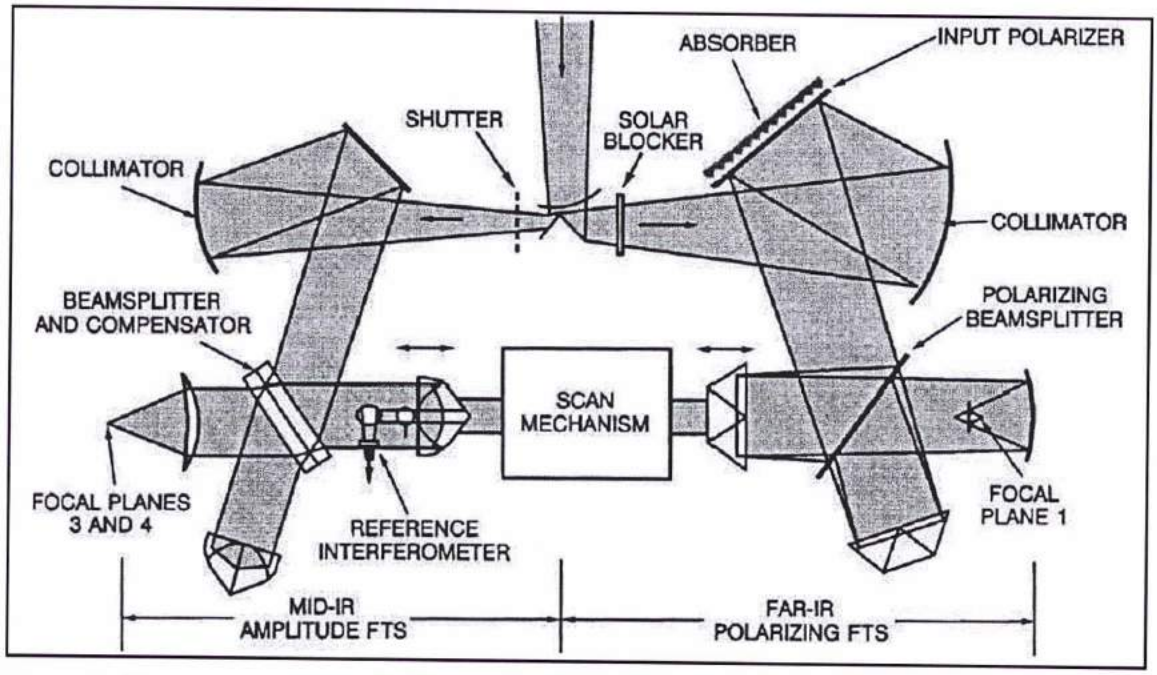

Figure 2.2: The conceptual layout of CIRS (Kunde et al., 1996). The single arrows show the light paths after been collected from the telescope, while the double arrows demonstrate the movable parts of the interferometers.

Table 2. 1 - Instrument specifications (Kunde et al., 1996; Flasar et al., 2004).

Mass	39.24 kg
Telescope's primary mirror diameter	50.8 cm
Telescope's secondary mirror diameter	7.6 cm
Focal Ratio	F/6
Telescope dimensions	89 cm x 76 cm x 52 cm
Maximum Power	32.89 W
Average operational power	26.37 W
Maximum bit rate	6 kbit/s
Data telemetry rate (kbps)	2, 4

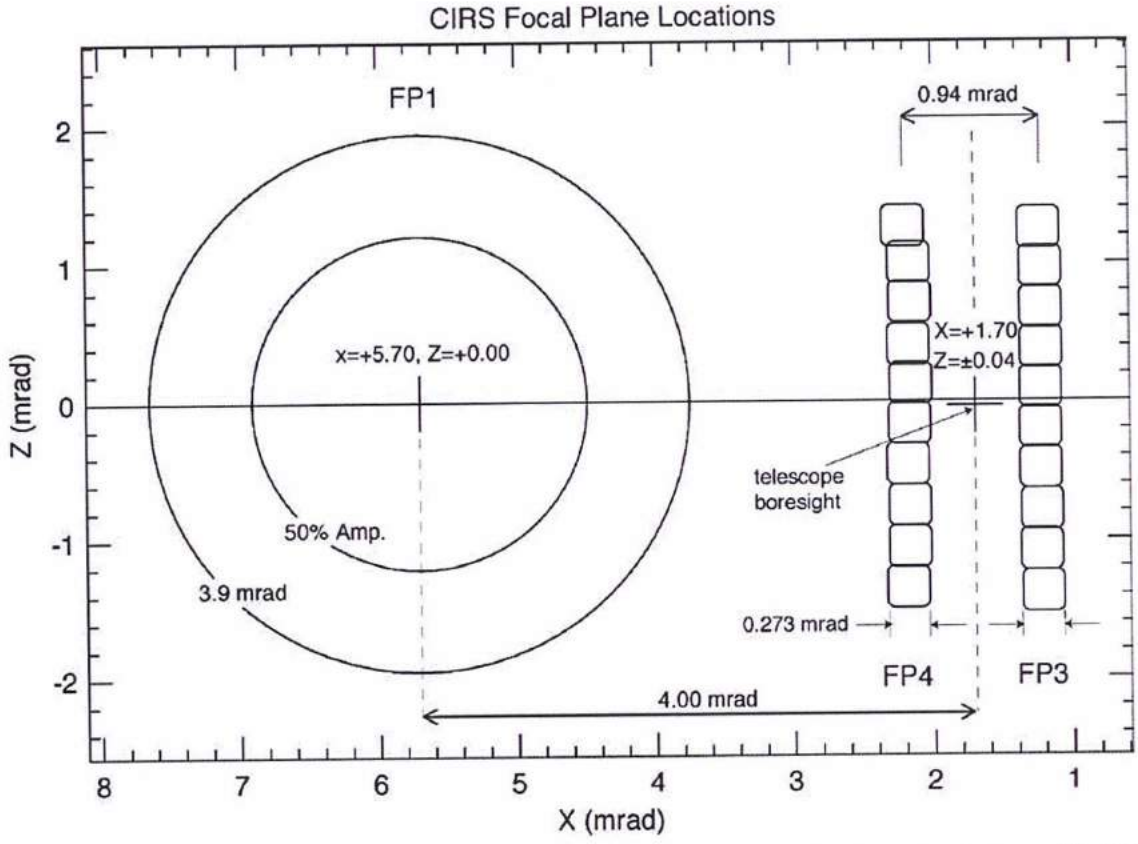

Figure 2.3: CIRS fields of view with correct relative positions and sizes. FP1 is the far-IR focal plane, while FP3 and FP4 are the mid-IR focal planes (Flasar et al., 2004). The far-IR detector has larger FOV than the mid-IR ones.

CIRS interferometers have one focal plane array (FPA), the Focal Plane 1 (FP1), sensing the far-IR portion of the emitted radiation (16.7 to 1000 microns) and a pair of focal plane arrays, the Focal Planes 3 and 4 (FP3, FP4), sensing the mid-IR (7.1 to 16.7 microns). In the primary proposal two focal planes the FP1 from 10 to 300 cm^{-1} and the FP2 ranging from 300 to 600 cm^{-1} covered the far-IR investigation. However, due to budget cuts, FP2 was not mounted but merged into one focal plane the FP1.

The FP1 is a polarizing interferometer, having a pair of thermopile detectors with a 3.9-mrad field of view (FOV) per pixel (Fig 2.3). The mid-IR interferometer is a traditional Michelson where the FP3 and FP4 have a photoconductive 10-element array of HgCdTe detectors and a photovoltaic 10-element array of HgCdTe detectors, respectively. Each pixel of the array has a 0.273-mrad FOV (Kunde et al., 1996). The Table 2.2 below lists the specifications of the focal planes.

Table 2.2: Focal Planes specifications (Kunde et al., 1996; Flasar et al., 2004).

Focal Plane	FP1	FP3	FP4
Spectral Range (cm^{-1})	10-600	600-1100	1100-1400
Detectors	Thermopile (dual)	Photoconductive (PC) (1 x 10 array)	Photovoltaic (PV) (1 x 10 array)
Pixel FOV (mrad)	4.3	0.27	0.27
Pixel AΩ (cm^2)	2.4×10^{-2}	1.5×10^{-4}	1.5×10^{-4}
Peak D* ($cm\ Hz^{1/2}W^{-1}$)	4×10^{-9}	2×10^{-10}	7×10^{-11}
Operational Temperature (K)	170	70, 75, 80, 85	70, 75, 80, 85

The CIRS telescope

CIRS telescope is of Cassegrain type, made from beryllium with a very low scattering surface. This configuration combines two mirrors: a primary F/6 concave parabolic reflector at 50.8 cm and a secondary convex hyperbolic one at 7.6 cm. The gold-enhanced surface of the primary mirror provides low scattering. Both mirrors share one focus, while the other focal point of the hyperbolic mirror is located where the image is to be observed. A supporting tube, cylindrical in shape, extends from the primary mirror center to the secondary mirror.

The primary dish reflects the incoming IR light beams towards its one focus, while the secondary mirror converges these rays to the other focus. Then, the light beam falls on a field splitting mirror, the Entrance Aperture Plate (EAP) (Kunde et al., 1996). The EAP divides the incoming light and directs it to the two interferometers via collimators and folding mirrors (see Fig. 2.2). Each collimator aligns the IR beam part to the fold mirror and then the light passes through a beamsplitter and onto retroreflectors (Kunde et al., 1996; Flasar et al., 2004).

The beamsplitters split the wave front of the incident ray in two separate beams, while the retroreflectors reflect the light back to its source with a minimum scattering. After being split, the recombined output beams go to the focal planes and are focused on the relative detectors. An electromechanical shutter is mounted in the mid-IR path, which can be used for internal calibration issues as it can be commanded to stop the incident beam. A solar blocking filter protects the FP1 thermopile detectors from any accidental solar illumination, rejecting rays shorter than 16.7 microns. The optimum operation temperature of the instrument is at 170 K except for the mid-IR detectors, the temperature of which is at around 80 K.

By applying the Fourier transform formalization at the interferogram we can reconstruct the original spectrum. Larger sample numbers in the interferogram give higher resolution of the final product. In contrast with the grating spectrometers, the FTS has no loses of the incident light, which is called the multiplex advantage. To achieve higher

resolution, the interferogram can be scanned more slowly and add a large number of interferograms (Lewis, 2004).

The far-IR interferometer (FP1)

For the far-IR interferometer, a polarizing Martin-Puplett type (Martin & Puplett, 1970) is mounted on CIRS in order to record the far-IR part of the incident light (Fig. 2.4). The linear polatization design hosts wire-grid polarizers to separate and recombine the incoming signal at FP1. CIRS wire-grid polarizers are nearly ideal for far-IR experiments. When the electromagnetic radiation meets the grid, the oscillating field parallel to its wires produces a wave originating from the electron movement along the wires, while the grid absorbs the rest of the light. Then, the radiation proceeds to the beamsplitter polarizer, located 45° in respect to the first polarizer, where it is split one more time into two orthogonal components. These beams fall in two roof top mirrors rotated at 90° and return back to the beamsplitter.

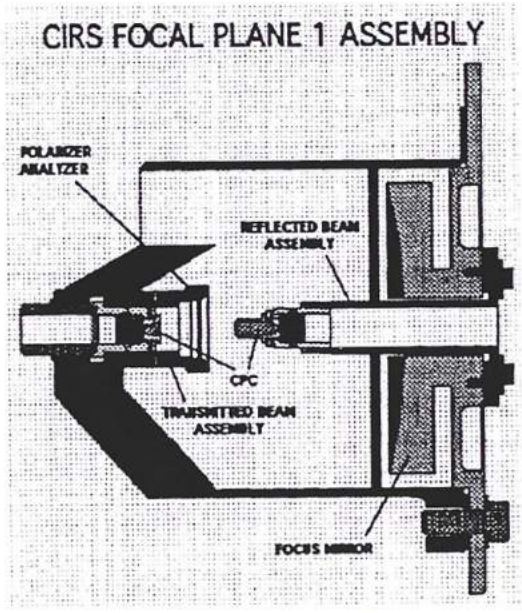

Figure 2.4: Cassini/CIRS FP1 assembly (Kunde et al., 1996). The polarizing grid and the concentrators are shown as well as the focus mirror.

The beamsplitter recombines these components which now have a phase difference of 90° and eventually send the recombined beam, which has now elliptical polarization, to the focal plane. A polarizer/analyser (Fig. 2.4) is placed in the front of the focal plane's detectors and it converts the polarization modulation into intensity modulation. The polarizer,

beamsplitter and analyser grids consist of photolithographic copper wires having each a diameter of 1 micron and a spacing of 2 microns, deposited on Mylar, a strong polyester film.

The modulated frequency is analogous to the wavenumber of the radiation, producing the resultant intensity of the combined beams, a conventional interferogram. The interferogram is a function of the path length difference between the two beams path which when they differ by integral number of wavelengths they interfere constructively. In any other path difference, they interfere destructively and they do not appear in the observed interferogram.

The polarizer/analyser splits the polarized beam into the transmitted component and the reflected one and sends them to the thermopile pair detectors. A Compound Parabolic Concentrator (CPC) is installed in the front of each thermopile detector (Fig. 2.4). Each detector receives one of the split components and now the final signal is gained, with no unmodulated intensity fluctuations and provided redundancy.

The mid-IR interferometer (FP3 and FP4)

The mid-IR interferometer is a conventional Michelson design (Michelson, 1881), having KBr beamsplitter and cube-corner retroflectors. After the split of the incoming radiation into two beams of almost equal intensity, one of them proceeds to the stationary mirror, while the other directs to the moveable arm of the interferometer. After having been reflected and transmitted once, the beams are recombined at the beamsplitter that is also a compensator and travel to the detectors. The interferometers specifications as well as the specifications of the focal planes are showed in Table 2.3 below.

Table 2.3: Interferometers specifications (Kunde et al., 1996; Flasar et al., 2004).

Specifications	Mid-IR	Far-IR
Type	Michelson	Martin-Puplett
Spectral Range (cm^{-1})	10-600	600-1400
Spectral Resolution (cm^{-1})	0.5-20	0.5-20
Integration time[5] (s)	5-52	5-52

The reference interferometer

The reference interferometer is the hardware component of CIRS, which provides an accurate calibration standard for the interferometer (Fig. 2.2). It is installed within the mid-IR interferometer of the instrument, uses a solid state 785 nm diode laser at 170 K providing a servo signal for velocity control. The laser is a source of monochromatic radiation and it is temperature depended. For redundancy the instrument is equipped with two laser diodes, selectable via command. The function of this interferometer is to generate a signal in order to sample the outputs from all the focal plane detectors of the instrument. Sampling of the created interferograms occurs at zero crossing of equally spaced reference fringes. The same signal is additionally used for handling the velocity of the scan mechanism.

The term zero path distance or zero path difference (ZPD) describes the relative distance between the two moving mirrors of the instrument in order to have the two arms of the interferometer at equal optical path length. When this distance is zero, all the light rays interfere constructively, producing the white light spike in the interferogram. When the interference is constructive for every wavenumber at the ZPD, the interferogram has the maximum relative intensity at one of the output ports and the minimum at the other. Thus the ZPD should be placed at every interferogram in order to ease the co-adding of interferograms and reduce the CIRS telemetry data rate. Such recording takes place due to a white light interferogram originating from the Light Emitting Diode (LED) mounted on the reference interferometer.

The scan mechanism

The scan mechanism is the same for the interferometers as well as for the reference interferometer and controls the sampling sequence and the moving mirrors' adjustment (Fig. 2.2). It follows the pattern of Voyager/IRIS and hosts the carriage device and the motor

[5] When using the Hamming apodization function. Unapodized widths have the corresponding scan times at about half as wide (Nixon et al., 2010).

responsible for the moving interferometer mirrors (the moving roof top mirror of FP1, the moving retroreflector for FP3, FP4 and the reference interferometer).

The CIRS detectors

During its flybys, the Cassini orbiter approaches Titan close enough at an altitude of no less than 1000 km, so that the IR spectrometer can perform not only downward viewing, but also limb profiling. This type of sounding needs a small field of view and for this reason high-efficiency photo-electronic detectors have been applied to the instrument (Nixon, 1998). CIRS detectors can be distinguished to a pair of thermopiles on the far-IR part of the instrument and to mercury cadmium telluride (HgCdTe) photoconductive (PC) and photovoltaic (PV) detectors on the mid-IR part. The thermopile detectors operate at 170K, which is the CIRS functional temperature, while both the PC and PV operate at 80K. A passive radiative cooler is mounted at this part of the instrument, which reduces the initial temperature to 80 K.

In general, thermopile detectors are passive uncooled devices, which require no electrical bias. Such devices have negligible 1/f noise and they do not sense substrate temperature variations (Foote et al., 1998). The thermal detectors of the far-IR sense the power of absorbed radiation. They receive one of the two components of the elliptical polarized beam from the polarizer/analyzer and improve the signal's gain by eliminating any unmodulated intensity fluctuations, providing redundancy. Each thermopile detector converts the incident infrared light into heat through an absorber, while a thermoelectric component creates an output voltage proportional to its internal temperature gradient.

The FP3 and FP4 detectors respond to the number of photons, which arrive per unit time. Both consist of HgCdTe linear arrays. A linear array of 1 x 10 photoconductive (PC) components is mounted in FP3, while a linear array of 1 x 10 photovoltaic (PV) components is mounted in FP4. Their back-to-back configuration is shown in Fig. 2.5. When photons hit the photoconductors, they generate free charge carriers and the resistance of the material is decreased. This results in a voltage change, which is the measured signal. On the other hand, when photons hit the photovoltaic detectors, electrons and holes are generated forming an electric field (Hanel et al., 2003). With this structure the instrument takes advantage of the low power dissipation which is less than 0.5 mW per element and a limited array detectivity by 1/f noise (Martineau et al., 1996).

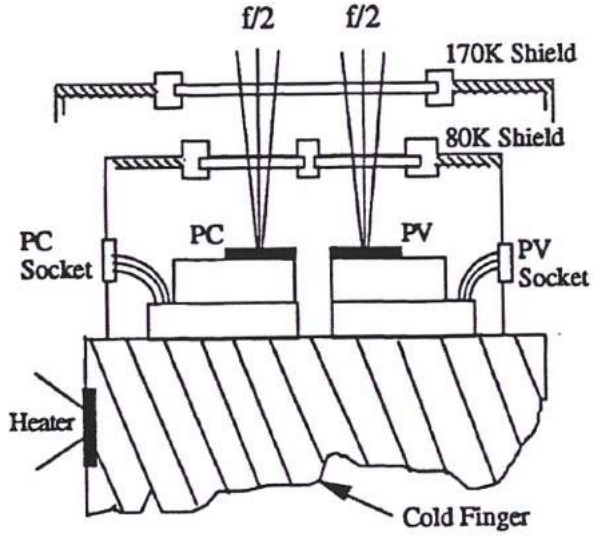

Figure 2.5: Configuration of photoconductive and photovoltaic arrays on FP3 and FP4 respectively (Martineau et al., 1996).

2.1.3 CIRS scientific objectives

CIRS measures the infrared emission from atmospheres, rings and surfaces, which are mainly used to map the temperature, the hazes and clouds and the chemical structure of the probed atmospheres and surfaces (Coustenis & Taylor, 2008). CIRS objectives are the following (http://cirs.gsfc.nasa.gov/science.html):

For Titan:

- Thermal and compositional mapping of atmosphere
- Surface temperature mapping

For Saturn:

- Thermal and compositional mapping of atmosphere
- Search for new molecular species

For Saturn's Rings:

- Determine the thermal structure
- Determine the material composition and particle size

For Saturn's Icy Satellites:

- Thermal and compositional mapping of surfaces
- Determination of subsurface regolith structure

The Cassini mission covers a large part of the Saturnian year, which is circa 29.5 terrestrial ones. In mid-2010, a full Saturnian year was completed since the Voyager 1 encounter. Moreover, ground and space borne observations have been published during the interval between the two *in situ* missions. Hence, CIRS infrared spectra, recovered during the Cassini mission period, determine both the temporal and the spatial variations of the gas composition of Titan's atmosphere in a global scale: its temperature and its opacity sources such as the aerosol distribution, the haze and the clouds are investigated. In addition, CIRS has gathered information throughout the last 8 years (2004 to 2012) and will hopefully continue to operate until 2017 when its extended mission will end. Thus, a wealth of data is available which have already changed our perspective of the atmospheric composition, dynamics and evolution over time.

As discussed before, CIRS is a more advanced instrumentation comparing to its ancestor, the Voyager 1/IRIS, which first sounded *in situ* the atmosphere of Titan. Not only does CIRS exploit its higher spectral resolution, but it also maps an extended spectral regime, larger than the one IRIS did in longer integration times. In fact, CIRS affords a programmable spectral resolution from 0.5 cm^{-1} to 20 cm^{-1} (Flasar et al., 2004). Its highly improved operability gives the opportunity to search for minor atmospheric species as well as for new isotopologues and calculate isotopic ratios. The determinations of the chemical composition of the atmosphere and the temperature are therefore done with much higher accuracy.

CIRS data analysis gives the opportunity to advance current modeling in atmospheric dynamics and general circulation and understand the complex photochemistry occurring on Titan's upper atmosphere. Moreover, the great success of its operation sets the requirements for future missions to the outer planets at high standards.

CIRS is not only dedicated to Titan's atmosphere but also to the other Saturnian moons and of course to the study of Saturn, its rings, their thermal properties, composition and surface. However, its achievements concerning these planetary bodies are beyond this study. Without doubt, CIRS is one of the most important experiments of the Cassini-Huygens mission.

2.2 Types of CIRS observations

The Cassini orbiter executes flybys of Titan, while is touring Saturn. Table 2.4 lists the Cassini flybys completed up to date (July 2012). The Composite Infrared Spectrometer on board Cassini operates during the Titan flyby sequence beginning at about 40 hours before the closest approach. Cassini approaches Titan with a velocity relative to the satellite ranging from 5.5 to 6.1 km/s. Fig. 2.6 below demonstrates the observation sequence during each flyby and the type of data, which CIRS can obtain moving towards the Closest Approach (C/A). All the far infrared types of the CIRS observations are listed in Table 2.5, while the mid-IR recording types are listed in Table 2.6.

T0 was the first Cassini flyby of Titan, which was performed just after the Saturn Orbit Insertion (SOI) of the spacecraft. However, the distances were too high compared to the observations which followed; hence, T0 data is excluded from our studies. A CIRS commanding error led to the corruption of most of the data obtained by TA flyby.

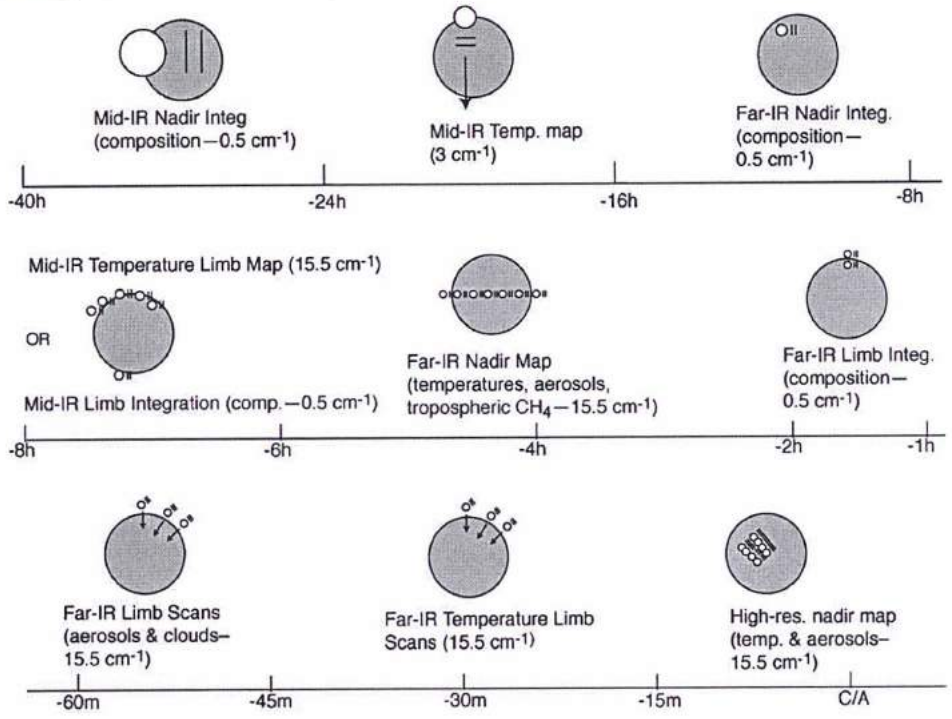

Figure 2.6: CIRS Titan timeline during a flyby. The fields of view of the instrument are shown. With the circle the FOV of FP1 is indicated and with the two parallel lines the linear arrays FOV of FP3 and FP4 are also plotted.

Table 2.4: Cassini Titan flybys. The date, the time from the closest approach, the Saturnian time and the position of Titan in the Saturnian magnetosphere during each flyby are also listed. Ls is the corresponding solar longitude of the flyby.

Year	Flyby	Date	Closest Approach	Ls
2004	T0	03 July 2004		293
	TA	28 October 2004	15:20:33	297
	TB	13 December 2004	11:38:13	299
2005	TC	13 January 2005		300
	T3	15 February 2005	6:54:21	300
	T4	01 April 2005	19:55:12	303
	T5	16 April 2005	19:11:46	304
	T6	22 August 2005	8:53:37	308
	T7	07 September 2005	7:50:26	309
	T8	28 October 2005	3:58:09	311
	T9	26 December 2005	18:54:15	313
2006	T10	15 January 2006	11:41:27	314
	T11	27 February 2006	8:25:19	315
	T12	19 March 2006	0:05:57	316
	T13	30 April 2006	20:53:31	317
	T14	20 May 2006	12:18:12	318
	T15	02 July 2006	9:12:19	320
	T16	22 July 2006	0:25:13	320
	T17	07 September 2006	20:12:04	322
	T18	23 September 2006	18:58:49	323
	T19	09 October 2006	17:23:24	323
	T20	25 October 2006	15:58:07	324
	T21	12 December 2006	11:41:31	326
	T22	28 December 2006	10:05:22	326
2007	T23	13 January 2007	8:34:00	327
	T24	29 January 2007	7:15:55	327
	T25	22 February 2007	3:10:59	328
	T26	10 March 2007	1:47:22	329
	T27	26 March 2007	0:21:52	329
	T28	10 April 2007	22:58:00	330
	T29	26 April 2007	21:32:52	331
	T30	12 May 2007	20:08:14	331
	T31	28 May 2007	18:51:27	332
	T32	13 June 2007	17:47:57	332
	T33	29 June 2007	16:59:46	333
	T34	19 July 2007	0:39:58	334
	T35	31 August 2007	6:34:25	335
	T36	02 October 2007	4:49:50	336
	T37	19 November 2007	0:52:51	338
	T38	05 December 2007	0:07:37	338

Year	Flyby	Date	Closest Approach	Ls
	T39	20 December 2007	22:56:41	339
2008	T40	05 January 2008	21:26:24	340
	T41	22 February 2008	17:39:08	341
	T42	25 March 2008	14:36:12	342
	T43	12 May 2008	10:09:59	344
	T44	28 May 2008	8:33:21	345
	T45	31 July 2008	2:13:11	347
	T46	03 November 2008	17:35:23	350
	T47	19 November 2008	15:56:28	351
	T48	05 December 2008	14:25:45	351
	T49	21 December 2008	12:59:52	352
2009	T50	07 February 2009	8:50:52	354
	T51	27 March 2009	4:43:37	355
	T52	04 April 2009	1:47:48	355
	T53	20 April 2009	0:20:46	356
	T54	05 May 2009	22:54:16	357
	T55	21 May 2009	21:26:42	357
	T56	06 June 2009	20:00:01	358
	T57	22 June 2009	18:32:36	358
	T58	08 July 2009	17:04:04	359
	T59	24 July 2009	15:34:04	359
	T60	09 August 2009	14:03:54	0
	T61	25 August 2009	12:51:39	0
	T62	12 October 2009	8:36:25	2
	T63	12 December 2009	1:03:15	4
	T64	28 December 2009	0:17:00	5
2010	T65	12 January 2010	23:10:37	5
	T66	28 January 2010	22:28:50	6
	T67	05 April 2010	15:50:39	8
	T68	20 May 2010	3:24:21	9
	T69	05 June 2010	2:26:28	10
	T70	21 June 2010	1:27:18	10
	T71	07 July 2010	0:22:45	11
	T72	24 September 2010	18:38:41	14
	T73	11 November 2010	13:37:02	15
2011	T74	18 February 2011	16:04:11	19
	T75	19 April 2011	05:00:39	20
	T76	8 May 2011	22:53:45	21
	T77	20 June 2011	18:32:01	23
	T78	12 September 2011	02:50:05	25
	T79	13 December 2011	20:11:24	28
2012	T80	2 January 2012	15:13:38	29
	T81	30 January 2012	13:39:48	30
	T82	19 February 2012	08:43:17	31
	T83	22 May 2012	01:10:11	33

Year	Flyby	Date	Closest Approach	Ls
2012	T84	7 June 2012	00:07:21	34
	T85	24 July 2012	20:03:08	36
	T86	26 September 2012	14:35:39	38

Table 2.5: Far-IR CIRS observation sequences

Type	Range (km)	Objective	Altitude (km)	Mapping geometry
FIRLMBINT Far-IR limb composition integration	25,000 to 40,000 (75-135 min of C/A)	Atmospheric composition (CO, H_2O, new species)	centered at 125 km[6] 225 km of limb	Composition of several flybys
FIRLMBAER Far-IR limb aerosol scan	<15,000 (45-75 min of C/A)	Aerosols, tropospheric abundance, surface temperature	40 km from limb	15.5 cm^{-1} samples two latitudes on the limb separated 5°
FIRLMBT Far-IR limb temperature sounding	<15,000 (10-45 min of C/A)	T-profiles of lower stratosphere tropopause 8-100 mbar	40 km from limb	15.5 cm^{-1} samples 2 latitudes on single limb separated 10°
FIRNADMAP Far-IR nadir temperature maps	60,000 (2:25-5 h of C/A)	T-profiles upper troposphere tropopause at 20-100 cm^{-1} surface temperatures	disk	15.5 cm^{-1}
FIRNADCMP Far-IR nadir composition integration	160,000 to 270,000 (9-13 h of C/A)	Atmospheric composition weak species new species	disk	O.5 cm^{-1} emission angle: 45-60° multiple flybys one location

Table 2.6: Mid-IR CIRS observation sequences

Type	Range (km)	Objective	Altitude (km)	Mapping geometry
MIRLMBINT mid-IR limb composition integration	100,000 to 180,000 (5-9 h from C/A)	minor species stratosphere	centered at 125 km 225 km of limb	O.5 cm^{-1}
MIRLMBMAP mid-IR limb map	120,000 (6 h from C/A)	T-profile upper stratosphere mesosphere v_4 CH_4	centered at 150 km 420 km of limb	15.5 cm^{-1} vertical resolution 36 km
MIDIRTMAP mid-IR nadir map	380,000 (13-22 h from C/A)	T-profile upper stratosphere nu4 CH_4	disk	3.0 cm^{-1} 6 slews cover the entire visible hemisphere
COMPMAP-TEMPMAP Mid-IR nadir composition temperature integration	500,000 - 1,000,000 (> 24h from C/A)	Atmospheric composition	meridian	O.5 cm^{-1}
HIRES	(0-10 min from C/A)	Surface mapping	disk	15.5 cm^{-1}

[6] The detectors are positioned twice at each altitude, which correspond to the lower and middle stratosphere respectively.

Since Titan's atmosphere experiences temperature inversion, the derived thermal spectrum consists of the emission part and the absorption part, which both depend on the temperature gradient of the probed atmospheric layers.

The FP3 pixel viewing modes are four: ODD, EVEN, CENTER and PAIRS. In the ODD mode only the 1, 3, 5, 7, 9 detectors are active, while in the EVEN mode the detectors 2, 4, 6, 8, 10 are only active. In the CENTER mode the 3, 4, 5, 6, 7 detectors are active, while in PAIRS mode the detectors 1&2, 3&4, 5&6, 7&8, 9&10 are combined and amplified.

As far as the FP4 pixel mode is concerned, we have the same modes: ODD, EVEN, CENTER and PAIRS. The active detectors are as in the FP3 modes, except that the detectors 4, 5, 6, 7, 8 are used in CENTER mode, to spatially match the detectors of FP3, which are numbered in reverse physical order. In the CO-ADD mode (COADD or NO-COADD) two successive scans are added together in the on-board electronics (buffers), to reduce the data rate by a factor of 2.

Normally, CIRS data is read out at a rate of 4 kbs and every 2 seconds 8 kbit datasets are transferred via the Bus Interface Unit (BIU) to the spacecraft Command Data Subsystem (CDS). CIRS has many ways of reducing the data rate, such as co-adding the spectra, dropping FP3 or FP4 readout (reduces by 45%), dropping FP3 and FP4 readout (reduces by 91%), or going into housekeeping-only mode.

The instrument electronics compress the data packets and transmit them to Earth by using the Deep Space Network (DSN). Then, the datasets are decompressed by software on the ground and go into a processing pipeline, which organizes the science data into binary tables creating the Vanilla database and interpolates housekeeping records. We will discuss more about the data calibration in the following section. The Vanilla software is a simple database query tool. However, the user can also access the binary data by using other programming retrieval tools.

2.3 Improving the CIRS data processing

2.3.1 Instrumental artifacts in CIRS data

The recordings of the Cassini Infrared Spectrometer onboard Cassini suffer from some quality problems having to do with quality, calibration, noise, etc. CIRS FP1, FP3 and FP4 interferograms are subject to the presence of single frequency (sine wave) ripples with varying period and amplitude and prominent sharp spikes or delta functions with periods of 0.125 s (8 Hz) and 2.0 s (0.5 Hz) respectively (Nixon et al., 2004). The source of the sine wave ripples is still unknown (Carlson et al., 2011). On the other hand, the source of the noise spikes is the electrical interference from the CIRS electrical sub-systems and especially the Bus Interface Unit (BIU) (Nixon et al., 2004). Figure 2.7 shows an example of such sine wave features in both FP3 and FP4 CIRS spectra. An example of prominent spikes is shown in Fig. 2.8.

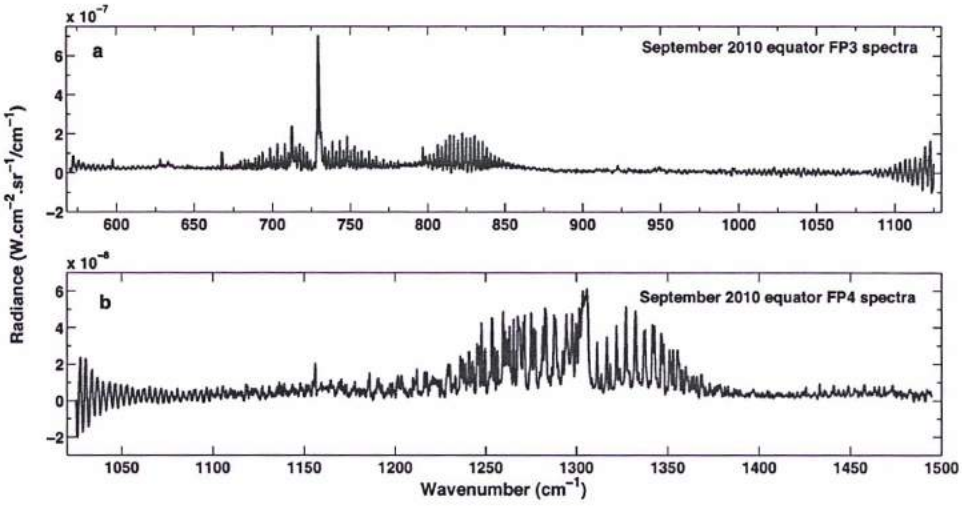

Fig. 2.7: FP3 averaged spectra as recorded from CIRS. The upper panel (a) shows the FP3 spectral average of September 2010 at equatorial latitudes, while the lower panel shows the FP4 one. The sine wave ripples are located below 600 cm^{-1} and above 1000 cm^{-1} at the FP3 selection and below 1050 cm^{-1} at the FP4 selection.

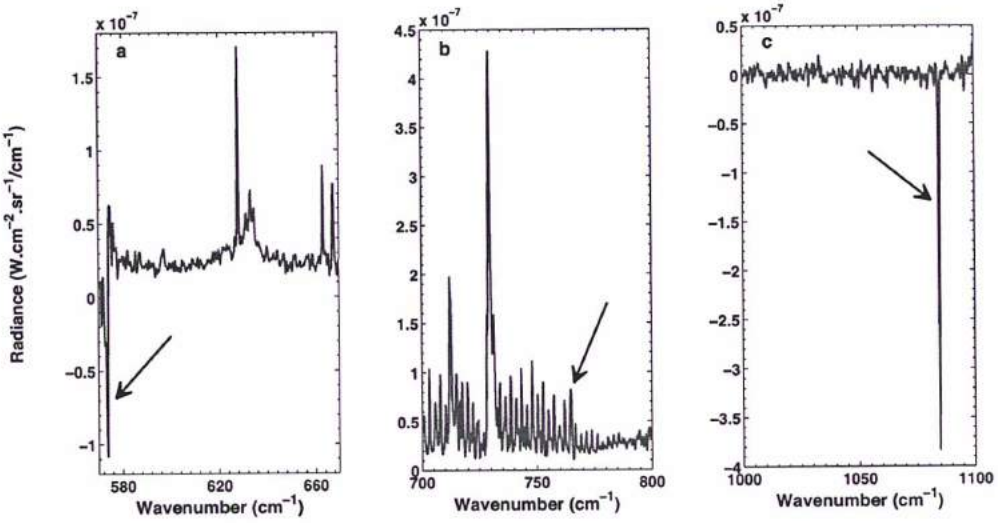

Figure 2.8: Prominent spikes at FP3 averaged CIRS spectra at the January 2007 query at 50°N. The left panel (a) zooms at the region of 580 to 660 cm^{-1} with a spike located at 574 cm^{-1}, the center (b) focuses on the 700 to 800 cm^{-1} where the spike is at 764 cm^{-1} and the right panel (c) shows the 1000 - 1100 cm^{-1} and the spike at 1085 cm^{-1}.

Each Cassini science instrument is connected to the Cassini's data bus through BIUs, which allow for two-way communication between the instruments and spacecraft (Henry, 2002). However, a bug exists when there is a heavy communication traffic, which affects the instruments' interferences. This bug has caused instrument resets and transmitted commands not to be received by the instrument (Linick et al., 2006). The CIRS BIU is queried 8 times per second by the Cassini Command Data Subsystem (CDS), on the spacecraft clock signal pulses and it produces a small spike. Data is transferred from CIRS to the CDS every 2 seconds, which causes a larger spike and this enhances its intensity (Nixon et al., 2004). The result in the spectrum is a series of spikes spaced by 12 cm^{-1} corresponding to the harmonics of 0.5 Hz. The 8 Hz spike at 191.38 cm^{-1} also appears in FP1 CIRS spectra as strong harmonics at 16 Hz (382.76 cm^{-1}) and 24 Hz (574.14 cm^{-1}). Unavoidably, both spikes impact atmospheric retrievals and can make interpretation problematic (Carlson et al., 2011).

2.3.2 Regular wavenumber calibration of the CIRS instrument

In-flight calibration of the absolute radiance expressed by the spectral responsivity has been performed on CIRS by using two separate techniques. The instrument is exposed to a blackbody source of accurately known temperature (shutter-closed) and to the deep space, which is assumed to be a perfect sink (Hanel et al., 2003; Flasar et al., 2004; Nixon et al., 2004). The former calibration task results the local calibration database ("current" Pipeline), while the latter the deep space calibration database (DS4000).

However, any new database edition may impact seriously the spectra. After having tested each correction algorithm, a new database inference is released to the CIRS data users with the new application. Hence, our purpose is not only to track any relative issues in the queries we make for our spectral analysis, but also to test each CIRS database using our radiative transfer code as well. In the next sections, I show the results of our testing procedure, how the new database inferences advance our analysis and measure the impact of the new release to radiative transfer calculation fits. I firstly retrieved spectra from CIRSDATA database in Meudon (Observatoire de Paris). The available database inferences are:

(a) v2.5 current pipeline with local calibration,

(b) v3.2 current pipeline with local calibration,

(c) DS4000 pipeline with deep-space calibration,

(d) Grand Average with unique average calibration over the mission.

The v3.2 current pipeline is the evolution of the v2.5 current pipeline, incorporating further refinement in the calibration algorithm. A spectral query with negative radiances is one of the occasional problems with the official CIRS current Pipeline. This problem has been experienced around from the beginning of the mission. The CIRS calibration team is working towards solving these issues and applies correction algorithms in both calibration sources in order to reduce spikes' effects on CIRS interferograms as well as vanish the presence of negative radiances.

The DS4000 is an independent database of CIRS data, which contains all consistent current pipeline data, but calibrated with using 4000 deep space spectra taken under the same conditions as the data in as close proximity to the data as possible. The introduction of such a data processing aims to resolve negative radiances and reduce the instrument's noise.

The Grand Average version of CIRS data has been developed in order to vanish negative radiances. This database is calibrated using a unique average for the entire mission. In principle, the comparison to the local (current) database will provide a much better signal-to-noise ratio and give good relative amplitude, but with baseline bias. The DS4000 provide spectra with also better signal-to-noise ratio without bias.

Another issue that should be addressed is whether an eventual systematic drift of calibrations as function of time exists, for example, if eventual detector degradation with time would result in a slow systematic drift of the radiation detection efficiency. After personal communications with Dr. D. Jennings, Dr. C. Nixon and Dr. R. Carlson from Goddard/NASA, such a case is not possible. No significant degradation of the CIRS radiance calibration has been observed over the mission of any of the 21 CIRS detectors.

As far as the detector's response is concerned, a local calibration in time takes place. That means that the calibration team uses observations of space and 170 K shutter taken around the same time as the science observations, to estimate the response. They continuously update the calibration during the mission, so that if the detector response ever degrades, it will automatically be accounted for. For instance, if 1000 detector counts correspond to 1 mW of radiance in 2007, but 900 counts correspond to 1 mW in 2012, their calibration will always compute the right radiance level, by looking at the "known" targets (space and shutter).

2.3.3 Retrieval of CIRS spectra and averaging procedure

In order to evaluate the impact of each new CIRS database that became available after corrections by the CIRS team at Goddard Space Flight Center on our atmospheric retrievals, and at the same time validate the improvement in the new database as we were asked to do, I have performed some tests using our radiative transfer code and running simulations using our updated atmospheric model for a given selection in the available developmental versions to determine the improvement and uncover any remaining calibration and/or other issues. I then compared the results of this fit to the ones retrieved using the spectra selected from previous official editions.

Because the purpose of this study is to obtain high precision inferences of the chemical and thermal composition, we always query for spectral averages which include a large number of spectra with given restricting parameters. We thus increase the signal-to-noise ratio. We mainly focus on nadir spectral observations and therefore we restrict the emission

angles to be less than 65°, in order to have reasonable airmasses in our calculations (airmass is the inverse cosine of the emission angle). These queries restricted the spacecraft range from 100 to 400,000 km and accepted all longitudes.

The radiative transfer code is applied to match the CIRS spectra. The fitting procedure is a simulation of the observations and comparison with the selected real spectra. We search for the best agreement between data and model through an iterative process. Then, we extract the mixing ratios of the atmospheric compounds. The comparison of the fits retrieved from each database shows if each new developmental database provides improved, worse or the same data.

2.3.4 Evaluating new CIRS databases and improving the data processing

Hereafter, I show three different validation tasks, we were asked to perform in order to evaluate the improvement in the CIRS data processing in each new database inference, and to validate the new calibration database which would then be implemented on the public access machines.

On 1 October 2010, we were asked from Ron Carlson, Research Associate Professor at the Catholic University of America, to validate the spike suppression algorithm has been developed with Ever Guandique, from ADNET systems Inc. This multi-parameter CIRS spike suppression algorithm is expected to reduce or vanish negative radiances from CIRS spectra, (Carlson et al., 2011). This algorithm employs deep space and shutter-closed interferograms for calibration averaged over several years. It matches the positions and intensities of the spikes to the observed spikes in each interferogram and performs checks to optimize and characterize the quality of the fitting process. The main idea is to calibrating the coadded Titan interferograms with non-coadded ("noadd") deep space and shutter-closed interferograms. The sine wave is modeled by a cubic polynomial exponentially damped cosine function.

Before de-spiking, each interferogram is over-sampled by a factor of 8 and has 8 times as many points as it had originally. Unfortunately, the continua are not always correct when such large deep space and shutter-closed averages are used for calibration across all three CIRS reference laser modes (Ron Carlson, pers. comm.). A good example of these negative

radiances is the query of a FP3 large average from March 01, 2009 to November 30, 2009[7] at high resolution (0.5 cm^{-1}) within a latitudinal bin at 25°S (Fig. 2.32-in red). In this selection, the presence of negative radiances is obvious. The resulted averaged spectrum is hereafter called Grand Average and is also shown in Fig. 2.9 (in blue).

The average spectrum of the current database version v2.5 has a continuum problem from 570 to 700 cm^{-1} with negative radiance we want to correct. One of the sequences of this query therein commanded co-added Titan interferograms to be recorded, along with a few coadded deep space and shutter-closed interferograms for calibration (Ever Guandique, pers. comm.). The negative radiances occur only for the co-added spectra in this sequence.

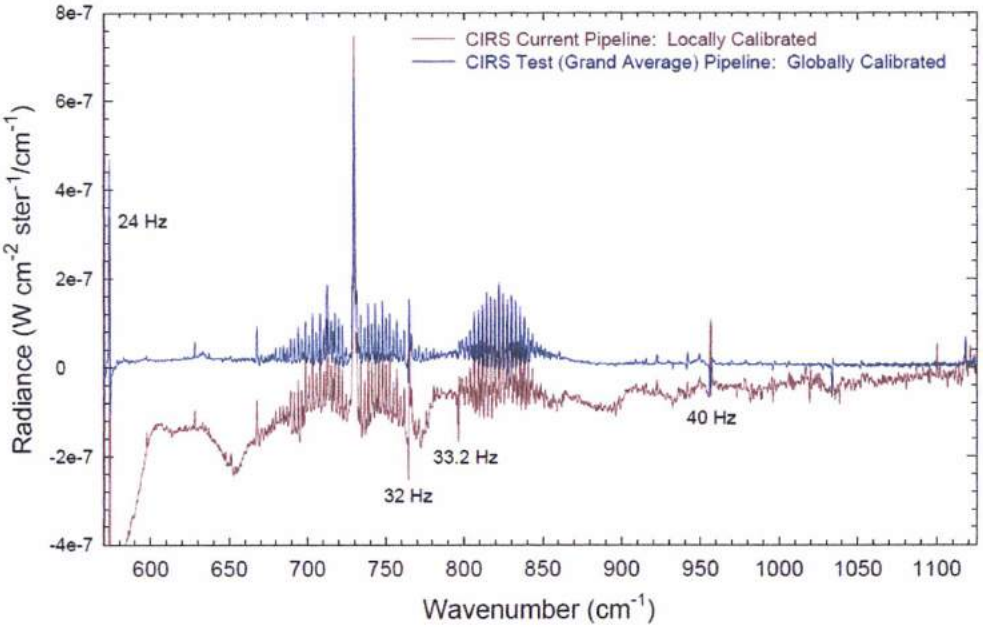

Figure 2.9: FP3 average spectrum from the current database v2.5 (in red) with calibration problems. It is for the time period 01 March - 30 November 2009, while the latitude range is from 20°S to 30°S at high resolution (0.5 cm^{-1}). The test-averaged spectrum (Grand Average) for the same conditions is plotted in blue (Ron Carlson, Ever Guandique pers. comm.).

Quite a few of the customary no-add Titan interferograms were recorded at a higher CIRS instrument temperature than the usual 76.3K, presumably because of the solar angle during the observations. These higher temperature Titan interferograms have to be calibrated separately using higher temperature deep-space and shutter-closed interferograms and then added to the 76.3K Titan calibrated spectra using a weighted average. To achieve a good signal-to-noise ratio for the higher temperature Titan spectrum, we may have to go backwards

[7] T51 to T62 Cassini Titan flybys

in time to earlier CIRS reference laser mode 1 time periods to average enough higher temperature deep-space and shutter-closed interferograms. The algorithm used about 12,000 deep-space and 1,200 shutter-closed noadd 76.3K interferograms for each of the ten FP3 detectors (11 - 20) in order to obtain a superior signal-to-noise rate for the calibrated Titan spectra. This calibration should yield the correct continuum. The resulted averaged spectrum is shown in Fig. 2.10 (in red) below.

One problem is that the 8 Hz spikes are very prominent in the 25°S spectrum if we use about 10,000 deep-space interferograms for each detector (11 - 20) averaged over the November, 2008 - July, 2010 reference laser mode 1 time period for the calibration. One suggestion is to use only about 4,000 deep-space interferograms averaged over a shorter time period that overlaps with the Titan observation. Such choice will cause the 8 Hz spikes to vanish, since the Titan and deep-space spikes should subtract out fairly well without any spike suppression (Ron Carlson pers. comm.). The extract of this algorithm, the Grand Average, (Fig. 2.10 red) is also compared to the DS4000 extract in Fig. 2.10 (in blue).

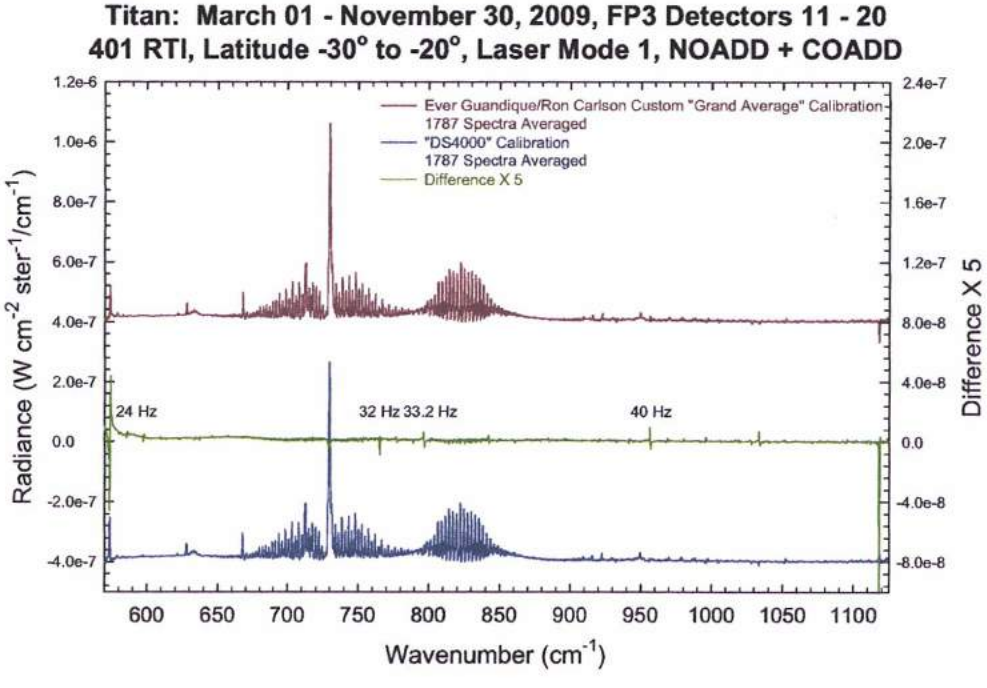

Figure 2.10: The difference between DS4000 (blue) and Grand Average (red) queries is showed by the green graph (Ron Carlson, Ever Guandique pers. comm).

On 6 October 2010, Marcia E. Segura, CIRS Operations Team leader in Goddard, asked us to validate the DS4000 database using our radiative transfer code. DS4000 spectra

have been treated as in the current pipeline, but calibrated with 4000 deep space spectra. In this approach, typically issues such as negative radiances are resolved and the noise is reduced. The current v2.5 (and lately v3.2) is the primary source for CIRS data users. The version 3.1 incorporates further refinement in the calibration algorithm. For interferograms collected using CIRS Flight Software Version 6, non-co-added data will have the 1/2 Hz noise spikes suppressed, while no noise suppression will be done on co-added data.

The first effort towards a better calibration of CIRS data was the "custom calibration" which was applied to support the Flight Software Version 6 (FSW6) by selecting 1,000 deep space spectra. The spectra were selected in order to match the conditions of the data to be calibrated and be recorded before the starting spacecraft event time (SCET). If such 1,000 spectra could not be found, then the selection procedure moves to the 1,000 deep space spectra, which match the data conditions after the ending SCET.

The Global calibration DS4000 takes into account 4,000 deep space spectra, which match the conditions of the data to be calibrated. Contrary to the custom calibration, it uses the 4,000 deep space spectra from the beginning of the mission and moving through the deep space by always using the most recent 4,000, replacing the older blocks.

The task was to provide the results of a comparison between the current v2.5 version of CIRSDATA and the DS4000 and check if this database resolved the negative radiances without loosing any information. The 3.1 (and 3.2) version was not released in this date.

On 3 May 2012, Marcia E. Segura, asked for validating the new dataset, which was generated with a similar algorithm than the one used to generate the DS4000 database, but with a phase correction algorithm applied from Nicolas Gorius, science collaborator, member of the CIRS science team. This new algorithm is expected either to correct most of the negative radiance or too-positive radiance outriders or be identified easily but the user. Outstanding outriders are being shifted back to level where they are expected to be.

My purpose is to provide to CIRS calibration team representatives the requested validation for each database release.

A) Grand Average *versus* DS4000

Using our line-by-line radiative transfer code I inferred a model simulation that I compared to both selections. When the best fits possible were found in the emission bands, I inferred the

abundances of the major molecules. The fits are illustrated in Fig. 2.11 a, b and the mixing ratios of the major species in Table 2.7 below. For all these spectra we have used the same temperature profile, which fits the v_4 methane band in the associated FP4.

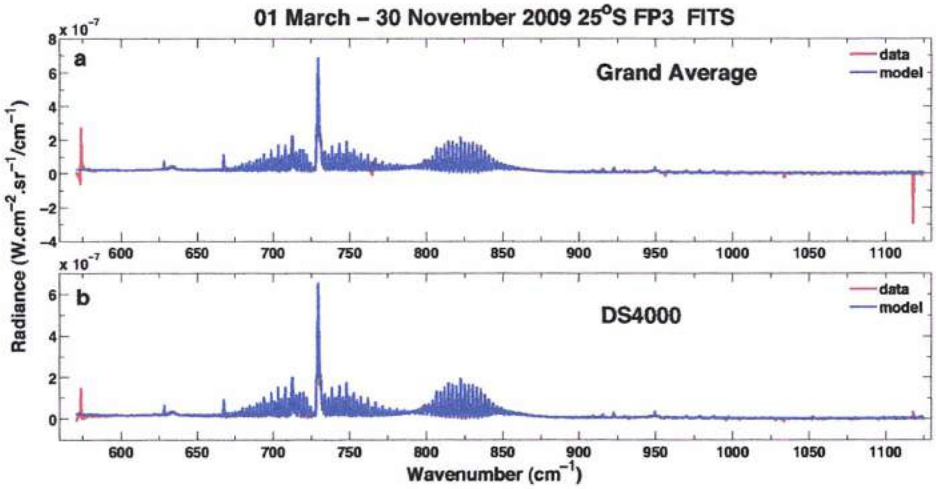

Figure 2.11: (panel a) Average spectrum best fit of the Grand Average selection file. The data are depicted in red color, while the model is in blue. (panel b): Average Spectrum best fit of the DS4000 selection file. The data are also illustrated in red color, while the model is in blue.

The plots (Fig. 2.11 a, b) are very similar except for:

a) Grand Average fit: correct continuum level at 570 cm^{-1}, but includes spikes

b) DS4000 fit: Continuum level has some problems before 600 cm^{-1} and it is lower than in the Grand Average selection, but most of the spikes are removed.

Table 2.7. The abundances of the major trace gases when fitting each selection and their difference

Molecule	Grand Average -fit	DS4000 -fit	Difference
C_2H_2	$2.4x10^{-6}$	$2.1x10^{-6}$	+14%
HCN	$5.6x10^{-8}$	$4.7x10^{-8}$	+20%
C_2H_6	$7.0x10^{-6}$	$6.2x10^{-6}$	+13%
C_3H_4	$4.8x10^{-9}$	$3.95x10^{-9}$	+20%

In general, the derived abundances for the major molecules in the FP3 range have a difference on the order of 15-20%. The continuum is 1.5 to 2 times higher in Grand Average spectrum between 600-890 cm^{-1}. Since the CIRSDATA v2.5 pipeline contains large calibration problems, the DS4000 is a large improvement with despiking. The Grand Average test database is still significantly different from DS4000 and yields higher abundances.

B) DS4000 *versus* v2.5

The characteristics of the selections I have chosen to perform this task are listed in the Table 2.8 below. I compared two spectral selections, one from the beginning of the mission and a recent one. According to the selections criteria the nadir-averaged spectra from both December 2006 and January 2010 were queried at high resolution (0.5 cm^{-1}) in FP3 and FP4. The December 2006 query is the first CIRS dataset consisting of adequate in number data at the latitude of 50°N. It incorporates observations from both flybys T21 (12/12/2006) and T22 (28/12/2006). The January 2010 selection, consisting of flybys T65 (12/01/2010) and T66 (28/01/2010), is the last query of satisfactory (in number) data of the year 2010 at the same latitudinal zone.

Table 2.8: CIRSFRANCE nadir selections used for the present test. I have gathered data from the DS4000 database as well as the v2.5 database at high resolution (0.5 cm^{-1}) at 50°N. Ls represents the corresponding solar longitude of each query. The number of spectra, the emission angle of the averaged spectral selection, the signal-to-noise ratio as well as the airmass of the collection are also listed.

50°N			DS4000				v2.5				
CIRS	Query	Ls	Number of spectra	Emission angle	S/N	Airmass	Number of spectra	Emission angle	S/N	Airmass	S/N Difference DS4000 - v2.5
FP4	Dec-06	326°	866	31.3	46.1	1.170	866	31.3	52.5	1.170	13.88%
	Jan-10	5°	234	53.1	27.5	1.666	234	53.1	27.6	1.666	0.36%
FP3	Dec-06	326°	1033	36	35.1	1.236	1033	36	32.4	1.236	-7.69%
	Jan-10	5°	284	53.9	21.3	1.697	284	53.9	27.6	1.697	29.58%

The v2.5 current pipeline presents an improvement by a factor of 30% on the S/N ratio in the FP3 query of January 2010. The DS4000 has higher S/N by a factor of 8% at the FP3 selection on December 2006.

In order to depict the differences between the two database inferences concerning the despiking result, I have overplotted the FP3 (Figs. 2.12, 2.13) and FP4 (Figs. 2.14, 2.15) spectra from each database. Their difference within the spectral range in each query is drawn in the lower panel of Figs. 2.12 -2.15 in black. DS4000 spectra FP4 on December 2006 (Fig. 2.14) have lower line radiances between 1020 and 1250 cm^{-1} than the v2.5 spectra. In the January 2010 FP4 (Fig. 2.15) spectra there is no such difference. In both FP4 files, the v2.5 data present ripples below 1050 cm^{-1} as it is shown in Figs. 2.14 and 2.15.

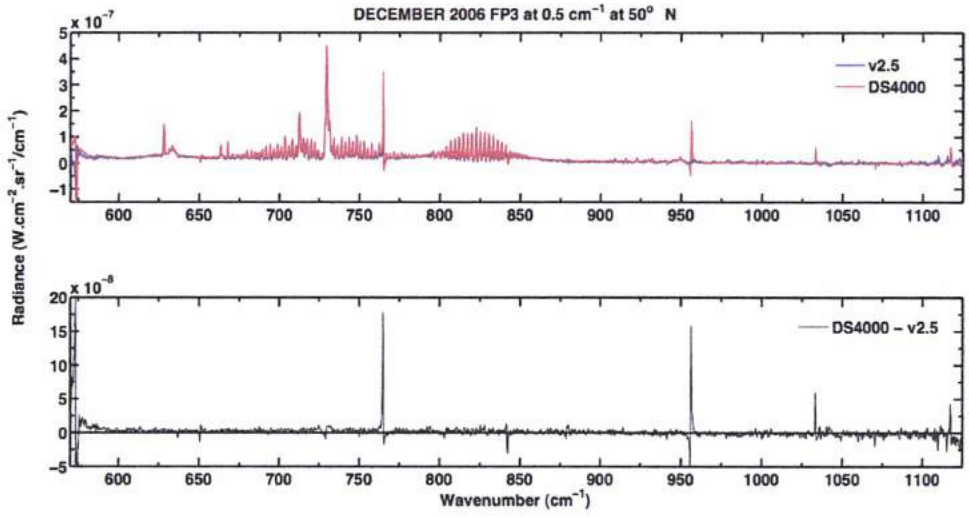

Figure 2.12: December 2006-FP3 average spectrum from the current database v2.5 (in red) and from the DS4000 (in blue). Their difference is plotted below (in black). Spikes of the DS4000 pipeline exist at 764, 956, 1033 and 1121 cm^{-1} wavenumber.

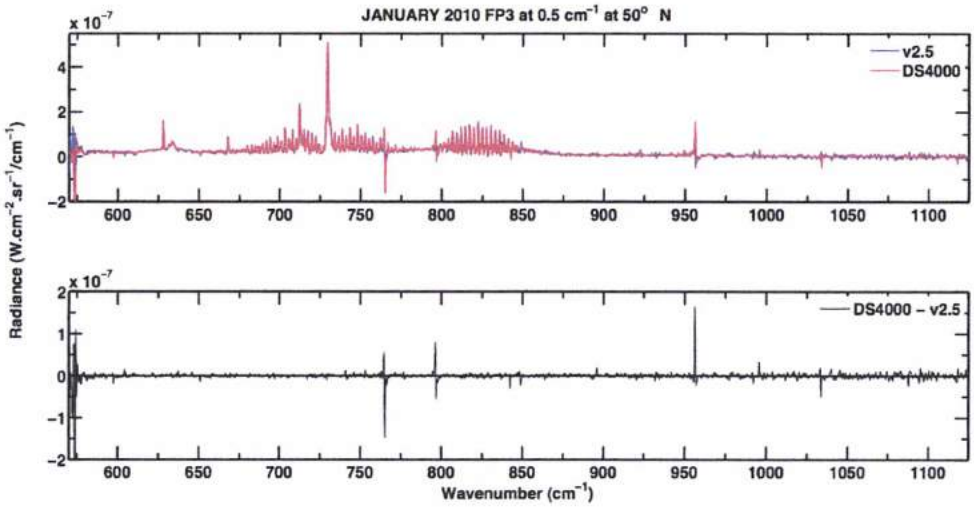

Figure 2.13: January 2010-FP3 average spectrum from the current database v2.5 (in red) and from the DS4000 (in blue). Their difference is plotted below (in black). Spikes of the DS4000 pipeline exist at 651, 764, 795, 842, 956 and 1033 cm^{-1} wavenumber.

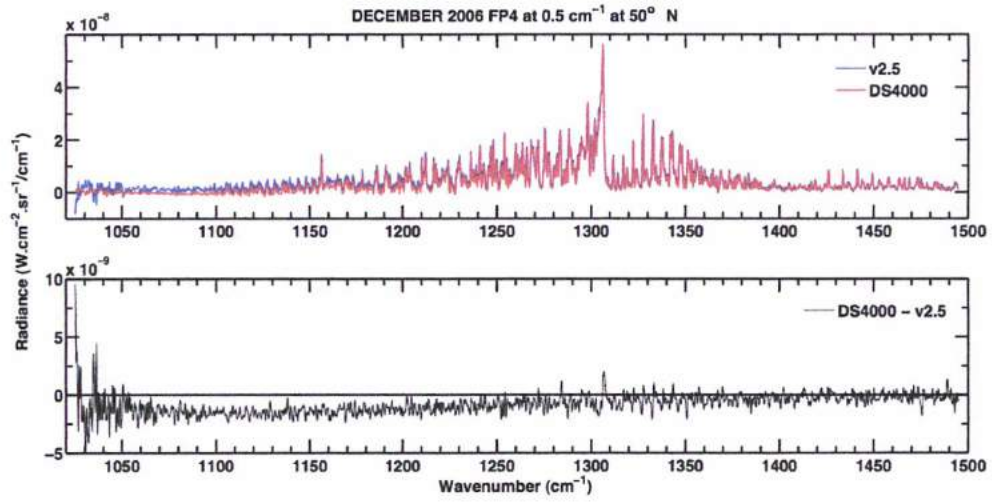

Figure 2.14: December 2006-FP4 average spectrum from the current database v2.5 (in red) and from the DS4000 (in blue). Their difference is plotted below (in black).

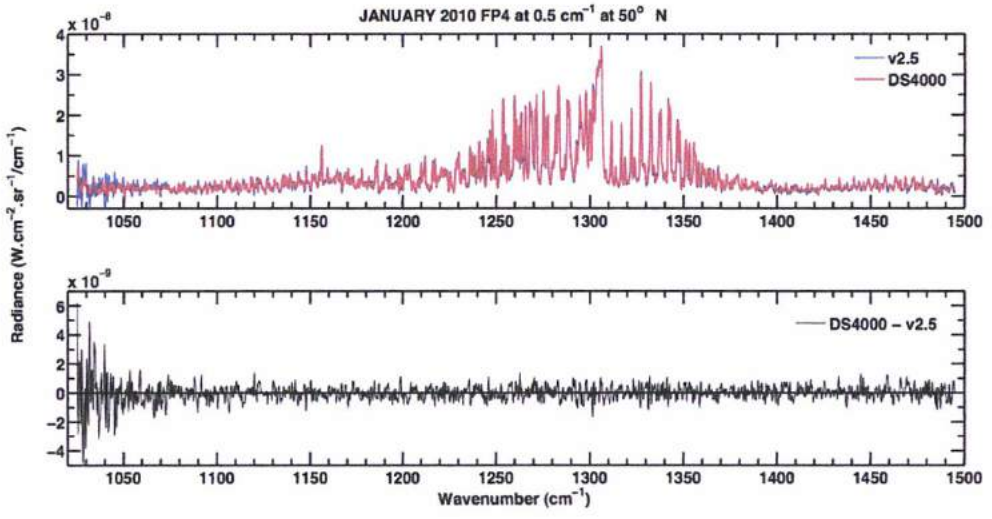

Figure 2.15: January 2010-FP4 average spectrum from the current database v2.5 (in red) and from the DS4000 (in blue). Their difference is plotted below (in black).

Both DS4000 FP3 averaged spectra show spikes at 764, 956 and 1033 cm^{-1}. In December 2006 query one more spike has been recorded 1171 cm^{-1}, while in the January 2010 query spikes are also present at 651, 795 and 842 cm^{-1}. The difference in radiance of the major spikes at 764 and 956 cm^{-1} between DS4000 and v2.5 is listed in the Table 2.9 below.

Table 2.9: The major spikes in CIRS FP3 spectra. The percentage corresponds to the relative difference between the DS4000 spectra and the v2.5 around the wavenumbers of 764 and 956 cm^{-1}.

Major spikes in spectra		
w/n (cm^{-1})	December 2006	January 2010
764	56%	42%
956	248%	68%

The spikes in DS4000 spectra are more prominent than in the v2.5. Especially, although December's 2006 spectra of v2.5 lacks spike around 956 cm^{-1}, the DS4000 spectra present a very prominent one.

Using our line-by-line radiative transfer code I produced a model simulation that I compared to both selections and when the best fits possible were found in the emission bands, I inferred the abundances of the major molecules. The fits of the FP3 spectra are illustrated in Figs. 2.16 and 2.17 from the v2.5 inference and in Figs. 2.18 and 2.19 from the DS4000. The retrieved mixing ratios of the major species from all fits are given in Tables 2.10 and 2.11 below. For each spectral selection I applied the same temperature profile with CH_4 at 1.48% (provided by R. Archterberg, at my request), which fits the ν_4 methane band in the associated FP4 spectra.

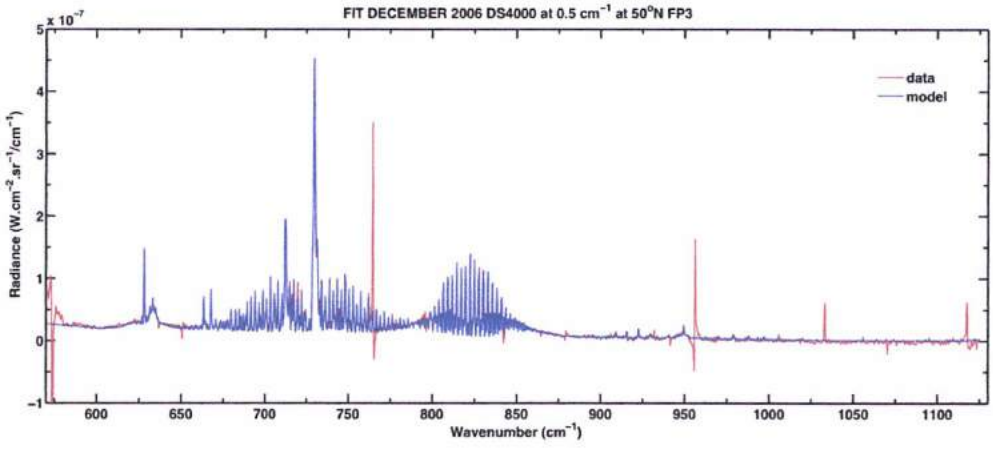

Figure 2.16: Fit of the December 2006-FP3 average spectrum from the DS4000 database at 50°N and high resolution (data in red, model in blue).

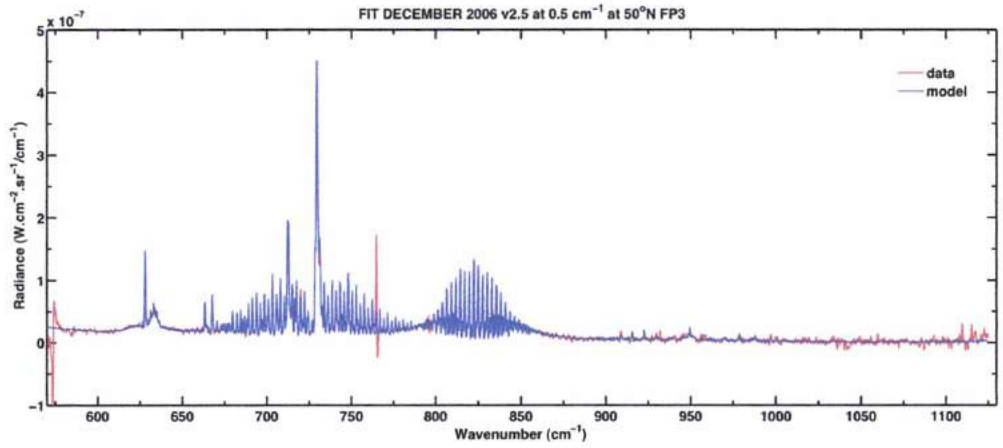

Figure 2.17: Fit of the December 2006-FP3 average spectrum from the v2.5 database at 50°N and high resolution (data in red, model in blue).

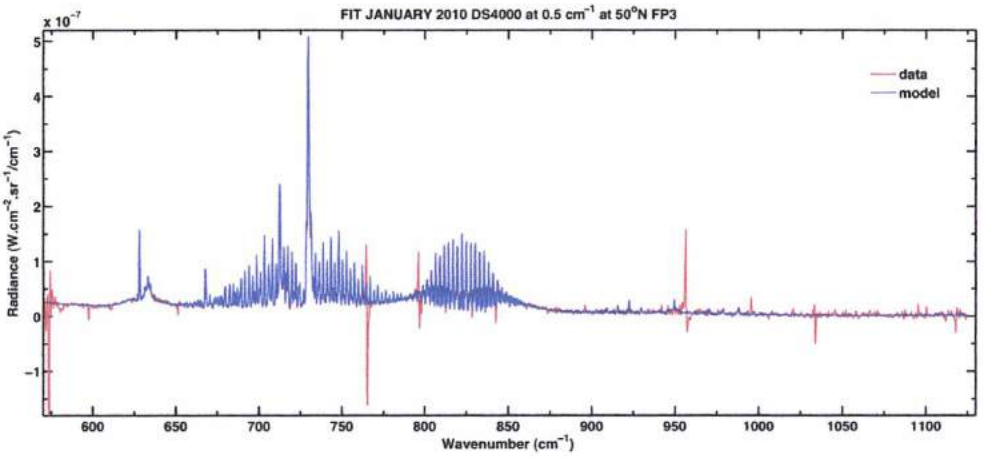

Figure 2.18: Fit of the January 2010-FP3 average spectrum from the DS4000 database at 50°N and high resolution (data in red, model in blue).

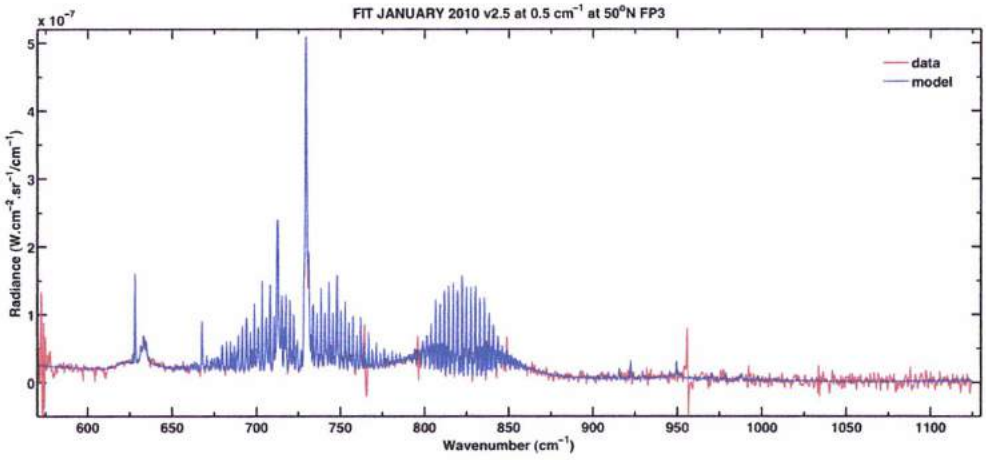

Figure 2.19: Fit of the January 2010-FP3 average spectrum from the v2.5 database at 50°N and high resolution (data in red, model in blue).

For the December 2006 query, the abundance of acetylene - C_2H_2 - (Tables 2.10 and 2.11) calculated from the v2.5 pipeline is significantly higher than the DS4000 one at about 26% and the HCN at about 10%. The rest molecules have similar mixing ratios retrieved from both database inferences, located within the error bars.

Table 2.10: The abundances of the major trace gases when fitting the January 2010 selections and their difference.

January 2010 abundances			
Molecule	v2.5	DS4000	Difference
C_2H_2	5.60×10^{-6}	5.10×10^{-6}	9.8%
HCN	8.00×10^{-7}	7.90×10^{-7}	1.3%
C_3H_4	1.22×10^{-8}	1.38×10^{-8}	-11.6%
C_4H_2	5.50×10^{-9}	5.20×10^{-9}	5.8%
CO_2	1.55×10^{-8}	1.39×10^{-8}	11.5%
C_2H_6	1.22×10^{-5}	1.05×10^{-5}	16.2%

Table 2.11: The abundances of the major trace gases when fitting the December 2006 selections and their difference.

December 2006 abundances			
Molecule	v2.5	DS4000	Difference
C_2H_2	3.90×10^{-6}	3.10×10^{-6}	25.8%
HCN	4.70×10^{-7}	4.30×10^{-7}	9.3%
C_3H_4	1.54×10^{-8}	1.60×10^{-8}	-3.8%
C_4H_2	8.10×10^{-9}	8.10×10^{-9}	0.0%
CO_2	1.60×10^{-8}	1.70×10^{-8}	-5.9%
C_2H_6	1.15×10^{-5}	1.15×10^{-5}	0.0%

We now focus on the continuum level in both pipelines. The continuum of December 2006 FP3 selection (Fig. 2.20) is higher in the DS4000 data than in v2.5 on the order of 45%, 20% and 13% within the spectral range of 575-590, 590-625 and 640-650 cm^{-1} respectively (Table 2.12). Instead, the continuum level in the January 2010 FP3 selection (Fig. 2.21) shows no significant differences between the two inferences.

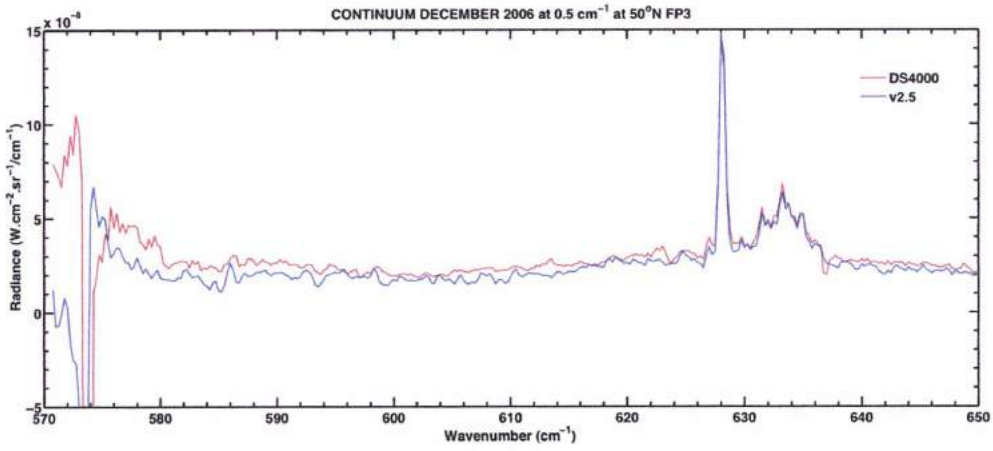

Figure 2.20: Plot of the December 2006-FP3 average spectrum at 50°N and 401 rti. The continuum from 570 to 650 cm^{-1} of both versions of CIRSDATA is higher in DS4000 (v2.5 in red, DS4000 in blue).

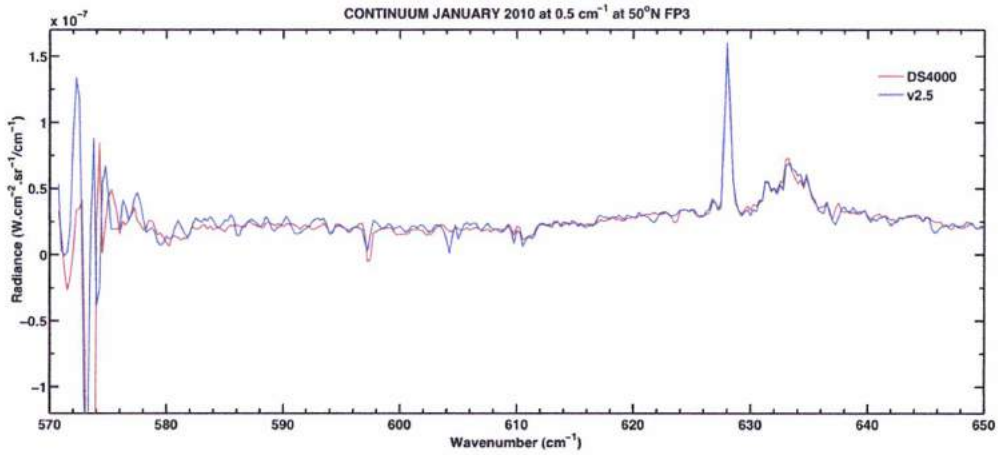

Figure 2.21: Plot of the January 2010-FP3 average spectrum 50°N and 401 rti. The continuum from 570 to 650 cm^{-1} of both versions of CIRSDATA are equal (v2.5 in red, DS4000 in blue).

Table 2.12. The differences between the continuum level of both pipelines at the December's 2006 selection within the region around C_3H_4 and C_4H_2. DS4000 continuum is higher than the v2.5.

December 2006 -FP3 continuum level (cm^{-1})	Difference between DS4000 and v2.5
575 - 590	40-50%
590 - 625	20%
640 - 650	13%

The continuum level appears in the DS4000 database lower than for v2.5 and negative in some cases. The FP4 spectra of the 2006 December selection (Fig. 2.22) shows significant differences between the two database inferences at about 50% from 1050 to 1120 and 1170 to 1200 (Table 2.13). Once again no significant difference is depicted in January 2010 FP4 data (Fig. 2.23).

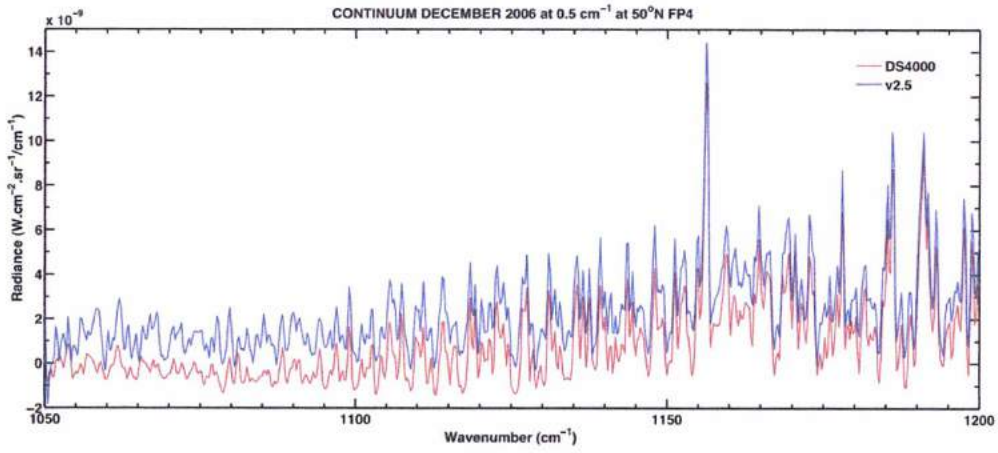

Figure 2.22: Plot of the December 2006-FP4 average spectrum at 50°N and high resolution. The continuum from 1050 to 1200 cm^{-1} of both versions of CIRSDATA is higher in v2.5 (v2.5 in red, DS4000 in blue).

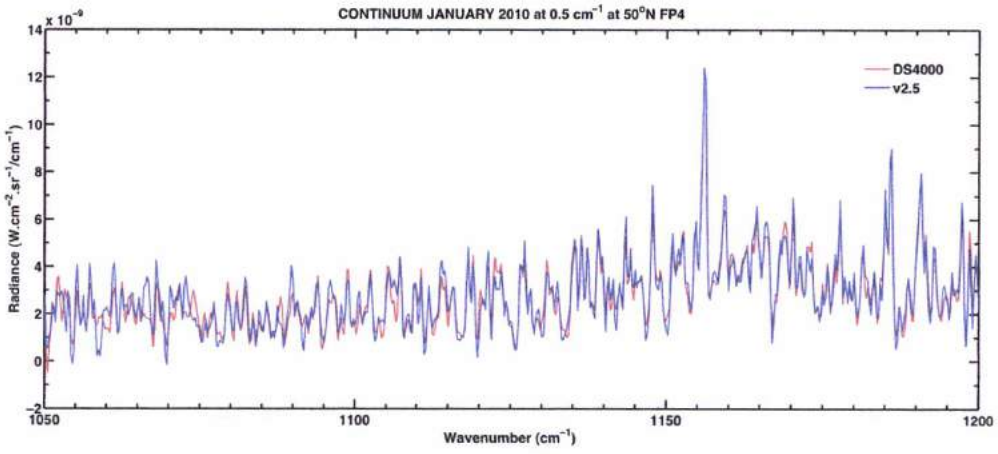

Figure 2.23: Plot of the January 2010-FP4 average spectrum 55°N and 401 rti. The continuum from 1050 to 1200 cm^{-1} of both versions of CIRSDATA are equal (v2.5 in red, DS4000 in blue).

Table 2.13. The differences between the continuum level of both pipelines at the FP4 December's 2006 selection. The v2.5 continuum is higher at about 50% than the DS4000 one.

December 2006 -FP4 continuum level (cm^{-1})	higher values difference between DS4000 and v2.5
1050 - 1120	-60% to -50%
1170 - 1200	-50%

C) v3.2 versus v2.5, DS4000 and DS4000 with phase correction

I have queried three selections from CIRSFRANCE database in Meudon on spectra produced during Titan flybys. I have asked for the same selection at FP3 and FP4 focal planes (and FP1 for the first two queries) within three versions of CIRSDATA:

(a) the calib_v3.2, which refers to the current pipeline with local calibration which has replaced the previous v2.5, hereafter v.3.2,

(b) the calib_v4.2, which is the DS4000 dataset, hereafter DS4000, and

(c) the calib_v4.3, which is also the DS4000 dataset but with the application of the new phase algorithm by N. Gorius, hereafter DS4000-PhC.

The first selection picked up spectra recorded by Cassini/CIRS on September 2010 (T72 flyby) focused on equatorial latitudes taken at high spectral resolution (0.5 cm^{-1}). The second selection contains averaged spectra from the first Titan flyby on July 2004 (T0) in medium resolution (2.5 cm^{-1}) focused on mid southern latitudes (50°S). It should be noted that the choice of T0 data (July 2004) was due to the fact that only these spectra were uploaded at the moment of the July 2004 query from the DS4000-PhC database. Although we do not take into account the data from this flyby in our radiative transfer calculations, this comparison may be helpful for the algorithm developers. The last selection refers to January 2007 at 50°N at high resolution from Cassini Titan T23 and T24 flybys.

I applied our radiative transfer code in order to fit C_2H_2, C_2H_6, HCN signatures at the three spectral inferences. I use the corresponding temperature profile as retrieved by the v_4 methane band at FP4 spectra (Achterberg et al., 2008; 2011) to then infer the major molecules' abundances after a best-fit modeling procedure.

On September 24, 2010 the Cassini orbiter performed its 72th Titan flyby (T72). Table 2.14 below lists the characteristics of both FP3 and FP4 queries in each database. These queries have focused on equatorial latitudes. No spectra were found for FP1 for this

selection's parameters. The number of spectra as well as the emission angles are the same in all database editions, while the Signal-to-Noise ratio values differ but not significantly.

Table 2.14: September 2010, equator, 0.5 cm^{-1}. Only slight differences in Signal-to-Noise ratios exists.

Focal Plane	CIRSDATA version	Number of spectra	Emission angle	Signal-to-Noise ratio
FP3	v3.2	1503	11.6	60.6
FP3	DS4000	1503	11.6	60.2
FP3	DS4000-PhC	1503	11.6	57.8
FP4	v3.2	1619	7.6	138.0
FP4	DS4000	1619	7.6	137.8
FP4	DS4000-PhC	1619	7.6	143.7

Figs. 2.24 and 2.25 below depict the comparison of these three database inferences. The upper plots contain all the database queries, while the lower panels of each figure show the difference with the DS4000-PhC and the nominal DS4000. It should be noted that the September 2010 selection at equator from the DS4000-PhC database still suffers from ripples on its edges in both FP3 and FP4. The negative differences in Fig. 2.24-lower panel- mean that the nominal DS4000 data have higher values in radiance than the DS4000-PhC ones in the FP3 spectral range. Instead, the differences plot in the lower panel of Fig. 2.25 shows that in FP4 the DS4000-PhC spectra have radiances higher than the corresponding nominal DS4000 ones. There is also a spike at 797 cm^{-1}, which exists in all database extracts.

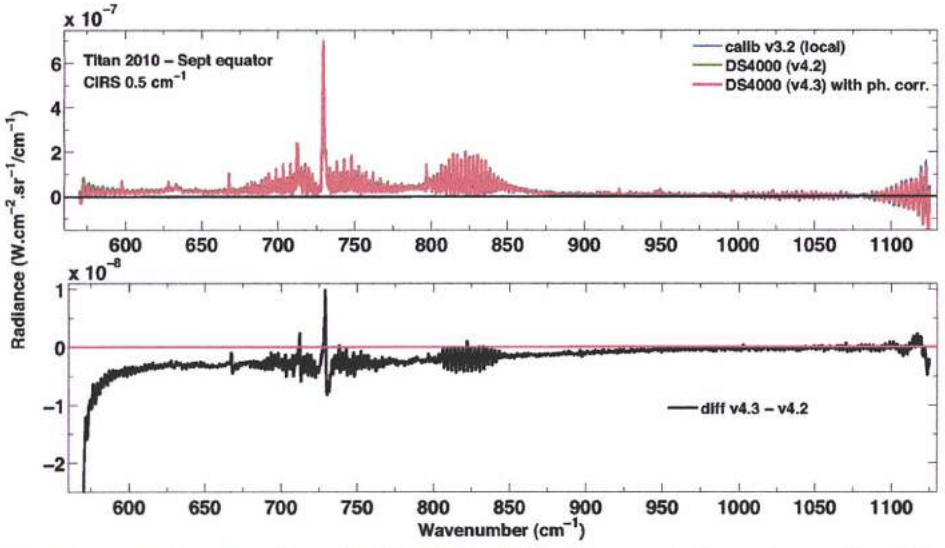

Fig. 12.24: FP3 averaged spectra from CIRSFRANCE. The upper panel shows the results of the database inferences (local calibration in blue, DS4000 in green and the new DS4000-PhC algorithm in red). The lower panel shows the difference between the two DS4000 versions (black). Ripples in the recorded radiation are obvious in both spectral edges.

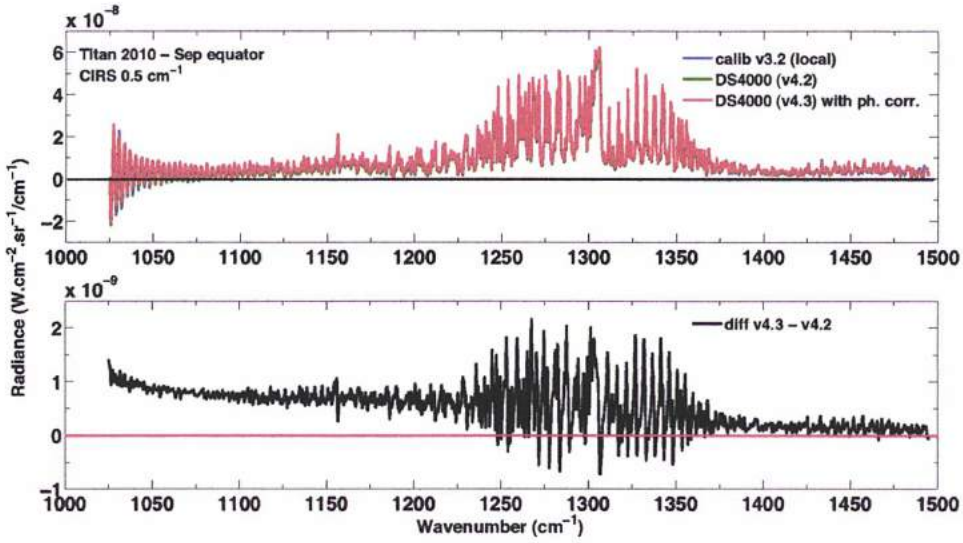

Fig. 2.25: FP4 averaged spectra from CIRSFRANCE. The upper panel shows the results of the database editions (local calibration in bleu, DS4000 in green and the new DS4000-PhC algorithm in red). The lower panel shows the difference between the two DS4000 versions (black). The presence of ripples from 1020 to 1100 cm^{-1} is shown.

I then solve the radiative transfer equation by using our radiative transfer code. In Figs. 2.26 and 2.27 below, I plot the best-fitting procedure results for each database version.

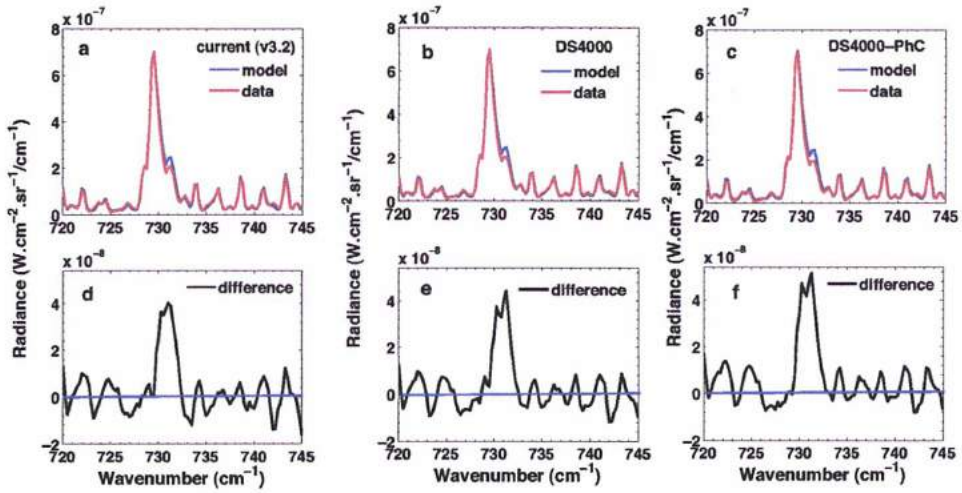

Fig. 2.26: Fits of the C_2H_2 signature in each database extract. The model is depicted in blue, while the data are in red. The panels a, b, c show the fit plot versus data of current (v3.2), DS4000 and DS4000 phase corrected database, while the panels d, e and f show the corresponding differences between model and data.

The P-wing of acetylene at 730 cm^{-1}, is better fitted when using the DS4000 databases (differences' plots -Fig. 2.22 d, e, f). The phase corrected DS4000 also better simulates the 13-

C_2H_2 isotopologue in the Q-branch. It should be noted however, that I have used constant-with-height distributions when producing the model atmosphere. Vertical distributions will give better fits of the Q-branch and minimize the differences.

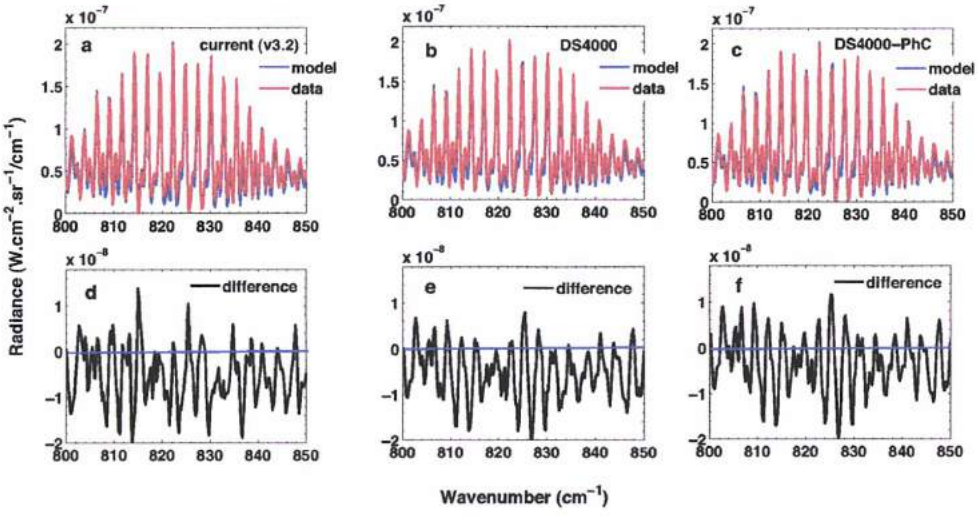

Fig. 2.27: As in the previous case, fits of the C_2H_6 signature in each database extract are plotted in this figure. The model is depicted in blue, while the data are in red. The panels a, b, c show the fit plot versus data of current (v3.2), DS4000 and DS4000 phase corrected database, while the panels d, e and f show the corresponding differences between model and data.

The differences of both DS4000 databases are smoother at ethane band at 822 cm^{-1} compare to the v3.2 fit (Fig. 2.27 d, e, f). The derived mixing ratios as well as the previous v2.5 edition mixing ratios are listed in Table 2.15 below. No differences have been found for the abundances of the 3 major molecules of the FP3 spectral region.

Table 2.15: C_2H_2, C_2H_6, HCN abundances as derived by applying our radiative transfer code in FP3 September 2010 averaged spectra at equator (0.5 cm^{-1}).

CIRSDATA	C_2H_2	C_2H_6	HCN
v2.5	3.4×10^{-6}	9.2×10^{-6}	2.1×10^{-7}
v3.2	3.9×10^{-6}	9.8×10^{-6}	2.1×10^{-7}
DS4000	3.9×10^{-6}	9.8×10^{-6}	2.1×10^{-7}
DS4000-PhC	3.8×10^{-6}	9.7×10^{-6}	2.0×10^{-7}

I concluded that the difference between the two DS4000 versions is less than 5% with respect to the phase corrected one, having somewhat lower values (Table 2.15).

The first Titan flyby (T0) by the Cassini orbiter occurred on July 3 2004 just after the Saturn Orbit Insertion of the spacecraft. Table 2.16 below lists the characteristics of this query in each database. The geometry of these queries follows the restrictions we have adapted when studying the previous selection. FP1 spectra have been retrieved.

Table 2.16: July 2004, 50°S, 2.5 cm^{-1}. The number of spectra for FP3 and FP4 between the local calibrated database and the deep space calibrated differ significantly. Consequently, the other characteristics also differ. FP1 spectra are the same.

Focal Plane	CIRSDATA version	Number of spectra	Emission angle	Signal-to-Noise ratio
FP3	v3.2	982	33.2	117.2
FP3	DS4000	97	26.7	34.5
FP3	DS4000-PhC	97	26.7	33.2
FP4	v3.2	929	37.1	267.3
FP4	DS4000	929	37.1	268.5
FP4	DS4000-PhC	929	37.1	267.7
FP1	v3.2	111	20.8	130.3
FP1	DS4000	111	20.8	130.3
FP1	DS4000-PhC	111	20.8	130.3

There is no difference in the FP1 spectra, as we can from the Table 2.15 and the Fig. 2.30. Following the implementation of the new phase algorithm in the DS4000 database, we find that the number of spectra that are now return from this query in FP3 is significantly reduced by a factor of 10 and therefore we have lower Signal-to-Noise ratios in our spectral averages. Figs. 2.28, 2.29 and 2.30 below depict the comparison between the two DS4000 versions in each focal plane. I have not plotted the FP1 DS4000 differences because both spectral averages were identical.

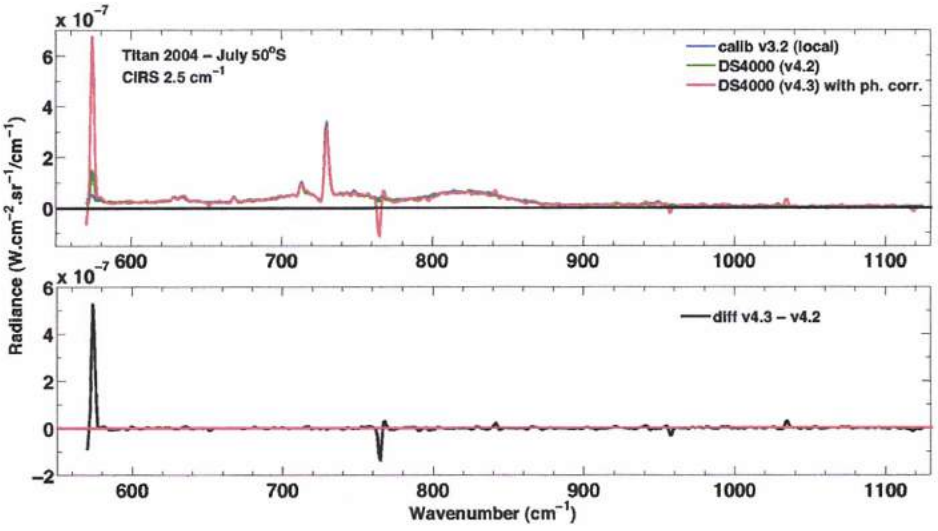

Fig. 2.28: FP3 averaged spectra from CIRSFRANCE. The upper panel shows the results of the database editions (local calibration in blue, DS4000 in green and the new DS4000 with the phase correction algorithm in red). The lower panel shows the difference between the two DS4000 versions (black).

The new algorithm produces higher radiances at 570 cm^{-1} compared to the nominal version, and negative radiances at around 765 cm^{-1}. Negative radiances are also found at around 960 cm^{-1}.

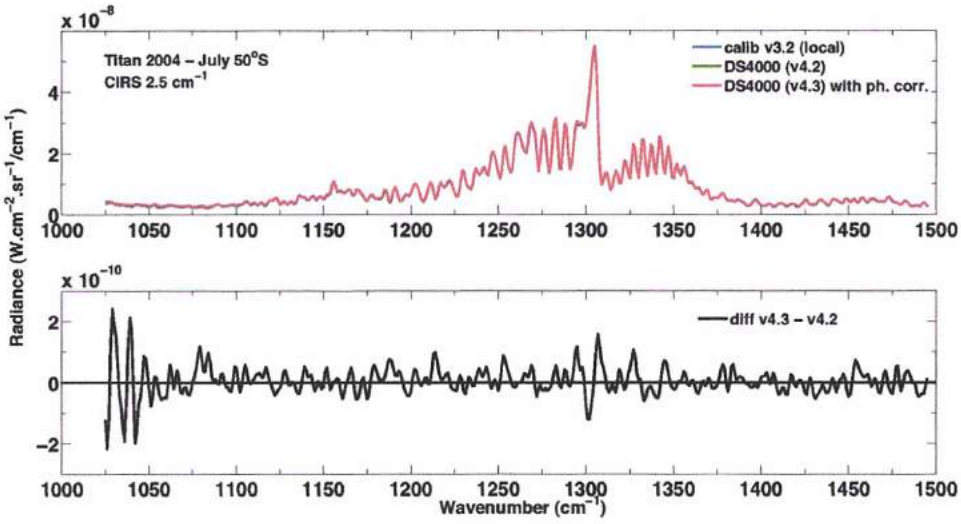

Fig. 2.29: FP4 averaged spectra from CIRSFRANCE. The upper panel shows the results of the database editions (local calibration in blue, DS4000 in green and the new DS4000 with the phase correction algorithm in red). The lower panel shows the difference between the two DS4000 versions (black).

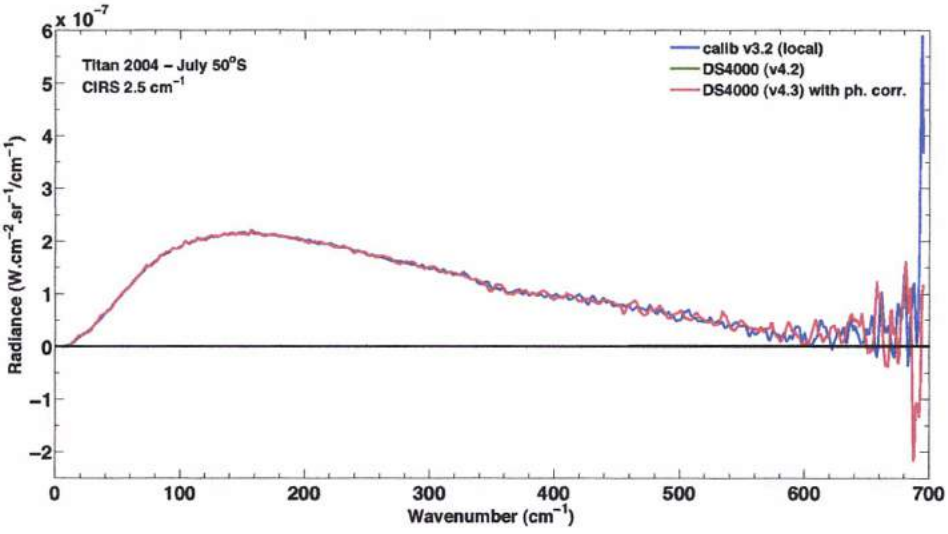

Fig. 2.30: FP1 averaged spectra from CIRSFRANCE. The upper panel shows the results of the database editions (local calibration in bleu, DS4000 in green and the new DS4000 with the phase correction algorithm in red).

The T23 and T24 flybys of Titan took place in January 2007. Table 2.17 below lists the characteristics of this query in each database. As previously, all queries have been restricted to emission angles less than 65°, focused on equatorial latitudes, the spacecraft range was restricted from 100 to 400,000 km and all longitudes were accepted. I now focus on the northern latitudes at 50°N. The number of spectra as well as the emission angles are the same in all database editions, while the Signal-to-Noise ratio values slightly differ.

Table 2.17: January 2007, 50°N, 0.5 cm^{-1}. As far as the recorded number of spectra are concerned as well as the emission angles, there are no difference. Any differences in the Signal-to-Noise ratios are insignificant.

Focal Plane	CIRSDATA version	Number of spectra	Emission angle	Signal-to-Noise ratio
FP3	v3.2	545	23.0	24.7
FP3	DS4000	545	23.0	24.2
FP3	DS4000-PhC	545	23.0	24.2
FP4	v3.2	356	3.9	30.3
FP4	DS4000	356	3.9	30.7
FP4	DS4000-PhC	356	3.9	30.7

The following Figs. 2.31 and 2.32 show the comparison of these three database inferences for the January 2007 50°N query.

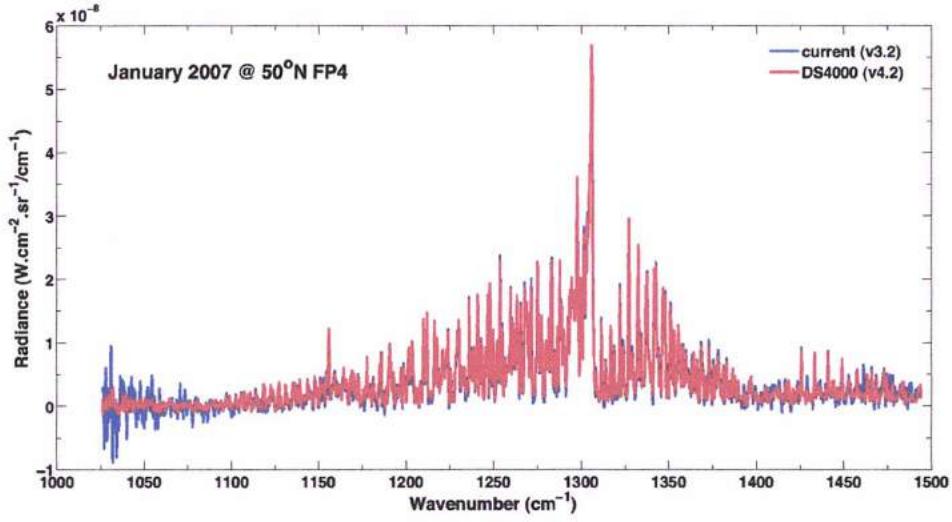

Fig. 2.31: Comparison between the current v3.2 database (blue) and the DS4000 one (red) FP4 averaged spectra of January 2007 at 50°N from CIRSDATA. The deep space calibration eliminates the noise in the continuum.

The continuum of this selection in its v3.2 version suffers from negative radiances below 1000 cm^{-1} (Fig. 2.31) while, in the DS4000 database inference these spectral features do not exist.

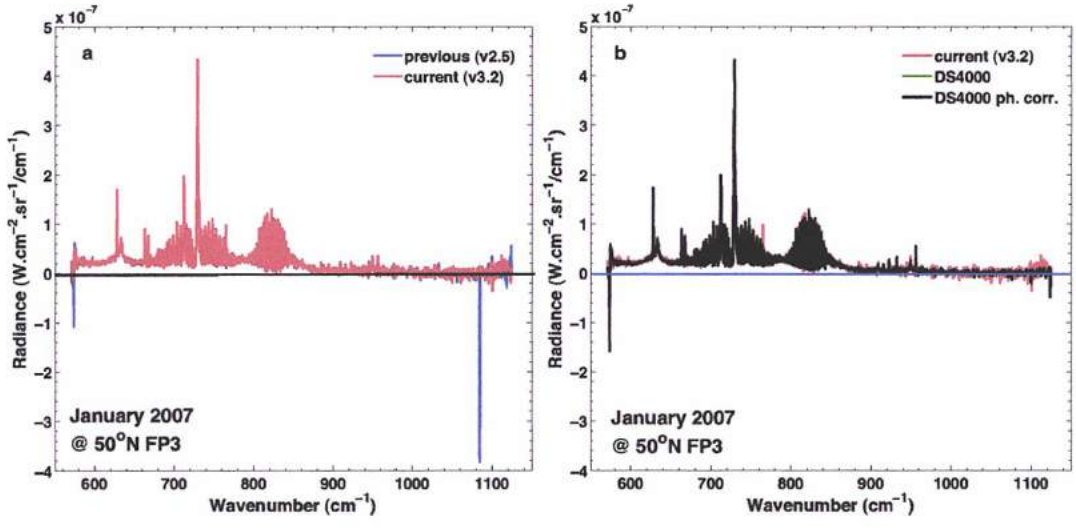

Fig. 2.32: Plot of the FP3 averaged spectra of January 2007 at 50°N from CIRSDATA. (a) Comparison between the previous edition v2.5 database (blue) and the current v3.2 database (red). Negative radiances and spike from 570 to 574 cm^{-1} as well as the spike at 1085 cm^{-1} have been vanished in the current edition. (b) Comparison between the current v3.2 database (red), the nominal DS4000 database (green) and the DS4000-PhC database (black).

The spike at 573 cm^{-1} appears again in deep space calibration data. Negative radiance from 1000 to 1100 cm^{-1} still exists, but the problem with the bad pixel at 765 cm^{-1} has been fixed. DS4000 and the DS4000-PhC are exactly the same and there is a question concerning the extent of the phase correction algorithm application in the DS4000. I ran our radiative transfer code in order to fit the data of these three database inferences. The fits of ethane are plotted in Fig. 2.33.

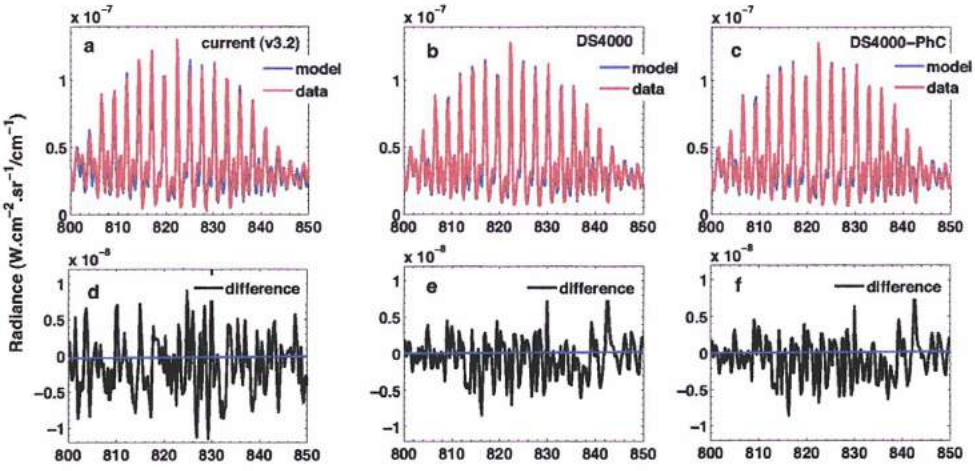

Fig. 2.33: Fits of the C_2H_6 signature in each database extract. The model is depicted in blue, while the data are in red. The panels a, b, c show the fit plot versus data of current (v3.2), DS4000 and DS4000 phase corrected database, while the panels d, e and f show the corresponding differences between model and data. As it is shown in the difference plot, ethane is fitted better using the DS4000 spectral averages.

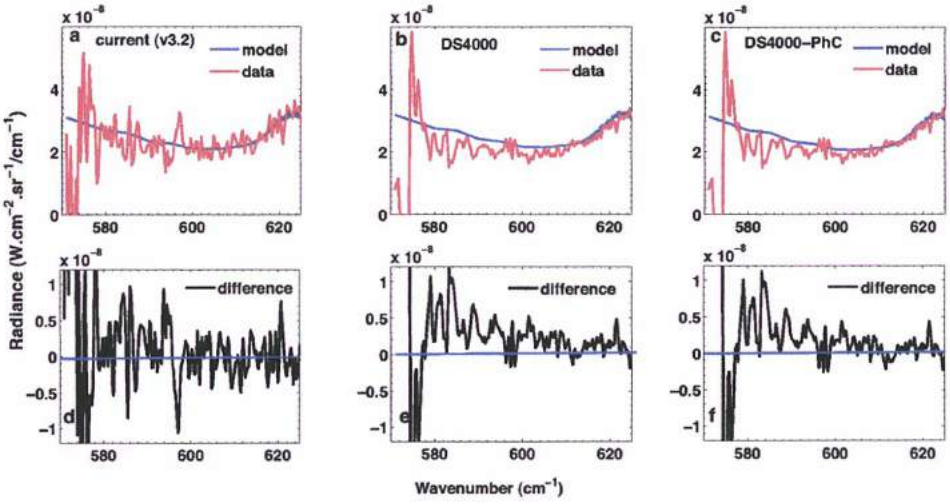

Fig. 2.31: Fits of the continuum at FP3 spectra in each database extract. The model is depicted in blue, while the data are in red. The panels a, b, c show the fit plot versus data of current (v3.2), DS4000 and DS4000 phase corrected database, while the panels d, e and f show the corresponding differences between model and data. The continuum is better calibrated with the DS4000 editions.

The abundances from the best-fit process for the 5 major molecules of the FP3 spectral region from the fit of the three inferences (DS4000-PhC, DS4000 and v3.2) are listed in the Table 2.18 below.

Table 2.18: The abundances of the major molecules as derived by applying our radiative transfer code in FP3 January 2007 averaged spectra at 50°N (0.5 cm^{-1}).

CIRSDATA	C_2H_2	C_2H_6	C_3H_4	C_4H_2	HCN
v2.5	2.5×10^{-6}	1.07×10^{-5}	2.0×10^{-8}	9.5×10^{-9}	5.8×10^{-7}
v3.2	2.8×10^{-6}	1.13×10^{-5}	2.1×10^{-8}	9.8×10^{-9}	6.0×10^{-7}
DS4000	2.6×10^{-6}	1.05×10^{-5}	1.9×10^{-8}	1.0×10^{-8}	5.8×10^{-7}
DS4000-PhC	2.8×10^{-6}	1.05×10^{-5}	1.9×10^{-8}	1.0×10^{-8}	6.0×10^{-7}

Ethane is better fitted with using the DS4000 inferences (Fig. 2.32). Ethane's abundance is slightly higher at about 5% using v3.2 to our calculations than using the rest databases, but located within the error bars. The rest molecules have similar mixing ratios using all the databases. The DS4000 database optimizes the continuum (Fig. 2.34). The differences between v2.5 and DS4000 for this selection are comparable to the January 2010 spectra (Table 2.10).

2.4 Conclusions

I have had the opportunity get access to the most recent CIRS databases, which are significantly improved, with respect to what was before and validate them. I have used five CIRSDATA editions: the current pipeline v3.2 and the previous v2.5, which have been locally calibrated, and the DS4000 and the phase corrected DS4000, with deep space calibration. Additionally, I also validated the Grand Average database, which employs deep space and shutter-closed interferograms for calibration averaged over several years.

To begin with the latter, the Grand Average calibration shows a better continuum level before 600 cm^{-1}, compared to the DS4000 and 1.5 to 2 times higher continuum between 600-890 cm^{-1}. It also diminishes the negative radiances, successfully. However, the Grand Average still contains spikes. Instead, most of the spikes are removed in DS4000. The derived abundances for the major molecules in the FP3 in Grand Average are higher on the order of 15-20% compared to the DS4000. Eventually, the Grand Average test database is still significantly different from DS4000 and yields higher abundances.

The DS4000 calibration of CIRSDATA is a large improvement with despiking. Indeed, the DS4000 version diminishes in several cases the noise in the continuum around 570 and 1050 cm^{-1} and fixes the bad pixel problem at 765 cm^{-1}. The abundances between DS4000 and the v3.2 are the almost the same in recent queries and their continuum levels have no differences. The retrieved abundances using DS4000 are more accurate compared to the v3.2 ones. The model shows that the shift I had to apply to my radiative transfer code calculations is smaller than the one in v3.2 and gives a better line shape.

However, when using old data queries, DS4000 has higher abundances and higher continuum level compared to the v3.2 (and the v2.5). The spike at 573 cm^{-1} appears again in DS4000 calibration data, although it has been vanished in current pipeline with local calibration in some cases. Moreover, DS4000 still suffers from ripples.

The new DS4000-PhC version of CIRSDATA, with respect to DS4000, reduces the negative radiances. In our radiative transfer simulations, the derived abundances have no significant variation comparing to the nominal DS4000 edition. However, ripples exist in several spectral selections. There is a question if the new phase correction algorithm has been applied to the entire DS4000 database, since the queries in some selections from the two DS4000 versions are identical.

I recommend the phase-corrected DS4000 database in future studies of Titan CIRS data for all users. If the newest database is not available, the DS4000 is still an improvement with respect to the v3.2.

Chapter 3

The Titan Atmospheric Model

This chapter introduces the fundamentals of the radiative transfer theory and the tool I use to model the stratosphere of Titan. It is a radiative transfer code that has been used in the past for retrievals of the thermal and chemical structure of Titan by the analysis of Voyager, ISO and Cassini data. I describe here the code upgrade we made in order to analyze the recent Cassini results using the latest laboratory spectroscopic line lists and advances in haze modeling. The simulations produced by this code are compared with the actual CIRS data to derive the abundances of the atmospheric constituents, which are given in the next chapter. I discuss here the inferences of the temperature profiles we need to extract first and how they are used to retrieve the atmospheric chemical composition. All the assumptions will be also defined.

3.1 The structure of Titan's atmosphere

Titan is the only planetary body of the Solar System, except for the Earth, that possesses a thick, nitrogen-dominated atmosphere (which creates a pressure of about 1,5 bar at the surface). On Titan, methane is the second most abundant atmospheric species with a mixing ratio of 2.19 ± 0.002 in the upper atmosphere (Waite et al., 2005), 1.6 ± 0.5 in the stratosphere (Flasar et al., 2005), $1.48 \pm 0.09\%$ in the lower stratosphere (139.8 - 75.5 km) and 5.65 ± 0.18 near the surface (6.7 km to surface) (Niemann et al., 2010). The interaction with the solar influx, the combination and dissociation of these two mother constituents initiates complex photochemical reactions in the upper atmosphere, which enrich the organic inventory of the satellite. Some of these organics condense and form a thick haze layer of aerosols covering the satellite globally or partially. The mixing ratios of these gases vary as a function of altitude, latitude and longitude and also time, due to atmospheric circulation. Titan is a cold environment, located at 10 AU and receiving 100 times less energy from the Sun, compared to the Earth.

Titan's temperature profile was first determined extensively by Lindal et al. (1983) from egress and ingress radio-occultation observations by Voyager 1. Its temperature

structure was shown to resemble the terrestrial one, divided into regions with a clearly defined tropopause, stratopause and mesopause. As in the Earth, the temperature profile of Titan's atmosphere shows inversions, caused by local heating. The mid-atmospheric heating source in the Earth is the stratospheric ozone layer, while the haze layer in Titan plays such a role. Both of these heat the local atmosphere by absorbing solar energy and give local temperature maximum (Coustenis & Taylor, 2008).

The Huygens probe obtained, among other, Titan's vertical atmospheric thermal structure during its descent in January 2005, before landing at 10.3°S and 192.3°W (Lebreton et al., 2005). The Huygens Atmospheric Structure Instrument (Fulchignoni et al., 2002) measured the deceleration of the probe from 1400 to 155 km and determined the atmospheric mass density. By assuming that the atmosphere is in hydrostatic equilibrium, the pressure profile can be inferred. Then, by considering the atmosphere at these levels as a perfect gas and assuming a value for the atmospheric mean molecular weight, the temperature as a function of altitude is derived.

At the altitude of 155 km, Huygens released its protection shield and HASI measured directly the atmospheric pressure and temperature by using its sensors from this level down to the surface by better than 1 K accuracy (Fulchignoni et al., 2005). The density and temperature profile derived from HASI is depicted in Figure 3.1 from the surface up to 1380 km.

HASI showed that Titan has a well-defined tropopause at about 44 km with 70.43 K. The HASI temperature measurements for this region are in agreement (1-2 K) with the Voyager measurements (Lindal et al., 1983). The stratopause is located at the altitude of 265 km with 188 K, 13 K warmer than the Voyager IRIS results. The mesopause has been identified at 494 km with 153 K. In this region, the temperatures are 5-10 K higher than the model predictions (Yelle et al., 1997). For altitudes over 500 km and up to 1020 km, which is the thermosphere, HASI shows temperatures variations of around 170 K (varying within ±10-15 K), caused by inversion layers, dynamic phenomena like gravity waves and graviational tides (Fulchignoni et al., 2005). In this part of the atmosphere, the HASI density measurements are higher by a factor of 2 compared to the re-interpretation of Voyager solar occultation measurements (Vervack et al., 2004).

Figure 3.1 also illustrates the engineering model based on Voyager data of Yelle et al. (1997) as well as the measurements of the Voyager radio occultation experimented revisited by Lellouch et al. (1989). No considerable difference exists from the surface up to an altitude

of 200 km among these models. The HASI temperature profile from 200 km and upwards shows occultations growing in amplitude.

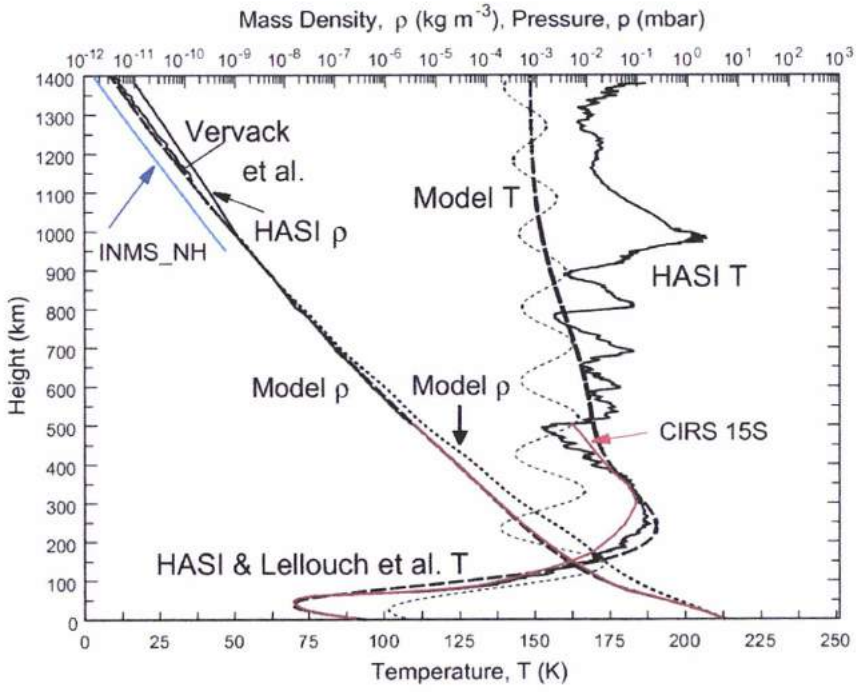

Figure 3. 1 - HASI density and temperature profile. The Yelle et al. (1997) (dashed line) and the Lellouch et al. (1989) Voyager radio occultation data are also shown for comparison (adapted from Strobel (2010). CIRS retrieved temperature profile from the T3 Cassini Titan flyby is plotted (red solid curve) (Flasar et al., 2005). INMS density results are also shown (blue solid line)(Muller-Wodarg et al., 2008).

Titan's atmosphere is more extensive than the atmosphere of the Earth and its exosphere begins much higher. Indeed, the homopause level is located at 1,195±65 km according to Cassini/INMS mass spectrometer results from TA flyby (80-90 km on Earth), while the exobase is found to be at 1429±5 km (Waite et al., 2005) (400-500 km on Earth).

3.1.1 The Troposphere

The troposphere, the atmospheric part which lays above the surface, has a negative temperature vertical gradient. HASI measured the surface temperature at 93.65 ± 0.25 K (Fulchignoni et al., 2005). Only 10% of the incoming solar radiation reaches Titan's surface. The other solar photons are scattered by haze and cloud layers. Part of this scattered radiation is reflected back to space, while some of it is absorbed by the aerosols and the atmospheric gases (Coustenis & Taylor, 2008). The surface absorbs the incident radiation and heats the lower atmosphere, producing atmospheric convection depending on the local temperature gradient.

The infrared emission of the surface heats the lower tropospheric layers, which become less dense than the colder layers above. The density difference produces vertical movement of the atmospheric layers and the hotter layers rise, while the colder fall. The convection does not occur when the temperature gradient is shallow and it is only possible when the gradient value reaches the adiabatic lapse rate. For Titan, this rate is at 1.4 K/km.

Such convective instabilities occur in the lower part of optically thick atmospheres. In the upper part of the atmosphere, the density becomes quite low due to radiative cooling caused by infrared emission to the space and reduces the temperature. The temperature gradient becomes sub-adiabatic and the convection stops. Titan's troposphere reaches a minimum of 70.43 K at 44 km with a pressure of 115 ± 1 hPa (Fulchignoni et al., 2005). In this level, a temperature inversion occurs and the stratosphere begins.

3.1.2 The Stratosphere

The lower part of Titan's stratosphere is quasi-isothermal near the altitude of 50 km. No absorption occurs in the lower stratosphere, above the tropopause, and the temperature lapse rate is almost zero, which indicates that the temperature is constant with height. In the mid and upper Titan's stratosphere, similar to Earth's, the temperature increases with the altitude. From 50 km to 300 km, the temperature increases due to the heating caused by the absorption of UV and visible solar radiation.

In Titan's stratosphere, the temperature has a high static stability with a lapse rate at about 1K/km. The convection stops and the atmosphere is stratified in layers, which are mixed. On Earth, the ozone layer is the main absorber and the heating source of the stratosphere. On Titan, aerosols and methane are the main radiation absorbers. The aerosols, the methane, the acetylene and the ethane re-emit isotropically in infrared wavelengths and this mechanism cools the stratosphere, balancing the solar heating. The temperature reaches a maximum value of 186 K at the altitude of 250 km, as derived from HASI measurements (Fulchignoni et al., 2005), which defines the location of the stratopause.

Cassini/CIRS also retrieved the atmospheric temperature from remote sensing probing. Its results are not consistent with HASI measurements about the location of the stratopause which CIRS places at about 312 with 183 K (Flasar et al., 2005; Vinatier et al., 2007a). This difference is illustrated in Figure 3.1. This discrepancy and how it affects radiation transfer calculations is discussed in Section 3.2 below.

3.1.3 The Mesosphere

Above the stratopause, the temperature decreases again with the altitude and it reaches a minimum of 152 K at 490 km, the mesopause (Fulchignoni et al., 2005). In this region, HASI measured perturbations due to dynamic phenomena and inversion layers. Between the tropopause and the mesopause, the atmosphere remains fairly well mixed by turbulence produced by a variety of instabilities in wave motions and the mean flow (Coustenis & Taylor, 2008).

3.1.4 The Thermosphere

Above the mesopause, the atmospheric temperature rises up to the exobase due to the absorption of solar EUV from nitrogen, methane and acetylene (Lellouch et al., 1990). In these altitudes, the pressure values are a few microbars and gas densities are quite low. The solar EUV photons as well as energetic particles from the Saturnian magnetosphere, pass through this layer, causing ionization, dissociation of the molecules and releasing kinetic energy. Such mechanisms heat the gas and the temperature gradient increases rapidly with height.

The thermosphere is the most extensive part of the atmosphere, in which the energy is transported by thermal conduction. Diffusion is the dominant process and the atmosphere starts to separate into its lighter and heavier components.

3.2 HASI and CIRS temperature profiles determinations and discrepancies

Two separate instruments of the Cassini-Huygens mission have retrieved the vertical temperature profiles of Titan's stratosphere. CIRS on board the Cassini orbiter senses remotely the emitted infrared radiation during Cassini Titan flyby. HASI on board the Huygens probe measured *in situ* the temperature during its descent following the procedure described previously. The HASI data correspond to the Huygens trajectory through the atmosphere near the equator. Instead, CIRS profiles are retrieved remotely from recordings that correspond to different latitudes.

CIRS temperatures profiles are retrieved from an inversion method, which is described in Appendix A. In brief, the temperature profile is retrieved by using the methane v_4 band at 1304 cm^{-1} as a thermometer in the stratosphere. Methane's mole fraction versus altitude is well known from Huygens/GC-MS *in situ* measurements from the surface up to about 140 km (Fig. 3.2) and we adopt it to retrieve the temperature (Niemann et al., 2010).

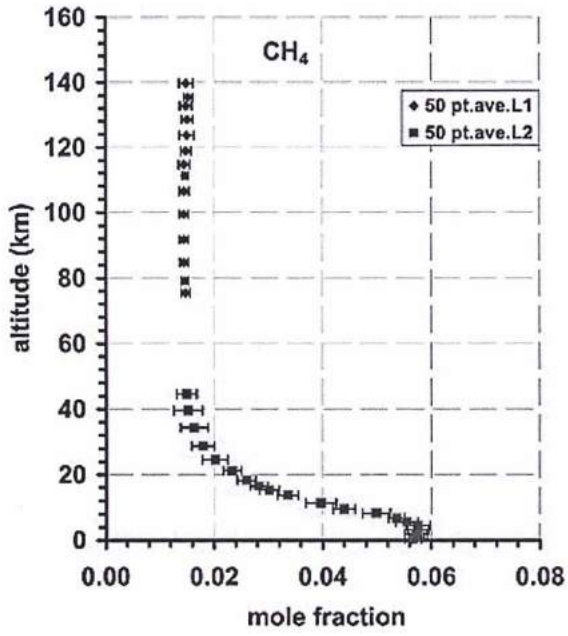

Figure 3. 2 -Methane mole fraction as measured in situ by GC-MS during Huygens descent (adapted from Niemann et al. 2010). With blue diamonds leak L1 data are depicted, while with red squares leak L2 data are plotted.

By introducing the FP4 CIRS spectra into an inverse algorithm (Achterberg et al., 2008; 2011), we retrieve the temperature profile related to each CIRS selection of interest. This algorithm solves the radiative equation, which is an inverse ill-posed problem, by considering a reference temperature profile for optimizing the results as the initial guess. Two are the main profiles used as the original guess in the retrievals, the one derived from Huygens/HASI (Fulchignoni et al., 2005) and the second retrieved from Cassini/CIRS T3 Titan flyby (Flasar et al., 2005) (Fig. 3.1). The HASI profile is a result of *in situ* measurements during the Huygens probe descent. From 1400 km down to 155 km, the temperature was retrieved indirectly from the acceleration measurements and by assuming hydrostatic equilibrium and an ideal gas state for this atmospheric region.

Below 155 km and after the thermal shield release, HASI measured directly the temperature and the pressure by using sensors exposed to the environment. CIRS T3 profile at 15°S was retrieved from a combination of CIRS nadir and limb-viewing spectra. Voyager radio-occultation data (Lindal et al., 1983) as well as radiative mesospheric models (Yelle, 1991) were used as the initial guess in order to interpolate the values between nadir and limb spectra (5-60 mbar) (Flasar et al., 2005). Since HASI data were obtained by in situ measurements, its results should be considered as reliable for the equatorial latitudes.

3.2.1 The stratopause temperature and level discrepancy between CIRS and HASI observations

The CIRS temperature profile retrieval at 15°S from T3 flyby is close to the HASI landing date and descent path but it does not agree in the upper stratosphere with the HASI results (Fig. 3.1). HASI shows a hotter stratosphere than CIRS, with the stratopause located at about 250 km at 186 K (Fig. 3.3). The CIRS profile locates the stratopause higher at 316 K with 183 K (Flasar et al., 2005).

The cause of this discrepancy remains unsolved. I spent, however, some time at the beginning of my PhD interacting with both with the CIRS and the HASI team (Prof. M. Fulchignoni and Dr. F. Ferri) and with the help of Dr. D. Strobel, trying to shed some light to this problem. We also discussed the Huygens probe descent parameters with ESA representatives, among which J-P. Lebreton and P. Couzin from Thales Alenia Space, ESA's prime contractor for building the Huygens probe.

The HASI temperature at this level being 185 K, leads to a computation of the infrared radiance with the HASI derived atmosphere inconsistent with the observed CIRS radiance of the 7.7 μm methane band (Lebreton et al., 2009; Strobel et al., 2009). The methane v_4 band probes the 150-350 km region, around the stratopause and the HASI profile is too warm.

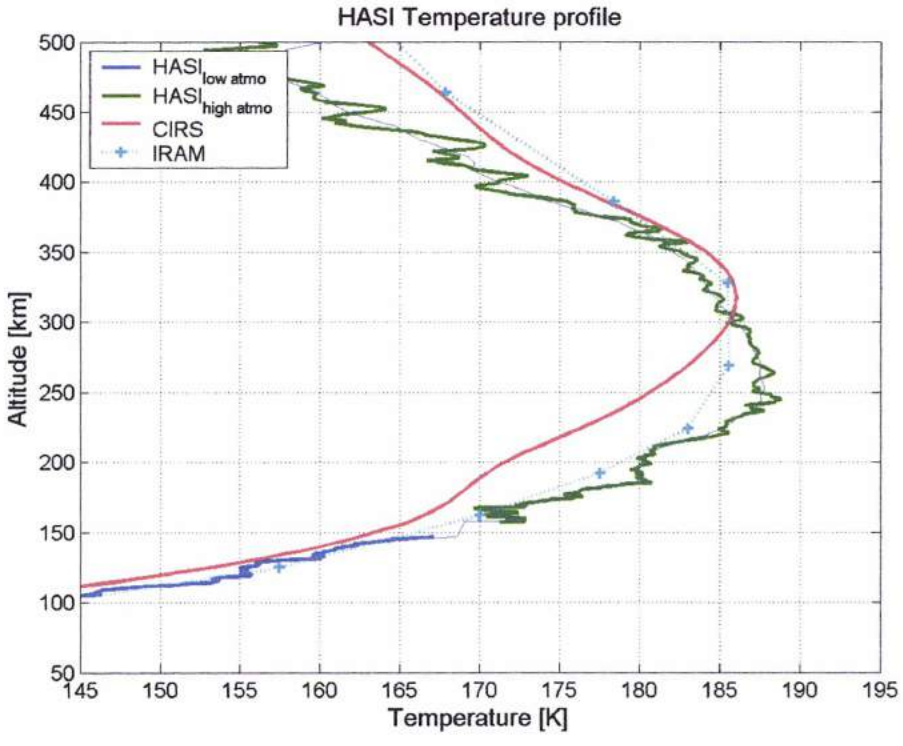

Figure 3. 3 - Stratopause location: Comparison among HASI CIRS and IRAM (credit F. Ferri).

We also have ground-based observations in the submillimeter range, from the Institut de Radio Astronomie Millimétrique (IRAM)/Plateau de Bures telescope that can help in this problem. IRAM heterodyne measurements inferred a temperature profile sounding altitude range from 80 to 800 km at very high spectral resolution. Carbon monoxide line wings probe the Titan atmosphere from 80 to 180 km (Hidayat et al., 1998) and at these levels the HASI profile is similar with the IRAM one, while the CIRS one is too cold (Fig. 3.4). Hydrogen cyanide lines probe higher altitudes (300-500 km in the center and 100-200 km in the wings) (Hidayat et al., 1997) and the HASI profile is too cold.

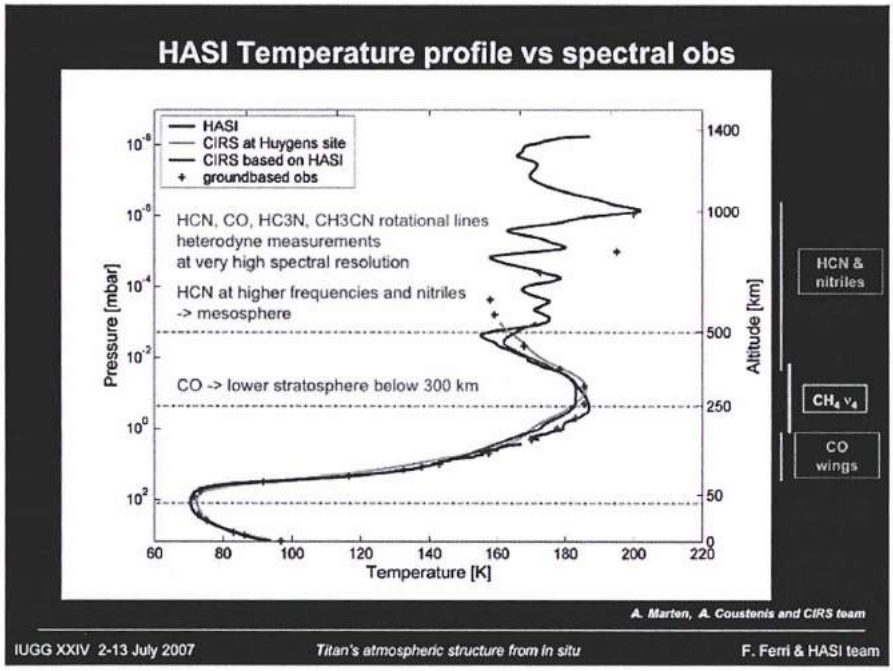

Figure 3. 4 - Comparison of HASI temperature profile and CIRS and ground based observations (credit F. Ferri).

In conclusion, without having solved the problem, we can say that the HASI near-equator data directly sounding the lower atmosphere are the more reliable, while at higher altitudes, where HASI only indirectly infers the temperature, CIRS inferences may be the correct ones.

3.2.2 Impact of the original assumption in the temperature calculations

In order to deal with the question of how the radiative transfer calculations are affected by the choice of the initial profile in temperature retrievals, I have performed radiative transfer calculations on the same CIRS data FP3 and FP4 queries. I have selected 4 queries from CIRSDATA, two at equatorial latitudinal bins and two at 50°N. Since HASI data were obtained at 10°S, the application of CIRS T3-based temperature profile at equatorial selections can give an estimation of the temperature profile influence to the resulted abundances. On the other hand, I ran the same test in northern selections where the stratospheric temperatures are indeed lower compared to the equatorial ones. Table 3.1 below lists the characteristics of the selections used in these tests.

Table 3. 1 - List of CIRS queries used for estimation of the effect of different temperature profiles in radiative transfer calculations. All selections refer to high resolution spectra (0.5 cm^{-1}).

Focal Plane	Year	Month	Latitude	Total number of spectra	Signal-to-noise	Airmass	Cassini Flyby	Ls (°)
FP3	2008	Feb-Mar-Jul	50°N	145	12.4	1.19	T41-T45	341-347
FP4	2008	Feb-Mar-Jul	50°N	166	12.8	1.14	T41-T45	341-347
FP3	2010	Jan	50°N	284	21.3	1.69	T65-T66	005-006
FP4	2010	Jan	50°N	234	27.6	1.66	T65-T66	005-006
FP3	2009	Mar-Jul	0°	86	18.3	1.75	T51-T59	355
FP4	2009	Mar-Jul	0°	84	39.2	1.71	T51-T59	355
FP3	2010	Sep	0°	1504	50	1.2	T72	014
FP4	2010	Sep	0°	1622	136.9	1.01	T72	014

The retrieved temperature profiles for each selection, using both HASI and CIRS-T3 profiles as the initial guess, are illustrated in Figure 3.3. (R. Achterberg has provided all temperature profiles by my request).

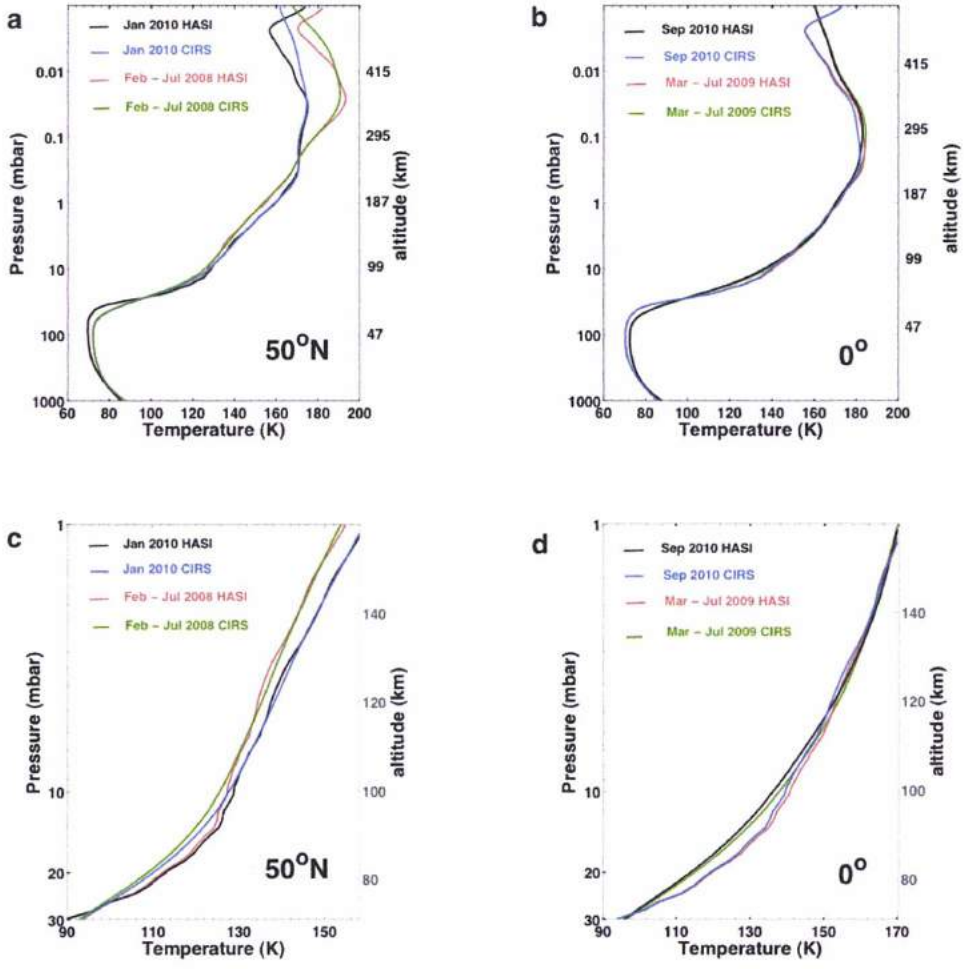

Figure 3. 5 - Temperature profiles retrieved by assuming both HASI and CIRS-T3 profiles as the initial guess. The lower panel (c, d) focuses on the 1-30 mbar region.

The HASI-based temperature profiles (Fig. 3.5 a, b) in the region of 1 to 10 mbar show slight variations compared to the relative CIRS-based ones. Below 10 mbar (Fig. 3.5 c, d), the HASI-based profiles are hotter than the CIRS ones by 5 K. Tables 3.2 and 3.3 below list the retrieved abundances when using these profiles and their difference at 50°N and equator respectively.

Table 3. 2 - Retrieved abundances by using both CIRS- and HASI- based profiles for two queries at 50°N.

Molecule	FEB 2008 CIRS-based	FEB 2008 HASI-based	Difference HASI vs CIRS	JAN 2010 CIRS-based	JAN 2010 HASI-based	Difference HASI vs CIRS
CO_2	$1.73x10^{-8}$	$1.80x10^{-8}$	4%	$1.60x10^{-8}$	$1.55x10^{-8}$	-3%
C_2H_2	$4.70x10^{-6}$	$5.60x10^{-6}$	19%	$5.30x10^{-6}$	$6.30x10^{-6}$	19%
C_2H_4	$1.90x10^{-7}$	$2.00x10^{-7}$	5%	$2.30x10^{-7}$	$2.30x10^{-7}$	0%
C_2H_6	$1.20x10^{-5}$	$1.27x10^{-5}$	6%	$1.35x10^{-5}$	$1.35x10^{-5}$	0%
C_3H_4	$1.80x10^{-8}$	$1.82x10^{-8}$	1%	$1.18x10^{-8}$	$1.17x10^{-8}$	-1%
C_4H_2	$9.50x10^{-9}$	$9.50x10^{-9}$	0%	$5.50x10^{-9}$	$5.40x10^{-9}$	-2%
HCN	$9.50x10^{-7}$	$1.20x10^{-6}$	26%	$9.00x10^{-7}$	$1.50x10^{-6}$	17%

Table 3. 3 - Retrieved abundances by using both CIRS- and HASI- based profiles for two queries at equator.

Molecule	MAR-JUL 2009 CIRS-based	MAR-JUL 2009 HASI-based	Difference HASI vs CIRS	SEP 2010 CIRS-based	SEP 2010 HASI-based	Difference HASI vs CIRS
CO_2	$1.41x10^{-8}$	$1.41x10^{-8}$	0%	$1.44x10^{-8}$	$1.44x10^{-8}$	0%
C_2H_2	$3.15x10^{-6}$	$3.20x10^{-6}$	2%	$3.90x10^{-6}$	$4.00x10^{-6}$	3%
C_2H_4	$1.30x10^{-7}$	$1.20x10^{-7}$	-8%	$1.40x10^{-7}$	$1.30x10^{-7}$	-7%
C_2H_6	$9.60x10^{-6}$	$9.30x10^{-6}$	-3%	$9.80x10^{-6}$	$9.50x10^{-6}$	-3%
C_3H_4	$6.30x10^{-9}$	$6.20x10^{-9}$	-2%	$8.30x10^{-9}$	$8.20x10^{-9}$	-1%
C_4H_2	$1.10x10^{-9}$	$1.00x10^{-9}$	-9%	$1.00x10^{-9}$	$9.40x10^{-10}$	-6%
HCN	$1.80x10^{-7}$	$1.55x10^{-7}$	-14%	$2.10x10^{-7}$	$1.60x10^{-7}$	-24%

At mid-latitudes all molecular abundances are within 10%, except for HCN, with the CIRS-based profile generally giving higher abundances. This is expected, because the HASI profile was inferred above the Huygens landing site, which was at 10°S. In the northern latitudes, the divergence depending on the profile is more pronounced, with most of the molecular abundances still within 10% whatever the temperature profile. Only the emission bands of C_2H_2 and HCN are more affected by the temperature variation as expected, still within the 20% level, since the HASI original assumption gives rise to higher abundances.

3.3 The opacity sources on Titan

Voyager 1 observations showed that the main infrared opacity sources of the Titan's atmosphere are the main molecules' absorption, N_2, CH_4 and H_2. Usually symmetrical atoms like N_2 do not interact with the infrared radiation field due to the fact that they lack dipole moment. However, at longer wavelengths collisions between these molecules produce a temporal dipole moment and therefore opacity (Coustenis & Taylor, 2008). The trace gaseous species also contribute to the infrared opacity of the atmosphere (Fig. 3.6).

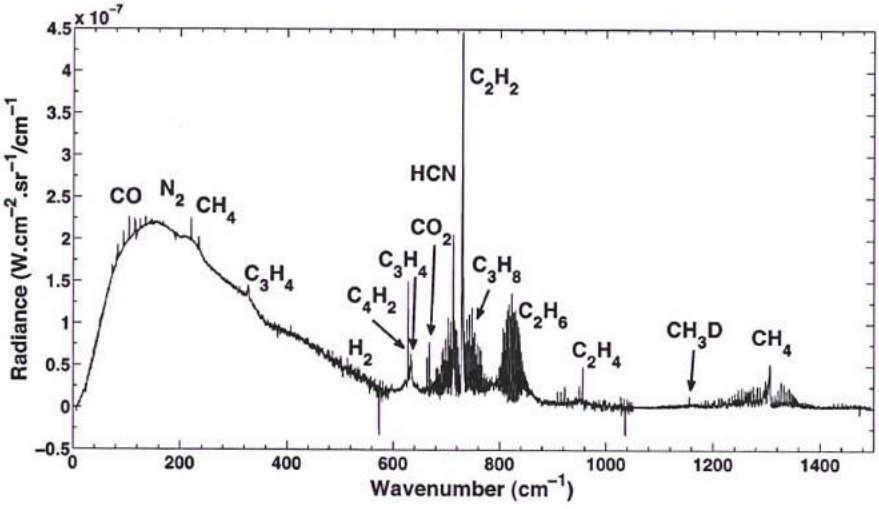

Figure 3. 6 - A complete composite averaged CIRS spectrum of 2007 flybys (T23-T39) at high resolution (0.5 cm^{-1}) at 50°N. The positions of the major molecules and trace gases are illustrated in the figure.

The continuum of the spectrum is influenced by two factors essentially: (a) the temperature of the surface and the troposphere and (b) the haze opacity in the troposphere and the stratosphere caused by the aerosols (Coustenis et al., 2007). The temperature is adjusted from an initial guess profile and the surface temperature is considered to be at 93.7 K according to Huygens/HASI *in situ* measurement after the probe's touchdown (Fulchignoni et al., 2005) at 10°S. CIRS brightness measurements at 19 μm showed that the surface temperatures in North pole is 3 K lower and at the South pole 2 K lower, compared to the equatorial one (Jennings et al., 2009).

The aerosols are the end product of the complex photochemistry that occurs on Titan's upper atmosphere and they strongly affect the thermal balance of the entire satellite. They are the main heating source of the stratosphere, since they absorb the 40-60% of the sunlight, depending on the altitude, as measured by the Huygens/DISR (Tomasko et al., 2008a). V1/IRIS measurements provided the aerosol distribution between the tropopause at 40 km and

the upper stratosphere at 300 km (Samuelson & Mayo, 1991). They showed that the stratospheric opacities increase monotonically with the wavenumber from 250 to 600 cm^{-1}. According to experimental results, aerosols are dark in the visible and bright in the infrared (Ramirez et al., 2002). DISR measured directly the haze particles' vertical distribution from the altitude of 150 km down to the surface (Tomasko et al., 2005).

As Cassini approaches Titan during each flyby, its radial component of the velocity is negative, it goes to zero at closest approach, and then it becomes positive. For a nadir viewing geometry this should, in theory, produce a Doppler shift on the observed CIRS spectra. It is probably a very small effect, but the question is if we can give an evaluation of it.

After personal communication with Dr. C. Nixon from Goddard/NASA, we evaluated the Doppler effect and came to the conclusion that is probably too small to significantly affect CIRS results. A rough estimation of the size follows below. Cassini approaches Titan at typically 20,000 km/h, or 5.5 km/s. The Doppler shift is defined as:

$$\frac{\Delta L}{L} = \frac{\Delta v}{c} = \frac{5.5}{3x10^5} \approx 2x10^{-5}$$

Thus, the shift is about 2 parts in 100,000, applied to frequency/wavenumber. For example, at 1000 cm^{-1} the shift should be about 0.02 cm^{-1}, but at 100 cm^{-1} would be 0.002 cm^{-1}, while the maximum would be about 0.03 cm^{-1} at 1500 cm^{-1}. However, larger wavenumber shifts have been noticed, likely due to other effects, they can be noticeable (~0.1 cm^{-1}) and should be corrected for empirically.

3.4 Radiative Transfer on Titan

The theory of radiative transfer is a quantitative assessment of the relation between the interactions of the matter with radiation (absorption, scattering and emission of radiant energy on a microscopic scale) and the resulting radiation field (Hanel et al., 2003). Atmospheric emission, which at planetary temperatures occurs mainly in the thermal-infrared part of the spectrum, depends on the composition and thermal structure of the atmosphere. Absorption and scattering mainly occur at ultraviolet, visible and near-infrared wavelengths and depend on the prevailing molecular opacity and on aerosol and cloud properties.

3.4.1 The radiative transfer process

The emission of an infrared source is described both by Planck's law and Kirchhoff's law. The former gives the radiant energy emitted by a black body at the same temperature and wavelength as the source, while the latter determines that the absorption of a body equals to its emissivity. The radiative transfer equation (RTE) describes how the optical properties of the medium are related to the spectrum we measure.

When we have a beam which passes through a medium, a portion is absorbed by the material due its physical properties and according to Kirchhoff's law the body should emit the same amount of heat as if it was a black body in the same temperature described by Planck's law. In physical terms, while a radiation with the intensity $I(\mu)$ passes through a path within a medium of a distance Δx, the medium absorbs a fraction of $\kappa \Delta x I(\mu)/\mu$ and emits a fraction of thermal radiation of $\kappa \Delta x B/\mu$ (Twomey, 2002) where μ is the cosine of the emission angle measured from the vertical, κ is the absorption coefficient of the medium and $B(\nu,T)$ represents the Planck radiance ($B(\nu,T) = \frac{2h\nu^3}{c^2}\frac{1}{e^{h\nu/kT}-1}$) at the frequency ν and the temperature T. Hence, the fraction of the total intensity which propagates through the medium can be written as:

$$\Delta I(\mu) = -I_{absorbed} + I_{emitted} = -\frac{1}{\mu}\kappa \Delta x I(\mu) + \frac{1}{\mu}\kappa \Delta x B$$

or

$$\mu \frac{\Delta I(\mu)}{\kappa \Delta x} = -I(\mu) + B$$

But since $\Delta\tau = \kappa\Delta x$, where τ is the optical depth of the influenced layer, the above equation takes the general form of the RTE:

$$\mu\frac{dI(\mu)}{d\tau} = -I(\mu) + B$$

Then, one can write this differential equation such as:

$$e^{\tau/\mu}\mu\frac{dI(\mu)}{d\tau} = e^{\tau/\mu}\left(-I(\mu) + B\right)$$

However, since $\frac{d\left(e^{\tau/\mu}I(\mu)\right)}{d\tau} = e^{\tau/\mu}\frac{dI(\mu)}{d\tau} + I(\mu)e^{\tau/\mu}\frac{1}{\mu}$ the RTE can be written as:

$$\frac{d\left(e^{\tau/\mu}I(\mu)\right)}{d\tau} = \frac{1}{\mu}e^{\tau/\mu}B$$

Then, by integrating both parts of the latter relation in respect to the optical depth, we derive:

$$\int_0^{\tau_o}\frac{d\left(e^{\tau/\mu}I(\mu)\right)}{d\tau}d\tau = \int_0^{\tau_o}B\frac{1}{\mu}e^{\tau/\mu}d\tau$$

The intensity of the radiation is the initial I_o when $\tau = 0$ at the level of emergence and $I=I(\tau_o)$ when $\tau = \tau_o$ at the level of emission and by applying these boundary values in the above integral equation we derive (Hanel et al., 2003):

$$I(\tau_o) = I_o e^{-\tau_o/\mu} + \int_0^{\tau_o}B\frac{d\tau}{\mu}e^{(\tau-\tau_o)/\mu} \quad (1)$$

Equation (1) describes the intensity of a propagating radiation through layered gaseous media such as planetary atmospheres. The first term of the second part of (1) corresponds to the surface contribution, while the second term depicts the atmospheric contribution.

The emerging radiation from the surface I_o is the fraction of the Planck function emission at the same temperature. According to the Beer-Lambert law, the transmittance of the atmosphere T_r can replace the exponential expression in (1). Therefore, following the above consideration, the spectral radiance measured remotely by the CIRS instrument is (Hanel et al., 2003):

$$I(\mu,\nu) = \varepsilon_\nu B(\nu,\mathrm{T}_s)T_r(\mu,\nu,z_s) + \int_{z_s}^{z_{top}}B(\nu,\mathrm{T}(z))\frac{\partial T_r(\mu,\nu,z)}{\partial z}dz \quad (2)$$

where μ=cosine of the emission angle and ν=frequency

Here, the term ε_v is the emissivity[8] of the surface at the temperature T_s. The altitude z can be derived by the equation $z = -\ln p$, where the atmospheric pressure is denoted by the symbol p. With the index "s" the surface level values are indicated. The z_{top} refers to the highest altitude from the surface where the atmospheric gases sense the recorded radiance. The transmittance T_r can also be written in the following form:

$$T_r(\mu,\nu,z) = \int_{\delta\nu} \phi(\nu,\nu') e^{-\tau(\nu',z)/\mu} d\nu' \quad (3)$$

The term $\phi(\nu,\nu')$ is the instrument spectral response function[9] extending over the spectral interval $\delta\nu$ with central number ν. By definition, the transmittance is the rate of the radiation, which passes a gaseous sample versus the incident one. The exponential expression in equation (3) comes from the Beer-Lambert law where τ is the optical depth.

On Titan, since the stratospheric haze absorbs most of the surface radiance, the first term of the equation (2) can be neglected. This assumption simplifies the equation (2) in the form (Hanel et al., 2003):

$$I(z,\mu) = \int_{z_s}^{z_{top}} B(\nu,T(z)) \frac{\partial T_r(\mu,\nu,z)}{\partial z} dz \quad (4)$$

It should be noted, however, that both scattering and surface reflection have been neglected in (2) and (4). Indeed, in the thermal part of the spectrum, where absorption and emission by atmospheric gases dominate and solar radiation is negligible, scattering processes can often be neglected and the solution becomes considerably simpler (Hanel et al., 2003).

3.4.2 The solution of the radiative transfer equation

In physical terms, the intensity of the radiation $I(\mu,\nu)$ of the equation (4) is known (the recorded data), while what causes it (the quantity in the integral) is unknown. Hence, the solution of the equation (4) provides the transmission of the absorbing gasses of the atmosphere related to the recorded radiation and, eventually, the composition of the probed atmospheric region as well as the thermal structure.

The problem is how to retrieve the atmospheric parameters from a set of measurements. The infrared data depends on the spectral range, the spectral resolution, the

[8] The emissivity is the ratio of the radiated energy by the surface to relative black body energy radiated (for the black body ε_v=1)

[9] The spectral response function determines the ability of an instrument to record radiation in a specific wavelength comparing to the one in another wavenumber where the response is unity. Practically, it evaluates the operational spectral range.

observational geometry and the signal-to-noise (*S/N*) ratio (Hanel et al., 2003). Several models have been proposed to solve equation (4). These solutions can be divided into two kinds:

a) To those which solve directly the equation (4) by producing a model which is then compared to the data and
b) To those which solve indirectly the relation (4) by importing the recorded data to an inversion algorithm.

The forward approach is the direct integration over the frequencies of equation (4) and the use of the fine parameters of the absorbing bands (Scott, 1974) to produce a synthetic model of the atmosphere. By assuming the abundances of the contributing species and following an iterative best-fit process, the model spectrum is fitted to the real data. Then, the atmospheric composition can be retrieved.

The inversion approach is an alternative tool that allows for the calculation of the values of atmospheric parameters from the recorded radiation intensities by solving the inverse problem. Following a reversal sequence, we begin from the results of a physical process and seek for the embedded parameters which have caused the recorded results (Tarantola, 2005).

Most of the models proposed so far have been used for radiative transfer calculations in the terrestrial atmosphere (Snell et al., 1995; Berk et al., 1998; Stamnes et al., 1998). Apparently, they contain assumptions and parameters which satisfy the conditions on the Earth but they need modifications before applied in other planetary atmospheres (Irwin et al., 2008).

Cassini/CIRS as well as its predecessor Voyager 1/IRIS have probed the infrared part of the spectrum of Titan's atmosphere and sent back to the Earth their recordings. Here, I describe the forward model I use to solve the radiative transfer equation (4) for interpreting CIRS FP1 and FP3 spectra.

We firstly consider an atmosphere in hydrostatic equilibrium with a vertical temperature structure and without any scattering effects. We model the atmosphere by dividing it into 80 variable individual pressure levels. Each layer is determined by the pressure values in its boundaries P_{i-1} and P_i, while the temperature in each one varies from $(T_{min})_i$ and $(T_{max})_i$. Considering a spectral region limited by frequencies ν_a and ν_b, we apply a fast line-by-line code introduced by Scott (1974) for all the layers and for all the temperatures of each layer from $(T_{min})_i$ to $(T_{max})_i$ (Scott & Chedin, 1981). The temperatures are imported by

the temperature profile retrieved from the FP4 CIRS recordings using a constrained inverse algorithm (Achterberg et al., 2008; 2011).

For each individual layer we assume local thermodynamic equilibrium (LTE) which means that the source function of each layer is given by the Planck function, stable in the layer between its top (z_{top}) and bottom (z_s), at the corresponding level temperature. According to Houghton, the LTE condition does not exist at high altitudes due to the difference between the Planck and the source functions in these layers (Houghton, 1986). Coustenis et al. (1989) calculated this altitude at $8x10^{-3}$ mbar or 550 km and set this value as the upper limit of the solution of equation (4).

The radiative transfer code integrates directly in frequency and uses the fine structure parameters of the absorbing gases (Scott, 1974). These spectroscopic parameters incorporated into the code have been provided from laboratory results through spectroscopic databases.

Since we have an atmosphere in non-isothermal state, the temperature contrast between different pressure levels of the atmosphere causes spectral variation. Then, the emerging radiation of equation (4) for each layer can be written as:

$$I(z,\mu) = \int_{z_s}^{z_{top}} B(z)W(z,\mu)dz$$

The function $W(z,\mu)$ is the weighting function of an opacity source. By definition, $W(z,\mu)$ is the partial derivative of the transmittance in the direction of the μ (the cosine of the emission angle), that is $W(z,\mu) = \frac{\partial T_r(\mu,\nu,z)}{\partial z}$. Since the Planck function varies quite rapidly with the height, the peak of the contribution function $C(z,\mu)$:

$$C(z,\mu) = B(z)W(z,\mu)$$

is more appropriate to describe the level of the maximum contribution of this source to the emerging radiation (Hanel et al., 2003). Fig. 3.7 depicts en example of the contribution functions of methane v_4 band Q-branch at 1304.4 cm^{-1} and its R-branch at 1291.8 cm^{-1}. The contribution of the central methane band peaks at about 0.5 mbar (approximately 225 km).

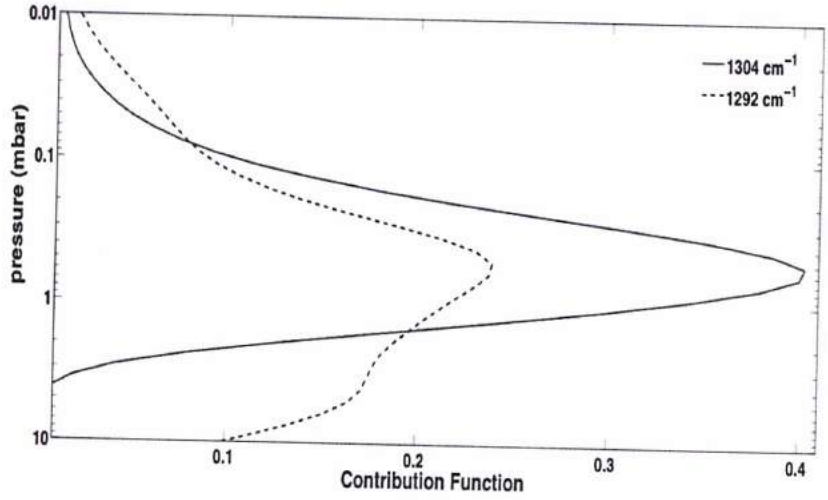

Figure 3. 7 - The contribution function related to the methane v_4 band. The solid [red] line represents the contribution function of the center of methane band, while the dashed line shows the contribution of the left wing.

The monochromatic radiance is then calculated by incorporating the contribution functions of the opacity sources to equation (4). The outcome of this procedure is a model spectrum which is then convolved with the Fourier Transform of the Hamming function used for smoothing the edges of the interferograms.

In our calculations we take into account the absorption of 39 molecules and their isotopologues. For each species, we have used the most recent spectroscopic parameters as they are published in online spectroscopic databases *HITRAN* (Rothman et al., 2009) and *GEISA*[10] (Jacquinet-Husson et al., 2011).

For deriving the abundances of Titan's trace stratospheric constituents we use constant-with-height distributions as well as vertically-varying distribution profiles. In the former case, the abundances are assumed to be constant-with-height above the condensation level and set to follow the corresponding saturation law below (Coustenis et al., 2007). The 2-D General Circulation Model (GCM) provides the latter profiles (Rannou et al., 2005). However, the minor trace gases of the stratosphere have not strong enough spectral lines in their emission bands to apply the relative vertical distribution profiles. The vertical mixing ratios are applied only for acetylene, hydrogen cyanide and ethane, since they probe multiple altitudes via optical thin and thick lines (Coustenis et al., 2010b).

[10] *HITRAN* website: http://www.cfa.harvard.edu/hitran/
GEISA website: http://ether.ipsl.jussieu.fr/etherTypo/?id=950

The fit of the continuum of the recorded spectrum is acquired by using a simple two-cloud system (Borysow & Tang, 1993; Coustenis & Bezard, 1995; Samuelson et al., 1997), one in the troposphere from 20 to 40 km and the other in the stratosphere, beginning from the height of 40 km and upward. The continuum is fitted by using the collision-induced absorption (CIA) opacity of the combination of the main molecules of the atmosphere (N_2-N_2, CH_4-N_2, H_2-N_2, CH_4-CH_4, CH_4-H_2, and H_2-H_2). The recently upgraded radiative transfer code adapts Vinatier et al. (2012) vertical distribution of the aerosol extinction coefficient for fitting the continuum at different latitudes, starting out with CIRS limb data and DISR measurements at the equatorial latitudes (Vinatier et al., 2010a; Vinatier et al., 2012b). We then adjust the haze opacity parameters in order to achieve the best fit of the continuum.

3.4.3 The Atmospheric Radiative Transfer code for Titan (ARTT)

The Atmospheric Radiative Transfer code for Titan (ARTT) is a forward model which solves the radiative transfer equation (4) for the atmosphere of Titan. It is a fast *line-by-line* and *layer-by-layer method* which sums all the contributions of the absorbing gases in an inhomogeneous atmosphere (Scott, 1974; Scott & Chedin, 1981).

The method incorporates both the atmospheric inhomogeneities and the instrument function and it directly integrates the radiance over a band of specific frequencies in order to compute the radiance in a single layer. It is called line-by-line due to the calculation of each spectral line of the atmospheric gases in the layers of interest. For this purpose, it adapts the spectroscopic files of the molecules of interest as inputs in the code which are provided from laboratory studies. It relies on (a) a precise temperature profile and (b) on the correct representation of all opacity sources (Coustenis et al., 1989a).

ARTT is based on the precise knowledge of the thermal structure or of the opacity sources of the atmosphere. Then, it produces a model spectrum which is compared to the real data to infer one or the other of the parameters. An iterative process during which we adjust the abundances of the molecules of interest, allows us to obtain best fits of the data. We firstly derive the transmittances monochromatically for the whole spectral region for a determined set of atmospheric conditions and then we reconstruct them for any atmospheric conditions to generate a mean weighted spectrum.

The scheme of the fitting procedure is the following. We firstly incorporate a precise model of thermal structure of the probed atmospheric region to the synthetic spectra.

We then also assume either constant-with-height abundances or vertical distributions of the absorbing gases. By an iterative best-fit process, we fit the synthetic spectra to the real data at FP1 (10-600 cm^{-1}) or at FP3 (600-1100cm^{-1}).

ARTT takes the gravity and the radius of Titan as constant values considering the satellite as a perfect sphere. Moreover, it takes into account the secant of the observations, which can be modified by the user. The other inputs of the software are the pressure levels and the temperature vertical profile which can be adjusted to fit the spectra. The code then simulates the vertical pressure and temperature distribution for a specific selection. This is necessary in order to model the Planck function for the recorded infrared radiation. Afterwards, we induce the mixing ratios of the major molecules (nitrogen, methane, hydrogen and argon) of the atmosphere.

The next step is to incorporate the spectroscopic parameters of the trace gases. ARTT is a fast line-by-line code and therefore it reads all the line lists from each file and calculates the relative contribution. Each molecular mixing ratio can be constant-with-height or vary vertically with height. All the available spectroscopic line lists have been incorporated in the software during the installation procedure. Finally, the continuum is simulated through the presence of a two-cloud model which reproduces the opacity in between lines, and is due to the absorption from aerosols or particle condensates. The haze distribution we apply to the data is adapted from Vinatier et al. (2012b) spectral discription near the equator that we adjust to match our spectra at different latitudes.

After having extracted the model, the code compares it with the recorded spectra. This comparison is the outcome of the whole procedure and leads to the determination of the thermal and chemical structure of Titan. The comparison between the synthetic and the observed spectra is dual. In general, we try to accomplish the best possible match of the Q-branch (the center) of all the molecules. That can be done visually through an iterative process. However, for large and extended emission bands (as for CH_4, C_2H_2 and C_2H_6 for instance) we may want the best fit throughout the band. In that case, the best fit can be deducted from the difference between the model and the data by minimizing the residuals. When the difference is minimal, we assume a best fit. We have applied a specific code using regression analysis to optimize these differences. The software upgrade has optimized the computational time which is literally depended on the hardware. Generally, each radiative transfer calculation takes 2-3 minutes.

When I started my PhD thesis in 2008, the version of the CIRS database also installed in Meudon servers was at its v2.3 version with local calibration applies to the CIRS spectra up

to T44 flyby (28/5/2008). Today, the available inventory of CIRS spectra has been expanded to include the most recent Cassini Titan T86 flyby (26/9/2012). While waiting for the validation of the most recent calibration, sevaral CIRS databases are currently available in Meudon: the v3.2 with local calibration, the DS4000 with deep space calibration, the DS4000 with the application of phase correction algorithm and the Grand Average with deep space calibration over several years.

The version of the radiative transfer software I received from my predecessors was the ARTT 0.3.8 (Atmospheric Radiative Transfer for Titan, version 0.3.8), based on spectroscopic parameters adopted from *GEISA*[11] *(97 and 2003* editions), *HITRAN*[12] (*2004* and *2004* editions) and line lists from individual researchers. The spectroscopic line parameters contained in these databases change frequently to include necessary updates. One of my tasks was to search for weak features in the CIRS spectra and to try to search for new molecules. The lack of a perfect fit of the major molecules did not allow for such a fine spectroscopic research in the regions around the major emission bands of C_2H_2, HCN and C_2H_6. Within the past four years, I have searched regularly in the available databases in order to retrieve any updates of the molecules included in the model and to improve the fits. However, the ARTT 0.3.8 version did not allow us to easily include such updates. Several years after the last upgrade of the ARTT radiative transfer code we had to move to a newer version in order to:

a) Make the software more user-friendly and improve its flexibility
b) Include new aerosol description (Vinatier et al., 2012b) to fit the spectrum continuum
c) Improve and update the spectroscopic parameters
    1) New spectroscopic atlases have been released with more accurate parameters and enhanced line lists following contemporary laboratory work such as the *HITRAN 2008* (Rothman et al., 2009) and the *GEISA 2009* (Jacquinet-Husson et al., 2011).
    2) Incorrect scale of propane ν_{26} line strengths at 748 cm^{-1} included in *GEISA 2003*, the band of which should be multiplied by a factor of 0.420 (Nixon et al., 2009).
    3) Isotopologue investigation in Titan atmosphere requires new molecules to be added to the code.

[11]Gestion et Etude des Informations Spectroscopiques Atmosphériques: Management and Study of Spectroscopic Information (Jacquinet-Husson et al., 2005)
[12] HIgh-resolution TRansmission molecular AbsorptioN database (Rothman et al., 2005)

3.4.4 The improved ARTT software

The new software upgrade took place in LESIA (Laboratoire d'études spatiales et d'instrumentation en astrophysique) at the Paris Observatory in Meudon, France and in the Astrophysics Laboratory of the University of Athens, Greece. Stefanos Stamogiorgos, software engineer, assisted in this procedure, focussing on the programmatic part of the upgrade.

One of the aspects we had to tackle was the low flexibility of the code in implementing new spectroscopic data and making any sort of changes in the input parameters. First of all, there was a lack of a readme file with guidelines on how to use the source files in order to create the executable files, which we would use in order to create our graphs. In addition, there was no manual on the actions, which had to be taken in order to find how to enrich the molecular database of the program. By studying the workflow of the program and by adding breakpoints into the source code of the program, we managed to identify the actions needed in order to complete the upgrade. Moreover, the use of the program had to be more user-friendly and for this reason we added output messages to the software and replaced or removed any messages left of the debugging process.

The code also had to meet the demands of the increased number of data imported, which increased the computational time. For this reason, we had to remove any delays on the workflow by using less memory resources and by removing some redundant conditional statements and iterative processes. So, the new version has better stability and an increased performance compared to the previous version since the number of the calculated molecules has almost been doubled but the calculations time has remained the same.

The new edition of the radiative transfer software is completely compatible with the files used by the previous one and therefore the migration from the one version to the other is bug-free.

3.4.5 Description of the new aerosol model

The ARTT code has also been upgraded in the sense of new aerosol distribution to fit the continuum. As noted previously, the continuum was fitted by adapting a simple two-cloud system, one in the troposphere and the other in the stratosphere (Borysow & Tang, 1993; Coustenis & Bezard, 1995; Samuelson et al., 1997). As opacity sources were considered the

collisions-induced absorption (CIA) between the major molecules (N_2, CH_4 and H_2) and its combinations. In the new ARTT model we have adapted the recent aerosol distribution provided by Vinatier et al. (2012b), which put constrains at the refractive indices of Titan's aerosols in the mid infrared part of the spectrum.

Vinatier et al. (2012b) have combined CIRS remote limb observations at 15°S and 0.95 mbar (193 km) and Huygens/DISR *in situ* measurements at 10°S to model the extinction cross-section in mid-infrared (600-1500 cm^{-1}). The extinction cross-section is derived by the ratio of the aerosol volume extinction coefficient to the aerosol number density. The former was retrieved by the CIRS limb data (Vinatier et al., 2012b), while the latter by DISR measurements. According to (Tomasko et al., 2008b) the aerosol number density of 5 particles per cm^{-3} at 80 km decreases exponentially with a scale height of 65 km from the altitude of 80 km up to 150 km (Fig. 3.8).

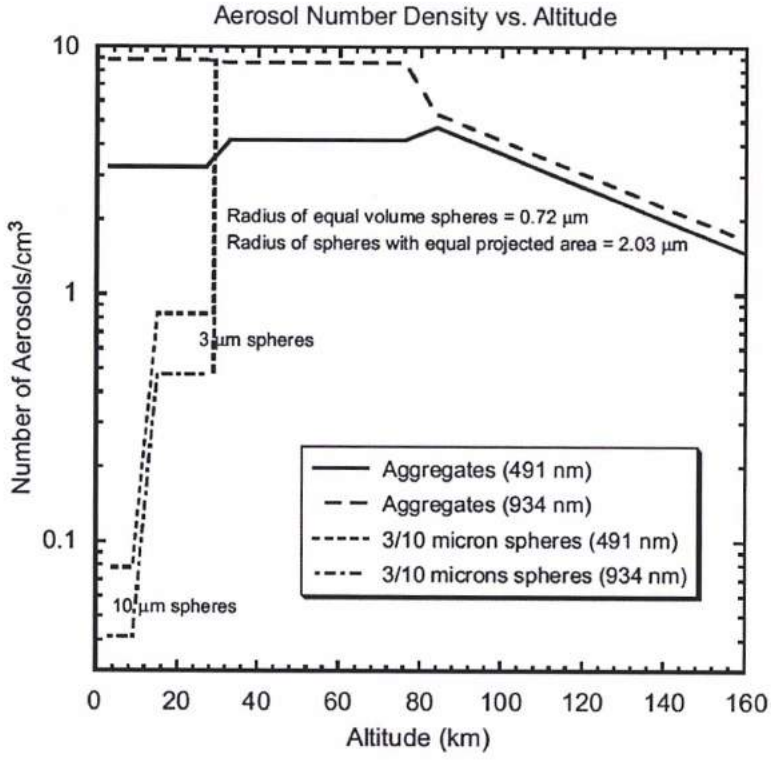

Figure 3. 8 - Aerosol number density versus the altitude by DISR measurements, adapted from Tomasko et al. (2008b). The value of 5 particles per cc at 80 km is the maximum of the haze aerosol concentration. The predictions of a fractal algorithm, which was used to describe the haze particles, agree with the measurements. This means that above 80 km some hydrocarbons condense onto fractal aggregate particles, which may fill the voids in particles and therefore cause higher single scattering albedos (Tomasko & West, 2009).

Vinatier et al. (2012b) assumed the same scale height for altitudes above 150 km. Although no relative measurements exist for higher than 150 km, this assumption agrees with Vinatier et al. (2010a) results. Anderson & Samuelson (2011) have derived the aerosol volume extinction coefficient in far-infrared (70-600 cm^{-1}) at 15°S. The calculated extinction cross-section by Vinatier et al., combined with the latter results of is illustrated in Fig. 3.9. Both parts of the complex refractive index are interlinked by a special form of Hilbert transforms, which are termed Kramers-Kronig relation (KKR) (Lucarini, 2005). By applying the KKR, through an iterative process, the real and the imaginary parts of the refractive index as a function of the wavenumber is calculated numerically (color lines in Fig. 3.9).

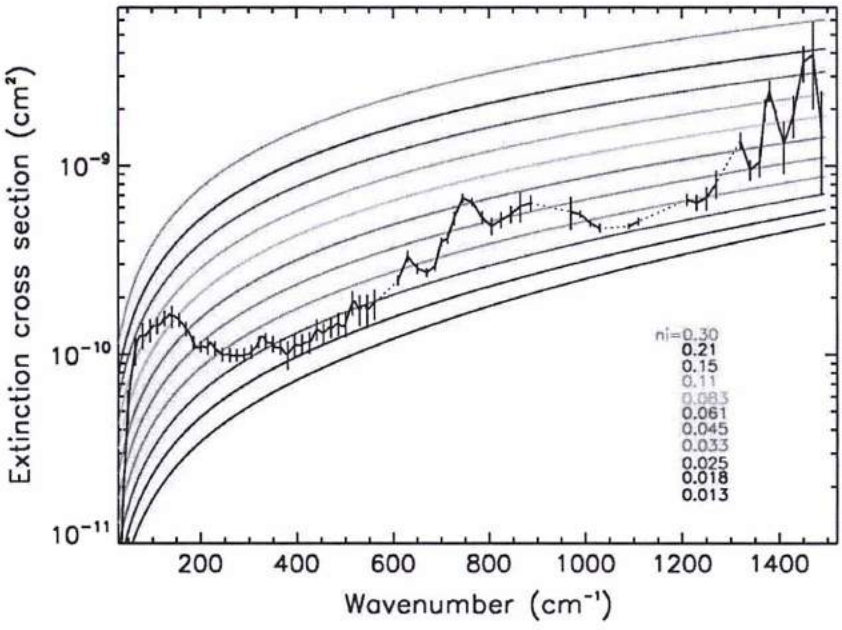

Figure 3. 9 - Aerosol extinction cross-section in the range of 30 to 1500 cm-1 (adapted from Vinatier et al. (2012)). The observed extinction cross-section (black) is plotted with 1-σ error bars. The calculation was performed by assuming a constant real part of the refractive index equal to 1.69, while the imaginary part of the refractive index ni varying within the range of 0.01 and 0.2. The color lines are calculations assuming a fractal cluster of 3000 monomers with individual radii of 0.05 μm and fractal dimension of 2 as predicted by (Cabane et al., 1992) and observed by DISR (Tomasko et al., 2008b). The ni used for each model calculation is shown in the legend. The imaginary part of the refractive index of Titan's aerosols varies between 0.018 and 0.2.

The extinction cross-section is the imaginary part of the complex refractive index. In an opaque medium, the real part the complex refractive index of describes the refraction, while its imaginary part the absorption loss. The results of Vinatier et al. (2012b) calculations of the complex refractive index are plotted in Fig. 3.10. Within the region spectral region of 600 to 1500 cm^{-1}, the imaginary part of the refractive index n_i presents maxima at 630, 700, 750,

900, 1300 and 1450 cm^{-1}. These results differ from Khare et al. (1984), being less absorbent than tholins in the thermal infrared (Fig 3.10). Similar results have been reported in the literature (de Kok et al., 2007b; Rannou et al., 2010; Vinatier et al., 2010a; Anderson & Samuelson, 2011).

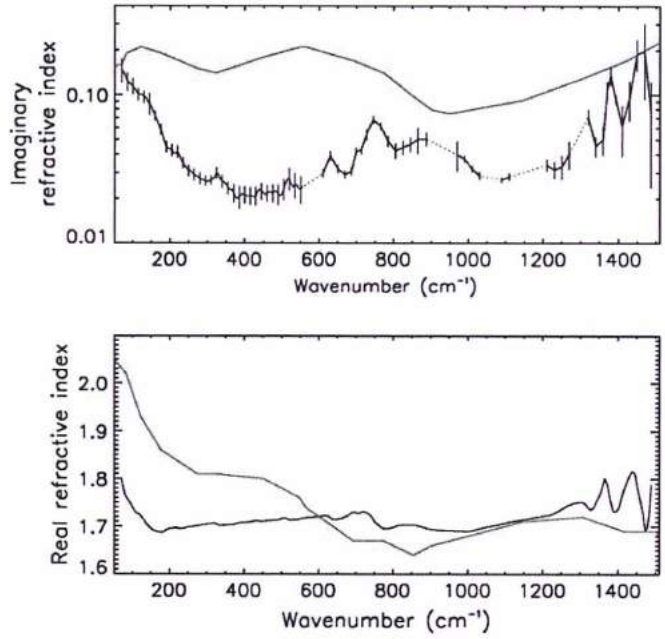

Figure 3. 10 - The real (upper panel) and the imaginary (lower panel) parts of the refractive index of Titan's aerosols (adapted from Vinatier et al. (2012b)). The indices as obtained of Khare et al. (1984) for tholins are illustrated in blue.

By integrating the volume extinction coefficient over the altitude for two given altitudes, we derive the optical depth of the haze aerosols. I have applied these values to our radiative transfer code to fit the continuum. However, although this distribution can be applied in all latitudes, there are differences between the north to the south hemisphere and these values should be adjusted in order to obtain the best fit. In Chapter 4, I show that this description if adjusted in latitude can provide results as to the haze distribution on Titan's disk.

3.4.6 The updated spectroscopic parameterization

The spectroscopic parameters of the main molecules (CH_4, CH_3D, CO, CO_2, HC_3N, C_2N_2, C_2H_2, C_2H_4, C_4H_2, C_3H_4, H_2O, C_6H_6, C_2HD, HCN, $HC^{15}N$, C_2H_6, C_3H_8 and CH_3CN) and the

isotopologues ($^{13}CH_3D$, $^{13}CH_4$, $^{13}C^{12}CH_2$) incorporated in our radiative transfer code have been significantly modified in both *GEISA* and *HITRAN* databases, since the last release of the code in 2006, including recent laboratory works. The line lists of these molecules have more precise spectral parameters. Therefore, ARTT had to be upgraded in order to include these improved features in its inventory. The increased accuracy of the fundamental parameters (line position, intensity and line shape) improves the retrieved fit between the model and the real data. The wealth of CIRS data allows us to use large spectral averages, with which the identification of minor isotopologues is easier. All these new identified isotopologues ($^{13}C_2H_6$, $H^{13}C^{14}N$, $H^{13}CCCN$, $^{13}CO_2$, $^{13}C^{18}O^{16}O$) should be added as well as candidate isotopologues (DCN, $H^{16}OD$, $H^{17}OH$, $H^{17}OD$, $H^{18}OH$ and $H^{18}OD$, $HC^{13}CCN$, $HCC^{13}CN$, $^{12}C^{18}O^{16}O$, $^{12}C^{17}O^{16}O$, $^{13}C^{17}O^{16}O$, $^{12}C^{18}O^{17}O$ and $^{12}C^{18}O_2$) in case of future detection. Then, the radiative transfer calculations are more reliable, which is prerequisite for remote sensing interpretation of CIRS spectra.

I have upgraded our Atmospheric Radiative Transfer for Titan (ARTT 1.0.0) following the previously described requirements. First of all, the main databases from which we adopt the spectroscopic parameters are *GEISA* and *HITRAN*, two independent spectroscopic databases available online[13] for spectroscopic studies. Both atlases are widely used and have a significant impact on radiative transfer studies and the interpretation of spectra. Specifically, *GEISA* has a planetary applications heritage than in terrestrial sciences, while on the contrary, *HITRAN* has an Earth sciences one. We have improved the following spectroscopic parameters incorporated in the code by updating the existing ones:

a) Methane (CH_4), ($2H_1$) methane (CH_3D), carbon monoxide (CO), carbon dioxide (CO_2), cyanoacetylene (HC_3N), cyanogen (C_2N_2), acetylene (C_2H_2), ethylene (C_2H_4), diacetylene (C_4H_2), water (H_2O), benzene (C_6H_6), monodeuterated acetylene (C_2HD) and the isotopologues $^{13}CH_3D$, $^{13}CH_4$ and $^{13}C^{12}CH_2$ line lists are provided by the latest *GEISA* 2009 release (Jacquinet-Husson et al., 2011), which have replaced the relative old spectroscopic files. This edition of *GEISA* database contains all the line lists data, which were adapted from individual researches in the previous ARTT 0.3.8 edition (see also Table 3.1).
b) Both line lists for hydrogen cyanide (HCN) and its 15-N isotopologue ($HC^{15}N$) were taken from *HITRAN 2008* atlas (Rothman et al., 2009) and replaced the previous versions.

[13] GEISA website: http://ether.ipsl.jussieu.fr/etherTypo/?id=950, HITRAN website: http://www.cfa.harvard.edu/hitran/

c) The spectroscopic parameters of ethane (C_2H_6) were treated as follows: For the spectroscopic range between 613-843 cm^{-1} the line lists from *GEISA 2009* are adopted, while at the region of 1350-1496 cm^{-1} the spectroscopic data of the code is still incorporated by the Vander-Auwera et al. (2007) files. Although the *GEISA 2009* contains the data of Vander-Auwera et al. work, it lacks the latter spectral range.

d) For the methylacetylene (C_3H_4), the files from G. Graner (pers. comm.) were kept due to conflicts of relative C_3H_4 *GEISA 2009* data and the code. As noted in *GEISA 2009* paper, the same dataset of the ν_9 and ν_{10} bands at 331 and 639 cm^{-1} respectively, was provided by G. Graner to the new *GEISA* distribution (Jacquinet-Husson et al., 2011). Therefore, the C_3H_4 spectroscopic parameters we use are consistent with the latest *GEISA* update.

d) For the propane (C_3H_8) bands, the previous data was replaced by the new extract from *GEISA 2009* at 700-800 cm^{-1}. Additional line lists at 1308-1582 cm^{-1} were imported from the CIRS team website (http://blizzard.astro.cornell.edu/drupal/) line list which has been calculated by J.-M. Flaud (31 Oct. 2008) (Flaud et al., 2010), since *GEISA 2009* gives only the former data.

e) For the acetonitrile (CH_3CN), *GEISA 2009* provides data ranging from 890 to 1650 cm^{-1}. These lines are imported in the code. However, for the region of 318 to 1135 cm^{-1} the *PNNL* data from the previous ARTT version was kept.

As a second step, we have added new isotopologues in the new release of ARTT. The identification of isotopologues in Titan's atmosphere is essential for radiative transfer studies. Isotopologues are molecular entities which differ in their isotopic composition. The isotopic compounds have at least one atom which consists of a different number of neutrons from the one of the main molecule, it exhibits different vibration states and can therefore be observed in infrared spectra. The knowledge of isotopic ratio sets constrains on the origin and evolution of a planetary atmosphere, understands its dynamics and describes contemporary chemical and photochemical paths.

Moreover, contributions from isotopologues may influence the observed spectra and could possibly explain any misfits between the data and the model (Coustenis et al., 2010b). The minor isotopologues exhibit extremely low abundances in Titan's atmosphere. The identification of isotopologues in Titan's infrared spectrum can be obtained only where the adequate spectroscopic data files are available. *GEISA 2009* distribution has been updated to

include such line lists. In *HITRAN*, the minor isotopologues are embedded with the main molecule.

Eighteen new minor isotopologues have been added to the ARTT code, one for ethane ($^{13}C_2H_6$), two for hydrogen cyanide (DCN and $H^{13}C^{14}N$), three for cyanoacetylene ($H^{13}CCCN$, $HC^{13}CCN$ and $HCC^{13}CN$), five for water ($H^{16}OD$, $H^{17}OH$, $H^{17}OD$, $H^{18}OH$ and $H^{18}OD$) and seven for carbon dioxide ($^{13}CO_2$, $^{12}C^{18}O^{16}O$, $^{12}C^{17}O^{16}O$, $^{13}C^{17}O^{16}O$, $^{13}C^{18}O^{16}O$, $^{12}C^{18}O^{17}O$ and $^{12}C^{18}O_2$). The spectroscopic parameters of all these molecules have been adopted from *GEISA 2009*, except for $H^{13}C^{14}N$ and cyanoacetylene. The $H^{13}C^{14}N$ line lists have been adopted by *HITRAN 2008*, while cyanoacetylene minor isotopologues have been picked up from the CIRS team website. In fact, they are Jolly et al. (2007) data, modified by C. Nixon in *GEISA* format.

Some of these minor isotopologues have been detected in Titan's atmosphere. The first identification of ^{13}C-ethane ($^{13}C_2H_6$) ν_{12} band was derived from CIRS spectra (Nixon et al., 2008a). $H^{13}C^{14}N$ has been detected in Titan from ground –based observations of IRAM/JCMT data in May-June 1995 (Hidayat et al., 1997) and from Submillimeter Array data in February 2004 (Gurwell, 2004). The same molecule has been inverted from CIRS limb data at 83°N (Vinatier et al., 2007b).

The existence of three cyanoacetylene minor isotopologues has been studied by Jennings et al. (2008) in CIRS spectra. The $H^{13}CCCN$ has identified for the first time at 658.7 cm^{-1} but it has been impossible to detect the other two, $HC^{13}CCN$ and $HCC^{13}CN$ at 663 cm^{-1} because they are blended with the stronger ν_5 band of the main isotopologues at 663.3 cm^{-1} (Jennings et al., 2008).

As far as the carbon dioxide minor isotopologues are concerned, Nixon et al. (2008b) reported a 6.5σ detection of $^{13}CO_2$ and a possible 3.5σ detection of $^{13}C^{18}O^{16}O$ at 648.75 and 662.5 respectively using CIRS data. The detection of the latter is noted as possible due to need for higher resolution spectroscopic data (Nixon et al., 2008b).

It should be noted that although the ^{13}C-isotopologue of diacetylene has been detected in Titan's atmosphere at 627.9 cm^{-1} (Jolly et al., 2010), it has not been included in the current ARTT upgrade. *GEISA 2009* lacks the line lists of this isotopologues. From the new molecules in ARTT, DCN, water minor isotopologues, $^{12}C^{18}O^{16}O$, $^{12}C^{17}O^{16}O$, $^{13}C^{17}O^{16}O$, $^{12}C^{18}O^{17}O$ and $^{12}C^{18}O_2$ have not been detected yet in Titan's infrared spectrum. The Table 3.4 below lists these molecules and their sources.

In the following Figs. 3.11 - 3.20, I have plotted the output of the modeled emission features of all the molecules included in the new upgraded radiative transfer software.

Table 3. 4 - List of the spectroscopic parameters adopted for the ARTT upgrade. The source the line lists of each molecule of the previous version is also shown.

Molecule	ARTT 0.3.8	ARTT 1.0.0
CH_4	GEISA 2003	GEISA 2009
CH_3D	GEISA 2003	GEISA 2009
CO	GEISA 2003	GEISA 2009
CO_2	GEISA 2003	GEISA 2009
HCN	HITRAN 2004 and HITRAN 2008	HITRAN 2008
HC_3N	Jolly et al. (2007)	GEISA 2009
C_2N_2	GEISA 2003	GEISA 2009
C_2H_2	GEISA 2003	GEISA 2009
C_2H_6	Vander Auwera et al. (2007)	Vander Auwera et al. (2007) at 1350-1496 cm-1 GEISA 2009 at 613-843 cm-1
C_2H_4	Blass et al. (2001) and Rotger 2006 pers. comm.	GEISA 2009
C_3H_4	Rotger et al. (2008) G. Graner pers. comm.	G. Graner pers. comm.
C_3H_8	GEISA 2003	GEISA 2009 at 700-800 cm-1 CIRS team site at 1308-1582 cm-1
C_4H_2	Arié and Johns (1992) for nu8 and hot bands	GEISA 2009
H_2O	GEISA 2003	GEISA 2009
C_6H_6	Dang-Nhu et al. (1989)	GEISA 2009
C_2HD	Jolly et al. (2008)	GEISA 2009
CH_3CN	PNNL line lists	PNNL at 318-1135 cm-1 GEISA 2009 at 890-1650 cm-1
$^{13}CH_3D$	Bezard et al. (2007)	GEISA 2009
$H^{12}C^{15}N$	HITRAN 2008	HITRAN 2008
$^{13}CH_4$	GEISA 2003	GEISA 2009
$^{13}C^{12}CH_2$	GEISA 2003	GEISA 2009
$H^{13}CCCN$	NO	CIRS team web site
$HC^{13}CCN$	NO	CIRS team web site
$HCC^{13}CN$	NO	CIRS team web site
$^{13}C^{16}O_2$	NO	GEISA 2009
$^{12}C^{18}O^{16}O$	NO	GEISA 2009
$D^{12}C^{14}N$	NO	GEISA 2009
$H^{13}C^{14}N$	NO	HITRAN 2008
$^{12}C^{13}CH_6$	NO	GEISA 2009
$H^{16}OD$	NO	GEISA 2009
$H^{17}OH$	NO	GEISA 2009
$H^{17}OD$	NO	GEISA 2009
$H^{18}OH$	NO	GEISA 2009
$H^{18}OD$	NO	GEISA 2009
$^{12}C^{17}O^{16}O$	NO	GEISA 2009
$^{13}C^{17}O^{16}O$	NO	GEISA 2009
$^{13}C^{18}O^{16}O$	NO	GEISA 2009
$C^{18}O^{17}O$	NO	GEISA 2009
$^{12}C^{18}O_2$	NO	GEISA 2009

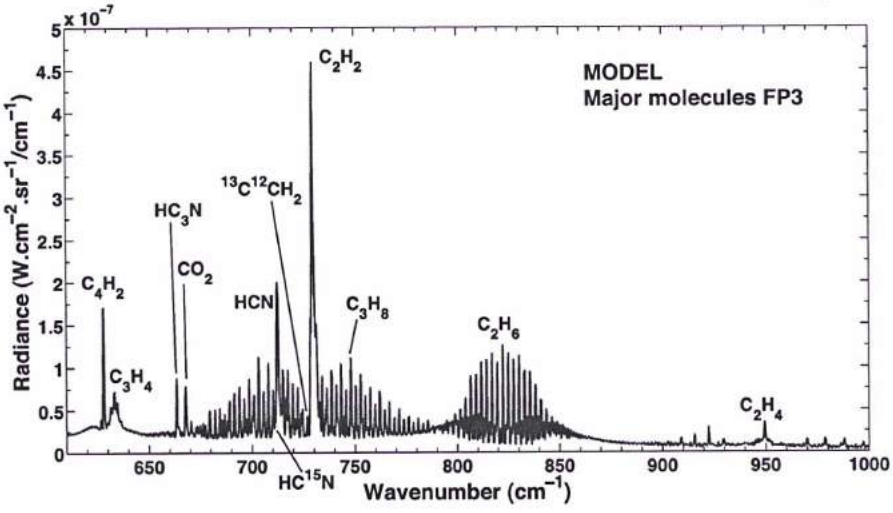

Figure 3. 11 - Output of the model simulation of all the major molecules of the FP3 part of CIRS spectrum.

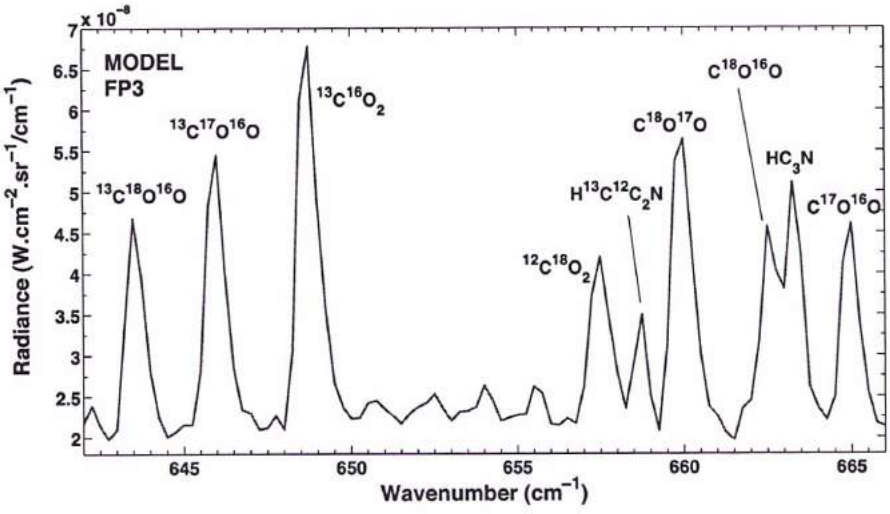

Figure 3. 12 - Output of the model simulation of the FP3 but with zoom in the spectral region from 642 to 665.9 cm^{-1}. The 13-C isotopologues of carbon dioxide are located in this spectral region as well as the ones of cyanoacetylene. $^{13}C^{18}O^{16}O$ has emission band at 643 cm^{-1}, $^{13}C^{17}O^{16}O$ at 646 cm^{-1}, $^{13}C^{16}O_2$ at 648 cm^{-1}, $^{12}C^{18}O_2$ at 657 cm^{-1}, $^{12}C^{18}O^{17}O$ at 660 cm^{-1}, $^{12}C^{18}O^{16}O$ at 662.5 cm^{-1} and $^{12}C^{17}O^{16}O$ at 664.9 cm^{-1}. $^{12}C^{18}O^{16}O$, $^{12}C^{17}O^{16}O$, $^{13}C^{17}O^{16}O$, $^{12}C^{18}O^{17}O$ and $^{12}C^{18}O_2$ have not been detected yet in Titan's infrared spectrum. Only $H^{13}C^{12}C_2N$ has been detected at 658 cm^{-1} (Jennings et al., 2008). The rest two are blended with the Q-branch of HC_3N at 663 cm^{-1} and higher resolution than CIRS is needed to separate them. ARTT can identify them as we can see in Fig. 3.13, but only with using much higher resolution for its calculations.

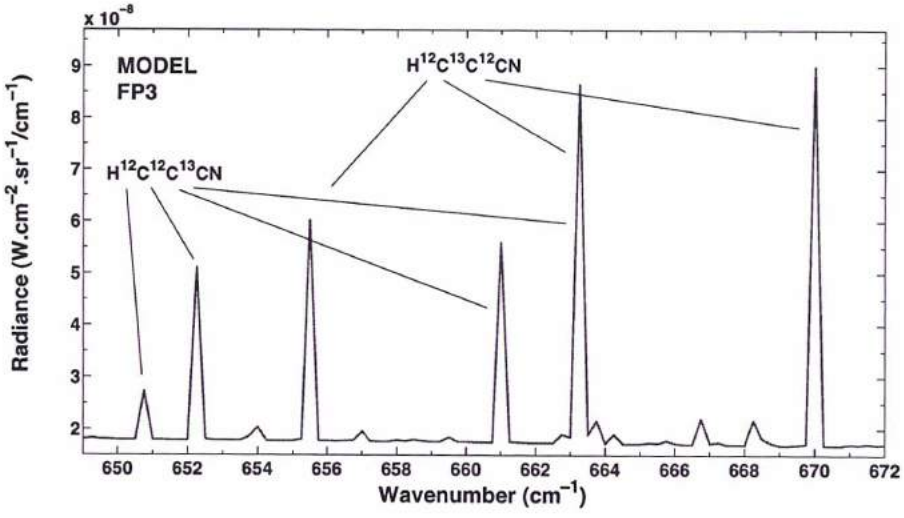

Figure 3. 13 - The output of the model by taking into account only the two 13-C isotopologues of cyanoacetylene, which are blended with HC_3N at 663 cm^{-1}. These calculations have been made by using a resolution of 0.001 cm^{-1}, two orders of magnitude higher than the CIRS one (0.5 cm^{-1}). The signatures of these isotopologues are indeed blended, but they can be identified by the other bands. The HC_3N has not been plotted. $HCC^{13}CN$ has emission bands at 650, 652.3, 661 cm^{-1} and 663.2, while $HC^{13}CCN$ has emission bands at 655, 663.2 and 670 cm^{-1}(Anderson & Samuelson, 2011).

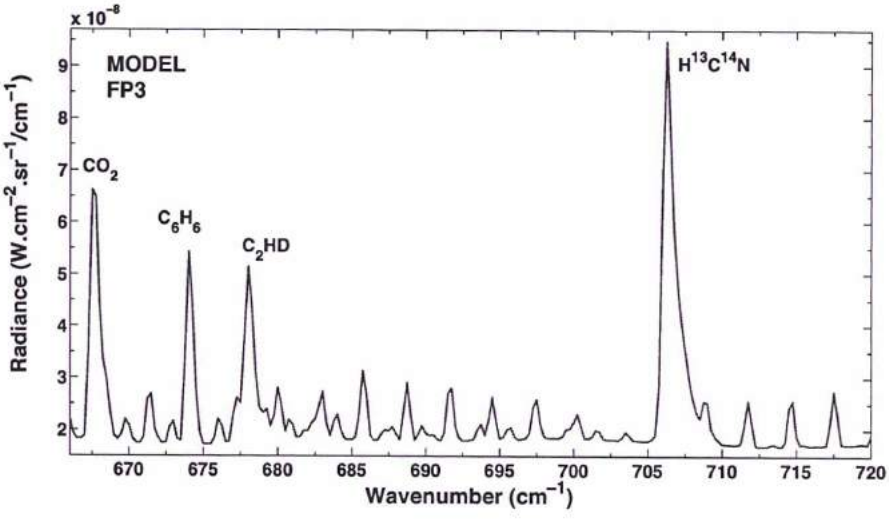

Figure 3. 14 - The results of the model simulation within 664 and 720 cm^{-1}, where the weak v_4 band of C_6H_6 exists at 674 cm^{-1}. In this region, there is also the signature of C_2HD at 674 cm^{-1} and 13-C HCN isotopologues at 706 cm^{-1}.

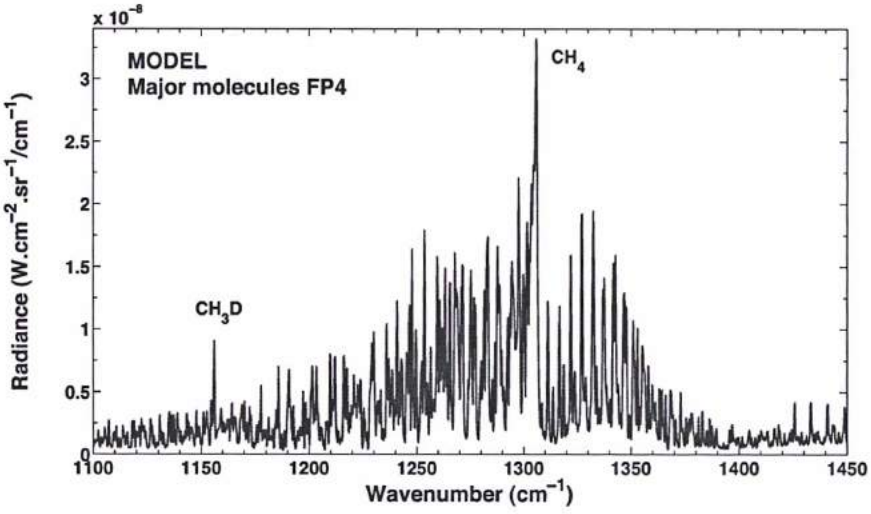

Figure 3. 15 - The outcome of the model simulation at FP4, where methane v_4 band dominates the spectra.

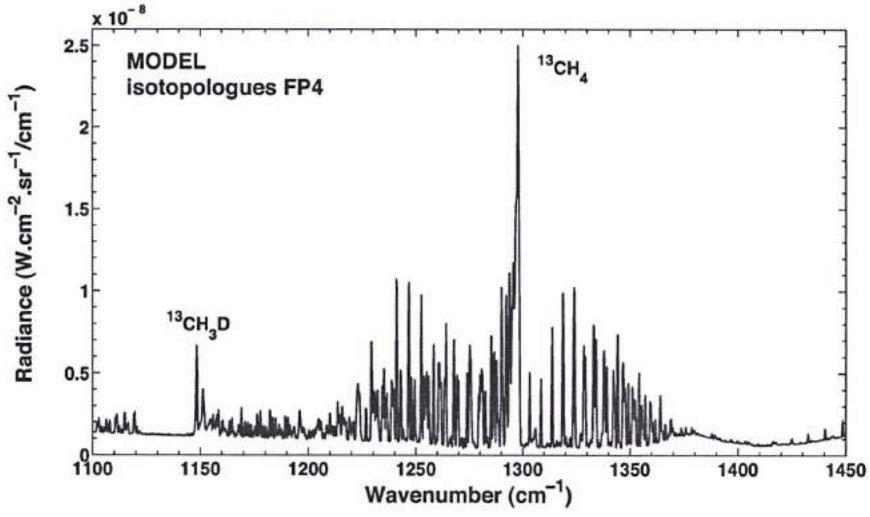

Figure 3. 16 - Model simulation at FP4 with methane v_4 band discarded. The signature and the position of 13-C isotopologues of molecules in Fig. 3.15 is obvious.

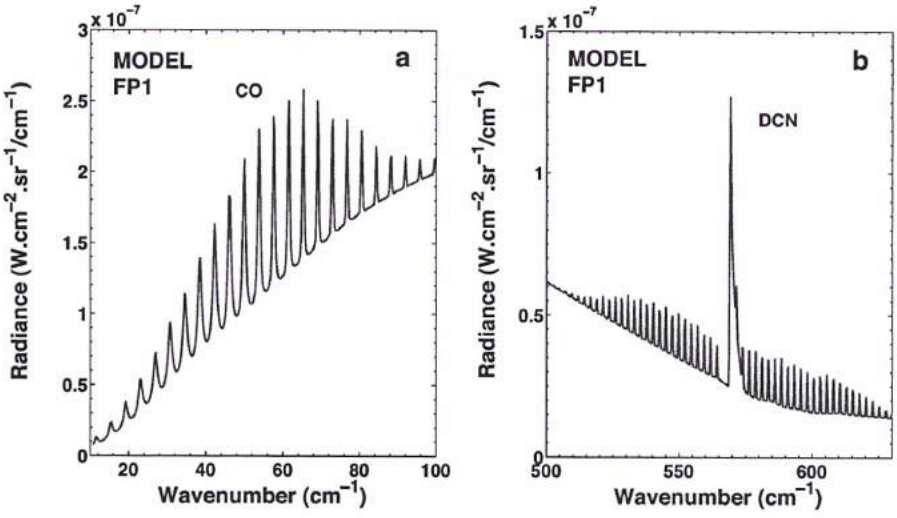

Figure 3. 17 - Model simulation at FP1. Panel a shows the CO emission, while panel b shows the DCN model signature. The latter has been not yet detected in CIRS data.

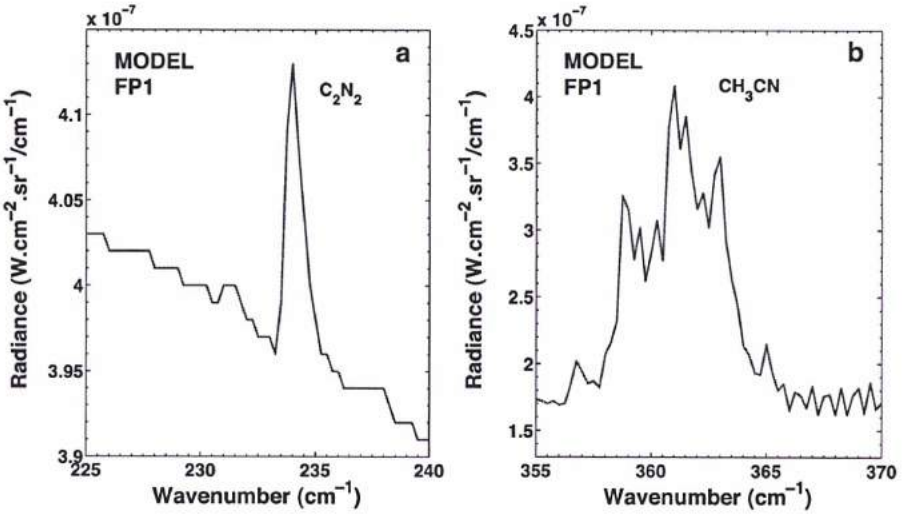

Figure 3. 18 - The outcome of model simulation at FP1. Panel a shows the cyanogen emission, while panel b shows acetonitrile model calculations. Acetonitrile has also emission band at the FP3 part of CIRS spectra (Fig. 3.19-b).

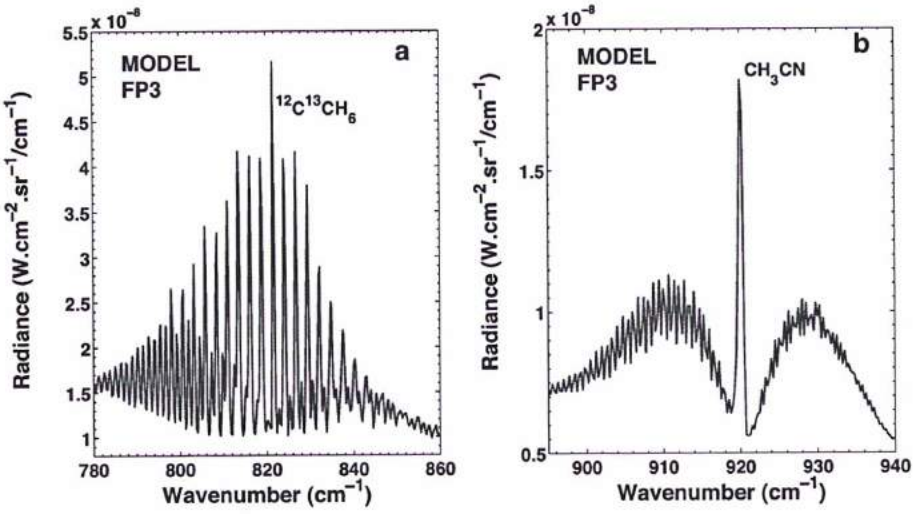

Figure 3. 19 - Panel (a) illustrates the outcome of model simulation of 13-C isotopologues of ethane at FP3. Panel (b) shows acetonitrile model calculations.

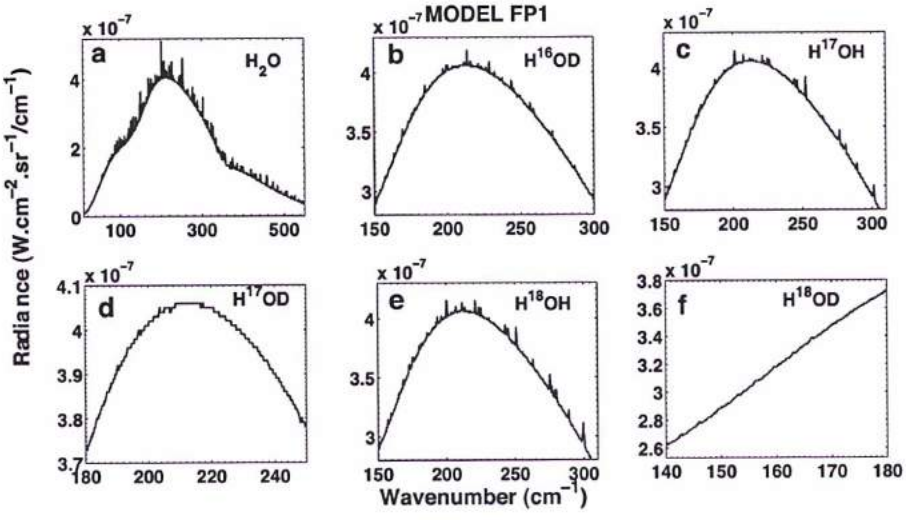

Figure 3. 20 - Water vapor isotopologues model calculations at FP1. Only the signature of the major isotopologues has been identified in Titan's atmosphere (panel a).

3.4.7 Improved simulation of the observations

Tests on the main molecules

We have compared the output of our new upgraded radiative transfer code (ARTT 1.0.0) with the previous version (ARTT 0.3.8) in order to quantify what has changed. For this purpose, we have applied the spectral CIRS FP3 selection of May 2010 at medium resolution at 50°N. This selection contains 160 spectra recorded from the T68 Cassini flyby. We had firstly applied the relative temperature profile as retrieved from the corresponding FP4 data and then, through an iterative process, we had been running the code until we reached the best fit. This procedure had been done for both ARTT versions. Fig. 3.20 below illustrates outcome of these simulations.

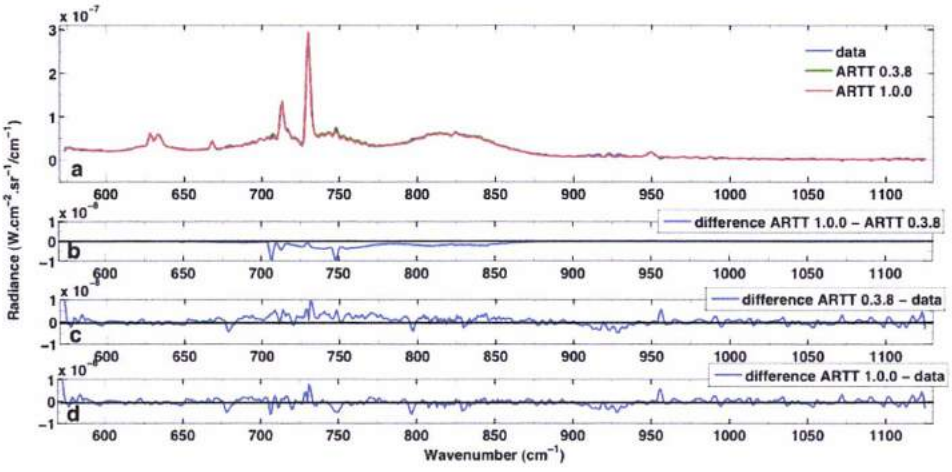

Figure 3. 21 - Comparison of the outcome of the two models for the same CIRS selection and comparison to the data (panel a). In panel b, the difference between the two models is illustrated. In panel c, we depict the difference between the model of ARTT 0.3.8 and the data. Similarly, the difference between the model of ARTT 1.0.0 and the data is showed in panel d.

From the difference plot (Fig. 3.21-b) we can see that the old version has higher emission from 670 to 870 cm^{-1} (negative differences). On the other hand, from 940 to 1000 cm^{-1}, the old model has lower emission (positive differences). Indeed, from 770 to 680 cm^{-1} both models seem identical, but from 660 to 700 cm^{-1} the old version has a slightly higher emission as well as from 700 to 720 cm^{-1} and from 720 to 750 cm^{-1}. The emission of the old model becomes higher in the region of 740 to 800 cm^{-1} and continues similarly from 760 to 870cm^{-1}.

Eventually, from 880 to 1100 cm^{-1} both fits seem identical. Judging from the differences between each model and the data, the new version fits better the data at the range between 670 to 870 cm^{-1}, while in the rest wavenumbers the result is the same. In this point, we have to note that we have used the same continuum fit with the same adjustments. We will discuss the reason of the differences between ARTT 1.0.0 and ARTT 0.3.8 below. The major molecules in this spectral region (CIRS/FP3) are: HCN, C_2H_2, C_3H_8, C_2H_6, C_2H_4 and CO_2. We examine these molecules one by one. Table 3.5 summarizes the test results of the two ARTT versions.

HCN:

Hydrogen cyanide is one of the dominant trace gaseous species in the spectral range of 650 to 780 cm^{-1}. However, the line lists for this molecule are from the same database distribution (*HITRAN 2008*. The following plot (Fig. 3.22) illustrates the HCN lines from the spectroscopic files adapted in old and new ARTT versions at the spectroscopic range of interest (CIRS/FP3). Although the files come from the same database version (*HITRAN 2008*), they are not the same it is depicted in Fig. 3.23.

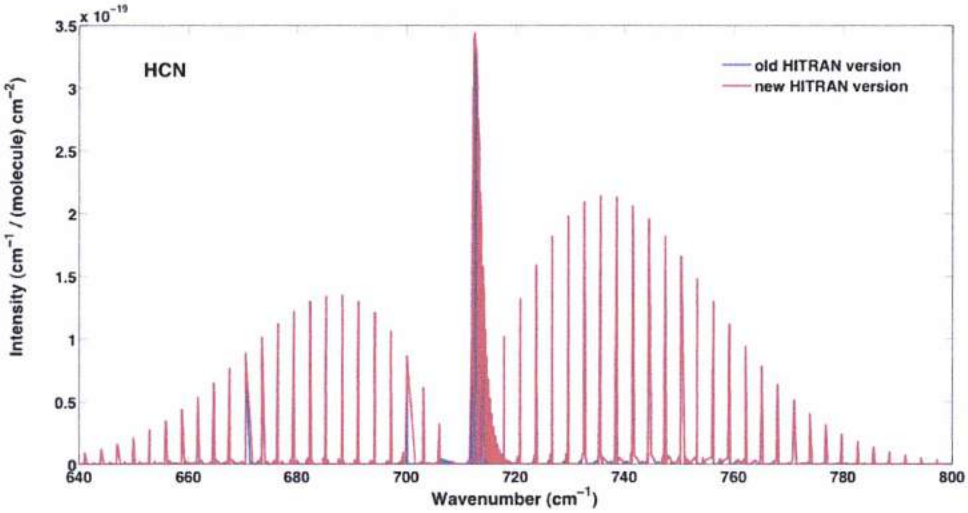

Figure 3. 22 - HCN lines series comparison between the two files adapted in old and new radiative transfer code within the range 640-800 cm^{-1}. Although the line lists files come from the same version of the HITRAN database (2008) some lines have been discarded in the existing file. The HITRAN 2008 line lists used in 0.3.8 version is shown in blue solid line, while the HITRAN 2008 file used in 1.0.0 version is shown in red solid line.

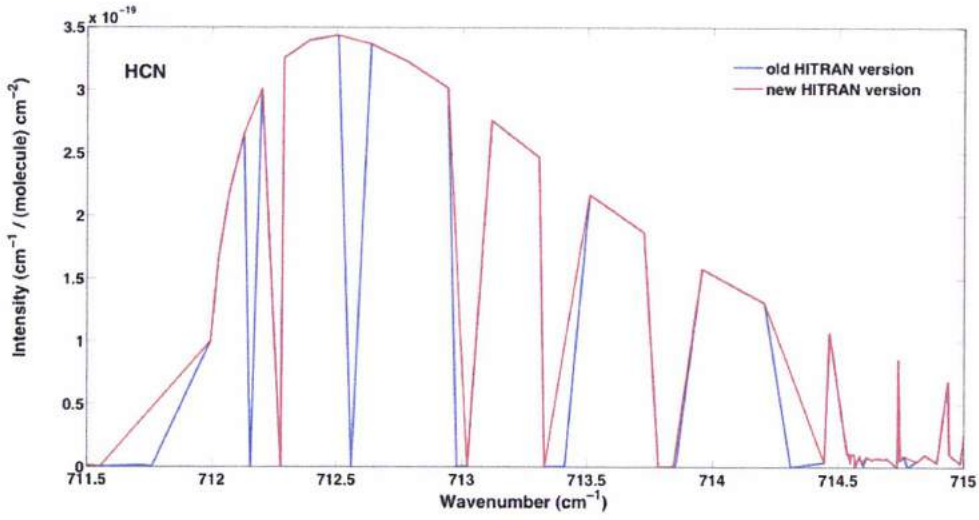

Figure 3. 23 - The same comparison with Fig. 3.22, but focused on the HCN Q-branch.

The HCN file adapted in the old version (0.3.8) is different from the one used in the latest version although they are both retrieved from *HITRAN 2008*. The old file includes lines with low intensity, which have been discarded from the latest version within the range from 711 to 715 cm^{-1}. The ARTT 0.3.8 version HCN line lists are an old *HITRAN 2008* edition, which contained lines with the identified low intensity and, apparently, the *HITRAN* administrators have upgraded the HCN file after 2010. This observation shows the significance of the new upgrade.

C_2H_2:

The next plot (Fig. 3.24) shows the updates of C_2H_2 spectroscopic dataset in *GEISA 2009*.

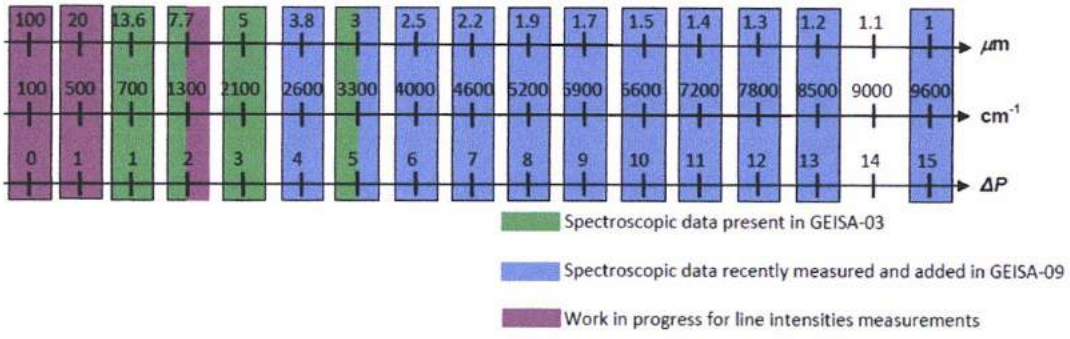

Figure 3. 24 - GEISA 2009 upgrade for C_2H_2 (adopted from Fig. 8 of Jacquinet-Husson et al., 2011).

The C_2H_2 upgrade in *GEISA 2009* contained new lines, but not in the region of FP3, therefore both ARTT versions produce the same signature in FP3 spectral simulation. Indeed, the

difference between the two models in Fig. 3.19 is close to zero for acetylene. Any deviance from the zero level can be explained by the contribution of the HCN emission.

C_3H_8:

Both models have high negative difference within the region between 700 and 800 cm^{-1} (Fig. 3.21-b). In this region, except for the P-wing of acetylene, the contribution of ν_{26} C_3H_8 emission band exists. The differences are indeed significant. Since the acetylene is the same in both models, we have to focus on the propane spectroscopic files. This difference can be explained by the fact that the GEISA 2009 lines contains the *GEISA 2003* ones multiplied by a factor of 0.420 (Jacquinet-Husson et al., 2011) because the *2003* line lists for propane ν_{26} band are incorrectly scaled (Nixon et al., 2009). When comparing the abundances retrieved by both code versions, the relation between the 0.3.8/1.0.0 is 0.420 as described above. The adoption of the new spectroscopic file for propane in ARTT 1.0.0 fixes this malfunction.

C_2H_6:

Both models have notable negative difference within the region between 800 and 880 cm^{-1} (Fig. 3.20-b). The lines lists used in ARTT 1.0.0 have been separated into two files. One was adopted from Vander-Auwera et al. (2007) at 1350-1496 cm^{-1} (FP4-region) and the other from GEISA 2009 at 613-843 cm^{-1} (FP3-region). For the FP3 part, the differences are notable. The same fit is achieved with a value 7.5% higher in 1.0.0 than in 0.3.8. The previous ARTT version calculates the fits by adopting C_2H_6 lines from Vander-Auwera et al. (2007). This difference can be explained by the fact that the *GEISA 2009* lines intensities are lower by a factor of 2.3% than the ones from Vander Auwera et al. (2007).

C_2H_4:

The differences in the region of C_2H_4 (900-1000 cm^{-1}) are indeed significant. Contrary to previous results, the ARTT new edition generates simulations with higher emission than the older version. The previous ARTT version used spectroscopic lines from Blass et al. (2001) and Rotger (2006 pers. comm.-Rotger et al., 2008), while the latest ARTT version adopts the *GEISA 2009* line lists. Rotger et al. (2008) have published measurements on the ν_{10} band of ethylene at 1442 cm^{-1}. Blass et al. (2001) line lists are not mentioned in the GEISA 2009 paper (Jacquinet-Husson et al., 2011). The abundance for the fit of CIRS data using the new *GEISA 2009* line lists is 4% lower compared to the previous code edition.

CO_2:

The new *GEISA 2009* database release includes line transitions of nine carbon dioxide isotopologues: $^{12}C^{16}O_2$ (the main), $^{13}C^{16}O_2$, $^{16}O^{12}C^{18}O$, $^{16}O^{12}C^{17}O$, $^{16}O^{13}C^{18}O$, $^{16}O^{12}C^{17}O$, $^{18}O^{12}C^{17}O$, $^{12}C^{18}O_2$ and $^{13}C^{18}O_2$. The first four isotopologues existed in *GEISA 2003* (Jacquinet-Husson et al., 2005), while the rest ones are new entries in the latest edition (Jacquinet-Husson et al., 2011). Except for the main molecule, all the isotopologues are new entries also in the ARTT 1.0.0 code. It should be noted that we have excluded the $^{13}C^{18}O_2$ since it has no transition lines in the spectral range of CIRS. The changes in line lists can be summarized as the increase in the number of transitions since the *GEISA 2009* version contains:

a) lowered minimum intensities (up to 10^{-30} $cm^{-1}/(molecule\ cm^{-2})$) at 296K and

b) merged line-lists of *CDSD-296* databank and JPL near infrared.

In CIRS FP3 spectra, the emission of carbon dioxide at 667 cm^{-1} has no significant difference when using the previous and the new ARTT version (Fig. 3.21-b). However, when fitting the same spectral selection by using both codes, the difference in abundance is at about 2% higher values for 1.0.0. This can be explained by the increase of the number of the transition lines of CO_2 in the new *GEISA* edition (Fig. 3.25).

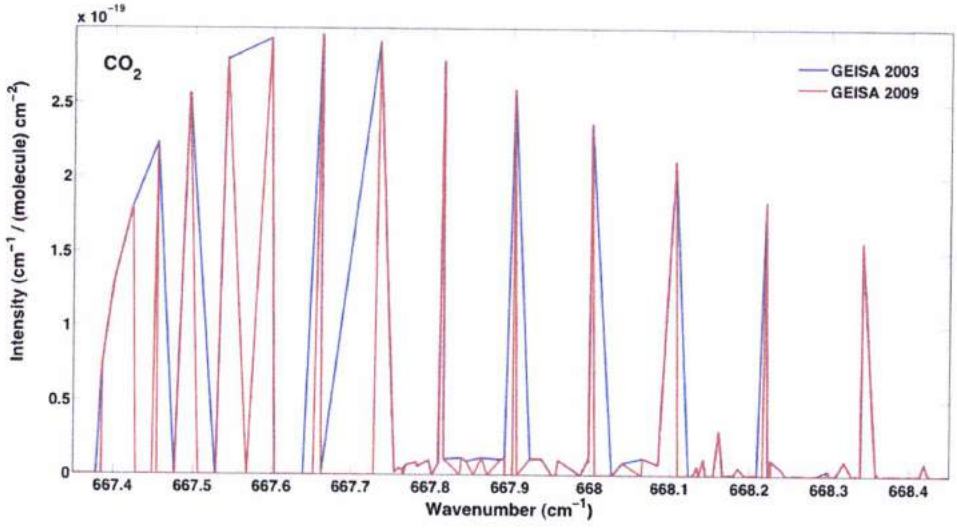

Figure 3. 25 - Focus on the Q-branch of CO_2 line lists comparison between GEISA 2003 line lists (blue solid line) and GEISA 2009 (red solid line). Here, the significantly increased number of transition lines is depicted.

C_4H_2:

The following plot (Fig. 3.26) illustrates the spectroscopic lines from the files used in old and new ARTT versions. The lines used in 0.3.8 version are from Arie & Johns (1992), while the new ones are from Jolly et al. (2010) in *GEISA 2009*. However, the abundances for fitting the same selection with the two code versions are the same.

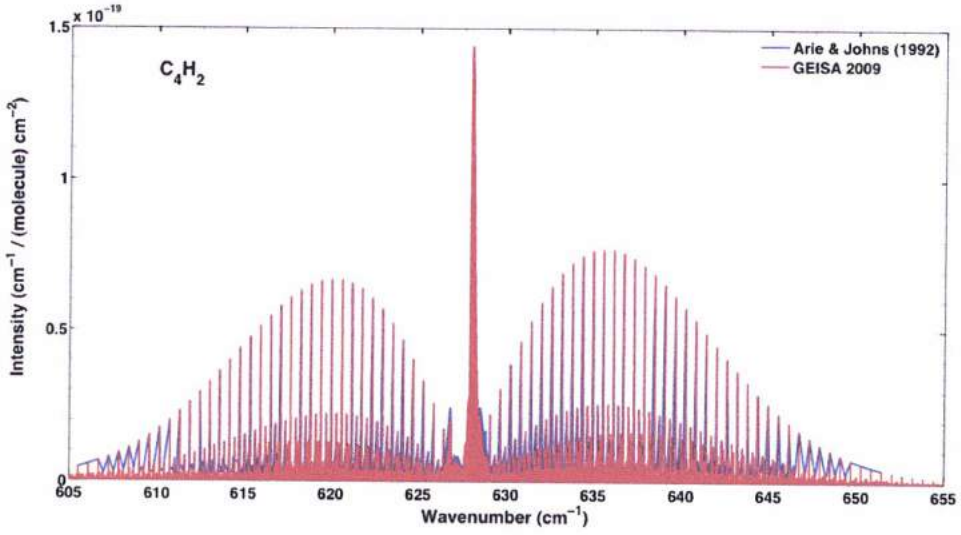

Figure 3. 26 - Line lists comparison between Arie & Johns (1992) (blue solid line) and GEISA 2009 (red solid line).

Table 3. 5 - The major molecules within the spectroscopic region of comparison

Molecule	0.3.8	1.0.0	Comments
HCN	HITRAN 2008	HITRAN 2008 (about 14% higher abundances with the new spectroscopic files)	The spectroscopic files are the same but the one in 0.3.8 has "almost zero" lines. These lines have been discarded from the latest file in 1.0.0 version.
C_2H_2	GEISA 2003	GEISA 2009	No upgrade has been imported from the 2003 version to the latest 2009 at the FP3 spectral region. The emission is the same. Change in the emission of ν26 propane band.
ν_{26} C_3H_8	GEISA 2003	GEISA 2009	The GEISA 2009 lines file contains the GEISA 2003 ones multiplied by a factor of 0.420. The CIRS/team site has the same file with GEISA 2009 file. Difference in fits. The same fit is achieved with a value 7.5% higher in 1.0.0 than in 0.3.8.
C_2H_6	Vander Auwera et al. (2007)	GEISA 2009 at 613-843 cm^{-1} and Vander Auwera et al. (2007) at 1350-1496 cm^{-1}	Devi et al. (2010) have found that ethane in ν_9 line intensities are 10-15% lower than in Vander Auwera et al. (2007) which mean that GEISA 2009 values are 10-15% higher. GEISA 2009 lines intensities are lower by a factor of 2.3% than the ones from Vander Auwera et al. (2007).
C_2H_4	Blass et al. (2001) and Rotger 2006	GEISA 2009	4% lower abundance for fitting the molecule comparing to the 0.3.8 one.
CO_2	GEISA 2003	GEISA 2009	No significant change in the emission signature of the main isotopologue at 667 cm^{-1}. The abundance of 1.0.0 fit is 2% higher than in the previous version.
C_4H_2	Arié and Johns (1992) for ν_8 and hot bands	GEISA 2009	GEISA 2009 adopts Jolly et al. (2010) line lists. No change in fits' abundances between the two versions.

The work described hereabove on the comparisons among the code versions, serves the purpose of helping adjusting new inferences to past ones, without having to redo all the

calculations and also understanding any discrepancies found with previous results, while identifying significant and real variations.

3.5 Conclusions

The new radiative transfer code upgrade functions in an enhanced and optimized way and allows for an improved fit to the data, thanks to the updated haze and spectroscopic parameters. Furthermore, the previous version generated the synthetic spectra by taking into account 21 molecules. In the upgraded edition, ARTT can search for 18 additional molecules and isotopologues provided from the latest available spectroscopic databases with more precise molecular parameters. The molecular inventory of the code has been almost doubled. This allows us first of all improve the fit with molecules such as those that have been recently detected by Nixon et al., (2008a; 2008b) and Jennings et al. (2008). Secondly, the research for the presence of more complex and new weak species, as will be discussed in Chapter 4. Moreover, by using large spectral averages from CIRS data, the identification of more minor isotopologues is easier.

Some problems of the previous version have been fixed, such as the propane v_{26} line strengths which are corrected. Additionally, the continuum is better fitted due to the more accurate aerosol distribution, which has been adopted. The computational time stays within acceptable levels considering the amount of calculations, which the software performs during each simulation.

Chapter 4

Titan's stratosphere by Cassini/CIRS

The Cassini-Huygens mission in the Kronian system has revealed a complex world in its largest satellite, Titan. The stratospheric organic chemistry, resulting from several processes like photodissociation and recombination starting with the mother molecules N_2 and CH_4, comprises a large number of hydrocarbons and nitriles. In addition, a few oxygen compounds were detected, possibly of external origin. The research so far has concluded that the relations between Titan's atmospheric veil with the surface, and probably the interior, are very close. Hence, the study of the atmospheric composition, and especially its trace gaseous molecules and their isotopologues, from the surface to the upper atmosphere, is crucial for obtaining a complete picture of the moon.

After giving the basis for my research (processes, method), I present the results of yearly CIRS spectral averages analyses during the Cassini nominal mission, which were published in *Icarus* (Coustenis et al., 2010b). This study provided us with the latitudinal distribution of temperature and composition from South to the North in Titan's stratosphere and allowed me to train in CIRS spectral processing and analysis.

In this Chapter, I also present more time-resolved results of the Cassini/CIRS spectra analysis which I have performed, in order to investigate the temperature structure and the trace gaseous composition of Titan's stratosphere from the beginning of the mission up to early 2012. This work has been recently published in the *Astrophysical Journal* (Bampasidis et al., 2012a). I report in this Chapter the inferred variations in temperature and chemical composition in the stratosphere during the Cassini mission, which include Titan's Northern Spring Equinox (NSE) in mid-2009.

During these studies, I also worked on the mixing ratios of benzene and HC_3N, weaker molecules, hence more difficult to determine and not yet published in their entirety. For benzene, we have obtained vertical distributions from the surface of Titan to the upper atmosphere by applying the 1-D photochemical model of Lavvas et al. (2008a;b). This work was presented in *Faraday Discussions 147*: Chemistry of the Planets, which was held in Saint Jacut de la Mer (France) from 14 to 16 June 2010 (Bampasidis et al., 2010b).

Moreover, we have applied our own radaitive transfer code to analyze CIRS data in the focal plane 1 (FP1) in order to search for water vapor, following a first detection by ISO (Coustenis et al. 1998). Our own analysis verified the calculations performed with another radiative transfer code used by our collaborators at the GSCF and in Oxford. The results of this study have been recently published in *Icarus* (Cottini et al., 2012a).

Recently, we have also focused on changes observed in the emission bands of several components at higher northern and southern latitudes than the ones we usually explore and the evolution in time that we find indicate a seasonal cycle which affects some species (like HC_3N and the haze products) more than others. This work was recently accepted for publication in the *Astrophysical Journal Letters* (Jennings et al., 2012, *in press*).

I complete this Chapter by describing some perspectives for the future where we look at the possible detection of some weak species or new molecules in large averages and also in the evolution with time of some of the most abundant species in Titan's atmosphere since the Voyager times.

4.1 Titan's stratosphere before the Cassini-Huygens mission

Cassini entered into Saturn insertion orbit (SOI) on 2 July 2004 and since then it observes Titan closely through several programmed flybys. The Composite Infrared Spectrometer (CIRS) (Flasar et al., 2004) operates during most of them, delivering numerous infrared spectra with spectral resolutions varying between 0.5 cm^{-1}, 2.5 cm^{-1}, and 15.5 cm^{-1}. A detailed description of the instrument was given in Chapter 2 along with a description of my personal contribution to the improvement of the CIRS data processing. In order to analyze CIRS spectra, we also had to upgrade the existing radiative transfer code to produce a new powerful software version that incorporates all the recent spectroscopic data (Rothman et al., 2009; Jacquinet-Husson et al., 2011) and a new aerosol model (Flasar et al., 2004; Vinatier et al., 2012b). The procedure and the results of this upgrade were described in Chapter 3. Before now describing the data I have used in my work here, I will briefly discuss the pre-Cassini knowledge of Titan's stratospheric thermal structure and composition as relevant to my research.

4.1.1 Voyager 1 & 2 encounters

Infrared spectroscopy has provided the characterization of Titan's temperature and chemical structure. The first *in situ* measurements in the thermal radiation of Titan were obtained during the Voyager 1 encounter, in November 1980, right after Titan's northern spring equinox. The Infrared Spectrometer Radiometer (IRIS) on board the spacecraft (Hanel et al., 1980) performed disk-resolved observations of Titan's stratosphere at different latitudes and longitudes with a spectral resolution of 4.3 cm^{-1} in the 200 and 1500 cm^{-1} region.

The results of the V1/IRIS spectral analysis provided the temperature of the stratosphere as well as its composition. Molecular nitrogen was determined to be the dominant species, followed by methane in a few percent mole fraction (Broadfoot et al., 1981; Hanel et al., 1981; Tyler et al., 1981). Voyager also detected a rich inventory of trace gases in the atmosphere consisting of hydrocarbons and nitriles. Indeed, acetylene, ethylene, ethane and hydrogen cyanide were identified through their emission spectral signatures (Hanel et al., 1981). Moreover, methyl acetylene and propane were tentatively identified (Maguire et al., 1981) and confirmed since then, while diacetylene, cyanoacetylene and cyanogen were also found in the stratosphere (Kunde et al., 1981). The existence of mono-deuterated methane was reported a little later (Kim & Caldwell, 1982), while the first oxygen-bearing compound (CO_2) was also identified in the V1/IRIS spectra a year later (Samuelson et al., 1983).

Equatorial vertical atmospheric refractivity profiles were yield by Voyager 1 radio occultation measurements (Radio Science System-RSS) from the surface up to 200 km. These measurements were used to retrieve vertical thermal profiles (Lindal et al., 1983). These temperature profiles depended on the atmospheric composition and a pure nitrogen atmosphere was assumed at the time. Lellouch et al. (1989) reanalyzed the V1/RSS measurements and updated the thermal profiles by using a more precise atmospheric composition, including methane and various Argon molecular fractions.

A thorough analysis of IRIS spectra provided the vertical and spatial variations of the temperature and composition from 53°S to 70°N in 1980. The temperature profiles used in these studies were retrieved from the best fit of the ν_4 methane emission band at different latitudes (Coustenis et al., 1989a;1989b;1991; Coustenis & Bezard, 1995). The warmest region was found to be close to the equator (5-7°S). A temperature decrease of about 17 K at 0.4 mbar (225 km) was observed between the 5°S and 70°N, while a shorter decrease of about

3 K was observed at the south hemisphere from 5°S to 53°S (Flasar & Conrath, 1990; Coustenis & Bezard, 1995).

As far as the trace gaseous concentrations are concerned, no longitudinal variation has been found by V1/IRIS data in Titan's stratosphere between 4 and 9 mbar (Coustenis et al., 1989a). HCN increased significantly from pole to pole, while carbon dioxide mole fraction remained constant in respect to the latitude. The abundances of the other trace constituents presented variations from the equatorial latitudes and northwards. Ethane, acetylene and propane showed a moderate increase by a factor of two. Methyl acetylene, ethylene and diacetylene showed significant enrichments at latitudes northern than 50°N. The other nitriles, cyanogen and cyanoacetylene have no spectral signatures from 50°N and southwards (Fig 1.3 in Chapter 1). The results of this research are listed in Table 1 below.

Table 4. 1 - Trace gaseous abundances of Titan's stratosphere from Coustenis & Bezard (1995) retrieved from V1/IRIS spectra in 1980.

Molecule	Sample I (lat. in °) (53°S)	H (32°S)	G (7°S)	A, B, C (7°N)	D (30°N)	E (50°N)	F (70°N)	North/ south (E/I)
C_2H_2	$2.5 \pm 0.3 \times 10^{-6}$	$3.0 \pm 0.4 \times 10^{-6}$	$2.7 \pm 0.2 \times 10^{-6}$	$3.0 \pm 0.3 \times 10^{-6}$	$2.7 \pm 0.5 \times 10^{-6}$	$5.5 \pm 1.0 \times 10^{-6}$	$6.5 \pm 2.1 \times 10^{-6}$	2.2 ± 0.5
C_2H_6	$1.5 \pm 0.5 \times 10^{-7}$	$1.5 \pm 0.3 \times 10^{-7}$	$1.5 \pm 0.3 \times 10^{-7}$	$1.5 \pm 0.4 \times 10^{-7}$	$1.5 \pm 0.5 \times 10^{-7}$	$1.0 \pm 0.3 \times 10^{-6}$	$1.5 \pm 0.5 \times 10^{-6}$	7 ± 3
C_2H_4	$1.15 \pm 0.1 \times 10^{-5}$	$1.35 \pm 0.1 \times 10^{-5}$	$1.65 \pm 0.1 \times 10^{-5}$	$1.3 \pm 0.1 \times 10^{-5}$	$1.25 \pm 0.15 \times 10^{-5}$	$1.85 \pm 0.2 \times 10^{-5}$	$1.65 \pm 0.3 \times 10^{-5}$	1.6 ± 0.2
C_3H_4	$3.5 \pm 0.7 \times 10^{-9}$	$4.5 \pm 0.7 \times 10^{-9}$	$8.0 \pm 0.6 \times 10^{-9}$	$5.0 \pm 0.9 \times 10^{-9}$	$6.0 \pm 1.6 \times 10^{-9}$	$3.3 \pm 0.2 \times 10^{-9}$	$3.7 \pm 0.3 \times 10^{-9}$	9.5 ± 2
C_3H_8	$6.0 \pm 1.5 \times 10^{-7}$	$6.0 \pm 1.4 \times 10^{-7}$	$9.0 \pm 1.6 \times 10^{-7}$	$5.0 \pm 1.7 \times 10^{-7}$	$7.0 \pm 3.0 \times 10^{-7}$	$1.0 \pm 0.3 \times 10^{-6}$	$1.2 \pm 0.5 \times 10^{-6}$	1.7 ± 0.7
C_4H_2	$1.0 \pm 0.3 \times 10^{-9}$	$1.3 \pm 0.3 \times 10^{-9}$	$1.7 \pm 0.3 \times 10^{-9}$	$1.4 \pm 0.4 \times 10^{-9}$	$1.2 \pm 0.4 \times 10^{-9}$	$1.5 \pm 0.2 \times 10^{-8}$	$2.7 \pm 0.4 \times 10^{-8}$	15 ± 5
HCN	$4.7 \pm 0.5 \times 10^{-8}$	$7.0 \pm 0.8 \times 10^{-8}$	$2.2 \pm 0.2 \times 10^{-7}$	$1.7 \pm 0.2 \times 10^{-7}$	$2.4 \pm 0.4 \times 10^{-7}$	$1.1 \pm 0.2 \times 10^{-6}$	$1.5 \pm 0.3 \times 10^{-6}$	23 ± 4
C_2N_2	$<1.5 \times 10^{-9}$	$<1.5 \times 10^{-9}$	$<1 \times 10^{-9}$	$<1.5 \times 10^{-9}$	$<2 \times 10^{-9}$	$1.5 \pm 0.2 \times 10^{-8}$	$2.2 \pm 0.3 \times 10^{-8}$	>10
HC_3N	$<1.5 \times 10^{-9}$	$<1.5 \times 10^{-9}$	$<1.5 \times 10^{-9}$	$<1.5 \times 10^{-9}$	$<2 \times 10^{-9}$	$2.5 \pm 0.5 \times 10^{-8}$	$4.5 \pm 0.9 \times 10^{-8}$	>17
CO_2	$1.3 \pm 0.2 \times 10^{-8}$	$1.5 \pm 0.2 \times 10^{-8}$	$1.5 \pm 0.15 \times 10^{-8}$	$1.4 \pm 0.2 \times 10^{-8}$	$1.1 \pm 0.25 \times 10^{-8}$	$1.3 \pm 0.5 \times 10^{-8}$	$1.3 \pm 0.55 \times 10^{-8}$	1 ± 0.4
			Haze optical depth for $\sigma > 600$ cm^{-1}[a]					
τ_A/τ_{Sample}	0.83 ± 0.06	0.93 ± 0.06	1.34 ± 0.15	1.00	1.00 ± 0.09	2.11 ± 0.10	2.83 ± 0.40	2.54 ± 0.27

[a] Relative to the equatorial optical depth, calculated at wavenumbers 650, 900, 1000, and 1100 cm^{-1}.

A few months later, in August 1981, Voyager 2 flew by Titan, but at a distance 170 times greater. The analysis of V2/IRIS spectra probing the atmosphere in the altitude range of 80-130 km. V2 results confirm the ones from V1 and the temperature structure which was retrieved from V2/IRIS showed a decrease from equator to northern latitudes of about a 10 K.

No significant temporal variations were observed within this time interval of 9 months between the two encounters. No significant latitudinal variations were recorded for acetylene, ethane and propane within the error bars. Like in the V1/IRIS spectra, HCN showed a significant increase at higher northern latitudes (50°N) by a factor of 2. C_4H_2 and C_3H_4 also presented the same enhancement. Only upper limits were derived for C_2H_4, HC_3N, C_2N_2 and CH_3D. The results are listed in Table 4.2 below (Letourneur & Coustenis, 1993).

Table 4. 2 - Trace gaseous abundances of Titan's stratosphere from Letourner & Coustenis (1992), retrieved from V2/IRIS spectra in 1981.

Abundances	Sample A (=B+C+D)	Sample B 50 N	Sample C 28 N	Sample D 6 N
Acetylene (C_2H_2)	$2.6^{+1.1}_{-1.3} \times 10^{-6}$	$2.6^{+1.5}_{-1.5} \times 10^{-6}$	$2.6^{+1.1}_{-1.5} \times 10^{-6}$	$2.7^{+1.3}_{-1.5} \times 10^{-6}$
Ethylene (C_2H_4)	$<1 \times 10^{-6}$	—	—	—
Ethane (C_2H_6)	$1.4^{+0.7}_{-0.6} \times 10^{-5}$	$1.9^{+2.3}_{-1.6} \times 10^{-5}$	$1.4^{+0.8}_{-0.9} \times 10^{-5}$	$1.2^{+0.6}_{-0.9} \times 10^{-5}$
Methyl acetylene (C_3H_4)	$6.0^{+2.2}_{-2.5} \times 10^{-9}$	$1.2^{+0.6}_{-0.7} \times 10^{-8}$	$6.0^{+2.2}_{-2.5} \times 10^{-9}$	$6.0^{+2.5}_{-3} \times 10^{-9}$
Propane (C_3H_8)	$5^{+3}_{-4} \times 10^{-7}$	$2.2^{+1.6}_{-2} \times 10^{-6}$	$5.0^{+3}_{-4} \times 10^{-7}$	$7.0^{+4.4}_{-5.8} \times 10^{-7}$
Diacetylene (C_4H_2)	$1.4^{+0.7}_{-1} \times 10^{-9}$	$2.8^{+2.5}_{-2.3} \times 10^{-9}$	$1.4^{+0.5}_{-0.9} \times 10^{-9}$	$1.3^{+0.8}_{-1} \times 10^{-9}$
Hydrogen cyanide (HCN)	$2.8^{+1}_{-1.5} \times 10^{-7}$	$6.0^{+2.7}_{-4} \times 10^{-7}$	$2.8^{+1}_{-1.4} \times 10^{-7}$	$2.2^{+1}_{-1.3} \times 10^{-7}$
Carbon dioxide (CO_2)	$1.1^{+0.5}_{-0.5} \times 10^{-8}$	$1.1^{+1.6}_{-1} \times 10^{-8}$	$1.0^{+0.7}_{-0.6} \times 10^{-8}$	$1.5^{+1.5}_{-0.7} \times 10^{-8}$
Cyanogen (C_2N_2)	$<2 \times 10^{-9}$	—	—	—
Cyano acetylene (HC_3N)	$<3 \times 10^{-9}$	—	—	—
Monodeuterated methane (CH_3D)	$<2 \times 10^{-5}$	—	—	—

4.1.2 Infrared Space Observatory (ISO)

Almost two Titan seasons after the Voyager close fly-by, Titan's stratosphere was again observed by the Infrared Space Observatory (ISO) in 1997, close to northern autumnal equinox. The ISO spectrometers performed disk-averaged observations within the 7-30 μm region with a grating spectral resolution (>10^6), an order of magnitude higher than Voyager/IRIS.

The nominal thermal profile retrieved from ISO is warmer than any of the IRIS-inferred thermal profiles at pressures lower than 1 mbar. The ISO higher resolution measurements helped to separate the spectroscopic signatures of C_4H_2 and C_3H_4 (at around 630 cm^{-1}) as well as of the HC_3N and CO_2 (contributing at around 660 cm^{-1}), which were blended in the IRIS data. The abundances of the trace constituents retrieved from ISO spectra are listed in Table 4.3 below with the Voyager 1 equatorial abundances for comparison. The latter are the outcome of a recalculation in 2003 of the V1 values from Coustenis et al. (1995) by using updated spectroscopic lines for the contributing molecules. It should be noted that the V1 values are latitude-depended and the ISO results are disk-average abundances. Additionally, the altitudes which are probed should be taken into consideration as well as the fact that ISO data incorporate also a limb contribution. The equatorial V1 retrievals are therefore the closer for an actual comparison with the ISO ones (Coustenis et al., 2003) as indicated at the Table 4.3.

Table 4. 3 - Trace gaseous abundances of Titan's stratosphere from Coustenis et al. (2003), retrieved from ISO spectra taken in 1997. The Voyager equatorial values have been recalculated by adopting updated spectroscopic parameters.

Molecule or isotopic ratio	Abundance	
	Voyager equator	ISO disk-average
C_2H_2	$2.85^{+1}_{-1.2} \times 10^{-6}$	$5.5 \pm 0.5 \times 10^{-6}$
C_2H_4	$1.5^{+0.5}_{-0.8} \times 10^{-7}$	$1.2 \pm 0.3 \times 10^{-7}$
C_2H_6	$1.5^{+0.6}_{-0.8} \times 10^{-5}$	$2.0 \pm 0.8 \times 10^{-5}$
C_3H_4	$6.5^{+2.0}_{-2.5} \times 10^{-9}$	$1.2 \pm 0.4 \times 10^{-8}$
C_3H_4 (allene)		$<2.0 \times 10^{-9}$
C_3H_8	$7.0 \pm 4.0 \times 10^{-7}$	$2.0 \pm 1.0 \times 10^{-7}$
C_4H_2	$1.5 \pm 0.7 \times 10^{-9}$	$2.0 \pm 0.5 \times 10^{-9}$
C_6H_6 (benzene)		$4.0 \pm 3.0 \times 10^{-10}$
HCN	$1.95^{+0.5}_{-0.9} \times 10^{-7}$	$3.0 \pm 0.5 \times 10^{-7}$
CO_2	$1.45^{+0.35}_{-0.55} \times 10^{-8}$	$2.0 \pm 0.2 \times 10^{-8}$
H_2O at 400 km		8×10^{-9}
CH_3D	$1.1^{+0.7}_{-0.6} \times 10^{-5}$	$6.7^{+2.9}_{-1.9} \times 10^{-6}$
D/H	$1.5^{+1.4}_{-0.5} \times 10^{-4}$	$8.7^{+3.2}_{-1.9} \times 10^{-6}$
HC_3N	$<1.0 \times 10^{-9}$	$5.0 \pm 3.5 \times 10^{-10}$
C_2N_2	$<1.0 \times 10^{-9}$	

The ethane mole fraction remained constant compared to the V1 era as well as those of CO_2, C_2H_4, C_3H_8, C_3H_4 and C_4H_2 within the error bars. On the other hand, acetylene and HCN exhibited an increase of 30% in the ISO spectra. Cyanoacetylene was observed in disk-averaged spectra for the first time at 553 cm^{-1}. One of the most important discoveries of the ISO Short Wavelength Spectrometer (SWS) was the firm detection of two water vapor signatures near 40 micron (Coustenis et al., 1998) and of benzene in Titan's atmosphere at 674 cm^{-1} with a maximum emission coming from atmospheric levels between 0.2 and 20 mbar (Coustenis et al., 2003).

4.1.3 Ground-based observations

Ground-based observations of Titan offer significant information on the stratospheric composition as well as on the vertical distribution of molecular abundances is several cases.

After CO_2, the other oxygen-bearing species, carbon monoxide (CO), was discovered on Titan by Lutz et al. (1983) with near infrared observations at the Mayall telescope of Kitt Peak National Observatory (KPNO) - USA. Acetonitrile (CH_3CN) was firstly detected by Bezard et al. (Bezard et al., 1993) from spectra acquired at the Institut de Radioastronomie Milimetrique - IRAM - (Spain) radiotelescope. Using the same facility, Marten et al. (2002) provided the first vertical profiles of Titan's stratospheric nitriles (HCN, HC_3N and CH_3CN), as also reported by Paubert et al. (1984). Moreover, the isotopic ratios of $^{12}C/^{13}C$ from HCN

(Hidayat et al., 1997), $^{14}N/^{15}N$ from HCN (Marten et al., 2002) and $^{16}O/^{18}O$ (Gurwell, 2008) were measured, but the latter have not been fully published yet. Millimeter observations at IRAM also delivered the vertical profile of HCN (Paubert et al., 1987; Tanguy et al., 1990).

NASA Infrared Telescope Facility (IRTF) ethane measurements (Kostiuk et al., 1997; 2005; Livengood et al., 2002) at 12 μm (emission coming from 7 to 0.1 mbar) gave values comparable to the V1/IRIS results. The first spectrally-resolved detection of the propane emission band on Titan's stratosphere was made at NASA/IRTF (Roe et al., 2003). A south spring polar accumulation of ethylene was also shown just before solstice (Roe et al., 2004b) at Keck Observatory spectra using the Long Wavelength Spectrometer (LWS). These spectra were taken from the south polar region of Titan, which had not been observed by Voyager 1. High-resolution spectroscopy at 3 μm provided measurements of HCN and C_2H_2 high in Titan's stratosphere and mesosphere and CH_3D in Titan's troposphere (Geballe et al., 2003; Kim et al., 2005). In the Table 4.4 below, I have gathered these and more the ground-based observations of Titan's stratospheric trace gases published so far to the best of our knowledge.

Recently, the Heterodyne Instrument of the Far-Infrared (HIFI) on board ESA's Herschel Space Observatory (de Graauw et al., 2010; Pilbratt et al., 2010) reported the first detection of hydrogen isocyanide (HNC) in Titan's atmosphere at 18.14 cm^{-1} (Moreno et al., 2011), during observations of Titan on June 14 and December 31, 2010 and provided abundances of several species (Courtin et al., 2011; Moreno et al., 2012).

Table 4. 4 - Trace gaseous abundances of Titan's stratosphere from ground-based observations. To compare them with the Cassini data, we take into account only the observations pertaining to Titan's center and in the stratosphere, essentially at altitudes between 1 and 10 mbar (100-200 km roughly) depending on the molecule (see contribution functions and text for more details).

Species	OBSERV. DATE	Ls	ABUNDANCE	ALTITUDE (km)	LATITUDE	INSTRUMENT	REFERENCE	RESOLVING POWER	cm^{-1}	COMMENTS
C_2H_2	10/1/1997	194	$4.92\pm0.43 \times 10^{-6}$	stratosphere	disk average	ISO	Coustenis et al. 2003	1650-2000		reanalysis of Coustenis et al. 2003 values
	21/11/2001	257	$7.00\pm4.50 \times 10^{-6}$	300	disk average	KECK II NIRSPEC	Kim et al. 2005	2.5×10^4	3225 - 3472	DATA: reanalysis of Geballe et al. 2003 observations. The tempareture profile used in this work is consistent with Yelle (1991) and Strobel et al. (1992), but not with Lellouch et al. (1990)
			$5.60\pm3.30 \times 10^{-6}$	200						
			$4.00\pm2.30 \times 10^{-6}$	100						
C_2H_4	04/1974-04/1975	282-295	$1.10\pm0.90 \times 10^{-7}$	stratosphere	disk average	Kitt Peak National Observatory	Gillett, 1975 & Orton, 1992	2.0×10^{-2}		The abundance has been adjusted lowered by a factor of 35% (see Coustenis et al. 2007; 2010) since the original value was derived by using old spectroscopic data
	10/1/1997	194	$8.48\pm1.00 \times 10^{-8}$	stratosphere	disk average	ISO	Coustenis et al. 2003	1650-2000		reanalysis of Coustenis et al. 2003 values
C_4H_2	10/1/1997	194	$1.67\pm0.42 \times 10^{-9}$	stratosphere	disk average	ISO	Coustenis et al. 2003	1650-2000		reanalysis of Coustenis et al. 2003 values
	21/11/2001	257	$< 1.00 \times 10^{-7}$	stratosphere	disk average	KECK II NIRSPEC	Kim et al. 2005	2.5×10^4	3225 - 3472	ν_4 band. Reanalysis of Geballe et al. 2003 observations, T-profile: consistent with Yelle 1991 and Strobel et al. (1992) but not with Lellouch et al. (1990). Below 1 mbar the V1/ISO profile adapted

Species	OBSERV. DATE	Ls	ABUNDANCE	ALTITUDE (km)	LATITUDE	INSTRUMENT	REFERENCE	RESOLVING POWER	cm^{-1}	COMMENTS
C_2H_6	04/1974-04/1975	282-295	$1.00\pm0.30 \times 10^{-5}$	stratosphere	disk average	Kitt Peak National Observatory	Gillett, 1975 & Orton, 1992	2.0×10^{-2}		The abundance has been adjusted lowered by a factor of 35% (see Coustenis et al. 2007, 2010) since the original value was derived by using old spectroscopic data
	08/1993	153	$1.96\pm2.42 \times 10^{-5}$	stratosphere	center	IRTF (IRHS)	Livengood et al. 2002	1.0×10^{6}	841-851	ν_9 band. Position of Titan: Near Saturn opposition. Ethane well-mixed all over the atmosphere
			$5.80\pm3.30 \times 10^{-6}$	stratosphere	west					
	10/1995	179	$9.40\pm9.40 \times 10^{-6}$	120 - 300	disk average	IRTF (IRHS)	Kostiuk et al. 1997	1.0×10^{6}	841-851	ν_9 band. Temperature profile: Yelle et al. 1992 is a report which is finally published in Yelle et al. 1997
	10/1995	179	$1.17\pm0.44 \times 10^{-5}$	stratosphere	east	IRTF (IRHS)	Livengood et al. 2002	1.0×10^{6}	841-851	ν_9 band. Position of Titan: Near Saturn opposition. Ethane well-mixed all over the atmosphere. Update of Kostiuk et al. (1997)
			$1.36\pm0.71 \times 10^{-5}$	stratosphere	west					
	09/1996	190	$1.60\pm0.77 \times 10^{-5}$	stratosphere	east	IRTF (IRHS)	Livengood et al. 2002	1.0×10^{6}	841-851	ν_9 band. Position of Titan: Near Saturn opposition. Ethane well-mixed all over the atmosphere
			$5.20\pm5.90 \times 10^{-6}$	stratosphere	west					
	08/1993 - 09/1996	153 - 190	$8.80\pm2.20 \times 10^{-6}$	stratosphere	disk average	IRTF (IRHS)	Livengood et al. 2002	1.0×10^{6}	841-851	ν_9 band. Position of Titan: Near Saturn opposition. Ethane well-mixed all over the atmosphere
	10/1/1997	194	$1.12\pm0.45 \times 10^{-5}$	stratosphere	disk average	ISO	Coustenis et al. 2003	1650-2000		reanalysis of Coustenis et al. 2003 values

Species	OBSERV. DATE	Ls	ABUNDANCE	ALTITUDE (km)	LATITUDE	INSTRUMENT	REFERENCE	RESOLVING POWER	cm^{-1}	COMMENTS
C_2H_6	18/12/2003	286	$3.00\pm1.50 \times 10^{-6}$	stratosphere	15N-40S West	NAO Subaru 8.2-m	Kostiuk et al. 2005	$1\text{-}25\times 10^{6}$	851	Titan position: Summer solstice at January 2003, high stratospheric winds should rapidly mix C_2H_6 horizontally
			$9.00\pm5.00 \times 10^{-6}$	stratosphere	5°N-50°S East					
			$8.00\pm3.00 \times 10^{-6}$	130 - 300	Simultaneously East & West					
	08/93 - 12/2003	153 - 286	$8.60\pm3.00 \times 10^{-6}$	100 - 300	disk average	IRTF (IRHS) - NAO Subaru 8.2-m (HIPWAC)	Kostiuk et al. 2010	1.0×10^{6}	851	Bands of other constituents with weaker signatures may contribute to the total measured radiance at ethane's band. Thus, if those molecules do not be distinguished from the spectrum, the derived values for C_2H_6 are higher than the real ones and therefore the ground based measurements experience differences. CIRS (Coustenis et al., 2010) and Kostiuk et al., 2010) agree in ethane abundance although the former probes in lower atmospheric altitudes (Kostiuk et al., 2010). However, C_2H_6 is well mixed in the stratospheric layers almost independed from the altitude (c.f. Vinatier et al. 2010b).

Species	OBSERV. DATE	Ls	ABUNDANCE	ALTITUDE (km)	LATITUDE	INSTRUMENT	REFERENCE	RESOLVING POWER	cm^{-1}	COMMENTS
HCN	8/9/1986 - 6/5/1987	76 - 84	$7.50\pm0.80 \times 10^{-8}$	100	disk average	IRAM 30-m	Tanguy et al. 1990		2.95	Ripple effect in data. Best fit at 170 km, first detection of HCN in September 1986 using IRAM (Paubert et al. 1987)
			$3.30\pm0.90 \times 10^{-7}$	170						
			$6.20\pm2.10 \times 10^{-7}$	200						
			$5.20\pm6.60 \times 10^{-6}$	300						
	22/5/1995	174	$5.00\pm1.10 \times 10^{-8}$	100	disk average	IRAM 30-m	Hidayat et al. 1997		2.95	
			$1.50\pm0.50 \times 10^{-7}$	170						
			$3.50\pm1.10 \times 10^{-7}$	200						
	10/1/1997	194	$2.42\pm0.40 \times 10^{-7}$	stratosphere	disk average	ISO	Coustenis et al. 2003	1850		reanalysis of Coustenis et al. 2003 values
	07/1997 and 12/1999	200 and 232	$4.00\pm2.00 \times 10^{-8}$	100	disk average	IRAM 30-m	Marten et al. 2002		2.95	S/N has improved by a factor of 6 from Hidayat et al. (1997). Dates of observations: 04/1996, 07/1997, 12/1998 and 12/1999
			$2.10\pm0.80 \times 10^{-7}$	170						
			$4.50\pm1.50 \times 10^{-7}$	200						
			$5.20\pm1.60 \times 10^{-7}$	250						
			$5.80\pm2.00 \times 10^{-7}$	300						

Species	OBSERV. DATE	Ls	ABUNDANCE	ALTITUDE (km)	LATITUDE	INSTRUMENT	REFERENCE	RESOLVING POWER	cm^{-1}	COMMENTS
C_2H_6	15/1/2005	300	$9.30\pm7.30 \times 10^{-6}$	250 - 316	disk center	NAO Subaru 8.2-m (HIPWAC)	Livengood et al. 2006	$1\text{-}25 \times 10^{6}$	851	ABUNDANCE: retrieved by assuming a uniform ethane fraction profile. GEISA2009 has replaced the mentioned spectroscopic lines with recent of Vander Auwera et al. 2007 as well as PNNL lines
			$8.20\pm2.10 \times 10^{-6}$							ABUNDANCE: retrieved by assuming gradient form of ethane (uniform up to stratopause, increase after). GEISA2009 has replaced the mentioned spectroscopic lines with recent of Vander Auwera et al. 2007 as well as PNNL lines
			$9.70\pm4.90 \times 10^{-6}$							ABUNDANCE: retrieved by assuming discontinuous form for ethane (uniform about one scale height above the stratopause, uniform at an enhanced concentration above that point). GEISA2009 has replaced the mentioned spectroscopic lines with recent of Vander-Auwera et al. (2007) as well as PNNL lines
C_3H_8	10/1/1997	194	$1.67\pm0.83 \times 10^{-7}$	stratosphere	disk average	ISO	Coustenis et al. 2003	1850		reanalysis of Coustenis et al. 2003 values
	14/12/2002	272	$6.20\pm1.20 \times 10^{-7}$	90 – 250	disk average	TEXES/ IRTF	Roe et al. 2003	1.0×10^{5}	748	ν_{26} band of propane: first resolved detection, latitude independent, constant-to-height

Species	OBSERV. DATE	Ls	ABUNDANCE	ALTITUDE (km)	LATITUDE	INSTRUMENT	REFERENCE	RESOLVING POWER	cm^{-1}	COMMENTS
HCN	07/1997 and 12/1999	200 and 232	$6.60\pm2.00 \times 10^{-7}$	350	disk average	IRAM 30-m	Marten et al. 2002		2.95	S/N has improved by a factor of 6 from Hidayat et al. (1997). Dates of observations: 04/1996, 07/1997, 12/1998 and 12/1999
			$7.50\pm2.50 \times 10^{-7}$	400						
			$8.00\pm2.50 \times 10^{-7}$	450						
	21/11/2001	257	$1.00\pm0.20 \times 10^{-7}$	200	disk average	KECK II NIRSPEC	Kim et al. 2005	2.5×10^{4}	3225 - 3472	Re-analysis of Geballe et al. (2003) measurements
			$4.10\pm2.00 \times 10^{-7}$	300						
			$1.00\pm0.25 \times 10^{-6}$	400						
			$5.00\pm2.00 \times 10^{-6}$	500						
	1/2/2004	288	$3.00\pm1.00 \times 10^{-7}$	83	disk average	SMA	Gurwell 2004		11.8	
			$4.00\pm2.00 \times 10^{-7}$	200						
			$5.00\pm5.00 \times 10^{-6}$	300						
	22/6/2010 16/7/2010	011	$5.90\pm0.90 \times 10^{-7}$	300	disk average	Herschel Space Observatory	Courtin et al. 2011			
			$5.10\pm0.30 \times 10^{-7}$	250						
			$4.80\pm0.40 \times 10^{-7}$	200						
C_3H_4	10/1/1997	194	$1.19\pm0.40 \times 10^{-8}$	stratosphere	disk average	ISO	Coustenis et al. 2003	1650-2000		reanalysis of Coustenis et al. 2003 values
CO_2	10/1/1997	194	$1.82\pm0.18 \times 10^{-8}$	stratosphere	disk average	ISO	Coustenis et al. 2003	1650-2000		reanalysis of Coustenis et al. 2003 values
HNC	14/6/2010 31/12/2010	010 017	$2.60\pm0.80 \times 10^{-8}$	500	disk average	Herschel Space Observatory	Moreno et al. 2011		18.1	
			$4.50\pm1.20 \times 10^{-9}$	400						
			$1.10\pm0.30 \times 10^{-9}$	300						
			$4.00\pm1.00 \times 10^{-10}$	200						

4.2 Titan's active methane cycle

Methane is the second most abundant species, in Titan's thick, nitrogen-dominated atmosphere [2.19±0.002% in the upper atmosphere (Waite et al., 2005), 1.6±0.5% in the stratosphere (Flasar et al., 2005), 1.48±0.09% in the lower stratosphere and 5.65±0.18 near the surface (Niemann et al., 2010)]. The existence of a large number of hydrocarbons and nitriles in Titan's atmosphere, as were firstly shown in Voyager 1/IRIS observations (Hanel et al., 1981; Coustenis et al., 1989a), originates through methane and nitrogen photolysis essentially and recombination with nitrogen, as predicted by Strobel (1974).

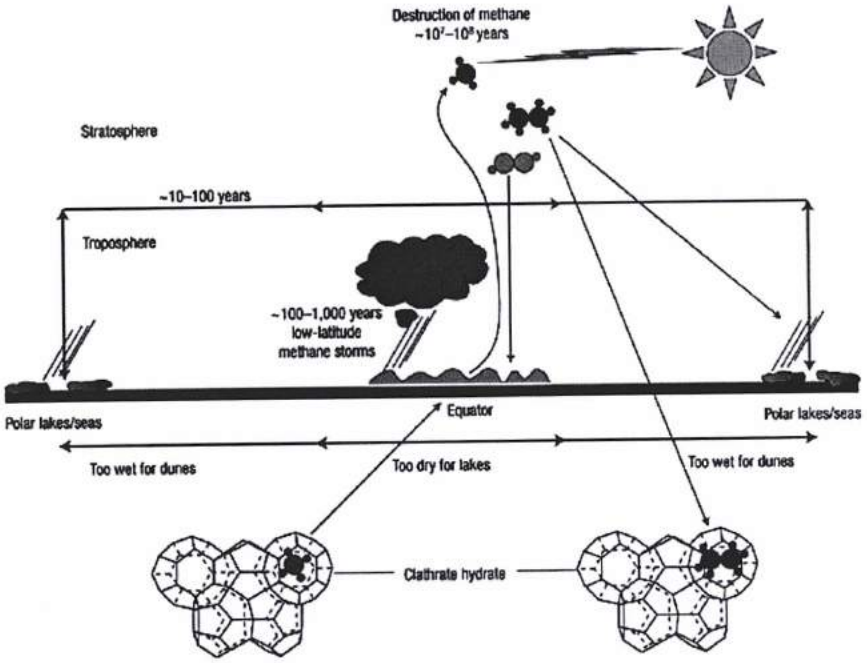

Figure 4. 1 - The methane cycle on Titan (Atreya et al., 2006).

The products of the photochemistry, which occurs above the level of 700 km in the atmosphere, are short-lived radicals of CH_n (n=1,2,3). The self-reaction between CH_3 radicals forms ethane, which is the most abundant methane photolysis product. Ethane is a stable molecule and hence a key molecule in the methane cycle from the time it is formed until it precipitates on the surface (Choukroun & Sotin, 2012).

The products of methane photolysis are a high variety of complex hydrocarbons and once methane is dissociated, the chemical procedure is irreversible. These organics form the haze layer, which obscures the lower atmosphere and the surface at visible wavelengths. Substantial quantities of these aerosols accumulate on the surface.

Part of the organic surface deposits form liquid lake-like features, discovered by Cassini, which are extremely significant in photochemical modeling and habitability. When aerosols reach the equatorial surface, the environment is dry enough for them to remain in solid state and dunes are formed. However, the methane-based hydrologic cycle has not been well constrained yet by the Cassini-Huygens mission.

Photochemical reactions and hydrogen escape dissociate methane in the upper atmosphere (Strobel, 1974; Yung et al., 1984; Wilson & Atreya, 2004; Lavvas et al., 2008b) and if no source replenishes it, it will be totally depleted from the satellite within 10-100 million years (Strobel, 1974; Atreya et al., 2006). Like the hydrological cycle on the Earth, this procedure is expected to be irreversible. The study of possible methane sources in Titan's environment is crucial to understand the methane cycle. The sources that could replenish the dissociated atmospheric methane in Titan's atmosphere are still unknown, but they are possibly located on the surface and in the interior (see following Chapter). Atreya et al. (2006) and other investigators have suggested methane outgassing from the interior and/or hydrothermal sources to satisfy the mission methane.

In my PhD studies, I have looked at Titan's environment from different points of view, from the atmosphere to the surface conditions and even to some of the possibly associated internal processes, as will be discussed in the next chapter. The methane cycle is the leading theme among all these processes and helps us understand the various physical and geological processes, while by studying the processes themselves we better understand this alcanological cycle, whose importance is major in the work presented here.

4.3 Photochemistry

Gaseous species are ideal agents for tracing the photochemical and dynamical processes occurring on Titan's atmosphere. The combination of Voyager, of other space-borne and of Earth-based observations of Titan provides constraints to photochemical models.

4.3.1 Complex photochemistry in the upper atmosphere

The chemical and physical pathways involved in the chemical evolution of the atmosphere of Titan have been described by several photochemical models (Yung et al., 1984; Toublanc et al., 1995; Wilson & Atreya, 2004; Lavvas et al., 2008a;2008b). These models estimate the resulting vertical concentration profiles of the different molecules starting from dissociation of N_2 and CH_4 and then fulfilling a volatile chemical cycle. Solar EUV and UV photons are the main sources of photo-dissociation (Agren et al., 2009; Galand et al., 2010). Other photo-dissociation sources are galactic cosmic rays and energetic particles from the Saturnian magnetosphere (Fig. 4.2) (Krasnopolsky, 2009).

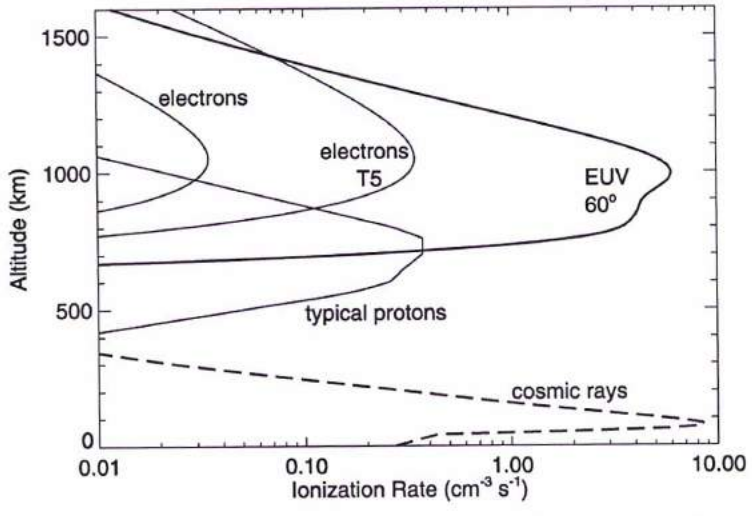

Figure 4. 2 - Sources of ionization in Titan's atmosphere. The EUV solar flux has been calculated for a solar zenith angle at 60°. Electrons T5 represent the nighttime electron distribution in Titan's ionosphere which was observed by Cassini flyby T5 (Krasnopolsky, 2009).

The photochemical processes provide the pathways for the formation of ethane, acetylene and hydrogen cyanide in the higher atmospheric levels. These molecules play a key role: after their formation, they diffuse down to the lower atmosphere where they produce

higher hydrocarbons and nitriles and perhaps aromatic compounds. Besides, methane dissociation probably also occurs in the lower stratosphere through photocatalytic processes involving acetylene and polyynes. Polyynes are the group of organics in which single and triple bonds alternate. The simplest member of this group is acetylene.

Contrary to the very short lifetime of C_2H_2 on Earth (Rudolph et al., 1984), acetylene experiences a seasonal variation during a Titan year (29.5 yrs) and reaches almost the abundances recorded by Voyager 1 in 1980. The end products of the chemical evolution of methane in the atmosphere are complex refractory organic compounds and ethane. Figures 4.3 - 4.5 summarize the complex photochemical reactions occurring in Titan's upper atmosphere according the Yung et al. (1984) and Wilson & Atreya (2004) models.

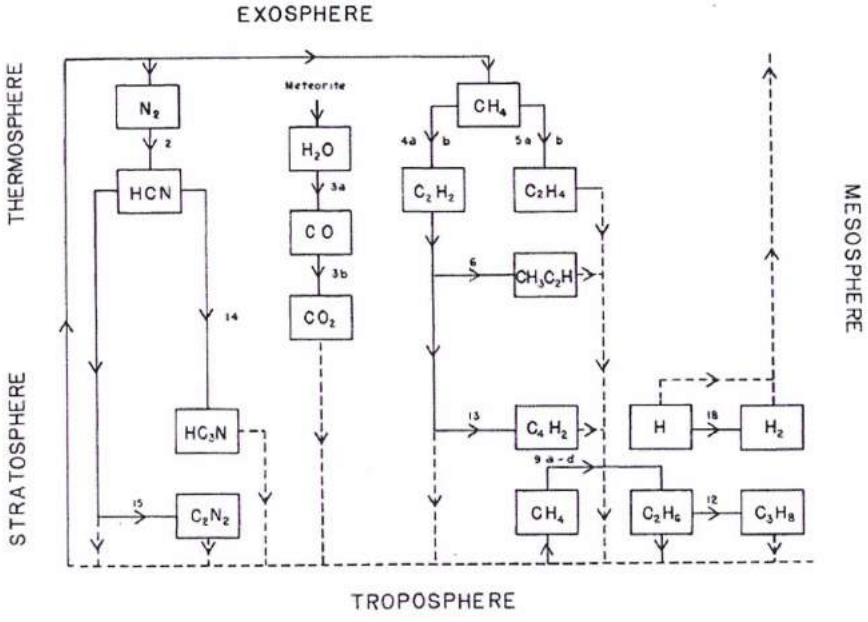

Figure 4. 3 - Plot of the relation among observed molecules and parent molecules. Numbers refer to the chemical cycles described in Yung et al. (1984).

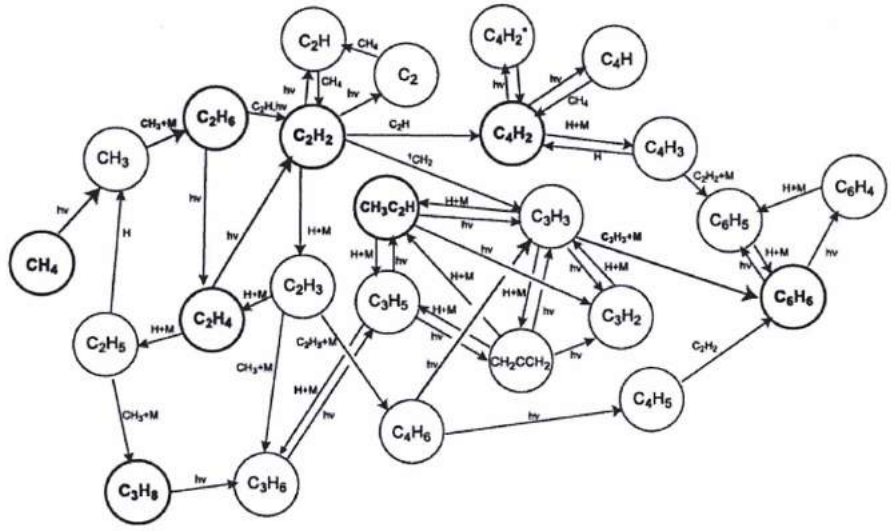

Figure 4. 4 - Plot of the hydrocarbon chemistry in Titan according to Wilson & Atreya (2004). The stable species and the principal reactions are plotted in bold.

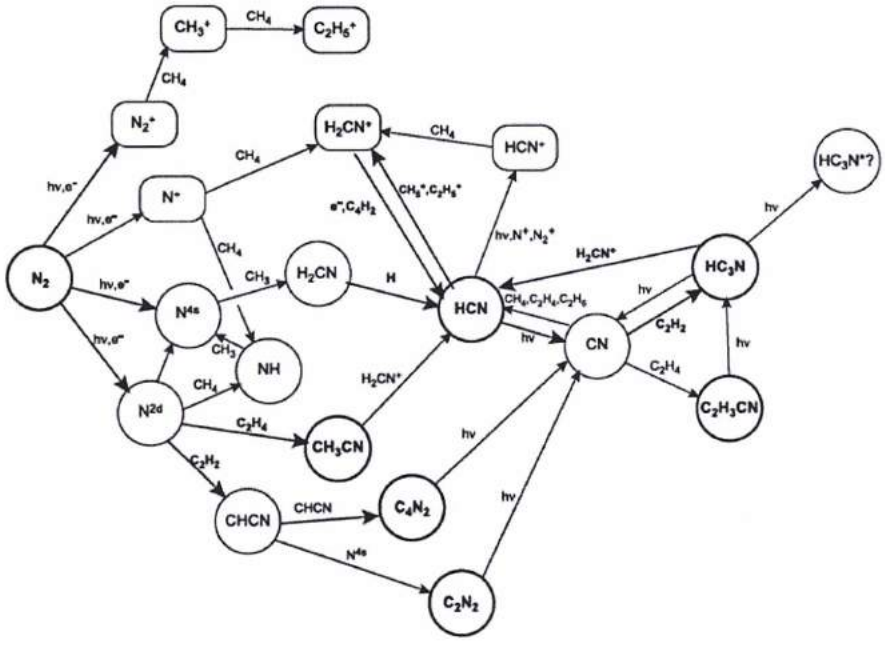

Figure 4. 5 - Plot of the nitrile chemistry in Titan according to Wilson & Atreya (2004). The stable species and the principal reactions are plotted in bold. Boxes represent the ions.

As the haze particles fall through the atmosphere and grow, they become detectable with imaging systems such as the Cassini Imagine Science Subsystem (ISS) at about 500 km altitude and are ubiquitous throughout the stratosphere (Porco et al., 2005). Since they are

strong absorbers of solar UV and visible radiation, they heat the stratosphere and drive wind systems in the middle atmosphere, like the ozone layer in the Earth's middle atmosphere.

4.3.2 The photochemical model of Lavvas et al.

We have been extensively collaborating with Dr. Panayiotis Lavvas, currently Chargé de Recherche at the French National Research Center. He had developed a 1-D coupled radiative convective photochemical microphysical model to investigate the spatial and temporal variability of Titan's atmosphere and its photochemical haze (Lavvas et al., 2008a;2008b) during his PhD (A. Coustenis, co-advisor) which he updated and upscaled in the past years. The model consists of three parts: the radiative transfer calculations, the chemistry sub-model and the microphysics sub-model (Fig. 4.6).

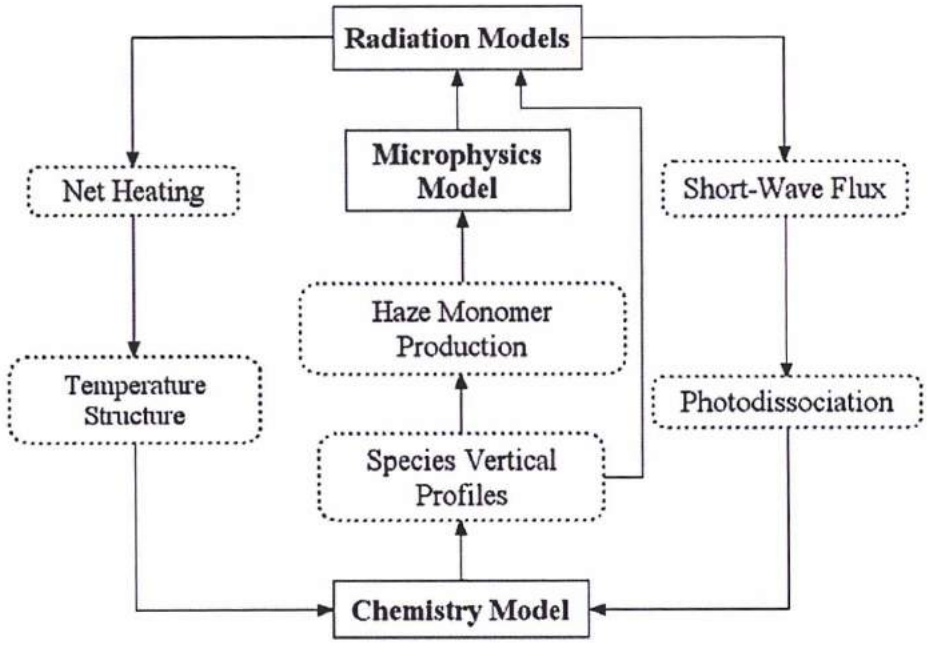

Figure 4. 6 - Flow chart of the model. The model operates in a self-consistent manner (adapted by Lavvas et al. 2008a).

The model firstly incorporates detailed radiation transfer calculations which describe the short and long wave fluxes. These calculations provide the vertical radiation field and the thermal structure which are used for simulating photochemical processes in the atmosphere.

The photolysis of Titan's major compounds (N_2, CH_4) produces the haze particles in its atmosphere. The chemical sub-model solves the time-depended continuity equation for the profiles of the contributing molecules' abundances. The haze pathways lead to haze monomer production at each altitude.

The growth of the haze particles from an initial monomer is described by the microphysical branch of the model. Haze particles are assumed to be spherical with no fractal structure and the haze particle production rate is quite different from the Gaussian. The model generates the vertical haze distribution from the vertical production rates. Then, the calculated aerosol and gas opacities are included in the radiation transfer calculations in order to find their influence in the temperature profile and geometric albedo. The model thermal structure depends on the haze vertical distribution. This iterative process occurs until the equilibrium is reached.

By applying this model to Titan's atmospheric envelope we derive a better understanding of the unknown connection mechanism between the production of neutral gases and their transformation to haze particles. The model reproduces well the observations (Lavvas et al., 2008b) as we have also reported in Coustenis et al. (2010b).

4.4 Composite Infrared Spectrometer (CIRS) data selection

My work in studying Titan's stratosphere is twofold. I first studied the composition and temperature as retrieved from CIRS spectra averaged yearly during the nominal mission (2004-2008) and then looked at the evolution of the thermal structure and chemical composition from the beginning of the mission in 2004 up to early 2012 with more time-resolved selections. Large averages have been also used for the study of water vapor and the weak species and of course to search for new molecules as I describe hereafter.

For all selected CIRS datasets, I have restricted the emission angles to be less than 65°. I sum all longitudes (because it was demonstrated that no longitudinal variations are expected (Coustenis et al., 2007; Teanby et al., 2008) and retrieve spectra only for different latitudinal bins.

As discussed in Coustenis et al. (2007), we need to correct the data for any latitude smearing effect observed for high emission angles and/or data taken at latitudes higher than 50°N (Fig. 4.7). The sounded latitudes can be about 5° lower when the line-of-sight intercepts the surface at 55°N or 55° S. Thus, the actual latitude of the stratospheric altitudes observed being rather 50°N and 50°S, respectively. The latitudes listed in data Tables below (4.4-4.14) are corrected for this effect.

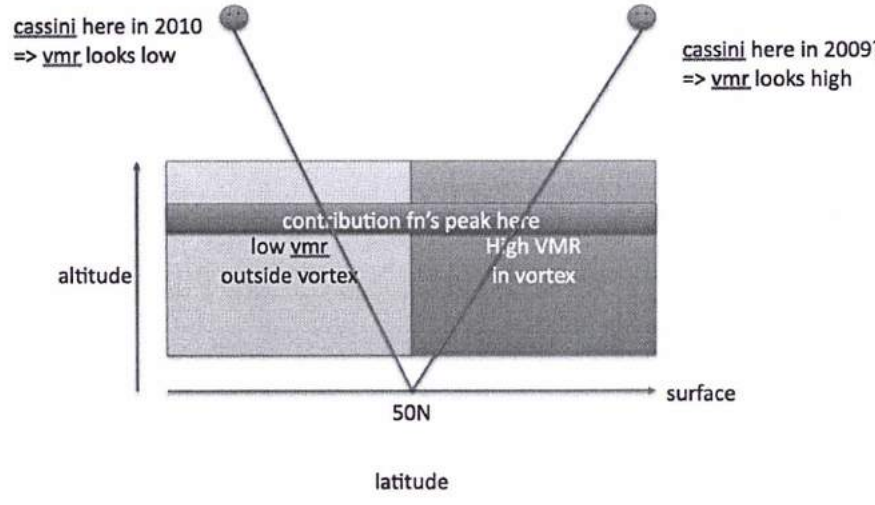

Figure 4. 7 - Illustration of the Cassini changing viewing aspect for the same surface intersect latitude at 50°N. The contribution functions peak at about 150 km (provided by Dr. N. Teanby). This plot shows that the actual location at which CIRS data are acquired depends highly on the emission angle of the observation. However, in this work we have taken into account this so-called smearing effect (Coustenis et al. 2007) and corrected the line of sight before the retrievals.

4.4.1 CIRS data: yearly spectral averages from the Cassini-Huygens nominal mission (2004-2008)

In our paper Coustenis et al. (2010b), we gathered nadir CIRS spectra from the first 44 Cassini flybys which have been performed within the first 4 years of the Cassini-Huygens mission. It was the first time that Titan was explored continually and that study is complementary to the previous one described in Coustenis et al. (2007). The spectra analyzed in the 2007 study were obtained within the first two years of the mission (July 2004-January 2006, flybys TB-T10). A full description of the instrument and the processing and calibration procedure can be found in Chapter 2 of this manuscript.

As in Coustenis et al. (2007), in the 2010 study we averaged CIRS FP3 and FP4 spectra from the CIRSDATA database in latitudinal bins of 10° ranging from 85°S to 80°N in both mid and high resolutions (2.54 and 0.53 cm^{-1} respectively). We have excluded the T0 and TA flybys from our queries. Data from T0, the first Cassini flyby of Titan, was omitted since they were obtained at distances too high to be compared to the observations which followed. Most of the data obtained from TA flyby were corrupted due to a CIRS command error. Tables 4.5 and 4.6 list the high and medium resolution spectra that I assembled and used in Coustenis et al. (2010b - c.f. Table 1).

Table 4. 5 - Characteristics of the CIRS nadir spectral selections from Titan flybys TB-T44 at high resolution of 0.53 cm^{-1} (adapted from Table 1 of Coustenis et al., 2010b).

Mean Latitude	FP3			FP4		
	Spectra	airmass	S/N	Spectra	airmass	S/N ratio
70°N	1117	1.21	34.4	2011	1.32	102.6
60°N	2413	1.25	48.0	2147	1.25	91
50°N	2316	1.12	48.7	4302	1.09	117
42°N	5328	1.08	84.5	4098	1.12	133.7
33°N	7002	1.12	116.8	8222	1.14	242.6
25°N	8607	1.09	140.3	7942	1.09	277.6
15°N	5249	1.07	114.9	9299	1.06	340.2
5°N	11981	1.03	173.8	10899	1.04	383.7
5°S	10873	1.04	161.7	10903	1.07	392.3
15°S	4144	1.15	92.6	3567	1.25	229.6
25°S	2446	1.13	62.9	3457	1.07	206.8
33°S	3574	1.13	85.0	2949	1.24	197.4
42°S	2190	1.24	65.7	3332	1.28	205.8
50°S	2154	1.15	60.7	1968	1.16	149.4
60°S	2081	1.28	60.8	1845	1.26	145.1
70°S	778	1.45	39.1	2543	1.41	173.0

Table 4. 6 - Characteristics of the CIRS nadir spectral selections from Titan flybys TB-T44 at high resolution at 2.54 cm^{-1} (adopted from Table 1 of Coustenis et al., 2010b).

Mean Latitude	FP3			FP4		
	Spectra	airmass	S/N	Spectra	airmass	S/N
70°N	528	1.27	59.2	530	1.24	135.7
60°N	1184	1.21	84.9	1617	1.03	201.2
50°N	6133	1.11	203.9	6471	1.12	382.9
42°N	8066	1.13	227.3	7170	1.15	480.5
33°N	8173	1.12	337.2	11154	1.13	721.7
25°N	12614	1.11	444.9	10317	1.13	861.1
15°N	13018	1.07	479.3	14509	1.08	1123.8
5°N	15639	1.09	534.8	15741	1.09	1231.8
5°S	19953	1.05	575.5	19726	1.04	1357.3
15°S	18953	1.05	524.3	19140	1.05	1338
25°S	7426	1.11	323	8266	1.10	861.2
33°S	6948	1.08	296.8	5791	1.12	706
42°S	5085	1.12	244.9	4722	1.12	613.1
50°S	2908	1.10	176.8	3035	1.12	475.4
60°S	1353	1.16	121.6	1270	1.16	313.3
70°S	1379	1.33	126.8	1421	1.28	330.2

4.4.2 CIRS data: monthly averages from the beginning of the Cassini-Huygens mission (July 2004) up to early 2012.

In the more recent study, in 2012, we looked at more time-resolved data now that a large number of spectra have become available. We have thus used all available and exploitable data at high spectral resolution (0.5 cm^{-1}) and I performed averages of the spectra acquired during one or several flybys as necessary to attain a high signal-to-noise ratio for my calculations. To do this, I have queried for spectra averaged over a given date (flyby, or over a month) and attributable to a given latitudinal bin between (50°S and 50°N) containing a large number of spectra in general, with some exceptions (Bampasidis et al., 2012a).

The TB-T9 flybys (December 2004-December 2005) at 50°N and 50°S contain insufficient data in the right conditions (signal-to-noise, emission angle, distance, region, etc) for our purposes and they are excluded. During the flybys that followed, CIRS acquired a large number of spectra in FP3 and FP4 at high, medium and low spectral resolutions (0.53, 2.54 and 15 cm^{-1} respectively) in surface-intercepting (nadir) and horizontal viewing (limb) geometry conditions. However, the spacecraft did not always track all latitudes and in the northern hemisphere data from only late 2007 to 2010 are available. Moreover, an instrument anomaly followed by a reboot of CIRS took place in December 2006, depriving us of data from that time.

Tables 4.7 and 4.9 contain nadir averages at high resolution (0.5 cm^{-1}) for the northern hemisphere (FP3 and FP4 spectra respectively), while Tables 4.8 and 4.10 contain the datasets for the southern hemisphere (FP3 and FP4 spectra respectively). The selections we made in order to enhance the signal-to-noise ratio cover different latitudes on Titan. Each query was restricted to emission angles lower than 65°. The average signal-to-noise ratio is given in the Tables, as well as the corresponding Cassini Titan fly-by(s) and the relative solar longitude (Ls). Following the same selection criteria I have also analyzed 6 datasets of medium resolution spectra (2.54 cm^{-1}) taken at FP3 and FP4 spectral ranges for January 2008 (flyby T40), April 2009 (flybys T52-T53) and May 2010 (T68). Table 4.11 and 4.12 list these mid-resolution data characteristics acquired at FP3 and FP4 respectively.

Table 4. 7 - Titan flybys and FP3 data acquisition characteristics from March 2007 to September 2011 averaged in northern latitudinal bins (adapted from Bampasidis et al. 2012a).

Year	Month	Latitude	Total number of spectra	Signal-to-noise	Airmass	Cassini Flyby	Ls (°)
2007	Mar	50°N	357	18.6	1.02	T26-T27	329
"	Dec	50°N	335	19.9	1.25	T38-T39	338-339
2008	Feb-Mar-Jul	50°N	145	12.4	1.19	T41-T45	341-347
2009	Mar	50°N	517	25	1.35	T51	355
"	Apr-May	50°N	275	15.3	1.01	T52-T55	355-357
"	Jun	50°N	476	25.6	1.88	T56-T57	358
2010	Jan	50°N	284	21.3	1.69	T65-T66	005-006
2006	Jul	30°N	551	34	1.17	T15-T17	320
2007	May	28°N	934	44.7	1.06	T30-T31	331-332
"	Dec	31°N	905	45.4	1.14	T38-T39	338-339
2008	Mar	30°N	992	42.3	1.01	T42	342
"	Dec	36°N	262	20.5	1.03	T48-T49	351-352
2009	Dec	30°N	748	44.5	1.46	T63-T64	004-005
2010	Jun	35°N	599	37.4	1.24	T69-T70	010
2011	Sep	32°N	771	46.8	1.49	T78	025
2006	Jan	1°N	1291	56.2	1.01	T10	314
"	Jul	1°N	2118	71.8	1.01	T15-T16	320
2007	Apr-May	1°N	189	23.9	1.21	T28-T29	330-331
"	Jun	1°N	1497	62.5	1.06	T32-T33	332-333
"	Aug	1°N	152	19.3	1.01	T35	335
2008	Jan	1°N	589	39.4	1.07	T40	340
"	May	2°N	597	47	1.55	T43-T44	344-345
2009	Mar-Jul	1°N	86	18.3	1.75	T51-T59	355
"	Oct	1°N	72	14.9	1.19	T62	002
"	Dec	1°N	283	25.6	1.01	T63-T64	004
2010	Sep	3°N	1504	58.9	1.02	T72	014
2011	May	11°N	921	50	1.20	T76	021

Table 4. 8 - Titan flybys and FP3 data acquisition characteristics from February 2006 to January 2012 averaged in southern latitudinal bins (adapted by Bampasidis et al. 2012a).

Year	Month	Latitude	Total number of spectra	Signal-to-noise	Airmass	Cassini Flyby	Ls (°)
2006	Mar	1°S	1515	61.3	1.04	T12	316
2007	Oct	1°S	93	17	1.28	T19-T20	323-324
"	Jul	1°S	232	23.3	1.01	T34	334
"	Nov	1°S	813	44.5	1.01	T37	338
"	Dec	3°S	276	25.3	1.01	T38-T39	338-339
2008	Feb	1°S	426	39.8	1.46	T41	341
2010	Apr-May	1°S	466	33.0	1.01	T67	008
"	Jun	1°S	391	30.6	1.02	T69-T70	010
"	Jul	1°S	985	49.8	1.08	T71	011
2011	Dec	2°S	1047	52.1	1.19	T79	028
2006	Feb	30°S	666	37.7	1.88	T11	315
"	May	30°S	536	35.3	1.33	T14	318
2008	Nov	38°S	1055	39.9	1.02	T46-T47	350-351
2009	Dec	24°S	961	40	1.08	T63-T64	004-005
2010	May	24°S	911	44.9	1.30	T68	009
2012	Jan	30°S	1980	56.1	1.49	T80-T81	029
2006	Oct	50°S	568	30.9	1.18	T19-T20	323
2007	Jan	50°S	925	37.0	1.04	T23-T24	327
"	Mar-May	50°S	341	28.2	1.64	T26-T31	329-332
"	Jul-Aug	50°S	647	39.6	1.70	T34-T35	334
"	Dec	50°S	467	31.7	1.53	T38-T39	338-339
2008	Jul	50°S	34	9.6	1.28	T41	341
2009	Mar	50°S	198	17.2	1.09	T51	355
"	May	50°S	1288	45.2	1.25	T54-T55	357
2010	Apr	50°S	124	16.0	1.69	T67	008

Table 4. 9 - Titan flybys and FP4 data acquisition characteristics from March 2007 to September 2011 averaged in northern latitudinal bins (adapted by Bampasidis et al. 2012a).

Year	Month	Latitude	Total number of spectra	Signal-to-noise	Airmass	Cassini Flyby	Ls (°)
2007	Mar	50°N	1376	64.6	1.03	T26-T27	329
"	Dec	50°N	342	34.4	1.26	T38-T39	338-339
2008	Feb-Mar-Jul	50°N	166	12.8	1.14	T41-T45	341-347
2009	Mar	50°N	417	30	1.28	T51	355
"	Apr-May	50°N	1481	49.9	1.01	T52-T55	355-357
"	Jun	50°N	575	35.8	1.65	T56-T57	358
2010	Jan	50°N	234	27.6	1.67	T65-T66	005-006
2006	Jul	30°N	567	67.1	1.17	T15-T16	320
2007	May	30°N	1789	125	1.06	T30-T31	331-332
"	Dec	30°N	657	81.8	1.18	T38-T39	338-339
2008	Mar	30°N	1013	86.5	1.02	T42	342
"	Dec	35°N	394	74.1	1.03	T48-T49	351-352
2009	Dec	30°N	764	83.9	1.36	T63-T64	004-005
2010	Jun	36°N	503	69.6	1.25	T69-T70	010
2011	Sep	28°N	1107	106	1.39	T78	025
2006	Jan	2°N	869	107.3	1.01	T10	314
"	Jul	1°N	1840	152.0	1.01	T15-T16	320
2007	Apr-May	3°N	93	37.5	1.20	T28-T29	330-331
"	Jul	1°N	198	51.9	1.02	T34	334
"	Aug	1°N	146	45.5	1.02	T35	335
2008	Jan	1°N	449	80.3	1.09	T40	340
"	Feb	1°N	439	86.2	1.59	T41	341
"	May	3°N	64	32.9	1.70	T43-T44	344-345
2009	Dec	1°N	322	64.8	1.03	T63-T64	004
2010	Apr-May	1°N	233	54.1	1.01	T67	008
2011	May	7°N	765	99.8	1.18	T76	021

Table 4. 10 - Titan flybys and FP4 data acquisition characteristics from February 2006 to January 2012 averaged in southern latitudinal bins (adapted by Bampasidis et al. 2012a).

Year	Month	Latitude	Total number of spectra	Signal-to-noise	Airmass	Cassini Flyby	Ls (°)
2006	Mar	1°S	1515	142.1	1.09	T12	316
"	Oct	1°S	96	39.4	1.26	T19-T20	323-324
2007	Jun	1°S	2545	195.1	1.09	T32-T33	332-333
"	Nov	1°S	869	106.7	1.01	T37	338
"	Dec	1°S	382	70.9	1.02	T38-T39	338-339
2009	Mar-Jul	1°S	84	39.2	1.71	T51-T59	355
"	Oct	1°S	60	26.6	1.09	T62	002
2010	Jun	1°S	367	69.4	1.01	T69-T70	010
"	Jul	1°S	913	110.8	1.13	T71	011
"	Sep	3°S	1622	136.9	1.01	T72	014
2011	Dec	10°S	1866	157	1.24	T79	028
2006	Feb	30°S	666	96	1.21	T11	315
"	May	30°S	551	85.5	1.26	T14	318
2008	Nov	31°S	1055	106.4	1.01	T46-T47	350-351
2009	Dec	28°S	980	103.4	1.12	T63-T64	004-005
2010	May	24°S	1028	114.3	1.21	T68	009
2012	Jan	30°S	2083	133.8	1.15	T80-T81	029
2006	Oct	50°S	546	78.8	1.16	T19-T20	323
2007	Jan	50°S	842	95.8	1.07	T23-T24	327
"	Mar-May	50°S	320	63.1	1.42	T26-T31	329
"	Jul-Aug	50°S	538	86.8	1.68	T34-T35	334
"	Dec	50°S	456	77.5	1.59	T38-T39	338-339
2008	Jul	50°S	51	25.6	1.62	T41	341
2009	Mar	50°S	584	73.4	1.13	T51	355
"	May	50°S	892	91.0	1.33	T54-T55	357
2010	Apr	50°S	525	35.4	1.71	T67	008

Table 4. 11 - Titan flybys and medium FP3 resolution data acquisition characteristics from January 2008 to June 2010 averaged in 50°N, 0° and 50°S at medium resolution (2.53 cm^{-1}).

Year	Month	Latitude	Total number of spectra	Signal-to-noise	Airmass	Cassini Flyby	Ls (°)
2008	Jan	50°N	459	60.2	1.26	T40	340
2009	Apr	50°N	1193	87.1	1.08	T52-T53	355-356
2010	May	50°N	160	46.7	1.84	T68	009
2010	May	0°N	396	87.5	1.12	T68	009
2010	May-Jun	50°S	484	77.1	1.74	T68-T70	009-010

Table 4. 12 - Titan flybys and medium FP4 resolution data acquisition characteristics from January 2008 to June 2010 averaged in 50°N, 0° and 50°S at medium resolution (2.53 cm^{-1}).

Year	Month	Latitude	Total number of spectra	Signal-to-noise	Airmass	Cassini Flyby	Ls (°)
2008	Jan	50°N	495	106.9	1.27	T40	340
2009	Apr	50°N	4447	227.0	1.01	T52-T53	355-356
2010	May	50°N	163	67.2	1.84	T68	009
2010	May	0°N	390	192.7	1.13	T68	009
2010	May-Jun	50°S	473	173.9	1.78	T68-T70	009-010

4.4.3 CIRS data: large averages for water vapor detection

In order to detect and retrieve the abundances for water vapor, I have used our radiative transfer code (ARTT) to simulate large CIRS averages in the FP1. These calculations offer a chance to compare the results of our radiative transfer code with the retrievals of the NEMESIS code - Non-linear Optimal Estimator for Multivariate Spectral Analysis (Irwin et al., 2008).

The water vapor detection in Titan's atmosphere can be achieved only through large spectral averages, because, as demonstrated by the ISO first detection in 1997 data (Coustenis et al., 1998) the emission signatures are rather weak. In our paper Cottini et al. (2012a), we queried for 3 FP1 selections within the season of Titan's northern winter which is from December 2004 up to December 2008. These FP1 datasets are listed in Table 4.13 below.

Table 4. 13 - Titan flybys and medium FP1 resolution data acquisition characteristics from December 2004 to December 2008.

Latitude	Total number of spectra	Airmass	Cassini Flyby
80°S-45°S	1700	1.22	T40
45°S-10°S	3800	1.27	T52-T53
0-30°N	7000	1.21	T68

4.5 The method for the analysis of the spectra

I have analyzed the Cassini/CIRS spectra using a method described in previous articles (Coustenis et al. 2007; 2010). In brief, we model Titan's thermal infrared spectrum using a line-by-line monochromatic radiative transfer code upgraded from the one we used in previous Titan atmospheric structure retrievals (ARTT, for Atmospheric Radiative Transfer for Titan, c.f. Bampasidis et al. 2012 and references within).

I computed synthetic nadir spectra in each of the FP1 (10-600 cm^{-1}), FP3 (600-1100 cm^{-1}) and FP4 (1100-1400 cm^{-1}) spectral ranges, which I then compare to the observations in order to retrieve the vertical temperature profile (from the ν_4 methane band emission in the FP4, at 7.7 micron) and the composition of Titan's atmosphere (from the gaseous molecular signatures in FP1 and FP3). The dominant emission bands in the CIRS/FP4 spectra (1100-1500 cm^{-1}) are the methane ν_4 band at 1304 cm^{-1} and the CH_3D ν_6 band at 1156 cm^{-1}. Several molecules have emission bands in this region, but their signature has not been verified yet, like the propane band ν_{24} at 1472 cm^{-1} (Nixon et al., 2009). The 13-C bearing isotope of CH_3D has also a weak emission at 1148 cm^{-1}. Figure 4.8 below depicts the contribution functions of these molecules at May 2009 CIRS selection at 50°S and high resolution (0.5 cm^{-1}).

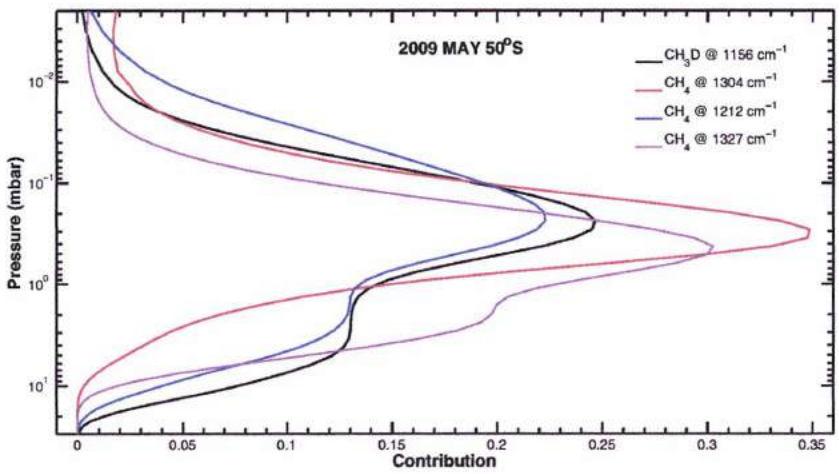

Figure 4. 8 - The contribution functions of CH_3D at 1156 cm^{-1} (black), CH_4 - Q branch at 1304 cm^{-1} (red), CH_4 - R branch at 1212 cm^{-1} (blue) and CH_4 - P branch at 1327 cm^{-1} (magenta). The corresponding selection is the one of May 2009 at 50°S in high resolution.

As shown in the contribution function of CH_3D (Fig. 4.8), the atmospheric region which is probed in this band at 50°S is between 0.03 and 10 mbar with a peak at 0.24 mbar. Similarly,

the Q-branch of CH_4 peaks at 0.29 mbar with a FWHM between 0.04 and 1 mbar. As far as the methane wings are concerned, the R- and P-branches probe the atmosphere between 0.01-7 mbar and 0.1-5 mbar respectively.

The best fit for the selection of May 2009 at 50°S in the FP4 region is illustrated in Figure 4.9 below. The 3-σ standard deviation due to noise alone in this region is about $2x10^{-10}$ $Wcm^{-2}sr^{-1}/cm^{-1}$. When other sources of uncertainties (in the methane abundance, the thermal structure, the calibration and the continuum fit) are included, the total error is about $2x10^{-9}$ $Wcm^{-2}sr^{-1}/cm^{-1}$. The misfit between the model and data from 1180 to 1250 cm^{-1} has not been yet understood; perhaps is caused by uncertainties in methane line lists (Coustenis et al., 2010b).

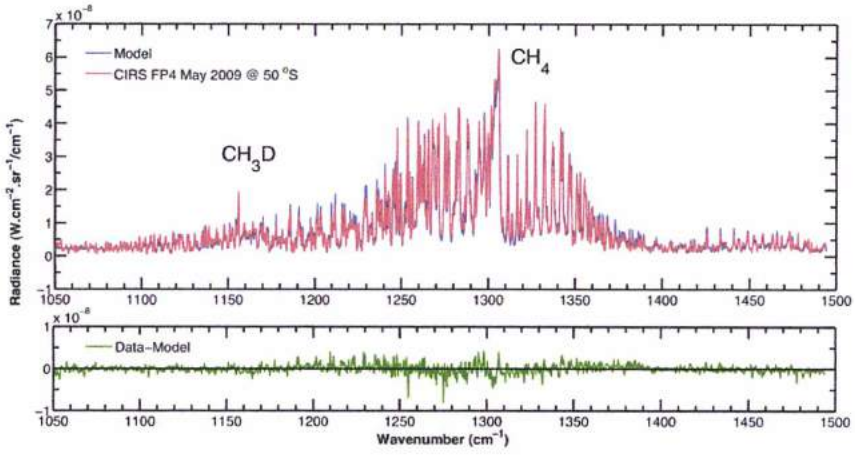

Figure 4. 9 - (Upper) Fit of CH_3D at 1156 cm^{-1} and CH_4 at 1304 cm^{-1}. (Lower) Difference between data and the model. The selection is the one of May 2009 at 50°S in high resolution (0.5 cm^{-1}).

The way the radiative transfer calculations work is that either the opacity is known and the thermal composition inferred or the temperature profile is injected in the code and the mixing ratios inferred. To get the temperature profiles from the ν_4 methane band, we use the CH_4 vertical mixing ratio profile in the stratosphere as measured by the Huygens probe (Niemann et al., 2010), which yields 1.48% above the cold trap, compatible with the CIRS inferences from FP1 (Flasar et al., 2005). We also take 0.11% for H_2 (Samuelson et al., 1983) and 98.41% for N_2. We then use the inversed temperature profiles to infer the abundances of the emitting gases.

In the ARTT code, I have included more constituents relevant to Titan's chemistry following a procedure which is described in detail in Chapter 3. The contributing molecules to the synthetic model spectra are therefore 26 in total, which is all the so-far detected

hydrocarbons, nitriles and oxygen compounds in addition to the main molecules N_2, H_2, CH_4 and Argon.

Furthermore, the updated list of ARTT molecules includes the $^{13}CH_4$, $^{13}CH_3D$, $^{12}C^{13}CH_2$ and $H^{15}CN$ isotopologues that are essential in fitting the emission bands of methane, acetylene and hydrogen cyanide respectively and allow us to infer the $^{12}C/^{13}C$ and $^{14}N/^{15}N$ ratios. Finally, new oxygen and hydrocarbon isotopologues that were recently detected (Jennings et al., 2008; Nixon et al., 2008a) are also incorporated.

As said in Chapter 3, the need for a massive upgrade was obvious since new spectroscopic parameters for the molecules found in the FP3 and FP4 spectral ranges became available from recent laboratory studies, as for instance in the case of ethane and propane spectroscopic parameters, both of which were provided from the individual line lists of Vander Auwera et al. (2007) and Flaud et al. (Flaud et al., 2010) respectively. These new line lists are from the GEISA 2009 (Jacquinet-Husson et al., 2011) and the HITRAN 2008 (Rothman et al., 2009) databases, in which all these updates have been included.

More in detail, the analysis we perform comprises the following steps: we begin by inferring the temperature profiles by the inversion of the observed n_4 methane emission band at 1305 cm^{-1} in CIRS/FP4 individually for each selection (Tables 4.5-6, 4.9-10 and 4.12-14). These thermal profiles are provided by R. Achterberg of the GSFC following the method described extensively in Achterberg et al. (2008; 2011). Once the vertical thermal structure is known, the contribution function of each molecule incorporated in the model can be calculated (thus providing the altitude/pressure range from where the maximum of the emission originates) and more importantly its abundance can be retrieved when the best fit is achieved.

The *a priori* reference temperature profile for these calculations was the 15°S profile from Flasar et al. (2005). As I have described in Chapter 3, Section 3.2, I have also run tests using the HASI measured temperature structure in the stratosphere and troposphere (Fulchignoni et al., 2005). At the equatorial latitudes, the impact of these thermal profiles in the abundances retrievals is at about 10% less for all molecular abundances, except for HCN (20%). This small impact is expected because the HASI profile was inferred above the Huygens landing site (10°S). In the northern latitudes, the divergence is more pronounced (within 20% of increase in abundance) for the molecules with the stronger emission bands (C_2H_2, C_2H_6 and HCN). Most of the molecular abundances vary by less than 10% whatever the initial temperature profile (see Tables 3.2 and 3.3).

Then, I adapt each individual temperature profile to solve the radiative transfer equation in the FP3 (and FP1 for the water vapor) part of the CIRS spectrum. Through an iterative best-fit process, I derive the trace gases abundances of the various components in each selection of data (Tables 4.5-6, 4.7-8, 4.11 and 4.13-14).

For all of the molecules analyzed here in surface-intercepting (nadir) geometry conditions, I use only constant-with-height abundance profiles above the condensation level relevant to stratospheric levels of 0.1-20 mbar essentially (roughly 80-280 km). Only C_2H_2, HCN and C_2H_6 can provide some vertical information and there I have tested vertical profiles against the observations. The others do not have strong enough emission bands to provide the retrieval of vertically-dependent information.

Moreover, in order to fit the continuum observed in the spectra, I have adapted the haze description with wavenumber recently reported in Vinatier et al. (2012b) adjusted to match the level of radiance observed between the molecular bands in each selection. This distribution provides the aerosol refractive index from CIRS spectra in the far and mid-infrared regions near 15°S and 20°S.

4.6 Titan's stratospheric composition during the nominal Cassini-Huygens mission

The study of CIRS data obtained during the Cassini-Huygens mission has significantly advanced our perspective of Titan's atmospheric chemical structure. In the paper of Coustenis et al. (2007), the authors have analyzed the CIRS spectra retrieved from flybys TB to T10 (December 2004-January 2006) and reported meridional variations of trace gases. Figure 4.10 illustrates the results of this work.

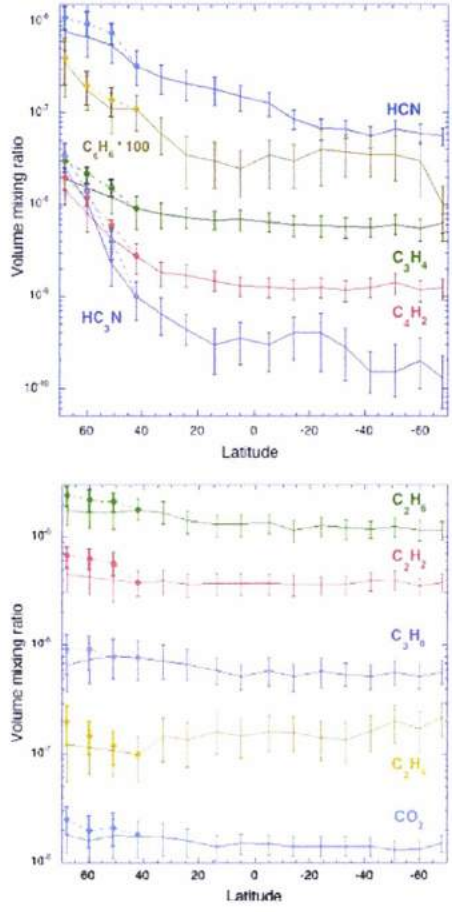

Figure 4. 10 - Latitudinal variations reported in Coustenis et al. 2007. The upper panel shows the molecules the abundance of which increases with the latitude above 50°N, while the molecules of the lower panel remain almost constant with latitude.

The abundances of C_3H_4, C_4H_2, HCN, C_6H_6 and HC_3N show significant enhancement above 50°N. The other molecules (CO_2, C_2H_6, C_2H_2, C_2H_4 and C_3H_8) remain fairly stable with latitude. C_2H_4 and C_3H_8 show a decrease in the abundance near the North pole. Similar observations have been reported from Voyager data (Coustenis & Bezard, 1995), but the

enhancement was greater (Fig. 4.11).

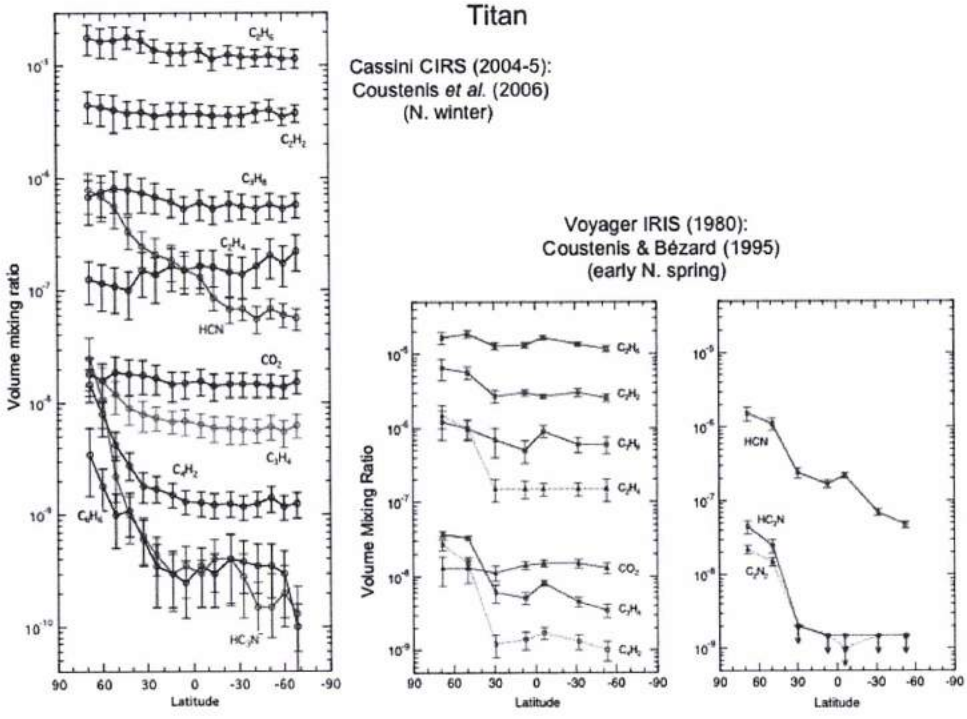

Figure 4. 11 - Latitudinal distribution of major organic trace gases from Voyager (Coustenis & Bezard, 1995) and Cassini (Coustenis et al., 2007), adapted from Coustenis et al. 2010b.

However, due to the Cassini position during the first 10 flyby of Titan, the most northern latitude observed was the 60°N one. Since there is a significant enhancement of the trace gases mixing ratios polewards to the north, further analysis of polar data is needed. Thanks to the Cassini mission, a wealth of spectra became available in order to study Titan at all latitudes.

In the paper of Coustenis et al. (2010b), which I have co-authored, we have used large spectral averages from flybys TB to T44 that cover the whole nominal mission of the Cassini orbiter. These averages provide more detailed abundances retrievals as well as improved meridional variations as described hereafter.

4.6.1 Titan's stratospheric chemistry retrieval

In Coustenis et al. (2010b), we have divided Titan's globe into latitudinal bins of 10° from 90°S to 90°N with emission angles less than 50° and searched to determine spatial variations in temperature and composition from 2004 to 2008, more refined with respect to previous studies. No longitudinal variations existing in the chemical composition of the stratosphere (Coustenis et al. 2007) and the longitudinal variations in temperature not being significant (Achterberg et al., 2008), we summed up all longitudes.

This work was a great introduction for me in CIRS data analysis by using ARTT (**A**tmospheric **R**adiative **T**ransfer code for **T**itan) and the ensuing interpretation. It was also important that through that project I got familiar with the radiative transfer code modifications and began to interact with the CIRS data acquisition and calibration team in Goddard.

The modeling procedure is described in Section 4.4 and the data used are listed in Tables 4.5 and 4.6. Due to the detection of C_2HD (Coustenis et al., 2008) and $^{13}CH_3D$ (Bezard et al., 2007), these molecules have been included in the 2010 version of ARTT.

The vertical distributions of the molecules are assumed to be constant with altitude with the exception of acetylene, for which we tried some vertical profiles. We have also used distributions predicted from General Circulation Models (Rannou et al., 2005). Contrary to the previously described analysis of the temporal and spatial variations of the Titan's stratosphere, the GCM distributions for C_2H_2 work well (Coustenis et al. 2010b).

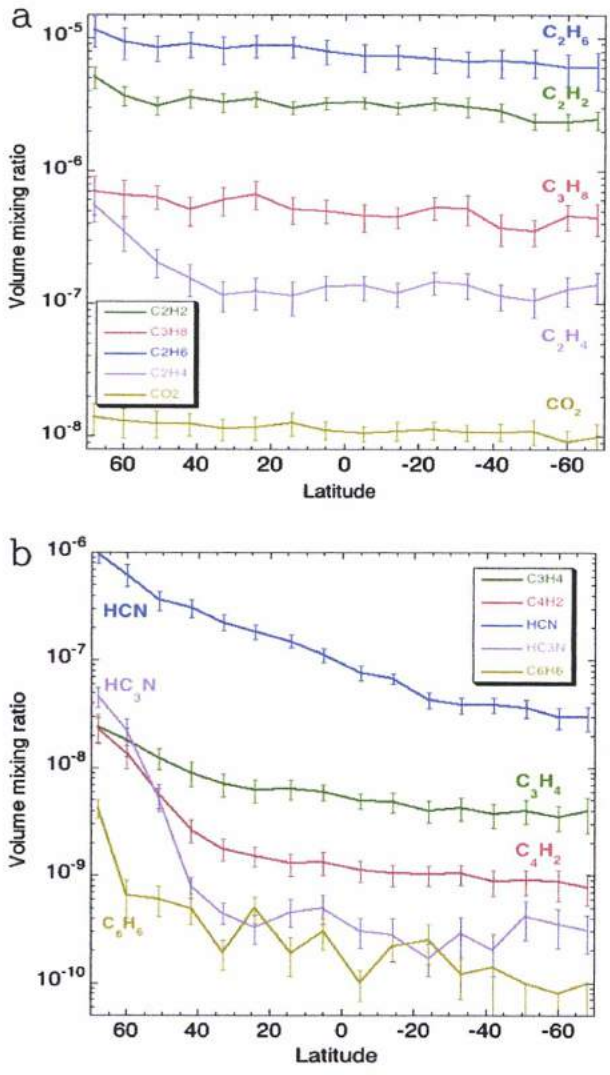

Figure 4. 12 - Latitudinal variations reported in Coustenis et al. (2010b) with 3-σ error bars. For latitudes lower than 40°S, only upper limits are illustrated for benzene.

We confirm the meridional variations reported in Coustenis et al. (2007) with a significant enhancement at northern latitudes with new smaller uncertainties. Figure 4.12 illustrates the latitudinal variations during Cassini prime mission.

Differences in the mixing ratios have been found for ethane and for other species (C_2H_4 and C_3H_8) compared to the previous work (Coustenis et al. 2007). The decrease in the abundance near the North pole of C_2H_4 and C_3H_8 is not confirmed. Instead, the propane's mixing ratio increases slightly, while the values for ethylene are higher.

Ethane, acetylene, propane and carbon dioxide show abundance increase from South to North by a factor ranging from 1.5 to 2. The mixing ratios of benzene and

cyanoacetylene increase even more significantly to the North by factors of 30 and 150 respectively. The other molecules have enriched values by factors within 3 and 8 (Coustenis et al.*, 2010b). In the 2007 study, the enrichments found in the North were not at the levels of the Voyager ones. The ones in the 2010 study are lower with respect to the ones observed at the time of the Voyager encounter.*

The results of our work are compatible with the ones of Teanby et al. (Teanby et al.*, 2009a) and with the isotopic ratio retrievals of Bezard et al. (2007), Nixon et al. (2008a; 2008b) and Vinatier et al. (2007b). Additionally, our findings are in good agreement with photochemical models (Lavvas et al. 2008a; 2008b) and GCM models (Crespin et al., 2008).*

The main reason of the observed enhancement from the southern latitude to the northern ones seems to be the stratosphere which is in the shadow of Titan's pole during winter. During the polar night, the mesosphere is illuminated by the sunlight and Saturnian magnetospheric energetic electrons. Thus, HCN and other nitriles are formed in the upper atmospheric layers, they diffuse downwards and accumilate close to the polar region (Yung, 1987; Coustenis et al., 1989a).

4.7 Temporal and spatial variations during the Cassini-Huygens mission

Latitudinal variations in Titan's stratospheric thermal and chemical structure have been previously reported from Cassini CIRS limb and nadir data analyses (Flasar et al., 2005; Coustenis et al., 2007; 2008; 2010b; de Kok et al., 2007a; Teanby et al., 2007; 2008; 2009b; Vinatier et al., 2007a; 2010b; Nixon et al., 2008b).

In this section, I investigate the possible thermal and chemical evolution within 2006 and 2012, complementing and refining previous studies (Teanby et al. 2008; 2010; Achterberg et al. 2011) by adding temporal resolution. I focus on Titan's stratosphere and lower mesosphere between ~120 and 500 km in altitude and latitudes from 50°S to 50°N.

4.7.1 Thermal evolution of Titan's stratosphere during the Cassini mission

The temperature profiles used in this study were retrieved by Dr. R. Achterberg by fitting of the n_4 methane band at 1305 cm^{-1} for the 2006-2012 CIRS data acquisition period (see Fig. 4.9 above). These retrievals were obtained by a constrained algorithm which is an inverse approach of the radiative transfer equation solution (Achterberg et al. 2008; 2011). A more general view of solving inversely the radiative transfer equation is presented in Appendix B of this manuscript.

The *a priori* reference profile was the one published in Flasar et al. (2005) and retrieved from 15°S observations by use of CIRS nadir and limb data from the T3 Cassini flyby. The gap in altitude between nadir and limb measurements in the stratosphere was fulfilled by interpolation using as initial guess the updated Voyager radio occultation profile. The characteristics of this profile are given in the online supplementary material of Flasar et al. (2005) paper and in Chapter 3. The results are shown in Figure 4.13a-e below. The precision of these temperature profiles depends on the number of spectra and the calibration accuracy. The random error imported in the measurements due to the instrument's noise is at about 0.1 K. Systematic errors come from uncertainties in methane abundance and the absorption coefficients (Coustenis et al., 2007). The temperature error bars are about 0.7 K at 1 mbar and about 5 K at 5 mbar (Achterberg et al., 2011).

Figure 4.13f shows the temperature profiles retrieved from limb data obtained by Sandrine Vinatier. Figures 4.13a-e show the results on the temperature as a function of latitude from nadir data inferences described in Table 4.7-4.10, using the altitude information

contained in the lines of the n_4 methane band. Figure 4.13a,b (upper panel) shows the temperature structure inferred at two latitudes (50°N and 30°N) at certain dates during the Cassini mission.

In the northern hemisphere, the temperature decreases in the mesosphere, which is more sensitive to the seasonal insolation variations. This decrease starts from the stratopause level above 0.1 mbar, where the temperature significantly decreases from 2007 to 2010. Since the beginning of the Cassini mission, the warm northern lower mesosphere has cooled by about 14 K at 50°N (Figure 4.13a) and by about 8 K at 30°N (Figure 4.13b) at around 250 to 300 km in altitude, which was also suggested by Achterberg et al. (2011).

In the mid-stratosphere (around 200 km), the northern polar region initially began cooling from 2007 up to 2009, while in 2010 a slight warming is observed again at both 50°N and 30°N. Temperature decrease (by 8 K maximum) with time in the lower mesosphere is also observed at the equatorial and southern latitudes. No significant changes are found in the equatorial mid-stratospheric temperatures (Figure 4.13c).

Similarly, in the southern hemisphere (at 30°S and 50°S - Figure 4.13d,e respectively), small temperature variations are observed that are always less than 10 K and more typically 2-4 K between 0.5 and 10 mbar within the error bars. Mid-stratospheric measurements for southern latitudes at 30°S (Figure 4.13d) show cooling between 2010 and early 2012 by 3 K, while no significant variations occurred from 2006 to 2008. More importantly, the general shape of the thermal structure is changing and we find a more isothermal profile at higher latitudes losing the marked stratopause present in earlier years.

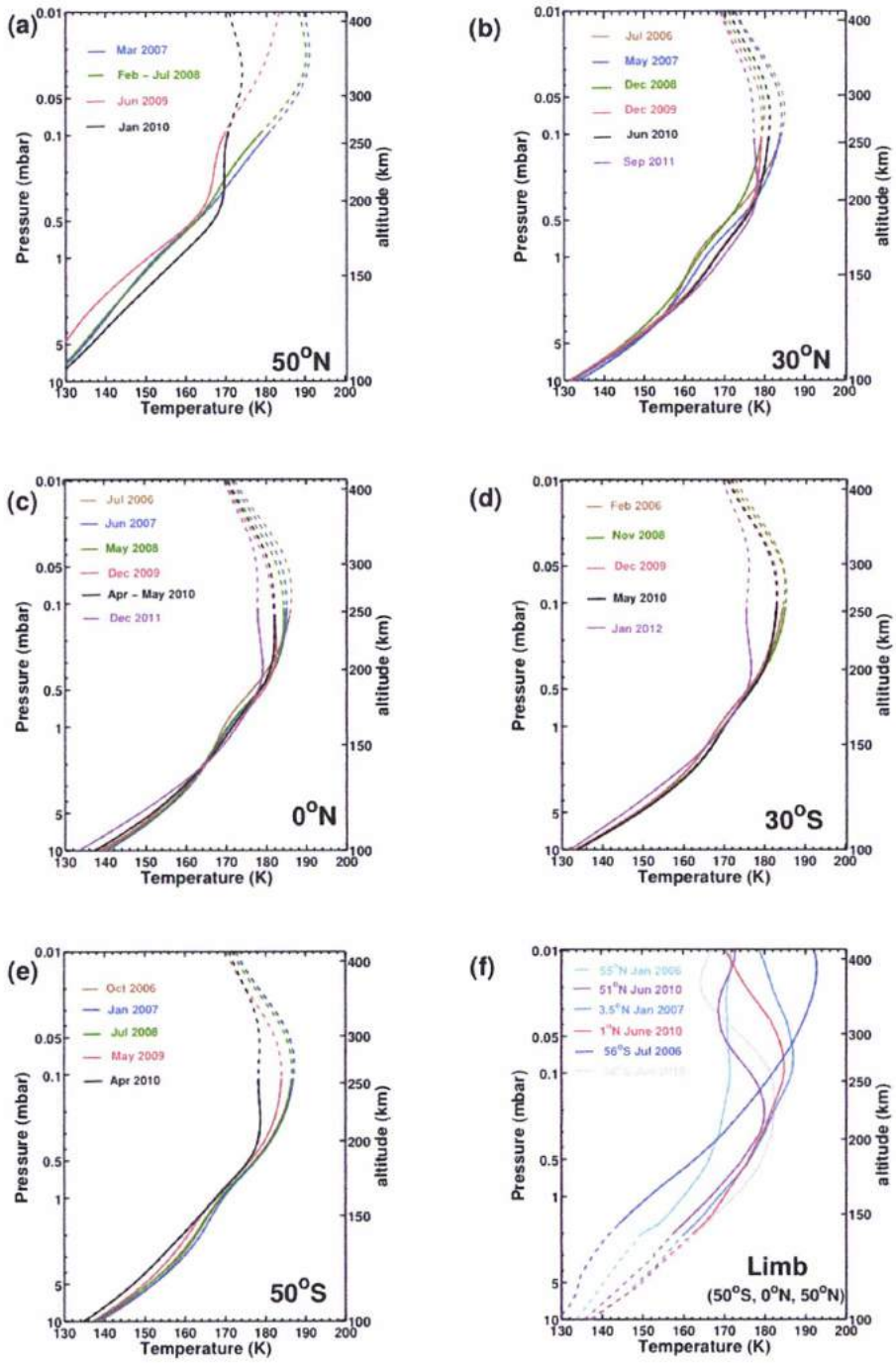

Figure 4. 13 - Retrieved thermal profiles from CIRS nadir data at (a) 50°N, (b) 30°N, (c) equator, (d) 30°S, (e) 30°S and (f) from limb data for the 2006-2010 limb data and from several dates. Panel f illustrates the temperature profiles corresponding to June 2010 at 50°S (pink solid line), 1°N (red solid line), 51°N (violet solid line) from CIRS limb observations acquired with a 15.5 cm^{-1} spectral resolution. They are compared with thermal profiles of the 2006-2007 period (northern winter) at similar latitudes. For the nadir temperature profiles the typical error bars uncertainty are about 0.7K at 1 mbar and about 5K at 5 mbar, while for limb retrievals is 1-2K. Dashed lines indicate the altitude levels above or below which, the temperature has higher uncertainties or is not accurately constrained (Bampasidis et al. 2012a).

The latter phenomenon is confirmed from CIRS limb data analysis (Figure 4.13f). We retrieved the temperature profiles at 50°S, 1°N and 51°N from CIRS limb observations acquired in June 2010 with the FP4 at 15.5 cm^{-1} spectral resolution. The temperature uncertainty is about 1 to 2 K. Figure 4.13f shows the temperature profiles retrieved from June 2010 compared with temperature profiles retrieved using CIRS limb spectra acquired in the 2006-2007 period with a 0.5 cm^{-1} spectral resolution (Vinatier et al. 2010b). In the lower mesosphere, between 250-300 km, the temperature is lower by 10 K at 50°S and 3 K at 0°N in 2010 than in the 2006-2007 period, while at 50°N the 2010 temperature is about 3 K higher than the 2006 value.

In the stratosphere, below ~250 km, from 2006 to 2010, the temperature at 50°N increased by about 10 K, shows no significant variation at the equator and has increased at 50°S more than 10 K. The difference between the 2007 and 2010 temperature profiles from limb data furthermore indicates not only a significant cooling (by more than 20 K in the 300-400 km range), but also a trend for the temperature to become more vertically uniform and the pronounced mesosphere to be dampened, as we find from the nadir data.

These changes at northern latitudes suggest a weakening of the descending branch of the middle atmosphere meridional circulation (Achterberg et al. 2011), which implies less adiabatic heating and hence lower temperatures. Moreover, the changes in the circulation affect the distribution of aerosols (Vinatier et al. 2012b), which in turn affect the thermal structure.

4.7.2 Chemical composition variation during the Cassini-Huygens mission

After fixing the temperature profile, I inject it in our radiative transfer code, in order to derive the mixing ratios of the contributing molecules from their emission bands in the CIRS FP3 and FP4 spectra through an iterative procedure. When the best fit between the model simulation and the observation is accomplished, I infer the corresponding abundances (see also Bampasidis et al. 2012 and Coustenis et al. 2010b). For each selection, I match the continuum level between the emission signatures by adapting the new model of haze distribution of Vinatier et al. (2012b).

The emission bands of Titan's hydrocarbon trace gases, nitriles and CO_2 are contained in the 600-1100 cm^{-1} region of the spectrum. These molecules (C_2H_2, C_2H_4, C_2H_6, C_3H_4, C_3H_8, C_4H_2, HCN, CO_2, HC_3N) have been previously detected in Voyager/IRIS spectra, ground based data and/or ISO/SWS recordings. The presence of all of the above-mentioned molecules has been verified in Cassini/CIRS FP3 spectra. The list of the molecules detected in Titan's spectra, is presented in Table 4.14 below. Table 4.15 summarizes the candidate molecules that are expected to be detected in CIRS FP3 and FP4 spectra and which are discussed further in this Chapter 3, Section 3.4.6, when we describe our search for weak molecules. All these molecules are included in the model.

Table 4. 14 - List of the currently detected molecules and isotopologues in Titan's atmosphere in the FP3 region.

molecule	cm^{-1}
C_4H_2	628
C_3H_4	633
$^{13}C^{18}O^{16}O$	643
$^{13}C^{16}O_2$	648.5
$H^{13}C^{12}C_2N$	658.7
HC_3N	663.2
CO_2	667.4
C_6H_6	674
C_2HD	678
$H^{13}CN$	706
$HC^{15}N$	711.5
HCN	712.7
$^{13}C^{12}CH_2$	728.5
C_2H_2	729.5
C_3H_8	748
C_2H_6	822
$C^{13}C^{12}H_6$	822
C_2H_4	949.5

Table 4. 15 - Candidate molecules that are expected to be detected in CIRS FP3 and FP4 spectra

molecule	cm^{-1}
DCN	554
$^{13}C^{17}O^{16}O$	646
$^{12}C^{18}O_2$	657
$^{12}C^{18}O^{17}O$	660
$^{12}C^{18}O^{16}C$	662.5
$HCC^{13}CN$	663.2
$HC^{13}CCN$	663.2
$^{12}C^{17}O^{16}O$	664.9

The continuous probing of Titan's stratosphere by CIRS provides information for the evolution of the chemical composition. Towards this end, I have calculated the abundances of the trace gases from the beginning of the mission up to early 2012.

In order to define the stratospheric regions probed by the emission observed in the different gaseous bands, we calculate the contribution functions $C(z,\mu)$ by using the formula (see Chapter 3, Section 3.4.2):

$$C(z,\mu) = B(z)W(z,\mu)$$

With $W(z,\mu)$ we describe the weighting function and $B(z)$ the Planck function. The contribution functions of the molecules present in the FP3 region are plotted in Figures 4.14-4.18 below.

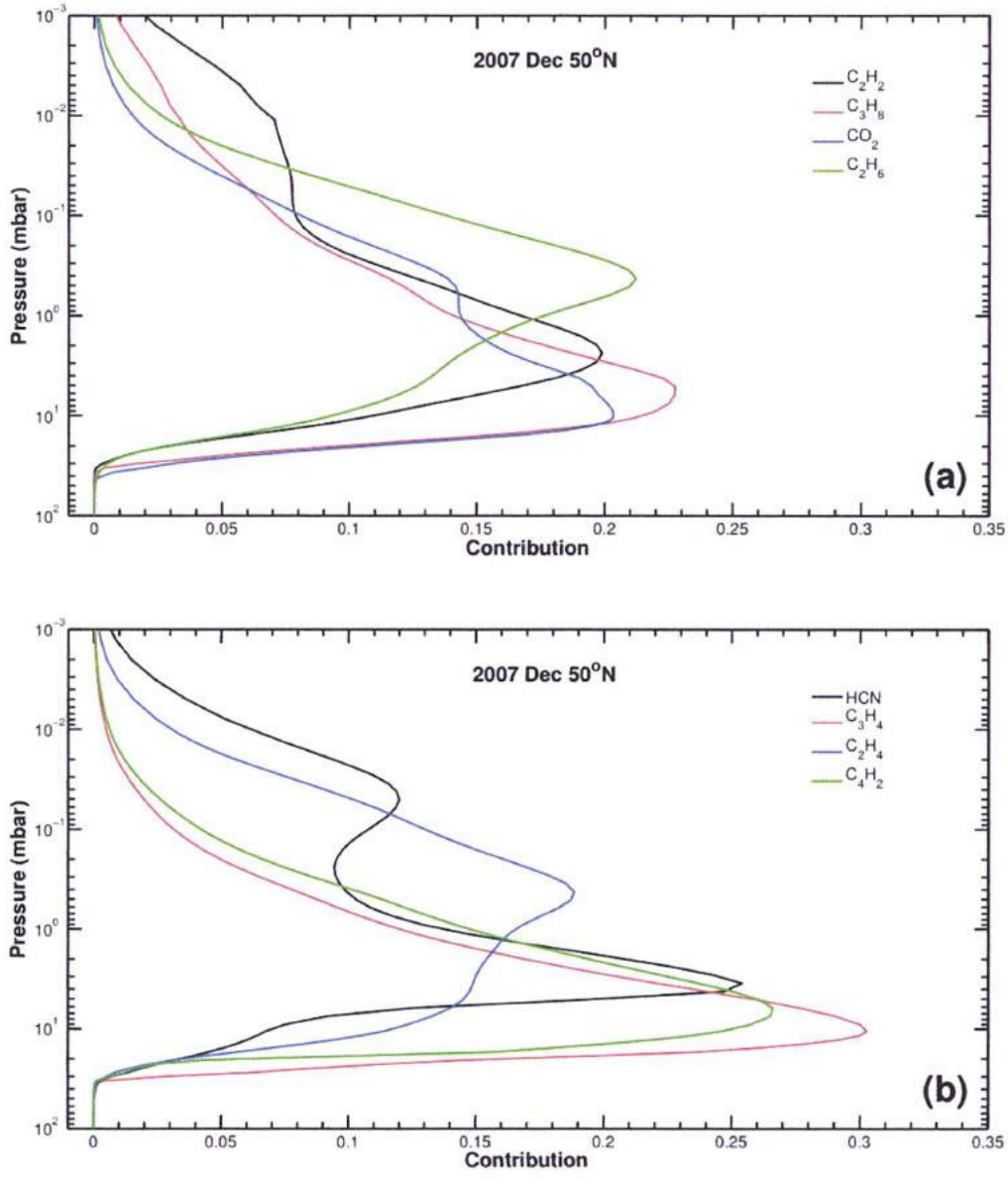

Figure 4. 14 - Contribution functions of most of the hydrocarbons, nitriles and carbon dioxide that have emission bands in Titan's CIRS FP3 spectra at 50°N high-resolution data.

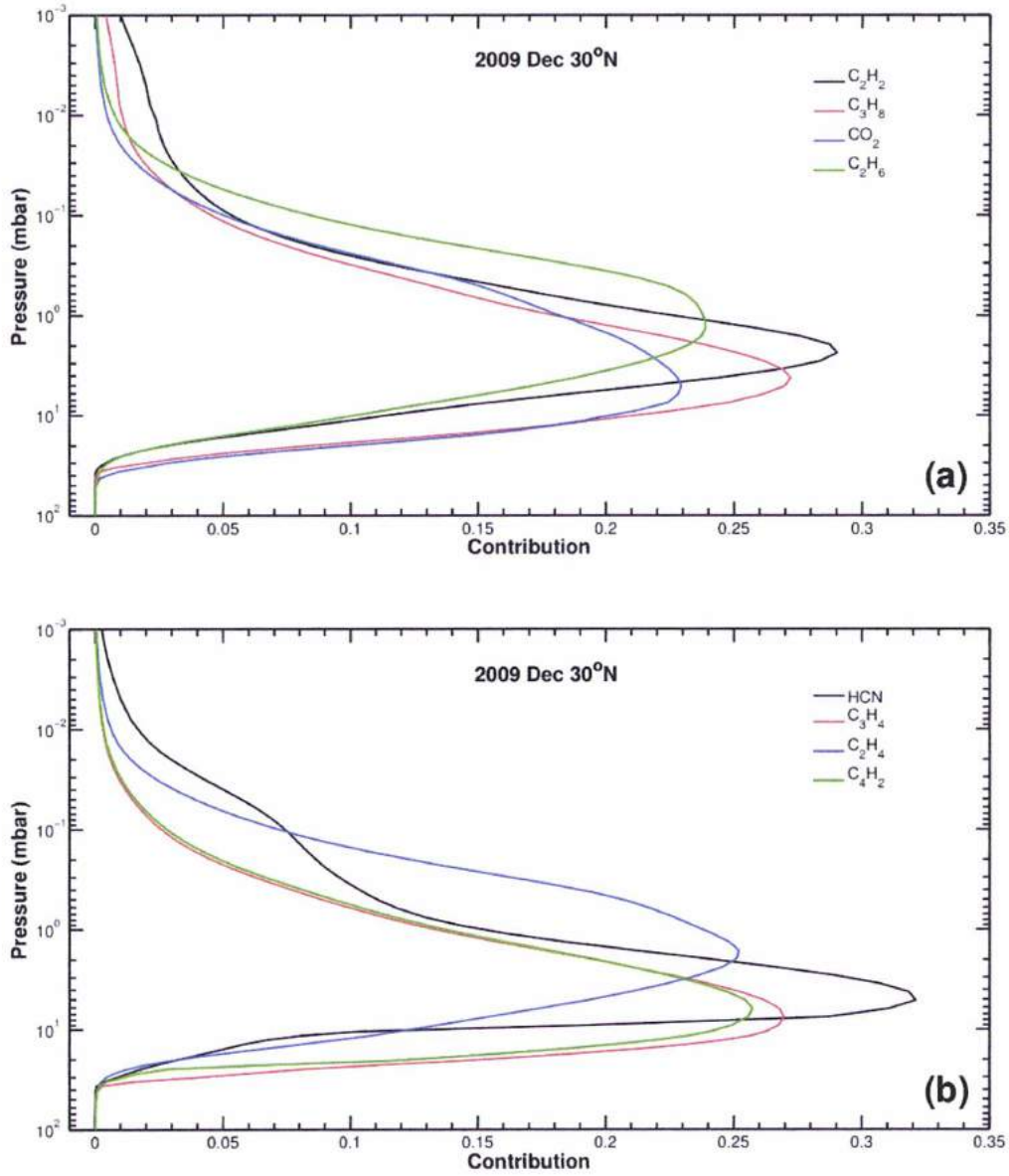

Figure 4. 15 - Contribution function of most of the hydrocarbons, nitriles and carbon dioxide that have emission bands in Titan's CIRS FP3 spectra at 30°N high-resolution data.

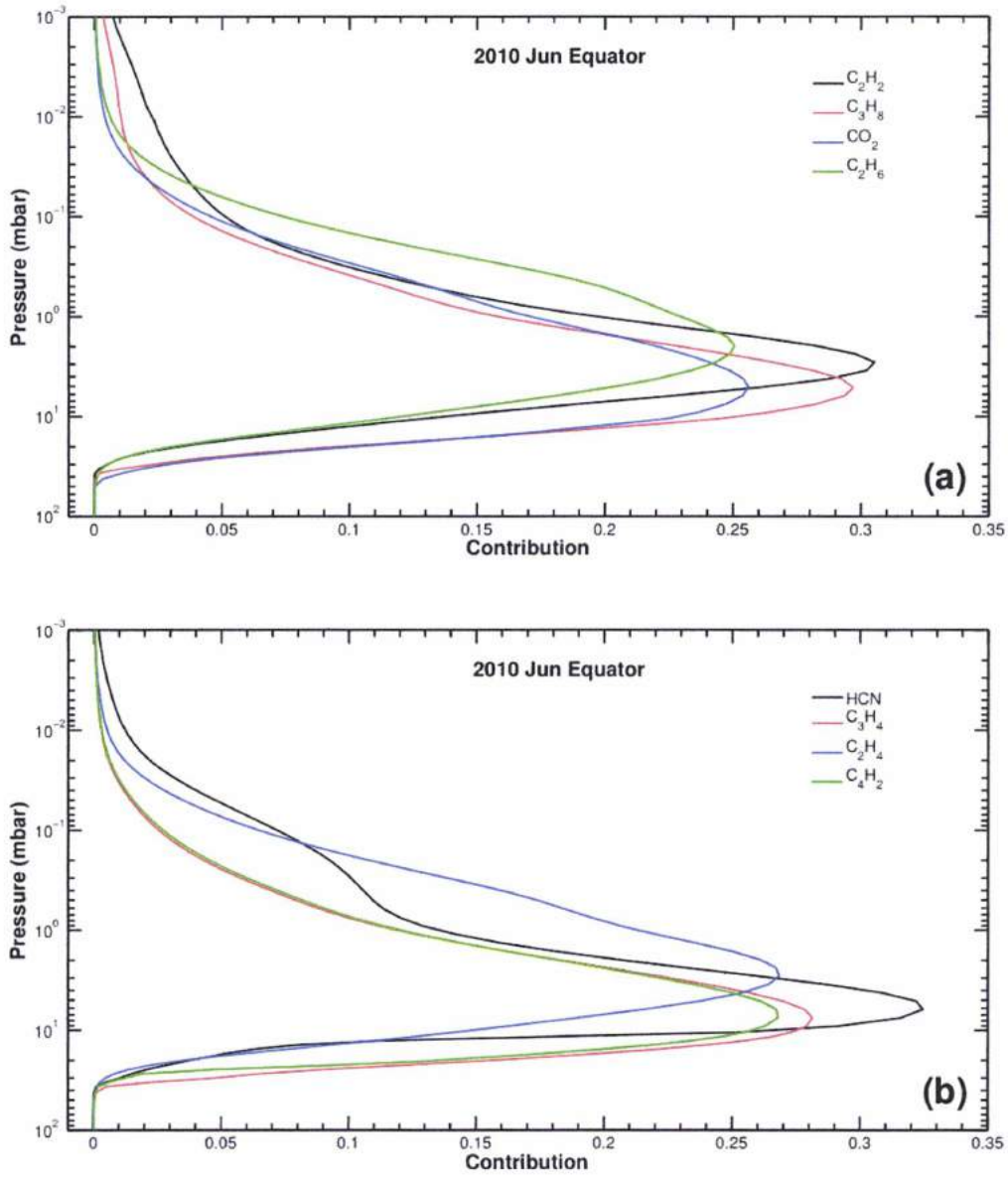

Figure 4. 16 - Contribution function of most of the hydrocarbons, nitriles and carbon dioxide that have emission bands in Titan's CIRS FP3 spectra at 0°N high-resolution data.

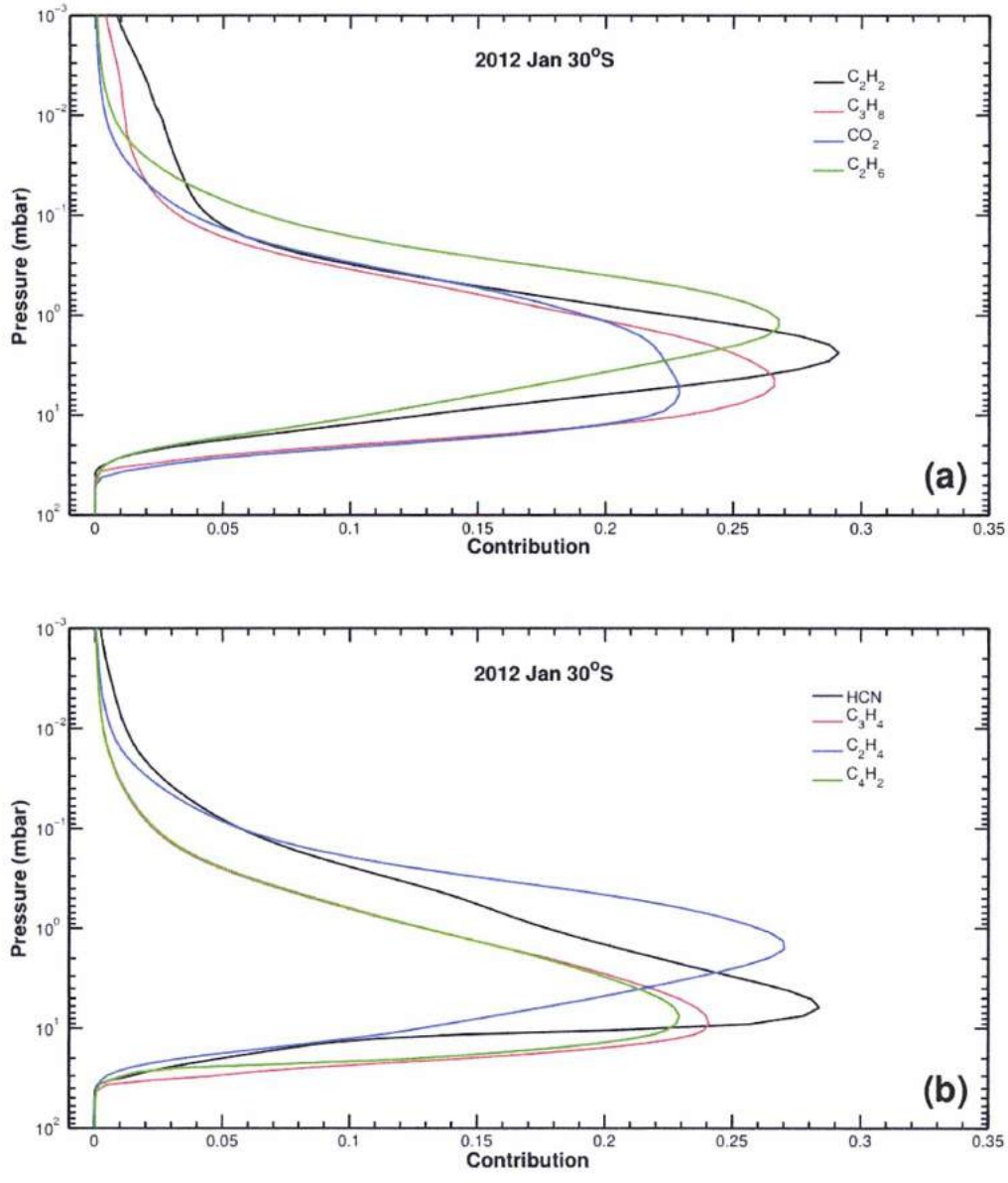

Figure 4. 17 - Contribution functions of most of the hydrocarbons, nitriles and carbon dioxide that have emission bands in Titan's CIRS FP3 spectra at 30°S high-resolution data.

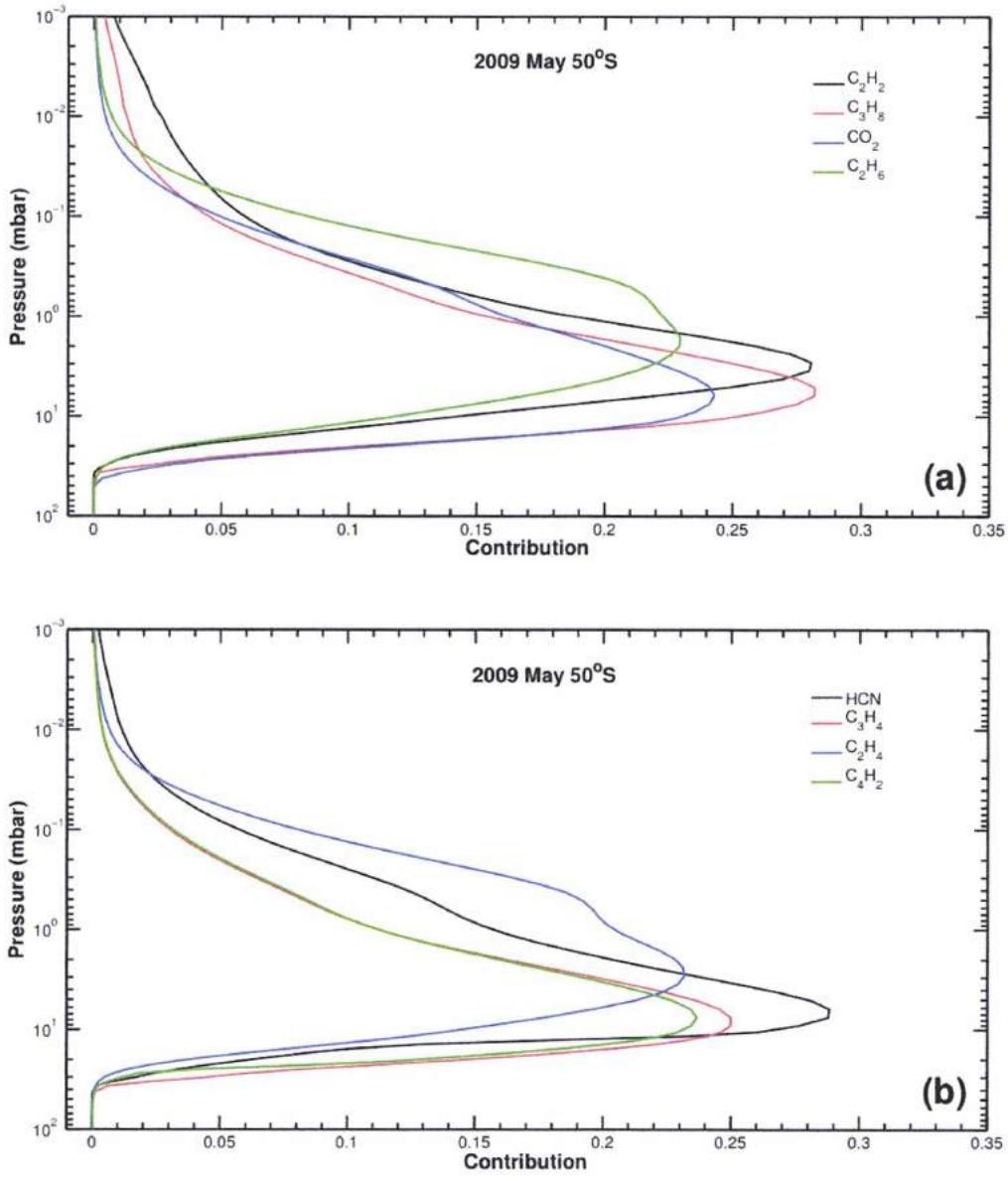

Figure 4. 18 - Contribution function of most of the hydrocarbons, nitriles and carbon dioxide that have emission bands in Titan's CIRS FP3 spectra at 50°S high-resolution data.

The dominant bands in the FP3 region are those of acetylene, hydrogen cyanide and ethane at 729.5 and 712.5 and 822 cm^{-1} respectively. For achieving the best fit, after fitting the continuum, we match these bands first for each selection. The following Figures 4.19-4.21 show the result of the best-fit process for some of the aforementioned selections throughout the FP3 region.

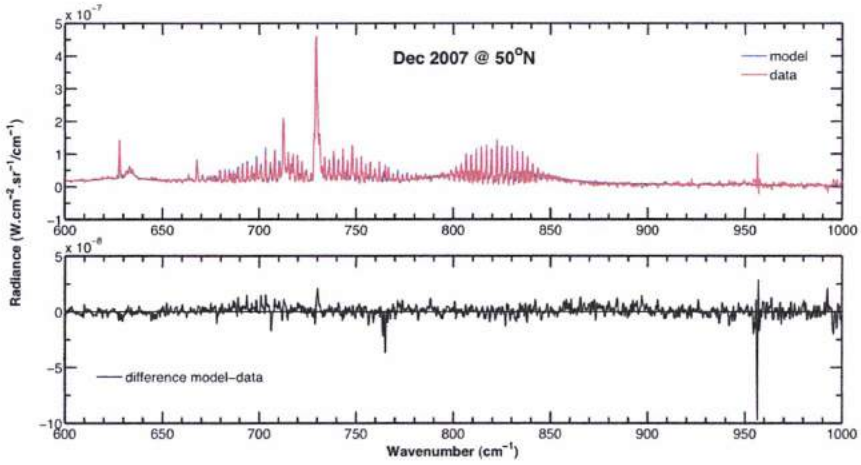

Figure 4. 19 - (Upper panel) The best fit achieved (in blue the model) between 600 and 1000 cm^{-1} for the December 2007 Titan spectrum at 50°N (in red). (Lower panel) Plot of the difference between model and data. The peaks at 765 and 955 cm^{-1} are caused by electrical artificial inferences - spikes (see Chapter 2).

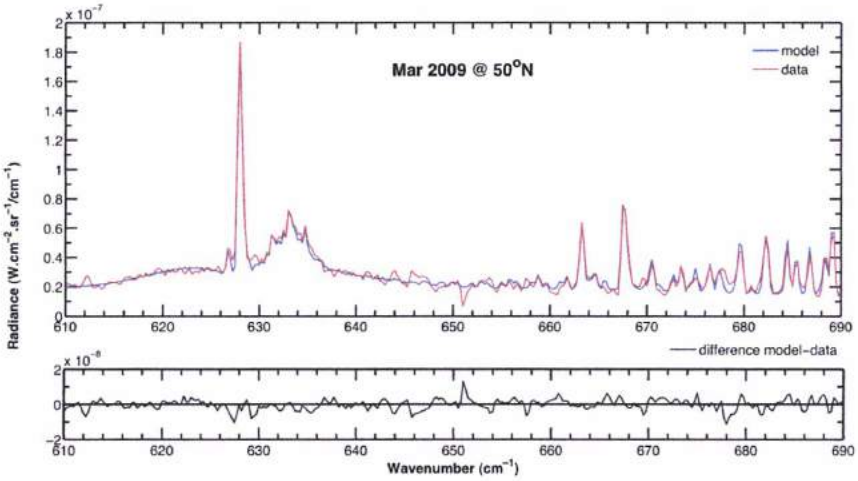

Figure 4. 20 - (Upper panel) The best fit obtained (in blue the model) between 610 and 690 cm^{-1} for the March 2009 Titan's spectrum at 50°N (in red). (Lower panel) Plot of the difference between model and data. The C_4H_2, C_3H_4, HC_3N and CO_2 emission bands are at 628, 633, 663 and 667 cm^{-1} respectively.

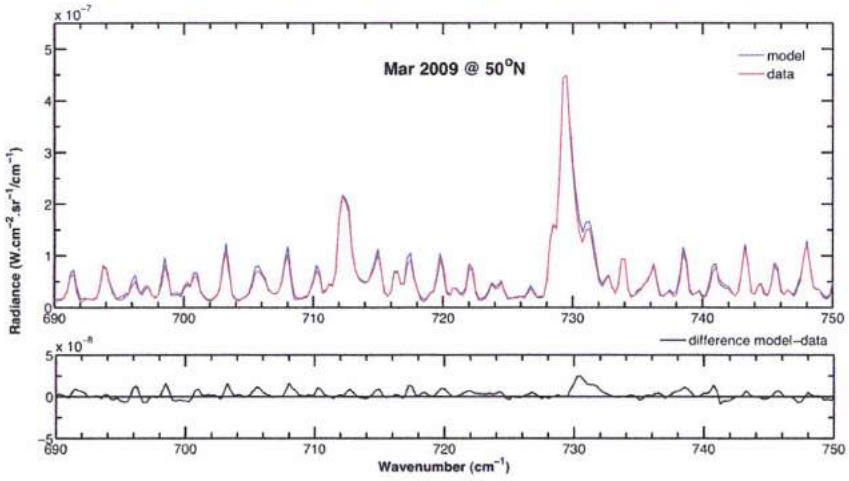

Figure 4. 21 - (Upper panel) The best fit found (in blue the model) between 690 and 750 cm^{-1} for the March 2009 Titan's spectrum at 50°N (in red). (Lower panel) Plot of the difference between model and data. The HCN and C_2H_2 emission bands are at 713 and 730 cm^{-1} respectively. The isotopologues of $H^{13}CN$, $HC^{15}N$ and $^{13}C^{12}CH_2$ are also fitted at 706, 712 and 729 cm^{-1} respectively.

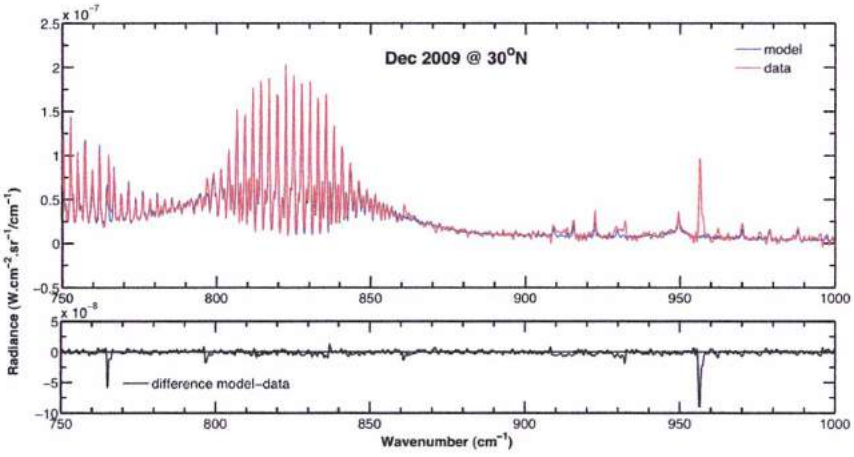

Figure 4. 22 - (Upper panel) The best fit found between 750 and 1000 cm^{-1} for the December 2009 Titan's spectrum at 30°N (in red the data, in blue the model). (Lower panel) Plot of the difference between model and data. The negative peaks at 765 and 955 cm^{-1} are caused by spikes in the spectrum. The 13-C isotopologue of C_2H_6 ($^{13}C^{12}CH_2$) is included.

In Figures 4.24a-h, I show the Cassini/CIRS mixing ratio inferences which are found above the condensation level with the associated error bars. Two are the main types of the uncertainties: systematic errors in our model atmosphere and spectroscopic data and random errors due to instrumental noise itself at the location of the emission peak, the uncertainty in the placement of the continuum above which the emission rises and the uncertainty on the thermal profile and its influence on the line formation region (Coustenis et al., 1995; 2010b).

Other systematic errors are from calibration uncertainties, temperature profile inconsistencies in the datasets and haze description uncertainties.

The Noise Equivalent Spectral Radiance (NESR) is the signal when the instrumental signal-to-noise ratio (S/N) is unity (Hanel et al., 2003). NESR varies with the wavenumber as it shown in Figure 4.23 below, which is provided by Dr. R. Carlson (GSFC and IACS).

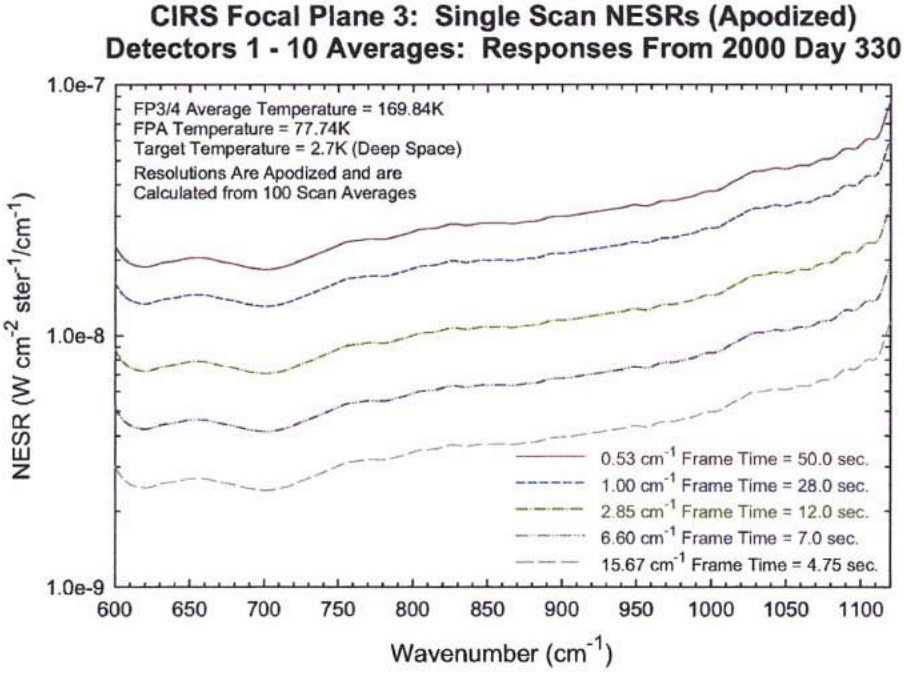

Figure 4. 23 - CIRS NESR as a function of wavenumber (provided by Dr. R. Carlson, *pers. communication*).

The ratio of NESR to the square root of the total number of averaged spectra is the 1-σ standard deviation. The estimation of uncertainties has included the temperature profile errors as described above, calibration, and line positions.

Except for the early mission dates (within 2004-2005) and sometimes in the northern selections (e.g. February 2008), the noise level is low in our usually large averages. The errors from the instrument noise are small in temperature retrievals, about 0.1 K (Achterberg et al., 2008; Coustenis et al., 2010b). We only consider the relative uncertainties that mainly originated in the uncertainties of methane abundance and temperature (all within 15%) and neglect the systematic errors which are the same for all selections.

Propane (C_3H_8) and ethylene (C_2H_4) show ratios that have error bars of about ±35% and they are not as reliable as the other inferences for the temporal or spatial variations. These

molecules are affected by abundance retrieval difficulties and some insufficient laboratory spectroscopic data. The strong P-branch of the C_2H_2 band influences the retrieval of the C_3H_8 abundance from its emission at 748 cm^{-1}. Around 765 and 950 cm^{-1}, the spectrum suffers from some electrical interference artifacts ("spikes", see Chapter 2 for further information).

The retrieved abundances at southern latitudes (50°S and 30°S), as well as near the equator, remain rather constant-in-time during the Cassini mission within the error bars. C_2H_4 and C_3H_8 are identified as complicated molecules to process, in particular at the mid and southern latitudes. In general, for the other molecules, the equatorial data yield higher abundances than the 30 or 50°S inferences by about 20%, almost at the same level for all molecules. The mixing ratios at 30°N are 20% higher than the equatorial values except for the acetylene which is almost 10% higher.

When moving from the South to the North, I have found a definitive trend for increased gaseous content in the stratosphere. Additionally, the enhanced abundances have been observed in most cases at latitudes higher than 30°N during the duration of the northern latitudes.

In the latitudinal bin of 50°N, all abundances except for CO_2, are thus significantly enhanced with respect to 50°S and the equator. These results are consistent with our previous work with this model (Coustenis et al. 2007; 2010b) and with Voyager 1 results (Coustenis et al. 1991; Coustenis & Bézard 1995). The 50°N values are higher than the 30°N by 20% and by 40% with respect to the equator.

These enhancements appear to be greatest for the shortest-lived chemicals which are explained by a combination of chemistry and dynamics. The vertical distributions are steepest for the shortest-lifetime species in a purely chemical model, while the presence of a circulation cell in the real atmosphere, with subsidence in the polar regions (at the north pole during the period of the observations), causes the lower stratosphere to be greatly enriched in these species at the winter pole as compared to the equator. The study of the temporal evolution of this enhancement in the higher northern regions within the Cassini mission duration, as well as changes observed with time at southern polar regions are described in more detail by Teanby et al. (2008; 2010 and 2012, *in press*) as well as in a work to which we contributed and will be published by Vinatier et al (2012, *in preparation*).

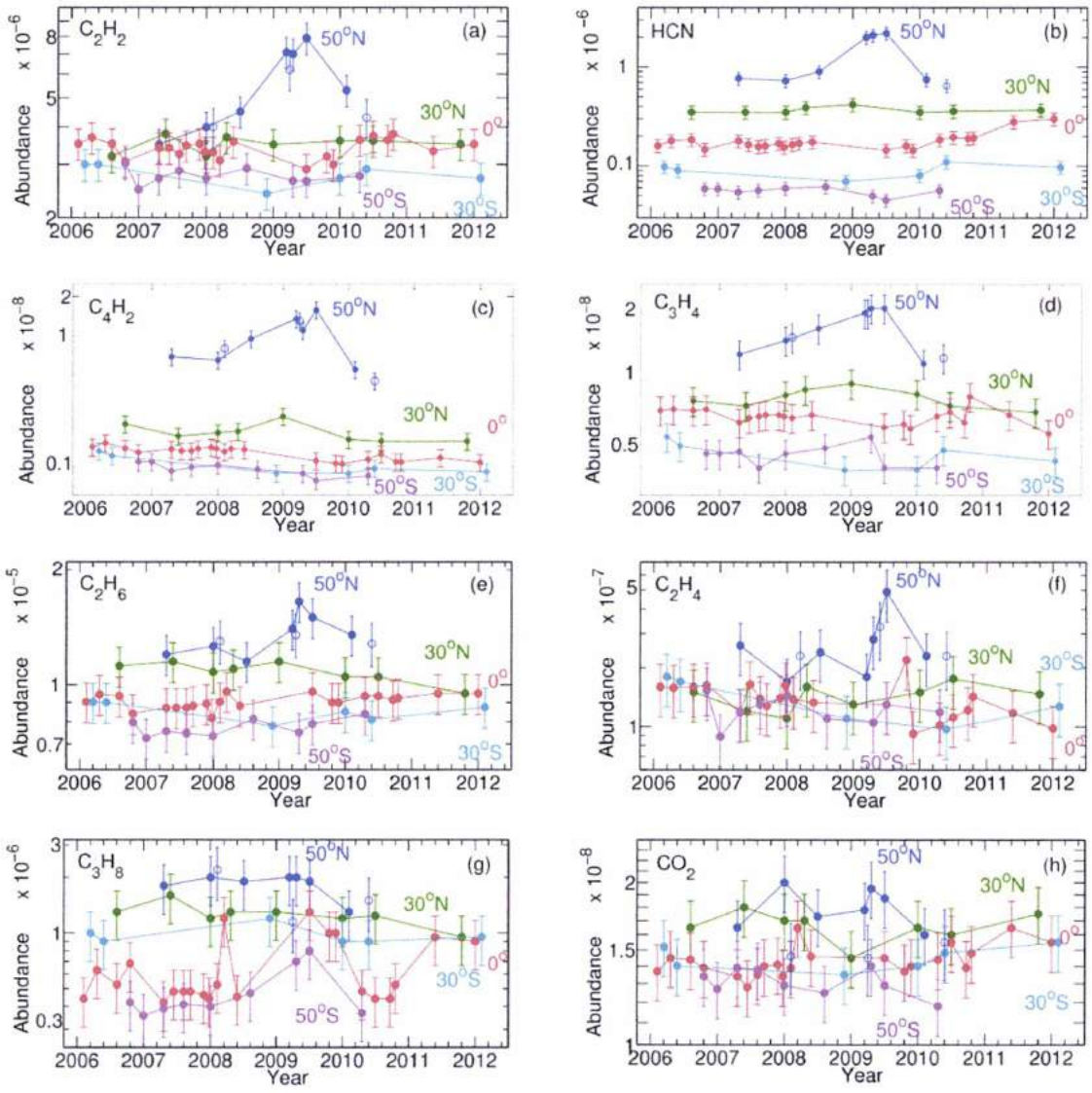

Figure 4. 24 - Time-latitude composition variations for the major trace gases of Titan's stratosphere: (a) C_2H_2, (b) HCN, (c) C_4H_2, (d) C_3H_4, (e) C_2H_6, (f) C_2H_4, (g) C_3H_8 and (h) CO_2 with 3-σ estimated error bars. The latitudes mapped from 2006 to 2012 are: 50°S (violet), 30°S (light blue), equator (red), 30°N (green) and 50°N (blue). Connected filled circles are high resolution observations (0.5 cm^{-1}), while open circles are medium resolution data (2.5 cm^{-1}) for 2008, 2009 and 2010 (which sometimes coincide with the higher resolution values). The 3-σ estimated error bars are indicated (Bampasidis et al., 2012a).

Titan experienced the northern spring equinox (NSE) on 15 August 2009. My research covering the Cassini mission duration, allowed us to infer variations as a function of latitude and time. At 50°N, we have found indication for an increase in abundance from 2006 to mid-2009 for almost all molecules compared to the 2008 and 2010 values. The exceptions are propane and carbon dioxide which do not seem to vary in time at any

latitude (see g and h plots of Fig. 4.24). C_3H_8 seems to have increased abundances around NSE, but the data analysis results for this molecule at lower latitudes is rather uncertain. We have detected a maximum around the time of the Northern Spring Equinox in mixing ratios with increases in abundances by about 30-40% for C_3H_4 and C_2H_6, 60-70% for C_2H_2 and C_4H_2 and about a factor of 2 for HCN and C_2H_4 (albeit with higher uncertainties) relative to the adjacent time periods in 2008 and 2010. Ethane shows variations with time only at this higher latitude.

The observed increase in abundance for some molecules is followed by a strong decrease which reduces considerably the observed enhancement by 2010. It is a quick decrease, within 1-2 terrestrial years and brings the abundances back to their levels prior to the ascent.

There is only one CIRS FP3 selection at high resolution available in nadir viewing geometry after the NSE and one in lower resolution. The latter confirms this result, but further verification is required. Additionally, both high and low-resolution nadir data taken in the 2010-2012 period seem to support the observed increase as well as the follow-up decrease (see open circles in Fig. 4.24).

We have also derived the $^{12}C/^{13}C$ ratio in CH_4 and C_2H_2 to be 95 ± 15. Similarly, the $^{14}N/^{15}N$ ratio in HCN has been inferred to be 50 ± 10 for the latitudes analyzed in this section as an average. The $^{12}C/^{13}C$ ratio is consistent with results reported by Vinatier et al. (2007b) and Nixon et al. (Nixon et al., 2008a; 2008b) and with the terrestrial inorganic standard value (88.9, Fegley 1995). The $^{14}N/^{15}N$ ratio is also consistent with the values given by Vinatier et al. (2007b) and about 4.8 times lower than the terrestrial value (272, Fegley 1995).

Much stronger chemical and temperature variations have been reported at higher northern or southern latitudes (poleward of 70°N or 70°S) within the recent years (Vinatier et al., 2012b; Teanby et al., 2012, *in press*).

4.7.3 Comparison between nadir and limb data at the NSE

I have tried to verify the NSE enhancement by performing limb data analysis in collaboration with Dr. S. Vinatier. However, there are no available high-resolutio limb spectra of this period at 50°N, only in July 2009 we have spectra taken at 15 cm^{-1} resolution during the T59 Cassini flyby. The comparison with this data delivered a discrepancy. No

enhancement is observed in T59 limb spectra. We have checked if this discrepancy comes from the temperature profile used in both retrievals (nadir and limb).

The limb temperature profile is indeed hotter by about 10 K at 1 mbar compared to the nadir one, while their difference is less significant in higher altitudes (Fig. 4.25). I have to note here, that the limb temperature profiles have been retrieved from limb spectra from S. Vinatier, while R. Achterberg provided the nadir temperature profiles. Since limb spectra do not give information below 2 mbar, the initial guess used for retrieving both profiles does not affect the results.

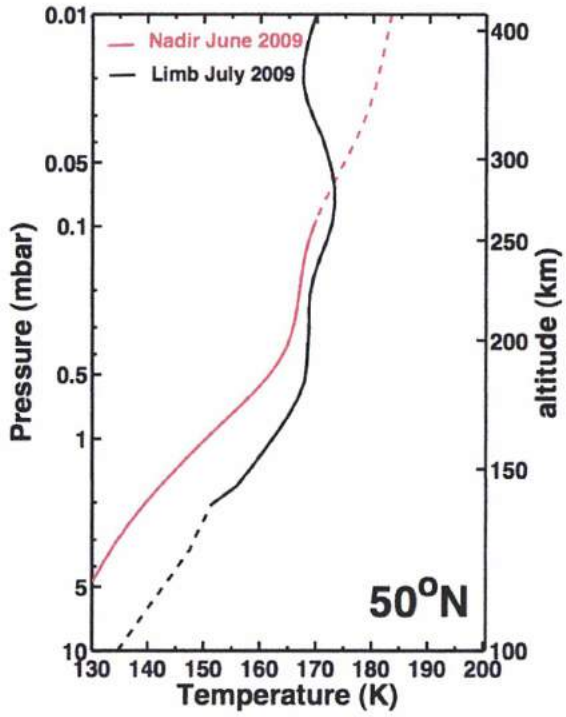

Figure 4. 25 - Comparison of the vertical temperature profiles between limb and nadir selections at northern spring equinox. The nadir temperature profile has been retrieved by R. Achterberg by using 0.5 cm^{-1} spectra, while the limb one has been retrieved by S. Vinatier by using 15 cm^{-1} spectra. The profiles present a 10 K difference at 1 mbar.

We have run some tests in order to understand the discrepancy in the thermal profiles. The nadir temperature profile could not fit the limb FP4 data except for the altitude of 213 km or 0.3 mbar (see Fig. 4.26).

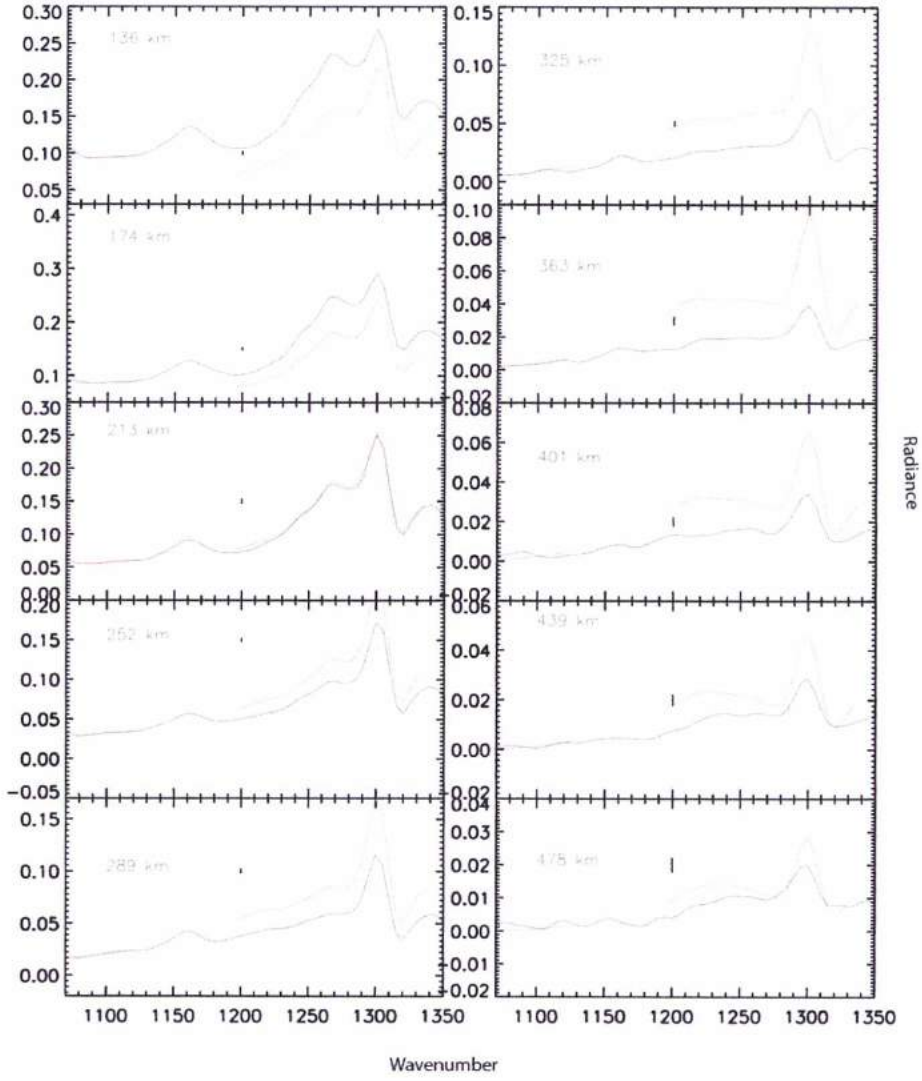

Figure 4. 26 - Fits of the limb data (in black) of the July 2009 selection by using the temperature profile of June 2009 nadir query to model the observations (in red). Data and model fit only at 213 km or 0.3 mbar.The plot was provided by S. Vinatier. Radiance is in $x10^{-7}$ $Wcm^{-2}sr^{-1}/cm^{-1}$, while the Wavenumber is in cm^{-1}.

Then, we tried to fit the nadir FP4 data of June 2009 by using the limb temperature profile (Fig. 4.27). The temperature profile retrieved from the limb T59 selection (July 2009) did not fit well the wings of CH_4 band at 1304 cm^{-1}. The temperature profile is hotter by 10 K than the nadir temperature profile and a colder profile is needed for the probed altitudes.

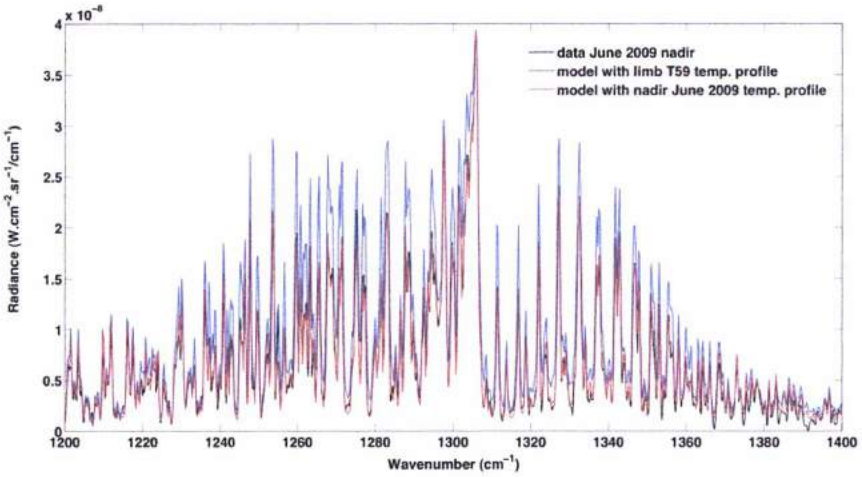

Figure 4. 27 - Fit of the ν_4 methane band at 1304 cm^{-1} by using ARTT and the limb temperature retrieval. This temperature profile is too hot in the probed atmospheric level for fitting the nadir data, especially in the wings.

The contribution functions of the methane Q-branch and its wings when we used the limb temperature profile are plotted below (Fig. 4.28). The contribution functions confirm that the methane central branch as well as its wings peak at the pressure levels where nadir and limb thermal profiles have a 10 K difference and are therefore not compatible.

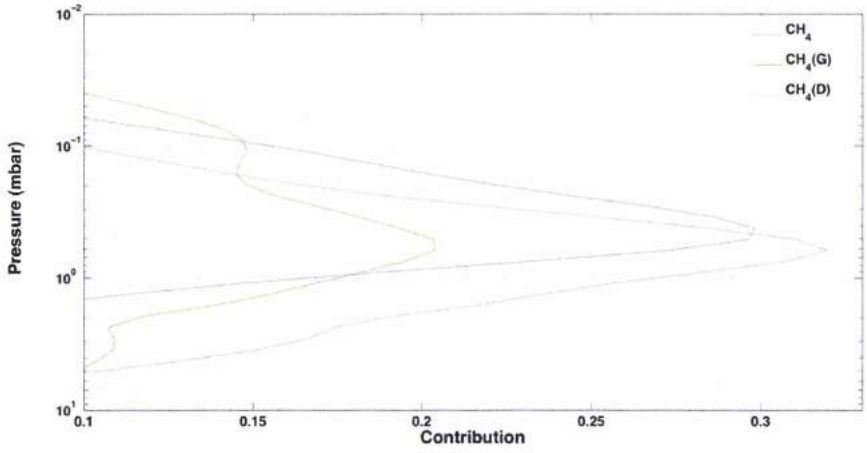

Figure 4. 28 - Contribution functions of ν_4 methane band at 1304 cm^{-1} and its wings derived from the limb temperature profile. $CH_4(G)$ is the left wing, while $CH_4(D)$ is the right wing.

The contribution functions of methane Q-branch and its wings when we used the nadir temperature profile are plotted below (Fig. 4.28).

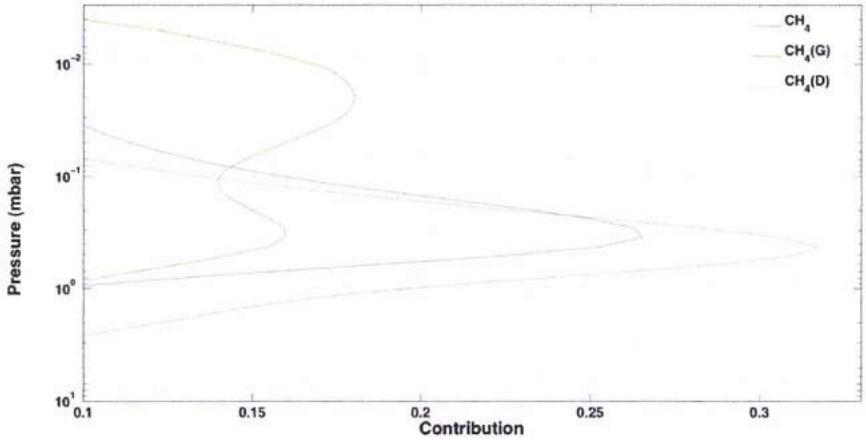

Figure 4. 29 - Contribution functions of ν_4 methane band at 1304 cm^{-1} and its wings derived from the nadir temperature profile. $CH_4(G)$ is the left wing, while $CH_4(D)$ is the right wing.

From the contribution functions' plots above (Figs. 4.28-4.29), we confirm the difference between the regions probed by the two thermal profiles. The left wing of methane peaks at different altitudes. Moreover, there is a discrepancy in the retrieved abundances between limb July 2009 selection and nadir June 2009 selection (Fig. 4.30). HCN and C_2H_6 have similar limb values with the nadir ones in the probed pressure level at 0.1 mbar. We have a discepancy for C_2H_2.

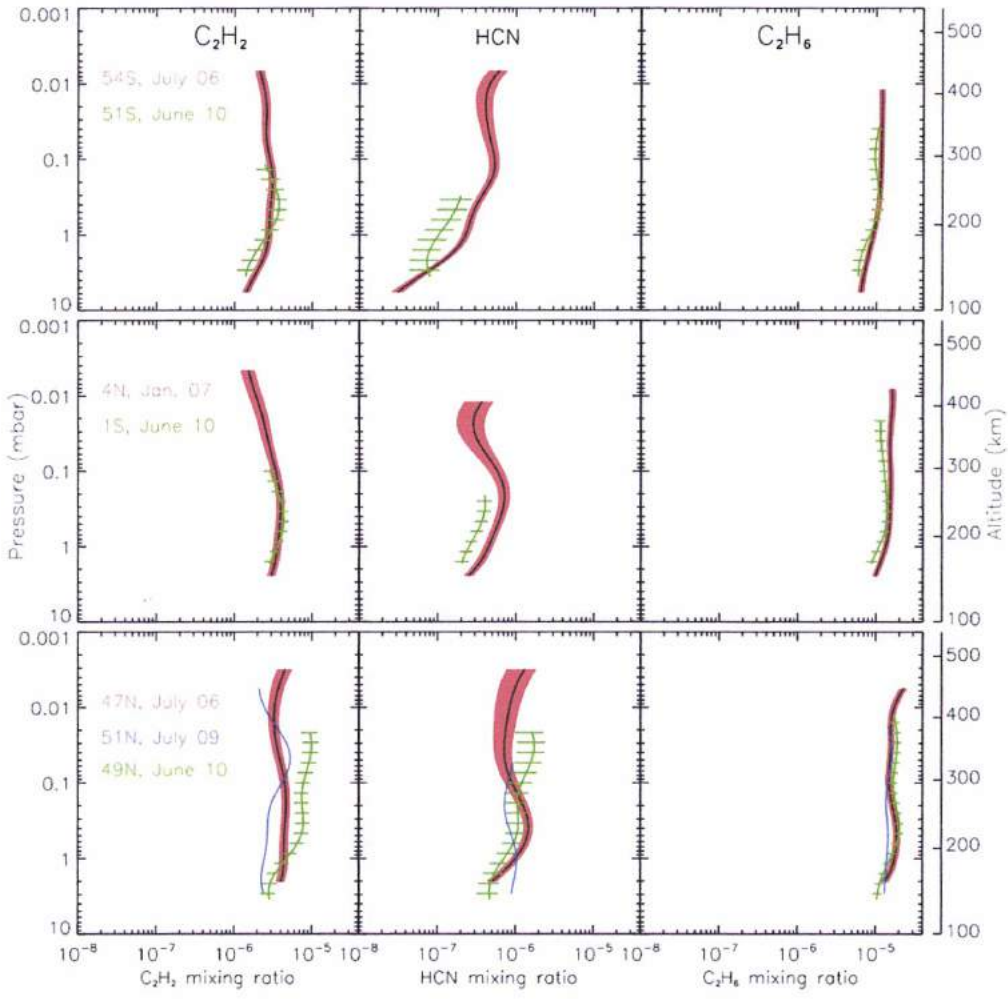

Figure 4. 30 - Variations in the vertical distributions of the main stratospheric molecular constituents on Titan between 2006-2007 and 2010 from CIRS limb data. Retrieved mixing ratio profiles of C_2H_2 (left panel), C_2H_6 (right panel) and HCN (middle panel) in June 2010 (in green) are shown. They are compared with mixing ratio profiles derived from CIRS limb data acquired in 2006 and 2007 (in red). The altitude scale corresponds to the 2010 observations. 1-s uncertainties on the vertical mixing ratio profiles are indicated. The July 2009 retrieval (blue) presents comparable values for HCN and C_2H_6 with nadir results. The only exception is acetylene. For the interpretation of this discrepancy see text.

When we injected the limb temperature profile (adjusted to fit the nadir FP3 data) into ARTT and used vertical distributions derived from general circulation models (GCM-Rannou et al., 2005), for the major molecules C_2H_2, C_2H_6 and HCN, the model did not fit well the data because the thermal profile is too hot. Figure 4.31 illustrates the outcome of this simulation.

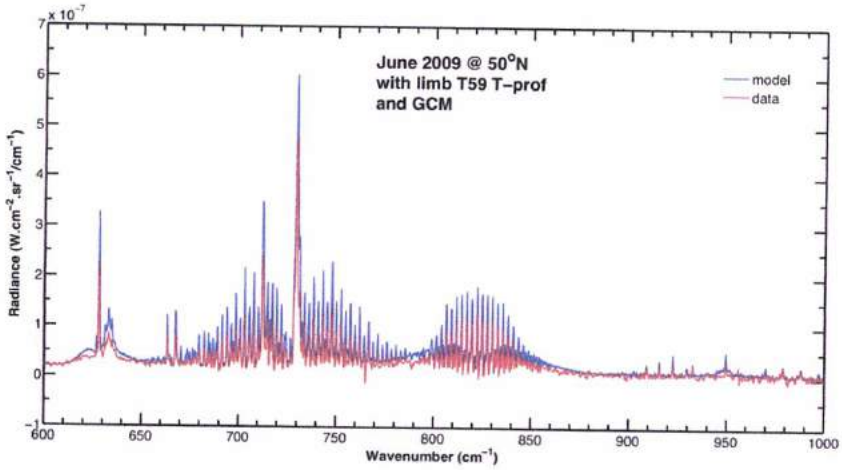

Figure 4. 31 - Fit of the nadir selection of June 2009 at 50°N when the thermal profile retrieved from limb measurement was adapted. Values predicted from General Circulation Models (Rannou et al. 2005) have been used. The misfit due to the temperature profile is obvious.

We then made the same fit, but with using the nadir June 2009 temperature profile instead of the limb one and the limb vertical distribution files for C_2H_2, HCN and C_2H_6 (see Fig. 4.32 below).

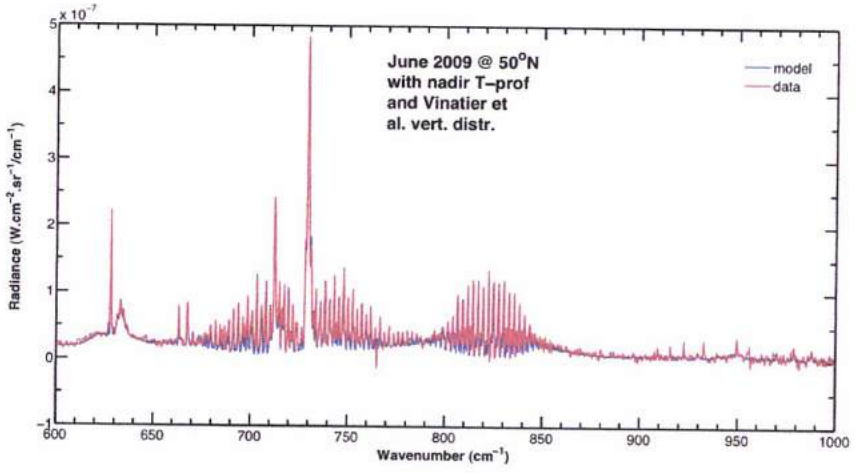

Figure 4. 32 - Fit of the nadir selection of June 2009 at 50°N when the thermal profile retrieved from nadir measurement was adapted. Vertical distributions provided from S. Vinatier have been used. Now the model spectra fit well the data.

The HCN and C_2H_6 limb vertical distributions fit the nadir data. The C_2H_2 limb vertical distribution is lower than the one we have calculated by using constant-to-height mixing ratio and it needs adjustment. The retrieved value for C_2H_2 is 6.25×10^{-6}. The vertical

distributions from S. Vinatier fit better the spectra compared with the GCM files that have a steeper slope.

In discussions that ensued, R. Achterberg pointed out that these observational selections are not comparable because they are not really looking at the same latitude as the limb observations in the ν_4 methane band are also looking at about 10 degrees of arc or more in front of the tangent points. Indeed, the 2009 selection is at a fairly high emission angle. Assuming that the latitudes used for averaging are the surface latitudes, the latitudes in the upper stratosphere can be different by several degrees, and at 50°N, the latitudinal temperature gradients are fairly large. Therefore we renounced in trying to fit the limb and the nadir selections taken at the same time but looking at different real estate and have focused on the nadir spectra.

4.7.4 Interpretation of the results

In this section, I have retrieved the abundances of trace gaseous compounds in Titan's stratosphere from 50°S to 50°N (Fig. 4.24). CO_2 presents no latitudinal variations anywhere because of its long photochemical lifetime. For the other molecules, mid and southern latitudes show no significant temporal variations during the Cassini mission. However, I confirm that a rapid change in the atmosphere took place at 50°N during the Cassini mission (Teanby et al., 2010, Bampasidis et al., 2012a). A compositional enhancement is reported with an indication for a maximum at the time of the Titan northern spring equinox (NSE - August 2009), followed by a sharp decrease of the gaseous chemical content within the next terrestrial year that remains to be confirmed with further data. These results are compatible with the findings of Teanby et al. (2010) in that I find HCN and C_2H_2 to display a rapid increase in northern latitudes up to mid-2009, while the abundances at equatorial and southern latitudes remain stable.

Short-term variations observed during the Cassini mission can arise from changes in the circulation around the equinox. The collapse of the detached aerosol layer (West et al., 2011) suggests that the dynamics during this period go through a rapid transition which should also affect the gas distribution. The rapid decrease after NSE for which the most straightforward explanation is that the vortex has shrunk somewhat, would be consistent with the weakening thermal gradient and the profile becoming more constant with height,

losing it warm mesosphere that we find here. Also compatible is the weakening of the winds as reported by Achterberg et al. (2008; 2011) and Teanby et al. (Teanby et al., 2009b). The finding also ties into the location of the maximum temperature gradient, which appears to be moving northward over the winter/spring season (Teanby et al., 2010, see Fig. 3, T panel). If 50°N is emerging from the vortex core, it would cause a large reduction in the abundances, hence explaining our observations. Thus, reduction at 50°N could be due to a weakening vortex with reduced lateral mixing across the vortex boundary (Teanby et al., 2010).

Another cause could be the spatial (due to Titan's inclination) variations in the energy input to Titan's atmosphere as a driver for changes in the advection patterns, which in turn provide a stronger variability in the latitudinal abundances of photochemical species. Cassini entered into Saturn Orbit Insertion (SOI) at Ls=293°. The NSE is at Ls=0° and the average insolation at the top of the atmosphere has been increased (Fig. 4.33).

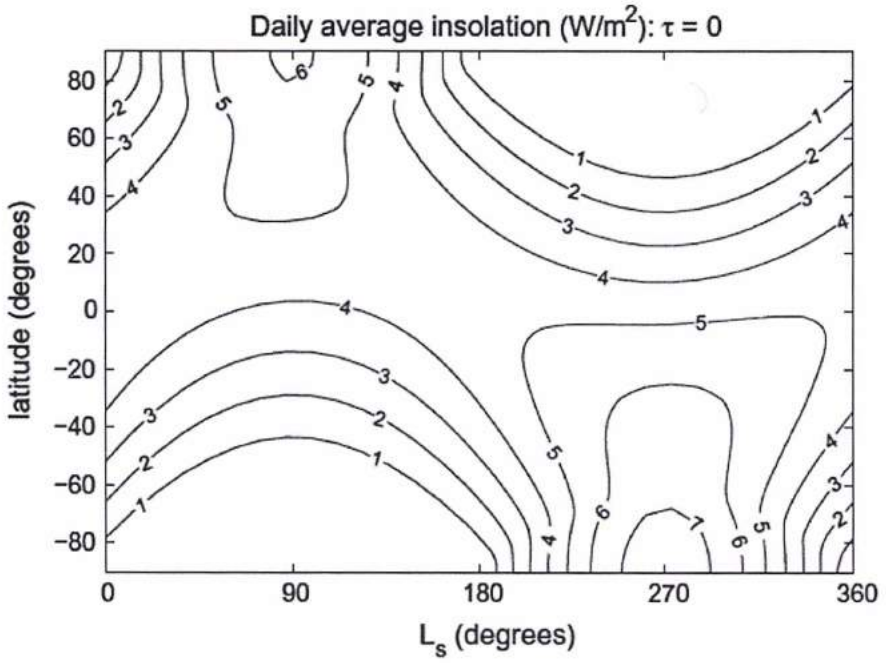

Figure 4. 33 - Daily averaged insolation as a function of time at the top of the atmosphere. Cassini entered into SOI at Ls 293° (adapted from Lora et al., 2011).

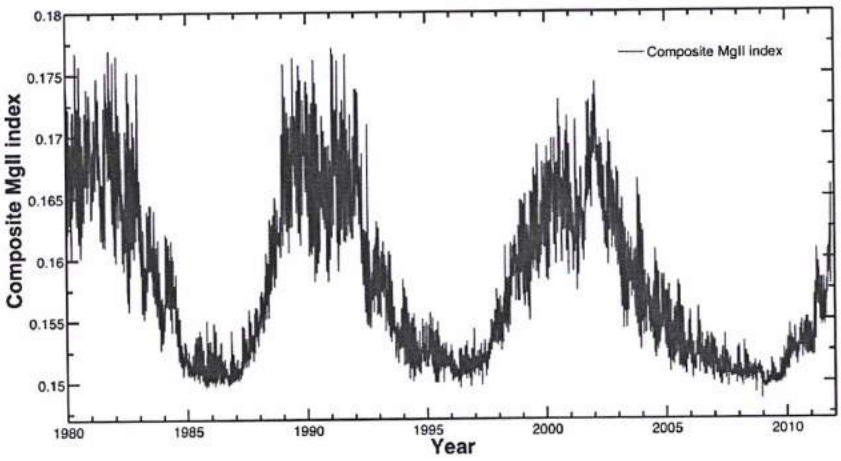

Figure 4. 34 - The Solar Cycle from 1980 (Voyager encounter at the Saturnian System) up to date. Cassini began touring the Saturnian System in mid-2004. This plot shows the Composite Mg II index which is frequently used as a proxy for spectral irradiance variability. It refers at 1 AU and it provides the solar activity at EUV and UV. As I have discussed with Prof. Moussas and Dr. L. Didkovsky (Univ. of Southern California/SSC) Mg II index represents the UV solar radiation (e.g. Viereck et al., 1999).

Changes in the solar output during the 11-year solar cycle (Fig. 4.34) can potentially affect the chemical production rates in Titan's atmosphere. However, during the Cassini mission, the Sun has presented an extended minimum with the first weak signs of increased output observed towards the end of 2009. The chemical lifetimes in Titan's stratosphere (at 200 km) range between ~1 year for C_2H_4 and C_3H_4, up to ~20 years for HCN, which are longer than the time-scales of some of the rapid changes observed. Thus, the temporal variability observed is more likely related to changes in the atmospheric circulation patterns due to progression of seasons (Bampasidis et al., 2012a).

4.8 Water vapor in CIRS spectra

The first detection of water vapor in Titan's atmosphere was made in disk-average observations taken with the Short Wavelength Spectrometer of the Infrared Space Observatory (ISO/SWS) yielding a mixing ratio of $4x10^{-10}$ at about 180 km (Coustenis et al., 1998). Due to their low signal-to-noise ratio, the first CIRS spectra could not provide the detection of water vapor and only an upper limit of $9x10^{-10}$ was inferred (de Kok et al., 2007b). After the end of the Cassini prime mission, more spectra are available and the signatures of the weak molecules can be detected in large spectral averages where the signal-to-noise ratio is high. Figure 4.35 shows the contribution function of water vapor. The contribution functions peak at 0.01 mbar (about 400 km), c.f. Coustenis et al. (1998).

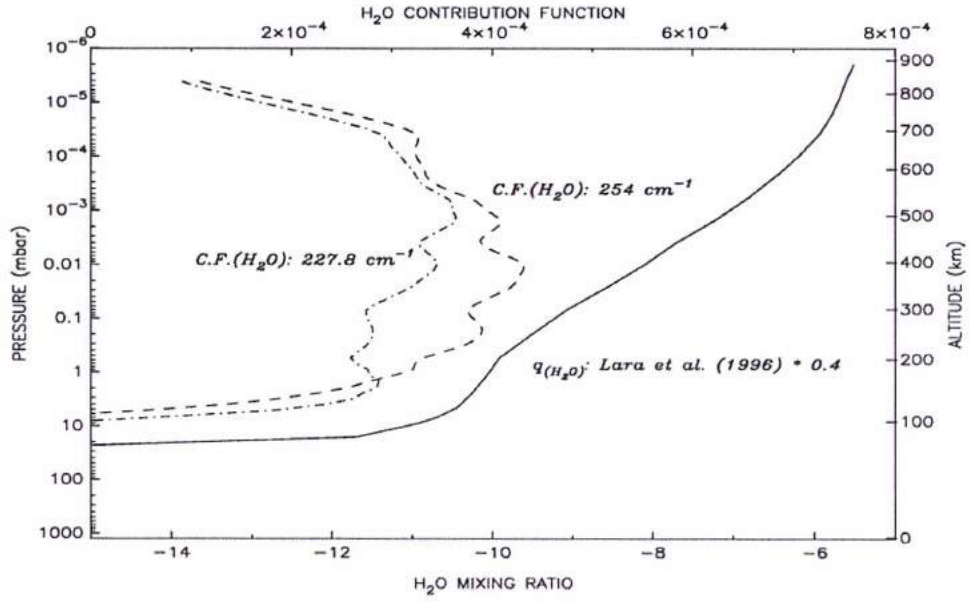

Figure 4. 35 -Contribution functions of water vapor (dashed line) and the vertical profile used for simulating the best-fit (adapted from Coustenis et al. 1998).

In the paper of Cottini et al. (2012a), which I have co-authored, we confirm the detection of stratospheric water vapor on Titan using CIRS spectra. The analysis of these observations was performed by using two independent radiative transfer codes: the NEMESIS code used by the Oxford team and by GSFC colleagues - Non-linear Optimal Estimator for Multivariate Spectral Analysis (Irwin et al., 2008) and our newly updated ARTT - Atmospheric Radiative transfer for Titan (Coustenis et al., 2007; 2010b; Bampasidis et al., 2012a). NEMESIS is a retrieval code that performs a combination of correlated-k forward

model computation (Lacis & Oinas, 1991) and the retrieval scheme based on the method of optimal estimation (Rodgers, 2000). I was asked by Dr. V. Cottini (GSFC/NASA) to work on specific CIRS queries by using ARTT in order to validate the NEMESIS results.

4.8.1 CIRS/FP1 observations in search of water vapor

Water vapor has rotation lines in the FP1 region of CIRS. CIRS/FP1 is a detector with a circular field of view and probes the far infrared region in the range of 10 to 600 cm^{-1}. The stronger water lines are located from 90 to 260 cm^{-1}. The selected datasets were queried from December 2004 up to December 2008. Three selections cover Titan up to 30°N (80°S-45°S, 45°S-10°S, 0°-30°N) in nadir viewing mode (Table 4.13).

With Dr. A. Coustenis, we have gathered large nadir FP1 spectral averages within the SCET[14] limits, as required by V. Cottini and analyzed them following a study already started about 2 years ago aiming to explore the FP1 region, but which was impeached by the difficulty to model the aerosols which are very important in that region. By focusing on the water lines and simulating summarily the continuum level, I have injected the temperature profile retrieved by R. Achterberg from the corresponding FP4 spectrum taken at the same time and at the same latitudes and conditions of geometry in order to fit the FP1 observations. I have simulated the observations and when the best fit was achieved, I have inferred the abundances. Also into account were taken the other molecules present in the region, namely HCN, C_4H_2, C_2N_2 and C_3H_4 and furthermore, we have extended the range of our calculations to the 300 (check) cm^{-1} region, while the Cottini et al. paper is constrained from 150 to 260 cm^{-1}.

[14] SCET: Spacecraft event time

4.8.2 Confirmation of the water vapor detection by ISO with CIRS

Water has emission bands at the FP1 spectral range of CIRS at 150.5, 170.4, 177.56, 202.77, 208.50, 227.8, and 253.93 cm^{-1}. The contribution functions of the water vapor lines are plotted in Figure 4.36 below. All of them peak at about 50 km.

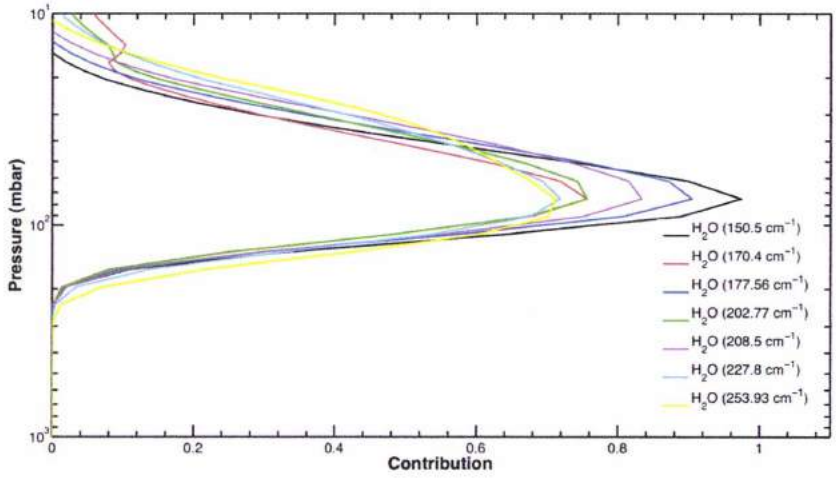

Figure 4. 36 - Contribution functions of water vapor. All the emission bands peak at about 50 km.

We first fit the continuum at the FP1 range thus providing an *ab initio* simulation of the aerosol contribution in there (as indicated and more properly done by de Kok et al. 2007a) which however serves our purpose sufficiently well since we focus on the lines. We then make different tests using various values for the water abundance, starting with of $1x10^{-10}$. By fitting the different lines, with particular accent to the line at 150 cm^{-1} which shows the strongest emission, and then getting weighted averages of the inferred best-fit values, we obtain a final best-estimated water vapor mixing ratio. Figure 4.37 below, shows the best-fits of the selection 0° - 30°N when using a constant-to-height mixing ratio for water vapor at $1x10^{-10}$. The vertical black lines in the upper plot indicate the positions of water lines. The model fits well the water lines. The peak of the data at 220 cm^{-1} is discussed in Section 4.10.

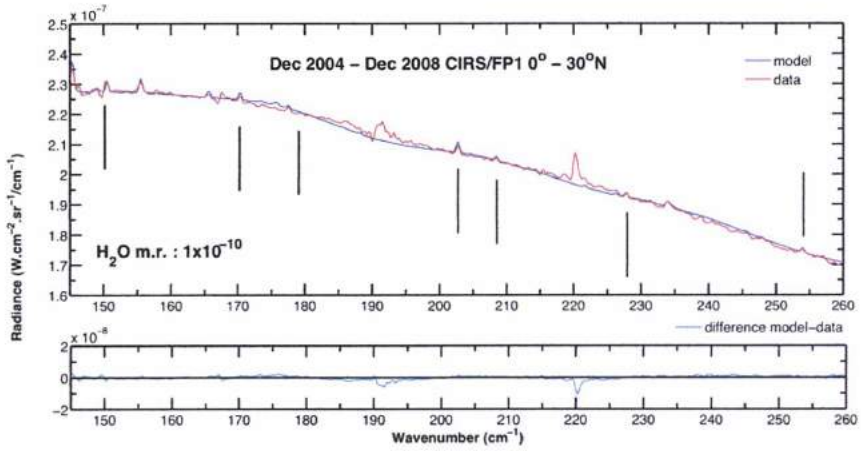

Figure 4. 37 - (Up) Best-fit plot at the 0°-30°N latitudinal bin achieved for water vapor abundance of $1x10^{-10}$. (Down) Plot of the difference between model and observations. The vertical black lines depict the positions of water lines in the spectrum.

The same constant value fits also the water lines for the 45°S-10°S selection (Fig. 4.38), except perhaps the 250 cm^{-1} line.

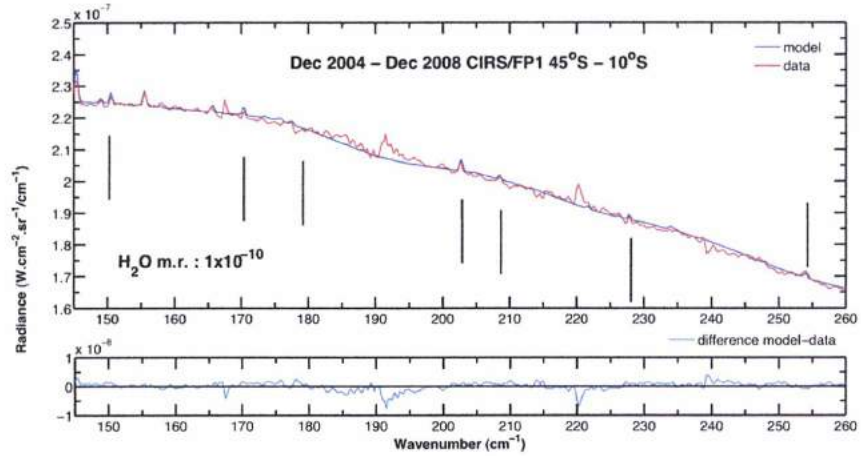

Figure 4. 38 - (Up) Best-fit plot at the 45°S-10°S latitudinal bin achieved for water vapor abundance of $1x10^{-10}$. (Down) Plot of the difference between model and observations. The vertical black lines depict the positions of water lines in the spectrum. Except for 250 cm^{-1}, all the water lines are fitted.

We then use a slightly higher value, at $2x10^{-10}$, and the line at 250 cm^{-1} is fitted but the fit is not well for the other lines (see Fig. 4.39).

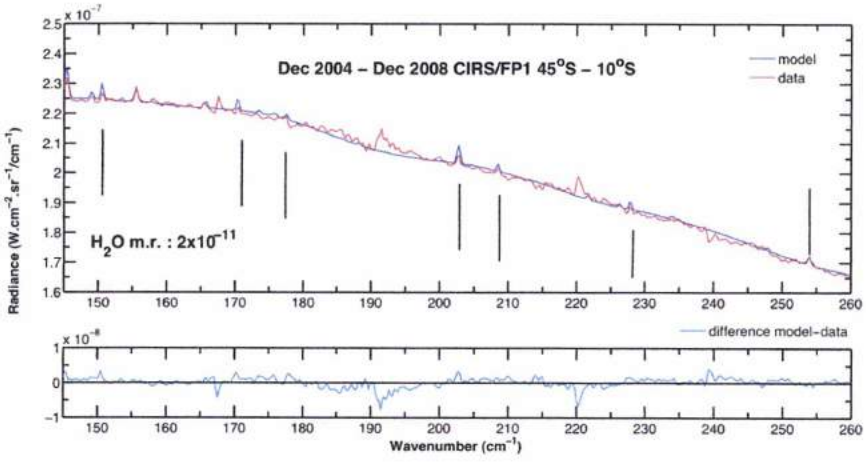

Figure 4. 39 - (Up) Best-fit plot at the 45°S-10°S latitudinal bin achieved for water vapor abundance of $2x10^{-10}$. (lower panel) Plot of the difference between model and observations. The vertical black lines depict the positions of water lines in the spectrum. Only the line at 250 cm^{-1} is well fitted.

For the latitudinal bin of 80°S-45°S, the simulation result is the same. The water vapor constant-with-height abundance of $1x10^{-10}$ fits all the lines except for the one at 250 cm^{-1} (Fig. 4.40), while the value of $2x10^{-10}$, fits better the 250 cm^{-1} line but not the others (Fig. 4.41).

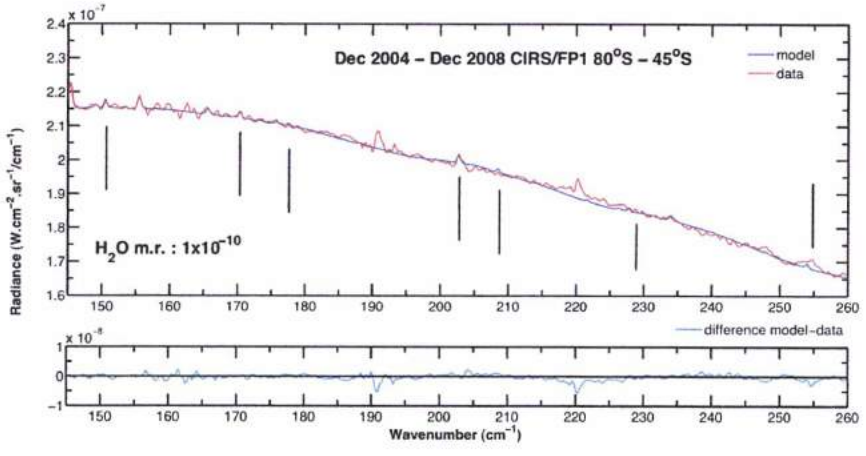

Figure 4. 40 - (Up) Best-fit plot at the 80°S-45°S latitudinal bin achieved for water vapor abundance of $1x10^{-10}$. (Down) Plot of the difference between model and observations. The vertical black lines depict the positions of water lines in the spectrum. Except for 250 cm^{-1}, all the water lines are fitted.

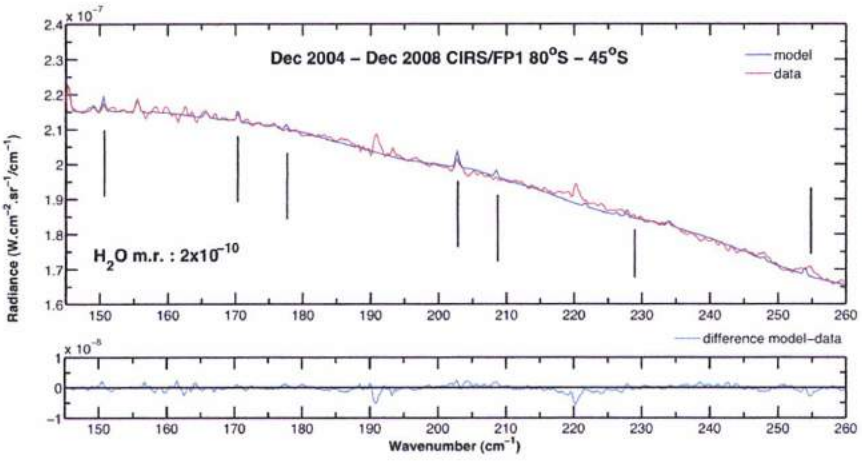

Figure 4. 41 - (Up) Best-fit plot at the 80°S-45°S latitudinal bin achieved for water vapor abundance of $2x10^{-10}$. (Down) Plot of the difference between model and observations. The vertical black lines depict the positions of water lines in the spectrum. Only the line at 250 cm^{-1} is well fitted.

We find that the 254 cm^{-1} water line is best fitted with $2\pm0.8x10^{-10}$. For the other lines the H_2O abundance is rather $1\pm0.4x10^{-10}$. The Full Width at Half Maximum (FWHM) of the contribution function for 254 cm^{-1} water line is slightly higher than for the others, so that seems to then bring us into compatibility with ISO, where a higher value is observed at higher altitudes for the 228 and 254 cm^{-1} lines $(4\pm2)x10^{-10}$. The ISO $4.0x10^{-10}$ constant value profile had a contribution function peaking at 180 km and not near 100 km (Coustenis et al., 1998). The error bar we find is $\pm2x10^{-10}$, and this includes all the uncertainties due to calibration, methane mixing ratio, Saturn background, etc. The water vapor value retrieved from Herschel Space Observatory data is in good agreement with the ISO results (Moreno et al., 2012, in press).

From the analysis of nadir spectra with the NEMESIS radiative transfer code, we have derived a mixing ratio of $(1.4\pm0.5)x10^{-10}$ at 93^{+37}_{-10} km (Table 1 of Cottini et al., 2012). In the same paper, using limb observations, we obtained mixing ratios of $(1.3\pm0.4)x10^{-10}$ at 115^{+47}_{-22} km and $(4.5 \pm 1.5)x10^{-10}$ at 230^{+45}_{-40} km of altitude, confirming that the water abundance has a positive vertical gradient as predicted by photochemical models (Cottini et al. 2012).

The important result from these simulations I have performed on the CIRS available FP1 water lines is that the CIRS result is compatible with the value found by ISO and that the photochemical models for water vapor should be revised. The ratio of CO_2/H_2O on both Saturn and Titan is unexpectedly large and Enceladus variable activity has been suggested to be its source (Moreno et al., 2012, in press).

4.9 Benzene vertical distribution profiles

In this section, I present the results of analysis of the averaged Cassini/CIRS (Composite Infrared Spectrometer) spectra at both medium (2.5 cm^{-1}) and high (0.5 cm^{-1}) resolutions during the first six-and-a-half years of the mission focused on the benzene mixing ratio.

4.9.1 Benzene in Titan's environment

The presence of benzene (C_6H_6) in Titan's atmosphere is extremely interesting, as it is the first and the simplest polycyclic aromatic hydrocarbon (PAH) detected. In particular, following its first detection at 674 cm^{-1} based on ISO/SWS data (Coustenis et al., 2003), benzene was also detected in the thermosphere (950-1150 km) by modeling Cassini/INMS data (Waite et al., 2007) and firmly in the stratosphere (100-200 km) in all latitudes (Flasar et al., 2005; Coustenis et al., 2007; 2010b). Moreover, benzene has been tentatively identified on Titan's surface by Huygens/ CGMS measurements (Niemann et al., 2005).

The unsaturated molecule of benzene has a six-carbon ring with three double bonds alternating with single ones. The length of its bonds are equal in all carbon pairs with a value of 139 pm, while the electron density in the regular hexagon of benzene is identical. It is well represented as a resonance hybrid of two equivalent forms with six pi electrons, and thus its conjugated molecule is more stable than typical alkenes. Comparing to the whole organic inventory, aromatic substances perform different chemical behavior (McMurry, 2008). Benzene is a key compound for the synthesis of polycyclic aromatic hydrocarbons (PAHs) and may play an important role in the formation of the hydrocarbon haze of Titan. The planar molecule of benzene could help in understanding of the photochemical mechanisms occurred in Titan. When two benzene rings fuse together the molecule of naphthalene is created. Naphthalene has not yet been identified in Titan.

The presence of the cyclic conjugated molecule of benzene in Titan's atmosphere demonstrates multiple pathways to the possible synthesis of biological building blocks. Additionally, the existence of the liquids on the surface of the satellite (Stofan et al., 2007) in combination with the low temperature of 93 K (Fulchignoni et al., 2005) could host the proper environment for this biosynthesis. Recent laboratory experiments have showed that aromatic compounds could plausibly be produced on icy surfaces (Menor-Salván et al., 2008).

Considering all the above described characteristics, the prebiotic potential of Titan is significant and a large effort in astrobiological research has recently been focusing on Titan's environment (Raulin et al., 2008). The firm detection of hydrocarbons and especially acetylene and benzene has really enhanced the inventory of photochemical organic products. Moreover, the abundance of benzene in the thermosphere shows a value four times higher than in the stratosphere, as it discover by the Cassini/INMS (Waite et al., 2007).

Combined with acetylene, benzene could produce polycyclic aromatic hydrocarbons (PAHs) or/and simpler compounds, the polyphenyls. The polycyclic aromatic hydrocarbons (PAHs) seem to be the most interesting product of the photochemical chain. However, since Titan lacks oxygen and sufficient temperature as Early Earth had, probably different pathways from Earth's have been followed and polyphenyls may possibly be created (Delitsky & McKay, 2010).

4.9.2 Modeling benzene's vertical distribution

In collaboration with Dr. P. Lavvas, I have modeled the vertical distribution of C_6H_6 in the atmosphere of Titan, expending the work presented in Coustenis et al. (2010b) from a latitudinal point of view.

The signature of benzene (C_6H_6) at 674 cm^{-1} is very weak in the CIRS spectra and only by large averages and/or at medium resolution reliable abundances can be retrieved. For this reason, I have gathered the same Cassini/CIRS averaged spectra from Tb to T44 flybys as presented in (Coustenis et al., 2010b - Table 1). The new selections have been improved by the fact that new calibration inferences were incorporated in the CIRS database. These data cover the beginning of the mission on July 2004, until the T44 flyby in late May 2008. In this work, as no longitude variation has been observed in Titan's atmosphere, we have scanned the globe in latitude bins of about 10°, starting from the equator and ending at the poles. We have analyzed data of both medium and high spectral resolution (2.5 cm^{-1} and 0.5 cm^{-1} respectively).

We refer here only to nadir observations with emission angles restricted to less than 60°. The corresponding temperature profiles are retrieved by R. Achterberg following the method described in Achterberg et al (2008; 2011). The results of this research were presented at the Faraday Discussions 147: Chemistry of the Planets, which was held in Saint Jacut de la Mer (France) from 14 to 16 June 2010.

CIRS detected benzene above 40°S and its profile is significantly affected by the downwelling part of the circulation at this region. Benzene has been detected in a large abundance in Titan's upper atmosphere (Waite et al., 2005) and its formation has been correlated with ion-neutral chemical reactions taking place in the thermosphere (Vuitton et al., 2008). The contribution of neutral chemistry in C_6H_6 production is small and focused in the stratosphere. Thus, both production mechanisms, ion and neutral, must be included in the photochemical calculations. P. Lavvas has updated the photochemical model with the necessary ion reaction based on Vuitton et al. (2008) (see Figure 4.42).

Following our recent work in Coustenis et al. (2010b) on CIRS data analysis and photochemical modeling, we have thus applied this advanced version of Lavvas et al. (2008a;b) 1-D model, which is described in section 4.3.2. This advanced model then includes ion-chemistry at different latitudes of Titan's globe.

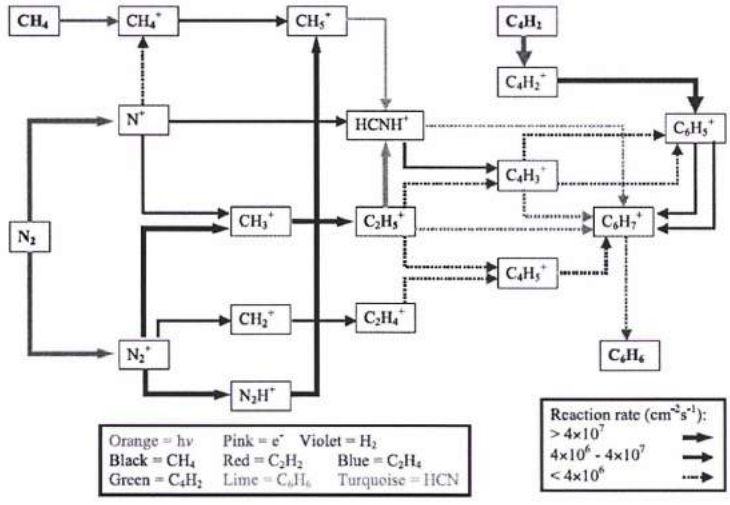

Figure 4. 42 - Principal chemistry reaction sequence for benzene (adapted from Vuitton et al. 2008).

I have compared the model results provided by P. Lavvas, with the abundances of benzene I retrieved from both Cassini/CIRS and the ones found from Cassini/INMS data for the stratosphere and thermosphere respectively. ***We have thus compared the benzene's vertical distributions at different latitudes towards the end of the nominal Cassini mission with the data and hence brought constraints to the photochemical model.***

The stratospheric C_6H_6 mixing ratios from the CIRS data show a significant increase towards Northern latitudes (c.f. Table 2 in Coustenis et al. 2010b) and here I present its

vertical profiles based on this photochemical model and focusing on these latitudes. (Fig. 4.43 a-j).

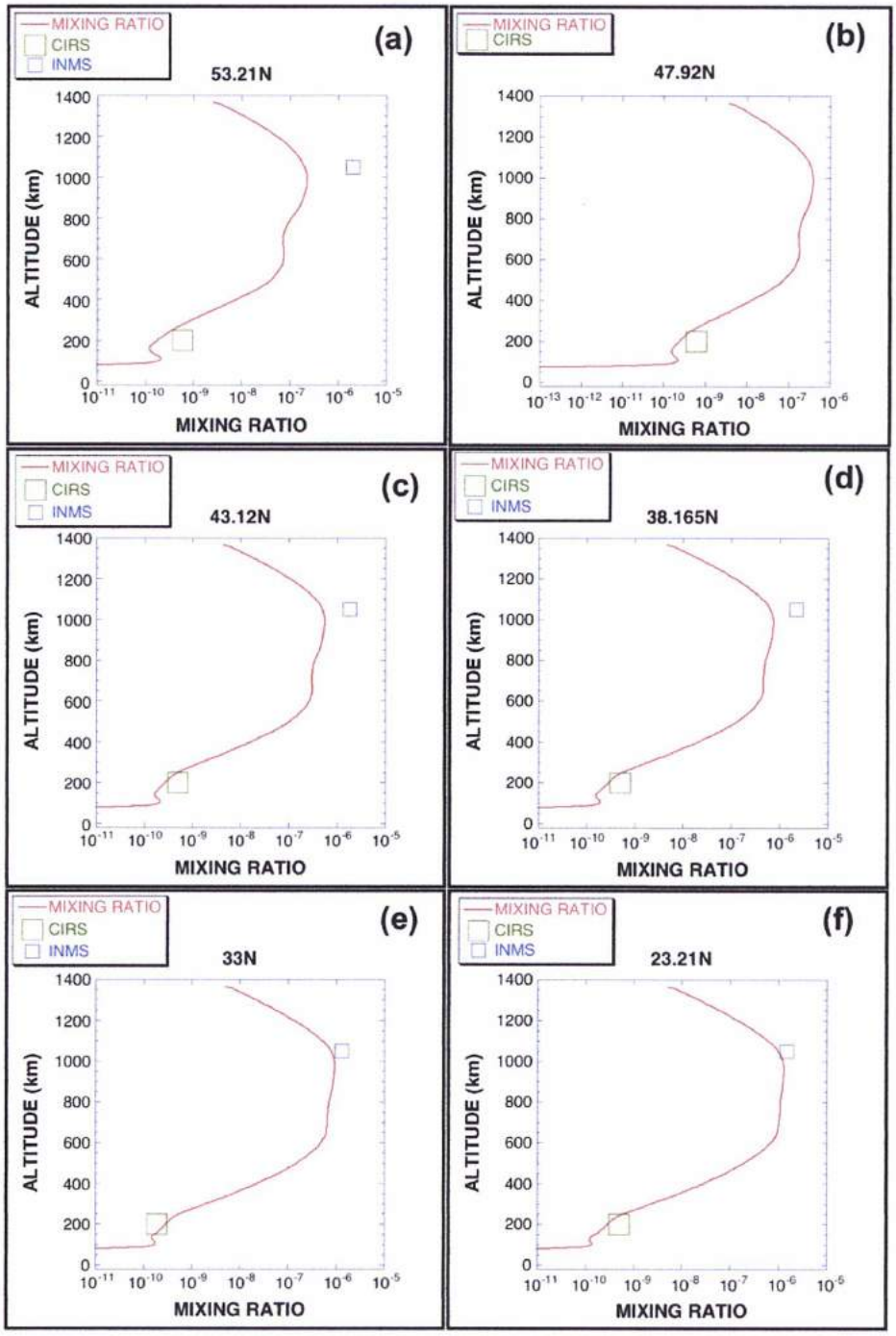

Figure 4. 43 - (a-f) Vertical distribution of benzene's abundances retrieved by the advanced 1-D photochemical model by Lavvas et al. (2008a;b) at the northern Titan's hemisphere. CIRS results are plotted with green boxes, while INMS with blue ones (Bampasidis et al., 2010).

From the model calculations, the benzene mole mixing ratio profiles exhibit an almost constant-with-height value from 600 km up to 1000 km in the upper atmosphere. In the stratosphere, CIRS measurements (green boxes) are well satisfied by the model except in the higher Northern latitudes. However, the model overestimates the benzene abundance for latitudes greater than 40° (Fig. 4.43a-f).

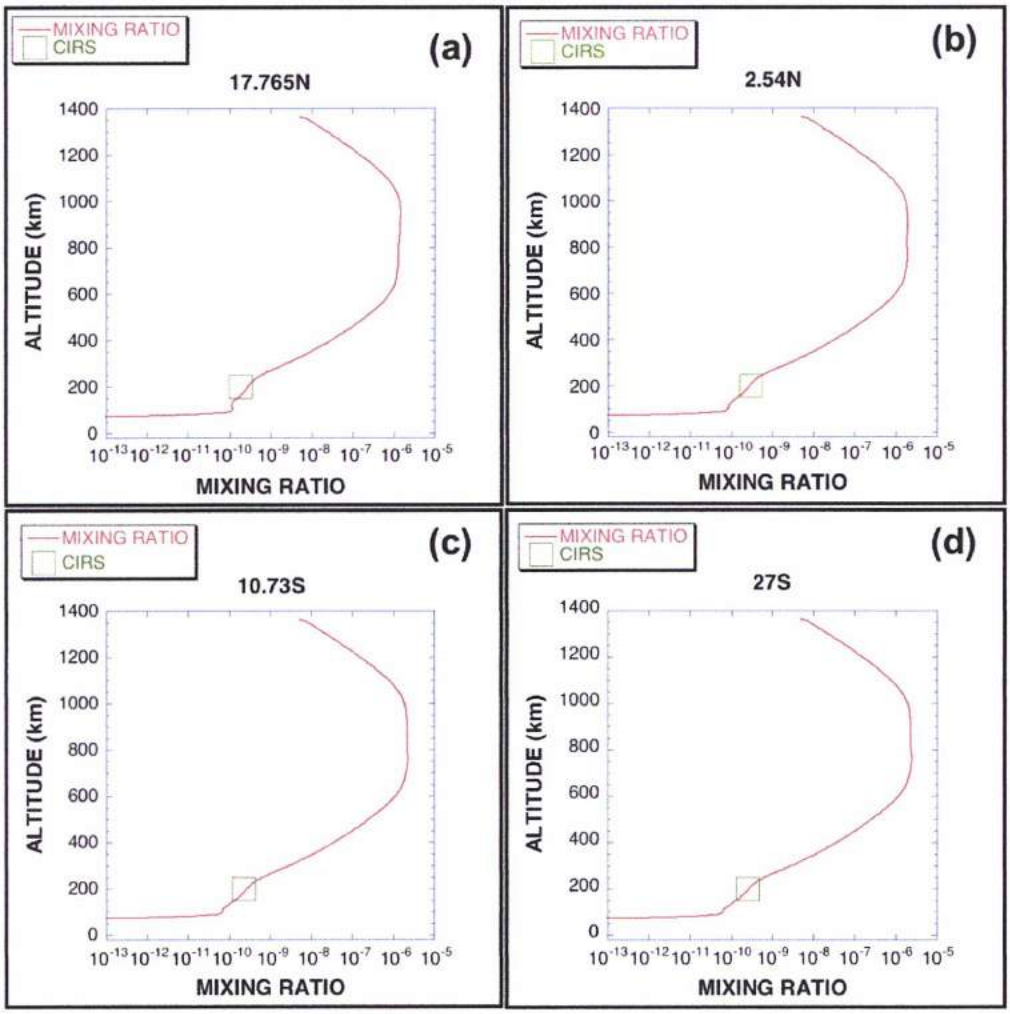

Figure 4. 44 - (a-d) Vertical distribution of benzene's abundances retrieved by the advanced 1-D photochemical model by Lavvas et al. (2008a;b) at the equatorial and sourthern Titan's hemisphere. CIRS results are plotted with green boxes (Bampasidis et al., 2010).

From the equatorial latitudes to the South pole, the model of C_6H_6 mixing ratio reproduces very well the CIRS inferences (Fig. 4.44 a-d). Furthermore, in Figs. 4.43a,c,d,e,f, the INMS results for the benzene retrieved abundance at 1100 km (Waite et al., 2007; Vuitton

et al., 2008; Cui et al., 2009) - in blue boxes - are also presented. The simulation also satisfies the INMS value for the latitudes of 23°N and 33°N (Figs. 4.43e,f). For higher latitudes from 38°N to 53°N (Figs. 4.43a,c,d) the model underestimates the INMS value which is suggestive of the contribution of dynamical effects that are not taken into account in the 1-D model. Overall, the model is quite consistent with the INMS data, although it presents a small underestimation of the C_6H_6 INMS abundance at some northern latitudes. The next step is to include in our analysis the INMS measurements for the whole latitude range, and we have been in discussions over this with Prof. H. Waite, PI of INMS.

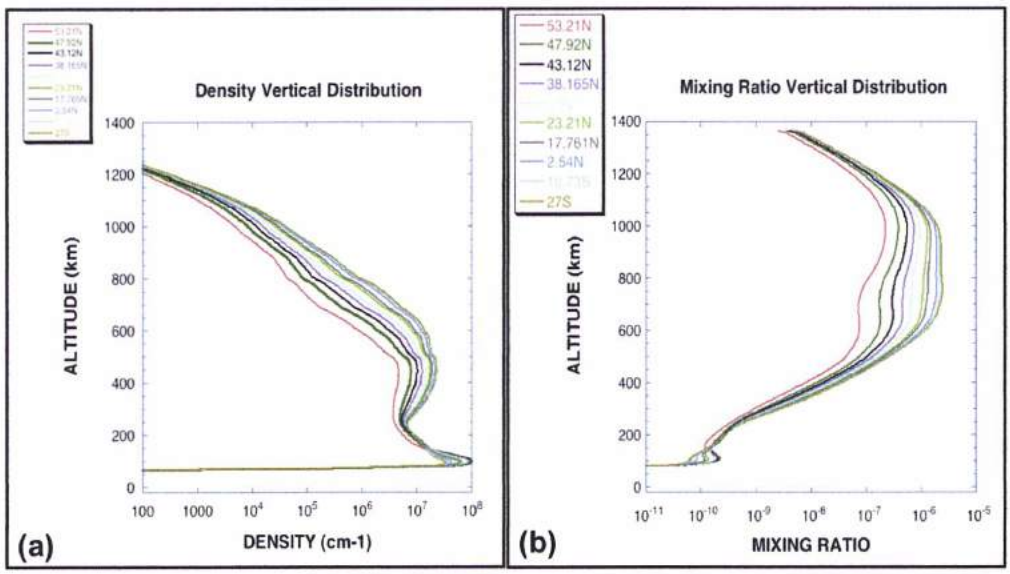

Figure 4. 45 - (a) Vertical distribution of benzene's density for latitudes. (b) Vertical distribution of benzene's abundance for latitudes (Bampasidis et al., 2010).

Finally, Figures 4.45a,b show the latitudinal variations of the mixing ratios and the density of benzene respectively.

Both the mixing ratio and the density profiles show a significant enhancement from northern latitudes to southern ones. Since the production of benzene is dependent on the number of the photons, this latitudinal change of vertical distribution can be easily explained if we take into consideration the fact that the photon flux is also enhanced southwards of the latitudes as shown in Figs. 4.45a,b (Bampasidis et al., 2010).

4.10 Winter condensates evolution between the North and South pole on Titan

By comparing large yearly averages of CIRS/FP3 at different time periods, I have discovered a dramatic depletion in the abundance of HC_3N at 50°N in 2010 of more than 50% (see Fig. 4.46) compared to 2006-2009 values. This was indicative of changes in the North pole concentrations at recent times.

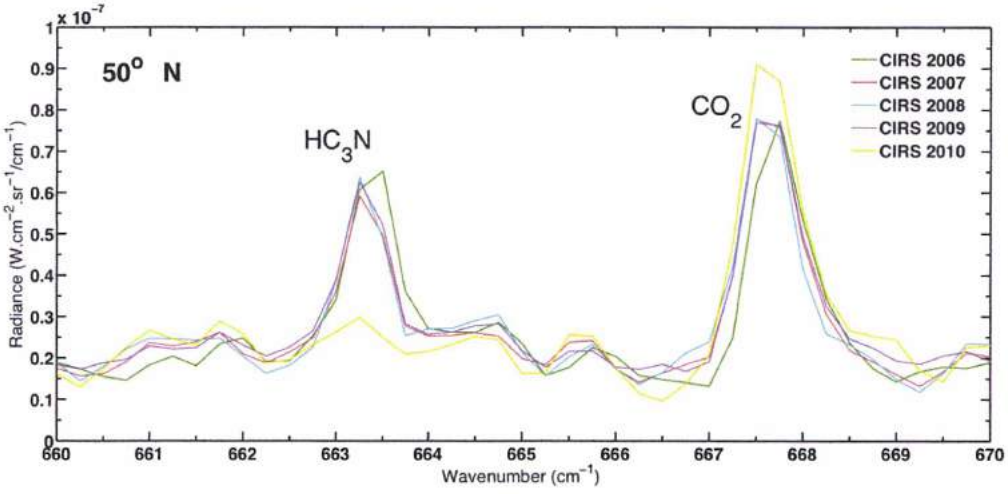

Figure 4. 46 - CIRS/FP3 annual data at 50°N. The depletion of HC_3N abundance is obvious in 2010 spectra.

In the paper of Jennings et al. (2012, *in press*), in which I participate, we associate the emission at 220 cm^{-1} seen for the first time to appear in southern CIRS/FP1 spectra, with stratospheric condensates enhancement rising in the south. Since the South pole of Titan moves deep into the winter season, the lack of solar EUV and UV provide downwelling accumulation of nitriles in the stratosphere and form condensates. However, the increase of the 220 cm^{-1} emission was much faster compared to the decrease in the north. Additionally, in the north, HC_3N is present in CIRS September 2011 spectra but not in June 2011 ones, suggesting that the mixing ratio of the molecule initiated its enhancement a year before the emission at 200 cm^{-1}.

The decrease of cyanoacetylene in the northern spectra indicated that changes in the condensates and gases are observed indicative of seasonal changes (Vinatier et al., 2012a; 2010b; Jennings et al., 2012, in press). The change in season is also evidenced in

the south by the appearance of the 200 cm^{-1} emission band (Fig. 4.47) described by an exponential law within a lifetime of 4.4 years (Jennings et al., 2012, in press).

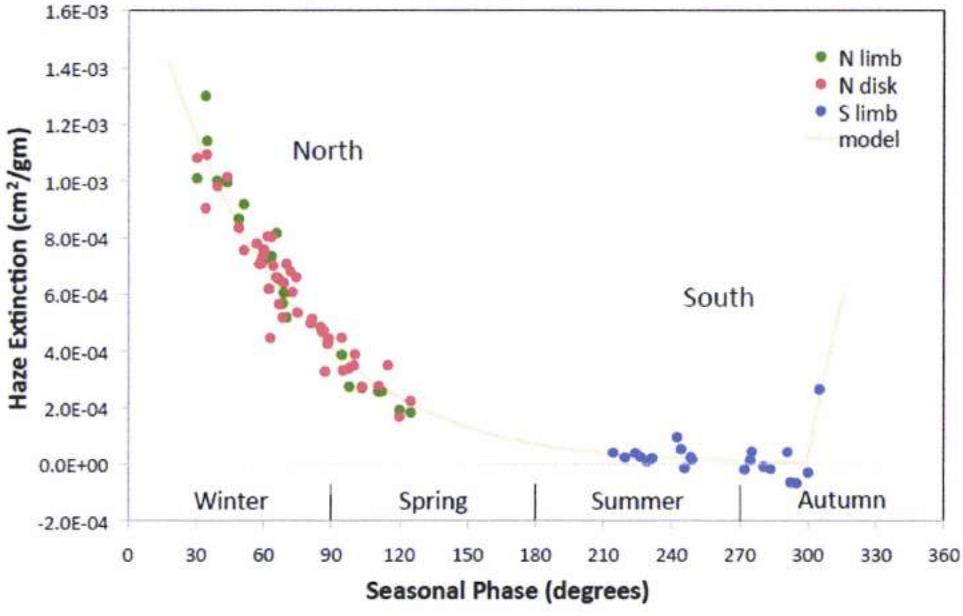

Figure 4. 47 - Haze observations in seasonal scale (adapted from Jennings et al. 2012, *in press*.).

The explanation is that during the southern summer, the sunlight influences significantly the trace gaseous composition in the stratosphere. Due to the low supply rate from the upper atmospheric layers, the condensates precipitate on the surface. However, as Titan's southern hemisphere moves into the winter, haze particles start to form and therefore the relative emission increases in the spectra.

4.11 Search for weaker molecules in CIRS spectra

Large CIRS nadir FP3 averages are necessitate to observing the signature of the weak trace gases and the isotopologues in Titan's atmosphere, since the use of such averages reduces the signal-to-noise ratio. Fortunately, CIRS has provided a huge number of datasets, which can be averaged in order to retrieve large averaged spectra. This work was presented at the EGU General Assembly 2012 in Vienna (Bampasidis et al., 2012b).

I have queried the 2009 CIRS annual FP3 spectra and assembled them in an average (Titan flybys T50 to T65) at 50°N, consisting of 1306 spectra at high resolution. Large averages for searching for weaker molecules are summarized in Table 4.16 below.

Table 4. 16 - Large FP3 and FP4 averages over 2009 at high resolution at 50°N.

Focal Plane	Total number of spectra	Airmass	Cassini Flyby
FP3	1306	1.31	T50-T65
FP4	2499	1.08	T50-T65

I have applied the relative temperature profile derived from the FP4 spectral selection in the FP3 and then fitted the major molecules during a best-fit iterative process. The results of the radiative transfer calculations are plotted in Figs. 4.48 and 4.49.

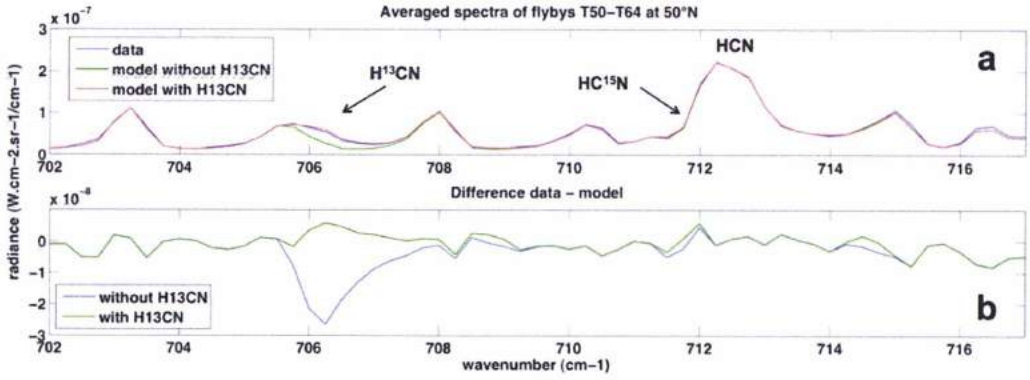

Figure 4. 48 - Comparison between CIRS nadir spectra and radiative transfer models. Hydrogen cyanide and the signature of its isotopologues are also shown. For $H^{13}CN$, only a 3-σ upper limit of $1.7x10^{-8}$ was derived. Top (a): Averaged spectra of T50 to T64 flybys at high resolution (0.5 cm^{-1}) (in blue) at 50°N, best-fit model with main gases and isotopologues (in red) and best-fit model without $H^{13}CN$ isotopologue at 706 cm^{-1} (in green). Bottom (b): Difference between model and data for both cases: with all gases and isotopologues (in green) and without $H^{13}CN$ 706 cm^{-1} (in blue).

In Figure 4.48-a, I have plotted the model atmosphere with and without the $H^{13}CN$ contribution. The residual between data and model in each fit is also depicted in Figure 4.48-b. For $H^{13}CN$ at 706.2 cm^{-1}, only a 3-σ upper limit of $1.7x10^{-8}$ has been derived, which is comparable with previous results in CIRS limb data (Vinatier et al., 2007b). I have also derived the $^{12}C/^{13}C$ ratio of this average at 64.7±14 which is consistent with the relative ratio of 68^{+16}_{-12} calculated in limb spectra at 83°N (Vinatier et al., 2007b), the estimation of 80.2±2 (Nixon et al., 2008b) and the Huygens GCMS *in situ* measurements (82.3±1) (Niemann et al., 2005). This ratio is similar to the terrestrial one (at 89).

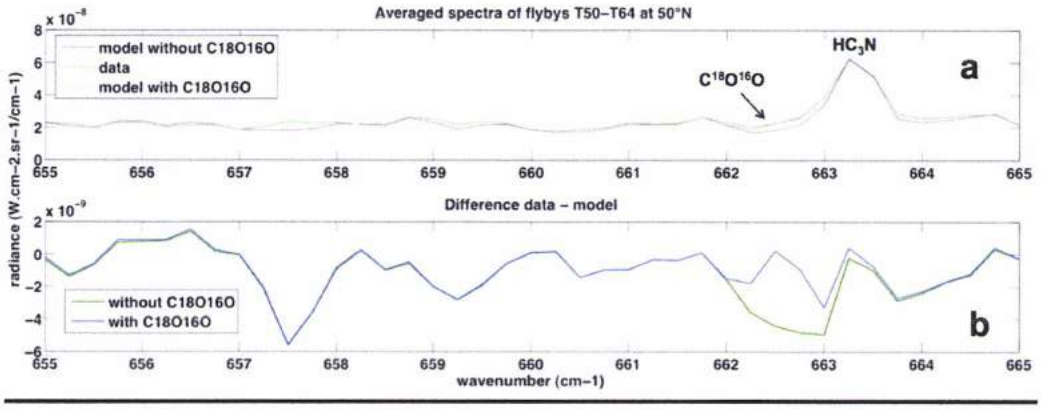

Figure 4. 49 - Comparison between CIRS nadir spectra and radiative transfer models. We have derived only a 3-σ upper limit of $8x10^{-10}$ for the isotopologue $^{13}C^{18}O^{16}O$ of carbon dioxide. Top (a): Averaged spectra of T50 to T64 flybys at high resolution (0.5 cm^{-1}) (in blue) at 50°N, best-fit model with main gases and isotopologues (in red) and best-fit model without $^{13}C^{18}O^{16}O$ isotopologue at 662.5 cm^{-1} (in green). Bottom (b): Difference between model and data for both cases: with all gases and isotopologues (in green) and without $^{13}C^{18}O^{16}O$ at 662.5 cm^{-1} (in blue).

The same procedure has been conducted for $^{13}C^{18}O^{16}O$ at 662.5 cm^{-1} (Fig. 4.49). We have derived only a 3-σ upper limit of $8x10^{-10}$ and the $^{16}O/^{18}O$ ratio at 386±130 which is comparable with previous estimations (Nixon et al., 2008b). However, this result is significantly lower than the terrestrial ratio (circa 500) (Bampasidis et al., 2012b).

This test shows that our upgraded radiative code with the new molecules incorporated can help detect the signatures of new isotopologues or even entirely new species by fitting better the data where already identified molecules appear. We aim to apply this search for new molecules in the future with large averages seeking to identify C_2H_5 or other such predicted molecules, see Table 4.15.

4.12 Future perspectives

Cassini will continue orbiting Saturn up to the next summer solstice in 2017. Thus, a considerable amount of CIRS spectra will be available for studying Titan's stratosphere. The follow-up of this study is to investigate temporal variations on Titan due to seasonal and dynamical effects. The reported peak and sharp decrease in the abundances at the northern spring equinox at 50°N needs confirmation from northern CIRS spectra when are available. Moreover, it will be very interesting to include in our photochemical analysis of benzene vertical distribution Cassini/INMS measurements in a global sense.

Seven years after Cassini's arrival to the Saturnian system, the combination of Voyager 1 Infrared Radiometer Spectrometer (IRIS) measurements from 1980, Cassini Composite Infrared Spectrometer (CIRS) continuous recordings from 2004 to 2010 and the intervening ground-based and space-borne observations with ISO provide almost a complete picture of the stratospheric evolution within a Titanian year.

The V1 measurements were taken at the same season compared to the one of Cassini/CIRS in mid-2009. The next step is to compare the previous results in temperature and composition variations from Voyager 1/IRIS and ISO with Cassini/CIRS ones. This can be complemented with the ground-based observations I have assembled in Table 4.4. Thus, we can describe the thermal and chemical evolution of Titan's stratosphere within a Titan year (29.5 years) and evaluate General Circulation Models predictions.

The cause of these variations should be also investigated. A further discussion on the influence of the solar cycle on Titan's stratospheric interannual variations in chemistry and temperature should be conducted. In fine, this allows us to set constraints on seasonal, photochemical and general circulation models for Titan and to better describe the physical processes in this complex environment.

Chapter 5

Numerical tools for analyzing the Titan lakes environment

In the previous Chapter, I have studied Titan's atmosphere focusing on the temporal and spatial variations of trace gases as derived from the Cassini Composite Infrared Spectrometer (CIRS) data during the Cassini-Huygens mission, from 2004 up to early 2012. Cassini's remote sensing measurements as well as Huygens' *in situ* observations have also revealed a variety of features on Titan's surface uniquely similar to the terrestrial ones. Comparative Planetology studies can provide essential information about the physical processes that form or formed these surface features.

Although Titan's atmosphere is the basic subject of my research, this active geological environment and the processes that occur or occurred on Titan's surface as well as the exchanges with its atmosphere and interior are also among my scientific interests. This is due to the fact that, besides my Physics background, I also possess a degree in Geology. The subject of my thesis included the study of "Titan's environment" and this of course bears relevance to the interactions between the atmosphere and the surface or even the interior and my contribution in that respect to Titan science is what is described in this chapter. I focused mainly on the manifestations of the methane cycle in its connecting the atmosphere, the surface and the interior.

To that effect, the Cassini/RADAR discovery of numerous liquid organic deposits - lakes - on the surface of Titan bearing witness to the condensation of methane and its products and their deposits on the surface. Without doubt, lakes are the ideal medium for linking the surface processes, the atmosphere and the interior on Titan. By studying the lakes, we can infer valuable information about the complex processes occurring within Titan's environment and understand better the pattern of the methane cycle on a global scale.

My contribution and involvement in the surface studies, which I describe in this Chapter, focus on lakes as a reference point and they concern either the study method tools or the observation data processing. The outcome of these studies provides further understanding

of the liquid extends contribution to the environment, their connection with the atmosphere and their contribution to Titan's methane cycle.

The lakes may also offer the proper habitability conditions for hosting biological building blocks on Titan, a possibility that motivated me to work on Titan's astrobiology, as it is described in Chapter 6. Moreover, these surface studies, mainly performed in collaboration with A. Coustenis, A. Solomonidou, E. Bratsolis and M. Hirtzig (but also with other international colleagues such as Jean-Pierre Lebreton and Hunter Waite), inspired me to propose the MEMS experiment for Titan, which is described in detail in Chapter 7.

Specifically, Titan's geologic environment is defined in Section 5.1 and the exchange processes as well as the relationship between the major geologic forces are described in Sections 5.2 and 5.3 respectively. In the Sections 5.4 and 5.5 that follow, I contribute to the study of the morphotectonic expressions of the Kraken Mare lake surroundings using geomorphologic numerical analysis tools. The Cassini RADAR image processing technique using a probabilistic filtering in which I got involved is discussed in Sections 5.7 and 5.9 respectively.

5.1 Titan's geological environment

Techniques and experiments adapted from Earth Science are also applied to distant rocky planets or satellites and provide essential information about the surface processes in other planetary environments. The Apollo Passive Seismic Experiment (PSE), a network of seismic instruments consisted of four seismometers deployed by the astronauts on the lunar surface between 1969 and 1972 provided the internal structure of the Moon (Dainty et al., 1974; Nakamura et al., 1982; Bulow et al., 2005). The recently selected Discovery mission to Mars, InSight (for Interior exploration using Seismic Investigations, Geodesy and Heat Transport), planned for launch in 2016, will perform geophysical experiments on the Red planet to determine its interior structure and reveal its thermal history.

This also can apply to Titan. After the Voyagers encounters of Titan, the existence a global deep was suggested (Flasar, 1983; Lunine et al., 1983). Both methane and ethane can exist in all three states (vapor, liquid and ice) in Titan's surface temperature and pressure conditions (94 K and 1.5 bar, respectively c.f. Fulchignioni et al., 2005) and they can cause precipitations perhaps responsible for some at least of the surface lakes. But, according to Lorenz (1993), methane drops would evaporate before reaching the surface and the existence

of pure methane surface deposit is then doubtful. According to Flasar (1983), the partial pressure of methane would be lowered in a mixture of methane and its photochemical by-products (ethane, propane). The Lunine et al. (1983) model suggested the presence of ethane surface ocean of 75% ethane, 20% CH_4 and 5% nitrogen about 1 km deep. Stevenson (1992) suggested that the hydrocarbon ocean may be located under the surface of Titan, by assuming a porous enough surface bedrock.

The global ocean hypothesis was rejected by post-Voyager ground-based RADAR echoes, which indicated that the surface of Titan is not homogeneous nor compatible with global liquid coverage. The high reflectivity echoes recorded by Very Large Array (New Mexico) radio-telescope suggested significant surface variability consisting of 'dirty' ice (Muhleman et al., 1990). Steward Observatory and the Multiple Mirror Telescope data also showed a variation in Titan's albedo (Lemmon et al., 1993), while Arecibo echoes in 2001 and 2002 marked areas of specular reflections, similar to small lake-like features (Campbell et al., 2003).

Moreover, Titan's atmosphere is transparent through methane windows in the near infrared (see § 1.1.4) and the Infrared Telescope Facility on Mauna Kea Earth-based observations have confirmed RADAR measurements (e.g. Griffith et al., 1991, Griffith 1993). This data have triggered updates to previous models about the presence of surface liquids and according to Dermott & Sagan (1995), liquid hydrocarbons could be restricted in small surface basins.

5.1.1 Cassini-Huygens surface observations

In January 2005, the Huygens probe performed the only *in situ* measurements to date of Titan's surface during its descent and landing (Lebreton et al., 2005). It observed the atmosphere and the surface during the descent from 170 km downwards with the Descent Imager/Spectral Radiometer (DISR) (Tomasko et al., 2002) and measured its composition above and on the landing site with the Gas Chromatograph and Mass Spectrometer (GC-MS) (Niemann et al., 2002). The Huygens Atmosphere Structure Instrument (HASI) (Fulchignoni et al., 2002) probed the atmospheric properties (T,p and density) during the descent from 1600 km downwards and determined the surface temperature and pressure, while the the Surface Science Package (SSP) (Zarnecki et al., 2002) investigated the local surface material.

Huygens measurements revealed that Titan's surface is mostly dry currently near the equator, but also compatible with the presence of wet ground close underneath the surface as indicated by the increase in methane gas following evaporation from the location where the warm Huygens probe landed. The surface is also suggested to be covered by water and hydrocarbon ice, silicate rocks and organics/tholins frozen material (Tomasko et al., 2005; Zarnecki et al., 2005; Lebreton et al., 2009).DISR images showed a well-developed surface network of channels (Fig. 5.1) close to the probe's landing site (Tomasko et al., 2005). Except for the Huygens observations of river-like features, Cassini/SAR has recorded a variety of fluvial channels networks on Titan's surface (Lorenz et al., 2008a) but with much lower spatial resolution. It has been suggested that the dry channels at the low latitudes are caused by earlier precipitation during a different season (Turtle et al., 2011).

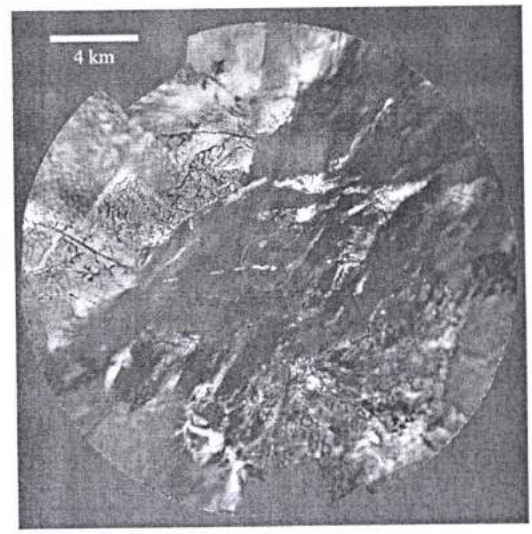

Figure 5. 1 - Titan's surface diversity, recorded from Huygens/DISR (Tomasko et al., 2005). The panoramic view from 8 km shows that the surface is solid and inhomogeneous at the Huygens landing area (the circle in the middle of the image).

Since its first flybys of Titan from 2004, the Cassini orbiter maps remotely Titan with the Imaging Science Subsystem (ISS) (Porco et al., 2004), the RADAR (Elachi et al., 2004) and the Visual and Infrared Mapping Spectrometer (VIMS) (Brown et al., 2004). The Composite Infrared Spectrometer (CIRS) (Flasar et al., 2004) is also used to map the surface temperatures. Figure 5.2 below shows the global map of Titan obtained by the RADAR instrument.

All of these instruments have confirmed the existence of a diverse solid surface with an inhomogeneous and complex topography (Elachi et al., 2005; Porco et al., 2005; Elachi et al., 2006). Titan's topography is relatively low and its lithosphere is too soft and flexible and/or heavily eroded for high mountains to exist (Lorenz et al., 2011), as it was expected (Perron & de Pater, 2004). However, the joint instrumental coverage of Titan's surface delivers a long list of features, which resemble the terrestrial ones in smaller scale height. Titan has mountains (e.g. Radebaugh et al., 2007, Lopes et al., 2010), and chains of mountains known as ridges (e.g. Soderblom et al., 2007, Mitri et al., 2010), faults (e.g. Radebaugh et al., 2011), canyons (Lorenz et al., 2008a), volcanic-like features (Barnes et al., 2006; Elachi et al., 2006; Stofan et al., 2006; Lopes et al., 2007), network river drainages (Tomasko et al., 2005; Elachi et al., 2006; Stofan et al., 2006; Barnes et al., 2007b; Lorenz et al., 2008a), lakes (Mitri et al., 2007; Stofan et al., 2007), impact craters (Wood et al., 2010), numerous longitudinal dunes (Elachi et al., 2006; Lorenz et al., 2006b; Radebaugh et al., 2008) and tropical oases (Griffith et al., 2012).

Cassini/SAR has also made the first detection of large liquid deposits on Titan's surface from data obtained during the Cassini T16 (July 2006) flyby at the northern polar latitudes. The RADAR instrument observed more than 75 topographic depressions which have very low RADAR reflectivity, circular or irregular shapes and filled with low dielectric constant material (Stofan et al., 2007).

Titan has indeed a very complex surface formed by multivariable geological processes. The very small number of impact craters, counted on the surface so far (Wood et al., 2010), indicates that it is an active planetary body where strong exogenic forces occur and contribute to the shape of its landform. The main source of these exogenic forces is Titan's thick nitrogen dominated organic atmosphere, which provides the erosion agents. In the relation between the atmosphere and the surface and how it affects the methane cycle, I essentially focus on the creation, evolution and contributions of the methane lakes and also concern myself with the dunes, sometimes called "sand seas".

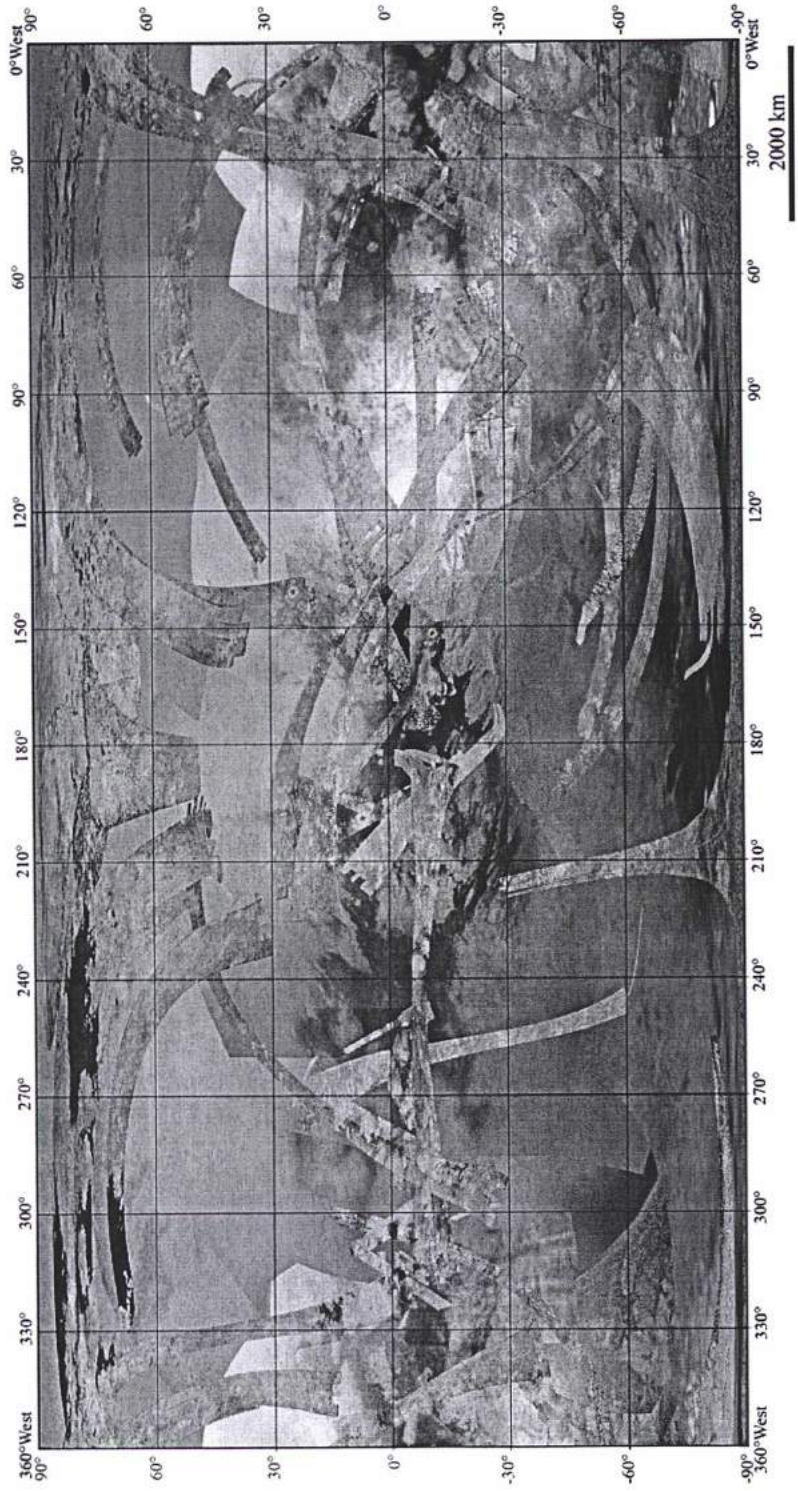

Figure 5. 2 - Global map of Titan's surface obtained from the beginning of the mission up to flyby T50 (February 2009). It shows the coverage derived from RADAR synthetic aperture (SAR) images overlaid onto the ISS map, in a simple cylindrical projection centered at 0°N and 180°W. Full resolution SAR images are shown in gray, lower resolution high altitude SAR (HiSAR) observations in blue, and the ISS base map in brown. Black and dark blue correspond to -20 db, white to 5 db (Stephan et al., 2009).

5.1.2 Surface material properties and Titan's substrate

To study the action of endogenetic and exogenetic forces on Titan's surface, we have to focus on the material of the ground and the substrate. Concerning the latter, a number of questions arise. We would like to find answers about its structure, its composition, whether it is globally the same and if it presents similarities with the terrestrial surface.

The Huygens *in situ* surface measurements were constrained in the region of the landing site (10.3° S, 192.3°W c.f. Lebreton et al., 2005). Huygens/SSP *in situ* data shows a damp porous ground material consisting of loosely packed grains, resembling mud to medium sand or clay consisting of water ice, clathrate and organics (Zarnecki et al., 2005; Lorenz et al., 2006a). The environmental conditions existing on the satellite indicate that Titan's crust mainly consists of mixtures of water ice, organic ices, tholins and nitriles (e.g. Soderblom et al., 2007) in temperature and pressure of about 90-94 K and 1,5 bar respectively (Fulchignoni et al., 2005; Jennings et al., 2009; Cottini et al., 2012b).

The discovery of lakes on Titan's polar regions by both RADAR and ISS provides information about the surface material and the interior and the surface-atmosphere-interior exchange processes. Morphotectonic analyses on Earth have shown a relation between the formation of lakes and the geologic interior forces in several cases. The question is if such a mechanism is responsible for the formation of surface topographic depressions on Titan, where the liquid deposited through the atmosphere is sequestrated creating lakes.

To address this issue, we have to compare the mechanic response of the terrestrial silicate substrate to tectonic stresses with Titan's icy bedrock response. Analogous tectonic behavior provides similar results on the surface. If the two planetary bedrocks are submitted to comparable mechanical processes, similar interpretation techniques can be applied. The study and the correlation of landform, tectonism and erosional processes is in the scientific field of Morphotectonics (e.g. Scheidegger, 2004).

In the paper of Solomonidou et al. (2012), we compare silicate and icy tectonism. According to Collins et al. (2009) the icy crusts of the outer planets moons exhibit similar brittle response to terrestrial silicate crust when stresses are applied. However, while water ice and silicate rocks have similar frictional strength on small planetary bodies with diameter less than 100 km (Beeman et al., 1988), in larger bodies when plastic yielding becomes important, the silicate rock is about 10 times stronger than the ice crust (Melosh & Nimmo, 2011). This

means that silicate rocks can be deformed for a longer period of time and under higher pressure of about one order of magnitude, without reaching the fracture point.

Therefore, we conclude that the tectonic behavior between silicate crust and the planetary ice at 100 K is comparable. This fact encouraged me to help adapt tools from the terrestrial geomorphology for studying Titan's surface, an effort that I describe in the next section.

5.2 Exchanges between atmosphere and surface in Titan's environment

The environmental exchanges between the atmosphere and the surface form specific types of surface features, which are either lakes (or seas, or rivers, or oases) that are mainly located at the polar regions in the current season, or dunes, which are distributed at the equatorial latitudes. As we have discussed in the previous Chapter, (Fig. 4.1) methane possesses a key role by driving an active hydrologic cycle (Atreya et al., 2006). Thus, the link between the atmosphere and the surface is the existence of lakes and dunes in addition to the erosional processes that reshape the already existed structures and resurface the entire terrain.

Lakes are mainly located in the polar regions of the moon, where the environmental conditions maintain the liquid state. On the contrary, the equator is dry enough to support the dune fields. However, recent radiative transfer analyses of VIMS data by Griffith et al. (2012) reported the existence of methane tropical liquids with a depth of 1 m within the latitudes from 20°N to 20°S. They suggested that these deposits are supplied by subsurface sources such as subterranean rivers. Therefore, the study of the surface liquids provides insights on the methane cycle.

5.2.1 Vast dune fields on Titan's surface

Cassini/RADAR images have shown many dune formations at equatorial latitudes mainly from 0°N to 30°N and in some isolated regions up to 55°N (Radebaugh et al., 2008). Due to their extent the equatorial dunes have been interpreted as sand seas (Lorenz et al., 2006b) and they are mainly concentrated in zonal east-west direction. The presence of these vast dune fields indicates the wind blow direction which is towards east, but they wrap around the topographically high features they meet like mountains and craters (Radebaugh et al., 2008).

Dunes are 1-2 km wide and 1-4 km apart, having up to 150 km height and more than 100 km in length (Elachi et al., 2006). Except from the RADAR swaths, the presence of the dunes has been confirmed by Cassini/ISS images (Porco et al., 2005) and the Cassini/VIMS spectra (Soderblom et al., 2007b; Barnes et al., 2008). These linear dunes differ in composition from their surrounding material (Radebaugh et al., 2008) and are clearly the result of the action of aeolian exogenic forces.

5.2.2 Liquid sequestration

The diversity of Titan's surface does not exclude the existence of surface liquid hydrocarbons. Theoretical studies and observations indicate that the presence of stable liquid phase on Titan's surface is plausible. The surface temperature ranges at about 90-94 K while the pressure at about 1,5 bar (Fulchignoni et al., 2005; Jennings et al., 2009; Cottini et al., 2012b) and compared to the triple points of main atmospheric constituents organic liquids can exist on the surface. Indeed, the triple points of nitrogen, methane, ethane and propane are 63.148, 90.68, 90.348 and 85.47 respectively (Jacobsen et al., 1986; Younglove & Ely, 1987).

The channel networks at the equatorial latitudes that Huygens/DISR observed resemble the common pattern of terrestrial river channels. Their presence indicates that liquid provided by heavy precipitation can flow on Titan's surface although, no rain was observed during the descent of Huygens (Tomasko et al., 2005).

Several channel networks deposit in large lakes. Hence, the channel liquid and the lake liquid should have many similarities. The chemical composition of Titan's lakes is considered to be a mixture of ethane, methane, propane, higher order hydrocarbons and nitriles (Cordier et al., 2009; 2012). Cassini/VIMS measurements of the Ontario Lacus during the December 2007 T38 flyby indicate that it is mainly consisted of liquid ethane (Brown et al., 2008), but

without giving a mixing ratio. According to Hayes et al. (2008) the imaginary dielectric properties of the liquid hydrocarbons of Ontario Lacus observed by Cassini are consistent with the experimental values of liquid natural gas, but not similar to the tholin ones. By analyzing the same VIMS spectra Moriconi et al. (2010) suggest that the region that surrounds the lake feature is dominated by propane, butane and acetylene. The existence of propane consistent with Cordier et al. (2009; 2012) model, while butane and acetylene can be exposed as sediments. It should be noted however, that Cordier et al. model does not take into account the temporal variation of lakes' chemical composition.

The study of Titan's liquids, as well as their relation to their environment, provides evidence about their formation, their evolution and their influence to the local area. However, Titan's exogenic and endogenic forces act upon the liquid deposits and shape their morphometry. By understanding the impact of Titan's geologic forces in the liquids of Titan, we will be able to determine links between these forces and the methane cycle. In the following sections, I will describe the techniques adapted from terrestrial Geomorphology and image processing that we have applied to Cassini data towards this direction.

5.3 Lakes on Titan

Titan's lakes with a mean diameter greater than 200 km are listed in the Table 5.1 below. Most of the other lakes are quite smaller with diameters less than 100 km. The northern great lakes of Titan, Kraken Mare, Ligeia Mare (the main target of the discovery candidate TiME mission) and Punga Mare, are large enough to be characterized as seas (according the IAU Committee on Planetary Nomenclature) and are illustrated in the Figure 5.3. Ontario Lacus is the largest lake located at the southern hemisphere.

Titan's lakes have been divided into three classes according their RADAR returns: (a) the dark – liquid filled lakes, (b) the granular - partially filled lakes and (c) the bright - empty lakes (Stofan et al., 2007). The dark lakes completely absorb the incident RADAR beam. SAR microwave radiation penetrates the liquid layer and interacts with the lakebed in the partially filled lakes. The granular lakes can be considered as the transition feature between dark lakes and empty basins. Empty lakes look brighter in SAR images compared to their exteriors and have a depth of 200-300 m (Hayes et al., 2008).

The area I have selected to study is the northern shoreline of Kraken Mare, where the island Mayda Insula is located. I have decided to work on this image because of the presence of this island. It presents an interesting landform inside the lake to study any morphometric correlations with the topography of the nearby shorelines.

Kraken Mare is the largest liquid surface basin of Titan. It covers an area of about 400,000 km^2 (Turtle et al., 2009), bigger than the Caspian Sea on Earth. Kraken Mare has been selected as a target of a future lake lander from the Titan-Saturn System Mission (TSSM) c.f. TSSM Final Report JPL D-48148 NASA Task Order NMO710851.

Table 5. 1 -Lakes[15] on Titan's surface with mean diameter greater than 200 km.

Name	Location	Diameter (km)
Kraken Mare	68°N, 310°W	1,170
Ligeia Mare	79°N, 248°W	500
Punga Mare	85.1°, 339.7° W	380
Jingpo Lacus	73°N, 336°W	240
Ontario Lacus	72°S, 175°W	235

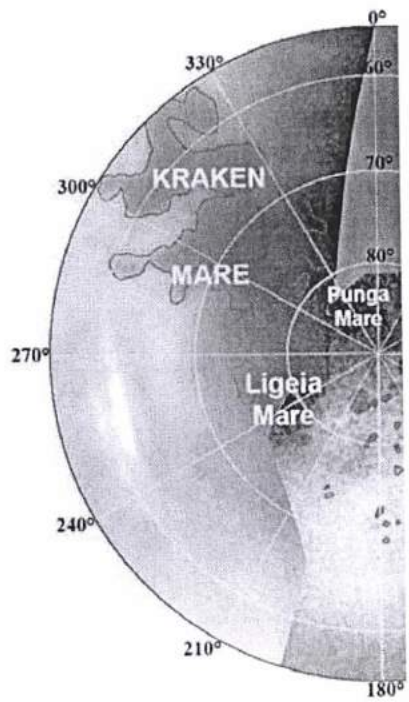

Figure 5. 3 - Titan's North Pole projection from Cassini/SAR, showing the extent of Titan's large north polar lakes. Jingpo Mare is the large unlabeled long narrow feature eastwards of Kraken Mare (credit: Turtle et al., 2009).

[15] http://planetarynames.wr.usgs.gov/

5.4 Numerical analysis in Cassini/SAR images

5.4.1 The context

Due to gravity and morphology, the surface liquid moves downwards to lower places, forming streams or rivers. On its way, the stream collects more liquid from the atmospheric deposit (rain, condensation, etc) and from other streams joining in. Usually, the river discharges its load into basins, which are lakes or seas. The main attribute of this work is to quantify the hierarchy of stream segments in the observed drainage network according to the ordering classification system proposed by Horton & Strahler (Horton, 1945; Strahler, 1952). This classification provides information about the degree of the evolution of the drainage network, describes the geologic history of the basin and eventually tells us the story of the lakes.

In the drainage system, the channel segment, which begins from the head of the stream, is assigned the value 1 and called first-order stream. When two first-order streams come together, they form a second-order stream, two second order streams form a third order stream, and so on. Having measured the length of the stream segments and its basins, it is possible to estimate the liquid budgets of this drainage and the hydrocarbon lake supply.

Several stream ordering systems have been proposed so far in the literature (Shreve, 1966; Woldenberg, 1966; Scheidegger, 1968; Doornkamp & King, 1971), but Strahler and Shreve methods are used widely today. In this latter method the order of channels increases only when two streams of the same order join together, while in the Shreve (1966) model the order number increases for all links of the network.

The statistical analysis of the streams number and lengths reveals some interesting aspects of the evolution of this specific area and studies the balance between the exogenic erosional forces and the endogenic tectonic movements. In addition, the measurement of the drainage density provides a useful numerical measure of the landscape dissection and runoff potential. Here, I present these considerations in association with the morphotectonics influence on Titan's surface.

5.4.2 Study of Mayda Insula in Kraken Mare with an eye to morphotectonics

During the near-polar Titan T25 flyby on February 22, 2007, the Cassini/SAR instrument observed a big island or a peninsula in the northern shoreline of Kraken Mare, the Mayda Insula (Fig 5.4). The same region was covered by the T28 flyby (Fig 5.5).

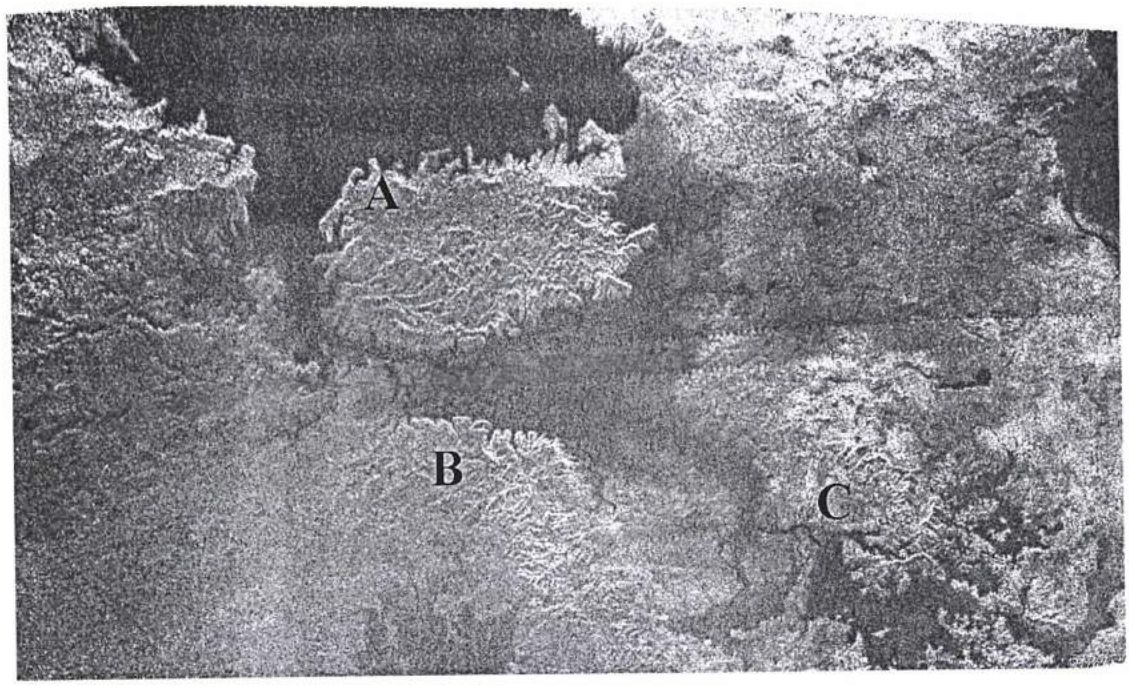

Figure 5. 4 - Part of the northern shoreline of Kraken Mare from Cassini/SAR taken during the T25 flyby. Mayda Insula is in the center of the image (79° N and 310° W). North is to the left (Credit: NASA/JPL-Caltech/ASI: PIA09180).

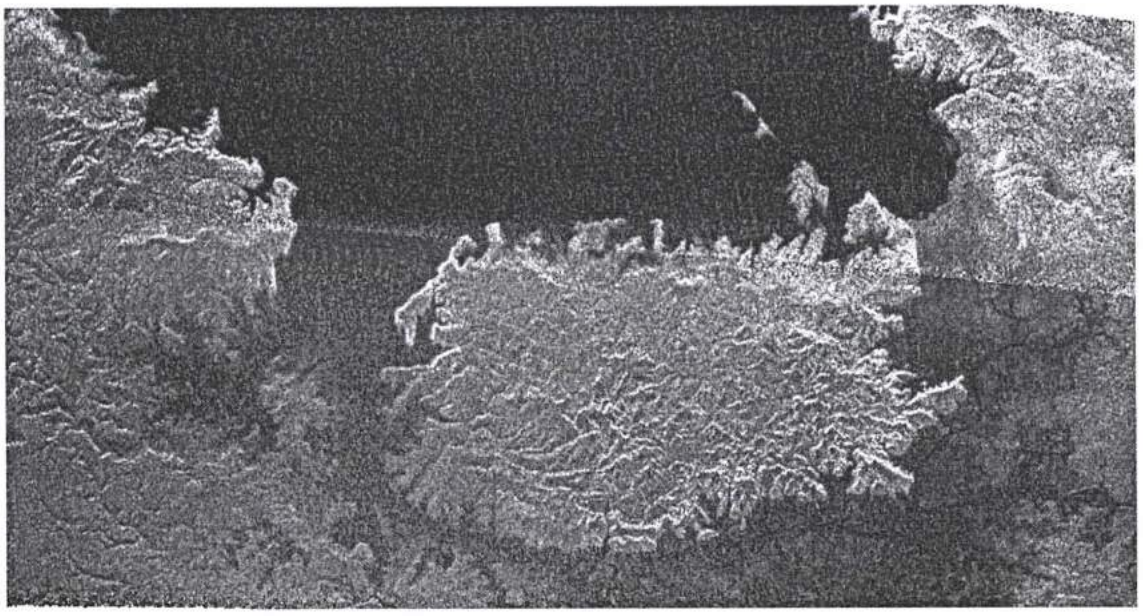

Figure 5. 5 - Mayda Insula from the Cassini Titan flyby T28. This figure is part of the swath which began at 20°S and 37°W and continued in the north-northeast direction. T28 flyby overlaps T25 (Credit: NASA/JPL-Caltech/ASI: PIA09217).

The Cassini/SAR took this image during its T25 flyby of Titan on February 22, 2007. It is in the synthetic aperture (SAR) mode at a nominal resolution of 128 pixels/degree, which is approximately 351 m/pixel. The definition of an ellipsoid for Titan is a sphere with a radius of 2575 km. This image is in an oblique cylindrical projection. In this geometry, the pixel spacing is exactly $\frac{\pi \cdot 2575}{180 \cdot 128} = 0.35111$ km in the direction of top to bottom. The island is about 90 km by 150 km across and it is centered at about 79°N and 310°W.

At the West-Southwest side next to the island, there is a surface of low radar reflectivity. It is not as dark as the lake at the other side of the island and no significant topography is observed on it. A similar plateau is also observed at the South coast of the island, but not at the East. This area has an increased radar brightness compared to the lake. The same features have been previously observed at the edges of the lakes in Northern Titan and they might be due to a reflection from the lake bottom where it is sufficiently shallow so that the bottom echo is not completely attenuated (Stofan et al., 2007). These features can be indicators of ground elevation.

Moreover, the East and West coasts seem scarped, while canyons in an average length of 20 km exist. Mountain ridges are extended to the coastline as well, while their slopes are large and they may have a tectonic origin, as I have discussed above. Furthermore,

remarkable topography with ridges has been developed in the Western part. The Northern region seems to be smoother than the other regions.

The question is whether the local topographic features are somehow related and whether there is any evidence of tectonic activity in this region. By studying the development of the drainage system, I can get constraints on the influence of the antecedent geological events and subsequent geologic changes.

For data acquisition, I cooperated with Dr. Randolph Kirk from the Astrogeology Science Center of the US Geological Survey already since 2007.

5.4.3 Methodology and application

The stream order classification is a statistical relationship of the stream segments in drainage basin (Scheidegger, 1968). In this work we use the Horton and Strahler's ordering system (Horton, 1945; Strahler, 1952) which is a classical approach. Horton's laws are certain topological invariants that are needed to be satisfied, whereas these laws connect the numbers and the lengths of streams of different orders in a drainage basin.

1. Law of Stream Numbers: The numbers of streams of different orders in a given drainage basin tend closely to approximate an inverse geometric series in which the first term is unity and the ratio is the bifurcation ratio.

2. Law of Stream Lengths: The average lengths of streams of each of the different orders in a drainage basin tend closely to approximate a direct geometric series in which the first term is the average length of streams of the first order.

After precipitation, surface liquids form at high latitudes shallow rills. The lowest order streams, the rills, are the smallest outlying tributaries on the edges of the network, according to the Horton and Strahler's ordering scheme. At each unique point, where two tributary streams join, a new stream originates. Whenever two tributaries of the same order meet, the outgoing stream has one order number higher than that of its ancestors. If two tributaries of different orders meet, the outgoing stream has the same order number with the higher ordered tributary. Eventually, all streams in the network combine to form the highest order (main) stream. The number of streams of order u is N_u, while $<L_u>$ is the average length of streams

of order u. Horton's Laws [4] state that the bifurcation ratio R_b and the length ratio R_L, given by:

$$R_b = \frac{N_u}{N_{u+1}} \quad \text{(Eq. 5.1)}$$

$$R_L = \frac{< L_{u+1} >}{< L_u >} \quad \text{(Eq. 5.2)}$$

are constant, or independent of u.

The Hortonian system ordering has a recursive nature since each arc's order depends on the order of its inflow tributaries and has been implemented in various Geographical Information System (GIS) tools (Gleyzer et al., 2004). The algorithm behind these stream ordering GIS procedures is not revealed. This is not a problem in terrestrial geomorphology, since the plethora of observations in a region optimizes the GIS application. However, in the case of Cassini/SAR images of Titan, the resolution does not allow recursive procedures and I made the decision to do it manually. Therefore, I have decided to use Computer-aided design software (CAD). The results of this procedure are illustrated in Figure 5.7 where the drainage of Mayda Insula is classified according the Horton-Strahler's system. The raw data are Cassini/SAR raster image PIA09180 (Figs. 5.4 and 5.5).

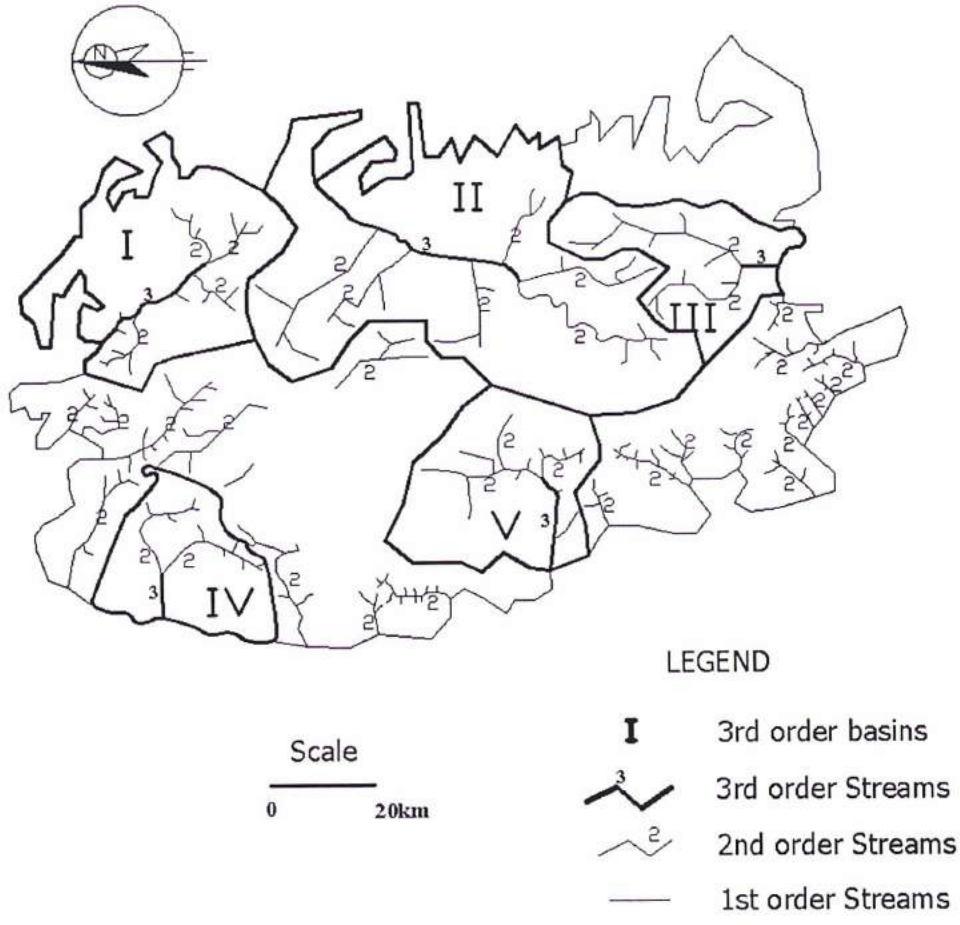

Figure 5. 6 - Mayda Insula drainage basins and stream classification (Cassini/SAR image PIA09180-PIA09217).

The unnumbered lines in Figure 5.6 are the 1st order streams whereas the 2nd order streams are marked by the label "2" and 3rd order streams by the label "3". The basins' borders of the 3rd order streams are designed with thick dark lines and mentioned by roman numbers.

Since there is no topographic map with contour lines available, but only a SAR image, I have designed the streamlines following the fluctuation of the color's intensity. Hence, it is possible to find more streams, especially of the 1st order group in an image taken in higher resolution. The outlined drainage and its development can be used as a tool to study the evolution of the local surface.

5.4.4 Numerical analysis of the drainage network

Table 5.2 below contains the results of the analysis of the 3rd stream order basins, according the Horton-Strahler's classification system. The Bifurcation Ratio R_b is also calculated according the Equation 1. Usually, the bifurcation ratio R_b has a range of 3 to 5 for well-drained networks, while values greater than 5 refer to deep and narrow basins.

Table 5. 2 - Number of Streams formed the 3rd order basins of the island and Bifurcation Ratio

3^{rd} order Basin	Stream Number				Bifurcation Ratio
	1^{st}	2^{nd}	3^{rd}	TOTAL	
	N_1	N_2	N_3	ΣN_u	R_b
I	12	4	1	17	3.00
II	13	6	1	20	2.17
III	8	2	1	11	4.00
IV	8	2	1	11	4.00
V	11	2	1	14	5.50
TOTAL	52	16	5	73	

From the morphologic point of view, I have divided the island's 3rd order drainage basins in two different regions. The criterion of this grouping is the degree of the 3rd order channels' development. The first group contains the 3rd order basins labeled as IV, V, III and the second one contains the basins labeled as II and I (Fig. 5.6). The longer the main branch of a stream network is, the more evolved its respective basin will be. Better evolution of a drainage basin means that the whole network has been operated for a long time without being influenced from other geologic or atmospheric events. In the region of interest, the third order basins I and II have their main stream well developed along to the basin's axis, compared to the other three basins.

The total length of the streams in the 3rd order basins is listed in Table 5.3. L_u is the length value for each branch of the drainage system. The lengths of the 3rd order branches of basin I, III, IV and V are shorter by a factor of about 0.8, 5.8, 4.4 and 1.4 respectively, compared to the longest 3rd order stream of basin II.

Table 5. 3 - Lengths of the streams formed the 3rd order basins of the island.

3rd order Basin	Stream Length			
	1st Order ΣL_1 (m)	2nd Order ΣL_2 (m)	3rd Order ΣL_3 (m)	TOTAL ΣL_u (m)
I	38,425.3	49,287.3	25,733.8	113,446.5
II	76,962.7	165,799.5	45,986.8	288,749.0
III	32,136.7	58,416.1	6,799.0	97,351.8
IV	17,857.3	49,628.5	8,456.5	75,942.3
V	48,650.1	36,025.7	18,827.3	103,503.1
TOTAL	214,032.2	359,157.2	105,803.4	678,992.8

Table 5.4 below, contains the number of the streams of each order of the rest of the island, where only 2nd order streams have been developed. I divide these streams in two groups, the Northern and the Southern, according the orientation of their flows. The last column of the Table 5.4 contains the total number of the streams of the entire island. The last column of Table 5.4 contains the percentage of these 2nd order streams compared to the total stream number of the island. Figure 5.7 below shows the 2nd order basins of the Northern and Southern region of island, which do not have 3rd order streams developed in.

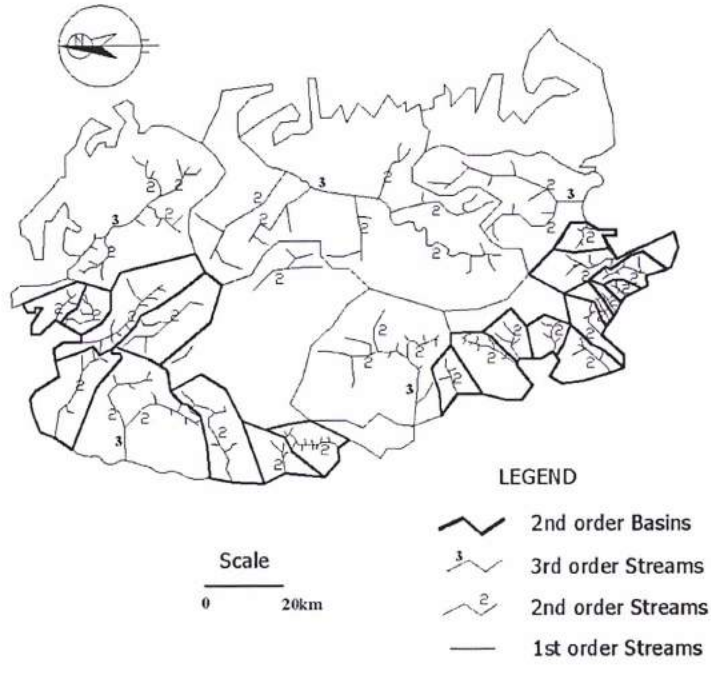

Figure 5. 7 - 2nd order Northern and Southern basins classification according to their orientation.

Table 5. 4 - Streams of the island, which they do not belong to a 3rd order basin.

Stream Order	North 2nd order Basins	South 2nd order Basins	Total Number of the streams of the island	% of the Total number of streams
1	37	37	126	59
2	9	12	37	57
3	0	0	5	-
Total	46	49	168	57

Consequently, according the drainage development, I divide Mayda Insula into two morphotectonic regions:

1. The eastern part (basins I and II), where the drainage networks are well developed,
2. The western part (basins II, IV and V), where the drainage networks are in initial stages of their evolution.

The average lengths of the Table 5.3 length values are calculated in the Table 5.5 below, in order to find the length ratio R_L according the Equation 2. $<L_u>$ is the average length of streams of order u in meters.

Table 5. 5 - Average length of the streams formed the 3rd order basins of Mayda Insula.

3rd order Basin	Average Stream Length		
	1st Order $\Sigma<L_1>$ (m)	2nd Order $\Sigma<L_2>$ (m)	3rd Order $\Sigma<L_3>$ (m)
I	3,202.1	12,321.8	25,733.8
II	5,920.2	27,633.3	45,986.8
III	4,017.1	29,208.0	6,799.0
IV	2,232.2	24,814.3	8,456.5
V	4,422.7	18,012.9	18,827.3

The stream length ratios R_L, the area A of each 3rd order basin and the Drainage Density D are listed in Table 5.6. The drainage density is calculated by the equation:

$$D = \frac{\sum L}{A} \quad \text{(Eq. 5.3)}$$

Table 5. 6 - Stream Length Ratio Area and Drainage Density of the 3rd order basins of the island.

Stream 3rd order Basin	Stream length Ratio $R_L(2,1)$	$R_L(3,2)$	Area of Basin A ($x10^3$ km^2)	Drainage Density D (km^{-1})
I	3.8	2.1	1.35	0.08
II	4.7	1.7	2.96	0.10
III	7.3	0.2	0.76	0.13
IV	11.1	0.3	0.72	0.11
V	4.1	1.0	1.05	0.10
TOTAL			6.84	

From Table 5.6, the length ratio R_L between the 3rd and 2nd order of streams of basins I to V ranges 0.2 to 2.1. When the ratio is greater than 2, then the 2nd order streams joint the 3rd ones in acute angles, like most of the tributaries in an intense topography.

5.4.5 Interpretation of the results

The study of drainage basins morphometric parameters reveals much information regarding the evolution and the dynamics of the "hydrological" processes on Titan surface, despite the fact that the liquid material is not water but hydrocarbons. The correlation between the geomorphic features that are expressed by these parameters and the local topography can provide a qualitative description of the region's development.

Stream order classification is a simple qualitative basis for understanding the development degree of a specific area through time. Generally, a basin is better drained when its stream order is higher. The 3rd order basins of Mayda Insula cover more than half of the total area of the island. On the other half of the island, low order basins exist, indicating a lower degree of development. Additionally, the 3rd order basins I, III, IV and V are located at the island's edges, while basin II, the best geomorphologically developed one, is situated in the centre of island's East part.

The 2nd order streams of the well-drained basin II are quite long and deployed at the ¼ of the surface of the island. The longest 2nd order stream of this basin seems to be shaped like a meander, another clue of the well-developed stage of basin II. The 3rd order streams of basins III and IV are not so much developed as their 2nd order stream ancestors.

The 1st order streams flow parallel or are consequent to the original slope of the surface. These rills are steep-sided, have short lengths and are V-shaped. The number of

these streams (52), as Table 5.2 shows, is greater than the total stream number of the 2nd (16) and 3rd (5) order at the 3rd order basins I, III, IV, V. Because of the almost vertical entrance of most of the tributaries into the main stream (Figs. 5.6-7), the drainage pattern can be described as rectangular.

The drainage density D, listed in Table 5.6, extends to zero, although there is a considerable degree of basin development. This can be explained by the existence of intermittent and ephemeral streams in the region as well as by the low image resolution. Although the designed drainage in Figures 5.6-7 seems to be dry, it can still operate (or operated in the past) and may evolve on the island's surface.

The heterogeneity of Mayda Insula's surface may have been caused by two factors: the atmospheric or the tectonic activity, operating separately or together. Tectonic activity indications on Titan's surface have been reported by Soderblom et al. *(2007). In the case of tectonic quiescence, either vertical or horizontal, the landscape will be eroded following the Davies erosion cycle (Davies, 1899).*

The bifurcation ratio is a numerical expression of the development degree of a basin. The bifurcation ratio for basin II is R_b=2.17, which means that the basin is well drained. The bifurcation ratio of the other 3rd order basins is greater than that of basin II, due to their lower drainage development. The ratio of basin V is greater than 5, which on the Earth is an indicator of a newly or an elevated surface.

The Horton law of stream lengths shows a geometric relationship between the average length of streams of a specific order and the corresponding order. The stream length ratio R_L is the measure of this relationship. When the ratio R_L is greater than 2, it means that the 2nd order tributaries enter into the 3rd streams at acute angles, as most of the streams on steeper slopes. The steeper the slope, the more acute the angle of the stream entrance is (Horton, 1945), which is the case of R_L(2,1) (Table 5.6). Our morphometric analysis shows the existence of steep slopes on the Western part of Mayda Insula. The stream length ratio R_L(3,2) (see Table 5.6) ranges between 0.2 and 2.1 that means smoother slopes than in the previous case. The magnitude of slope is one of the characteristics that determine the relief. Since the island basins have different slopes, they have experienced different elevations. Summarizing the results of the drainage network analysis and taking into account the stream length ratio R_L between 2nd order and 1st order streams, we can assume that the 2nd order basins I, III, VI and V are elevated after the drainage development of basin II.

5.5 Statistical analysis of Mayda Insula surface edifices

To have a deep insight of the topography of Mayda Island, I studied the close shoreline areas as well. Three regions with significant topography have been distinguished in the Cassini's RADAR image, marked with A, B, C in Fig. 5.4.

5.5.1 Statistical analysis of the angular distribution of the mountain ridges

In the following Tables 5.7-9, the angles of the mountain ridges in degrees are listed, for the three regions respectively, showing the orientation of their axis, according to the N-S direction.

Table 5. 7 - Angles of mountain ridges according the N-S direction, Region A - Mayda Insula. The positive angles are looking to the East and the negatives to the West.

Angles (deg) of the main Mountain Ridges of Region A – Island								
41.7	-5.6	6.6	-7.3	30.6	2.7	-47.8	71.4	19.4
39.5	-6.1	-12.2	-19.6	-10.0	42.9	-42.5	-2.2	22.8
41.4	20.5	-16.4	38.6	-30.1	39.0	39.9	-14.2	16.6
14.8	-8.7	26.4	27.3	-54.4	-0.5	59.4	-21.5	-25.9
-27.2	41.0	-11.7	46.3	52.1	-10.1	-0.1	34.8	21.1
12.1	-19.7	-19.1	-19.1	-30.9	-47.4	-18.7	-3.2	62.1
44.6	-6.5	15.9	-22.4	-23.9	-3.7			

Table 5. 8 - Angles of mountain ridges according the N-S direction, Region B - Western Mountains. The positive angles are looking to the East and the negatives to the West.

Angles (deg) of the main Mountain Ridges of Region B – Western Mountains								
20.8	13.7	-20.6	-5.8	20.8	53.1	-47.5	31.6	-30.5
7.5	30.7	43.7	-27.1	8.1	-19.0	-34.8	-5.2	-8.7
65.3	32.8	53.3	-10.6	70.2	47.0	14.5	25.7	24.4
30.4	-45.0	-2.7	36.2	-54.7	-2.9	-24.0	51.3	28.7
-58.2	-37.9	-27.0	12.8	38.3	0.0	-22.1	25.0	20.8
43.9	72.2	35.8	32.6	5.3	-17.3	-2.3		

Table 5. 9 - Angles of mountain ridges according the N-S direction, Region C - SW Mountains. The positive angles are looking to the East and the negatives to the West.

Angles (deg) of the main Mountain Ridges of Region C- SW Mountains				
-3.5	-39.9	30.3	16.7	0.0
16.1	8.3	47.1	12.8	16.7
51.4	54.1	13.8	0.0	22.1
40.9	-9.8	-57.1	11.0	-46.0
33.3	-39.9	44.1	35.3	-33.7
9.5				

The angle distributions of the mountain ridges' orientations are presented in Figs. 5.9-11. The normal curve is also included.

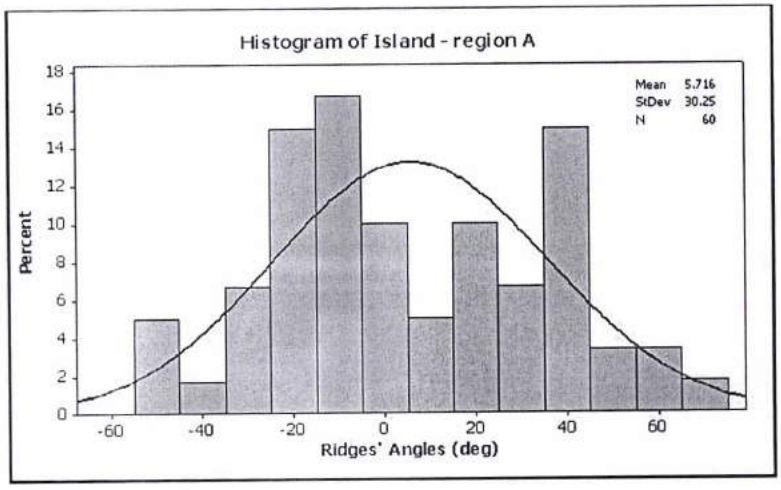

Figure 5. 8 - Histogram of the Island-region A.

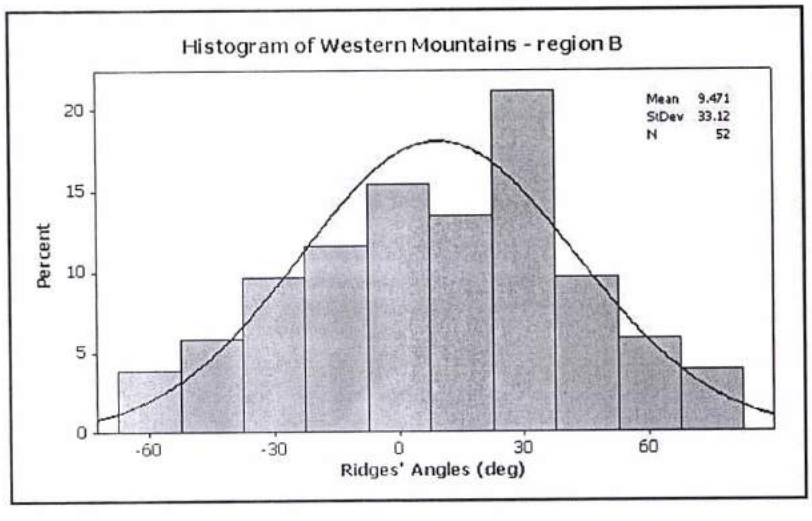

Figure 5. 9 - Histogram of the Western Mountains-region B.

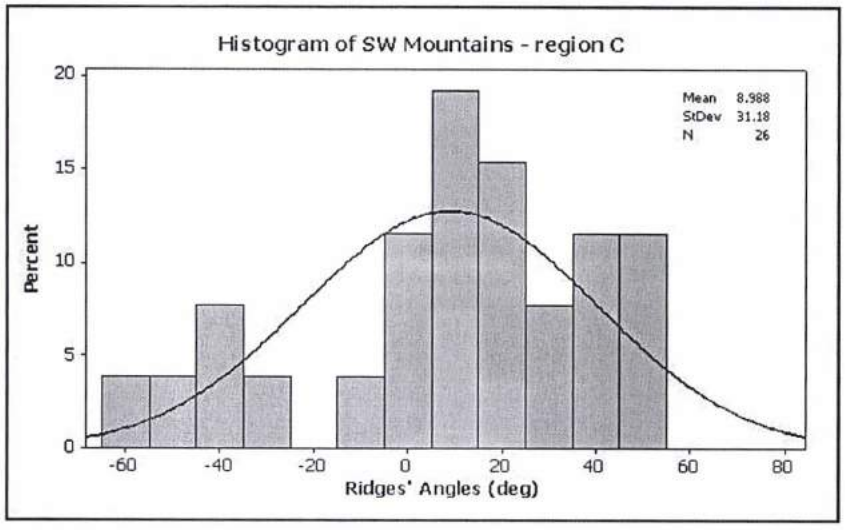

Figure 5. 10 - Histogram of the SW Mountains-region C.

To plot the island's histogram of Figure 5.9, I have taken into account 60 ridges. Similarly, 52 ridges have been plotted concerning the region western of the island (B) in Figure 5.10. For the region that is close to the eastern part of the island (C), 26 ridges have been plotted. These ridges have been recorded from Cassini/SAR during the T25 flyby and confirmed by the overlay of T28 few months later. Apparently, their distributions are not unique in the area and more ridges may exist, but in minor scale.

Analysis of the angular ridges' statistics:

Mayda Insula (A):

The angular distribution of the ridges (Fig. 5.9) shows two preferred directions: (a) 20° to 40° eastwards and (b) 20° westwards.

West Region (B):

The angular distribution of the mountain ridges in Figure 5.10 demonstrates an orientation at 30° eastwards.

Southwest Region (C):

The angular distribution of the mountain ridges in Figure 5.11 shows an orientation of 20° eastwards.

The prominent mountain ridges orientations of the area of interest are two. The first one is located in all the three regions (A, B and C in Figure 5.4) at 20° to 30° eastwards. The other one has been observed at the island at 20° westwards. The next interesting result of this statistical analysis is that at region A an opposite orientation exists. There are almost 30% of the ridges that are N-W oriented. Due to the low radar resolution, only a sample of the mountain ridges is examined. A high-resolution image could provide the accurate orientation of the ridges.

5.5.2 Correlation between ridge distribution and drained basins of Mayda Insula

The drainage basins are defined by the landscape and each basin has the same orientation as its main stream. Intense topography exists in the western part of Mayda Insula with a radial development of the 3rd order basins (Fig 5.7). Particularly:

- **3rd order basins:**

Basin I: The central stream (3rd order) of the basin is northwest oriented.

Basin II: As I have shown previously in the numerical analysis, basin II is the best-evolved 3rd order basin in length and occupied area. The central stream of the basin as well as the longer 2nd order channels are meander, are northeast oriented like the relevant mountain ridges. The drainage follows the regional topography. ***By taking into account that the northeast is dominant and that the basin II is well drained, I conclude that this direction is the older orientation of the landscape in the Insula and the near-by shoreline.***

Basin III: The central 3rd order stream of basin III has south direction.

Basins IV and V: The 3rd order channels of basins IV and V present western orientation.

- **2nd order basins:**

As I have mentioned before, the west part of the Mayda Insula consists of many drainage basins of 2nd order (Fig. 5.8). Next section is dedicated to these basins.

5.5.3 Statistical analysis of the angular distribution of the island's 2nd order streams in poor drained basins

As discussed above, the 2nd order streams are poorly drained in the Island of Mayda Insula (Fig. 5.8). In the other part of the island, except for the 3rd order basins, the 2nd order streams have been developed vertical to the coastline. The orientation of these streams is listed in Table 9, according to the N-S direction. The angle distribution of Table 5.13 is designed in Fig. 5.13, with the normal curve.

Table 5. 10 - 2nd Order Stream Angles Orientation according to N-S direction. The positive angles are looking to the East and the negatives to the West.

2nd Order Stream Angles (deg) to N-S direction			
83.7	-67.1	-56.7	-72.5
55.7	67.9	-39.8	-72.5
22.9	-42.1	4.5	-88.2
27.3	-72.3	11.3	31.9
55.6	-59.6	61.0	-26.7

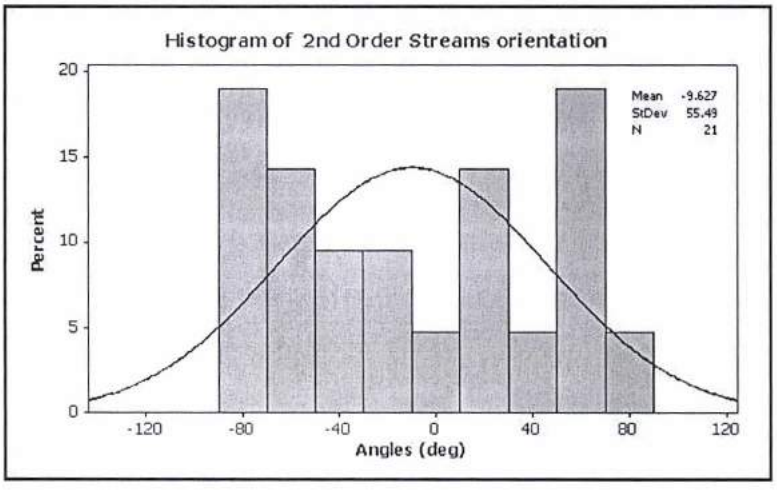

Figure 5. 11 - Histogram of 2nd order Streams orientation of Northern and Southern poorly drained basins.

There are two prominent orientations of the 2nd order channels in poorly drained basins. The Northern streams are oriented at 80°W and the Southern streams at 60°E. Comparing the two

histograms of the Mayda Insula (Figs. 5.10 and 5.13), the streams in poorly drained regions seem to be related to the axis of the mountain ridges of the surface.

5.6 Cassini/RADAR image processing

Titan's lakes were first recorded by the Cassini Titan Radio Detection and ranging Mapper - RADAR (Stofan et al., 2007). The RADAR instrument onboard the Cassini orbiter is designed to map Titan's surface as well as other Saturnian moons, its rings and Saturn itself. The main RADAR advantage is that the emitted microwave radiation penetrates the thick atmosphere almost unaffected. The idea is to combine RADAR recorded echoes with other remote sensing observations, especially VIMS, in order to retrieve a full view of Titan's surface.

5.6.1 RADAR instrument and its operational sequence

Cassini's RADAR instrument is a multimode sensor dedicated for surface observations. It can operate at four modes: Synthetic-Aperture Radar (SAR) imager, Altimeter, Scatterometer and Radiometer. It is expected to detect surfaces with backscatter coefficient as low as -40dB. It is the offspring of a joint effort between NASA's Jet Propulsion Laboratory (JPL) and Agenzia Spaziale Italiana (ASI).

Cassini's RADAR is a Ku-band (13.8 GHz - λ=2.17 cm) single-polarization instrument with a total mass of 43.3 kg. It uses the 4 m High Gain telecommunications Antenna (HGA) of Cassini. It operates in conjunction with the Cassini Ion and Neutral Mass Spectrometer (INMS) due to the fact that both instruments have similar geometry requirements. When the HGA is pointed to Earth for tracking, the RADAR is not operating. Five antenna microwave beams, one at the time (B1 to B5 in Fig. 5.12) are used in order to obtain the maximum path coverage. The RADAR transmits a set of pulses for a given time period and when the first echo burst returns the receiver is switched on. During each sequence the instrument collects 1 GB of data. These data are compressed to a specific format the Block Adaptive Quantizer (BAQ) (Elachi et al., 2004).

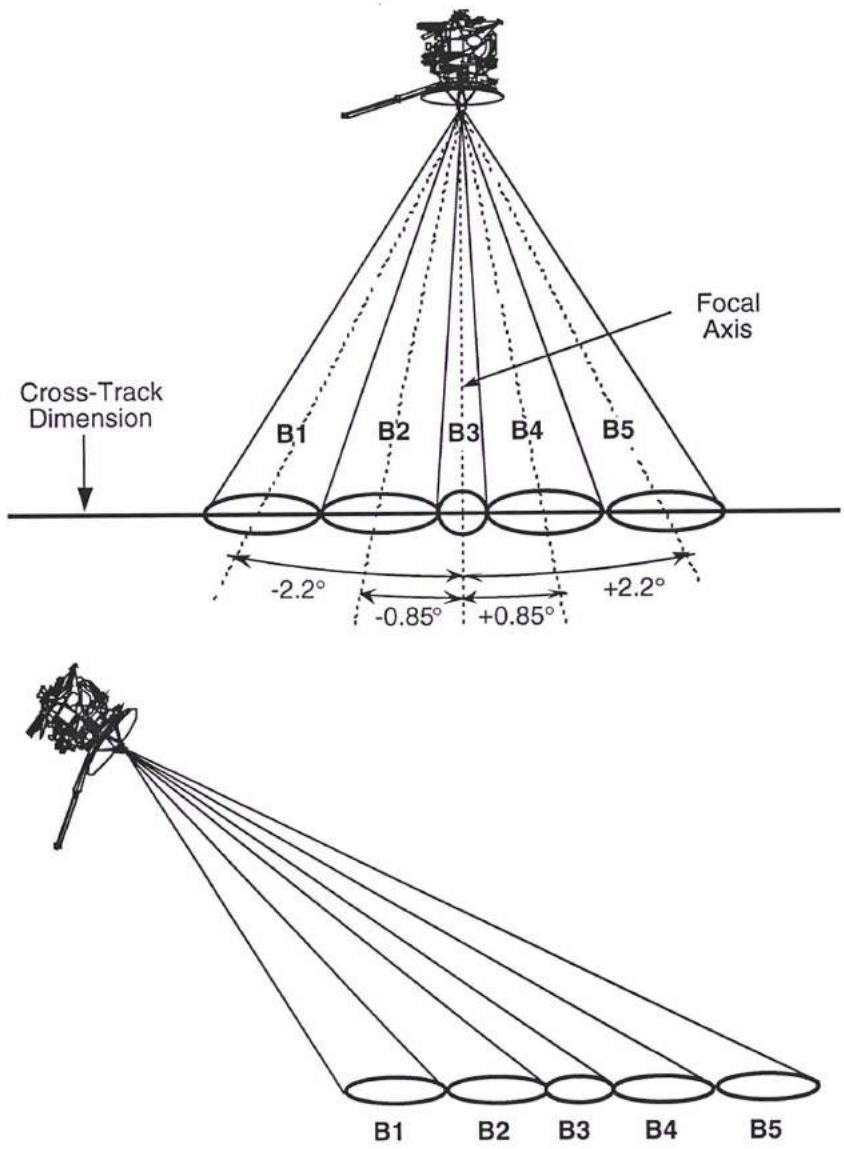

Figure 5. 12 - Cassini RADAR antenna beams. The top panel shows the nadir pointing for altimetry, while the bottom panel shows the imaging side-pointing (Elachi et al., 2004).

SAR can probe the surface with two resolutions: the High SAR Resolution (HiSAR) at 350-720 m per pixel and the low SAR resolution. The linear polarized electric field vector of the Cassini/RADAR is oriented to be approximately parallel to Titan's surface during SAR operation (Hayes et al., 2011). RADAR operates only during close flybys of Titan or other planetary objects of interest. Figure 5.13 illustrates the observational sequence during nominal Titan flybys, when the closest approach (C/A) is at an altitude of 1000 km or lower.

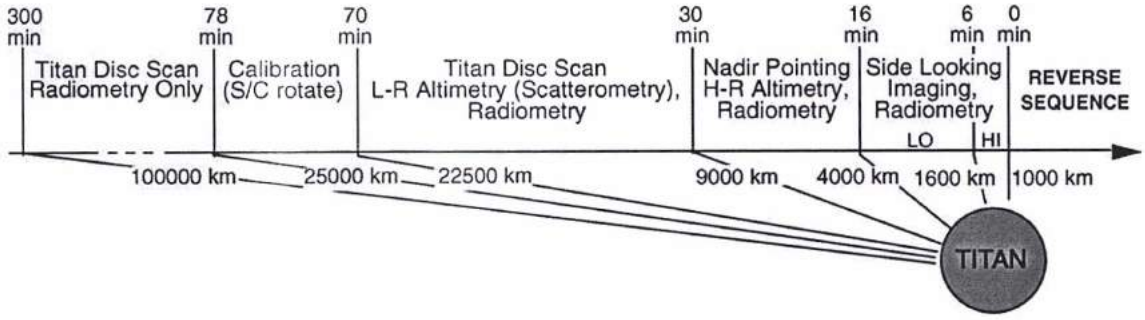

Figure 5. 13 - The sequence of the radar operational stages during a Titan flyby with closest approach at an altitude of 1000 km (Elachi et al., 2004).

The combination of the five individually illuminated sub-swaths derives the total width of RADAR swath and ranges from 120 to 450 km at the spacecraft altitudes from 1000 to 4000 km. Each nominal Titan flyby produces a SAR swath 5000 km long, which is about 1.1% of the satellite's surface. When the flyby has C/A at higher than 4000 km, no SAR images acquisition occurs (Elachi et al., 2004).

5.6.2 Speckle noise in Cassini/SAR images

RADAR observations are almost unaffected by the atmospheric conditions. The recorded echoes can distinguish different types of surface regions through the measurement of their emissivity or radar reflectivity. The instrument measures the normalized backscatter cross-section of Titan's surface.

However, the backscatter recordings suffer from both speckle and instrument noise. The speckle noise is a multiplicative granular noise that appears when the surface features are rough compared to the illuminating coherent radiation (Goodman, 1976). It is caused by the constructive and destructive interference of the RADAR returns, which are scattered by many elementary reflectors (Lee et al., 1994; Patel et al., 2011). The speckle noise exists in all types of coherent imaging systems and it reduces the resolution of the image as well as the detectability of the target (Goodman, 1976). Its presence in SAR images overlays real structures and causes grey value variations even in homogenous image parts, making automatic segmentation difficult.

When suppressing multiple views of the same surface element, the speckle noise follows a Gaussian probability distribution (Chitroub et al., 2002). The multilook technique

averages incoherently the independent neighboring pixels to estimate the characteristics of the same ground area.

5.7 Filtering and segmentation of the Cassini/SAR images on Titan

The liquid of the Titan exhibits very low reflectivity and therefore the lakeshores can be easily distinguished from the surroundings. Long-term observations of the lakeshores' evolution may show temporal variations of the liquid volume and provide evidence about the methane cycle. However, the automatic segmentation of the shores becomes problematic by the existence of the RADAR speckle noise.

In order to reduce this speckle noise in Cassini/SAR images, we have applied a despeckle filter that yields the SAR restored images. In the next two subsections, I describe the application of the filtering procedure in SAR images as well as a segmentation method. The filtering technique, based in probabilistic methods, is described in (Bratsolis & Sigelle, 2003) and the application we have performed in Cassini/SAR images in (Bratsolis et al., 2012) which I have co-authored.

5.7.1 Total Sum Preserving Regularization (TSPR) filtering

The filter is based on a membrane model Markov random field approximation optimized by a synchronous local iterative method, the outcome of which is a total sum preserving regularization (TSPR) for the pixel values of the image. The image is considered as a random element drawn from a pre-specified set of possible images. The problem is ill posed, since we try to recover the real image from the recordings. An iterative algorithm is then applied to optimize the image reconstruction.

To retrieve the maximum information of the TSPR filter application in a SAR image we needed a 32-bit version of the image. All SAR data of the Cassini-Huygens mission are available in NASA Planetary Data System (PDS) except for the most recent ones, which are in raw format. NASA/PDS database contains a pair of Short Burst Data Record (SBDR) and Long Burst Data Record (LBDR) files for each flyby. The only difference between the datasets formats is whether or not two data fields are included: the sampled echo data and the altimeter profile. The altimeter profile is an intermediate processing result between sampled

echo data and a final altitude estimate. LBDRs include the echo data but not the altimeter profile[16].

Using the Integrated Software for Imagers and Spectrometers (ISIS)[17] that US Geological Survey has developed, Cassini/SAR images can be retrieved. The software packages, the installation procedure and an assistance forum are available online as well. ISIS inputs the JPL Cassini RADAR science data products and extracts 32-bit images which can be processed by GIS software applications and other numerical computing software.

A 32-bit version of Cassini/SAR image PIA08630[18] was provided by Dr. A. Hayes (Fig. 5.14). We have chosen a SAR image with lakes for a test case, since the contrast between the lakes and the surroundings is significant. This image was taken during the Cassini T16 Titan flyby on July 21, 2006. It is centered near 80°N, 92°W and its dimensions are 420 km horizontally and 150 km vertically. The dark patches are lakes, filled with organics. This data is an 860x6200 array and is in a band sequential ISIS 3 format with an oblique cylindrical projection. The image covers an area 750x3100 in pixel size and the pixel scale is set to 175.558 meters per pixel. The actual SAR resolution is around 350 meters per pixel and the image contains some interpolation.

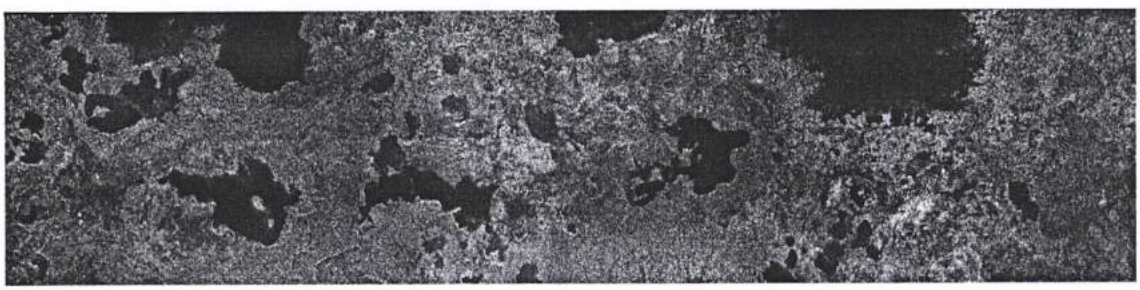

Figure 5. 14 - The initial Cassini/SAR image PIA08630 (Credit: NASA/JPL-CalTech/ASI).

The final form of despeckling (Fig. 5.15) gives a sum-preserving regularization for the pixel values of the image. The TSPR method preserves the mean values of local homogeneous regions and decreases the standard deviation up to six times.

[16] http://starbrite.jpl.nasa.gov/pds/viewProfile.jsp?dsid=CO-V/E/J/S-RADAR-3-LBDR-V1.0

[17] http://isis.astrogeology.usgs.gov/

[18] http://photojournal.jpl.nasa.gov/catalog/pia08630

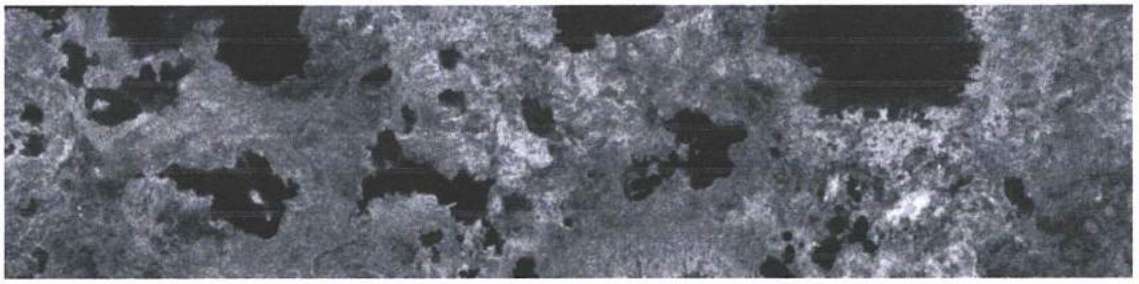

Figure 5. 15 - The filtered Cassini/SAR image PIA08630 using Bratsolis et al. (2012) despeckle filter.

5.7.2 Supervised segmentation

The TSPR filter can be used as intermediate stage for the extraction of meaningful regions that correspond to structural units in the scene or distinguish objects of interest. The speckle noise has not been completely removed from the filtering and we apply an image segmentation method in order to divide the image into specific regions where the pixels share common properties.

The segmentation method classifies regions of an image following a specific criterion. The supervised method of minimum Euclidean distance uses the mean values of each member and calculates the Euclidean distance from each classified object to the nearest class segmenting the image into different regions of interest or different labels.

In our case, we have selected three classes: the dark lakes (black), the granular lakes (grey) and the background (light grey). For each value of normalized backscatter, we subabstract the mean values that correspond to the region of interest. After using the despeckling filter TSPR we apply the segmentation method. The resulted image is illustrated in Figure 5.16 below.

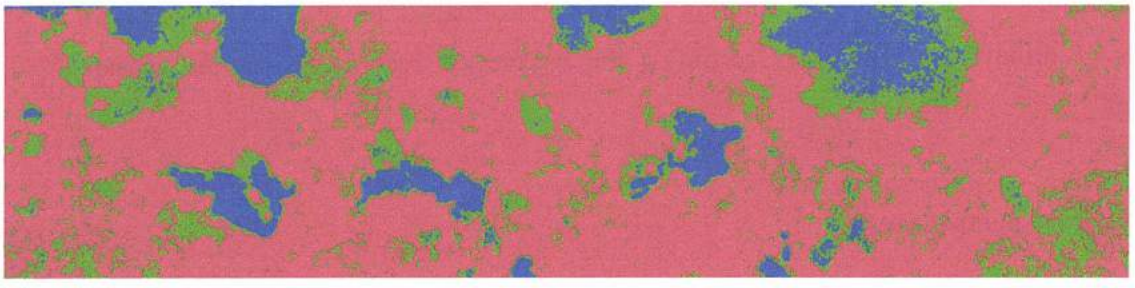

Figure 5. 16 - The segmented image after filtering. Dark lake with low backscatter are illustrated with blue, the granular lakes with green and the local background is colored red.

The dark part of lakes are indicated in blue, in green it is the granular part of lakes and in red the local background. The temporal variation of the dark spots can provide information on the evolution of the lake system and consequently help us to better understand the methane cycle on Titan (Atreya et al., 2006) and therefore the mechanisms linked with the lake surface features, their origin and fate, through a global temporal and spatial coverage (Hayes et al., 2011). The proposed filtering and segmentation method would be a helpful tool in enhancing the return of the analysis of all SAR data acquired on Titan and other objects as well as in the exploitation of such data from future missions to Titan.

I apply the TSPR filter and supervising segmentation procedure on a different surface feature where the contrast between the RADAR echoes is not obvious. I have selected the SAR image of Sinlap crater (11.3°N, 16.0°W)- PIA 07368 (Fig. 5.17-left). This crater has a diameter of about 60 km and the bright surrounding material indicates impact origin. The central panel of Figure 5.17 shows the results of the despeckle filtering and the supervised segmentation procedure for the Sinlap crater.

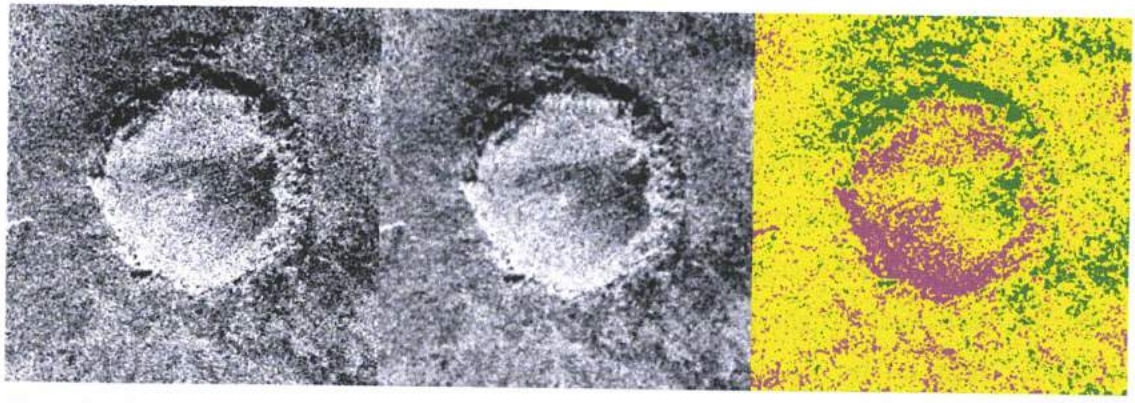

Figure 5. 17 - Application of the filtering and segmentation procedure to Sinlap crater: Initial image (left) PIA07368 (Credit: NASA/JPL-CalTech/ASI). Filtered image (center) and Segmented image (right).

The segmentation outcome of our filtering procedure in Sinlap crater (Fig. 5.17-left) shows regions of different surface types according the backscatter recording after the speckle removal.

5.7.3 Future perspectives

With the filtering and segmentation procedure described above, accurate isolation of distinct surface features from their surroundings can be achieved. As we can see from Figures

5.16 and 5.17-right, the shapes of the surface edifices can be determined and then classified. The technique I described above removes the speckle noise from RADAR images and provides the shapes of regions of interest. We can then optimize the results of the direct comparison of Cassini/RADAR images with the images retrieved from ISS and VIMS of the same area. Several similar efforts have been reported so far (Barnes et al., 2007a; Soderblom et al., 2007a; Le Mouelic et al., 2008; Tosi et al., 2010).

One of the most challenging projects I plan to be engaged in is to superimpose VIMS images in which the atmospheric contribution is constrained by M. Hirtzig's radiative transfer code over the despeckled and segmented RADAR images of the same region. We have already been cooperating with Dr. R. Lopes to this direction.

In the paper of Solomonidou et al. (2010), which I have co-authored, we have worked on the two recognized (at that time) cryovolcanic candidate areas, Tui Regio and Hotei Regio, on which we applied the Principal Component Analysis tool. The paper was published in the anniversary volume of the Hellenic Journal of Geosciences[19] for the 40 years since the foundation of Geology and Geoenvironment Department of the University of Athens. The main goal was to identify regions of interest that present brightness or color alterations using VIMS data within the possible cryovolcanic areas that suggest deposition of material coming from the interior and having a different chemical composition than the surrounding surface. Hence, a variety of materials within a certain geological terrain suggests either past or still ongoing activity of different and distinct geological processes or the deposition of different and distinct material from various sources.

The surface contributes significantly to Titan's methanological system (Hayes et al., 2011) and its lakes are an integral part of the methane cycle. By studying the filtered images of the same regions of Titan, taken at different time periods, we can study the existence of possible ephemeral or seasonal changes on the surface. These studies are also of interest to the astrobiological research, which I discuss in Chapter 6, the design of future mission instrumentation and the determination of regions of interest for future landing sites, which I describe in Chapter 7.

[19] formely Annales Géologiques des Pays Hélléniques

Chapter 6

Habitability of Titan and other icy moons

Despite great strides in biosciences, the roots, the sources and the initial conditions of life emergence on Earth remain largely unknown. Due to the erosional and tectonic activity occurring on Earth, the traces of the geological record have been inevitably erased. Extraterrestrial environments can provide the necessary information for finding the missing link, looking at the conditions for the emergence of life or at least for characterizing Earth as a habitat.

Current missions and data analysis revealed that among the main candidates for finding signs of past and/or current life within our Solar System, besides Mars, are the icy moons of the giant planets Europa, Ganymede, Callisto, Titan and Enceladus. These planetary bodies may host the proper conditions for the emergence or the maintenance of life, providing the concentration of the necessary ingredients and the proper chemical inventory for biochemical reactions.

Due to their high astrobiological significance, they have been selected as targets of future exploration programs, ESA's Jupiter Icy Moons Explorer (JUICE) and and the NASA-ESA joint study of the Titan-Saturn System Mission. Indeed, one of the major objectives of both missions is to explore the habitability potential of these icy moons. It was that astrobiological significance that triggered my interest and formed my final decision to engage with Titan studies.

For this reason, I have studied and compared Titan and Enceladus, in collaboration with Dr. A. Coustenis, Prof. F. Raulin and A. Solomonidou considering the recent discoveries of the Cassini-Huygens mission. This study entitled as "Life in the Saturnian Neighborhood" has been published as a chapter in Cellular Origin, Life in Extreme Habitats and Astrobiology book series of Springer Editions, edited by Prof. J. Seckbach[20] (Coustenis et al., 2012). In this work, we look for similarities as well as differences among the aforementioned satellites,

[20] http://www.springer.com/series/5775

which may impact their habitability conditions. Our main purpose in this book chapter is to underline the presence of liquid water considerably further from the Sun than previous models of the Habitable Zone envisaged and to emphasize that both Titan and Enceladus host unique conditions for the emergence of biological building blocks in their environment and to recommend a future mission dedicated to these moons to perform astrobiological studies. Comparative planetology among the icy moons of the outer planets allows us to better bring forward common characteristics of the atmosphere and the surface that allow us to look into the origin and evolution of these bodies. On this subject, we have written a paper which was published in the *Journal of Cosmology* (Solomonidou et al., 2011).

Accordingly, in this chapter, I describe the habitability of the icy moons of our Solar System more from the astronomical point of view and looking at them as potential habitats.

6.1 Introduction and context

The scientific field of Astrobiology (also bioastronomy or exobiology) investigates the origin and the evolution of life on Earth in the past, present and future. Extending to the terrestrial analogues, Astrobiology explores the possibility of life forms existing in extraterrestrial environments hosting suitable conditions for life emergence and/or sustainability.

Astrobiology adapts knowledge obtained from different scientific disciplines namely astrophysics, geology, physics, chemistry, geochemistry, biology and more, in order to understand the appropriate aspects concerning the creation of our Solar System and the initiation of life. It focuses on extraterrestrial environments, posing the unanswered question on the origin of life on Earth and elsewhere and how humans can detect it (Des Marais et al., 2002; Raulin, 2007).

Planetary habitability is the ability of a planetary environment to support and sustain life forms. The habitability potential of a planet or a satellite depends on a combination of factors, which are considered to be essential for life appearance, evolution and maintenance. Crucial factors are, among other, the orbital properties of the planetary body, its stability, its bulk composition, the existence of an atmosphere and a surface, as well as the proper chemical ingredients.

The region around a star or a planet that is favorable for life in any form is called habitable zone (HZ) (Huang, 1959). Within the habitable zone a planetary environment can have the required temperature, pressure and luminosity conditions to allow water to remain in

a stable liquid state on its surface (Hart, 1979). In such a zone, living organisms may arise and evolve.

Life emergence on Earth sets the habitability constraints. Terrestrial life is the final product of a long complex chemical evolution, requiring at least four raw ingredients: (a) the existence of liquid water, (b) a stable environment (c) carbonaceous matter as nutrients and (d) energy. The fulfillment of these prerequisites over a long period of time can be considered as an indicator of suitable environments for hosting the proper biological building blocks, which may lead to the formation of primitive life structures (Kasting et al., 1993).

The basic definition of the habitable zone refers to the existence of liquid water on the surface. In this framework, the boundaries of the habitable zone of the Solar System (Fig. 6.1), extend from 0.95 AU to 1.2 AU.

The inner boundary of the habitable zone is the specific distance from the star where the surface liquid water of a planetary body has been vaporized due to runaway greenhouse effect. In this case, water is vaporized rapidly and dissociated by solar UV radiation in the upper atmosphere. Subsequently, hydrogen under high temperature conditions, escapes to space, breaking the water cycle (Kasting, 1988). The outer limit of the habitable zone is the specific distance from the star where the local atmospheric conditions have failed to produce a satisfactory greenhouse effect that could keep the temperature at the planetary atmosphere above the freezing point (Lammer et al., 2009). Alternatively, it is the distance from the star where CO_2 begin to condense (Kasting et al., 1993), but CO_2 ice clouds in the atmosphere still allow for the surface temperature to be above the freezing point of water (Forget & Pierrehumbert, 1997).

However, what makes a planetary body habitable is more complex than fulfilling the distance limitation. Lammer et al., (2009) defines 4 classes of habitable planets. The first Class I consists of Earth-type planets in which life can evolve following the terrestrial analogue. These planets host the proper atmospheric conditions to maintain their surface liquid water stable over a long period of time in geological terms, in combination with active plate tectonics.

Class II habitats are planets in which life may evolve like in Class I, but due to different stellar and geophysical conditions, they have followed different evolutionary paths (Taylor, 2011). Early Venus and early Mars belong to this class. According to Pioneer Venus and Venus Express measurements, Venus (Kulikov et al., 2006; Svedhem et al., 2007) which lies below the inner threshold of the habitable zone, at 0.72 AU, has kept its surface water during its early stage, before experiencing a runaway greenhouse effect (Kasting, 1988;

Cockell, 1999). Mars orbits at 1.52 AU and managed to stay warm between 3.5 and 4 billion years ago to allow for the existence of liquid water on the surface (Craddock & Howard, 2002; Ehlmann et al., 2011) producing characteristic landforms such as ocean shorelines, fluvial channels and valleys (Carr & Head, 2003; McEwen et al., 2007).

Liquid water can also exist under the surface in several planetary bodies, below their icy crust, as in the case of the icy satellites of the outer planets. According to Lammer et al., (2009), the planetary bodies where the internal ocean interacts directly with silicates, like Jupiter's Europa, belong to the Class III habitats. In this structure, the silicates provide various chemicals and energy through hydrothermal or volcanic activity.

The Class IV habitats are the planets or satellites which have huge water underground deposits without interacting with silicate material. These subsurface oceans of the icy satellites of the gas giants may be in direct contact with heat sources below their icy crust or encapsulated between two ice layers, or liquids above ice. This is the case of Jupiter's Ganymede and Callisto and Saturn's Titan. In this context, the determination of the habitable zone limits can be expanded. The question is if these underground water deposits can support any life forms. Except for water liquid, life requires other essential elements such as nitrogen and phosphorus in addition to hydrogen and oxygen. If this situation maintains for long timescales, the liquid underground water may become capable of sustaining life. Similar conditions have been considered for the terrestrial case where a coupled sea/ice system could provide the necessary conditions for life emergence on the primitive Earth (Trinks et al., 2005). In the paper by Solomonidou et al. (2011), which I have co-authored, we review the surface features of Ganymede, Europa, Titan and Enceladus, their internal structure and their astrobiological potential.

The role of a planetary field is also crucial for habitability. A strong intrinsic magnetic field protects the atmosphere from the direct interaction with the solar wind and thus, the quick loss through sputtering process is avoided. Additionally, the magnetic field traps high-energy particles into radiation belts, avoiding harmful radiation levels on the surface. The magnetopause of a magnetized planetary body, like the Earth or the possibly early Mars and early Venus, deflects the solar wind plasma globally except for the polar regions, where the solar plasma reaches the ionosphere. In the case of an unmagnetized (or weakly magnetized) body, like the Venus, Mars and Titan, the ionosphere shields the surface from the solar wind flow (e.g. Lammer et al., 2009).

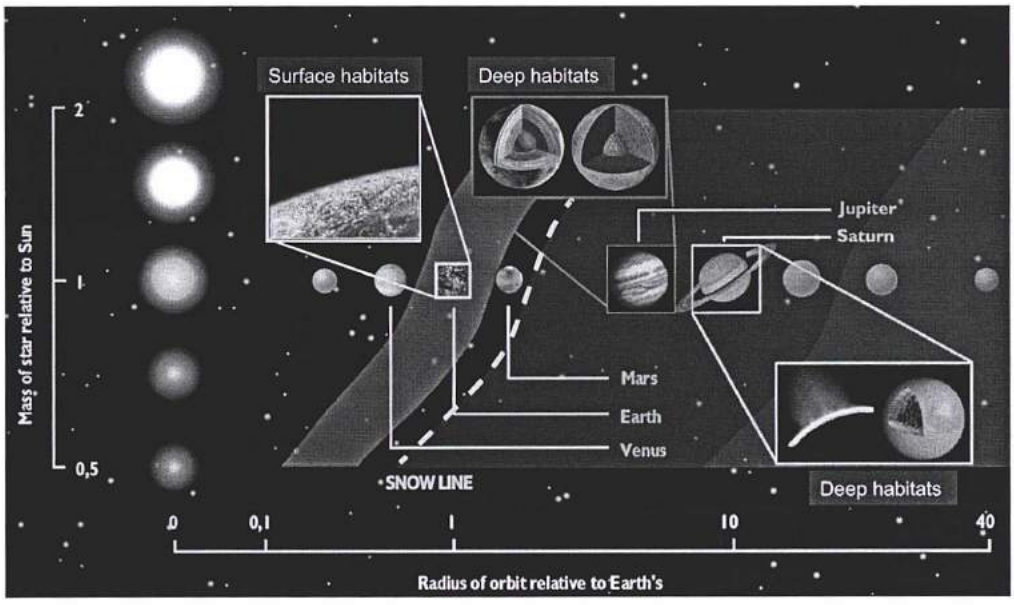

Figure 6. 1 - The habitable zone in our galaxy. Habitability should not be restricted to the places where liquid water may exist at the surface of moons and planets. A much larger domain exists beyond the snow-line, where very large liquid reservoirs can exist below the icy crusts of the moons and planets, see also Lammer et al., 2009. (image credit: http://media.egu2012.eu/media/filer_public/2012/04/19/egu_juice_press.pdf).

Titan, Enceladus and Europa host the proper ingredients for developing (today or in the past) life-friendly conditions and, therefore, the interest for an astrobiological investigation of these planetary objects is enormous. Since 2004, the discoveries of the Cassini-Huygens mission in the Saturnian System have revolutionized our considerations as to whether these bodies could harbor life (now or in the future) or at least provide us with valuable information on the origin and evolution of life on Earth.

6.2 Titan as a possible habitat

Titan is a good candidate for astrobiological studies as its environment exhibits many similarities with the Earth's. Current investigations have shown that Titan fulfills many of life's prerequisites for an organic portfolio due to its atmosphere. Both the remote observations from the Cassini orbiter and the *in situ* measurements from the Huygens probe have significantly advanced our perspective of Titan's system and its potential to harbor the essential ingredients for life.

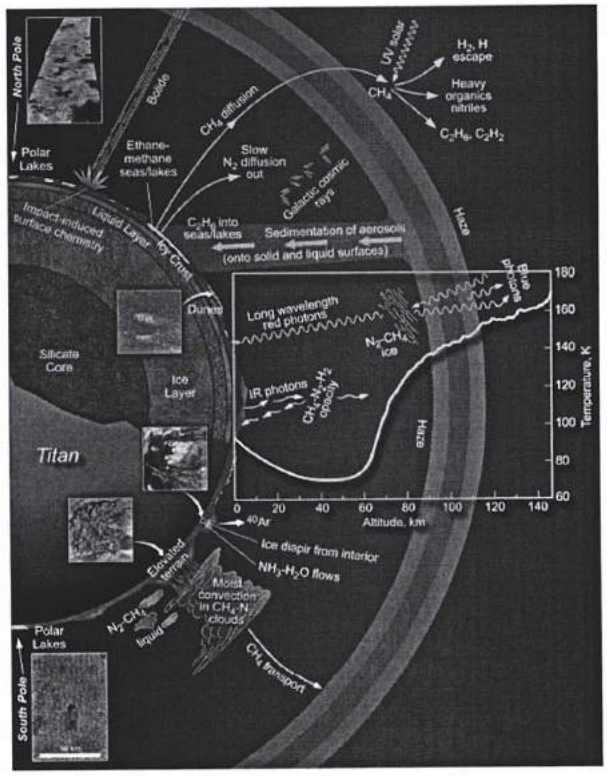

Figure 6. 2 - Schematic illustration of the connections between Titan's interior, surface, atmosphere, and cosmic environment. Images show lakes close to the north and south poles, mid-latitude terrains with dunes, and fluvial features carved in the ice crust. It is based on an original figure from Lunine (1993) with Cassini VIMS, Radar and Huygens DISR images added (adapted from the TSSM *Final Report*).

Titan is indeed a very complex world much like Earth (Fig. 6.2). A thick nitrogen-based atmosphere, four times denser than the terrestrial one, where a rich organic chemistry occurs, shrouds its surface. Besides this rich organic budget, we also find a geologically active surface including lake-like features filled with organic liquid (Stofan et al., 2007). Additionally, past models and recent discoveries reveal that Titan probably contains a vast subsurface liquid water ocean (Lorenz et al., 2008c; Beghin et al., 2009a; Iess et al., 2012).

From the outer limits of its atmosphere, to deep in its interior, Titan is a living planetary body with an evolving environment. Titan, along with comets, is considered as a planetary scale natural laboratory for prebiotic chemistry and a possible habitat for extraterrestrial life (albeit probably different from the terrestrial one). Studying Titan could be beneficial to our understanding of the origin of life on Earth. The low solar influx, the composition of Titan's atmosphere and the possible presence of an internal water ocean, give us the opportunity to study the conditions prevailing on the primitive Earth.

6.2.1 Titan's prebiotic atmospheric environment

Titan can be considered as a huge abiotic factory. The total organic abundance in the atmosphere, the lakes and dunes exceeds the carbon inventory in the Earth's globe (ocean, biosphere and fossil fuel reservoirs) by more than one order of magnitude (Lorenz et al., 2008b).

Its atmosphere consists mainly of nitrogen (98%) and methane at about 2.2% in the upper layers (Waite et al., 2005), 1.4% in the stratosphere and 5% on the surface (Niemann et al., 2010). Interactions among Saturn's magnetosphere and Titan's ionosphere and atmosphere, involving solar EUV and UV radiation, energetic ions and electrons, energetic particles from the Saturnian magnetosphere and galactic cosmic rays, photo-dissociate both nitrogen and methane and trigger a complex photochemistry.

The Cassini Ion and Neutral Mass Spectrometer (INMS) is extensively studying *in situ* Titan's upper atmosphere during low altitude Cassini flybys. INMS showed the presence of many organic species at detectable levels, at very high altitudes (1100 - 1300 km) establishing that this active photochemistry produces complex organic species and nitriles. Extrapolation among the INMS measurements (limited to mass up to 100 Daltons) and Cassini Cosmic Plasma Spectrometer (CAPS) data strongly suggests that high molecular weight species (up to several 1000 Daltons) may be present in the ionosphere (Waite et al., 2007; Vuitton et al., 2009). These observations open new avenues in our perception of the organic content and chemistry occurring in Titan's atmosphere. These detected compounds initiate the process of haze formation starting at about 950 km (Waite et al., 2007) to finally condense out on the surface after descending through the atmosphere.

Through photodissociation in this dynamic evolving environment, the second most abundant atmospheric constituent, methane, is destroyed irreversibly producing a variety of trace gases such as hydrocarbons (e.g. ethane, acetylene, and propane). Furthermore, CH_4 in combination with nitrogen, gives rise to nitriles like hydrogen cyanide, acetonitrile, and cyanoacetylene. Many of these organic products have been detected in the stratosphere (between 70 and 500 km in altitude) by the Cassini Composite Infrared Spectrometer - CIRS (e.g. Flasar et al., 2005, Coustenis et al., 2007; 2010), which has confirmed the Voyager 1/IRIS observations (Hanel et al., 1981; Kunde et al., 1981; Maguire et al., 1981; Kim & Caldwell, 1982; Samuelson et al., 1983; Coustenis et al., 1989a; 1995). These space detections have complemented ground-based (e.g. Hidayat et al., 1997, Tanguy et al., 1990, Kostiuk et al., 1997, Roe et al., 2004) and space-born discoveries of water vapor (Coustenis et

al., 1998) and acetonitrile (Bezard et al., 1993). The chemical inventory in Titan's atmosphere further includes oxygen compounds like CO (Lutz et al., 1983) and CO_2 (Samuelson et al., 1983). Moreover, the presence of water vapor (Cottini et al., 2012a) and benzene (Coustenis et al., 2007; 2010b) has been unambiguously confirmed by the CIRS instrument after the initial ISO discoveries (Coustenis et al., 1998; 2003).

The CIRS instrument investigates Titan's atmosphere since 2004 and will continue to do so up to 2017, when the Cassini Solstice mission ends. The atmospheric chemical composition provided by CIRS sets up constraints for astrobiological studies. Some of these gases can be considered as key molecules in terrestrial prebiotic chemistry, such as hydrogen cyanide (HCN), cyanoacetylene (HC_3N) and cyanogen (C_2N_2). Moreover, HCN is considered as a prebiotic molecule, a precursor of life (see Raulin et al., 2005 and references therein). Determining the origin and evolution of these molecules on Titan could provide us clues on how life began on Earth.

All of the organic compounds, detected in Titan's atmosphere, were also produced in simulation prebiotic experiments. The first simulation of the reactions that took place in the primitive terrestrial atmosphere was the Miller-Urey experiment (Miller, 1953; Miller & Urey, 1959). Miller modeled the Early Earth atmosphere in a glass reactor with a mixture of methane, ammonia, hydrogen and water vapor in the presence of liquid water at 1 bar, following Urey's assumption. He applied electrical sparks to simulate lightning flashes which might have occurred in the early troposphere. The outcome of this experiment was the formation of key organic compounds like formaldehyde and hydrogen cyanide which are considered as precursors of biological amino acids. More complex experiments were conducted later by Sagan & Khare (1971) using UV radiation as the energy source. Two types of products were formed (see Raulin et al., 2005 and references therein): simple volatile organic compounds (i.e. HCN, HC_3N, HCHO) which can participate in prebiotic reactions and macromolecular products, refractory organics, usually named "tholins" (Sagan & Khare, 1979). Tholins represent laboratory analogues of Titan's aerosols and are useful to interpret many observational data which require information on the aerosols. As experimental analogues of Titan's atmospheric particles, tholins also permit the study of the behavior of the aerosols in Titan's conditions in the laboratory. These organics release biological amino acids in an aqueous solution (Khare et al., 1986).

Titan lacks liquid water surface deposits and therefore is an ideal environment to study the processes of chemical evolution under anhydrous conditions (Raulin & Owen, 2002).

Several laboratory experiments have shown the existence of hydrocarbon and nitriles (Thompson et al., 1991; de Vanssay et al., 1995; Coll et al., 1998; 1999).

Schaefer and Fegley (2007) predict that Earth's early atmosphere contained CH_4, H_2, H_2O, N_2, and NH_3, similar to the components used in the Miller–Urey synthesis of organic compounds, often related to Titan's and Enceladus' atmospheric inventory. Furthermore, according to Trainer et al. (2006), the processes that formed the haze on Titan and on early Earth have many similarities with what could have served as a primary source of organic material to the surface.

The Huygens Aerosol Collector Pyrolyser (ACP) experiment provided the first direct *in situ* chemical analysis of Titan's aerosols. The instrument collected haze particles in Titan's stratosphere and troposphere during the probe's descent phase, heated them at different temperatures and sent the produced gases for analysis to Huygens Gas Chromatograph-Mass Spectrometer (GC-MS). The results thus obtained indicated that the aerosols are made of a refractory nucleus, composed of H, C and N atoms (Fig. 6.3), and producing NH_3 and HCN after pyrolysis at 600 °C (Israel et al., 2005).

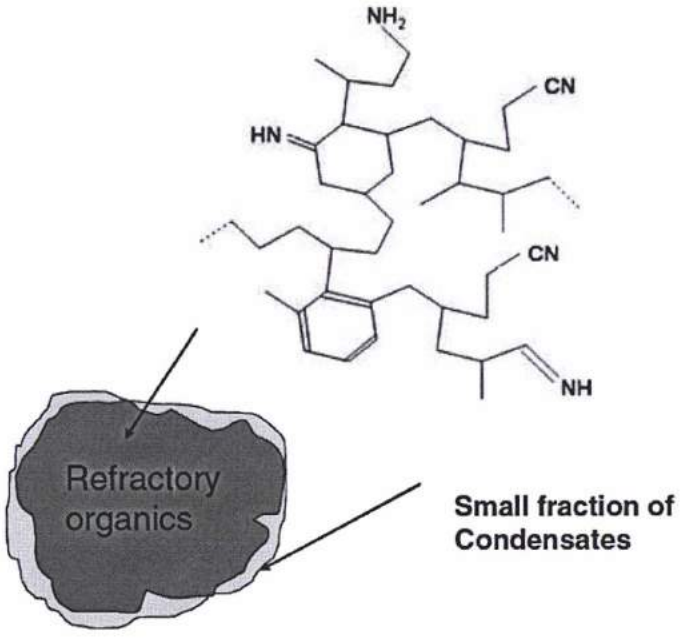

Figure 6. 3 - Composition of Titan's aerosols from the Huygens/ACP (Raulin, 2008a).

ACP results strongly support the tholin hypothesis (Nguyen et al. 2007 and references therein). They also suggest that Titan's aerosols may evolve if in contact with water ice on its surface, and could produce a variety of organics of biological interest, such as amino acids

(Neish et al., 2010; Ramirez et al., 2010). However, Huygens/GCMS did not detect a large variety of organic compounds in the low atmosphere (Niemann et al., 2005). Moreover, we do not know anything yet about the nature and quantity of the condensates, nor of the elemental composition or the molecular structure of the refractory part of the aerosols.

The Cassini-Huygens mission has revealed the details of the organic and methane hydrologic cycles on Titan (Atreya et al., 2006; Raulin, 2008a; Lebreton et al., 2009). Methane on Titan plays the part of water on Earth. It can exist in all three forms : as a gas, liquid and solid, since the mean surface temperature is almost 94 K (Fulchignoni et al., 2005), approaching the triple point of methane.

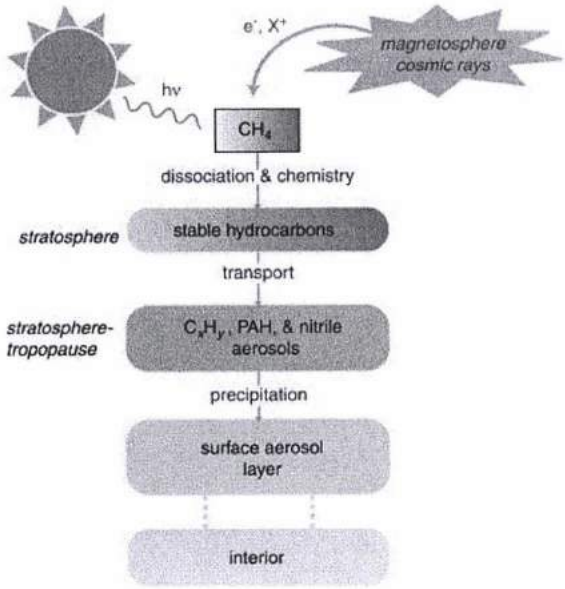

Figure 6. 4 - Illustration of methane sink in Titan (Atreya et al., 2006).

When methane condenses in the form of haze, it is done irreversibly (Fig. 6.4). Taking into account the rate of methane photo-dissociation and the formation of organic products in Titan's atmosphere, methane should therefore have disappeared after 10-100 million years (Atreya et al., 2006). As a consequence, we are either witnessing the extinction of methane or - more likely - looking at a source, which replenishes the methane gaseous abundance in the atmosphere.

Today, on Earth, methane is mainly a by-product of the metabolism of many living organisms. A legitimate question may be if the same occurs on Titan. Huygens/GCMS *in situ* measurements have shown that the carbon-13 isotopic ratio from methane is compatible rather with inorganic values methane, and therefore Titan's methane is not considered of biogenic origin (Niemann et al., 2005; 2010). Although the sinks of atmospheric methane on Titan are

relatively well understood, the major sources of replenishment in the atmosphere are still very model-dependent.

Comparatively to the Earth, Titan lacks both oxygen and hydrogen. However, with several percent of methane in dinitrogen, the atmosphere of Titan is one of the most favorable atmospheres for prebiotic synthesis. Analogies are obvious between the current organic chemistry occurring on Titan and the prebiotic chemistry which was once active on the primitive Earth, prior to the emergence of life (e.g. McKay & Smith, 2005). Although liquid water extents are absent on Titan's surface, both chemistries are similar.

A thick methane-induced organic haze was possibly formed on early Earth. Before the rise of the atmospheric oxygen in the terrestrial atmosphere 2.5 Gyrs ago, it is considered possible that the abundance of methane gas was 10 to 20 times higher than the today's value of 1.6×10^{-6} (Pavlov et al., 2003). If the atmospheric CO_2/CH_4 ratio had become equal to 10 at the mid-Achaean era, an organic haze could have formed on this early environment (Pavlov et al., 2000; DeWitt et al., 2009). This hydrocarbon haze produced the anti-greenhouse effect which reduced the temperature of the atmosphere (Kasting & Howard, 2006). Titan experiences the same anti-greenhouse effect (McKay et al., 1999). The absence of vast amounts of CO_2 on Titan is one of the major differences between the two atmospheric envelopes. On the other hand, hydrogen cyanide and other prebiotic molecules are among the starting materials for biosynthesis. The existence of hydrocarbons, and in particular acetylene and benzene, has really enlarged the borders of photochemical organic products to a degree that is still unknown today on Titan.

Especially, the presence of benzene (C_6H_6) is extremely interesting, as it is the only polycyclic aromatic hydrocarbon (PAHs) discovered on Titan today. PAHs could contribute to the synthesis of biological building blocks in liquid deposits on Titan's surface in low temperature. Recent laboratory experiments confirmed that aromatic compounds could be plausibly produced on icy surfaces (Menor-Salván et al., 2008).

Benzene was first detected at 674 cm^{-1} in Infrared Space Observatory (ISO/SWS) data (Coustenis et al., 2003) with a mixing ratio of 4×10^{-10}. It was then also detected in the thermosphere (950-1150 km) from the analysis of Cassini/INMS data (Waite et al., 2007) and firmly in the stratosphere (100-200 km) at all latitudes by Cassini/CIRS (Flasar et al., 2005; Coustenis et al., 2007; 2010b). Moreover, It has been tentatively identified on Titan's surface by Huygens/CGMS (Niemann et al., 2005).

Titan lacks oxygen and sufficiently high temperatures compared to the primitive Earth. The abundances of hydrocarbons are higher on Titan than those on Earth by a factor of

about 10^2-10^4. Apparently, evolutionary pathways different from the ones operating on Earth must have been followed on Titan and polyphenyls could possibly be created (Delitsky & McKay, 2010).

6.2.2 Titan's active terrestrial-like surface

Titan is an evolving planetary body with several terrestrial shaped surface features distributed globally. The Cassini-Huygens mission has observed a small number of impact craters (Wood et al., 2010), which implies an active surface environment that erased almost all traces of past activity and records. Indeed, as on Earth, sedimentological and meteorological processes, mark the surface of Titan. Erosional processes have been reported on Titan's surface (Jaumann et al., 2008; Lopes et al., 2010). Huygens/DISR recorded well developed rivers, like dedritic networks, close to the probe's landing site at 10°S and 192°W (Tomasko et al., 2005), see Fig. 6.5.

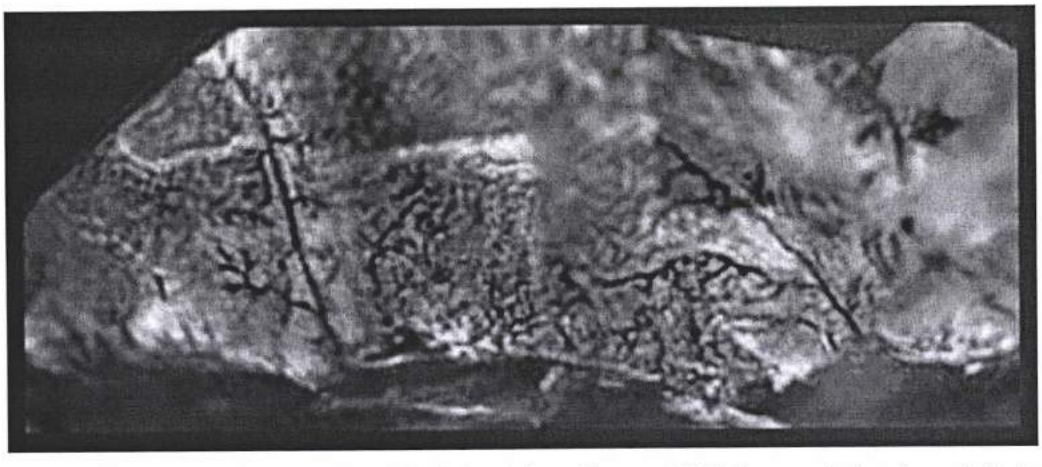

Figure 6. 5 - Channels on Titan's surface (black lines) from Huygens/DISR images during the probe's descent (Tomasko et al. 2005).

Particles from the complex layering of organic aerosols in Titan's atmosphere fall down and deposit on the surface. Cassini/RADAR observations link this aerosol rain to the generation of extensive organic dunes, which shape an equatorial belt (Fig. 6.6).

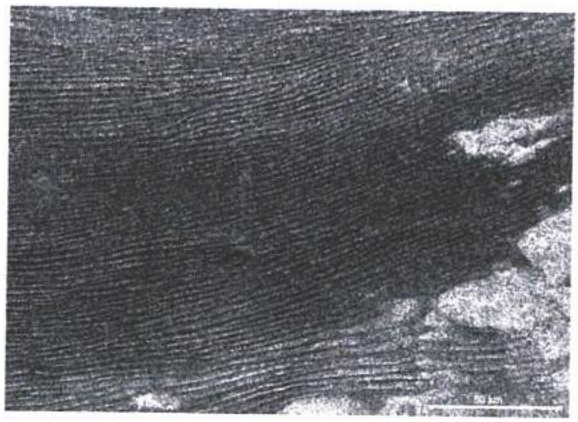

Figure 6. 6 - Linear dunes on Titan from T8 flyby, Oct. 2005 at 8° S, 264° W (Radebaugh, 2009).

Titan's dunes are believed to be composed of ice and organics grains that possibly derive from a combination of the surface ice and the organic aerosols dropped from the atmosphere (Lorenz et al., 2006b; Radebaugh et al., 2008). Hence, the upper atmosphere is linked intimately with the surface and the intervening atmosphere. Despite the low surface temperature at about 94 K (Fulchignoni et al., 2005; Jennings et al., 2009), the organics that accumulate on the surface can evolve once in contact with water ice and may form organic molecules of astrobiological interest.

Cassini/RADAR unveiled large liquid deposits (Fig. 6.7) on Titan's surface distributed at polar regions (Stofan et al., 2007; Hayes et al., 2008; 2010) and the equator (Griffith et al., 2012).

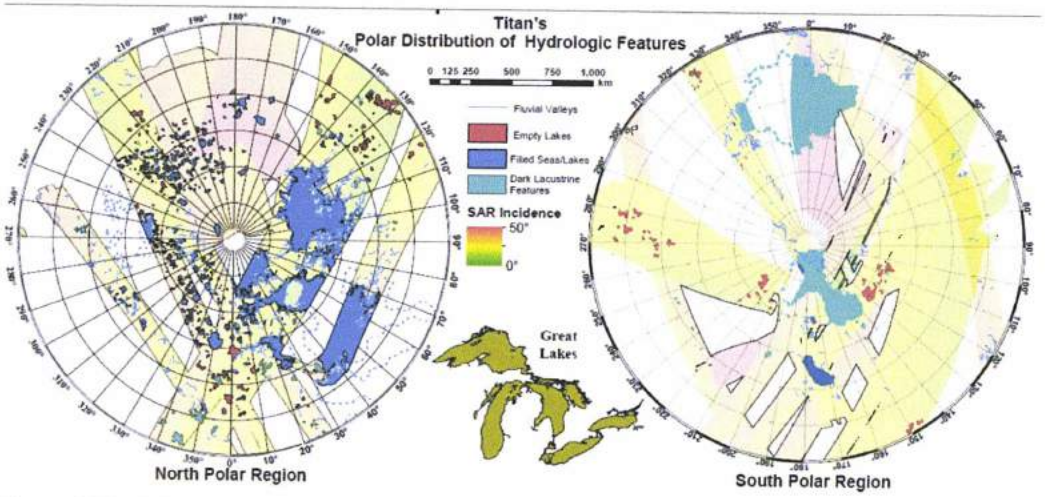

Figure 6. 7 - Map of almost 655 lakes and sea features observed by the Cassini/Radar. These maps are in azimuthal projection at the North Pole of Titan. The projection A (left) shows the radar swath mosaic up to May 2007 flybys. The projection B represents the spatial distribution of mapping units. Lake Michigan is illustrated for comparison (Hayes et al., 2008).

With its lakes and seas, Titan is the only body in the Solar System hosting large liquid bodies on its surface except for the Earth. These very dark radar spots were finally proved to be filled with liquid, most probably with ethane rich mixtures (Brown et al., 2008). The features range in size from less than 10 km^2 to at least 100,000 km^2.

The cosmic rays that reach Titan's surface have a quite low flux (Raulin et al., 1992), which means that, in combination with the low temperature, the reaction rate in the upper layers of the liquid remains very low. The surface liquid deposits can then offer the proper stable environmental conditions for prebiotic chemistry which depends on the long duration, the freezing degree, the dissolved organics and the sedimentary deposition to the lakes' bottom (Tokano, 2009). Pure methane lakes develop and freeze in short geological periods of time, and, therefore, such lakes have no prebiotic significance. Instead, deep lakes (> few hundred meters deep), consisting of a mixture of ethane, methane and nitrogen (Cordier et al., 2009; 2012), can favor stable composition at the bottom with accumulation of acetylene, as the latter sinks being denser than the liquid. The deeper layers do not show any significant movement and create an isolated environment with the proper constituents for prebiotic chemistry.

Cassini Imaging Science Subsystem (ISS) images have allowed for the compilation of a nearly global surface map and the monitoring of both the surface and atmosphere for activity. Repeated south-polar imaging by ISS revealed differences consistent with ponding of hydrocarbon liquids on the surface due to precipitation from a large storm (Turtle et al., 2011).

The large lakes or seas on Titan's surface are primary targets of future lake landers. I have proposed a specific experiment to be incorporated as payload in a future lander mission. The concept of this experiment is to use a series of micro-probes in order to sense the deep isolated layers of the liquid deposit as well as its floor (Bampasidis et al., 2011b). The experiment is fully described in the next Chapter.

6.2.3 Titan's internal ocean

The source of the methane replenishment may lie beneath the lakes in an underground "aquifer" (or "methanofer") system hinted at strongly by Cassini data. The existence of an ocean layer below the surface is crucial for defining the habitability potential of the moon.

According to Lammer et al., 2009, due to this encapsulated water layer, Titan can be considered as Class IV habitat.

Remote sensing data from the Cassini orbiter imply that Titan's interior is partially differentiated. Indeed, Cassini Radio Science (RSS) data provided variations of its degree 2 coefficient gravitational potential, which supports internal density variations (Rappaport et al., 2008).

The Cassini Synthetic-Aperture RADAR (SAR) images, acquired between the October 2004 and May 2007 flybys, revealed a 0.36° faster than synchronous rotation of the moon. Lorenz et al. (2008c) then suggested that the crust is decoupled from the interior by a subsurface water ocean.

HASI-PWA measured the electrical conductivity of the atmosphere during the descent of the Huygens Probe through Titan's atmosphere in January 2005. The sensor detected an extremely low frequency (ELF) radio wave during the descent which was oscillating very slowly for a radio wave (36 Hz) and increased slightly in frequency as the probe reached lower altitudes (Hamelin et al., 2007). The ELF waves on the Earth are reflected by both the surface of the Earth and its ionosphere. However, Titan's surface is a poor reflector because of its low conductivity and so these waves penetrate the interior. The recorded wave could have been reflected by the liquid-ice boundary of a subsurface ocean of water and ammonia predicted by theoretical models (Simoes et al., 2007). Beghin et al. (2009; 2012) interpreted the ELF wave as a Schumann resonance between the ionosphere and a modestly conducting ocean at 30-50 km below the surface.

Cassini's acceleration measurements during flybys from 2006 to 2011 discovered large solid tides caused to Titan by Saturn at about 10 m in height. If the interior is uniform, such solid tides should be only at 1 m in height. Therefore, this finding implies the existence of an internal ocean of liquid water, assuming a depth of 100 km beneath the surface (Iess et al., 2012).

Titan internal structure models also support the presence of such an internal ocean (Grasset & Sotin, 1996; Grasset et al., 2000; Tobie et al., 2005; Mitri et al., 2008). Thermal evolution models suggested that Titan may have an icy crust between 50 and 150 km thick, lying over a liquid water ocean, a couple of hundred kilometers deep, with some amount (a few to 30%, but most likely ~10%) of ammonia dissolved in it, acting as an antifreeze material. This corresponds to a pH of around 11.5. The pressure reaches ~ 5 kbar at 200 km depth, and it could include hot spots reaching -20°C.

Tobie et al. (2005) suggested a layered interior structure, consisting of a rocky core overlaid by high pressure ice, a liquid layer overlaid by low pressure ice and finally a solid icy crust. Fortes (2000) claimed that underneath Titan's icy crust, at 200 km, lies an ammonia–water solution ocean. Mitri et al. (2008) assumed pockets of methane clathrates trapped within an ammonia-water ocean.

The possible Titan's internal structure from the interior to the surface is as follows: (a) a silicate core, (b) a high-pressure water ice layer, (c) an ammonia-rich ocean and (d) an ice layer covered by a crust of organics and ices (Tobie et al., 2005; Fortes et al., 2007; Fortes, 2012), see Figure 6.8. However, the exact inner structure of Titan can only be identified by seismic experiments. For this reason I support the installation of a seismic network on Titan's surface (Bampasidis et al., 2011a; 2012c).

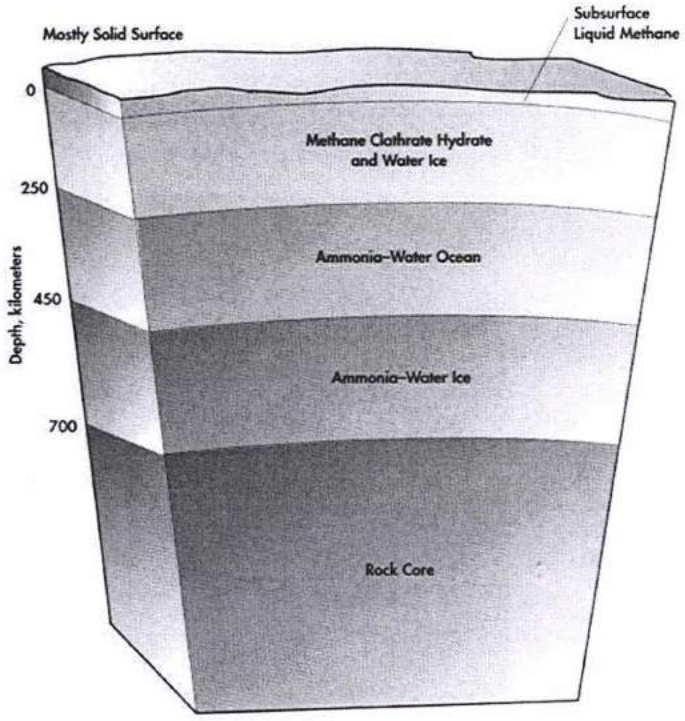

Figure 6. 8 - Model of the interior structure of Titan. The ammonia-water ocean lies at about 250 km in depth, below the crust and the methane clathrate hydrate ice layer (credits: L. Spilker).

Such an internal liquid ocean with the presence of methane clathrates could exsolute and produce overpressure and subsequently the ammonia-water could erupt to the surface leading to explosive cryovolcanic phenomena (Fortes et al., 2007).

Cryovolcanism is an activity that resembles terrestrial volcanic processes following a similar mechanisms and patterns but in cold environmental conditions with different initial

and depositional products. An ice volcano erupts liquids and gases from the interior of an ice shell, when they are denser than the surrounding solid. The required heat for melting the material comes from tidal friction. On Titan, fluid water mobilized and made buoyant by ammonia and/or methane and/or other materials, is ejected from the interior to the surface. Cryovolcanism is a dynamic process that links the interior, the surface and the atmosphere, while it is believed to be a significant source of the methane in the atmosphere on Titan (Tobie et al., 2006).

Cassini data support the presence of cryovolcanism on Titan since traces of cryomagma flows are believed to exist across parts of the surface (Sotin et al., 2005; Lopes et al., 2007). Several regions have been proposed to change reflectance on Titan's surface so far, with the three more often cited: Tui Regio (20°S, 130°W), Hotei Regio (26°S, 78°W) and Sotra Facula (12.5°S, 39.8°W) (Barnes et al., 2006; Soderblom et al., 2007a; Nelson et al., 2009a; 2009b). These features are wide crater-like with lobate flows originate from them (Soderblom et al., 2009; Lopes et al., 2010).

The theory of methane clathrates trapped in an internal liquid ocean enhances the astrobiological interest. According to the "clathrate gun" hypothesis, potential movement and rise of the temperature in an underground liquid deposit could trigger the sudden release of methane from its clathrate buried in permafrost or seabeds (Kennett et al., 2003) or an ocean like on Titan's case. Further temperature enhancement leads to further methane clathrate destabilization which could easily trigger cryovolcanic eruptions (Kennett et al., 2003). Such process on Titan could increase the temperature values, creating an environment more favorable for life to exist.

6.2.4 Is it possible to find life forms in Titan's environment?

Water is frozen solid on Titan's surface and much too cold to support terrestrial-type life. The list of liquid candidates, present on the surface, includes liquid methane and related molecules like ethane. While liquid water is widely regarded as necessary for life, it is not a strict requirement. The new hydrogen findings on Titan are consistent with conditions that could produce an exotic, methane-based life form, but do not prove its existence.

McKay and Smith (2005) assumed the possibility for a different form of life to exist in liquid hydrocarbons of Titan. Such a methanogenic life form could consume H_2 instead of O_2 that could be measured in the lower atmosphere. Towards that hypothesis, Strobel (2010) and

Clark et al. (2010) focused on the complex chemical activity on the surface of Titan, based on Cassini data.

According to Strobel (2010), hydrogen flows down through Titan's atmosphere and then disappears on the surface, resembling the terrestrial oxygen consumption. On Titan, the hydrogen as byproduct of UV dissociation in the upper atmosphere should be distributed fairly evenly throughout the atmospheric layers. Strobel (2010) described a downward flow of hydrogen molecules to the surface at a rate of about 10,000 trillion molecules per second, similar to the escape rate. Hydrogen cannot be stored in an underground space on Titan. The surface is too cold to drive chemical processes with a catalyst to convert hydrogen molecules and acetylene back to methane. Only an unknown mineral could provide the net energy needed for such reactions, acting as the catalyst on Titan's surface. The McKay and Smith (2005) assumption for methanogenic life, which consumes the hydrogen from the atmosphere, can explain its disappearance.

Methane-based life forms have not been yet detected anywhere, though there are liquid-water-based microbes on Earth that thrive on methane or produce it as a waste product. At Titan's low temperatures, a methane-based organism would have to use a substance that is liquid as its medium for living processes, but not water itself.

The effectiveness of methane as a medium for life compared to water or ammonia is under consideration. Water enables easier transport of substances in a cell than methane does, since it has higher solubility. On the contrary, methane's lesser chemical reactivity favors the easier formation of large structures corresponding to proteins (Benner et al., 2004). In addition, the possible existence of cryovolcanic activity suggests higher temperatures within the ocean and the volcanic conduit where heat transfer between the interior and upper layers would be critical in creating and sustaining any kind of subsurface oceanic life (Grasset et al., 2000).

6.2.5 Concluding remarks for Titan's astrobiological case

Taking into account all the characteristics described above, the prebiotic potential of Titan is significant. Titan seems to be an ideal planet-size laboratory for increasing our knowledge of the evolution of the Earth's atmosphere. However, the full extent of current geologic activity is still under investigation.

As we have mentioned in the Book Chapter by Coustenis at al. (2012), Titan, although it presents many similarities to the primitive Earth, should not be considered as a frozen analogue. It is an evolving planetary body with an active complex chemistry occurring from the upper atmosphere to its surface. One of the by-products of this chemistry, the macromolecular material, is included in atmospheric refractory organics, the Titan's tholins, which are eventually deposited on the solid surface (dunes) or in the lakes. Both laboratory and theoretical works have provided an assumption of the composition of these compounds.

Laboratory experiments show that the accumulation of these aerosols on the surface, if they are in contact with liquid water, can release many compounds of biological interest, such as amino acids (Khare et al., 1986). Similar processes could be particularly favorable in areas of Titan's surface where cryovolcanism may occur.

Titan lakes fulfill the habitability criteria as far as the presence of carbonaceous material and the stable environment. McKay & Smith (2005) suggested that methanogenic life on Titan's surface liquids could derive the energy they need by consuming hydrocarbons. The isolated environment of Titan's deep lakes can offer the proper conditions to increase the concentration of high order organics in their deep layers and their floor.

Therefore, a dedicated future mission to Titan's lakes could, in principle, investigate the presence of organic material as well as the thermodynamic conditions of their environment. If no vertical convection occurs within the deep layers of the lakes, the local environment is favorable for maintaining the formation of biological building blocks and their chemical evolution. The experiment I have proposed, which incorporates Micro-Electro-Mechanical Systems (MEMS) to be included as payload of a future Lake Lander probe, could measure the temperature, the pressure of the liquid and produce a 3D topographic map of the bottom (Bampasidis et al., 2011b). Any temperature inversions would indicate vertical movement of the liquid. This experiment is described in detail in the following Chapter.

The existence of an internal water-ammonia ocean is suggested both by modeling and by Cassini-Huygens mission results. The question is whether there are exchanges between this ocean and the surface (and eventually atmosphere) system. Are the lakes such a link? The possibility of life signs in the internal liquid water deposit cannot be excluded. Models have also predicted that during the first tens millions of years after Titan's formation, its global ocean was in direct contact with the atmosphere on one side and with

the bedrock on the other. This structure may provide conditions favorable for an efficient prebiotic chemistry towards the emergence of life. However, similar conditions are not incompatible with life as we know it on Earth (Fortes, 2000; Raulin, 2008a; 2008b).

Astrobiological studies on Titan can also provide insights regarding the future of life on Earth. On Titan a methane cycle occurs similar to the water cycle on Earth. However, the source of methane atmospheric budget replenishment is still unknown. Titan can help us understand the climate change in a planetary atmosphere when the main compound of a global cycle is rapidly lost. As it is mentioned in the Nixon et al. white paper[21], which I co-authored, climate change studies on Earth showed an increase in the mean surface temperature of the planet. If such an increase continues, the evaporation of the water ocean will also increase. Water vapor will reach the stratosphere where it will be irreversibly photolyzed, as H_2 escapes to space. CO_2 levels will rise, and the Earth will heat up and dry out (e.g. Li et al., 2009). Therefore, Titan studies can provide crucial information about the atmospheric equilibrium on the Earth.

[21] Submitted to National Research Council of US in response to the Planetary Science Decadal Survey Call in 2009.

6.3 Enceladus, an active small satellite

Enceladus is the sixth satellite of Saturn in size, quite small compared to Titan, with a mean radius of 252 km (a tenth of Titan's). The first images of the satellite were taken by the Voyager space missions, which illustrated a highly reflective surface with few impact craters implying for a young surface. V1 also showed that the satellite is orbiting within the extended Saturn's E-ring (Smith et al., 1981). Its mass is 1.08×10^{20} kg, while its mean density is 1,610 kg/m^3 (Jacobson et al., 2006). It orbits Saturn at 3.95 R_S (Saturnian radii, R_S=60,330 km, e.g. Postberg et al., 2008) between the moons Mimas and Tethys. Due to the small mass and the weak gravitational field, the satellite has a negligible atmosphere (Parkinson et al., 2007).

The surface of Enceladus is fully covered by ice, having albedo values of about 1, the highest in the Solar System (Fig. 6.9). Its mean surface temperature is about 75 K. The surface features are mainly smooth and cratered terrains, rifts, ridges, grooves, escarpments and extensive linear fractures in the South pole. Cassini/VIMS indicates that the surface consists of CO_2 and organics (Brown et al., 2006).

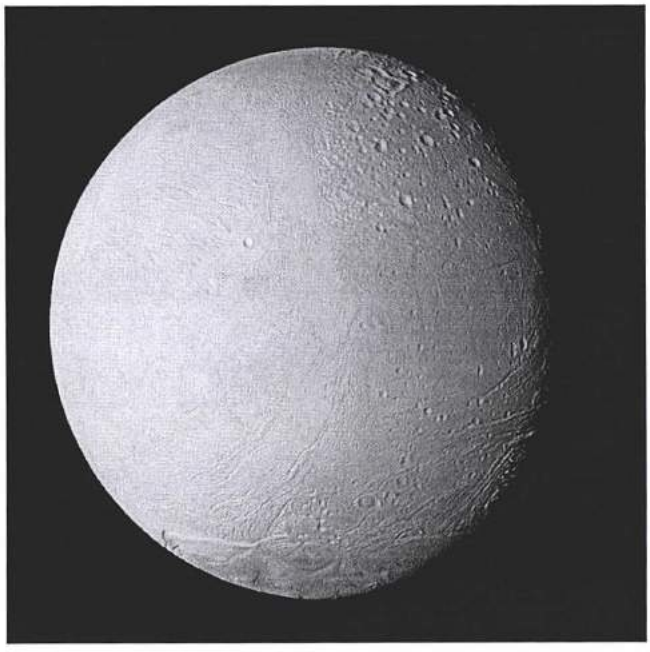

Figure 6. 9 - Enceladus from Cassini/ISS. It is a mosaic of the moon's leading (or western) hemisphere. The southern polar regions are geologically younger than the northern ones. This image was taken during the November 21, 2009 flyby over Enceladus (credits: PIA11684, NASA/JPL/Space Science Institute).

The Cassini-Huygens mission has significantly improved our knowledge of Enceladus during 19 close flybys so far. One of the most important discoveries of Cassini was the existence of large plumes ejected from its south polar region as firstly discovered by its Magnetometer (MAG) (Dougherty et al., 2006). This finding is relevant to astrobiology since it implies a complex organic chemistry occurring in the interior of Enceladus along with the appropriate thermal energy, in the presence of liquid water at short distances from the surface.

6.3.1 Enceladus plumes and habitability

By studying Enceladus, an example of active cryovolcanism in icy satellites, we can understand the processes that shape the surfaces of other icy moons. These processes include tidal heating, possible internal convection, cryovolcanism, and ice tectonics. Moreover, the plume source region on Enceladus samples a warm, chemically rich environment that may facilitate complex organic chemistry and biological processes.

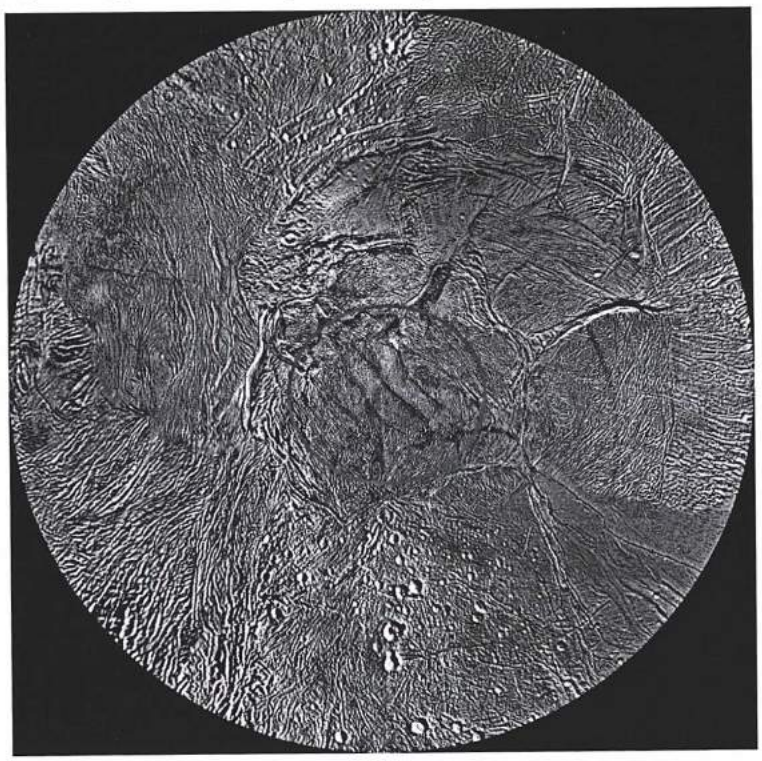

Figure 6. 10 - The south pole of Enceladus with the linear depressions "Tiger Stripes" indicated by the red circle (captured by Cassini/ISS). The plumes are ejected from these fractures (credits: PIA12566, NASA/JPL/Space Science Institute, Porco et al. 2006).

The geyser-like features on Enceladus are ejected from its south pole from a series of sub-parallel fractures named as "Tiger Stripes" (Fig. 6.10), spewing a series of jets more than 1000 km into space, see Figure 6.11 (Porco et al., 2006; Spencer et al., 2006). Their shape is linear while their structure typically about 500 m in depth, 2 km in width and around 130 km in length, flanked on both sides by prominent 100 m high ridges. Cassini/CIRS mapped higher temperatures from these linear features compared to the surrounding area (Spencer et al., 2006). The mass production rate of the plume gas has been estimated to be at about 150 kg/s from occultation data (Tian et al., 2007). If this value remains from the formation of the satellite, it is sufficient to remove a significant fraction (~20%) of Enceladus' mass (Kargel, 2006).

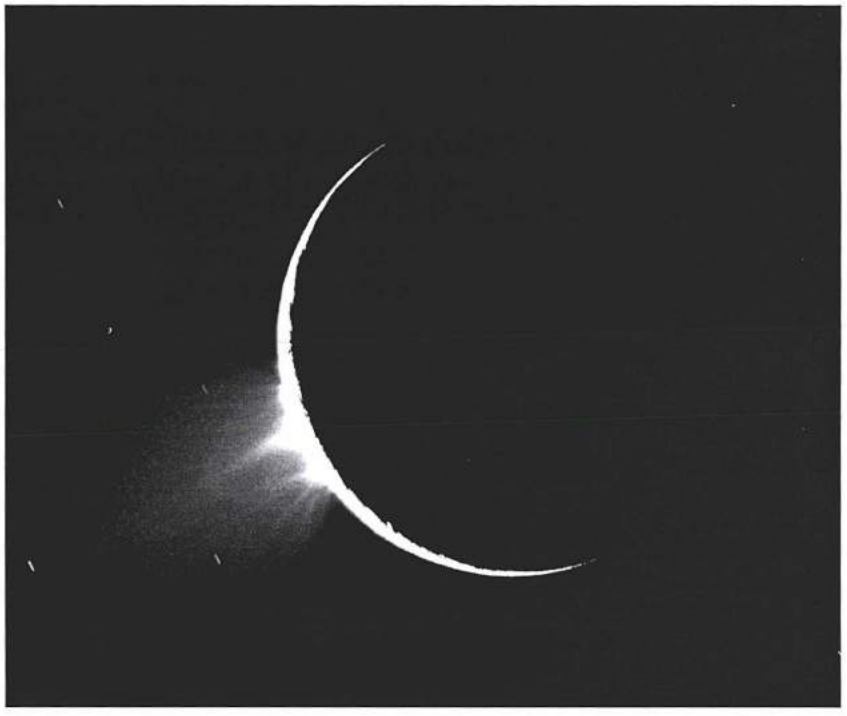

Figure 6. 11 - Enceladus' plumes ejected from the south polar region by Cassini/ISS (Porco et al., 2006).

The Cassini Cosmic Dust Analyzer (CDA) showed that the plumes' columns consist of small ice grains with low concentration in salt far away from the satellite. Close to the surface, large grains enriched with sodium and potassium dominate the plume's column (Postberg et al., 2011).

Cassini/INMS data identified H_2O vapor as the predominant component of Enceladus' plumes, CO_2 as the second most abundant, in addition to methane and trace quantities of acetylene and propane and other organics. During the flyby of 9 October 2008, Cassini dived

into the south polar plume at a distance of 339 km and INMS recorded the presence of ammonia and other various organic compounds, deuterium and ^{40}Ar, as well as complex organics like benzene and other species such as methanol and formaldehyde (Waite et al., 2009).

The Cassini Ultraviolet Imaging Spectrograph (UVIS) observed an occultation of the Sun by the plumes of Enceladus on 18 May 2010. Water vapor was confirmed as the dominant component, while the upper limit for N_2 was less than 0.5%. Combination of the results of the three Cassini instruments (CDA, INMS and UVIS) supports the existence of an internal liquid reservoir with gas escaping through the narrow channels in the Tiger Stripes region (Hansen et al., 2011). Cassini/CAPS detected positive water group ions (Tokar et al., 2009), water-cluster molecular ions (Coates et al., 2010) and charged nanometer-sized grains (Jones et al., 2009; Hill et al., 2012) in the plumes of Enceladus. Moreover, Cassini /RPWS-LP detected a cold dense plasma in the same material (Shafiq et al., 2011).

The chemical composition of the plume and surface material of Enceladus suggests the presence of a very hot interior, for such a frozen satellite, implying internal temperatures on the order of 500-800 K. Such hot interior decomposes ammonia into N_2 and drives reactions with hydrocarbons (Matson et al., 2007).

Several models have been proposed so far regarding the geyser mechanism occurred on Enceladus' surface, which can be divided into two categories. The first assumes that an underground ocean forms the plumes (Schmidt et al., 2008; Tobie et al., 2008; Postberg et al., 2009; Behounkova et al., 2012; Matson et al., 2012), see Figure 6.12, while the second one suggests that the ejected material originates from warmed, melted or crushed ice by tectonic motions (Nimmo et al., 2007), see Figure 6.13. Most of the models suggest the existence of a liquid water environment underneath the Tiger Stripes.

Since Enceladus is not in hydrostatic equilibrium (Schubert et al., 2007; 2010) a simple and very general stratigraphic interior is being suggested which consists of a 169 km rocky core overlain by an icy 82 km mantle (Barr & McKinnon, 2007; Fortes et al., 2007; Schubert et al., 2007).

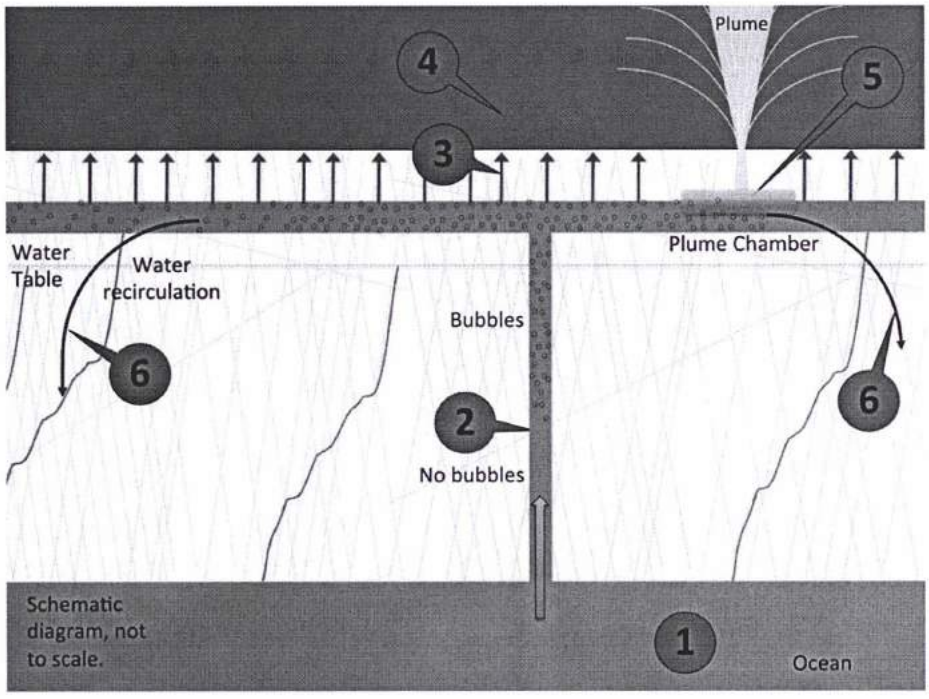

Figure 6. 12 – Schematic model of the interior mechanism occurring in Enceladus' south polar region: #1 indicates the internal water ocean, #2 shows the fracture from where the water ocean exsoluted gases rises towards the surface. #3 indicates thermal anomalies where heat from the water is being conducted through ices to the surface and radiated to space (#4). The label 5 marks the plume chamber which feeds the geysers. The label 6 indicates the return of the water back to the ocean after the ejection of the volatiles (adapted from Matson et al. 2012).

Figure 6. 13 - Internal model of Enceladus based on tectonic meltwater. Tidal flexing causes heating along the fractures (Nimmo et al., 2007).

Enceladus fulfills most of the habitability prerequisites. It could be hosting a large water ocean in its interior enriched with organic compounds and energy sources as well. The

difference from the terrestrial-type large oceans are the lack of sunlight, oxygen compounds and the organics produced on a surface crust environment. Similar environments and ecosystems exist and evolve on Earth as well, like the one located deep inside South Africa's surface, where sulfur-reducing bacteria consume hydrogen and sulfate, produced by radioactive decay (McKay et al., 2008; Muyzer & Stams, 2008).

Additionally, life forms existing in extreme terrestrial environments like the magmatic volcanic rocks, which are produced through metasomatism. Metasomatism is the change of the chemical composition of rocks, when they interact with fluids. The metasomatosis of the volcanic rocks under the presence of water produces methanogens of hydrogen on which the primary productivity is based on. The question is if the methane detected by Cassini in the plumes has a biological related origin (McKay et al., 2008).

6.3.2 Conclusions and questions about Enceladus' astrobiological potential

Enceladus, Saturn's most active moon, is the place in the Solar System System where we have observational evidence of a habitable environment already occurring in terms of energy, organics, stable environment and liquid water. Despite its small size, the moon can possess sufficient dynamical energy to drive a plume ejection 1000 km in space out of the moon's south pole and eventually feed the outer E-ring of Saturn (Postberg et al., 2009). In a model by Cooper et al. (2009), the astrobiological parameters that support life on Enceladus are evaluated as higher than for Europa due to a less extreme state of oxidation and greater residual abundance of organics. The quest of habitability on Enceladus includes: the presence of liquid water (either in a subsurface ocean, in the plume vent regions, or elsewhere); the extension and long-term stability of the water liquid; the interactions of the liquid reservoir and the surface; the degree of thickness and uniformity of the ice crust; the available energy sources and finally the presence of any biomarkers or biological building blocks.

6.4 Jupiter's satellites as astrobiological targets: Ganymede, Europa and Callisto

Since we lack long-term remote and *in situ* observations of these icy moons, comparative studies operate supplementary to our perspective of these worlds. In our paper, Solomonidou et al. (2011), we study the surface aspects of Jupiter's Ganymede and Europa and Saturn's Titan and Enceladus and try to find which of their similarities are connected with astrobiological implications. In this section, I have expanded the comparison among the Saturnian moons Titan and Enceladus and the Jovial Ganymede and Europa by considering also Callisto.

6.4.1 Ganymede, the biggest satellite of the Solar System

Ganymede is the biggest satellite in our Solar System with a diameter of 5,272 km, a mass of 148.2 x 10^{21} kg and a density of 1940 kg/m^3. It orbits Jupiter at 1.07 million km and its surface has a mean temperature of about 110 K. It is the only moon that possesses a magnetosphere (Kivelson et al., 2002), generated by currents flowing in a conducting liquid, which indicates the existence of the deep ocean. It is covered by a thin exosphere consisting mainly of oxygen in the forms of O_2, O and O_3 (Noll et al., 1996; Calvin & Spencer, 1997; Hall et al., 1998).

Most of Ganymede's surface coverage displays dark regions which are filled with impact craters (Prockter et al., 1998) and brighter regions covered by terrains curved by tectonic ridges and grooves (Fig. 6.14) (Pappalardo et al., 1998a; Patterson et al., 2010). Several non-water ice materials have been found in the surface of the satellite such as $MgSO_4$ and possibly Na_2SO_4 (McCord et al., 1998a; 2001).

Figure 6. 14 - Natural color view of Ganymede from Galileo/SSI. The picture was taken during the first Galileo encounter of the satellite. North is on the top of the image and the Sun illuminates the moon from the right. The bright spots are young impact craters and their ejecta. The dark areas are geologically older, while the light areas are younger, tectonically deformed regions. The brown/gray color is due to mixtures of rocky materials and ice (credit: NASA/JPL-PIA00716).

Galileo gravitational measurements showed that Ganymede is fully differentiated into a core and a mantle (Anderson et al., 1996). It consists of an iron-rich sulfide core in liquid state, a silicate-rich mantle covered by an icy crust up to 100 km (Fig. 6.15).

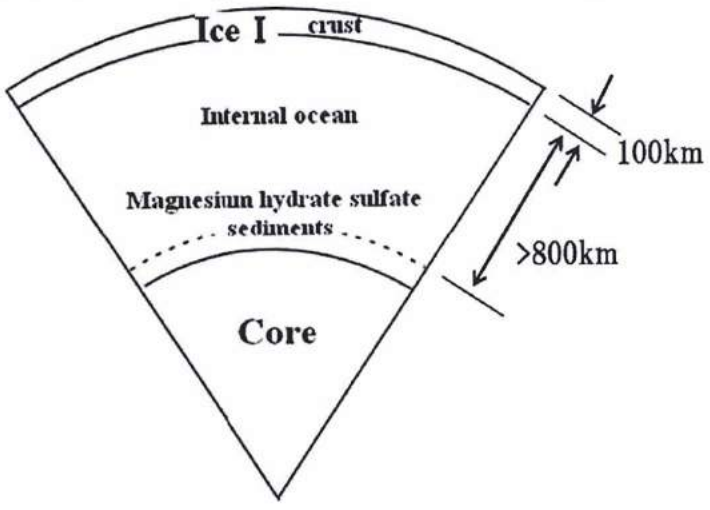

Figure 6. 15 - The interior structure of Ganymede (adapted by Nakamura & Ohtani, 2011).

A liquid ocean possibly exists 200 km below the surface, between layers of ice (McCord et al., 2001). Reflectance spectra from Galileo/NIMS discovered hydrated minerals on

Ganymede's surface, similar to Europa's (McCord et al., 1998a), derived from the encapsulated internal ocean.

6.4.2 Europa as a habitat

Jupiter's Europa is the smallest of the four large Galilean satellites with diameter of 3,122 km, a mass of 48 x 10^{21} kg and a density of 3,010 kg/m^3 (Fig. 6.16). It orbits Jupiter at 671,000 km and its surface has a mean temperature of about 100 K.

Figure 6. 16 - The training hemisphere of Europa from the Galileo mission in natural color. Dark brown areas represent rocky material from the interior. The fractures in the crust are also shown (credits: Galileo/SSI-PIA00502, NASA/JPL/DLR).

As shown by the Galileo mission, the lack of many impact craters on its surface (Pappalardo et al., 1998b) indicates that it is relatively young and active,. It is mainly composed of water ice (Dalton, 2010; Dalton et al., 2010) and the most typical surface structures are linear chains, the *lineae* (e.g. Figueredo & Greeley (2004)). Reflectance spectra from Galileo's Near Infrared Mapping Spectrometer (NIMS) showed that the surface of

Europa also contains hydrated salt minerals such as magnesium sulfates and sodium carbonates (McCord et al., 1998b).

Hubble Space Telescope observations showed that Europa possesses a tenuous exosphere mainly consisting of molecular oxygen (Hall et al., 1995) which has not biological origin. However, it may interact with the possible internal liquid ocean and thus it may have biological significance.

The interior of Europa is differentiated as reported from Galileo gravitational data (Anderson et al., 1997). It is primarily composed of silicate rock (Sohl et al., 2010) and an iron-rich core (Anderson et al., 1998). Galileo's magnetometer data showed that Europa has an induced magnetic field, which suggests the presence of a subsurface conductive layer (Kivelson et al., 2000). The layer is likely a salty liquid water ocean decoupled from the icy crust no more than 100 km thick (Fig. 6.17) (Schenk & McKinnon, 1989; Zimmer et al., 2000; Schenk & Pappalardo, 2004). The big difference compared to Ganymede, the large satellite, is that the liquid layer is almost certainly in direct contact with the silicates.

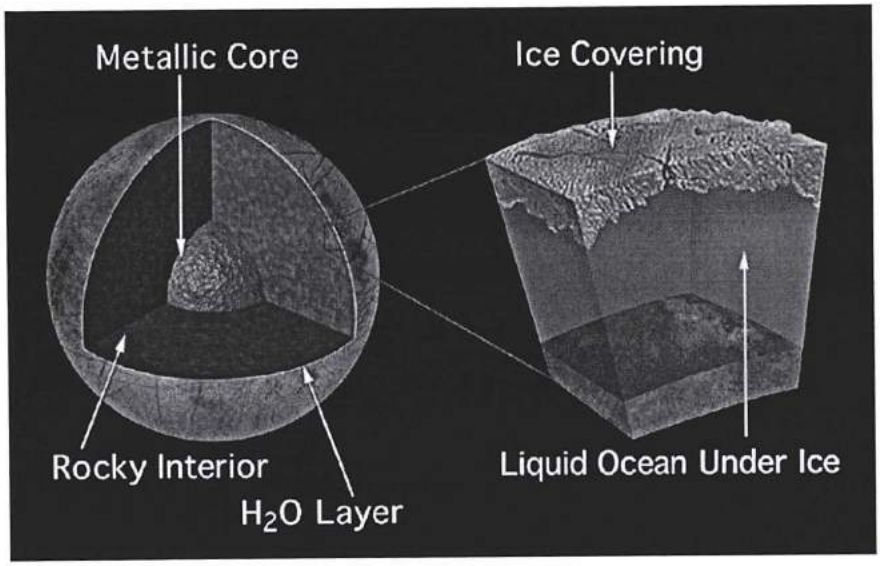

Figure 6. 17 - (left) The layered interior of Europa and (right) a proposed model for its interior suggesting a thin icy crust of 200 km (credits: NASA/JPL/Galileo/SSI-PIA01669).

Jupiter probably generates large tidal waves on Europa, due to its small but non-zero obliquity, which keep the ocean warm (Tyler, 2008). The composition of this internal ocean is different from the terrestrial ones. The Earth's ocean major component is sodium chloride, while Europa's should have a highly conductive component such as magnesium sulfate (McCord et al., 1998b; Fanale et al., 2001), or sulfuric acid hydrate (Carlson et al., 2005).

Recent analyses of Galileo images suggest that ice-water dynamics are active. Surface features may be formed from exchanges between the ice shell and shallow subsurface water deposits. This mechanism provides transfer of energy and nutrients between the surface and the interior, increasing the associated habitability potential (Schmidt et al., 2011).

6.4.3 Callisto, the heavily-cratered moon

Callisto is the third largest moon in the Solar System after Ganymede and Titan with a diameter of 4821 km, while its mass is at 107.6 x 10^{21} kg and its density at 1830 kg/m^3. Its surface has a mean temperature of about 134 K (Fig. 6.18). Of the four Galilean moons, Callisto orbits farthest from the giant planet at 1883 x 10^3 km (Anderson et al., 2001). Due to its orbital distance, Callisto is less affected by the magnetosphere of Jupiter compared to the other Galilean satellites (Cooper et al., 2001) and it has a tenuous carbon dioxide exosphere (Carlson, 1999).

The surface of Callisto is heavily cratered which means that no surface processes occur on it (Greeley et al., 2000).

Figure 6. 18 - The only complete global color image of Callisto obtained by the Galileo orbiter. Callisto is uniformly cratered (the bright scars on the darker surface) (credits: Galileo/SSI/PIA03456 NASA/JPL/DLR).

Callisto is very similar to Ganymede, but it is only partially differentiated and does not have an intrinsic field (Spohn & Schubert, 2003).

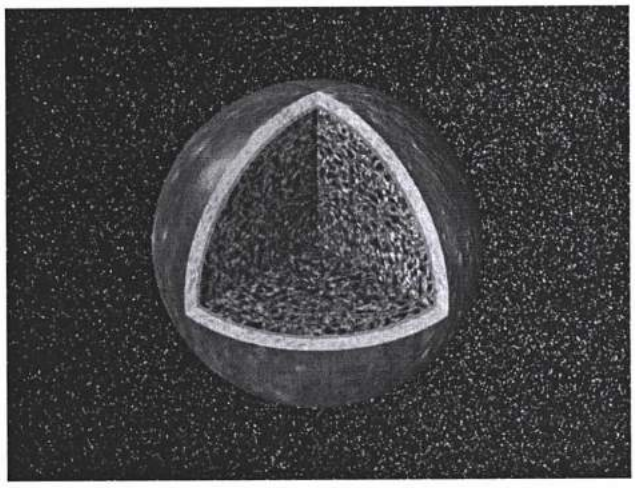

Figure 6. 19 - The interior of Callisto from Galileo data. An internal ocean lies probably beneath the 200 km icy crust (credit: NASA/JPL/PIA01478).

The thickness of Callisto's icy lithosphere is between 80 and 150 km (6.19). It possesses a deep water-ammonia ocean similar to Ganymede with a thickness between 70-90 km beneath the crust indicated by Galileo magnetometer and gravity data (Khurana et al., 1998; Zimmer et al., 2000; Spohn & Schubert, 2003; Kuskov & Kronrod, 2005). Beneath the ocean the interior is composed by rock and ice and the rock percentage increasing by the depth without having a core (Nagel et al., 2004).

6.4.4 Habitability of Ganymede, Europa and Callisto

Surface properties of the satellites provide indications about their interior structure. Callisto has a dark, geologically old, heavily cratered ice surface and from its rotational data that its density is equally distributed (Anderson et al., 2001). The rotation measurements of the three inner Galilean moons (Ganymede, Europa and Io) indicate differentiated interiors. Moreover, Ganymede's surface features indicate possible past tectonic processes. Europa probably hosted more recent tectonic movements, with a thinner ice crust. The nearer a moon is to Jupiter the hotter its interior. Callisto's internal structure may be the original structure of all the moons.

The gravitational pull of Jupiter induces stresses to its moons and as a result their interiors are heated. Except for Callisto, the tidal heating melts the interior ice, allowing for rock and iron to sink downwards and for water to lift to the surface. Ganymede has a thick ice crust. Europa experiences stronger tidal heating and has a thinner crust. The geological and structural data of Ganymede and Europa provide promising worlds for astrobiological studies.

Gravitational forces from Jupiter and other Galilean satellites cause tidal friction on Europa and provide the proper energy for the internal ocean to remain in liquid state. Large amounts of energy at the bottom the ocean could form hydrothermal vents like the ones seen on Earth. Such vents can provide the proper temperature status and ingredients to support life forms. Greenberg (2010) suggested complex aerobic organisms could exist on Europa, providing evidence of oxygen concentration within the ocean greater than that of the Earth's. Since the salts' concentration is large, only extremophile organisms (like halophiles) could survive (Cooper et al., 2001; Marion et al., 2003).

Ganymede is colder than Europa, which lowers possibly its habitability potential. However, Ganymede possesses an intrinsic magnetic field which protects the satellite from incident radiation and thus, provide the necessary tools to concentrate biological building block ingredients (Trinks et al., 2005). Its dark terrain is of astrobiological interest due to the existence of organic materials (McCord et al., 1998a). Additionally, nutrient-rich material provided from magmatic events could exist in the internal ocean (Barr et al., 2001).

Europa does not have an intrinsic magnetic field, but its icy crust provides some natural shielding to the sub-surface liquid ocean, protecting it from direct exposure to the intense radiation environment of Jupiter's magnetosphere.

6.5 Conclusions

Earth has drastically evolved since its formation 4.5 billion years ago and most of the traces of the initial environmental conditions have been erased. It is therefore difficult to retrace the processes of the emergence of life on Earth around 4 billion years ago, or even of the formation and evolution of its atmospheric organic content. Astrobiology could provide crucial information from extraterrestrial locales with similarities to our planet's early stages.

According to the Lammer et al. (2009) classification, Saturn's Titan and Enceladus and Jupiter's Ganymede, Europa and Callisto can be considered as habitats, since they have encapsulated internal water deposit. The question is if these moons have compositional, structural and other similarities among them or compared to the Earth with astrobiological implications. In Coustenis et al. (2012) and in Solomonidou et al. (2011) we try to provide answers. Titan's surface differs significantly from Enceladus and the other Galilean moons due to the presence of the thick atmosphere. Erosional processes act and shape the surface globally, resulting a flat topography (Lorenz et al., 2011).

The surface of Titan and the other outer planets' satellites appears initially as an unfavorable place for life, at least for terrestrial-type life. The absence of liquid water on the surface makes them unlikely to support any terrestrial-type life. If liquid water exists under the surface, it is not in direct contact with a silicate core (with the exception of Europa), which is isolated from the subsurface ocean by a layer of a high-pressure ice phase.

However, exotic types of life could be found in the internal large reservoirs of the outer planets. Ganymede, Callisto, Europa, Titan and Enceladus have encapsulated water oceans, which may maintain an exotic type of life, using liquid hydrocarbons as solvents (McKay & Smith, 2005). According to Stoker et al. (1990), terrestrial bacteria can satisfy their energy and carbon needs by consuming tholins, the laboratory analogue of Titan's aerosols.

On the other hand, living organisms have been found on Earth under extreme environmental conditions in deep oceanic layers. Such environments, with low-temperature and high-pressure conditions, are the cold seeps and the hydrothermal vents (e.g. Ritt et al., 2010). Single-cell Archaea and Eubacteria microbes have been discovered to consume methane and hydrogen sulfide from seep and hydrothermal vents. Additional laboratory experiments and in situ studies of deep subglacial isolated lakes in Antarctica (Kapitsa et al., 1996) would improve our understanding in this field, as the physical properties of deep subglacial lakes resemble those found on outer planets' moons (Bulat et al., 2009).

The satellites of the giant planets like Ganymede, Callisto, Europa, Titan or Enceladus are possible habitable environments and astrobiological targets. According to current models of internal structure, the existence of subsurface oceans is expected for most of the icy moons of the outer planets (e.g. Sohl et al., 2010, Schubert et al., 2010 and references therein). The common properties that need to be satisfied on all bodies in order to sustain a liquid subsurface ocean are (Solomonidou et al., 2011): (a) The heat

production, which mainly originates from radiogenic heating or other triggering mechanisms (e.g. McKinnon, 1999, Tobie et al., 2005); other heat sources are the dissipation of tidal energy due to the orbital interaction between the satellites and their planets, the exothermal geochemical production of heat like hydration and crystallization of solids (e.g. Sohl et al., 2010, Hussmann et al., 2010); (b) The efficiency of heat transfer, which is based on thermal diffusion and thermal convection (e.g. Hussmann et al., 2010); (c) The components that decrease the melting point of ice and support the ocean's liquid state (e.g. Sohl et al., 2010, Tobie et al., 2010); an antifreeze component like a solution of water with ammonia should exist in the ocean in order to remain in the liquid state; and (d) The stability of the crust against convection (e.g. McKinnon, 1998 , Rainey & Stevenson, 2003).

The internal ocean could provide the proper isolation to the satellites of the outer planets to form possible habitable environments. The discovery of hydrocarbon lakes on Titan's surface and the possible existence of subsurface liquid oceans in Ganymede, Callisto, Europa, Titan and Enceladus suggest reconsidering the habitable zone definition and limits (Lammer et al., 2009).

However, life forms that do not influence the atmosphere of their host planet on a global scale will not necessarily be remotely detectable. In the Solar System's neighborhood, such potential habitats can only be investigated with space missions (see Chapter 7). For the Jovian and Saturnian satellites the proposed future missions will address the question of the hypothesized internal liquid water ocean for their icy moons (see following Chapter).

Although it is a difficult challenge to search for life forms in the environments of outer planets' moons, such studies will profoundly improve our understanding of the origin and the evolution of life and the habitable environment on our own planet.

Chapter 7

Future exploration of the satellites of the outer planets

-MEMS devices for icy moons

The gas giants are massive planets, mainly composed of hydrogen and helium, but with no well-defined planetary surface. Our Solar System has four gas giants: Jupiter, Saturn, Uranus and Neptune. They are also known as Outer Planets[22] since they orbit beyond the asteroid belt. Recently, many extrasolar gas giants have been detected, for which our Solar System giant planets serve as archetypes.

Jupiter, followed by Saturn are the largest planets of the Solar System. They both have their own system of numerous natural satellites in multivariable sizes (more than 60 moons each). Unique among these moons are Jupiter's Ganymede, Callisto and Europa and Saturn's Titan and Enceladus. All of them are active worlds likely to have a differentiated internal structure with encapsulated oceans. The scientific interest in these objects is considerable, concerning their correlation with the origin of the Solar System, the terrestrial-like processes and features they exhibit, as well as their habitability potential.

The planetary environments of Jupiter and Saturn have been studied by the missions Pioneer 10 and 11, Voyager 1 and 2, Ulysses, Galileo, Cassini-Huygens and New Horizons for Jupiter and Pioneer 11, Voyager 1 and 2 and Cassini-Huygens for Saturn. The Galileo mission to Jupiter and the Cassini-Huygens mission to Saturn have significantly advanced our knowledge about the biggest outer planets of the Solar System and their systems. The Cassini-Huygens mission, in particular, studies in depth Saturn, its satellites and its rings and will continue touring up to 2017.

However, numerous questions have been raised so far, which cannot be addressed by these missions, mainly due either to the instrumentations' limitations. Without doubt, both systems of Jupiter and Saturn should be revisited by new missions.

---

[22] Pluto orbits also outside the asteroid belt, but the International Astronomical Union (IAU) categorized it as a Dwarf Planet in 2006.

Titan and Europa were identified, among others, as main targets for future exploration by NASA in their 2003 and 2011 Decadal Surveys. ESA has recently performed extended studies for the outer planets satellites exploration (TandEM, TSSM, EJSM) and finally selected JUICE, as the first large mission to be launched within the Cosmic Vision 2015-2025 Program. In this Chapter, I present some of the studies for future missions in which I have had the chance to somehow contribute or to participate and in particular some individual experiments concepts for icy moons that I have explored and proposed.

7.1 Recent mission studies to Jupiter: From EJSM to JUICE

Jupiter is the biggest planet of our Solar System. It has a mass of $1{,}898.6 \times 10^{24}$ kg and a radius of 71,492 km at the equator. Its mean distance to the Sun is 778.57×10^{6} km and it completes a full revolution of the Sun every 11.86 years. Jupiter has the strongest magnetic field of the Solar System (4.2 gauss on the surface at the equator, 14 gauss on the surface at the North pole and 11 gauss on the surface at its South pole) and the biggest magnetosphere, which extends up to 75 Jupiter radii.

Jupiter is considered as a gas giant along with Saturn, Uranus and Neptune since it mainly consists of a gaseous envelope, without a surface. Its atmosphere is hydrogen-dominated (89.8%) with helium (at about 10%), while the rest of the gases are methane, ammonia, hydrogen deuteride, ethane and water vapor in traces.

It has 63 natural satellites and among them the four so-called "Galilean" (because they were discovered by Galileo Galilei in 1610), Ganymede, Europa, Callisto and Io. Ganymede is the biggest satellite of our Solar System. The Jovian system has been investigated by the spacecraft Pioneer 10 (1973) and 11 (1974), Voyager 1 (1979) and 2 (1979), Ulysses (1992 and 2004), Cassini-Huygens (2000) and New Horizons (2007), during their flyby maneuvers. The Galileo spacecraft entered into Jovian orbit in December 1995 and operated until September 2003, when it fell onto the giant planet. Galileo also released a probe, which entered the planet's atmosphere in December 1995 and collected measurements for 57.6 min until the atmospheric pressure crushed it.

A new NASA mission is on its way to the Jovian System: The Juno mission[23], which was launched in August 2011 and will enter into orbit insertion at 2016. The eight instruments of Juno will study Jupiter's gravitational and magnetic potential as well as its composition. However, this mission lacks a lander vehicle for the *in situ* exploration of an icy moon.

7.1.1 The Europa Jupiter System Mission (EJSM)

EJSM (Europa Jupiter System Mission) was a joint NASA and ESA mission study, which would focus on the exploration of Jupiter and its moons. It was a L-scale (large) mission consisting of two orbiters, the Jupiter Ganymede Orbiter (JGO) and the Jupiter Europa Orbiter (JEO). JGO would be developed by ESA and it was a continuation of the LAPLACE proposal (Blanc et al., 2009), submitted in response to ESA's Cosmic Vision 2015-2025 Call mission (*EJSM, NASA/ESA Final Report*, 30 January 2009). It would focus mainly on Ganymede and Callisto and the Jupiter system. JEO, on the other hand, would have been developed by NASA and it would focus mainly on Europa and explore its habitability. Both orbiters' payloads were designed to study the moons' surfaces, interiors, their gravitational fields and magnetospheres and their atmospheric environments. Table 7.1 below describes the main payload proposed for this mission (*EJSM, NASA/ESA Final Report*, 30 January 2009).

[23] http://juno.wisc.edu/juno-mission.html; http://missionjuno.swri.edu/

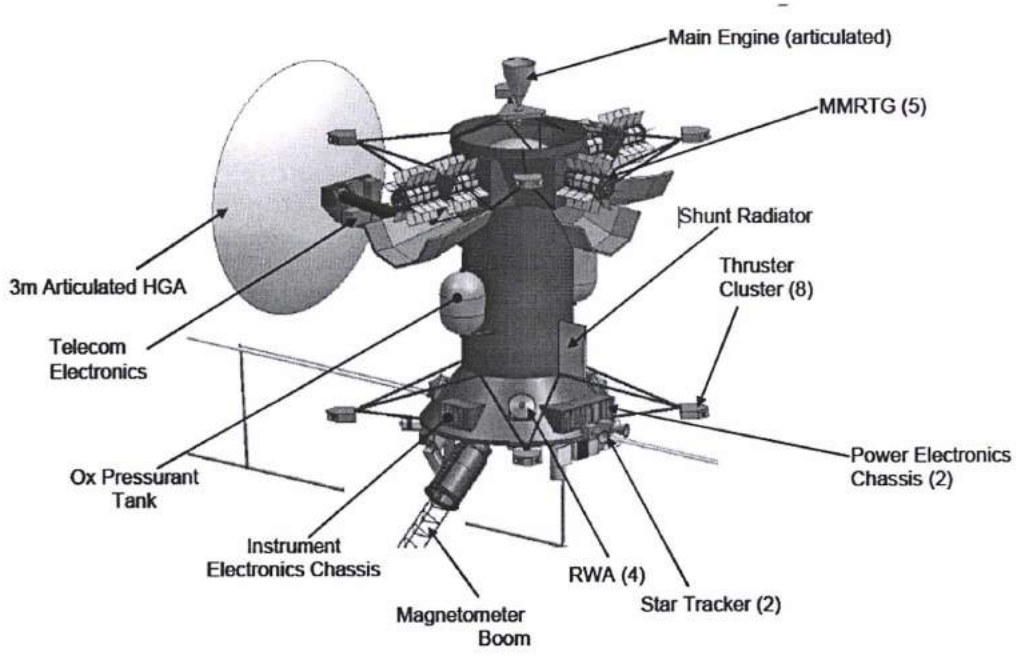

Figure 7. 1 - NASA's Jupiter Europa Orbiter (credit: NASA/EJSM Final Report)

Figure 7. 2 - ESA's Jupiter Ganymede Orbiter (credit: ESA)

Table 7. 1 EJSM payload (EJSM Final Report).

Orbiters	Science Payload	
	Instrumentation	Main objectives
JGO/JEO	Laser Altimeter	Surface topography – coherence with gravity, tides
JGO/JEO	Radio Science	Interior state of moons, presence of a deep ocean and other gravity anomalies
JGO/JEO	Ice Penetrating Radar	Structure of the subsurface & identify warm ice and/or anomalies within the ice shell
JGO/JEO	Visible-IR Spectrometer	Composition of non-ice components on Ganymede & Callisto; State & crystalinity of surface ices
JGO/JEO	Ultraviolet Spectrometer	Composition & dynamics of the atmospheres of Ganymede & Callisto
JEO	Ion and Neutral Mass Spectrometer	Composition of sputtered products from Europa
JGO/JEO	Thermal Instrument	Map temperature anomalies and thermal inertia of surface materials on Ganymede
JEO	Narrow Angle Camera	Local-scale geologic processes on Europa, Ganymede & Callisto; Io volcano monitoring; Jupiter cloud dynamics & structure
JGO/JEO	Wide and Medium Angle Camera	Global morphology of Ganymede; Global to regional scale morphology of Callisto
JGO/JEO	Magnetometer	Ganymede's intrinsic magnetic field and its interaction with the Jovian field
JGO/JEO	Plasma and Particles	Interaction between Ganymede & Callisto and the space environment to constrain induction responses
JGO	Submillimeter Wave Sounder	Dynamics of Jupiter's' stratosphere; Vertical profiles of wind speed and temperature

EJSM was in competition with a mission concept for the exploration of the Kronian system which focused on Titan (the Titan Saturn System Mission or TSSM) for a slot among the L-class Cosmic Vision Program missions. After the initial studies, the Europa Jupiter System Mission (EJSM) mission was prioritized by NASA and ESA to be launched first in order to explore the Jupiter System. The Titan Saturn System Mission (TSSM) mission, which will be described later in this Chapter, was to be developed and launched later for the Saturnian System. However, due to budget cuts, NASA could not support in the immediate future the development of such a large-scale mission as JEO and terminated that study. ESA has decided to continue with the same objectives and some enhancement with respect to the JGO, but with a unique spacecraft dedicated to study the icy moons of Jupiter : Ganymede, Callisto and Europa. In this context, the ESA Jupiter Icy Moons Explorer mission (JUICE) was proposed as a reformulation of JGO. The mission has won the competition for the first L-class mission of ESA's Cosmic Vision 2015-2025 Program. It has been selected for the L1 slot of ESA's Cosmic Vision science program on May 2, 2012. Two other proposals were competing: ATHENA, a big X-Ray telescope and NGO, a concept of three satellites to detect gravity waves. The complete instrument payloads, as well as, the instrument contractors have not yet

been decided. A NASA contribution towards the payload is under consideration. The participation of NASA will be limited to a few instruments perhaps and to co-investigators.

7.1.2 The Jupiter Icy Moons Explorer mission (JUICE)

Science goals

The Jupiter Icy Moons Explorer mission (JUICE) will visit the Jupiter system focusing on the investigation of Ganymede mainly, but also Callisto and to a lesser extent of Europa as potential habitats and on the exploration of Jupiter. JUICE will study the conditions that may have led to the emergence of habitable environments among these icy satellites and their internal oceans. The mission will also focus on characterizing the diversity of processes in the Jupiter system, including gravitational coupling between the Galilean satellites and their long term tidal influence on the system as a whole (ESA/SPC(2012)12)[24].

Mission profile

The mission[25] will be launched in June 2022 on an Ariane 5 rocket carrier and will perform a 7.3-year cruise towards Jupiter, based on an Earth-Venus-Earth-Earth gravitational assist. The Jupiter orbit insertion will occur in January 2030, and will be followed by a tour around the Jupiter system. It will comprise a transfer to Callisto (11 months), a phase studying of Europa (with 2 flybys) and Callisto (with 3 flybys) lasting one month. Then, a "Jupiter high-latitude phase" will begin that includes 9 Callisto flybys (lasting 9 months) and the transfer to Ganymede which will last 11 months. In September 2032 the spacecraft will insert into orbit around Ganymede, starting with elliptical and high altitude circular orbits (for 5 months) followed by a phase at a medium altitude (500 km) circular orbit (of 3 months) and by a final

[24] http://planetary.s3.amazonaws.com/assets/resources/ESA/ESA-SPC_20120417_selection-L1-mission.pdf
http://sci.esa.int/juice
http://media.egu2012.eu/media/filer_public/2012/04/19/egu_juice_press.pdf

[25] http://sci2.esa.int/cosmic-vision/JUICE_Yellow_Book_Issue1.pdf

phase at a low altitude (200 km) circular orbit (for 1 month). The end of the nominal mission is planned to be in June 2033.

Spacecraft description

The spacecraft is three-axis stabilized and powered by solar panels, providing around 650 W at end of mission. Communication to Earth is provided by a fixed 3.2 m in diameter high-gain antenna, in X and Ka bands, with a downlink capacity of at least 1.4 Gbit/day.

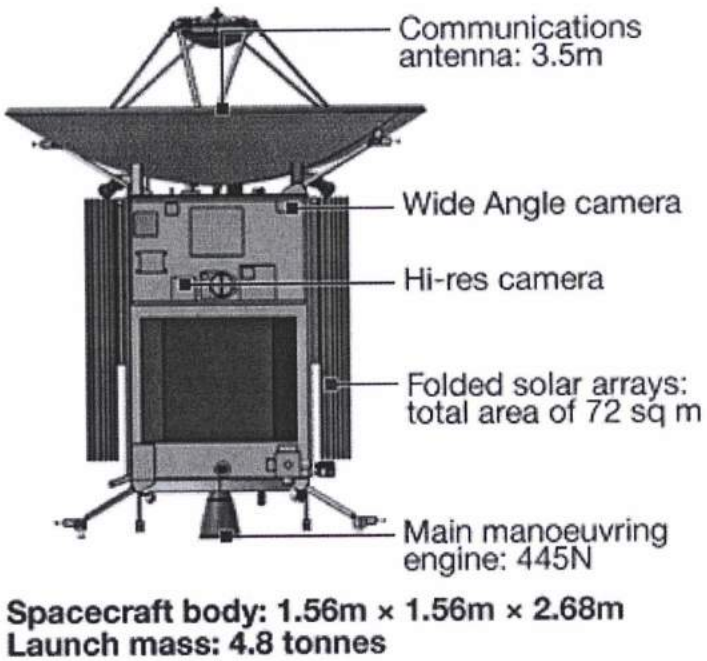

Figure 7. 3 The JUICE spacecraft design (credit: ESA)

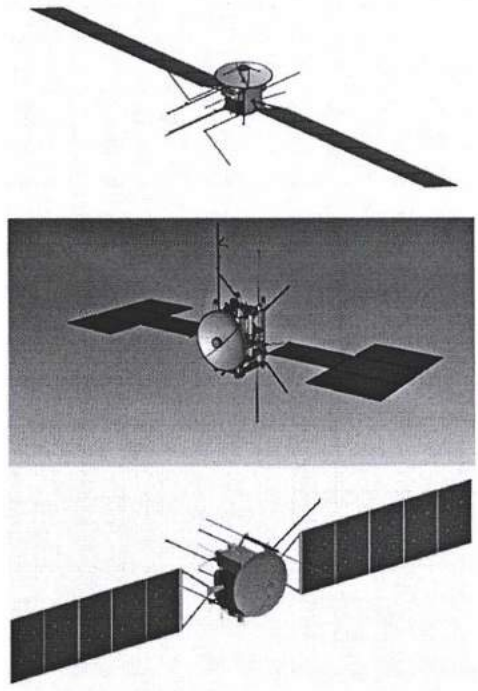

Figure 7. 4 - Design solutions for JUICE from three studies (credit: ESA)

The spacecraft's dry mass at launch will be approximately 1.8 tons. The proposal has identified a model payload based on a suite of 11 instruments weighting about 104 kg (see JUICE Yellow Book Issue 1)[26]:

- Narrow angle camera
- Wide angle camera
- Visible and Infrared Hyperspectral Imaging Spectrometer
- Ultraviolet Imaging Spectrometer
- Submillimeter Wave Instrument
- Laser Altimeter
- Ice penetrating radar
- Magnetometer
- Particle Package
- Radio and Plasma Wave instrument
- Radio Science Instrument and Ultrastable Oscillator

[26] http://sci.esa.int/science-e/www/object/index.cfm?fobjectid=49837

JUICE will provide a thorough investigation of the Jovian System and especially on the potential habitable worlds Ganymede, Callisto and Europa, since they satisfy the habitability prerequisites: the existence of water, the energy supply, the proper chemistry and the stability over time.

My PhD Thesis supervisor, Dr. A. Coustenis, was the European Science co-Lead of the JUICE Science Study Team which defined all the steps of the mission during its study by ESA and NASA and then by ESA alone (JUICE) and in cooperation with the Space Physics Team of the University of Athens, we focused on a twofold contribution in the JUICE mission: (a) instrument calibration and (b) outreach activities.

With Dr. Mathieu Hirtzig, we developed and are currently still exploiting a multi-stream radiative transfer code (Hirtzig et al., 2011) with which we can process spectro-imaging data. In particular, after correcting the atmospheric contribution in Cassini Visual and Infrared Mapping Spectrometer (VIMS) observations (Brown et al., 2004), we can deduce Titan's surface spectrum, by inverting the I/F reflectivity. But this code can be further applied to the inflight data of the foreseen JUICE/Visible infrared Hyperspectral Imaging Spectrometer (VIRHIS) instrument included in the model payload of the JUICE mission by the Science Definition Team during Earth and Venus flybys. The RT code can be further used to yield spectral calibration constraints for the instrument.

In addition to the evident scientific interest of the outer planets community, a mission to the Jovian system will certainly attract the interest of the layman (public). As a member of the Space Physics Group of the University of Athens, I have a long-term experience in designing outreach events, exhibitions and activities (see Chapter 8) as well as in web page design and administration. I am the web master of the Planetary and Solar System Sciences Division of the European Geosciences Union (EGU/PS) site[27], the official web site of Titan and Saturnian System Mission (TSSM)[28] and I have created the TSSM main article in Wikipedia[29]. Moreover, I have created the supporting site of the proposed Titan Aerial Explorer (TAE)[30], together with Stefanos Stamogiorgos, software engineer. The EGU/PS web site was selected and presented by the EGU administrators as a prototype example of development to other division web masters in the recent EGU General Assembly (Vienna,

[27] http://www.egu.eu/inside-egu/divisions-and-present-officers/division-planetary-and-solar-system-sciences/inside-ps/administration.html

[28] http://www.lesia.obspm.fr/cosmicvision/tssm/tssm-public/

[29] http://en.wikipedia.org/wiki/Titan_Saturn_System_Mission

[30] http://users.sch.gr/gbabasides/joomla/index.php

2012). ESA plans to set up web sites focusing on the JUICE mission, which will be upgraded as the mission progresses and I will contribute towards this effort. All of this I will further develop in the next chapter. As regards the future missions, my contributions were in particular centered around providing an atmosphere-surface interaction combined approach for the possible instrumentation aboard the orbiters (through my experience with Cassini/CIRS and Cassini/VIMS, see Chapters 4 and 5) and the HASI instrument aboard Huygens, but also through novel ideas that I will describe more in detail hereafter on future *in situ* instrumentation in case of a balloon or a lake lander, in particular.

7.2 Mission studies to Saturn and Titan: KRONOS, TSSM and TAE

Saturn is the second largest planet of the Solar System after Jupiter. Its radius is 60,330km, while its mass is 568.46×10^{24} kg. It orbits around the Sun at about 10 AU and it takes almost 29.5 years for a full revolution. It has an intrinsic magnetic field at 0.2 gauss at the equator, which is perfectly symmetric. This field creates the second largest magnetosphere in the Solar System after Jupiter (Blanc et al., 2005; Belenkaya et al., 2006; Gombosi et al., 2009). As the Cassini magnetometer discovered, the main source of neutrals in the Saturnian magnetosphere is Enceladus (Dougherty et al., 2006). Its magnetopause extends up to 20 Saturnian radii at the orbit of Titan.

The Saturnian atmosphere is dominated by hydrogen at about 96%, while the rest 3% is helium. It experiences the most intense storms of the Solar System with its equatorial zonal winds to present a slowing from 450 m/s down to 250 m/s in respect to the Voyager era.

Saturn has 62 natural satellites known today and a unique planetary ring system. Its rings are mainly composed of ice particles, rocky debris and dust and they are separated into nine continuous rings and three discontinuous arcs.

I got involved in future mission planning to the Saturnian System in February 2007, during my MSc studies. I have participated in the starting workshops for planning future missions in response to ESA's Cosmic Vision 2015-2025 Call, conducted in Meudon-Paris Observatory from 12 to 15 February 2007. There were two workshops in which Prof. Xenophon Moussas (my PhD co-supervisor) and myself were invited to attend, representing the Astrophysics laboratory of the University of Athens. The outcome of the work of the Consortium formed at the time were two separate L-scale (large) mission proposals to Saturn,

the Kronos mission (Marty et al., 2009a;b), and to Titan and Enceladus, the TandEm mission (Coustenis et al., 2009a). The TandEM concept was later merged with a NASA Flagship mission (Titan Explorer, Leary et al. 2008) to form the TSSM concept.

I contributed to both proposals and was therefore included in associated publications or communications. Hereafter, I describe first the mission concept for the study of Saturn with probes and then the TSSM mission, a very complete and challenging mission concept and compare it to other smaller mission proposals for a balloon or a lake lander.

7.2.1 The KRONOS mission

The Kronos mission focused on studying Saturn as a whole system, from its magnetosphere and its atmospheric environment to its interior. The basic concept of this mission was to probe globally the giant planet with two probes and remote sensing techniques through a carrier which would also serve as relay and derive the chemical and isotopic composition of the giant planet. Kronos would be an equally ambitious mission compared to Cassini-Huygens with instrumentation improved by several orders of magnitude in resolution and enhanced capabilities. A. Coustenis was co-Lead of the proposal with Bernard Marty and Tristan Guillot. The Kronos study is well-described in the papers of Marty et al. (2009a;b) published in *Experimental Astronomy* Journal, which I co-authored.

The ESA contribution to the mission were the two probes, while NASA (via its New Frontiers program) would provide the carrier which would also perform some remote measurements and telecom. Kronos would analyze in depth the chemical and isotopic composition of the Saturnian atmosphere. Such studies provide essential clues about the formation and the evolution of Saturn and the Solar System in general, since the giant planets are made of protosolar nebula gases. The study of the meteorology and atmospheric dynamics would be also a major goal of the mission in order to understand the evolution of its atmosphere since the planet's formation. The Kronos orbiter and probes would measure the temperature vertically and zonally, the winds, the cloud properties, the radiative balance and the convection mechanisms.

The mission would measure the Saturnian gravity with high accuracy in order to yield constraints about its interior. Gravitational data would also determine if the interior rotates as a solid body or not. The knowledge of the composition and the conductivity of the interior

would help understanding better the asymmetric magnetosphere of the planet. Kronos would also observe directly the Saturnian rings.

Data from the Kronos mission compared with the results from the Juno mission could have provided the opportunity to learn about the dynamics and the evolution of our Solar System's giants. Additionally, since advanced space telescopes like KEPLER[31] are now able to observe extrasolar planets, parallel studies could also give detailed information about the physics, chemistry and thermodynamic state of other solar systems.

The mission architecture

The Kronos mission proposal consisted of a spacecraft, which carried two atmospheric probes launched into the atmosphere of the planet. Each probe was planned to make *in situ* temperature measurements down to the pressure limit of 10 bars. The spacecraft design is similar to the one from the Juno mission. Two other ring probes have also been proposed to be included in order to study the rings and their particles within a distance of a few kilometers, similar to that of the Galileo entry probe.

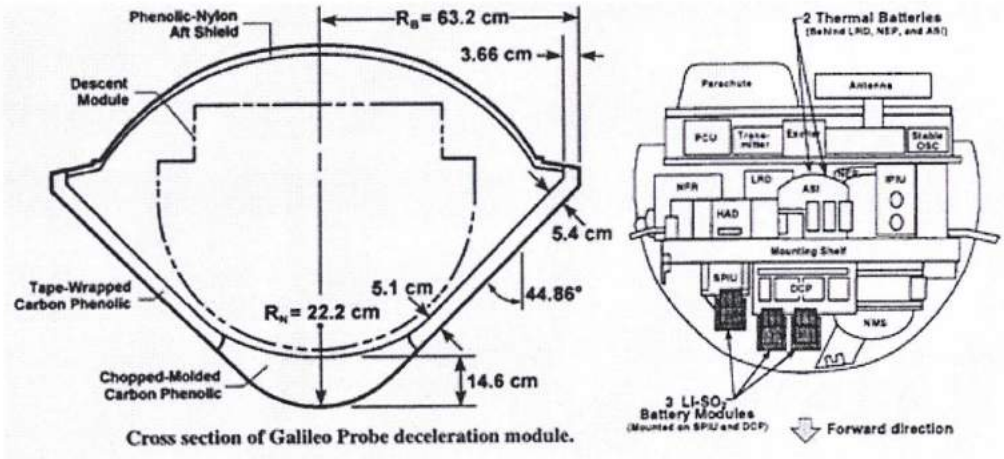

Figure 7. 5 - The cross section of the Galileo probe. The Galileo probe's heritage would be used as the basis of the Kronos probes design (Galileo Probe Deceleration Module Final Report, Doc No. 84SDS2020, General Electric Re-entry Systems Operations, 1984; Project Galileo Mission and Spacecraft, 1983) (Marty et al., 2009a).

The carrier would arrive to Saturn after an interplanetary journey by taking advantage of Earth, Venus and Jupiter gravitational assists as Cassini did. The initial proposal mission

[31] http://kepler.nasa.gov/

suggested a launch at 2017 and the journey to Saturn would last about 11 years. ESA selected to support the EJSM and TSSM proposals for the slot of a large-scale mission study to the outer planets, discarding Kronos. However, the concept was recognized as very interesting, and is carried forward today in studies performed essentially in the USA.

After the synthesis of the Kronos Consortium in Meudon in 2007, I have performed a study at the University of Athens focusing on the atmospheric entry probes' payload of the Kronos mission. The probes would sound the atmospheric composition and dynamics from the upper Saturnian atmosphere downwards to the level of about 10 bar. I was interested to get involved in the atmospheric structure experiment, which would measure the atmospheric density, pressure and temperature during the probe's descent. The Kronos Atmospheric Structure Instrument (ASI) on board the entry probes design would benefit the Huygens Atmospheric Structure Instrument (HASI) heritage (Fulchignoni et al., 2002).

I have investigated some of the possible modifications on the HASI instument to adapt to the higher pressures of the deeper Saturnian atmosphere and focused on the temperature sensors which would perform direct measurements during the descent phase after the release of the probe's shield. Each HASI temperature sensor was a dual element platinum resistance thermometer (Fulchignoni et al., 2002) designed to meet the Cassini/Huygens mission requirements.

However, the environmental conditions in Saturn differ significantly from Titan's. Indeed, the Galileo probe survived for about 58 minutes before melting from the high atmospheric pressure of 20 bar and the temperature of about 150°C inside Jupiter's atmosphere. Piezoresistive micro-machined temperature sensors can obtain direct measurements[32] in Saturn's high pressure environment, using a Wheatstone bridge circuit configuration.

My main concern was also to minimize the probe's payload weight and that research led to the study of implementing Micro-Electro-Mechanical System (MEMS) technology in future missions to outer planets. A further study of MEMS devices and their implementation as distinctive future experiments in icy moons are described later in this Chapter.

[32] http://www.kistler.com/mediaaccess/000-614e-09.09.pdf

7.2.2 The Titan and Enceladus Mission (TandEM)

My involvement in future mission planning to Titan and Enceladus began in early 2007 in Meudon, when Prof. X. Moussas and I participated to the Workshop of the TandEM Consortium conducted in Salle des Conférences du Château of the Paris-Meudon Observatory (Atelier CIAS). This Workshop set up the baselines for the study of a future flagship mission dedicated to these planetary objects. TandEM was a multi-national cooperative effort, in which 155 expert scientists and engineers participated (Coustenis et al., 2009a). The Proposal Lead was Athena Coustenis.

The TandEM mission was planned to be launched around 2018 or later and wanted to address several of the Cosmic Vision 2015-2025 call themes with the help of an orbiter, a balloon, and several landers/penetrators to be delivered to the satellite around 2030. Its design was based on the Cassini-Huygens architecture and it was expected to surpass the latter's legacy by exploring Titan and Enceladus in full close-up and *in situ* coverage over long periods of time, which is not currently possible.

The study's task assignments of the Astrophysics Laboratory of University of Athens were the study of Titan surface, the mission architecture and the outreach campaign. During my MSc dissertation, I studied the surface of the northern part of Titan and tried to identify tectonic signs on the crust. However, we found that the resolution of the available Cassini/Synthetic Aperture RADAR (SAR) images was not sufficient to produce topographic and geologic maps. For this reason, I took advantage of the involvement of the University of Athens in TandEM's Titan surface and mission architecture working groups to suggest improved RADAR instrumentation characteristics for the mission. A high resolution RADAR on an orbiter revolving around Titan for a long period of time would help in the study of surface evolution and its interactions with the lower atmosphere. TandEM's RADAR was expected to provide solutions to a series of under-study matters such as:

1. Determination of the active (or not) local tectonic field
2. Determination of the age of Titan's surface
3. Chemical composition and source of liquid surface deposits
4. Depth measurement of lakes
5. Correlation between the surface lithology and the surface features.

In order to understand the internal structure of Titan Dr. A. Coustenis and I worked together on including seismic instrumentation in the TandEM strawman payload. I have

studied the technical difficulties of robotic emplacement of this very sensitive sensor system on Titan's surface and set the surface constrains for its installation. The ideal position of a seismometer is the one which will guarantee the accurate recording of the ground vibration above the instrument's threshold. Moreover, the instrument's legs should contact firmly with the local surface at the landing site. The presence of dust and sand grains can influence significantly the instrument's performance. The location should be on a flat surface away from dunes and drainage networks. This study led to the proposal of implementing seismometers in future missions to icy moons, which is described later in the Chapter.

Prof. X. Moussas and I were the co-leaders of the TandEM Outreach working Group. We have organized several outreach activities and participated or attended in many outreach events globally. A detailed list and a description of our outreach projects and their evaluation is in Chapter 8. In collaboration with A. Coustenis and X. Moussas I will continue to support the outreach campaign of the Titan future mission.

TandEM mission concept

The mission concept of TandEM (Fig. 7.6) consisted of two moderate-size spacecraft the Titan-Enceladus Orbiter with the Enceladus penetrators and the Carrier for the Titan *in situ* investigation elements which were the Titan Montgolfier-hot air balloon and the three lander/mini-probes (Coustenis et al., 2009a).

After its arrival, the orbiter would perform several flybys of Titan and Enceladus and carry the Enceladus landers/penetrators. The carrier spacecraft wwoud release the Titan hot air balloon and up to three entry probes. To facilitate the telecommunication with the *in situ* vehicles, the carrier could be converted into an orbiter and perform science measurements like occultations using the telecom link between the two orbiting spacecraft. The telecom relay between the Titan *in situ* elements and the Earth orbiter would be provided by the orbiter.

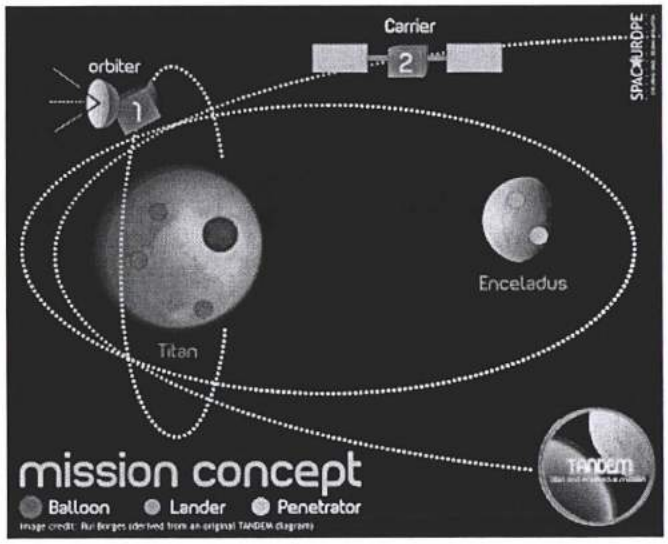

Figure 7. 6 - TandEM mission concept (Coustenis et al., 2009a). Design by Dr. M. Hirtzig.

According to the initial mission scenario, the Titan-Enceladus orbiter would perform 12 Enceladus flybys as well as 2 Titan flybys and 3 or 4 more Titan flybys before entering into Titan Orbit Insertion (TOI). Then, the orbiter would enter in Titan polar orbit, in order to support the *in situ* mission elements. For enchanced performance, the spacecraft would be maneuvered to a polar orbit before the delivery of the balloon and the entry probes by the carrier.

The Montgolfière consisted of a balloon and a gondola. The balloon would be filled by Titan's gas, heated by the energy from the two Multi-Mission Radioisotope Thermoelectric Generators (MMRTGs) which were located in the gondola with the scientific equipment. Titan's dense nitrogen atmosphere with temperatures less than 100 K at the first 70 km above the surface is favorable for a hot air balloon flight. The average operation altitude of the Montgolfière is 10 km above the surface.

The Titan mini-probes design would follow mainly the Huygens probe experience as well as the GEP-ExoMars (Geophysics Package). The parachute system would have been similar to the one used for the Huygens Entry Descent and Landing (EDL) sequence. These probes would be powered by Radioisotope Thermoelectric Generators (RTGs). Figure 7.7 shows the design of a penetration module.

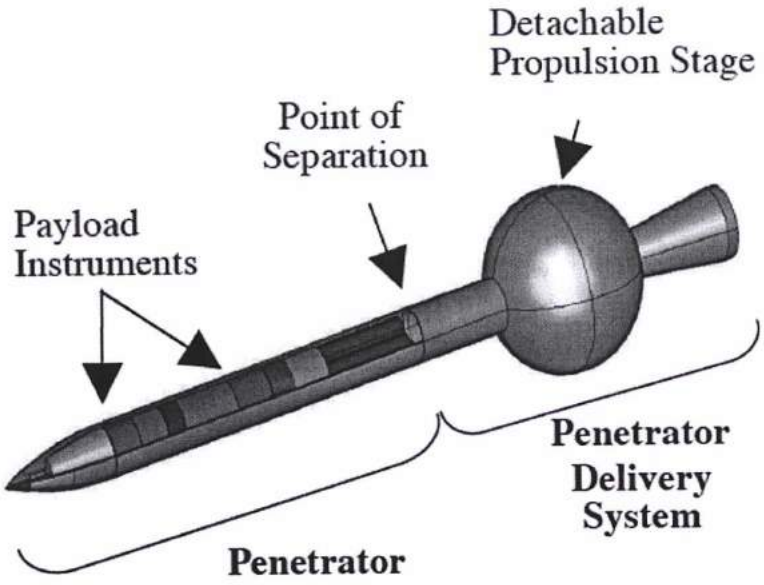

Figure 7. 7 - TandEM penetration probe (Coustenis et al., 2009a).

These penetrators could be released by the Montgolfière or the carrier. They could include seismometers as payload and thus construct a seismic network on the surface of Titan. Two penetrators would be delivered to Enceladus surface from the Titan-Enceladus orbiter.

TandEM, along with the LAPLACE mission to Jupiter (Blanc et al., 2009) proposals were the two finalists selected by ESA in October 2007 for further study in the framework of the 2015-2025 Cosmic Vision Plan as L-class missions in collaboration with NASA. Both studies were accepted as fully responsive to the Cosmic Vision Goals.

An international team of scientists and engineers with 16 US and 15 European members, the Joint Science Definition Team (JSDT), was then formed in order to develop a mission to Titan that would address the key questions left by the Cassini-Huygens mission. The JSDT merged the NASA Titan Explorer study for a mission to Titan (Leary et al., 2008) and the TandEM study into a single one named "Titan and Saturn System Mission" (TSSM)[33]. The TSSM JSDT also examined the Decadal Survey of 2003 documents of the US National Academy of Sciences, which regarded Titan and Europa as the highest priority targets for future missions.

[33]http://www.lesia.obspm.fr/cosmicvision/tssm/tssm-public/
http://sci.esa.int/science-e/www/area/index.cfm?fareaid=106
http://opfm.jpl.nasa.gov/titanriskreduction/

7.2.3 The Titan-Saturn System Mission (TSSM)

Titan Saturn System Mission (TSSM) is a Flagship (large) mission which was to be developed jointly by NASA and ESA (*TSSM Final Report* JPL D-48148 NASA Task Order NMO710851). TSSM could study for several years Titan's atmospheric and surface environment and explore extensively one of Titan's lakes. TSSM is planned to be launched after 2025 and after a 9-year interplanetary voyage it would reach the Saturnian System. The duration of the nominal mission will be four years.

I have been given the unique opportunity to participate in the design of a future mission dedicated to Titan, the subject of my PhD Thesis. I got involved in the TSSM mission study from its very beginning. During the 15-month preparation for the selection procedure, I supported Dr. A. Coustenis, one of my Thesis supervisors and European lead of the TSSM Consortium, in administration issues. One of my administration duties was, and still is, the web support of the mission. I am the web master of the TSSM official web site and I have also created the TSSM main article in Wikipedia, the web sites of which are the following:

- *http://www.lesia.obspm.fr/cosmicvision/tssm/tssm-public/*
- *http://en.wikipedia.org/wiki/Titan_Saturn_System_Mission*

I have also, more essentially, been involved in the definition of Cassini-like instruments on board TSSM, which would study the atmosphere and the surface like the infrared spectrometer which would follow in the steps of the Voyager/IRIS and Cassini/CIRS instruments (see Chapter 4), as well as the spectro-imager similar to VIMS with improved capabilities from my experience described in Chapter 5. The corresponding instruments on TSSM would be TiRS and HiRIS (see description heareafter, in Table 7.2).

My other interest in future Titan exploration, more focused, is the lakes study. Cassini has identified their existence, but crucial information about their nature, structure, origin and evolution is not to be addressed by the current mission. Cassini monitors remotely the lakes and only *in situ* exploration could calculate their liquid volume, identify their bottom topography and their contribution to the active methane cycle. The TSSM concept also includes a lake lander, which could provide the relevant information. For this purpose, I have proposed the emplacement of micro-probes in the lake lander payload. The main idea is to use Micro-Electro-Mechanical-Systems (MEMS) technology is to establish a network of micro-probes spread in the interior of a lake. These devices are lightweight, low cost and highly

reliable. The concept and the constraints of MEMS experiment are described in detail in the following section.

The TSSM concept

The current TSSM concept foresees a carrier to be launched on an Atlas V 551 who would reach Saturn by using an ion propulsion system, the Solar Electric Propulsion (SEP) to gain thrust from ion beams as well as gravity assist trajectory, capable of accomplishing outer planet missions. TSSM basic concept consists of three space vehicles (Fig. 7.8):

a) The orbiter, which will tour mainly around Titan for two years, after performing seven close-up Enceladus' flybys. On Enceladus, the orbiter will sample the plumes and make subsurface measurements.
b) The hot air balloon (Montgolfière) will probe both Titan's atmosphere and surface at a latitudinal bin of circa 20° around the equator, being in low altitude orbit of 10 km for at least six months.
c) The Lake Lander will perform the first extraterrestrial oceanographic experiment by landing and floating on the largest of Titan's lakes, the Kraken Mare.(however the lake to be explored could be a different target depending on the mission arrival time).
d) The TSSM orbiter after its arrival to Saturn will perform a 24-month system tour including sixteen flybys of Titan and seven close flybys of Enceladus. Four of these Enceladus flybys will be over the poles at 100 km, one at 300 km and two at 1000 km. During this tour, the orbiter will encounter several icy moons and it will observe Saturn. It will release the hot air balloon during its first flyby of Titan, while the lake lander will be released at the second flyby.
e) After this phase, the orbiter will enter into highly elliptical orbit to conduct a two month concurrent aerobraking and aerosampling phase in Titan's atmosphere, reaching the altitude of 600 km. Then it will execute a final periapsis raise burn to achieve a 1500 km circular, 85° mapping orbit. The duration of this phase will be 20 months.
f) Finally, the orbiter will perform a maneuver, which will start the orbit decay assisted by the influence of Saturn's perturbations and Titan's atmospheric drag. In this stage it will observe the magnetospheric interaction between Saturn and Titan.

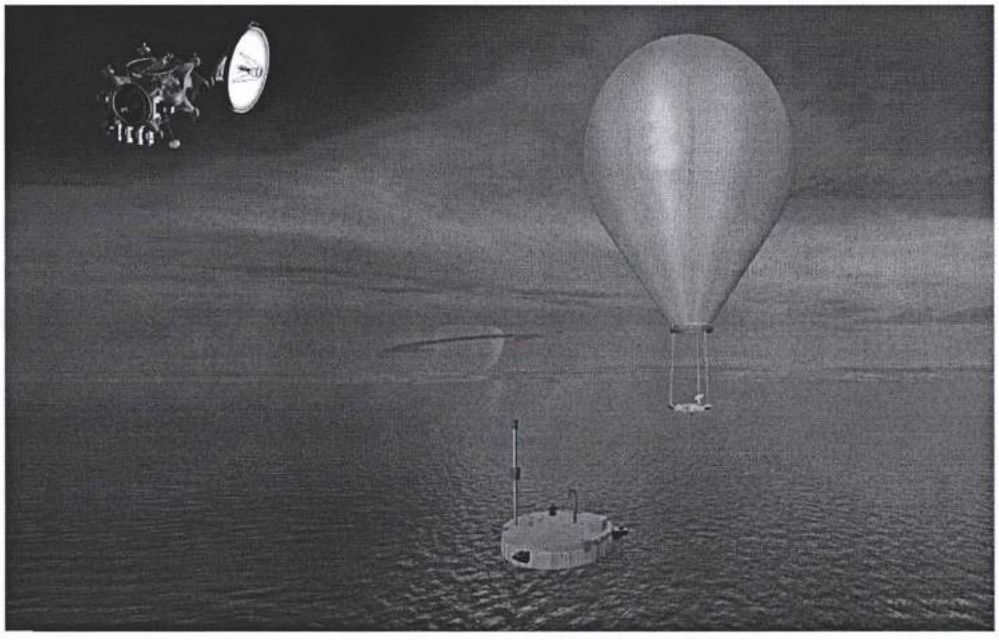

Figure 7. 8 - The TSSM basic concept: the orbiter, the balloon and the lake lander (TSSM Final Report. JPL D-48148 NASA Task Order NMO710851).

The TSSM orbiter is a three-axis stabilized spacecraft. The basic elements of the spacecraft as well as the positions of the Montgolfère and lander on the mothership are illustrated in Figure 7.9, while its payload is listed in Table 7.2. The orbiter is also the carrier of the two other vehicles of the mission.

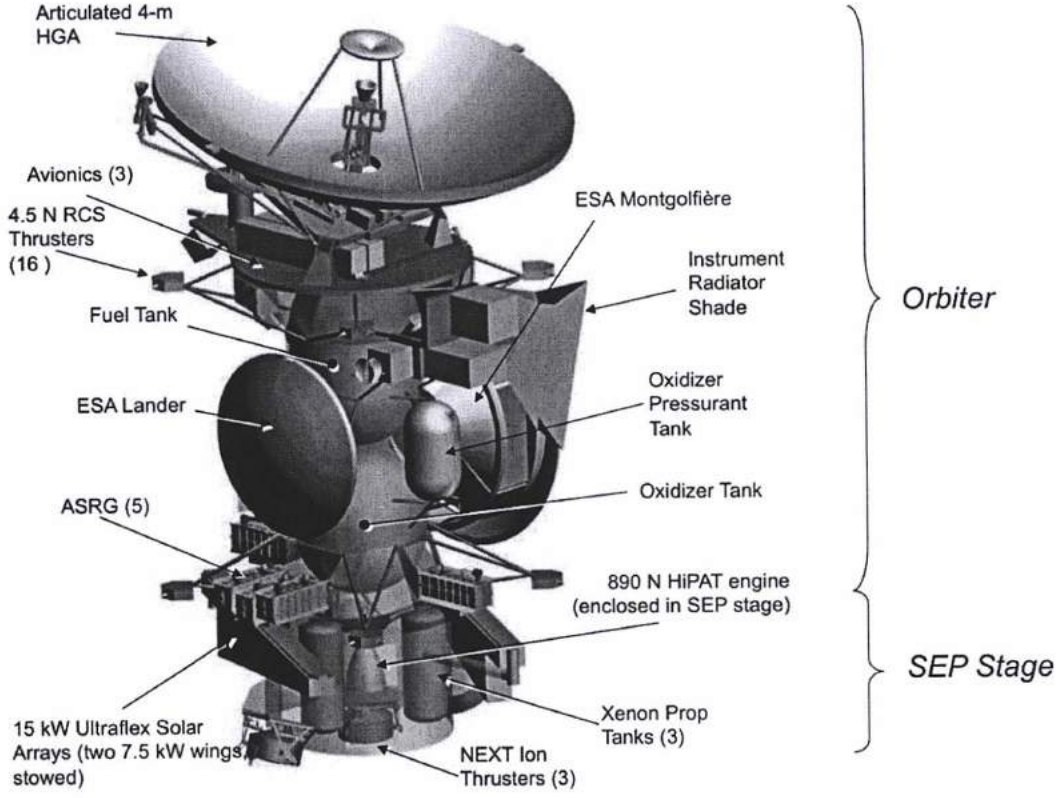

Figure 7. 9 - The TSSM orbiter (TSSM Final Report. JPL D-48148 NASA Task Order NMO710851).

Table 7. 2 - The orbiter's payload (TSSM Final Report. JPL D-48148 NASA Task Order NMO710851)

	Orbiter planning Payload	Instrument Capabilities
HiRIS	High-Resolution Imager and Spectrometer (near IR)	1–6 μm global mapping at 50 m/pixel in three colors. Adjustable spectral editing for surface/atmosphere studies.
TiPRA	Titan Penetrating Radar and Altimeter	>20 MHz global mapping of subsurface reflectors with 10 m altitude resolution in altimetry mode & >10 m depth resolution. Lower data rate sounding mode with ~100 m depth resolution ~1 km x 10 km spatial resolution.
PMS	Polymer Mass Spectrometer	TOF MS with M /ΔM ~10,000 for masses up to 10,000 Da. From 600 km to upper atmospheric in situ analysis of gases and aerosol precursors.
SMS	Sub-Millimeter Spectrometer	Heterodyne spectrometer with scanning mirror. Direct winds from Doppler and temperature mapping from ~200-1000 km altitude; carbon dioxide and nitrile profiles.
TIRS	Thermal Infrared Spectrometer	Passively cooled Fourier spectrometer, 7–333 μm. Organic gas abundance, aerosol opacity and temperature mapping 30–500 km.
MAPP	Magnetometer	Tri-axial fluxgate sensors. Noise level ~11pT$_{rms}$. Interaction of field with ionosphere: internal and induced field.
	Energetic Particle Spectrometer	TOF Analyzer w/ss detectors to measure magnetospheric particle fluxes, ~10 keV to >MeV with 150° x 15° FOV.
	Langmuir Probe	Swept voltage/current probe. In situ electron density and temperature, ion speed constraint, including during aerosampling.
	Plasma Spectrometer	Electrostatic analyzer with Linear electric field TOF MS. Measures ion and electron fluxes at ~5 eV to ~5 keV. M/ΔM~10.
RSA	Radio Science and RSA Accelerometer	All components part of spacecraft telecom system. Lower stratosphere and troposphere T profile. Gravity field.

The Montgolfière is a hot air balloon to be released by the orbiter during the first flyby. It will be powered with 100 W by. Figure 7.10 shows the entry system of the balloon capsule, while Figure 7.11 illustrates the position of the instrumentation in the gondola. From the altitude of 40 km the balloon will start to be filled by air and 1.7 W from the a Multi-Mission Radioisotope Thermoelectrical Generator (MMRTG) will warm the air for buoyancy at about 10 km above the surface. The Montgolfère will then navigate with the winds at 1-2 m/s. The balloon's gondola will be equipped with scientific instrumentation in order to perform atmospheric measurements, imaging, spectrometry, subsurface radar profiling, and electric and magnetic field measurements (Table 7.3). The nominal mission of the Montgolfère will last 6 months.

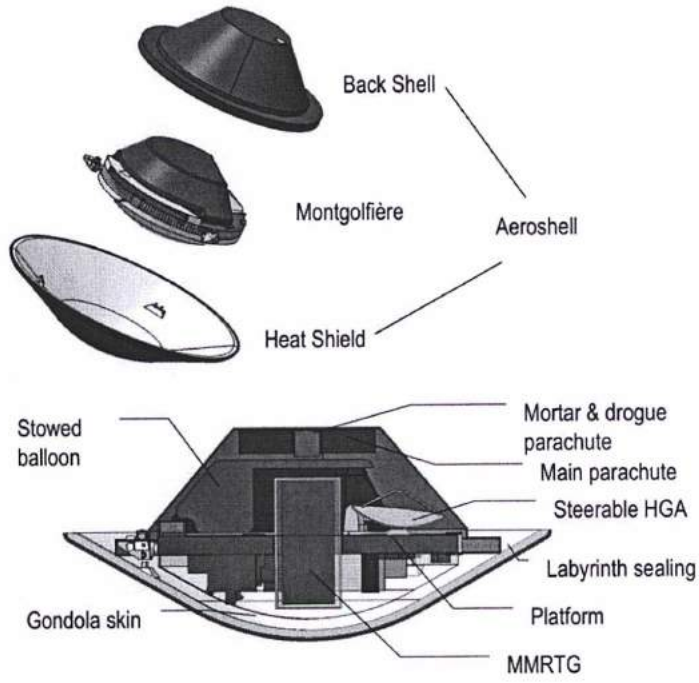

Figure 7. 10 - The TSSM Montgolfière gondola and a view of the entry system aeroshell (*TSSM Final Report.* JPL D-48148 NASA Task Order NMO710851).

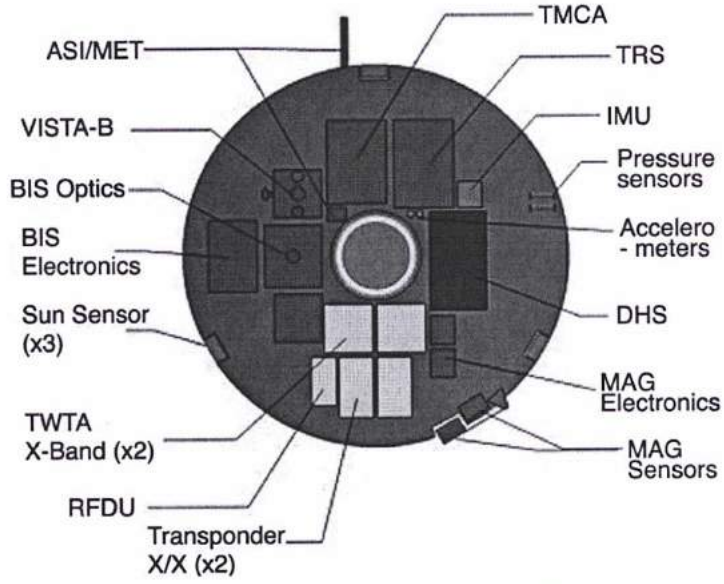

Figure 7. 11 - Positions of the payload in the Montgolfière's gondola (*TSSM Final Report.* JPL D-48148 NASA Task Order NMO710851).

Table 7. 3 - The Montgolfière payload (TSSM Final Report. JPL D-48148 NASA Task Order NMO710851).

	Montgolfier planning Payload
BIS	Balloon Imaging Spectrometer (1–5.6 μm)
VISTA-B	Visual Imaging System for Titan Balloon
ASI/MET	Atmospheric Structure Instrument/ Meteorological Package
TEEP-B	Titan Electric Environment Package
TRS	Titan Radar Sounder (>150 MHz)
TMCA	Titan Montgolfier Chemical Analyzer (1–600 Da Mass Spectrometer)
MAG	Magnetometer
MRST	Radio Science using spacecraft / Montgolfier telecom system

The Lake Lander will follow an entry, descent and landing (EDL) procedure like the Huygens EDL, while the orbiter will be in continuous contact with it. The target location will be the Northern largest lake of Titan, Kraken Mare. Figure 7.12 illustrates the aeroshell of the Lake lander, while Figure 7.13 shows its payload.

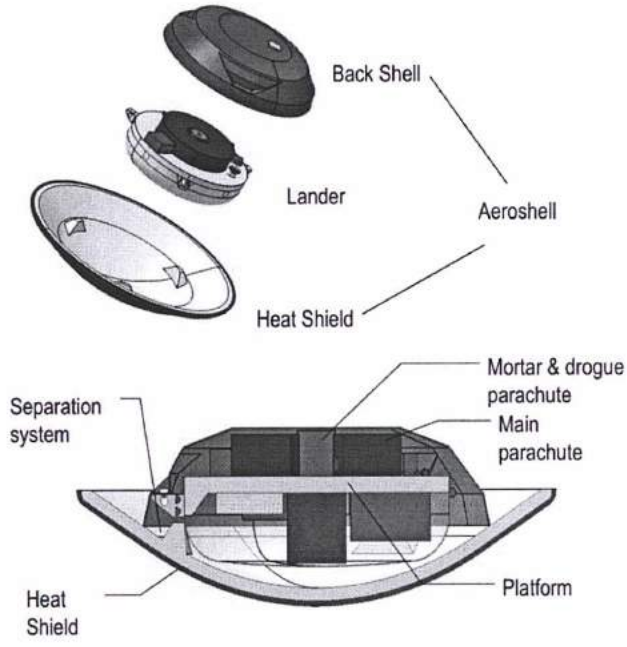

Figure 7. 12 - The TSSM lake lander (*TSSM Final Report.* JPL D-48148 NASA Task Order NMO710851).

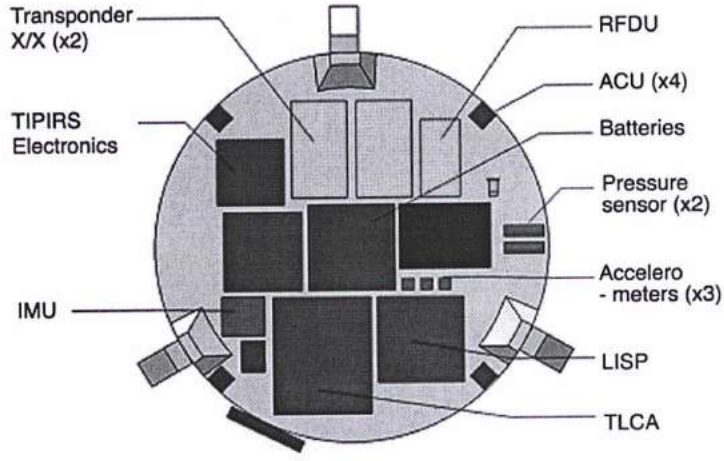

Figure 7. 13 - The positions of the lake lander payload (*TSSM Final Report.* JPL D-48148 NASA Task Order NMO710851).

The probe will be powered by batteries like Huygens and its nominal mission is designed to last for 9 hours, 5 hours in the descent phase and 3-4 hours after the touchdown on the lake's surface. The floating configuration of the lake Lander is depicted in Figure 7.14 and its instrumentation is listed in Table 7.4.

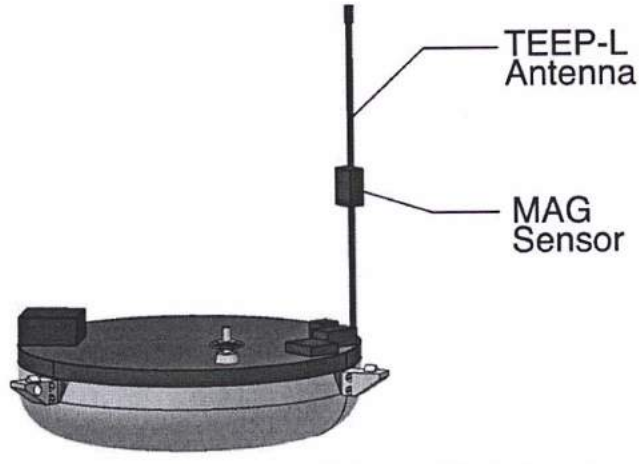

Figure 7. 14 - The TSSM Lake Lander (*TSSM Final Report.* JPL D-48148 NASA Task Order NMO710851).

The TSSM mission is planned to be supported by ground based radio telescopes (Coustenis et al., 2009c), following the heritage of the Huygens data retrieval in 2005 (Witasse et al., 2006).

Table 7. 4 - The Lake Lander Payload (TSSM Final Report. JPL D-48148 NASA Task Order NMO710851).

	Lake Lander Planning Payload
TLCA	Titan Lander Chemical Analyzer (GCMS)
TiPI	Titan Probe Imager + Lamp
ASI/MET- TEEP	Atmospheric Structure Instrument/ Meteorological Package + Titan Electric Environment Package
SPP	Surface Properties Package + Acoustic Sensor Package with Magnetometer
LRST	Radio Science using spacecraft/lander telecom system

The TSSM competitor for the final selection as the next L-scale mission was the Europa Jupiter System Mission (EJSM). In February 2009, a down-selection meeting was conducted in Washington DC by the NASA and ESA management and the Europa Jupiter System Mission was selected as the most technically feasible to pursue first. ESA's Solar System Working Group recommended, and NASA agreed, that TSSM would be the EJSM follow up mission within the next decade. However, as I have mentioned above, the EJSM project has been terminated and ESA carries forward alone with JUICE mission to the Jupiter System.

The future exploration of the Saturnian moons, and especially of Titan and Enceladus, has been supported by several white papers which I have co-authored with the Titan Working Group (TWG). These white papers were submitted in 2009 in response to National Research Council (NRC) Planetary Science Decadal Survey 2013-2022[34].

In the Lunine et al. white paper, we highlighted the significance and the scientific merit of a future mission to Titan. In the white paper of Spilker et al. we recommended the continuation of Cassini mission operation by exceeding its function for 7 more years, the Cassini Solstice Mission, which NASA accepted. In Nixon et al. article we recommended Titan exploration to be as a high priority target, the continuation of funding for large ground and space based telescopes in order to perform long-term observations of Titan and to support laboratory experiments that provide constraints in Titan science. Titan was identified in that paper as the only credible analogue to the Earth's seasonal-dependent and climatic variations and as such an important study object. Seasonal variations of Titan's atmospheric chemistry are an important part of my PhD studies (see Chapter 4). The laboratory support as well as the launch of an orbiter to sample *in situ* Titan's upper atmosphere with high resolution instrumentation was the subject of the Yelle's et al. white paper. In the Allen et al. white paper, we recommended a mission concept similar to TSSM to be delivered at Titan, considering its

[34] http://sites.nationalacademies.org/SSB/CurrentProjects/ssb_052412

high astrobiological interest. In the Coustenis et al. white paper, we also recommended a balloon mission to Titan as high priority for decadal science and to invest in reducing the risks of such a flight. In the Atkinson et al. white paper, we recommended that probes be sent to giant planets beyond Jupiter.

The NRC Committee recommended in March 2011 the continuation of the study of TSSM and considering the mission's flexibility, NASA anticipates future studies to divide this large flagship mission into separate flight opportunities in varying sizes (see NASA response to Planetary Science Decadal Survey Report (9-22), 26/7/2011).

7.2.4 Titan Aerial Explorer (TAE)

Besides TSSM other concepts for future missions in medium scale sizes to Titan have been proposed such as Aerial Vehicle for In-Situ and Airborne Titan Reconnaissance (AVIATR), Titan Mare Explorer (TiME), Titan Lake Probe and Titan Aerial Explorer (TAE).

AVIATR (Figs. 7.15 - 7.16) is a proposal suggestive of alternative concept to the Titan balloon mission. Since Titan experiences low gravity and a dense atmosphere, a nuclear powered airplane could fly more than 20 times easier than on Earth. It could sample directly the atmosphere and cover huge swaths of Titan's landscape (Barnes et al., 2012). Although very interesting, this proposal did not get selected among the Discovery mission studies.

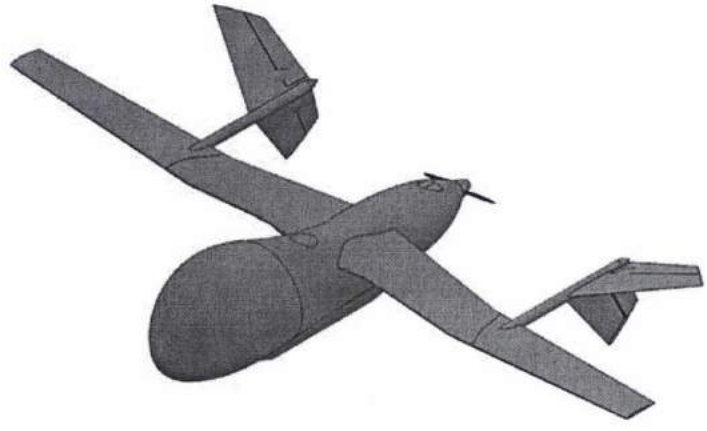

Figure 7. 15 - AVIATR air vehicle exterior blueprint (Barnes et al., 2012).

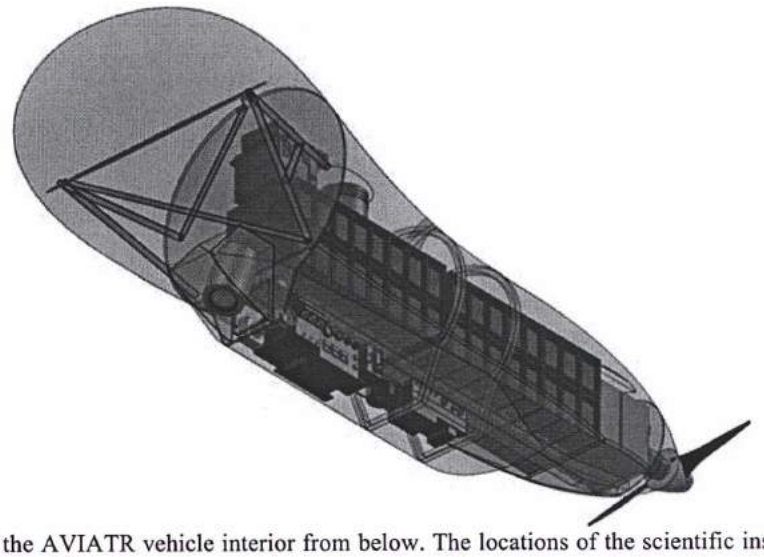

Figure 7. 16 - View of the AVIATR vehicle interior from below. The locations of the scientific instrumentation is showed (Barnes et al., 2012).

TiME (Fig. 7.17) is a probe focusing on exploring Titan's lakes and especially the Ligeia mare. This lake lander could study the chemical composition and the geological characteristics of the hydrocarbon pools (Stofan et al., 2010a; b).

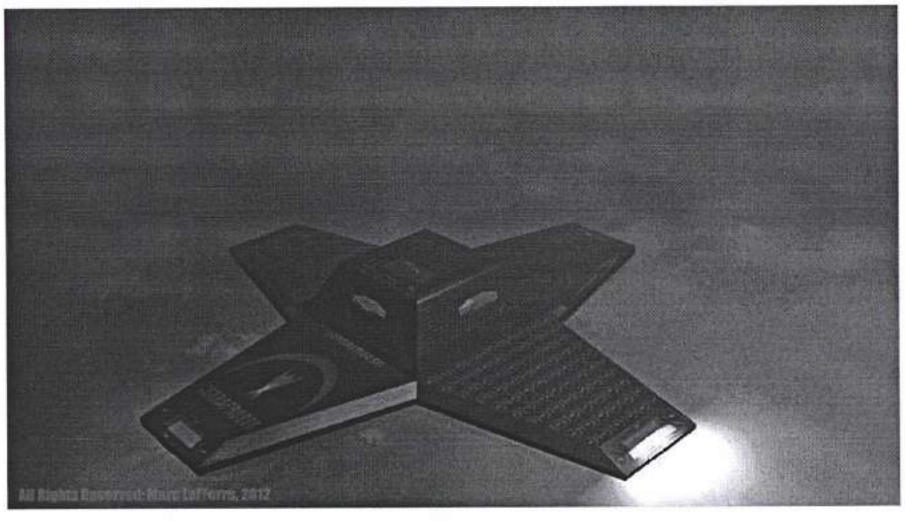

Figure 7. 17 - Artist's view of the TiME sailing Leigia Mare on Titan (Stofan et al., 2010a; b).

The TiME concept was studied until 2012 but was not downselected among the 3 Discovery mission proposals, so in August 2012, the study was terminated. InSight - Interior exploration using Seismic Investigations, Geodesy and Heat Transport - a mission to Mars was selected, InSight will study the interior of Mars by performing a seismic experiment and probing the rate of the heat which escapes from the interior.

Titan Lake Probe (Fig. 7.18) is a lake lander, similar to what we had proposed in TSSM, which could be considered as part of a larger mission or as a stand-alone mission. The main objective of this proposal is to investigate the lake deposit and the physical properties of the liquids like the TiME concept (Waite et al., 2010).

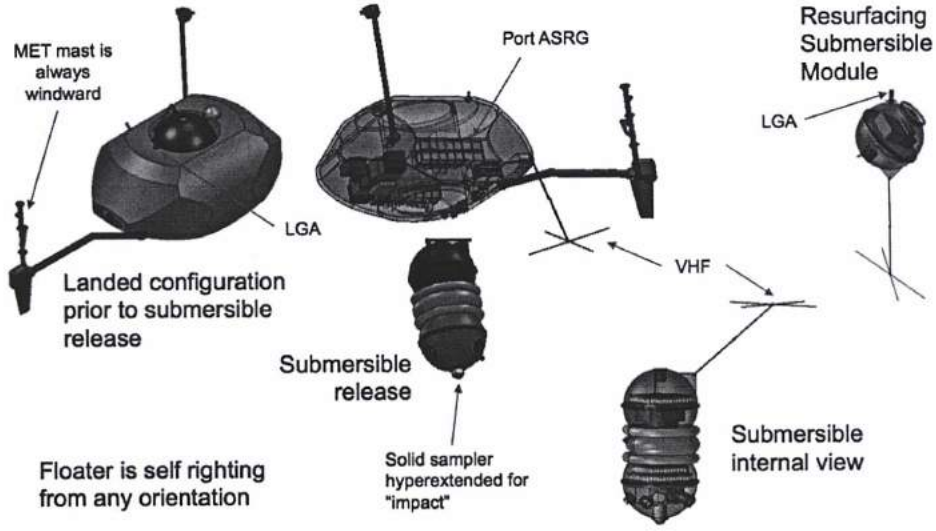

Figure 7. 18 - Titan Lake Probe (credit: Waite et al. 2010, Decadal mission concept study)

Titan Aerial Explorer (TAE) was developed by Dr. J. Lunine and the TAE team in response to ESA 2010 Cosmic Vision call for M-class (medium) missions (Hall et al., 2011). TAE was a helium-filled high-pressure balloon, which was planned to fly in the lower atmosphere of Titan at an altitude of 8 km from 3 to 6 months on Titan's equatorial latitudes. The data transmission of about 1 Gbit (total) to Earth would be established directly, avoiding the intervention of an orbiter. As a follow-up to the TSSM mission with similar concept and objectives, my interest in TAE was obvious, as I will describe hereafter.

I have also created the web page of the mission proposal using flexible web tools in order to achieve a quick impact to the scientific community and the public, which is:
http://users.sch.gr/gbabasides/joomla/index.php

The TAE concept

The Titan Aerial Explorer (TAE) mission is a super-pressure helium balloon, 4.6 m in diameter and spherical in shape. It combines the mobility and coverage of an orbiter with the

capability for high resolution and *in situ* observations demonstrated by the Huygens lander. The balloon would be powered by two Advanced Stirling Radioisotop Generators (ASRGs) (Figure 7.19) but without propulsion (Hall et al., 2011).

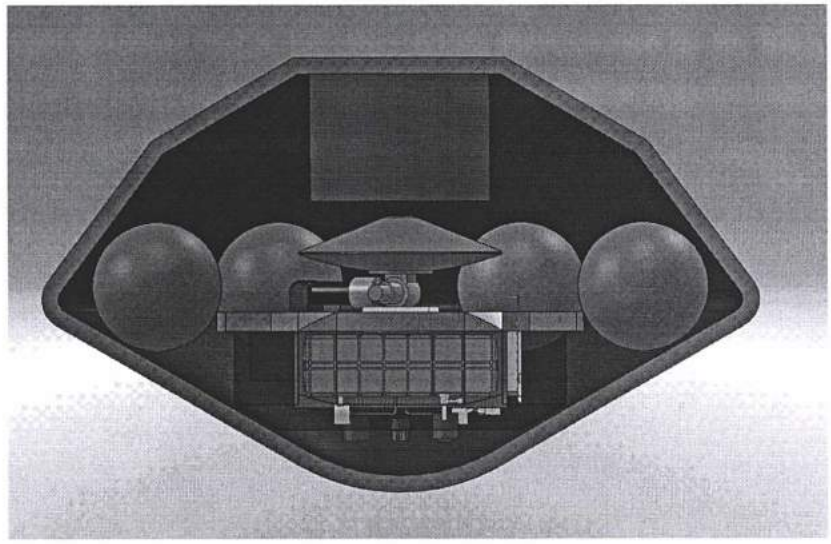

Figure 7. 19 - The gondola of TAE (credits: Hall et al., 2011)

The mission would launch within the 2020-2023 timeframe on a carrier spacecraft containing the aerostat encased in a Huygens-like entry system. It would arrive at Titan after a 9-year trajectory. When the carrier would encounter Titan, it would release the Descent Module onto the pre-determined entry, descent and inflation trajectory. The entry probe would enter Titan's atmosphere at mid-latitude, deploy a parachute, release the aeroshell heat shield and backshell, initiate balloon inflation, release the helium tanks and establish neutral buoyancy at ~8 km altitude (Figure 7.20).

Although TAE aerostat and TSSM Montgolfière air platform have similar objectives in Titan science, they present differences in architecture. In Table 7.5 below, I summarize the results of the comparison between TSSM Montgolfière and TAE. TSSM balloon is twice in diameter compared to the TAE one and it will be filled by Titan gas, which means that there is no need to carry special tanks, and therefore it has more space for scientific instrumentation. Instead, TAE balloon is a high-pressure helium filled balloon and has to carry the gas from the Earth. This fact influences the amount of data which will be collected and transmitted to Earth from both vehicles. The Montgolfière gondola will host 8 scientific instruments which will provide data volume three orders of magnitude larger than TAE.

Both vehicles will be powered by Radioisotop generators: TAE by ASRG and TSSM Montgolfière by MMRTG. ASRGs are preferable power sources compared to MMRTGs, since they combine reduced mass, increased power output and reduced cost. Nevertheless, the Montgolfière architecture can easily adopt ASRG.

One more difference between the proposed balloon concepts is that the Montgolfière will use the orbiter in order to transmit data to Earth, while TAE will establish a direct-to-Earth link.

Table 7. 5 - Comparison between TSSM Montgolfiére and TAE.

	TSSM Montgolfiére	TAE balloon
Gas	Titan gas	Helium
Diameter	10.5 m	4.6 m
Power	Multi-Mission Radioisotope Thermoelectrical Generator (MMRTG)	Advanced Stirling Radioisotop Generator (ASRGs)
Scheduled mission duration	6 months	3-6 months
Low altitude orbit	10 km	8 km
Communication link	Orbiter intervation	Direct
Payload	see Table 7.3	No magnetometer Imaging spectrometer probes from 4.6 to 5.6 μm (TSSM balloon: 1 - 5.6 μm)
Total data volume	up to 1.3 Tb	up to 1 Gb

By comparing the two, it is obvious that both the Montgolfière and TAE can provide satisfactory proposals for future Titan exploration. However, the the former could be considered as a more complete option since it carries more instruments onboard including a magnetometer and its imaging spectrometer provides a wider range of wavenumber. Furthermore, if the Montgolfière concept manages to adopt ASRGs instead of MMRTG, it will enhance its energy budget. Finally, the scientific value of the TSSM hot air balloon can be increased by the possible emplacement of a simple seismometer in its heat shield.

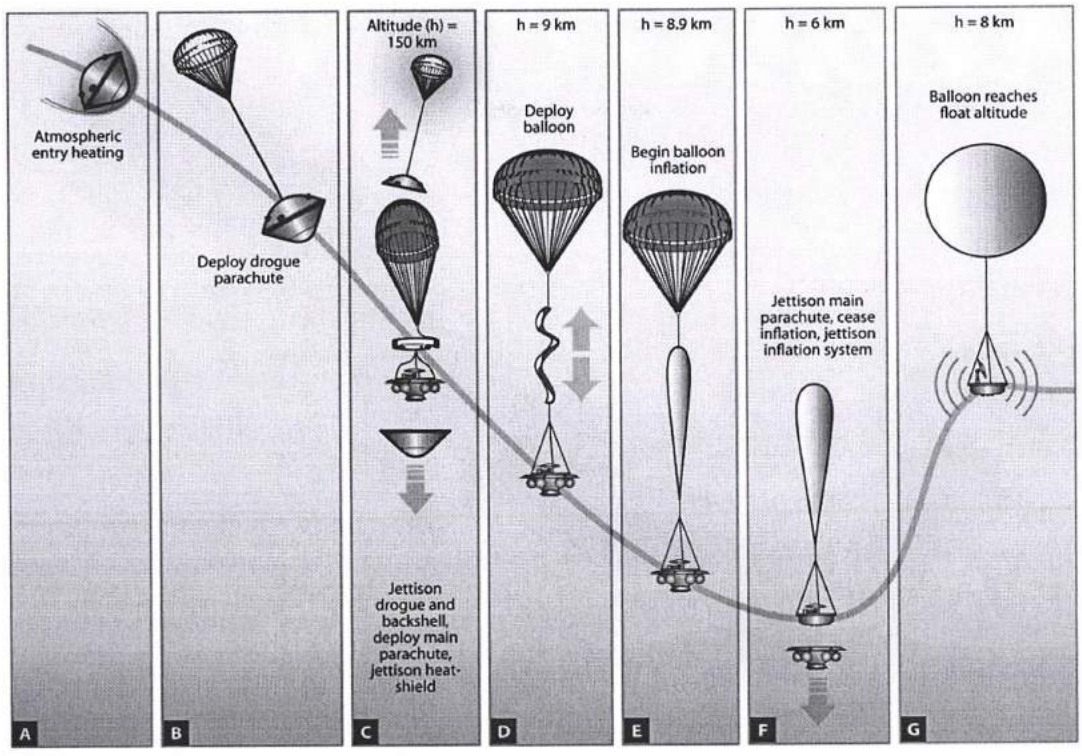

Figure 7. 20 - The entry, descent and inflation sequence of TAE (credits: Hall et al. 2011)

The threshold science mission was to fly over one Titan hemisphere and the goal is a complete circumnavigation of Titan (assumed to require 6 months at 1 m/s net zonal movement). Science data are sent back to earth via a direct-to-earth communication system located on the aerostat.

TAE made the first selection from 47 to 14 mission concepts, and was judged excellent in science, but finally it was not selected. The major concern was about the implementation and especially the availability of ASRGs, provided from US.

7.3 Micro-Electro-Mechanical-Systems (MEMS) for Titan Lakes

In order to overcome portability and consumption restrictions in any future outer planetary missions' requirements, new alternative technologies should be considered. Towards this direction, the adaption of Micro-Electro-Mechanical-Systems (MEMS) devices has been proposed, as part of the science surface properties package of a future probe to Titan like the TSSM Lake Lander (Bampasidis et al., 2009; 2011b).

In this section, I describe how I propose MEMS devices to operate as micro-laboratories by including RF wavelength emitters and temperature and pressure sensors. These micro-machines could obtain the 3D sounding of the liquid deposit, its chemical composition and detect the presence of any biomarkers in a broader area. The temperature and pressure micro-sensors could provide the vertical pressure, temperature and density profile of the liquid deposit (Bampasidis et al., 2011b). Obviously, the utilization of any innovative instrumentation requires complete knowledge of the environmental issues and parameters and, of course, deep understanding of their complexity.

The MEMS pattern, due to its very small shape and size without reducing their operational performance, is the ideal payload for a future Lake Lander probe in Titan and outer planetary space missions in general. As this unique technology is new in the space field, further analysis and testing necessitates. MEMS implementation in Titan's exotic environment is a great challenge for science, engineering and space physics.

As a MEMS device can be considered any small-size product within the range of a micron to a centimetre which also combines mechanical, as well as, electrical structures. Although H. C. Nathanson in late 1960s constructed the first MEMS device (Nathanson et al., 1967), only after the 1980s minor integrated circuits were massively produced in microscopic scale (Stark & Bernstein, 1999).

Due to their small size and shape (20 μm to 1 mm), MEMS have unique properties, which increase the performance of every scientific experiment for a wide range of uses and applications. MEMS can provide an excellent rate of the optimum shape to the rendering performance relation. MEMS devices are able to easily locate impossibly approachable places by traditional instrumentation. They can successfully substitute quite larger in size and shape conventional devices, giving the user the opportunity to explore the structure of the nature in minor scales. Therefore, because of the minimization of the cost in their manufacture and

operation stages, MEMS instruments are preferable for scientific applications, improving the quality and widening the range of the obtained data.

7.3.1 MEMS devices in the space scene

The advantage of implementing MEMS techniques in Aerospace and Space systems become obvious when the reduced requirements in size, mass, power issues of many Aerospace/Space applications are taken into account (Janson et al., 1999). Minimizing the electronic instrumentation assembly is a promising approach when it employs MEMS. The MEMS revolutionizing technology includes all the properties of the larger devices, which are replaced in an inexpensive way. Therefore, the presence of MEMS in space systems offers important financial advantages to space agencies by severely shrinking the cost of any mission. Indeed, MEMS are reducing the weight of future spacecraft without diminishing the scientific performance of the instrument.

Among many other applications, MEMS devices have already been used in the adaptive optics imaging technology in some major telescopes (Krishnamoorthy & Bifano, 1995; Roggemann et al., 1999; Dayton et al., 2002; Zhou & Bifano, 2006). Moreover, the Jet Propulsion Laboratory (JPL) has already developed a new MEMS deformable mirror (DM) system for NASA's adaptive space-based telescopes and in particular for Terrestrial Planet Finding (TPF) mission (Stewart et al., 2006).

Likewise, several proposals have recently been reported for future space missions and telescopes, exploiting the new leading edge MEMS technology. Especially, MEMS techniques have been incorporated as detectors, spectrophotometer and an infrared camera of the new proposed telescope called MTEL (MEMS Telescope for Extreme Lightning) in order to observe the extreme lightning occurring in the upper atmosphere (Nam et al., 2008). MEMS devices seem also appropriate for observing fast moving objects and transient events by the proposed space-based telescope called Obscura (Park et al., 2008). MEMS have also been implemented in Space Infrared telescope for Cosmology and Astrophysics (SPICA), the Japanese coronagraph which is planned to be launched in 2017 (Swinyard et al., 2009). Although the use of MEMS in space applications is in fairly early stage, they will certainly optimize the scientific value of any mission.

7.3.2 Scientific Goals and Objectives

I proposed the implementation of MEMS technology as part of the payload of a future lake lander in Titan. I have presented this proposal at several meetings and have had the opportunity to discuss it with international experts like Dr. Hunter Waite who was interested for a submarine in a Titan lake and Dr. Jean-Pierre Lebreton Huygens Project Scientist/Mission manager.

A MEMS experiment would expand the scientific potential of a future *in situ* space mission to Titan, as these devices can provide miscellaneous measurements, all included in a single capsule. These micro-machines will be able to:

1. Construct a topographic map of the lake floor
2. Probe the temperature and the pressure of the liquid layers
3. Contribute to comparative Planetology
4. Investigate the presence of any biomarkers in a broader area

My study includes several micro probes in the concept of the mission, in order to establish a broad network in the lake, when these devices are released from the lander during its descent. The MEMS network can provide a three dimensional sounding of the lake's bottom topography. This unique map will be constructed by the RF signals transmitted from each device and received by the sensor on-board the Lake Lander. The floor of the lake hosts clues about the processes, which created and shaped the lake and any signs of exchange material with the interior.

As far as the structure of the lakes on Titan is concerned, the contribution of this experiment will be important as well. Firstly, the depth of the lake will be identified, enabling researchers to test their models. Nowadays, only assumptions have been used to determine the lake depth either by studying the surrounding topography of the lake in accordance with terrestrial models, or correlating the lake size to the depth of the Earth's 20 largest lakes (Hayes et al., 2008; Lorenz et al., 2008b; Paillou et al., 2008; Griffith et al., 2012). When the volume of the liquid inventory is calculated, it can be considered in the schema of the methane cycle occurring on Titan (Atreya et al., 2006). The existence of hydrothermal vents on the lake floor could also provide information on the methane cycle of Titan and its hidden source, which replenishes the atmospheric abundance.

MEMS data can also provide information about the interaction of Titan's liquefiers with the lower atmosphere. Particularly, a methane dominated lake affects seriously the local atmospheric status due to the cooling effect of the methane evaporation. This cooling, causes a reduction of the lake surface temperature and as a result an atmospheric downward heat current balances the whole pattern and saturation with methane of the local air mass (Mitri et al., 2007). On the other hand, a lake abundant in ethane is independent of evaporative cooling and it could contribute to the atmospheric convection by remaining in liquid state during the winter like their large terrestrial analogues (Brown et al., 2009).

Measuring the local temperature and pressure profile with the MEMS sensors, scientists will be able to evaluate such current models and determine the local atmospheric heat flux. The incognizance of both composition and structure of Titan's lakes increase the significance of such an *in situ* experiment. The temperature and pressure sounding of the liquid deposit with MEMS experiment will provide the vertical distribution of thermodynamic variables (pressure, temperature, density) beneath the lake surface. This set will supplement HASI vertical distribution profiles (Fulchignoni et al., 2005; Harri et al., 2006) and improve the study of Titan as a system.

MEMS experiment will be the first extraterrestrial oceanographic experiment. New opportunities will be opened for comparative Planetology between Earth and Titan especially looking in terrestrial seas and lakes and their equivalents on Titan.

One of the perspectives of the MEMS experiment would be to investigate the existence of biomarkers located inside Titan's lakes. Molecular biological markers, or biomarkers, are organic structures, sedimentary grown, which contain important information about the precursors of origin of life (Peters et al., 2005). Due to the geologically fresh surface of Titan, with few impact craters (Wood et al., 2010), most of the clues of the moon's past have been erased. However, in isolated environments, like a deep lake, past geological traces can be detected, remaining there under the protection of the liquid.

Similar organic products, like the terrestrial *Stromatolites*, which emerged one or two billion years ago in Earth (Grotzinger & Knoll, 2003), might be well-preserved at the bottom of a deep lake in Titan, encapsulating evidence from past geological environments (Fig. 7.21). These patterns could be easily identified during the topographic sounding of the floor of the hydrocarbon lake with the MEMS experiment. Therefore, this innovative micro-system could become a significant tool to astrobiological research as well.

Figure 7. 21 - Terrestrial Stromatolites (http://www-eaps.mit.edu/geobiology/biomarkers/whatis.html photo: R.V. Burne).

Except for Titan, the proposed instrumentation can be incorporated in the payload of any future space mission to other planetary bodies which consist of liquid layers like Europa and even to Enceladus. To sum up, as Titan resembles Earth more than any other planetary body in the Solar System, any results from Titan can be used for studying the terrestrial environments and help scientists to test and evaluate their models for Earth.

7.3.3 The MEMS payload

MEMS devices feature low power consumption, high-modulation depth, high emissivity and a long lifetime. In general MEMS devices combine:

1) Very small size (20 μm to 1 mm)
2) Fast pulsing (thanks to low mass of the emitter)
3) Limitation of low output power (450 mW)
4) Reduction of the thermal mass of the system
5) Enhancement of the modulated performance
6) Extremely low cost

Design considerations

The microcapsules will be released from the lake lander during the last stage of the Entry, Descent and Landing (EDL) procedure as well as after the touchdown. Each capsule will include a MEMS Unit (MEMS-U). The MEMS-U consists of one temperature and one pressure sensor for direct measurements and the RF signal transmitter. A similar design is depicted in Figure 7.22. The RF receiver unit would be on board the lake lander probe (Bampasidis et al., 2011b). The functional specificity of the temperature and pressure sensors is that they should interact with the environment being outside of the MEMS capsule.

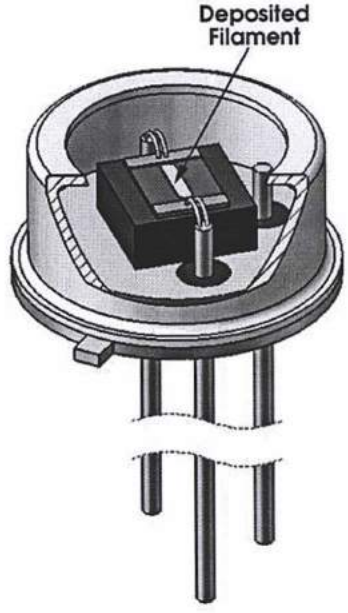

Figure 7. 22 - Deposited filament MEMS emitter (source: Brian Elias, Photonics Spectra (Elias, 2008))

The capsule will encounter harsh and unknown environmental conditions which may affect the performance of the experiment. In order to implement such a payload, several issues should be addressed which are mainly the absorption of the RF signals by the medium and the operation in low temperatures range. Therefore, the physical properties of the liquid should be discussed.

The question is if the transmitted RF will be attenuated from the medium before reaching the receiver. If the liquid material behaves as a partial conductor (when consisting of ionic contaminants for instance), it will prevent RF propagation in long distances. Such liquid conductors set the independent operation of these RF emitters inside the liquid under

discussion. Media with high permittivity and permeability cause a strong attenuation of the RF signal power. One scenario to avoid the attenuation is to connect the devices by a wire to the mother ship. This pattern can also support the microprobes with energy originated by the carrier.

The only information about the composition of the Titan lakes is provided by the remote measurements from Cassini. However, the exact blend of the lakes is still unknown. As I have described in Chapter 5, the main constituent is expected to be ethane, but more hydrocarbons could be mixed in lesser quantities as well. Modeling results about the composition of Titan's lakes show that the major lake liquid constituents are hydrocarbons, mainly ethane, methane and nitrogen (Table 7.6) (Cordier et al., 2009; 2012).

Table 7. 6 - Main constituents of lakes on Titan and the hydrogen bonding strength of each one.

Main Solvent	m.r. poles (90 K) (Cordier et al., 2009; 2012)	H-bond
C_2H_6	$7.64x10^{-1}$	poor
N_2	$4.90x10^{-3}$	no
CH_4	$9.69x10^{-2}$	poor
C_3H_8	$7.42x10^{-2}$	poor
Main Solutes		
HCN	$2.09x10^{-2}$	strong
C_4H_{10}	$1.21x10^{-2}$	poor
C_2H_2	$1.15x10^{-2}$	poor
CH_3CN	$9.89x10^{-4}$	poor

Hence, we should consider the conductivity of such solvent, which is crucial for the proposed experiment. Nitrogen is a non-electrical conductive and it is used as a refrigerant in superconductive applications. Alkanes do not conduct electricity and do not get polarized by an electric field, since they are covalent compounds and do not contain freely moving ions. Aliphatic hydrocarbons have non-polar liquids and weak hydrogen bonding liquids. These liquids are non-polar which means that they allow for the propagation of RF waves throughout the medium.

An electrical conductive mixture can be produced if the hydrogen and nitrogen are connected by hydrogen bonding. To participate in hydrogen bonding, the nitrogen should be polar and charged, which is not the case for free nitrogen. Hence, no hydrogen bond exists. The possibility that the HCN solves in a minor percentage in the liquid ethane and nitrogen does not lead to hydrogen bonding too. Additionally, nitrogen's solution with HCN does not produce free charges.

In conclusion, according to the models that calculate the composition of Titan's lakes, the RF signals emitted from the MEMS-U will be properly propagated in the liquid.

The mean surface temperature in Titan's environment at the equator is approximately 94 K, as it has been determined by the Huygens probe (Fulchignoni et al., 2005) and 2 or 3 K lower in the polar regions as measured remotely by CIRS (Jennings et al., 2009). MEMS devices, will be released by the Lake Lander at low height and either they will flow on the liquid's surface or dive in the liquid. They have to be qualified for such low temperatures.

From experimental experience using MEMS devices at low temperatures, the micro-devices are already adaptable in cryogenic conditions. In the SPICA coronagraph (Swinyard et al., 2009) the micro-scale machines are designed to operate in cryogenic conditions, while the whole telescope will be cooled down to 4.5 K (Enya et al., 2009).

Any temperature measurement is correlated on the variance of an attribute of the exposed material with any ambient temperature change. MEMS resonator-based oscillators have been proposed to be used as Complementary metal-oxide semiconductor (CMOS) temperature sensor with a resolution of 0.008 K (Jha et al., 2007). The MEMS pressure sensing technique is based on the silicon piezoresistive effect, where any pressure change will cause deflection and internal stain change, which will result an output voltage variation (Lin & Yun, 1998; Li et al., 2010). Usually, a Wheatstone bridge circuit delivers such voltage measurements, in order to correlate them with the applied pressure.

RF MEMS Switches are currently under development at the NASA Goddard Space Flight Center[35] (Fig. 7.23).

[35] *http://eed.gsfc.nasa.gov/562/mems_accelerometer.htm*

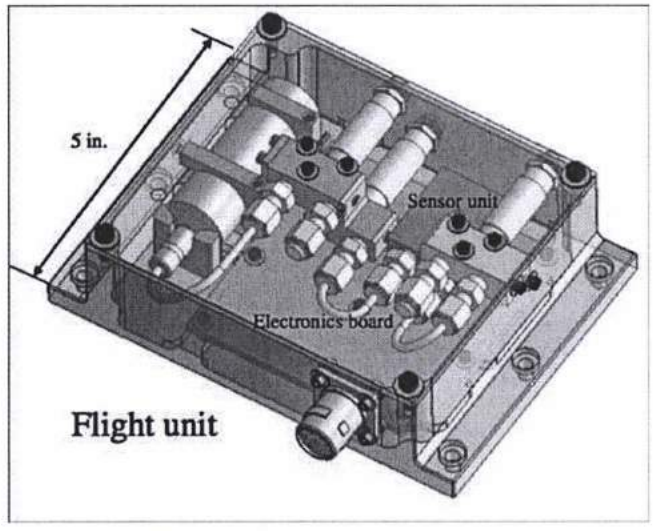

Figure 7. 23 - A pattern of the MEMS 5-inces package (source: NASA, Nano ChemSensor Unit (NCSU) Experiment http://128.102.216.35/factsheets/view.php?id=118)

7.3.4 Description of the experiment

The MEMS experiment will be developed in two phases. Phase One is the deployment of the MEMS micro-shells network (Fig. 7.24). Phase two starts when the devices begin to emit (Fig. 7.25). The deployment will take place during the descent phase of the EDL procedure of the probe. Few meters before the touchdown, the probe will release the MEMS shells to the atmosphere which will begin simultaneously to operate as micro-laboratories. This procedure will be continued after the landing, when the probe releases more MEMS directly to the liquid. Some of these devices will float on the surface of the liquid and other will dive without stopping transmitting.

Schematically, this deployment will provide a broad network of floating and submarine RF sources, while the signal receiver will be aboard the Lake Lander. In a sense, this ambitious experiment can easily accomplish both the 3D sounding of the lake as well as its thermal profile.

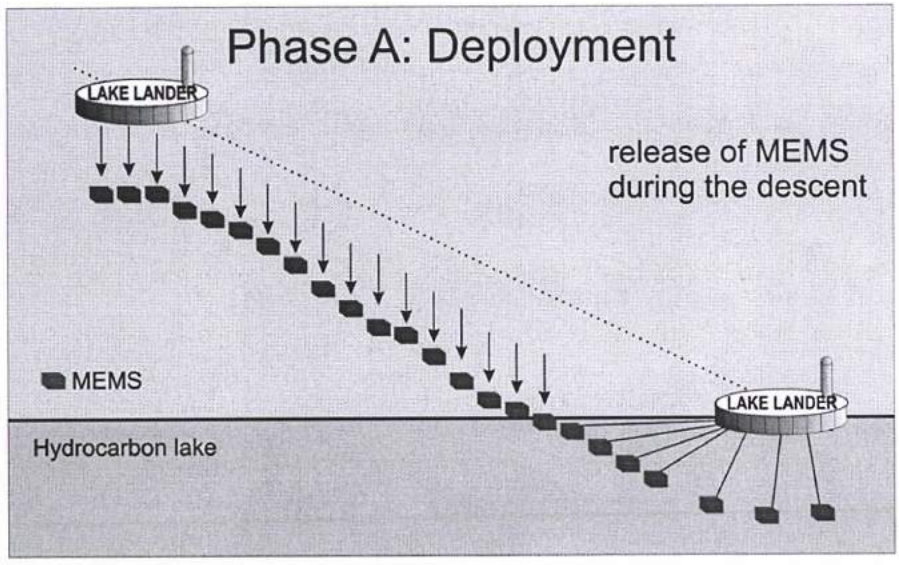

Figure 7. 24 - Phase One of the MEMS experiment during the EDL procedure.

Subsequent to Phase One, these devices will float or dive into the liquid hydrocarbons and continuously transmit data to the Lander depending on the duration of their power supplies.

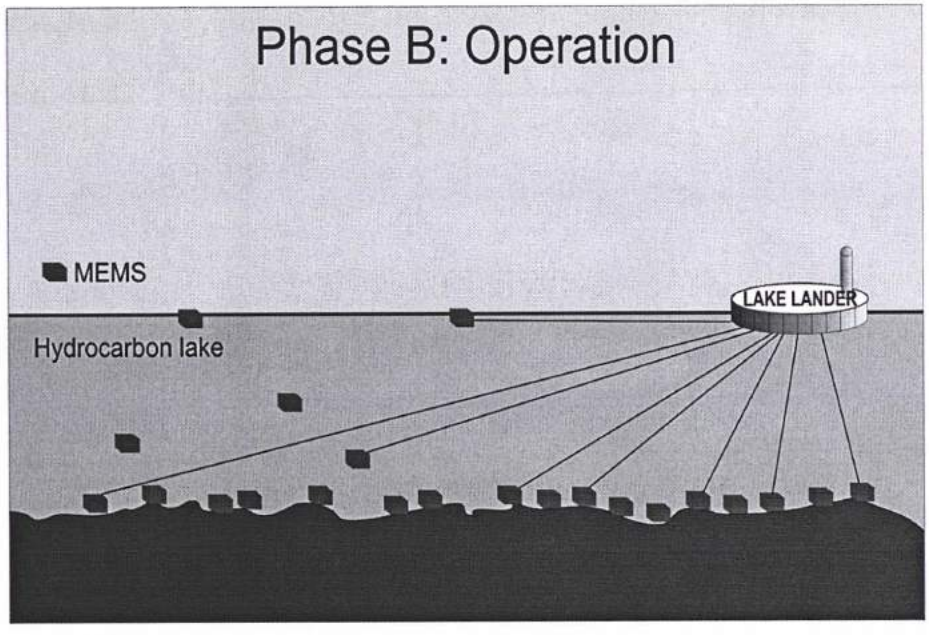

Figure 7. 25 - Phase Two of the MEMS experiment.

The MEMS experiment will vertically measure the temperature and the pressure of the liquid deposit. Moreover, the recorded reflections of the RF signal emitted by MEMS-U will construct the topographical map of the bottom of the lake.

Although it is desirable to have many devices in order to establish a network, the major issue of portability comes up. However, MEMS devices suit perfectly this kind of requirements because of their small shape, size and weight.

7.4 Seismometers on icy moons

The icy moons of the Outer Solar System possess evidence about the origin and evolution of their systems and the Solar System in general. In terms of surface morphology, internal structure as well as their environmental uniqueness, Saturn's moons Titan and Enceladus and Jupiter's Ganymede and Europa are the best representatives to that perspective. In this section, I would like to propose a seismic experiment for the icy moons as a payload of future missions' landers. I also suggested pre-target areas with internal dynamic potential and multivariable surface expressions. Through these experiments, it will be possible to identify active regions along the satellites, which will provide important information regarding the fluid transfer processes towards the surface, as well as, determining the presence of a subsurface liquid deposit (Bampasidis et al., 2011a).

7.4.1 Scientific Goals and Objectives

The scientific goals of the future seismic experiment are:

1. Unveil the internal structure of the moon
2. Detect tectonic activity
3. Confirm or not the existence of internal ocean

The icy satellites of the outer planets can significantly contribute to the study of geological processes across the Solar System. Comparative Planetology can enlighten fundamental mysteries concerning the origin and the evolution of Earth and the Solar System in general and predict future geological events. However, the internal geological structure of each planet or moon can only be determined by *in situ* measurements.

The local or global tectonic field, meteoroid impacts and the moon's tidal deformations induced by Jupiter or Saturn's gravity field, as well as temperature and pressure

fluctuations, may originate ground vibrations within the icy moons. These ground vibrations provide information about the nature of the subsurface material, its fracture and its chemical composition. The Cassini-Huygens mission heritage encourages scientists to discuss about launching future missions towards the outer planets' satellites. In this section, I examine the possibility of installing seismic equipment on icy satellites of the outer planets, setting the minimum technical requirements and describing scientific achievements and possible problems. Data obtained by a seismic experiment, in combination with the analysis results from remote observations, will provide us with details about the interiors of the moons and their connection with the observed surface features (Bampasidis et al., 2011a).

7.4.2 The payload of the experiment

A seismograph is the basic instrument for measuring the ground vibration. It mainly consists of the seismometer and the unit that records the signal. The seismometer consists of three sensors placed in the same sealed case. Each sensor is a pendulum that when it is triggered by the ground movement, it moves from its equilibrium position. This movement is the record of the instrument. The sensors can measure any ground motion within a frequency range usually of 0.001 Hz to 100 Hz, at the north/south, east/west and vertical component in orthogonal system.

Both low and high frequencies can be recorded by broadband seismometers used on Earth. Newer seismographs measure ground movements smaller than 1 nm. There are several kinds of such instruments available, depending on the surface's location. With the usage of seismic instruments, we will extend our knowledge of planets' interior at the Solar System. Additionally, both these space and terrestrial observations will help us understand better the origin and trace the evolutionary path of our own planet.

Table 7.7 below lists the main seismic instrument's requirements considering the specifications of the shortest modern seismic instruments which operate in extreme conditions on Earth like the deep ocean floor (Romanowicz et al., 2006). Similar sensors can be easily found in the global market.

Table 7. 7 - The requirements of the seismic instrument

Seismic Sensors			
Power	Mass	Velocity Bandwidth	Operational temperature
0.32 W	0.200g each	0.001-100Hz	below 100 K

Future mission's instruments on the icy satellites' surface of the outer planets will meet abnormal physical conditions during the entry descent and after landing of their carrier. To achieve the seismograph's accuracy in a specific location the environmental factors (mainly temperature and pressure) should be considered. The ground vibration is the input signal to the system. If the ground vibrates within a range of 0.001 Hz to 100 Hz, the motion signal will be recorded by each one of the three sensors. The sensor system contains a transducer, the device that converts the mechanical motion into electrical signal. A piezoelectric accelerometer can be used as a transducer to sense any weak or strong ground motion in a low frequency range (up to 100 Hz) without using extra power to operate (Garcia et al., 1999).

Once the sensor records a motion, a signal will be sent at the Main Processor Unit (MPU) of the system. The MPU is responsible for the operation, the administration and the maintenance of the instrument and contains the core of the application software. After receiving and recording the signal from the MPU, it will be transferred to the next component of the instrument, the Multiplexer (MUX) by using a line interface circuit, which provides the connectivity between MPU and MUX. MUX data files will be compressed, converted to the right format and prepared for transmission.

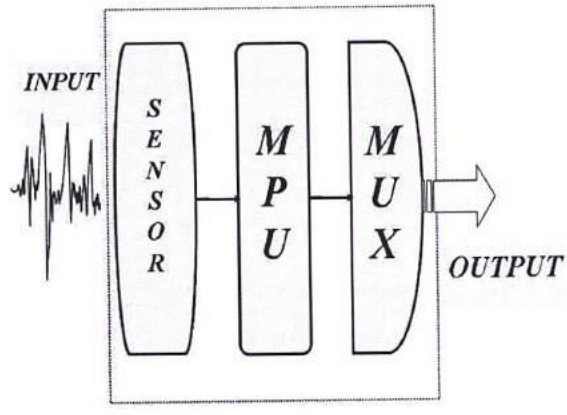

Figure 7. 26 - Functional procedure of the seismic instrument.

Because of the continuous function of the seismometer, a service for bulky data is needed. The transmission frame protocols will be defined similar to the protocols of the lander's instrumentation. Figure 7.26 shows the basic functional procedure of a seismic instrument to be operated on icy moons according to the requirements mentioned above. The configuration of the system is illustrated in a simplified plot. All the components inside the dashed line in Figure 7.26 are parts of the same physical equipment, the seismograph.

The experimental constraints and conditions of the implementation of seismic instrumentation on the surface of icy moons and the possibly emerged problems and difficulties are listed in Table 7.8 below.

Table 7. 8 - Engineering constraints and conditions for a future space seismic experiment on icy moons

Constraints and Conditions	Possible Problems and Difficulties		
	Science	Engineering	Precautions
Fluctuations in temperature	Accuracy affected	Malfunction of the sensors	Special thermal shield
Surface characteristics	Sensors' deformation	Loose the equilibrium position	Special installation and stabilization needed
Dense atmosphere	Chemical Corrosion	Insufficient solar power to recharge batteries	Shield case
Stability of the apparatus	First time in space exploration	Orientation lost	Robotic installation of the seismometer
Maintenance	No recordings	Impossible to repair	Autonomous System
Data transmission	Radio frequency signals	A permanent link needed	Orbiter and large ground radiotelescopes
Exact recordings	3D plotting	Different devices	Seismic network needed
Ground/wind noise	Low Signal to Noise ratio	Stable structure	A shallow hole needed for installation
Power	Continuous operation	Batteries	Radioisotope thermoelectric Generator (RTG)

MEMS technology can be implemented in future seismic experiments on icy moons (Bampasidis et al., 2012b). A MEMS device is in experimental state in the Arizona State University, which is in collaboration with the MET Tech (USA) and the Moscow Institute of Physics and Technology (Russia).

Table 7.9 lists the characteristics of the Arizona State University MEMS device. The sensing element is manufactured with silicon-based microfabrication. It has been integrated with molecular electronic transducer technology (MET), c.f. Hongyu Yu (pers. comm.) and Knapmeyer et al. (2012). It performs high sock tolerance and therefore seems ideal when the geophysical network scenario development will be adopted.

Table 7. 9 – The Arizona State University MEMS device specifications (Hongyu Yu, pers. comm)

Specification	Value
Sensor Type	Molecular Electronic Transducers
Proof Mass	None
Size [mm]	40 x 40 x 40
Power Consumption [W]	0.3
Total Mass [g]	50 (sensing part)
Channels	3
Useful Freq. Range	0.01-50[Hz]
Self Noise (current version)	2×10^{-6} m/S^2/Hz$^{0.5}$ @ 2.5 Hz
Self Noise (expected in 1 year)	1×10^{-9} m/S^2/Hz$^{0.5}$ @ 1 Hz
Shock	Potentially up to 20,000[g]
Installation	Any angle

7.4.3 The concept of the experiment

Seismic waves refract when they pass from the fringes of layers with different densities or changes in temperature, since the local seismic velocities are different. These boundaries are tracers of changes in rock types of the interior (Fig. 7.27). The waves can be detected through a network of sensors providing constraints for the modeling of the internal structure. Seismic

waves from distant events travel deeper into the interior of a planetary body than waves from nearby events. Hence, measuring events at various distances by seismometers can provide the variance with depth of seismic velocities within icy moons.

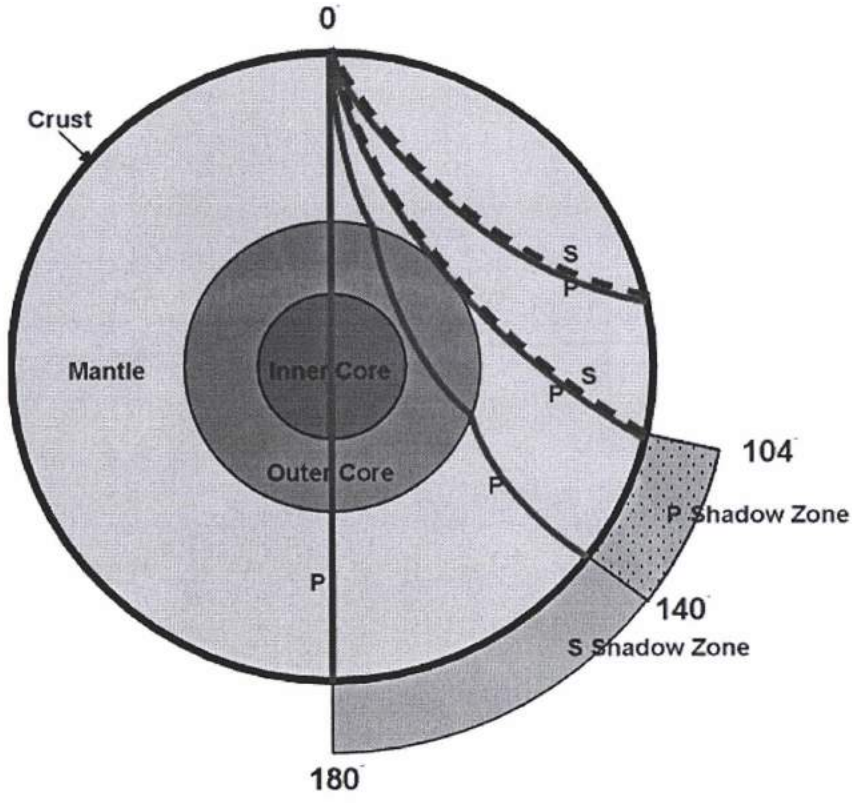

Figure 7. 27 - Seismic waves propagation through the Earth. The Earth is a differentiate medium. The two types of body waves, initiated by earthquakes or by explosions, travel through the interior and provide crucial information about the internal structure. The primary waves (P) compress the material and can travel either through solid or fluid media. On the other hand, the secondary waves (S) shear the medium and can only travel trough solids. Hence, the recordings of P and S waves on the surface can give us clues about the nature of the interior of a planetary body (credit: JL Ahern, 2009).

A seismic network has been proposed (see Fig. 7.28) to be part of the geophysical payload of forthcoming missions (Lorenz et al., 2009; Lange et al., 2011). A seismic network can consist of an array of sensors based on the promising MEMS technology as well as several piezoelectric transducers and new developments based on laser-interferometric sensing or convection in electrolytic liquids.

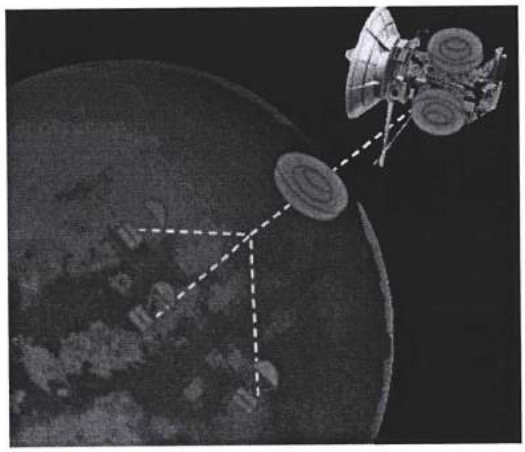

Figure 7. 28 - Titan network mission scenario. Detailed long-term surface studies require data collection though out a geophysical network (Lange et al., 2011). Seismic equipment can be included as payload of such a mission. As in other planetary bodies except for the Earth (Moon, Mars, Venus) Saturn's icy moons seem ideal targets for seismic experiments since they possibly possess active interior.

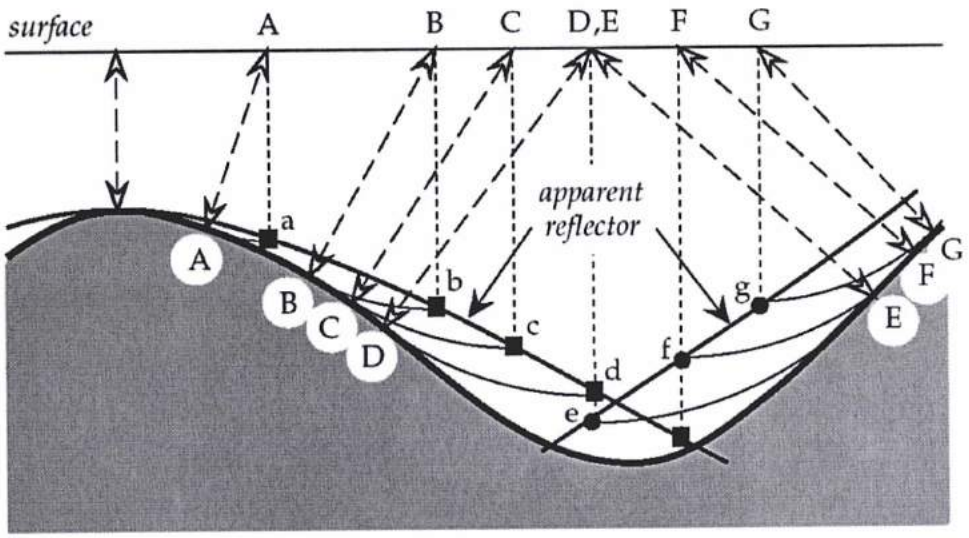

Figure 7. 29 - Geophones on the terrestrial surface. This figure illustrates the operation of a geophone network above a syncline structure (Stein & Wysession, 2003). A network of geophones can receive signals of seismic waves and thus records not only the ground movement but also the interior structure.

This network, which resembles a geophone array (Fig. 7.29) widely used on the Earth, can detect ground motions caused by natural (passive experiment) or controlled sources (active experiment). Space seismic exploration is high priority in NASA programs. Insight mission to

Mars newly selected by NASA as the next Discovery mission will consist of sophisticated geophysical instrumentation which will sound Mars deep interior.

Possible locations for ground-based experiments

The ideal location for the location of seismic equipment will have to ensure that its recordings will represent accurately and separately every ground vibration. For this purpose, the seismic instruments on Earth should be placed in a hole of approximately 0.5 m depth. Thus, less ground noise will be recorded. Noise on an icy surface can be originated by the atmosphere due to its seasonal and diurnal effects as reviewed in Hirtzig et al. (2009) for Titan's case. Noise can be produced also from the local wind and meteor impacts.

In the case of Titan, its dense atmosphere protects the surface from meteoroid impacts and few craters have been observed so far (Elachi et al., 2005; Wood et al., 2010). Therefore, the seismometers will record merely interior events. On the other hand, the same instrumentation will also measure vibrations caused by impacts on Enceladus, Ganymede and Europa.

The proper contact between the feet of the seismograph and the local surface at the landing area stands for another issue to be confronted. Any particles and dust can easily perturb the seismic sensors during their function and cause random errors at the sensor's record. This type of surface features has been already found on Titan. The Huygens probe landed on a relatively soft solid surface analogous to wet clay, lightly packed snow and wet or dry sand (Zarnecki et al., 2005). Moreover, the Descent Imager and Spectral Radiometer's (DISR) surface images showed rounded stones approximately 15 cm in diameter to lie on top of a finer-grained surface in variable spatial distribution (Tomasko et al., 2005). If the icy pebbles lying over the instrument's feet move or/and melt, the equilibrium position of the seismic equipment will be disturbed and the sensors will misplace their initial orientation. The measurements should be corrected if such a micro-movement of the probe is noticed.

7.5 Conclusions

Since 2004, the Cassini-Huygens mission has made exciting discoveries at the Saturnian system and especially at its satellites, Titan and Enceladus. Titan may be representative of many planetary bodies and consequently, the understanding of its internal geology will enlighten the inner structure of an entire class of planets and moons (Coustenis & Taylor, 2008). Similarly, Enceladus, despite its small size, it is extremely interesting due its huge geysers, which mainly feed the E-ring of Saturn. These plumes show that the moon is geologically active, hosting a possible internal water ocean which is the source of its vents (Dougherty et al., 2006; Collins & Goodman, 2007).

Likewise, the Galilean satellites of Jupiter present many similarities with rocky planetary bodies in terms of their surface features and atmospheric environments. Europa hosts a relatively stable environment, an internal ocean and in combination with its young surface, the moon houses a great astrobiological potential (Kargel et al., 2000). On the other hand, Ganymede seems to be a partially geologically active satellite with an intrinsic magnetic field (Pappalardo et al., 1998a; Patterson et al., 2010).

Future missions at icy moons of the outer planets will be a great opportunity to study them comparatively and give proofs of active planetary systems. Jupiter's Ganymede, Callisto and Europa will be the main targets of a future ESA mission at the outer planets to study the emergence of habitable worlds and the Jovian system as a whole. The Jupiter Icy moons Explorer (JUICE) mission will study in depth the icy satellites of Jupiter. It will focus on detailed investigations on Ganymede, Europa and Callisto in order to understand their surface geology, detect the presence of a liquid ocean in their interior and study their habitability potential.

Saturn's Titan and Enceladus could be also studied in the future to improve our understanding of their atmospheric circulation, the surface geological processes and tectonics and their internal oceans, among other. The icy moons of the gas giants can also provide hints regarding the emergence of life and the climate of the Earth.

To study Titan as a system, the Titan Saturn System Mission (TSSM) or smaller more focused concepts have been proposed based on interdisciplinary scientific interest in order to understand the nature of the geological playground, surface formation and its interaction with the atmosphere, meteorology and aeronomy. They could determine the present-day structure and levels of activity of Titan and Enceladus. Such a mission could

also identify heat sources, internal reservoirs of volatiles (in particular methane and ammonia) and eruptive processes and astrobiological processes which possibly occur in its organic environment. The mission would also investigate the relation and the interaction between Titan and Saturn and between Enceladus and Saturn.

The utilization of Micro-Electro-Mechanical Systems (MEMS) technology will give to the future missions the opportunity to improve the exploration. By exploiting their small shape, these prospective devices can reach distant areas where traditional instrumentation is unable to visit. MEMS are some of the most innovative technologies available today. The challenges inherent in using MEMS applications in exotic space environments will surely advance the current technological innovations. Irrespective of that, the impact of this kind of experiment in space science will be enormous, even when operating at rudimentary level. Although several technically originated issues arise from MEMS implementation due to the lack of long time utilization in space missions, they can be compounded by the fact of the reduction of piece-part instrumentation. MEMS can operate in extremely unfavorable conditions by overcoming any technological limitations, thus establishing a benchmark for future experiments.

The MEMS experiment I propose for the lake lander will monitor extensively the ground beneath the liquid and quantitatively define precisely its chemical composition. As a consequence, a MEMS experiment in Titan's lakes will appreciably enlighten our view of the largest Saturnian moon, unraveling a crucial link for understanding atmospheric dynamics and geological processes on it. This conceptual project, after surviving a rigorous testing procedure, can be part of any planetary mission establishing a path for forthcoming surveys.

The seismic experiment which I also would like to propose can identify the existence of liquid internal deposits, with a great astrobiological potential. Isolated environments that consist of water and organics, components that have already been identified on most icy satellites, providing ideal conditions for the survival of biological building blocks. Since only the seismic instrumentation can map the subsurface layers, determine their composition and structure and measure their thickness, I would suggest mounting it in a future mission as part of a landing probe payload.

I believe that these sophisticated experiments should be part of the framework of a future mission on icy moons. As micro-devices are in compliance with the enhanced technological capabilities and meet the NASA and ESA regulations, they seem to be the key

for solving the issues of investigation of the remotest regions of Titan, Enceladus, Ganymede and Europa.

Chapter 8

Titan and the Cassini-Huygens mission as educational resources

Growing and living in a technology-dominated world, it is indispensable for people to become confident in their ability to understand Mathematics and Science (Furner & Ramirez, 1999). Alternative educational resources, different from traditional tools and techniques, can be used as supplementary material in order to attract them to these disciplines. Astronomy and Space Science are excellent fields to use for this purpose. However, the public is occasionally discouraged to get involved in Astronomy by the complexity of modern technology. Despite the intense interest in astronomical phenomena and the contemporary facilities like Internet or a great amount of exceptional publications and TV broadcasts, most people have not got familiar with astronomical phenomena yet. The role of Space Scientists is vital in reducing the distance between Astronomy and the public. The Committee on the Planetary Science Decadal Survey Steering group of the National Research Council of USA strongly recommended and NASA administration agreed to spend at least 1% of the cost of each space mission for education and public outreach activities[36].

In this Chapter, I describe the incorporation of Titan and the Cassini-Huygens mission as resources in formal and informal/outreach educational activities. I also present the results of a project conducted in a secondary education group of pupils in Greece, using Astronomy and especially the Cassini-Huygens mission as a tool for attracting them to science tasks, testing and enhancing their knowledge, abilities and perspective.

The outcome of the outreach activities have been presented in the European Planetary Science Congress (EPSC) in 2006 in Berlin, Germany (Moussas et al., 2006), in the EPSC in 2009 in Potsdam, Germany (Coustenis et al., 2009d; Moussas & Bampasidis, 2009), in the International Astronomical Union Symposium (IAU) in Paris, France in 2009 (Moussas et al., 2011b), in the EPSC in Rome, Italy in 2010 (Bampasidis et al., 2010b) and in the European

[36] NASA response to NRC report, 16/7/11

Geophysical Union (EGU) General Assembly in 2010 (Moussas et al., 2010b) and 2012 (Moussas et al., 2012; Solomonidou et al., 2012), both in Vienna, Austria.

8.1 Introduction

It has been reported that the majority of students of all levels are usually unable to change their previous beliefs and intuitions about physical phenomena, even though they have attended adequate science courses offered by their national curricula (Swann, 1951; Halloun & Hestenes, 1985; Barrington & Hendricks, 1988; Halloun, 1997). Many students continue to use the so called quasi-Aristotelian theory for analyzing nature, being led by their everyday experience, notwithstanding the proved scientific explanations (DiSessa, 1981; White, 1983). Additionally, pupils often do not succeed in solving mathematical problems, because they do not understand the framework of a problem and therefore cannot demonstrate a correct solution (Frykholm & Glasson, 2005).

A more effective way of describing Physics is required in order to overcome people's previous beliefs (White, 1983). Educators have to inspire pupils in demanding modern learning environments and give them the opportunity to engage in productive discussions pertaining to challenges of Science and Technology. Motivating pupils to use contemporary scientific and technological achievements could accomplish significant improvement of teaching effectiveness. The teacher should go beyond the traditional way of teaching and focus on a more student–oriented approach (Heacox, 2002). Obviously, a strong motivator is needed, which can make the children visualize Science and understand the scientific phenomena as well as the embedded mathematics.

The past academic year (2011-12), I had the opportunity to teach Science lessons in a state school of Athens, Greece. My students had not attended Science lessons before and it was a great opportunity for me to incorporate the Cassini-Huygens advents in the secondary education school curriculum. I tried to test whether such a topic could enhance the effectiveness of my teaching and eventually evaluate the results in order to check the degree to which I succeeded the target.

Astronomical issues can be used as an essential pedagogical tool towards this goal. The Astronomy field has already been successfully selected for conceptual change in Science (Vosniadou, 1991).

8.2 The educational value of Titan and the Cassini-Huygens mission

I have been studying the Cassini-Huygens discoveries since 2006. My participation and contribution to the Kronos, TandEM and later TSSM and TAE mission studies gave me the opportunity to interact with many scientists worldwide, experts in Planetary Science. The number of these exchanges increased during my PhD Thesis studies and had significantly benefited me and advanced my knowledge in Titan science as well in Physics and Mathematics. In the meantime, I have been thinking of the possible benefit for the broader public from similar interactions.

The Astrophysics Laboratory's Space Group of the University of Athens, and especially my Thesis supervisors Prof. X. Moussas and P. Preka-Papadema have a long-term experience in educational and outreach activities. Together with my supervisors, we considered the possibility of implementing the Cassini-Huygens mission concept, which is the most successful human exploration project, to attract students and the general public in the disciplines of Science and Mathematics (Moussas et al., 2006). An ideal educational and outreach resource for our purposes should be intriguing and both Titan and the Cassini-Huygens mission are indeed attractive objects.

From the ancient years, people have been always intrigued to seek for terrestrial-like analogues and habitable worlds throughout the Solar System and beyond. As I have described in the previous Chapters, Titan satisfies these prerequisites since its environment presents many similarities to the terrestrial one and it is also one of the prime targets for astrobiology research.

Since 2004, Titan is under deep investigation by the Cassini-Huygens mission, which will last until 2017. The mission's discoveries are often in the headlines worldwide. This material is easily accessible through the World Wide Web, so students, teachers and the layman public can obtain a wealth of information about the Saturnian system.

The Cassini-Huygens mission is a state-of-the-art result of efforts in Science and Engineering and its findings have advanced significantly our knowledge of the Saturnian system. It is a perfect example of the contemporary technology achievements of the application of Science in real life situations. The mission is in the forefront of NASA outreach activities. NASA has already scheduled the 10th edition of "Cassini Scientist for a day", a global annual contest[37], which gives the opportunity for students of all grades (7-18 years old)

[37] http://saturn.jpl.nasa.gov/education/scientistforaday10thedition/

to interact with the Cassini material and the local Cassini experts. My involvement in this event will be described later in this Chapter.

Titan and the Cassini-Huygens mission are exceptional tools for astronomical educational and outreach activities since they combine most of the prerequisites of ideal educational resources: intriguing concept, accessibility, interactivity, illustrative knowledge transitivity, applicability to real life situations and gradual approach to knowledge. Finally, it is worth noting that the interdisciplinary character of the Cassini-Huygens mission is an additional positive element for Science education and outreach.

8.3 Titan and the Cassini-Huygens mission in informal/outreach activities

The starry sky has always seemed mysterious and familiar at the same time to humans from the ancient era to modern times. Today, from ground and space telescopes, a wealth of data revolutionizes our knowledge for our living planet and the entire Universe in a way never imagined before. This digital evolution, currently available worldwide, allows the humanity to benefit from all the space applications. The introduction of young people and the general public into the space field seems essential for not only cultivating astronomical culture and skills, but also for becoming more familiar with scientific work.

In collaboration with the Space Group of the University of Athens, I have organized, participated or attended numerous outreach activities focalized on the general audience in order to conceptualize astronomical phenomena and especially Saturn and Titan to enhance people's knowledge and perceptions. These public events encourage and help young people to love Astronomy and the Solar System, to understand why we need to study Titan and the Saturnian system and to develop their critical thinking, self-expression and creative talents. An overview of these events is listed in Table 8.1 below.

Engaging Cassini-Huygens and Titan in outreach activities has proved very efficient. The concept is to use all the available material to show to the layman public that the human progress is strongly related with the advents in Science, Mathematics and Technology. Beyond its tremendous importance for both Science and Technology, the Cassini-Huygens mission can be successfully employed as an attractor of the general public to Science, Mathematics, Engineering and Technology during outdoor and indoor events.

For this purpose, we perform a virtual time travel from the roots of the Astronomy to the contemporary space era. Two are the major milestones of this journey: the Antikythera Mechanism, which is the most sophisticated astronomical device survived from the Antiquity and the Cassini-Huygens mission (Moussas & Bampasidis, 2009; Moussas, 2010a; 2011a; 2012). Through an introductory lecture, the public becomes capable to visualize the concept of the spacecraft, its operation and usage and learn the high engineering capabilities of it. People can easily visualize the celestial movements of the Solar System and comprehend the fundamental principles that govern the Universe.

I have strongly supported this specific outreach field because of my broad knowledge of Titan science and the Cassini-Huygens mission as well as my personal interest in both of them. Usually in the framework of each event, I perform also a series of simple science experiments, which are the offspring of the collaboration among the Space Group, the British Council in Athens and the Science Communication Unit of the University of West England in Bristol[38].

Prof. X. Moussas and I were the co-leaders of the TandEM Outreach working Group. Distinctive activities/events have been designed for this study. Our plans of outreach activities included interactive web pages, images and video related to the mission (from its developmental stage until the nominal operation at Titan and Enceladus). We will exploit the wide spread of social media especially to interact with the young people. Conventional activities have been also considered such as newsletter release, TV broadcasts, specific publications, lectures, CD/DVD release, card games, collaboration with communities.

The planned outreach activities will be divided into three phases: (a) before the launch of the mission, (b) during the cruise to the Saturnian System and (c) during the nominal mission. As for the first phase, the purpose of the outreach is to keep the layman public interest alive. Towards this goal, the discoveries of Cassini-Huygens mission, which is planned to operate up to 2017, will be used. During the spacecraft cruise to the Saturn System, the outreach activities and events will exploit the first inflight data of the mission from its flyby maneuvers and the Juno results from Jupiter.

Going beyond the level of demonstration, with the contribution of local scientific and amateur astronomers who are considered to be effective Astronomical and Science ambassadors (Berendsen, 2005; Gibbs & Berendsen, 2006), people are actively engaged by

[38]http://www1.uwe.ac.uk/research/sciencecommunicationunit/projecthighlights/uwesciencecommunicators.aspx

performing observations and simulation experiments focusing on the giant planetary systems of our space neighbourhood.

Through these events, people are empowered to conceptualize various astronomical assets by making their own observations and learn the usage of scientific instrumentation, like the telescope and the coronagraph. By these means, Science and Astronomy approach the public and equip young people with critical thinking skills (Coustenis et al., 2009d; Bampasidis et al., 2010b). In particular, children can experience astronomical observations by watching the Sun during the daylight whereas during night, they watch the Moon, the planets, the stars and the constellations.

In addition, children are strongly encouraged to design posters and perform oral presentations in subjects related to Physics and Astronomy. In the meantime, scientists can easily emphasize the importance of funding Science as an investment for society and as a key factor for improving the quality of human life.

Through these activities, pupils enjoy exploring the fundamentals of Science and Technology, which might have a positive long-term impact on their careers and lives (Furner & Ramirez, 1999). The general public has the opportunity to meet experts in space science, scientists, astronomers and engineers and inquire them about astronomical assets concerning the space research, the Earth and the evolution of the Solar System and Cosmology.

At these events, visitors get an up–close view of scale models of spacecraft constructed for young children and are informed about space agencies' missions and their future projects for the exploration of the Universe. Through these events and exhibitions we aim to empower social interactions, encourage the school community to get involved into Space Science and Astronomy and discuss the merits of major global issues like global warming and pollution.

The majority of these outreach events have been presented in numerous conferences worldwide. Table 8.1 below lists the outreach activities I have been engaged. The feedback from the people attended these activities and especially the children encourage me to adapt similar techniques to formal education practices, in which I am engaged since 2001. Due to their interdisciplinary value, Titan and the Cassini-Huygens mission can be easily incorporated into the national science curriculum material.

Table 8. 1 - List of outreach events

Event	Location	Date	Number of visitors
	EUROPE		
Observation of the Venus transit Univ. of Athens	Athens, Greece	6/6/2012	100
Exhibition Antikythera Mechanism University of Evora	Evora, Portugal	19-23/09/2011	1000
Exhibition and Lecture Antikythera Mechanism and the Sun Stadium of Peace and Friendship	Athens, Greece	02-05/09/2011	3000
2nd Festival for the child Lectures and Observation of the starry sky Salamis island	Salamis, Greece	09/07/2011	300
Exhibition and Lecture Antikythera Mechanism and Astrophysics for pupils Hellenic Physical Society Summer School	Heretria and Gianitsa Greece	26-28/06/2011	150
Exhibition and Lecture Antikythera Mechanism Hellenic Foundation for Culture Science and Technology of the Ancient World	Athens, Greece	08/06/2011- 30/09/2011	2200
Exhibition and Lecture Antikythera Mechanism Papastrateion Centre	Agrinio, Greece	16/05/2011	800
Exhibition and Lecture Antikythera Mechanism European University Cyprus Cyprus Science Festival	Nicosia and Limassol Cyprus	27/04/2011- 14/05/2011	800
Exhibition and Lecture Antikythera Mechanism and Astrophysics for pupils Hellenic Physical Society	Naousa, Greece	11-13/03/2011	200
Exhibition and Lecture Antikythera Mechanism and Astrophysics for pupils	Portaria, Thessalia, Greece	11-13/02/2011	200

Event	Location	Date	Number of visitors
Hellenic Physical Society Observation of the Sun Yard of the National and Kapodistrian University of Athens for school pupils	Athens, Greece	09/02/2011	80
Exhibition and Lecture, Antikythera Mechanism	Lemnos, Greece	28/01/2011	58
Exhibition and Lecture Antikythera Mechanism Municipality of Myrina	Lemnos, Greece	27/01/2011	65
Partial Solar Eclipse, Propylaea Acropolis	Athens, Greece	4/1/2011	200
Lecture, Antikythera Mechanism	Rhodes, Greece	2010	120
Astronomical Institute SAS (AISAS) Exhibition of the Antikythera Mechanism	Tatranska Lomnica, Slovakia	01/10-07/11/2009	351
Observation of the Sun University of Athens, International Year of Astronomy 2009 100 hours of Astronomy Exhibition	Athens, Greece	3&5&11/2009	200
34th Convention of Polish Astronomical Society, Institute of Physics of the Jagielonian University Exhibition of the Antikythera Mechanism	Krakow, Poland	15/9-30/10/2009	350
Exhibition Festival International des Sciences Les Rencontres de la Terre	Athens, Greece	12-15/10/2009	2200
3rd Scientific Symposium: "Science and Art" Hellenic Physical Society and Harokopion University	Athens, Greece	09-11/10/2009	300
7th General Conference of the Balkan	Alexandroupolis,	09-13/9/2009	300

Event	Location	Date	Number of visitors
Physical Union 6th Hellenic Conference on Amateur Astronomy Exhibition and Lecture	Greece Alexandroupolis, Greece	25-27/9/2009	400
Partnership Opportunity for Learning: Astronomy Resources for Inspiring Seniors – Aurora Polaris Grundtvig Learning Partnership Olsztyn Planetarium	Olsztyn, Poland	06/5–20/9/2009	10,000
Observation of the Sun and Lectures University of Athens, AURORA Polaris, Eudemos Amateur observatory, Union of secondary education teachers of Dodecanese Exhibition	Rhodes, Greece	15/5/2009	350
The 13th Science Picnic of Polish Radio and the Copernicus Science Centre - The largest outdoor event in Europe promoting Science	Warsaw, Poland	30/5/2009	4000
Exhibition and Lecture Museum Gustavianum Uppsala University	Uppsala, Sweden	31/1–26/4/2009	10,000
Exhibition and Lecture Conference and Cultural Center of the University of Patras	Patras, Greece	05-08/4/2009	2000
Observation of the Sun and Lecture: The Sun, our nearest Star University of Athens	Athens, Greece	05/4/2009	150
Exhibition and Lecture Culture Center City of Rethymnon	Rethymnon, Greece	27–30/3/2009	300
Observation of the Sun Primary school of Nea Chili, Amateur Astronomic Club of Thrace	Alexandroupolis, Greece	27/3/2009	200
Astronomy Week Amateur Astronomic Club of Thrace	Orestiada, Greece	23-27/3/2009	150
The beauty of Astronomy, Astrophysics, the leading edge of research	Kranidi, Argolida, Greece	3/2009	700

Event	Location	Date	Number of visitors
Communication with the ISS 1st Lyceum of Alexandroupolis - Amateur Astronomic Club of Thrace	Alexandroupolis, Greece	11/2/2009	530
Exhibition and Lecture Inauguration of the International Astronomy Year, IAU Symposium 260 and Art Exhibition	UNESCO Headquarters, Paris, France	15–23/1/2009	1000
Exhibition and Lecture Ionic Centre	Athens, Greece	22/10–14/12/2008	7000
Exhibition Zappeion Megaron, Research and Technology Show 2007 and 2008	Athens, Greece	11/2007 and 11/2008	4500
Exhibition HELEXPO/Annual International Commercial Exhibition of Greece	Thessalonica, Greece	9/2008	4000
Lecture, Intermediate school of Kassos, The Antikythera Mechanism, The senior Calculator	Kassos, Greece	30/7/2008	60
Observation of the Sun 10th Primary School of Alexandroupolis Amateur Astronomic Club of Thrace	Alexandroupolis, Greece	21/5/2008	110
Observation of the Sun 5th High School of Alexandroupolis Amateur Astronomic Club of Thrace	Alexandroupolis, Greece	15/5/2008	200
Exhibition and Lecture City of Chios	Chios, Greece	09/2/2008	200
Municipal Theatre of Alexandroupolis Amateur Astronomic Club of Thrace	Alexandroupolis, Greece	05/5/2007	180
Lecture, The Sun and us	Rhodes, Greece	2007	60
Lecture, The Sun and us	Kassos, Greece	2007	45
Total Solar Eclipse	Castellorizo, Greece	29/3/2006	300
Total Solar Eclipse Amateur Astronomic Club of Thrace	Alexandroupolis, Greece	29/3/2006	370

Event	Location	Date	Number of visitors
Total Solar Eclipse Amateur Astronomic Club of Thrace	Orestiada, Greece	29/3/2006	500
Lecture, The Sun	Rhodes, Greece	28/3/2006	70
Lecture, Antikythera Mechanism	Kassos, Greece	2006	90
Lecture, The Sun	Rhodes, Greece	2005	90
Observation, Venus Transit	Rhodes, Greece	08/6/2004	1100
	AFRICA		
Exhibition and Lecture Planetarium Science Center Bibliotheca Alexandrina Alexploratorium	Alexandria, Egypt	1–30/11/2008	2000
Exhibition Centre de Recherche en Astronomie Astrophysique et Géophysique (CRAAG)	Algiers Observatory, Algeria	2/11/2008	50
Abet Greek School in Cairo	Cairo, Egypt	Permanent exhibition inaugurated on 29/11/2008	300
Exhibition 7em Salon d'Astronomie	Constantine, Algeria	30/10–1/11/2008	6000
	USA		
Exhibition Antikythera Mechanism NASA/Kennedy Space Center Launch of JUNO	Cape Canaveral, USA	03/08/2011	3000
Exhibition Gods, Myths and Mortals: Discover Ancient Greece Children's Museum of Manhattan National Touring Exhibition	New York, USA	From 2007 to 2010	more than 500,000

Discussion

Since the beginning of civilizations Planetary Sciences have played a crucial role in the development of human thought. Without doubt, the recent advents in computer hardware, telecommunications and the Internet have definitely facilitated the impact of Space Sciences among young people. Besides, as children experience a continuously evolving technological society, the need for new and challenging educational devices seems obvious.

The astronomical knowledge has significantly increased with time and people have become familiar with scientific facts. Since serving the social benefit is the major commitment of Astronomy, it seems crucial in the contemporary harsh environment to approach the layman public (Clough, 2011). People's perspective of Science and Astronomy in particular is a significant concern of modern scientific communities (Wallace et al., 2012). By general consensus, conventional methods for making science accessible to the public have failed. However, due to the large impact of pseudoscience on people of different social and cultural backgrounds, it is imperative to teach real science to the public in order to clarify any misconceptions.

Astronomers and scientists have to produce innovative methods to attract people and bring Astronomy at the forehead of education. This can only be achieved by following successful pedagogical principles and tools, aiming to make Science accessible and promote lifelong Science learning (Linn et al., 2003). An example of this kind is the use of films (Efthimiou & Llewellyn, 2006), or user-friendly computer software (Furner & Ramirez, 1999; Keating et al., 2002), visual representations (Gazit et al., 2005) or the wealth of the Internet (Cohen, 1999). The outreach activities focus on both children and the general public. The real focus, however, should be on the development of creative and critical thinking throughout the society.

Concerning the educational process, the interaction of the scientific community with school educators improves their teaching skills and effectiveness by including astronomical assets to the design of their lesson plans. In the contemporary school environment, Astronomy is indeed an efficient tool which allows the educators to self evaluate their work on Science lessons and intrigue their students in a learner-friendly environment.

Pupils understand the existence of multiple pathways towards knowledge, develop the ability to express ideas about Physics and Astronomy and eventually think outside the box. Adequately trained teachers readily act as local science distributors to their pupils and

community. Moreover, more students have decided to follow a scientific career, being inspired by the interdisciplinary value of astronomical issues.

Advances of Science have always proved to be beneficial to the humanity and people's quality of life. The outreach projects try to strengthen public interest in Astronomy, by providing alternative paths of learning and expanding their expectations. The participation of people in the events we have organized or participated is increasing, showing their interest in Space Research matters (Fig. 8.2).

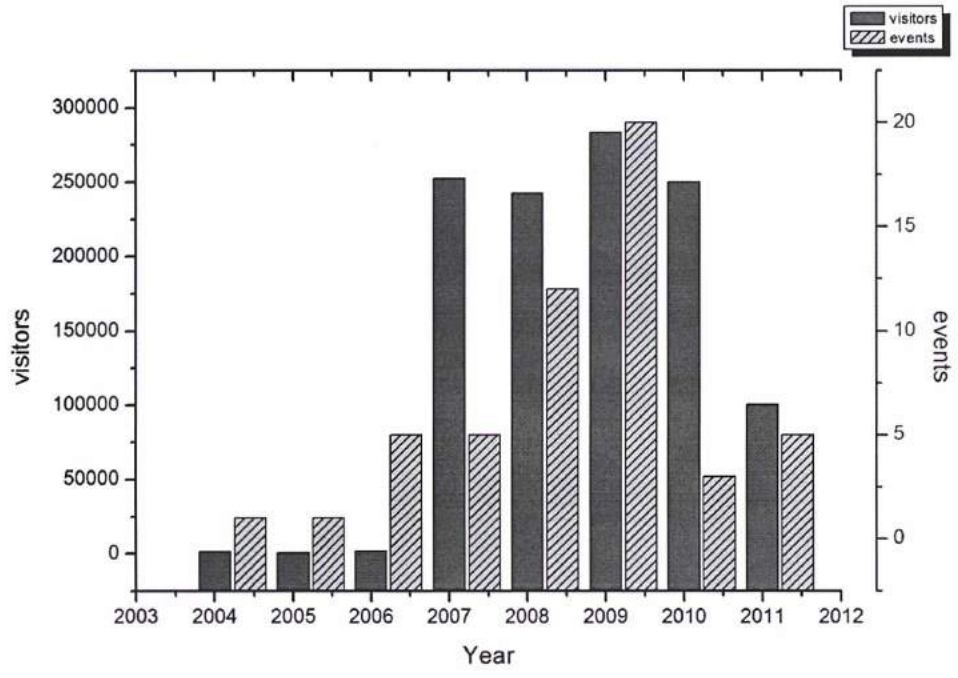

Figure 8. 1 - Annual report of activities listed in Table 8.1 and the number of participants

Both seniors and youngsters can now understand the physical phenomena, adapt indisputably a new way of thinking and leave behind their previous beliefs and intuitions. Through Science, people move beyond the barriers imposed by pseudoscience and start negotiating with their issues using a thoroughly scientific way. Teachers can enrich their inventory with the proper tools to effectively empower their pupils with all the necessary science and mathematical skills. Indeed, Astronomy and Astrophysics stand as excellent attractors of pupils to Science and Technology.

8.4 Titan and Cassini-Huygens mission in formal education

Astronomy can be used in formal education, not only as an independent discipline but also as an attractor to Science and Mathematics and as an evaluation tool for testing pupils' knowledge and perspective about fundamental Science. In order to attract young students from all levels (7-18 years old) A. Solomonidou, Prof. X. Moussas and I became the coordinators of the very successful NASA student contest the "Cassini Scientist for a day" (Solomonidou et al., 2012) the concept of which is described in the next section. This international contest is focusing on the Cassini mission for the last 10 years with Saturn's Titan always being in the center of attention.

Towards this goal I have performed a twofold project. One group of my students participated in the NASA's student contest. Following the two-year successful contest, in May 2012, I conducted a small-scale student research program in a group of Greek students of secondary education in a state school. These students have also participated in the NASA contest.

The goal of this research was dual. I first applied this project to the pupils in order to introduce them to Science issues, which they would face in the next grade. In my point of view, creating positive perspective to Science before pupils begin their science lessons is crucial and Titan and Cassini-Huygens mission provide the essential tools to achieve it.

The second goal of this research was to produce a negotiated interaction between the students and an exchange of information. Through this procedure I was able to evaluate the contribution of each pupil in his/her group and, eventually, self-evaluate my project and the impact of Titan and the Cassini-Huygens to the students. In the forthcoming academic year, this small-scale study will be distributed among the teachers throughout Greece.

8.4.1 NASA - Cassini Outreach school contest: Scientist for a day

NASA holds a very active, productive and student oriented Outreach Group. For the last 10 years the members of this Group focus in maintaining in high levels the interest of teachers and students towards the joint NASA-ESA successful mission Cassini-Huygens with the school essay contest "Cassini Scientist for a day". This mission has attracted global attention and the Outreach Group focus in the international participation in every contest or event regarding Cassini.

The "Cassini Scientist for a Day" contest is a chance for students of all grades (7-18 years old) to describe where they think the cameras on Cassini should be pointed during upcoming observations scheduled for every year's fall. A science team of expertise designs the scientific plan for each year by setting three possible targets within the Saturnian system, including Saturn itself. Each of the three targets has a scientific importance that justifies a possible future observation by Cassini. The task is to choose a target focused on the best science return and explain the reason, in an essay of about 500 words. They also have the option to do team work through groups of maximum three students. For the years 2010 and 2011 (2012 contest is currently under planning), the Space Physics Group of the University of Athens in association with external colleagues has been selected as the coordinator of NASA for the international competition in Greece. This kind of school competition in Greece is particularly important since students rarely have the opportunity to experience and participate actively in similar tasks. Under the guidance of the Cassini Outreach team, A. Solomonidou, Prof. X. Moussas and I have informed, explained and spread the rules of the competition at primary, secondary and high schools all over Greece. We kept open communication with students, teachers and parents for questions and guidance. For the 2010 contest, the target number one was a close-up view of the moon Rhea, number two was a video of Titan, Tethys and Enceladus dancing under Saturn's rings and target three captured a day on Saturn. The main preference of about 60% was target number two. For the 2011 contest, the target number one was Hyperion, number two Rhea & Titan and number three Saturn. Again most arguments were in favor of target number two (67%), showing a preference trend on Titan.

The participation in the contest for 2010 (first time in Greece) was unexpectedly high and thoroughly satisfied at about 150 original essays, while for 2011 the participation increased up to 75%. The winners awarded through a ceremony, which was held in the old amphitheatre of the University of Athens, which was fully packed (Fig. 8.1).

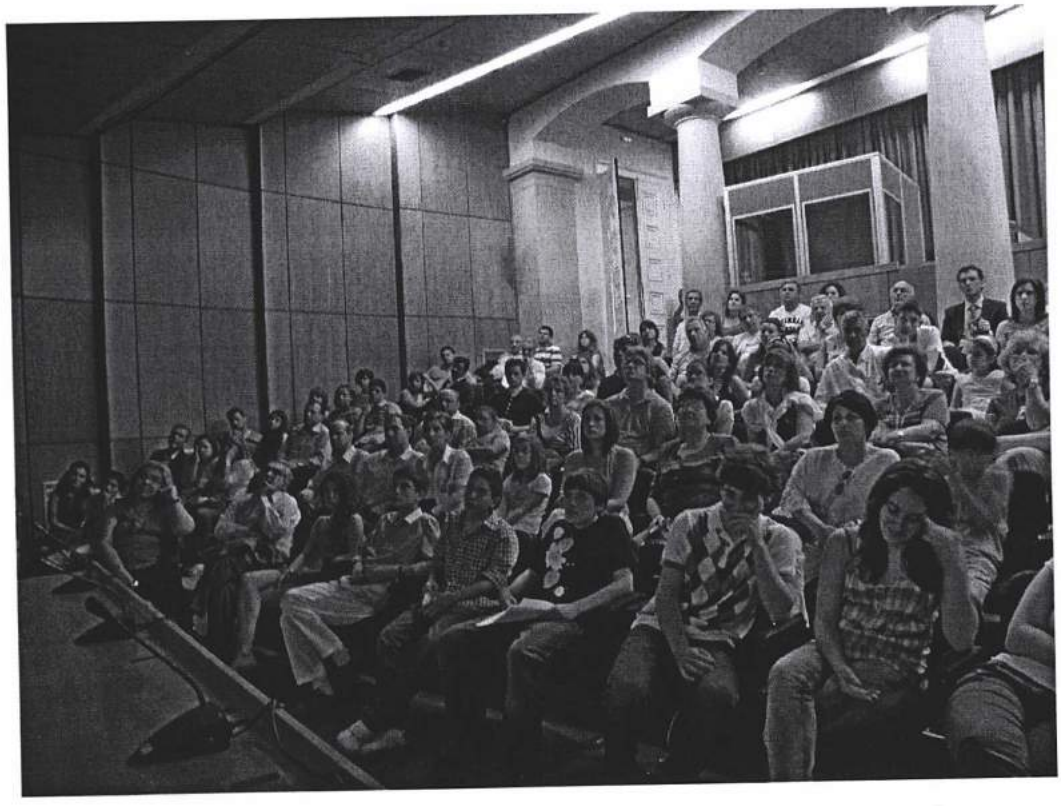

Figure 8. 2 - The winner's ceremony of the NASA contest 'Cassini Scientist for a day' in Greece, May 2012

A big number of the participants of the 2010 contest are either participating in the new contest of 2011-2012 or –since some of them have graduated– are still in touch with the members of our group for study guidance. The 2011 contest's increased number of participation indicated the progress of this competition and its future involvements in school interests. This year (2011 edition) we organized a similar ceremony, with lectures on the topic by specialists as well as some lectures by the pupil and an extra event at the Island of Salamis.

8.4.2 Evaluation project

Student profile

In order to evaluate the impact of the contest in my students I have decided to perform a group activity research in the classroom. All learners who participated in this research were studying at the First Grade of the 20th High School of Athens, Greece within the academic year 2011-2012 and all of them have previously participated in the NASA contest. Classes were mixed and a total of 35 students were involved in this study, 21 boys and 14 girls. Their average age was 12 years old and they only had attended introductory Science lessons during their studies in the Elementary level. However, except for Geography and Biology, Science is not included in this Class Curriculum.

8.4.3 The method

I adapted cooperative group-based activities by using worksheets for three 45-minute teaching hours. Cooper & Mueck (1990) described this type of educational practice as a structured, systematic instructional strategy in which small groups work together towards a common goal. Although students in Greece are not used to working in groups (Alexopoulou & Driver, 1996), this particular state school has been selected from the Ministry administration as a pilot-school to adapt such educational practices. Hence, the target group is quite familiar with group-based work.

The pre-task activity consisted of an introductory lecture, which explained the tasks and linked the forthcoming activity to the Cassini contest. This lecture lasted for about ten minutes. After having attended the pre-task activity, the students were asked to form self-selected groups of 3 to 5 members. They formed 8 groups, 4 of them consisting of 5 students, 3 groups of 4 students and one group of 3 students (Table 8.2).

Table 8. 2 - Group formation

Members in Groups	5	4	3
Number of Groups	4	4	1

Each student had his own worksheet in which he was asked to write down the response of the whole group to the activity's tasks. On the other hand, only one sheet with planetary facts was given to the group as supporting material. By this approach, all students were forced to participate by filling their worksheets and interact with their team members using the common material. The worksheet was divided into 3 individual activities. A short description of the worksheet is given in the Table 8.3 below.

Table 8. 3 - Main points of the tasks' worksheet

Activity	Tasks
1	a) Classify the planets given their density and their distance from the Sun
	b) Mention the position of the Earth
	c) Retrieve information about Titan and Saturn from the web
2	a) Produce a scaled solar system
	b) Find the larger satellites of the Solar System
	c) Retrieve information for Titan and the Cassini-Huygens mission
	d) Describe briefly what Cassini orbiter does
3	a) Mention your favorite planet to visit
	b) List scientific disciplines necessary for space missions
	c) List 3 favorite objects to bring onboard in case of selection as astronaut
	d) Mention a song which fits a future space mission

Acting as a facilitator, I had a minor intervention, mainly observing and monitoring students' work rather than participating as a group member, so as not to influence the final outcome.

Before starting the activity 3, I performed a short demonstration of two experiments, similar to the ones I performed in informal outreach activities. In particular, a simulation of a rocket launch and one of zero atmosphere pressure were demonstrated by using every day materials. An empty film canister played the role of the rocket body. When I lit half of a commercial fizzing antacid tablet and few drops of water, their chemical reaction produced carbon dioxide, which in turn gave the canister the proper impulse to launch for a few meters. Then, I put in a kitchen vacuum packer an inflated balloon or preferably marshmallows and then I pumped the air out from the container. The latter experiment demonstrates what happens to the astronauts in space. More details about both experiments can be easily queried in the internet. This type of experiments can be easily performed by the students as well, showing them the strong connection between Science and real life situations.

The task cycle closed by asking the students to answer an on-line questionnaire related to the whole project. Most of the questions follow the 5-point Likert scale (Likert, 1932), and evaluate the group activity by testing their satisfaction. The questionnaire can be accessed in the following website:

http://users.sch.gr/gbabasides/joomla/index.php?option=com_ckforms&view=ckforms&id=2

8.4.4 Problems related to group-based activities

Working with groups has a beneficial impact in learning process especially in Science disciplines as well as to the development of the communicative skills of the student (Heller et al., 1992). In this group-based project, I have faced the common difficulties mentioned in literature: the free-ride effect and how to evaluate each group member individually.

People participating in groups lower their sense of individual responsibility (Armstrong, 2012) and usually the free-rider effect takes place when skilled members do most of the work (Kerr & Bruun, 1983; Karau & Williams, 1993) .

The outcome of the group work in formal education can be easily evaluated whether it meets the initial goals or not. However, it is difficult to estimate the degree of participation of each individual member of the group in the final result. The same issue has been reported in other disciplines such as English as a foreign language (Foster, 1998), in which group-based activities are a widespread practice. For a successful outcome, students should be convinced for the beneficial purpose of the task and be serious and committed. Additionally, each group member must have a specific role in the task (Ellis, 2003).

8.4.5 Data analysis

The activity was performed as planned within the time limit of three 45-minute teaching hours. All the students participated, submitted the worksheets and filled in the online questionnaire. All the answer sheets were presented in a whole-class context.

The favorite planet for a future travel was Mars which gained 23% of the students, while the Saturnian system was less favorite (20%). Students explained that they selected Mars due to its proximity to the Earth, the results of current water research and the possibility of life existence on it. On the other hand their favorite object was the personal computer at 30%, followed by the mobile phone at 25%. It is worth noting that none of them questioned the possibility of a mobile phone functioning in space. These choices show the degree to which the everyday use of technology influences contemporary teenagers. Finally, although they are technologically influenced, 30% of them did not like the web search activities.

As far as the outcome of the online questionnaires is concerned, Table 8.4 below lists the results. This questionnaire illustrates the satisfaction of the students after finishing the group task. I have decided to give a more general census questionnaire in order to avoid repetitions from the contest.

Table 8. 4 - Results of the online questionnaire

Question	Very well	Well	Moderate	Little	Dislike
General Satisfaction	49	42	9	0	0
The concept	40	39	21	0	0
Exploit Previous knowledge of Science	30	17	20	16	17
Instructions	37	49	14	0	0
Interesting task	46	48	6	0	0
Experiments helpful	57	17	14	9	3
Teacher as a facilitator	94	3	0	3	0
Ability to solve similar problems in the future	11	54	26	9	0
Satisfaction of their participation in the NASA contest	92	8	0	0	0
Attend Astronomy lessons in the future	42	32	19	4	3
Astronomy issues in Science disciplines	44	32	14	5	5
Group cooperation	43	26	14	14	3
All the group member help understanding	32	20	31	6	11
No help from rest the members	38	14	11	17	20

Most of the students were satisfied (91%) from the activity and the concept (79%), while the majority of them (96%) found the subject interesting. Almost half of the students (47%) used successfully the knowledge obtained from their elementary studies, which means that they believe they have a good basis for the forthcoming class. Sixty-five per cent of the students feel more confident to solve similar problems in the future. About 65% of the pupils would like to attend lessons devoted to Astronomy and prefer more astronomic subjects in Science lessons. The students' favorite activity was the design of a scaled solar system by a percentage of 31 followed by the experiment demonstration at 20%. All the students were satisfied by their participation in the NASA contest.

About the feedback for the teacher, the vast majority (94%) appreciated his facilitating role to the activity. Additionally, most of the students understood the task instructions (86%), which means that they are well structured and related to their age and educational level.

Almost three quarters of the participants enjoyed the experimental demonstration, which helped them understand the concept of activity 3. Concerning the performance of group work, half of the students cooperated effectively and interacted with the rest team members.

8.5 Conclusions

As described above, the interdisciplinary value of Titan and the Cassini-Huygens mission is apparent and the public interest worldwide is enormous. This can be used as a magnificent educational instrument, not only to model physical phenomena, but also to become involved in the whole curriculum of the learning procedure. Titan and the Cassini-Huygens mission can motivate children and the general public to understand modeling, identify the scientific way of thinking and initiate or encourage their interest to scientific disciplines. The interaction of the public with the Cassini-Huygens concept emphasizes the technological applications and their large impact to our lives. Without doubt, Cassini-Huygens seriously and generously contributes effectively in promoting Science and Technology to the broader public.

The proposed group work based activity follows the concept of the formative assessment (Ainsworth & Viegut, 2006) in which the teacher applies procedures during the learning process to improve his students' performance. This activity focuses on a qualitative feedback from the student. The high percentages of satisfaction, in combination with their will to implement more astronomic aspects in the Science lessons, encourages me to work towards this direction.

Although the involved students were familiar with working in small groups, only 50% of them felt that they had cooperated properly. This is explained by the fact that the groups were self-formed. Since the free-rider effect had appeared, it would have worked out more efficiently if I had organized the groups according to their level in order to form groups of equal power (Davies, 2009).

This activity has significantly enhanced the students' self-confidence and their ability to solve scientific problems in the future. With such activities, students have developed problem solving and their presentational and communicational skills. Moreover, this kind of group work activities introduces students in the Science discipline.

Conclusions

During my Thesis study, I have investigated different aspects of Titan's environment, focusing mainly on its middle atmosphere but with some non-negligible contribution to its surface science as well. The Thesis manuscript can be divided into two major parts, one concerning the techniques of analyzing Cassini/CIRS data and the other purely scientific. The outcome of the scientific research is then used as a basis for presenting Titan's habitability potential and experiments' design for future missions.

During my research, while covering the Cassini mission, I have managed to infer variations as a function of latitude and time. I have confirmed that a rapid change in the atmosphere took place at 50°N (Bampasidis et al., 2012a). I was led to this conclusion after finding an indication for a compositional enhancement from 2006 to mid-2009 during Titan's northern spring equinox (NSE) on 15 August 2009 for almost all molecules compared to the 2008 and 2010 values. These results are compatible with the findings of Teanby et al. (2010). An additional, new contribution from our work was that the observed increase is followed by a strong decrease of the gaseous chemical content within the next terrestrial year that remains to be confirmed with further data but which has strong implications on the seasonal variations and the behavior of the northern vortex.

To perform this analysis, I have made use of data obtained from Cassini/CIRS on which I have applied the radiative transfer code (Atmospheric Radiative Transfer for Titan - ARTT) I have upgraded. ARTT functions in an enhanced and optimized way, providing an improved fit to the data, thanks to the updated haze and spectroscopic parameters. Thus, ARTT can search for 18 additional molecules and isotopologues compared to the previous version, includes recently detected molecules (Nixon et al. 2008a; 2008b, Jennings et al. 2008) and allows for further research concerning the presence of more complex and new weak species or the identification of more minor isotopologues.

Moreover, I was involved in the evaluation of CIRS data inferences (current pipeline, DS4000 and Grand Average) by testing the outcome of new calibration algorithms applied by the CIRS calibration Team in Goddard. I concluded that a new release of DS4000 database, the Phase-Corrected, should be exploited in future studies using CIRS data for all users. If the latter database is not available, the DS4000 still constitutes an improvement with respect to the current pipeline (v3.2).

As far as the surface is concerned, I have searched for links of the atmosphere with the surface and the interior, since my Thesis subject was on the environment of Titan. Titan's surface liquids (lakes and their surroundings) can provide one such linking point. The surface liquids reveal information concerning the evolution and the dynamics of the "hydrological" processes on Titan surface. The correlation between the geomorphic features that are expressed by the Hortonian morphometric parameters, on which I have worked, and the local topography can provide a qualitative description of the region's development. The analysis of the Mayda Insula drainage shows the existence of steep slopes on its Western part. Since the island basins have various slopes, I assumed that they have experienced various elevations.

Moreover, I have contributed to the research of possible morphotectonic expressions on Titan through a comparative study between Cassini observations and terrestrial tectonic systems. From the above, we managed to make suggestions about possible formation mechanisms of the observed features (Solomonidou et al., 2012). Furthermore, in Bratsolis et al. (2012), I got involved in the application of a despeckle filtering technique for obtaining restored Cassini/SAR images. This tool is based on probabilistic methods and in combination with a segmentation technique, makes possible the extraction of regions of interest from the local background.

The analysis of atmospheric and surface Titan data has also enhanced our understanding of the habitability potential of the satellite as it gives better access to the properties involved in the environment and the stability of the system for supporting the emergence of biological building blocks. The experiment I have proposed, to be included as payload of a future Lake Lander probe incorporating Micro-Electro-Mechanical Systems (MEMS), could measure the thermodynamic parameters of the liquid and produce a 3D topographic map of the lake's bottom (Bampasidis et al., 2011b). I have also proposed a seismic experiment which will be able to identify the existence of liquid internal deposits, with a great astrobiological potential (Bampasidis et al., 2011a).

Finally, the interdisciplinary value of Titan and the frequent, amazing discoveries in the Saturnian system by the Cassini-Huygens mission can be used as a magnificent educational instrument. I have adapted the achievements of the Cassini-Huygens mission on Titan to motivate children and the general public to get involved in scientific disciplines related to Astronomy.

Appendices

Appendix A

The inversion approach of the Radiative Transfer Equation solution

The inversion approach

The inversion approach is a method which allows the calculation of the values of atmospheric parameters from the recorded infrared intensities. In brief, we describe the whole system following a reversal sequence, beginning from the results of a physical process and seeking for the embedded parameters which cause the recorded results (Tarantola, 2005). At first, we should seek for the temperature structure of the atmosphere. Titan's atmospheric temperature is considered as a function of the vertical distance from the satellite's center and the planet-graphical coordinates.

The equation (4) follows the generic form of the *homogeneous Fredholm integral equation of the first kind* in one – linear – dimension which can be formally illustrated as:

$$g(y) = \int_a^b K(y,x) f(x) dx \quad (5)$$

The function $g(y)$ corresponds to the recorded radiance in our case and can be considered as a known term as well as the continuous Kernel function $K(y,x)$ which is the partial derivative of the transmittance in respect to the altitude. On the other hand, the $f(x)$ function illustrates the Planck function, the source of the emission.

The term *inverse problem* is common in Astronomy and in other experimental branches of Science and Engineering such as image and signal processing, geophysics, remote sensing etc, when researchers try to determine the parameters of a physical system by using the interaction data of its sample and the radiation emitted by a known source (e.g. Rawlinson et al., 2010; Bertero and Boccacci, 1998). The Kernel function $K(y,x)$ in (5) is at least known in principle while $g(y)$ is only known in a determined set of points y_i where $i=1,...,m$ is a finite set of quantities with a certain accuracy (Hansen, 1992).

A.1 The quest for the proper solution

In order to understand whether we can proceed to a direct calculation of the above equation, we should firstly formulate the mathematical framework of these problems. To begin with, the class X of functions $f(x)$ is considered as Hilbert space. Both the set of the linear functionals $\{F_n\}_{n=1}^{N}$ and the set of the values of these functionals $\{g_n\}_{n=1}^{N}$ are also defined in the class X, such as:

$$F_n(f) = g_n,\ n=1,\ldots,\ N.$$

Since X is a Hilbert space, the functionals should be continuous and they should be the scalar inner product of the function f and the function $\phi_n \in X$ such as (Bertero et al., 1985):

$$(f,\phi_n)_X = g_n,\ n=1,\ldots,\ N.$$

The solution of such an integral in order to uncover the sought function $f(x)$ can be accomplished by using numerical methods.

When one solves the linear Fredholm integral equation of the first kind, one should take into account that this form is an **ill-posed problem**. As firstly defined by Hadamard (1923) any modeling of physical phenomena should satisfy the next three attributes:

a) the existence of a solution,

b) the uniqueness of the solution, and

c) the stability of the solution (continuous dependence) on the observed data.

When all these conditions are satisfied, these problems are called well-posed. On the other hand, when part of the *boundary data* is not available due to the insufficient number of measurements or heterogeneities and singularities, the problem becomes ill-posed (Xin et al., 2010). In these kinds of problems the solution is extremely sensitive to arbitrarily small oscillations of the system and hence, the data is not really a solution in a physical sense. Indeed, the solution amplifies the noise producing a large and wildly oscillating function which eventually covers the physical solution. As a consequence, a unique existing solution is entirely corrupted by a small error in data, which apparently refers to a loss of information.

The whole issue is linked with the compactness of the operator associated with the Kernel function which cannot have a continuous inverse (Kress, 1999). In our case of Titan's infrared radiation, the high frequency components in the function $f(x)$ are smoothed out by the integration with Kernel $K(y,x)$ in equation (4). Inversely, the calculation of the $f(x)$

function from $g(y)$ will amplify the high frequency in $g(y)$ (Hansen, 1992; Bertero & Boccacci, 1998).

Therefore, an approximate, but stable and reliable, and eventually meaningful solution should be quested by applying additional parameters to the problem which describes the expected physical properties of the system. We should also seek to filter out the high frequency components of the data in order to avoid instabilities on the solution.

To do so, the intensity recording of the instrument $I(\mu,\nu)$ or the $g(y)$ function should have a linear relation with $B(z,\mathrm{T})$ or $f(x)$ function which will be correct only when:

a) $g(y)$ function is related to $f(x)$ by form (5)

b) The recordings on the detectors should have the same or a constant ratio to the y_n value of $g(y)$ function. Then, the equation (5) can be written as:

$$g_n(y) = \int P(y_n - y)\left[\int_a^b K(y,x)f(x)dx\right]dy \quad n = 1,...,N \quad (6)$$

where $P(y_n - y) = \delta(y - y_n)$.

In this point of our discussion, it should be mentioned that the latter (6) equation ignores the noise contribution to the measurements. Eventually, each value of $g(y)$ function of the instrument's recordings is a linear functional of the $f(x)$ function. In other words, $g(y)$ numbers are the norm [$f(x)$] from the vector space $K(y,x)$ to its field of scalars. Therefore, the equation (4) can be solved by numerical analytical methods.

A.2 Linearization

The radiance $I(\mu,\nu)$ and the transmission function $T_r(\mu,\nu,z)$ are known values by the CIRS recordings and spectroscopic databases respectively. The Planck function $B(\nu,\mathrm{T}(z))$ remains the unknown parameter. Therefore, the equation (4) should be solved to derive the $B(\nu,\mathrm{T}(z))$ values. The solution of the radiative transfer equation (4) can be approached as follows (Vinatier, 2007):

$$I_{\nu_i} = \sum_{j=1}^{N} B(\nu_i, T(z_j))\Delta T_r(j)$$

$$I_{\nu_i} = \sum_{j=1}^{N} B\left[\nu_i, T^o(z_j) + \Delta T_j\right]\Delta T_r(j)$$

for N layers and $\Delta T_j = T(z_j) - T^o(z_j)$ and by applying the Taylor series for the B function we derive:

$$I_{\nu_i} = \sum_{j=1}^{N}\left[B(\nu_i, T^o(z_j)) + \frac{\partial B(\nu_i, T)}{\partial T}\Delta T_j\right]\Delta T_r(j)$$

$$I_{\nu_i} = I^o{}_{\nu_i} + \sum_{j=1}^{N}\frac{\partial B(\nu_i, T)}{\partial T}\Delta T_j \Delta T_r(j)$$

but since $\Delta I = I_{\nu_i} - I^o{}_{\nu_i}$

$$\Delta I = \sum_{j=1}^{N}\frac{\partial B(\nu_i, T)}{\partial T}\Delta T_j \Delta T_r(j)$$

$$\Delta I = \sum_{j=1}^{N}\frac{\partial I_{\nu_i}}{\partial T}\Delta T_j$$

and if we define K_{ij} as:

$$K_{ij} = \frac{\Delta I_i}{\Delta T_j} = \frac{\partial B(\nu_i, T(z_j))}{\partial T_j}\Delta T_r(\nu_i, z_j)$$

we can have the linear form:

$$\Delta I = K\Delta T \quad (7)$$

A.3 The K_{ij} matrix

To begin with, we assume that the temperature is a depended quantity by the altitude r_i and the latitude φ_j. Thus, we can define the array of n-element vectors:

$$T(r_i, \phi_j) = T_{ij}$$

where $i = 1,...,n$ and $j = 1,...,q$, which means that we divide the atmospheric region in N layers.

Moreover, since the measurements are remotely recorded, errors due to orbiter's position in respect to the planetary body should be also considered. Furthermore, the atmospheric pressure is either not accurately known on a constant gravitational potential surface or outside the sounding region. Therefore, we introduce a single shift ξ_l in all tangent heights at a given tangent point latitude $(\varphi_t)_l$, when $l=1,...,p$. CIRS spectral radiance recordings depend on frequency ν, altitude r_t and latitude φ_t (Achterberg et al., 2008). Then, we define the m-element vector:

$$I_k = [\nu, r_t, \varphi_t]_k$$

where $k = 1,...,m$.

Secondly, the quantities to be retrieved are incorporated to a single column vector x the elements of which are the arrays of temperature T_j, the neperian logarithm of the derivative of the transmittance in respect to the altitude $\ln\left(\frac{d\tau_c}{dr}\right)_{ij} = b_j$ and the tangent point shifts ξ_l.

$$x = \begin{bmatrix} T_1 \\ \vdots \\ T_q \\ b_1 \\ \vdots \\ b_q \\ \xi_1 \\ \vdots \\ \xi_p \end{bmatrix}$$

This is the vertical temperature and aerosol profile of Titan's atmosphere for both limb and nadir measurements. The column vector x is a [(2nq+l) x 1] vector.

On the other hand, we define a forward spectral radiance model vector $h(x)$ with m-elements such as the measurements I_k. Then, by calculating the partial derivatives of the model h in respect to the n-elements vectors T_j and b_j we derive:

$$L_j = \frac{\partial h}{\partial T_j} \text{ and } M_j = \frac{\partial h}{\partial b_j}$$

L_j and M_j are (m x n) Jacobian matrices. Additionally, the partial derivatives of the model radiances h in respect to the p-elements shifts at each tangent point latitude are:

$$u_l = \frac{\partial h}{\partial \xi_p}$$

All these Jacobian matrices (L_j and M_j) and the vector u_l construct the (m x (2nq+p)) array K:

$$K = [L_1,...,L_q, M_1,...,M_q, u_1,...,u_p]$$

Having a reference set of atmospheric parameters and in our case the temperature $T^o(z_j)$ derived by the a combination of CIRS limb and nadir data and Voyager 1 radio occultation results (Flasar et al., 2005) or by the Huygens Atmospheric Structure Instrument (HASI) (Fulchignoni et al., 2005), we can consider a forward model $h(x)$ and by expanding it by applying the first order of Taylor series we derive:

$$h(x) = h(x^o) + K(T - T^o)$$
$$h(x) - h(x^o) = K\Delta T$$
$$\Delta h(x) = K\Delta T$$

where $h(x)$ are the measurements and $h(x^o)$ is the model using the reference values $T^o(z_j)$ and which is the same expression as (7).

A.4 Numerical Solution

If we followed the classical least squares approach, since the problem has become at the linear form of (7):

$$\Delta I = K\Delta T$$

we would minimize the residual:

$$\|\Delta I - K\Delta T\|^2$$

ΔI and ΔT are the perturbation quantities with respect to a reference temperature $T^o(z)$, the radiance $I^o(\nu_i)$ is calculated using the reference value of $T^o(z)$. The matrix K_{ij} is the functional derivative at ν_i with respect to T at level z_j

$$\Delta T = T(z_j) - T^o(z_j)$$
$$\Delta I = I(\nu_j) - I^o(\nu_j)$$

The solution should confront the same problems with the original equation. The regularization technique is usually applied in solving inversion problems and Tikhonov's approach in Hilbert spaces is one of the most famous (Tikhonov & Arsenin, 1977) by introducing the parameter γ as a constraint which determines the relative weight which is applied. The regularization can be applied in both the integral and linear system derived from integral's discritization since the effect on the smooth solution is the same (Hansen, 1992).

Let's expand the perturbation in temperature ΔT in a set of basis vectors such as (Conrath et al., 1998; Hanel et al., 2003):

$$\Delta T = Fa$$

where by F is the matrix the columns of which are the basis vectors and α is the vector of the expansion coefficients.

Hence, we minimize the function:

$$\|\Delta I - K\Delta T\|^2 + \|\gamma a\|^2$$

which means that according to Tikhonov's approach we can minimize the following penalty function[39] in respect to α :

$$Q = (\Delta I - KF\alpha)^T E^{-1}(\Delta I - KF\alpha) + \gamma\alpha^T\alpha$$

With E we represent the measurement error covariance matrix. The first term illustrates the usual penalty function of the least square fittings, while the second one is a measure of the departure of the solution from the reference profile. Since we want to minimize the previous function Q in respect to a, we should apply the following matrix identity:

$$\frac{\partial(Ax+b)^T C(Dx+e)}{\partial x} = (Dx+E)^T C^T A + (Ax+b)^T CD$$

Then, the partial derivative of Q in respect to a becomes:

$$\frac{\partial Q}{\partial a} = (\Delta I - KFa)^T \left(E^{-1}\right)^T (-KF) + (\Delta I - KFa)^T \left(E^{-1}\right)(-KF) + 2\gamma a^T$$

and from the definition of the covariance matrix $\left(E^{-1}\right)^T = E^{-1}$, the derivative takes the form:

$$\frac{\partial Q}{\partial a} = 2(\Delta I - KFa)^T \left(E^{-1}\right)(-KF) + 2\gamma a^T$$

By setting $\frac{\partial Q}{\partial a} = 0$, we quest for the minimization:

$$(\Delta I - KFa)^T E^{-1} KF = \gamma a^T$$

Now, by applying the identity $(ABC)^T = C^T B^T A^T$ and by replacing the $KF = G$ we derive:

[39] By the superscript T we define the transpose matrix.

$$\left(\Delta I^T - a^T G^T\right)E^{-1}G = \gamma a^T$$
$$\Delta I^T E^{-1}G - a^T G^T E^{-1}G = \gamma a^T$$
$$\Delta I^T E^{-1}G = a^T\left(\gamma I + G^T E^{-1}G\right)$$
$$\Delta I^T = a^T\left(\gamma I + G^T E^{-1}G\right)\left(E^{-1}G\right)^{-1}$$
$$\Delta I^T = a^T\left(\gamma I + G^T E^{-1}G\right)G^{-1}E$$
$$\Delta I^T = a^T\left(\gamma G^{-1}E + G^T E^{-1}GG^{-1}E\right)$$
$$\Delta I^T = a^T\left(\gamma G^{-1}E + G^T\right)$$

where I is the unit matrix, and by transposing the last expression we have:

$$\left(\Delta I^T\right)^T = \left[a^T\left(\gamma G^{-1}E + G^T\right)\right]^T$$

which leads to:

$$\Delta I = \left(\gamma G^{-1}E + G^T\right)^T a$$
$$\Delta I = \left(\left(\gamma G^{-1}E\right)^T + G\right)a$$
$$\Delta I = \left(\gamma E\left(G^{-1}\right)^T + G\right)a$$
$$\left(\gamma E\left(G^{-1}\right)^T + G\right)^{-1}\Delta I = a$$

Now its time to seek for an expression containing the temperature difference ΔT hence we multiply with the F matrix and replace again the $G = KF$:

$$F\left(\gamma E\left(G^{-1}\right)^T + G\right)^{-1}\Delta I = Fa$$
$$F\left(\gamma E\left((KF)^{-1}\right)^T + KF\right)^{-1}\Delta I = Fa$$
$$F\left(\gamma E\left((KF)^T\right)^{-1} + KFI\right)^{-1}\Delta I = Fa$$
$$\Delta T = F\left(\left(\gamma E + (KF)(KF)^T\right)\left((KF)^T\right)^{-1}\right)^{-1}\Delta I$$

Therefore, the minimization of Q gives the following expression:

$$\Delta T = FF^T K^T\left[\gamma E + KFF^T K^T\right]^{-1}\Delta I \quad (8)$$

which can be written as:

$$\Delta T = SK^T\left[\gamma E + KSK^T\right]^{-1}\Delta I \quad (9)$$

where $S = FF^T$, a two-point correlation matrix of the basis vector F (e.g. Conrath et al, 1998). And if we define:

$$V = SK^T\left[\gamma E + KSK^T\right]^1$$

we derive:

$$\Delta T = V\Delta I \quad (10)$$

We then separate the stratosphere into N levels, which in Titan's case are 200 (Achterberg et al., 2008). Now, we are able to apply a constrained inversion algorithm, by assuming local thermodynamic equilibrium (LTE).

Once a system is supposed to be in LTE, although the intensive parameters of the system still change within space and time in each of the 200 levels, they vary slowly enough to support the thermodynamic equilibrium assumption. Then, its thermodynamic condition is determined only by its temperature which describes both the distribution of the velocity of the contained particles and the radiance of the radiation as a function of frequency. Thus, the radiation field within each atmospheric layer approaches the black body emission.

Hence, the recorded energy can be approximated as a function of the thermal radiation and the vertical distribution of the absorber. The total contribution of the outgoing infrared radiation of the atmosphere consists of the partial contribution of each atmospheric level. The region of the maximum contribution is located where the optical depth equals unity.

Due to the nonlinearity of the problem an iterative process of (10) is necessary. Only the correlation matrix $S = FF^T$ of the basis vector is present in the final expression and the basis vector. The error covariance matrix due for the temperature retrieval due to the instrument's noise propagation is (Hanel et al., 2003):

$$R = VEV^T$$

If we assume that the existing random measurement errors at two random points in the spectrum are uncorrelated, the diagonal elements of the (mxm) matrix R equal the square of the Noise Equivalent Spectral Radiance (NESR) of each measurement associated with the CIRS instrument (Achterberg et al., 2008). In fact, NESR is the signal of the instrument when the signal-to-noise ratio equals unity (Hanel et al., 2003). The rms error estimate for the i-th level is:

$$\sigma_{T_i} = (\sum_j V_{ij}^2 E_{ij})^{1/2}$$

For the CIRS averaged spectra, the effective NESR is derived by the:

$$\frac{NESR(i)}{\sqrt{N}}$$

where N is the number of spectra. The error estimate σ_{T_i} refers only to the precision or reproductivity of the retrievals in the presence of random measurement error (Conrath et al., 1998).

The functional derivatives or the contribution functions or kernels are determined from the equation mentioned in §4.4.2, the $K_{ij} = B(z)W(z,\mu)$.

However, if we assume that the temperature dependence of the Planck function is strong compared to that of the transmittance the K_{ij} can be written as (Hanel et al., 2003):

$$K_{ij} = \frac{\partial B\left[\nu_i, T(z_j)\right]}{\partial T_i} \frac{\partial Tr(\mu, \nu_i, z_j)}{\partial z_j}$$

The vertical profiles of the temperature retrieval correspond to a specific spectral query in FP1, FP3 and FP4 part of the recorded spectrum. We directly apply this profile to fit the ν_4 methane band in the FP4 data and then we apply it to the other two focal planes, as it is described previously in the direct solution of the radiative transfer equation.

Appendix B

Atmospheric Radiative Transfer code for Titan (ARTT)

Installation and upgrade manual

B.1 History of the ARTT development

The core of ARTT is based in the radiative transfer software, first induced by Scott in 1974 (Scott, 1974). The program has been firstly applied in 1977 in the Laboratoire de Météorologie Dynamique (LMD) studies (Scott & Chedin, 1981) and several upgrades have been done up to date.

The first large upgrade was taken place in 1986 by Bruno Bezard, who modified the code initially for applying it in the Saturnian atmosphere and then for the Titan's case. This release of the code calculated the transmittance and the atmospheric radiance of Titan's atmospheric constituents based on spectroscopic parameters adapted from the *GEISA* 1977 database (*Gestion et Etude des Informations Spectroscopiques Atmosphériques*: Management and Study of Spectroscopic Information,(Chedin et al., 1982).

From 1986 to 2005, several modifications have been imported into the code, mainly adapting the new *GEISA* release updates (Husson et al., 1992; 1994). In 2006, two separate upgrades have been performed. GEISA 97 spectroscopic parameters (Jacquinet-Husson et al., 1998; 1999) were adapted in mid-2006, while at the end of the year the new spectroscopic files from the *GEISA 2003* version (Jacquinet-Husson et al., 2005) replaced the old ones, except for the HCN, HC_3N, C_2H_4, C_3H_4 and C_4H_2. For the HCN the *GEISA 97* lists were kept (Jacquinet-Husson et al., 1999). On the other hand, new spectroscopic files from Jolly et al. for the ν_5 stretching band at 663.2 cm^{-1} of HC_3N replaced the previous ones (Jolly et al., 2007). C_2H_4 lines were initially taken from Blass et al. (Blass et al., 2001) and M. Rotger 2006 (pers. comm.) (Rotger et al., 2008). The latter data were added later in the upgraded version of GEISA 2003 atlas (Jacquinet-Husson et al., 2008). The ν_9 band data of C_3H_4 was replaced from the files provided by G. Graner (pers. comm.). Only C_4H_2 ν_8 and $\nu_8+\nu_9-\nu_9$ hot

bands were replaced by Arie and Johns results (Arie & Johns, 1992), while the rest replaced by the *GEISA 2003* ones .

The 2006 version of the code could perform calculations for 14 individual molecules: methane (CH_4), ($2H_1$) methane (CH_3D), carbon monoxide (CO), carbon dioxide (CO_2), hydrogen cyanide (HCN), cyanoacetylene (HC_3N), cyanogen (C_2N_2), methylacetylene (C_3H_4), acetylene (C_2H_2), ethane (C_2H_6), ethylene (C_2H_4), propane (C_3H_8), diacetylene (C_4H_2) and water (H_2O).

With the 2006 upgrade, the user became capable of choosing between constant-to-height abundances and vertical distribution mixing ratios for the model calculations. Additionally, in this release, the software simulation is divided into 3 separated spectral regions, following CIRS data focal planes, FP1, FP3 and FP4 data in order to save valuable computational time. Moreover, two more molecules were added to the source code of ARTT:

a) Benzene (C_6H_6) from Dang-Nhu et al. lists (Dang-Nhu et al., 1989) was added to the code, followed its detection in Titan's atmosphere (Coustenis et al., 2003).

b) Monodeuterated acetylene C_2HD v_4 band at 451-581 cm^{-1} and v_5 at 600-761 cm^{-1} also was added from LISA (Laboratoire Interuniversitaire des Systemes Atmospheriques) spectroscopic database (http://www.lisa.univ-paris12.fr/). Acetylene-d1 was firstly detected on Titan in 2008 (Coustenis et al., 2008).

The latest upgrade before our effort was the 2007 one. In this upgrade, two more molecules were added:

a) Acetonitrile (CH_3CN) v_8, $2v_8$, v_4, v_7 bands were added to the code from Pacific Northwest National Lab – PNNL data (https://secure2.pnl.gov/nsd/nsd.nsf/Welcome)

b) The $^{13}CH_3D$ isotopologue of monodeuterated methane was added at 1148 cm^{-1} following its detection (Bezard et al., 2007).

Hydrogen cyanide (HCN) spectroscopic lines from *GEISA 97* (Jacquinet-Husson et al., 1999) were replaced from *HITRAN 2004* (HIgh-resolution TRansmission molecular AbsorptioN database) (Rothman et al., 2005) and later by *HITRAN 2008* files (Rothman et al., 2009). C_2H_6 bands were replaced by the ones provided from Vander Auwera et al. (2007). Following its detection (Coustenis et al., 2008), C_2HD v_4 and v_5 bands were updated provided by the work of Jolly et al. (Jolly et al., 2008). Moreover, three molecules are separated from their isotopologues: $HC^{14}N$ and $HC^{15}N$ adapted from *HITRAN 2004*, $^{12}CH_4$ and $^{13}CH_4$, $^{12}C_2H_2$ and

$^{13}C^{12}CH_2$ adapted from *GEISA 2003*. Eventually, this version takes into account for calculations 21 molecules and is named as ARTT 0.3.8.

B.2 ARTT Installation

In order to install the Atmospheric Radiative Transfer code for Titan (ARTT) the following software is prerequisite:

- Fortran compiler
- Gnuplot
- the make command
- an archive manager

As far as the hardware is concerned, the workstation should have:

- at least 2GB ram capacity
- Linux or Macintosh OS distribution

The source distribution of ARTT (ARTT-src-*.*.*-yyyy-mm-dd.tar.gz) contains all the source files for the installation of the program. In the name of the file we can find its version in the part of the name seen as '*' and the date that its development ended in the 'yyyy-mm-dd' part of the name. The current version is 1.0.0. The source folder contains the following folders:

- ARTT-work-*.*.*: This folder contains some sample files to be used for the modeling of the spectrum after the installation.
- cirs: This folder contains Cassini CIRS datasets
- db: Here we can find all the spectroscopic data files which are used for the calculation of the model.
- distrib: This folder contains the vertical profiles as derived by General Circulation Models (GCM).
- profils: This folder contains the thermal profiles.
- src: This folder contains the source files needed for the installation of ARTT.

The folder "ARTT-src-*.*.*-yyyy-mm-dd" contains some files too with data needed for the installation. The most important files from these is a file called "config.txt" which contains the installation path and the compiler options and a makefile with the installation procedure. If we execute the command "make" in the folder containing the source files then we can see the options for the installation of ARTT.

After installing ARTT a folder called "bin" is created, in the installation folder, which contains the executable files. Another folder called data is created in the path specified within the file "config.txt". This folder contains the following sub-folders:

- ARTT-work-*.*.*: If we execute the "make" command in this folder then a list with all the available actions is seen. In order to generate a model of Titan's atmosphere a template file is needed with the name "Name_of_the_model.mod"
- bandes-*.*.*: This folder contains the files "c3h8.dat" and "continuum.dat"
- cirs: In this folder we can find the data from CIRS used for the creation of the plot based on space data. This is a copy of the cirs folder of the source distribution.
- distrib: This folder contains the vertical distributions of the molecules. It is a copy of the initial distrib folder.
- profiles: This folder contains the thermal profiles. It is a copy of the initial profiles folder
- raies-*.*.*: This folder contains in binary format the data which were read during the installation procedure from the db file.

B.3 ARTT Upgrade procedure

To add a new molecule in our model, we should proceed through the following procedure. The sources databases for the spectroscopic files we search are the following:

Gestion et Etude des Informations Spectroscopiques Atmosphériques (GEISA) (Jacquinet-Husson et al., 2011) website: http://ether.ipsl.jussieu.fr/etherTypo/?id=950

High-resolution transmission (HITRAN) (Rothman et al., 2009) website: http://www.cfa.harvard.edu/HITRAN/HITRAN2008/

CIRS Team Website: http://blizzard.astro.cornell.edu/drupal/

Adopt GEISA linelists

The spectroscopic files, adopted from GEISA database are accessible in GEISA website. The steps are the following order:

We hit the Geisa-2009 link, then the Interactive access link and finally the Database Extract. The latter opens a webpage, which is divided with three different boxes. In the first box we select the molecules or the isotopologues we would like to download, in the second box we define the spectral range we are interested in and in the last box we check the columns we want. The following procedure should be done for every different molecule or isotope separately.

Each GEISA entry has its own id number instead of their name and therefore we should find the correct code from the GEISA list. This list is also posted in GEISA web site.

As far as the spectral range is concerned, it is not necessary to download different files for every spectral region (FP1, FP3, FP4). ARTT has the ability to read from the same file using the right parameters, besides the spectral range.

From the available parameters for of GEISA line lists, we select the A, B, C, D, F, G, I, parameters to be included in the download:

A: Wavenumber of the line

B: Intensity of the line at 296K

C: Air broadening pressure half-width

D: Energy of the lower transition level

F: Temperature dependence coefficient n of the air broadening half-width

G: Identification code for isotope as in GEISA

I: Identification code for molecule as in GEISA

Adopt HITRAN linelists

The procedure needed to get a molecule or an isotope from the HITRAN database is somewhat different from GEISA. HITRAN is also a web accessible database and it offers a

program called javaHAWKS. After downloading and installing javaHAWKS locally we proceed to the "HITRAN2008/By-Molecule/Uncompressed-files" folder. Every file in this folder corresponds to a specific molecule. In order to track down this molecule we must advice the corresponding HITRAN database table. After downloading the data file we open the JavaHAWKS program and complete the following steps:

- Click on "Select" tab
- In the field "HITRAN filename" enter the name of the data file
- Give a name in the output file
- Edit the selection parameters and hit the "Run select" button

Now the requested file is created locally and it contains the data specified in the "Selection Parameters" area.

The last step remaining is to complete the transformation of HITRAN data to ARTT format. The problem that we meet after downloading the data from HITRAN is that the wavenumber values should be in the first column and the molecule and isotope id numbers should be in the last 2 columns. The following program written in Fortran makes this conversion easy:

```
      program read_spectro

C ***** Program for the formatting of the spectrum files *****

      implicit none

C ********** Constants **********
      integer mtotre
     parameter(mtotre=100000)

C ********** Local variables **********

     character*80 fichin,fichout
     integer infre,isupre,np1,np2
     integer i,ntotre
     double precision freq1,freq2
     integer idcor
     double precision wn,ss,ffr,alfar
C ================================================================
```

```
      if(iargc().eq.2) then
        call getarg(1,fichin)
        call getarg(2,fichout)
      else
        write(*,*) 'Which file would you like to transform ?'
        read(*,*) fichin
        write(*,*) 'Which is the name of the output file you want ?'
        read(*,*) fichout
      endif
      open(unit=10,file=fichin,form='formatted',status='old')
      open(unit=11,file=fichout,form='formatted',status='replace'
      rewind 10
      rewind 11
      idcor=0

      do
           read(10,1002,err=100,end=300) i,wn,ss,ffr,alfar,freq1
1002        format(i3,f12.6,e10.4,10x,f5.4,5x,f10.4,f4.2)
           write(11,1003)wn,ss,ffr,alfar,freq1,i,idcor
1003        format(f12.6,1x,e10.4,f5.4,f10.4,36x,f4.2,2x,i3,1x,i1)
      enddo

300   write(*,*) 'File formatted succesfully'
      close(10)
      close(11)
      stop

100   write(*,*) 'Reading error'
      stop 1

200   write(*,*) 'Writing error'
      stop 2

      end
```

This program is executed in a terminal by command "gfortran -o read_hitran read_hitran.f" where read_hitran is the name of the executable file which will be created, while and read_hitran.f is the name of the source file containing the code above. Then we should execute the command "./read_hitran". The output of this program is the HITRAN file

in the correct ARTT format. Important note: during the execution of the read_hitran program we will be asked to enter the name of the output file, we must not enter the same name as the input file.

Add a new molecule in ARTT

After retrieving the desired spectroscopic files from the online databases, the incorporation procedure is the following:

1) We create a copy of the installation folder of a previous installation and we will make all the subsequent changes in this folder. It is essential to keep a backup of the previous installation folder in case of a data loss.

2) We add the data file from GEISA or HITRAN in the folder /db and we edit it in order to change the number corresponding to the molecule's database id (it is the number in the final column in most cases). We replace this number with a molecule id, which doesn't exist in our code. In order to find all the existing molecule numbers it is better to search in the spectroFP1-2-3.don files first. Alternatively, we can edit the spectro.f file but it is a bit more risky. If we update a molecule, which already exists in our database, we don't have to change the molecule's id, since the new file will replace the old one.

3) The following procedure must be done for the files spectroFP1.don spectroFP2.don spectroFP3.don:

   - We open the file spectroFP*.don and we augment the number before the following text "nombre d'associations fichier-molecule" by one.
   - We add a new line with the idgeisa we added before. The wninf and wnsup columns must have values that cover the desired spectrum.
   - In the fichier column we put a number which must be unique and less than 65 (this number will be used later for the identification of the data file). It is crucial that the name of every molecule or isotope will be only 6 characters long.

4) Then we open the /src directory and edit the files "trans_rad.f", "linelists.f" and "distrib.f".

5) In the file trans_rad.f in the line 22 we change the value of the variable named mcorps in the new number of molecules in our radiative transfer code. In the file distrib.f we

must change the format identifier 627 to ensure that all the new molecules will be printed.

6) In the file linelists.f we have to be very careful. We add a couple of lines like the following :

```
fichier(56)='db/geisa_C3H8.dat'
forma(56)='(f12.6,1x,d11.4,f6.4,f10.4,36x,f4.2,i3,i3)'
```

7) These lines describe the file we have added in the /db folder. The number inside the parenthesis is the unique identifier of the file under the fichier column in the spectroFP*.don files. In the first line we add the exact path to the new file and in the second line we edit the format in Fortran language. The argument f12.6 means that we have a number with twelve digits, six of which are the decimal fraction. The argument 36x means that we have 36 blank spaces. The argument d11.4 means that we have a number in exponential form with four decimal digits.

8) In the file compounds.inc we must augment the nbcomp parameter to the number of molecules that our radiative transfer database contains. It is always the same number we add in the file trans_rad.f. Then we must add the right number in the end of every set of variables. When we add an isotope of an already existing molecule all the values we must add except the molecular weight are the same as the ones of the original molecule. It is crucial that the name of the molecule will be only 6 characters long.

After the installation the number of molecules in the line 21 in the .mod files should be edited.

Note: This manual is based in Stefanos Stamogiorgos Bachelor dissertation.

Appendix C1

Thermal and chemical structure variations in Titan's stratosphere during the Cassini mission

Journal Article published in *The Astrophysical Journal*, 760, 144.

The Astrophysical Journal, 760:144 (8pp), 2012 December 1 doi:10.1088/0004-637X/760/2/144

THERMAL AND CHEMICAL STRUCTURE VARIATIONS IN TITAN'S STRATOSPHERE DURING THE *CASSINI* MISSION

Georgios Bampasidis[1,2], A. Coustenis[1], R. K. Achterberg[3], S. Vinatier[1], P. Lavvas[4], C. A. Nixon[5], D. E. Jennings[5], N. A. Teanby[6], F. M. Flasar[5], R. C. Carlson[5,7], X. Moussas[2], P. Preka-Papadema[2], P. N. Romani[5], E. A. Guandique[5,8], and S. Stamogiorgos[2]

[1] Laboratoire d'Études Spatiales et d'Instrumentation en Astrophysique (LESIA), Observatoire de Paris, CNRS, UPMC Univ. Paris 06, Univ. Paris-Diderot, 5, place Jules Janssen, F-92195 Meudon Cedex, France; gbabasid@phys.uoa.gr
[2] Faculty of Physics, National and Kapodistrian University of Athens, Panepistimioupolis, GR 15783 Zographos, Athens, Greece
[3] Department of Astronomy, University of Maryland, College Park, MD 20742, USA
[4] GSMA, Université Reims Champagne-Ardenne, F-51687 Reims Cedex 2, France
[5] Goddard Space Flight Center, Greenbelt, MD 20771, USA
[6] School of Earth Sciences, University of Bristol, Bristol BS8 1RJ, UK
[7] IACS, Catholic University of America, and NASA/Goddard Space Flight Center, USA
[8] Adnet Systems, Inc., Rockville, MD, USA
Received 2012 September 8; accepted 2012 October 8; published 2012 November 16

ABSTRACT

We have developed a line-by-line Atmospheric Radiative Transfer for Titan code that includes the most recent laboratory spectroscopic data and haze descriptions relative to Titan's stratosphere. We use this code to model *Cassini* Composite Infrared Spectrometer data taken during the numerous Titan flybys from 2006 to 2012 at surface-intercepting geometry in the 600–1500 cm^{-1} range for latitudes from 50°S to 50°N. We report variations in temperature and chemical composition in the stratosphere during the *Cassini* mission, before and after the Northern Spring Equinox (NSE). We find indication for a weakening of the temperature gradient with warming of the stratosphere and cooling of the lower mesosphere. In addition, we infer precise concentrations for the trace gases and their main isotopologues and find that the chemical composition in Titan's stratosphere varies significantly with latitude during the 6 years investigated here, with increased mixing ratios toward the northern latitudes. In particular, we monitor and quantify the amplitude of a maximum enhancement of several gases observed at northern latitudes up to 50°N around mid-2009, at the time of the NSE. We find that this rise is followed by a rapid decrease in chemical inventory in 2010 probably due to a weakening north polar vortex with reduced lateral mixing across the vortex boundary.

Key words: infrared: planetary systems – planets and satellites: atmospheres – planets and satellites: composition – planets and satellites: individual (Titan) – radiation mechanisms: thermal – radiative transfer

Online-only material: color figures

1. CONTEXT AND OBSERVATIONS

Latitudinal variations in Titan's stratospheric thermal and chemical structure have been reported in the past from *Cassini* data acquired by the Composite Infrared Spectrometer (CIRS) (Flasar et al. 2005; Teanby et al. 2006; Coustenis et al. 2007, 2008, 2010; de Kok et al. 2007; Teanby et al. 2007, 2008, 2009a; Vinatier et al. 2007, 2010; Nixon et al. 2008a; Achterberg et al. 2008, 2011). Here, we explore the thermal and chemical evolution discernible within the timeframe from 2006 to 2012, thus complementing and refining previous reports from earlier stages of the mission. We study Titan's neutral atmosphere between ~120 and 300 km in altitude (the stratosphere and lower mesosphere) and latitudes from 50°S to 50°N.

CIRS is a Fourier Transform Spectrometer, aboard the *Cassini* orbiter, consisting of two interferometers probing the far-infrared (10–600 cm^{-1}) and mid-infrared (600–1500 cm^{-1}) ranges with an apodized spectral resolution varying from 15.5 to 0.5 cm^{-1}. CIRS scans Titan's atmosphere through three separate focal planes that share the same telescope: FP1 (10–600 cm^{-1}), FP3 (600–1100 cm^{-1}), and FP4 (1100–1500 cm^{-1}) (Flasar et al. 2004). We focus here mainly on FP3 and FP4 high-resolution observations (0.5 cm^{-1}) but also some medium resolution ones (2.5 cm^{-1}).

Prior to 2006 (flybys T0–T9) insufficient data at the right conditions for our purposes (signal-to-noise, emission angle, distance, region, etc.) were acquired. During the flybys that followed, CIRS obtained a large number of spectra in FP3 and FP4 at high, medium, and low spectral resolutions (0.53, 2.54, and 15 cm^{-1}), respectively, in surface-intercepting (nadir) and horizontal viewing (limb) geometry conditions, albeit not always covering all latitudes, so that in the northern hemisphere we have data only from late 2007 to 2010. An instrument anomaly followed by a reboot of CIRS took place in December 2006, thus depriving us of data from that time. We otherwise use all available and exploitable data at high spectral resolution (0.5 cm^{-1}) and perform averages of the spectra acquired during one or several flybys as necessary to attain a high signal-to-noise ratio for our calculations.

Tables 1 and 2 list the CIRS FP3 nadir northern and southern averages, respectively, at high resolution (0.5 cm^{-1}), while Tables 3 and 4 list the associated FP4 averages. The average signal-to-noise ratio is shown as well as the corresponding *Cassini* Titan flyby(s) and the relative solar longitude (Ls). The selections we made in order to enhance the signal-to-noise ratio cover different latitudes on Titan (we sum all longitudes because no longitudinal variations were found in our studies; Coustenis et al. 2007, 2010). The averaged spectra created from the high-resolution nadir data in the several latitudinal bins (between 50°S and 50°N) contain a large number of spectra in general, with some exceptions (as indicated in Tables 1–4). As discussed in Coustenis et al. (2007), we have taken care to correct the

Table 1
Titan Flybys and FP3 Data Acquisition Characteristics from 2007 March to 2011 September Averaged in Northern Latitudinal Bins

Year	Month	Latitude	Total Number of Spectra	Signal-to-noise	Airmass	*Cassini* Flyby	Ls (°)
2007	Mar	50°N	357	18.6	1.02	T26–T27	329
"	Dec	50°N	335	19.9	1.25	T38–T39	338–339
2008	Feb–Mar–Jul	50°N	145	12.4	1.19	T41–T45	341–347
2009	Mar	50°N	517	25	1.35	T51	355
"	Apr–May	50°N	275	15.3	1.01	T52–T55	355–357
"	Jun	50°N	476	25.6	1.88	T56–T57	358
2010	Jan	50°N	284	21.3	1.69	T65–T66	005–006
2006	Jul	30°N	551	34	1.17	T15–T17	320
2007	May	28°N	934	44.7	1.06	T30–T31	331–332
"	Dec	31°N	905	45.4	1.14	T38–T39	338–339
2008	Mar	30°N	992	42.3	1.01	T42	342
"	Dec	36°N	262	20.5	1.03	T48–T49	351–352
2009	Dec	30°N	748	44.5	1.46	T63–T64	004–005
2010	Jun	35°N	599	37.4	1.24	T69–T70	010
2011	Sep	32°N	771	46.8	1.49	T78	025
2006	Jan	1°N	1291	56.2	1.01	T10	314
"	Jul	1°N	2118	71.8	1.01	T15–T16	320
2007	Apr–May	1°N	189	23.9	1.21	T28–T29	330–331
"	Jun	1°N	1497	62.5	1.06	T32–T33	332–333
"	Aug	1°N	152	19.3	1.01	T35	335
2008	Jan	1°N	589	39.4	1.07	T40	340
"	May	2°N	597	47	1.55	T43–T44	344–345
2009	Mar–Jul	1°N	86	18.3	1.75	T51–T59	355
"	Oct	1°N	72	14.9	1.19	T62	002
"	Dec	1°N	283	25.6	1.01	T63–T64	004
2010	Sep	3°N	1504	58.9	1.02	T72	014
2011	May	11°N	921	50	1.20	T76	021

Table 2
Titan Flybys and FP3 Data Acquisition Characteristics from 2006 February to 2012 January Averaged in Southern Latitudinal Bins

Year	Month	Latitude	Total Number of Spectra	Signal-to-noise	Airmass	*Cassini* Flyby	Ls (°)
2006	Mar	1°S	1515	61.3	1.04	T12	316
2007	Oct	1°S	93	17	1.28	T19–T20	323–324
"	Jul	1°S	232	23.3	1.01	T34	334
"	Nov	1°S	813	44.5	1.01	T37	338
"	Dec	3°S	276	25.3	1.01	T38–T39	338–339
2008	Feb	1°S	426	39.8	1.46	T41	341
2010	Apr–May	1°S	466	33.0	1.01	T67	008
"	Jun	1°S	391	30.6	1.02	T69–T70	010
"	Jul	1°S	985	49.8	1.08	T71	011
2011	Dec	2°S	1047	52.1	1.19	T79	028
2006	Feb	30°S	666	37.7	1.88	T11	315
"	May	30°S	536	35.3	1.33	T14	318
2008	Nov	38°S	1055	39.9	1.02	T46–T47	350–351
2009	Dec	24°S	961	40	1.08	T63–T64	004–005
2010	May	24°S	911	44.9	1.30	T68	009
2012	Jan	30°S	1980	56.1	1.49	T80–T81	029
2006	Oct	50°S	568	30.9	1.18	T19–T20	323
2007	Jan	50°S	925	37.0	1.04	T23–T24	327
"	Mar–May	50°S	341	28.2	1.64	T26–T31	329–332
"	Jul–Aug	50°S	647	39.6	1.70	T34–T35	334
"	Dec	50°S	467	31.7	1.53	T38–T39	338–339
2008	Jul	50°S	34	9.6	1.28	T41	341
2009	Mar	50°S	198	17.2	1.09	T51	355
"	May	50°S	1288	45.2	1.25	T54–T55	357
2010	Apr	50°S	124	16.0	1.69	T67	008

data for any latitude smearing effect observed for high emission angles and/or data taken at latitudes higher than 50°N. So that the latitudes sounded can be about 5° lower when the line of sight intercepts the surface at 55°N or 55°S, the actual latitude at the vertical of the stratospheric altitudes being observed is then rather 50°N and 50°S, respectively. The latitudes listed in the tables are corrected for this effect.

We have applied a radiative transfer code to analyze the CIRS data spanning the 2006–2012 timeline, during which the *Cassini* mission performed 71 Titan flybys (Tables 1–4). Besides the

Table 3
Titan Flybys and FP4 Data Acquisition Characteristics from 2007 March to 2011 September Averaged in Northern Latitudinal Bins

Year	Month	Latitude	Total Number of Spectra	Signal-to-noise	Airmass	*Cassini* Flyby	Ls (°)
2007	Mar	50°N	1376	64.6	1.03	T26–T27	329
"	Dec	50°N	342	34.4	1.26	T38–T39	338–339
2008	Feb–Mar–Jul	50°N	166	12.8	1.14	T41–T45	341–347
2009	Mar	50°N	417	30	1.28	T51	355
"	Apr–May	50°N	1481	49.9	1.01	T52–T55	355–357
"	Jun	50°N	575	35.8	1.65	T56–T57	358
2010	Jan	50°N	234	27.6	1.67	T65–T66	005–006
2006	Jul	30°N	567	67.1	1.17	T15–T16	320
2007	May	30°N	1789	125	1.06	T30–T31	331–332
"	Dec	30°N	657	81.8	1.18	T38–T39	338–339
2008	Mar	30°N	1013	86.5	1.02	T42	342
"	Dec	35°N	394	74.1	1.03	T48–T49	351–352
2009	Dec	30°N	764	83.9	1.36	T63–T64	004–005
2010	Jun	36°N	503	69.6	1.25	T69–T70	010
2011	Sep	28°N	1107	106	1.39	T78	025
2006	Jan	2°N	869	107.3	1.01	T10	314
"	Jul	1°N	1840	152.0	1.01	T15–T16	320
2007	Apr–May	3°N	93	37.5	1.20	T28–T29	330–331
"	Jul	1°N	198	51.9	1.02	T34	334
"	Aug	1°N	146	45.5	1.02	T35	335
2008	Jan	1°N	449	80.3	1.09	T40	340
"	Feb	1°N	439	86.2	1.59	T41	341
"	May	3°N	64	32.9	1.70	T43–T44	344–345
2009	Dec	1°N	322	64.8	1.03	T63–T64	004
2010	Apr–May	1°N	233	54.1	1.01	T67	008
2011	May	7°N	765	99.8	1.18	T76	021

Table 4
Titan Flybys and FP4 Data Acquisition Characteristics from 2006 February to 2012 January Averaged in Southern Latitudinal Bins

Year	Month	Latitude	Total Number of Spectra	Signal-to-noise	Airmass	*Cassini* Flyby	Ls (°)
2006	Mar	1°S	1515	142.1	1.09	T12	316
"	Oct	1°S	96	39.4	1.26	T19–T20	323–324
2007	Jun	1°S	2545	195.1	1.09	T32–T33	332–333
"	Nov	1°S	869	106.7	1.01	T37	338
"	Dec	1°S	382	70.9	1.02	T38–T39	338–339
2009	Mar–Jul	1°S	84	39.2	1.71	T51–T59	355
"	Oct	1°S	60	26.6	1.09	T62	002
2010	Jun	1°S	367	69.4	1.01	T69–T70	010
"	Jul	1°S	913	110.8	1.13	T71	011
"	Sep	3°S	1622	136.9	1.01	T72	014
2011	Dec	10°S	1866	157	1.24	T79	028
2006	Feb	30°S	666	96	1.21	T11	315
"	May	30°S	551	85.5	1.26	T14	318
2008	Nov	31°S	1055	106.4	1.01	T46–T47	350–351
2009	Dec	28°S	980	103.4	1.12	T63–T64	004–005
2010	May	24°S	1028	114.3	1.21	T68	009
2012	Jan	30°S	2083	133.8	1.15	T80–T81	029
2006	Oct	50°S	546	78.8	1.16	T19–T20	323
2007	Jan	50°S	842	95.8	1.07	T23–T24	327
"	Mar–May	50°S	320	63.1	1.42	T26–T31	329
"	Jul–Aug	50°S	538	86.8	1.68	T34–T35	334
"	Dec	50°S	456	77.5	1.59	T38–T39	338–339
2008	Jul	50°S	51	25.6	1.62	T41	341
2009	Mar	50°S	584	73.4	1.13	T51	355
"	May	50°S	892	91.0	1.33	T54–T55	357
2010	Apr	50°S	525	35.4	1.71	T67	008

high resolution spectra, we also have analyzed six data sets at medium resolution (2.54 cm^{-1}) taken in FP3 and FP4 in January 2008 (flyby T40), April 2009 (flybys T52–T53), and May 2010 (flyby T68). They contain 459, 1193, and 160 spectra each in FP3 and a similar or higher number in the FP4. Each selection at high or medium spectral resolution was restricted to emission angles lower than 65° for optimum radiative transfer treatment.

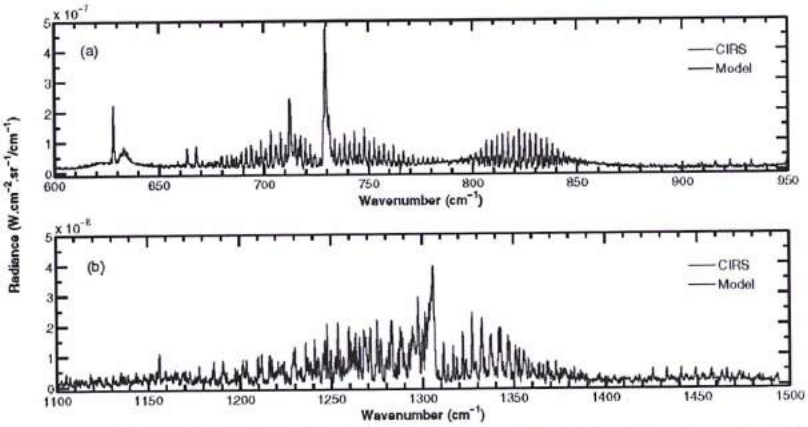

Figure 1. Example of fit of the FP3 (a) and FP4 (b) spectrum of Titan taken by *Cassini* CIRS in June 2009 at flybys T56–T57 at 50°N, containing 476 spectra for FP3 and 575 spectra for FP4.

(A color version of this figure is available in the online journal.)

2. DATA ANALYSIS

The *Cassini*/CIRS spectra are analyzed using a method extensively described in previous articles (Coustenis et al. 2007, 2010). In brief, we model Titan's thermal infrared spectrum by use of a line-by-line monochromatic radiative transfer code updated from the one we used in previous Titan atmospheric structure retrievals (Coustenis et al. 2010, and references therein). In this new release (ARTT, for Atmospheric Radiative Transfer for Titan), we have included more constituents relevant to Titan's chemistry (26 species in total, all the so-far detected hydrocarbons, nitriles, and oxygen compounds in addition to the main molecules N_2, H_2, CH_4, and argon). Our list of molecules includes in particular the $^{13}CH_4$, $^{13}CH_3D$, $^{12}C^{13}CH_2$, and $H^{15}CN$ isotopologues which are essential in fitting the emission bands of methane, acetylene, and hydrogen cyanide and allow us to infer the $^{12}C/^{13}C$ and $^{14}N/^{15}N$ ratios. Furthermore, new oxygen and hydrocarbon isotopologues as detected by Jennings et al. (2008) and Nixon et al. (2008b) are included. Spectroscopic parameters for the molecules found in the FP3 and FP4 spectral ranges are from GEISA 2009 (Jacquinet-Husson et al. 2011) and HITRAN 2008 (Rothman et al. 2009) databases, with several updates, as for instance in the case of ethane and propane, both of which are simulated from the individual line lists of Vander Auwera et al. (2007) and Flaud et al. (2010), respectively.

We first retrieve temperature profiles by the inversion of the observed ν_4 methane emission band at 1305 cm^{-1} in CIRS FP4 following the method described in Achterberg et al. (2008, 2011). We use the CH_4 vertical mixing ratio profile in the stratosphere as measured by the Huygens probe (Niemann et al. 2010) and compatible with the CIRS inferences from FP1 (Flasar et al. 2005), which yields 1.48% above the cold trap.

The initial guess temperature profile for these calculations was the 15°S profile from Flasar et al. (2005), in a process described in detail in Achterberg et al. (2008). We also made tests using the HASI measured temperature structure in the stratosphere and troposphere (Fulchignoni et al. 2005), as discussed in the next section. We then use the temperature profiles to solve the radiative transfer equation in the FP3 part of the spectrum for the mixing ratios of the various components seen in emission at different epochs and latitudes (Tables 1 and 2).

For all the molecules analyzed here in "nadir" geometry conditions, we adopt constant-with-height profiles above the condensation level relevant to stratospheric levels of 0.1–20 mbar essentially (roughly 80–280 km). As explained in detail in Section 4.4 of Coustenis et al (2010), the use of constant vertical profiles does not allow for a good fit of the whole C_2H_2 emission band centered at 729 cm^{-1}. We therefore first derive the C_2H_2 abundance that fits the Q-branch and then adjust the fit in the wings of the band to infer the other mixing ratios of the weaker species in the 620–780 cm^{-1} region. In order to model the continuum observed in the spectra, we have used the haze dependence as reported in Vinatier et al. (2012a) giving the aerosol refractive index from CIRS spectra in the far- and mid-infrared regions near 15°S and 20°S, adjusted to match the level of radiance observed in between the molecular bands in our selections.

3. TEMPERATURE EVOLUTION OF TITAN'S STRATOSPHERE DURING THE *CASSINI* MISSION

Figure 1 shows an example of fits obtained in the FP3 (600–1000 cm^{-1}) region and in the FP4 (1100–1500 cm^{-1}) region. The latter is used for all spectral selections to derive the corresponding temperature profile.

Figures 2(a)–(d) show the results of the temperature as a function of latitude, using the altitude information contained in the resolved lines of the ν_4 methane band. Figures 2(a) and (b) (upper panel) show the temperature structure inferred at two latitudes (50°N and 30°N) at certain dates during the *Cassini* mission. The temperature profiles discussed hereafter were calculated using as an initial guess the one from Flasar et al. (2005).

But we have also run tests using thermal profiles retrieved from the same CIRS FP4 selections but by adopting into the

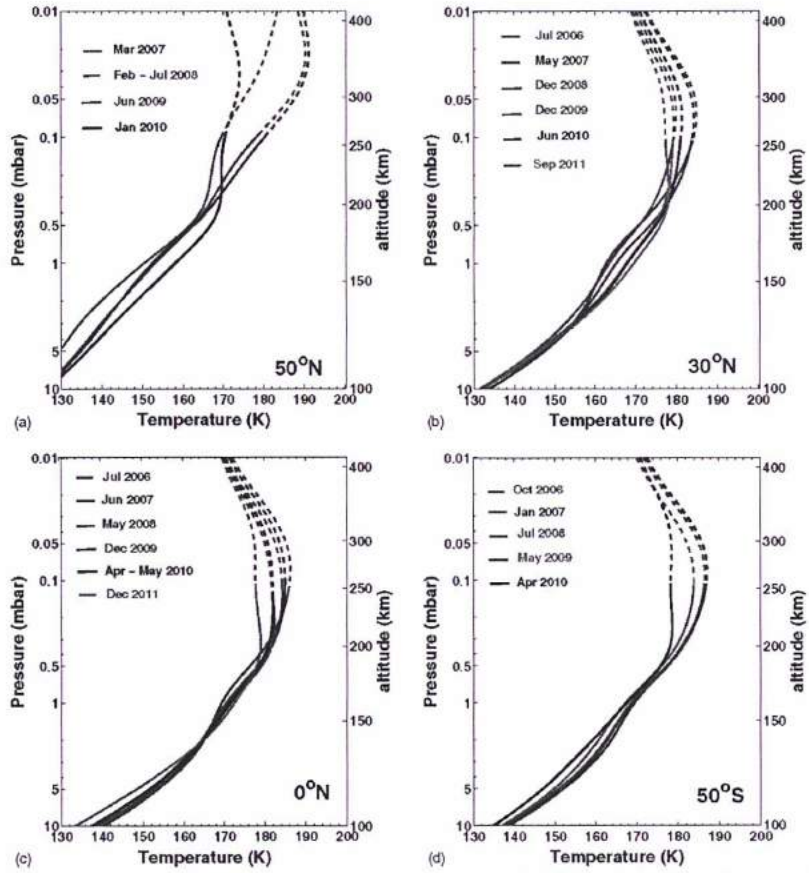

Figure 2. Retrieved thermal profiles from CIRS nadir data at (a) 50°N, (b) 30°N, (c) equator, and (d) 30°S. The typical error bar uncertainty is about 0.7 K at 1 mbar and at most 4 K at 5 mbar. Dashed lines indicate the altitude levels above which the temperature has higher uncertainties.
(A color version of this figure is available in the online journal.)

constrained inversion algorithm (Achterberg et al. 2008) as the a priori reference profile the HASI temperature structure (Fulchignoni et al. 2005). We find that at the equatorial latitudes all molecular abundances are affected by 10% or less, except for HCN (20%). This small impact is expected because the HASI profile was inferred above the Huygens landing site, which was at 10°S. In the northern latitudes, the divergence is more pronounced (as much as 20% of decrease in abundance) for some molecules (the ones with the stronger emission bands: C_2H_2 and HCN), however, even at 50°N, all the other molecular abundances vary by less than 10% whatever the initial temperature profile.

In the northern hemisphere, we find a decrease in temperature in the mesosphere (more sensitive to the seasonal insolation variations), starting from the stratopause above 0.1 mbar, where the temperature significantly decreases from the earlier to the later mission dates. The warm north polar lower mesosphere has cooled (as also suggested previously by Achterberg et al. 2011) and now we find the decrease to be about 12 K at 50°N (Figure 2(a)) and about 7 K at 30°N (Figure 2(b)) at around 250–300 km in altitude, since the beginning of the *Cassini* mission. In the mid-stratosphere below 200 km, the northern polar region initially began cooling from 2007 up to 2009, while in 2010 a slight warming is observed again at both 50°N and 30°N.

The cooling with time in the lower mesosphere (by 8 K maximum) is also witnessed at the equatorial and southern latitudes. On the contrary, in the stratosphere (lower atmospheric levels), no significant changes are found in the equatorial temperatures (Figure 2(c)) and this holds for latitudes down to

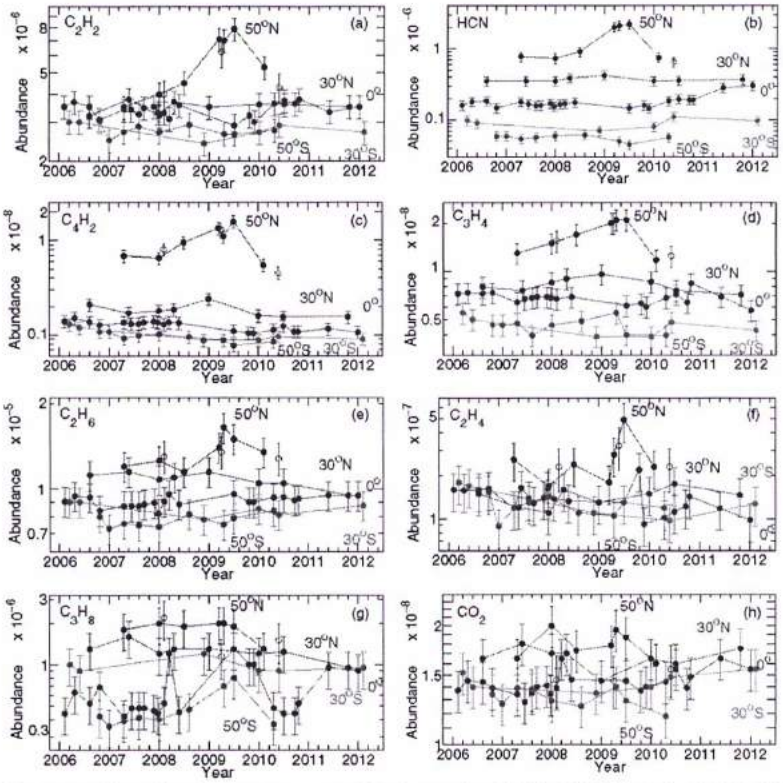

Figure 3. Time–latitude composition variations for the major trace gases of Titan's stratosphere: (a) C_2H_2, (b) HCN, (c) C_4H_2, (d) C_3H_4, (e) C_2H_6, (f) C_2H_4, (g) C_3H_8, and (h) CO_2. The latitudes investigated from 2006 to 2012 are: 50°S (violet), 30°S (light blue), equator (red), 30°N (green), and 50°N (blue). Connected filled circles are high resolution observations (0.5 cm^{-1}), while open circles are medium resolution data (2.5 cm^{-1}) for 2008, 2009, and 2010 (and sometimes coincide with the higher resolution values). The 3σ estimated error bars are indicated (see the text).

(A color version of this figure is available in the online journal.)

30°S. More to the south (50°S, Figure 2(d)), some temperature variations are observed in the stratosphere, typically 2–4 K between 1 and 10 mbar, but this is within error bars. More importantly, the general shape of the thermal structure is changing and we find the temperature gradient to be weakening, resulting in a more isothermal profile at higher latitudes with a loss of the marked stratopause present in earlier years.

These changes at northern latitudes suggest a weakening of the descending branch of the middle atmosphere meridional circulation (Achterberg et al. 2011), which implies less adiabatic heating and hence lower temperatures. Moreover, the changes in the circulation affect the distribution of aerosols (Vinatier et al. 2012a), which in turn affect the thermal structure.

4. CHEMICAL COMPOSITION CHANGES OVER THE *CASSINI* MISSION

With the thermal profiles described above injected in our radiative transfer code, we derived the abundances of the molecules from the best fits obtained of their emission bands in the Titan CIRS FP3 spectra (Figure 1(b)). We show the *Cassini*/CIRS mixing ratio inferences for Titan's gases as found above the condensation level in Figures 3(a)–(h) with the associated errors.

Since the model parameters for all these calculations are the same (in terms of calibration, methane profile, haze description model, etc.), we only consider the relative uncertainties, due to noise (rather small in our usually large averages, except for the early mission dates and sometimes in the north), the temperature profiles and any remaining uncertainties regarding some of the spectroscopic data (all within 15%). Exceptions are C_3H_8 and C_2H_4, which are affected by abundance retrieval difficulties and some insufficient laboratory spectroscopic data. In the case of C_3H_8, at 748 cm^{-1}, a major hindrance is the mixing with the C_2H_2 lines while the spectrum of C_2H_4, around 950 cm^{-1}, suffers from some electrical interference artifacts ("spikes") and also interference from C_3H_8 contribution and other emission

bands. As a consequence, these two molecules show ratios that have error bars on the order of ±30% and are not as reliable as the other inferences for the temporal or spatial variations.

At southern latitudes (50°S and 30°S, Figure 3) as well as near the equator, we find the abundances of the gaseous species to remain rather constant during the *Cassini* mission within the error bars. In general (with the exception of C_2H_4 and C_3H_8, identified as complicated molecules to process, in particular at the mid and southern latitudes), the equatorial data yield abundances higher by about 20% than the 30 or 50°S inferences (which are almost at the same level for all molecules). The mixing ratios at 30°N are in general higher than the equatorial values by 10%–20%. We found a definitive trend for increased gaseous content in the stratosphere when moving from the south to the north, and, in addition, significantly enhanced abundances during the whole mission duration at northern latitudes, observed in most cases at latitudes higher than 30°N.

At 50°N, all abundances except for CO_2 are thus enhanced with respect to 55°S and the equator, consistent with our previous work with this model (Coustenis et al. 2007, 2010) and with *Voyager 1* results (Coustenis et al. 1991; Coustenis & Bézard 1995), almost at the same season as in mid-2010 (A. Coustenis et al., in preparation). In average, and at the maximum, the 50°N values are higher than the 30°N by 20% and by 40% with respect to the equator. These enhancements appear to be greatest for the shortest-lived chemicals. This is explained by a combination of chemistry and dynamics: the vertical distributions are steepest for the shortest-lifetime species in a purely chemical model, while the presence of a circulation cell in the atmosphere, with subsidence in the polar regions (at the north pole during the period of the observations), causes the lower stratosphere to be greatly enriched in these species at the winter pole compared to the equator. The study of the temporal evolution of this enhancement in the higher northern regions within the *Cassini* mission duration, as well as changes observed with time at southern polar regions, is described by Teanby et al. (2008, 2010, 2012).

Furthermore, at 50°N, we find an indication for an increase in abundance from 2006 to mid-2009 for almost all molecules (the exceptions are propane and carbon dioxide which do not seem to vary in time at any latitude, lower double panel of Figure 3). We detect a maximum around the time of the NSE (Northern Spring Equinox, 2009 August 15) in mixing ratios with increases in abundances by about 30%–40% for C_3H_4 and C_2H_6, 50%–70% for C_2H_2 and C_4H_2, and about a factor of 2 or more for HCN and C_2H_4 (albeit with higher uncertainties for the latter) relative to the adjacent time periods in 2008 and 2010. Ethane shows variations with time only at this higher latitude. We note that C_3H_8 seems to have increased abundances around NSE, but the data analysis results for this molecule at lower latitudes are rather uncertain. The results on the increase and the reported values near April 2009 presented for C_2H_2 (7×10^{-6}) and HCN (2×10^{-6}) in these figures (just before the maximum in June 2009) are in excellent agreement with the findings of Teanby et al. (2010), as shown in their Figure 4, panels (c) and (d). Although there is a hint in their Figure 4, Teanby et al. do not yet see the increase in abundance that we report here for C_4H_2 but we are still compatible within error bars at values near 2×10^{-8} in 2009.

The observed increase in abundance for some molecules is followed by a strong decrease which reduces considerably the observed enhancement by 2010. This decrease settles in quickly, within 1–2 terrestrial years and brings the abundances back to their levels prior to the ascent. Admittedly we have so far only one high-resolution nadir selection after the NSE and one in lower resolution confirming this result, so that the finding probably requires further verification. However, both high- and low-resolution nadir data taken in the 2010–2012 period seem to support the increase and follow-up decrease.

We inferred the $^{12}C/^{13}C$ ratio in CH_4 and C_2H_2 to be 95±15 and the $^{14}N/^{15}N$ ratio in HCN to be 50±10 for the latitudes on which we investigate here as an average. The $^{12}C/^{13}C$ ratio is consistent with results reported by Vinatier et al. (2007) and Nixon et al. (2008a, 2008b) and with the terrestrial inorganic standard value (88.9; Fegley 1995). The $^{14}N/^{15}N$ ratio is also consistent with the values given by Vinatier et al. (2007) and about 4.8 times lower than the terrestrial value (272; Fegley 1995).

Since the C_2H_2 emission band at 729 cm^{-1} contains information at several altitudes through the central and wing lines, we have also tested a vertical profile predicted for Ls = 358° by the GCM models (Rannou et al. 2005), which does not match the shape of the C_2H_2 band, but is not too off with respect to the actual values.

At higher northern or southern latitudes, poleward of 70°N, the situation has dramatically changed in recent years with much stronger chemical and temperature variations (Vinatier et al. 2012b; Teanby et al. 2012) but at the latitudes considered here, we do not observe them which gives us hints as to the location and the extent of the winter polar vortex.

5. DISCUSSION OF THE RESULTS AND POSSIBLE INTERPRETATIONS

In this work, we estimate the abundances of the trace gases in Titan's stratosphere from 50°S to 50°N. We find no significant temporal variations at mid- and southern latitudes during the *Cassini* mission. We monitor and quantify the compositional enhancement at 50°N, and find indication for a maximum at the time of the Titan northern spring equinox (NSE, mid-2009), followed by a sharp decrease of the gaseous chemical content within the next Earth year or so. Our results are compatible with the findings of Teanby et al. (2010) in that we find HCN and C_2H_2 to display a rapid increase in northern latitudes up to mid-2009 while the abundances at equatorial and southern latitudes remain stable. CO_2 presents no latitudinal variations anywhere because of its long photochemical lifetime.

The peak in abundance is observed around the northern spring equinox, during which we know a rapid change in the atmosphere took place. Indeed, short-term variations observed during the *Cassini* mission can arise from changes in the circulation around the time of the equinox. The collapse of the detached aerosol layer (West et al. 2011) suggests that the dynamics during this period go through a rapid transition which should also affect the gas distribution. The rapid decrease after mid-2009, for which the most straightforward explanation is that the vortex has shrunk somewhat, would be consistent with the weakening thermal gradient we find here and that of the winds also reported by Achterberg et al. (2008, 2011) and Teanby et al. (2009b). The finding also ties into the location of the maximum temperature gradient, which appears to be moving northward over the winter/spring season (Teanby et al. 2010; Figure 3, T panel). If 50°N is emerging from the vortex core, it would cause a large reduction in the abundances, hence explaining our observations. Thus, decreasing abundances at 50°N could be

due to a weakening vortex with reduced lateral mixing across the vortex boundary (Teanby et al. 2010).

Another cause could be the spatial variations in the energy input to Titan's atmosphere (due to Titan's inclination) as a driver for changes in the advection patterns, which in turn provide a stronger variability in the latitudinal abundances of photochemical species. Changes in the solar output during the 11 year cycle can potentially affect the chemical production rates in Titan's atmosphere. On the other hand, for the time period of the *Cassini* mission, the Sun has been remarkably stable going through an extended minimum with the first weak signs of increased output observed toward the end of 2009. The chemical lifetimes in Titan's stratosphere (at 200 km) range between ~1 year for C_2H_4 and C_3H_4 up to ~20 years for HCN, which are longer than the timescales of some of the rapid changes observed. Thus, the temporal variability observed during the *Cassini* mission is more likely related to changes in the atmospheric circulation patterns due to progression of seasons.

We thank Nicolas Gorius, Marcia Segura, and Florence Henry for help with the data acquisition and processing during this project. We also acknowledge support from the CNES *Cassini* program.

REFERENCES

Achterberg, R. K., Conrath, B. J., Gierasch, P. J., Flasar, F. M., & Nixon, C. A. 2008, Icarus, 194, 263
Achterberg, R. K., Gierasch, P. J., Conrath, B. J., Flasar, F. M., & Nixon, C. A. 2011, Icarus, 211, 686
Coustenis, A., Achterberg, R., Conrath, B., et al. 2007, Icarus, 189, 35
Coustenis, A., & Bézard, B. 1995, Icarus, 115, 126
Coustenis, A., Bézard, B., Gautier, D., Marten, A., & Samuelson, R. 1991, Icarus, 89, 152
Coustenis, A., Jennings, D. E., Jolly, A., et al. 2008, Icarus, 197, 539
Coustenis, A., Jennings, D. E., Nixon, C. A., et al. 2010, Icarus, 207, 461
de Kok, R., Irwin, P. G. J., Teanby, N. A., et al. 2007, Icarus, 186, 354
Fegley, B. 1995, in A Handbook of Physical Constants, ed. T. Ahrens (Washington, DC: Am. Geophys. Pub.), 320
Flasar, F. M., Achterberg, R. K., Conrath, B. J., et al. 2005, Science, 308, 975
Flasar, F. M., Kunde, V. G., Abbas, M. M., et al. 2004, Space Sci. Rev., 115, 169
Flaud, J. M., Kwabia Tchana, F., Lafferty, W. J., & Nixon, C. A. 2010, Mol. Phys., 108, 699
Fulchignoni, M., Ferri, F., Angrilli, F., et al. 2005, Nature, 438, 785
Jacquinet-Husson, N., Crepeau, L., Armante, R., et al. 2011, J. Quant. Spectrosc. Radiat. Transfer, 112, 2395
Jennings, D. E., Nixon, C. A., Jolly, A., et al. 2008, Astrophys. J. Lett., 681, L109
Niemann, H. B., Atreya, S. K., Demick, J. E., et al. 2010, J. Geophys. Res., 115, E12006
Nixon, C. A., Achterberg, R. K., Vinatier, S., et al. 2008a, Icarus, 195, 778
Nixon, C. A., Jennings, D. E., Bézard, B., et al. 2008b, Astrophys. J. Lett., 681, L101
Rannou, P., Lebonnois, S., Hourdin, F., & Luz, D. 2005, Adv. Space Res., 36, 2194
Rothman, L. S., Gordon, I. E., Barbe, A., et al. 2009, JQSRT, 110, 533
Teanby, N. A., Irwin, P. G. J., de Kok, R., & Nixon, C. A. 2010, Astrophys. J. Lett., 724, L84
Teanby, N. A., Irwin, P. G. J., de Kok, R., et al. 2006, Icarus, 181, 243
Teanby, N. A., Irwin, P. G. J., de Kok, R., et al. 2007, Icarus, 186, 364
Teanby, N. A., Irwin, P. G. J., de Kok, R., et al. 2008, Icarus, 193, 595
Teanby, N. A., Irwin, P. G. J., de Kok, R., et al. 2009a, Icarus, 202, 620
Teanby, N. A., Irwin, P. G. J., de Kok, R., et al. 2009b, Phil. Trans. R. Soc. A, 367, 697
Teanby, N. A., Irwin, P. G. J., Nixon, C. A., et al. 2012, Nature, in press
Vander Auwera, J., Mouzzen-Ahmadi, N., & Flaud, J.-M. 2007, Astrophys. J., 662, 750
Vinatier, S., Bézard, B., Anderson, C. M., et al. 2012b, in Titan Through Time Workshop 2012, ed. V. Cottini, C. Nixon, & R. Lorenz (NASA, FSGC), 45
Vinatier, S., Bézard, B., Fouchet, T., et al. 2007, Icarus, 188, 120
Vinatier, S., Bézard, B., Nixon, C. A., et al. 2010, Icarus, 205, 559
Vinatier, S., Rannou, P., Anderson, C. M., et al. 2012a, Icarus, 219, 5
West, R. A., Balloch, J., Dumont, P., et al. 2011, Geophys. Res. Lett., 38, L06204

Appendix C2

Titan trace gaseous composition from CIRS at the end of the Cassini-Huygens prime mission

Journal article published in *Icarus* (2010),
Volume 207, pp. 461-476.

Icarus 207 (2010) 461–476

Contents lists available at ScienceDirect

Icarus

journal homepage: www.elsevier.com/locate/icarus

Titan trace gaseous composition from CIRS at the end of the Cassini–Huygens prime mission

A. Coustenis [a,*], D.E. Jennings [b], C.A. Nixon [b,c], R.K. Achterberg [c], P. Lavvas [d], S. Vinatier [a,e], N.A. Teanby [f], G.L. Bjoraker [b], R.C. Carlson [g], L. Piani [a,h], G. Bampasidis [i], F.M. Flasar [b], P.N. Romani [b]

[a] Laboratoire d'Etudes Spatiales et d'Instrumentation en Astrophysique (LESIA), Observatoire de Paris-Meudon, 5, Place Jules Janssen, 92195 Meudon Cedex, France
[b] NASA/Goddard Space Flight Center, Code 693, Greenbelt, MD 20771, USA
[c] Department of Astronomy, University of Maryland, College Park, MD 20742, USA
[d] Department of Planet. Science, University of Arizona, Tucson, AZ 85721, USA
[e] Laboratoire de Météorologie Dynamique, IPSL, CNRS/UPMC, F-75252 Paris Cedex 05, France
[f] AOPP, Department of Physics, Univ. of Oxford, Clarendon Lab., Parks Rd., Oxford OX1 3PU, UK
[g] IACS, Catholic University of America, and NASA/Goddard Space Flight Center, Planet. Systems Lab. – Code 693.0, Greenbelt, MD 20771, USA
[h] Muséum de l'Histoire Naturelle, Case Postale 52-61, rue Buffon, F-75005 Paris, France
[i] Faculty of Physics, National and Kapodistrian Univ. of Athens, Panepistimiopolis, GR-15783 Zographos, Athens, Greece

ARTICLE INFO

Article history:
Received 14 July 2009
Revised 20 November 2009
Accepted 20 November 2009
Available online 11 December 2009

Keywords:
Titan
Abundances, atmospheres
Organic chemistry
Satellites, atmospheres
Spectroscopy
Atmospheres, chemistry
Atmospheres, composition
Satellites, composition

ABSTRACT

This paper reports on the results from an extensive study of all nadir-looking spectra acquired by Cassini/CIRS during the 44 flybys performed in the course of the nominal mission (2004–2008). With respect to the previous study (Coustenis, A., and 24 colleagues [2007]. Icarus 189, 35–62, on flybys TB–T10) we present here a significantly richer dataset with, in particular, more data at high northern and southern latitudes so that the abundances inferred here at these regions are more reliable. Our enhanced high-resolution dataset allows us to infer more precisely the chemical composition of Titan all over the disk. We also include improved spectroscopic data for some molecules and updated temperature profiles. The latitudinal distributions of all of the gaseous species are inferred. We furthermore test vertical distributions essentially for acetylene (C_2H_2) from CIRS limb-inferred data and from current General Circulation Models for Titan and compare our results on all the gaseous abundances with predictions from 1-D photochemical-radiative models to check the reliability of the chemical reactions and pathways.

1. Introduction

Our understanding of Titan's atmospheric chemical composition has recently been enhanced by the data returned by the Cassini instruments. We analyze here a full set of spectra recorded by the Composite Infrared Spectrometer (CIRS) aboard the Cassini spacecraft taken during the 44 Titan flybys spanning the 4 years of nominal mission. Previous composition studies of subsets of this dataset were published by Flasar et al. (2005), Teanby et al. (2006, 2007, 2008a,b, 2009), Coustenis et al. (2007, 2008), Vinatier et al. (2007, 2009), Nixon et al. (2008a,b, 2009), and Jennings et al. (2008) among others.

In a previous paper (Coustenis et al., 2007) we analyzed and discussed a set of nadir CIRS data from the first year of Cassini observations (Tours TB–T10). The abundances of all known gaseous constituents were retrieved at different locations of Titan's disk. Besides these well-known trace species, a firm detection of benzene (C_6H_6), first reported in ISO data (Coustenis et al., 2003), was provided by CIRS at 674 cm^{-1}. We use this band here to study its latitudinal variations. The detection of C_2HD was also obtained from the analysis of the extra emission observed at 678 cm^{-1} (Coustenis et al., 2003, 2008). The D/H ratio on Titan was determined from the CH_3D band at 8.6 μm and found to be $1.17^{+0.16}_{-0.21} \times 10^{-4}$ (Coustenis et al., 2007). Bézard et al. (2007) furthermore reported the detection of $^{13}CH_3D$ at 1148 cm^{-1} and determined a D/H ratio of $1.32^{+0.15}_{-0.11} \times 10^{-4}$. Nixon et al. (2008a,b) and Jennings et al. (2008) used CIRS data to retrieve information on the $^{12}C/^{13}C$ and other isotopic ratios in Titan. Finally, there is ongoing work on the analysis of CIRS limb data to infer information on the vertical profiles of several gaseous constituents of Titan's stratosphere at nine latitudes between 56°S and 80°N (Vinatier et al., 2007, 2009; Teanby et al., 2007, 2008a,b).

* Corresponding author. Fax: +33 1 45 07 74 26.
E-mail address: athena.coustenis@obspm.fr (A. Coustenis).

0019-1035/$ - see front matter © 2009 Elsevier Inc. All rights reserved.
doi:10.1016/j.icarus.2009.11.027

The results published in Coustenis et al. (2007) and Teanby et al. (2008a) indicated that no longitudinal variations existed for any of the gases. On the other hand, the retrievals of the meridional variations of the trace constituents showed an enhancement for some of them towards the North pole. However, due to the geometry of the observations from 2004 to 2006, the most northern latitude exploited was limited to about 60°N. Molecules showing a significant enhancement at northern latitudes are the nitriles (HC_3N, HCN) and the complex hydrocarbons (C_4H_2, C_3H_4). The results were tied to predictions by dynamical–photochemical models (Hourdin et al., 2004; Lavvas et al., 2008a,b; Crespin et al., 2008).

With respect to the results published in Coustenis et al. (2007), we improve here on the analysis by exploiting a far larger number of spectra with a significantly higher number taken at the higher resolution of 0.53 cm^{-1}. The more complete coverage of Titan's disk, combined with the larger number of spectra at high resolution available, allows for the inference of more precise abundances for the trace gases and for a more adequate definition of meridional variations, in particular in the northern regions, which were not fully observed previously.

2. Nadir observations in the FP3 and FP4 CIRS ranges

For a full description of the CIRS spectroscopic observations and the instrument capabilities we refer the reader to Flasar et al. (2004) and for the general procedure applied to the data in our studies, see Coustenis et al. (2007).

The CIRS nadir spectra characterize various regions on Titan from roughly 85°S to 80°N with a variety of emission angles. We have studied the emission observed in the CIRS FP3 and FP4 detector arrays (covering roughly the 600–1500 cm^{-1} spectral range) with apodized FWHM (full width to half maximum) resolutions of 2.54 or 0.53 cm^{-1}. The more recent Cassini/CIRS observations (T10–T44, until May 2008) have allowed for a more complete coverage of the higher northern latitudes on Titan, where previously only a few spectra were available (Teanby et al., 2006; Coustenis et al., 2007). We include here a large number of both mid- and high-resolution CIRS spectra at all latitudes from 90°N to 90°S at emission angles smaller than 50° and we perform averages in order to focus on a given latitudinal range and also in order to enhance the S/N ratio (see Table 1). The airmass numbers and the S/N ratios given in Table 1 represent averages of the mean values in each spectral average. As said in the previous section, the lack of longitudinal variations in gas abundance that we have demonstrated in Coustenis et al. (2007) justifies the latitudinal binning, while longitudinal variations in temperature (Achterberg et al., 2008b) are small enough to be ignored for our purposes.

The composite spectral averages thus produced in the 600–1500 cm^{-1} range covered by the FP3 and FP4 detectors (Fig. 1) show several signatures of previously identified molecules: hydrocarbons (CH_4, CH_3D, C_2H_2, C_2H_4, C_2H_6, C_3H_4, C_3H_8, C_4H_2, C_6H_6), nitriles (HCN, HC_3N) and CO_2. We have included all of these species in our model, but we have not included all the isotopes of C, N and O discovered today for lack of complete spectroscopic data. In addition, C_2HD, as observed at 678 cm^{-1} (Coustenis et al., 2008) is incorporated in our model but the associated abundance and its relative variations were extensively discussed in the earlier paper.

Small offsets in the wavenumber of the spectra were corrected by cross-correlation with a synthetic spectrum. These instrumental offsets were generally small compared to the resolution and were at most ±0.1 cm^{-1}. However, these small adjustments reduced the misfit between model and data by up to 25%.

Table 1
Characteristics of the spectral selections from Titan flybys TB–T44 used in this study for medium spectral resolution of 2.5 cm^{-1} and high spectral resolution, 0.5 cm^{-1}. The latitudes in the first column refer to atmospheric levels at around 5 mbar and take into account the latitude smearing effect (see text). The latitude coverage for each selection is actually around the mean value (for example 5°S means spectra from 10°S to the equator). We sum all spectra from all longitudes in columns 2 and 5. The emission angles are restricted to 50° everywhere and the retrieved average airmass is given in columns 3 and 6. The S/N indicated in columns 4 and 7 is the average signal-to-noise ratio for all spectra combined. It varies with wavelength across the spectrum depending on the CIRS data NESR (noise equivalent spectral radiance).

Mean latitude	FP3			FP4		
	Spectra	Airmass	S/N ratio	Spectra	Airmass	S/N ratio
TB–T44 high-resolution nadir spectral selections						
70N	1117	1.21	34.4	2011	1.32	102.6
60N	2413	1.25	48.0	2147	1.25	91
50N	2316	1.12	48.7	4302	1.09	117
42N	5328	1.08	84.5	4098	1.12	133.7
33N	7002	1.12	116.8	8222	1.14	242.6
25N	8607	1.09	140.3	7942	1.09	277.6
15N	5249	1.07	114.9	9299	1.06	340.2
5N	11,981	1.03	173.8	10,899	1.04	383.7
5S	10,873	1.04	161.7	10,903	1.07	392.3
15S	4144	1.15	92.6	3567	1.25	229.6
25S	2446	1.13	62.9	3457	1.07	206.8
33S	3574	1.13	85.0	2949	1.24	197.4
42S	2190	1.24	65.7	3332	1.28	205.8
50S	2154	1.15	60.7	1968	1.16	149.4
60S	2081	1.28	60.8	1845	1.26	145.1
70S	778	1.45	39.1	2543	1.41	173.0
TB–T44 medium-resolution nadir spectral selections						
70N	528	1.27	59.2	530	1.24	135.7
60N	1184	1.21	84.9	1617	1.03	201.2
50N	6133	1.11	203.9	6471	1.12	382.9
42N	8066	1.13	227.3	7170	1.15	480.5
33N	8173	1.12	337.2	11,154	1.13	721.7
25N	12,614	1.11	444.9	10,317	1.13	861.1
15N	13,018	1.07	479.3	14,509	1.08	1123.8
5N	15,639	1.09	534.8	15,741	1.09	1231.8
5S	19,953	1.05	575.5	19,726	1.04	1357.3
15S	18,953	1.05	524.3	19,140	1.05	1338
25S	7426	1.11	323	8266	1.10	861.2
33S	6948	1.08	296.8	5791	1.12	706
42S	5085	1.12	244.9	4722	1.12	613.1
50S	2908	1.10	176.8	3035	1.12	475.4
60S	1353	1.16	121.6	1270	1.16	313.3
70S	1379	1.33	126.8	1421	1.28	330.2

Our analysis here is based essentially on the high-resolution data acquired by CIRS, with the medium-resolution spectra used as a check for consistency.

3. Modeling

Our method in deriving abundances of the trace constituents on Titan has been largely described in previous articles (see Coustenis et al., 2007a and references therein). In brief, we use a line-by-line radiative transfer code to simulate the Titan spectrum and through iterative processes we derive the abundances of the various constituents observed in Titan's atmosphere. We begin with temperature profiles obtained by inversion of the emission observed in the ν_4 methane band at 1305 cm^{-1}, assuming 1.4% of CH_4 in the stratosphere as measured by the Huygens probe and compatible with the CIRS inferences from FP1 (Flasar et al., 2005; Niemann et al., 2005). We use these profiles to then solve the radiative transfer equation in the FP3 part of the spectrum for the mixing ratios of the various components.

Our model includes collision-induced absorption and a two-cloud system to represent the haze opacity (see Coustenis

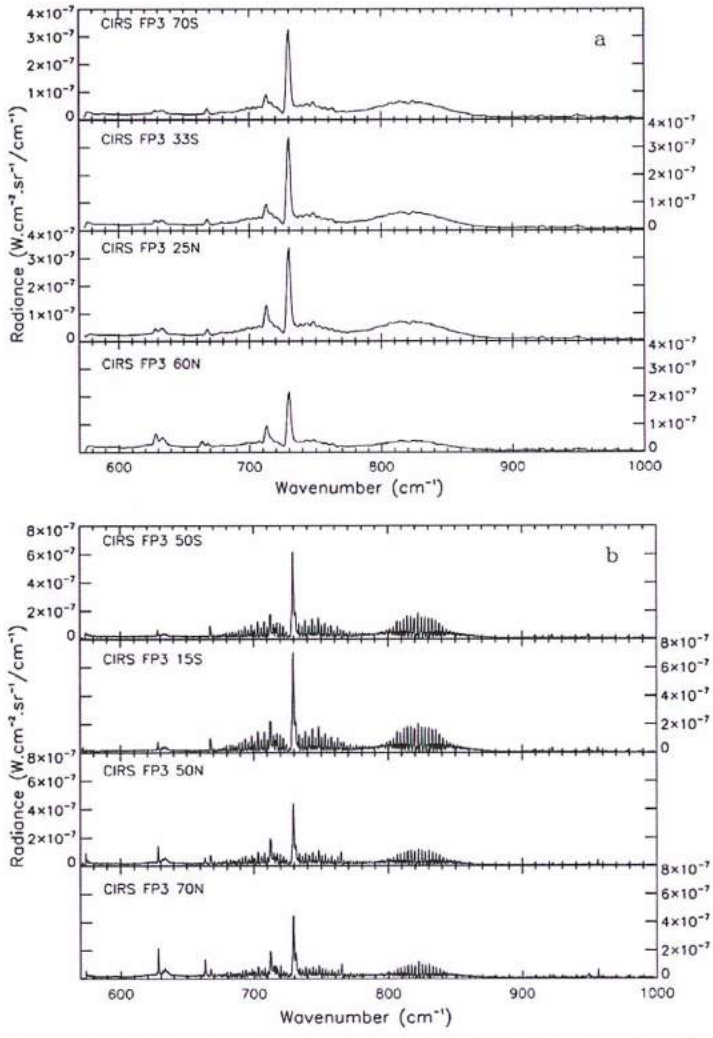

Fig. 1. Spectral averages performed over TB–T44 Titan flybys as described in Table 1 for different latitudes binned in 10°: (a) at medium resolution (2.5 cm $^{-1}$); (b) at high resolution (0.5 cm $^{-1}$).

et al. (2007) for more details). With respect to that previous study, although we still essentially use the new GEISA 2008 database (Jacquinet-Husson et al., 2008), we have added here some improvements in the spectroscopic treatment of some molecules:

(a) Following its detection (Coustenis et al., 2008) we have added C_2HD in our model.

(b) We have included new spectroscopic parameters for C_2H_6 (Vander Auwera et al., 2007) which are now in the new GEISA database and allow for a much better representation of its emission features throughout the spectrum.

(c) We have added the new isotopic lines for HCN from the HITRAN database (Rothman et al., 2009).

(d) We have also used new HC_3N spectroscopic parameters which come from the recent laboratory work of Jolly et al. (2007).

Even though all the neutral species are contained in our model, we lack spectroscopic data and have not included several of the isotopic species that have been detected to date on Titan, nor all the propane bands (Nixon et al., 2009).

For all the molecules analyzed here, with the exception of C_2H_2, C_2H_6 and HCN, we adopt only constant-with-height profiles above the condensation level, because there are not enough strong lines in their emission bands to allow for the retrieval of altitude-dependent information. Only C_2H_2 – with a resolved band at 730 cm^{-1} that probes multiple altitudes via strong and weak (optically thick and thin) lines, allows for an unambiguous discrimination between different vertical distributions. However, the C_2H_6 and HCN vertical distributions extracted from GCM models or from limb calculations and tested here also produce a slight improvement of the spectral fit with respect to the constant-with-height profiles, as will be discussed hereafter.

4. Analysis of the data

We use the information contained in the ν_4 methane band at 1305 cm^{-1} to retrieve temperature profiles, which are then injected in the radiative transfer equation for the other molecules to solve for the gaseous opacities. By comparison with the observations a best fit is obtained through an iterative process. For each selection (see Table 1) the continuum level between emission signatures is matched by varying the haze/cloud opacity. With the exception of C_2H_2, and in some cases – but not systematically – of HCN and C_2H_6, the vertical distributions of the trace constituents were assumed to be constant-with-height above the condensation level and set to follow their saturation vapor pressure curve below.

4.1. The FP4 region

Temperature profiles were retrieved from zonally-averaged spectra over all of the temperature maps up through T40, for a methane abundance of 1.4%. The spectra were averaged in 10° latitude bins, based on the latitude of surface intercept, with the emission angle restricted to <50°. For the procedure of this retrieval of Titan's stratospheric temperatures by CIRS see Achterberg et al. (2008a). The analyzed nadir mapping data presented in that paper sampled latitudes between 90°S and 60°N, providing temperatures for pressure levels roughly in the 0.2–5-mbar range (in some cases, the contribution functions can reach 10 mbar). The latitude range for the temperature profiles has been extended in this work to 90°N and they are inferred using the Huygens Atmospheric Structure (HASI) profile (Fulchignoni et al., 2005) as the initial guess, so that below the altitudes where CIRS can retrieve temperature information, the profiles are set to the HASI data. Some of the temperature profiles retrieved from the inversion of the emission observed in the methane ν_4 band at 1305 cm^{-1} are shown in Fig. 2.

Using these temperature profiles, we then performed radiative transfer simulations of Titan's spectrum starting with the FP4 (1100–1500 cm^{-1}) spectral region where the emission from 1200 to 1400 cm^{-1} is mainly due to methane opacity. However, CH_3D, C_3H_8, C_2H_6 and other molecules contribute at shorter and longer wavelengths. CH_3D has a strong emission band at 1156 cm^{-1}, diagnostic of regions around 0.3 mbar, Fig. 3. The fit in this band gives us access to the D/H ratio in Titan, as discussed extensively in Coustenis et al. (2007, 2008).

The best fits at 15°S in the FP4 region are shown in Fig. 4 with residuals for other latitudes. The ν_4 CH_4 band yields information at different altitude levels as testified by the contribution functions of the Q-branch and its wings (Fig. 3). The $3-\sigma$ standard deviation due to noise alone in the FP4 region is about 2×10^{-10} W cm^{-2} sr^{-1}/cm^{-1}. When other error sources are included (CH_4 abundance, lack of precise spectroscopic parameters for the CH_4 and CH_3D bands, thermal structure uncertainties, calibration issues, continuum level, etc., as described in Section 4.6) the total uncertainty is on the order of 2×10^{-9} W cm^{-2} sr^{-1}/cm^{-1}. Some of the remaining misfits in this region can be explained by the presence of molecular bands or isotopes not included in our model.

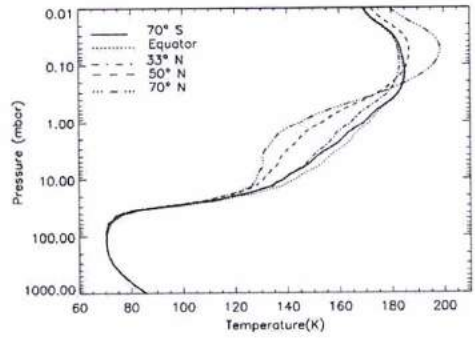

Fig. 2. Temperature profiles at different latitudes for medium resolution. From 70°S to about 30°N, the profiles are very similar and close in shape. In the troposphere, the profiles are set to match the HASI temperature data, while the HASI profile is also used as an initial guess in the stratosphere for our temperature retrievals.

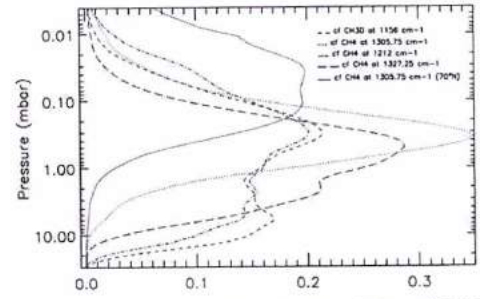

Fig. 3. Contribution functions of methane at the center and wings and of CH_3D, calculated at high resolution for equatorial latitudes and, in addition, at 70°N, for methane.

Thus, the misfit of the spectrum between 1370 and 1500 cm^{-1} could be due to an uncertain representation of the C_2H_6 bands, the ν_6 at 1376 and the ν_8 and 1468 cm^{-1}, as well as to the several predicted propane bands (ν_{18} at 1378, ν_7 at 1464 and ν_{24} at 1472 are expected), and spectral aliasing beyond 1430 cm^{-1} due to numerical filtering in the instrument (see Nixon et al., 2009). Also note the weak emission of $^{13}CH_3D$ at 1148 cm^{-1}. The cause for the returning discrepancy between the model and the observed radiance between 1180 and 1250 cm^{-1} has not been clearly identified, but can be due to uncertainties in the CH_4 spectroscopic data.

4.2. Trace gas abundances from the FP3 region

The 600–1000 cm^{-1} spectral region in Titan's spectrum contains the signature of many hydrocarbons, two nitriles and an oxygen compound (C_2H_2, C_2HD, C_2H_4, C_2H_6, C_3H_4, C_3H_8, C_4H_2, C_6H_6, HCN,

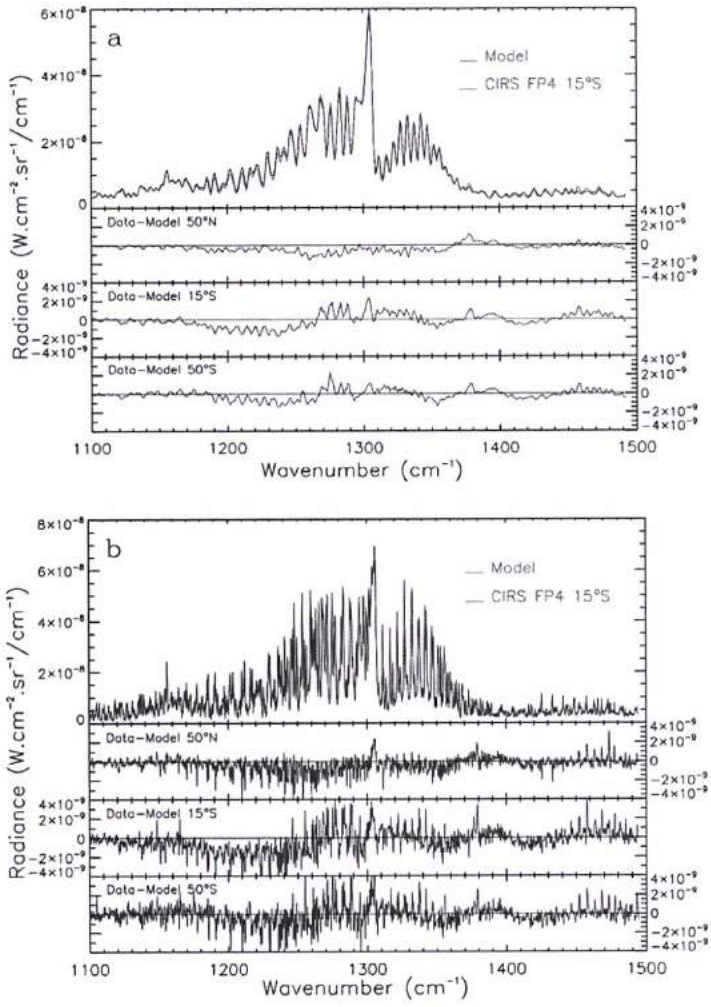

Fig. 4. The best fit to the FP4 region including the CH_4 band at 1305 cm^{-1} and the CH_3D band at 1156 cm^{-1}. The methane abundance in the stratosphere is taken to be 1.4%. Upper panel: medium resolution; lower panel: high resolution. When all error sources are included for this region, the total uncertainty is on the order of 2×10^{-9} W cm^{-2} sr^{-1}/cm^{-1}. See text for more details.

HC_3N and CO_2). All of these molecules are included in our model. Using our radiative transfer code, we perform simulations of the 600–1000 cm^{-1} region and compare them to the spectral averages described in Table 1 for all the different latitudinal bins. The contribution functions of a selection of molecules for two latitudes (5°S and 50°N) are shown in Fig. 5.

Fig. 6 shows examples of fits in the FP3 medium and high-resolution data as a whole for five different latitudes. The fits are generally quite good, within the $3-\sigma$ standard deviation error, except for a few localized areas which can be associated in their majority either to insufficient spectroscopic data (in particular for C_3H_8 or isotopes, at frequencies identified hereafter) or to noise interference features in the Titan spectrum.

4.3. The 600–700 cm^{-1} region: C_4H_2, C_3H_4, HC_3N, CO_2, C_6H_6

The 600–700 cm^{-1} region of Titan's spectrum recorded by the FP3 of CIRS is very rich in spectral signatures. Several molecules have their stratospheric contributions through emission bands with their centers or wings located here. From the molecules

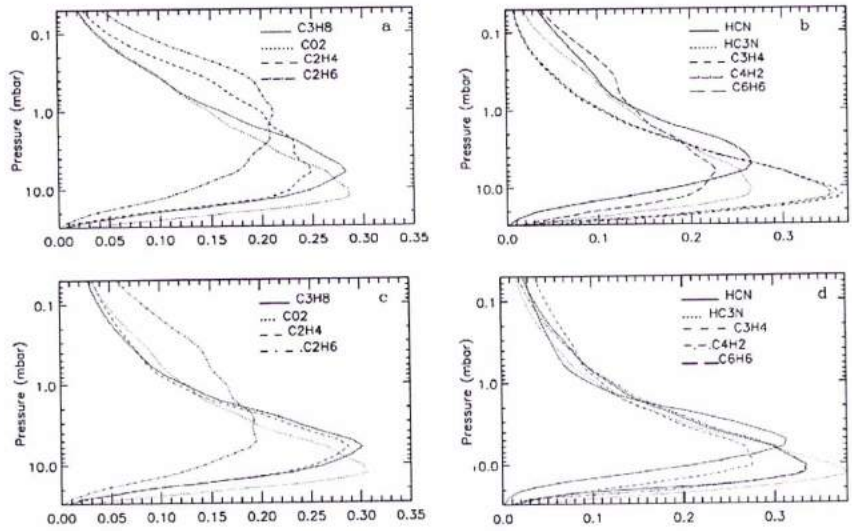

Fig. 5. Contribution functions of some molecules at different latitudes for high resolution: (a and b) are at 5°S and (c and d) are at 50°N. For latitudes near the equator or the South, the contribution functions are similar to the ones shown here for 5°S.

already known to exist on Titan, C_4H_2, C_3H_4, HC_3N, CO_2 and C_6H_6 have their band centers at 628, 633, 663, 667 and 674 cm^{-1} respectively. All of these molecules have been included in our gaseous model (Coustenis et al., 2007). In addition, C_2HD was identified at 678 cm^{-1} and included in this model (Coustenis et al., 2008). Furthermore, the left wing of the C_2H_2 band, centered at 728 cm^{-1}, significantly contributes here, as does, to a lesser amount the R-branch of the HCN band (centered at 713 cm^{-1}). In order to simulate this region, we first obtain the best possible fit for the C_2H_2 and HCN bands (as explained in the following section).

Fig. 7 shows the fits and the residuals in this region (610–690 cm^{-1}). The $3-\sigma$ standard deviation due to noise alone in the FP3 region for spectra taken at mid-latitudes is about 1.2×10^{-10} W cm^{-2} sr^{-1}/cm^{-1} for the high-resolution data (negligible with respect to other sources of errors). This is also the case for the medium resolution data. When other error sources are included (see Section 4.6) the uncertainty level (at $3-\sigma$) on the emission observed increases and is given on the figure. Some of the remaining misfits in this region can be explained by the presence of molecular bands or isotopes not included in our model, such as the isotopes of CO_2, which have been identified at 648.5 and 662.5 cm^{-1} (Nixon et al., 2008b), as well as those of HC_3N at 658.7 and 663.0 cm^{-1} (Jennings et al., 2008).

4.4. C_2H_2 and HCN

We have tried to simulate as well as possible the emission observed in the whole C_2H_2 band between 680 and 760 cm^{-1}. We have used both constant-with-height mixing ratios and vertical distributions inferred from the study of CIRS limb data or provided by the General Circulation Model (hereafter GCM) for Titan of Rannou et al. (2005).

Note that there are several systematic instrumental interference features in the FP3 spectrum that have been identified. One such noise feature is near the center of the C_2H_2 Q-branch, at 729.25 cm^{-1}, and could be the cause of the imperfect fit. Also, another strong interference affects the spectrum near 765 cm^{-1}. If any event the simulations obtained when using the constant vertical profiles (Fig. 8) do not allow for a good fit of the whole C_2H_2 band (Fig. 9a–c). When the center of the band, at 729 cm^{-1}, is fitted, the simulated emission in the wings is in excess of the observations, especially in the left wing (R-branch). From the contribution functions of C_2H_2 shown in Fig. 8, it is clear that these regions probe different atmospheric levels and hence require a vertical distribution with a slope which gives lower abundances at lower altitudes, like the ones inferred from limb CIRS data and from the GCM simulations. For the purposes of our fit then when using constant profiles, and in order to derive the abundances of the weaker-band species (like HC_3N, CO_2, C_2HD and C_6H_6) embedded in that part of the spectrum, we need to reduce the C_2H_2 abundance until we fit the left wing. The corresponding C_2H_2 abundance is significantly different from the one that fits the center of the Q-branch (by up to 80%).

Therefore, after having obtained the best possible fits with the constant-with-height profiles for all latitudes, we then turned to testing vertical distributions for acetylene, HCN and C_2H_6. We obtained vertical distributions for these three constituents from the GCM calculations (Crespin et al., 2008) for $L_S = 300$. In addition, for C_2H_2 we tested the vertical profiles produced by CIRS limb inferences (Vinatier et al., 2007).

Fig. 8 then also shows the C_2H_2 GCM vertical distributions tested in this work for latitudes of 50°S, 15°S and 50°N. The distributions for the mid and southern latitudes are similar in shape and in mixing ratio (Fig. 8) in the 0.5–20 mbar range probed by the C_2H_2 band center and wings as shown by the contribution functions (Fig. 8). On the contrary, the 50°N GCM-inferred distribution is quite different, both in shape and in abundance.

The GCM distributions that we tested worked well in satisfying both the Q-branch and the wings of the acetylene band for C_2H_2 abundance values close to the ones inferred by fitting the Q-branch

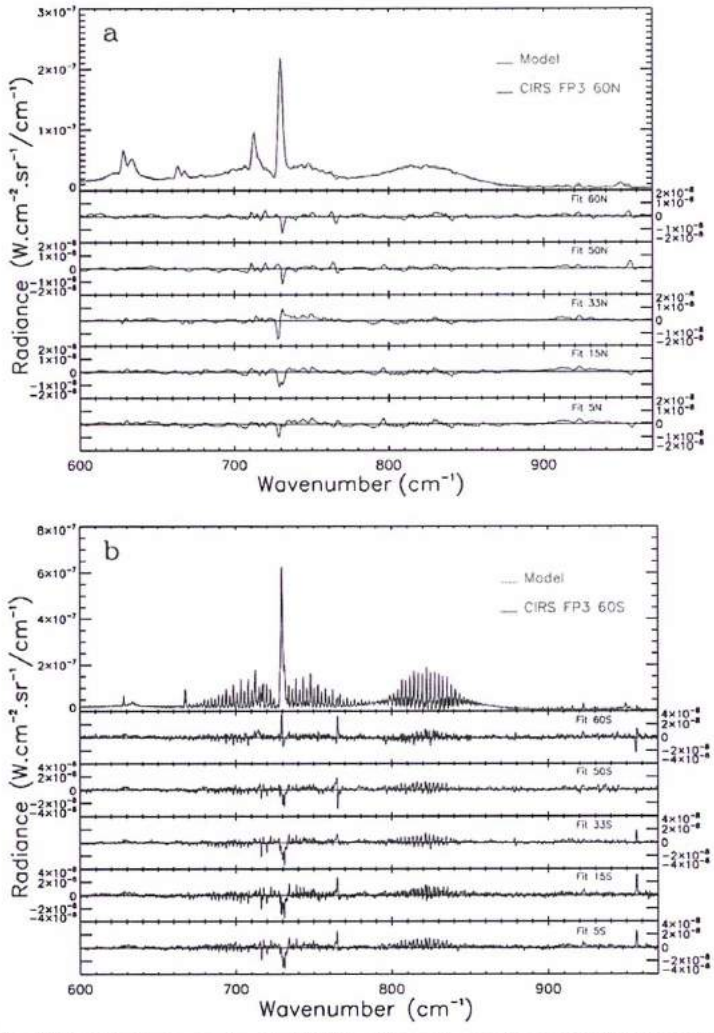

Fig. 6. Best global fits to the FP3 region at medium (a) and high (b) resolutions, using everywhere constant-with-height molecular profiles.

with constant-with-height profiles at mid-latitudes. They also work well for the shape reproduction at higher northern and southern latitudes, but they need in each case to be adjusted by significant multiplying factors (about 0.3 for the North and 0.5 for the South). This means that these distributions need to be significantly reduced in abundance to match the data at high northern and southern latitudes. But in general, their use allows for a better fit to the data than with constant-with-height profiles. This is the case also for the vertical profiles inferred from CIRS limb data (Vinatier et al., 2007), so that the vertical distributions always provide a better fit to the whole acetylene band simultaneously. The abundances retrieved for the minor species embedded within the C_2H_2 wings (and in particular HCN and C_3H_8) are the same, since we always first adjust the C_2H_2 mixing ratio to match the observed emission in the left and right wings of the acetylene band before further exploring the abundances of other species.

The vertical profiles used for HCN have allowed for a slightly improved fit to the band at 713 cm^{-1}. We can thus say that the nadir data hold proof that a vertical distribution with a marked slope (as inferred in the models and by the CIRS limb data analysis

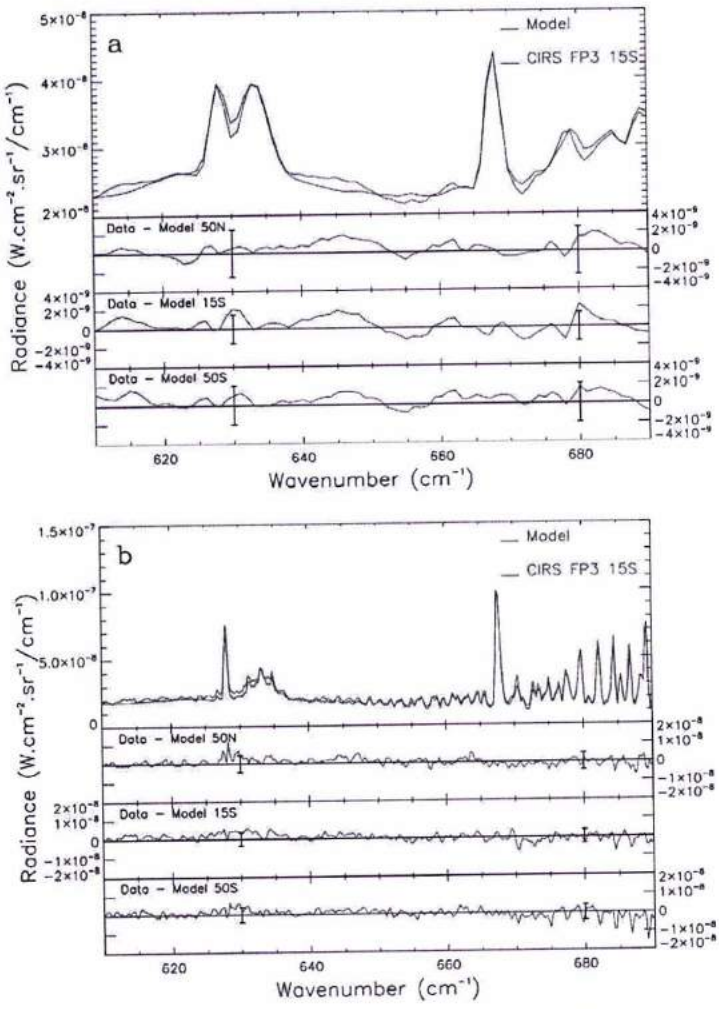

Fig. 7. Fits in the 610–690 cm^{-1} region of the 5°S Titan spectrum, using constant-with-height profiles, at medium (a) and high resolution (b), showing the C_4H_2, C_3H_4, HC_3N, CO_2, C_6H_6 and C_2HD bands, as well as the residual radiances after fitting this region at 50°S, 15°S and 50°N. The 3 – σ error bars (see text for details) on the radiance are indicated.

(Teanby et al., 2008a,b; Vinatier et al., 2007, 2009)) is required. But no further information can be inferred as a function of altitude from the nadir spectra.

4.5. The ethane and ethylene abundances

Ethane and ethylene dominate the emission observed in the 750–1000 cm^{-1} spectral region, with band centers at 821 and 949 cm^{-1} for the ν_9 and ν_7 bands respectively (Fig. 10). The ethylene retrieval is difficult due to the strong interference from a noise feature at 956 cm^{-1}.

New spectroscopic data was made available for C_2H_6 from Vander Auwera et al. (2007), which greatly improves the fit in the C_2H_6 band at 821 cm^{-1} and allows us to include the ν_6 and ν_8 bands in the 1350–1500 cm^{-1} region. The region also contains weak propane bands at 869 and 922 cm^{-1} (Nixon et al., 2009). Also a possible gradient in the haze simulation could be affecting the continuum.

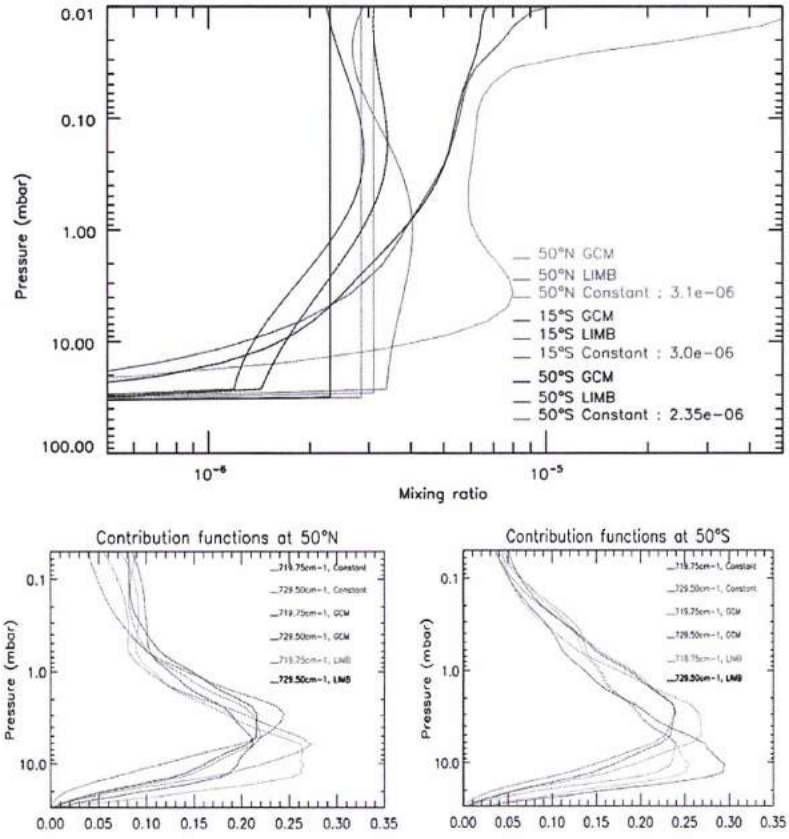

Fig. 8. Upper panel: vertical distributions for C_2H_2 tested here: the GCM model (Crespin et al., 2008) and the limb-inferred profiles (Vinatier et al., 2007) are shown, along with the constant-with-height best-fit distributions. In order to fit the center and the wings of the 729 cm^{-1} band in the high-resolution data at 50°N, 15°S and 50°S the vertical distributions need to be adjusted by certain multiplying factors. Also shown (lower panel) are the contribution functions as calculated with the GCM profiles for 50°N and 50°S; the latter is also representative of equatorial and mid-latitudes.

The new fit obtained in the ethane band now yields much smaller abundances (by 45–60%) with respect to what was previously found (Coustenis et al., 2007) due to the higher band strength (by 1.44 with respect to the previous GEISA version). When a vertical distribution is used, we get a slightly better match to the data, but within uncertainties, we cannot distinguish between the constant-with-height and the vertical profiles.

4.6. The uncertainties

The uncertainties on the abundances inferred here are calculated as explained in Coustenis et al. (2007), Section 4.1. We take into account

- the instrument noise on the location of the emission peak (negligible with respect to other sources of error given the large number of spectra we generally sum up in a sample, with the exception of higher northern latitudes for medium resolution),
- the uncertainty on the position of the continuum level above which the emission rises, and
- the uncertainty on the temperature profile and its impact on the line formation region.

In addition, systematic errors due to the uncertainty on the CH_4 abundance, on the spectroscopic data, calibration problems and inconsistencies in the samples or the datasets used, were also taken into account when the absolute error bars are given.

The precision on the temperature profile inferences described in Section 4.1 is discussed in Achterberg et al. (2008a) and in Coustenis et al. (2007). The uncertainty from the instrument noise is small (0.1 K or so) so the main errors are systematic, mainly originating in the uncertainty of the CH_4 abundance: about 1 K around 1 mbar, increasing to ~4 K about 5 mbar and from the sensitivity to the initial guess (~2 K or so).

Due to the large number of spectra considered here, as well as to the improved spectroscopic parameters for C_2H_6, C_3H_4, HC_3N

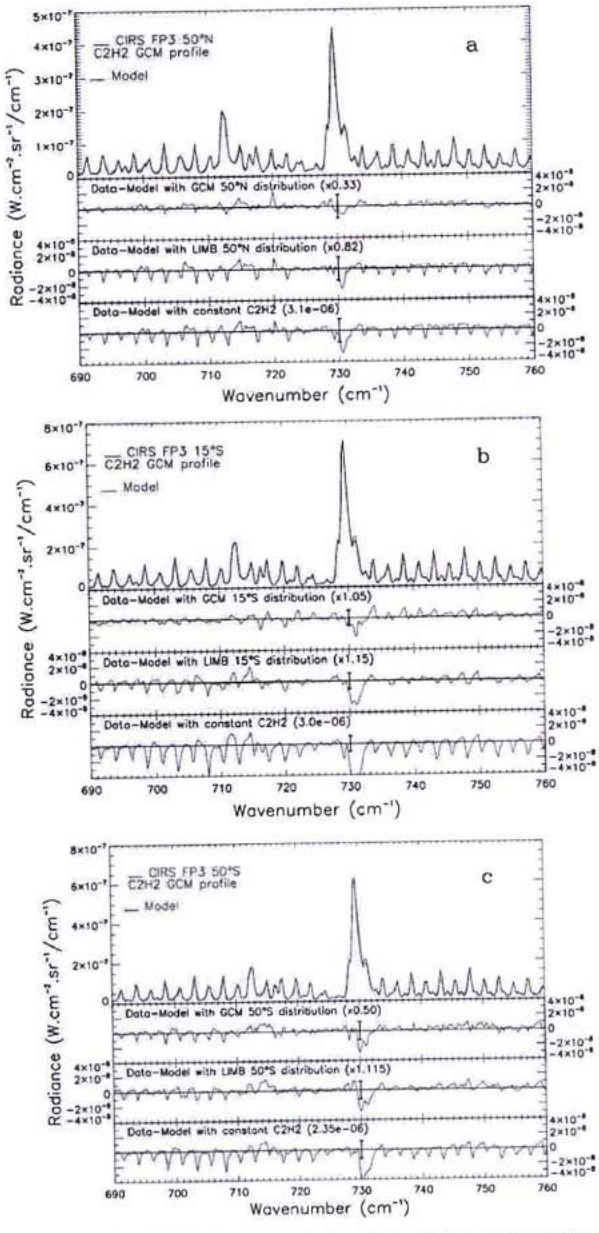

Fig. 9. The fit produced at high resolution for (a) 50°N, (b) 15°S and (c) 50°S as well as the residuals to the fits found when the GCM or a constant-with-height or the limb-inferred vertical mixing ratios are used for C_2H_2. The constant vertical profile is forced to fit the center of the C_2H_2 Q-branch. The misfit near 730 cm^{-1} is due to the fact that the very close right wing of the band eludes fitting on all occasions, perhaps due to a noise feature in that region (see text). 3 – σ error bars are indicated.

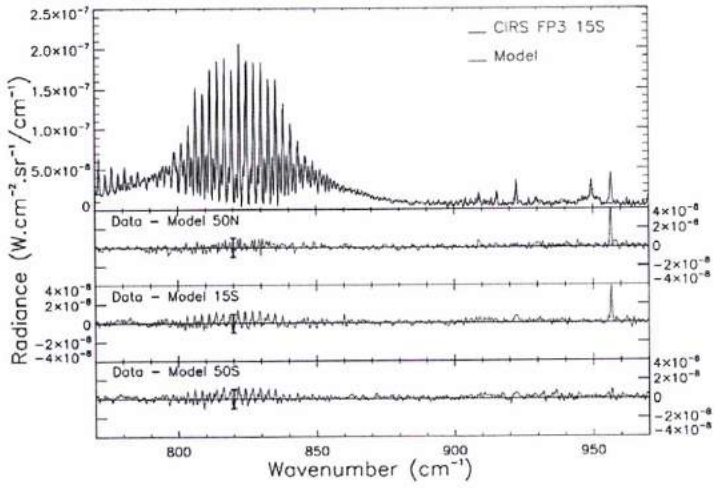

Fig. 10. Fit to the 750–1000 cm $^{-1}$ region with the emissions mainly of ethane and ethylene, with constant in altitude profiles, for high-resolution spectra and at different latitudes. The fit to the ethane band with new spectroscopic parameters has significantly improved the fit to the emission in the band, but there is still room for improvement in the 800–840 cm $^{-1}$ region, although a vertical distribution for C_2H_6 slightly improves the fit. The fit to the ethylene band is also shown. There is a strong bad pixel feature interfering near 957 cm $^{-1}$. 3 – σ error bars are indicated.

and some isotopes, we have been able to considerably reduce the error bars on our inferences with respect to previous papers.

5. Meridional variations of the trace gaseous constituents

We have inferred the meridional variations for the different constituents present in the CIRS spectra from 600 to 1500 cm^{-1}. They are shown in Fig. 11a and b, along with the 3 – σ error bars including all uncertainties. For some latitudes, the mixing ratios inferred from high-resolution data, are given in Table 2. Benzene and HC_3N are difficult to detect at low southern latitudes. However, while the HC_3N emission is clearly observed, even at low latitudes, C_6H_6 eludes firm detection. Thus, for latitudes <40°S in Fig. 11b, the values for C_6H_6 are upper limits.

As in Coustenis et al. (2007), we find that the observed enrichment reported here for some species at high northern latitudes is less at this epoch (mid-winter at the northern pole) than at the time of the Voyager encounter just after spring equinox (Coustenis and Bézard, 1995). The gases showing a strong enhancement in the North are the complex hydrocarbons (C_3H_4, C_4H_2, and C_6H_6) and the nitriles (HCN and HC_3N). For most of these gases, the increase strongly manifests itself starting at around 40°N, with the exception of HCN which exhibits a regular increase from South to North. Other constituents with a smaller increase in abundance (also from about 40°N and northwards) are: C_2H_2, C_2HD (whose detection and abundance results are given in Coustenis et al. (2008)) and C_2H_4. Propane (C_3H_8) is now found to be constant or slightly increasing in the North (contrary to inferences from the limited North-pole dataset we had used in Coustenis et al. (2007)), while C_2H_6 and CO_2 remain constant (Fig. 11a). When relative errors are considered (too small to appear in Fig. 11a and b), there is a possible indication for a notch (small unexpected decrease) near 50°N in the abundances of C_2H_2 and HCN and near 50°S for C_2H_4 and C_3H_8. For the 50°N possible minimum in the abundance of the aforementioned species, Vinatier et al. (2009) report such an occurrence at 0.01 mbar (around 350 km) for C_2H_2 and HCN in results they present from CIRS limb data analysis. Teanby et al. (2008a,b) also inferred such abundance minima which they interpret as a combined effect of poleward advection of air from southern latitudes, a mixing barrier at around 60°N and eddy transport towards the equator in the lower stratosphere. Our results here are in agreement with these inferences, although the altitudes of the limb data are not the same as the ones probed by the nadir data analyzed here. Furthermore, the abundance minimum in our case cannot be confirmed given the error bars and there is nowhere an indication of anything similar for 50°S.

6. Interpretation of the results and discussion

Our findings on the trace gas abundances (Fig. 11 and Table 2) reported here mostly support the results in the previous paper (Coustenis et al., 2007) with the advantage that our new uncertainties are smaller and we have secured more reliable spectroscopic data for some molecules (HCN, HC_3N, C_2H_6), as well as information on new species (C_2HD, see Coustenis et al., 2008). This allows us to improve, in particular, the inferences at high North and South latitudes. Indeed, differences in Titan's composition between this paper (Table 2) and the previous one pertain mainly to the ethane abundance and to mixing ratios found at higher latitudes for some species (such as C_2H_4 and C_3H_8 for instance, compare Fig. 11a and b here with Fig. 16a and b in Coustenis et al. (2007)). Thus, while this new study confirms – with more precision – the abundances and the latitudinal trend attributed to C_2H_6, C_2H_2, CO_2, C_3H_4, C_4H_2 and some of the weaker components (HC_3N and C_6H_6), the decrease in abundance near the North pole for C_3H_8 and C_2H_4 is invalidated here. Indeed, with the larger number of spectra available at northern latitudes in this study we find propane to slightly increase and ethylene to be significantly more abundant. The differences in results between this work and the 2007 cannot be attributed to temporal variations but rather to: (a) the lack of a sufficient number of

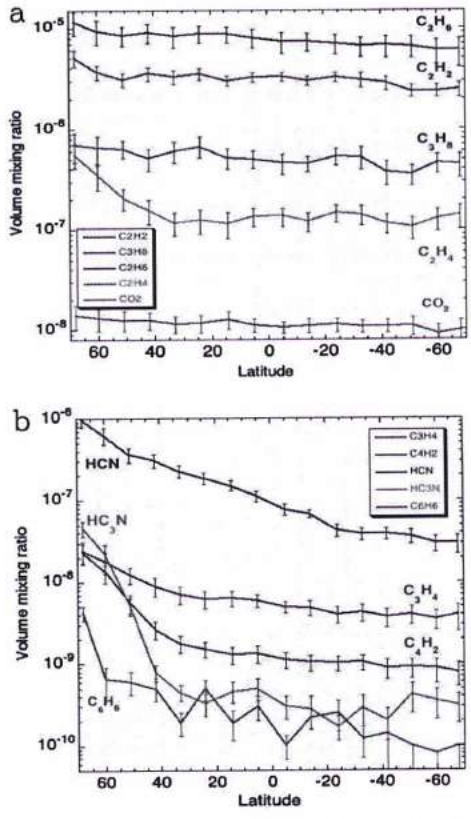

Fig. 11. (a and b) Meridional variations of trace gases on Titan. Error bars represent $3-\sigma$ standard deviations including all error sources (relative error bars, without systematic errors) are too small to appear on this figure for most molecules. Only upper limits were inferred for C_6H_6 at latitude <40°S.

spectra available in 2007 for high latitudes and (b) the new spectroscopic parameters available (mainly for ethane).

In summary, we find the main trace gases (C_2H_6, C_2H_2 and C_3H_8) and CO_2 to increase from South to North by factors between 1.5 and 2. C_6H_6 and HC_3N are found to exhibit dramatic increases to the North by factors of about 30 and 150 respectively. All other gases show enhancement by factors between 3 and 8 (see Fig. 11). Hourdin et al. (2004) have shown that the meridional circulation on Titan, dominated by global Hadley cells, can be responsible for the accumulation of chemical species and aerosols at high northern latitudes and have also predicted the magnitude of the enrichment in stratospheric constituents to be related to their condensation altitudes (the meridional advection increases the concentrations in the air rising from the troposphere, where most of the species condense). In a recent paper, Teanby et al. (2009) have shown that these enhancements occur in inverse proportion to the photochemical lifetime of the species, so that the enhancement is greatest for the shortest-lived chemicals. This is explained by a combination of chemistry and dynamics: the vertical gradients are steepest for the shortest-lifetime species in a purely chemical model: however the presence of a circulation cell in the real atmosphere with downwelling in the polar regions (North pole at present epoch) causes the lower stratosphere to be greatly enriched in these species compared to the equator. Our results compare well, within error bars, with the findings of Teanby et al. (2009) as concerns meridional variations of the species reported in their paper and all trends are confirmed, although somewhat higher abundances are found in general in the Oxford retrievals for the complex hydrocarbons and the nitriles.

We also compared the findings in this paper with gas abundances in Titan's stratosphere reported in other papers by the CIRS team members. We are in good agreement with isotopic ratios and values reported by Bézard et al. (2007) and Nixon et al. (2008a,b). We have tested the vertical distributions for C_2H_2, C_2H_6 and HCN as recovered from limb data analyses by Vinatier et al. (2007, 2009) and we find them to be compatible with our nadir data for nine different latitudes between 50°S and 80°N. The abundances inferred from the limb data for other molecules as well are plotted in Figs. 12a and 12b. These values are compatible with ours at mid and low latitudes and slightly higher towards the North (as was also found in Coustenis et al. (2007)).

Hereafter, we compare our results with theoretical work and current models for Titan's atmosphere. Attempts to model the seasonally varying distribution of organic compounds in the middle atmosphere have used 2-D simulations with parameterizations of eddy and wave momentum flux convergences.

The Titan model proposed by Lavvas et al. (2008a,b) is a 1-D simulation coupling between photochemistry, radiation transfer and aerosol microphysics. The production of all main neutral gas species is followed from the initial photolysis of N_2 and CH_4, while the production of aerosols is described through specific chemical

Table 2
Mixing ratios for the Titan trace gaseous constituents in the stratosphere for a selected set of latitudes from nadir high-resolution data using constant-with-height distributions.

Molecule	Mixing ratios							
	70°S	50°S	33°S	15°S	5°N	33°N	50°N	70°N
Mixing ratios of trace gases in Titan's stratosphere								
C_2H_2	2.45E−06	2.35E−06	3.05E−06	2.97E−06	3.25E−06	3.30E−06	3.10E−06	5.10E−06
C_2HD	1.10E−09	7.00E−10	1.40E−09	7.50E−10	7.40E−10	1.00E−09	1.25E−09	2.00E−09
C_2H_4	1.38E−07	1.05E−07	1.40E−07	1.20E−07	1.35E−07	1.16E−07	2.05E−07	5.50E−07
C_2H_6	6.07E−06	6.50E−06	6.65E−06	7.30E−06	8.00E−06	8.80E−06	8.50E−06	1.15E−05
C_3H_4	3.98E−09	4.00E−09	4.20E−09	4.80E−09	5.90E−09	7.10E−09	1.23E−08	2.40E−08
C_3H_8	4.45E−07	3.50E−07	5.20E−07	4.50E−07	5.00E−07	6.00E−07	6.30E−07	6.95E−07
C_4H_2	7.80E−10	9.00E−10	1.04E−09	1.12E−09	1.32E−09	1.77E−09	5.60E−09	2.30E−08
C_6H_6	<1.00E−10	<1.00E−10	1.20E−10	2.20E−10	3.00E−10	1.90E−10	6.00E−10	4.20E−09
HCN	2.95E−08	3.60E−08	3.85E−08	6.70E−08	1.13E−07	2.25E−07	3.62E−07	9.70E−07
HC_3N	3.10E−10	4.20E−10	2.90E−10	2.80E−10	5.00E−10	4.50E−10	5.10E−09	4.60E−08
CO_2	9.90E−09	1.10E−08	1.08E−08	1.10E−08	1.11E−08	1.15E−08	1.25E−08	1.40E−08

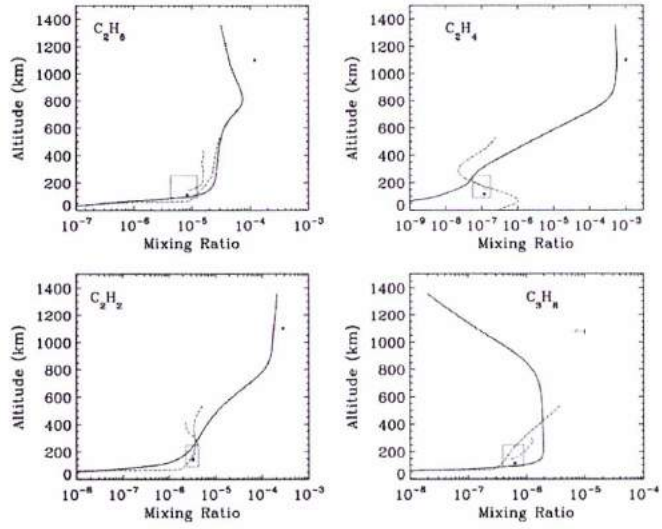

Fig. 12a. Comparison of the results from this work at 33°N for major hydrocarbons (points in green boxes) with the vertical profiles inferred from limb data (blue lines, 15°S, Vinatier et al., 2007; red lines, 30°N, Vinatier et al., 2009) and the model simulations (black curves). The points at 1100 km in altitude are the INMS results (Waite et al., 2007; Vuitton et al., 2008; Cui et al., 2009). In the green boxes, the horizontal dimension is the uncertainty on the mixing ratio, while the vertical side gives the extent of the contribution function at FWHM. The model correctly reproduces the results from nadir and limb CIRS data for these molecules within error bars. See text and Vinatier et al. (2009) for more details.

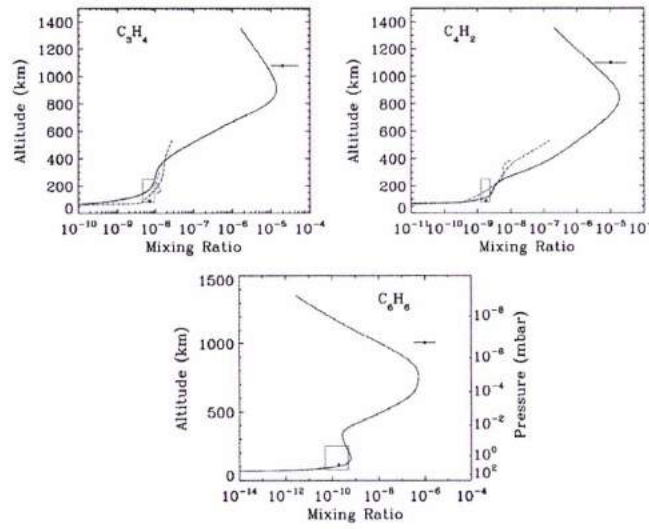

Fig. 12b. Same as Fig. 12a but for lesser hydrocarbons. The model gives a good representation of the CIRS findings from nadir data within uncertainties and tends to agree with limb-inferred vertical profiles.

pathways that are based on the simulated gas components. The contribution of both gases and aerosols are included in the simulation of the radiation transfer and vertical temperature profile providing in this way a self-consistent approach. Furthermore the model included heterogeneous chemistry processes on the surface of the produced aerosols, while the contribution of atmospheric mixing in the calculated vertical profiles is taken into account through an eddy mixing profile, retrieved based on the observed vertical mixing ratio profiles of argon and ethane. The model results are representative of 33°N latitude atmospheric conditions hence the comparisons are performed with our inferences near that latitude. Our purpose is to check the reactions and chemical pathways included in current photochemical models for Titan and to infer some insights on what works and what does not in our current understanding of Titan's chemistry.

Figs. 12a–12c shows the comparisons among various inferences of Titan's atmospheric composition and the model, all at equatorial or mid-latitudes, based on data taken at high resolution with CIRS. One set of these retrievals is our own work at 33°N, the others are the vertical profiles by Vinatier et al. (2007) at 15°S and at 30°N (Vinatier et al., 2009). In addition, the retrieved abundances in the thermosphere by INMS (Waite et al., 2005; Vuitton et al., 2007, 2008; Cui et al., 2009) are compared. Finally, water vapor was detected by ISO (Coustenis et al., 1998) and the abundance retrieved is given in Fig. 12c. Water vapor was also detected by CIRS and preliminary investigations show that the ISO abundance fits the data (Nixon et al., 2006).

There is a general good agreement between the observations and the model although there are specific cases for which the agreement is less good. The main hydrocarbon and nitrile species are well described by the model with the stratospheric abundances being in good agreement with our retrieved ones, except for the cases of C_2H_4 and HC_3N. For the former the simulated profile decreases further than the stratospheric value towards the surface, although the observations suggest a reversal in the mixing ratio profile, while for latter the simulated abundance is larger than the observed one at the specific latitude. These apparent discrepancies could be a manifestation of advection processes not captured by the 1-D character of the simulation. Another hint suggesting the presence of other processes taking place in the atmosphere is the case of C_3H_8 for which although the stratospheric abundance is in agreement with the CIRS nadir-retrieved value, the vertical profile from the limb observations suggests a different behavior than the simulated one. Furthermore, the HCN and C_2H_2 profiles at 30°N appear to decrease above 250 km relative to the equatorial profile that present a more monotonic altitude behavior, thus suggesting the contribution of advection phenomena. It is important also to note that the current model includes only the neutral chemistry contribution in the abundances of the simulated species. Although this is a good approach for most of the observed species, the contribution of ion-neutral chemistry reaction can become significantly important for some cases such as that of benzene (see Vuitton et al., 2009). Nonetheless, most of the CIRS-inferences reported here and from the limb data are well simulated by this 1-D mode, which proves to be a good tool to simulate vertical mid-latitude distributions of Titan's trace constituents, including the INMS results, while pointing to some issues with the currently adopted chemical pathways for Titan's atmosphere and the contribution of dynamical effects.

The results presented in this work were also compared with predictions by recent 2-D dynamical models such as the General Circulation Model (GCM) developed for Titan at the IPSL (Crespin et al., 2008 and references within). These models (Lebonnois et al., 2001, 2003; Hourdin et al., 2004; Crespin et al., 2008) used a series of 2-D models based on the Hourdin et al. (1995) GCM, with photochemical coupling, and radiative transfer calculations that included the opacities of the organic compounds and hazes. These models managed to reproduce much of the observed spatial distributions seen by Voyager IRIS and Cassini/CIRS. They suggest that the meridional distributions were dependent on both the

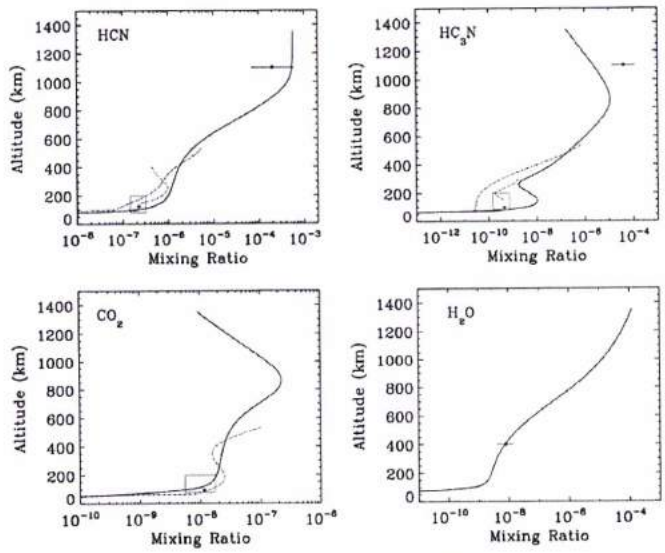

Fig. 12c. Same as Fig. 12a but for nitriles and oxygen compounds within the CIRS range. With the exception of a marginal fit for HC_3N, the model nicely reproduces the CIRS findings and the ISO-retrieved water vapor value. With respect to other vertical distributions retrieved from CIRS limb data, the model overestimates the HC_3N abundance.

meridional circulations and the mixing by barotropic eddies. These seasonal models predict that the circulation in the middle atmosphere is dominated by a pole-to-pole cell with ascent over the summer pole, followed by a circulation reversal during a short period after the equinox, with a brief transition period in which the ascending branch is at low latitudes and the circulation is more hemispherically symmetric. According to these models, and as described in Flasar et al. (2005), the subsidence over the winter pole accounts for the enhancement in the concentrations of the organic compounds that are observed (see also Teanby et al., 2008b, 2009).

We also find here a generally good agreement with the equatorial and the northern (winter) pole distributions. In particular, the observed enrichment reported here at high northern latitudes, slightly stronger after spring equinox (Voyager) than for mid-winter (Cassini) is found in the GCM. The vertical distribution predicted for C_2H_2 by the GCM for mid-latitudes is also compatible with our observations with minimal adjustment. Note, however, that at higher northern and southern latitudes, the GCM acetylene profiles require a strong reducing adjustment factor while also vertical profiles inferred by limb CIRS data are not reproduced by the GCM (Crespin et al., 2008). An additional disagreement can be found in the model predictions for the southern hemisphere (currently summer pole), where the model produces a secondary cell in the low stratosphere, which maintains an enrichment over this pole and a depleted region at 30°S, both of which features are not observed (see Fig. 10 of Crespin et al. (2008)). However, spatial mapping provided by CIRS, both in the nadir- and limb-viewing modes, shows a structure that is quite complex, particularly near the North (winter) polar vortex, that the 2-D models cannot adequately explain. Teanby et al. (2008b) reported that the isoclines of several compounds, including HCN, HC_3N, C_3H_4, and C_4H_2 have an altitude–latitude structure that is tilted in the middle atmosphere, and these compounds exhibit a depletion zone near the vortex in the mesosphere. Clearly, the 2-D parameterizations need to include additional transport processes to account for behavior like this. Understanding the seasonal change of the polar vortex—its buildup in the late fall and early winter, its mature phase into early spring, and its subsequent break-up—and the attendant changes in the organic concentrations will be key in elucidating these processes.

In spite of this important breakthrough in modeling Titan's circulation (Achterberg et al., 2008b), 3-D models may be required before the complexity of Titan's atmospheric composition and dynamics can be satisfactorily reproduced in a model.

Acknowledgments

We gratefully recognize the contribution and valuable help of Alexandre Laurent and Zhi-Fang Xu in the CIRS data preparation and processing. We also thank GCM modelers (A. Crespin and S. Lebonnois) for providing listings of their vertical distributions at our averaged latitudes. We are grateful to the CIRS team as a whole for valuable assistance with the science and the data preparation and processing described here. In particular, we would like to thank Jacqueline Mondellini for the data processing in Meudon and the planning and processing team at Goddard.

References

Achterberg, R.K., Conrath, B.J., Gierasch, P.J., Flasar, F.M., Nixon, C.A., 2008a. Titan's middle-atmospheric temperatures and dynamics observed by the Cassini Composite Infrared Spectrometer. Icarus 194, 263–277.

Achterberg, R.K., Conrath, B.J., Gierasch, P.J., Flasar, F.M., Nixon, C.A., 2008b. Observation of a tilt of Titan's middle-atmospheric super-rotation. Icarus 197, 549–555.

Bézard, B., Nixon, C.A., Kleiner, I., Jennings, D.E., 2007. Detection of $^{13}CH_3D$ on Titan. Icarus 191, 397–400.

Coustenis, A., Bézard, B., 1995. Titan's atmosphere from Voyager Infrared Observations: IV. Spatial variations of temperature and composition. Icarus 115, 126–140.

Coustenis, A., Salama, A., Lellouch, E., Encrenaz, Th., Bjoraker, G., Samuelson, R.E., de Graauw, Th., Feuchtgruber, H., Kessler, M.F., 1998. Evidence for water vapor in Titan's atmosphere from ISO/SWS data. Astron. Astrophys. 336, L85–L89.

Coustenis, A., Salama, A., Schulz, B., Ott, S., Lellouch, E., Encrenaz, Th., Gautier, D., Feuchtgruber, H., 2003. Titan's atmosphere from ISO mid-infrared spectroscopy. Icarus 161, 383–403.

Coustenis, A., and 24 colleagues, 2007. The composition of Titan's stratosphere from Cassini/CIRS mid-infrared spectra. Icarus 189, 35–62.

Coustenis, A., Jennings, D., Jolly, A., Bénilan, Y., Nixon, C., Gautier, D., Vinatier, S., Bjoraker, G., Romani, P., 2008. Detection of C_2HD and the D/H ratio on Titan. Icarus 197, 539–548. doi:10.1016/j.icarus.2008.06.003.

Crespin, A., Lebonnois, S., Vinatier, S., Bézard, B., Coustenis, A., Teanby, N.A., Achterberg, R.K., Rannou, P., 2008. Diagnostics of Titan's stratospheric dynamics using Cassini/CIRS data and the IPSL General Circulation Model. Icarus 197, 556–571. doi:10.1016/j.icarus.2008.05.010.

Cui, J., and 12 colleagues, 2009. Analysis of Titan's neutral upper atmosphere from Cassini Ion Neutral Mass Spectrometer measurements. Icarus 200, 581–615.

Flasar, F.M., and 44 colleagues, 2004. Exploring the Saturn system in the thermal infrared: The Composite Infrared Spectrometer. Space Sci. Rev. 115, 169–297.

Flasar, F.M., and 44 colleagues, 2005. Titan's atmospheric temperatures, winds, and composition. Science 308, 975–978.

Fulchignoni, M., and 42 colleagues, 2005. Titan's physical characteristics measured by the Huygens Atmospheric Instrument (HASI). Nature 438, 785–791.

Hourdin, F., Talagrand, O., Sadourny, R., Courtin, R., Gautier, D., McKay, C.P., 1995. Numerical simulation of the general circulation of the atmosphere of Titan. Icarus 117, 358–374.

Hourdin, F., Lebonnois, S., Luz, D., Rannou, P., 2004. Titan's stratospheric composition driven by condensation and dynamics. J. Geophys. Res. 109, E1205. 15 pp.

Jacquinet-Husson, N., and 50 colleagues, 2008. The GEISA spectroscopic database: Current and future archive for Earth's planetary atmosphere studies. JQSRT 109, 1043–1059.

Jennings, D.E., and 10 colleagues, 2008. Isotopic ratios in Titan's atmosphere from Cassini CIRS limb sounding: HC_3N in the North. Astrophys. J. 681, L109–L111.

Jolly, A., Benilan, Y., Fayt, A., 2007. New infrared integrated intensities and extensive line list for the HC_3N bending modes. J. Mol. Spectrosc. 242 (1), 46–54.

Lavvas, P.P., Coustenis, A., Vardavas, I.M., 2008a. Coupling photochemistry with haze formation in Titan's atmosphere. Part I: Model description. Planet. Space Sci. 56, 27–66.

Lavvas, P.P., Coustenis, A., Vardavas, I.M., 2008b. Coupling photochemistry with haze formation in Titan's atmosphere. Part II: Results and validation with Cassini/Huygens data. Planet. Space Sci. 56, 67–99.

Lebonnois, S., Toublanc, D., Hourdin, F., Rannou, R., 2001. Seasonal variations of Titan's atmospheric composition. Icarus 152, 384–406.

Lebonnois, S., Hourdin, F., Rannou, P., Luz, D., Toublanc, D., 2003. Impact of the seasonal variations of composition on the temperature field of Titan's stratosphere. Icarus 163, 164–174.

Niemann, H.B., and 17 colleagues, 2005. The abundances of constituents of Titan's atmosphere from the GCMS instrument on the Huygens probe. Nature 438, 779–784.

Nixon, C.A., Jennings, D.E., de Kok, R., Coustenis, A., 2006. Water in Titan's stratosphere from Cassini CIRS observations. Bull. Am. Astron. Soc. 38, 529.

Nixon, C.A., and 10 colleagues, 2008a. The $^{12}C/^{13}C$ ratio in Titan hydrocarbons from Cassini/CIRS Infrared Spectra. Icarus 195, 778–791.

Nixon, C.A., Jennings, D.E., Bézard, B., Teanby, N.A., Achterberg, R.K., Coustenis, A., Vinatier, S., Irwin, P.G.J., Romani, P.N., Flasar, F.M., 2008b. Isotopic ratios in Titan's atmosphere from Cassini CIRS limb sounding: CO_2 at low and midlatitudes. Astrophys. J. 681, L101–L103.

Nixon, C.A., Jennings, D.E., Flaud, J.-M., Bézard, B., Teanby, N.A., Irwin, P.G.J., Ansty, T.M., Coustenis, A., Flasar, F.M., 2009. Titan's prolific propane: The Cassini CIRS perspective. Planet. Space Sci. 57 (13), 1573–1585.

Rannou, P., Lebonnois, S., Hourdin, F., Luz, D., 2005. Titan atmosphere database. Adv. Space Res. 36, 2194–2198.

Rothman, L.S., and 44 colleagues, 2009. The HITRAN 2008 molecular spectroscopic database. J. Quant. Spectrosc. Radiat. Trans. 110, 553–572.

Teanby, N.A., and 11 colleagues, 2006. Latitudinal variations of HCN, HC_3N and C_2N_2 in Titan's stratosphere derived from Cassini CIRS data. Icarus 181, 243–255.

Teanby, N., and 11 colleagues, 2007. Vertical profiles of HCN, HC_3N and C_2H_2 in Titan's atmosphere derived from Cassini/CIRS data. Icarus 186, 364–384.

Teanby, N.A., and 10 colleagues, 2008a. Global and temporal variations in hydrocarbons and nitriles in Titan's stratosphere for northern winter observed by Cassini/CIRS. Icarus 193, 595–611.

Teanby, N.A., and 12 colleagues, 2008b. Titan's winter polar vortex structure revealed by chemical tracers. J. Geophys. Res. 113, E12003.

Teanby, N.A., Irwin, P.G.J., de Kok, R., Nixon, C.A., 2009. Dynamical implications of seasonal and spatial variations in Titan's stratospheric composition. Philos. Trans. R. Soc. A 367, 697–711.

Vander Auwera, J., Moazzen-Ahmadi, N., Flaud, J.-M., 2007. Towards an accurate database for the 12 μm region of the ethane spectrum. Astrophys. J. 662, 750–757.

Vinatier, S., and 10 colleagues, 2007. Vertical abundance profiles of hydrocarbons in Titan's atmosphere at 15°S and 80°N retrieved from Cassini/CIRS spectra. Icarus 188, 120–138.

Vinatier, S., and 10 colleagues, 2009. Analysis of Cassini/CIRS limb spectra of Titan acquired during the nominal mission. I: Hydrocarbons, nitriles, and CO_2 vertical mixing ratio profiles. Icarus, in press, doi:10.1016/j.icarus.2009.08.013.

Vuitton, V., Yelle, R.V., McEwan, M.J., 2007. Ion chemistry and N-containing molecules in Titan's upper atmosphere. Icarus 191, 722–742.

Vuitton, V., Yelle, R.V., Cui, J., 2008. Formation and distribution of benzene on Titan. J. Geophys. Res. 113 (E5), E05007.

Vuitton, V., Yelle, R.V., Lavvas, P., 2009. Composition and chemistry of Titan's thermosphere and ionosphere. Philos. Trans. R. Soc. A: Math. Phys. Eng. Sci. 367 (1889), 729–741.

Waite, J.H., and 20 colleagues, 2005. Ion Neutral Mass Spectrometer results from the first flyby of Titan. Science 308, 982–986.

Waite, J.H., Young, D.T., Cravens, T.E., Coates, A.J., Crary, F.J., Magee, B., Westlake, J., 2007. The process of tholin formation in Titan's upper atmosphere. Science 316 (5826), 870–875.

Appendix C3

Water vapor in Titan's stratosphere from Cassini CIRS far-infrared spectra

Journal article published in *Icarus* (2012),
Volume 220, pp. 855-862.

Icarus 220 (2012) 855–862

Contents lists available at SciVerse ScienceDirect

Icarus

journal homepage: www.elsevier.com/locate/icarus

Water vapor in Titan's stratosphere from Cassini CIRS far-infrared spectra

V. Cottini [a,*], C.A. Nixon [a,b], D.E. Jennings [a], C.M. Anderson [a], N. Gorius [a,c], G.L. Bjoraker [a], A. Coustenis [d], N.A. Teanby [e], R.K. Achterberg [a,b], B. Bézard [e], R. de Kok [f], E. Lellouch [d], P.G.J. Irwin [g], F.M. Flasar [a], G. Bampasidis [d,h]

[a] Planetary Systems Laboratory, NASA Goddard Space Flight Center, Greenbelt, MD 20771, USA
[b] Department of Astronomy, University of Maryland at College Park, College Park, MD 20742, USA
[c] Department of Physics, The Catholic University of America, Washington, DC 20064, USA
[d] LESIA-Observatoire de Paris, CNRS, UPMC Univ. Paris 06, Univ. Paris-Diderot, France
[e] School of Earth Sciences, University of Bristol, Wills Memorial Building, Queen's Road, Bristol BS8 1RJ, UK
[f] SRON, Sorbonnelaan 2, 3584 CA Utrecht, Netherlands
[g] Atmospheric, Oceanic and Planetary Physics, University of Oxford, Parks Rd., Oxford OX1 3PU, UK
[h] Faculty of Physics, National and Kapodistrian University of Athens, Athens, Greece

ARTICLE INFO

Article history:
Received 17 April 2012
Revised 7 June 2012
Accepted 9 June 2012
Available online 26 June 2012

Keywords:
Spectroscopy
Atmospheres, Composition
Satellites, Atmospheres
Titan

ABSTRACT

Here we report the measurement of water vapor in Titan's stratosphere using the Cassini Composite Infrared Spectrometer (CIRS, Flasar, F.M. et al. [2004]. Space Sci. Rev. 115, 169–297). CIRS senses water emissions in the far infrared spectral region near 50 μm, which we have modeled using two independent radiative transfer codes (NEMESIS (Irwin, P.G.J. et al. [2008]. J. Quant. Spectrosc. Radiat. Trans. 109, 1136–1150) and ART (Coustenis, A. et al. [2007]. Icarus 189, 35–62; Coustenis, A. et al. [2010]. Icarus 207, 461–476). From the analysis of nadir spectra we have derived a mixing ratio of 0.14 ± 0.05 ppb at an altitude of 97 km, which corresponds to an integrated (from 0 to 600 km) surface normalized column abundance of $3.7 \pm 1.3 \times 10^{14}$ molecules/cm^2. In the latitude range 80°S to 30°N we see no evidence for latitudinal variations in these abundances within the error bars. Using limb observations, we obtained mixing ratios of 0.13 ± 0.04 ppb at an altitude of 115 km and 0.45 ± 0.15 ppb at an altitude of 230 km, confirming that the water abundance has a positive vertical gradient as predicted by photochemical models (e.g. Lara, L.M., Lellouch, F., Lopez-Moreno, J.J., Rodrigo, R. [1996]. J. Geophys. Res. 101(23), 261; Wilson, E.H., Atreya, S.K. [2004]. J. Geophys. Res. 109, E6; Hörst, S.M., Vuitton, V., Yelle, R.V. [2008]. J. Geophys. Res., 113, E10). We have also fitted our data using scaling factors of ~0.1–0.6 to these photochemical model profiles, indicating that the models over-predict the water abundance in Titan's lower stratosphere.

1. Introduction

Water is present in its various forms in many regions of the Solar System, from the atmospheres of the inner planets and shadows of lunar craters, to the mantles of icy satellites and beyond to the Kuiper Belt Objects (KBOs) and Oort Cloud Comets. Liquid water is also an essential ingredient for life on Earth and a potential clue in the search for life or habitability conditions in the rocks of Mars, the internal ocean of Europa or Titan, and the volcanic vents of Enceladus. On Titan, Saturn's largest satellite that hosts a dense nitrogen-dominated atmosphere, water is a trace species in the atmosphere. However, water plays a significant role since it is one of the sources of oxygen for the observed active photochemistry on Titan (e.g. Lara et al., 1996; Wilson and Atreya, 2004; Hörst et al., 2008).

Titan's known oxygen compounds to date are carbon monoxide (CO, ~47 ppm), carbon dioxide (CO_2, ~15 ppb) and water vapor (H_2O), where the abundances are quoted for the low-latitude stratosphere (de Kok et al., 2007a). CO_2 was first detected by Voyager 1 (Samuelson et al., 1983), while CO was first seen by ground-based observations in the near-IR (Lutz et al., 1983). Subsequent observations in the sub-millimeter led to controversy as to whether CO was well-mixed or not (Hidayat et al., 1998; Gurwell, 2004). CO emission lines were later observed by the Cassini Composite Infrared Spectrometer (CIRS), thus improving the previous abundance estimate (de Kok et al., 2007a; Teanby et al., 2009). Water was first detected in Titan's atmosphere by the Infrared Space Observatory (ISO) in 1997 (Coustenis et al., 1998). Two lines near 40-μm observed by the Short Wavelength Spectrometer (SWS) were modeled using a uniform mixing ratio above the condensation level and a value of 0.4 ppb was detected. An early

* Corresponding author. Address: NASA/GSFC, Code 693, Bldg. 34, Rm. S121, 8800 Greenbelt Rd., Greenbelt, MD 20771, USA.
E-mail address: valeria.cottini@nasa.gov (V. Cottini).

0019-1035/$ - see front matter © 2012 Elsevier Inc. All rights reserved.
http://dx.doi.org/10.1016/j.icarus.2012.06.014

attempt to measure H_2O with Cassini CIRS was unsuccessful due to poor signal-to-noise (S/N) ratios in early versions of the calibration pipeline spectra and a limited number of available spectra. Therefore, only an upper limit of 0.9 ppb could be retrieved (de Kok et al., 2007a). Since then, water emission in the CIRS data has been definitely observed, albeit without deriving any further information on its abundance and distribution (Bjoraker et al., 2008). The Cassini Ion and Neutral Mass Spectrometer (INMS) detected H_2O in the upper atmosphere – between 950 and 1200 km – with a mixing ratio in the range of $\sim(0.4–3.4) \times 10^{-5}$ (Cui et al., 2009).

While the presence of these oxygen compounds is now well-established, some details about their origin remain to be determined. Early photochemical models assumed that CO originated from episodic outgassing from Titan's interior along with nitrogen (N_2) or ammonia (NH_3) and methane (CH_4), whereas water molecules entered the top of the atmosphere and were photochemically dissociated to produce hydroxyl radicals (OH) (Wong et al., 2002; Wilson and Atreya, 2004). The combination of OH and CO led to the production of CO_2. However, Hörst et al. (2008) have recently challenged this model, arguing instead that both CO and CO_2 are the result of upper-atmospheric chemistry that occurs between in-falling oxygen species reacting with carbon produced by CH_4 photodissociation. In this hypothesis, water enters Titan's atmosphere either in the form of H_2O or OH (since the latter is quickly converted to H_2O within the atmosphere) together with oxygen (O and O^+). These forms of oxygen are thought to be deposited on Titan at two different altitudes. O^+ ions have been observed flowing into Titan's atmosphere (Hartle et al., 2006a,b) and they are thought to be deposited in the upper atmosphere around 1100 km (Hörst et al., 2008) where their interaction with methyl (CH_3) radicals leads to the formation of CO. Water is instead deposited at 750 km due to micrometeoritic ablation (English et al., 1996) where it is photolyzed to OH. The latter finally combines with CO to form CO_2 and possibly other complex species.

Saturn's rings and the icy satellites that surround the giant planets, and also interplanetary dust, are probable sources of the water (oxygen) in Titan's atmosphere and recent results from INMS indicate that the plumes of Enceladus are the dominant source (e.g. Dougherty et al., 2006). Observations and models of the neutral H_2O, OH, and O torus formed from the Enceladus plume show that material from Enceladus extends well beyond Titan's orbit (Melin et al., 2009; Cassidy and Johnson, 2010; Fleshman et al., 2012). Based on Herschel measurements of the Enceladus torus combined with modeling of the fate of the species within the torus, Hartogh et al. (2011) showed that the flux of O/O^+ into Titan is consistent with an Enceladus source for the oxygen seen in Titan CO, except for the fact that Enceladus does not seem to provide enough OH/H_2O.

In this paper, we analyze the spectra acquired by CIRS in the far infrared spectral region in order to retrieve the water vapor vertical or spatial distribution in Titan's atmosphere. CIRS has been acquiring spectra of Titan since the beginning of the Cassini prime mission (July 2004). After 2 years of the extended mission (XM), which included the 2009 equinox, in July 2010 Cassini entered in the Solstice Mission (SM), which is scheduled to last until 2017. Since an upper limit for H_2O was reported by de Kok et al. (2007a) there has been a considerable increase of the number of data collected by CIRS and significant improvements to their calibration. The increased signal to noise (S/N) ratio not only permits a definitive detection of H_2O from the analysis of CIRS far infrared spectra, but it allows us to constrain its vertical and latitudinal profile.

2. Selected dataset

CIRS (Flasar et al., 2004) is comprised of three Focal Planes observing in the spectral range 10–1400 cm^{-1} with spectral resolutions from 0.5 to 15.5 cm^{-1}. Focal Plane 1 detector (FP1) is characterized by a circular field of view (FOW) of 3.9 mrad. It records data in the far infrared spectral range (10–600 cm^{-1}) with a spectral resolution of 0.5 cm^{-1}, allowing us to observe the water vapor signature, and by modeling, to retrieve its abundance. Water presents its rotational lines in the CIRS FP1 spectral region up to 400 cm^{-1}, with the strongest and most visible lines in the range positioned between 90 and 260 cm^{-1}. We focus here on the range from 150 to 260 cm^{-1} for the water detection, as this is the range of maximum responsivity of FP1. At lower wavenumbers the on-board electronics of CIRS create a moving interference spike that can affect the spectrum up to 150 cm^{-1}. Therefore, we exclude wavenumbers shorter of 150 cm^{-1}. We use data from two different types of observations to obtain independent measurements: the far infrared on-disk integrations (FIRNADCMP) and the far infrared limb integrations (FIRLMBINT). Water is a trace species with relatively weak lines and therefore it cannot be observed in an individual spectrum. An average of a few thousand spectra of on-disk observations and a few hundred spectra of limb observations is necessary to achieve sufficient signal-to-noise (Fig. 1).

Limb observations have the FP1 Focal Plane centered around two different altitudes – hereafter limb 1 and 2 – and are therefore used to constrain the water vapor abundance in the stratosphere around 115 and 230 km respectively, well above the 45 km tropopause. Since the contribution functions of water for on-disk observations peak around 97 km (Fig. 2), the retrieved water vapor abundance derived from these measurements can be compared with the lowest altitude targeted by our limb integrations around 115 km.

For the water detection and retrieval of quantitative information together with possible latitudinal variations, multiple Titan flybys must be utilized to enhance the signal. To date, 35 limb integrations of approximately 1 h in duration (~60 high-resolution spectra) have been obtained covering latitudes from 87°S to 80°N. The nadir integrations are more numerous (about 92 successfully executed, of typical duration 5 h, ~300 spectra) as they occur in a less contested observing time further from the Titan closest-approach period. They also have a more or less complete spatial coverage of Titan's latitudes and longitudes with an average footprint size of ~15° great circle arc.

We focus on one season of on-disk observations acquired from December 2004 to December 2008 (northern winter on Titan) in order to reach a compromise between obtaining a large number of spectra and a sufficiently homogeneous dataset. Inside this time period for on-disk observations acquired from a maximum distance of 300,000 km and with a maximum emission angle of 60°, we selected latitudinal bins (80–45°S, 45–10°S, and 0–30°N) centered around three latitudes for which observation-derived temperature profiles were available (see model description in Section 3 and Fig. 3). The number of spectra averaged in these latitudinal bins were approximately 1700, 3800 and 7000 respectively and their average emission angles were 35°, 38° and 34°.

CIRS limb spectra are acquired in much smaller numbers, therefore to reach a sufficient signal-to-noise ratio we consider only one average of about 320 spectra acquired from December 2004 and September 2009, encompassing the entire southern hemisphere and mid-latitudes within the range 90°S to 20°N. During this time period and at these latitudes data can be considered quite homogeneous as shown in Teanby et al. (2010), therefore we model this average using a temperature profile retrieved for 15°S. We exclude from this analysis the higher northern latitudes where the stratospheric temperature profile changes significantly. We have also selected data acquired by the spacecraft at a range less than 45,000 km in order to limit the size of the projected detector footprint on the limb to less than 150 km.

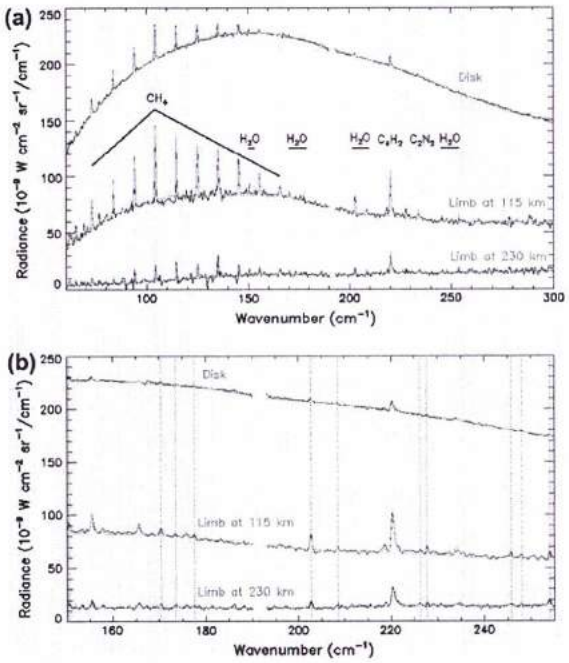

Fig. 1. (a) In black, the average of CIRS far-IR on-disk observations is plotted (~7000 spectra acquired from December 2004 to December 2008 in the latitudinal range of 0–0°N), limb observations centered around 115 and 230 km (respectively ~320 and ~280 spectra acquired from December 2004 to September 2009 in the latitudinal range of 90–20°S) and their fit (in green, blue, red respectively) assuming a constant water mole fraction above the condensation altitude. In (b) the retrieval spectral range is shown with the main water lines indicated by vertical dotted lines. (For interpretation of the references to color in this figure legend, the reader is referred to the web version of this article.)

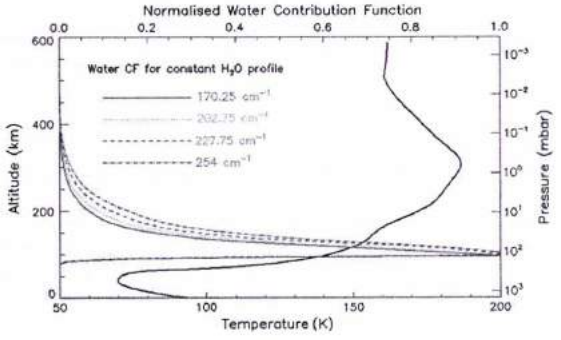

Fig. 2. Contribution functions of the different atmospheric layers to the water vapor line emission computed for four wave numbers. The solid line shows a temperature profile for 15°N.

3. Data analysis and model

In the selected part of the FP1 spectral range, Titan's spectrum is formed by (i) the contribution of thermal emission of the surface and atmospheric layers, (ii) the seven pairs (Anderson and Samuelson, 2011) of collision induced absorption (CIA) opacities between the main atmospheric molecules – N_2, CH_4 and H_2 – due to Titan's dense lower atmosphere, (iii) the photochemical aerosol plus

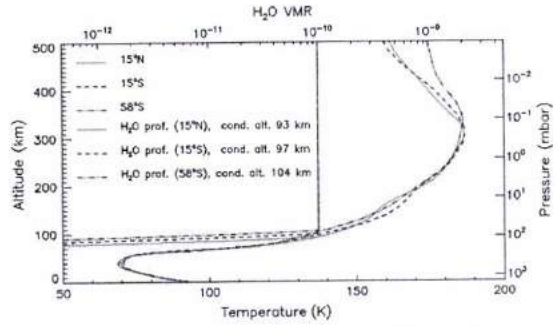

Fig. 3. Atmospheric vertical temperature–pressure profiles retrieved from CIRS data for three latitudes (58°S, 15°S, 15°N) from Anderson and Samuelson (2011) from the surface to 3.3×10^{-7} bar, corresponding to an altitude range of 0–600 km. *A priori* constant with altitude water vapor profiles are also shown for the three temperatures profiles. The constant mixing ratio profile along the atmosphere (*a priori* assumed to be 0.1 ppb) is decreased to follow the saturation vapor pressure curve in the lower stratosphere below the condensation altitude ('cond. alt.' in the figure), where the relative humidity reaches 100%. Using the saturation vapor pressure equation of water over ice of Murphy and Koop (2005) and assuming the temperature profiles retrieved at 58°S, 15°S, 15°N we find a condensation altitude of about 104, 97 and 93 km respectively.

stratospheric condensates, and (iv) the ro-vibrational emission lines of atmospheric species seen by CIRS at the latitudes considered in our study: CH_4, CO, H_2O, C_4H_2.

These quantities were used as input to the NEMESIS retrieval code (Irwin et al., 2008) to perform a combination of forward model computation and retrieval scheme based on the method of optimal estimation (Rodgers, 2000). The computation of the forward model spectrum used the correlated-k approach of Lacis and Oinas (1991) and included a Hamming apodization of Full Width at Half Maximum (FWHM) of 0.5 cm^{-1} to reproduce the instrumental line shape. The retrieval scheme was used to optimize the fits and determine the model free parameters including the water vapor abundance. This method was successfully applied to model the FP1 spectrum in Cottini et al. (2012) to retrieve surface temperature. We solve the radiative transfer equation for 147 spherical atmospheric layers, using as a source function the thermal emission of the surface, for which a unit surface emissivity is assumed, and that of the atmospheric layers. The retrieval algorithm then iteratively computes a synthetic spectrum, compares it to the data and after applying a cost function, determines the best estimate for the physical parameters in the model – the stratospheric aerosol profile and any necessary adjustments to the temperature profile and the mole fraction of included atmospheric gases. The cost function includes two components: one that measures the quality of the fit to the spectra (similar to a χ^2 test) and another that measures the deviation of the retrieved parameters from a set of *a priori* quantities.

The continuum due to the CIA was calculated according to Borysow and Frommhold (1986a,b,c, 1987), Borysow (1991), and Borysow and Tang (1993). For the N_2–CH_4 pair, we used CIA coefficient values increased by 50% as required to fit the continuum of the Cassini Descent Imager Spectral Radiometer (DISR) data (Tomasko et al., 2008) and the CIRS spectra (de Kok et al., 2010).

We have modeled the haze emission/absorption using the extinction cross sections of the hazes included in de Kok et al. (2007b). Since scattering is negligible at these wavelengths for particles smaller than few microns, we have omitted it from our computations.

We have adopted the atmospheric vertical temperature–pressure profiles retrieved from CIRS data for three latitudes (58°S, 15°S, 15°N) from Anderson and Samuelson (2011) from the surface to 3.3×10^{-7} bar, corresponding to an altitude range of 0–600 km (Fig. 3). Spectroscopic information for the gas rotational lines in the far-infrared range was extracted from the HITRAN 2004 database (Rothman et al., 2005). For CH_4 we have adopted the revised mole fraction of 1.48% in the stratosphere (Niemann et al., 2010) acquired by the Gas Chromatograph Mass Spectrometer (GCMS) on the Huygens probe during in its descent to Titan's surface. In the stratosphere for H_2 we assumed a uniform volume mixing ratio of 0.1% (Courtin et al., 2008). The geometry of the observations was also included in the computations.

An accurate model of the instrumental FOV is required to successfully reproduce CIRS spectra and measure water abundance. The FP1 FOV is circular and has a sensitivity with a quasi-exponential decrease from the center to the edge and a FWHM of 2.4 mrad. For on-disk spectra the homogeneity of the field of view usually permits simple modeling with a single ray calculated for the detector center. For limb spectra, we have to take into account the rapid decrease in atmospheric density with height and the variations of temperature and gas volume mixing ratio profile with altitude. In such cases, the FOV is not assumed to be uniform and a multiple ray model is required to fit the data. We modeled the FOV using the minimum number of rays for which the synthetic spectrum and the water retrieval computation results became stable; this corresponds to nine rays with a step in altitude of 25 km. We also recomputed some of the results using 39 rays (step of 5 km) in order to show a smoother limb contribution function. The spectral radiance measured by the FP1 detector is modeled by a convolution of the emerging radiance at each point in the FOV (as described in Nixon et al. (2009) and in Teanby and Irwin (2007)), weighted by a response function for CIRS FP1 detector. This beam profile was determined for CIRS FP1 (Flasar et al., 2004) using Jupiter as a point source. As 95% of the integrated response is contained in a radius of 1.95 mrad from the FOV center, the detector observes a maximum altitude range of about 70 km.

Independent line-by-line calculations to simulate the same on-disk FP1 selections were also made using the Atmospheric Radiative Transfer (ART) code that has recently been applied to CIRS data in Coustenis et al. (2010, 2007). The code uses the most recent aerosol extinction dependence inferred from Vinatier et al. (2012) and temperature profiles derived by fitting the ν_4 methane band at 1304 cm^{-1} in FP4 averages taken at similar conditions as the FP1 spectra. The spectroscopic parameters for all the observed molecules and isotopes are from GEISA 2009 (Jacquinet-Husson et al.,

2011) and HITRAN 2008 (Rothman et al., 2009). The results from these two different codes are very similar and their difference is smaller than the error bars on the data.

In Fig. 1a the on-disk and two limb observation averages are shown together with their fits. Fig. 1b shows only the spectral range used for the water line analysis.

4. Results

We have retrieved the water vapor abundance from both on-disk and limb data assuming different vertical profiles. These were a constant water mixing ratio profile and three vertically increasing profiles from recent photochemical models: (a) Hörst et al. (2008), (b) Wilson and Atreya (2004) and (c) Lara et al. (1996). The latter profile was adopted in Coustenis et al. (1998) for the first water detection on Titan by ISO. The constant mixing ratio profile (*a priori* assumed to be 0.1 ppb) was decreased to follow the saturation vapor pressure curve in the lower stratosphere below the altitude where the relative humidity reaches 100% (see Fig. 3). Using the saturation vapor pressure equation of water over ice of Murphy and Koop (2005) and assuming the temperature profile retrieved at 15°N we find a condensation altitude of 93 km. For temperature profiles retrieved at 15°S and 58°S we find respectively condensation altitudes of 97 km and 104 km. We have also computed the contribution functions – normalized inversion kernels – showing the sensitivity of each atmospheric layer to a variation of the H_2O mixing ratio. These contribution functions were computed for each profile and for all of the most intense water lines in order to provide an altitude range of validity of the retrieved values (Figs. 2 and 4). Fig. 2 shows the contribution functions for on-disk observations computed at four different wave numbers; at 254 cm^{-1} (one of the two lines used for the ISO water retrieval) the upper shoulder of the contribution function is wider and sensitive to higher altitudes compared to the other wave numbers used for the water retrieval in this work. In our case the fit of the 254 cm^{-1} line improves when using a profile increasing with altitude rather than a constant profile. In Fig. 4 we show only the contribution functions computed at wavenumber 202.75 cm^{-1}, where the most intense water line in the CIRS spectrum occurs (discounting the line at 150.5 cm^{-1} that is unusable due to an instrumental interference).

For water retrievals obtained using a scaled constant water profile we show the retrieved mixing ratio values at the altitude where the water contribution function peaks for the assumed profile (Table 1). For the vertical error we use the Full Width Half Maximum (FWHM) of the contribution function for the corresponding water profile. We also retrieve a scaling factor to the water profile from each of the photochemical models considered in this work (Table 1).

4.1. On-disk water retrieval

To measure the water abundance from the on-disk average (0–30°N) data we first use a constant water profile. We retrieve a volume mixing ratio of 0.14 ± 0.05 ppb at 97 km (FWHM 93–130 km). This value corresponds to a surface-normalized H_2O total column density of $3.7 \pm 1.3 \times 10^{14}$ molecules/cm^2.

The largest source of error for the on-disk observations is due to the fact that the maximum of the contribution function occurs in the region where the water abundance is rapidly changing due to condensation. Other sources of error include small variations of the temperature profile in the stratosphere, random noise from the detectors, and a small dependence in altitude sensitivity with wavenumber.

We also fit the water lines for the three other water vertical distribution profiles (Lara et al., 1996; Wilson and Atreya, 2004; Hörst et al., 2008) and obtained the necessary scale factors to fit the data, which are shown in Table 1. These values, ranging between 0.11 and 0.63 times the considered profiles, show the retrieved water mole fraction to be less than predicted from these previous models.

We have analyzed two additional latitudinal bins from 45°S to 10°S and from 80°S to 45°S, centered on the latitudes corresponding to the temperature profiles previously retrieved from CIRS at 15°S and 58°S respectively (Anderson and Samuelson, 2011). See Fig. 3. The observed water mixing ratio indicates the absence of any significant latitudinal variations within the error bars in these

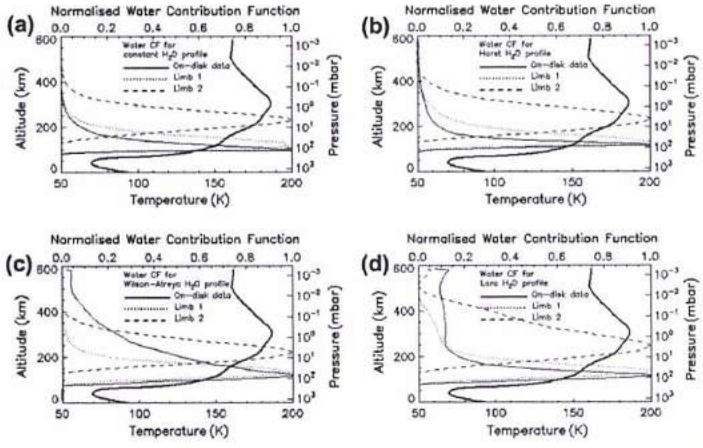

Fig. 4. Contribution functions of water vapor line emission and temperature profile for 15°N. In (a–d) we show the contribution functions computed at 202.75 cm^{-1} for different water profile models: (a) a constant water vertical profile; (b) profile from model D in Hörst et al. (2008); (c) profile from Wilson and Atreya (2004) and (d) profile from Lara et al. (1996).

Table 1
Water vapor abundance results.

Water vapor retrieved mole fractions	On-disk average (0–30°)N	Limb retrieval 1	Limb retrieval 2
Constant VMR profile	(0.14 ± 0.05) ppb at 97^{+33}_{4} km	(0.13 ± 0.04) ppb at 115^{+50}_{29} km	(0.45 ± 0.15) ppb at 230^{+45}_{40} km
Scaling factor to H_2O profile from Hörst (model D)	0.18 ± 0.05 at 118^{+20}_{12} km	0.14 ± 0.05 at 129^{+45}_{17} km	0.23 ± 0.07 at 232^{+67}_{50} km
Scaling factor to H_2O profile from Wilson–Atreya	0.14 ± 0.05 at 118^{+85}_{22} km	0.13 ± 0.05 at 129^{+66}_{24} km	0.18 ± 0.08 at 222^{+62}_{53} km
Scaling factor to H_2O profile from Lara	0.48 ± 0.07 at 115^{+20}_{30} km	0.63 ± 0.07 at 133^{+42}_{27} km	0.45 ± 0.08 at 247^{+33}_{100} km

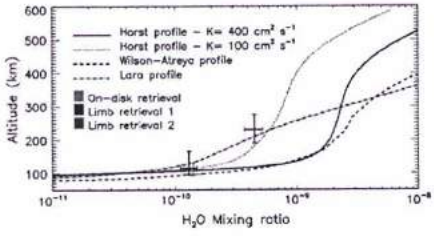

Fig. 5. Water vapor mole fraction retrieved from CIRS on-disk and two limb observations assuming a water profile constant with altitude over the condensation level. Water profiles from three photochemistry models are also shown for comparison. The Hörst et al. (2008) water vapor profile was derived assuming two different eddy diffusion coefficients – 100 $cm^2 s^{-1}$ and 400 $cm^2 s^{-1}$ (the second being the one recommended in their model; dotted curve plus solid curve). Also the profiles in Wilson and Atreya (2004; dashed curve) and in Lara et al. (1996; dot-dash curve).

latitude ranges. It should be stressed that in this work we did not analyze the water stratospheric content at high northern latitudes that were experiencing winter during this time period. To model spectra at these latitudes for a large average is particularly complex since the stratospheric temperature was changing quickly with latitude. In addition the temperature profiles for high northern latitudes are not yet available for the lower stratospheric region sensed by the CIRS water lines.

The results obtained simultaneously for on-disk data using the independent line-by-line ART code simulations of the same FP1 selections confirm the retrieved water vapor value reported above within the error bars.

4.2. Limb water retrieval

The measurement of water vapor obtained by modeling the limb 1 spectrum under the assumption of a constant mixing ratio profile is equal to 0.13 ± 0.04 ppb. According to the position of the peak of the corresponding contribution function, the radiance mostly originates from a region centered at 115 km (FWHM 95–165 km). Modeling the limb 2 spectrum we retrieved a water mixing ratio using a constant water profile of 0.45 ± 0.15 ppb at an altitude of 230 km (FWHM 190–275 km). These values indicate an increase of the water mole fraction with altitude in the stratosphere from 115 km to 230 km of about three times.

The scaling factors to the model water profiles obtained from the two types of limb retrievals are shown in Table 1 and again illustrate the smaller amount of stratospheric water vapor detected by CIRS with respect to the ones predicted by the models considered in this study.

5. Conclusions

In this work we modeled CIRS data using a constant-with-height water vapor profile and assigned the retrieved mixing ratio to the altitude where the contribution function peaks.

By combining on-disk and limb observations we are able to constrain the vertical profile of water in the stratosphere from 12 mbar to 10^{-3} mbar, corresponding to altitudes between 93 and 280 km (considering the widths of the contribution functions).

In Fig. 5 we compare our water vapor retrieved values with the models of (Lara et al., 1996; Wilson and Atreya, 2004; Hörst et al., 2008).

The measurement of the stratospheric vertical profile of water adds useful constraints to the photochemical models of Titan's atmosphere. Qualitatively, the increase of the water mixing ratio with altitude is in agreement with an external source of oxygen and a lower altitude sink due to condensation. However, quantitatively, our retrieved abundance seems to be less (from ~0.1 to ~0.6) than predicted from the models considered in this work (see Table 1). We also observe that since the scaling factors to the photochemical models (a)–(c) in Table 1 are slightly different for the two limb altitudes, it implies that these models might have a slope for H_2O not quite consistent with CIRS data. However, due to the rapid variation of the water vapor mole fraction with altitude in the atmospheric region where water freezes, and where CIRS is actually observing (on-disk and limb 1 spectra), we should be cautious in assigning a slope to the water profile.

Coustenis et al. (1998) fitted the ISO data with a scaling factor to the Lara et al. (1996) water profile of $0.4^{+0.3}_{-0.2}$. We fitted the CIRS data assuming the same profile multiplied by a scaling factor of 0.48 ± 0.07 (corresponding to a water column density of $3.8 \pm 1.0 \times 10^{14}$ molecules cm^{-2}). This result agrees with the scaling factor from the ISO analysis although this agreement may be fortuitous because most of the ISO emission originates from above 300 km, with the contribution functions peaking around 400 km (Fig. 3 of Coustenis et al. (1998)). Since the beam size of ISO was much larger than Titan there is a strong emission from the limb occurring at high altitudes where 0.4 times the Lara et al. (1996) profile is used. Due to its higher spatial resolution, the contribution functions for the CIRS nadir selection using the Lara et al. (1996) profile cover the range 95–145 km (at half maximum).

ISO also retrieved a water vapor abundance of 0.4 ppb assuming a constant mole fraction above the condensation level (Coustenis et al., 1998); we assign the same relative error bars as those derived by ISO for the scaled Lara et al. (1996) profile: +0.3 and −0.2. From CIRS on-disk observations we retrieved a volume mixing ratio of 0.14 ± 0.05 ppb around 97 km for latitudes 0–30°N. Our retrieval is only marginally consistent with the ISO determination of $0.4^{+0.3}_{-0.2}$ ppb above the water vapor condensation altitude. However it is necessary to make the assumption that the ISO results pertain to the same condensation altitude that we retrieve because unfortunately it is not reported in the ISO paper.

We now discuss how our retrieved water abundances compare with current models of oxygen photochemistry on Titan. The retrieved scaling factors are all less than one, implying that there are still uncertainties in our understanding of oxygen processes on Titan.

In photochemical models of Titan prior to 2000 (e.g. Lara et al., 1996), in order to allow atmospheric production of CO, it was postulated that CO could be produced through a chemical reaction between OH (available from H_2O influx into the upper atmosphere)

and CH_3. However, it was emphasized by Wong et al. (2002) that this reaction does not produce CO as previously assumed but instead it produces H_2O (Pereira et al., 1997).

Hence an influx of H_2O or OH does not produce any significant abundance of CO and therefore CO_2 can be produced by an H_2O influx only with CO already present ($OH + CO \rightarrow CO_2 + H$). For this reason these models were unable to reproduce the observed CO abundance and were substituted by other models that suggest the existence of primordial CO in the atmosphere (Wilson and Atreya, 2004), or instead CO produced in the atmosphere using an external influx of O^+ rather than H_2O or OH (Hörst et al., 2008).

In the pre-Cassini model of Wilson and Atreya (2004) water is photolyzed to OH, which combines with CO to form CO_2 and other complex species. In this model, CO is assumed to be primordial on Titan and the water abundance profile derives from the amount necessary to form the observed CO_2. This assumption was challenged by the Hörst et al. (2008) model, in which oxygen species are assumed to arrive from outside the Moon and form carbon monoxide as well as carbon dioxide in the atmosphere. The values of the input fluxes of O and OH were adjusted to reproduce the observed abundances of CO and CO_2. In the Hörst et al. (2008) model water profiles were produced for six different values (from $K_0 = 100\ cm^2\ s^{-1}$ to $K_0 = 1000\ cm^2\ s^{-1}$) of the eddy coefficient in the lower atmosphere, since the stratospheric abundances of photochemically produced species are highly dependent on this parameter. As shown in Fig. 5, the water abundance retrieved in our study is best fit by the water profile with the lowest eddy diffusion coefficient value considered in their model ($K_0 = 100\ cm^2\ s^{-1}$). This is lower than the value ($K_0 = 400\ cm^2\ s^{-1}$) they identified as best reproducing CIRS observations of hydrocarbon species and adopted in this work for comparison with our retrievals. However our results show that even the Hörst model with $K_0 = 100\ cm^2\ s^{-1}$ still has excessive water at the altitudes of our measurements.

Therefore, our work clearly points towards further refinement of oxygen chemistry in photochemical models of Titan's atmosphere.

Acknowledgments

Valeria Cottini is supported by the NASA Postdoctoral Program. Thanks to S. Hörst, E. Wilson and S. Atreya for providing their photochemical water profiles for comparison, and to Paul Romani for water chemistry discussions. The US-based authors were funded by the NASA Cassini Mission during the period in which this work was performed. N. Teanby was supported by the Leverhulme Trust and the UK Science and Technology Facilities Council.

References

Anderson, C.M., Samuelson, R.E., 2011. Titan's aerosol and stratospheric ice opacities between 18 and 500 μm: Vertical and spectral characteristics from Cassini CIRS. Icarus 212, 762–778.

Bjoraker, G., Achterberg, R., Anderson, C., Samuelson, R., Carlson, R., Jennings, D., 2008. American Astronomical Society. DPS Meeting #40, #31.12, Bulletin of the AAS, 40, 448.

Borysow, A., 1991. Modelling of collision-induced infrared-absorption spectra of H_2–H_2 pairs in the fundamental band at temperatures from 20 K to 300 K. Icarus 92 (2), 273–279.

Borysow, A., Frommhold, L., 1986a. Theoretical collision-induced rototranslational absorption spectra for modeling Titan's atmosphere—H_2–N_2 pairs. Astrophys. J. 303, 495–510.

Borysow, A., Frommhold, L., 1986b. Theoretical collision-induced rototranslational absorption spectra for the outer planets—H_2–CH_4 pairs. Astrophys. J. 304, 849–865.

Borysow, A., Frommhold, L., 1986c. Collision-induced rototranslational absorption spectra of N_2–N_2 pairs for temperatures from 50 to 300 K. Astrophys. J. 311, 1043–1057.

Borysow, A., Frommhold, L., 1987. Collision-induced rototranslational absorption spectra of CH_4–CH_4 pairs at temperatures from 50 to 300 K. Astrophys. J. 318, 940–943.

Borysow, A., Tang, C., 1993. Far infrared CIA spectra of N_2–CH_4 pairs for modelling of Titan's atmosphere. Icarus 105, 175–183.

Cassidy, T.A., Johnson, R.E., 2010. Collisional spreading of Enceladus' neutral cloud. Icarus 209 (2), 696–703.

Cottini, V. et al., 2012. Spatial and temporal variations in Titan's surf ace temperatures from Cassini CIRS observations. Planet. Space Sci. 60, 62–71.

Courtin, R.D., Sim, C., Kim, S., Gautier, D., Jennings, D.E., 2008. Latitudinal variations of tropospheric H_2 on Titan from the Cassini CIRS investigation. Bull. Am. Astron. Soc. 40, 446.

Coustenis, A. et al., 1998. Evidence for water vapor in Titan's atmosphere from ISO/SWS data. Astron. Astrophys. 336, L85–L89.

Coustenis, A. et al., 2007. The composition of Titan's stratosphere from Cassini/CIRS mid-infrared spectra. Icarus 189, 35–62.

Coustenis, A. et al., 2010. Titan trace gaseous composition from CIRS at the end of the Cassini–Huygens prime mission. Icarus 207, 461–476.

Cui, J., Yelle, R.V., Vuitton, V., Waite, J.H., Kasprzak, W.T., Niemann, H.B., Gell, D., Borggren, N., Magee, B., Müller-Wodarg, I.C.F, 2009. Analysis of Titan's neutral upper atmosphere from Cassini ion neutral mass spectrometer measurements. Icarus 200, 581–615.

de Kok, R. et al., 2007a. Oxygen compounds in Titan's stratosphere as observed by Cassini CIRS. Icarus 186, 354–363.

de Kok, R., Irwin, P.G.J., Teanby, N.A., Nixon, C.A., Jennings, D.E., Fletcher, L., Howett, C., Calcutt, S.B., Bowles, N.E., Flasar, F.M., Taylor, F.W., 2007b. Characteristics of Titan's stratospheric aerosols and condensate clouds from Cassini CIRS far-infrared spectra. Icarus 191 (1), 223–235.

de Kok, R., Irwin, P.G.J., Teanby, N.A., 2010. Far-infrared opacity sources in Titan's troposphere reconsidered. Icarus 209 (2), 854–857.

Dougherty, M.K. et al., 2006. Identification of a Dynamic Atmosphere at Enceladus with the Cassini Magnetometer. Science 311, 1406–1409.

English, M.A., Lara, L.M., Lorenz, R.D., Ratcliff, P.R., Rodrigo, R., 1996. Ablation and chemistry of meteoric materials in the atmosphere of Titan. Adv. Space Res. 17, 157–160.

Flasar, F.M. et al., 2004. Exploring the Saturn system in the thermal infrared: The Composite Infrared Spectrometer. Space Sci. Rev. 115, 169–297.

Fleshman, B.L., Delamere, P.A., Bagenal, F., Cassidy, T., 2012. The roles of charge exchange and dissociation in spreading Saturn's neutral clouds. J. Geophys. Res., in press. http://dx.doi.org/10.1029/2011JE003996.

Gurwell, Mark A., 2004. Submillimeter Observations of Titan: Global Measures of Stratospheric Temperature, CO, HCN, HC_3N, and the Isotopic Ratios $^{12}C/^{13}C$ and $^{14}N/^{15}N$. Astrophys. J. 616, L7–L10.

Hartle, R.E. et al., 2006a. Preliminary interpretation of Titan plasma interaction as observed by the Cassini Plasma Spectrometer: Comparisons with Voyager 1. Geophys. Res. Lett., 33.

Hartle, R.E. et al., 2006b. Initial interpretation of Titan plasma interaction as observed by the Cassini Plasma Spectrometer: Comparisons with Voyager 1. Planet. Space Sci. 54, 1211–1224.

Hartogh, P. et al., 2011. Direct detection of the Enceladus water torus with Herschel. Astron. Astrophys. 532 (Article ID L2).

Hidayat, T. et al., 1998. Millimeter and submillimeter heterodyne observations of Titan: The vertical profile of carbon monoxide in its stratosphere. Icarus 133, 109–133.

Hörst, S.M., Vuitton, V., Yelle, R.V., 2008. Origin of oxygen species in Titan's atmosphere. J. Geophys. Res. 113, E10.

Irwin, P.G.J. et al., 2008. The NEMESIS planetary atmosphere radiative transfer and retrieval tool. J. Quant. Spectrosc. Radiat. Trans. 109, 1136–1150.

Jacquinet-Husson, N. et al., 2011. The 2009 edition of the GEISA spectroscopic database. J. Quant. Spectrosc. Radiat. Trans. 112, 2395–2445.

Lacis, A.A., Oinas, V., 1991. A description of the correlated k distributed method for modeling nongray gaseous absorption, thermal emission, and multiple scattering in vertically inhomogeneous atmospheres. J. Geophys. Res. 96, 9027–9063.

Lara, L.M., Lellouch, F., Lopez-Moreno, J.J., Rodrigo, R., 1996. Vertical distribution of Titan's atmospheric neutral constituents. J. Geophys. Res. 101 (23), 261.

Lutz, B.L., de Bergh, C., Owen, T., 1983. Titan – Discovery of carbon monoxide in its atmosphere. Science 220, 1374–1375.

Melin, H., Shemansky, D.E., Liu, X., 2009. The distribution of atomic hydrogen and oxygen in the magnetosphere of Saturn. Planet. Space Sci. 57 (14–15), 1743–1753.

Murphy, D.M., Koop, T., 2005. Review of the vapour pressures of ice and supercooled water for atmospheric applications. Q. J. R. Meteorol. Soc. 131, 1539–1565.

Niemann, H.B. et al., 2010. The composition of Titan's lower atmosphere and simple surface volatiles as measured by the Cassini–Huygens probe gas chromatograph mass spectrometer experiment. J. Geophys. Res. 115, E12006.

Nixon, C.A. et al., 2009. Infrared limb sounding of Titan with the Cassini Composite Infrared Spectrometer: Effects of the mid-IR detector spatial responses. Appl. Opt. 48, 1912–1925.

Pereira, R.A., Baulch, D.L., Pilling, M.J., Robertson, S.H., Zeng, G., 1997. Temperature and pressure dependence of the multichannel rate coefficients for the CH_3 + OH system. J. Phys. Chem. A 101, 9681–9693.

Rodgers, C.D., 2000. Inverse Methods for Atmospheric Sounding: Theory and Practice. World Scientific, Singapore.

Rothman, L.S. et al., 2005. The HITRAN 2004 molecular spectroscopic database. J. Quant. Spectrosc. Radiat. Trans. 96, 139–204.

Rothman, L.S. et al., 2009. The HITRAN 2008 molecular spectroscopic database. J. Quant. Spectrosc. Radiat. Trans. 110, 533–572.

Samuelson, R.E. et al., 1983. CO_2 on Titan. J. Geophys. Res. 88, 8709–8715.

Teanby, N.A., Irwin, P.G.J., 2007. Quantifying the effect of finite field-of-view size on radiative transfer calculations of Titan's limb spectra measured by Cassini–CIRS. Astrophys. Space Sci. 310, 293–305.

Teanby, N.A. et al., 2009. Titan's stratospheric C_2N_2, C_3H_4 and C_4H_2 abundances from Cassini/CIRS far-infrared spectra. Icarus 202, 620–631.
Teanby, N.A., Irwin, P.G.J., de Kok, R., Nixon, C.A., 2010. Seasonal changes in Titan's polar trace gas abundance observed by cassini. The Astrophysical Journal Letters 724 (2010), L84.
Tomasko, M.G. et al., 2008. A model of Titan's aerosols based on measurements made inside the atmosphere. Planet. Space Sci. 56, 669–707.
Vinatier, S., Rannou, P., Anderson, C.M., Bézard, B., de Kok, R., Samuelson, R.E., 2012. Optical constants of Titan's stratospheric aerosols in the 70–1500 cm^{-1} spectral range constrained by Cassini/CIRS observations. Icarus 219, 5–12.
Wilson, E.H., Atreya, S.K., 2004. Current state of modeling the photochemistry of Titan's mutually dependent atmosphere and ionosphere. J. Geophys. Res. 109, E6.
Wong, A., Morgan, C.G., Yung, Y.L., Owen, T., 2002. Evolution of CO on Titan. Icarus 155 (2), 382–392.

Appendix D1

A despeckle filter for the Cassini synthetic aperture radar images of Titan's surface

Journal article published in *Planetary Space & Science*,
Volume 61, pp. 108-113.

Planetary and Space Science 61 (2012) 108–113

Contents lists available at ScienceDirect

Planetary and Space Science

journal homepage: www.elsevier.com/locate/pss

A despeckle filter for the Cassini synthetic aperture radar images of Titan's surface

Emmanuel Bratsolis [a,*], Georgios Bampasidis [a,b], Anezina Solomonidou [b,c], Athena Coustenis [b]

[a] Faculty of Physics, University of Athens, Athens GR-15784, Greece
[b] LESIA, Observatoire de Paris - Meudon, 92195 Meudon Cedex, France
[c] Faculty of Geology and Geoenvironment, University of Athens, Athens GR-15784, Greece

ARTICLE INFO

Article history:
Received 24 December 2010
Received in revised form
30 March 2011
Accepted 7 April 2011
Available online 18 May 2011

Keywords:
Titan
Lakes
Radar imaging
Filtering
Segmentation

ABSTRACT

Cassini synthetic aperture radar (SAR) images of Titan, the largest satellite of Saturn, reveal surface features with shapes ranging from quasi-circular to more complex ones, interpreted as liquid hydrocarbon deposits assembled in the form of lakes or seas. One of the major problems hampering the derivation of meaningful texture information from SAR imagery is the speckle noise. It overlays real structures and causes gray value variations even in homogeneous parts of the image. We propose a filtering technique which can be applied to obtain restored SAR images. Our technique is based on probabilistic methods and regards an image as a random element drawn from a prespecified set of possible images. The despeckle filter can be used as an intermediate step for the extraction of regions of interest, corresponding to structured units in a given area or distinct objects of interest, such as lake-like features on Titan. This tool can therefore be used, among other, to study seasonal surficial changes of Titan's polar regions. In this study we also present a segmentation technique that allows us to separate the lakes from the local background.

1. Introduction

Cassini–Huygens, the extremely successful NASA/ESA joint mission to the Saturnian system, has already accomplished six years of extended investigation. Titan being one of the most intriguing objects in the Solar system, hosting an Earth-like environment, is one of the main targets of this mission. Titan's landscape has been observed by multiple flybys that examine the surface expressions through Cassini's infrared and radar instrumentation.

Cassini's RADAR instrument operates in the Ku-band (13.78 GHz, $\lambda = 2.17$ cm), at both high and low resolution, viewing Titan's surface in four modes: imaging, altimetry, scatterometry and radiometry (Elachi et al., 2004).

The SAR mode is used at altitudes lower than 4000 km, resulting in spatial resolution ranging from about 350 m to more than 1 km. Images are acquired either left or right of nadir using 1–5 looks while a swath, 120–450 km in width, is created from five antenna beams. SAR coverage is dependent on spacecraft range and orbital geometry (Elachi et al., 2004) and radar backscatter variations in SAR images can be interpreted in terms of variations of surface geometry (incidence angle, azimuth angle, and the polarization vector), near-surface roughness, or near-surface dielectric properties.

The images obtained using SAR revealed that Titan hosts a very complex surface formed with features such as lakes, mountains, fluvial river networks, possible volcanic-like features and dunes (Jaumann et al., 2008; Lopes et al., 2010 and references therein) which resemble Earth-like geomorphological structures (Coustenis and Hirtzig, 2009). However, both the material and the environmental conditions shaping their respective surfaces are considerably different. Despite these differences, the exogenic mechanisms forming the surficial expressions may be similar. Indeed, one dominating terrestrial surface-affecting procedure is the water cycle while on Titan an active methane cycle is at play (Atreya et al., 2006). The impact of the endogenic processes in the surface construction on Titan is still under investigation through geophysical interior models (e.g. Tobie et al., 2005). Radar images provided evidence of drainage and branching channel networks with subdivided channels (Perron et al., 2006; Soderblom et al., 2007; Lorenz et al., 2008; Burr et al., 2009), as well as distinct fluvial erosional patterns (Jaumann et al., 2008) that indicate dynamic and evolved surface processes. Additionally, SAR imagery observed lake-like features in several swaths (Stofan et al., 2007; Turtle et al., 2009; Hayes et al., 2010; Wye et al., 2010).

Other features, identified by radar, are the potentially volcanic in origin structures (Elachi et al., 2005; Lopes et al., 2007a; Soderblom et al., 2009; Nelson et al., 2009; Wall et al., 2009), the impact craters

* Corresponding author. Tel.: +30 2105813069.
E-mail address: ebrats@phys.uoa.gr (E. Bratsolis).

0032-0633/$ - see front matter © 2011 Published by Elsevier Ltd.
doi:10.1016/j.pss.2011.04.003

(Wood et al., 2010), the mountain chains (e.g. Radebaugh et al., 2007) and the linear dunes (Elachi et al., 2006; Radebaugh et al., 2008).

2. Lacustine features of Titan's surface

The thermodynamical conditions dominating Titan as well as its chemical profile allow the hydrocarbon liquid phase to exist on its surface (Kouvaris and Flasar, 1991; Thompson et al., 1992; Atreya et al., 2006). Indeed, the temperature of its icy surface has been measured in situ (10.34°S, 192.34°W) (Tomasko et al., 2005) by Huygens at 93.7 K (Fulchignoni et al., 2005), while the Cassini composite infrared spectrometer (CIRS) found by remote observations an average temperature of 92 K between 2004 and 2008 (Jennings et al., 2009).

Cassini RADAR instrumentation confirmed the presence of lake-like features on the surface of Titan. Several models have suggested organic precipitation on Titan (Toon et al., 1988; Lorenz, 1993; Graves et al., 2008) either violently through torrential storms (Hueso and Sanchez-Lavega, 2006) or smoothly through drizzle at the lower atmosphere (Tokano et al., 2006) and rainfalls originated from occasional short-lived clouds (Griffith et al., 2000, 2005; Lorenz et al., 2005), such phenomena have not been recorded yet.

The first recording of organic liquid pools was accomplished during the T16 flyby at the northern polar locations, where more than 75 lake candidate features were identified (Sotin, 2007; Stofan et al., 2007). In 2008, the Cassini/RADAR swaths counted in both north and south polar regions, above 50°N and 50°S, respectively, more than 655 lake-like features (Hayes et al., 2008). SAR imaging shows lake-like features separated into three classes: dark lakes, granular lakes, and bright lakes (Hayes et al., 2008). Dark lakes are interpreted as liquid filled, while bright lakes are interpreted as empty basins and granular lakes are inferred as transitional between dark and bright lake features. From a geomorphological aspect the lakes on Titan span over the range of observed morphologies on Earth (Stofan et al., 2007; Mitri et al., 2007; Hayes et al., 2008). They are rimmed features, from circular to irregular and some with distinct edges, steep margins and smooth surfaces (Stofan et al., 2007) and they show very low microwave backscatter. Some of them are surrounded by a drainage network of dark channels, which may supply them with liquid (Stofan et al., 2007), while some are not.

It is suggested that this liquid is a methane/ethane mixture, with smaller concentrations of nitrogen and higher order hydrocarbons/nitriles (Lunine et al., 1983; Mitri et al., 2007; Brown et al., 2008; Raulin, 2008).

The lakes' radiometric brightnesses which appear to be warmer than the surrounding region (Janssen et al., 2009) are consistent with the high emissivity expected for a smooth surface with the real part of the low dielectric constant between 1.7 and 1.9 of liquid ethane–methane solutions (Lopes et al., 2007b) with most possible value the 1.9. However, the imaginary part is still under investigation (Notarnicola et al., 2009).

This study provides a qualitative method of recognition of lake-like features from Cassini SAR images. The intended goal is to label regions in an image into three classes (dark lakes, granular lakes and the local background). First, a filtering technique is applied to obtain the restored image. Then, a method of supervised segmentation is used. The segmentation method based on the minimum Euclidean distance is used here.

3. Filtering

Strip mapping SAR consists of a large antenna which is synthesized from many small antennas and remains fixed with respect to the radar platform, so that the large antenna illuminates a strip of the ground. This technique is used to improve the azimuthal resolution. As the platform moves, a sequence of closely spaced pulses is emitted and the returned waveforms are recorded. An image is computed after the coherent sum of reflected monochromatic microwaves. The image is distorted by a strong granulation, called speckle. Speckle noise exists in all types of coherent imaging systems and its presence reduces the resolution of the image and the detectability of the target. Speckle noise is not only signal dependent but is also spatially correlated and reduces the effectiveness of image reduction. The Cassini RADAR measures the normalized backscatter cross-section (σ_0) of Titan's surface (Ulaby et al., 1982). The SAR textures are generally affected by multiplicative speckle noise. In order to reduce the speckle noise, the multilook technique, based on incoherently averaging the independent neighboring pixels, is used to estimate the characteristics of the same ground area.

The statistical characteristics of multilook data depart considerably from those of single-look data. Multilook data tend to mix some physical and statistical properties of the terrain. The terrain appears more homogeneous and the multilook averaging will tend to be close to the Gaussian statistics (Chitroub et al., 2002).

Speckle noise overlays real structures and causes gray value variations even in homogeneous parts of the image and also makes automatic segmentation of such images difficult. We propose here a filtering technique that can be applied to obtain the SAR restored images. After filtering the structured parts of the image can be much better separated. The total sum preserving regularization (TSPR) filter, is based on a membrane model Markov random field approximation optimized by a synchronous local iterative method (Bratsolis and Sigelle, 2003). The final form of despeckling gives a sum-preserving regularization for the pixel values of the image.

Image formation is the process of computing (or refining) an image both from raw sensor data that is related to that image and from prior information about that image. Information about the image is contained in the raw sensor data, and the task of image formation is to extract this information so as to compute the image.

Image space is the set $\mathcal{F}$ of model images that represent the true, underlying physical distributions that are measured by the sensors.

Working in a probabilistic imaging problem, an a priori knowledge about an image is most naturally incorporated through the use of a prior probability distribution (or prior) $P(f)$ on the image space. Our objective here is to reconstruct the original (or true) image from its degraded version.

A random field is an appropriate model for image values. Random variables characterized by conditional priors that account for local interactions are often used as natural and convenient priors in imaging problems. These priors are placed directly on the image space. However, the fundamental probability distribution on the field is the joint probability distribution $P(f)$, and this is difficult or impossible to specify directly. One needs to verify that the chosen specification of conditional distributions is sufficient and consistent in the sense that a unique joint probability distribution corresponds to this set of conditional probability distributions.

Assume that an image is formed on a finite rectangular lattice when the sensors of this lattice select one scene from $\mathcal{F}$. Let us note the finite lattice of sites as $S=\{s\}_{s=1..N}$ with $S\subset Z^2$. Each site $s\in S$ has a set of neighbors r noted $\mathcal{N}_s$. If $s=(i,j)$ four-connectivity is assumed in the following: $\mathcal{N}_s=\{(i-1,j);(i+1,j);(i,j-1);(i,j+1)\}$.

A random process $\{f_s|s\in S\}$ with f_s random variables following the joint probability function $P(f)$ is a "random field". In the special case where $P(f_s|\{f_r\neq s\})=P(f_s|\{f_r\}_{r\in\mathcal{N}_s})$ the random field is

called a "Markov random field" (MRF). By the Hammersley–Clifford theorem MRFs and Gibbs random fields on a finite lattice are equivalent under the positivity condition (Besag, 1974).

Let g be the degraded observed image and f the restored image. The general problem is now to estimate f from a set of input data g.

The Bayes theorem allows us to obtain the a posteriori probability for the field f given the data g:

$$P(f|g)=\frac{P(g|f)P(f)}{P(g)} \tag{1}$$

where $P(f)$ is the a priori probability for the field f, $P(g|f)$ is the conditional probability for the data g given f and $P(g)$ is the probability of g, which is independent of f.

Considering a multilook image, we assume for the conditional probability $P(g|f)$ a Gaussian distribution (Chitroub et al., 2002) and we have

$$P(g|f)=\frac{\exp-\left[\sum_s \frac{(f_s-g_s)^2}{2\sigma^2}\right]}{C_1} \tag{2}$$

where σ is the standard deviation of the Gaussian distribution and C_1 a normalization constant.

The probability $P(f)$ is given by

$$P(f)=\frac{\exp-\left[\beta\sum_{(r,s)}(f_s-f_r)^2\right]}{C_2} \tag{3}$$

where β is a smoothness factor, C_2 a normalization constant, and the sum runs on all pairs of neighboring sites. From (1) we obtain

$$P(f|g)=\frac{1}{Z}\exp-U(f) \tag{4}$$

where Z, also called the a posteriori partition function, is a normalization constant and $U(f)$ is the total a posteriori potential function, which is written as

$$U(f)=\sum_s \frac{(f_s-g_s)^2}{2\sigma^2}+\beta\sum_{(r,s)}(f_s-f_r)^2 \tag{5}$$

The related local conditional potential functions are given by

$$V_s(f)=\frac{(f_s-g_s)^2}{2\sigma^2}+\beta\sum_{r\in N_s}(f_s-f_r)^2 \tag{6}$$

The a posteriori usual maximum (MAP) estimate is assigned to the value f which maximizes (4), i.e. which minimizes the a posteriori energy $U(f)$ (Bratsolis and Sigelle, 2003). We accept as a fast method of optimization a synchronous minimization of the local potential energies which we named synchronous local iterative method.

Our final TSPR filter is an iterative filter which uses the equation given by

$$f^{(n+1)}=\lambda g+(1-\lambda)\mathcal{R}*f^{(n)} \quad \forall n\geq 1 \tag{7}$$

where $*$ is the 2-D convolution operation. Thus, at each step the current pixel value will depend in a regularizing manner on its neighboring ones, according to the magnitude of parameter λ. It is also obvious that positivity is preserved when $0\leq\lambda\leq 1$. $\mathcal{R}$ is a normalized matrix given by

$$\mathcal{R}=\begin{bmatrix} 0 & 0.25 & 0 \\ 0.25 & 0 & 0.25 \\ 0 & 0.25 & 0 \end{bmatrix}$$

According to the notation of our method, it is evident that $\sigma_0=g_s$ and $\langle\sigma_0\rangle=\langle g_s\rangle=\langle f_s\rangle$. The TSPR method preserves the mean values of local homogeneous regions and decreases the standard deviation up to six times (Bratsolis and Sigelle, 2003).

4. The segmentation method

The purpose of segmentation is to divide the image into specific regions that correspond to structural units in the scene or distinguish objects of interest. These regions are characterized by spatially connected, non-overlapping sets of pixels sharing common properties.

In general, image segmentation is a classification problem. A classification problem can be formalized as a pair $(\mathcal{O},\mathcal{C})$, where $\mathcal{O}$ denotes a set of objects and $\mathcal{C}$ a collection of disjoint subsets $\mathcal{C}_1,\ldots,\mathcal{C}_l$ that partitions $\mathcal{O}$. The problem is to determine the subset $\mathcal{C}_j\subset\mathcal{C}$ to which a given object $o\in\mathcal{O}$ belongs. The supervised method of minimum Euclidean distance uses the mean values (or vectors) of each member and calculates the Euclidean distance from each classified object to the nearest class segmenting the image into different regions of interest or different labels (Richards, 1999). In our case we choose three regions of interest: dark lakes (black label), granular lakes (dark gray label) and local background (light gray label). The TSPR filter can be used as an intermediate step before the extraction of the regions of interest.

As Euclidean distance here, we define the distance

$$d_e=\sqrt{(f_s-\mu_i)^2} \tag{8}$$

where μ_i with $i=1,\ldots,3$ presents the mean values ($\langle\sigma_0\rangle$) corresponding to three sampled regions of interest. The algorithm is applied for every site s and for every value f_s of the restored (filtered) image. The value μ_i which minimize the distance d_e gives the characteristic label (black, dark gray or light gray) to the segmented image of Fig. 4, where μ_1 corresponds to -20.27 db, μ_2 to -18.64 db and μ_3 to -13.78 db.

We begin our analysis with the Cassini SAR image (PIA08630, NASA/JPL) acquired during the T16 flyby on July 22, 2006, at high latitudes near the north pole. This image is centered near 80°N, 92°W. Our image has dimensions 750×3100 in pixel size and the pixel scale is set to 175.558 m per pixel ($\sim 256^{*}$), but the actual SAR resolution is around 350 m per pixel and the image has been subjected to some interpolation. Cassini SAR images across this region contain numerous very dark splotches with sharp-edged boundaries, which may be filled with hydrocarbon liquid.

After using the despeckling filter TSPR we apply the segmentation method. Figs. 1 and 2 illustrate the initial image derived form the Cassini SAR while Fig. 3 is the filtering result of the previous image. The despeckling TSPR filter is used to smooth out the multiplicative

Fig. 1. Initial image of lakes (PIA08630, NASA/JPL) after subtraction of negative σ_0.

Fig. 2. Initial image of lakes (PIA08630, NASA/JPL) after subtraction of negative σ_0 and subtraction of values greater than $\langle\sigma_0\rangle + 3\,std(\sigma_0)$.

Fig. 3. Filtered image.

Fig. 4. Image ratio between the initial (Fig. 2) and the despeckled (Fig. 3) image.

Table 1
Characteristics of the sampled regions of interest.

Regions of interest	Before filtering $\langle\sigma_0\rangle \pm std(\sigma_0)$ (db)	After filtering $\langle\sigma_0\rangle \pm std(\sigma_0)$ (db)
Region 1 (black)	-20.27 ± 0.44	-20.26 ± 0.13
Region 2 (dark gray)	-18.64 ± 2.03	-18.53 ± 0.69
Region 3 (light gray)	-13.78 ± 3.57	-13.19 ± 1.32

noise of SAR images without missing important textural details from the regions of interest. Consequently, Fig. 3 seems smoother than Fig. 2. Fig. 4 depicts the ratio between the initial and the despeckle image. In this figure the lakes' interior is presented smoother than the surrounding area. This can be explained as the dark lakes are not really speckled regions. From the initial data (and σ_0 in non-dimensional values) the samples of the region 2 (granular lake) and the region 3 (local background) we take a value for the ratio $std(\sigma_0)/\langle\sigma_0\rangle$ equal to 0.4 and for the region 1 (dark lakes) equal to 0.05 which means that the region 1 is flatter than we were waiting.

The characteristics of the sampled regions of interest are listed in Table 1.

We can see the segmentation results in Fig. 5, where the black area corresponds to the dark lakes, the dark gray to the granular lakes and the light gray to the local background.

5. Discussion

Titan is indeed an active planetary body and both endogenic and exogenic processes have most possibly left their marks on the surface. Hence, one should focus on the surface geomorphology in order to identify any local tectonic field and estimate the importance as well as influence of each forming mechanism.

The TSPR filter, in combination with the minimum Euclidean distance method of supervised segmentation, can be used to extract regions of interest on the surface of Titan, such as lakes or seas using Cassini SAR images. Such despeckle filter can be applied in studying other surface features on Titan like the drainage networks, the equatorial dunes and the impact craters, where different textures appear.

Our approach allows to isolate each distinct surface feature from its surroundings and to study their distribution through out the surface. Then, in combination with radiative transfer modeling using Cassini visual and infrared mapping spectrometer (VIMS) data, we can infer about the relation between surface composition and morphotectonic structures. When we determine in a more accurate way the shapes of several surface structures, we will be able to study their global distribution and perform effectively classifications.

Since the Cassini mission extended its operational duration, new swaths, overlapping the liquid areas, have shown that the lakes have been evolving during the past years. Recent studies, focused on lake Ontario, the largest lake of the southern hemisphere, showed a significant recession of its shoreline (Turtle et al., 2009; Hayes et al., 2010; Wall et al., 2010) and support the hypothesis that these liquid deposits are not stable structures but evolve with time by expanding in winter and shrinking in the summer (Sotin, 2007). Applying the segmentation method on the same area at various periods of time, we can identify possible enhancements or reductions of the liquid coverage of the region. In particular, the temporal variation of the dark spots can provide information on the evolution of the lake system and consequently help us to better understand the methane cycle on Titan and therefore the mechanisms linked with the lake surface features, their origin and fate, through a global temporal and spatial coverage.

The passage from qualitative to quantitative results, requires to apply the aforementioned method in the same regions of interest with the same observational characteristics at different time periods in order to measure the surface each time.

Using this temporal dataset will help us evaluate the volume variation through time and estimate the hydrocarbon loss rate,

Fig. 5. Segmented image after filtering.

a critical parameter for the global methane cycle (Atreya et al., 2006).

Cassini evolves in the Saturnian system since 2004 and will continue returning data until at least 2017 in the extended mission. Although Cassini SAR recordings have unveiled new characteristics of Titan's surface, more advanced instrumentation with higher resolution is necessary to give a full picture of this complex environment.

A new long-term mission to Titan which will perform efficient in situ experiments in order to study widely the nature and the dynamics of its environment would be required.

Several proposals have been studied to this end. Recently, the 2008 study of a flagship mission, Titan Saturn System Mission (TSSM), focused on Titan and Enceladus exploration (Reh et al., 2008; Coustenis et al., 2009). TSSM consists of an orbiter, a lake lander and a balloon (montgolfière) and aims to a complete investigation scrutinizing thoroughly the whole satellite from the exosphere to its interior. The montgolfière would contain advanced instrumentation such as the Titan radar sounder (> 150 MHz), which could perform a detailed surface investigation. In addition to topography, the radars on both the orbiter and the montgolfière would provide extended information regarding the lakes coverage. The proposed filtering and segmentation method in this paper would be a helpful tool in enhancing the return of the analysis of all SAR data acquired on Titan and other objects as well as in the exploitation of future missions to Titan.

Acknowledgments

The authors would like to gratefully acknowledge the assistance of Dr. Alexander Hayes in providing us with raw SAR Cassini data and with a thorough and constructive review of the manuscript and subsequent fruitful discussions. We are also grateful to another anonymous referee for helpful comments and suggestions.

A. Solomonidou is supported by the "HRACLEITOS II" project, co-financed by Greece and the European Union.

References

Atreya, S.K., Adams, E.Y., Niemann, H.B., Demick-Montelara, J.E., Owen, T.C., Fulchignoni, M., Ferri, F., Wilson, E.H., 2006. Titan's methane cycle. Planetary and Space Science 54, 1177–1187.

Besag, J., 1974. Spatial interaction and the statistical analysis of lattice systems (with discussion). Journal of the Royal Statistical Society Series B 36, 192–236.

Bratsolis, E., Sigelle, M., 2003. Fast SAR image restoration, segmentation and detection of high-reflectance regions. IEEE Transactions on Geoscience and Remote Sensing 41, 2890–2899.

Brown, R.H., Soderblom, L.A., Soderblom, J.M., Clark, R.N., Jaumann, R., Barnes, J.W., Sotin, C., Buratti, B., Baines, K.H., Nicholson, P.D., 2008. The identification of liquid ethane in Titan's Ontario Lacus. Nature 454, 607–610.

Burr, D.M., Jacobsen, R.E., Roth, D.L., Phillipis, C.B., Mitchell, K.L., Viola, D., 2009. Fluvial network analysis on Titan: evidence for subsurface structures and west-to-east wind flow, southwestern Xanadu. Geophysical Research Letters 36, L22203.

Chitroub, S., Houacine, A., Sansal, B., 2002. Statistical characterization and modeling of SAR images. Signal Processing 82, 69–92.

Coustenis, A., Hirtzig, M., 2009. Cassini–Huygens results on Titan's surface. Research in Astronomy and Astrophysics 9, 249–268.

Coustenis, A., Atreya, S., Balint, T., Brown, R., Dougherty, M., Ferri, F., Fulchignoni, M., Gautier, D., Gowen, R., Griffith, C., Gurvits, L., Jaumann, R., Langevin, Y., Leese, M., Lunine, J., McKay, C., Moussas, X., Muller-Wodarg, I., Neubauer, F., Owen, T., Raulin, F., Sittler, E., Sohl, F., Sotin, C., Tobie, G., Tokano, T., Turtle, E., Wahlund, J.E., Waite, J., Baines, K., Blamont, J., Coates, A., Dandouras, I., Krimigis, T., Lellouch, E., Lorenz, R., Morse, A., Porco, C., Hirtzig, M., Saur, J., Spilker, T., Zarnecki, J., Choi, E., Achilleos, N., Amils, R., Annan, P., Atkinson, D., Benilan, Y., Bertucci, C., Bezard, B., Bjoraker, G., Blanc, M., Boireau, L., Bouman, J., Cabane, M., Capria, M., Chassefière, E., Coll, P., Combes, M., Cooper, J., Coradini, A., Crary, F., Cravens, T., Daglis, I., de Angelis, E., de Bergh, C., de Pater, I., Dunford, C., Durry, G., Dutuit, O., Fairbrother, D., Flasar, F., Fortes, A., Frampton, R., Fujimoto, Galand, M., Grasset, O., Grott, M., Haltigin, T., Herique, A., Hersant, F., Hussmann, H., Ip, W., Johnson, R., Kallio, E., Kempf, S., Knapmeyer, M., Kofman, W., Koop, R., Kostiuk, T., Krupp, N., Kuppers, M., Lammer, H., Lara, L.M., Lavvas, P., Le Moulic, S., Lebonnois, S., Ledvina, S., Li, J., Livengood, T., Lopes, R., Lopez-Moreno, J.J., Luz, D., Mahaffy, P., Mall, U., Martinez-Frias, J., Marty, B., McCord, T., MenorSalvan, C., Milillo, A., Mitchell, D., Modolo, R., Mousis, O., Nakamura, M., Neish, C., Nixon, C., Nna Mvondo, D., Orton, G., Paetzold, M., Pitman, J., Pogrebenko, S., Pollard, W., Prieto-Ballesteros, O., Rannou, P., Reh, K., Richter, L., Robb, F., Rodrigo, R., Rodriguez, S., Romani, P., Ruiz Bermejo, M., Sarris, E., Schenk, P., Schmitt, B., Schmitz, N., Schulze-Makuch, D., Schwingenschuh, K., Selig, A., Sicardy, B., Soderblom, L., Spilker, L., Stam, D., Steele, A., Stephan, K., Strobel, D., Szego, K., Szopa, C., Thissen, R., Tomasko, M., Toublanc, D., Vali, H., Vardavas, I., Vuitton, V., West, R., Yelle, R., Young, E., 2009. TandEM: Titan and Enceladus mission. Experimental Astronomy 23, 893–946.

Elachi, C., Allison, M.D., Borgarelli, L., Encrenaz, P., Im, E., Janssen, M.A., Johnson, W.T.K., Kirk, R.L., Lorenz, R.D., Lunine, J.I., Muhleman, D.O., Ostro, S.J., Picardi, G., Posa, F., Rapley, C.G., Roth, L.E., Seu, R., Soderblom, L.A., Vetrella, S., Wall, S.D., Wood, C.A., Zebker, H.A., 2004. Radar: the Cassini Titan Radar Mapper. Space Science Reviews 115, 71–110.

Elachi, C., Wall, S., Allison, M., Anderson, Y., Boehmer, R., Callahan, P., Encrenaz, P., Flamini, E., Francescheti, G., Gim, Y., Hamilton, G., Hensley, S., Janssen, M., Johnson, W., Kelleher, K., Kirk, R., Lopes, R., Lorenz, R., Lunine, J., Muhleman, D., Ostro, S., Paganelli, F., Picardi, G., Posa, F., Roth, L., Seu, R., Shaffer, S., Soderblom, L., Stiles, B., Stofan, E., Vetrella, S., West, R., Wood, C., Wye, L., Zebker, H., 2005. Cassini Radar views the surface of Titan. Science 308, 970–974.

Elachi, C., Wall, S., Janssen, M., Stofan, E., Lopes, R., Kirk, R., Lorenz, R., Lunine, J., Paganelli, F., Soderblom, L., Wood, C., Wye, L., Zebker, H., Anderson, Y., Ostro, S., Allison, M., Boehmer, R., Callahan, P., Encrenaz, P., Flamini, E., Francescetti, G., Gim, Y., Hamilton, G., Hensley, S., Johnson, W., Kelleher, K., Muhleman, D., Picardi, G., Posa, F., Roth, L., Seu, R., Shaffer, S., Stiles, B., Vetrella, S., West, R., 2006. Titan Radar Mapper observations from Cassini's T3 fly-by. Nature 441, 709–713.

Fulchignoni, M., Ferri, F., Angrilli, F., Ball, A.J., Bar-Nun, A., Barucci, M.A., Bettanini, C., Bianchini, G., Borucki, W., Colombatti, G., Coradini, M., Coustenis, A., Debei, S., Falkner, P., Fanti, G., Flamini, E., Gaborit, V., Grard, R., Hamelin, M., Harri, A.M., Hathi, B., Jernej, I., Leese, M.R., Lehto, A., Lion Stoppato, P.F., Lpez-Moreno, J.J., Mikinen, T., McDonnell, J.A.M., McKay, C.P., Molina-Cuberos, G., Neubauer, F.M., Pirronello, V., Rodrigo, R., Saggin, B., Schwingenschuh, K., Seiff, A., Simes, F., Svedhem, H., Tokano, T., Towner, M.C., Trautner, R., Withers, P., Zarnecki, J.C., 2005. In situ measurements of the physical characteristics of Titan's environment. Nature 438, 785–791.

Graves, S.D.B., McKay, C.P., Griffith, C.A., Ferri, F., Fulchignoni, M., 2008. Rain and hail can reach the surface of Titan. Planetary and Space Science 56, 346–357.

Griffith, C.A., Hall, J.L., Geballe, T.R., 2000. Detection of daily clouds on Titan. Science 290, 509–513.

Griffith, C.A., Penteado, P., Baines, K., Drossart, P., Barnes, J., Bellucci, G., Bibring, J., Brown, R., Buratti, B., Capaccioni, F., Cerroni, P., Clark, R., Combes, M., Coradini, A., Cruikshank, D., Formisano, V., Jaumann, R., Langevin, Y., Matson, D., McCord, T., Mennella, V., Nelson, R., Nicholson, P., Sicardy, B., Sotin, C., Soderblom, L.A., Kursinski, R., 2005. The evolution of Titan's mid-latitude clouds. Science 310, 474–477.

Hayes, A., Aharonson, O., Callahan, P., Elachi, C., Gim, Y., Kirk, R., Lewis, K., Lopes, R., Lorenz, R., Lunine, J., Mitchell, K., Mitri, G., Stofan, E., Wall, S., 2008. Hydrocarbon lakes on Titan: distribution and interaction with a porous regolith. Geophysical Research Letters 35, L09204.

Hayes, A., Wolf, A., Aharonson, O., Zebker, H., Lorenz, R., Kirk, R., Paillou, P., Lunine, J., Wye, L., Callahan, P., Wall, S., Elachi, C., 2010. Bathymetry and absorptivity of Titan's Ontario Lacus. Journal of Geophysical Research 115, E09009.

Hueso, R., Sanchez-Lavega, A., 2006. Methane storms on Saturn's moon Titan. Nature 442, 428–431.

Jaumann, R., Brown, R.H., Stephan, K., Barnes, J.W., Soderblom, L.A., Sotin, C., Le Mouelic, S., Clark, R.N., Soderblom, J., Buratti, B.J., Wagner, R., McCord, T.B., Rodriguez, S., Baines, K.H., Cruikshank, D.P., Nicholson, P.D., Griffith, C.A.,

Langhans, E., Lorenz, R.D., 2008. Fluvial erosion and post-erosional processes on Titan. Icarus 197, 526–538.
Janssen, M.A., Lorenz, R.D., West, R., Paganelli, F., Lopes, R.M., Kirk, R.L., Elachi, C., Wall, S.D., Johnson, W.T.K., Anderson, Y., Boehmer, R.A., Callahan, P., Gim, Y., Hamilton, G.A., Kelleher, K.D., Roth, L., Stiles, B., Le Gall, A., 2009. the Cassini Radar Team, 2009. Titan's surface at 2.2-cm wavelength imaged by the Cassini Radar radiometer: calibration and first results. Icarus 200, 222–239.
Jennings, D.E., Flasar, F.M., Kunde, V.G., Samuelson, R.E., Pearl, J.C., Nixon, C.A., Carlson, R.C., Mamoutkine, A.A., Brasunas, J.C., Guandique, E., Achterberg, R.K., Bjoraker, G.L., Romani, P.N., Segura, M.E., Albright, S.A., Elliott, M.H., Tingley, J.S., Calcutt, S., Coustenis, A., Courtin, R., 2009. Titan's surface brightness temperatures. Astrophysical Journal 691, L103–L105.
Kouvaris, L.C., Flasar, F.M., 1991. Phase equilibrium of methane and nitrogen at low temperatures: application to Titan. Icarus 91, 112–124.
Lopes, R.M.C., Mitchell, K.L., Stofan, E.R., Lunine, J.I., Lorenz, R., Paganelli, F., Kirk, R.L., Wood, C.A., Wall, S.D., Robshaw, L.E., Fortes, A.D., Neish, C.D., Radebaugh, J., Reffet, E., Ostro, S.J., Elachi, C., Allison, M.D., Anderson, Y., Boehmer, R., Boubin, G., Callahan, P., Encrenaz, P., Flamini, E., Francescetti, G., Gim, Y., Hamilton, G., Hensley, S., Janssen, M.A., Johnson, W.T.K., Kelleher, K., Muhleman, D.O., Ori, G., Orosei, R., Picardi, G., Posa, F., Roth, L.E., Seu, R., Shaffer, S., Soderblom, L.A., Stiles, B., Vetrella, S., West, R.D., Wye, L., Zebker, H.A., 2007a. Cryovolcanic features on Titan's surface as revealed by the Cassini Titan Radar Mapper. Icarus 186, 395–412.
Lopes, R.M.C., Mitchell, K.L., Wall, S.D., Mitri, G., Janssen, M., Ostro, S.J., Kirk, R.L., Hayes, A., Stofan, E.R., Lunine, J.I., Lorenz, R., Wood, C.A., Radebaugh, J., Paillou, P., Zebker, H.A., Paganelli, F., 2007b. the Cassini RADAR Team, 2007. The lakes and seas of Titan. Transactions of EOS, American Geophysical Union 88, 569–576.
Lopes, R.M.C., Stofan, E.R., Peckyno, R., Radebaugh, J., Mitchell, K.L., Mitri, G., AWood, C.A., Kirk, R.L., Wall, S.D., Lunine, J.I., Hayes, A., Lorenz, R., Farr, T., Wye, L., Craig, J., Ollerenshaw, R.J., Janssen, M., Legall, A., Paganelli, F., West, R., Stiles, B., Callahan, P., Anderson, Y., Valora, P., Soderblom, L., 2010. the Cassini RADAR Team, 2010. Distribution and interplay of geologic processes on Titan from Cassini radar data. Icarus 205, 540–558.
Lorenz, R.D., 1993. The life, death and afterlife of a raindrop on Titan. Planetary and Space Science 41, 647–655.
Lorenz, R.D., Griffith, C.A., Lunine, J.I., McKay, C.P., Renn, N.O., 2005. Convective plumes and the scarcity of Titan's clouds. Geophysical Research Letters 32, L01201.
Lorenz, R.D., Lopes, R.M., Paganelli, F., Lunine, J.I., Kirk, R.L., Mitchell, K.L., Soderblom, L.A., Stofan, E.R., Ori, G., Myers, M., Miyamoto, H., Radebaugh, J., Stiles, B., Wall, S.D., Wood, C.A., Team, T.C.R., 2008. Fluvial channels on Titan : initial Cassini radar observations. Planetary and Space Science 56, 1132–1144.
Lunine, J.I., Stevenson, D.J., Yung, Y.L., 1983. Ethane ocean on Titan. Science 222, 1229–1230.
Mitri, G., Showman, A.P., Lunine, J.I., Lorenz, R.D., 2007. Hydrocarbon lakes on Titan. Icarus 186, 385–394.
Nelson, R.M., Kamp, L.W., Lopes, R.M.C., Matson, L., Kirk, R., Hapke, B., Wall, S.D., Boryta, M.D., Leader, F.L., Smythe, W.D., Mitchell, K., Baines, K.H., Jaumann, R., Sotin, C., Clark, R.N., Cruickshank, D.P., Drossart, P., Lunine, J., Combes, M., Bellucci, G., Bibring, J.-P., Capaccioni, F., Cerroni, P., Coradani, A., Formasiano, V., Filacchione, G., Langevin, Y., McCord, T., Menella, V., Nicholson, P.D., Sicardy, B., Itrwin, P.J., Pearl, J.C., 2009. Photometric changes on Saturn's Titan: evidence for active cryovolcanism. Geophysical Research Letters 36, L04202.
Notarnicola, C., Ventura, B., Casarano, D., Posa, F., 2009. Cassini radar data: estimation of Titan's lake features by means of Bayesian inversion algorithm. IEEE Transactions on Geoscience and Remote Sensing 47, 1503–1511.
Perron, J.T., Lamb, M.P., Koven, C.D., Fung, I.Y., Yager, E., Adamkovics, M., 2006. Valley formation and methane precipitation rates on Titan. Journal of Geophysical Research 111, E11001.
Radebaugh, J., Lorenz, D., Kirk, R.L., Lunine, J.I., Stofan, E.R., Lopes, R.M.C., Wall, S.D., 2007. the Cassini Radar Team, 2007. Mountains on Titan observed by Cassini Radar. Icarus 192, 77–91.
Radebaugh, J., Lorenz, R.D., Lunine, J.I., Wall, S.D., Boubin, G., Reffet, E., Kirk, R.L., Lopes, R.M., Stofan, E.R., Soderblom, L., Allison, M., Janssen, M., Paillou, P., Callahan, T., Spencer, C., The Cassini Radar, T., 2008. Dunes on Titan observed by Cassini Radar. Icarus 194, 690–703.
Raulin, F., 2008. Planetary science: organic lakes on Titan. Nature 454, 587–589.
Reh, K., Lunine, J., Matson, D., Magner, T., Lebreton, J.-P., Coustenis, A., 2008. TSSM Final Report on the NASA Contribution to a Joint Mission with ESA, JPL D-48148, NASA Task Order NMO710851.
Richards, J.A., 1999. Remote Sensing Digital Image Analysis. Springer-Verlag, Berlin, p. 240.
Soderblom, L.A., Tomasko, M.G., Archinal, B.A., Becker, T.L., Bushroe, M.W., Cook, D.A., Doose, L.R., Galuszka, D.M., Hare, T.M., Howington-Kraus, E., Karkoschka, E., Kirk, L., Lunine, J.I., McFarlane, E.A., Redding, B.L., Rizk, B., Rosiek, M.R., See, C., Smith, P.H., 2007. Topography and geomorphology of the Huygens landing site on Titan. Planetary and Space Science 55, 2015–2024.
Soderblom, L.A., Brown, R.H., Soderblom, J.M., Barnes, J.W., Kirk, R.L., Sotin, C., Jaumann, R., Mackinnon, d.J., Mackowski, D.W., Baines, K.H., Buratti, B.J., Clark, R.N., Nicholson, P.D., 2009. The geology of Hotei Regio, Titan: correlation of Cassini VIMS and RADAR. Icarus 204, 610–618.
Sotin, C., 2007. Planetary science: Titan's lost seas found. Nature 445, 29–30.
Stofan, E.R., Elachi, C., Lunine, J.I., Lorenz, R.D., Stiles, B., Mitchell, K.L., Ostro, S., Soderblom, L., Wood, C., Zebker, H., Wall, S., Janssen, M., Kirk, R., Lopes, R., Paganelli, F., Radebaugh, J., Wye, L., Anderson, Y., Allison, M., Boehmer, R., Callahan, P., Encrenaz, P., Flamini, E., Francescetti, G., Gim, Y., Hamilton, G., Hensley, S., Johnson, W.T.K., Kelleher, K., Muhleman, D., Paillou, P., Picardi, G., Posa, F., Roth, L., Seu, R., Shaffer, S., Vetrella, S., West, R., 2007. The lakes of Titan. Nature 445, 61–64.
Thompson, W.R., Zollweg, J.A., Gabis, D.H., 1992. Vapor–liquid equilibrium thermodynamics of N_2 + CH_4—model and Titan applications. Icarus 97, 187–199.
Tobie, G., Grasset, O., Lunine, J.I., Mocquet, A., Sotin, C., 2005. Titans internal structure inferred from a coupled thermal-orbital model. Icarus 175, 496–502.
Tokano, T., McKay, C.P., Neubauer, F.M., Atreya, S.K., Ferri, F., Fulchignoni, M., Niemann, H.B., 2006. Methane drizzle on Titan. Nature 442, 432–435.
Tomasko, M.G., Archinal, B., Becker, T., Bezard, B., Bushroe, M., Combes, M., Cook, D., Coustenis, A., de Bergh, C., Dafoe, L.E., Doose, L., Doute, S., Eibl, A., Engel, S., Gliem, F., Grieger, B., Holso, K., Howington-Kraus, E., Karkoschka, E., Keller, H.U., Kirk, R., Kramm, R., Kuppers, M., Lanagan, P., Lellouch, E., Lemmon, M., Lunine, J., McFarlane, E., Moores, J., Prout, G.M., Rizk, B., Rosiek, M., Rueffer, P., Schroder, S.E., Schmitt, B., See, C., Smith, P., Soderblom, L., Thomas, N., West, R., 2005. Rain, winds and haze during the Huygens probe's descent to Titan's surface. Nature 438, 765–778.
Toon, O.B., McKay, C.P., Courtin, R., Ackerman, T.P., 1988. Methane rain on Titan. Icarus 75, 255–284.
Turtle, E.P., Perry, J.E., McEwen, A.S., DelGenio, A.D., Barbara, J., West, R.A., Dawson, D.D., Porco, C.C., 2009. Cassini imaging of Titan's high-latitude lakes, clouds, and south-polar surface changes. Geophysical Research Letters 36, L02204.
Ulaby, F.T., Moore, R.K., Fung, A.K., 1982. Microwave Remote Sensing: Active and Passive, vol. 2. Artech House, Norwood, Mass.
Wall, S.D., Lopes, R.M.C., Stofan, E.R., Wood, C.A., Radebaugh, J.L., Horst, S.M., Stiles, B.W., Nelson, R.M., Kamp, L.W., Janssen, M.A., Lorenz, R.D., Lunine, J.I., Farr, T.G., Mitri, G., Paillou, P., Paganelli, F., Mitchell, K.L., 2009. Cassini RADAR images at Hotei Arcus and western Xanadu, Titan: evidence for geologically recent cryovolcanic activity. Geophysical Research Letters 36, L04203.
Wall, S., Hayes, A., Bristow, C., Lorenz, R., Stofan, E., Lunine, J., Le Gall, A., Janssen, M., Lopes, R., Wye, L., Soderblom, L., Paillou, P., Aharonson, O., Zebker, H., Farr, T., Mitri, G., Kirk, R., Mitchell, K., Notarnicola, C., Casarano, D., Ventura, B., 2010. Active shoreline of Ontario Lacus, Titan: a morphological study of the lake and its surroundings. Geophysical Research Letters 37, L05202.
Wood, C.A., Lorenz, R., Kirk, R., CLopes, R.M., Mitchell, K.L., Stofan, E., 2010. Impact craters on Titan. Icarus 206, 334–344.
Wye, L., Zebker, H.A., Hayes, A.G., Lorenz, R.D., Notarnicola, C., Ventura, B., Casarano, D., the Cassini Radar Team, 2010. Constraining depths and wave heights for Titan's lakes with Cassini RADAR Data. In: American Geophysical Union, Fall Meeting 2010, abstract P31C-1552.

Appendix D2

Morphotectonic features on Titan and their possible origin

Journal article in press submitted in *Planetary Space & Science*,
http://dx.doi.org/10.1016/j.pss.2012.05.003.

ARTICLE IN PRESS

Planetary and Space Science ∎ (∎∎∎∎) ∎∎∎–∎∎∎

Contents lists available at SciVerse ScienceDirect

Planetary and Space Science

journal homepage: www.elsevier.com/locate/pss

Morphotectonic features on Titan and their possible origin

Anezina Solomonidou [a,b,*], Georgios Bampasidis [b,c], Mathieu Hirtzig [b], Athena Coustenis [b], Konstantinos Kyriakopoulos [a], Karen St. Seymour [d,e], Emmanuel Bratsolis [c], Xenophon Moussas [c]

[a] Department of Geology and Geoenvironment, National & Kapodistrian University of Athens, 15784 Athens, Greece
[b] LESIA-Observatoire de Paris, CNRS, UPMC Univ. Paris 06, Univ. Paris-Diderot, 92195 Meudon Cedex, France
[c] Department of Physics, National & Kapodistrian University of Athens, 15784 Athens, Greece
[d] Department of Geology, University of Patras, 26504 Patras, Greece
[e] Concordia University, Department of Geography, H3G1M8 Montréal, Canada

ARTICLE INFO

Article history:
Received 26 December 2010
Received in revised form
12 January 2012
Accepted 3 May 2012

Keywords:
Titan
Morphotectonic features
Icy satellites
Cryovolcanism
Internal structure

ABSTRACT

Spectro-imaging and radar measurements by the Cassini–Huygens mission suggest that some of the Saturnian satellites may be geologically active and could support tectonic processes. In particular Titan, Saturn's largest moon, possesses a complex and dynamic geology as witnessed by its varied surface morphology resulting from aeolian, fluvial, and possibly tectonic and endogenous cryovolcanic processes. The Synthetic Aperture Radar (SAR) instrument on board Cassini spacecraft, indicates the possibility for morphotectonic features on Titan's surface such as mountains, ridges, faults and canyons. The mechanisms that formed these morphotectonic structures are still unclear since ensuing processes, such as erosion may have modified or partially obscured them. Due to the limitations of Cassini–Huygens in the acquisition of *in situ* measurements or samples relevant to geotectonics processes and the lack of high spatial resolution imaging, we do not have precise enough data of the morphology and topography of Titan. However we suggest that contractional tectonism followed by atmospheric modifications has resulted in the observed morphotectonic features. To test the possibility of morphotectonics on Titan, we provide in this work a comparative study between Cassini observations of the satellite versus terrestrial tectonic systems and infer suggestions for possible formation mechanisms.

1. Introduction

Tectonic or structural geology is the field of geological research that focuses on the study of features observed on the crust of the Earth and that of other planets investigating the processes, forces and movements that resulted in them. Tectonism encompasses geological events not caused by exogenous processes such as erosion and meteoritic impacts. Tectonism being compressional or extensional is related with important endogenous processes such as terrestrial volcanism and most probably with extraterrestrial cryovolcanism. Morphotectonics correlate landscape morphology to tectonism (Rosenau and Oncken, 2009; Scheidegger, 2004; Lidmar-Bergström, 1996) by studying landform evolution and degradation, since tectonic features are subsequently subjected to exogenous processes. Major morphotectonic features on Earth are represented by mountains, ridges, faults and escarpments, as well as by significant types of linear features such as rifts, grabens and other linear terrestrial terrains that are subjected to erosion subsequently to deformational events (e.g., Scheidegger, 2004). However, geology on Earth is dominated by active plate tectonics where rigid lithospheric plates float and move on a plastic asthenosphere.

Although the other planetary bodies in our Solar System possess different surface and internal conditions, bodies like Titan, Europa and Enceladus may possess a liquid water layer underneath their icy crust. If confirmed, then similarly to rocky plate tectonics on Earth, rigid ice plates may rupture and collide, floating over such a liquid substrate layer, resulting in surficial features, which may be reminiscent of terrestrial edifices. It is therefore possible that other planets and moons in the Solar System harbor "tectonic activity" in varying degrees and even exhibit morphotectonic features on their surfaces, which are subsequently modified by exogenous processes.

Venus appears to have no plate tectonics due to a high surface temperature and a higher density of its lithosphere compared to that of the mantle, which prevents a subduction regime, despite the fact that the mantle is convecting (Nimmo and McKenzie, 1998). However, the planet shows deformation and morphotectonic features such as faults, mountain crests and rifts, which probably originated from lithospheric movements in association with volcanism (Jull and Arkani-Hamed, 1995; Nimmo and McKenzie, 1998). In the case of Mars, two major regions are known to display morphotectonic features: the Tharsis volcanic plateau, which was possibly formed after crustal deformation in

* Corresponding author at: Department of Geology and Geoenvironment, National & Kapodistrian University of Athens, Greece. Tel.: +30 69 45 40 29 03.
E-mail addresses: asolomonidou@geol.uoa.gr, Anezina.Solomonidou@obspm.fr (A. Solomonidou).

0032-0633/$ - see front matter © 2012 Elsevier Ltd. All rights reserved.
http://dx.doi.org/10.1016/j.pss.2012.05.003

Please cite this article as: Solomonidou, A., et al., Morphotectonic features on Titan and their possible origin. Planetary and Space Science (2012), http://dx.doi.org/10.1016/j.pss.2012.05.003

association with active diapirism from the mantle (Mège and Masson, 1996) and the Elysium region, which was a result of volcanic activity (Hall et al., 1986). Io, Jupiter's moon, presents morphotectonic features with no apparent association to plate tectonic activity. The mountains of Io are formed by stresses at the bottom of the lithospheric layer and subsequent uplift through thrust faulting system (Schenk and Bulmer, 1998).

A good candidate for the study of morphotectonic features in the Solar System appears to be Titan. With a diameter of 5150 km (1/3 that of the Earth), Titan is the largest satellite of the Saturnian System and the second in the Solar System, after Ganymede the moon of Jupiter. The temperature and pressure conditions at the surface near the equator are 93.65 ± 0.25 K and 1.467 ± 1 hPa, as measured by the Huygens probe Atmospheric Structure Instrument (HASI) (Fulchignoni et al., 2005). Titan is recognized as a world bearing several resemblances to our own planet, with respect to its atmosphere and to its surface morphology. Titan's dense atmosphere consists mainly of nitrogen (~97%), methane (1.4%) and hydrogen (~0.2%) with traces of hydrocarbons, nitriles, oxygen compounds and argon (see table 6.4 in Coustenis and Taylor, 2008). This complex atmosphere renders the surface difficult to access and analyze, apart from within a few methane spectral windows in the near-infrared where the methane absorption is weak (Griffith et al., 1991). Thirty-two years after the Voyager encounter in 1980, Cassini is today able to probe Titan's surface with a spatial resolution reaching a few hundred meters per pixel (RADAR), while the Huygens probe achieved the first *in situ* measurements in 2005 (for instruments and resolutions see Section 2). Even though Titan's surface morphology resembles that of the Earth, it is made of materials and subjected to surface conditions very distinct from the terrestrial ones. Indeed, morphotectonic features such as mountains (e.g. Radebaugh et al., 2007; Lopes et al., 2010), ridges (Soderblom et al., 2007b; Mitri et al., 2010), faults (e.g., Radebaugh et al., 2011), rectangular drainage patterns and cryovolcanic structures are most likely controlled, at least in part, by tectonism (Burr et al., 2009).

Atmospheric processes, like cloud formation and precipitation create extensive fluvial features on the surface, as observed by Huygens near its landing site and constitute the visible part of an active methane cycle (Atreya et al., 2006; Coustenis and Taylor, 2008; Lorenz and Mitton, 2008; Raulin, 2008; Brown et al., 2009; Coustenis and Hirtzig, 2009; Lebreton et al., 2009). The preservation limit of 100 Myr for this atmospheric methane requires a reservoir that would replenish occasionally the atmosphere (Lunine and Atreya, 2008). One of the most predominant theories suggests that methane sources exist in Titan's interior (e.g., Tobie et al., 2006; Fortes et al., 2007). Since volcanism is a major process associated with the terrestrial carbon release (Bolin, 1981), cryovolcanism may play a similar role in the methane supply (Sotin et al., 2005), as well as significantly influence Titan's surface morphology.

Geophysical models suggest that Titan's partially differentiated interior consists of a silicate core (~1800 km thick), a high-pressure ice mantle (~400 km), a liquid layer of aqueous ammonium sulfate (50–150 km thick), and an external icy shell 100–170 km thick that possibly contains clathrate hydrates (Tobie et al., 2005; Fortes et al., 2007; Grindrod et al., 2008). Castillo-Rogez and Lunine (2010) suggested possible dehydration of the core's hydrated silicates, which impacts the geophysical structure of the satellite as well as the possible internal ocean. Regarding the icy shell, the methane stored as clathrate hydrates within the ice shell is a plausible methane reservoir that can replenish the atmosphere via cryovolcanism (Sotin et al., 2005). Indeed, surface discontinuities such as faults and fractures, which are probably the result of tectonic and volcanic-like processes, could provide the pathways of internal methane release to the atmosphere. The morphotectonic structures on Titan's surface provide good evidence of such a mechanism, in the same way as, over extensive zones of geological weaknesses, magma and volatiles are released on the Earth's surface.

In the last eight years, despite continuous observations by Cassini and the development of models and interpretations based on them, we still lack long-term *in situ* measurements and geophysical data of Titan's interior, in order to be in a position to accurately evaluate its endogenetic potential and how it affects morphotectonic features. However, in this work we attempt to use similarities between the surficial morphotectonic features on Titan and on Earth as the key for deciphering Titan's endogenetic processes, in spite of the fact that our understanding of Earth's endogenetic processes is rather recent (Wilson, 1973).

2. Titan surface observations

From the interpretation of Voyager 1 recordings, a global ocean of dissolved ethane and nitrogen, several kilometers deep, was first assumed to cover the entire surface of Titan (Flasar, 1983; Lunine et al., 1983). However, ground- and space-based observations refuted this assumption by unveiling, within the methane "windows" of weaker methane absorption (centered at 0.94, 1.08, 1.28, 1.59, 2.03, 2.8 and 5 μm), a solid surface with heterogeneous bright and dark features (Muhleman et al., 1990; Griffith, 1993; Smith et al., 1996; Gibbard et al., 1999; Meier et al., 2000; Coustenis et al., 2001). The Cassini orbiter arrived at the Saturnian System in 2004 equipped with two spectro-imagers capable to probe down to the surface via several of the near-infrared windows: the Visual and Infrared Mapping Spectrometer (VIMS—with a typical resolution of 10–20 km/pixel) and the Imaging Science Subsystem (ISS—with a typical resolution of 1 km/pixel). In the scope of this paper we also make use of the RADAR data from Cassini with a spatial resolution from 300 m to 1.5 km/pixel. In addition, Huygens probe measurements and observations by the Descent Imager Spectral Radiometer (DISR—Tomasko et al., 2005), the Surface Science Package (SSP—Zarnecki et al., 2005), and the Gas Chromatograph Mass Spectrometer (GCMS—Niemann et al., 2005, 2010) provided additional information of Titan's geology. The actual landing site on the Saturnian satellite appears to be a relatively soft surface similar to tar or dry sand, tinted by methane ready to evaporate and providing ample evidence for fluvial and aeolian processes.

2.1. Surface expressions

2.1.1. Geological features formed by non-tectonic processes

Endogenous, as well as exogenous dynamic processes have created diverse terrains with extensive ridges and grooves, impact units, icy flows, caldera-like structures, layered plains and stable liquid lakes (Mitri et al., 2007; Stofan et al., 2007). In addition, Cassini's radar has partially revealed the topography of Titan's surface, indicating several types of surficial expressions, which are non-tectonic. Features like dunes, lakes and drainage network are attributed solely to fluvial, aeolian and impact processes (Fig. 1). Thus, their formation is the result of exogenous processes with no influence of internal activity.

2.1.2. Morphotectonic features

Cassini's remote instrumentation and the Huygens lander brought evidence of many features on Titan's surface, which were probably formed by extension or compression of parts of the planetary solid crust due to endogenetic geological and geophysical processes (Radebaugh et al., 2007; Soderblom et al., 2007b;

Please cite this article as: Solomonidou, A., et al., Morphotectonic features on Titan and their possible origin. Planetary and Space Science (2012), http://dx.doi.org/10.1016/j.pss.2012.05.003

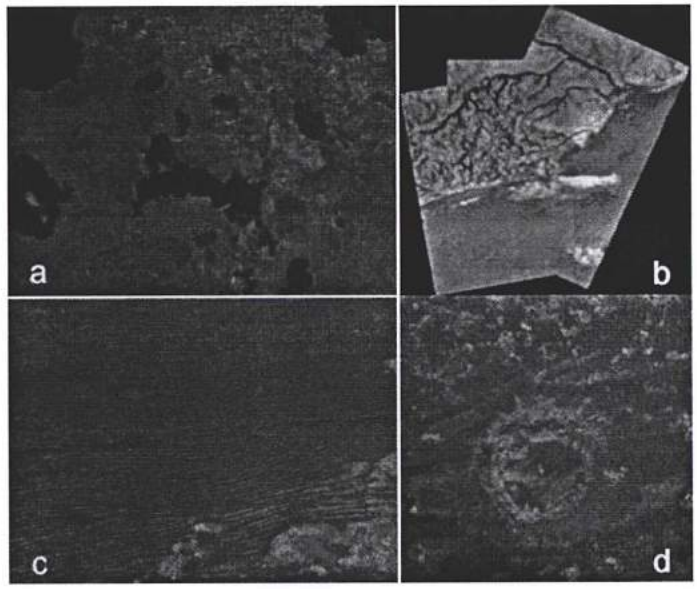

Fig. 1. Surface features on Titan. (a) Hydrocarbon liquid lakes at the North pole (Cassini Radar Mapper, JPL, ESA, NASA). (b) Complex network of narrow drainage channels formed by fluvial processes near the Huygens probe landing site (NASA/JPL). (c) Sand dunes formed by aeolian processes (NASA). (d) Afecan (26°N, 200°W) impact crater, discovered in 2008 (NASA/JPL).

Lopes et al., 2010). Furthermore, these features can be modified under the influence of exogenetic processes: the resultant morphotectonic structures are mainly mountains, ridges, faults, and structures of probable cryovolcanic origin as we will argue further down. Titan, despite its small size, displays surface features that resemble the structure of terrestrial volcanic fields albeit they are much more extensive. For example, Hotei Regio (see Section 4.2) covers an area of 140,000 km^2, which is an order of magnitude larger than Harrat Khaybar (14,000 km^2) in Saudi Arabia, which represents one of the most extensive volcanic fields on Earth (Camp et al., 1991).

2.2. Silicate and icy tectonism

A surface feature largely owes its shape to the material composing the planetary body's crust and to the forces that formed it. The response of the crustal material to the applied stresses, defines to a large extent the main topographic terrain of an area, along with the atmospheric conditions. Even though geological features such as mountains, faults and rifts on Titan present similar visual characteristics, the type of material that builds the features plays an important role. Indeed, the properties of the source material such as viscosity, elasticity and density in addition to the geological forces control the structural characteristics of the feature such as height, expansion and gradient slope.

On Titan, the surface should probably be composed mainly of mixtures of water and other ices, organics–tholins, nitriles (e.g. Soderblom et al., 2007a), while, most likely, its interior is composed of rock and high-pressure ice (Tobie et al., 2005). Since the well-known tectonic features of Earth are closely linked to silicate geology, we must first assess the similarities and differences between water ices and silicates, so that our comparative study can be based on reasonable assumptions. The icy crust of the outer system satellites possibly reacts in a brittle fashion to the application of stresses, similarly to the Earth's rocky upper crust (Collins et al., 2009). Both on Titan and Earth this reaction changes in proportion with depth. However, while water ice and silicate rock exhibit similar frictional strength (Beeman et al., 1988), when ductile yielding becomes important, ice is about ten times weaker than silicate rock (Melosh and Nimmo, 2011). The major differences and similarities between water ice and silicates are noted in Collins et al. (2009) and summarized in Table 1.

Table 1 shows that silicate materials, when compared to water ice, exhibit higher viscosity, Young modulus i.e. the ratio of linear stress to linear strain and melting temperature, but display lower density. As a result, the homologous temperature, on which rheology depends, is reached at greater depths in silicate environments while silicate magma eruptions are statistically more possible to occur than eruptions of ice (Collins et al., 2009). Nevertheless, both icy and silicate systems seem to follow some similar general deformation principles and mimic each other's behavior. Also, since ice topography could viscously relax over geologic time (e.g. Dombard and McKinnon, 2006) and elastic, brittle and ductile deformation could occur in the icy crust, tectonic-like movements, resembling the silicate plate behavior, are plausible.

3. Morphotectonic observations of mountains

3.1. Mountains and ridges

RADAR, VIMS as well as DISR data have provided some details of the characteristics of Titan's mountains and ridges. The term mountain describes large uplifted localized landforms while the term

Please cite this article as: Solomonidou, A., et al., Morphotectonic features on Titan and their possible origin. Planetary and Space Science (2012), http://dx.doi.org/10.1016/j.pss.2012.05.003

Table 1
Comparison between silicate and ice properties.

Properties	Water ice	Silicate	Similarity
Homologous temperature	0.4	0.4	Yes
Melting temperatures	273.15 K	950–1500 K	No
Density	Low (in solid state)	High	No
Young Modulus	~10 GPa	~100 GPa	No
Low stress and strain	Elastic deformation	Elastic deformation	Yes
High strain, low temperature	Brittle deformation	Brittle deformation	Yes
Low strain, high temperature	Ductile deformation	Ductile deformation	Yes

Table 2a
Major mountain and ridge features on Titan.

Location	Orientation	Heights	Characterization	Flyby/Time	Instrument (reference)
10°N, 15°W 15°N, 45°W		380–570 m	Blocks of mountains	T3/February 2005	RADAR (Radebaugh et al., 2007)
20°N, 87°W	E–W	~300 m	Ridges	T3/February 2005	RADAR (Williams et al., 2011)
40°S, 340°W			Hills	T7/September 2005	RADAR (Lunine et al., 2008)
5°S, 12.5°S 63°W, 67°W	E–W	~860–2000 m	Curvilinear mountains/Ridges	T8/October 2005	RADAR (Radebaugh et al., 2007; Mitri et al., 2010; Lopes et al., 2010)
10°S, 210°W		~400 m	Mountainous region	T9/December 2005 T13/April 2006	VIMS/RADAR (Barnes et al., 2007)
10.4°S, 192.4°W	W–E	100–150 m	Ridges	Huygens/January 2005	DISR (Tomasko et al., 2005; Soderblom et al., 2007b)
30°S, 315°W	NW–SE	~1500 m	Mountain ranges	T20/October 2006	VIMS (Sotin et al., 2007)
52°N, 347°W	E-W	~1400 m	Mountain block	T30/May 2007	RADAR (Stiles et al., 2009; Mitri et al., 2010)
30°S, 107°W	S–W	~800 m	Mountains	T43/May 2008	RADAR (Mitri et al., 2010)
2°S, 127°W	E–W	1930 m	Ridges	T43/May 2008	RADAR (Mitri et al., 2010)

Table 2b
Proposed mechanisms for the formation of mountains and ridges of Titan.

Proposed mechanism	Description	Observations	Terrestrial analog
Lithospheric shortening (Mitri et al., 2010)	Folding of the upper crust due to past high heat flux from the interior and high temperature gradients in the ice shell	Curvilinear mountains/ Ridges T8, T30, T43	Folded mountains: Rocky Mountains, North America
Tectonic stresses of the ice shell (Mitri and Showman, 2008)	Transitions of the ice shell over a liquid subsurface ocean, from a conductive state to a convective state, causes tectonic stresses and movements that influence the surface	Model	Rocky Mountains, North America
Crustal compression/ upthrust blocks (Radebaugh et al., 2007 scenario 1)	Localized compression due to thickening of the crust linked with the cooling of Titan at areas where fault structures exist	Linear mountains T8, T3 (15°N, 45°W)	Eroded mountains: Acadian Mountains, USA Mountain-building due to Sevier/Laramide Orogeny
Crustal stresses/upwelling of material (Sotin et al., 2007)	Generation of extensive stresses that penetrate the icy shell and create pathways for the internal material	High-standing mountain ranges T20	Tectonic and magmatic aspects on geological terrains: Mid Atlantic Ridge, Atlantic Ocean Ahaggar Mountains, North-central Sahara Desert
Crustal extension (Tobie et al., 2006; Radebaugh et al., 2007 scenario 2)	Recent crustal thickening due to localized extension	Blocks and grabens T8	Mountains due to extension: Basin and Range Province (Harcuvar Mountains, Gila Mountains, Maricopa Mountains) (Radebaugh et al., 2007)
Blocks of impact ejecta (Radebaugh et al., 2007 scenario 3)	Deposition of ejecta blocks around craters in a radial manner	Blocks of mountains T3	Ejecta patterns: Meteor crater, Arizona
Dissection and erosion (Radebaugh et al., 2007 scenario 4; Lunine et al., 2008)	Erosion and incision of terrains that form regional uplifted structures	Mountainous region T13	Erosional geomorphological structures: Colorado Plateau, USA (Lorenz and Lunine, 2005; Radebaugh et al., 2007). It is dissected by a number of long north–south trending normal faults while deep entrenchment of streams and differential erosion have formed high standing crustal blocks

mountain ridges (in this paper we will refer to mountain ridges as ridges), chains of elevated (uplifted) ground that extend for some distance. The major mountains and ridges on Titan are listed along with their location and observational characteristics in Table 2a.

Table 2a points at two intriguing aspects: mountain-like edifices exist at almost all latitudes on Titan; however, they are concentrated in the equatorial region at latitudes between 30°S and 30°N (Lopes et al., 2010). Their height is significantly lower than that of the terrestrial mountains ranging from 100 to 2000 m (Barnes et al., 2007; Radebaugh et al., 2007; Soderblom et al., 2007b; Sotin et al., 2007; Mitri et al., 2010). This may be partly due to erosional processes, as it is suggested by the blanket-like

Please cite this article as: Solomonidou, A., et al., Morphotectonic features on Titan and their possible origin. Planetary and Space Science (2012), http://dx.doi.org/10.1016/j.pss.2012.05.003

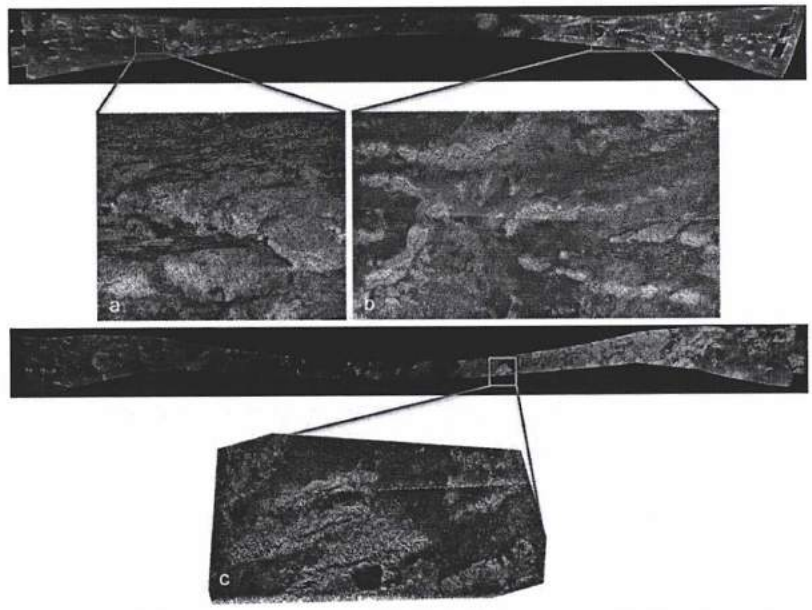

Fig. 2. Major mountainous regions on Titan. (a) Mountain extends for almost 240 km (NASA/JPL). (b) Long bright ridges with multiple mountain peaks were observed in T8 on October 28, 2005 (linear mountains extend from 13-5°S to 198-225°W) (e.g., Radebaugh et al., 2007; Lopes et al., 2010), and extend over 480 km (NASA/JPL). (c) Three radar bright parallel ridges (2°S, 127°W) within the mountainous area of Xanadu from T43 of May 12, 2008, the length of the image is almost 400 km (e.g., Mitri et al., 2010) (NASA/JPL/Space Science Institute).

materials that surround these structures (Radebaugh et al., 2007). Alternative hypotheses include the construction of Titan's mountains with materials with properties preventing height growth (Radebaugh et al., 2008) and the effects of high temperature gradients on the ice shell which, according to the calculations of Mitri et al. (2010), result in mountains from 100 to 2700 m high. Similarly to Earth where terrain topography is defined by the interaction of tectonism and erosion (Montgomery and Brandon, 2002), we suggest here that there is a strong connection between slope morphology and erosional rates on Titan due to its extreme conditions of hydrocarbon rainfall and/or winds.

Fig. 2 presents three portions of the T8 and T43 RADAR swaths that provide the most reliable evidence so far for the existence of mountains and ridges on Titan.

3.2. Related mechanisms and terrestrial analogs

The mechanisms for mountain formation on Titan are summarized in Table 2b and include pure extension (Tobie et al., 2006; Sotin et al., 2007; Radebaugh et al., 2007—scenario 2), pure compression (Radebaugh et al., 2007—scenario 1; Mitri et al., 2010) and transitions between compressional and extensional stresses (Mitri and Showman, 2008). Extensional deformation is observed on all icy moons, but if orogenesis on Titan can be attributed to compressional forces this will render Titan unique.

Orogenesis in the terrestrial analog is predominantly a compressional event due to the coming together of the lithospheric plates floating on the plastic asthenosphere. The phenomenon is attributed to global convection initiated from the liquid external core and might not be random but with peaks related to the orbit of our Solar System around the galactic center. Terrestrial orogenesis results in forms and tectonic structures such as folds and thrust faults. Such compressional structures are represented by the mountain chains of the Rocky Mountains, the Andes and the Himalayas. Fig. 3 shows the Rocky Mountains, an almost 5000 km long mountain chain, extending from Canada to the western United States. This region was formed by subduction of the Pacific plate beneath the North American plate (Bird, 1998), when two tectonic plates of different densities sank one beneath the other inducing internal compressive forces within the plates. Mitri et al. (2010) argued for Titan that ice floes of altered densities, moving on a liquid layer, could reproduce structures and simulate phenomena similar to subduction. If this hypothesis is confirmed in the near future by geophysical measurements and modeling, and under the assumption that ice floes would react exactly like silicate plates to the stresses simulating subduction, something not impossible as shown in Table 1, then we may infer that what we see on Titan is an Earth-like mountainous terrain with peaks and extensive ranges.

Formation of mountains due to extension on Earth is represented by the classical example of the Basin and Range area and other examples listed in Table 2b. The geomorphology of Basin and Range (Hawkesworth et al., 1995) consists of separate and semi-parallel mountain ranges as seen in Fig. 4. The formation of the area is attributed to crustal extension and associated development of large faults along which mountains were elevated and valleys have submerged. These endogenous tectonic processes resulted in a geological terrain characterized by morphotectonic

Please cite this article as: Solomonidou, A., et al., Morphotectonic features on Titan and their possible origin. Planetary and Space Science (2012), http://dx.doi.org/10.1016/j.pss.2012.05.003

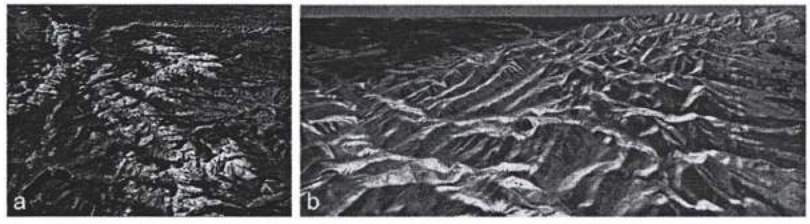

Fig. 3. Rocky Mountains, USA (a) in Landsat TM scene with DEM data (Credit: Federation American Scientists FAS). (b) 3-D perspective view by combining two spaceborne radar images (PIA01840 NASA/JPL).

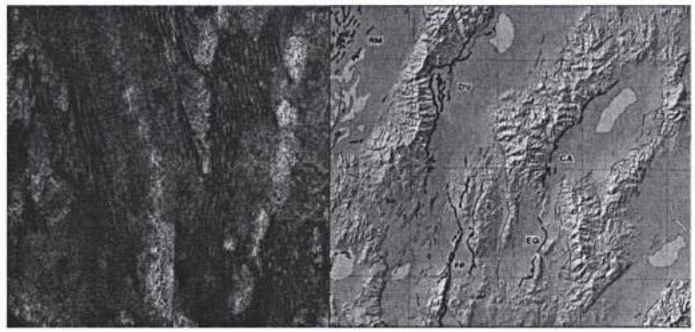

Fig. 4. (left) Fault-block mountains on Titan (portion of Fig. 2b) (PIA03566 NASA/JPL) formed possibly through crustal extension (Radebaugh et al., 2007). (right) Relief map of the Basin and Range province in west-central Nevada (USGS) displaying the parallel ranges and valleys created by crustal thinning and fracturing by extensive stresses.

features such as linear mountain ranges and valleys. Fluvial, aeolian and other exogenous processes subsequently modified these features.

However, convective stresses on silicate bodies tend to be larger and their rheological length scales are typically greater (Table 1). In Titan therefore it is essential to note that local/regional rather than global stress mechanisms are commonly suggested in the models for mountain building. Regional or local stress mechanisms invoked in these models include (a) convection, which depends in the ice shell thickness, (b) local gravity, and (c) ice viscosity, which depends on the temperature and mostly on the grain-size (Barr and Pappalardo, 2005; Collins et al., 2009). Indeed, on large icy satellites, layers of high- and low-pressure ice may convect separately (McKinnon, 1998).

Among the local stress mechanisms presented above, one can include lateral pressure gradients that may have as a consequence the lateral flow of floating ice shells on their low viscosity base. Rigid ice floes rupturing and colliding are reminiscent of plate tectonics albeit in a random fashion. This could lead to the creation of blocks of high-standing topography that would subsequently be subjected to erosional processes. Such elevated morphotectonic features on Titan, as mountains, ridges, hills and ranges, indicate a formation preference around the equatorial zone of the moon (Barnes et al., 2007; Radebaugh et al., 2007; Mitri et al., 2010).

4. Morphotectonics of faults and transverse processes

In this section, we describe Titan's morphotectonic features as a combination of a formation process and one or more superimposed "transverse processes" that occurred at the same time or subsequently, modifying the initial shape of the feature.

4.1. Tectonic control on Titan's linear features: Faults, fractures, canyons and drainage networks

In geology, a fault is a rupture that separates a rock unit into two parts, moving one relatively to another, in a microscale or a whole field in a macroscale. A variety of geological processes are associated with faults and therefore their analysis is very important. For instance, geologists consider the direct relation of earthquakes with faults, or the penetration of igneous rocks on Earth's crust along faults, or also the interaction of faults in the development of sedimentary basins. On the other hand, canyons are another type of crustal scars, formed on Earth by the accelerated erosion by rivers entrenched after tectonic activity and trying to reach base-line elevation (Schumm et al., 2002). On Titan the observed faults, fractures, canyons and ground lineaments are most likely the results of crustal movements due to tectonic and/or volcanic processes as well as structures associated with fluvial networks controlled by tectonism (Table 3). An investigation of canyon formation can augment our understanding of Titan's geology. A study in 2009 by Burr et al. (2009) provided evidence on the influence of subsurface tectonic activity on drainage patterns as observed by SAR data. Based on that, we can infer that these fluvial networks are morphotectonic features since there are indications that both tectonic and fluvial processes operate for their formation. Titan studies based on observations and mapping, have suggested the presence of fault formations. Table 3 summarizes their major observations by Cassini.

Please cite this article as: Solomonidou, A., et al., Morphotectonic features on Titan and their possible origin. Planetary and Space Science (2012), http://dx.doi.org/10.1016/j.pss.2012.05.003

As expected from the study of other icy satellites, the majority of formation mechanisms suggest extensional style tectonism. In the areas where fluvial networks seem to be controlled by tectonic patterns, the surface material seems to have the proper elasticity to create linear fractures. At the Huygens landing site, as proposed by Soderblom et al. (2007b), the linear structures can function as the ideal path for the hydrocarbon liquids to escape towards the surface. Furthermore, the observed radial fault system around the possible calderas of Hotei Regio (Soderblom et al., 2009), argue in favor of cryovolcanism since the identification of radial faults around caldera formations also on Earth, are indicators of ground elevation due to volcanic activity.

Fig. 5 displays a complex feature on Titan (71°S, 240°W), which — even if it is not confirmed by radar data processing yet — it appears to be a canyon-like morphotectonic feature since it consists of a sinuous dark, rather narrow feature with tributary-like off shoots and it is limited on all sides by high albedo i.e. elevated terrains (e.g. Radebaugh et al., 2007). The morphology of the bright and the dark shape of this region resembles the terrestrial analog, which is the Grand Canyon in the United States. This terrestrial feature is adjacent to the Basin and Range Province that was mentioned earlier. The formation of the Grand Canyon on Earth is the end result of the extensional tectonics that formed the Basin and Range Province and of continuous rifting and erosion (Sears, 1990).

From Table 3 we can distinguish a tendency for preferential formation of these features between 10°S and 26°S, that is, within the zone where mountains are formed. Such observations imply crustal movements are more frequent within this zone than around the poles, including compressional and extensional stresses. However, Titan's limited-coverage observations (less than 50% of the surface), with instruments incapable of precisely unveiling its geology, make this aspect a subject for future exploration.

4.2. *Cryovolcanism and association with morphotectonics*

Plate tectonics and volcanism are strongly associated on Earth (McDonald, 1982) and this can also be the case on Titan in the presence of tectonic features overlying a liquid water ocean. These can function as leading 'pathways' for the ammonia–water cryomagma to reach the surface and for the release of methane. Liquid pockets with methane clathrates and with a high ammonia mass concentration in a water solution can dissociate in the ice shell and eventually exsolve on the surface and in the atmosphere (Tobie et al., 2006; Mitri et al., 2008). Hence, cryovolcanism can also act as the dynamic force that deforms tectonic features. Cryovolcanism is believed to represent an important geological process in the history of several icy Saturnian satellites and other icy satellites, such as Triton (Kargel, 1994; Fagents, 2003; Lopes et al., 2007a). Gaidos (2001) stated that tectonic extension could trigger cryovolcanic eruptions by reducing the minimum normal stress in an aquifer to a value

Table 3
Major fault, fracture and canyon formations on Titan.

Location	Characterization	Proposed mechanism	Flyby/Time	Instrument (reference)
15°S, 155°W	Conjugate-like faults	i. Large scale tectonic modification of bedrock material. ii. Fluvial sapping of bedrock that enlarges tectonic zones of weakness.	T0/July 2004 TA/October 2004 TB/December 2004	ISS (Porco et al., 2005)
10°S, 145°W 0°N, 180°W	Joints and/or faults	Control by a subsurface tectonic structural fabric due to orbital processes (diurnal tides, non-synchronous rotation: tensional stresses)	T13/April 2006 T44/May 2008	RADAR (Burr et al., 2009)
10°S, 192°W	Linear fault patterns/ canyon-like formations	Preexisting faults reactivated from cryovolcanism and filled with deposited material and formed canyon-like systems	Huygens DISR/ January 2005	DISR (Soderblom et al., 2007b)
15°S, 100°W	Lithospheric fault-blocks	Extensional crustal stresses	Model	(Radebaugh et al., 2011)
26°S, 78°W	Radial fault system	i. Hot plume uplift and crust elevation-fault formation due to extension stresses. ii. Large ancient impact crater.	T47/November 2008	VIMS (Soderblom et al., 2009)

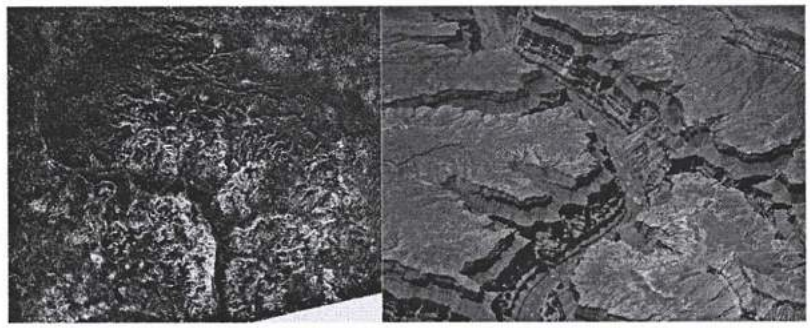

Fig. 5. (left) Radar image showing canyon-like systems on Titan (71°S, 240°W) (PIA12036 NASA/JPL). (right) Massive canyon formation on Earth, Grand Canyon, USA (USGS).

Please cite this article as: Solomonidou, A., et al., Morphotectonic features on Titan and their possible origin. Planetary and Space Science (2012), http://dx.doi.org/10.1016/j.pss.2012.05.003

below the pore pressure. On Titan, a few topographic features are candidates for large volcanic edifices (Table 4).

The mechanism of cryovolcanism resembles terrestrial type volcanism, however the cryomagma differs from the terrestrial magma in composition, texture and temperature. Indeed, the cryomagma i.e. aqueous solutions of ammonia, methane, salts, etc., can be found at temperatures well below the freezing point of pure water and degassing replaces the traditional silicate volcanism. Cryovolcanic structures are openings, or ruptures, on a planetary surface or crust, allowing for various internal products like water, other chemical components, gases and cryoclastic ash to escape from the planet's interior (Fortes et al., 2007).

On Titan, internal heating due to radiogenic decay and tidal forces along with pressure fluctuations may trigger cryomagma eruptions. The cryolava deposition would then happen at temperatures much lower than the terrestrial ones (Davies et al., 2010). In general, the temperatures of most terrestrial magma types range from 1150 to 1470 K while a plausible range of the Titan cryomagma temperatures is between 177 and 239 K (Mitri et al., 2008). Besides predictions from theoretical modeling we also have surface features indicating possible cryovolcanism on Titan. Indeed, lobate and fan shaped features seen in radar images have been interpreted as cryovolcanic in origin, as for instance, the lobate circular structure of Ganesa Macula (50°N, 87°W) (Lopes et al., 2007a). The structure contains bright rounded features, interpreted as cryovolcanic flows, while the curved or linear shapes are lineaments that could be caused by elevation of the crust due to cryovolcanic activity (Lopes et al., 2007a). Other such features like Tui Regio, Hotei Regio and Sotra Facula are more extensively discussed hereafter. The identification of cryovolcanic structures is rendered difficult mainly for two reasons: firstly, the masking of cryovolcanic features by the interaction with major exogenetic processes, e.g. by fluvial or aeolian deposits (Lopes et al., 2010). As an example of the latter case, Lopes et al. (2010) report in the Winia Fluctus (45°N, 30°W) a dune field, which has partially covered a cryovolcanic edifice. Secondly, the Cassini instrumentation with relevance to cryovolcanic investigations (SAR and VIMS) is not adequate on terms of spatial and spectral resolution (Elachi et al., 2004; Brown et al., 2004).

However, we have currently some cryovolcanic candidate features. The most probable ones are three areas located close to the equator. Tui Regio, as well as Hotei Regio, lie within the bright region of Xanadu (100°N, 15°S), a large, reflective equatorial area. Tui Regio presents relatively high 5-μm reflectivity and its size is 1500 km long and 150 km wide (McCord et al., 2006). It is a massive flow-like terrain, which resembles flow fields in volcanic areas on Earth. In 2006, Barnes et al. (2006) noted that there are two bright and long areas within Tui Regio that are filled with a material darker than the surrounding terrain, forming a trench. These areas, located within the northwestern portion of Tui Regio's flow and including the trending dark linear marks (Fig. 6), may have a regional tectonic origin (Barnes et al., 2006). Additionally, the latter authors pointed out a linear dark feature with similar spectral behavior which surrounds the southern bright region, suggesting that it might also be formed by regional tectonics. A recent and very reliable candidate for cryovolcanic activity is Sotra Facula; an area 235 km in diameter including a 1 km high mountainous peak next to a 1.5 km wide crater-like feature from which lobate flows seem to originate (Kirk et al., 2010; Lopes et al., 2010). Indeed, this area displays varying topography with adjacent uplifts and pit features suggesting probable tectonic control. Hotei Regio is also another candidate for the presence of tectonic features within a probable cryovolcanic region (Wall et al., 2009). Hotei Regio extends over 700 km and includes a 1 km wide topographic depression, characterized as a basin filled with flow-like features, a ridge-like mountainous terrain that surrounds the basin, dendritic channels, two caldera-like structures, dark blue patches (as seen in VIMS infrared images; a color that suggests enrichment in water ice), and possible alluvial deposits (Soderblom et al., 2009). Hotei Arcus, a bright arc in the southern margin of Hotei Regio, may represent a heavily eroded crater (Barnes et al., 2005). This assumption reinforces the hypothesis of interplay among the different types of processes. Soderblom et al. (2009) correlated VIMS and RADAR images in order to unveil the geological history of this area. Their interpretation suggests that a wide range of processes occurred — or are still occurring — in this varied terrain, including tectonism. Furthermore, they suggested that impact-induced faults created

Table 4
Candidates of major cryovolcanic features on Titan and their association with volcanotectonic processes.

Location	Name	Description	Possible tectonic features
20°S, 130°W	Tui Regio	Flow-like region	Trending dark linear marks on VIMS data (Barnes et al., 2006)
26°S, 78°W	Hotei Regio	Volcanic-like terrain	Circular tectonic features (Soderblom et al., 2009)
15°S, 42°W	Sotra Facula	Volcanic-like terrain	Topographic elevation, mountain-like structures (unidentified) (Lopes et al., 2007b)

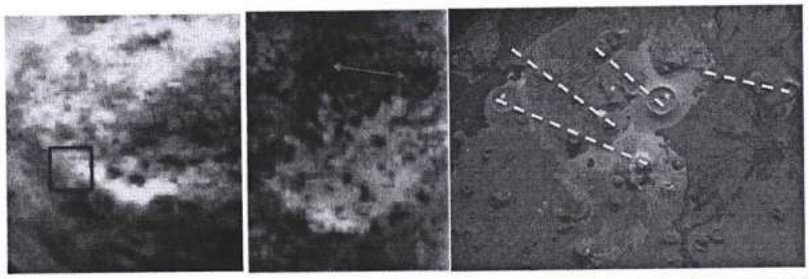

Fig. 6. Area on Tui Regio (left) with possible tectonic influence; two dark patches on Hotei Regio (middle) assumed to be volcanic caldera ridges (NASA/JPL/University of Arizona); Harrat Khaybar (right), massive volcanic terrain in western Saudi Arabia on Earth; the dashed lines indicate the linear trend of the volcanic vents suggesting tectonic control (NASA).

Please cite this article as: Solomonidou, A., et al., Morphotectonic features on Titan and their possible origin. Planetary and Space Science (2012), http://dx.doi.org/10.1016/j.pss.2012.05.003

zones of weakness on which volcanism and tectonism occurred. The two dark morphotectonic features (Fig. 6) north of Hotei Regio, are interpreted as cryovolcanic calderas by Soderblom et al. (2009).

A terrestrial region that appears to resemble the evolution of Hotei Regio is Harrat Khaybar, located in north of Medina in Saudi Arabia. It is a 14,000 km^2 volcanic field that was formed by eruptions along a 100 km N–S linear vent system. The area contains multiple volcanic rock types, lava flows, and volcanic structures such as calderas and domes (e.g., Baker et al., 1973). The internal mechanism that most likely formed the terrain is a mantle plume causing diffused lithospheric extension (Chang and Van der Lee, 2011). The association of the volcanic centers that lie over a linear zone of weakness with the Red Sea transform fault i.e. conservative plate boundary—where plates slide past each other along transform faults, characterizes them as geological structures that are presently active (Rehman, 2010). This suggests that local movements of parts of the crust, probably affect areas of great extent like Hotei Regio and Harrat Khaybar, even if they are not located precisely in the center of the active area. In the case of Harrat Khaybar, the adjacent Red Sea fault continues to propagate: its rifting causes seafloor spreading, triggering the volcanic centers of the region (Camp et al., 1991). Such a process illustrates the relation between the terrestrial volcanic terrains and tectonism, a relation that seems possible for Titan's case as well.

Tui Regio, Hotei Regio and Sotra Facula are all located in the 15°S–30°S latitudinal zone which is close to the southern margin of Xanadu (Soderblom et al., 2009), implying that the region might be an extensive zone of crustal weakness. The existence of possible volcanic and tectonic features within a specific area seem to be manifestations of the most active region of Titan like the boundaries of tectonic plates on Earth. Although still under investigation in Titan's case, the definite identification and understanding of morphotectonic features in these regions is crucial in order to determine the presence and origin of zones of crustal weakness, which will in turn impose additional constraints on cryovolcanism on Titan. Indeed, on Earth, as well as on other planetary bodies, the interplay of volcanism and tectonism causes the formation of extensive and distinct geological terrains.

The moons of Jupiter, Europa and Ganymede, possibly also display similarities with the morphotectonics of Earth (volcanism–tectonism) and of the Saturnian icy satellites (cryovolcanism–tectonism). Fig. 7a shows Europa's ridges, junctions and domes, as seen by the Galileo instrument Solid State Imager (SSI), which are typical geological expressions on this moon. The ridges are most likely formed by cryovolcanic processes probably causing deposition of subsurface materials over surface units, accompanied by tectonic movements, that formed the lineaments (Figueredo and Greeley, 2004). This extensional volcano-tectonic mechanism is similar to the terrestrial mid-oceanic rifting (Prockter et al., 2002). On Ganymede, volcanic processes may have occurred in the past, but current evidence suggests the presence of tectonic processes (e.g., Head et al., 2002). The linked tectonic–cryovolcanic hypothesis suggests graben rupture (depressed block of ice bordered by parallel faults) due to lithospheric extension and cryovolcanic deposition caused by flooding of the internal material (cryovolcanic resurfacing) (e.g., Schenk and McKinnon, 1985; Murchie et al., 1986). Also fault blocks operating as zones of weakness can act as pathways for the bright material onto the surface while the crustal movements could produce the bright ridges (e.g., Head et al., 1997, 2002) (Fig. 7b).

Ganymede, and partially Europa, are the targets of a future mission proposal to the Jovian system, which will, among others, could explore the icy moons' interior heat potential, as well as, the surface motion and morphology, with improved and enhanced instrumentation in order to better understand their surface composition, internal structure, dynamics and the morphotectonics. Further investigation and comparison of the morphotectonic features of many of the icy satellites will shed light on the potential different internal mechanisms that operate in the Solar System.

5. Discussion

The morphotectonic structures presented here are related to the most elevated, as well as the most fractured features observed on Titan. Major mountainous regions are concentrated in mid-latitudes between 30°S and 30°N and probable cryovolcanic areas are located within the same zone (20°S–30°S). Linear features are displayed also within the same region (10°S–26°S). Fig. 8 represents a location map of the major morphotectonic features presented in this study.

We have argued here that all these features are related to surface stress fields. In analogy with terrestrial morphotectonic structures, the shape, size and morphology of Titan's observed mountains, ridges, hills and linear features such as faults, major fractures and canyons probably originate through some form

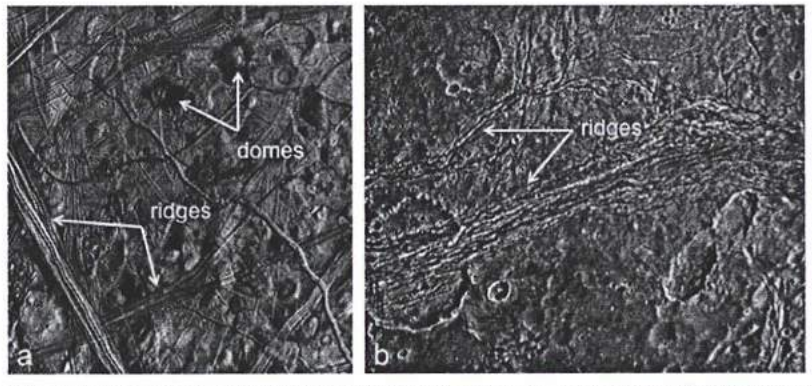

Fig. 7. (a) Europa's major geo-structures that may have formed due to volcanic and tectonic processes acting together (NASA/JPL-Caltech). (b) Ganymede's grooved and tectonic terrain (NASA/JPL/Brown University).

Please cite this article as: Solomonidou, A., et al., Morphotectonic features on Titan and their possible origin. Planetary and Space Science (2012), http://dx.doi.org/10.1016/j.pss.2012.05.003

compressional and extensional tectonic activity. Titan's rigid crust and the probable existence of a subsurface ocean create an analogy with terrestrial, at least surficial, plate tectonics.

If in future missions a number of Titan's surface features are definitely identified as a result of compressional processes, as it has been proposed here, and despite the fact that large stresses are required to form compressional features (Pappalardo and Davis, 2007), then this will render Titan unique among the rest of icy satellites where extensional features are dominant (Jaumann et al., 2009) and will ratify the thesis of Mitri et al. (2010) that some of Titan's mountains represent folds and/or thrusts.

On the other hand, in regard to the extensional features on Titan as compared to their terrestrial analogs one may question if there are some essential differences in the development and propagation of fractures in the icy crusts vis-à-vis the silicate crusts.

However, before addressing these questions, one should initially examine which factors control tectonism on a planetary body; essential stress mechanisms that can be either global, regional and local. Global stress mechanisms include tides, non-synchronous planetary rotation, polar wander, despinning, orbital recession and radiogenic decay. One major stress mechanism is provided by *convection*. Another array of mechanisms is due to volume changes up to the large density contrast between ice-I and water and is applicable to icy satellites (Collins et al., 2009). Finally, "impacts" represent another local stress mechanism. To global, regional or local stresses, Solar System bodies and particularly their crusts may react in a brittle, ductile or more rarely elastic fashion, producing corresponding landforms. In this respect it is essential to compare and contrast the mechanical properties of icy and silicate crusts, as well as, the order in which stress mechanisms occur, to find correlations between the morphotectonic features on Earth and those on Titan (Radebaugh et al., 2007; Collins et al., 2009).

Thus, a question arises: is there some essential difference in the development and propagation of faults in the icy crust with respect to a silicate crust? As indicated in Table 1, ice and silicates mainly share a similar crystal structure, differ in melting temperature but when ice involves water and methane, an additional similarity with the silicates is found in the three physical states of the material (solid, liquid, gas).

Earth and Titan share all the global stress mechanisms and sources of internal heat such as radiogenic decay, heating by applied tidal forces and primordial heat.

However the analogy probably stops here since Earth has preserved a capital of its primordial heat. The outer core of the Earth with a thickness of 2890–5150 km has a temperature range of 4400–6100 °C, similar to the photosphere of the Sun. Furthermore the total heat flux from Earth's interior ranges from 0.08 to 0.4 W m^{-2} (Pollack et al., 1993; Davies and Davies, 2010). Due to the state (liquid) and composition (Fe–Ni) of Earth's outer core, *thermal runaways* occur at the core–mantle interface and resurface as hot spots, causing local mantle convection and induce plate motion which implies the breaking of continents (Africa) or supercontinents (Pangea).

Hot spot volcanism is found in the middle of lithospheric plates and on the margins of extensional plates. Volcanism also occurs in compressional plate margins followed by orogenesis (mountain building). Titan's primordial heat flux from the satellite's interior is of the order of 0.02–0.06 W m^{-2} and Mitri et al. (2010) proposed that it can similarly result in crustal fold processes and mountain building.

On Titan, stress mechanisms even if global, as in the case of tides, can have very local effects: for instance Saturnian tidal forces result in a concentration of morphotectonic structures mainly around Titan's equator. It is not a random event that all the three candidates for cryovolcanic areas are concentrated in Titan's equatorial zone. Actually, it will be surprising if future detailed observations refute the case for cryovolcanism on Titan in this area, given positive indications from current studies (Lopes et al., 2010; Solomonidou et al., in preparation). Morphotectonic features resulting from tidal-induced convection have different ages, as can be shown from superposition and cross-cutting relationships. Mountains are old (20–100 million years—Radebaugh et al., 2007) and probable cryovolcanic areas are younger (less than 10,000 years for Hotei Regio—Soderblom et al., 2009). This is to be expected since tidal-induced convection will cause ice elevations with subsequent breaking of the surface ice and formation of fractures (extension). The ice floats may collide

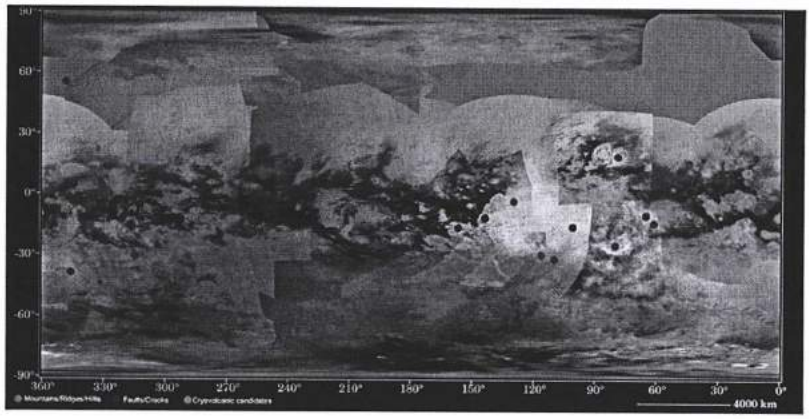

Fig. 8. Location map of the major morphotectonic features on Titan (background map credit: NASA/JPL). In green: mountains, ridges and hills; in blue: linear features, faults, fractures, canyons; in red: probable cryovolcanic regions. (For interpretation of the references to color in this figure legend, the reader is referred to the web version of this article.)

Please cite this article as: Solomonidou, A., et al., Morphotectonic features on Titan and their possible origin. Planetary and Space Science (2012), http://dx.doi.org/10.1016/j.pss.2012.05.003

against each other (compression) forming mountain- or ridge-like features. Subsequent extension of the so-formed fractures will provide the pathways for cryovolcanism, which will be the younger event.

Primordial heat, as well as, heat produced by radiogenic decay and heat induced by tidal forces can be dissipated both by conduction and/or convection. It has been shown that transitions from a conductive to a convective state for an ice shell, overlying a pure liquid ocean (Tobie et al., 2005), can have major effects on surface morphotectonics (Mitri and Showman, 2008). The same authors have shown that thermal convection can occur under a range of conditions in the ice-I shells of Titan and two possible scenarios can follow. A thin ice with a low viscosity base (I) and a thick ice with a high viscosity base (II). Thus, Mitri and Showman (2008) proposed oscillations in the thermal state of the ice-I shell of the Saturnian satellites, which may cause repeated episodes of extensional and compressional tectonism. Similarly on Earth, a current widely accepted internal evolution model suggests that expansion and contraction processes are due to internal thermal runaway cycles and can be important in controlling geotectonic mechanisms (Rice and Fairbridge, 1975; Fowler, 1986; Baumgardner, 1994, 2003; Benn et al., 2006).

Thermal stresses are responsible for updoming, weakening and subsequent fracturing of the crust of a planetary body. On Earth, such a paradigm is provided by the continent of Africa where hot spot activity has resulted in updoming, fracturing and volcanism (East African Rift, Ahaggar Mountains, Table 2a). On Titan, zones of tectonic weakness have probably formed in an analogous manner i.e. as a consequence of thermal stresses and weakening of the crust with concomitant formation of open fissures, which act as pathways for the ejection of material from the interior (cryovolcanism) as it has already been proposed for Enceladus and Europa (Manga and Wang, 2007).

Localized compression and crustal thickening can also lead to mountain building on Titan. Linear mountains in T3 and T8 swath, seen in radar data, probably have formed this way (Fig. 3a and b; Table 2b). A terrestrial analog can be provided by the Laramide Orogeny. The Laramide event that affected Western-North America during Late Cretaceous and Early Paleogene time, involved compressive forces, conductive heating and crustal thickening that eventually led to mountain building (orogeny) (Dickinson and Snyder, 1978). A similar example is provided by the Acadian Orogeny during middle Paleozoic, which has affected the Eastern-North America as the result of collision of Baltica plate with the Laurentia.

The proposed formation mechanism for Titan's mountains, mainly the ones observed during T8, T30 and T43 flybys (Fig. 2c), concerns folding of the upper crust due to high heat flows from the interior and high temperature gradients in the past (Table 2b). A terrestrial analog, the Rocky Mountains chain in Western-North America (Fig. 3), was formed over an area where high values of mantle heat flow occur (Bird, 1998).

For the high-standing ranges of the T20 radar swath a formation mechanism has been proposed by Sotin et al. (2007) involving the generation of stresses by tectonic extension that penetrate the icy shell and create pathways for the internal material. This finds a terrestrial analog in the formation of the Mid Atlantic Ridge in Atlantic Ocean where divergent tectonic plates are associated with magma upwelling due to partial melting of the upper mantle in the interior.

Other surface features on Titan that seem to be the result of intense forces of tectonic extension are the probable blocks and grabens seen in T8 radar swath (Tobie et al., 2006; Radebaugh et al., 2007). On Earth, the Basin and Range Province in USA (Fig. 4; Table 2b) is such a large terrain subjected to forces of tectonic extension. As it can be seen from Fig. 4 a striking structural similarity exists in the morphology of the T8 mountain range on Titan and the Basin and Range Province on Earth. Alternative proposed mechanisms for *mountain formation* on Titan do not involve crustal movements: Radebaugh et al. (2007) argue that blocks of mountains viewed in T3 swath could have been formed by *impact ejecta*. Such deposits resemble those of Meteor Crater in Arizona, USA where blocks of ejecta deposited 1200 m away from the rim create hilly features (Ramsey, 2002). Furthermore, two terrestrial analogs presented and described in this study that seem to have a major resemblance with *canyon-like* and *cryovolcanic* features seen on Titan, are the Grand Canyon (Fig. 5) and the Harrat Khaybar (Fig. 6). Both terrestrial terrains consist of a number of geological features that have been subject to multiple processes. Titan's surface seems to be as complex as the Earth's and may be the end result of the action of multiple processes as well.

The fact that the mountains and ridges seem to be concentrated around Titan's equatorial band is a very strong argument for tidal forces shaping these morphotectonics features. However, Lopes et al. (2010) showed that mountains exist at other latitudes, a possible sign for a global source of stress as well. It is plausible that radiogenic decay would heat uniformly the entire satellite, similarly to what occurs on Earth (Dickin, 1995), and lead to morphotectonic structures evenly distributed all over the body's crust. We argue, nevertheless, that mountain ranges are more extensive at the equator of the satellite as a result of tidal forces since the very geometry of tides causes local stresses larger at the equator than anywhere else, inducing convection and therefore enhancing mountain formation. This mountain formation can be contrasted with that on Earth where mountains occur globally along collisional plate boundaries. Furthermore, as noted hereabove, radiogenic heat production on small bodies like Titan or even Mars has significantly decreased over a long period of time (e.g., Schubert et al., 1986; Grasset and Sotin, 1996; Grott and Breuer, 2008). It should be noted here that Saturn's tides are still heating up Enceladus' interior (Hurford et al., 2007).

The existence of tectonism on Titan can provide significant insights on the internal structure of the Saturnian satellite. In reference to the terrestrial paradigm, where rigid lithospheric plates *'float'* on a weaker asthenosphere, it could provide indirect evidence for the existence of a subsurface ocean on Titan. The importance of deciphering morphotectonic features on Titan that can be linked to tectonism has also consequences in elucidating the methane cycle on Titan in analogy with the link between terrestrial tectonics and the global terrestrial carbon cycle (Bolin, 1981; Ruddiman, 1997). More specifically, Titan's tectonic activity can probably be directly related to the replenishment of the atmosphere in methane (Sotin et al., 2005; Atreya et al., 2006; Tobie et al., 2006; Coustenis and Taylor, 2008; Lunine and Atreya, 2008; Mitri et al., 2008).

Finally, the origin of some morphological features can be attributed to exogenous processes such as *meteorite impacts* (Moore and Pappalardo, 2011), *aeolian processes* (Stofan et al., 2006; Radebaugh et al., 2009) and *fluvial erosion* (Porco et al., 2005; Tomasko et al., 2005), especially *monsoonal rainfall* causing flooding mainly in the equatorial region (Tokano, 2011).

The Cassini–Huygens mission has significantly improved our understanding of Titan and the coupling of its atmosphere and surface. Since 2004 and for another five years, Titan is investigated by Cassini's flybys. However, only limited surface coverage will be achieved at high spatial resolution. Therefore, the composition and evolution of its diverse surface features will still demand extensive future investigation.

Acknowledgments

The authors are grateful to Julie Castillo, Ellen Stofan and an anonymous referee for extremely constructive and extensive

Please cite this article as: Solomonidou, A., et al., Morphotectonic features on Titan and their possible origin. Planetary and Space Science (2012), http://dx.doi.org/10.1016/j.pss.2012.05.003

comments that have immensely helped in improving the original manuscript. MH and AC acknowledge financial support from the French Agence Nationale de la Recherche (ANR Project: CH4@Titan, PI: Athena Coustenis).

Anezina Solomonidou has been co-financed by the European Union (European Social Fund—ESF) and Greek national funds through the Operational Program "Education and Lifelong Learning" of the National Strategic Reference Framework (NSRF)—Research Funding Program: Heracleitus II. Investing in knowledge society through the European Social Fund.

References

Atreya, S., Adams, E., Niemann, H., Demick-Montelara, J., Owen, T., Fulchignoni, M., Ferri, F., Wilson, E., 2006. Titan's methane cycle. Planetary and Space Science 54, 1177–1187.

Baker, P.E., Brosset, R., Gass, I.G., Neary, C.R., 1973. Jebel al Abyad: a recent alkalic volcanic complex in western Saudi Arabia. Lithos 6, 291–313.

Barnes, J.W., Brown, R.H., Turtle, E.P., McEwen, A.S., Lorenz, R.D., Janssen, M., Schaller, E.L., Brown, M.E., Buratti, B.J., Sotin, C., Griffith, C., Clark, R., Perry, J., Fussner, S., Barbara, J., West, R., Elachi, C., Bouchez, A.H., Roe, H.G., Baines, K.H., Bellucci, G., Bibring, J.P., 2005. A 5-micron-bright spot on Titan: evidence for surface diversity. Science 310, 92–95.

Barnes, J.W., Brown, R.H., Radebaugh, J., Buratti, B.J., Sotin, C., LeMouelic, S., Rodriguez, S., Turtle, E.P., Perry, J., Clark, R., Baines, K.H., Nicholson, P.D., 2006. Cassini observations of flow-like features in western Tui Regio, Titan. Geophysical Research Letters 33, L16204.

Barnes, J.W., Radebaugh, J., Brown, R.H., Wall, S., Soderblom, L., Lunine, J., Burr, D., Sotin, C., Lemouelic, S., Rodriguez, S., Buratti, B.J., Clark, R.N., Baines, K.H., Jaumann, R., Nicholson, P.D., Kirk, R.L., Lopes, R., Lorenz, R.D., Mitchell, K., Wood, C.A., 2007. Near-infrared spectral mapping of Titan's mountains and channels. Journal of Geophysical Research 112, E11006.

Barr, A.C., Pappalardo, R.T., 2005. Onset of convection in ice I with composite Newtonian and non-Newtonian rheology: application to the icy Galilean satellites. Journal of Geophysical Research 110, E12005.

Baumgardner, J.R., 1994. Runaway subduction as the driving mechanism for the Genesis Flood. In: Proceedings of the Third International Conference on Creationism, Technical Symposium Sessions. Creation Science Fellowship, Pittsburgh, pp. 63–75.

Baumgardner, J.R., 2003. Catastrophic plate tectonics: the physics behind the Genesis Flood. In: Proceedings of the Fifth International Conference on Creationism, pp. 113–126.

Beeman, M., Durham, W., Kirby, S., 1988. Friction of ice. Journal of Geophysical Research 93, 7625–7633.

Benn, K., Mareschal, J.-C., Condie, K.C., 2006. Archean geodynamics and environments. Geophysical Monograph Series, 164.

Bird, P., 1998. Formation of the Rocky Mountains, Western United States: a continuum computer model. Science 239, 1501–1507.

Bolin, B., 1981. Carbon Cycle Modelling. Plenum Press, New York.

Brown, R.H., Baines, K.H., Bellucci, G., Bibring, J.-P., Buratti, B.J., Capaccioni, F., Cerroni, P., Clark, R.N., Coradini, A., Cruikshank, D.P., Drossart, P., Formisano, V., Jaumann, R., Langevin, Y., Matson, D.L., McCord, T.B., Mennella, V., Miller, E., Nelson, R.M., Nicholson, P.D., Sicardy, B., Sotin, C., 2004. The Cassini Visual and Infrared Mapping Spectrometer (Vims) Investigation. Space Science Reviews 115, 111–168.

Brown, R.H., Lebreton, J.-P., Waite, J.H., 2009. Titan from Cassini–Huygens. Springer-Verlag, Berlin Heidelberg.

Burr, D.M., Jacobsen, R.E., Roth, D.L., Phillips, C.B., Mitchell, K.L., Viola, D., 2009. Fluvial network analysis on Titan: evidence for subsurface structures and west-to-east wind flow, southwestern Xanadu. Geophysical Research Letters 36, L22203.

Camp, V., Roobol, M., Hooper, P., 1991. The Arabian continental alkali basalt province: Part II. Evolution of Harrats Khaybar, Ithnayn, and Kura, Kingdom of Saudi Arabia. Geological Society of America Bulletin 103, 363–391.

Castillo-Rogez, J., Lunine, J.I., 2010. Evolution of Titan's rocky core constrained by Cassini observations. Geophysical Research Letters 37, L20205.

Chang, S.J., Van der Lee, S., 2011. Mantle plumes and associated flow beneath Arabia and East Africa. Earth and Planetary Science Letters 302, 448–454.

Collins, G.C., McKinnon, W.B., Moore, J.M., Nimmo, F., Pappalardo, R.T., Prockter, L.M., Schenk, P.M., 2009. Tectonics of the outer planet satellites. In: Schultz, R.A., Watters, T.R. (Eds.), Planetary Tectonics. Cambridge University Press, pp. 264–350.

Coustenis, A., Taylor, F.W., 2008. Titan: Exploring an Earth-Like World. World Scientific Publishing.

Coustenis, A., Hirtzig, M., 2009. Cassini–Huygens results on Titan's surface. Research in Astronomy and Astrophysics 9, 249.

Coustenis, A., Gendron, E., Lai, O., Veran, J.-P., Woillez, J., Combes, M., Vapillon, L., Fusco, T., Mugnier, L., Rannou, P., 2001. Images of Titan at 1.3 and 1.6 μm with adaptive optics at the CFHT. Icarus 154, 501–515.

Davies, A.G., Sotin, C., Matson, D., Castillo-Rogez, J., Johnson, T., Choukroun, M., Baines, K., 2010. Atmospheric control of the cooling rate of impact melts and cryolavas on Titan's surface. Icarus 208, 887–895.

Davies, J.H., Davies, D.R., 2010. Earth's surface heat flux. Solid Earth 1, 5–24.

Dickin, A.P., 1995. Radiogenic Isotope Geology. Cambridge University Press.

Dickinson, W.R., Snyder, W.S., 1978. Plate Tectonics of the Laramide Orogeny, 141. Geological Society of America Memoir, Boulder.

Dombard, A.J., McKinnon, W.B., 2006. Folding of Europa's icy lithosphere: an analysis of viscous-plastic buckling and subsequent topographic relaxation. Journal of Structural Geology 28, 2259–2269.

Elachi, C., Allison, M.D., Borgarelli, L., Encrenaz, P., Im, E., Janssen, M.A., Johnson, W.T.K., Kirk, R.L., Lorenz, R.D., Lunine, J.I., Muhleman, D.O., Ostro, S.J., Picardi, G., Posa, F., Rapley, C.G., Roth, L.E., Seu, R., Soderblom, L.A., Vetrella, S., Wall, S.D., Wood, C.A., Zebker, H.A., 2004. Radar: the Cassini Titan Radar Mapper. Space Science Reviews 115, 71–110.

Fagents, S.A., 2003. Considerations for effusive cryovolcanism on Europa: the post-Galileo perspective. Journal of Geophysical Research 108, E12.

Figueredo, P.H., Greeley, R., 2004. Resurfacing history of Europa from pole-to-pole geological mapping. Icarus 167, 287–312.

Flasar, F.M., 1983. Oceans on Titan? Science 221, 55–57.

Fortes, A.D., Grindrod, P.M., Trickett, S.K., Vocadlo, L., 2007. Ammonium sulfate on Titan: possible origin and role in cryovolcanism. Icarus 188, 139–153.

Fowler, A.C., 1986. Thermal runaways in the Earth's mantle. Studies in Applied Mathematics 74, 1–34.

Fulchignoni, M., Ferri, F., Angrilli, F., Ball, A.J., Bar-Nun, A., Barucci, M.A., Bettanini, C., Bianchini, G., Borucki, W., Colombatti, G., Coradini, M., Coustenis, A., Debei, S., Falkner, P., Fanti, G., Flamini, E., Gaborit, V., Grard, R., Hamelin, M., Harri, A.M., Hathi, B., Jernej, I., Leese, M.R., Lehto, A., Lion Stoppato, P.F., López-Moreno, J.J., Mäkinen, T., McDonnell, J.A.M., McKay, C.P., Molina-Cuberos, G., Neubauer, F.M., Pirronello, V., Rodrigo, R., Saggin, B., Schwingenschuh, K., Sieff, A., Simões, F., Svedhem, H., Tokano, T., Towner, M.C., Trautner, R., Withers, P., Zarnecki, J.C., 2005. In situ measurements of the physical characteristics of Titan's environment. Nature 438, 785–791.

Gaidos, E.J., 2001. Cryovolcanism and the recent flow of liquid water on Mars. Icarus 153, 218–223.

Gibbard, S.G., Macintosh, B., Gavel, D., Max, C.E., de Pater, I., Ghez, A.M., Young, E.F., McKay, C.P., 1999. Titan: high-resolution speckle images from the Keck Telescope. Icarus 139, 189–201.

Grasset, O., Sotin, C., 1996. The cooling rate of a liquid shell in Titan's interior. Icarus 123, 101–112.

Griffith, C.A., 1993. Evidence for surface heterogeneity on Titan. Nature 364, 511–513.

Griffith, C.A., Tobias, O., Wagener, R., 1991. Titan's surface and troposphere, investigated with ground-based, near-infrared observations. Icarus 93, 362–378.

Grindrod, P., Fortes, A., Nimmo, F., Feltham, D., Brodholt, J., Vocadlo, L., 2008. The long-term stability of a possible aqueous ammonium sulfate ocean inside Titan. Icarus 197, 137–151.

Grott, M., Breuer, D., 2008. Constraints on the radiogenic heat production rate in the Martian interior from viscous relaxation of crustal thickness variations. Geophysical Research Letters 35, L05201.

Hall, J., Solomon, S., Head, J., 1986. Elysium region, Mars: tests of lithospheric loading models for the formation of tectonic features. Journal of Geophysical Research 91, 11377–11392.

Hawkesworth, C., Turner, S., Gallagher, K., Hunter, A., Bradshaw, T., Rogers, N., 1995. Calc-alkaline magmatism, lithospheric thinning and extension in the basin and range. Journal of Geophysical Research 100, 10271–10286.

Head, J.W., Pappalardo, R.T., Collins, G., Greeley, R., 1997. Tectonic resurfacing on Ganymede and its role in the formation of the grooved terrain. In: Proceedings of the Lunar and Planetary Science Conference, XXIX. Houston, Texas, Abstract 535.

Head, J.W., Pappalardo, R., Collins, G., Belton, M., Giese, B., Wagner, R., Breneman, H., Spaun, N., Nixon, B., Neukum, G., Moore, J., 2002. Evidence for Europa-like tectonic resurfacing styles on Ganymede. Geophysical Research Letters 29, 2151.

Hurford, T.A., Helfenstein, P., Hoppa, G.V., Greenberg, R., Bills, B.G., 2007. Eruptions arising from tidally controlled periodic openings of rifts on Enceladus. Nature 447, 292–294.

Jaumann, R., Roger, C., Nimmo, F., Hendrix, A., Buratti, B., Tilmann, D., Moore, J., Schenk, P., Ostro, S., Srama, R., 2009. Icy satellites: geological evolution and surface processes. Saturn from Cassini–Huygens, 637. Springer.

Jull, M.G., Arkani-Hamed, J., 1995. The implications of basalt in the formation and evolution of mountains on Venus. Physics of the Earth and Planetary Interiors 89, 163–175.

Kargel, J.S., 1994. Cryovolcanism on the icy satellites. Earth, Moon and Planets 67, 101–113.

Kirk, R.L., Howington-Kraus, E., Barnes, J.W., Hayes, A.G., Lopes, R.M., Lorenz, R.D., Lunine, J.I., Mitchell, K.L., Stofan, E.R., Wall, S.D., 2010. La Sotra y las otras: topographic evidence for (and against) cryovolcanism on Titan. AGU, Fall Meet, Abstract P22A-03.

Lebreton, J.-P., Coustenis, A., Lunine, J.I., Raulin, F., Owen, T., Strobel, D., 2009. Results from the Huygens probe on Titan. Astronomy and Astrophysics Review 17, 149–179.

Lidmar-Bergström, K., 1996. Long term morphotectonic evolution in Sweden. Geomorphology 16, 33–59.

Lopes, R.M.C., Mitchell, K.L., Stofan, E.R., Lunine, J.I., Lorenz, R., Paganelli, F., Kirk, R.L., Wood, C.A., Wall, S.D., Robshaw, L.E., Fortes, A.D., Neish, C.D., Radebaugh, J., Reffet, E., Ostro, S.J., Elachi, C., Allison, M.D., Anderson, Y., Boehmer, R., Boubin, G., Callahan, P., Encrenaz, P., Flamini, E., Francescetti, G., Gim, Y., Hamilton, G., Hensley, S., Janssen, M.A., Johnson, W.T.K., Kelleher, K., Muhleman, D.O., Ori, G., Orosei, R., Picardi, G., Posa, F., Roth, L.E., Seu, R., Shaffer, S., Soderblom, L.A., Stiles, B., Vetrella, S., West, R.D., Wye, L.,

Please cite this article as: Solomonidou, A., et al., Morphotectonic features on Titan and their possible origin. Planetary and Space Science (2012), http://dx.doi.org/10.1016/j.pss.2012.05.003

Zebker, H.A., 2007a. Cryovolcanic features on Titan's surface as revealed by the Cassini Titan Radar Mapper. Icarus 186, 395–412.
Lopes, R.M.C., Stofan, E.R., Mitri, G., Robshaw, L.E., Mitchell, K.L., Wood, C.A., Radebaugh, J., Kirk, R.L., Wall, S.D., Lorenz, R., Lunine, J.I., Craig, J., Paganelli, F., Soderblom, L., The Cassini Radar Team, 2007b. Much like Earth: distribution of geologic processes on Titan from Cassini RADAR data. In: Proceedings of the 38th Lunar and Planetary Science Conference. Boulder, Colorado, Abstract 1357, pp. 78–79.
Lopes, R.M.C., Stofan, E.R., Peckyno, R., Radebaugh, J., Mitchell, K.L., Mitri, G., Wood, C.A., Kirk, R.L., Wall, S.D., Lunine, J.I., Hayes, A., Lorenz, R., Farr, T., Wye, L., Craig, J., Ollerenshaw, R.J., Janssen, M., LeGall, A., The Cassini RADAR Team, 2010. Distribution and interplay of geologic processes on Titan from Cassini radar data. Icarus 205, 540–558.
Lorenz, R.D., Lunine, J.I., 2005. Titan's surface before Cassini. Planetary and Space Science 53, 557–576.
Lorenz, R.D., Mitton, J., 2008. Titan Unveiled: Saturn's Mysterious Moon Explored. Princeton University Press.
Lunine, J.I., Atreya, S.K., 2008. The methane cycle on Titan. Nature Geosciences 1, 159–164.
Lunine, J.I., Stevenson, D.J., Yung, Y.L., 1983. Ethane ocean on Titan. Science 222, 1229–1230.
Lunine, J.I., Elachi, C., Wall, S.D., Janssen, M.A., Allison, M.D., Anderson, Y., Boehmer, R., Callahan, P., Encrenaz, P., Flamini, E., Francescheti, G., Gim, Y., Hamilton, G., Hensley, S., Johnson, W.T.K., Kelleher, K., Kirk, R.L., Lopes, R.M., Lorenz, R., Muhleman, D.O., Orosei, R., Ostro, S.J., Paganelli, F., Paillou, P., Picardi, G., Posa, F., Radebaugh, J., Roth, L.E., Seu, R., Shaffer, S., Soderblom, L.A., Stiles, B., Stofan, E.R., Vetrella, S., West, R., Wood, C.A., Wye, L., Zebker, H., Alberti, G., Karkoschka, E., Rizk, B., McFarlane, E., See, C., Kazeminejad, B., 2008. Titan's diverse landscapes as evidenced by Cassini RADAR's third and fourth looks at Titan. Icarus 195, 415–433.
Manga, M., Wang, C.-Y., 2007. Pressurized oceans and the eruption of liquid water on Europa and Enceladus. Geophysical Research Letters 34, L07202.
McCord, T.B., Hansen, G.B., Buratti, B.J., Clark, R.N., Cruikshank, D.P., D'Aversa, E., Griffith, C.A., Baines, E.K.H., Brown, R.H., Dalle Ore, C.M., Filacchione, G., Formisano, V., Hibbits, C.A., Jaumann, R., Lunine, J.I., Nelson, R.M., Sotin, C., The Cassini VIMS Team, 2006. Composition of Titan's surface from Cassini VIMS. Planetary and Space Science 54, 1524–1539.
McDonald, K.C., 1982. Mid-ocean ridges: fine scale tectonic, volcanic and hydrothermal processes within the plate boundary zone. Annual Review of Earth and Planetary Sciences 10, 155.
McKinnon, W.B., 1998. Geodynamics of icy satellites. In: Schmitt, B., et al. (Eds.), Solar System Ices. Kluwer, Dordrecht, Netherlands, pp. 525–550.
Mège, D., Masson, P., 1996. A plume tectonics model for the Tharsis province, Mars. Planetary and Space Science 44, 1499–1546.
Meier, R., Smith, B.A., Owen, T.C., Terrile, R.J., 2000. The surface of Titan from NICMOS observations with the Hubble Space Telescope. Icarus 145, 462–473.
Melosh, H.J., Nimmo, F., 2011. Long-term strength of icy vs. silicate planetary bodies. In: Proceedings of the 42nd Lunar and Planetary Science Conference. The Woodlands, Texas, Abstract 2306.
Mitri, G., Showman, A.P., 2008. Thermal convection in ice-I shells of Titan and Enceladus. Icarus 193, 387–396.
Mitri, G., Showman, A.P., Lunine, J.I., Lorenz, R.D., 2007. Hydrocarbon lakes on Titan. Icarus 186, 385–394.
Mitri, G., Showman, A.P., Lunine, J.I., Lopes, R.M.C., 2008. Resurfacing of Titan by ammonia-water cryomagma. Icarus 196, 216–224.
Mitri, G., Bland, M.T., Showman, A.P., Radebaugh, J., Stiles, B., Lopes, R.M.C., Lunine, J.I., Pappalardo, R.T., 2010. Mountains on Titan: modeling and observations. Journal of Geophysical Research 115, E10002.
Montgomery, D.R., Brandon, M.T., 2002. Topographic controls on erosion rates in tectonically active mountain ranges. Earth and Planetary Science Letters 201, 481–489.
Moore, J.M., Pappalardo, R.T., 2011. Titan: an exogenic world? Icarus 212, 790–806.
Muhleman, D.O., Grossman, A.W., Butler, B.J., Slade, M.A., 1990. Radar reflectivity of Titan. Science 248, 975–980.
Murchie, S.L., Head, J.W., Helfenstein, P., Plescia, J.B., 1986. Terrain types and local-scale stratigraphy of grooved terrain on Ganymede. Journal of Geophysical Research 91, E222–E238.
Niemann, H.B., Atreya, S.K., Bauer, S.J., Carignan, G.R., Demick, J.E., Frost, R.L., Gautier, D., Haberman, J.A., Harpold, D.N., Hunten, D.M., Israel, G., Lunine, J.I., Kasprzak, W.T., Owen, T.C., Paulkovich, M., Raulin, F., Raaen, E., Way, S.H., 2005. The abundances of constituents of Titan's atmosphere from the GCMS instrument on the Huygens probe. Nature 438, 779–784.
Niemann, H.B., Atreya, S.K., Demick, J., Gautier, D., Haverman, J., Harpold, D., Kasprzak, W., Lunine, J., Owen, T., Raulin, F., 2010. Composition of Titan's lower atmosphere and simple surface volatiles as measured by the Cassini–Huygens probe gas chromatograph mass spectrometer experiment. Journal of Geophysical Research 115, E12006.
Nimmo, F., McKenzie, D., 1998. Volcanism and tectonics on Venus. Annual Review of Earth and Planetary Sciences 26, 23–51.
Pappalardo, R.T., Davis, D.M., 2007. Where's the compression? Explaining the lack of contractional structures on icy satellites. Workshop on Ices, Oceans, and Fire: Satellites of the Outer Solar System, vol. 1357, pp. 108–109.
Pollack, H.N., Hurter, S.J., Johnson, J.R., 1993. Heat flow from the Earth's interior: analysis of the global data set. Reviews of Geophysics 31, 267–280.
Porco, C.C., Baker, E., Barbara, J., Beurle, K., Brahic, A., Burns, J.A., Charnoz, S., Cooper, N., Dawson, D.D., Del Genio, A.D., Denk, T., Dones, L., Dyudina, U., Evans, R.A., Fussner, S., Giese, B., Grazier, K., Helfenstein, P., Ingersoll, A.P., Jacobson, R.A., Johnson, T.V., McEwen, A., Murray, C.D., Neukum, G., Owen, W.M., Perry, J., Roatsch, T., Spitale, J., Squyres, S., Thomas, P., Tiscareno, M., Turtle, E.P., Vasavada, A.R., Veverka, J., Wagner, R., West, R., 2005. Imaging of Titan from the Cassini spacecraft. Nature 434, 159–168.
Prockter, L.M., Head, J.W., Pappalardo, R.T., Sullivan, R.J., Clifton, A.E., Giese, B., Wagner, R., Neukum, G., 2002. Morphology of Europan bands at high resolution: a mid-ocean ridge-type rift mechanism. Journal of Geophysical Research 107, E5.
Radebaugh, J., Lorenz, R.D., Kirk, R.L., Lunine, J.I., Stofan, E.R., Lopes, R.M.C., Wall, S.D., The Cassini Radar Team, 2007. Mountains on Titan observed by Cassini Radar. Icarus 192, 77–91.
Radebaugh, J., Lorenz, R.D., Lunine, J.I., Wall, S.D., Boubin, G., Reffet, E., Kirk, R.L., Lopes, R.M., Stofan, E.R., Soderblom, L., Allison, M., Janssen, M., Paillou, P., Callahan, P., Spencer, C., 2008. Dunes on Titan observed by Cassini Radar. Icarus 194, 690–703.
Radebaugh, J., Lorenz, R.D., Farr, T., Paillou, P., Savage, C., Spencer, C., 2009. Linear dunes on Titan and earth: initial remote sensing comparisons. Geomorphology 121, 122–132.
Radebaugh, J., Lorenz, R.D., Wall, S.D., Kirk, R.L., Wood, C.A., Lunine, J.I., Stofan, E.R., Lopes, R.M.C., Valora, P., Farr, T.G., Hayes, A., Stiles, B., Mitri, G., Zebker, H., Janssen, M., Wye, L., LeGall, A., Mitchell, K.L., Paganelli, F., West, R.D., Schaller, E.L., The Cassini Radar Team, 2011. Regional geomorphology and history of Titan's Xanadu province. Icarus 211, 672–685.
Ramsey, M.S., 2002. Ejecta distribution patterns at Meteor Crater, Arizona: on the applicability of lithologic end-member deconvolution for spaceborne thermal infrared data of Earth and Mars. Journal of Geophysical Research 107, E8.
Raulin, F., 2008. Astrobiology and habitability of Titan. Space Science Reviews 135, 37–48.
Rehman, S., 2010. Saudi Arabian geothermal energy resources an update. In: Proceedings of the World Geothermal Congress, pp. 1–6.
Rice, A., Fairbridge, R.W., 1975. Thermal runaway in the mantle and neotectonics. Tectonophysics 29, 59–72.
Rosenau, M., Oncken, O., 2009. Fore-arc deformation controls frequency-size distribution of megathrust earthquakes in subduction zones. Journal of Geophysical Research 114, B10311.
Ruddiman, W.F., 1997. Tectonic Uplift and Climate Change. Plenum Press.
Scheidegger, A., 2004. Morphotectonics. Springer, Berlin.
Schenk, P., Bulmer, M., 1998. Origin of mountains on Io by thrust faulting and large-scale mass movements. Science 279, 1514–1518.
Schenk, P., McKinnon, W.B., 1985. Dark halo craters and the thickness of grooved terrain on Ganymede. Journal of Geophysical Research 90, 775–C783.
Schubert, G., Spohn, T., Reynolds, R.T., 1986. Thermal histories, compositions and internal structures of the moons of the solar system. Satellites, 224–292.
Schumm, S.A., Dumont, J.F., Holbrook, J.M., 2002. Active Tectonics and Alluvial Rivers. Cambridge University Press, New York.
Sears, J.W., 1990. Geological structure of the Grand Canyon supergroup, Grand Canyon Geology. University Press. (pp. 71–82).
Smith, P.H., Lemmon, M.T., Lorenz, R.D., Sromovsky, L.A., Caldwell, J.J., Allison, M.D., 1996. Titan's surface, revealed by HST imaging. Icarus 119, 336–349.
Soderblom, L.A., Kirk, R.L., Lunine, J.I., Anderson, J.A., Baines, K., Barnes, J., Barrett, J., Brown, R., Buratti, B., Clark, R., Cruikshank, D., Elachi, C., Janssen, M., Jaumann, R., Karkoschka, E., LeMouelic, S., Lopes, R., Lorenz, R., McCord, T., Nicholson, P., Radebaugh, J., Rizk, B., Sotin, C., Stofan, E., Sucharski, T., Tomasko, M., Wall, S., 2007a. Correlations between Cassini VIMS spectra and RADAR SAR images: implications for Titan's surface composition and the character of the Huygens Probe Landing Site. Planetary and Space Science 55, 2025–2036.
Soderblom, L.A., Tomasko, M.G., Archinal, B.A., Becker, T.L., Bushroe, M.W., Cook, D.A., Doose, L.R., Galuszka, D.M., Hare, T.M., Howington-Kraus, E., Karkoschka, E., Kirk, R.L., Lunine, J.I., McFarlane, E.A., Redding, B.L., Rashar, R., Rosiek, M.R., See, C., Smith, P.H., 2007b. Topography and geomorphology of the Huygens landing site on Titan. Planetary and Space Science 55, 2015–2024.
Soderblom, L.A., Brown, R.H., Soderblom, J.M., Barnes, J.W., Kirk, R.L., Sotin, C., Jaumann, R., Mackinnon, D.J., Mackowski, D.W., Baines, K.H., Buratti, B.J., Clark, R.N., Nicholson, P.D., 2009. The geology of Hotei Regio, Titan: correlation of Cassini VIMS and RADAR. Icarus 204, 610–618.
Solomonidou, A., Hirtzig, M., Bratsolis, E., Bampasidis, G., Coustenis, A., Kyriakopoulos, K., Le Mouelic, S., Stephan, K., Jaumann, R., Drossart, P., Sotin, C., Seymour, K., Moussas, X. New processing of Cassini/VIMS data on potentially geologically varying regions, in preparation.
Sotin, C., Jaumann, R., Buratti, B.J., Brown, R.H., Clark, R.N., Soderblom, L.A., Baines, K.H., Bellucci, G., Bibring, J.P., Capaccioni, F., Cerroni, P., Combes, M., Coradini, A., Cruikshank, D.P., Drossart, P., Formisano, V., Langevin, Y., Matson, D.L., McCord, T.B., Nelson, R.M., Nicholson, P.D., Sicardy, B., Le Mouélic, S., Rodriguez, S., Stephan, K., Scholz, C.K., 2005. Release of volatiles from a possible cryovolcano from near-infrared imaging of Titan. Nature 435, 786–789.
Sotin, C., LeMouelic, S., Brown, R.H., Barnes, J., Soderblom, L., Jaumann, R., Buratti, B.J., Clark, R.N., Baines, K.H., Nelson, R.M., Nicholson, P., VIMS Science Team, 2007. Cassini/VIMS observatoire of Titan during the T20 flyby. In: Proceedings of the 37th Lunar and Planetary Science. League City, Texas, Abstract 2444.
Stiles, B.W., Hensley, S., Gim, Y., Bates, D.M., Kirk, R.L., Hayes, A., Radebaugh, J., Lorenz, R.D., Mitchell, K.L., Callahan, P.S., Zebker, H., Johnson, W.T.K., Wall, S.D., Lunine, J.I., Wood, C.A., Janssen, P.S., Pelletier, F., West, R.D., Veeramacheneni, C., The Cassini RADAR Team, 2009. Determining Titan surface topography from Cassini SAR data. Icarus 202, 584–598.

Please cite this article as: Solomonidou, A., et al., Morphotectonic features on Titan and their possible origin. Planetary and Space Science (2012), http://dx.doi.org/10.1016/j.pss.2012.05.003

Stofan, E.R., Lunine, J.I., Lopes, R., Paganelli, F., Lorenz, R.D., Wood, C.A., Kirk, R.L., Wall, S., Elachi, C., Soderblom, L.A., Ostro, S., Janssen, M., Wye, L., Zebker, H., Anderson, Y., Allison, M., Boehmer, R., Callahan, P., Encrenaz, P., Flamini, E., Francescetti, G., Gim, Y., Hamilton, G., Hensley, S., Johnson, W., Kelleher, K., Muhleman, D., Picardi, G., Posa, F., Roth, L., Seu, R., Shaffer, S., Stiles, B., Vetrella, S., West, R., 2006. Mapping of Titan: results from the first Titan radar passes. Icarus 185, 443–456.

Stofan, E.R., Elachi, C., Lunine, J.I., Lorenz, R.D., Stiles, B., Mitchell, K.L., Ostro, S., Soderblom, L., Wood, C., Zebker, H., Wall, S., Janssen, M., Kirk, R., Lopes, R., Paganelli, F., Radebaugh, J., Wye, L., Anderson, Y., Allison, M., Boehmer, R., Callahan, P., Encrenaz, P., Flamini, E., Francescetti, G., Gim, Y., Hamilton, G., Hensley, S., Johnson, W.T.K., Kelleher, K., Muhleman, D., Paillou, P., Picardi, G., Posa, F., Roth, L., Seu, R., Shaffer, S., Vetrella, S., West, R., 2007. The lakes of Titan. Nature 445, 61–64.

Tobie, G., Grasset, O., Lunine, J.I., Mocquet, A., Sotin, C., 2005. Titan's internal structure inferred from a coupled thermal-orbital model. Icarus 175, 496–502.

Tobie, G., Lunine, J.I., Sotin, C., 2006. Episodic outgassing as the origin of atmospheric methane on Titan. Nature 440, 61–64.

Tokano, T., 2011. Precipitation climatology on Titan. Science 331, 1393–1394.

Tomasko, M.G., Archinal, B., Becker, T., Bézard, B., Bushroe, M., Combes, M., Cook, D., Coustenis, A., de Bergh, C., Dafoe, L.E., Doose, L., Doutè, S., Eibl, A., Engel, H.U., Gliem, F., Grieger, B., Holso, K., Howington-Kraus, E., Karkoschka, E., Keller, H.U., Kirk, R., Kramm, R., Küppers, M., Lanagan, P., Lellouch, E., Lemmon, M., Lunine, J., McFarlane, E., Moores, J., Prout, G.M., Rizk, B., Rosiek, M., Rueffer, P., Schröder, S.E., Schmitt, B., See, C., Smith, P., Soderblom, L., Thomas, N., West, R., 2005. Rain, winds and haze during the Huygens probe's descent to Titan's surface. Nature 438, 765–778.

Wall, S.D., Lopes, R.M.C., Stofan, E.R., Wood, C.A., Radebaugh, J.L., Horst, S.M., Stiles, B.W., Nelson, R.M., Kamp, L.W., Janssen, M.A., Lorenz, R.D., Lunine, J.I., Farr, T.G., Mitri, G., Paillou, P., Paganelli, F., Mitchell, K.L., 2009. Cassini RADAR images at Hotei Arcus and western Xanadu, Titan: evidence for geologically recent cryovolcanic activity. Geophysical Research Letters 36, L04203.

Williams, D.A., Radebaugh, J., Lopes, R.M.C., Stofan, E., 2011. Geomorphologic mapping of the Menrva region of Titan using Cassini RADAR data. Icarus 212, 744–750.

Wilson, T.Z., 1973. Mantle plumes and plate motions. Tectonophysics 19, 149–164.

Zarnecki, J.C., Leese, M.R., Hathi, B., Ball, A.J., Hagermann, A., Towner, M.C., Lorenz, R.D., McDonnell, J.A.M., Green, S.F., Patel, M.R., Ringrose, T.J., Rosenberg, P.D., Atkinson, K.R., Paton, M.D., Banaszkiewicz, M., Clark, B.C., Ferri, F., Fulchignoni, M., Ghafoor, N.A.L., Kargl, G., Svedhem, H., Delderfield, J., Grande, M., Parker, D.J., Challenor, P.G., Geake, J.E., 2005. A soft solid surface on Titan as revealed by the Huygens surface science package. Nature 438, 792–795.

Please cite this article as: Solomonidou, A., et al., Morphotectonic features on Titan and their possible origin. Planetary and Space Science (2012), http://dx.doi.org/10.1016/j.pss.2012.05.003

Appendix D3

Imaging of potentially active geological regions on Saturn's moons Titan and Enceladus, using Cassini-Huygens data: With emphasis on cryovolcanism

Journal article published in *Hellenic Journal of Geosciences* (2010),
Volume 45, pp. 257-268.

Imaging of potentially active geological regions on Saturn's moons Titan and Enceladus, using Cassini-Huygens data: With emphasis on cryovolcanism*

Anezina Solomonidou[1,2], Georgios Bampasidis[2,3], Konstantinos Kyriakopoulos[1], Emmanuel Bratsolis[3], Mathieu Hirtzig[4], Athena Coustenis[2] & Xenophon Moussas[3]

[1]*Faculty of Geology and Geoenvironment, National & Kapodistrial University of Athens, Panepistimiopolis, 157 84 Athens, Greece*
[2]*LESIA, Observatoire de Paris – Meudon, 92190 Meudon Cedex, France*
[3]*Faculty of Physics, National & Kapodistrial University of Athens, Panepistimiopolis, 157 84 Athens, Greece*
[4]*LMD – IPSL, Paris, France*
email: asolomonidou@geol.uoa.gr

ABSTRACT: Since 2004, investigations, measurements and data analysis by the Cassini-Huygens mission showed that Titan, Saturn's largest satellite, presents complex, dynamic and Earth-like geology. Endogenous, as well, as exogenous dynamic processes, have created diverse terrains with extensive ridges and grooves, impact units, caldera-like structures, layered plains and liquid hydrocarbon lakes. Observations by the Cassini Visual Infrared Spectrometer instrument (VIMS) have indicated possible cryovolcanic terrains in the areas called Tui Regio (20°S, 130°W) and Hotei Regio (26°S, 78°W). In addition, Cassini's investigation over another icy moon of Saturn, Enceladus, identified its cryovolcanic activity and partially revealed its unique topography indicating several types of surface expressions. We present a comparative study of volcanic analogues from Earth and Enceladus that derive insight on the origin of some of these features. In this work, we focus on the analysis of VIMS data using the Principal Component Analysis technique in order to identify regions of altered chemical composition on Titan. The analysis of VIMS data suggests that possible cryovolcanic activity formed both the Tui Regio and the Hotei Regio.
Key-words: *Planetary geology, icy satellites, Titan, Enceladus, cryovolcanism, spectroscopy.*

ΠΕΡΙΛΗΨΗ: Μακροχρόνιες έρευνες, μετρήσεις και αναλύσεις δεδομένων από την αποστολή Cassini-Huygens από το 2004, έδειξαν ότι ο Τιτάνας, ο μεγαλύτερος δορυφόρος του Κρόνου, παρουσιάζει περίπλοκη, δυναμική και παρόμοια με τη Γη γεωλογία. Ενδογενείς, όσο και εξωγενείς δυναμικές διεργασίες, έχουν δημιουργήσει ποικίλα γεωλογικά πεδία με εκτεταμένες ράχες και αύλακες, κρατήρες πρόσκρουσης, δομές καλδέρας, πεδιάδες με στρωμάτωση καθώς και λίμνες υδρογονανθράκων. Παρατηρήσεις από το Cassini Visual Infrared Mapping Spectrometer (VIMS) όργανο, έχουν δείξει πιθανές κρυοηφαιστειακές εκτάσεις στις περιοχές Tui Regio (20 ° N, 130 ° Δ) και Hotei Regio (26°N, 78°Δ). Επιπλέον, η έρευνα του Cassini στον παγωμένο δορυφόρο του Κρόνου, Εγκέλαδο, επιβεβαίωσε την κρυοηφαιστειακή του δραστηριότητα και αποκάλυψε μερικώς τη μοναδική του τοπογραφία, παρουσιάζοντας ποικίλους τύπους επιφανειακών εμφανίσεων. Παρουσιάζουμε μια συγκριτική μελέτη, δείχνοντας ηφαιστειακά ανάλογα της Γης και του Εγκέλαδου, που παρέχουν πληροφορίες για τη δημιουργία κάποιων σχηματισμών. Σε αυτή τη μελέτη, επικεντρωνόμαστε στην ανάλυση δεδομένων VIMS, χρησιμοποιώντας τη μέθοδο Ανάλυσης Κύριων Συνιστωσών σε περιοχές με διαφορετική χημική σύσταση. Οι αναλύσεις των VIMS δεδομένων των προαναφερθέντων εκτάσεων δείχνουν ότι τόσο η περιοχή Tui Regio όσο και η περιοχή Hotei Regio πιθανά σχηματίστηκαν από κρυοηφαιστειακή δραστηριότητα.
Λέξεις-κλειδιά: *Πλανητική Γεωλογία, Παγωμένοι δορυφόροι, Τιτάνας, Εγκέλαδος, κρυοηφαιστειότητα, φασματοσκοπία.*

INTRODUCTION

Icy moons are small celestial bodies whose surfaces are partially, if not principally, covered by ice, mostly water ice (JOHNSON, 2004). The most remarkable icy moons around the giant planets are Jupiter's Ganymede, Neptune's Triton, Uranus's Miranda and Saturn's Titan and Enceladus in a variety of sizes, composition and temperatures. It was thought that due to the abundance of water ice, the large distance from the Sun, the absence of internal energy sources and of an atmosphere in most cases, the geology of these bodies would be simple, or rather simpler than the geology of Earth; however, subsequent images have shown complex surfaces with several notable morphological formations. Furthermore, the composition, as well as, the structure of the surfaces of the icy moons depends on geological and geophysical factors (JOHNSON, 2004).

Titan is the second largest moon in the Solar system after Jupiter's Ganymede, with a radius of 2,575 km (LINDAL *et al.*, 1983) and spherical geometry. Titan has a unique atmosphere, in that it is dense and consists mainly of N_2 (98.4%), as on Earth. CH_4 (1.4%), H_2 (0.1%) and traces of argon, ethane, acetylene, propane and more complex hydrocarbons and nitriles, as well as condensates and organic aerosols (COUSTENIS & TAYLOR, 2008) constitute the rest of the atmosphere. The identification of such atmospheric compo-

* Απεικόνιση των πιθανών ενεργών γεωλογικών περιοχών στους δορυφόρους του Κρόνου Τιτάνα και Εγκέλαδο: Μελέτη για την κρυοηφαιστειότητα με τη χρήση υπέρυθρων φασματικών δεδομένων

nents endorse theories suggesting that even though Titan is far out of the habitable zone, it is one of the most likely worlds in our solar system of astrobiological interest (RAULIN, 2008). Except for the new atmospheric discoveries such as the organic chemistry in the ionosphere, new components in the neutral atmosphere and the properties of the troposphere, Cassini-Huygens' most surprising discovery was Titan's complex and Earth-like geology (COUSTENIS & TAYLOR, 2008). As far as the surface is concerned, one of the moon's exceptional characteristics is the existence of surface liquid bodies that resemble terrestrial lakes (STOFAN *et al.*, 2007). Other surface formations, were captured both by the Cassini orbiter's *remote sensing* instrumentation such as the Synthetic Aperture Radar (SAR) (ELACHI *et al.*, 2005); the Visual and Infrared Mapping Spectrometer (VIMS) (BROWN *et al.*, 2004) and the Imaging Science System (ISS) (PORCO *et al.*, 2004; MCCORD *et al.*, 2006), as well as by the Huygens probe's *in situ* instruments i.e.: the Surface Science Package (SSP) (ZARNECKI *et al.*, 2005), the Descent Imager and Spectral Radiometer (DISR) (TOMASKO *et al.*, 2005) and the Gas Chromatograph Mass Spectrometer (GCMS) (FULCHIGNONI *et al.*, 2005). The surface discoveries include extensive mountains, ridges, dendritic networks, dunes, lakes, channels, canyons and riverbeds. Of even higher importance is the possible existence of active zones on the satellite due to past or recent cryovolcanic and tectonic activity (e.g. SODERBLOM *et al.*, 2007; LORENZ *et al.*, 2008; SOLOMONIDOU *et al.*, 2010). Caldera-like edifices characterized by radial faults, features resembling lava flows and other possible volcanic structures and deposits, within large areas of volcanic-like terrains, in addition to spectral data indications, suggest that Titan is a world that once suffered cryovolcanic activity which could possibly still be active. The suggestion of an active cryovolcanic interior that supplies the atmosphere with methane is compatible with the current level of methane in Titan's atmosphere. According to calculations, the lifetime of atmospheric methane is limited to 10-100 Myrs (WILSON *et al.*, 2004). If we assume that methane in the atmosphere should be replenished, then Titan needs a reservoir that would supply the atmosphere with enough methane to maintain the atmospheric abundance. The requirement of sufficient supplies of methane in combination with the volcanic-like expressions did trigger the theory of active cryovolcanism on Titan (TOBIE *et al.*, 2006).

Other than Titan, the Cassini mission unveiled another unique world among Saturn's icy moons. Enceladus is a significantly smaller satellite than Titan (500 km in diameter), it presents however, extremely interesting surface features including cratered as well as smooth terrains, extensive linear cracks, scarps, troughs, belts of grooves in addition to the spectacular phenomenon of volcanic geysers that Cassini instrumentation captured in 2005 in the south pole (PORCO *et al.*, 2006). High-resolution data from Cassini magnetometer (MAG) (DOUGHERTY *et al.*, 2006), ISS (PORCO *et al.*, 2006) and the Ultraviolet Imaging Spectrograph (UVIS) (HANSEN *et al.*, 2006), reported cryovolcanic activity in the form of jets in the southern Polar region, at the geological surface expressions called "Tiger stripes". The accumulation of multiple jets resulted in the formation of a massive fountain that reached over 435 km in height (PORCO *et al.*, 2006).

Our work provides: i/ an overview of the geology of Titan and Enceladus, ii/ terrestrial analogues and iii/ the results of our data analysis regarding Titan's potentially active regions. This study implicates the presence of cryovolcanism on Titan's surface.

GEOLOGY AND CRYOVOLCANISM ON TITAN & ENCELADUS

Cryovolcanism

Cryovolcanism is considered to be one of the principal geological processes that have shaped several of the icy moons' surfaces. This activity can be described as ice-rich volcanism, while the cryovolcanic ejecta are referred to as cryomagma. The cryomagma appears in the form of icy cold liquid and, in some cases, as partially crystallised slurry (KARGEL, 1994). The possibility of volcanic resurfacing on icy moons was first noted by LEWIS (1971, 1972) and subsequently addressed by CONSOLMAGNO & LEWIS (1978), but it was not until after the Voyager flybys of Jupiter and Saturn that evidence for past and present tectonic and volcanic activity on moons such as Europa, Ganymede, and Enceladus was brought to light. In our Solar system the only observed recent eruptions are limited to Earth and three other locations: 1) Io, moon of Jupiter; 2) Triton, moon of Neptune; and, 3) Enceladus, moon of Saturn. Titan is also major candidate for past and/or present cryovolcanic activity awaiting for a definitive evidence.

Subsequent to the Cassini-Huygens findings, the term 'cryovolcanism' has been associated with Titan more than any other Saturnian moon (SODERBLOM *et al.*, 2009). Even though, for the case of Enceladus the cryovolcanic origin of the plume is now confirmed (PORCO *et al.*, 2006), the cryovolcanic activity on Titan presents a controversial scientific issue within the scientific community. However, some facts are in favor of such processes like the theory of cryomagma being relevant to the formation of prebiotic compounds (e.g. FORTES, 2000).

The composition of the material called cryomagma on Titan's surface is still unknown, due to the lack of *in situ* measurements and in depth investigations, which may reveal its properties. Cryovolcanic features on Titan's surface are believed to be a significant source of the methane present in the atmosphere (LORENZ & MITTON, 2008). Considering this, a model has been suggested regarding the evolution of Titan, indicating that the methane supply may be trapped in a methane-rich ice and episodically released by cryovolcanic phenomena (TOBIE *et al.*, 2006). However, the definite answer of the composition of Titan's cryomagma is still a subject of research.

According to TOBIE *et al.* (2006) the methane could have

originated through three distinct episodes: the first following the silicate core formation, accretion and differentiation period; a second episode approximately 2000 million years ago when convection commenced in the silicate core; and finally, a geologically recent period, circa 500 million years ago, where subsequent cooling and crystallization of the outer layer occurred. FORTES *et al.* (2007) suggested that ammonium sulphate is the possible origin of cryovolcanism. Titan's interior is broadly described by these authors, from the core to the crust, in distinct layers: a serpentinite core, a high-pressure ice VI mantle, where ice VI has a differentiated crystalline structure ordering and density than typical water ice, a liquid layer of aqueous ammonium sulphate and an externally heterogeneous shell of methane clathrate with low-pressure ice Ih (similarly as ice VI) and solid ammonium sulphate (FORTES *et al.*, 2007).

The geological map below (Fig. 1) has been derived from albedo and texture variations and indicates that the circular feature shows signs of several series of flows, as shown by the black lines (SOTIN *et al.*, 2005). The black circle indicates a caldera, similar to vents that appear above reservoirs of molten material associated with volcanoes on Earth. The colours of the map are representative of the brightness of the features where yellow-green to light brown are the bright patches; blue are the dark patches, red the mottled material and finally the yellow area marks the location of the volcano (SOTIN *et al.*, 2005).

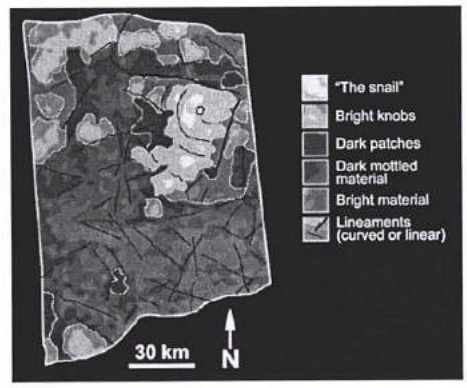

Fig. 1. Geological map of Titan possible volcano (SOTIN *et al.*, 2005).

Enceladus

Cassini's observations on Enceladus did reveal distinct geological features. The surface of Enceladus is covered by smooth and cratered terrains, ridges, grooves, escarpments and extensive linear fractures (JOHNSON, 2004). The most interesting and youthful terrain seen on this moon called "Tiger Stripes" and presents a very complex structure and evolution. The Tiger Stripes (Fig. 2) are tectonic structures consisting of four sub-parallel, linear depressions located in the south polar region (PORCO *et al.*, 2006). In 2005 Cassini's instrumentation and especially the ISS experiment provided evidence of active cryovolcanism (Fig. 3), emanating from a series of jets located within the Tiger Stripes (PORCO *et al.*, 2006).

The jets of water ice from the fractures of Tiger Stripes produce a plume of gas and particles like NH_3, Na, K salts (WAITE *et al.*, 2009). These tectonic fractures, discharge material by endogenic dynamic and most probably hydrothermal activity. The source of the jets is a controversial issue as extensive internal stratification as well as dynamic modeling, is required for the source to be identified. The recent discovery of salts in Saturn's E-ring composition, which is fed from Enceladus' plumes (POSTBERG *et al.*, 2009), suggests that the source of jets is possibly a "chamber" of liquid water that lies underneath the ice shell (TOBIE *et al.*, 2008). Alternatively, the material could derive from originally warm ice that is heated and explodes by the dissociation of clathrate hy-

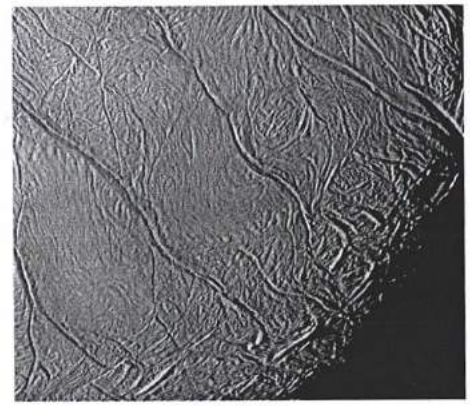

Fig. 2. Tiger Stripes on Enceladus (NASA).

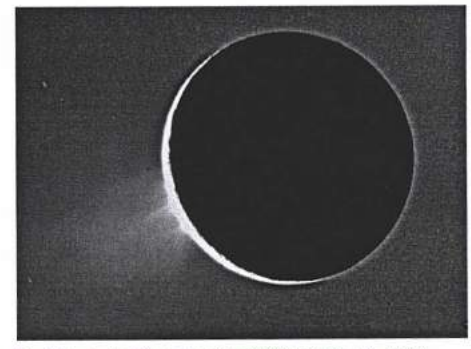

Fig. 3. Enceladus' Plume from Cassini/ISS (PORCO *et al.*, 2006).

drates (KIEFFER *et al.*, 2006). The clathrate hydrates are crystalline water-based ices where the host molecule is water and the trapped-guest molecule is typically a gas. The VIMS instrument detected simple organic compounds in the Tiger Stripes. Such chemical composition which consists of liquid water, ammonia, carbon dioxide, Na and K salts, benzene and other hydrocarbons (WAITE *et al.*, 2009), has not been found in any other region on Enceladus (BROWN *et al.*, 2006). The presence of liquid water might also make it possible for Enceladus to support life (LAMMER *et al.*, 2009).

Recent data from Cassini reported pockets of heat that appear along a fracture named Baghdad Sulcus (Fig. 15), one of the Tiger Stripes that erupt with jets of water vapor and ice particles (HURFORD *et al*, 2009). The temperature along Baghdad Sulcus exceeds 180 Kelvin (WAITE *et al.*, 2009). As is the case for Titan's Hotei Regio, Tiger Stripes on Enceladus and in particular Baghdad Sulcus represent tectonic zones of weakness from which the internal materials find their way to the surface. The idea of a subsurface sea becomes all the more compelling since Enceladus' south polar region (Tiger Stripes area) is actually a half-kilometer deep basin distinguishing from the surrounding expressions (COLLINS & GOODMAN, 2007). Such figure, like the deep basin in Tiger stripes, resembles Titan's Hotei Regio which is a basin lying one kilometer deeper than the surrounding area (SODERBLOM *et al.*, 2009). This basin could be the surface expression of a subsurface sea (COLLINS & GOODMAN, 2007).

Titan

Titan's geology has been extensively studied using Cassini image data. In this research, we investigate and process data acquired from VIMS in order to identify areas of cryovolcanic deposition.

The most intriguing problem in regard to the decoding of Titan's surface is the atmospheric veil that covers the surface. This veil prevents any direct observation from Earth and space-based telescopes. However, VIMS on board Cassini has the ability to acquire partial surface images, taken within the so-called "methane windows" centered at 0.93, 1.08, 1.27, 1.59, 2.03, 2.8 and 5 μm, where the methane atmospheric absorption is weak (MCCORD *et al.*, 2008; COUSTENIS

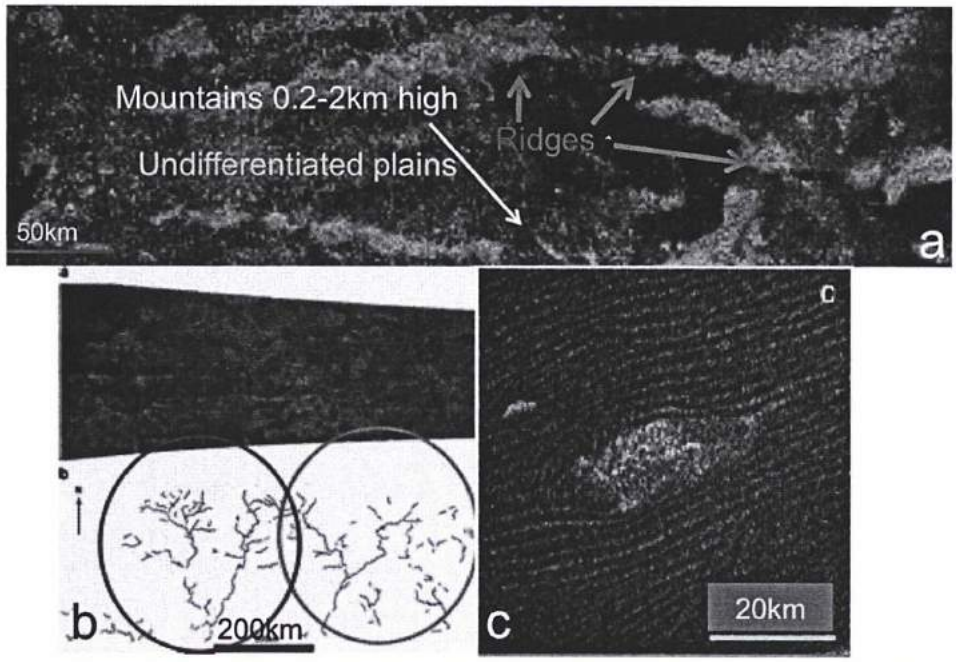

Fig. 4. (a) Ridges and mountains on Titan's surface. The radar bright features are part of the undifferentiated plains (LOPES *et al.*, 2010). The proposed processes that formed this terrain have possibly tectonic origin. (b) Dendritic networks as seen with SAR and morphological map (LORENZ *et al.*, 2008). The system is located at the western end of Xanadu close to our area of interest, Tui Regio. (c) Sand dunes around the Belet sand sea on Titan. The dunes are formed due to Aeolian processes. The bright figures are topographic obstacles that advance the formation of the dunes (RADEBAUGH *et al.*, 2009).

et al., 2005). In general, Titan's surface appears to have smooth and rough areas of various altitudes which include extensive mountains and ridges (Fig. 4a) (LOPES *et al.*, 2010), longitudinal dunes (Fig. 4c) (RADEBAUGH *et al.*, 2009), dendritic networks (Fig. 4b) (LORENZ *et al.*, 2008), liquid lakes (Fig. 6) (STOFAN *et al.*, 2007) and impact craters that are intermittently filled by atmospheric precipitations (ELACHI *et al.*, 2005). RADEBAUGH *et al.* (2008) suggests that mountains on Titan range from 200 m to 2000 m in height (Fig. 4a). Erosional processes that operate at the area where mountains lie, are probably the reason of the significant short height of the mountains. However, there is also the assumption that the mountains are built by material with properties that prevent the altitudinal growth (RADEBAUGH *et al.*, 2008). RADEBAUGH *et al.* (2007) mentioned that the notably SAR bright features on Titan's surface most probably correspond to mountains and tectonic ridges which represent mountain chains (Fig. 4a). In particular, the tectonic ridges could have suffered atmospheric precipitation (i.e. hydrocarbon rain) acquiring a rough and fractured surface (SODERBLOM *et al.*, 2007). Rivers are common on Titan, while in some cases a few craters are traversed by them (WOOD *et al.*, 2009). The observation of river systems with dendritic patterns (Fig. 4b) (LORENZ *et al.*, 2008), in addition to the observation of storm clouds (PORCO *et al.*, 2005), suggest that rainfall may be a continuing erosional force erasing impact craters. Other surficial structures observed on Titan are impact craters. Of particular importance is the small number of impact craters which has been observed by the Cassini/Radar which suggests that the surface of Titan is relatively young (i.e. WALL *et al.*, 2009).

The consideration of Titan's young surficial age indicates the possible existence of active regions among the satellite. Contrary to impact craters, surficial structures that are seen commonly on Titan are the dunes (Fig. 4c). The dunes are generally smooth surfaces that diverge around topographic obstacles resembling terrestrial dunes (RADEBAUGH *et al.*, 2009). Moderately variable winds that either follow one mean direction or alternate between two different directions have formed the observed longitudinal dunes (LORENZ *et al.*, 2006).

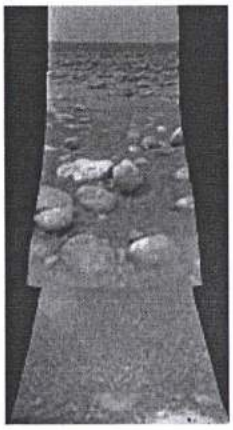

Fig. 5. Titan's surface from the Huygens probe (TOMASKO *et al.*, 2005).

Our knowledge regarding Titan's surface deposits is limited to the data acquired from Huygens' landing site. The Huygens captured image was that of a dark plain covered in pebbles mainly composed of water ice (Fig. 5) (TOMASKO *et al.*, 2005). The size of pebbles is estimated to be roughly 10-15 cm. There is evidence of erosion at the base of the icy rocks, indicating possible fluvial activity (TOMASKO *et al.*, 2005). The surface is darker than originally expected, consisting of a mixture of water and hydrocarbon ice. It is believed that

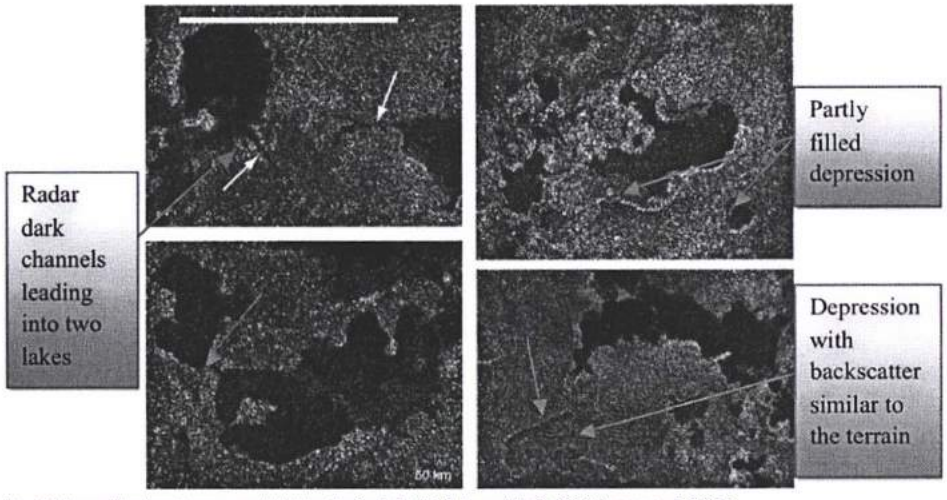

Fig. 6. Lakes on Titan's surface as recorded during the Cassini's T16 flyby on July 22, 2006 (STOFAN *et al.*, 2007a).

the visible ground "powder" in the image is possibly precipitation from the hydrocarbon haze above (TOMASKO *et al.*, 2005).

One of the moon's exceptional characteristics is the existence of large liquid bodies described as lakes of surface liquids (Fig. 6) (STOFAN *et al.*, 2007). These features resemble terrestrial lakes consitute a unique characteristic displayed by the icy moons. Based on data provided by the Cassini/Radar, the presence of hydrocarbon lakes on Titan's surface is now well established (Fig. 6) (LOPES *et al.*, 2007a).

Candidates of cryovolcanic areas on Titan

Our study involves two major areas on Titan that are the most significant, as well as, interesting cryovolcanic candidates. These areas are Tui Regio and Hotei Regio (Fig. 7) lying within the bright region of Xanadu (100°N, 15°S). Tui Regio is centered at 130°W, 20°S and presents relatively high 5 μm reflectivity. Its size is 1,500 km long and 150 km wide. This bright area has been identified as a surface feature and not as the image capture of fog, due to the area's spectral behavior at 2.7 mm (MCCORD *et al.*, 2006). Tui Regio is a massive flow-like terrain, which resembles flow field volcanic areas on Earth. Another area whose spectrum matches that of Tui Regio is Xanadu's Hotei Regio. Hotei Regio is centered at 78°W, 26°S and comprises a 700 km wide field that is probably volcanic in origin. VIMS images confirm the interpretation that the area is a low basin surrounded by higher terrains with possible calderas, fault structures and extensive cryovolcanic flows (SODERBLOM *et al.*, 2009).

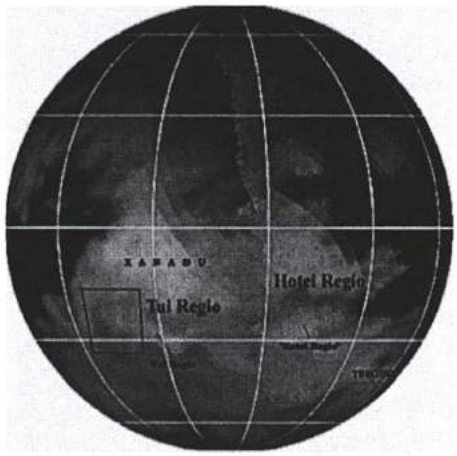

Fig. 7. The location of Tui Regio and Hotei Regio on Titan's globe (BARNES *et al.*, 2006).

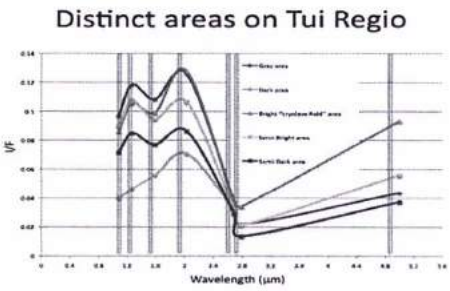

Plot 1. Spectral plot of five distinct areas at the seven atmospheric spectral windows.

Method and Data analysis

Both Tui Regio and Hotei Regio are suggested to be geologically young due to the fact that both present anomalously bright and spectrally distinct areas that have not changed from seasonal precipitation (BARNES *et al.*, 2006).

In order to investigate geologically the regions of interest, it is essential to study their chemical composition that lead to the aforementioned brightness as well as their morphology in order to derive the geological factors that led to their formation.

We have processed spectral images acquired from VIMS, for both areas in the seven narrow spectral windows centered at 0.93, 1.08, 1.27, 1.59, 2.03, 2.8 and 5 μm for which absorption by atmospheric methane is minimal.

The main goal is to identify the composition as well as the alterations of the components that compose the possible cryovolcanic structures. We have used the principal components (PCs) of the Principal Component Analysis (PCA) method. The PCA method involves a mathematical procedure that transforms a number of possibly correlated variables into a smaller number of uncorrelated ones called principal components (JOLLIFFE, 2002). The PCA is well adapted to our study, as our primary concern is to determine the minimum number of factors that will account for the maximum variance of the data we use in this particular multivariate analysis. The main goal of PCA is to reduce the dimensionality of a data set consisting of a large number of interrelated variables, while retaining as much as possible of the variation present in the data set. This is achieved by transforming, the principal components (PCs) into a new set of variables, which are uncorrelated, and which are ordered so that the first few retain most of the variation present in all of the original variables (JOLLIFFE, 2002).

PCA images for both Tui Regio and Hotei Regio allowed us to isolate areas with distinct and diverse false coloring, which imply areas of distinct and diverse spectral and chemical composition (Fig, 9; 11). Such chemical diversity suggests that endogenic and/or exogenic geodynamic processes have formed these regions.

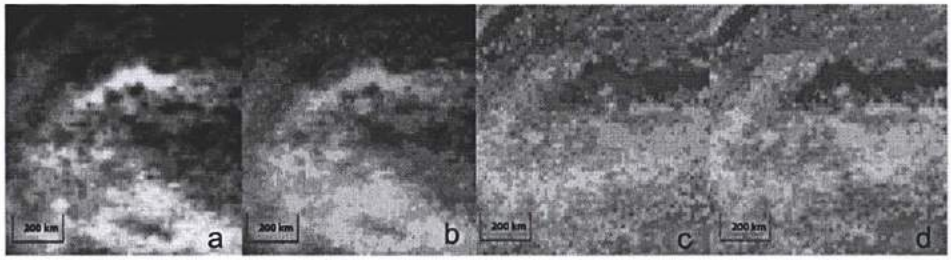

Fig. 8. Reprojection of Tui Regio: (a) Gray scale 2.03 μm, (b) RGB false colors R: 5 μm, G: 2 μm, B: 1.08 μm, (c) PCA R: 1st, G: 2nd, B: 3rd components, (d) PCA R: 3rd, G: 2nd, B: 1st components.

RESULTS

Tui Regio

We have isolated five distinct areas (Fig. 9) within Tui Regio. The Principal Component Analysis projections (Fig. 8c, d) showed areas of different colors and brightness suggesting diversity in surface composition. The PCA method is compatible to gray scale (a) and RGB (b) projections of Tui Regio. The visually brighter areas represent the highest I/F values and the darker areas the lowest, where I stands for the intensity of reflected light measured by the instrument and F the plane-parallel flux of sunlight incident on the satellite normalized for Titan (THEKAEKARA, 1973; BARNES *et al.*, 2007; BROWN *et al.*, 2004).

The plot (Plot 1) of "Bright cryolava field" terrain is different from the other plots, presenting higher I/F values. This suggests that, additionally, this area is extremely brighter than the rest of the region. The wavelengths at which this area presents obvious alterations are the 2 μm, 2.8 μm and 5 μm.

Hotei Regio

We have also isolated five distinct areas within Hotei Regio's probable volcanic field (Fig. 11). The PCA projections (Fig. 10c, d) are presented in false colors areas of different spec-

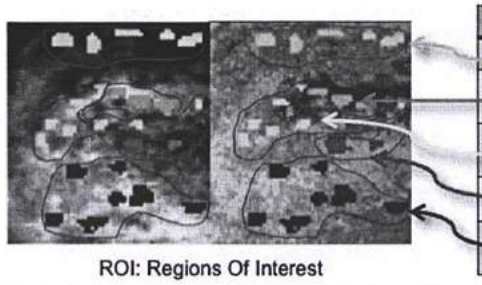

Gray scale	PCA	ROI Color
Dark area	Green area	Cyan
Bright "cryolava field" area	"Lava field" (Dark pink)	Green
Semi-Bright area	"Lava field edges" (light pink)	Yellow
Semi-Dark area	Bright Blue area	Red
Gray area	"Deposits" (pink-yellow mixture)	Blue

Fig. 9. Isolated areas with the use of visual colour alterations, which suggest areas of spectral difference.

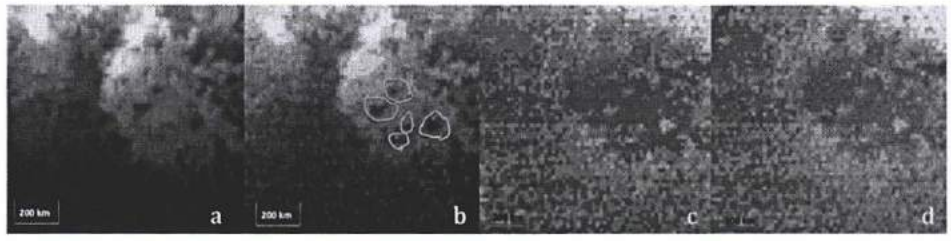

Fig. 10. Reprojection of Hotei Regio: (a) Gray scale 2.03 μm, (b) RGB false colors R: 5 μm, G: 2 μm, B: 1.08 μm, (c) PCA R: 1st, G: 2nd, B: 3rd components, (d) PCA R: 3rd, G: 2nd, B: 1st components.

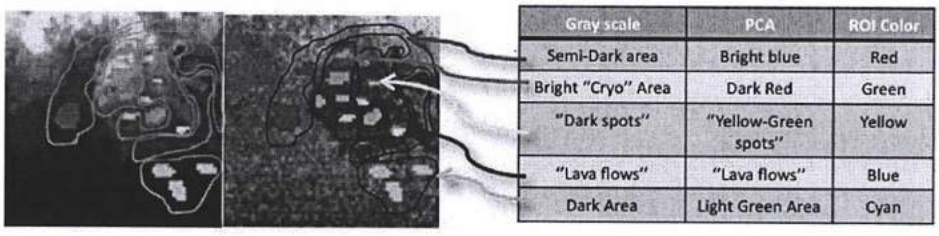

Fig. 11. Isolated areas with the use of visual color alterations, which suggest areas of spectral difference.

tra and brightness, suggesting alterations in surface composition. Thus, the area suggested to be cryovolcanic is distinguished from the surroundings. The only compatible figures with the surrounding area are the caldera-like structures (pointed by green lines, [b]), which probably reveal the primal surficial material, before resurfacing (i.e the surrounding area). The PCA images are compatible to gray scale (a) and RGB (b) projections of Hotei Regio.

Hotei Regio's spectral graph (Plot 2) indicates that the "Bright Cryovolcanic area" presents the highest I/F values and remains brighter than the other areas at all wavelengths. In addition, the "Dark area" remains darker with low values of I/F at all wavelengths. Surprisingly, the spectra from caldera-like structures present medium I/F values, lying almost in the average between the brighter ("volcanic area") and the darker ("primal surface") at most wavelengths. This is compatible with terrestrial caldera structures that consist partially of primary surficial components on which the volcano is being built, as well as new material coming from the interior.

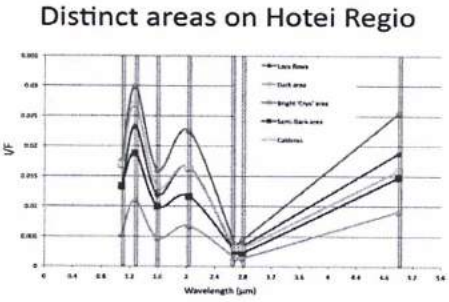

Plot 2. Spectral plot of five distinct areas at the seven atmospheric spectral windows.

DISCUSSION

Whilst it offers a particularly interesting opportunity for research, the existence of past or current cryovolcanic activity on Titan's surface, especially in areas with high reflectance, as observed by Cassini's VIMS instrument, is currently a highly controversial subject. This study has focused on evidence derived from Tui Regio and Hotei Regio, in order to analyze and interpret the data gathered from the VIMS instrument. The spectrographic analysis of VIMS data shows that the visually bright flow-like figure, seen in Tui Regio, has the highest I/F value from its surroundings, especially in the 2.03 μm, 2.8 μm and 5 μm spectral windows (Plot 1), suggests compositional variability in the material between the dark and the bright spots. Furthermore, the dark area presents the lowest I/F values at all wavelengths of the seven spectral windows. This suggests that the flow field has possibly been deposited over the initial (dark) material after single or multiple diachronic eruptions. If Tui Regio is a massive cryolava flow field, then it resembles the terrestrial Carrizozo flow field in New Mexico. Hotei Regio's field displays a low basin with flow-like features lying in the basin interior and at the margins. The flow field has higher I/F values at all wavelengths than the semi-dark and dark areas that either surround the field or lie within it (Plot 2). The dark areas present significantly lower I/F values. Even though the caldera-like structures are seeing as dark as the surrounding areas at VIMS images, they demonstrate medium I/F values suggesting altered chemical composition. The medium I/F values compared with the other areas, suggest that the calderas consist of the initial substrate (dark) material and the cryomagmatic (bright) new material. Such a combination could result in the formation of rough surfaces with high textural variability. The VIMS analysis for the caldera-like structure of Hotei Regio reinforces the theory that assumes the volcanic origin of the area's pattern. In addition, the area resembles the terrestrial volcanic terrain, Harrat Khaybar as well Enceladus' volcanic-tectonic zone of weakness, Tiger Stripes.

Further investigation and comparison of similar features from the three bodies, Titan-Enceladus-Earth, could provide information regarding their formation and future development. Titan, as described in detail hereabove, is perhaps one of the most intriguing objects in our Solar system. The combination of Titan's nitrogen atmosphere and the geologically complex and dynamic surface possesses the satellite as an

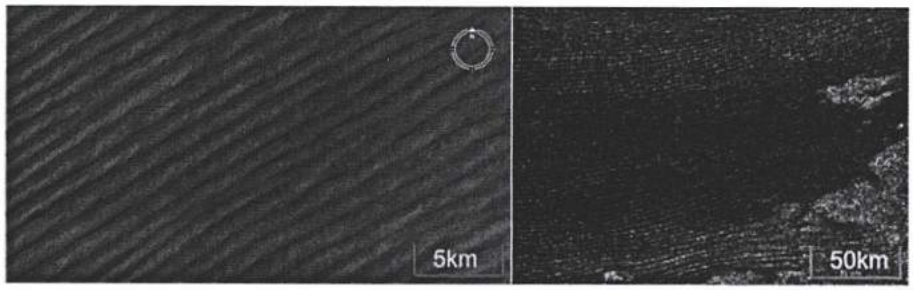

Fig. 12. (left) Longitudinal Sand dunes in Saudi Arabia (NASA). (right) Longitudinal equatorial dunes on Titan (RADEBAUGH *et al.*, 2009).

Earth-like body (COUSTENIS & TAYLOR, 2008). In addition, many atmospheric aspects such as the climate and the meteorology, as Titan displays a 'methanological' weather cycle of clouds, rainfall and evaporation that parallels the 'hydrological' cycle of the Earth, as well as, its complex morphology, make Titan an extremely important astrobiological place. Specifically, cryovolcanism has important astrobiological implications, as it provides a mechanism to expose Titan's organics to liquid water, transforming hydrocarbons and nitriles into more evolved and oxidized prebiotic species (NEISH *et al.*, 2006). Also it has been suggested that life could exist in the lakes of liquid methane on Titan (MCKAY & SMITH, 2005). The existence of liquid bodies identified as lakes exposed on the surface (STOFAN *et al.*, 2007), the equatorial dunes (Fig. 4c), dendritic flows, potential tectonics and volcanism, enhance Titan's resemblance to our own planet. Prior to this discovery, such combination of surface features and dense nitrogen atmosphere had only been identified on Earth.

All the aforementioned aspects, which mainly are the nitrogenic atmosphere, the liquid lakes, as well as the Earth-like geological structures, suggest that Titan resembles Earth more than any other body in the Solar System; despite the huge differences in temperature and other environmental conditions. Thus, an holistic understanding of Titan's system will help us better understand Earth's evolution starting with its primordial phase since early Earth probably looked much like Titan looks today (OWEN, 2005). In general, the activity of cryovolcanism might operate in analogy to terrestrial hydrovolcanic eruptions (SOLOMONIDOU *et al.*, 2010). Fig. 13 shows the supervolcano of Lake Toba in North Sumatra, Indonesia, which is 100 km long and 30 km wide, in comparison with the possible supervolcanic structure called Ganesa Macula (50°N, 87°W) (LOPES *et al.*, 2007b). The Volcanic Explosivity Index (VEI) for Lake Toba, which provides a relative measure of the explosiveness of volcanic eruptions (scale 0-8), was set to be 8 values and the total amount of erupted material volume of 2,800 km³. Taking into consideration the amount of the erupted material, the size of the volcanic structure and the hazards that could affect the satellite, we can assume that supervolcanoes could be hosted in Titan's geological history. The candidate cryovolcanic figures Ganesa Macula, Tui Regio and Hotei Regio could resemble the supervolcanic structures seen on Earth.

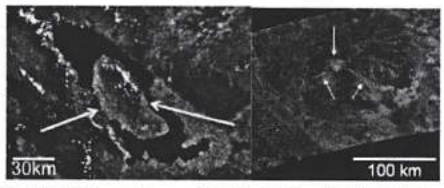

Fig. 13. (left) Supervolcano on Earth. Lake Toba (USGS). (right) Possible supervolcano on Titan. For both figures, the central part of calderas is indicated by the white arrows (LOPES *et al.*, 2007b).

In this study, we focus on the volcanological structures like the ones seen in Tui Regio and Hotei Regio that resemble terrestrial volcanic terrains and characteristics. Tui Regio is a massive (1,500 km) flow field-like figure that could possibly have formed after accumulation of cryolava flows erupted at different times, following the area's topography. On Earth, a massive edifice resembling Tui Regio, emerges in the Tularosa Basin in south-central New Mexico, USA. Carrizozo flow field (Fig. 14) is 75 km long and covers 328 km². The volume of eruptive material was 4.3 km³ (BLEACHER *et al.*, 2008). The field was probably formed from periodic deposition of eruptive material spewing from a source located 27 m

Fig. 14. (up) Carrizozo flow field, New Mexico, USA (USGS). (down) One of the largest candidate cryovolcanic flows on Titan, Tui Regio.

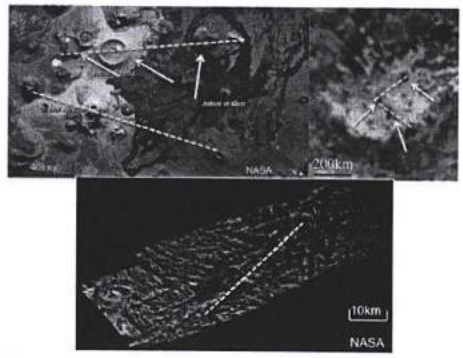

Fig. 15. (up left) Harrat Khaybar volcanic terrains, North of Medina, Saudi Arabia (NASA). (up right) Possible cryovolcanic terrain on Titan, Hotei Regio (SODERBLOM *et al.*, 2009). (down) Baghdad Sulcus, volcanic fracture on the south pole of Enceladus, Tiger Stripes (NASA). Pockets of heat have been appeared along the fracture. The white arrows indicate structures of tuffs, domes and calderas for Harrat Khaybar and possible dome and caldera formations for Hotei Regio. Additionally, the red arrows indicate lava flows and possible cryovolcanic flows within the volcanic terrain. The yellow dashed lines indicate areas that are possibly tectonic zones of weakness from which internal material may pass through.

high named Little Black Peak. The peak consists of three nested cinder cones and a solidified lava pond. The Titanian analogue (Fig. 14) is the possible cryovolcanic flow, Tui Regio; one of the largest seen on Titan. It presents similar shape as Carrizozo flow field (Fig. 14).

As indicated above, Hotei Regio is probably a massive cryovolcanic terrain that consists of caldera-like figures and depositional areas filled with lava flows. One terrestrial terrain that resembles Hotei Regio is the Harrat Khaybar volcanic field (Fig. 15), which is located at North of Medina in Saudi Arabia. The western half of the Arabian Peninsula contains extensive lava fields known as haraat (PINT, 2006). One such field is the 14,000 km² volcanic field that was formed by eruptions along a 100 km N-S vent system over the past 5 million years. The area contains a wide range of volcanic rock types, spectacular landforms and several generations of dark fluid basalt lava flows (PINT, 2006). Jabal Abyad, in the center of the image, was formed from more viscous, silica-rich lava classified as a rhyolite. While the 322 m high Jabal al Qidr exhibits stratovolcano, Jabal Abyad is a lava dome. To the west (image top center) is the impressive Jabal Bayda. This symmetric structure is a tuff cone, formed by eruption of lava in the presence of water. The combination produces wet, sticky pyroclastic deposits that can build a steep cone structure, particularly if the deposits consolidate quickly (PINT, 2006). In Fig. 15, we present a comparison between Earth's, Titan's and Enceladus' possible volcanic terrains and tectonic zones of weakness that consist the passage for internal material to deposit on the surfaces.

REFERENCES

BARNES, J.W. and 11 co-authors (2006). A 5-Micron-Bright Spot on Titan: Evidence for Surface Diversity. *Geophys. R. Lett.*, 33, L16204.

BARNES, J.W. and 10 co-authors (2007). Global-scale surface spectral variations on Titan seen from Cassini/VIMS. *Icarus*, 186, 242-258.

BLEACHER, J.E., GARRY, W.B. & J.R. ZIMBELMAN (2008). Observations of surface textures that are indicative of lava sheet inflation in monogenetic flow fields: Insights from the McCartys and Carrizozo flow fields. *Geol. Society of America*, 40, 114.

BROWN, R.H. and 21 co-authors (2004). The Cassini Visual And Infrared Mapping Spectrometer (Vims) Investigation. *Space Science Reviews*, 115, 111-168.

BROWN, R.H. and 26 co-authors (2006). Composition and Physical Properties of Enceladus' Surface. *Science*, 311, 1425-1428.

COLLINS, G.C. & J.C. GOODMAN (2007). Enceladus' south polar sea. *Icarus*. 189, 72–82.

CONSOLMAGNO, G.J. & J.S. LEWIS (1978). The evolution of icy satellite interiors and surfaces. *Icarus*, 34, 280-293.

COUSTENIS, A., HIRTZIG, M., GENDRON, E., DROSSART, P., LAI, O., COMBES, M. & A. NEGRAO (2005). Maps of Titan's surface from 1 to 2.5 μm. *Icarus*, 177, 89-105.

COUSTENIS, A. & W.C. TAYLOR (2008). *Titan - Exploring an Earth-like World*. Scientific Publishing Company, Singapore, Eds.

DOUGHERTY, M.K., KHURANA, K.K., NEUBAUER, F.M., SAUR, C.T., LEISNER, J. & J.S. BURTON (2006). Identification of a Dynamic Atmosphere at Enceladus with the Cassini Magnetometer. *Science*, 311, 1406.

ELACHI, C. and 21 co-authors (2004). Radar: The Cassini Titan Radar Mapper. *Space Science Reviews*, 115, 71-110.

ELACHI, C. and 30 co-authors (2005). Cassini Radar Views the Surface of Titan. *Science*, 308. 970-974.

FORTES, A.D. (2000). Exobiological implications of a possible subsurface ocean inside Titan. *Icarus*, 146, 444–452.

FORTES, A.D., GRINDROD, P.M., TRICKETT, S.K. & L. VOCADLO (2007). Ammonium sulfate on Titan: Possible origin and role in cryovolcanism. *Icarus*, 188, 139–153.

FULCHIGNONI, M. and 41 co-authors (2005). In situ measurements of the physical characteristics of Titan's environment. *Nature*, 438, 785-791.

HANSEN, C.J., ESPOSITO, L., STEWART, A.I., COLWELL, J., HENDRIX, A., PRYIOR, W., SHEMANSKY, D. & R. WEST (2006). Enceladus' Water Vapor Plume. *Science*, 311, 1422.

HURFORD, T.A., BILLS, B.G., HELFENSTEIN, P., GREENBERG, R., HOPPA, G.V. & D.P. HAMILTON (2009). Geological implications of a physical libration on Enceladus. *Icarus*, 203, 541–552.

IVANOV, B.A., BASILEVSKY, A.T. & G. NEUKUM (1997). Atmospheric entry of large meteoroids: implication to Titan. *Planetary and Space Science*, 45. 993–1007.

JOHNSON, T. (2004). Geology of the Icy planets. *Space science reviews*, 166, 401-420.

JOLLIFFE, I.T. (2002). *Principal Component Analysis*. Springer series in statistics. New York: Springer.

KARGEL, J.S. (1994). Cryovolcanism on the icy satellites. *Earth, Moon, and Planets*, 67, 101-113.

KIEFFER, S.W., LU, X., BETHKE, C.M., SPENCER, J.R., MARSHAK, S. & A. NAVRITSKY (2006). A Clathrate Reservoir Hypothesis for Enceladus' South Polar Plume. *Science*, 314, 1764 - 1766.

LAMMER, H. and 16 co-authors (2009). What makes a planet habitable? *Astronomy and astrophysics review*, 17, 181-249.

LEWIS, J.S. (1971). Satellites of the Outer Planets: Their Physical and Chemical Nature. *Icarus*, 15, 174.

LEWIS, J.S. (1972). Metal/silicate fractionation in the Solar System. *Earth Planet. Sci. Lett.*, 15, 286-290.

LINDAL, G.F., WOOD, G.E., HOTZ, H.B., SWEETNAM, D.N., ESHELMAN, V.R. & G.L. TYLER (1983). The atmosphere of Titan: An analysis of the Voyager 1 radio occultation measurements. *Icarus*, 53, 348-363.

LOPES, R.M.C. and 15 co-authors (2007a). The Lakes and Seas of Titan. *Eos, Transactions American Geophysical Union*, 88, 569-570.

LOPES, R.M.C. and 42 co-authors (2007b). Cryovolcanic features on Titan's surface as revealed by the Cassini Titan Radar Mapper. *Icarus*, 186, 395–412.

LOPES, R.M.C. and 24 co-authors and the Cassini Radar Team (2010). Distribution and interplay of geologic processes on Titan from Cassini radar data. *Icarus*, 205, 540–558.

LORENZ, R.D. & J. MITTON (2008). Titan Unveiled. Princeton University Press.

LORENZ, R.D. and 39 co-authors (2006). The sand seas of Titan: Cassini RADAR observations of longitudinal dunes. *Science*, 312, 724–727.

LORENZ, R.D. and 15 co-authors and the Cassini Radar Team (2008). Fluvial channels on Titan: Initial Cassini radar observations. *Planetary and Space Science*, 56, 1132-1144.

McCORD, T.B. and 16 co-authors and the Cassini VIMS Team (2006). Composition of Titan's Surface from Cassini VIMS. *Planetary Space Science*, 54, 1524–1539.

McCORD, T.B. and 13 co-authors (2008). Titan's surface: Search for spectral diversity and composition using the Cassini VIMS investigation. *Icarus*, 194, 212-242.

McKAY, C.P. & H.P. SMITH (2005). Possibilities for methanogenic life in liquid methane on the surface of Titan. *Icarus*, 178, 274-276.

NEISH, C.D., LORENZ, R.D., O' BRIEN, D.P and the Cassini Radar Team (2006). The potential for prebiotic chemistry in the possible cryovolcanic dome Ganesa Macula on Titan. *International Journal of Astrobiology*, 5(1), 57-65.

OWEN, T. (2005). Huygens rediscovers Titan. *Nature*, 438, 756-757.

PINT, J.J. (2006). Prospects for Lava-Cave Studies in Harrat Khaybar, Saudi Arabia. *AMCS Bulletin*, 19, 197-200.

PORCO, C.C. and 19 co-authors (2004). Cassini Imaging Science: Instrument Characteristics And Anticipated Scientific Investigations At Saturn. *Space Science Reviews*, 115, 363-497.

PORCO, C.C. and 35 co-authors (2005). Imaging of Titan from the Cassini spacecraft. *Nature*, 434, 159-168.

PORCO, C.C. and 24 co-authors (2006). Cassini Observes the Active South Pole of Enceladus. *Science*, 311, 1393-1401.

POSTBERG, F. and 7 co-authors (2009). Sodium salts in E-ring ice grains from an ocean below the surface of Enceladus. *Nature*, 459, 1098–1101.

RADEBAUGH, J., LORENZ, R., KIRK, R.L., LUNINE, J.I., STOFAN, E.R., LOPES, R.M.C., WALL, S.D. and the Cassini Radar Team (2007). Mountains on Titan observed by Cassini Radar. Icarus, 192, 77–91.

RADEBAUGH, J., LOPES, R.M.C., STOFAN, E.R., VALORA, P., LUNINE, J.I., LORENZ, R.D. and the Cassini Radar Team (2008). Mountains on Titan as Evidence of Global Tectonism and Erosion. *39th Lunar and Planetary Science Conference* XXXIX, 1391, 2206.

RADEBAUGH, J., LORENZ, R., FARR, T., PAILLOU, P., SAVAGE, C. & SPENCER, C. (2009). Linear dunes on Titan and earth: Initial remote sensing comparisons. *Geomorphology*, 121(1-2), 122-132.

RAULIN, F. (2008). Astrobiology and habitability of Titan. *Space Science Reviews*, 135, 37-48.

SODERBLOM, L.A. and 26 co-authors (2007). Correlations between Cassini VIMS spectra and RADAR SAR images: Implications for Titan's surface composition and the character of the Huygens Probe Landing Site. *Planetary and Space Science*, 55, 2025-2036.

SODERBLOM, L.A. and 12 co-authors (2009). The geology of Hotei Regio, Titan: Correlation of Cassini VIMS and RADAR. *Icarus*, 204, 610-618.

SOLOMONIDOU, A., COUSTENIS, A., BAMPASIDIS, G., KYRIAKOPOULOS, K. & X. MOUSSAS (2010). Possible cryovolcanic and tectonic processes on Titan and Enceladus: Similarities to terrestrial systems. *European Geosciences Union*, Vienna, 12, 4355.

SOTIN, C. and 25 co-authors (2005). Release of volatiles from a possible cryovolcano from near-infrared imaging of Titan. *Nature*, 435, 786-789.

STOFAN, E.R. and 37 co-authors (2007). The lakes of Titan. *Nature*, 445, 61-64.

THEKAEKARA, M.P. (1973). The Extraterrestrial Solar Spectrum. *Eds. Institute of Environmental Sciences. Mount Prospect Illinois*, 71-133.

TOBIE, G., JONATHAN, I.L. & C. SOTIN (2006). Episodic outgassing as the origin of atmospheric methane on Titan. *Nature*, 440, 61–64.

TOBIE, G., CADEKC, O. & C. SOTINA (2008). Solid tidal friction above a liquid water reservoir as the origin of the south pole hotspot on Enceladus. *Icarus*, 196, 642-652.

TOMASKO, M.G. and 39 co-authors (2005). Rain, winds and haze during the Huygens probe's descent to Titan's surface. *Nature*, 438, 765-778.

WAITE, J. H. and 14 co-authors (2009). Liquid water on Enceladus from observations of ammonia and ^{40}Ar in the plume. *Nature*, 460, 487–490.

WALL, S. D. and 16 co-authors (2009). Cassini RADAR images at Hotei Arcus and western Xanadu, Titan: Evidence for geologically recent cryovolcanic activity. *J. Geophys. Res.*, 109, E06002.

WILSON, E.H. & S.K. ATREYA, (2004). Current state of modelling the photochemistry of Titan's mutually dependent atmosphere and ionosphere. *Geophys. Res. Lett.*, 36, L04203.

WOOD, C.A., LORENZ, R., KIRK, R., LOPES, R., MITCHELL, K., STOFAN, E. and the Cassini Radar Team (2009). Impact craters on Titan. *Icarus*, 206, 334-344.

ZARNECKI, J.C. and 25 co-authors (2005). A soft solid surface on Titan as revealed by the Huygens Surface Science Package. *Nature*, 438, 792-795.

Appendix E1

Life in the Saturnian Neighborhood

Book Chapter published in the book *Life on Earth and other Planetary Bodies* (2012),
Series: Cellular Origin, Life in Extreme Habitats and Astrobiology,
Volume 24, pp. 485-522
Hanslmeier, Arnold; Kempe, Stephan; Seckbach, Joseph (Eds.)
Springer Books

LIFE IN THE SATURNIAN NEIGHBORHOOD

ATHENA COUSTENIS[1], FRANCOIS RAULIN[2], GEORGIOS BAMPASIDIS[1,3], AND ANEZINA SOLOMONIDOU[1,3]
[1]LESIA, Observatoire de Paris, CNRS, UPMC Univ Paris 06, Univ. Paris-Diderot–Meudon, France
[2]LISA-IPSL, CNRS/UPEC & Univ. Paris Diderot, 61 Avenue Général de Gaulle, F-94000 Créteil, France
[3]National & Kapodistrian University of Athens, Athens, Greece

1. Introduction and Context

Charles Darwin's vision, in 1859, of the origin and evolution of life on Earth, paved the way for future biological searches and studies on our planet and on other planetary bodies. The DNA decoding by James Watson and Francis Crick (1953) confirmed both the complexity and the symmetry of living particles. Following their strides, astrobiology, the study of evidence for life outside the Earth, is not only the research of the origin, distribution, and evolution of life in the whole universe but also that of structures and processes related to life and its destiny (Raulin, 2007). In general, astrobiology brings together different scientific disciplines such as astrophysics, geology, chemistry, geochemistry, biology, and more in order to shed light on the many aspects regarding the creation of our solar system as well as the initiation of life. Starting with the terrestrial paradigm, astrobiology focuses on extraterrestrial environments, posing the unanswered question on the origins of life on Earth and elsewhere, while investigating the more easily accessible organic compounds—and in particular the prebiotic chemistry—on other celestial bodies.

It is generally admitted today that life arose on Earth as the derivative of a long chemical evolution, implying three major raw ingredients: liquid water, carbonaceous matter, and energy, working together over time. Since life primitive structures should be able to emerge, evolve, and develop in suitable environments, the quest for possible habitats outside our planet is focused on places where these ingredients are or have been present.

With the discovery of planets beyond our solar system and the search for current living organisms or for favorable conditions for past and future life in exotic places such as Mars, Europa, Titan, and Enceladus, the notion of habitability takes a new dimension. In this chapter, we focus on habitability issues and possible living forms around Saturn. Saturn has 62 known natural satellites to this date, and the discoveries from the Cassini–Huygens mission, which started in 2004, have revolutionized our perception about whether these bodies could harbor life

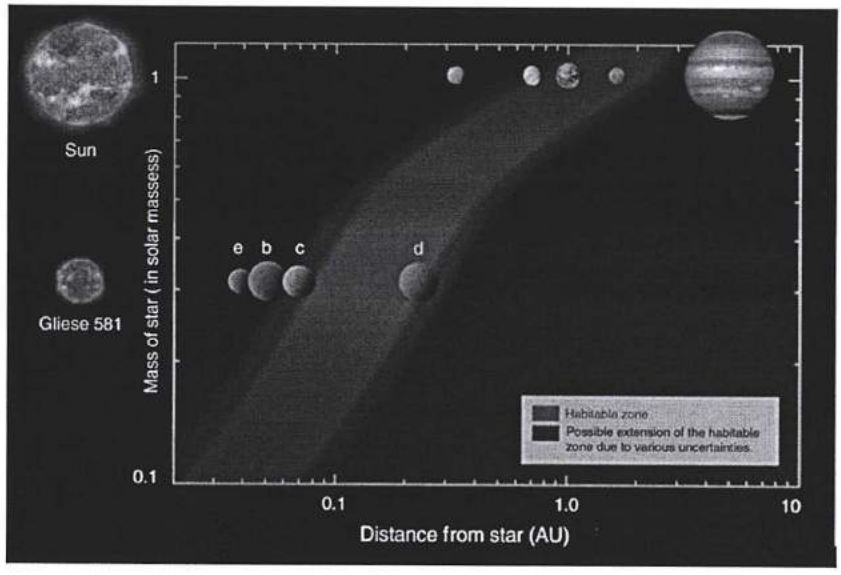

Figure 1. Map of the habitable zone's (*HZ*) limits. Earth is in the middle of the HZ for the solar system while Mars and Venus lie in its boundaries. The planetary bodies *e*, *b*, *c*, and *d* are exoplanets. Gliese 581 is *red dwarf* star 20.3 light years from Earth (NASA).

(now or in the future) or at least provide us with valuable information on the origin and evolution of life in the solar system. In the latter case, at least two of the Kronian satellites, Titan and Enceladus, can certainly offer a lot.

Discovered in 1655 by the Dutch astronomer Christiaan Huygens, Titan is the largest satellite of Saturn, bigger than planet Mercury, at 5,152 km in diameter. Titan rotates around the Sun within 29.5 years following Saturn on its trek. As a result, Titan experiences seasons, each of which lasts about 7.5 terrestrial years. Moreover, Titan orbits around Saturn within 16 Earth-days almost synchronously; thus, its solid surface rotates very slowly. Instead, due to strong zonal winds (Bird et al., 2005; Lorenz et al., 2008b), its atmosphere is in super-rotation. Due to Titan's distance from the Sun of about 9.5 astronomical units (AU), the satellite receives slightly more than 1% of the solar flux that the Earth registers at the top of its atmosphere at 1 AU (Fig. 1). In addition, Titan revolves far enough from the giant planet (about 20 Saturnian radii), to avoid any critical interactions with the rings or the magnetosphere. Although sometimes Titan moves close enough to Saturn to allow its atmosphere to interact with the energetic particles of the magnetosphere of Saturn. Together with the solar photons, these interactions play a key role in Titan's chemical evolution. Indeed, Titan possesses an extensive atmosphere made mostly of N_2 with a column density ten times that of Earth's (Fig. 2). Furthermore, Titan's astrobiological potential is enhanced by the presence

Figure 2. (*left*) Titan's thick, orange, and smoggy atmosphere (NASA); (*right*) Earth's atmosphere as seen from space (NASA); the cloudy nature of both atmospheric envelopes and also commonalities. Both Titan and Earth experience a greenhouse effect and complex photochemical reactions in their upper atmospheric layers.

of a rich organic chemistry which is produced in its atmosphere, thanks to the presence of its second most abundant gas, methane (about 1.4% in the stratosphere and 5% on the ground), and on the surface from the interactions among the various constituents.

Thus, Titan's unique and dense atmosphere harbors a whole host of organic trace gases: hydrocarbons and nitriles (e.g., Coustenis et al., 2007, 2010b). Its surface presents many morphological similarities with the Earth's, which surprisingly show similar structural diversity, but the raw materials are different from those on our own planet. With an environment very rich in organics, Titan, along with comets, is thus often considered as one of the best targets to search for prebiotic chemistry at a full planetary scale and a possible habitat for extraterrestrial life in all probability different from the terrestrial one. More importantly, our understanding of the origin of life on Earth could greatly benefit from studying Titan, where the low solar influx, the composition of the atmosphere, and the possible presence of an internal water ocean give us the opportunity to study the conditions prevailing on the primitive Earth.

After more than 8 years of close observations by remote sensing and *in situ* instruments on board the Cassini–Huygens mission, Titan is revealed as an evolving planet, geologically active, not only from erosional processes in the face of the lack of impact craters (Lopes et al., 2010) but also because of its possible cryovolcanism (Tobie et al., 2005; Barnes et al., 2006; Nelson et al., 2009a, b; Soderblom et al., 2009) and morphotectonism (Solomonidou et al., 2012), aeolian and fluvial erosion (Fulchignoni et al., 2005; Israel et al., 2005; Niemann et al., 2005; Owen, 2005; Tomasko et al., 2005; Zarnecki et al., 2005; Jaumann et al., 2008;

Lorenz and Mitton, 2008; Raulin, 2008; Lebreton et al., 2009), clouds and precipitations, and a methane cycle very similar to the water cycle on Earth (Bird et al., 2005; Atreya et al., 2006; Coustenis and Taylor, 2008; Brown et al., 2009a; Coustenis and Hirtzig, 2009). The organic chemistry products are found on Titan all the way from the upper atmosphere to the surface and possibly in the interior, indicating close exchanges between the different elements and planetary layers (interior-surface-atmosphere).

Enceladus, first observed by Sir Frederick William Herschel in 1789, is another intriguing moon of Saturn. Although it is quite small compared to Titan, with a mean radius of 252 km, the large plumes ejected from its south-polar region, as first discovered by the Cassini–Huygens mission magnetometer (Dougherty et al., 2006), make it very important for astrobiology. These geyser-like features mainly consist of water vapor and ice and include organic compounds (Dougherty et al., 2009; Waite et al., 2009). This strongly suggests the potential presence of a complex organic chemistry ongoing in the interior and the presence of liquid water, providing grounds for the search of a liquid ocean at short distances under the surface.

Enceladus is an unambiguous example of a cryovolcanically active icy satellite identified in the outer solar system and can be used to understand active processes that are thought to have once played and/or are still possibly playing (e.g., Titan's case) a role in shaping the surfaces of other icy moons. These processes include tidal heating, possible internal convection, cryovolcanism, and ice tectonics, which all can be studied as they currently happen on Enceladus. Moreover, the plume source region on Enceladus samples a warm, chemically rich, environment that may facilitate complex organic chemistry and biological processes.

What is the level of complexity reached by the organic chemistry in Titan and Enceladus? What is the correlation between the interior, the surface, and the atmosphere, especially regarding the biological aspects? What are the habitability potentialities in the Kronian environment, in particular for Titan? Such are the questions that further exploration of Titan and Enceladus should answer in the coming years (Brown et al., 2009b). After all, Darwin's evolutionary ideas could also be successfully applied *sensu lato* in the Saturnian neighborhood.

2. Habitability Issues for Outer Planetary Satellites

Liquid water is established as the necessary solvent in which life emerges and evolves. Water, as an abundant compound in our galaxy, can be found in various places, from cold dense molecular clouds to hot stellar atmospheres (e.g., Cernicharo and Crovisier, 2005; Hanslmeier, 2010). The thermodynamic behavior of water, which enables it to remain liquid in a large range of temperatures and pressures and to be a strong polar–nonpolar solvent, makes it essential for maintaining stable biomolecular and cellular structures (Des Marais et al., 2002).

A large number of organisms are capable of living in water. However, in a deposit of pure water, life will probably never spontaneously originate and evolve,

since while there are many organisms living in water, none we know of is capable of living on water alone, because life requires other essential elements such as nitrogen and phosphorus in addition to hydrogen and oxygen. Moreover, no known organism is made entirely of water. "Just water" is therefore not an auspicious place for the emergence and evolution of life.

The concept of the habitable zone (Fig. 1) is, of course, based on our understanding of life on Earth and is related to the presence of liquid water on a body's surface. But the requirements for extraterrestrial life do not have to be the same, suggesting that life could exist outside the habitable zone (Cohen and Stewart, 2002), in particular if liquid water exists underneath the surface. Furthermore, the changes that occurred on Earth's primordial atmosphere under the influence of early primitive plant life (Wolstencroft and Raven, 2002) require that diachronic alternation be taken into account regarding the habitability opportunities of a planetary body. In addition, internal processes such as volcanic activity, hydrothermal movements, and radioactive decay that possibly occur within satellites located outside the habitable zone could affect the radiation and thermal level of the body and thus change significantly the environmental conditions favoring life (Horneck, 2008).

Of the large satellites of the gas giants, there are those that may house underground water deposits in direct contact with heat sources below their icy crust and those expected to have either liquid water layers encapsulated between two ice layers or liquids above ice. In the study for the emergence of life elements on such satellites, the timescale is of essence. If it is long enough, the liquid water underground ocean may host life. Thus, the icy satellites of the outer planets of the solar system, as well as the recently discovered exoplanets, host unique conditions which may inhibit the emergence of life precursors in isolating environments that can prevent the concentration of the ingredients necessary for life or the proper chemical inventory for the relevant biochemical reactions. Conversely, according to Trinks et al. (2005), a coupled sea/ice system could in theory provide the necessary conditions for life emergence in the primitive Earth. Additional laboratory experiments and *in situ* studies of deep subglacial isolated lakes in Antarctica (Kapitsa et al., 1996) would improve our understanding in this field, as the physical properties of deep subglacial lakes resemble those found on both Jupiter's moon Europa and Saturn's moon Enceladus (Bulat et al., 2009).

As a consequence, the satellites of the giant planets like Europa, Enceladus, Ganymede and Titan are possible habitable environments and valid targets in the research for life with space missions and/or telescopes. However, life structures that do not influence the atmosphere of their host planet on a global scale will not be remotely detectable. In the solar system's neighborhood, such potential habitats can only be investigated with appropriate designed space missions, as in the case of Europa, where the Europa Jupiter Space Mission (Clark et al., 2009) will attempt to look for the hypothesized internal liquid water ocean. In the case of the Saturnian satellites (see hereafter), proposed future missions shall also address this question.

3. Titan: Organic Factory and Habitat

Retracing the processes, which allowed for the emergence of life on Earth around 4 billion years ago, is a difficult challenge. Our planet has drastically evolved since that time, and most of the traces of what were the initial environmental conditions have been erased as a consequence of plate tectonics and erosion. It is thus crucial for astrobiologists to find extraterrestrial locales with similarities to our planet's early stages. This will provide a way to study in the present time some of the processes, which occurred on the primitive Earth, when prebiotic chemistry was in its young stages (Fig. 3). For instance, a subsurface ocean in the interior of the satellite of a gas giant (as on Europe, Enceladus, Titan, etc.) may be habitable for some kind of life form—even though not necessarily an Earth analogue-but also information on the terrestrial-like atmospheric and surface conditions on any planetary body can provide valuable information.

Titan is a good candidate in this instance as its atmosphere exhibits more similarities with the Earth's today—and even more so in the past than any other solar system body (e.g., Coustenis and Taylor, 2008). Recent Cassini–Huygens findings have revolutionized our understanding of Titan's system and its potential for harboring the "ingredients" necessary for life (Coustenis and Taylor, 2008;

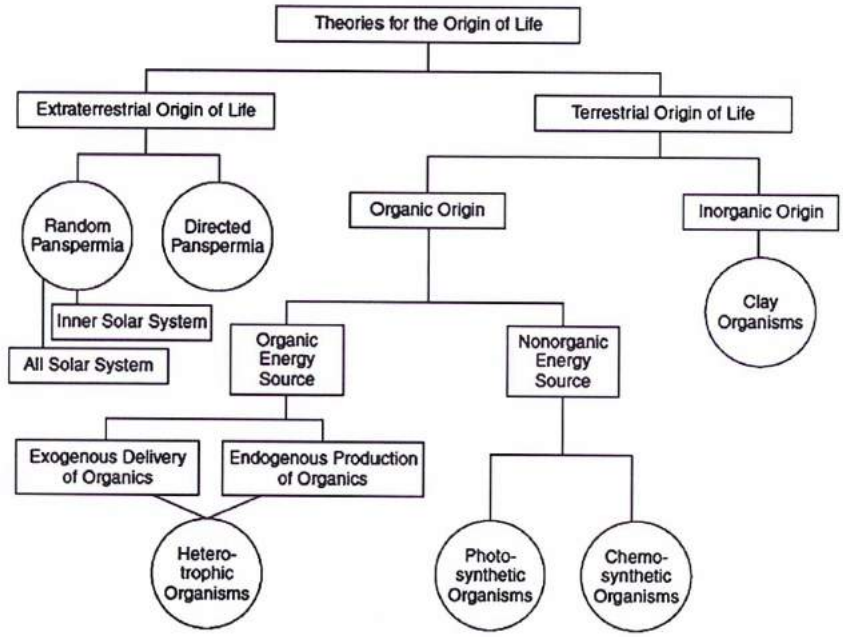

Figure 3. A scheme of possible theories on the origin of terrestrial and extraterrestrial life. The chemistry of the raw materials as well as energy sources plays key roles to each evolutionary path (From Davis and McKay (1996) and McKay et al. (2008)).

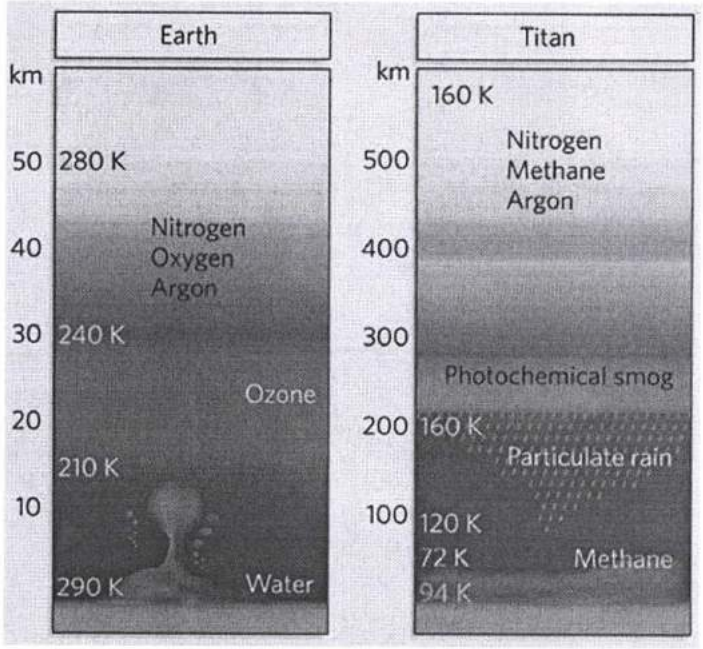

Figure 4. Atmospheric structure comparison of Earth and Titan. Both atmospheres are nitrogen-dominated, but on Titan, methane plays the role of water on Earth. Both atmospheres have an important haze content, and condensation processes are expected similarly on both bodies (Owen, 2005).

Lorenz and Mitton, 2008). Recent discoveries reveal that beyond its rich organic budget, and sufficient energy sources to drive chemical evolution, Titan also probably contains a vast subsurface ocean (Lorenz et al., 2008b).

Titan is indeed a very complex world much as our own planet. It is the only one other than Earth, that possesses a thick nitrogen-based atmosphere, four times denser than on our own atmosphere, with a rich organic chemistry (Fig. 4). It also has a geologically complex and active surface including lake-like features filled with organic liquid (e.g., Stofan et al., 2007). The physical processes within this world invite further close-up investigation that will provide a better understanding of the terrestrial processes as well.

Current investigations have shown that Titan fulfills many of life's prerequisites for a carbonaceous portfolio. Due to its nitrogen atmosphere, which is not in chemical equilibrium but like a chemical factory initiates the formation of complex positive and negative ions in the high thermosphere as a consequence of induced magnetospheric–ionospheric–atmospheric interactions involving EUV, UV radiation, energetic ions, and electrons (as recently demonstrated by the Cassini Ion and Neutral Mass Spectrometer, INMS). In this dynamic evolving environment, the second most abundant atmospheric constituent, methane, is dissociated irreversibly to produce a variety of trace gases such as hydrocarbons

(e.g., ethane, acetylene, and propane) and in combination with the nitrogen, nitriles (e.g., hydrogen, cyanide, acetonitrile, cyanoacetylene), which are detected in the stratosphere (between 70 and 500 km in altitude) by the Composite Infrared Spectrometer (CIRS) onboard Cassini (e.g., Coustenis et al., 2007, 2010b). Literally, some of these gases would be considered as signs of life if they were on our planet (HCN is considered a prebiotic molecule, a precursor of life). Hence, finding how they form on Titan could give us clues on how life began on Earth.

The Cassini–Huygens mission has revealed the essential details of the organic and methane hydrologic cycles that we see today on Titan (Raulin et al., 2008; Brown et al., 2009b; Lebreton et al., 2009). Methane on Titan seems to play the role of water on Earth, with a similar complex cycle as shown in Fig. 5 (Atreya et al., 2006). On Titan, where methane is photodissociated and forms ethane and other organic products in the atmosphere, it should have disappeared after 10–100 million years, with around 34 Myrs as a nominal period (Atreya et al., 2006).

The intriguing question then is of how methane gets replenished in the atmosphere. On Earth today, it is life itself that refreshes the methane supply since methane is a by-product of the metabolism of many organisms. Hence, could this mean there is life on Titan? However, the Huygens Gas Chromatograph Mass Spectrometer (GCMS) data have shown that methane is not of biogenic origin, because the isotopic ratios are compatible with inorganic values (Niemann et al., 2005, 2010). Thus, the sinks of atmospheric methane on Titan are relatively well understood, but the major sources of replenishment are still very model dependent, as will be discussed later.

3.1. THE ATMOSPHERIC ORGANIC-RICH ENVIRONMENT OF TITAN

Although Titan's atmosphere is much colder than Earth's, it presents many direct similarities with our planet (Fig. 4), at different levels which have been pointed out since Voyager days. To begin with, both are made of the same main constituent, dinitrogen. A similar vertical structure from the troposphere to the ionosphere is also present, as well as a surface pressure of 40% larger than that of the Earth's (Fulchignoni et al., 2005). This is the only case of an extraterrestrial planetary atmospheric pressure so similar to that of Earth. Furthermore, a very exciting and complex organic chemistry takes place in Titan's atmosphere.

The direct analysis of the ionosphere by the Cassini Ion and Neutral Mass Spectrometer (INMS) instrument during the low-altitude Cassini flybys of Titan shows the presence of many organic species at detectable levels, at very high altitudes (1,100–1,300 km). Extrapolation of the INMS measurements (limited to mass up to 100 Da) and of Cassini Plasma Spectrometer (CAPS) data strongly suggests that high molecular weight species (up to several 1,000 Da) may be present in the ionosphere (Waite et al., 2007). These observations open a fully new vision of the organic processes occurring in Titan's atmosphere, with a strong implication of the ionospheric chemistry in the formation of complex organic

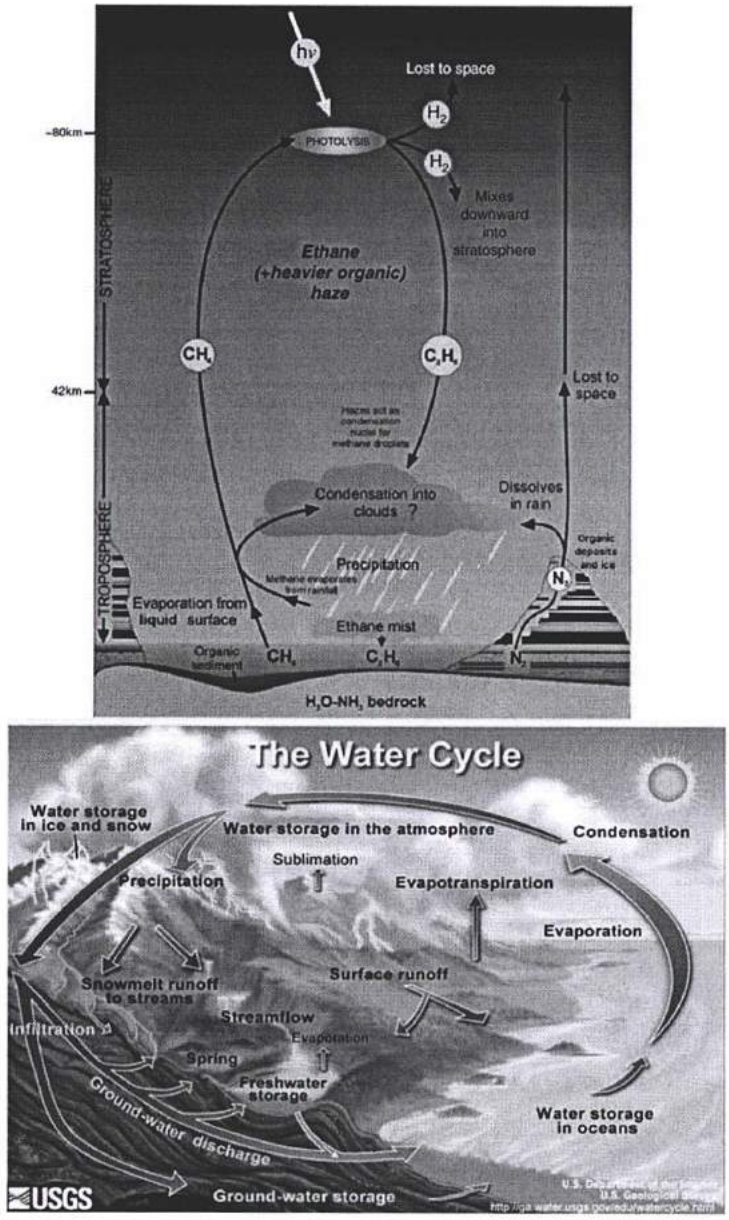

Figure 5. Titan's methane (*upper*) and Earth's water (*lower*) cycles in the atmosphere (USGS). Titan has a methane cycle resembling Earth's water cycle in its processes.

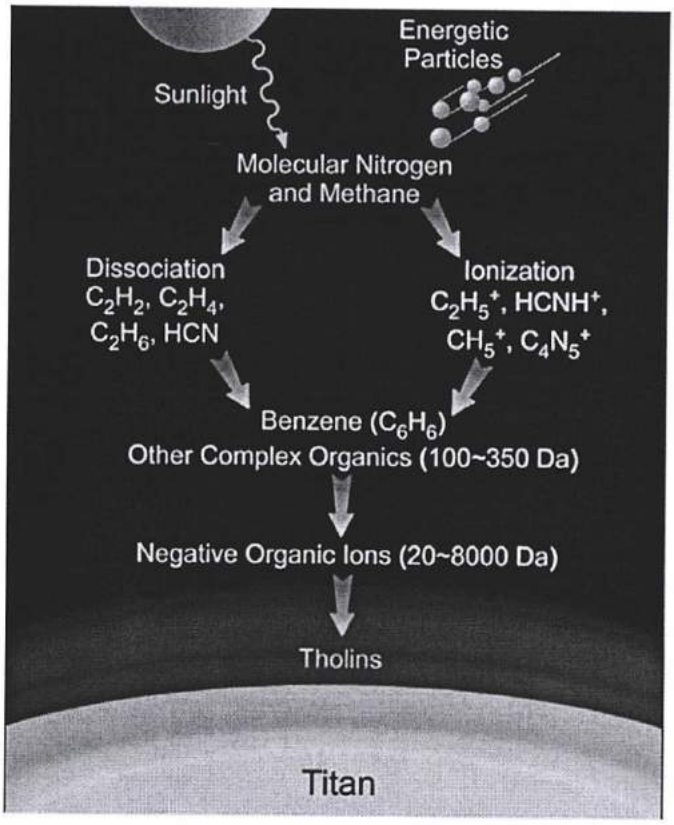

Figure 6. Organic chemistry in Titan's upper atmosphere. At the upper layers of the atmosphere, sunlight and energetic particles from Saturn's magnetosphere destroy CH_4 and N_2 and produce complex organic molecules that assemble to form negative ions from which tholins (hydrocarbon–nitrile aerosols) possibly form and diffuse in the lower parts of the atmosphere. Cassini/INMS measurements showed evidence for their formation around 1,000 km in altitude (Waite et al., 2007), and the Cassini/CIRS instrument detects the neutral chemistry in the stratosphere (Flasar et al., 2005).

compounds in Titan's environment (Fig. 6), which was not envisaged before. These compounds are detectable in solar and stellar UV occultations and initiate the process of haze formation starting at about 950 km (Waite et al., 2007) to finally condense out.

In the neutral atmosphere of Titan (between roughly 100 and 500 km), as we mentioned above, CH_4 chemistry is coupled with N_2 chemistry producing the formation of many organics in gas and particulate phase: hydrocarbons, nitriles, and complex refractory organics. Several photochemical models describing the chemical and physical pathways involved in the chemical evolution of the atmosphere of Titan have been published for the last 20 years (Yung et al., 1984;

Toublanc et al., 1995; Wilson and Atreya, 2004; Lavvas et al., 2008). These papers estimate the resulting vertical concentration profiles of the different molecules. Based on these models, the cycling of volatile chemicals starts with the dissociation of N_2 and CH_4 through electron, photon, and cosmic rays impacts in Titan's atmosphere. The primary processes allow for the formation of acetylene (C_2H_2) and hydrogen cyanide (HCN) in the high atmosphere. These molecules play a key role in the general chemical scheme: once they are formed, they diffuse down to the lower levels where they allow the formation of higher hydrocarbons and nitriles and perhaps aromatic compounds. Additionally, methane dissociation probably also occurs in the low stratosphere through photocatalytic processes involving acetylene and polyynes. The end products of the chemical evolution of methane in the atmosphere are complex refractory organic compounds and ethane.

As these aerosols and haze particles fall through the atmosphere and grow, they become detectable with imaging systems such as the Cassini Imaging Science Subsystem (ISS) at about 500 km altitude and are ubiquitous throughout the stratosphere (Porco et al., 2005). They are strong absorbers of solar UV and visible radiation and play a fundamental role in heating Titan's stratosphere and driving wind systems in the middle atmosphere, much as ozone does in the Earth's middle atmosphere.

Experiments that simulate the reactions taking place in Titan's atmosphere (such as the Miller-Urey experiment) produce refractory organics, usually named tholins (Sagan and Khare, 1979) ("tholins" are solid products in the laboratory mimicking complex refractory organics: Nguyen et al. (2007); and references therein). Tholins represent laboratory analogues of Titan's aerosols and are useful to interpret many observational data which require information on the aerosols. As being experimental analogues of Titan's atmospheric particles, tholins also allow the study of the aerosols behavior in Titan's conditions with the tools available in the laboratory. Several organic compounds have already been detected in Titan's upper and lower atmosphere (Waite et al., 2007; Coustenis et al., 2010b). The list includes hydrocarbons (both with saturated and unsaturated chains) and nitrogen-containing organic compounds, exclusively nitriles, as expected from laboratory simulation experiments (Fig. 6). Moreover, since the Cassini arrival in the Saturnian system in 2004, the presence of water vapor and benzene has been unambiguously confirmed by the CIRS instrument.

3.2. TITAN'S PREBIOTIC RELEVANCE

Several of the organic processes that are occurring today on Titan form some of the organic compounds which are considered as key molecules in terrestrial prebiotic chemistry, such as hydrogen cyanide (HCN), cyanoacetylene (HC_3N), and cyanogen (C_2N_2). In fact, with several percent of methane in dinitrogen, the atmosphere of Titan is one of the most favorable atmospheres for prebiotic synthesis, although it almost lacks both oxygen and hydrogen. Concerning the hydrocarbon trace budget, photochemical models imply that light hydrocarbons are destroyed mostly

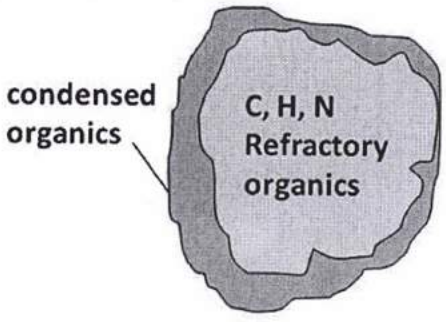

Figure 7. Composition of Titan's aerosols.

by reactions with OH^- and Cl^- radicals. Contrary to the very short lifetime of C_2H_2 on Earth (Rudolph et al., 1984), acetylene on Titan shows a seasonal variation during a Titan year (29.5 terrestrial years) and reaches almost the abundances recorded by Voyager 1 in 1980 (Coustenis et al., 2010a).

The Aerosol Collector Pyrolyser (ACP) experiment on Huygens provided the first direct *in situ* chemical analysis of Titan's aerosols. It collected haze particles from the stratosphere and the troposphere, heated them at different temperatures, and sent the produced gases for analysis to the GCMS instrument. The obtained results indicated that the aerosols are made of a refractory nucleus, composed of H, C, and N atoms (Fig. 7) and producing NH_3 and HCN after pyrolysis at 600°C (Israel et al., 2005). This strongly supports the tholin hypothesis. It also strongly suggests that Titan's aerosols may evolve once in contact with water ice on the surface and may produce a variety of organics of biological interest, such as amino acids (Neish et al., 2010; Ramirez et al., 2010).

Analogies are thus obvious between the organic chemistry activity currently occurring on Titan and the prebiotic chemistry which was once active on the primitive Earth, prior to the emergence of life (e.g., McKay and Smith, 2005). Indeed, in spite of the absence of permanent bodies of liquid water on Titan's surface, both chemistries are similar. As noted earlier, many resemblances can also be made between the role of methane on Titan and that of water on the Earth, with a complex cycle that has yet to be fully understood. Indeed, on Titan, methane can exist as a gas, liquid, and solid, since the mean surface temperature is almost 94 K (Fulchignoni et al., 2005), approaching the triple point of methane.

The atmosphere we enjoy today on Earth is probably radically different from the primitive one dating back to 4.6 billion years ago when our planet was nothing more than a molten ball of rock surrounded by an atmosphere of hydrogen and helium. In the absence of a magnetic field at those early stages, the intense solar wind from the young Sun blew this early atmosphere away. Then, as Earth cooled enough to form a solid crust, it was covered with active volcanoes, ejecting

water vapor, carbon dioxide, and ammonia to form an early toxic atmosphere. Eventually, light from the Sun broke down the ammonia molecules exsolved by the volcanoes, releasing nitrogen into the atmosphere. Over billions of years, the quantity of nitrogen built up to the levels we see today. Although life formed just a few hundred million years later, it was not until the evolution of bacteria, 3.3 billion years ago, that the early Earth atmosphere changed into the one we know today. During the period from 2.7 to 2.2 billion years ago, these early bacteria—known as cyanobacteria—used energy from the Sun for photosynthesis and released oxygen as a by-product. They also trapped carbon dioxide in organic molecules. In just a few hundred million years, these bacteria completely changed the Earth's atmosphere composition, bringing us to the current mixture of 21% oxygen and 78% nitrogen. Schaefer and Fegley (2007) predict that Earth's early atmosphere contained CH_4, H_2, H_2O, N_2, and NH_3, similar to the components used in the Miller–Urey synthesis of organic compounds, often related to Titan's and Enceladus's atmospheric inventory. Furthermore, Trainer et al. (2006) looked at the processes that formed haze on Titan and on early Earth and found many similarities for what could have served as a primary source of organic material to the surface.

Before the rise of the atmospheric oxygen in the terrestrial atmosphere 2.5 Gy ago, it considered possible that the abundance of methane gas was 10–20 times higher than the today's value of 1.6×10^{-6} (Pavlov et al., 2003). Hence, if the atmospheric CO_2/CH_4 ratio had become equal to 10 at the mid-Achaean era, an organic haze could have formed on this early environment (Pavlov et al., 2000; DeWitt et al., 2009). This hydrocarbon haze produced the anti-greenhouse effect which reduced the temperature of the atmosphere (Kasting and Howard, 2006). Titan also hosts a thick methane-induced organic haze, similar to the one predicted for the early Earth and, consequently, experiences the same anti-greenhouse effect (McKay et al., 1999). The absence of vast amounts of CO_2 on Titan is one of the major differences between the two atmospheric envelopes. On the other hand, hydrogen cyanide and other prebiotic molecules are among the starting materials for biosynthesis. The existence of hydrocarbons, and in particular acetylene and benzene, has really enlarged the borders of photochemical organic products.

Especially, the presence of benzene (C_6H_6) seems extremely interesting, as it is the only polycyclic aromatic hydrocarbon (PAHs) discovered on Titan today. The presence of PAHs on Titan's atmosphere is very important as they could contribute to the synthesis of biological building blocks. Moreover, the combination of the liquid deposits on the surface of Titan and the low temperature could host the proper environment for this biosynthesis. Recent laboratory experiments showed that aromatic compounds could be plausibly produced on icy surfaces (Menor-Salván et al., 2008). Benzene was first detected at 674 cm^{-1} based on Infrared Space Observatory (ISO/SWS) data (Coustenis et al., 2003) with the mixing ratio of 4×10^{-10} and was then also detected in the thermosphere (950–1,150 km) from the analysis of Cassini/INMS data (Waite et al., 2007) and firmly in the stratosphere (100–200 km) at all latitudes by Cassini/CIRS

measurements (Flasar et al., 2005; Coustenis et al., 2007, 2010b). Moreover, benzene has been tentatively identified on Titan's surface by Huygens/CGMS measurements (Niemann et al., 2005).

As Titan lacks oxygen and sufficiently high temperatures, as did primitive Earth, different evolutionary pathways from Earth must have been followed on Titan, and polyphenyls may possibly be created (Delitsky and McKay, 2010). The abundances of hydrocarbons are higher on Titan than those on Earth by a factor of about 10^2–10^4. Moreover, the temporal variations of the hydrocarbon traces on Titan experience a full cycle during the Titan year (Coustenis et al., 2010a) and are probably influenced by local or regional sources and sinks. Photochemical models are trying to reproduce these phenomena. Taking into account all the above-described characteristics, the prebiotic potential of Titan is enormous, and a huge effort in astrobiological studies is focused on its environment. Eventually, Titan still seems to be the ideal planet-size laboratory for increasing our knowledge of the evolution of the Earth's atmosphere.

3.3. ORGANIC CHEMISTRY AND MORPHOLOGY OF TITAN'S ACTIVE SURFACE

The Cassini–Huygens mission has significantly enhanced our understanding of Titan as the largest abiotic organic factory in the solar system. The abundance of methane and its organic products in the atmosphere, seas, and dunes exceeds the carbon inventory in the Earth's ocean, biosphere, and fossil fuel reservoirs by more than an order of magnitude (Lorenz et al., 2008a). As discovered by the Cassini/INMS, in the high atmosphere, heavy ions are formed (Waite et al., 2007).

Measurements throughout the atmosphere, both remote and *in situ*, have indicated the presence of numerous hydrocarbon and nitrile gases, as well as a complex layering of organic aerosols that persists all the way down to the surface of the moon (Tomasko et al., 2005; Coustenis et al., 2007; de Kok et al., 2007). Radar observations suggest that the ultimate fate of this aerosol "rain" is the generation of expansive organic dunes that produce an equatorial belt around the surface. Condensation of these species on aerosol particles is a probable explanation for these atmospheric characteristics. These particles, for which no direct data on their chemical composition were previously available, were analyzed by the Aerosol Collector and Pyrolyser instrument aboard Huygens probe. ACP results show that the aerosol particles are made of refractory organics which release HCN and NH_3 during pyrolysis.

This supports the tholin hypothesis (as described in section 3.1). From these new *in situ* measurements, it seems very likely that the aerosol particles are made of a refractory organic nucleus, covered with condensed volatile compounds (Israel et al., 2005). However, Huygens/GCMS did not detect a large variety of organic compounds in the low atmosphere (Niemann et al., 2005).

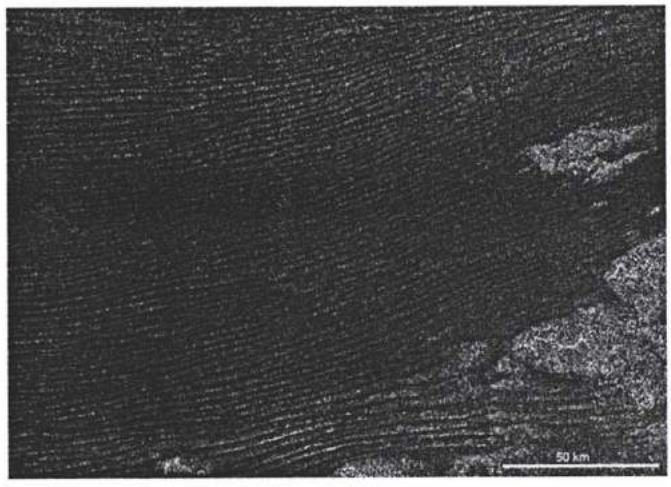

Figure 8. Linear dunes on Titan (Radebaugh et al., 2010). Titan's dunes are believed to be composed of ice and organics grains that possibly derive from a combination of the surface ice and the organic chemicals that fall through in Titan's atmosphere.

Moreover, the nature and abundances of the condensates have not been measured. Even more importantly for astrobiology, neither the elemental composition nor the molecular structure of the refractory part of the aerosols has been determined.

Eventually, these complex organic molecules are deposited on Titan's surface in large quantities, where data from Cassini's instruments hint at their existence. Hence, the upper thermosphere is linked intimately with the surface and the intervening atmosphere. In spite of the low surface temperature, the organics reaching the surface are probably evolving once in contact with water ice and may form organic molecules of biological interest.

Radar observations suggest that the ultimate fate of this aerosol "rain" is the generation of expansive organic dunes that produce an equatorial belt around the surface. Indeed, the surface of Titan shows also the presence of sedimentological and meteorological processes, as we see on Earth: There are many large dune areas (Lorenz et al., 2006; Radebaugh et al., 2008, 2010) (Fig. 8) where the terrestrial silica sand is probably replaced, once more, by water ice particles, mixed with the organic material of the aerosols.

Cassini's radar instrument finally unveiled what appears to be a land of lakes in Titan's northern polar regions (see Fig. 9) (Stofan et al., 2007). Cassini/ISS images also show a kidney-shaped dark feature about 200 km in length, named Ontario Lacus, that is outside the area of radar coverage and has recently been confirmed by the Cassini Visual and Infrared Mapping Spectrometer (VIMS)

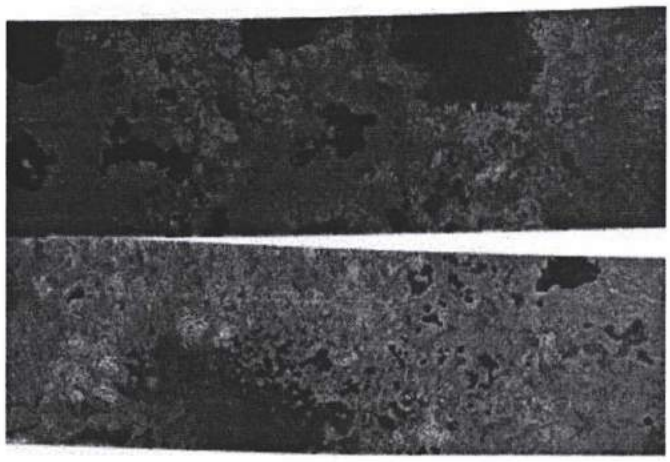

Figure 9. Lakes discovered in Titan's north-polar region by the Synthetic Aperture Radar (SAR) on board Cassini–Huygens mission (NASA/JPL). The dark patches are believed to be filled with hydrocarbon liquid.

not only to be a lake but also to be composed of ethane liquid (Brown et al., 2008). In the absence of a massive surface ocean but with analogues to all other terrestrial hydrological phenomena present, Titan's methane cycle is very exotic.

The liquid bodies are one of the main astrobiological aspects of Titan. Cassini's cameras (ISS) have allowed scientists to compile a nearly global surface map and to monitor the surface and atmosphere for activity. Intriguingly, repeated south-polar imaging by ISS revealed differences consistent with ponding of hydrocarbon liquids on the surface due to precipitation from a large storm. More recent ISS images of high northern latitudes illustrate the full extents (>500,000 km^2) of hydrocarbon seas, also observed by Cassini's radar. These observations demonstrate dynamic processes at work on Titan and indicate that the poles harbor liquid-hydrocarbon reservoirs, the extents of which differ from pole to pole and which may be coupled to seasonally varying circulation (Turtle et al., 2009).

The lakes and seas observed on Titan in the polar regions (Mitri et al., 2007; Stofan et al., 2007) make Titan the only body in the solar system having large liquid bodies on its surface. These very dark features at the high northern latitudes of Titan were finally shown to be liquid-filled (most probably with ethane-rich mixtures (Brown et al., 2008)) basins—classifying them as lakes.

The features range in size from less than 10 km^2 to at least 100,000 km^2. They are limited to the region poleward of 55°N. Currently, Cassini's instruments have identified and mapped almost 655 geological structures referred as lakes and/or basins (Fig. 10) (Hayes et al., 2008). Titan is thus the only planetary body, other than the Earth, with long-standing bodies of liquid on its surface (although direct observational evidence of the longevity of Titan's surface liquids remains

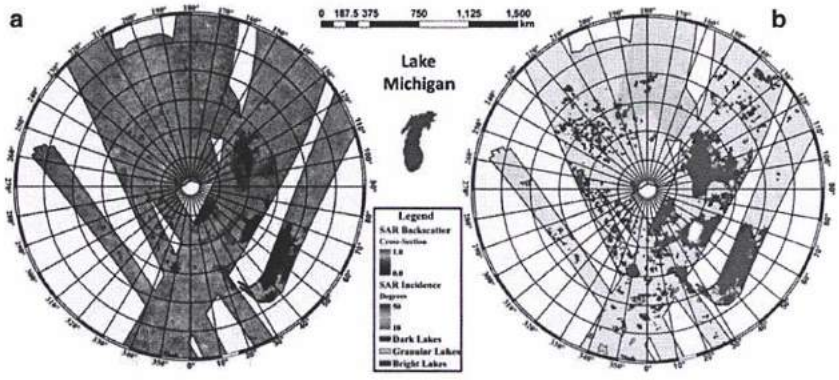

Figure 10. Map of almost 655 lakes and sea features by the Cassini radar system in azimuthal projection at the north pole of Titan. Map A (*left*) shows the radar swath mosaic up to May 2007 flybys. Map B (*right*) represents the spatial distribution of mapping units. Lake Michigan is illustrated for scale purposes (Hayes et al., 2008).

to be obtained). All of this suggests that Titan maybe even more similar to primitive Earth than we thought. However, the degree of complexity which can be reached from such an organic chemistry in absence of permanent liquid water bodies on Titan's surface is still unknown, although it could be quite high.

McKay and Smith (2005) noted the astrobiological importance of these geological features that are filled with liquid hydrocarbons, since there is a possibility for a different form of life to exist in such environments. It has been hypothesized that such a methanogenic life form consumes H_2 instead of O_2 that could be measured in the lower atmosphere. Two papers, by Strobel (2010) and Clark et al. (2010), based on data from the Cassini orbiter focus on the complex chemical activity on the surface of Titan. Strobel (2010) shows that hydrogen flows down through Titan's atmosphere and then somehow disappears on the surface. One of the most interesting phenomena occurring on Titan is that important quantities of atmospheric hydrogen precipitates and disappears when reach the surface. Such process resembles the oxygen consumption as occurring on Earth although in Titan's case, the element is hydrogen (Strobel, 2010).

Even though this is not supportive to the Titan's terrestrial-type life theory, it represents a hypothetical second form of life independent from water-based life we know on Earth. Strobel (2010) describes densities of hydrogen in different parts of the atmosphere and the surface. Previous models had predicted that hydrogen molecules, a by-product of ultraviolet sunlight breaking apart acetylene and methane molecules in the upper atmosphere, should be distributed fairly evenly throughout the atmospheric layers. The authors found a disparity in the hydrogen densities that lead to a flow down to the surface at a rate of about 10,000 trillion hydrogen molecules per second. This is about the same rate at which the molecules escape out of the upper atmosphere. Strobel (2010) states

that it is not likely for hydrogen to be stored in a cave or underground space on Titan. Titan's surface is also so cold that a chemical process that involved a catalyst would be needed to convert hydrogen molecules and acetylene back to methane, even though overall there would be a net release of energy. The energy barrier could be overcome if there were an unknown mineral acting as the catalyst on Titan's surface.

Another possible indicator for life on Titan is the lack of acetylene on the surface since there is no clear evidence of this compound in the received data to date, while it is expected to have been deposited through the atmosphere. It has been suggested that this could be due to the fact that some form of life on the surface is using acetylene as an energy source (Clark et al., 2010). This theory is largely debated and controversial among the scientific community, especially due to suggestions of nonbiological origin of this phenomenon; however, it has the merit to propose new interesting astrobiological theories. In detail, Clark et al. (2010) map hydrocarbons on the surface from Cassini/VIMS data and find a lack of acetylene. McKay and Smith (2005) had identified acetylene as the best energy source for methane-based life on Titan. While nonbiological chemistry offers one possible explanation, these authors believe these chemical signatures bolster the argument for a primitive, exotic form of life or precursor to life on Titan's surface. According to one theory put forth by astrobiologists, the signatures fulfill two important conditions necessary for a hypothesized "methane-based life", which would consume not only methane but also hydrogen. However, one other possibility is that sunlight or cosmic rays are transforming the acetylene in icy aerosols in the atmosphere into more complex molecules that would fall to the ground with no acetylene signature.

To date, methane-based life forms are only hypothetical. Scientists have not yet detected this form of life anywhere, though there are liquid-water-based microbes on Earth that thrive on methane or produce it as a waste product. At Titan's low temperatures, a methane-based organism would have to use a substance that is liquid as its medium for living processes, but not water itself. Water is frozen solid on Titan's surface and much too cold to support life as we know it. The list of liquid candidates includes liquid methane and related molecules like ethane. While liquid water is widely regarded as necessary for life, there has been extensive speculation published in the scientific literature that this is not a strict requirement. The new hydrogen findings are consistent with conditions that could produce an exotic, methane-based life form, but do not prove its existence.

3.4. INTERIOR MODELS FOR TITAN AND ITS POSSIBLE SUBSURFACE OCEAN

Regarding Titan's interior structure, since the only *in situ* data from its surface are the Huygens probe recordings, only modeling assumptions can be presented. Structural models for planetary interiors suggest that Titan, like Europa, Ganymede,

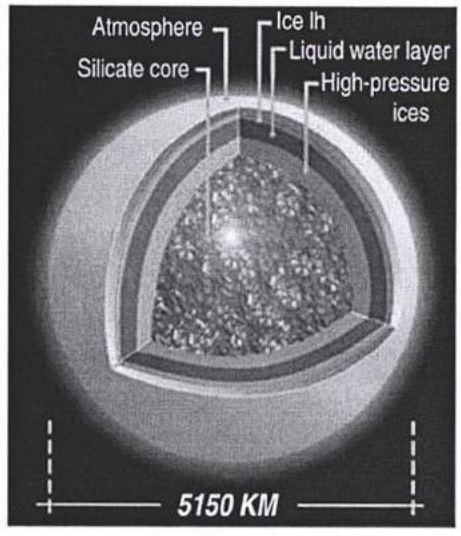

Figure 11. Illustration of Titan's internal structure with a liquid ocean between two subsurface ice layers (From Tobie et al., 2005). Cassini–Huygens recorded extremely low-frequency radio waves which supports the existence of this liquid subsurface layer (NASA/LPGN).

and Callisto, has maintained internal liquid water reservoirs, probably mixed with some ammonia and more speculatively sulfur and possibly entrained methane clathrates (Fig. 11).

Another possible location to look for life on Titan would be in an undersurface liquid water ocean. The presence of such an internal ocean is supported by Titan internal structure models (Tobie et al., 2005; Mitri et al., 2008), radar and gravity Cassini measurements (Lorenz et al., 2008b), and the Huygens Atmospheric Structure Instrument (HASI) experiment. Beghin et al. (2009) thus interpreted the extremely low-frequency electric signal recorded by HASI as a Schumann resonance between the ionosphere and a modestly conducting ocean (since the ice is not conductive) roughly 30–50 km below the surface. Thermal evolution models suggest that Titan may have an ice crust between 50 and 150 km thick, lying atop a liquid water ocean a couple of 100 km deep, with some amount (a few to 30%, most likely ~10%) of ammonia dissolved in it, acting as an antifreeze material (Lorenz et al., 2008b). This correspond to a pH around 11.5. The pressure reaches~5 kbars at 200 km depth, and it could include hot spots reaching −20 °C. Such conditions are not incompatible with life as we know it on Earth (Fortes, 2000; Raulin, 2008; Raulin et al., 2009).

Tobie et al. (2005) suggested a layered interior structure of Titan, consisting of a rocky core overlaid by high-pressure ice, a liquid layer overlaid by low pressure ice, and finally a solid icy crust (Fig. 11). An earlier model by Fortes (2000)

noted that underneath Titan's icy crust, at a depth of approximately 200 km, there lies an ammonia–water solution ocean in which life could survive. Another, more recent model by Mitri et al. (2008) suggests pockets of methane clathrates trapped within an ammonia–water ocean which could exsolute and produce overpressure and consequently the ammonia–water can erupt to the surface leading to cryovolcanic phenomena.

With regard to Titan's morphology and internal dynamic geology, it has been suggested that there may be active cryovolcanoes on Titan (Sotin et al., 2005; Lopes et al., 2007) since traces of former flows have been found across parts of the surface. A wide variety of Cassini data support the presence of cryovolcanism on Titan. Indeed, at least two regions have been observed to change reflectance on Titan's surface (Tui Regio 20°S, 130°W; Hotei Regio 26°S, 78°W) (Barnes et al., 2006; Nelson et al., 2009a, b), and one of them (Hotei Regio) in addition to a recent discovery (Sotra Facula 15°S, 42°W) in radar images exhibit lobate "flow" forms (Soderblom et al., 2009; Lopes et al., 2010), consistent with the morphology of volcanic terrain, supporting the hypothesis of cryovolcanic eruptions (Sotin et al., 2005).

However, on Titan, fluid water mobilized and made buoyant by ammonia and other materials could replace terrestrial melted silicates. Cryovolcanism suggests a dynamic process than involves the interior, the surface, and the atmosphere as well. It is a multi-complex activity that resembles terrestrial volcanic processes as it follows a similar pattern although in extremely altered conditions and different initial and depositional products. Cryovolcanism on Titan is believed to be a significant source of the methane in the atmosphere (Tobie et al., 2006). An underground liquid ocean, several hundred kilometers deep at the surface of Titan, is suggested to be the source of cryomagma, hence outgassing methane into the atmosphere and thus replenishing the destroyed amounts.

There are indeed studies suggesting the presence of an internal ammonia–water ocean (Grasset and Sotin, 1996; Grasset et al., 2000; Tobie et al., 2005; Mitri et al., 2007) while another study has modeled and suggested an ocean filled with methane clathrate pockets that lead to explosive cryovolcanism (Fortes et al., 2007).

The theory of trapped methane clathrates in the potential liquid ocean is of a major astrobiological interest. The presence of methane clathrates in an aqueous environment is attached to the "clathrate gun" hypothesis. This hypothesis suggests that potential movement and rise of the temperature in an underground liquid reservoir could trigger the sudden release of methane from methane clathrate compounds buried in permafrost or seabeds (Kennett et al., 2003) or an ocean like on Titan's case. The initiation of such process leads to further temperature rise and further methane clathrate destabilization that could easily cause and trigger cryovolcanic eruptions (Kennett et al., 2003). For Titan, a dynamic process like the one suggested by the clathrate gun hypothesis could result to increase of temperature values, creating an environment more favorable for life to exist.

With respect to the astrobiological interest, there is a controversy about the effectiveness of methane as a medium for life compared to water or ammonia. Water has higher solubility than methane, enabling easier transport of substances in a cell, while methane's lesser chemical reactivity allows for the easier formation of large structures corresponding to proteins (Benner et al., 2004). In addition, the cryovolcanic activity suggests higher temperatures within the ocean and the volcanic conduit where heat transfer between the interior and upper layers would be critical in sustaining any subsurface oceanic life (Grasset et al., 2000).

Thus, the possibility of life in this ocean cannot be excluded. Moreover, models also predict that during the first tens millions of years after Titan's formation, the ocean was in direct contact with the atmosphere on one side and with the bedrock on the side. This could have provided conditions very favorable for an efficient prebiotic chemistry toward the emergence of life, with the possible involvement of hydrothermal vents. Thus, the internal ocean of Titan not only is habitable but could be inhabited.

Hence, in spite of the low temperature, Titan is not a congealed Earth: The chemical system is not frozen. Titan is an evolving planetary body and so is its chemistry. Once deposited on Titan's surface, the aerosols and their complex organic content may follow a chemical evolution of astrobiological interest. Laboratory experiments show that, once in contact with liquid water, Titan tholins can release many compounds of biological interest, such as amino acids (Khare et al., 1986). Such processes could be particularly favorable in zones of Titan's surface where cryovolcanism may occur. The N_2–CH_4 by-products in Titan's atmosphere eventually end up as sediments on the surface, where they accumulate presently at a rate of roughly 0.5 km in 4.5 Gyr.

Long-term chemical evolution is impossible to study in the laboratory: *In situ* measurements of Titan's surface thus offer a unique opportunity to study by a ground-truth approach some of the many processes which could be involved in prebiotic chemistry, including isotopic and enantiomeric fractionation (Nguyen et al., 2007).

There are suggestions that Titan is presently geologically active on the surface (Nelson et al., 2006, 2009a, b) and in its interior. If Titan is currently active, then these results raise the following questions: What is the full extent of current geologic activity? What are the ongoing processes? Are Titan's chemical processes today supporting a prebiotic chemistry similar to that under which life evolved on Earth?

Although the chemical reactions that lead to life on Earth take place in liquid water, the reactions themselves are almost entirely between organics. The study of organic chemistry is therefore an important, and arguably richer, adjunct to the pursuit of liquid water in the solar system. Titan's organic inventory is impressive, and carbon-bearing compounds are widespread across the surface in the form of lakes, seas, dunes, and, probably, sedimentary deltas at the mouths of channels.

4. Enceladus: Liquid Water Far Away from the Sun

Discovered by William Herschel in 1789, Enceladus is arguably a place in the solar system where a demonstrably habitable environment already occurs and evaluating its astrobiological potential should be an overarching goal of Enceladus research. Although Enceladus is a relative small planetary body (500 km in diameter), significant chemical processes could produce primitive life structures. Obviously, oxidation/reduction reactions necessitate supporting redox-based life (Gaidos et al., 1999). Fe- and Ni-bearing dust particles can operate as reducing agents on Enceladus, which exist since planetary formation from the ancient solar nebula.

As concerns oxidant agents on Enceladus, Gaidos et al. (1999) also noted their production through E-ring particles, charged from the Saturnian magnetospheric environment. Then, some suitable geological process is needed to mix the reducing and oxidizing compounds. In a model by Cooper et al. (2009), the astrobiological parameters that support life on Enceladus are evaluated as higher than for Europa due to a less extreme state of oxidation and greater residual abundance of organics.

Indeed, Enceladus, Saturn's most active moon as observed from Cassini, presents a mystery in the studies of planetary science and, more specifically, in geophysics. The enigma evolves around how a small moon can possess sufficient dynamical energy to drive a geyser plume rising 600 miles in space out of the moon's south pole, eventually feeding its material to the outer E-ring of Saturn (Postberg et al., 2009). The heat source for Enceladus is still an open question, as is the possibility for life to exist on this small satellite if an underground liquid water ocean or liquid water subsurface pockets exist to explain the plumes (Kieffer and Jakosky, 2008).

The geyser plumes arise from the warm surface surrounding and including four parallel faults located at the moon's south pole, the "Tiger Stripes" fractures (Porco et al., 2006; Spencer et al., 2006), spewing a series of jets more than 600 km high (Fig. 12). The mass production rate of the plume gas has been estimated to be ~150 kg/s from occultation data (Tian et al., 2007). This value is surprisingly high, sufficient to remove a significant fraction (~20%) of Enceladus's mass over the age of the solar system (Kargel, 2006).

Data obtained by the VIMS instrument on board Cassini indicate CO_2 and organics as possible components (Brown et al., 2006). Data processing showed components that Cassini's INMS identified H_2O as the predominant component, CO_2 as the second most abundant, methane, and trace quantities of acetylene and propane (Waite et al., 2009). During the 9th of October 2008 flyby, Cassini dived into the south-polar plume, and INMS reported the presence of ammonia and other various organic compounds like deuterium and ^{40}Ar, as well as complex organics like benzene and other probable species such as methanol and formaldehyde (Waite et al., 2009). The chemical composition of the plume and surface material of Enceladus suggests the presence of a heat source in its interior, hot

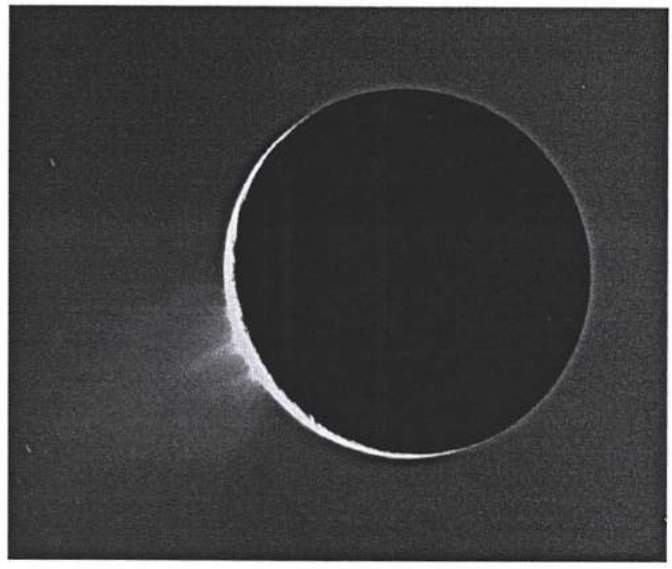

Figure 12. Enceladus's plumes ejected from the south-polar region captured by Cassini/ISS (Porco et al., 2006).

enough to decompose ammonia into N_2 and to drive reactions with hydrocarbons, implying internal temperatures on the order of 500–800 K (Matson et al., 2007).

There is a plethora of competing theories regarding the triggering and exsolution of geysers from the Tiger Stripes. The main controversy lies on as to whether the plumes are formed by a massive underground ocean (Tobie et al., 2008; Postberg et al., 2009) (Fig. 13a) or if the material generates from ice warmed, melted, or crushed by tectonic-like motions (Nimmo et al., 2007) (Fig. 13b).

Given the aforementioned observations and analysis, it is now known that Enceladus contains enough heat to drive complex and dynamic geologic activity. Interpretation of Cassini data with a view to explain the major internal reservoir that triggers and feeds this dynamic process points to a possible underground liquid ocean beneath the icy crust. Since the prerequisites for life to emerge are the simultaneous existence of energy, organic compounds, and liquid water that have been found on Enceladus, it seems that it possesses all the necessary components to support life.

In general, as described above, the south-polar region of Enceladus presents extremely high temperatures while the exsoluted vapor has also been shown to contain simple organic compounds. Most theories regarding the origin of this active region suggest that it is very likely for a liquid water environment to exist beneath the Tiger Stripes. This hypothesis enables the parallelism between potential biological ecosystems on Enceladus and the already existing on Earth (Fig. 14).

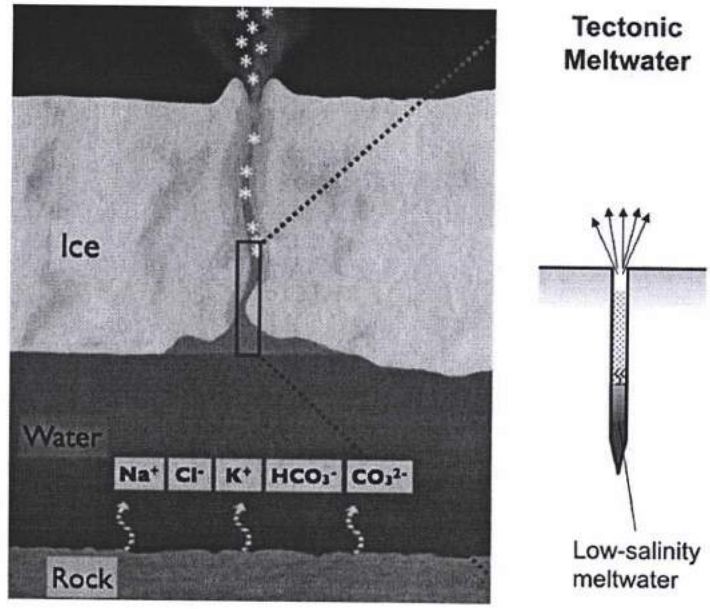

Figure 13. (*left*) Modeling of a possible internal ocean on Enceladus filled with water and chemical compounds. This model tries to explain the significant abundance of sodium salts of Saturn's E-ring, probably originating in Enceladus plumes (Postberg et al., 2006). (*right*) Internal model of Enceladus based on tectonic meltwater. Heating along fractures is caused by tidal flexing (Nimmo et al., 2007).

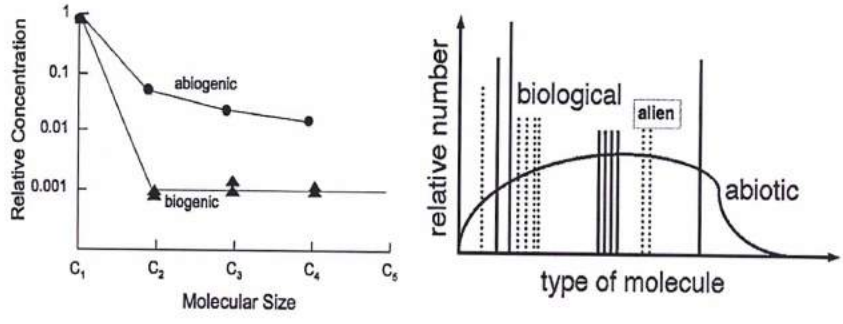

Figure 14. Indications for biological and nonbiological processes in relation to molecular parameter (*left*) terrestrial abiogenic production of hydrocarbons from McCollom and Simoneit (1999) and its biogenic pendant from Devai and Delaune (1996). (*right*) Organic distribution for abiotic, biological, and possible alien life on Enceladus (Both figures from McKay et al., 2008).

The standards for life that Enceladus' possible ocean does not fall into are the sunlight, the oxygen compounds, and the organics produced on a surficial-crust environment. Environments and ecosystems that do not meet the aforementioned prerequisites exist and evolve on Earth as well. Such an environment is located deep inside South Africa's surface, where sulfur-reducing bacteria consume hydrogen and sulfate, produced by radioactive decay (McKay et al., 2008; Muyzer and Stams, 2008). In addition, other analogous to Enceladus ecosystems are found within the magmatic volcanic rocks, which are produced through the activity of metasomatism. The metasomatosis of the volcanic rocks under the reaction of water produces methanogens of hydrogen on which the primary productivity is based on (McKay et al., 2008). Cassini's data showed that methane is present in the plumes. The terrestrial comparison regarding the ecosystems suggests that plume's methane may be biological in origin (McKay et al., 2008).

Specific questions relevant to the goal of understanding habitability on Enceladus include: Is liquid water present on Enceladus, either in a subsurface ocean, in the plume vent regions, or elsewhere? How extensive and long lived is the water, if present, and what is its chemistry? How does the liquid reservoir communicate with the surface? How thick is the ice crust and how uniform is that thickness? What energy sources are available for life? Is life present there now?

VIMS observations of several other satellites of Saturn, in the near-infrared region, show that their surface is covered by dark materials. This is particularly the case with Dione but also with Phoebe, Iapetus, Hyperion, Epimetheus and even with the F-ring (Clark et al., 2009). This dark material could be made of cyanide compounds and could be of cometary origin (Clark et al., 2009).

Spectral signatures of hydrocarbons have also been found from VIMS data on Iapetus and Phoebe suggesting the presence of organic compounds such as PAH's, kerogen-, or coal-like structure compounds (Cruishank et al., 2008).

Some of these satellites may also have internal liquid water pockets and thus may present the requisite essential for the emergence and development of life: liquid water and organic compounds. The solstice mission may be able to discover such properties and thus extend drastically the list of planetary bodies of important astrobiological interest in the Saturnian system.

5. Discussion: What Can Titan and Enceladus Tell Us About Life?

The complex mechanisms that have led to the emergence and development of life on Earth are still under investigation. Despite the great strides on biological sciences, the roots, the sources, and the initial conditions of life still remain unknown. Some answers can be found in extraterrestrial environments, hopefully in our solar system neighborhood or in exoplanets orbiting Sun-type stars. Without doubt, every planetary body, with a possible astrobiological potential, is a target for further investigations. Currently, after years of explorations, extended missions, and data analysis, it appears that among the main candidates for finding signs of

past or current life within our solar system are Mars, Enceladus, Europa, and Titan (not in any particular order of priority or importance).

In this context, Titan and Enceladus, both orbiting Saturn, seem ideal locations for further investigation. As said before, their astrobiological importance is obvious, because they propose uniquely all the necessary ingredients for life emerging and evolution. Not surprisingly, scientists expect that their study will provide some important insights on the origin of life.

The surface of Titan appears, like the surface of Mars or Europa, as an unlikely location for extant life, at least for terrestrial-type life. Even though Titan presents terrestrial-type geology with complex structures formed mostly from dynamic processes, the absence of water on the surface makes it unlikely to support terrestrial-type life. Liquid water, if it exists, is not presently in contact with a silicate core, which is isolated from the subsurface ocean by a layer of a high-pressure ice phase (Tobie et al., 2005). However, Fortes (2000) noted that Titan's internal water ocean might support terrestrial-type life that had been introduced there previously or formed when liquid water was in contact with silicates early in Titan's history. According to McKay and Smith (2005), photochemically derived sources of free energy on Titan's surface could maintain an exotic type of life, using liquid hydrocarbons as solvents. Similarly, Stoker et al. (1990) stressed that terrestrial bacteria can in fact satisfy their energy and carbon needs by "eating" tholin. In this sense, a methane-rich atmosphere may act as a "poor planet's photosynthesis," providing a means to capture the free energy from ultraviolet light and make it available for metabolic reactions.

Consequently, it cannot be excluded that life may have emerged on or in Titan. In spite of the extreme conditions in this environment, life may have been able to adapt and to persist. Even though the possible current conditions (pH, temperature, pressure, salt concentrations) are not incompatible with life, as we know it on Earth (Fortes, 2000), the detection of a potential biological activity in the putative liquid mantle seems very challenging. Furthermore, as mentioned above, another possible location to look for life on Titan would be in a possible subsurface liquid water ocean, and thus, it seems astrobiologically essential to confirm its presence.

Marine geologists and Marine biologists are nowadays close to confirm after many years of research and analysis that in the lower part of Earth's ocean, below the thermocline, where the environmental conditions are extremely different than on the surface, life exists. In deep oceanic layers that suffer from low temperature and high pressure, there are two extreme environments where life is abundant. Such environments are the cold seeps (vents) (e.g., Ritt et al., 2010) and the hydrothermal vents. Cold seeps are areas resembling brine pools, from which methane and hydrogen sulfide and other hydrocarbon-rich fluid seepage are released into the ocean. In such conditions, types of life exist, feeding on single-cell Archaea and Eubacteria microbes that consume the methane and hydrogen sulfide from the seep. The environmental and living conditions described above resemble that of Titan's hypothesized internal liquid ocean. Similarly, the temperature is low,

the pressure is high, and possible hydrovolcanic events exist, releasing methane and sulfides in the liquid ocean. Thus, there are many aspects of Titan that might argue for the presence of some sort of very basic life on Titan.

6. Future Exploration of the Kronian Satellites

Could Titan be providing us with hints as to the future of our own planet? Indeed, in addition to the past, Titan appears to be an analogue, albeit with different working materials, of the future state of the Earth when surface conditions preclude stable equatorial/midlatitude oceans. If we are to focus on the Earth and its climate, as well as on its organic chemistry, we need in the future to concentrate on another object in the solar system that sustains an active hydrologic cycle with surface liquids, meteorology, and climate change. The Cassini–Huygens mission has firmly established that Titan is such a body, in which the active working fluid of the hydrologic cycle is methane. The cycle is active but different from the Earth because Titan lacks a surface methane ocean. It possesses, however, methane lakes and seas, fluvial erosion, rounded pebbles, and liquid methane in the soil at the Huygens site.

With Titan, we are observing an active hydrologic cycle subjected to seasonal, annual, and longer term changes, as on the Earth. Moreover, the future increase in the solar luminosity make it almost inevitable that eventually water on the Earth will no longer be trapped in our ocean and troposphere but will escape rapidly in a process we see today for methane on Titan. The late stages of this evolution—an Earth with liquid water in the polar regions, in the crust, but no longer in an ocean—may be echoed by the configuration we see today in Titan's methane hydrologic cycle.

Our understanding of the future of living beings on Earth (and hence the habitability in many ways of our planet) may then have something to gain from a thorough exploration of Titan's current state.

Enceladus, on the other hand, may hold the key to understanding an important source of energy, plate tectonics, and volcanism. Indeed, many tectonic features on Enceladus may be analogous to features observed on other icy satellites such as Europa, Ganymede, and perhaps Titan. Thus, the study of the tectonics of Enceladus, which is currently active, can be used as a natural laboratory to investigate the response to stresses of the other surfaces of the outer solar system. Moreover, Enceladus possesses a warm, chemically rich, environment that may facilitate complex organic chemistry and biological processes.

The Cassini–Huygens mission has enormously advanced our knowledge of the Saturnian system and the satellites within. As far as Titan and Enceladus are concerned, the wealth of data retrieved by the Cassini–Huygens mission will definitely be the reference point for future planetary investigation. However, the key contribution to planetary science of Cassini may be the questions raised rather than those answered. Some drawbacks of the mission, such as insufficient

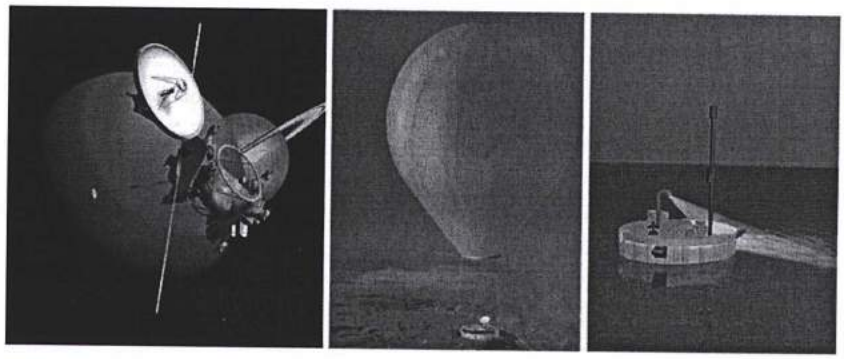

Figure 15. The TSSM basic concept. The orbiter (*left*), the balloon (*center*), and the lake lander (*right*) (Reh et al., 2008).

global coverage which has inhibited a full mapping of the atmospheric structure, composition, and temporal variations as well as the surface features of Titan and Enceladus, point to the need for further studies. Similarly, the part of the Titan's atmosphere between 400 and 950 km will remain unexplored (Coustenis et al., 2009). In addition, we will lack *in situ* measurements since the Cassini orbiter can only perform flybys of Titan and Enceladus, and the single vertical profile of the atmosphere taken by Huygens probe is limited to its landing site.

It is clear that Titan's organic chemistry and the possible subsurface ocean (among other) remain to be investigated. In particular, joint measurements of large-scale and mesoscale topography and gravitational field anomalies on Titan from an orbiter and from an aerial platform would impose important constraints on the thickness of the "lithosphere", the presence of mass anomalies at depth, and any lateral variation of the ice mantle thickness. As discussed above, it is astrobiologically crucial to confirm the presence of such an internal ocean, even though the water layer may not be in contact with the silicate core, like on Europa.

Lessons from Huygens will be used in the future to go back to Titan and explore in details its surface, in many locations. The intriguing discoveries of geological activity, excess warmth, and outgassing on Enceladus (due perhaps to the ejection of water and organics from subsurface pockets bathed in heat or by some other mechanism) mandate a follow-up investigation of that tiny Saturnian world that can only be achieved with high-resolution remote observations and detailed in situ investigations of the near-surface south-polar environment.

Among other options, a flagship (large) mission, TSSM (for Titan/Saturn System Mission), was proposed (Reh et al., 2008; Coustenis et al., 2009), jointly studied by NASA and ESA. TSSM could explore extensively one of the Titan's lakes and study for several months Titan's atmospheric and surface environment (Fig. 15).

This concept would also investigate the astrobiological perspective of Titan and Enceladus. In particular, since hydrocarbon lakes on Titan's surface may harbor evidence for present or past life, the proposed lake lander would play a crucial role. Similarly, the balloon platform would be responsible for understanding how volatile-rich worlds evolve and how organic chemistry and planetary evolution interact on large spatial and temporal scales.

The primary science goals of TSSM are to understand Titan's and Enceladus' atmospheres, surfaces, and interiors; to determine the pre- and proto-biotic chemistry that may be occurring on both objects; and to derive constraints on the satellites' origin and evolution, both individually and in the context of the complex Saturnian system as a whole. Many internal processes play crucial roles in the evolution of Titan and Enceladus. The formation and replenishing of Titan's atmosphere and the jet activity at Enceladus' south pole are intimately linked to the satellite's interior structure and dynamics. Open issues are listed below:

1. To determine their present-day structure and levels of activity
2. To determine whether the satellites underwent significant tidal deformation and whether they possess intrinsic or induced magnetic fields and significant seismicity
3. To identify heat sources, internal reservoirs of volatiles (in particular methane and ammonia), and eruptive processes
4. To detect plausible evidence for life by analysis of hydrocarbons in the plume during close encounters

A mission like TSSM would answer important astrobiological questions with precise measurements as follows:

1. What degree of complexity is reached by Titan's organic chemistry in the different parts of the geological system?
2. Is Titan a habitable world? Does it have an undersurface liquid water ocean or episodical liquid water bodies on the surface?
3. Is there currently, has there been or will there be biological activity on Titan?

To answer these questions and complement the Cassini–Huygens exploration of Titan, a dedicated orbiter and in situ elements would help by providing data and analyses directly in the atmosphere, on the surface, and the interior of Titan. The exchanges among the different media and the external processes that affect Titan on time lapses of days, years, or seasons beg for further investigation, even beyond the solstice Cassini mission which will be operating until 2017. Besides TSSM, other concepts for future missions to return to Titan have been proposed

Such as a simple orbiter to perform close-up investigations of the surface and the atmosphere of Titan (JET, C. Sotin, PI). Further more, several in situ elements have been proposed like:

The Aerial Vehicle for In-Situ and Airborne Titan Reconnaissance (AVIATR), an alternative proposal to a Titan balloon mission. Since Titan experiences low gravity and a dense atmosphere, such a nuclear-powered airplane

could fly more than 20 times easier than on Earth. It could sample directly the atmosphere and cover huge swaths of Titan's landscape (Barnes et al., 2010; McKay et al., 2010).

Titan Mare Explorer (TiME) is a proposed probe focusing on exploring Titan's lakelike features. This lake lander could study the chemical composition and the geological characteristics of the hydrocarbon pools (Lorenz et al., 2009; Stofan et al., 2009).

Similarly, Titan lake probe is a lake lander which could be considered as part of the TSSM mission or as a stand-alone mission. The main objective of this proposal is to investigate the lake deposit and the physical properties of the liquids like the TiME concept (Waite et al., 2010).

Future exploration of the Saturnian neighborhood shall no doubt bring forth extremely important insights on our quest for the possibility of life and habitable sites elsewhere.

7. References

Atreya SK, Adams EY, Niemann HB, Demick-Montelara JE, Owen TC, Fulchignoni M, Ferri F, Wilson EH (2006) Titan's methane cycle. Planet Space Sci 54:1177–1187

Barnes JW, Brown RH, Radebaugh J, Buratti BJ, Sotin C, Le Mouelic S, Rodriguez S, Turtle EP, Perry J, Clark R, Baines KH, Nicholson PD (2006) Cassini observations of flow-like features in western Tui Regio, Titan. Geophys Res Lett 33:16204–16204

Barnes JW, McKay C, Lemke L, Beyer RA, Radebaugh J, Atkinson D (2010) AVIATR: Aerial Vehicle for In-Situ and Airborne Titan Reconnaissance. In: 41st Lunar and planetary science conference, vol 41, Texas, 1–5 Mar, p 2551

Béghin C, Canu P, Karkoschka E, Sotin C, Bertucci C, Kurth WS, Berthelier JJ, Grard R, Hamelin M, Schwingenschuh K, Simoes F (2009) New insights on Titan's plasma-driven Schumann resonance inferred from Huygens and Cassini data. Planet Space Sci 57: 1872–1888

Benner R, Benitez-Nelson B, Kaiser K, Amon RMW (2004) Export of young terrigenous dissolved organic carbon from rivers to the Arctic Ocean. Geophys Res Lett 31:05305–05305

Bird MK, Allison M, Asmar SW, Atkinson DH, Avruch IM, Dutta-Roy R, Dzierma Y, Edenhofer P, Folkner WM, Gurvits LI, Johnston DV, Plettemeier D, Pogrebenko SV, Preston RA, Tyler GL (2005) The vertical profile of winds on Titan. Nature 438:800–802

Brown RH, Clark RN, Buratti BJ, Cruikshank DP, Barnes JW, Mastrapa RME, Bauer J, Newman S, Momary T, Baines KH, Bellucci G, Capaccioni F, Cerroni P, Combes M, Coradini A, Drossart P, Formisano V, Jaumann R, Langevin Y, Matson DL, McCord TB, Nelson RM, Nicholson PD, Sicardy B, Sotin C (2006) Composition and physical properties of Enceladus' surface. Science 311:1425–1428

Brown RH, Soderblom LA, Soderblom JM, Clark RN, Jaumann R, Barnes JW, Sotin C, Buratti B, Baines KH, Nicholson PD (2008) The identification of liquid ethane in Titan's Ontario Lacus. Nature 454:607–610

Brown ME, Schaller EL, Roe HG, Chen C, Roberts J, Brown RH, Baines KH, Clark RN (2009a) Discovery of lake-effect clouds on Titan. Geophys Res Lett 36:01103–01103

Brown R, Lebreton J-P, Waite H (eds) (2009b) Titan from Cassini-Huygens. Springer, New York, p 535

Bulat S, Alekhina I, Petit JR (2009) Life detection strategy for subglacial Lake Vostok, Antarctica: lessons for Jovian moon Europa. Goldschmidt conference, Davos, Switzerland, p 173

Cernicharo J, Crovisier J (2005) Water in space: the Water World of ISO. Space Sci Rev 119:29–69

Clark RN, 11 co-authors (2008) Compositional mapping of Saturn's satellite Dione with Cassini VIMS and implications of dark material in the Saturn system. Icarus 193:372–386

Clark K, Stankov A, Pappalardo RT, Greeley R, Blanc M, Lebreton J-P (2009) Europa Jupiter system mission. Joint summary report, NASA/ESA. JPL D-48440 and ESA-SRE(2008)1

Clark RN, Curchin JM, Barnes JW, Jaumann R, Soderblom L, Cruikshank DP, Brown RH, Rodriguez S, Lunine J, Stephan K, Hoefen TM, Le Mouelic S, Sotin C, Baines KH, Buratti BJ, Nicholson PD (2010) Detection and mapping of hydrocarbon deposits on Titan. J Geophys Res 115:E10005

Cohen J, Stewart I (2002) Evolving the Alien: The Science of Extraterrestrial Life. Ebury Press.

Cooper JF, Cooper PD, Sittler EC, Sturner SJ, Rymer AM (2009) Old faithful model for radiolytic gas-driven cryovolcanism at Enceladus. Planet Space Sci 57:1607–1620

Coustenis A, Hirtzig M (2009) Cassini-Huygens results on Titan's surface. Res Astron Astrophys 9:249–268

Coustenis A, Taylor FW (2008) Titan: exploring an earthlike world, Series on atmospheric, oceanic and planetary physics, vol 4. World Scientific, Singapore

Coustenis A, Salama A, Schulz B, Ott S, Lellouch E, Encrenaz TH, Gautier D, Feuchtgruber H (2003) Titan's atmosphere from ISO mid-infrared spectroscopy. Icarus 161:383–403

Coustenis A, Achterberg RK, Conrath BJ, Jennings DE, Marten A, Gautier D, Nixon CA, Flasar FM, Teanby NA, Bezard B, Samuelson RE, Carlson RC, Lellouch E, Bjoraker GL, Romani PN, Taylor FW, Irwin PGJ, Fouchet T, Hubert A, Orton GS, Kunde VG, Vinatier S, Mondellini J, Abbas MM, Courtin R (2007) The composition of Titan's stratosphere from Cassini/CIRS mid-infrared spectra. Icarus 189:35–62

Coustenis A, Atreya S, Balint T, Brown R, Dougherty M, Ferri F, Fulchignoni M, Gautier D, Gowen R, Griffith C, Gurvits L, Jaumann R, Langevin Y, Leese M, Lunine J, McKay C, Moussas X, Muller-Wodarg I, Neubauer F, Owen T, Raulin F, Sittler E, Sohl F, Sotin C, Tobie G, Tokano T, Turtle E, Wahlund JE, Waite J, Baines K, Blamont J, Coates A, Dandouras I, Krimigis T, Lellouch E, Lorenz R, Morse A, Porco C, Hirtzig M, Saur J, Spilker T, Zarnecki J, Choi E, Achilleos N, Amils R, Annan P, Atkinson D, Benilan Y, Bertucci C, Bezard B, Bjoraker G, Blanc M, Boireau L, Bouman J, Cabane M, Capria M, ChassefiŠre E, Coll P, Combes M, Cooper J, Coradini A, Crary F, Cravens T, Daglis I, de Angelis E, de Bergh C, de Pater I, Dunford C, Durry G, Dutuit O, Fairbrother D, Flasar F, Fortes A, Frampton R, Fujimoto M, Galand M, Grasset O, Grott M, Haltigin T, Herique A, Hersant F, Hussmann H, Ip W, Johnson R, Kallio E, Kempf S, Knapmeyer M, Kofman W, Koop R, Kostiuk T, Krupp N, Kuppers M, Lammer H, Lara LM, Lavvas P, Le Mouélic S, Lebonnois S, Ledvina S, Li J, Livengood T, Lopes R, Lopez-Moreno JJ, Luz D, Mahaffy P, Mall U, Martinez-Frias J, Marty B, McCord T, Menor Salvan C, Milillo A, Mitchell D, Modolo R, Mousis O, Nakamura M, Neish C, Nixon C, Nna Mvondo D, Orton G, Paetzold M, Pitman J, Pogrebenko S, Pollard W, Prieto-Ballesteros O, Rannou P, Reh K, Richter L, Robb F, Rodrigo R, Rodriguez S, Romani P, Ruiz Bermejo M, Sarris E, Schenk P, Schmitt B, Schmitz N, Schulze-Makuch D, Schwingenschuh K, Selig A, Sicardy B, Soderblom L, Spilker L, Stam D, Steele A, Stephan K, Strobel D, Szego K, Szopa C, Thissen R, Tomasko M, Toublanc D, Vali H, Vardavas I, Vuitton V, West R, Yelle R, Young E (2009) TandEM: Titan and Enceladus mission. Exp Astron 23:893–946

Coustenis A, Bampasidis G, Nixon C, Vinatier S, Achterberg R, Jennings D, Teanby N, Carlson R, Lavvas P, Flasar FM (2010a) Titan's atmospheric chemistry and its variations. Titan through time; A workshop on Titan's past, present and future, NASA Goddard Space Flight Center, USA, p 68

Coustenis A, Jennings DE, Nixon CA, Achterberg RK, Lavvas P, Vinatier S, Teanby N, Bjoraker GL, Carlson RC, Bampasidis G, Flasar F, Romani PN (2010b) Titan's meridional stratospheric composition: CIRS observations and modelling. Icarus 207:461–476

Cruikshank DP, 26 co-authors (2008) Hydrocarbons on Saturn's satellites Iapetus and Phoebe. Icarus 193:334–343

Darwin CR (1859) On the origin of species by means of natural selection, or the preservation of favoured races in the struggle for life. John Murray, London

Davis WL, McKay CP (1996) Origins of life: a comparison of theories and application to Mars. Orig Life Evol Biosph 26:61–73

de Kok R, Irwin P, Teanby N, Nixon C, Jennings D, Fletcher L, Howett C, Calcutt S, Bowles N, Flasar F (2007) Characteristics of Titan's stratospheric aerosols and condensate clouds from Cassini CIRS far-infrared spectra. Icarus 191:223–235

Delitsky ML, McKay CP (2010) The photochemical products of benzene in Titan's upper atmosphere. Icarus 207:477–484

Des Marais DJ, Harwit MO, Jucks KW, Kasting JF, Lin DNC, Lunine JI, Schneider J, Seager S, Traub WA, Woolf NJ (2002) Remote sensing of planetary properties and biosignatures on extrasolar terrestrial planets. Astrobiology 2:153–181

Devai I, Delaune RD (1996) Light hydrocarbon production in freshwater marsh soil as influenced by soil redox conditions. Water Air Soil Pollut 88:39–46

DeWitt HL, Trainer MG, Pavlov AA, Hasenkopf CA, Aiken AC, Jimenez JL, McKay CP, Toon OB, Tolbert MA (2009) Reduction in haze formation rate on prebiotic Earth in the presence of hydrogen. Astrobiology 9:447–453

Dougherty MK, Khurana KK, Neubauer FM, Russell CT, Saur J, Leisner JS, Burton ME (2006) Identification of a dynamic atmosphere at Enceladus with the Cassini Magnetometer. Science 311:1406–1409

Dougherty MK, Esposito LW, Krimigis SM (eds) (2009) Saturn from Cassini-Huygens. Springer, New York, p 805

ESA (2010) Web site on Huygens probe. http://sci.esa.int/huygens/

Flasar FM, Achterberg RK, Conrath BJ, Gierasch PJ, Kunde VG, Nixon CA, Bjoraker GL, Jennings DE, Romani PN, Simon-Miller AA, Bezard B, Coustenis A, Irwin PGJ, Teanby NA, Brasunas J, Pearl JC, Segura ME, Carlson RC, Mamoutkine A, Schinder PJ, Barucci A, Courtin R, Fouchet T, Gautier D, Lellouch E, Marten A, Prange R, Vinatier S, Strobel DF, Calcutt SB, Read PL, Taylor FW, Bowles N, Samuelson RE, Orton GS, Spilker LJ, Owen TC, Spencer JR, Showalter MR, Ferrari C, Abbas MM, Raulin F, Edgington S, Ade P, Wishnow EH (2005) Titan's atmospheric temperatures, winds, and composition. Science 308:975–978

Fortes AD (2000) Exobiological implications of a possible ammonia-water ocean inside Titan. Icarus 146:444–452

Fortes AD, Grindrod PM, Trickett SK, Vočadlo L (2007) Ammonium sulfate on Titan: possible origin and role in cryovolcanism. Icarus 188:139–153

Fulchignoni M, Ferri F, Angrilli F, Ball AJ, Bar-Nun A, Barucci MA, Bettanini C, Bianchini G, Borucki W, Colombatti G, Coradini M, Coustenis A, Debei S, Falkner P, Fanti G, Flamini E, Gaborit V, Grard R, Hamelin M, Harri AM, Hathi B, Jernej I, Leese MR, Lehto A, Lion Stoppato PF, Lopez-Moreno JJ, Makinen T, McDonnell JAM, McKay CP, Molina-Cuberos G, Neubauer FM, Pirronello V, Rodrigo R, Saggin B, Schwingenschuh K, Seiff A, Simoes F, Svedhem H, Tokano T, Towner MC, Trautner R, Withers P, Zarnecki JC (2005) In situ measurements of the physical characteristics of Titan's environment. Nature 438:785–791

Gaidos EJ, Nealson KH, Kirschvink JL (1999) Biogeochemistry: life in ice-covered oceans. Science 284:1631–1633

Grasset O, Sotin C (1996) The cooling rate of a liquid shell in Titan's interior. Icarus 123:101–112

Grasset O, Sotin C, Deschamps F (2000) On the internal structure and dynamics of Titan. Planet Space Sci 48:617–636

Hanslmeier A (2010) Water in the universe. Springer, London/New York, p 239

Hayes A, Aharonson O, Callahan P, Elachi C, Gim Y, Kirk R, Lewis K, Lopes R, Lorenz R, Lunine J, Mitchell K, Mitri G, Stofan E, Wall S (2008) Hydrocarbon lakes on Titan: distribution and interaction with a porous regolith. Geophys Res Lett 35:09204–09204

Horneck G (2008) Astrobiology. In: Artmann GM, Chien S (eds) Bioengineering in cell and tissue research. Springer, Berlin/Heidelberg, pp 641–666

Israel G, Szopa C, Raulin F, Cabane M, Niemann HB, Atreya SK, Bauer SJ, Brun JF, Chassefiére E, Coll P, Cond E, Coscia D, Hauchecorne A, Millian P, Nguyen MJ, Owen T, Riedler W, Samuelson RE, Siguier JM, Steller M, Sternberg R, Vidal-Madjar C (2005) Complex organic matter in Titan's atmospheric aerosols from in situ pyrolysis and analysis. Nature 438:796–799

Jaumann R, Brown RH, Stephan K, Barnes JW, Soderblom LA, Sotin C, Le Mouélic S, Clark RN, Soderblom J, Buratti BJ, Wagner R, McCord TB, Rodriguez S, Baines KH, Cruikshank DP, Nicholson PD, Griffith CA, Langhans M, Lorenz RD (2008) Fluvial erosion and post-erosional processes on Titan. Icarus 197:526–538

JPL/NASA (2010) Web site on Cassini mission. http://saturn.jpl.nasa.gov/index.cfm
Kapitsa AP, Ridley JK, de Q. Robin G, Siegert MJ, Zotikov IA (1996) A large deep freshwater lake beneath the ice of central East Antarctica. Nature 381:684–686
Kargel JS (2006) Enceladus: cosmic gymnast, volatile miniworld. Science 311:1389–1391
Kasting JF, Howard MT (2006) Atmospheric composition and climate on the early Earth. Philos Trans R Soc B Biol Sci 361:1733–1742
Kennett JP, Cannariato KG, Hendy IL, Behl RJ (2003) Methane hydrates in quaternary climate change: the clathrate gun hypothesis. American Geophysical Union, Washington, DC
Khare BN, Sagan C, Ogino H, Nagy B, Er C, Schram KH, Arakawa ET (1986) Amino acids derived from Titan tholins. Icarus 68:176–184
Kieffer SW, Jakosky BM (2008) Enceladus – oasis or ice ball? Science 320:1432–1433
Lavvas PP, Coustenis A, Vardavas IM (2008) Coupling photochemistry with haze formation in Titan's atmosphere, Part I: Model description. Planet Space Sci 56:27–66
Lebreton J-P, Coustenis A, Lunine J, Raulin F, Owen T, Strobel D (2009) Results from the Huygens probe on Titan. Astron Astrophys Rev 17:149–179
Lopes RMC, Mitchell KL, Stofan ER, Lunine JI, Lorenz R, Paganelli F, Kirk RL, Wood CA, Wall SD, Robshaw LE, Fortes AD, Neish CD, Radebaugh J, Reffet E, Ostro SJ, Elachi C, Allison MD, Anderson Y, Boehmer R, Boubin G, Callahan P, Encrenaz P, Flamini E, Francescetti G, Gim Y, Hamilton G, Hensley S, Janssen MA, Johnson WTK, Kelleher K, Muhleman DO, Ori G, Orosei R, Picardi G, Posa F, Roth LE, Seu R, Shaffer S, Soderblom LA, Stiles B, Vetrella S, West RD, Wye L, Zebker HA (2007) Cryovolcanic features on Titan's surface as revealed by the Cassini Titan Radar Mapper. Icarus 186:395–412
Lopes RMC, Stofan ER, Peckyno R, Radebaugh J, Mitchell KL, Mitri G, Wood CA, Kirk RL, Wall SD, Lunine JI, Hayes A, Lorenz R, Farr T, Wye L, Craig J, Ollerenshaw RJ, Janssen M, LeGall A, the Cassini RADAR Team (2010) Distribution and interplay of geologic processes on Titan from Cassini radar data. Icarus 205: 540–558
Lorenz R, Mitton J (2008) Titan unveiled: Saturn's mysterious moon explored. Princeton University Press, Princeton
Lorenz RD, Wall S, Radebaugh J, Boubin G, Reffet E, Janssen M, Stofan E, Lopes R, Kirk R, Elachi C, Lunine J, Mitchell K, Paganelli F, Soderblom L, Wood C, Wye L, Zebker H, Anderson Y, Ostro S, Allison M, Boehmer R, Callahan P, Encrenaz P, Ori GG, Francescetti G, Gim Y, Hamilton G, Hensley S, Johnson W, Kelleher K, Muhleman D, Picardi G, Posa F, Roth L, Seu R, Shaffer S, Stiles B, Vetrella S, Flamini E, West R (2006) The sand seas of Titan: Cassini RADAR observations of longitudinal dunes. Science 312:724–727
Lorenz RD, Mitchell KL, Kirk RL, Hayes AG, Aharonson O, Zebker HA, Paillou P, Radebaugh J, Lunine JI, Janssen MA, Wall SD, Lopes RM, Stiles B, Ostro S, Mitri G, Stofan ER (2008a) Titan's inventory of organic surface materials. Geophys Res Lett 35:02206
Lorenz RD, Stiles BW, Kirk RL, Allison MD, del Marmo PP, Iess L, Lunine JI, Ostro SJ, Hensley S (2008b) Titan's rotation reveals an internal ocean and changing zonal winds. Science 319:1649–1651
Lorenz RD, Stofan ER, Lunine JI, Kirk RL, Mahaffy PR, Bierhaus B, Aharonson O, Clark BC, Kantsiper B, Ravine MA, Waite JH, Harri A, Griffith CA, Trainer MG (2009) Titan Mare Explorer (TiME): a discovery mission to Titan's hydrocarbon lakes. AGU Fall Meet Abstr 51:1199–1199
Matson DL, Castillo JC, Lunine J, Johnson TV (2007) Enceladus' plume: compositional evidence for a hot interior. Icarus 187:569–573
McCollom TM, Simoneit BRT (1999) Abiotic formation of hydrocarbons and oxygenated compounds during thermal decomposition of iron oxalate. Orig Life Evol Biosph 29:167–186
McKay CP, Smith HD (2005) Possibilities for methanogenic life in liquid methane on the surface of Titan. Icarus 178:274–276
McKay CP, Lorenz RD, Lunine JI (1999) Analytic solutions for the antigreenhouse effect: Titan and the early Earth. Icarus 137:56–61
McKay CP, Porco Carolyn C, Altheide T, Davis WL, Kral TA (2008) The possible origin and persistence of life on Enceladus and detection of biomarkers in the plume. Astrobiology 8:909–919

McKay C, Barnes JW, Lemke L, Beyer RA, Radebaugh J, Atkinson D, Flasar FM (2010) Titan's atmosphere and surface in 2026: the AVIATR Titan Airplane Mission, Titan Through Time, NASA Goddard Space Flight Center, 6–8 Apr, p 31

Menor-Salván C, Ruiz-Bermejo M, Osuna-Esteban S, Muñoz-Caro G, Veintemillas-Verdaguer S (2008) Synthesis of polycyclic aromatic hydrocarbons and acetylene polymers in ice: a prebiotic scenario. Chem Biodivers 5:2729–2739

Mitri G, Showman AP, Lunine JI, Lorenz RD (2007) Hydrocarbon lakes on Titan. Icarus 186:385–394

Mitri G, Showman AP, Lunine JI, Lopes RMC (2008) Resurfacing of Titan by ammonia-water cryomagma. Icarus 196:216–224

Muyzer G, Stams AJM (2008) The ecology and biotechnology of sulphate-reducing bacteria. Nature Rev Microbiology 6:441–454

Neish CD, Somogyi A, Smith MA (2010) Titan's primordial soup: formation of amino acids via low-temperature hydrolysis of tholins. Astrobiology 10:337–347

Nelson RM, Brown RH, Hapke BW, Smythe WD, Kamp L, Boryta MD, Leader F, Baines KH, Bellucci G, Bibring JP, Buratti BJ, Capaccioni F, Cerroni P, Clark RN, Combes M, Coradini A, Cruikshank DP, Drossart P, Formisano V, Jaumann R, Langevin Y, Matson DL, McCord TB, Mennella V, Nicholson PD, Sicardy B, Sotin C (2006) Photometric properties of Titan's surface from Cassini VIMS: relevance to titan's hemispherical albedo dichotomy and surface stability. Planet Space Sci 54:1540–1551

Nelson RM, Kamp LW, Lopes RMC, Matson DL, Kirk RL, Hapke BW, Wall SD, Boryta MD, Leader FE, Smythe WD, Mitchell KL, Baines KH, Jaumann R, Sotin C, Clark RN, Cruikshank DP, Drossart P, Lunine JI, Combes M, Bellucci G, Bibring J-P, Capaccioni F, Cerroni P, Coradini A, Formisano V, Filacchione G, Langevin Y, McCord TB, Mennella V, Nicholson PD, Sicardy B, Irwin PGJ, Pearl JC (2009a) Photometric changes on Saturn's Titan: evidence for active cryovolcanism. Geophys Res Lett 36:04202–04202

Nelson RM, Kamp LW, Matson DL, Irwin PGJ, Baines KH, Boryta MD, Leader FE, Jaumann R, Smythe WD, Sotin C, Clark RN, Cruikshank DP, Drossart P, Pearl JC, Hapke BW, Lunine J, Combes M, Bellucci G, Bibring JP, Capaccioni F, Cerroni P, Coradini A, Formisano V, Filacchione G, Langevin RY, McCord TB, Mennella V, Nicholson PD, Sicardy B (2009b) Saturn's Titan: surface change, ammonia, and implications for atmospheric and tectonic activity. Icarus 199:429–441

Nguyen MJ, Raulin F, Coll P, Derenne S, Szopa C, Cernogora G, Israël G, Bernard JM (2007) Carbon isotopic enrichment in Titan's tholins? Implications for Titan's aerosols. Planet Space Sci 55:2010–2014

Niemann HB, Atreya SK, Bauer SJ, Carignan GR, Demick JE, Frost RL, Gautier D, Haberman JA, Harpold DN, Hunten DM, Israel G, Lunine JI, Kasprzak WT, Owen TC, Paulkovich M, Raulin F, Raaen E, Way SH (2005) The abundances of constituents of Titan's atmosphere from the GCMS instrument on the Huygens probe. Nature 438:779–784

Niemann HB, Atreya SK, Demick JE, Gautier D, Haberman JA, Harpold DN, Kasprzak WT, Lunine JI, Owen TC, Raulin F (2010) The composition of Titan's lower atmosphere and simple surface volatiles as measured by the Cassini-Huygens probe gas chromatograph mass spectrometer experiment. J Geophys Res-Planets 115:22

Nimmo F, Spencer JR, Pappalardo RT, Mullen ME (2007) Shear heating as the origin of the plumes and heat flux on Enceladus. Nature 447:289–291

Owen T (2005) Planetary science: Huygens rediscovers Titan. Nature 438:756–757

Pavlov AA, Kasting JF, Brown LL, Rages KA, Freedman R (2000) Greenhouse warming by CH4 in the atmosphere of early Earth. J Geophys Res 105:11981–11990

Pavlov AA, Hurtgen MT, Kasting JF, Arthur MA (2003) Methane-rich proterozoic atmosphere? Geology 31:87–90

Porco CC, Baker E, Barbara J, Beurle K, Brahic A, Burns JA, Charnoz S, Cooper N, Dawson DD, Del Genio AD, Denk T, Dones L, Dyudina U, Evans MW, Fussner S, Giese B, Grazier K, Helfenstein P, Ingersoll AP, Jacobson RA, Johnson TV, McEwen A, Murray CD, Neukum G, Owen WM, Perry J, Roatsch T, Spitale J, Squyres S, Thomas P, Tiscareno M, Turtle EP,

Vasavada AR, Veverka J, Wagner R, West R (2005) Imaging of Titan from the Cassini spacecraft. Nature 434:159–168

Porco CC, Helfenstein P, Thomas PC, Ingersoll AP, Wisdom J, West R, Neukum G, Denk T, Wagner R, Roatsch T, Kieffer S, Turtle E, McEwen A, Johnson TV, Rathbun J, Veverka J, Wilson D, Perry J, Spitale J, Brahic A, Burns JA, Del Genio AD, Dones L, Murray CD, Squyres S (2006) Cassini observes the active south pole of Enceladus. Science 311:1393–1401

Postberg F, Kempf S, Schmidt J, Brilliantov N, Beinsen A, Abel B, Buck U, Srama R (2009) Sodium salts in E-ring ice grains from an ocean below the surface of Enceladus. Nature 459:1098–1101

Radebaugh J, Lorenz RD, Lunine JI, Wall SD, Boubin G, Reffet E, Kirk RL, Lopes RM, Stofan ER, Soderblom L, Allison M, Janssen M, Paillou P, Callahan P, Spencer C, The Cassini Radar Team (2008) Dunes on Titan observed by Cassini Radar. Icarus 194:690–703

Radebaugh J, Lorenz R, Farr T, Paillou P, Savage C, Spencer C (2010) Linear dunes on Titan and earth: Initial remote sensing comparisons

Ramirez SI, Coll P, Buch A, Brassé C, Poch O, Raulin F (2010) The fate of aerosols on the surface of Titan. Faraday Discuss 147:419–427

Raulin F (2007) Question 2: why an astrobiological study of Titan will help us understand the origin of life. Orig Life Evol Biosph 37:345–349

Raulin F (2008) Planetary science: organic lakes on Titan. Nature 454:587–589

Raulin F, Gazeau MC, Lebreton JP (2008) Latest news from Titan. Planet Space Sci 56:571–572

Raulin F, McKay CP, Lunine J, Owen T (2009) Titan's astrobiology. In: Brown R, Lebreton J-P, Waite H (eds) Titan from Cassini-Huygens, Springer, New York, pp 215–233

Reh K, Lunine J, Matson D, Magner T, Lebreton J-P, Coustenis A (2008) TSSM final report on the NASA contribution to a joint mission with ESA, JPL D-48148, NASA Task Order NMO710851

Ritt B, Sarrazin J, Caprais J-C, Noel P, Gauthier O, Pierre C, Henry P, Desbruyeres D (2010) First insights into the structure and environmental setting of cold-seep communities in the Marmara Sea. Deep-Sea Res I Oceanogr Res Pap 57:1120–1136

Rudolph J, Ehhalt DH, Khedim A (1984) Vertical profiles of acetylene in the troposphere and stratosphere. J Atmos Chem 2:117–124

Sagan C, Khare BN (1979) Tholins – organic chemistry of interstellar grains and gas. Nature 277:102–107

Schaefer L, Fegley B (2007) Outgassing of ordinary chondritic material and some of its implications for the chemistry of asteroids, planets, and satellites. Icarus 186:462–483

Soderblom LA, Brown RH, Soderblom JM, Barnes JW, Kirk RL, Sotin C, Jaumann R, MacKinnon DJ, Mackowski DW, Baines KH, Buratti BJ, Clark RN, Nicholson PD (2009) The geology of Hotei Regio, Titan: correlation of Cassini VIMS and RADAR. Icarus 204:610–618

Solomonidou A, Bampasidis G, Hirtzig M, Coustenis A, Kyriakopoulos K, Seymour K, Bratsolis E, Moussas X (2012) Morphotectonic features on Titan and their possible origin. Planet Space Sci in press

Sotin C, Jaumann R, Buratti BJ, Brown RH, Clark RN, Soderblom LA, Baines KH, Bellucci G, Bibring JP, Capaccioni F, Cerroni P, Combes M, Coradini A, Cruikshank DP, Drossart P, Formisano V, Langevin Y, Matson DL, McCord TB, Nelson RM, Nicholson PD, Sicardy B, Lemouelic S, Rodriguez S, Stephan K, Scholz CK (2005) Release of volatiles from a possible cryovolcano from near-infrared imaging of Titan. Nature 435:786–789

Spencer JR, Pearl JC, Segura M, Flasar FM, Mamoutkine A, Romani P, Buratti BJ, Hendrix AR, Spilker LJ, Lopes RMC (2006) Cassini encounters Enceladus: background and the discovery of a south polar hot spot. Science 311:1401–1405

Stoker CR, Boston PJ, Mancinelli RL, Segal W, Khare BN, Sagan C (1990) Microbial metabolism of tholins. Icarus 85: 241–256

Stofan ER, Elachi C, Lunine JI, Lorenz RD, Stiles B, Mitchell KL, Ostro S, Soderblom L, Wood C, Zebker H, Wall S, Janssen M, Kirk R, Lopes R, Paganelli F, Radebaugh J, Wye L, Anderson Y, Allison M, Boehmer R, Callahan P, Encrenaz P, Flamini E, Francescetti G, Gim Y, Hamilton G, Hensley S, Johnson WTK, Kelleher K, Muhleman D, Paillou P, Picardi G, Posa F, Roth L, Seu R, Shaffer S, Vetrella S, West R (2007) The lakes of Titan. Nature 445:61–64

Stofan ER, Lunine J, Lorenz R, Aharonson O, Bierhaus E, Clark B, Kirk R, Kantsiper B, Morse B (2009) Titan Mare Explorer (time): a discovery mission to a Titan sea. American Astronomical Society, DPS meeting #41, Puerto Rico, USA, vol 41

Strobel DF (2010) Molecular hydrogen in Titan's atmosphere: implications of the measured tropospheric and thermospheric mole fractions. Icarus 208:878–886

Tian F, Stewart AIF, Toon OB, Larsen KW, Esposito LW (2007) Monte Carlo simulations of the water vapor plumes on Enceladus. Icarus 188:154–161

Tobie G, Grasset O, Lunine JI, Mocquet A, Sotin C (2005) Titan's internal structure inferred from a coupled thermal-orbital model. Icarus 175:496–502

Tobie G, Lunine JI, Sotin C (2006) Episodic outgassing as the origin of atmospheric methane on Titan. Nature 440:61–64

Tobie G, Čadek O, Sotin C (2008) Solid tidal friction above a liquid water reservoir as the origin of the south pole hotspot on Enceladus. Icarus 196:642–652

Tomasko MG, Archinal B, Becker T, Bézard B, Bushroe M, Combes M, Cook D, Coustenis A, de Bergh C, Dafoe LE, Doose L, Douté S, Eibl A, Engel S, Gliem F, Grieger B, Holso K, Howington-Kraus E, Karkoschka E, Keller HU, Kirk R, Kramm R, Küppers M, Lanagan P, Lellouch E, Lemmon M, Lunine J, McFarlane E, Moores J, Prout GM, Rizk B, Rosiek M, Rueffer P, Schröder SE, Schmitt B, See C, Smith P, Soderblom L, Thomas N, West R (2005) Rain, winds and haze during the Huygens probe's descent to Titan's surface. Nature 438:765–778

Toublanc D, Parisot JP, Brillet J, Gautier D, Raulin F, McKay CP (1995) Photochemical modeling of Titan's atmosphere. Icarus 113:2–26

Trainer MG, Pavlov AA, DeWitt HL, Jimenez JL, McKay CP, Toon OB, Tolbert MA (2006) Organic haze on Titan and the early Earth. Proc Natl Acad Sci USA 103:18035–18042

Trinks H, Schröder W, Biebricher C (2005) Ice and the origin of life. Orig Life Evol Biosph 35:429–445

Turtle EP, Perry JE, McEwen AS, DelGenio AD, Barbara J, West RA, Dawson DD, Porco CC (2009) Cassini imaging of Titan's high-latitude lakes, clouds, and south-polar surface changes. Geophys Res Lett 36:02204–02204

Waite JH, Young DT, Cravens TE, Coates AJ, Crary FJ, Magee B, Westlake J (2007) The process of tholin formation in Titan's upper atmosphere. Science 316:870–875

Waite JH, Lewis WS, Magee BA, Lunine JI, McKinnon WB, Glein CR, Mousis O, Young DT, Brockwell T, Westlake J, Nguyen MJ, Teolis BD, Niemann HB, McNutt RL, Perry M, Ip WH (2009) Liquid water on Enceladus from observations of ammonia and 40Ar in the plume. Nature 460:487–490

Waite JH, Brockwell T, Elliot J, Reh K, Spencer J, Outer Planets Satellites Decadal S (2010) Titan lake probe: the ongoing NASA Decadal Study Preliminary Report, EGU General Assembly, vol 12, Vienna, Austria, 2–7 May, p 14762

Watson JD, Crick FHC (1953) A structure for deoxyribose nucleic acid. Nature 171:737–738

Wilson EH, Atreya SK (2004) Current state of modeling the photochemistry of Titan's mutually dependent atmosphere and ionosphere. J Geophys Res (Planets) 109:06002–06002

Wolstencroft RD, Raven JA (2002) Photosynthesis: likelihood of occurrence and possibility of detection on Earth-like planets. Icarus 157:535–548

Yung YL, Allen M, Pinto JP (1984) Photochemistry of the atmosphere of Titan – comparison between model and observations. Astrophys J Suppl Ser 55:465–506

Zarnecki JC, Leese MR, Hathi B, Ball AJ, Hagermann A, Towner MC, Lorenz RD, McDonnell JAM, Green SF, Patel MR, Ringrose TJ, Rosenberg PD, Atkinson KR, Paton MD, Banaszkiewicz M, Clark BC, Ferri F, Fulchignoni M, Ghafoor NAL, Kargl G, Svedhem H, Delderfield J, Grande M, Parker DJ, Challenor PG, Geake JE (2005) A soft solid surface on Titan as revealed by the Huygens Surface Science Package. Nature 438:792–795

Appendix E2

Water Oceans of Europa and Other Moons: Implications For Life in Other Solar Systems

Journal article published in *Journal of Cosmology* (2011),
Volume 13, pp. 4191-4211
Online publication: http://journalofcosmology.com/Planets103.html.

Journal of Cosmology, 2011, Vol 13. 4191-4211.

Water Oceans of Europa and Other Moons: Implications For Life in Other Solar Systems

Solomonidou, A.[1,2], Coustenis, A.[2], Bampasidis, G.[2,3], Kyriakopoulos, K.[1], Moussas, X.[3], Bratsolis, E.[3], Hirtzig, M.[2]

[1]Department of Geology and Geoenvironment, National & Kapodistrian University of Athens, Greece,
[2]LESIA, Observatoire de Paris-Meudon, 92195 Meudon Cedex, France,
[3]Department of Physics, National & Kapodistrian University of Athens, Greece.

Abstract

The icy satellites around Jupiter and Saturn have been revealed as recently or presently active bodies of high interest for geology and astrobiology. Several of them show promising conditions for internal structures involving liquid water oceans. The surface features observed on Jupiter's Europa and Ganymede as well as Saturn's Titan and Enceladus moons display interesting evidence and multicomplex geological figures, which resemble terrestrial geo-terrains in terms of structure and possibly followed similar formation mechanisms. All aforementioned satellites consist of differentiated interiors that are stratified into a high-density rocky core, a mantle and an icy crust. The confirmation of the presence of a liquid water ocean within these satellites would have important implications on the existence of solid bodies with internal liquid water in the outer Solar System well beyond the "habitable zone", with important astrobiological consequences. Indeed, an underground liquid ocean could provide a possible habitat by resembling terrestrial life-hosting environments like the deep oceans and the hydrothermal active vents. In this study we review the surficial aspects of Europa, Ganymede, Titan, and Enceladus and connect them to possible models of interior structure, with emphasis on the astrobiological implications.

Keywords: Icy satellites, internal ocean, planetary geology, Europa, Titan, Ganymede, Enceladus

Anezina Solomonidou
National & Kapodistrian University of Athens / Observatoire de Paris-Meudon
Panepistimiopolis, Zografou
15783 Athens, Greece
Email: asolomonidou@geol.uoa.gr
Phone: +30-2107276854
Fax: +30-2107276725

1. Introduction

Europa, Ganymede, Titan, Enceladus

Icy satellites of the gaseous giants, Jupiter and Saturn, at orbits beyond the ice-line, constitute extremely interesting planetary bodies due to – among other - their unique geological (Prockter et al. 2010) and surface composition characteristics (Dalton, 2010; Dalton et al. 2010; Fortes & Choukroun, 2010), the possible internal water ocean underneath their icy crust and the habitability potential (Schubert et al. 2010; Tobie et al. 2010; Hussmann et al 2010; Sohl et al. 2010). Two of the largest Jovian satellites, Ganymede and Europa, as well as Saturn's Enceladus and Titan, show not only surface features similar to the terrestrial planets and especially the Earth, but also internal heating and occasionally volcanism. Hereafter we summarize some of the characteristics of these moons.

In the neighborhood of Jupiter, two moons are good candidates for the internal liquid water ocean and together form today the main targets of the Europa Jupiter System Mission (EJSM), a concept studied by ESA and NASA for a launch in 2020.

Europa hosts one of the smoothest surface topographies in the Solar System, composed essentially of water ice and other (Dalton, 2010; Dalton et al. 2010), and displays structures like linear chains (lineae) (e.g. Figueredo & Greeley, 2004), which most likely are crack developments caused primarily by diurnal stresses (Prockter et al. 2010) and display the main characteristics of ridges. Other structures are domes (pits that are surface depressions), dark spots and very few craters (Pappalardo et al. 1998a) as the Galileo mission showed. Internal stratigraphic modeling suggests that the satellite is primarily composed of silicate rock (olivine-dominated mineralogy) (e.g. Schubert et al. 2004; Sohl et al. 2010) and most probably an iron-rich core (Anderson et al. 1998). It is also suggested that the icy crust is decoupled from the moon's deeper interior due to the presence of a subsurface liquid ocean (e.g. Schenk &Mckinnon, 1989; Zimmer et al. 2000; Schenk et al. 2004). The cracks, faults and lineae observed on the surface, have most probably been formed by endogenic processes that lead to tectonic movements and imply the presence of a subsurface ocean that interact with the crust. Also, Europa suffers heavily bombardment by charged particles from the Jovian magnetosphere that lead to surface material decomposition and form the tenuous atmosphere composed mainly of oxygen (Shematovich & Johnson, 2001; Coustenis et al. 2010).

On the other hand, Ganymede, the largest satellite of the Solar System, is the only known moon to possess a magnetosphere (Kivelson et al. 2002). Most of Ganymede's surface coverage displays dark and brighter regions. The former are filled with impact craters while the latter are covered by terrains curved by tectonic ridges and grooves (e.g. Pappalardo et al. 2004; Patterson et al. 2010). Its internal structure possibly consists of a relatively small iron-rich core, overlain by silicate rocky material, which is covered by an icy crust. It is believed that a liquid ocean exists within the mantle almost 200 km deep (e.g. McCord et al. 2001). The satellite possesses a thin oxygen atmosphere (Hall et al. 1998; Coustenis et al. 2010 and references therein).

The aforementioned information for Europa and Ganymede has been provided mostly from ground-based but also from *in situ* missions such as Pioneer 10 and 11, Voyager and more recently and efficiently Galileo. Taking into account the geological and structural elements of both satellites, they readily become promising worlds of astrobiological potential. The forthcoming Europa Jupiter System Mission (EJSM) which is composed of two orbiters, one dedicated to Europa and one to Ganymede, will provide detailed investigation of these satellites (e.g. Blanc et al. 2009).

Orbiting at circa 10 AU, the Kronian satellites Titan and Enceladus, stand as intriguing objects as the Jovian satellites. The Cassini-Huygens mission has unveiled the multivariable Earth-like geology of Titan since its arrival in 2004. Furthermore, Titan is the only one planetary object except the Earth that possesses a unique nitrogen and full of organics atmosphere (e.g. Coustenis & Taylor, 2008). Recently, a subsurface liquid ocean was suggested at Titan based on thermal and orbital calculations (e.g. Tobie et al. 2005) spin rate measurements and SAR reflectivity observations (Lorenz et al. 2008; Stiles et al. 2010; Hussmann et al. 2010). The surface investigation brought to light many geological expressions such as extensive mountains, ridges, dendritic networks, dunes, lakes, channels, canyons and riverbeds (Lopes et al. 2010). Furthermore, there is the possible existence of active zones on the satellite due to past or recent cryovolcanic and tectonic activity (e.g. Soderblom et al. 2007; Lorenz et al. 2008; Nelson et al. 2009a; 2009b).

Another Saturnian satellite, Enceladus, has been shown by Cassini to be one of the most active objects in the Solar System despite its minor size. Indeed, jets from its southern polar region consisted mainly of water ice particles that reach over 435 km in height, enrich the E-ring of Saturn (Dougherty et al. 2006; Porco et al. 2006; Waite et al. 2006). The source of such activity could be a large internal liquid deposit, most likely an underground liquid ocean (e.g. Porco, 2008; Collins et al. 2007; Postberg et al. 2009). The surface expressions observed on Enceladus include craters and smooth terrains that consist of extensive linear cracks, scarps, troughs and belts of grooves.

Due to their complex surfaces and intriguing interiors, both Saturnian satellites, require new long-term missions with advanced instrumentation and possibly *in situ* elements. Such a concept was proposed within the Titan Saturn System Mission (TSSM), studied by ESA and NASA and could be launched after EJSM, around 2025. The mission consists in an orbiter, a Titan montgolfière hot air balloon and a Titan lake lander for simultaneous *in situ* and remote exploration of Titan and Enceladus.

A number of evidences, either surficial expressions or geophysical factors, endorse the existence of internal oceans beneath the four aforementioned satellites. The consideration of the possible implications from geological features on the surface and their possible relation to the interior is presented in the review hereafter.

2. Geology: Surface features and their implications

The diversity of geological features on Europa and Ganymede

Without doubt, the surface expressions observed on a planetary body are the signatures of both external and internal processes as occurred with time. Hence, although the environmental conditions and the working material are different from the terrestrial case, in the presence of similarities in the surface features observed, the heritage of Earth science can be used as a tool for their study on other bodies.

Europa and Ganymede present a major diversity in terms of appearance and surface geological structures and therefore in terms of the surface-shaping forces. Europa seems to be subject to active tectonism and cryovolcanism since it displays a young, smooth and active surface. On the contrary, Ganymede is heavily cratered on most of its surface and internal processes like cryovolcanism seem to have played only a minor role in the surface modification since there is little indication of resurfacing. In general, erosion as well as mass movement and landform degradation seem to play an important role in resurfacing as it reduces the topographic relief by moving surface materials to a lower gravitational potential (Moore et al. 2010).

The most distinct and characteristic morphotectonic features on Europa are the lineations that intersect the entire upper part of the satellite's crust (Fig. 1). These formations are probably the major resurfacing mechanism since their genesis is based on the intersection of any two parts of the surface by bedding or/and cleavage. Figure 2 displays a scheme of intersect lineae formation as seen on the Earth (Park, 1997). The tectonic activity that forms these edifices along with the heating from the subsurface diapirs (mobile material that was forced into more brittle surrounding rocks and follows an upward direction) composes the dominant dynamic potential of the satellite.

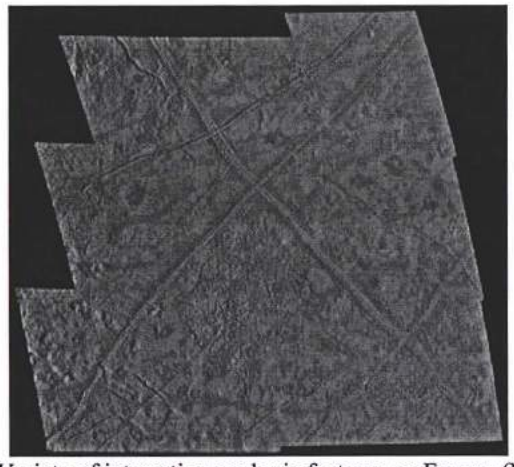

Fig. 1. Variety of interesting geologic features on Europa (NASA).

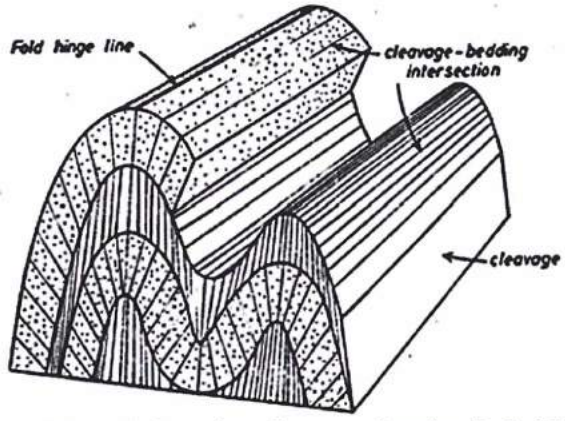

Fig. 2. Schematic formation of intersect lineation (Park, 1997).

Geissler et al. (1998) proposed four different classes of lineaments that vary with age and wipe out Europa's geologic history through time. Their size ranges from 1 to 20 km and they are separated into (a) incipient-simple colorless cracks, (b) ridges that are wider than the cracks, (c) multiple ridged triple bands and (d) ancient bands (Fig. 3). A distinct intersecting 1,500 km feature, Agenor Linea, is a candidate active region as found in photometric observations (Hoppa et al. 1998; Geissler et al. 1998).

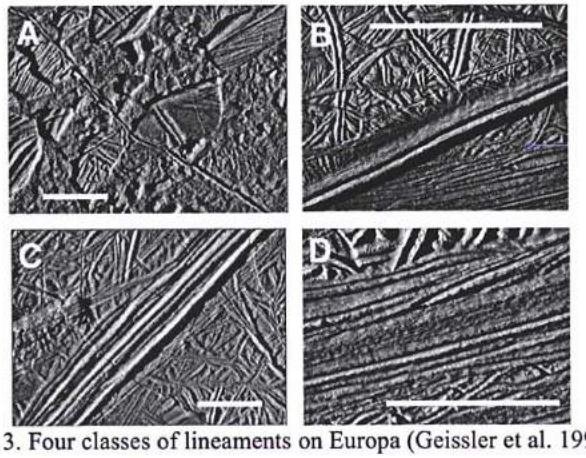

Fig. 3. Four classes of lineaments on Europa (Geissler et al. 1998).

Other geological expressions seen on Europa by Galileo are features that are called 'lenticulae' and 'chaos'. In terrestrial geology, a lenticulae feature is a depositional body that is thick in the middle and thin at the edges, resembling a convex lens in cross-section. Both features have probably formed by rising diapirs that produced partial melt. On Europa, the lenticulae are ovoidal features ranging from 5 to 20 km in diameter (Pappalardo et al. 1998) while the chaos structures, like Conamara Chaos (8°N, 274°W), are larger features presenting blocky material (Carr et al. 1998; Spaun et al. 1998; Sotin et al. 2002). Another hypothesis for the genesis of lenticulae features suggests a correlation between them and the chaos formations. This hypothesis by Greenberg (2008) assumes that the lenticulae are chaos formations in smaller dimension that low-resolution Galileo imaging interpreted wrongfully as distinct structures.

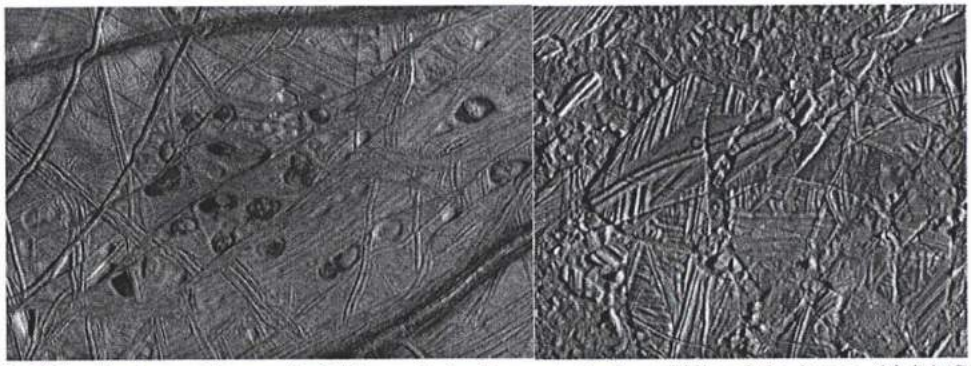

Fig. 4. (left) Lenticulae on Europa (reddish semi-circular spots in the middle of the image. (right) Conamara Chaos, area covered with big blocks of crust that are mixed and moved suggesting they floated on a liquid layer (Galilleo Project/NASA). The area of chaos terrain shows plate-like features (marked with A) with ridges and valleys, and regions lower than the plates (marked with B). Also, plate displacement is obvious with surface expressions like faults or ridges deviating from their linear structure (marked with C).

In contrast to Europa's flattened topography and homogeneous surface, Ganymede possesses two distinct types of terrain. The dominant terrain comprises the brighter regions marked with geological expressions such as extensive ridges, grooves and faults while its age considers as the youngest in comparison with the rest of the surface (Pappalardo et al. 1998) (Fig. 5).

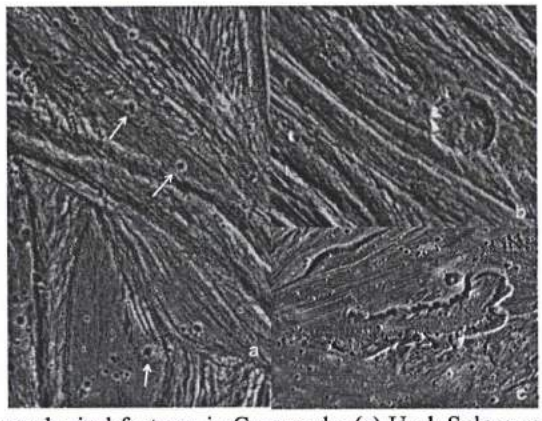

Fig. 5. Bright terrain's major geological features in Ganymede. (a) Uruk Sulcus region is filled with ridges (red dashed line), grooves, craters (white arrows) and generally displays a smooth area. (b) Nippur Sulcus region display an extensive crater overlying ridges and troughs. (c) Sippar Sulcus region contains a large curvilinear scarp or cliff or possibly a caldera. If this structure is identified as caldera then it is the basic evidence for a surficial edifice of active past or present cryovolcanism on Ganymede (NASA/JPL/Brown University).

The other geological terrain-type is the dark terrain (Prockter et al. 1998) (Fig. 6), which is the oldest one in terms of age, heavily cratered with astrobiological interest due to the existence of organic materials (McCord et al. 1998). Considering the fact that the satellite is heavily cratered and the dark terrain comprises one of the oldest terrains of the Galilean satellites (Zahnle et al. 1998), this surface is an indicator of the system's cratering history (Pappalardo et al. 1998).

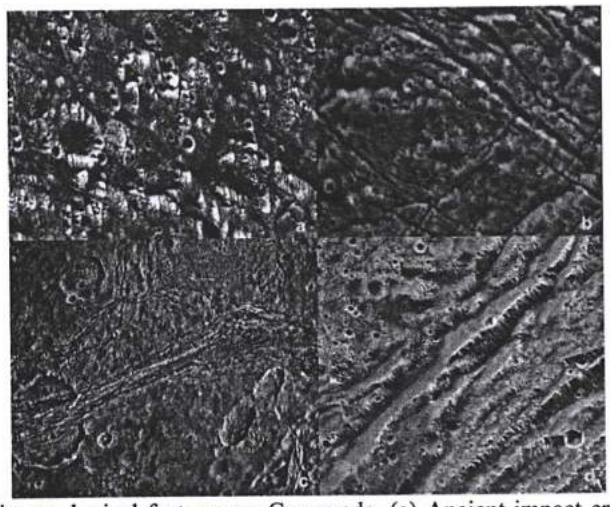

Fig. 6. Dark terrain's major geological features on Ganymede. (a) Ancient impact craters visible at the middle left. (b) Grooves – northwest to southeast sets of fractures that possibly traverse a chain of craters. (c) Tectonics in the dark terrain: sets of ridges and grooves and fault blocks traverse the extensive crater located at the lower left part of the image and deforms it. (d) Series of scarps cut through the heavily cratered and old dark terrain (NASA/JPL/Brown University).

The regions that are particularly interesting in terms of geology are the transitional regions (Fig. 7). Such regions correspond to surface areas that constitute a transition from the dark terrain to the bright grooved terrain of Ganymede. Even though cratering is present on both types of terrain, the dark ones seem heavily and more extensively bombarded (Showman & Malhotra, 1999) suggesting that they represent the oldest preserved (non-resurfaced) surfaces on Ganymede. Pappalardo et al. (2004) suggested that the modification of the dark terrain's material due to tectonic and cryovolcanic resurfacing formed the primary bright terrain.

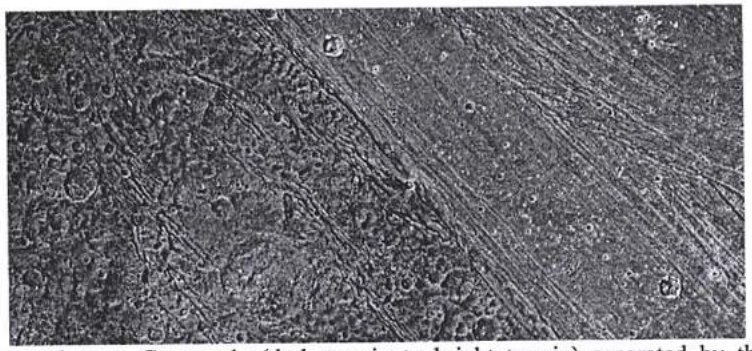

Fig. 7. Transitional region on Ganymede (dark terrain to bright terrain) separated by the red dashed line (NASA/JPL).

Another significant region on Ganymede is the Galileo Regio (Fig. 8), which has likely been formed during an active geologically period (Casacchia, 1984). The Galileo Regio is a heavily cratered area but not an impact crater. It seems to have been shaped under the influence of tectonic processes and young and bright material that arose from the interior (Harland, 2000).

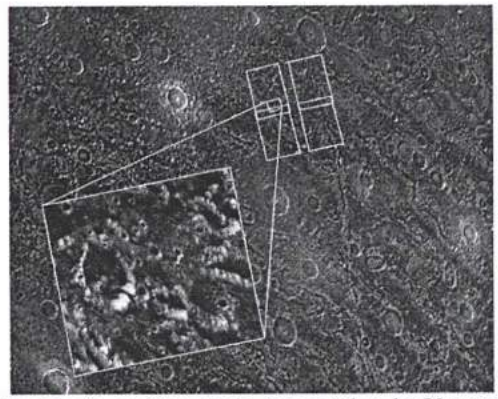

Fig. 8. Galileo Regio on Ganymede. Image taken by Voyager (NASA).

Both moons, Europa and Ganymede illustrate their own fascinating surface geology. Many factors contribute to their formation with the most influencing ones being the internal dynamics like tides, volcanism and tectonics as well as external factors like impact cratering.

Active worlds: Titan and Enceladus and their habitability

Even though Titan and Enceladus' surface expressions are very different in terms of composition, materials and size, they highly resemble the Earth's geomorphology. Titan's surface consists of structures like mountains, ridges, faults and canyons (Fig. 9), formed most probably by tectonic processes, as discovered by the Cassini-Huygens mission (Brown et al. 2009; Lopes et al. 2010; Mitri et al. 2010). Titan, other than its atmospheric uniqueness, is also the only among outer planet satellites where aeolian and fluvial processes operate to erode, transport, and deposit material (Moore et al. 2010).

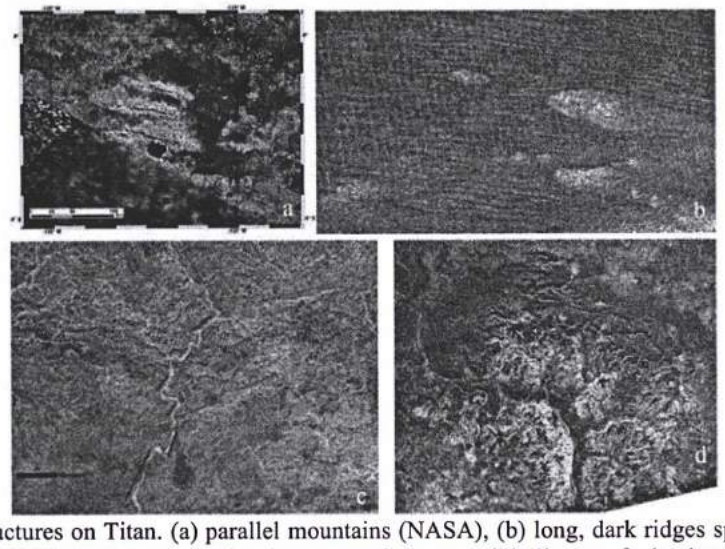

Fig. 9. Tectonic structures on Titan. (a) parallel mountains (NASA), (b) long, dark ridges spaced around one to two kilometers apart (NASA), (c) rectangular river network that possibly lie over faults that control the direction that methane can flow across the surface (NASA/JPL/Devon Burr), (d) canyon systems along with bedrocks, channels and high cliffs (NASA/JPL).

The phenomenon that most probably formed terrestrial-like volcanic structures like calderas, flows and domes on Titan, is cryovolcanism. Currently, there are three possible cryovolcanic regions. These are Tui Regio (20°S, 130°W), Hotei Regio (26°S, 78°W) and Sotra Facula (15°S, 40°W). The latter is considered as the most promising one with obvious surface expressions of peaks, flows and one caldera structure (Fig. 10).

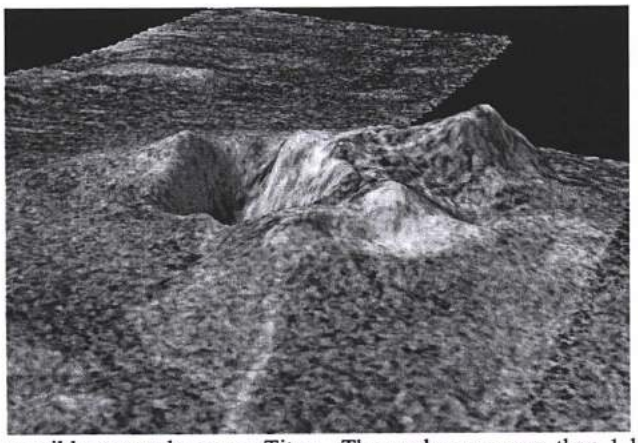

Fig. 10. Sotra Facula, a possible cryovolcano on Titan. The peaks are more than 1 km high and the craters-caldera almost 1.5 km deep. Furthermore, flow features about 100 meters thick are obvious following a radial pattern around the craters (NASA/JPL-Caltech/USGS/University of Arizona).

Furthermore, aeolian and fluvial processes acting on Titan's surface create edifices such as lakes, seas, riverbeds, sand dunes, shorelines, and dendritic drainage networks (Fig. 11). External impact phenomena like impact craters are rarely observed on the surface due to the resurface activity.

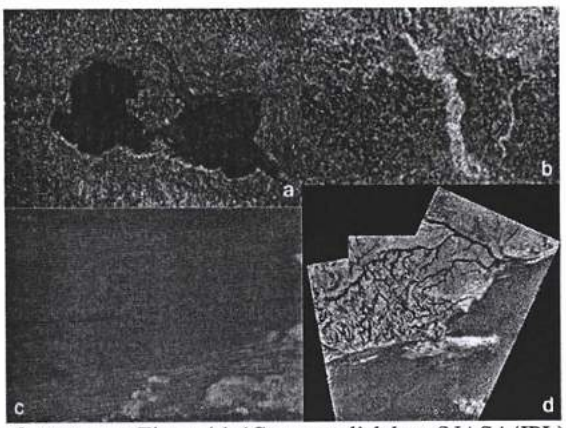

Fig. 11. Fluvial and aeolian features on Titan. (a) 'Connected' lakes (NASA/JPL), (b) riverbeds (NASA), (c) sand dunes (NASA/JPL), (d) dendritic drainage networks (NASA/JPL).

Similarly to Titan, Enceladus presents major tectonic features and active cryovolcanism. The most fascinating phenomenon occurs on Enceladus currently due to its tremendous internal dynamic convective forces that cause Geyser-like fountains at its southern pole that could reach more than 400-km in height (Porco et al. 2005). The rest of Enceladus' surface is covered by smooth and cratered terrains, rifts, ridges, grooves, escarpments and extensive linear fractures (Johnson, 2004). The geology of this tectonized moon is a field of active scientific research awaiting for new observations. Up to date, the observations and analysis showed two types of tectonic terrains. The north pole consists of heavily cratered landforms while the central region and southern pole of tectonic molded terrain with cryovolcanic features.

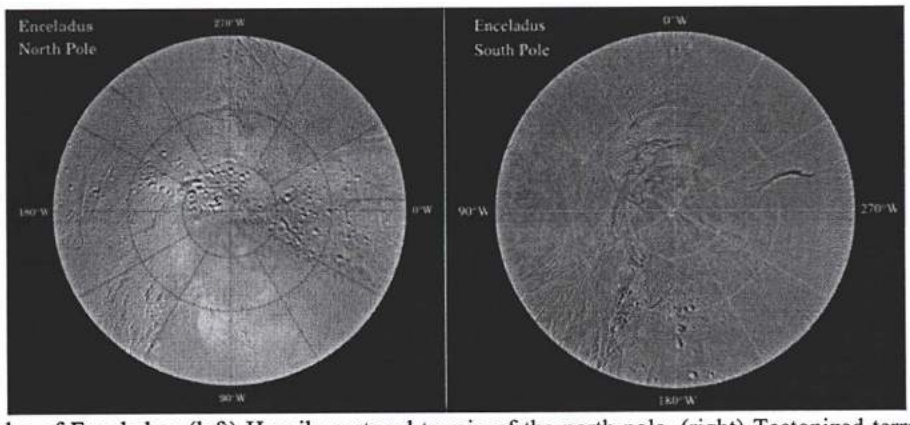

Fig. 12. Poles of Enceladus. (left) Heavily cratered terrain of the north pole. (right) Tectonized terrain (ridges, grooves, rifts) with fissures that emanate cryovolcanic material (NASA/JPL).

3. Interior models and liquid water subsurface oceans in giant planets' satellites

Our current knowledge of the icy moons' internal stratification and their composition is being built on a combination of spacecrafts data, laboratory experiments, and theoretical geophysical modeling. Resembling Earth's moon in terms of structure, icy moons consist of a core, a mantle, and a crust, with the specificity of the existence of a liquid ocean lying within the icy mantle (Fig. 13).

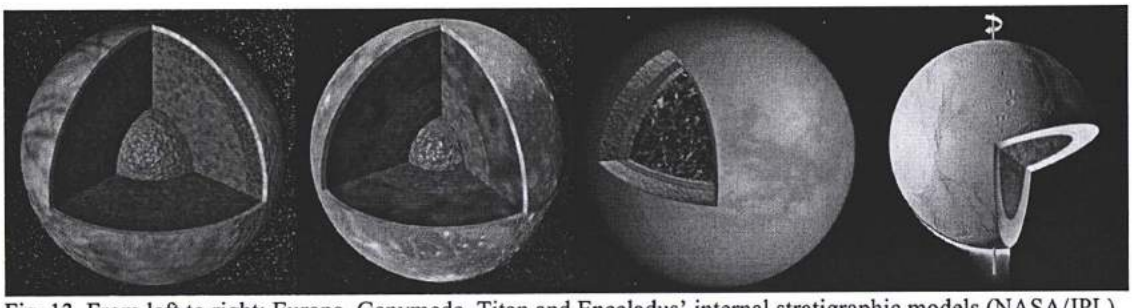
Fig. 13. From left to right: Europa, Ganymede, Titan and Enceladus' internal stratigraphic models (NASA/JPL).

According to current models of internal structure, the existence of subsurface oceans is expected for most of the icy moons of the Outer planets (e.g. Sohl et al. 2010; Schubert et al. 2010 and references therein). Even if an ocean is not currently hidden within the interior, it is suggested that a liquid layer was present in the past but cooled to ice over time. An example of such case is Neptune's moon Triton.

Evidence for hydrated sulfate salts on the surfaces of Europa and Ganymede from spectroscopic data support the possible existence of subsurface oceans (McCord et al. 1998; 2001; Cassidy et al. 2010; Fortes et al. 2010 and references therein) suggesting the deposition of minerals following internal hydrothermal events. In addition, Galileo's magnetometer (e.g. Khurana et al. 1998; Kivelson et al. 2002), detected induced magnetic fields at Europa and Ganymede that imply the presence of an electrically conductive subsurface layer (e.g. Sohl et al. 2010). Furthermore, the detection of a low viscosity layer underneath the icy crust again endorses the presence of a subsurface liquid ocean inducing recent geological activity (Stern & McKinnon, 1999; Ruiz & Fairen, 1999).

The common properties that need to be satisfied on all bodies in order to sustain a liquid subsurface ocean are:

(a) Heat production which mainly originates from radiogenic heating or other triggering mechanisms (e.g. McKinnon, 1999; Tobie et al. 2005). In the absence of an internal liquid layer, the tidal deformation of the ice shell remains very small as there is no decouple of the core and the mantle, thus the resulting stress and consequent heating is negligible (Moore & Schubert, 2000). Other possible heat sources are the dissipation of tidal energy due to orbital interaction between the satellites and their planets, or the exothermal geochemical

production of heat like hydration and crystallization of solids (e.g. Sohl et al. 2010; Hussmann et al. 2010).

(b) Efficiency of heat transfer, which is based on thermal diffusion and thermal convection (e.g. Hussmann et al. 2010).

(c) Components capable of decreasing the melting point of ice and supporting the ocean's liquid state (e.g. Sohl et al. 2010; Tobie et al. 2010). The composition of such oceans should offer an antifreeze constituent like a solution of water with ammonia, so that it remains in liquid state. The aqueous evolution of a possible internal ocean depends on the several chemical interactions between liquid water and rocks, on the hydrodynamic processes within the ocean (degassing), on the freezing of the expected plumes as well as on the presence of secondary organic and inorganic species (Sohl et al. 2010).

(d) Stability of the crust against convection, keeping the ocean subsurficial as well as preventing stagnant lid convection (e.g. McKinnon, 1998; Rainey & Stevenson, 2003).

The Voyager and Galileo missions data suggest that the internal stratification of Europa consists of an iron core (300 to 800 km) covered by a rocky mantle probably 100 km thick that it is overlain by a liquid water ocean less than ten kilometers thick. The ocean is covered by a surficial icy layer possibly 15 km thick (Fig. 13). The Galileo magnetometer's measurements that showed the crust had shifted by almost 80°, also indicated that the mantle is not attached to the crust, thus reinforcing the theory of an internal ocean (Kivelson et al. 2000; Greenberg, 2005). Nevertheless, the most convincing evidence for the liquid water ocean is the existence of the controversial 'chaos terrain' (Fig. 4) that possibly formed by melt-through from below (O'brien et al. 2002). The controversy debates on the mechanisms that formed the terrain, whether through induced impacts or cryovolcanic processes, as well as on the thickness and state of the ice shell. On one hand, one model (Fig. 14a) suggests that the ocean is a warm convective ice layer located several kilometers below the icy crust and on the other hand the other model (Fig. 14b) suggests a liquid ocean hidden more than 100 km below the crust.

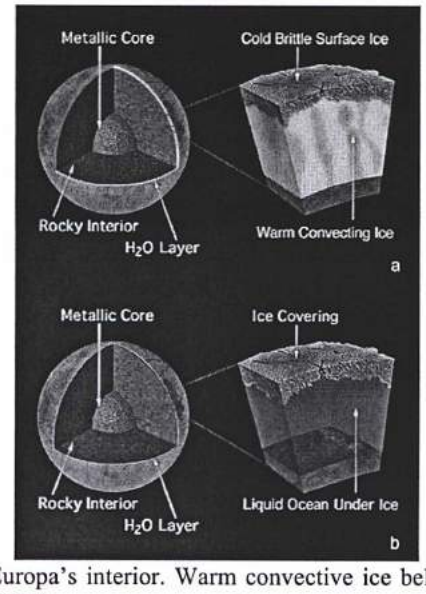

Fig. 14. Stratigraphic models of Europa's interior. Warm convective ice below the ice crust (a); Liquid ocean under the ice coverage (b) (NASA/JPL).

The radioactive decay cannot provide the amount of heat required to modify entirely the satellite surface, as observed on Europa. In this case, the surface temperature is limited to 110K at the equator and 50K at the poles; such cold temperatures make the ice locally as hard as terrestrial igneous granite (McFadden et al. 2007). On the other hand, hydrothermal activity has the potential to reshape the surface crust. Recent studies suggested that the influence of Jupiter on Europa due to its small but non-zero obliquity probably generates large tidal waves that keep the ocean warm (Tyler, 2008).

If the heat propagation and the buoyant oceanic currents are not intense then the ice shell will be thick and a warm ice layer will be formed at the bottom of the shell (Fig.15b). During the hydrothermal processes this warmer ice will rise and slide like the terrestrial glaciers. Such movements can cause surface modification and produce structures like the 'chaos terrain'. Other features supporting the existence of a thick ice layer are the large impact craters surrounded by concentric rings filled with ice. Geophysical models, associating the mere presence of these structures to the amount of heat generated by the tides, suggest an icy crust 10-30 km thick with a warm ice layer at the bottom and a liquid ocean probably 100 km thick (Schenk et al. 2004). Additionally, a scenario that consists of a thick icy crust of almost 15 km suggests a stratigraphic model with a 100 km deep ocean, which may be extremely deep, about10 times deeper than the deepest point of Earth's oceans, the Challenger Deep on the Mariana Trench, which is 11 km below sea level and the lowest elevation of the surface of the Earth's crust. The potential ocean of Europa would contain an amount of water twice the entire terrestrial surface hydrological system.

Alternatively to the previous model, if the heat flow and the plumes are intense then the ice shell is expected to be thin (Fig. 15a). The fragmentation of such a thin crust is most probably expressed with tectonic-like formations like the Conamara region. The debate regarding the thickness of Europa's crust gave birth to an alternative hypothesis regarding the thin ice model, which suggests a thin upper crust layer, almost 200-m thick, that behaves elastically and is in contact with the surface through zones of weakness like multiple linear ridges (Billings & Kattenhorn, 2005).

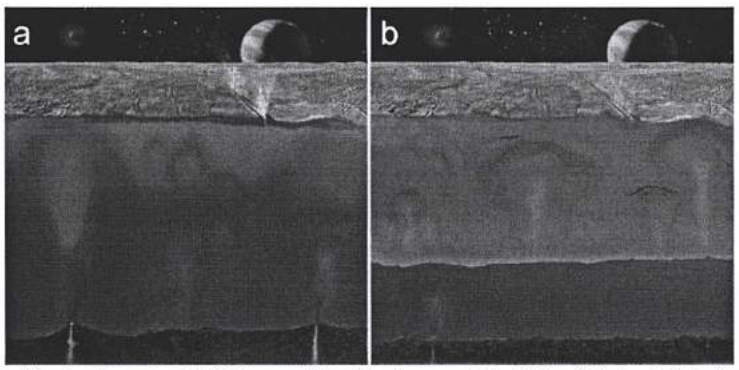

Fig. 15. Two models for the icy crust thickness. The thin ice model ~200m (a) the thick ice model ~15 km (b) (NASA/JPL).

Europa's case supports the existence of a stagnant lid underneath its crust (Fig. 16) (Showman & Han, 2004). The stagnant lid is a relatively cold and stiff conductive layer covering the warmer convective icy interior (Schubert et al. 2004). Since the expected activity within Europa's interior is upwelling thermal diapirism, the stagnant lid can prevent cold near-surface icy material from sinking towards the ocean.

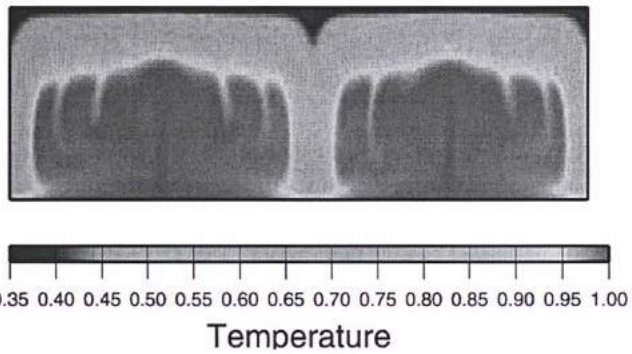

Fig. 16. Simulation of convection within Europa's ice shell (Showman and Han, 2004).

Compared to the Earth's oceans, the composition of Europa's hidden ocean should be significantly different. The Earth's ocean major component is sodium chloride while Europa's should be magnesium sulfate as indicated by Galileo data (e.g. Fanale et al. 2001). Indeed, Europa's weak magnetic moment is induced by the varying part of the Jovian magnetosphere (Schilling et al. 2007) and requires a highly conductive subsurface ocean. Such conductive materials candidates are the magnesium sulfate (e.g. McCord et al. 1998) or sulfuric acid hydrate (Carlson et al. 2005).

Similarly, Ganymede consists of a four-layer interior, based on measurements regarding its gravity field, mass, density and size. Geophysical models suggest two kinds of internal stratigraphy, one of an undifferentiated mixture of rock and ice and one of a differentiated body consisting of a rocky core, an extended icy mantle and an icy crust. We think the latter model is the most plausible as it is compatible with the gravity field measurements made by Galileo (e.g. Sohl et al. 2002). Such intrinsic magnetic field supports the existence of an iron-rich core (Hauk et al. 2006). The thickness of the layers in the interior depends on both the fraction of olivine and pyroxene and the amount of sulfur in the core (e.g. Sohl et al. 2002) (Fig. 17). Thus, the 2,634-km-radius Ganymede consists of an 800 km iron sulfide core, an almost 900-km thick outer ice mantle and a silicate-rich mantle 700 km thick (e.g. Kuskov et al. 2005).

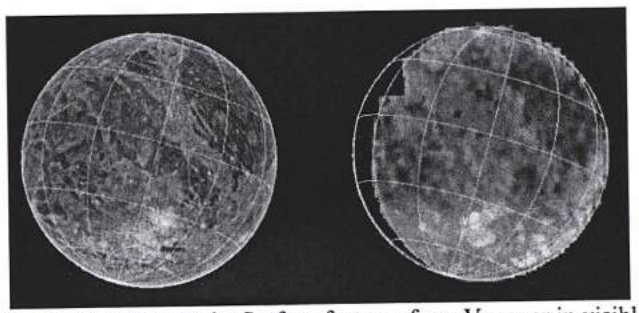

Fig. 17. Ice and mineral deposits on Ganymede. Surface features from Voyager in visible light (left); Minerals in red and ice grains in blue in infrared light from Galileo (NIMS, Galileo Mission, JPL, NASA).

Although the mechanisms that formed Ganymede's complex surface are still unidentified, multiple scenarios have been proposed. Most of the scenarios agree on a general mechanism that uses tectonism as the main chisel that formed and shaped the existing structures, especially the grooved terrain (Sohl et al. 2002). On the other hand, and in contrast with the other three aforementioned satellites, cryovolcanism does not seem to participate actively in the geodynamic processes. The radiogenic heating from within the satellite as well as tidal heating from past events are considered as the main forces that generate the stresses that lead to tectonic movements and eventually to tectonic structures.

Contrary to Ganymede, probably Titan but especially Enceladus provide evidence of past and current cryovolcanism that shapes their surfaces. The mechanisms that formed Titan's surface by endogenic factors are still unknown, although the central idea is focused on cryovolcanism and morphotectonism, with the latter being the short- and long-term surficial expressions of any tectonic activity originated from endogenic processes (Solomonidou et al. 2010). However, it is possible that Titan underwent a period of tectonism resembling those on Europa's and Ganymede's.

According to geophysical models, Titan's differentiated interior consists of a serpentinite core (~1,800 km), a high-pressure ice mantle (~400 km), a liquid layer of aqueous ammonium sulphate (50 to 150 km wide), and an externally heterogeneous icy few kilometers wide (Tobie et al. 2005; Fortes et al. 2007).

The subsurface instability due to the interactions within an interior liquid ocean causes the modification of extended features on Titan's surface, whether they derive from cryovolcanic or morphotectonic dynamic processes. Currently, all the geophysical models that try to explain the geodynamics of Titan support the existence of an oceanic layer that decouples the mantle from the icy crust. Additionally, the identification of a small but significant asynchronicity in Titan's rotation from Cassini SAR data favors the aforementioned decoupling (Lorenz et al. 2008). Internal geodynamic activity can transport effusively the explosive material from the oceanic layer to the surface and form the cryovolcanic structures like the lobate flows in Sotra Facula.

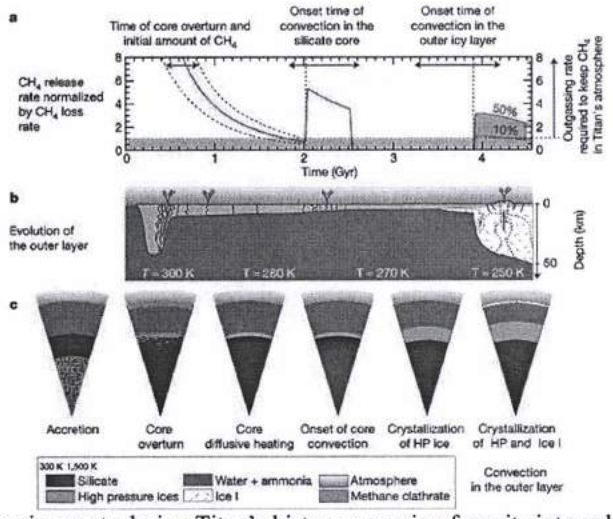

Fig. 18. Possible cryovolcanic events during Titan's history emerging from its internal liquid ocean (Tobie et al. 2006).

Tobie et al. (2006) suggested a cryovolcanic model for Titan's case to solve the mystery of Titan's methane replenishment since it is should vanish in 100 Ma. These authors suggested that episodic methane outgassing events occurred through three distinct episodes covering a chronological period from 2000 Ma ago until 500 Ma ago (Fig. 18). The internal ocean provides the 'magma' chamber by means of material, while convective processes are the triggering mechanisms that initiate the dynamic activity. A convective model of a stagnant lid is capable to explain such activities (Solomatov 1995) as explained for Europa's case earlier. However, the ice shell for Titan's case is expected to be thicker. In opposition, several studies suggest that Titan is not currently convective (Mitri et al. 2010; Nimmo and Bills, 2010).

The uniqueness of Titan's tectonism - even though not yet confirmed - lies in that the tectonic processes are contractional rather than extensional, setting Titan out as the only planetary body in the Solar System other than the Earth, where contractional deformation occurs.

Mitri et al. (2010) proposed an internal thermal model, focused on the changes in volume of a potential underground ocean caused by heat flux variations during freezing or melting. The authors suggest that the continuing cooling of the moon can develop global volume contraction, as described by Tobie et al. (2005; 2006).

Cassini's data proved that, despite its small size (about 505 km in diameter), Enceladus is an active planetary body that spews material through hydrothermal vents resembling terrestrial geysers. This moon is not in hydrostatic equilibrium (Schubert et al. 2007; Schubert et al. 2010), thus a simple and very general stratigraphic interior is being suggested: it consists of a 169 km rocky core overlain by an icy 82 km mantle (Barr and McKinnon, 2007; Fortes, 2007; Schubert et al. 2007). The subsurface ocean is lying between the two layers, and supplies the fountains observed at the south polar region through cracks called 'Tiger Stripes' (e.g. Porco, 2008; Postberg et al. 2009). The moon's tidal dissipation is proposed as the triggering mechanism as well as the cause of the dynamic phenomena like tectonics (convection-conduction, expansion contraction) and cryovolcanism (e.g. Mitri and Showman, 2008; Mitri et al. 2010) that formed the surface expressions described in the previous section.

4. Discussion: Internal activity and surface modification

The possible existence of subsurface liquid oceans underneath the crusts of the icy moons of Jupiter (Europa and Ganymede) and Saturn (Titan and Enceladus), places them in a potential group of planetary bodies where life could emerge and evolve. Other than data processing that provide evidence and information about the internal liquid layers, the surficial expressions that are related to the hydrothermal and dynamic processes occurring within these layers are the surface evidence that could lead to their identification. Specifically, the cryovolcanic and morphotectonic structures seen on the aforementioned satellites are the surface expressions of the internal activity while they are formed by modification of the crustal layer and deposition of material coming from the subsurface ocean. Therefore, investigating these surface exposures and associating them to terrestrial features where water is involved could shed some light on the investigation of internal liquid water oceans in the icy

moons. Trying to model the triggers of internal active phenomena, basic geophysical models usually propose liquid water reservoirs while the geodynamic models point at both radioactive decay and tidal stresses, caused by the giant planets Jupiter and Saturn. We shall herein try and reconcile both views.

The major and most significant structures on Europa's surface are the bunch lineae (e.g. Prockter et al. 2010) (Fig. 3). Data analysis showed that the geometry and the spectral properties vary depending on age, which indicates an evolutionary sequence (Geissler et al. 1998; Dalton, 2010). This means that persistent and drastic processes occur in order to form these features. Such processes seem to be different types of cryovolcanism in which multiple eruptions of ice (warmer than crustal ice) emerge through 'tectonic' crustal weaknesses (Figueredo & Greeley, 2004). This tectonic formation resembles the terrestrial mid-ocean ridges (MOR), which are the extensive opening seafloor terrains, and considered to be a global rather than a local phenomenon. MOR are dynamic and volcanically active structures that constantly provide and deposit new material from the mantle to create new oceanic crust. As seen in Figure 4, the red streaks, as well as the red spots called lenticulae, are most possibly evidence of upwelling warmer material emerging from the liquid layer while colder ice near the surface sinks downwards. After spectroscopic analysis, the red streaks are thought to be rich in magnesium sulfate, another hint in favor of their internal origin (McCord et al. 1998; Dalton et al. 2010). Furthermore, the lineament formations like the dark and red streaks present the basic resurfacing system that dominate on Europa's surface. Their formation is an indicator for current geological activity. Additionally, the thermal diapirism that most likely formed these structures, as well as the red spots, would imply that convective upwelling thermal plumes originate in the lower boundary of the convective system and gets in contact with the cold stagnant lid with the icy plumes (Showman & Han, 2004). Such temperature ranges indicate possible habitability at the upper part of the ice shell. Consequently, Europa's surface morphology is directly connected to the internal dynamic processes and provides evidence of a subsurface interactive ocean.

Unlike Europa's conflicting oceanic hydrothermal system that originates in a rocky sea layer, Ganymede's ocean lays between two icy layers that decouple it from the mantle. Barr et al. (2001; 2004) suggested that large magmatic events due to convective plumes could occur at Ganymede's rock – ice boundary. The surface expressions that are most possibly connected to tectonism are the deep fault structures like the horst-and-graben (resembling terrestrial continental rifts) as well as many cracks that are observed in Ganymede's bright terrain (Showman & Malhotra, 1999). Tidal heating events, either past or current, could cause dynamic forces that modify the icy lithosphere. The main mechanism that deforms tectonically the lithosphere is most likely warm liquid plumes that rise from the upper mantle to the surface, following a pattern similar to the plume-lithosphere interactions at the Hawaiian Swell which cause thinning and instabilities at the crust layer (Moore et al. 1998). Even though the plume theory indicates cryovolcanic processes, little evidence of such activity has been detected on Ganymede. Notably, the extreme morphological difference between the bright and the dark terrain as described in a previous section suggests a massive geological event or set of events that caused such large-scale geo-terrain alteration. Hence, it is possible that the extensive tectonic forces that fractured the dark terrain partially affected the bright terrain as well. Such tectonic weaknesses could display pathways to small cryovolcanic events that lead to resurface processes. However, tilt-block faulting and shears (Head et al. 2002) are some of the structures that appear bright within the dark terrain suggesting that tectonic cracks functioned as path for warm internal oceanic material to pass through like what occurred in the bright terrain. In terms of tectonics, and similarly to the other icy moons, there is no evidence of compressional deformation (Showman et al. 1997). Since the deformational pattern is extensional, the question is whether it is a global or a local phenomenon. Collins et al. (1998) studied observations of grooved terrains of specific stratigraphic ages that have consistent directions over hundreds of kilometers, something that indicates global stressing phenomena. On Earth stressing phenomena could occur where severe forces cause convective currents in the ocean. In a similar way, the plume convection within Ganymede's oceanic layer could create enough turbulence and temperature-pressure instabilities to cause global stressing phenomena with an impact on tectonism. Nevertheless, Ganymede presents styles of tectonism different from Europa's.

Following a pattern similar to the one mentioned for Ganymede, Enceladus' internal tidal stresses and radioenergetic decay produce warm pockets of material, the plumes, that subsequently form the geyser formations at the south polar region. The major and most valuable evidence of Enceladus' cryovolcanic activity, supporting as well the ocean existence, is this geyser formation or geyser accumulation that form a fountain of more than 400 km, as observed by Cassini. The jets initiate from four sub-parallel linear depressions, which are tectonic in origin. Other surface expressions are scarps, ridges, and shields (Collins et al. 2009). On the other hand, Titan's surface structures related to its dynamic interior that also support the existence of a subsurface ocean are the three cryovolcanic candidate regions Tui Regio, Hotei Regio and Sotra Facula and many morphotectonic structures like mountains, ridges and canyons (e.g. Solomonidou et al. 2010 and references therein). Generally, in the case of both moons it is thought that their ice shells transit from a conductive to a

convective state; since they probably overlay a pure liquid ocean (Tobie et al. 2005) this can have major effects on surface morphotectonics (Mitri and Showman, 2008). Indeed, thermodynamic oscillations within the ice shells may trigger repeated extensional and compressional events. In the presence of a subsurface ocean underneath Titan and as a consequence of local stress mechanisms, parts of the icy crust could behave like rigid ice floes due to lateral pressure gradients. If such floating occurs, many morphotectonic features like faults and canyons can relate their formation to this event. Furthermore, radial contraction of the internal high-pressure ice polymorphs could possibly amend the radial expansion caused during the cooling stage of the moon (Mitri and Showman, 2008), in which the existence of a liquid layer plays a significant role. As a result, the overall global contraction could form mountainous chains (Radebaugh et al. 2007).

These four satellites are dynamic planetary bodies and the internal ocean most likely plays an important role on the formation and modification of their surfaces. The properties on which the presence of an internal ocean depends were mentioned earlier (section 3). Another issue that should be taken under consideration is the set of properties that determine the possible exchange of material between the subsurface and the surface. These are the mechanical properties of the lithosphere as proposed by Tobie et al. (2010).

The formation of the surface signature of any upwelling activity depends on:

(a) the chemical interaction between the material in motion and the local environment, which travels through the conduit path from the source to the surface.
(b) the magnitude of the forces that triggers this motion.
(c) the complexity of the structure of the conduit path which could be an extensive tectonic zone of weakness. From such a structure, multiple cryovolcanic eruptions could emanate.
(d) the influence of the atmosphere on the surface as described in Tobie et al. (2010).

Titan and Enceladus display cryovolcanic expressions in specific regions. On Titan these zones appear on a latitudinal ring around 20°S - 30°S, while on Enceladus they lay at the southern pole. On the contrary, Europa and Ganymede do not host evidence of such large and localized structures. Considering these surface expressions, as well as the morphotectonic structures described earlier, we infer that different endogenic conditions occurred. Firstly, the upwelling material within Europa and Ganymede could spread throughout the lithosphere, while in Titan and Enceladus it would pass through more localize exsolution paths. On Titan and especially on Enceladus the cryovolcanic expressions illustrate instant energy relief of the hydrodynamic activity, while Europa and Ganymede could experience continuous relaxation. This can possibly explain the fractal development of lineae structures on Europa. Moreover, the gravitational field, as well as other heat and transfer mechanisms, play in each satellite a major role in the distribution of the upwelling material and the formation of the surface structures. In order to evaluate the above implications it is essential to record the spatial and temporal variations of the structures observed.

5. Habitability issues for outer planet satellites

The existence of an internal liquid ocean underneath the icy crusts of the giant planet satellites could serve as a potential abode for life. The location of the ocean close to the surface provides food for thought on habitability zones, and conditions for life in general, in the Solar System.

Indeed, the discovery of hydrocarbon surficial lakes on Titan and the possible existence of subsurface liquid oceans in Europa, Ganymede, Titan, and Enceladus reveal alternative concepts to the classical definition of the habitable zone, and suggest the need for reconsidering its limits (Lammer et al. 2009). Currently, more and more studies regarding the planetary habitability propose the icy moons with subsurface oceans as potential worlds for initiating and/or sustaining some sort of life forms (Fortes, 2000; Raulin, 2008; Raulin et al. 2010; Coustenis et al. 2011 and references therein). Figure 19 presents the possible locations of the liquid layers within the icy satellites of Jupiter as well as their habitability potential.

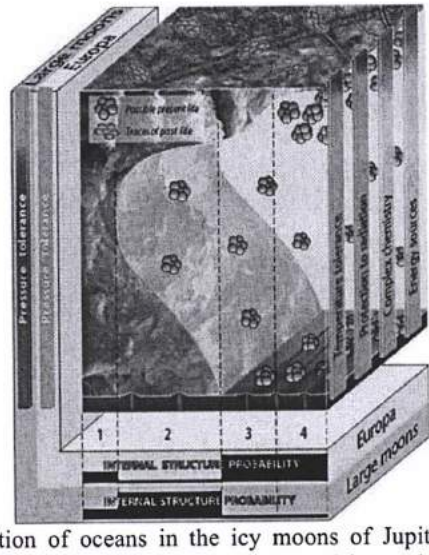

Fig. 19. Possible schematic location of oceans in the icy moons of Jupiter as a function of depth. Europa probably agrees with internal structures 3 (thick upper icy layer <10 km and a thick ocean) or 4 (very thin upper icy layer 3-4 km). Ganymede is closer to 1 (completely frozen) or 2 (three-layered structures impeding any contact between the liquid layer and the silicate floor) (Lammer et al. 2009). The color scales on the right side indicate the physical and chemical constraints on which habitability depends on.

For Europa, the assumed internal processes that trigger the geodynamic phenomena are the tidal stresses, which produce considerably less energy than radioenergetic decay. Europa is being compressed and stretched when affected by the gravitational forces of Jupiter and the other Galilean satellites and thus, the resulting tidal friction provides enough energy, as well as temperature, for an extensive ocean to exist underneath the crust. The provision of large amounts of energy at the bottom layer of an ocean can conceivably form hydrothermal vents like the ones seen on Earth. Notably, life could emerge around hydrothermal vents, which are important geological forms in terms of life propagation. Greenberg (2010) suggests that even ecology including complex organisms could exist on Europa. The author provided evidence of oxygen concentration within the ocean greater than that of the Earth's, which is suggested as an indicator for aerobic organisms. Nevertheless in the case where the concentration of salts is large, only extremophile organisms (like halophiles) could survive (Cooper et al. 2001; Marion et al. 2003).

Ganymede lays between structures 1 and 2 in the scheme shown on Fig. 19 indicating that it is much colder than Europa, a factor that lowers its habitability potential. On the other hand, reinforcing Ganymede's possibility for life to exist, Barr et al. (2001) imply that magmatic events could form pockets of liquid, which would then ascent buoyantly carrying nutrients to the internal ocean. Based on their calculations, a water plume could reach Ganymede's ocean and carry nutrient-rich material with an eruption time of 3 hours to 16 days. Additionally, Ganymede's system could provide the necessary tools to concentrate biological building block ingredients (Trinks et al. 2005) especially since it possesses a magnetic field that is able to protect life from harmful radiation and lies in a relatively quiet radio zone.
On Titan, terrestrial bacteria can absorb their energy and carbon needs from the tholins that exist in its thick atmosphere (Stoker et al. 1990). Furthermore, photochemically derived sources of free energy on the surface could maintain an exotic type of life, using liquid hydrocarbons as solvents (McKay & Smith, 2005). Other than the atmospheric properties that are favorable to life, the possible existence of an underground ocean might support terrestrial-type life that had been introduced previously or formed when liquid water was in contact with silicates early in Titan's history (Fortes, 2000). Furthermore, the possible amount of ammonia dissolved within the ocean is suggested to be ~10% (Lorenz et al. 2008), something that corresponds to a pH of 11.5, while at a depth of 200 km the pressure reaches ~ 5 kbars and hot plumes within the potential ocean could be generated (Coustenis et al. 2011 and references therein). The aforementioned conditions are not unfavorable to the emergence and maintenance of life (e.g. Fortes, 2000; Raulin, 2008).

Enceladus' extremely high temperatures at the south polar region are probably generated by the hydrodynamic processes that form the fountain, as previously described, and thus enhance the potential for habitability. The most convincing theory, after Cassini data analysis, suggests that a liquid ocean exists beneath the Tiger Stripes. There are standards for life that Enceladus' possible ocean is not consistent with: the sunlight, the oxygen compounds, and the organics produced on a surficial-crust environment. However, terrestrial regions like the

deep oceans that do no satisfy the aforementioned prerequisites for life, still function as active ecosystems (McKay et al., 2008; Muyzer and Stams, 2008). There, sulfur-reducing bacteria consume hydrogen and sulfate, produced by radioactive decay. Notably, the comparison with the terrestrial ecosystems suggests that plume's methane may be biological in origin (McKay et al., 2008). Hence, Enceladus displays an internal warm and chemically rich ocean that may facilitate complex organic chemistry and biological processes (Coustenis et al. 2011).

In conclusion, the confirmation of the existence of a subsurface liquid ocean underneath the crust of the icy moons of Jupiter and Saturn will revolutionise our perspective regarding the habitability potentials of such planetary bodies. Indeed, liquid water may exist well outside the traditional habitability zone, which is merely based on the presence of liquid water on the surface. For planetary habitability, the principal criteria are the presence of liquid water anywhere on the body, as well as the existence of environments able to assembly complex organic molecules and provide energy sources: this can well be underneath the surface in some cases, if stability conditions are met. The four satellites described in this study seem to fulfill some or all of the above requirements. However, it is of high priority to revisit these bodies with new missions and advanced instrumentation (such as gravitational and magnetic field sounding systems and in situ element detectors) in order to obtain altimetry and *in situ* monitoring of tidally-induced surface distortion data (Sohl et al. 2010) that could unveil in detail the internal stratigraphy of the moons and the specificity of the subsurface oceans. Future large missions, or smaller dedicated ones, to the Galilean and Khronian systems would allow us to better understand the mechanics behind the astrobiological potential of worlds with subsurface oceans, and shed some light on the emergence of life on our own planet.

6. Acknowledgement

A.Solomonidou is supported by the "HRAKLEITOS II" project, co-financed by Greece and the European Union.

7. References

Anderson, J. D., Schubert, G., Jacobson, R. A., Lau, E. L., Moore, W. B., Sjogren, W. L. (1998). Europa's Differentiated Internal Structure: Inferences from Four Galileo Encounters. Science, 281, 2019-2022.
Barr, A. C., Pappalardo, R. T.,Stevenson, D. J. (2001). Rise of deep melt into Ganymede's ocean and implications for astrobiology. Lunar and Planetary Science XXXII, 1781.
Barr, A. C., Pappalardo, R. T., Zhong, S. (2004). Convective instability in ice I with non-Newtonian rheology: Application to the icy Galilean satellites. Journal of Geophysical Research, 109, E12008.
Billings, S. E., Kattenhorn, S. A. (2005). The great thickness debate: Ice shell thickness models for Europa and comparisons with estimates based on flexure at ridges. Icarus, 177, 397-412.
Blanc, M., and 42 colleagues. (2009). LAPLACE: A mission to Europa and the Jupiter System for ESA's Cosmic Vision Programme. Experimental Astronomy, 23, 849-892.
Carlson, R. W., Anderson, M. S., Mehlman, R., Johnson, R. E. (2005). Distribution of hydrate on Europa: Further evidence for sulfuric acid hydrate. Icarus, 177, 461-471.
Carr, M. H., and 21 colleagues. (1998). Evidence for a subsurface ocean on Europa. Nature, 391, 363-365.
Casacchia, R., Strom, R. G. (1984). Geologic evolution of Galileo Regio, Ganymede. Journal of Geophysical Research, 89, B419-B428.
Cassidy, T., Coll, P., Raulin, F., Carlson, R. W., Johnson, R. E., Loeffler, M. J., Hand, K. P., Baragoila, R. A. (2010). Radiolysis and Photolysis of Icy Satellite Surfaces: Experiments and Theory. Space Science Reviews, 153, 299–315.
Collins, G. C., Head, J. W., Pappalardo, R. T. (1998). Formation of Ganymede grooved terrain by sequential extensional episodes: Implications of Galileo observations for regional stratigraphy, Icarus, 135, 345-359.
Collins, G.C., Goodman, J.C. (2007). Enceladus' south polar sea. Icarus, 189, 72-82.
Collins, G.C., McKinnon, W.B., Moore, J.M., Nimmo, F., Pappalardo, R.T., Prockter, L.M., Schenk, P.M., (2009). Tectonics of the outer planet satellites. Planetary Tectonics, Cambridge University Press.
Cooper, J. F., Johnson, R. E., Mauk, B. H., Garrett, H. B., Gehrels, N. (2001). Energetic Ion and Electron Irradiation of the Icy Galilean Satellites. Icarus, 149, 133-159.
Coustenis, A., Taylor, F.W. (2008). Titan: Exploring an Earth-like world. World Scientific
Publishing.
Coustenis, A., Tokano, T., Burger, M. H., Cassidy, T. A., Lopes, R. M. C., Lorenz, R. D., Retherford, K. D., Schubert, g. (2010). Atmospheric/Exospheric Characteristics of Icy Satellites. Space Science Reviews, 153, 155–184.
Coustenis, A., Raulin, P., Bampasidis, G., Solomonidou, A. (2011). Life in the Saturnian neighborhood, book chapter in Life on Earth and other planetary bodies, Springer Books, *Submitted for publication.*
Dalton, J. B. (2010). Spectroscopy of Icy Moon Surface Materials. Space Science Reviews, 153, 219–247.
Dalton, J. B., Cruikshank, D. P., Stephan, K., McCord, T. B., Coustenis, A., Carlson, R. W., Coradini, A. (2010). Chemical Composition of Icy Satellite Surfaces. Space Science Reviews, 153, 113–154.
Dougherty, M.K., Khurana, K.K., Neubauer, F.M., Russell, C.T., Saur, J., Leisner, J.S., Burton, M.E. (2006). Identification of a Dynamic Atmosphere at Enceladus with the Cassini Magnetometer. Science, 311, 1406 - 1409.
Fanale, F. P., Li, Y.-H., De Carlo, E., Farley, C., Sharma, S. K., Horton, K., Granahan, J. C. (2001). An experimental estimate of Europa's ``ocean" composition-independent of Galileo orbital remote sensing. Journal of Geophysical Research, 106, 14595-14600.
Figueredo, P. H., Greeley, R. (2004). Geologic mapping of the northern leading hemisphere of Europa from Galileo solid-state imaging data. Journal of Geophysical Research, 105, 22629-22646.
Fortes, A.D. (2000). Exobiological Implications of a Possible Ammonia-Water Ocean inside Titan, Icarus, 146, 444-452.

Fortes, A.D., Grindrod, P.M., Trickett, S.K., Voc˘adlo, L. (2007). Ammonium sulfate on Titan: Possible origin and role in cryovolcanism. Icarus, 188, 139–153.
Fortes, A. D., Choukroun, M. (2010). Phase Behaviour of Ices and Hydrates. Space Science Reviews, 153, 185–218.
Geissler, P. E., and 14 colleagues. (1998). Evidence for non-synchronous rotation of Europa. Nature, 391, 368.
Greenberg, R., (2005). Europa: The Ocean Moon: Search for an Alien Biosphere, Springer Praxis Books.
Greenberg, R. (2008). Unmasking Europa In: The Search for Life on Jupiter's Ocean Moon. Springer.
Hall. D. T., Feldman, P. D., McGrath, M. A., Strobel, D. F. (1998). The Far-Ultraviolet Oxygen Airglow of Europa and Ganymede. Astrophysical Journal, 499, 475.
Harland, David M. (2000). Jupiter Odyssey: The Story of NASA's Galileo Mission. Springer.
Hauk, S. A., Aurnou, J. M., Dombard, A. J. (2006). Sulfur's impact on core evolution and magnetic field generation on Ganymede. Jour. Geophys. Res., 111, E09008.
Head, J. W., and 10 colleagues. (2002). Evidence for Europa-like tectonic resurfacing styles on Ganymede. Geophysical Research Letters, 29, 2151.
Hussmann, H., Choblet, G., Lainey, V., Matson, D. L., Sotin, C., Tobie, g., Van Hoolst, T. (2010). Implications of Rotation, Orbital States, Energy Sources, and Heat Transport for Internal Processes in Icy Satellites. Space Science Reviews, 153, 317–348.
Johnson, T.V., (2004). Geology of the icy satellites. Space Science Reviews 116, 401-420.
Khurana, K. K., Kivelson, M. G., Russel, C. T. (1998). Induced magnetic fields as evidence for subsurface oceans in Europa and Callisto. Nature, 395, 777 780.
Kivelson, M.G., Khurana, K. K., Russell, C. T., Volwerk, M., Walker, R. J., Zimmer, C. (2000). Galileo Magnetometer Measurements: A Stronger Case for a Subsurface Ocean at Europa. Science, 289, 1340–1343.
Kivelson, M.G., Khurana, K. K., Coroniti, F.V. (2002). The Permanent and Inductive Magnetic Moments of Ganymede. Icarus, 157, 507–522.
Kuskov, O. L., Kronrod, V. A. (1998). Models of Internal Structure of Jupiter Satellites: Ganymede, Europa, and Callisto. Astron. Vestn., 32, 49–57.
Lammer, H., Bredehöft, J. H., Coustenis, A., Khodachenko, M. L., Kaltenegger, L., Grasset, O., Prieur, D., Raulin, F., Ehrenfreund, P., Yamauchi, M. (2009). What makes a planet habitable? The Astronomy and Astrophysics Review, 17, 181-24.
Lopes, R.M.C., and 18 colleagues. (2010). Distribution and interplay of geologic processes on Titan from Cassini radar data. Icarus, 205, 540-558.
Lorenz, R.D., Stiles, B.W., Kirk, R.L., Allison, M.D., Persi del Malmo, P., Iess, L., Lunine, J.I., Ostro, S.J., Hensley, S. (2008). Titan's Rotation Reveals an Internal Ocean and Changing Zonal Winds. Science, 319, 1649 - 1651.
Marion, G. M., Fritsen, C. H., Eicken, H., Payne, M. C. (2003). The Search for Life on Europa: Limiting Environmental Factors, Potential Habitats, and Earth Analogues. Astrobiology, 3, 785-811.
McCord, T. B., and 11 colleagues. (1998). Salts on Europa's Surface Detected by Galileo's Near Infrared Mapping Spectrometer. Science, 280, 1242-1245.
McCord, T. B., and 12 colleagues. (1998). Non-water-ice constituents in the surface material of the icy Galilean satellites from the Galileo near-infrared mapping spectrometer investigation. Journal of Geophysical Research, 103, 8603-8626.
McCord, T. B., Hansen, G. B., Hibbits, C. A. (2001). Hydrated salt minerals on Ganymede's surface: Evidence of an ocean below. Science, 292, 1523-1525.
McFadden, L., Weissman, P., Johnson, T. V. (2007). The Encyclopedia of the Solar System. Elsevier, 432.
McKay, C. P., Smith, H. D. (2005), Icarus, 178, 274–276.
McKay, C.P., Porco, C., Altheide, T., Davis, W.L. and Kral, T.A. (2008). The Possible Origin and Persistence of Life on Enceladus and Detection of Biomarkers in the Plume, Astrobiology, 8, 909-919.
McKinnon, W.B. (1999). Convective instability in Europa's floating ice shell. Geophys. Res. Lett. 26, 951–954.
Mitri, G., Showman, A.P., (2008). Thermal convection in ice-I shells of Titan and Enceladus.
Icarus, 193, 387-396.
Mitri, G., Bland, M.T., Showman, A.P., Radebaugh, J., Stiles, B., Lopes, R.M.C., Lunine, J.I., Pappalardo, R.T. (2010). Mountains on Titan: Modeling and observations. J. Geophys. Res., 115, E10002.
Moore, W. B., Schubert, G., Tackley, P. (1998). Three-Dimensional Simulations of Plume-Lithosphere Interaction at the Hawaiian Swell. Science, 279, 1008-1011.
Moore, W. B., Schubert, G. (2000). The tidal response of Europa. Icarus, 147, 317-319.
Moore, J. M., Howard, A. D., Schenk, P., Wood, S. E. (2010). Erosion, Transportation, and Deposition on Outer Solar System Satellites: Landform Evolution Modeling Studies. American Geophysical Union, P31D-04.
Nelson, R. M., and 32 colleagues. (2009a). Photometric changes on Saturn's Titan: evidence for active cryovolcanism, Geophysical Research Letters, 36, L04202.
Nelson, R. M., and 28 colleagues. (2009b). Saturn's Titan: Surface change, ammonia, and implications for atmospheric and tectonic activity, Icarus, 199, 429-441.
Nimmo, F., Bills, B.G. (2010). Shell thickness variations and the long-wavelength topography
of Titan. Icarus, 208, 896–904.
Muyzer, G. and Stams, A.J.M. (2008) The ecology and biotechnology of sulphate-reducing bacteria, Nature Reviews. Microbiology, 6, 441-454.
O'Brien, D. P., Geissler, P., Greenberg, R. (2002). A Melt-through Model for Chaos Formation on Europa. Icarus, 156, 152-161.
Pappalardo, and 10 colleagues. (1998a). Geological evidence for solid-state convection in Europa's ice shell. Nature, 391, 365-368.
Pappalardo, R.T., and 14 colleagues. (1998b). Grooved Terrain on Ganymede: First Results from Galileo High-Resolution Imaging. Icarus, 135, 276-302.
Pappalardo, R.T., Collins, g. C., Head, J. W., Helfenstein, P., McCord, T. B., Moore, J. M., Prockter, L. M., Schenk, P. M., Spencer, J. (2004) Geology of Ganymede. In Jupiter: The Planet, Satellites & Magnetosphere, pp. 363-396.
Park, R.G. (1997). Foundations of Structural Geology. Routledge, pp. 216.
Patterson, G. W., Collins, G. C., Head, J. W., Pappalardo, R. T., Prockter, L. M., Lucchitta, B. K., Kaym J. P. (2010). Global geological mapping of Ganymede. Icarus, 207, 845-867.
Porco, C.C., and 35 colleagues. (2005). Imaging of Titan from the Cassini spacecraft, Nature, 434, 159-168.
Porco, C.C., and 24 colleagues. (2006). Cassini observes the active south pole of Enceladus. Science, 311, 1393–1401.
Porco, C. (2008). The restless world of Enceladus. Scientific American, 299, 26–35.
Postberg, F., Kempf, S., Schmidt, J., Brillantov, N., Beinsen, A., Abel, B., Buck, U., Srama, R. (2009). Sodium salts in E Ring ice grains from an ocean below Enceladus' surface. Nature, 459, 1098-1101.
Prockter, L. M., and 14 colleagues. (1998). Dark Terrain on Ganymede: Geological Mapping and Interpretation of Galileo Regio at High Resolution. Icarus, 135, 317-344.

Prockter, L. M., Lopes, R. M. C., Giese, b., Jaumann, R., Lorenz, R. D., Pappalardo, R. T., Patterson, G. W., Thomas, P. C., Turtle, E. P., Wagner, R. J. (2010). Characteristics of Icy Surfaces. Space Science Reviews, 153, 63–111.
Radebaugh, J., Lorenz, R.D., Kirk, R.L., Lunine, J.I., Stofan, E.R., Lopes, R.M.C., Wall, S.D., the Cassini Radar Team, (2007). Mountains on Titan observed by Cassini Radar. Icarus 192, 77-91.
Raulin, F. (2008). Astrobiology and habitability of Titan. Space Science Reviews, 135, 37-48.
Raulin, F., Hand, K. P., McKay, C. P., Viso, M. (2010). Exobiology and Planetary Protection of icy moons. Space Science Reviews, 153, 511–535.
Ruiz, J., Fairen, A. G. (1999). Seas under ice: Stability of liquid-water oceans within icy worlds. In Earth, Moon, and Planets, 97, 79-90.
Schenk, P., McKinnon, W. (1989). Fault offsets and lateral crustal movement on Europa: Evidence for a mobile ice shell, Icarus, 79, 75-100.
Schenk, P. M., Chapman, C. R., Zahnle, K., Moore, J. M. (2004) Chapter 18: Ages and Interiors: the Cratering Record of the Galilean Satellites In Jupiter: The Planet, Satellites and Magnetosphere, Cambridge University Press.
Schilling, N., Neubauer, F., Saur, J. (2007). Time varying interaction of Europa with the Jovian magnetosphere: Constraints on the conductivity of Europa's subsurface ocean. Icarus, 192, 41–55.
Schubert, G., Anderson, J.D., Spohn, T., McKinnon, W.B. (2004) Interior composition, structure and dynamics of the Galilean satellites. In: Jupiter. The planet, satellites and magnetosphere. Cambridge planetary science 1, pp. 281-306.
Schubert, G., Anderson, J.D., Travis, B.J., and Palguta, J. (2007). Enceladus: Present internal
structure and differentiation by early and long-term radiogenic heating. Icarus, 188, 345–355.
Schubert, G., Hussmann, H., Lainey, V., Matson, D. L., McKinnon, W. B., Sohl, F., Sotin, C., Tobie, G., Turrini, D., Van Hoolst, T. (2010). Evolution of Icy Satellites. Space Science Reviews, 153, 447-484.
Shematovich, V. I., Johnson, R. E. (2001). Near-surface oxygen atmosphere at Europa. Advances in Space Research, 27, 1881-1888.
Showman, A. P., Malhotra, R. (1997). Tidal Evolution into the Laplace Resonance and the Resurfacing of Ganymede. Icarus, 127, 93-111.
Showman, A. P., Malhotra, R. (1999). The Galilean Satellites. Science, 286, 77-84.
Showman, A. P., Han, L. (2004). Numerical simulations of convection in Europa's ice shell: Implications for surface features. J. Geophys. Res. 109.
Soderblom, L.A., and 18 colleagues. (2007). Topography and geomorphology of the Huygens landing site on Titan. Planetary and Space Science, 55, 2015-2024.
Sohl, F., Spohn, T., Breuer, D., Nagel, K. (2002). Implications from Galileo Observations on the Interior Structure and Chemistry of the Galilean Satellites. Icarus, 157, 104–119.
Sohl, F., Choukroun, M., Kargel, J., Kimura, J., Pappalardo, R., Vance, S., Zolotov, M. (2010). Subsurface Water Oceans on Icy Satellites: Chemical Composition and Exchange Processes. Space Science Reviews, 153, 485–510.
Solomatov, V.S. (1995). Scaling of temperature- and stress-dependent viscosity convection. Phys. Fluids, 7, 266–274.
Solomonidou, A., Bampasidis, g., Coustenis, A., Kyriakopoulos, K., Seymour, K. S., Hirtzig, M., Bratsolis, E., Moussas, X. (2010). Morphotectonics on Titan and Enceladus. Planetary and Space Sciences, *submitted.*
Sotin, C., Head, J. W., Tobie, G. (2001). Europa: Tidal heating of upwelling thermal plumes and the origin of lenticulae and chaos melting. Geophys. Res. Lett., 29, 74-1.
Spaun, N. A., Head, J. W., Collins, G. C., Prockter, L. M., Pappalardo R. T. (1998), Conamara Chaos Region, Europa: Reconstruction of mobile polygonal ice blocks, Geophys. Res. Lett., 25, 4277–4280.
Stern, S.A.,McKinnon, W.B., (1999). Triton's surface age and impactor population revisited (evidence for an internal ocean). In: Proc. Lunar Planet. Sci. Conf. 30th. Abstract 1766.
Stiles, B. W., and 14 colleagues. (2010). ERRATUM: "Determining Titan's Spin State from Cassini Radar Images". The Astronomical Journal, 139, 311.
Stoker, C. R., Boston, P. J., Mancinelli, R. L., Segal, W., Khare, B. N., Sagan, C. (1990). Icarus, 85, 241–256.
Tobie, G., Grasset, O., Lunine, J.I., Mocquet, A., and Sotin, C. (2005). Titan's internal structure inferred from a coupled thermal-orbital model. Icarus, 175, 496-502.
Tobie, G., Lunine, J.I., Sotin C. (2006). Episodic outgassing as the origin of atmospheric methane on Titan. Nature, 440, 61-64.
Tobie, G., and 10 colleagues. (2010). Surface, Subsurface and Atmosphere Exchanges on the Satellites of the Outer Solar System. Space Science Reviews, 153, 375–410.
Trinks, H., Schröder, W., Biebricher, C. (2005). Ice And The Origin Of Life, Origins of Life and Evolution of Biospheres, 35, 429-445.
Tyler, R. H. (2008). Strong ocean tidal flow and heating on moons of the outer planets. Nature, 456, 770–772.
Waite, J. H., and 13 colleagues. (2006). Cassini Ion and Neutral Mass Spectrometer: Enceladus Plume Composition and Structure. Science, 311, 1419-1422.
Zahnle, K., Dones, L. (1998). Cratering Rates on the Galilean Satellites. Icarus, 136, 202-222.
Zimmer, C., Khurana, K. K., Kivelson, M. G. (2000). Subsurface Oceans on Europa and Callisto: Constraints from Galileo Magnetometer Observations. Icarus, 147, 329-347.

Appendix F1

Kronos: exploring the depths of Saturn with probes and remote sensing through an international mission

Journal article published in *Experimental Astronomy* (2009),
Volume 23, pp. 947-976 and 977-980.

Exp Astron (2009) 23:947–976
DOI 10.1007/s10686-008-9094-9

ORIGINAL ARTICLE

Kronos: exploring the depths of Saturn with probes and remote sensing through an international mission

B. Marty · T. Guillot · A. Coustenis · the Kronos consortium · N. Achilleos · Y. Alibert · S. Asmar · D. Atkinson · S. Atreya · G. Babasides · K. Baines · T. Balint · D. Banfield · S. Barber · B. Bézard · G. L. Bjoraker · M. Blanc · S. Bolton · N. Chanover · S. Charnoz · E. Chassefière · J. E. Colwell · E. Deangelis · M. Dougherty · P. Drossart · F. M. Flasar · T. Fouchet · R. Frampton · I. Franchi · D. Gautier · L. Gurvits · R. Hueso · B. Kazeminejad · T. Krimigis · A. Jambon · G. Jones · Y. Langevin · M. Leese · E. Lellouch · J. Lunine · A. Milillo · P. Mahaffy · B. Mauk · A. Morse · M. Moreira · X. Moussas · C. Murray · I. Mueller-Wodarg · T. C. Owen · S. Pogrebenko · R. Prangé · P. Read · A. Sanchez-Lavega · P. Sarda · D. Stam · G. Tinetti · P. Zarka · J. Zarnecki

Received: 7 December 2007 / Accepted: 2 April 2008 / Published online: 13 May 2008

Abstract *Kronos* is a mission aimed to measure in situ the chemical and isotopic compositions of the Saturnian atmosphere with two probes and also by remote sensing, in order to understand the origin, formation, and evolution of giant planets in general, including extrasolar planets. The abundances of noble gases, hydrogen,

B. Marty (✉)
CRPG, Nancy-Université, CNRS, BP 20, 54501 Vandoeuvre, Cedex, France
e-mail: bmarty@crpg.cnrs-nancy.fr

T. Guillot
Observatoire de la Côte d'Azur, BP 4229, 06304 Nice Cedex 04, France
e-mail: guillot@obs-nice.fr

A. Coustenis · B. Bézard · P. Drossart · T. Fouchet · D. Gautier · E. Lellouch · R. Prangé · P. Zarka
Laboratoire d'Etudes Spatiales et d'Instrumentation en Astrophysique (LESIA),
Observatoire de Paris-Meudon, 5, place Jules Janssen, 92195 Meudon Cedex, France

A. Coustenis
e-mail: Athena.Coustenis@obspm.fr

carbon, nitrogen, oxygen, sulfur and their compounds, as well as of the D/H, $^{4}He/^{3}He$, $^{22}Ne/^{21}Ne/^{20}Ne$, $^{36}Ar/^{38}Ar$, $^{13}C/^{12}C$, $^{15}N/^{14}N$, $^{18}O/(^{17}O)/^{16}O$, $^{136}Xe/^{134}Xe/^{132}Xe/^{130}Xe/^{129}Xe$ isotopic ratios will be measured by mass spectrometry on two probes entering the atmosphere of Saturn at two different locations near mid-latitudes, down to a pressure of 10 Bar. The global composition of Saturn will be investigated through these measurements, together with microwave radiometry determination of H_2O and NH_3 and their 3D variations. The dynamics of Saturn's atmosphere will be investigated from: (1) measurements of pressure, temperature, vertical distribution of clouds and wind speed along the probes' descent trajectories, and (2) determination of deep winds, differential rotation and convection with combined probe, gravity and radiometric measurements. Besides these primary goals, Kronos will also measure the intensities and characteristics of Saturn's

N. Achilleos
Atmospheric Physics Laboratory, Department of Physics and Astronomy, University College London, Gower Street, London WC1E 6BT, UK

Y. Alibert
Inst Phys, University of Bern, CH-3012 Bern, Switzerland

S. Asmar
Jet Propulsion Laboratory, Pasadena, CA 91109, USA

D. Atkinson
Department of Electrical and Computer Engineering, University of Idaho, Moscow, ID 83844-1023, USA

S. Atreya
Department of Atmosphere Ocean and Space Science, University of Michigan, Ann Arbor, MI 48109, USA

G. Babasides · X. Moussas
Space Group, Laboratory of Astrophysics, Faculty of Physics, National and Kapodistrian University of Athens, Panepistimiopolis, 15783 Zographos, Athens, Greece

K. Baines · T. Balint
Jet Propulsion Laboratory, 4800 Oak Grove Blvd, Paadena, CA 91109-8099, USA

D. Banfield
Department of Astronomy, Cornell University, Ithaca, NY 14853, USA

S. Barber · I. Franchi · M. Leese · A. Morse · J. Zarnecki
Open University, Walton Hall, Milton Keynes MK7 6AA, UK

G. L. Bjoraker · F. M. Flasar · P. Mahaffy
NASA, Goddard Space Flight Ctr Code 693, Greenbelt, MD 20771, USA

M. Blanc
Centre d'Etudes Spatiales des Rayonnements (CESR), Toulouse, France

S. Bolton
Southwest Research Institute, San Antonio, TX, USA

N. Chanover
New Mexico State University, Las Cruces, NM 88003, USA

magnetic field inside the D ring as well as Saturn's gravitational field, in order to constrain the abundance of heavy elements in Saturn's interior and in its central core. Depending on the preferred architecture (flyby versus orbiter), Kronos will be in a position to measure the properties of Saturn's innermost magnetosphere and to investigate the ring structure in order to understand how these tiny structures could have formed and survived up to the present times.

Keywords Saturn · Atmosphere · Probes · Cosmic vision

S. Charnoz
AIM, Université Paris 7/CEA/CNRS, 91191 Gif sur Yvette, France

E. Chassefière
Service d'Aéronomie du CNRS/IPSL, 91371 Verrières-le-Buisson, France

J. E. Colwell
Department of Physics, University Cent Florida, Orlando, FL 32816, USA

E. Deangelis · A. Milillo
NAF/Instituto di Fisica dello Spazio Interplanetario, via del Fosso del Cavaliere 100, 00133, Rome, Italy

M. Dougherty
Imperial College London, South Kensington Campus, London SW7 2AZ, UK

I. Mueller-Wodarg
Imperial College Sci Technol and Med, Space and Atmosphere Phs grp, University of London, London SW7 2BW, UK

R. Frampton
Boeing NASA Systems, MC H012-C349, 5301 Bolsa Ave, Huntington Beach, CA 92647-2099, USA

L. Gurvits · S. Pogrebenko
Joint Institute for VLBI in Europe, P.O. Box 2, 7990 AA Dwingeloo, The Netherlands

R. Hueso · A. Sanchez-Lavega
Departamento de Fisica Aplicada I, E.T.S. Ingenieros, Universidad del Pais Vasco, Alameda Urquijo s/n, 48013 Bilbao, Spain

B. Kazeminejad
Deutsches Zentrum für Luft-und Raumfahrt (DLR), German Space Operations Center (GSOC), 82234 Wessling, Germany

T. Krimigis · B. Mauk
Appl Phys Lab, Johns Hopkins University, Laurel, MD 20723, USA

A. Jambon
MAGIE UMR 7047, Université Pierre et Marie Curie, 4 place Jussieu, 75252 Paris Cedex 05, France

G. Jones
Max Plank Inst. Gravitat Phys, Albert Einstein Inst, Katlenburg-Lindau, Germany

Y. Langevin
Institut d'Astrophysique Spatiale Bat. 121, 91405 Orsay Campus, France

J. Lunine
Department of Planetary Science, University of Arizona, Tucson, AZ 85721, USA

1 Introduction

Giant planets are mostly made of the gas that was present in the protosolar disk before the terrestrial planets accreted (Fig. 1). Their comparative study is thus essential to understand planet formation in general and the origin of the Solar System. Saturn in particular appears to be a natural target for near-future exploration, after the fine characterization of Jupiter by Galileo and Juno and before future ambitious missions to Uranus and Neptune. Saturn, the ring planet, is mysterious in many aspects, and plays a key role to understanding planet formation, the evolution of solar and extrasolar giant planets, planetary meteorology, magnetospheric interactions, dynamo generation and the physics of planetary rings.

Saturn, like Jupiter, has an atmosphere that appears to be enriched in elements other than hydrogen and helium with respect to the solar composition. This enrichment may be the result of planetary precursors formed at low temperatures, or of a progressive enrichment of the protosolar disk, with profound consequences for understanding the formation of the Solar System. The different formation scenarios that result can be disentangled by a study of the atmospheric composition of Saturn in noble gases and major volatile (H, C, N, S, O) elemental and isotopic compositions, which requires in situ measurements Table 1.

Noble gases are particularly relevant in this study, because: (1) they are chemically inert and their abundances are determined by physical processes such as phase partitioning, and (2) their isotopic compositions present large-scale inhomogeneities between the original protosolar nebula composition and sub-reservoirs of the solar system that make them isotopic tracers as well. Indeed, analyses of meteorites point to the existence of a primordial reservoir of volatiles

M. Moreira
Laboratoire de Géochimie et Cosmochimie (UMR 7579 CNRS), Institut de Physique du Globe de Paris, Université Paris, 7, 4 place Jussieu, 75252 Paris cedex 05, France

C. Murray
Queen Mary & Westfield College, University of London, London E1 4NS, UK

T. C. Owen
Institute of Astronomy, University of Hawaii, Honolulu, HI 96822, USA

P. Read
Clarendon Laboratory, University of Oxford, Oxford OX1 3PU, UK

P. Sarda
Groupe géochimie des Gaz Rares, Département des Sciences de la Terre, Université Paris Sud, UMR CNRS 8148 (IDES), 81405 Orsay Cedex, France

D. Stam
Astronomical Institute "Anton Pannekoek" Kruislaan 403, 1098 SJ Amsterdam, The Netherlands

G. Tinetti
Institut d'Astrophysique de Paris, CNRS, Université Pierre et Marie Curie, 75014 Paris, France

Present address:
P. Sarda
Laboratoire de Sciences de la Terre, Ecole Normale Supérieure de Lyon cedex 07, France

1 Introduction

Giant planets are mostly made of the gas that was present in the protosolar disk before the terrestrial planets accreted (Fig. 1). Their comparative study is thus essential to understand planet formation in general and the origin of the Solar System. Saturn in particular appears to be a natural target for near-future exploration, after the fine characterization of Jupiter by Galileo and Juno and before future ambitious missions to Uranus and Neptune. Saturn, the ring planet, is mysterious in many aspects, and plays a key role to understanding planet formation, the evolution of solar and extrasolar giant planets, planetary meteorology, magnetospheric interactions, dynamo generation and the physics of planetary rings.

Saturn, like Jupiter, has an atmosphere that appears to be enriched in elements other than hydrogen and helium with respect to the solar composition. This enrichment may be the result of planetary precursors formed at low temperatures, or of a progressive enrichment of the protosolar disk, with profound consequences for understanding the formation of the Solar System. The different formation scenarios that result can be disentangled by a study of the atmospheric composition of Saturn in noble gases and major volatile (H, C, N, S, O) elemental and isotopic compositions, which requires in situ measurements Table 1.

Noble gases are particularly relevant in this study, because: (1) they are chemically inert and their abundances are determined by physical processes such as phase partitioning, and (2) their isotopic compositions present large-scale inhomogeneities between the original protosolar nebula composition and sub-reservoirs of the solar system that make them isotopic tracers as well. Indeed, analyses of meteorites point to the existence of a primordial reservoir of volatiles

M. Moreira
Laboratoire de Géochimie et Cosmochimie (UMR 7579 CNRS), Institut de Physique du Globe de Paris, Université Paris, 7, 4 place Jussieu, 75252 Paris cedex 05, France

C. Murray
Queen Mary & Westfield College, University of London, London E1 4NS, UK

T. C. Owen
Institute of Astronomy, University of Hawaii, Honolulu, HI 96822, USA

P. Read
Clarendon Laboratory, University of Oxford, Oxford OX1 3PU, UK

P. Sarda
Groupe géochimie des Gaz Rares, Département des Sciences de la Terre, Université Paris Sud, UMR CNRS 8148 (IDES), 81405 Orsay Cedex, France

D. Stam
Astronomical Institute "Anton Pannekoek" Kruislaan 403, 1098 SJ Amsterdam, The Netherlands

G. Tinetti
Institut d'Astrophysique de Paris, CNRS, Université Pierre et Marie Curie, 75014 Paris, France

Present address:
P. Sarda
Laboratoire de Sciences de la Terre, Ecole Normale Supérieure de Lyon cedex 07, France

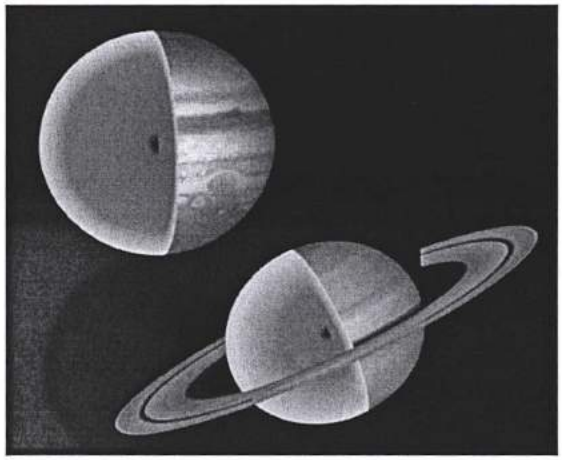

Fig. 1 Interiors of Jupiter and Saturn highlighting the importance of hydrogen and helium for the structure of these two planets (*yellow* indicates that hydrogen is in molecular form, *red* that it is metallic, and the central dense core is shown in *blue*)

with an isotopic composition different from that of the Sun. The discovery of this reservoir through its isotopic signature in Saturn's atmosphere would have a direct impact on the primordial history of the Solar System and on the study of meteorites and comets. Generally, the elemental and isotopic determinations of Saturn's atmospheric composition would permit to explore sources of matter and processes of formation for the giant planets.

Table 1 Composition measurements in Saturn's deep atmosphere and their consequences

Species	Consequence
He	Determine extent of helium sedimentation in Saturn's interior. Crucial for accurate understanding of the thermal evolutions of Saturn and Jupiter
Ne	Test prediction of Ne capture in He droplets. Refine H He phase separation diagram
CH_4	Fine determination crucial to understand the formation of the planet
NH_3 NH_4SH	Key to decide between models of planetesimal delivery and planet formation. Important for Saturn's meteorology
H_2S NH_4SH	Key for planetesimal delivery, with possibility that the abundance is linked to that of rocks deep inside. Important for Saturn's meteorology
H_2O	(by radiometry); Key to understand the planet's structure, formation, and meteorology
Ar, Kr, Xe	Key to decide between models of planetesimal delivery and planet formation. Link with the compositions of the Sun and protosolar disk
CO, PH_3, AsH_3, GeH_4	Disequilibrium species are important to understand convection in Saturn's deep atmosphere. Help to further test planetesimal delivery models
D/H	Test models that predict it should be similar to Jupiter and to the protosolar value
$^{12}C/^{13}C$	Test models that predict value similar to Earth
$^{14}N/^{15}N$	Important to understand whether N was delivered as N_2 or as NH_3. Test models of planetesimals delivery
$^{20}Ne/^{22}Ne$	Origin of gas, Test evaporation processes in the early solar system
$^{36}Ar/^{38}Ar$ Kr, Xe isotopes	Origin of gas, Test evaporation processes of these gases in planetesimals

Another means to better understand the formation of the Solar System is through a determination of the planet's core mass and global composition: we do not yet know whether Saturn possesses more or less heavy elements than Jupiter, and we do not know which planet has the largest core. This impacts directly on the formation models of these planets and of the Solar System as a whole.

Saturn is also fascinating for its intriguing meteorology. Contrary to Jupiter, whose rotation axis is almost perpendicular to its orbit, Saturn has an inclination of 20° (similar to that of the Earth), plus rings which lead to marked seasonal variations. Perhaps as a result of this, Saturn undergoes the most intense storms of the Solar System, with planet-wide events that can last for months. Its zonal wind pattern is similar to Jupiter, but appears to vary significantly, as shown by the mysterious slowing of Saturn's equatorial jet from 450 m/s in the Voyager era, down to 250 m/s at the arrival of the Cassini spacecraft. Two key elements are missing to model the causes of these variations: Saturn's deep water abundance as a powerful source of convective potential energy, and Saturn's deep rotation field.

Another surprising finding of the Cassini–Huygens mission has been the fact that Saturn's magnetic field is considerably modified by the rings, with two consequences: (1) our inability to measure the deep rotation rate in the magnetic dynamo region; (2) the impossibility to measure the planet's true magnetic field, but instead, a filtered, perfectly asymmetric field. A measurement of the planetary magnetic field inside the D ring would provide the data necessary to understand the planet's magnetic field generation and to analyze gravity data using proper constraints on the rotation rate.

The next section discusses the primary scientific goals that are driving the mission, namely the study of the origin of the Solar System and the study of planetary atmospheres, as well as the secondary goals which require a feasibility assessment, and finally the physics of magnetic fields and of planetary rings.

2 Science objectives

2.1 Planet formation and the origin of the solar system

Saturn and Jupiter formed 4.55 Ga ago, from the same disk of gas and solids that formed the Sun and eventually the entire Solar System (e.g., [1]). A significant fraction of their mass is composed of hydrogen and helium, the two lightest and most abundant elements in the Universe. Disks with hydrogen and helium are almost ubiquitous when stars appear, but these disks fade away rapidly, on timescales of only a few million years (e.g., [2]). This implies that Jupiter and Saturn had to form rapidly in order to capture their hydrogen and helium envelopes, more rapidly than e. g. terrestrial planets which took tens of millions of years to attain their present masses, and retained only negligible amounts of the primordial gases as part of their final composition. Thus by studying these giant planets, we have access to information on the composition and early evolution of the protosolar disk that led to the birth of the *entire* Solar System.

In spite of the recognition of the importance of such knowledge, data on the composition and structure of the giant planets, which hold more than 95% of the mass of the Solar System, excluding the Sun, remains scarce. The masses of

the central cores of Jupiter (0 to 15 $M_\oplus$ where $M_\oplus$ is the mass of the Earth) and of Saturn (8 to 26 $M_\oplus$), as well as the total masses of heavy elements (10 to 40 $M_\oplus$, and 20 to 30 $M_\oplus$, respectively) are poorly constrained [3]. Along the same lines, the abundance of oxygen, the third most abundant element in the Universe after H and He and a key element for planetary formation, is unknown in the well-mixed atmospheres of both Jupiter and Saturn [4]. Jupiter's composition was measured in situ by the Galileo probe in 1995 down to a pressure level of 22 Bar [5]. On Jupiter, the abundances of 8 major elements have been measured, while in contrast, on Saturn we only have reliable data for C, He, and model-dependant results on N and S (Fig. 2). The Galileo measurements at Jupiter include a highly precise determination of the planet's helium abundance, crucial for calculations of the structure and evolution of the planet.

Several key species (carbon, nitrogen, sulfur, argon, krypton and xenon), were found to be enriched in Jupiter's atmosphere compared to the solar composition mixture, which directly impacts theories on the formation of the Solar System. Figure 2 shows that planet formation models that attempt to reproduce the abundances measured in Jupiter yield very different results for Saturn, with key elements being oxygen (in the form of water) and the noble gases. Specifically a model based on direct adsorption on low-temperature planetesimals yields a high, uniform enrichment of all species other than H, He and Ne [5]. A model in which gases are trapped into crystalline ice as clathrates yields a very non-uniform enrichment of these species (e.g. [7, 8]). If the noble gases were not delivered

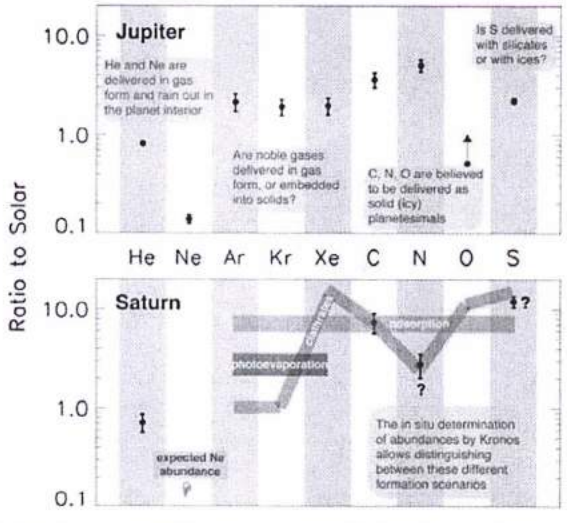

Fig. 2 Elemental abundances measured in the tropospheres of Jupiter (*top*) and Saturn (*bottom*) in units of their abundances in the protosolar nebula (from [6]). The elemental abundances for Jupiter are derived from the in situ measurements of the Galileo probe. The abundances for Saturn are spectroscopic determinations from Cassini for He/H and C/H, and model-dependant ground based measurements for N/H and S/H. Note that the retrieval of the helium abundance is indirect and uncertain, so that very precise He/H measurement is needed. Kronos will allow distinguishing between different formation scenarios whose predictions are shown as *green*, *blue* and *pink curves*, respectively (see text)

directly with the solids but as gas in a protosolar disk enriched in heavy elements by photoevaporation, one then expects enrichments in noble gases that are decoupled from other species and comparable to those found on Jupiter [3, 9]. The processes that formed the giant planets have implications for the other planets as well.

Kronos can therefore directly test scenarios of the formation of the solar system. In particular, Jupiter's nitrogen is highly depleted in ^{15}N by up to 40% compared to "planetary" N found in terrestrial planets and meteorites [10]. Together with measurements of lunar soils irradiated by the solar wind [11], this has led to the concept of an originally ^{15}N-depleted protosolar nebula gas, in which variable extents of ^{15}N-rich solid material were injected so as to yield the large range of N isotopic variations found among the solar system objects. Thus the $^{15}N/^{14}N$ ratio of the giant planetary atmospheres is expected to vary depending on the mixing ratio of solid and gaseous components that contributed to their formation, and a comparison between Jupiter and Saturn will yield information on the nature and strength of the contributing cosmochemical sources.

Noble gases are also excellent tracers for the origin and the evolution of major solar system reservoirs. Measurements of noble gas (Kr and Xe) isotopic ratios will also be of considerable importance for (1) assessing potential genetic relationship between solar system reservoirs and giant planet atmospheres, and (2) investigating possible atmospheric processes that might have fractionated atmospheric elements. For instance, cometary grains returned by the Stardust mission host a Ne component with an isotopic composition reminiscent of organic matter trapped in primitive meteorites rather than that of the solar nebula [12]. The measurement of the noble gas composition of the Saturn atmosphere is therefore requested to investigate the origin of Saturn atmospheric gases.

Other key measurements include the speciation and stable isotopic compositions of light elements (H, C, N, S) as well as trace gas species abundances (notably AsH_3, PH_3, GeH_4, CO). Last but not least, the very precise measurement of the helium and neon abundances will be the key to an understanding of the formation of helium droplets in the planet's interior and thus the evolution of Saturn and Jupiter (e.g., [13]).

Kronos will also allow us to obtain a measurement of Saturn's gravity field to be performed with unprecedented accuracy. Even from a single flyby of the carrier spacecraft, the close polar orbit and the use of both X and Ka bands guarantees improvements of several orders of magnitude compared to the measurements by Cassini–Huygens (Fig. 3). These accurate measurements will yield stringent constraints on the planetary interior structure. An important source of uncertainty for models is the unknown interior rotation of the planet. The determination of high order harmonics of the gravity field will allow a determination of whether Saturn's interior rotates as a solid body or not [14]. Additional constraints from the magnetic field measurements, radiometric measurements and similar observations at Jupiter with Juno will help precise the state of rotation of Saturn's interior. With further constraints on the helium and oxygen abundance measurements and on the basis of present models of Saturn's internal structure, we expect to determine the mass of the central core to within 10–20% accuracy, and to evaluate whether or not a layer of helium surrounds its core.

A combined analysis of in situ and remote Kronos measurements of Saturn's composition, global water abundance, high accuracy gravity and magnetic fields will

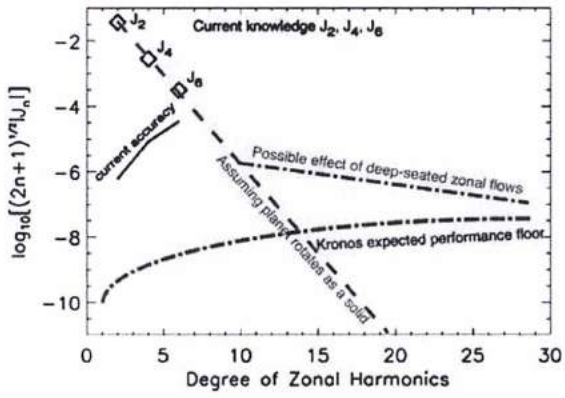

Fig. 3 A comparison of Saturn's currently measured gravitational moments to expected values depending on Saturn's deep rotation state (solid vs. deep-seated zonal flows), and Kronos expected performances based on Ka-band radio measurements during one or several polar fly-bys (based on similar calculations for Jupiter and the Juno spacecraft)

provide us with a detailed view of the planet's structure (Fig. 3). The comparison with similar measurements at Jupiter will yield a unique set of data that will permit us a global understanding of the evolution of the giant planets and their formation within the solar system. Within the next 20 years, we expect thousands of extrasolar planets to be characterized, but with only limited information (e.g. mean density, major atmospheric gases). The parallel study of Saturn and Jupiter enabled by Kronos is fundamental to understand giant planets both from a global statistical perspective, and in fine detail.

2.2 Meteorology and atmospheric dynamics

The dynamics and circulation of gaseous giant planetary atmospheres are important physical attributes for many disciplines, not only for planetary meteorology. Heat transport within the atmosphere and exchanges with the deep interior are crucial factors, affecting the long term evolution of the planet. Chemical transport/mixing within the atmosphere and interior are also of great importance to understand how the composition and structure of a giant planet has evolved since its formation. In addition, an understanding of the circulation, origin and maintenance of the jets, instabilities, waves and vortices in the atmospheres of all of the outer planets is of great interest for comparative planetary meteorology and oceanography. The belt-zone structure of zonal jets in the atmospheres of Jupiter and Saturn is especially relevant at the present time, in the light of the emerging discovery of apparently dynamically similar zonal structures in the Earth's oceans (e.g. [15] and new measurements of eddy momentum transports on Saturn from Cassini [Del Genio, 2007 #1686].

Up to the present time, cloud motion tracking from the Voyager 1 and 2 spacecraft in 1981, ground-based and Hubble Space Telescope since 1991 and the Cassini Orbiter since 2004, has been one of the main methods used to infer aspects of the general circulation of the planet (Fig. 4) [18 22]. A major and persistent problem is that the rotation period taken as a reference frame for the atmospheric motions is not fixed from radio-rotation measurements, and ranges between 10 hr 39 min 24 s and 10 hr 46 min [18, 23 25]. Recent measurements of Saturn's gravity field even

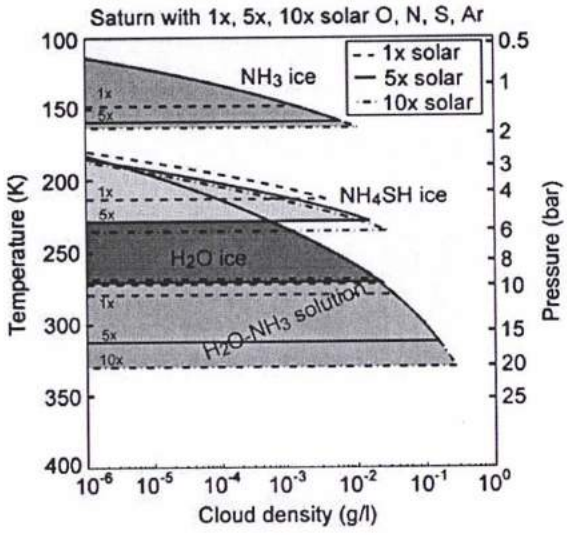

Fig. 4 Mean vertical distribution of cloud layers on Saturn, deduced from a simple thermochemical model [4, 16, 17]

suggest an interior rotation period as short as 10 hours 32 min [26]. As with Jupiter, Saturn's cloud-level meteorology may extend much deeper into its convective interior than the shallow 'weather layer' within which the observed patterns of wind and clouds may be observed from space. Observational constraints on such (deep) atmospheric dynamics are very difficult to obtain, not least because of some fundamental 'degeneracies' in the near-surface signatures of deep and shallow circulations i.e. very different processes (deep or shallow) may produce surface signatures that are more or less indistinguishable. A major objective of Kronos is therefore to obtain measurements (especially of Saturn's detailed gravity field; see Fig. 3) that can resolve some of these ambiguities and ascertain which aspects of Saturn's meteorology and circulation are deep-seated and which are shallow.

Images in the visual range by spacecraft have captured a plethora of meteorological phenomena immersed within the alternating pattern of zonal jets (Fig. 5), including: (1) cyclonic and anticyclonic eddies with closed circulations and sizes ranging from ~1,000 5,000 km [27, 28]. Particularly interesting is the strong cyclonic vortex found around the Southern Pole [18]. (2) Convective storms are relatively common at mid-latitudes [29, 30] and probably fuelled by "moist" ammonia and water vapour latent heat release [31]. A major event are the "Great White Spots" (GWS) that occur sporadically in Saturn (mainly at equatorial latitudes) attaining a size of 20,000 km before they spread zonally [32]. (3) Waves of different types have been detected at cloud level and in temperature maps. Most significant are those seen at cloud level on Saturn, as for example the mid-latitude northern "ribbon" that moves with a speed of 145 ms^{-1} [33] (Sromovsky et al. 1983), and the "hexagon" that surrounds the northern pole at 78° North [34] that appears to remain roughly stationary with respect to the planet rotation, at least as measured by the Voyager spacecraft.

This variety of meteorological phenomena are observed at clouds and hazes vertically distributed above the ammonia condensation level. The properties of the

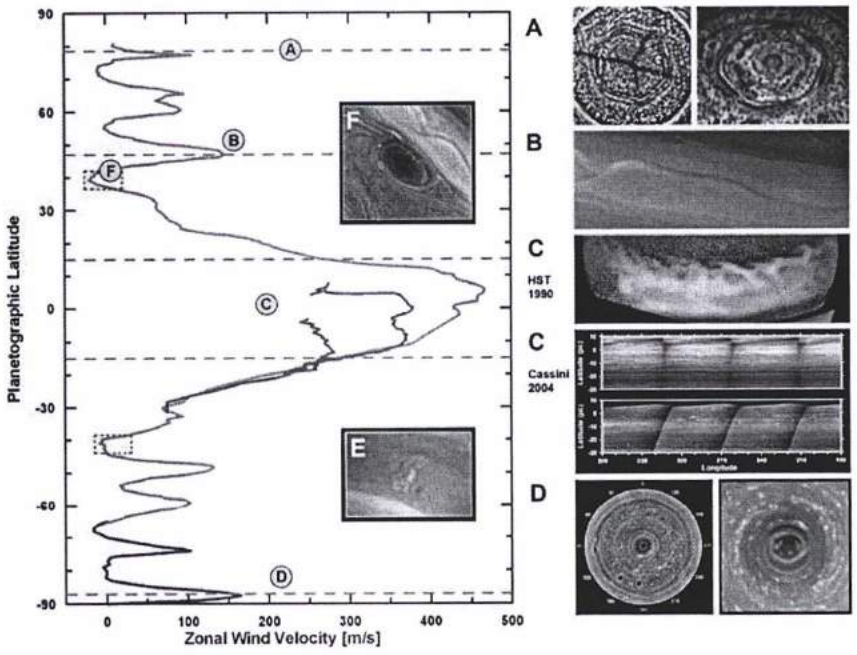

Fig. 5 General circulation of Saturn and relevant atmospheric features on its atmosphere. Winds at cloud level, relative to the interior reference frame measured by Voyager, traced by the Voyagers (*grey line*) and Cassini data of the Southernmost latitudes (*blue*) and equatorial region in different filters (*red* and *violet*). Relevant meteorological structures appear on the *insets*: a North polar hexagon in visible (Voyager 1) and infrared light (Cassini); b The Ribbon; c Saturn Great White Spot in the Equatorial Region in 1990 and the state of the equator as seen by Cassini in the methane absorption band and continuum filters; d The South Polar jet and the inner polar vortex; e Convective storms seen by Cassini; f Anticyclones from Voyager 1. The location of most convective storms appear marked with green dashed boxes

clouds and their temporal changes have been studied most recently by [35] and [36]. Related features are also seen at other levels from observations and retrievals of temperature and composition at infrared wavelengths [27]. The zonal jets are seen to extend into the stratosphere though decay with height [37]. Some eddy features are also evident at higher levels though some features such as Saturn's north polar hexagon seem to be confined to beneath the tropopause.

As with Jupiter, Saturn's cloud-level meteorology may extend much deeper into its convective interior than the shallow 'weather layer' within which the observed patterns of wind and clouds may be observed from space. Observational constraints on such (deep) atmospheric dynamics are very difficult to obtain, not least because of some fundamental 'degeneracies' in the near-surface signatures of deep and shallow circulations i.e. very different processes (deep or shallow) may produce surface signatures that are more or less indistinguishable. A major objective of Kronos is therefore to obtain measurements that can resolve some of these ambiguities and ascertain which aspects of Saturn's meteorology and circulation are deep-seated and which are shallow.

As a first step, Kronos will obtain the first detailed in situ measurements of the vertical structure of Saturn's atmospheric temperature, winds, radiative balance and cloud structure, to depths of up to 10 bar where direct solar heating is essentially negligible. The factors determining the atmospheric thermal and density structure in the outer planets depend on a complex mix of radiative heating and cooling, turbulent convection (both 'moist' and 'dry') and larger scale circulation systems. The distribution of radiative heating in the upper troposphere is affected strongly by the presence of clouds and hazes, whose distribution is itself determined by the ambient circulation, and the concentration of various volatiles. Figure 5 shows a much simplified 'typical' vertical distribution of clouds, modeled by assuming a particular composition at depth and adiabatic uplift until different components become saturated and begin to condense. Such a distribution may reflect a global mean picture, but observations indicate considerable local variability.

Seasonal effects are also much stronger on Saturn than on Jupiter, and have a major impact on thermal structure in the stratosphere and upper troposphere. While Kronos will not monitor such effects directly, they will influence the state of the atmosphere at the time of its encounter with Saturn, and will provide information by comparison with earlier missions (such as Cassini). The nature and distribution of convection in Saturn's atmosphere is a major objective of the Kronos mission. It is now widely thought that convection, modified by the latent heat effects of water condensation and consequent changes in molecular weight, is a critical component of the tropospheric circulation of both the gas giant planets [38].

Moist convection is highly intermittent and leads to massive storm cells ~1000 km wide which carry water and other material vertically over ~3 scale heights (~75 km) into the upper troposphere. In ways that are still not fully understood, moist convection works rather differently from terrestrial storms, due to the very low mean molecular weight of the atmosphere. As on Jupiter [39], lightning may also accompany vigorous convection at times, though detection at Saturn in association with particular convective events has been more elusive [30].

The horizontal distribution of convection is also highly variable. Figure 6 shows a Cassini VIMS image of Saturn at 5 μm which reflects the distribution of clouds and convection at 2–4 bar. This indicates that convection (both dry and moist) is organized by the winds in the deep troposphere into zonal bands on a finer scale than at the top of the troposphere. This drastic change, evident in the meteorology between the visible face of Saturn and its expression at just 5 bar, is indicative of the changes in the driving forces as one delves deeper into Saturn. We expect that by directly sampling the internal structure down to 10 bar, below most of the direct radiative heating/cooling of the atmosphere, we will have a more direct picture of the processes controlling the dynamics in Saturn's atmosphere driven from deep inside the planet rather than from solar input/radiative cooling.

The primary goals of the meteorology and atmospheric dynamics investigation on Kronos will be to determine the nature of the deep circulation, differential rotation and convection in Saturn's atmosphere by combining observations from the Kronos probes with remote sensing measurements from the carrier spacecraft. For the probes, this will require in situ determination of vertical profiles of temperature, horizontal winds and cloud properties (aerosol particle densities, size distributions and composition, including possible chromophores) throughout the troposphere to a

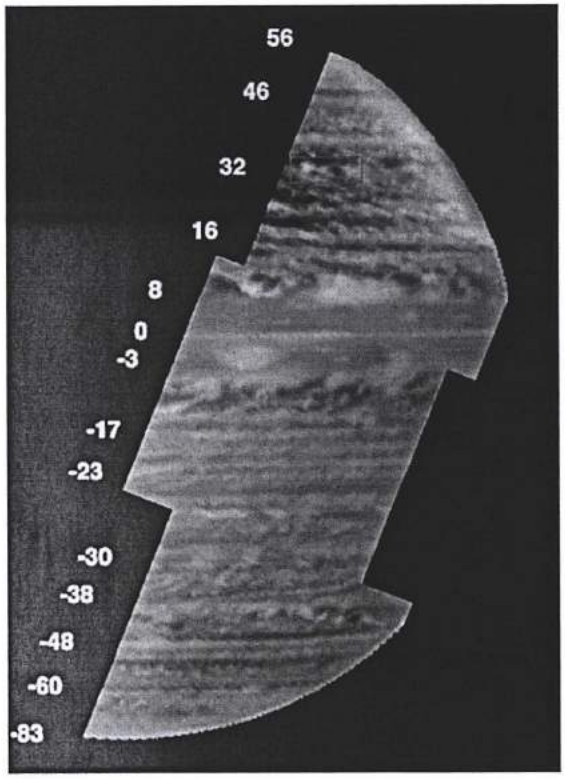

Fig. 6 Cassini VIMS image of Saturn at a wavelength of 5 μm [40, 41], showing cloud features and zonally banded structures at around 2 4 Bar. Here, the thermal image has been photometrically inverted to show high-opacity clouds as *white* and clearings in the deep cloud structure as *black*. This image mosaic reveals that, at depth, Saturn is an active, dynamic planet. *Bulky clouds near the equator* are likely convective in nature. At depth in mid and high latitudes Saturn exhibits a dense structure of alternating bands of clouds and clearings

pressure of up to 10 bar, at two dynamically distinct locations on Saturn. The profile of the water abundance will also be measured in order to constrain its role in moist convection processes. For the carrier, these goals will require measurements of temperature, deep cloud distributions, ammonia and water abundance distributions and deep winds, using a combination of near infrared and microwave radiometry, and gravity field measurements from a close periapsis pass.

2.3 Magnetic dynamo, magnetosphere and radiation environment

Like Jupiter, Saturn has a largely rotation-dominated planetary magnetosphere. But like Earth, solar wind convection and radial transport play major roles [42]. Understanding Saturn's magnetosphere (Fig. 7) will provide the "missing link" between the Jovian magnetosphere (then explored in-depth by Juno) and the Earth's magnetosphere (explored by many satellites).

The Kronos mission has the potential to resolve major open issues about Saturn's magnetic field, magnetic dynamo and internal rotation, its polar magnetosphere and radiation environment, and their couplings with the planet itself. Beyond planetology, redistribution of angular momentum via magnetic fields in astrophysical

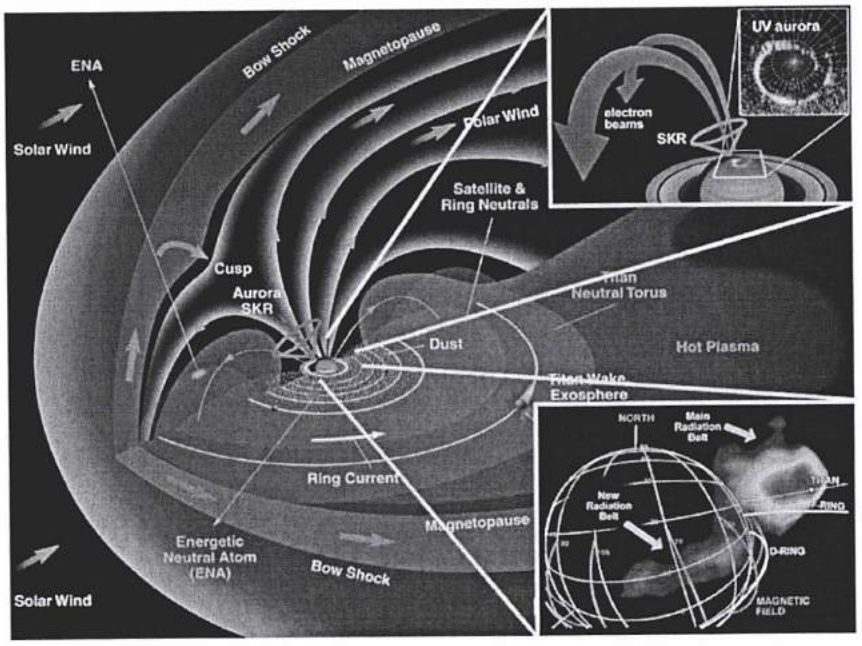

Fig. 7 *Saturn's magnetospheric regions and processes. Bottom inset* new radiation belt observed in ENA, *top inset* electron beams observed by Cassini and mapped to the aurora along field lines; auroral image by HST; orange cone sketches auroral (SKR) radio emissions

plasmas is a central question. Saturn's unique characteristics (neutral gas-dominated, dust-rich magnetosphere) make it an ideal model better than Jupiter for astrophysical situations such as the early phases of proto-star formation.

While all other magnetized planets in the Solar system have magnetic dipole axes tilted at an angle of 10° or more with respect to their rotation axes, Saturn's global magnetic field is almost perfectly axisymetric (angle of dipole tilt $\leq 0.7°$) [43], although a high-latitude 'anomaly' has been tentatively deduced from Saturn Kilometric Radiation (SKR) measurements [44]. Classical fluid dynamo theory [45] does not allow to maintain a field with perfect rotational symmetry, but new models do allow for the dipole tilt to be as small as 0.5°. Saturn's dynamo is thought to be produced by liquid 'metallic' hydrogen in its outer core, combined with strong convective motions and the rapid rotation of the planet itself (e.g. [46]). Accurate global field mapping is thus a key to both the composition and conductivity of Saturn's interior.

The Cassini spacecraft has already provided magnetometer measurements over several tens of close passes within $5R_S$ (average = $3.4R_S$) from Saturn's centre (R_{SS} = Saturn radius = 60,330 km). In addition the spacecraft made a closest approach at 1.33 R_S at the Saturn orbit insertion (SOI). Fluxgate magnetometer measurements near SOI suggested a possibly less symmetrical internal field within the radius of Saturn's D ring (1.11 R_S), as compared to the field model built from the more-distant periapses. Analysis is on-going, however further multiple passes and

high-resolution scalar magnetometry at these very small distances—which are beyond the scope of Cassini's trajectory—are required to improve our knowledge of higher-order components or 'multipoles' of Saturn's field.

Another unique aspect of Saturn's magnetospheric field is related to the drifting rotational signatures of the azimuthal field and SKR. A mission such as Kronos, especially with an orbiter element, is expected to provide additional close-range (<1.3 R_S) magnetic data for Saturn, of great value for addressing the origin and nature of its 'rotational anomaly', and characterize the internal (Enceladus ?) [47] or external (solar wind ?) [25] control of the period variability, in order to determine Saturn's true internal rotation rate.

At Jupiter, the most dramatic signature of the planet-magnetosphere coupling and dynamics is the aurora (best observed in the UV), including the near polar signatures of the satellites-magnetosphere interaction. This coupling involves electric currents flowing along field lines, energetic particle acceleration, and associated plasma waves and radio waves. The latter permit remote sensing of the coupling variability as well as insights to the microphysics of the emission (electron distribution function tapped). Juno will significantly advance our understanding of Jupiter's polar magnetosphere via its polar orbit with low altitude perijove, allowing in situ measurements of fields, plasmas, currents, particles, at the key region where the magnetospheric activity is focused along converging magnetic field lines. Similar measurements should be performed at Saturn (top right inset of Fig. 7) to better understand the magnetosphere-planet coupling.

Finally, Kronos should provide new insights to the inner radiation belt discovered by Cassini inside the D ring [48].

2.4 Ring science

Whereas observed since the seventeenth century, Saturn's rings are still one of the most puzzling structures in our Solar System. To constrain the origin of the rings and their evolution, in situ observations are needed, following Cassini's success. In addition, Saturn's rings are the closest example of an astrophysical *disk*, one of the most fundamental structures in the Universe. The outer edge of the rings system (the A–F region) is located on the Roche limit itself, allowing for substantial accretion processes. The outer regions of the rings therefore share common properties with a protoplanetary disk.

The origin of Saturn's rings is still not understood. They were possibly formed by fragmentation of comets destroyed by tides after a too close passage [49] or by the destruction of an ancient satellite [50]. Our limited knowledge of the physical properties of the ring particles prevents us from discriminating these different scenarios. A key information would be the precise size distribution of ring particles down below the 10 cm scale. Direct observation of ring particles would allow us to achieve a major ring science objective: the physics of accretion (similar to planet formation). Despite the strong tidal field of Saturn, limited accretion is theoretically possible (e.g., [51]). Recent works show that moonlets and ringlets may be the two sides of a same object [51]. Cassini has recently provided new indirect proofs of this [52]). Direct observation of these aggregates would be valuable and would unveil a new class of Solar System objects: temporary moons. Thus, an exotic accretion

physics could take place, resulting in the formation of temporary structures that need to be characterized in detail.

3 Mission profile

3.1 General mission architecture

The nominal mission includes two atmospheric probes delivered by a single carrier spacecraft. The primary science objectives of both elements is the formation of Saturn and the origin of its atmosphere. The probes enable in situ measurements of Saturn's atmosphere to be performed down to a pressure of 10 Bar. The carrier spacecraft is strongly inherited from Juno and enables a more global investigation of Saturn's atmospheric H_2O and NH_3, gravity and internal magnetic field, rings, and the inner magnetosphere.

3.2 Launcher requirements

Since Kronos was proposed as part of an international collaboration between ESA and NASA, the launch would have been possible with either a NASA or a European launch vehicle. Since the total mass of a flyby-based architecture with the two probes is estimated at less than 3000 kg, the projected launch vehicle for the mission could be an Atlas V-551.

3.3 Trajectory

Interplanetary trajectories to Saturn could be supported with chemical and/or solar electric propulsion (SEP) systems, combined with gravity assist at Earth and Venus, and for the relay trajectory architecture also at Jupiter. These trajectories result in flight times from ~6.3 years to ~17 years, although flight times over 12 years were found not desirable. Interplanetary and flyby/orbiter trajectory options are different for supporting relay or DTE architectures.

3.4 Direct to Earth communication

3.4.1 Flyby DTE trajectory

Using a direct-to-Earth (DTE) communication strategy decouples the probes from the carrier (after release) and thus allows for the most efficient, lowest cost and lowest risk mission architecture possible. This, of course, limits the data return from the probe mission, however, our preliminary analysis shows that the DTE capability meets the requirements for the Kronos mission. The probes are delivered on a Type II trajectory to Saturn to allow for probe entry at or near the sub-Earth point. Preliminary results suggest a longer flight time associated with DTE due to limits on the Jupiter gravity assist and to the probe entry geometry requirements. Preliminary launch characteristics for DTE and relay cases are shown in Tables 2 and 3.

Table 2 Preliminary launch characteristics for DTE option (shortest cruise for DTE)

EVVES case for DTE trajectory	
Launch vehicle	Atlas V-551
Departure condition	V_{inf}=4.1 km/s
Launch C3	C3=17 km^2/s^2
Launch mass	4,665 kg
Gravity assists	Earth–Venus–Venus–Earth
Arrival velocity	v_{inf}=5.8 km/s
Cruise time	11 years
Saturn arrival mass	3,345 kg
Mass post-SOI	2,721 kg
Sub-Earth point	~30° offset

3.4.2 DTE architecture

A relay architecture potentially provides the longest visibility between the probe and the carrier. This requires the relay spacecraft to be in a low inclination or equatorial orbit at a radial distance > 5 R_S. Zenith attenuation of radio signal is a function of probe depth, measured by atmospheric pressure. During the probe descent, the transmission of data must be performed in real time, with the data upload ending as the probe reaches its deepest point in Saturn's atmosphere. The preliminary DTE architecture includes a 200 MHz UHF link from the probes for direct-to-Earth communication to Earth, and an X-band link from the carrier for orbiter or flyby science and telemetry through the DSN. Data rate from the probe is the function of the antenna size, transmitter power, separation distance, and atmospheric conditions. Data compression potentially can increase the efficiency and thus the scientific return. Technology development in the areas of antenna design, telecom power, and frequency scanning and locking can vastly improve the expected performance. Preliminary analysis indicates that a data rate of ~60 bps from each probe is achievable without major new technology. This translates to a total data volume of

Table 3 Preliminary launch characteristics for relay options

Launch characteristics	
2015 EEJS Relay Trajectory	
Launch vehicle	Atlas V-551
Departure date	12/7/2015
Departure condition	V_{inf}=5.2 km/s
Launch C3	C3=29.5 km^2/s^2
Gravity assists	Earth–Earth–Jupiter
DSM	685 m/s
Arrival date	3/30/2022
Arrival velocity	v_{inf}=9.4 km/s
Cruise time	6.3 years
Dry mass	3,073 kg
Reference 2017 EEJS Relay Trajectory	
Launch year	January 2017
C3	C3=28 km^2/s^2
DSM	840 m/s
Arrival velocity	v_{inf}=5.8 km/s
Cruise time	7 years
Dry mass	2,935 kg

~0.44 Mb from the two probes. DTE potential at low frequencies (200–400 MHz) will be significantly (by an order of magnitude) improved with the next generation radio telescopes LOFAR (Low Frequency Array) and SKA (Square Kilometre Array.

Data link types on the relay architecture include: X-band telecom link for the carrier to the DSN; and 400 MHz UHF between the probes and relay spacecraft. Assuming a 400 K Saturn hot-body temperature noise at 400 MHz UHF frequency, and a corresponding 1.5 dB atmospheric attenuation at 10 Bar, the probes could support a data rate between of 512 bps, giving a total data volume of ~2 Mb from each probe.

On the carrier, the X-Band system uses ~35 W power and a 3 meter high gain antenna (HGA). Medium gain antenna and low gain antennas are likely necessary for maintaining links during cruise and safing scenarios. On the probes, the UHF LGA will work with an Electra transmitter at 20 W RF output. This requires an upgrade to the Electra transmitter, which currently operates at 12 W. Both ends of the radio link between the probes and the relay spacecraft must contain Ultra Stable Oscillators (USO) needed for radio interferometric (VLBI) and Doppler measurements (Doppler Wind Experiment -DWE- and Planetary Radio Interferometer and Doppler Experiment -PRIDE).

3.4.3 Ring science architecture

For the ring science purposes, we suggest an additional dedicated probe: Lora (Landers on Rings Array). Lora would not be a large probe, but rather a collection (2 to 3) of very small and simple probes, like "MicroProbes", containing only one efficient camera. The fleet of 2 to 3 identical probes would be dropped by Kronos during the flyby, and the probes would go directly into the rings at different locations, allowing to obtain high resolution images. One of the probes should target the ring plane, through a gap near a dense ring (B ring), in order to get information on the vertical structure of the ring.

3.5 Carrier

The spacecraft design is directly inherited from Juno replacing Juno's radiation vault mass with the probes. Juno is designed as an outer planet orbiter and already includes many of the components necessary to implement the mission. Low Intensity Low Temperature (LILT) solar panels from Juno and Bepi Colombo missions are baselined for Kronos, but require further tests for Saturn environment. The carrier is designed to deliver the probes to Saturn and to perform remote sensing measurement during its flyby. An orbiter configuration would include additional propellant tanks, and a modified power system to account for the higher power demands.

Structurally, the carrier consists of: (a) a spacecraft bus; (b) a propulsion system, including propellant tanks; (c) a power system, consisting of LILT solar arrays and batteries; (d) subsystems, including thermal management, CDH, GN&C, ACS, telecom; (e) and science instruments, including the MWR antennas. For the propulsion system both chemical and SEP were considered.

3.5.1 Carrier power system trades

At Saturn, the solar flux is about 15 W/m^2, or ~1% of that at Earth. Low Intensity Low Temperature (LILT) solar cells, developed by ESA for Rosetta, were tested up to ~70 W/m^2, while Juno's solar panels are designed to operate at Jupiter where the solar flux is ~55 W/m^2. New, high efficiency LILT cells could achieve a power output per unit area of 4 to 5 W/m^2, assuming a conversion efficiency of 30%. At this level of performance, according to a CNES study, a Juno-size solar panel could generate ~200 We, with the power system weighing ~300 kg (including batteries and conditioning system). Performance could be also increased with the development of concentrators.

Studies performed at both CNES and NASA [53, 54] demonstrated that short-lived missions could operate at Saturn using photovoltaic power generation. A flyby mission is expected to use batteries on both the probes and on the carrier spacecraft, and employ solar panels for backup only, in case not all data is transferred back to Earth in a single 8 hours telecom pass. For an orbiter mission the power requirement is expected to be continuous: near the periapsis the spacecraft would perform its science measurements, while during cruise to and from apoapsis it would perform data transfer to Earth, housekeeping, and recharge its batteries. This would have a significant impact of power system sizing. While solar power generation is expected to be the baseline configuration for the flyby architecture, future mission studies should also address the use of RPSs on an orbiter, in order to assess its impact on mission cost and architecture.

3.5.2 Saturn probes

Saturn's atmospheric circulation results in a distinct distribution of latitude bands and zones as seen most recently in the Cassini VIMS spectral data. Thus the Kronos mission should allow for the launch of two probes in different regions. The preliminary design calls for targeting one of the probes inside and one outside of the ±13° latitude band. Since the scale-height of Saturn is about twice that of Jupiter, it is not feasible for the probes to return data from the 50 to 100 Bar pressure levels—which would be required to measure the water abundance in situ—because of significant microwave absorption. Consequently, the probes will only be required to measure atmospheric composition and dynamics to about 10 Bar, while water and ammonia abundance will be measured using passive microwave radiometry from the carrier (like Juno) to 50–100 Bar.

The Saturn probes will use significant heritage from the Galileo probe (Fig. 8), including the thermal protection system (TPS), aeroshell design, and subsystems. Except for the TPS, heritage from the Huygens Titan probe will also prove extremely beneficial. Thanks to combined Huygens and Exomars, Europe has the technological background to provide for the Descent Modules of the two Kronos atmospheric probes. The gas giant-specific shield/aeroshell will be provided by NASA: its strong Galileo heritage will enable to get well-mastered interface specifications between the aeroshell and the descent module, and a controlled development. No development risk on US side is expected to be transferred to Europe's contribution, even via interface requirements.

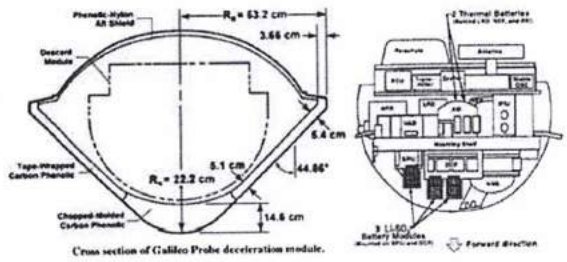

Fig. 8 Heritage Galileo descent module and probe (Galileo Probe Deceleration Module Final Report, Doc No. 84SDS2020, General Electric Re-entry Systems Operations, 1984; AIAA, "Project Galileo Mission and Spacecraft Design", Proc. 21st Aerospace Science Meeting, Reno, NV, January 10 13, 1983; Proc. AIAA'83, 21st Aerospace Science Meeting, Jan. 10 13, 1983, Reno, NV)

The probes are considered autonomous objects, consisting of a set of science instruments, and subsystems. Each probe is housed inside a protective aeroshell. Its total mass of ~330 kg consists of a 222 kg deceleration module, and 117 kg descent module. The descent module houses the science instruments and subsystems, while the deceleration module includes the aeroshell, TPS, parachutes and separation hardware.

4 Instruments

4.1 Elemental and isotopic measurements of Saturn's atmosphere

Saturn Probe measurements will be selected to meet the measurement requirements that address (1) theories of planetary origin and (2) fundamental knowledge of Saturn's atmospheric structure and meteorological processes. The instrument complement will include a mass spectrometer for chemical and isotopic composition determination, an atmospheric structure experiment, a Doppler Wind Experiment for retrieval of a vertical profile of zonal winds, and a nephelometer to determine the structure of the atmosphere to at least 10 Bar and to obtain the radiative balance at this depth. The instruments baselined for the Kronos Probe investigation have a solid heritage from previous probe missions such as Galileo [55] (Fig. 9) and Cassini/ Huygens [56].

4.2 Composition and isotopes

Light elements to be measured with an atmospheric probe mass spectrometer include H, C, N, S, P, Ge, As, and the noble gases He, Ne, Ar, Kr, and Xe. These measurements together with a determination of D/H, $^{13}C/^{12}C$, $^{15}N/^{14}N$, $^{3}He/^{4}He$, $^{20}Ne/^{22}Ne$, $^{38}Ar/^{36}Ar$, $^{36}Ar/^{40}Ar$, and the isotopic composition of Kr and Xe will provide a complete comparison with the Galileo Probe measurements at Jupiter and reveal key differences or similarities between these giant planets. However, we know that such a probe will not allow us to measure the deep, well-mixed abundance of oxygen, because of water condensation and meteorological processes. As the

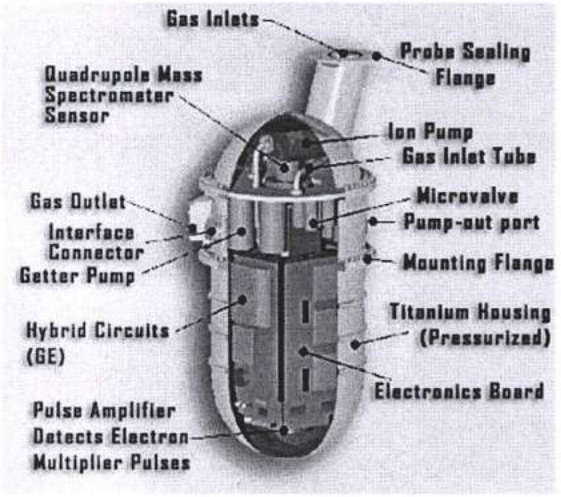

Fig. 9 The configuration of the Galileo Probe Mass Spectrometer (GPMS) that entered the Jupiter atmosphere on December 7, 1995 is shown. The Saturn Probe Gas Analysis Experiment will integrate several GPMS technologies with other advanced gas processing techniques to provide improved measurement sensitivity and precision at Saturn

abundance of oxygen in water is a key factor in the deduction of the composition and hence origin of giant planets, we propose to integrate on the orbital or flyby spacecraft a microwave sounder devoted to the remote sensing of water in the deep atmosphere of Saturn. Such an instrument is presently being developed for the Juno mission, to retrieve the O/H ratio in the deep troposphere of Jupiter.

Our present knowledge of the chemical and isotopic composition of the Jupiter and Saturn atmospheric chemical and isotopic composition is given in Table 4 together with the required precision of a Saturn Probe Gas Analysis System (GAS). The precisions listed represent a substantial improvement from the Galileo GPMS measurements. This performance will not only establish a full comparison with the Jupiter values, but will provide a robust data set for comparison with other planetary values. For example, differences in Xe isotopic fractionation between solar and meteoritic and between solar and terrestrial of <1% and <3% respectively per Dalton are resolvable with this precision. The static mass spectrometer design described

Table 4 SPMS measurement requirements

Elements	Jupiter/Sun	Saturn/Sun	KRONOS (%)	Isotopes	Jupiter	Saturn	Kronos (%)
He/H	0.81±0.02	~0.2	+1	D/H	$2.6\pm0.7\times10^{-5}$	$2.25\pm0.35\times10^{-5}$	<10
Ne/H	0.059±0.004	?	<5	$^{3}He/^{4}He$	$1.66\pm0.05\times10^{-4}$	?	<0.5
Ar/H	5.34±1.07	?	<5	$^{13}C/^{12}C$	0.0108±0.00005	0.011	<1
Kr/H	2.03±0.38	?	<25	$^{15}N/^{14}N$	$2.3\pm0.3\times10^{-3}$	?	<5
Xe/H	2.11±0.40	?	<25	Xe	<10% typical	?	<0.5
C/H	3.82±0.66	?	<10				
N/H	4.90±1.87	2 4 ?	<25				
S/H	2.88±0.69	?	<10				

Estimated Kronos precision might be higher or lower depending on abundances and measurement time during the descent spent on the species of interest. This will be explored in greater detail during the phase A study

below enables these precisions. The Jovian elemental ratios of C/H, N/H, S/H, and D/H in this table were measured in the molecular species CH_4, NH_3, H_2S, and H_2 respectively. The GPMS made continuous direct measurements of gases ingested into the vacuum of the instrument in the 2–150 Dalton mass range during the descent except for short periods of time when processed gases were introduced into the mass spectrometer.

4.2.1 GAS specifications

The proposed Saturn Probe Gas Analysis System has a high heritage in both successful atmospheric probe composition/isotope investigations conducted at Jupiter [4, 55, 57] and Saturn's moon Titan [58]. Elements of the GAS designed to improve the precision of the measurements are adapted from in situ calibration, static mass spectrometry, gas separation, chemical processing techniques and advanced pumping systems developed for the Rosetta mass spectrometer Ptolemy [59] and presently under development for the 2009 Mars Science Laboratory [60]. The mass spectrometer is a quadrupole mass spectrometer similar to more than a dozen that have been developed at the NASA Goddard Space Flight Center and successfully operated in the upper atmosphere of the Earth and Venus.

4.2.2 Noble gas enrichment and static mass spectrometry

The combination of a noble gas enrichment system, a gas scrubber that can remove all chemically active gases, a chemical getter pump in the MS analyzer region, and a high conductance valve between the MS and the WRP will enable static MS operations for higher precision noble gas measurements than were possible at Jupiter with the GPMS. The static measurements interrupt direct sampling of the atmosphere for a portion of the descent, but are necessary to obtain the desired precision. The noble gas enrichment system was proven on the Galileo Probe MS and consists of chemical getters and traps that can enrich the trace noble gases Kr and Xe. The Galileo Probe noble gas enrichment system was able to provide measurements to the sub ppb levels for isotopes of Jovian Xe.

4.2.3 Nitrogen combustion for $^{15}N/^{14}N$ isotope measurement

The $^{15}N/^{14}N$ ration on Jupiter was obtained from the NH_3^{++} signal at 8.5 and 9 Dalton for the two nitrogen isotopes. Due to the difficulty of removal of spectral interferences in this approach we provide an NH_3 oxidation reactor on GAS to produce N_2 so that this measurement can be carried out with higher precision. This element of GAS could be developed using techniques similar to those developed for Rosetta and Beagle 2, and expertise and techniques developed for the analysis of solar wind nitrogen implanted in the GENESIS targets.

4.3 Meteorology and atmospheric dynamics

In situ measurements that address the meteorology and atmospheric dynamics goals of the Kronos mission include density, pressure and temperature sounding to

characterize the atmospheric structure and instruments to measure the radiative balance, cloud structure, and zonal winds also down to a pressure of 10 Bar.

4.4 Measurements achieved with a Saturn probe nephelometer

The composition and precise location of cloud layers in Saturn are largely unknown. They may be composed of ammonia, ammonium hydrosulfide, or simply water. Because of this relative paucity of information on Saturn's clouds, the demands we place on a cloud particle sensor (nephelometer) are significant.

For Kronos, we have baselined a new instrument which would measure not only the amplitude phase function of the light scattered by the clouds from a laser source on the probe, but also the polarization ratio phase function as well. It does this at two wavelengths, separated by about an octave in wavelength near 1 μm. The phase functions are sampled at six discrete angles, chosen to maximize their leverage in distinguishing between different size, shape and aerosols compositions. These measurements at an optical depth unity as long as ~10 km permit to determine the aerosol number density, their particle size, an indication of the particle shape, and the particle's index of refraction at the two wavelength, which may be used to infer the molecular constituency of the aerosols.

4.5 Atmospheric structure instrument

The Kronos Atmospheric Structure Instrument (ASI) consists of three primary sensor packages: (1) a three axial accelerometer (ASI-ACC), (2) a pressure profile instrument (ASI-PPI), (3) temperature sensors (ASI-TEM). The proposed instrument will benefit from a strong heritage of the Huygens ASI experiment of the Cassini/Huygens mission [61]. The key in situ measurements will be atmospheric density, pressure and temperature profile by measuring deceleration of the entry vehicle and performing direct temperature and pressure measurements during the descent phase. The ASI-ACC will start to operate since the beginning of the entry phase, sensing the atmospheric drag experienced by the entry vehicle. Direct pressure and temperature measurements will be performed by the sensors having access to the atmospheric flow from the earliest portion of the descent until the end of the probe mission at approximately 10 Bar.

4.6 Measurements with a Doppler wind experiment

The primary goal of the Kronos Doppler Wind Experiment (DWE) is to measure a vertical profile of the zonal (east–west) winds along the probe descent path [62]. A secondary goal of the DWE is to detect, characterize, and quantify microstructure in the probe descent dynamics, including probe spin, swing, aerodynamic buffeting and atmospheric turbulence, and to detect regions of wind shear and atmospheric wave phenomena. The Kronos Doppler Wind Experiment (DWE) can be designed to work with a probe DTE architecture or a probe-to-relay architecture. Both options include USO requirements and differ only in the angle of entry and DTE geometry requirements (see Mission Design). For relay, the system comprises a probe and a carrier ultrastable oscillator (USO) as part of the probe/carrier communication

package. Involvement of several observing telescopes in interferometric mode (PRIDE) will significantly improve the accuracy and robustness of the measurements. The proposed experiment benefits from the strong heritage of both the Galileo and Huygens doppler wind experiments [63].

4.7 Instruments on the carrier spacecraft

Further definition of the carrier spacecraft will take place during the Kronos Phase A study. This may be a flyby spacecraft or a Saturn orbiter. Definition of the orbital instruments will also take place during this period. A key objective of the payload on the carrier spacecraft will be to secure deep, global abundances of H_2O and NH_3 and their distributions over al latitudes using microwave radiometry. The technology to implement these measurements is mature through the radiometers developed for the Juno mission. The mission objectives for the orbiter/flyby spacecraft are inherited from the Juno mission and include;

- Measurements of the global oxygen (water) and nitrogen (ammonia) abundances.
- Measurements of Saturn's internal mass distribution (core mass) via gravity science
- Measurements of Saturn's internal rotation and convection (whether Saturn rotates as a solid body) via gravity science (determination of high order gravitational moments; see)
- Measurements of Saturn's internal magnetic field sufficient to investigate the source location of the field.
- Measurements of the properties of Saturn's innermost magnetosphere (inner radiation belt, possible ring-associated currents, UV/IR/radio auroras, magnetic anomalies)
- Measurements of the deep atmospheric structure and dynamics via microwave sounding

4.7.1 Multi-frequency microwave radiometry

The design of the microwave radiometers will follow closely the Juno design, with the exceptions that the measurement at Saturn is considerably less driving. Without the strong synchrotron emission from Jupiter, the measurement noise will be less and thus the instrument design less complicated (beam pattern, etc.). Furthermore, the selection of wavelengths (frequencies) will be tuned to the Saturn atmosphere. As with Juno, it is expected that the radiometers will be a set (approximately 6) of frequencies ranging from 1 cm to 100 cm. Having the full latitude coverage is essential for understanding the roles of ammonia and water in Jovian meteorology and for placing the probe measurements in context.

4.7.2 X/Ka band up/downlink system for gravity science

Most of the uncertainty in our knowledge of Saturn's core stems from uncertainties in the equation of state and the gravity zonal harmonics *J4* and *J6* and to limited knowledge of how Saturn's deep interior rotates. Current uncertainties are 1% in *J4*

and 30% in *J6*. Kronos improves the knowledge of *J4* and *J6* by over 3 orders of magnitude (*J4* ~10 ppm accuracy, *J6* ~100 ppm accuracy). This removes the uncertainty regarding interior rotation and estimates the abundance of water, reducing the core mass uncertainty and total mass of heavy elements to a few Earth masses.

Using an existing Linear Ion Trap (LITS) as frequency reference (or an improved follow on) a DSN ground station (DSS25) transmits X and Ka-band radio signals to the spacecraft, then receives the transponded signals and very accurately measures their frequencies. Simultaneously, water vapor radiometers (WVR) at the DSN station measure Earth-atmospheric brightness temperatures in the direction of the antenna beam, thereby determining the zenith signal delay caused by the wet component of the troposphere, and ultimately the tropospheric correction (refraction) to the raw Doppler data. The same set of on-board instrumentation on the carrier spacecraft will enable multi-disciplinary VLBI tracking experiments with ultra-precise characterization of the state vector of the spacecraft, reaching tens of meters in the lateral direction.

4.7.3 Vector magnetometer

The instrument must be of sufficient sensitivity to measure perturbations caused by field aligned currents. The successful operation of the Cassini fluxgate magnetometer at Saturn makes it a natural candidate for inheritance for the design of the Kronos magnetometers. The new generation of digital fluxgate sensors have masses of the order ~200 g, and therefore make very little demand on overall payload mass. For a Cassini-like configuration, each sensor would be capable of measuring fields up to ~44.000 nT, well below the atmospheric depths at which the Kronos probes would be expected to operate.

4.7.4 Plasmas sensor

The instrument must quickly measure electron and ion energy angular distributions (100 eV–20 keV) from an effectively non-rotating platform.

4.7.5 Energetic particle sensor

This instrument must operate at the higher energies (20 keV—several MeV) while the plasma sensor functions at lower energies. Although a 1 MeV upper limit is sufficient to address magnetosphere–ionosphere coupling issues, higher energies (up to 30–50 MeV) are needed to study the radiation belts. In situ study of the new radiation belt seen by Cassini-MIMI inside the D-ring, would require a small ride-along particle detector on the probe itself. Such a sensor was carried by Galileo probe.

4.7.6 Plasma and radio wave receivers

Cassini and Stereo spacecraft carry radio and plasma waves spectro-polarimeters which can be programmed to operate according to very diverse setups (spectral and

temporal resolutions, snapshots or surveys, waveform capture, polarization measurement, etc.). In addition, they have goniometric capabilities, i.e. they enable the instantaneous determination of the direction of the brightest point source at each measurement, and thus the possibility to synthesize images of the radio-sources. The next generation of these radio spectro-goniopolarimeters has been miniaturized and could be implemented for resources of ~1 kg and ~1 W using development heritage from e.g. BepiColombo/MMO.

4.8 The Lora (Landers On Rings Array) MicroProbes

All the ring science objectives can be met by two to three very simple probes (MicroProbes), whose sole payload would be a high-resolution camera, dropped in different locations of the rings (A, B, C by order of priority). The only limit to the resolution is the time for data transfer before impacting into the rings. A Ritchey Chretien reflector, with 1m focal length and diffraction limited at 5×10^{-6} rad ($\geq$ a 15 cm diameter) would be suited. As the probes get closer to the ring, the resolution increases and allows to achieve the ring science objectives.

A low inclination impact angle is preferred (~1°), its feasibility depending on the arrival trajectory of the Kronos spacecraft. A high resolution imager for ring science that gives the required <1 10 m resolution images requires narrow angle cameras on the Lora probes that will be evaluated in the Kronos Phase A study. An example of synthetic images of A ring wakes at different resolution is shown in Fig. 10. Assuming a resolution of 6×10^{-6} radians/pixel (like the Cassini ISS-NAC), the minimal distance of approach to achieve a given resolution is given in Table 5.

The maximum scientific return is expected when the distance to the rings is <100 km. However, once the Lora probes are below 8,000 km, they could achieve a better resolution than the best Cassini images.

In order to stabilize and orient the spacecraft to allow a good pointing, a set of reactions wheels and gyros onboard are necessary. The small inertia of the probes may allow easy re-orientation during the descent.

4.8.1 Timeline for the Lora probe

In the current state of the design of the Kronos mission, the exact trajectory of the Lora probe has not been precisely determined. We assume below that the Lora Probe would be launched on an hyperbolic trajectory, with a ~1° inclination above the ring

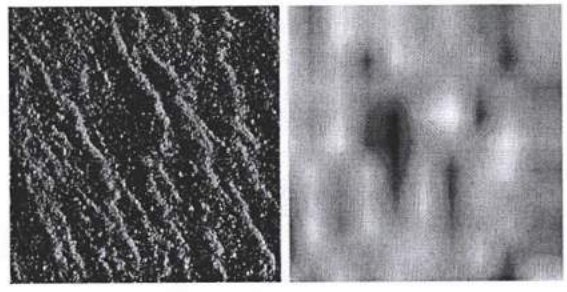

Fig. 10 Synthetic images of A ring wakes at 60 m resolution (*left*) and 60 resolution (*right*) (H. Salo)

Table 5 Ring science operations

Altitude above rings (km)	Resolution (m/pixel)	Science objective
2,000	10	Microstructure/aggregates
200	1	Ring thickness
20	0.1	Particle size distribution

plane, with nodes located around 10^5 km from Saturn's center. The velocity in the Saturn's inertial frame would be about ~ 27 km/s. With this approach geometry, the resulting timeline for the Lora probe is presented in Table 6.

During its descent to the ring plane, the Lora probe would transmit the collected data as soon as they are collected (in the spirit of what was done for the Huygens descent on Titan), because of the possible destruction of the probe during its crossing of the ring plane. If the Lora probe survives the ring-plane crossing, then new data could be collected and transmitted again to the Kronos spacecraft.

Since the Lora probe is meant to be a "microprobe" (i.e. with a single instrument and a simple communication system) its communication package would be designed primarily for communicating with the Kronos spacecraft only, which would record and transmit the data to Earth.

4.9 Saturn atmosphere wind diagnostics by means of radio measurements of the probe motion (PRIDE)

This experiment does not require special on-board instrumentation and can be conducted with radio signals in both communication scenarios, DTE and probe-to-carrier relay. In particular, it will provide additional input into measurements of the wind profile not requiring an a priori assumption on a one-dimensional model of the wind.

DTE could be used for additional measurements by determining an additional component of the probe's state vector. Indeed there is no need to limit the experiment to zonal component measurements since a meridional component could be measured as well. Even 3D diagnostics of the motion are not out of the question, i.e. the descent velocity can be included in the set of measured values from the experiment. To what extent the measured motion of the probe represents the wind depends on specifics of the atmosphere flight. A combination of Doppler and interferometric measurements can provide unambiguous determination of the descent trajectory—coordinates and their (at least first) derivatives.

Table 6 Timeline for the Lora probe

Time before impact (or ring-plane crossing)	Altitude above rings (km)	Resolution (m/pixel)	Science Objective
−1 h 9 min 21 s	2,000	10	Microstructure/aggregates
−6 min 56 s	200	1	Ring thickness
−41 s	20	0.1	Particle size distribution

5 Conclusions and summary

Multiple probes to the giant planets are critical for collecting the data required for understanding the formation of our solar system, and by extension, of extrasolar systems. Indeed, our giant planets can be studied in much finer detail than any exoplanet ever will, and they have preserved chemical and isotopic relics of early solar system reservoirs. In exploring the composition of Saturn with Kronos, we shall go back to the times when a tiny fraction of a molecular cloud collapsed to give birth to a special stellar system: the Sun and its planets. The probes will allow an in-depth exploration of Saturn and its comparison with results obtained by the Galileo mission at Jupiter. This comparison between the two most massive planets of the Solar System is a prerequisite to a detailed understanding of the origins of the Solar System. Kronos shall also investigate Saturn's complex atmospheric dynamics, which is a fantastic laboratory for this field of research. It will measure the planet's magnetic field very close to the planet's atmosphere and thus unfiltered by the rings, with direct consequences for understanding the planet's dynamo and deep rotation. Kronos also provides a possibility to study Saturn's rings in fine details. Altogether, through innovative approaches this international mission allows a combination of essential measurements that concern the ringed planet but impact many disciplines and the understanding of our origins.

References

1. Lissauer, J.J., Stevenson, D.J. In: Reipurth D. et al. (eds.) Protostars and Planets V, pp. 591–606. Univ. Arizona Press (2007)
2. Haisch, K.E., Lada, E.A., Lada, C.J.: Disk frequencies and lifetimes in young clusters. Astrophys. J. **553**, L153–L156 (2001)
3. Guillot, T., Hueso, R.: The composition of Jupiter: sign of a (relatively) late formation in a chemically evolved protosolar disc. Mon. Not. R. Astron. Soc. **367**, L47–L51 (2006)
4. Atreya, S.K., et al.: A comparison of the atmospheres of Jupiter and Saturn: deep atmospheric composition, cloud structure, vertical mixing, and origin. Planet. Space Sci. **47**, 1243–1262 (1999)
5. Owen, T., et al.: A low-temperature origin for the planetesimals that formed Jupiter. Nature **402**, 269–270 (1999)
6. Lodders, K.: Solar system abundances and condensation temperatures of the elements. Astrophys. J. **591**, 1220–1247 (2003)
7. Alibert, Y., Mousis, O., Benz, W.: On the volatile enrichments and composition of Jupiter. Astrophys. J. **622**, L145–L148 (2005)
8. Gautier, D., Hersant, F.: Formation and composition of planetesimals—Trapping volatiles by clathration. Space Sci. Rev. Space Sci. Rev. **116**, 25–52 (2005)
9. Guillot, T.: The interiors of giant planets: Models and outstanding questions. Annu. Rev. Earth Planet. Sci. **33**, 493–530 (2005)
10. Owen, T., Mahaffy, P.R., Niemann, H.B., Atreya, S., Wong, M.: Protosolar nitrogen. Astrophys. J. **553**, L77–L79 (2001)
11. Hashizume, K., Chaussidon, M., Marty, B., Robert, F.: Solar wind record on the moon: Deciphering presolar from planetary nitrogen. Science **290**, 1142–1145 (2000)
12. Marty, B., et al.: Helium and neon abundances and compositions in cometary matter. Science **319**, 75–78 (2008)
13. Fortney, J.J., Hubbard, W.B.: Phase separation in giant planets: inhomogeneous evolution of Saturn. Icarus **164**, 228–243 (2003)
14. Hubbard, W.B.: Gravitational signature of Jupiter's deep zonal flows. Icarus **137**, 357–359 (1999)
15. Maximenko, N. A., Bang, B., Sasaki, H. Observational evidence of alternating zonal jets in the world ocean. Geophys. Res. Lett. **32** (2005)

16. Atreya, S.K.: Atmospheres and Ionospheres of the Outer Planets and their Satellites, Chapter 3. Springer-Verlag, New York (1986)
17. Weidenschilling, S.J., Lewis, J.S.: Atmospheric and cloud structure of the Jovian planets. Icarus **20**, 465–476 (1973)
18. Sanchez-Lavega, A.: Viewpoint—How long is the day on Saturn? Science **307**, 1223–1224 (2005)
19. Sanchez-Lavega, A., Rojas, J.F., Sada, P.V.: Saturn's zonal winds at cloud level. Icarus **147**, 405–420 (2000)
20. Sanchez-Lavega, A., Perez-Hoyos, S., Rojas, J.F., Hueso, R., French, R.G.: A strong decrease in Saturn's equatorial jet at cloud level. Nature **423**, 623–625 (2003)
21. Porco, C.C., et al.: Cassini imaging science: Initial results on Saturn's rings and small satellites. Science **307**, 1226–1236 (2005)
22. Vasavada, A.R. et al.: Cassini imaging of Saturn: Southern hemisphere winds and vortices. J. Geophys. Res.—Planets **111** (2006)
23. Gurnett, D.A., et al.: Radio and plasma wave observations at Saturn from Cassini's approach and first orbit. Science **307**, 1255–1259 (2005)
24. Giampieri, G., Dougherty, M.K., Smith, E.J., Russell, C.T.: A regular period for Saturn's magnetic field that may track its internal rotation. Nature **441**, 62–64 (2006)
25. Zarka, P., Lamy, L., Cecconi, B., Prange, R., Rucker, H.O.: Modulation of Saturn's radio clock by solar wind speed. Nature **450**, 265–267 (2007)
26. Anderson, J.D., Schubert, G.: Saturn's gravitational field, internal rotation, and interior structure. Science **317**, 1384–1387 (2007)
27. Ingersoll, A.P., Beebe, R.F., Conrath, B.J., Hunt, G.E.: In: Saturn (ed. (eds.), T. G. a. M. S. M.), pp. 195–238. University of Arizona Press, Tucson (1984)
28. García-Melendo, E., Sánchez-Lavega, A., Hueso, R.: Numerical models of Saturn's long-lived anticyclones. Icarus **191**, 665–677 (2007)
29. Del Genio, A.D., et al.: Saturn eddy momentum fluxes and convection: First estimates from Cassini images. Icarus **189**, 479–492 (2007)
30. Dyudina, U.A. et al.: Lightning storms on Saturn observed by Cassini ISS and RPWS during 2004–2006. Icarus (2007)
31. Hueso, R., Sanchez-Lavega, A.: A three-dimensional model of moist convection for the giant planets II: Saturn's water and ammonia moist convective storms. Icarus **172**, 255–271 (2004)
32. Sanchezlavega, A., Battaner, E.: The nature of Saturns atmospheric great white spots. Astron. Astrophys. **185**, 315–326 (1987)
33. Sromovsky, L.A., Revercomb, H.E., Krauss, R.J., Suomi, V.E.: Voyager-2 observations of Saturns northern mid-latitude cloud features—morphology, motions, and evolution. J. Geophys. Res.—Space Physics **88**, 8650–8666 (1983)
34. Godfrey, D.A.: A hexagonal feature around Saturns north-pole. Icarus **76**, 335–356 (1988)
35. Karkoschka, E., Tomasko, M.: Saturn's vertical and latitudinal cloud structure 1991–2004 from HST imaging in 30 filters. Icarus **179**, 195–221 (2005)
36. Perez-Hoyos, S., Sanchez-Lavega, A.: On the vertical wind shear of Saturn's equatorial jet at cloud level. Icarus **180**, 161–175 (2006)
37. Pirraglia, J.A., Conrath, B.J., Allison, M.D., Gierasch, P.J.: Thermal structure and dynamics of Saturn and Jupiter. Nature **292**, 677–679 (1981)
38. Gierasch, P.J., et al.: Observation of moist convection in Jupiter's atmosphere. Nature **403**, 628–630 (2000)
39. Dyudina, U.A., et al.: Lightning on Jupiter observed in the H-alpha line by the Cassini imaging science subsystem. Icarus **172**, 24–36 (2004)
40. Baines, K.H., et al.: The atmospheres of Saturn and Titan in the near-infrared: First results of Cassini/VIMS. Earth Moon, Planets **96**, 119–147 (2005)
41. Baines, K.H., Momary, T.W., Roos-Serote, M.: The deep winds of Saturn: First measurements of the zonal windfield near the two-bar level. Bull. A. A. S. **37**, 658 (2005)
42. Blanc, M., et al.: Magnetospheric and plasma science with Cassini–Huygens. Space Sci. Rev. **104**, 253–346 (2002)
43. Davis, L., Smith, E.J.: A model of Saturn magnetic-field based on all available data. Journal of Geophysical Research-Space Physics **95**, 15257–15261 (1990)
44. Galopeau, P., Ortegamolina, A., Zarka, P.: Evidence of Saturns magnetic-field anomaly from Saturnian kilometric radiation high-frequency limit. Journal of Geophysical Research-Space Physics **96**, 14129–14140 (1991)
45. Cowling, T.G.: The magnetic field of sunspots. Mon. Not. R. Astron. Soc. **94**, 39 (1934)

46. Raedler, K.H.: Can the highly axisymetric magnetic field of Saturn be maintained by a dynamo? Adv. Space Res. **12**, 281–284 (1992)
47. Gurnett, D.A., et al.: The variable rotation period of the inner region of Saturn's plasma disk. Science **316**, 442–445 (2007)
48. Krimigis, S.M., et al.: Dynamics of Saturn's magnetosphere from MIMI during Cassini's orbital insertion. Science **307**, 1270–1273 (2005)
49. Dones, L.: A recent cometary origin for Saturns rings. Icarus **92**, 194–203 (1991)
50. Harris, A.: In: R. Greenberg, A. B. (eds) Planetary Rings. Univ. Arizona Press, Tucson (1984)
51. Canup, R.M., Esposito, L.W.: Accretion in the Roche zone—coexistence of rings and ringmoons. Icarus **113**, 331–352 (1995)
52. Tiscareno, M.S., et al.: 100-Metre-diameter moonlets in Saturn's A ring from observations of 'propeller' structures. Nature **440**, 648–650 (2006)
53. Balint, T.S., Kowalkowski, T.D., Folkner, W.M.: In 5th International Planetary Probe Workshop. Bordeaux, France (2007)
54. Langevin, Y.: In: Coustenis, A. (ed) Inst. for Space Astrophysics in Orsay, France; presented at the 1st Saturn Probes CV Workshop, February 2007, Meudon Observatory, Paris. Meudon France (2007)
55. Niemann, H.B., et al.: The Galileo probe mass spectrometer: Composition of Jupiter's atmosphere. Science **272**, 846–849 (1996)
56. Waite, J.H., et al.: Ion neutral mass spectrometer results from the first flyby of Titan. Science **308**, 982–986 (2005)
57. Mahaffy, P.R., et al.: Noble gas abundance and isotope ratios in the atmosphere of Jupiter from the Galileo probe mass spectrometer. Journal of Geophysical Research-Planets **105**, 15061–15071 (2000)
58. Niemann, H.B., et al.: The abundances of constituents of Titan's atmosphere from the GCMS instrument on the Huygens probe. Nature **438**, 779–784 (2005)
59. Wright, I.P., et al.: PTOLEMY—an instrument to measure stable isotopic ratios of key volatiles on a cometary nucleus. Space Sci. Rev. **128**, 363–381 (2007)
60. Mahaffy, P.R.: Exploration of the habitability of Mars: Development of analytical protocols for measurement of organic carbon on the 2009 Mars Science Laboratory. Space Sci. Rev. (2008), In press
61. Fulchignoni, M., et al.: The characterisation of Titan's atmospheric physical properties by the Huygens atmospheric structure instrument (HASI). Space Sci. Rev. **104**, 395–431 (2002)
62. Atkinson, D.H., Pollack, J.B., Seiff, A.: Galileo doppler measurements of the deep zonal winds at Jupiter. Science **272**, 842 (1996)
63. Atkinson, D.H., Pollack, J.B., Seiff, A.: The Galileo probe doppler wind experiment: Measurement of the deep zonal winds on Jupiter. J. Geophys. Res.—Planets **103**, 22911–22928 (1998)

Exp Astron (2009) 23:977–980
DOI 10.1007/s10686-008-9117-6

ERRATUM

Kronos: exploring the depths of Saturn with probes and remote sensing through an international mission

B. Marty · T. Guillot · A. Coustenis · the Kronos consortium · N. Achilleos · Y. Alibert · S. Asmar · D. Atkinson · S. Atreya · G. Babasides · K. Baines · T. Balint · D. Banfield · S. Barber · B. Bézard · G. L. Bjoraker · M. Blanc · S. Bolton · N. Chanover · S. Charnoz · E. Chassefière · J. E. Colwell · E. Deangelis · M. Dougherty · P. Drossart · F. M. Flasar · T. Fouchet · R. Frampton · I. Franchi · D. Gautier · L. Gurvits · R. Hueso · B. Kazeminejad · T. Krimigis · A. Jambon · G. Jones · Y. Langevin · M. Leese · E. Lellouch · J. Lunine · A. Milillo · P. Mahaffy · B. Mauk · A. Morse · M. Moreira · X. Moussas · C. Murray · I. Mueller-Wodarg · T. C. Owen · S. Pogrebenko · R. Prangé · P. Read · A. Sanchez-Lavega · P. Sarda · D. Stam · G. Tinetti · P. Zarka · J. Zarnecki · J. Schmidt · H. Salo

Published online: 5 August 2008

Erratum to: Exp Astron
DOI 10.1007/s10686-008-9094-9

In the originally published article, the names of co-authors Juergen Schmidt and Heikki Salo were omitted erroneously. The complete authorship is shown here.

The online version of the original article can be found under doi:10.1007/s10686-008-9094-9.

B. Marty (✉)
CRPG, Nancy-Université, CNRS, BP 20, 54501 Vandoeuvre, Cedex, France
e-mail: bmarty@crpg.cnrs-nancy.fr

T. Guillot
Observatoire de la Côte d'Azur, BP 4229, 06304 Nice Cedex 04, France
e-mail: guillot@obs-nice.fr

A. Coustenis · B. Bézard · P. Drossart · T. Fouchet · D. Gautier · E. Lellouch · R. Prangé · P. Zarka
Laboratoire d'Etudes Spatiales et d'Instrumentation en Astrophysique (LESIA), Observatoire de Paris-Meudon, 5, place Jules Janssen, 92195 Meudon Cedex, France

A. Coustenis
e-mail: Athena.Coustenis@obspm.fr

N. Achilleos
Atmospheric Physics Laboratory, Department of Physics and Astronomy,
University College London, Gower Street, London WC1E 6BT, UK

Y. Alibert
Inst Phys, University of Bern, CH-3012 Bern, Switzerland

S. Asmar
Jet Propulsion Laboratory, Pasadena, CA 91109, USA

D. Atkinson
Department of Electrical and Computer Engineering,
University of Idaho, Moscow, ID 83844-1023, USA

S. Atreya
Department of Atmosphere Ocean and Space Science,
University of Michigan, Ann Arbor, MI 48109, USA

G. Babasides · X. Moussas
Space Group, Laboratory of Astrophysics, Faculty of Physics,
National and Kapodistrian University of Athens,
Panepistimiopolis, 15783 Zographos, Athens, Greece

K. Baines · T. Balint
Jet Propulsion Laboratory, 4800 Oak Grove Blvd, Paadena, CA 91109-8099, USA

D. Banfield
Department of Astronomy, Cornell University, Ithaca, NY 14853, USA

S. Barber · I. Franchi · M. Leese · A. Morse · J. Zarnecki
Open University, Walton Hall, Milton Keynes MK7 6AA, UK

G. L. Bjoraker · F. M. Flasar · P. Mahaffy
NASA, Goddard Space Flight Ctr Code 693, Greenbelt, MD 20771, USA

M. Blanc
Centre d'Etudes Spatiales des Rayonnements (CESR), Toulouse, France

S. Bolton
Southwest Research Institute, San Antonio, TX, USA

N. Chanover
New Mexico State University, Las Cruces, NM 88003, USA

S. Charnoz
AIM, Université Paris 7/CEA/CNRS, 91191 Gif sur Yvette, France

E. Chassefière
Service d'Aéronomie du CNRS/IPSL, 91371 Verrières-le-Buisson, France

J. E. Colwell
Department of Physics, University Cent Florida, Orlando, FL 32816, USA

E. Deangelis · A. Milillo
NAF/Instituto di Fisica dello Spazio Interplanetario,
via del Fosso del Cavaliere 100, 00133, Rome, Italy

M. Dougherty
Imperial College London, South Kensington Campus, London SW7 2AZ, UK

I. Mueller-Wodarg
Imperial College Sci Technol and Med, Space and Atmosphere Phs grp,
University of London, London SW7 2BW, UK

R. Frampton
Boeing NASA Systems, MC H012-C349, 5301 Bolsa Ave,
Huntington Beach, CA 92647-2099, USA

L. Gurvits · S. Pogrebenko
Joint Institute for VLBI in Europe, P.O. Box 2, 7990 AA Dwingeloo, The Netherlands

R. Hueso · A. Sanchez-Lavega
Departamento de Fisica Aplicada I, E.T.S. Ingenieros,
Universidad del Pais Vasco, Alameda Urquijo s/n, 48013 Bilbao, Spain

B. Kazeminejad
Deutsches Zentrum für Luft-und Raumfahrt (DLR),
German Space Operations Center (GSOC), 82234 Wessling, Germany

T. Krimigis · B. Mauk
Appl Phys Lab, Johns Hopkins University, Laurel, MD 20723, USA

A. Jambon
MAGIE UMR 7047, Université Pierre et Marie Curie,
4 place Jussieu, 75252 Paris Cedex 05, France

G. Jones
Max Plank Inst. Gravitat Phys, Albert Einstein Inst, Katlenburg-Lindau, Germany

Y. Langevin
Institut d'Astrophysique Spatiale Bat. 121, 91405 Orsay Campus, France

J. Lunine
Department of Planetary Science, University of Arizona, Tucson, AZ 85721, USA

M. Moreira
Laboratoire de Géochimie et Cosmochimie (UMR 7579 CNRS),
Institut de Physique du Globe de Paris, Université Paris, 7,
4 place Jussieu, 75252 Paris cedex 05, France

C. Murray
Queen Mary & Westfield College, University of London, London E1 4NS, UK

T. C. Owen
Institute of Astronomy, University of Hawaii, Honolulu, HI 96822, USA

P. Read
Clarendon Laboratory, University of Oxford, Oxford OX1 3PU, UK

P. Sarda
Groupe géochimie des Gaz Rares, Département des Sciences de la Terre,
Université Paris Sud, UMR CNRS 8148 (IDES), 81405 Orsay Cedex, France

D. Stam
Astronomical Institute "Anton Pannekoek" Kruislaan 403, 1098 SJ Amsterdam, The Netherlands

G. Tinetti
Institut d'Astrophysique de Paris, CNRS, Université Pierre et Marie Curie, 75014 Paris, France

Present address:
P. Sarda
Laboratoire de Sciences de la Terre, Ecole Normale Supérieure de Lyon cedex 07, France

J. Schmidt
Universitaet Potsdam, Institut fuer Physik und Astronomie,
Karl-Liebknecht-Str. 24/25, D-14476 Potsdam-Golm, Germany

H. Salo
Department of Physical Sciences, Astronomy Division,
University of Oulu, FI-90014 Oulu, Finland
e-mail: heikki.salo@oulu.fi

Springer

Appendix F2

Sounding the interior of Titan's lakes by using Micro-Electro-Mechanical Systems

IEEE Electronic Refereed Conference Proceedings (2011)
DOI: 10.1109/ICSpT.2011.6064648.

Sounding the interior of Titan's lakes by using Micro-Electro-Mechanical Systems (MEMS)

Georgios Bampasidis, Anezina Solomonidou,
Emmanuel Bratsolis, Konstantinos Kyriakopoulos,
Xenophon Moussas, Panagiota Preka-Papadema
National & Kapodistrian University of Athens
Athens, Greece
gbabasid@phys.uoa.gr

Mathieu Hirtzig, Athena Coustenis
LESIA
Observatoire de Paris-Meudon
Meudon, France

Abstract—**The Synthetic Aperture Radar (SAR) instrumentation on board the Cassini orbiter has identified large hydrocarbon liquid deposits on the surface of Titan [e.g. 1], distributed mainly around its northern polar regions. Recent studies [2] suggest that the rims of these structures display seasonal changes, where the lakes appear to be shrinking. However, the precise depth, evolution and composition of these lake-like features are still unknown. The physical and chemical characteristics of the Titan lakes will be one of the major objectives of a future space mission to Titan [e.g. 3, 4]. We propose here the application of Micro-Electro-Mechanical Systems (MEMS) as part of a science surface properties package aboard a future Lake Lander. MEMS devices offer a low cost and reduced size of instrumentation in order to accomplish the 3-D sounding of the liquid deposit and detect the presence of any biomarkers in a broader area.**

Keywords: MEMS; Future mission; Titan.

I. INTRODUCTION

The Cassini-Huygens mission has been investigating the Saturnian System since July 2004 when it performed the Saturn Orbit Insertion (SOI). Titan, the largest satellite of Saturn, is one of the major targets of the mission mainly due to its dense atmosphere. Indeed, the Cassini-Huygens mission has revealed the complex organic nitrogen-dominated atmosphere of Titan, rich in methane (1.48% [5]) and the diversity of its multivariable surface [e.g. 6].

The temperature on Titan's surface has been measured *in situ* at almost 94 K [7], which is close to the triple point of methane, meaning that methane on the satellite can exist as liquid, gas and ice [8]. Literally, Titan hosts a complex and active organic global chemistry where methane plays a critical role in a cycle resembling the terrestrial hydrological one [9].

The presence of large hydrocarbon liquid deposits on Titan's surface was assumed before the Cassini-Huygens mission, considering the thermodynamics which dominate the satellite globally [e.g. 10, 11]. Although the existence of a planetary-scale ocean has been rejected, the Cassini orbiter has unveiled concentrations of large organic pools close to both poles [1, 12, 13]. However, the Cassini RADAR beams are not able to penetrate through the liquid surfaces hindering sounding their interior. Therefore such features can be described only by modeling [e.g. 14]. However, it is crucial to understand how these hydrocarbon liquids contribute in the active methane cycle. According to the contemporary photo-dissociation rate of methane, it should be vanished within a period of 10-100 Myrs [9], since currently no methane source has been identified to replenish it. Towards this direction, as well as the necessity of the thorough investigation of these features, a lake touchdown by a probe has been proposed, carried by a future mission [3].

The usage of Micro-Electro-Mechanical-Systems (MEMS) devices as infrared emitters has been recently proposed [15], as part of the science surface properties package of a future probe to Titan like the TSSM Lake Lander or the Titan Lake Explorer [3, 4]. In this paper we suggest MEMS devices to operate as micro-laboratories by including also radio frequency RF wavelength emitters and temperature and pressure sensors. Thus, these micro-machines could obtain the 3D sounding of the liquid deposit, its chemical composition and detect the presence of any biological building blocks within the liquid. Likewise, the temperature and pressure micro-sensors could provide the vertical pressure, temperature and density profile of the liquid deposit.

The MEMS pattern, owing to their very small shape and size without reducing their operational performance, seems ideal payload for a lake lander probe on Titan as well as outer planetary space missions in general. MEMS implementation in Titan's exotic environment is a great challenge for science, engineering and space physics.

In section II we present the advantages of MEMS devices, while in section III we report MEMS already used in space applications. The experiment concept and the MEMS technology embedded is described in Section IV and Section V contains the concluding remarks.

II. MICRO-ELECTRO-MECHANICAL-SYSTEMS (MEMS) DEVICES

Any small-size product within the range of a micron to a centimeter, which also combines mechanical and electrical structures, can be identified as a MEMS device. Although the first device was constructed by H. C. Nathanson in late 1960s [16], the industrial techniques were unable to produce such minor integrated circuits and only after the 1980s did start the massive production in microscopic scale [17].

Due to their small size (20 μm to 1 mm) and shape, MEMS present properties that increase the performance of every scientific experiment for a wide range of uses and applications. In general, they provide an excellent rate of the optimum shape to the rendering performance relation. Micro-devices can now be included in every part of any experiment and also visit impossibly approachable places by traditional instrumentation. They can successfully replace quite larger devices giving the user the opportunity to explore the micro-structure of the nature. Therefore, due to the minimization of the cost both in their manufacture and operation, MEMS instruments are preferable for scientific use by improving the quality and the amount of the obtained data range.

III. MEMS Devices In Space Scene

The benefit of implementing MEMS techniques in Aerospace and Space systems is obvious especially due to the reduced requirements in size, mass, power issues of many Aerospace/Space applications [18]. In order to overcome portability and consumption limitations in any future outer planetary missions, new alternative technologies have to be implemented. The minimization of the embedded electronic instrumentation is a promising approach when it employs MEMS Systems. Therefore, the presence of MEMS in space systems offers important monetary advantages to space agencies by severely shrinking the cost of any mission, while they are reducing the weight of future spacecrafts.

Among many other applications, MEMS devices have already been used on the adaptive optics imaging technology in major telescopes [19-22]. Moreover, JPL has already developed a new MEMS deformable mirror (DM) system for NASA's adaptive space-based telescopes and in particular for Terrestrial Planet Finding (TPF) mission [23]. Likewise, several proposals have recently been submitted for future space missions and telescopes, exploiting the new leading edge of MEMS technology. Especially, MEMS techniques have been incorporated as detectors, a spectrophotometer and an IR camera of the new proposed telescope called MTEL (MEMS Telescope for Extreme Lightning) in order to observe the extreme lightning occurring in the upper atmosphere [24]. MEMS devices seem also appropriate for observing fast moving objects and transient events by the proposed space-based telescope called Obscura [25]. Moreover, MEMS have also been implemented in Space Infrared telescope for Cosmology and Astrophysics (SPICA), the Japanese coronagraph which is planned for a launch in 2017 [26].

Without doubt, although the use of MEMS in space applications is in fairly early stage, they will certainly optimize the scientific potential of any future mission.

IV. Experiment Description

MEMS as components of the science surface properties package of a future Lake Lander probe to Titan are being discussed hereafter. We propose MEMS machines to operate as (a) infrared emitters inside the liquid and (b) micro-laboratories by including also radio frequency RF wavelength emitters as well as temperature and pressure sensors.

During the last stages of the descent of a probe in Titan's atmosphere and a few meters before landing on a liquid surface, the probe will release the MEMS devices (Fig. 1). This procedure will be continued after the landing, when the probe will release more MEMS directly into the liquid. From this point, they commence their operation by transmitting instantly as IR and RF emitters. Some of these devices will float on the surface of the liquid and other will dive without stopping transmitting depending on their weight and exterior design. Schematically, the proposed experiment will be consistent of two phases:

A. *Phase One: The Deployment*

Few meters before the touchdown of the vehicle, MEMS capsules will be released into the atmosphere and begin simultaneously to operate as micro-laboratories. Another group of MEMS can be also released after the landing of the lake vehicle inside the liquid environment (Fig. 1).

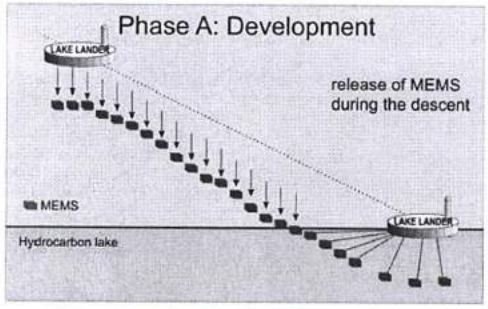

Figure 1: The deployment of the MEMS network during the entry descent and landing (EDL) procedure of the Lake Lander.

B. *Phase Two: The Operation*

Subsequently to Phase One, these devices will flow or dive into the liquid hydrocarbons and continuously transmit data to the Lander depending on the duration of their power supplies (Fig. 2).

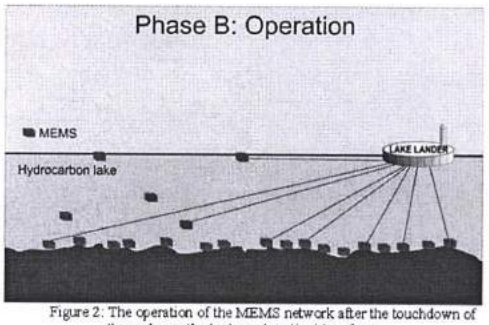

Figure 2: The operation of the MEMS network after the touchdown of the probe on the hydrocarbon liquid surface

This deployment will provide a broad network of surface and submarine IR and RF sources, while the signal receiver sensor will be aboard the Lake Lander. The MEMS micro-

probes will follow the swarm pattern [27] in which each apparatus single operation is a component of a large group of similar devices. Apparently, their combination will enhance the results.

C. MEMS components

As mentioned before, each MEMS device will include a combination of scientific instruments in micro scale. In particular, one pair of infrared (IR) and radio frequency (RF) emitters and two sensors for measuring the temperature and the pressure will be enclosed in each micro-shell. Additionally, MEMS technology can be part of the IR spectrometer's equipment aboard the Lake Lander.

1) Infrared Sources

Apart from traditional IR sources, micro-machined infrared emitters have been constructed, comprised of a photonic crystal modified micro-hotplate that emits thermally stimulated infrared radiation in a narrow band. As far as the performance of the device is concerned, it exhibits efficiencies in excess of 10 % greater than competitive technologies. These applications are like the deposited filament emitter, with the advantage of minimization of the filament which reduces the thermal mass of the system and enhances the modulated performance [28].

2) Micro-mirror

MEMS technology can be implemented at the IR spectrometer's architecture of a classical Michelson interferometer, being a transducer of the IR sensor. MEMS translational mirrors, covering an area of 1.1x1.5 mm^2 have been already tested giving reliable measurements at high scanning speed -in milliseconds- which enhances signal-to-noise ratio, suspended on a two long bending springs pattern [29]. A recent approach is the pantograph, which even though it exhibits less stability, it covers a surface mirror of 7 mm^2 providing a spectral resolution of 20 cm^{-1} [30]. The IR source can be based on silicon structure, a pattern which is already in long-term use for detecting gas in oil platforms without a failure recording [31]. In Titan's case, the target gases are mainly hydrocarbons, nitriles and carbon dioxide.

The surface temperature in Titan's environment is approximately 94 K, as it has been determined by the Huygens probe [7]. MEMS devices, released by the Lake Lander at low height and inside the liquid, have to be subjective to such low temperatures. In fact, micro-devices are already adaptable in cryogenic conditions. In the SPICA coronagraph [26] the included micro-scale machines are designed to operate in cryogenic conditions, while the whole telescope will be cooled down to 4.5 K [32]. This cryogenic environment can cause serious damage to the mirrors such as deformation and flaking. To achieve robust function in this harsh temperature conditions these micro-mirrors can be based on a silicon-on-insulator wafer, while their back surface can be made of polycrystalline silicon [33].

3) RF transmitter

The exact composition of the lake as well as its physical parameters are still unknown. If the liquid material behaves as a partial conductor (when consisting of i.e. ionic contaminants), it will prevent RF propagation in long distances. Such liquid conductors set the independent operation of these RF emitters inside the liquid under discussion, since their high permittivity and permeability cause strong attenuation of the signal power. For this reason the capsules which will be designed to dive in the lake can be connected by a wire with the mother ship as it shown in Figs 1, 2. This pattern can also support the micro probes with energy originated by the carrier. An overview of RF MEMS transmit/receive switches can be found in [34, 35]

4) Temperature and pressure sensors

The temperature and pressure sensors have the functional difference that they should interact with the environment surrounding the MEMS capsule.

Any temperature measurement is correlated on the variance of an attribute of the exposed material with any ambient temperature change. MEMS resonator-based oscillators have been proposed to be used as Complementary metal-oxide-semiconductor (CMOS) temperature sensor with a resolution of 0.008°C [36].

The MEMS pressure sensing technique is based on the silicon piezoresistive effect, where any pressure change will cause deflection and internal stain change, which will result output voltage variation [e.g. 37, 38]. Usually, a Wheatstone bridge circuit delivers such voltage measurements, in order to correlate them with the applied pressure.

V. CONCLUSION

The MEMS experiment will vertically measure the temperature and the pressure of the liquid deposit of an hydrocarbon lake on Titan's surface during a future mission, while at the same time it will operate as an internal source of infrared wavelengths giving the opportunity to the Lake Lander to analyze the composition of the lake by receiving its IR signals. Moreover, the recorded reflections of the RF signal emitted by MEMS will construct the topographical map of the bottom of the lake.

Although it is intentional to have many devices in order to construct a network, the major issue of portability comes up. However, micro-electro-mechanical devices suit perfectly in this kind of requirements because of their small shape, size and weight. Obviously, the utilization of any innovative instrumentation requires complete knowledge of the environmental issues and parameters and of course the deep understanding of their complexity.

In the contemporary market, MEMS can be easily found combining low cost and high reliability. These devices feature low power consumption, high-modulation depth, high emissivity and a long lifetime.

In a sense, this ambitious experiment can easily accomplish both the 3D sounding of the lake as well as its chemical composition.

MEMS devices combine:

1) Very small size (20 μm to 1 mm)
2) Fast pulsing (thanks to low mass of the emitter)
3) Limitation of low output power (450mW)

4) Reduction of the thermal mass of the system

5) Enhancement of the modulated performance

6) Extremely low cost.

ACKNOWLEDGMENT

The authors would like to thank Mr Dimosthenis Kouritis for fruitful discussions concerning the concept of the proposed experiment and Mr Theodosios Chatzistergos who provided valuable assistance with the figures. Anezina Solomonidou is financially supported by the European Union (European Social Fund – ESF) and Greek national funds through the Operational Program "Education and Lifelong Learning" of the National Strategic Reference Framework (NSRF) - Research Funding Program: Heracleitus II. Investing in knowledge society through the European Social Fund.

REFERENCES

[1] E. R. Stofan et al., "The lakes of Titan," *Nature*, vol. 445, pp. 61-64, 2007.

[2] E. P. Turtle et al., "Rapid and extensive surface changes near Titan's equator: evidence of April showers," *Science*, vol. 331, pp. 1414-1417, 2011.

[3] Stofan, E., et al., "The Titan Mare Explorer Mission : A Discovery mission to a Titan sea", EPSC-DPS 2011 Assembly. Nantes 3-8 Oct. 2011.

[4] TSSM, *NASA/ESA Final Report*, 30 January 2009.

[5] H. B. Niemann et al., "Composition of Titan's lower atmosphere and simple surface volatiles as measured by the Cassini-Huygens probe gas chromatograph mass spectrometer experiment," *Journal of Geophysical Research (Planets)*, vol. 115, pp. E12006, 2010.

[6] A. Coustenis and F. W. Taylor, "Titan: exploring an Earthlike World," *Series on atmospheric, oceanic and planetary physics, vol 4. World Scientific, Singapore*, 2008.

[7] M. Fulchignoni et al., "In situ measurements of the physical characteristics of Titan's environment," *Nature*, vol. 438, pp. 785-791, 2005.

[8] L. C. Kouvaris and F. M. Flasar, "Phase equilibrium of methane and nitrogen at low temperatures: Application to Titan," *Icarus*, vol. 91, pp. 112-124, 1991.

[9] S. K. Atreya et al., "Titan's methane cycle," *Planetary and Space Science*, vol. 54, pp. 1177-1187 2006.

[10] F. M. Flasar, "Oceans on Titan?," *Science*, vol. 221, pp. 55-57, 1983.

[11] J. I. Lunine, D. J. Stevenson, and Y. L. Yung, "Ethane ocean on Titan," *Science*, vol. 222, pp. 1229-1230, 1983.

[12] A. Hayes et al., "Hydrocarbon lakes on Titan: distribution and interaction with a porous regolith," *Geophysical Research Letters*, vol. 35, pp. E09204, 2008.

[13] G. Mitri, A. P. Showman, J. I. Lunine, and R. D. Lorenz, "Hydrocarbon lakes on Titan," *Icarus*, vol. 186, pp. 385-394, 2007.

[14] C. Notarnicola, B. Ventura, D. Casarano, and F. Posa, "Cassini radar data: estimation of Titan's lake features by means of a Bayesian inversion algorithm," *IEEE Transactions on Geoscience and Remote Sensing*, vol. 47, pp. 1503-1511, 2009.

[15] G. Bampasidis, A. Coustenis, A. Solomonidou, and X. Moussas, "MEMS techniques for sounding the interior of Titanic lakes," *European Planetary Science Congress, EPSC2009-722*, vol. Vol. 4, 2009.

[16] H. C. Nathanson, W. E. Newell, R. A. Wickstrom, and J. Davis, J. R., "The resonant gate transistor," *IEEE Transactions on Electron Devices*, 1967.

[17] B. Stark and J. Bernstein, "Reliability overview," *in MEMS reliability assurance guidelines for space applications (ed. B. Stark). JPL Publication 99-1*, 1999.

[17] S. W. Janson, H. Helvajian, and K. Breuer, "MEMS, microengineering and aerospace systems," *AIAA 99-3802*, 1999.

[19] D. Dayton et al., "Demonstration of new technology MEMS and liquid crystal adaptive optics on bright astronomical objects and satellites," *Optics Express*, vol. 10, pp. 1508-1508, 2002.

[20] R. Krishnamoorthy and T. Bifano, "MEMS arrays for deformable mirrors," *SPIE*, vol. 2641, 1995.

[21] M. C. Roggemann, V. M. Bright, B. M. Welsh, W. D. Cowan, and M. Lee, "Micro-electro-mechanical deformable mirrors for aberration control in optical systems," *Optical and Quantum Electronics*, vol. 31, pp. 451-468, 1999.

[22] Y. Zhou and T. G. Bifano, "Characterization of contour shapes achievable with a MEMS deformable mirror," *Proc. of SPIE*, vol. 6113, 2006.

[23] J. B. Stewart, T. G. Bifano, P. Bierden, S. Cornelissen, T. Cook, and B. M. Levine, "Design and development of a 329-segment tip-tilt piston mirrorarray for space-based adaptive optics," *Proc. of SPIE*, vol. 6113, pp. 181-189, 2006.

[24] S. Nam et al., "A telescope for observation from space of extreme lightnings in the upper atmosphere," *Nuclear Instruments and Methods in Physics Research Section A: Accelerators, Spectrometers, Detectors and Associated Equipment*, vol. 588, pp. 197-200, 2008.

[25] J. H. Park et al., "Obscura telescope with a MEMS micromirror array for space observation of transient luminous phenomena or fast-moving objects," *Optics Express*, vol. 16, pp. 20249-20249, 2008.

[26] B. Swinyard et al., "The space infrared telescope for cosmology and astrophysics: SPICA A joint mission between JAXA and ESA," *Experimental Astronomy*, vol. 23, pp. 193-219, 2009.

[27] W. Truszkowski, H. Hallock, C. Rouff, J. Karlin, J. Rash, and M. Hinchey, *Autonomous and autonomic systems: with applications to NASA intelligent spacecraft operations and exploration systems*. London: Springer-Verlag, 2009.

[28] B. Elias, "Match the emitter to the task," *Photonics Spectra*, vol. 42, 2008.

[29] M. Kraft, A. Kenda, T. Sandner, and H. Schenk, "MEMS-based compact FT-spectrometers - a platform for spectroscopic mid-infrared sensors," *IEEE Sensors*, pp. 130-133, 2008.

[30] A. Tortschanoff, M. Lenzhofer, A. Frank, A. Kenda, T. Sandner, and H. Schenk, "Improved MEMS based FT-IR spectrometer," *Int. Symposium on Optomechatronic Technologies*, pp. 116-121, 2009.

[31] R. W. Bernstein, A. Ferber, I. Johansen, S. T. Moe, H. Rogne, and D. T. Wang, "Optical MEMS for infrared gas sensors," *IEEE/LEOS Int. Conf. on Optical MEMS*, pp. 137-138, 2000.

[32] K. Enya, H. Kataza, and P. Bierden, "A Micro Electrical Mechanical Systems (MEMS)-based cryogenic deformable mirror," *Publications of the Astronomical Society of the Pacific*, vol. 121, pp. 260-265, 2009.

[33] S. Waldis, F. Zamkotsian, P. Lanzoni, W. Noell, and N. de Rooij, "Packaged MEMS micromirrors for cryogenic environment," *IEEE 21st Int. Conf. on Micro Electro Mechanical Systems*, pp. 758-761, 2008.

[34] K. Van Caekenberghe, "RF MEMS on the radar," *Microwave Magazine, IEEE*, vol. 10, pp. 99-116, 2009.

[35] S. K. Lahiri, H. Saha, and A. Kundu, "RF MEMS SWITCH: An overview at- a-glance," *4th Int. Conf. on Computers and Devices for Communication*, pp. 1-5, 2009.

[36] C. M. Jha et al., "Cmos-Compatible dual-resonator MEMS temperature sensor with milli-degree accuracy," *Int. Solid-State Sensors, Actuators and Microsystems Conf., TRANSDUCERS*, pp. 229-232, 2007.

[37] L. Lin and W. Yun, "MEMS pressure sensors for aerospace applications," *IEEE Aerospace Conf. Proc.* vol. 1, pp. 429-436, 1998.

[38] B. Li, G. Q. Zhang, D. G. Yang, H. Fengze, and H. Yang, "The effect of diaphragm on performance of MEMS pressure sensor packaging," *11th Int. Conf. on Electronic Packaging Technology & High Density Packaging*, pp. 601-606, 2010.

Appendix F3

Seismometers on the satellites of the Outer Solar System

IEEE Electronic Refereed Conference Proceedings (2011)
DOI: 10.1109/ICSpT.2011.6064647.

Seismometers on the Satellites of the Outer Solar System

Georgios Bampasidis, Anezina Solomonidou, Emmanuel Bratsolis, Konstantinos Kyriakopoulos, Xenophon Moussas, Panagiota Preka-Papadema
National & Kapodistrian University of Athens
Athens, Greece
gbabasid@phys.uoa.gr

Mathieu Hirtzig, Athena Coustenis
LESIA
Observatoire de Paris-Meudon
Meudon, France

Abstract— **The icy moons of the Outer Solar System are extremely interesting planetary bodies since they possess evidence about the origin and evolution of their systems and the Solar System in general. In terms of surface morphology, internal structure as well as their environmental uniqueness, Saturn's moons Titan and Enceladus and Jupiter's Europa and Io are the best representatives in that perspective. In this study, we propose a seismic experiment for the icy moons as a payload of future missions' landers. This suite of instruments comprises a gas monitoring sensor (micro Gas-Chromatograph) which will operate along with the seismic sensor. Data from the micro Gas-Chromatograph will give us the opportunity to correlate each time the recorded seismic data of the current gas-relief activity. We also suggest possible target areas with internal dynamic potential and multivariable surface expressions. Hence, it will be possible to identify active regions on the satellites, which will provide important information regarding the fluid transfer processes towards the surface as well as the presence of a subsurface liquid deposit.**

Keywords: Seismometer; Future mission; Icy moons; Titan; Enceladus; Europa; Io.

I. INTRODUCTION

Since 2004, the Cassini-Huygens mission has made exciting discoveries in the Saturnian system and especially with regard to its satellites Titan, the largest one, as well as the enigmatic Enceladus. Not only have their observations furthered our understanding of the complexity of these harsh environments, but many questions about their surface and interior have also been raised e.g. [1, 2].

Titan, the second largest moon of the Solar System may be representative of many planetary bodies and consequently, the understanding of its internal geology may allow scientists to enlighten the inner structure of an entire class of planets and moons [3]. Similarly, Enceladus, although it has minor dimensions (radius of 252 km), it is extremely interesting due its huge geysers which mainly feed the E-ring of Saturn. These plumes show that the moon is geologically active hosting a possible internal water ocean, the source of its vents [4, 5].

Likewise, the Galilean satellites of Jupiter present many similarities with rocky planetary bodies in terms of their surface features and atmospheric environments. Europa, the smallest of the Galilean satellites, hosts a relatively stable environment, a putative internal ocean in combination with a young evolving surface, and therefore the moon houses a great astrobiological potential [6]. On the other hand Io seems to be the most geologically active planetary moon through the solar system considering its huge volcanic activity occurring at the time of observation [7].

Without doubt, the icy satellites orbiting outer planets can significantly contribute to the study of geological processes across the solar system. Comparative Planetology can enlighten fundamental mysteries concerning the origin and the evolution of Earth and the solar system in general and predict future geological events. However, the internal geological structure of each planet or moon can only be determined by *in situ* measurements.

The local or global tectonic field, meteoroid impacts and moon's tidal deformations induced by Jupiter/Saturnian's gravity field as well as temperature and pressure fluctuations may cause ground vibrations within the icy moons. Such ground vibrations provide information about the nature of the subsurface material, its fracture and its chemical composition.

Therefore, the Cassini-Huygens mission heritage encourages scientists to discuss about launching future missions towards the outer planets' satellites. For that reason, two large L-Class missions set these moons as primary targets: Europa Jupiter System Mission (EJSM) [8] will investigate the subsurface, surfaces and atmospheres of Jupiter's satellites, while the Titan Saturn System Mission (TSSM) [9] will advance our current knowledge regarding the Saturnian icy moons. For further information the reader is referred to visit the NASA's website of the Outer Planet Flagship Mission (http://opfm.jpl.nasa.gov).

This paper examines the possibility of installing seismic experiments on icy satellites of the outer planets, setting the minimum technical requirements and describing scientific achievements and possible problems. The sections II and III contain a brief description of such space seismic equipment and the micro Gas Chromatograph (μGC) for gas sampling respectively, while in section IV the risks of such an instrument are discussed. Finally, the major goals of the proposed experiment are depicted in section V.

Data obtained by a seismic experiment, in combination with the analysis results of the μGC will provide us with details

about the interiors of the moons and their connection with the observed surface features.

II. Description Of The Seismic Instrument

The seismograph is the basic instrument for measuring any ground vibration. It mainly contains the seismometer and the unit which records the signal. The seismometer consists of three sensors placed in the same sealed case. Each sensor can be described as a pendulum that moves from its equilibrium position triggered by the ground movement. The sensors can measure any ground motion within a frequency range of 0.001 Hz to 100 Hz usually, at the north/south, east/west and vertical component in orthogonal system.

Both low and high frequencies can be recorded by broadband seismometers on Earth. Newer seismographs measure ground movements smaller than 1 nm. There are several kinds of these instruments depending from the surface's location.

By using seismic instruments we extend our knowledge of planets' interior at the Solar System. Additionally, both these space and telluric observations will help us understand better the origin and the evolutionary path of our own planet.

A. Instrument's specifications – technical requirements

The Table I below indicates the main seismic instrument's requirements considering the specifications of the shortest modern seismic instruments which operate in extreme conditions on Earth like the deep ocean floor [10]. Similar sensors can be easily found in the global market.

TABLE I. Seismic Instrument's Specifications

Power	Seismic Sensors		
	Mass	*Velocity Bandwidth*	*Operational temperature*
0.32 W	0.200g each	0.001-100Hz	below 100K

Future mission's instruments on the icy satellites' surface of the outer planets will operate in abnormal physical conditions during the entry descent and after landing of their carrier. To achieve the seismograph's accuracy in such a location the environmental factors (mainly temperature and pressure) should be considered.

B. System Hardware Architecture

The ground vibration is the input signal to the system. If the ground vibrates within a range of 0.001 Hz to 100 Hz, it will be recorded by each one of the three sensors. The sensor system contains a transducer, the device that converts the mechanical motion into electrical signal. A piezoelectric accelerometer can be used as a transducer to sense any weak or strong ground motion in a low frequency range (up to 100 Hz) without using extra power to operate [11].

Once the sensor records a motion, a signal will be sent at the Main Processor Unit (MPU) of the system. The MPU is responsible for the operation, the administration and the maintenance of the instrument and contains the core of the application software. After receiving and recording the signal from the MPU, it will be transferred at the next component of the instrument, the Multiplexer (MUX) by using a line interface circuit, which provides the connectivity between MPU and MUX.

At the MUX, data files will be compressed, converted to the right format and prepared for transmission. Because of the continuous function of the seismograph, a service for bulky data needed. The transmission frame protocols will be defined similar to the protocols of the lander's instrumentation.

Fig. 1 shows the basic functional procedure of a seismic instrument on icy moons according to the requirements mentioned above. The configuration of the system is illustrated in a simplified plot. All the components inside the dashed line in Fig. 1 are parts of the same physical equipment, the seismograph.

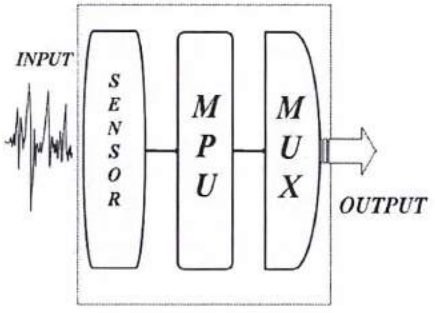

Figure 1. Functional procedure of the seismic instrument

III. Description Of The micro Gas Chromatograph

The purpose of the micro Gas Chromatograph (μGC) is to provide accurate information about the composition of the local gaseous environment. A successful relative experiment with the Gas Chromatograph Mass Spectrometer (GC-MS), was performed by the Huygens probe during its descent phase [12]. This instrument on Huygens only made measurements during the descent from 170 km to the surface and it provided us with valuable data in harsh environmental conditions. We propose the micro-GC as a payload of the lander to operate during the descent phase of the probe like in the Huygens case as well as after the touchdown. During terrestrial earthquakes close to volcanoes, amounts of gas are released, triggered by the ground vibration. In some cases this relief is used for earthquake prediction. Such instrumentation can be extremely useful on the surface of icy moons' locations where gas relief has been identified, like the tiger stripes of the Enceladus' South Pole.

The μGC tube/column mounted on the probe hosting the seismograph will be triggered when any vibration will be recorded by the seismic sensors. A presentation of a low power μGC column can be found in [13]. The instrument will also take samples of the local atmospheric envelope in several

specific times which will enable us to determine any temporal variations in chemical composition due to any recorded vibration as well as during in the descent phase of the lander. Such measurements can be extremely useful in the case of Enceladus if the probe landed close to the tiger stripes, the great linear surface fractures from where its plumes spread out.

In fig. 2 the procedure of the operation of the μGC is depicted.

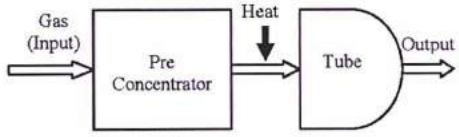

Figure 2. Operational flow diagram of the micro Gas Chromatograph

Briefly, the instrument will collect the sample from the local gas and collected material will be droved into the pre concentrator device where the concentration will be increased. Then, the sample will be heated in order to release the gas and it will be passed through the tube. This is the separation phase, critical to the analysis procedure where each component of the sampled gas needs its specific time to traverse the tube. Eventually, the identification stage follows this separation. The design of the signal condition circuit which converts the content of the separated gas to electric signal can follow the standards of [14]. The μGC will perform batch sampling like the Huygens/GC-MS did during Huygens Descent phase [15]. Hydrogen will be selected as the carrier gas like in the Huygens/GC-MS case [12].

By correlating the seismic soundings with the gas composition, we can infer about the significance of the internal gases and the mechanism beyond their relief. These measurements can help us solve the puzzle of icy moons interiors.

IV. Problems And Risks Of A Future Seismic Experiment On Outer Solar System

Terms and Conditions of the implementation of seismic instrumentation on icy moons and the possibly emerged problems and difficulties are listed in the Table II below.

TABLE II. Scientific And Technical Problems And Difficulties

Terms and Conditions	Possible Problems and Difficulties		
	Science	*Engineering*	*Precautions*
Fluctuations in temperature	Accuracy affected	Malfunction of the sensors	Special thermal shield
Surface characteristics	Sensors' deformation	Loose the equilibrium position	Special installation and stabilization needed
Dense atmosphere	Chemical Corrosion	Insufficient solar power to recharge batteries	Shield case
Stability of the apparatus	First time in space exploration	Orientation lost	Robotic installation of the seismometer
Maintenance	No recordings	Impossible to repair	Autonomous System
Data transmission	Radio frequency signals	A permanent link needed	Orbiter and large ground radiotelescopes
Exact recordings	3D plotting	Different devices	Seismic network needed
Ground/wind noise	Low Signal to Noise ratio	Stable structure	A shallow hole needed for installation
Power	Continuous operation	Batteries	Radioisotope thermoelectric Generator (RTG)

Since we lack any knowledge of seismic events on icy moons, data from a seismic instrument and global radar mapping for long periods of time will be of extreme importance. Obviously, due to power limitations, any instrument on these surfaces will operate continuously from the touchdown until its battery discharging. Therefore, a more durable energy source is necessary. A radioisotope thermoelectric generator (RTG) is to be considered.

An appropriate location for the placement of a seismic equipment will ensure that its recordings will represent accurately and separately every ground vibration. For this purpose, on Earth the seismic instruments should be placed in a hole of approximately 0.5 m depth. Thus, less ground noise will be recorded. Noise on an icy surface can be originated by the atmosphere due to its seasonal and diurnal effects as described in [16] for the Titan case. Noise can be produced also from the local wind and meteor impacts.

In the case of Titan, its dense atmosphere protects the surface from meteoroid impacts - few craters have been observed [17] – therefore, the seismometers will record merely interior events. On the other hand the same instrumentation on Enceladus, Io and Europa will also measure vibrations caused by external sources.

The proper contact between the feet of the seismograph and the local surface at the landing area stands for another issue to be confronted. Any particles and dust can easily perturb the seismic sensors during their function and cause random errors at the sensor's record. This type of surface features has already found on Titan. The Huygens probe landed on a relatively soft solid surface whose properties consisting of analogous to wet clay, lightly packed snow and wet or dry sand [18]. Moreover, the Descent Imager and Spectral Radiometer's (DISR) surface images showed rounded stones approximately 15 cm in diameter to lie on top of a finer-grained surface in variable spatial distribution [19]. If the icy pebbles lying over the instrument's feet move or/and melt, the equilibrium position of the seismic equipment will disturbed and the sensors will lose their orientation. The measurements should be corrected if such a micro-movement of the probe is noticed.

Experience gained from the Apollo Passive Seismic Experiment (PSE) on the Moon will be extremely useful for

such an ambitious effort. PSE was the first extraterrestrial network of seismic instruments and it consisted of four seismometers deployed by the astronauts on the lunar surface between 1969 and 1972 while Earth-based stations received data for eight years. The Apollo seismometers recorded 12,558 events and these seismic data have been recently reanalyzed [20]. A seismic experiment has also been performed on Mars as part of the Viking mission payload [21]. The Viking seismograph performed a long-term operation and measured ground vibrations without any significant seismic signals. The primary source of the recorded noise was the local wind. The dimensions of the equipment were 12x15x12 cm, weighted 2.2 kg and needed 3.5 W to operate.

V. Major Scientific Goals-Discussion

Icy moons of the outer planets seem to be or have been active like our own planet, as far as their atmospheric circulation, surface geological processes and tectonics are concerned. Each moon has its own atmospheric and geological record and therefore it should be treated separately. The internal structure of these satellites may be involved in some surface processes. Hence, since only the seismic instrumentation can map the subsurface layers, determine their composition and structure and measure their thickness, we will consider mounting it in a future mission as part of a landing probe payload.

Seismic waves from distant events travel deeper into the interior of a planetary body than waves from nearby events. Hence, measuring events at various distances by seismometers can provide the variance with depth of seismic velocities within icy moons.

Future missions to the outer planets icy moons will be a great opportunity for comparative planetology providing proofs of active planetary systems. A seismic experiment can identify the existence of liquid internal deposits, with a great astrobiological potential. Such isolated environments that consist of water and organics, components that have already been identified on most icy satellites, provide ideal conditions for the survival of biological building blocks. Table III lists the main benefits and advances in short terms of mounting seismic equipment in the surface of icy moons.

TABLE III. The Benefits Of Future Seismic Instrumentation

Features	Benefits of space seismic experiments	
	Icy moons	*Engineering*
Completed scientific experiment	Regional scale geology	New science- Planetary Seismology
Small size	Ideal as a payload for a space mission lander	Low power consumption
Continuous operation	Improve modeling for the three-dimensional internal structure	Service for bulky data needed
Evolution of seismic	Earthquake prediction Tidal effects caused by	No special software needs to be developed
instruments and applications	Jupiter/Saturn	

References

[1] A. Coustenis and M. Hirtzig, "Cassini-Huygens results on Titan's surface," *Research in Astronomy and Astrophysics*, vol. 9, pp. 249-268, 2009.

[2] R. H. Brown et al, "Composition and Physical Properties of Enceladus' Surface," *Science*, vol. 311, pp. 1425-1428, 2006.

[3] A. Coustenis and F. W. Taylor, "Titan: exploring an Earthlike World," *Series on atmospheric, oceanic and planetary physics, vol 4. World Scientific, Singapore*, 2008.

[4] M. K. Dougherty et al, "Identification of a Dynamic Atmosphere at Enceladus with the Cassini Magnetometer," *Science*, vol. 311, pp. 1406-1409, 2006.

[5] G. C. Collins and J. C. Goodman, "Enceladus' south polar sea," *Icarus*, vol. 189, pp. 72-82, 2007.

[6] J. S. Kargel et al, "Europa's Crust and Ocean: Origin, Composition, and the Prospects for Life," *Icarus*, vol. 148, pp. 226-265, 2000.

[7] R. Lopes and J. Spencer, "Io After Galileo: A view of Jupiter's volcanic moon," *Berlin, Springer*, 2006.

[8] EJSM, *NASA/ESA Final Report*, 30 January 2009.

[9] TSSM, *NASA/ESA Final Report*, 30 January 2009.

[10] B. Romanowicz et al, "The Monterey Bay broadband ocean bottom seismic observatory," *ANNALS OF GEOPHYSICS*, vol. 49, 2006.

[11] F. Garcia, E. L. Hixson, C. I. Huerta, and H. Orozco, "Seismic Accelerometer," *Instrumentation and Measurement Technology Conference, IMTC/99, Proceedings of the 16th IEEE*, vol. 3, pp. 1342-1346,

[12] H. B. Niemann et al, "The Gas Chromatograph Mass Spectrometer for the Huygens Probe," *Space Science Reviews*, vol. 104, pp. 553-591, 2002. 1999.

[13] J. A. Potkay, G. R. Lambertus, R. D. Sacks, and K. D. Wise, "A Low-Power Pressure- and Temperature-Programmable Micro Gas Chromatography Column," *Journal of Microelectromechanical Systems*, vol. 16, pp. 1071-1078, 2007.

[14] L. Hongfei, L. Chaoli, and C. Zhong, "Signal Conditioning Circuit Design for Micro Gas Chromatograph," *International Forum on Computer Science-Technology and Applications*, vol. 3, pp. 86-89, 2009.

[15] H. B. Niemann et al, "The abundances of constituents of Titan's atmosphere from the GCMS instrument on the Huygens probe," *Nature*, vol. 438, pp. 779-784, 2005.

[16] M. Hirtzig, T. Tokano, S. Rodriguez, S. le Mouelic, and C. Sotin, "A review of Titan's atmospheric phenomena," *Astronomy and Astrophysics Review*, vol. 17, pp. 105-147, 2009.

[17] C. Elachi et al, "Cassini Radar Views the Surface of Titan," *Science*, vol. 308, pp. 970-974, 2005.

[18] J. C. Zarnecki et al, "A soft solid surface on Titan as revealed by the Huygens Surface Science Package," *Nature*, vol. 438, pp. 792-795, 2005.

[19] M. G. Tomasko et al, "Rain, winds and haze during the Huygens probe's descent to Titan's surface," *Nature*, vol. 438, pp. 765 - 778, 2005.

[20] R. C. Bulow, C. L. Johnson, and P. M. Shearer, "New events discovered in the Apollo lunar seismic data," *Journal of Geophysical Research (Planets)*, vol. 110, pp. 10003, 2005.

[21] D. L. Anderson et al, "Seismology on Mars", *Journal of Geophysical Research*, vol. 82, pp. 4524-4546, 1977.

Bibliography

Achilleos, N., Arridge, C. S., Bertucci, C., Jackman, C. M., Dougherty, M. K., Khurana, K. K. & Russell, C. T. (2008). Large-scale dynamics of Saturn's magnetopause: Observations by Cassini. *Journal of Geophysical Research, 113*(A11), A11209.

Achterberg, R. K., Conrath, B. J., Gierasch, P. J., Flasar, F. M. & Nixon, C. A. (2008). Titan's middle-atmospheric temperatures and dynamics observed by the Cassini Composite Infrared Spectrometer. *Icarus, 194*, 263-277.

Achterberg, R. K., Gierasch, P. J., Conrath, B. J., Michael Flasar, F. & Nixon, C. A. (2011). Temporal variations of Titan's middle-atmospheric temperatures from 2004 to 2009 observed by Cassini/CIRS. *Icarus, 211*, 686-698.

Agren, K., Wahlund, J. E., Garnier, P., Modolo, R., Cui, J., Galand, M. & Muller-Wodarg, I. (2009). On the ionospheric structure of Titan. *Planetary and Space Science, 57* (14-15), 1821-1827.

Ainsworth, L. & Viegut, D. (2006). *Common formative assessments*: Thousand Oaks, CA: Corwin Press.

Alexopoulou, E. & Driver, R. (1996). Small-Group Discussion in Physics: Peer Interaction Modes in Pairsand Fours. *Journal of Research in Science Teaching, 33*, 1099-1114.

Anderson, C. M. & Samuelson, R. E. (2011). Titan's aerosol and stratospheric ice opacities between 18 and 500 μm: Vertical and spectral characteristics from Cassini CIRS. *Icarus, 212*(2), 762-778.

Anderson, J. D., Jacobson, R. A., McElrath, T. P., Moore, W. B., Schubert, G. & Thomas, P. C. (2001). Shape, Mean Radius, Gravity Field, and Interior Structure of Callisto. *Icarus, 153*, 157-161.

Anderson, J. D., Lau, E. L., Sjogren, W. L., Schubert, G. & Moore, W. B. (1996). Gravitational constraints on the internal structure of Ganymede. *Narure, 384*(6609), 541-543.

Anderson, J. D., Lau, E. L., Sjogren, W. L., Schubert, G. & Moore, W. B. (1997). Europa's Differentiated Internal Structure: Inferences from Two Galileo Encounters. *Science, 276*(5316), 1236-1239.

Anderson, J. D., Schubert, G., Jacobson, R. A., Lau, E. L., Moore, W. B. & Sjogren, W. L. (1998). Europa's Differentiated Internal Structure: Inferences from Four Galileo Encounters. *Science, 281*, 2019-2019.

Arie, E. & Johns, J. W. C. (1992). The bending energy levels of C_4H_2. *Journal of Molecular Spectroscopy, 155*, 195-204.

Armstrong, J. S. (2012). Natural Learning in Higher Education. *Encyclopedia of the Sciences of Learning. Heidelberg: Springer.*

Arridge, C. S., Khurana, K. K., Russell, C. T., Southwood, D. J., Achilleos, N., Dougherty, M. K., Coates, A. J. & Leinweber, H. K. (2008). Warping of Saturn's magnetospheric and magnetotail current sheets. *Journal of Geophysical Research, 113*(A8), A08217.

Atreya, S. K., Adams, E. Y., Niemann, H. B., Demick-Montelara, J. E., Owen, T. C., Fulchignoni, M., Ferri, F. & Wilson, E. H. (2006). Titan's methane cycle. *Planetary and Space Science, 54*(12), 1177-1187

Backes, H., Neubauer, F. M., Dougherty, M. K., Achilleos, N., Andre, N., Arridge, C. S., Bertucci, C., Jones, G. H., Khurana, K. K., Russell, C. T. & Wennmacher, A. (2005). Titan's Magnetic Field Signature During the First Cassini Encounter. *Science, 308*, 992-995.

Bampasidis, G., Coustenis, A., Achterberg, R. K., Vinatier, S., Lavvas, P., Nixon, C. A., Jennings, D. E., Teanby, N., Flasar, F. M., Carlson, R., Moussas, X., Preka-Papadema, P., Romani, P., Guandique, E. & Stamogiorgos, S. (2012a). Thermal and chemical structure variations in Titan's during the Cassini mission. *Astrophysical Journal,* 760, 144.

Bampasidis, G., Coustenis, A., Achterberg, R. K., Jennings, D. E., Nixon, C. A., Vinatier, S., Lavvas, P., Carlson, R., Teanby, N., Flasar, F. M., Guandique, E. & Stamogiorgos, S. (2012b). *Evolution of minor trace gases and isotopic ratios in Titan's stratosphere using CIRS/Cassini spectra.* Paper presented at the EGU General Assembly 2012, Vienna, Austria.

Bampasidis, G., Solomonidou, A., Coustenis, A., Knapmeyer, M. & Bratsolis, E. (2012c). *MEMS-based seismic sensors on Titan and Enceladus.* Paper presented at the International Planetary Probe Workshop 9, Toulouse, France.

Bampasidis, G., Solomonidou, A., Bratsolis, E., Kyriakopoulos, K., Moussas, X., Preka-Papadema, P., Hirtzig, M. & Coustenis, A. (2011a). *Seismometers on the satellites of the Outer Solar System.* Paper presented at the 2nd International Conference on Space Technology (ICST) Athens, Greece, 15-17 Sept., DOI: 10.1109/ICSpT.2011.6064647.

Bampasidis, G., Solomonidou, A., Bratsolis, E., Kyriakopoulos, K., Moussas, X., Preka-Papadema, P., Hirtzig, M. & Coustenis, A. (2011b). *Sounding the interior of Titan's lakes by using Micro-Electro-Mechanical Systems (MEMS).* Paper presented at the 2nd International Conference on Space Technology (ICST), Athens, Greece, 15-17 Sept., DOI: 10.1109/ICSpT.2011.6064648.

Bampasidis, G., Lavvas, P., Coustenis, A., Nixon, C., Achterberg, R., Jennings, D., Vinatier, S., Flasar, F. M., Moussas, X. & Preka-Papadema, P. (2010a). *Benzene in Titan's atmospheric envelope from Cassini/CIRS data.* Paper presented at the Faraday Discussions 147: Chemistry of the Planets, (14 - 16 June) Saint Jacut de la Mer (France).

Bampasidis, G., Solomonidou, A., Coustenis, A., Moussas, X., Lebreton, J. P., Kyriakopoulos, K., Preka-Papadema, P., Bratsolis, E. & Stamogiorgos, S. (2010b). *Future Saturn System Exploration Outreach Ideas.* Paper presented at the European Planetary Science Congress, 20-24 September, Rome, Italy.

Bampasidis, G., Coustenis, A., Solomonidou, A. & Moussas, X. (2009). MEMS Techniques for Sounding the Interior of Titanic Lakes. *European Planetary Science Congress, EPSC2009-722, Vol. 4.*

Barnes, J. W., Brown, R. H., Radebaugh, J., Buratti, B. J., Sotin, C., Le Mouelic, S., Rodriguez, S., Turtle, E. P., Perry, J., Clark, R., Baines, K. H. & Nicholson, P. D. (2006). Cassini observations of flow-like features in western Tui Regio, Titan. *Geophysical Research Letters, 33*, 16204.

Barnes, J. W., Brown, R. H., Soderblom, L., Buratti, B. J., Sotin, C., Rodriguez, S., Le Mouelic, S., Baines, K. H., Clark, R. & Nicholson, P. (2007a). Global-scale surface spectral variations on Titan seen from Cassini/VIMS. *Icarus, 186*, 242-258.

Barnes, J. W., Brown, R. H., Soderblom, L., Sotin, C., Le Mouelic, S. p., Rodriguez, S., Jaumann, R., Beyer, R. A., Buratti, B. J., Pitman, K., Baines, K. H., Clark, R. & Nicholson, P. (2008). Spectroscopy, morphometry, and photoclinometry of Titan's dunefields from Cassini/VIMS. *Icarus, 195*, 400-414.

Barnes, J. W., Lemke, L., Foch, R., McKay, C. P., Beyer, R. A., Radebaugh, J., Atkinson, D. H., Lorenz, R. D., Le Mouelic, S., Rodriguez, S., Gundlach, J., Giannini, F., Bain, S., Flasar, F. M., Hurford, T., Anderson, C. M., Merrison, J., Adamkovics, M., Kattenhorn, S. A., Mitchell, J., Burr, D. M., Colaprete, A., Schaller, E., Friedson, A. J., Edgett, K. S., Coradini, A., Adriani, A., Sayanagi, K. M., Malaska, M. J., Morabito, D. & Reh, K. (2012). AVIATR-Aerial Vehicle for In-situ and Airborne Titan Reconnaissance. A Titan airplane mission concept. *Experimental Astronomy, 33*, 55-127.

Barnes, J. W., Radebaugh, J., Brown, R. H., Wall, S., Soderblom, L., Lunine, J., Burr, D., Sotin, C., Mouelic, S. L., Rodriguez, S., Buratti, B. J., Clark, R., Baines, K. H., Jaumann, R., Nicholson, P. D., Kirk, R. L., Lopes, R., Lorenz, R. D., Mitchell, K. & Wood, C. A. (2007b). Near-infrared spectral mapping of Titan's mountains and channels. *Journal of Geophysical Research, 112*, E11006.

Barr, A. C. & McKinnon, W. B. (2007). Convection in Enceladus' ice shell: Conditions for initiation. *Geophysical Research Letters, 34*, 09202.

Barr, A. C., Pappalardo, R. T. & Stevenson, D. J. (2001). *Rise of Deep Melt into Ganymede's Ocean and Implications for Astrobiology.* Lunar and Planetary Science XXXII, 1781.

Barrington, B. L. & Hendricks, B. (1988). Attitudes toward science and science knowledge of intellectually gifted and average students in third, seventh, and eleventh grades. *Journal of Research in Science Teaching, 25*, 679-687.

Beeman, M., Durham, W. B. & Kirby, S. H. (1988). Friction of Ice. *Journal of Geophysical Research, 93*(B7), 7625-7633.

Beghin, C., Canu, P., Karkoschka, E., Sotin, C., Bertucci, C., Kurth, W. S., Berthelier, J. J., Grard, R., Hamelin, M., Schwingenschuh, K. & Simões, F. (2009a). New insights on Titan's plasma-driven Schumann resonance inferred from Huygens and Cassini data. *Planetary and Space Science, 57*, 1872-1888.

Beghin, C., Canu, P., Karkoschka, E., Sotin, C., Bertucci, C., Kurth, W. S., Berthelier, J. J., Grard, R., Hamelin, M., Schwingenschuh, K. & Simoμes, F. (2009b). New insights on Titan's plasma-driven Schumann resonance inferred from Huygens and Cassini data. *Planetary and Space Science, 57*, 1872-1888.

Beghin, C., Randriamboarison, O. l., Hamelin, M., Karkoschka, E., Sotin, C., Whitten, R. C., Berthelier, J.-J., Grard, R. j. & Simoμes, F. (2012). Analytic theory of Titan's Schumann resonance: Constraints on ionospheric conductivity and buried water ocean. *Icarus, 218*, 1028-1042.

Behounkova, M., Tobie, G., Choblet, G. & Cadek, O. (2012). Tidally-induced melting events as the origin of south-pole activity on Enceladus. *Icarus, 219*, 655-664.

Belenkaya, E. S., Alexeev, I. I., Kalegaev, V. V. & Blokhina, M. S. (2006). Definition of Saturn's magnetospheric model parameters for the Pioneer 11 flyby. *Annales Geophysicae, 24*, 1145-1156.

Bell, J. M., Westlake, J. & Waite, J. H. (2011). Simulating the time-dependent response of Titan's upper atmosphere to periods of magnetospheric forcing. *Geophysical Research Letters, 38*, 06202-06202.

Benner, R., Benitez-Nelson, B., Kaiser, K. & Amon, R. M. W. (2004). Export of young terrigenous dissolved organic carbon from rivers to the Arctic Ocean. *Geophysical Research Letters, 31*, 05305-05305.

Berendsen, M. L. (2005). Conceptual Astronomy Knowledge among Amateur Astronomers. *Astronomy Education Review, 4*(1), 1.

Berk, A., Bernstein, L. S., Anderson, G. P., Acharya, P. K., Robertson, D. C., Chetwynd, J. H. & Adler-Golden, S. M. (1998). MODTRAN Cloud and Multiple Scattering Upgrades with Application to AVIRIS. *Remote Sensing of Environment, 65*(3), 367-375.

Bertero, M. & Boccacci, P. (1998). *Introduction to Inverse Problems in Imaging.* Bristol: IOP Publishing.

Bertero, M., De Mol, C. & Pike, E. R. (1985). Linear inverse problems with discrete data: I - General formulation and singular system analysis. *Inverse Problems, 1*, 300-330.

Bertucci, C., Achilleos, N., Dougherty, M. K., Modolo, R., Coates, A. J., Szego, K., Masters, A., Ma, Y., Neubauer, F. M., Garnier, P., Wahlund, J. E. & Young, D. T. (2008). The Magnetic Memory of Titan's Ionized Atmosphere. *Science, 321*(5895), 1475-1478.

Bezard, B., Marten, A. & Paubert, G. (1993). *Detection of Acetonitrile on Titan.* Paper presented at the 25th DPS Meeting, Bulletin of the American Astronomical Society.

Bezard, B., Nixon, C. A., Kleiner, I. & Jennings, D. E. (2007). Detection of $^{13}CH_3D$ on Titan. *Icarus, 191*, 397-400.

Bird, M. K., Allison, M., Asmar, S. W., Atkinson, D. H., Avruch, I. M., Dutta-Roy, R., Dzierma, Y., Edenhofer, P., Folkner, W. M., Gurvits, L. I., Johnston, D. V., Plettemeier, D., Pogrebenko, S. V., Preston, R. A. & Tyler, G. L. (2005). The vertical profile of winds on Titan. *Nature, 438*, 800-802.

Bird, M. K., Dutta-Roy, R., Heyl, M., Allison, M., Asmar, S. W., Folkner, W. M., Preston, R. A., Atkinson, D. H., Edenhofer, P., Plettemeier, D., Wohlmuth, R., Iess, L. & Tyler, G. L. (2002). The Huygens Doppler Wind Experiment - Titan Winds Derived from Probe Radio Frequency Measurements. *Space Science Reviews, 104*, 613-640.

Blanc, M., Alibert, Y., André, N., Atreya, S., Beebe, R., Benz, W., Bolton, S., Coradini, A., Coustenis, A., Dehant, V., Dougherty, M., Drossart, P., Fujimoto, M., Grasset, O., Gurvits, L., Hartogh, P., Hussmann, H., Kasaba, Y., Kivelson, M., Khurana, K., Krupp, N., Louarn, P., Lunine, J., McGrath, M., Mimoun, D., Mousis, O., Oberst, J., Okada, T., Pappalardo, R., Prieto-Ballesteros, O., Prieur, D., Regnier, P., Roos-Serote, M., Sasaki, S., Schubert, G., Sotin, C., Spilker, T., Takahashi, Y., Takashima, T., Tosi, F., Turrini, D., Van Hoolst, T. & Zelenyi, L. (2009). LAPLACE: A mission to Europa and the Jupiter System for ESA's Cosmic Vision Programme. *Experimental Astronomy, 23*(3), 849-892.

Blanc, M., Kallenbach, R. & Erkaev, N. (2005). Solar System Magnetospheres. *Space Science Reviews, 116*(1), 227-298.

Blass, W. E., Jennings, L., Ewing, A. C., Daunt, S. J., Senesac, M. C. W. L., Hager, S. & Hillman D. C. Reuter J. M. Sirota, J. J. (2001). Absolute intensities in the v7 band of ethylene: tunable laser measurements used to calibrate FTS broadband spectra. *Journal of Quantitative Spectroscopy and Radiative Transfer, 68*, 467-472.

Borysow, A. & Tang, C. (1993). Far Infrared CIA Spectra of N_2-CH_4 Pairs for Modeling of Titan's Atmosphere. *Icarus, 105*, 175-183.

Brandt, P. C., Dialynas, K., Dandouras, I., Mitchell, D. G., Garnier, P. & Krimigis, S. M. (2012). The distribution of Titan's high-altitude (out to 50,000 km) exosphere from energetic neutral atom (ENA) measurements by Cassini/INCA. *Planetary and Space Science, 60*, 107-114.

Bratsolis, E., Bampasidis, G., Solomonidou, A. & Coustenis, A. (2012). A despeckle filter for the Cassini synthetic aperture radar images of Titan's surface. *Planetary and Space Science, 61*, 108-113.

Bratsolis, E. & Sigelle, M. (2003). Fast SAR image restoration, segmentation, and detection of high-reflectance regions. *IEEE Transactions on Geoscience and Remote Sensing, 41*(12), 2890-2899.

Broadfoot, A. L., Sandel, B. R., Shemansky, D. E., Holberg, J. B., Smith, G. R., Strobel, D. F., McConnell, J. C., Kumar, S., Hunten, D. M., Atreya, S. K., Donahue, T. M., Moos, H. W., Bertaux, J. L., Blamont, J. E., Pomphrey, R. B. & Linick, S. (1981). Extreme ultraviolet observations from Voyager 1 encounter with Saturn. *Science, 212*, 206-211.

Brophy, J. R. & Noca, M. (1998). Electric Propulsion for Solar System Exploration. *Journal of Propulsion and Power, 14*(5), 700-707.

Brown, M. E., Schaller, E. L., Roe, H. G., Chen, C., Roberts, J., Brown, R. H., Baines, K. H. & Clark, R. N. (2009). Discovery of lake-effect clouds on Titan. *Geophysical Research Letters, 36*, 01103.

Brown, R. H., Baines, K. H., Bellucci, G., Bibring, J. P., Buratti, B. J., Capaccioni, F., Cerroni, P., Clark, R. N., Coradini, A., Cruikshank, D. P., Drossart, P., Formisano, V., Jaumann, R., Langevin, Y., Matson, D. L., McCord, T. B., Mennella, V., Miller, E., Nelson, R. M., Nicholson, P. D., Sicardy, B. & Sotin, C. (2004). The Cassini Visual And Infrared Mapping Spectrometer (Vims) Investigation. *Space Science Reviews, 115*, 111-168.

Brown, R. H., Clark, R. N., Buratti, B. J., Cruikshank, D. P., Barnes, J. W., Mastrapa, R. M. E., Bauer, J., Newman, S., Momary, T., Baines, K. H., Bellucci, G., Capaccioni, F., Cerroni, P., Combes, M., Coradini, A., Drossart, P., Formisano, V., Jaumann, R., Langevin, Y., Matson, D. L., McCord, T. B., Nelson, R. M., Nicholson, P. D., Sicardy, B. & Sotin, C. (2006). Composition and Physical Properties of Enceladus' Surface. *Science, 311*, 1425-1428.

Brown, R. H., Soderblom, L. A., Soderblom, J. M., Clark, R. N., Jaumann, R., Barnes, J. W., Sotin, C., Buratti, B., Baines, K. H. & Nicholson, P. D. (2008). The identification of liquid ethane in Titan's Ontario Lacus. *Nature, 454*, 607-610.

Bulat, S., Alekhina, I. & Petit, J. R. (2009). *Life detection strategy for subglacial Lake Vostok, Antarctica: Lessons for Jovian moon Europa.* Goldschmidt Conference, 21-26 June Davos, Switzerland.

Bulow, R. C., Johnson, C. L. & Shearer, P. M. (2005). New events discovered in the Apollo lunar seismic data. *Journal of Geophysical Research (Planets), 110*, 10003.

Burr, D. M., Jacobsen, R. E., Roth, D. L., Phillips, C. B., Mitchell, K. L. & Viola, D. (2009). Fluvial network analysis on Titan: Evidence for subsurface structures and west-to-east wind flow, southwestern Xanadu. *Geophysical Research Letters, 36*, 22203-22207.

Cabane, M., Chassefiere, E. & Israel, G. (1992). Formation and growth of photochemical aerosols in Titan's atmosphere. *Icarus, 96*(2), 176-189.

Caldwell, J. (1977). Thermal radiation from Titan's atmosphere. In J. A. Burns (Ed.), *IAU Colloq. 28: Planetary Satellites* (pp. 438-450).

Calvin, W. M. & Spencer, J. R. (1997). Latitudinal Distribution of O_2 on Ganymede: Observations with the Hubble Space Telescope. *Icarus, 130*, 505-516.

Campbell, D. B., Black, G. J., Carter, L. M. & Ostro, S. J. (2003). Radar Evidence for Liquid Surfaces on Titan. *Science, 302*, 431-434.

Carlson, R. C., Guandique, E. A., Jennings, D. E., Albright, S. A., Pilorz, S. H., Brasunas, J. C., Kunde, V. G., Flasar, F. M., Gorius, N. J. P., Mamoutkine, A. A., Nixon, C. A., Bjoraker, G. L., Achterberg, R. K., Coustenis, A., Bampasidis, G., Hesman, B. E., Tingley, J. S., Kaelberer, M. S., Vinatier, S. & Cottini, V. (2011). *Removing Artifacts in the Calibration of Cassini CIRS Spectra of Saturn and Titan.* Paper presented at the 2011 EPSC-DPS Joint Meeting Nantes, France.

Carlson, R. W. (1999). A Tenuous Carbon Dioxide Atmosphere on Jupiter's Moon Callisto. *Science, 283*(5403), 820-821.

Carlson, R. W., Anderson, M. S., Mehlman, R. & Johnson, R. E. (2005). Distribution of hydrate on Europa: Further evidence for sulfuric acid hydrate. *Icarus, 177*, 461-471.

Carr, M. H. & Head, J. W. (2003). Oceans on Mars: An assessment of the observational evidence and possible fate. *Journal of Geophysical Research (Planets), 108*, 5042.

Chamberlain, J. W. (1963). Planetary coronae and atmospheric evaporation. *Planetary and Space Science, 11*(8), 901-960.

Chedin, A., Husson, N. & Scott, N. A. (1982). Une banque de donnees pour l'etude des phenomenes de transfert radiatif dans les atmospheres planetaires: la banque GEISA. *Bull. Inform. Centre Donnees Stellaires (France), 22*, 121.

Chitroub, S., Houacine, A. & Sansal, B. (2002). Statistical characterisation and modelling of SAR images. *Signal Processing, 82*(1), 69-92.

Choukroun, M. & Sotin, C. (2012). Is Titan's shape caused by its meteorology and carbon cycle? *Geophysical Research Letters, 39*, 04201.

Clark, R. N., Curchin, J. M., Barnes, J. W., Jaumann, R., Soderblom, L., Cruikshank, D. P., Brown, R. H., Rodriguez, S., Lunine, J., Stephan, K., Hoefen, T. M., Le Mouelic, S., Sotin, C., Baines, K. H., Buratti, B. J. & Nicholson, P. D. (2010). Detection and Mapping of Hydrocarbon Deposits on Titan. *J. Geophys. Res.*, 115, E10005.

Clough, M. P. (2011). The Story Behind the Science: Bringing Science and Scientists to Life in Post-Secondary Science Education. *Science & Education, 20*(7-8), 701-717.

Coates, A. J., Crary, F. J., Lewis, G. R., Young, D. T., Waite, J. H. & Sittler, E. C. (2007). Discovery of heavy negative ions in Titan's ionosphere. *Geophysical Research Letters, 34*, 22103.

Coates, A. J., Jones, G. H., Lewis, G. R., Wellbrock, A., Young, D. T., Crary, F. J., Johnson, R. E., Cassidy, T. A. & Hill, T. W. (2010). Negative ions in the Enceladus plume. *Icarus, 206*, 618-622.

Cockell, C. S. (1999). Life on Venus. *Planetary and Space Science, 47*, 1487-1501.

Cohen, K. C. (1999). *Internet Links for Science Education: Student-Scientist Partnerships.*

Coll, P., Coscia, D., Gazeau, M.-C., Guez, L. & Raulin, F. o. (1998). Review and Latest Results of Laboratory Investigations of Titan's Aerosols. *Origins of Life and Evolution of the Biosphere, 28*, 195-213.

Coll, P., Coscia, D., Smith, N., Gazeau, M. C., Ramirez, S. I., Cernogora, G., Israel, G. & Raulin, F. (1999). Experimental laboratory simulation of Titan's atmosphere: aerosols and gas phase. *Planetary and Space Science, 47*, 1331-1340.

Collins, G., McKinnon, W., Moore, J. M., Nimmo, F., Pappalardo, R. T., Prockter, L. M. & Schenk, H. (2009). Tectonics of the outer planet satellites. In T. R. Watters & R. A. Schultz (Eds.), *Planetary Tectonics* (pp. 264-350): Cambridge University Press.

Collins, G. C. & Goodman, J. C. (2007). Enceladus' south polar sea. *Icarus, 189*, 72-82.

Comas Solá, J. (1908). Observations des satellites principaux de Jupiter et de Titan. *Astronomische Nachrichten, 4290 (179)*(18), 289 - 290.

Conrath, B. J., Gierasch, P. J. & Ustinov, E. A. (1998). Thermal Structure and Para Hydrogen Fraction on the Outer Planets from Voyager IRIS Measurements. *Icarus, 135*, 501-517.

Cooper, J. & Mueck, R. (1990). Student involvement in learning: Cooperative learning and college instruction. *Journal on Excellence in College Teaching, 7*(1), 68-76.

Cooper, J. F., Cooper, P. D., Sittler, E. C., Sturner, S. J. & Rymer, A. M. (2009). Old Faithful model for radiolytic gas-driven cryovolcanism at Enceladus. *Planetary and Space Science, 57*(13), 1607-1620.

Cooper, J. F., Johnson, R. E., Mauk, B. H., Garrett, H. B. & Gehrels, N. (2001). Energetic Ion and Electron Irradiation of the Icy Galilean Satellites. *Icarus, 149*, 133-159.

Cordier, D., Mousis, O., Lunine, J. I., Lavvas, P. & Vuitton, V. (2009). An Estimate of the Chemical Composition of Titan's Lakes. *The Astrophysical Journal Letters, 707*, L128-L131.

Cordier, D., Mousis, O., Lunine, J. I., Lebonnois, S., Rannou, P., Lavvas, P., Lobo, L. Q. & Ferreira, A. G. M. (2012). Titan's lakes chemical composition: Sources of uncertainties and variability. *Planetary and Space Science, 61*, 99-107.

Cottini, V., Nixon, C. A., Jennings, D. E., Anderson, C. M., Gorius, N., Bjoraker, G. L., Coustenis, A., Teanby, N. A., Achterberg, R. K., Bezard, B., de Kok, R., Lellouch, E., Irwin, P. G. J., Flasar, F. M. & Bampasidis, G. (2012a). Water vapor in Titan's stratosphere from Cassini CIRS far-infrared spectra. *Icarus, 220*(2), 855-862.

Cottini, V., Nixon, C. A., Jennings, D. E., de Kok, R., Teanby, N. A., Irwin, P. G. J. & Flasar, F. M. (2012b). Spatial and temporal variations in Titan's surface temperatures from Cassini CIRS observations. *Planetary and Space Science, 60*, 62-71.

Courtin, R., Swinyard, B. M., Moreno, R., Fulton, T., Lellouch, E., Rengel, M. & Hartogh, P. (2011). First results of Herschel-SPIRE observations of Titan. *Astronomy and Astrophysics, 536*(L2).

Coustenis, A. (1989). L' atmosphere de Titan a partir des observations infrarouges de Voyager. *PhD Thesis, L' Universite de Paris VII.*

Coustenis, A., Achterberg, R. K., Conrath, B. J., Jennings, D. E., Marten, A., Gautier, D., Nixon, C. A., Flasar, F. M., Teanby, N. A., Bezard, B., Samuelson, R. E., Carlson, R. C., Lellouch, E., Bjoraker, G. L., Romani, P. N., Taylor, F. W., Irwin, P. G. J., Fouchet, T., Hubert, A., Orton, G. S., Kunde, V. G., Vinatier, S., Mondellini, J., Abbas, M. M. & Courtin, R. (2007). The composition of Titan's stratosphere from Cassini/CIRS mid-infrared spectra. *Icarus, 189*(1), 35-62.

Coustenis, A., Atreya, S., Balint, T., Brown, R., Dougherty, M., Ferri, F., Fulchignoni, M., Gautier, D., Gowen, R., Griffith, C., Gurvits, L., Jaumann, R., Langevin, Y., Leese, M., Lunine, J., McKay, C., Moussas, X., Muller-Wodarg, I., Neubauer, F., Owen, T., Raulin, F., Sittler, E., Sohl, F., Sotin, C., Tobie, G., Tokano, T., Turtle, E., Wahlund, J. E., Waite, J., Baines, K., Blamont, J., Coates, A., Dandouras, I., Krimigis, T., Lellouch, E., Lorenz, R., Morse, A., Porco, C., Hirtzig, M., Saur, J., Spilker, T., Zarnecki, J., Choi, E., Achilleos, N., Amils, R., Annan, P., Atkinson, D., Benilan, Y., Bertucci, C., Bezard, B., Bjoraker, G., Blanc, M., Boireau, L., Bouman, J., Cabane, M., Capria, M., Chassefiere, E., Coll, P., Combes, M., Cooper, J., Coradini, A., Crary, F., Cravens, T., Daglis, I., de Angelis, E., de Bergh, C., de Pater, I., Dunford, C., Durry, G., Dutuit, O., Fairbrother, D., Flasar, F., Fortes, A., Frampton, R., Fujimoto, M., Galand, M., Grasset, O., Grott, M., Haltigin, T., Herique, A., Hersant, F., Hussmann, H., Ip, W., Johnson, R., Kallio, E., Kempf, S., Knapmeyer, M., Kofman, W., Koop, R., Kostiuk, T., Krupp, N., Kuppers, M., Lammer, H., Lara, L. M., Lavvas, P., Le Mouelic, S., Lebonnois, S., Ledvina, S., Li, J., Livengood, T., Lopes, R., Lopez-Moreno, J. J., Luz, D., Mahaffy, P., Mall, U., Martinez-Frias, J., Marty, B., McCord, T., Menor Salvan, C., Milillo, A., Mitchell, D., Modolo, R., Mousis, O., Nakamura, M., Neish, C., Nixon, C., Nna Mvondo, D., Orton, G., Paetzold, M., Pitman, J., Pogrebenko, S., Pollard, W., Prieto-Ballesteros, O., Rannou, P., Reh, K., Richter, L., Robb, F., Rodrigo, R., Rodriguez, S., Romani, P., Ruiz Bermejo, M., Sarris, E., Schenk, P., Schmitt, B., Schmitz, N., Schulze-Makuch, D., Schwingenschuh, K., Selig, A., Sicardy, B., Soderblom, L., Spilker, L., Stam, D., Steele, A., Stephan, K., Strobel, D., Szego, K., Szopa, C., Thissen, R., Tomasko, M., Toublanc, D., Vali, H., Vardavas, I., Vuitton, V., West, R., Yelle, R. & Young, E. (2009a). TandEM: Titan and Enceladus mission. *Experimental Astronomy, 23*, 893-946.

Coustenis, A., Bampasidis, G., Nixon, C., Vinatier, S., Achterberg, R., Jennings, D., Teanby, N., Carlson, R., Lavvas, P. & Flasar, F. M. (2010a). *Titan's atmospheric chemistry and its variations.* Paper presented at the Titan Through Time; A Workshop On Titan's Past, Present and Future, April 6th - 8th, NASA Goddard Space Flight Center.

Coustenis, A. & Bezard, B. (1995). Titan's atmosphere from Voyager infrared observations. IV: Latitudinal variations of temperature and composition. *Icarus, 115*, 126-140.

Coustenis, A., Bezard, B. & Gautier, D. (1989a). Titan's atmosphere from voyager infrared observations : I. The gas composition of Titan's equatorial region. *Icarus, 80*(1), 54-76.

Coustenis, A., Bezard, B. & Gautier, D. (1989b). Titan's atmosphere from Voyager infrared observations. II - The CH_3D abundance and D/H ratio from the 900-1200/cm spectral region. *Icarus, 82*, 67-80.

Coustenis, A., Bezard, B., Gautier, D., Marten, A. & Samuelson, R. (1991). Titan's atmosphere from Voyager infrared observations. III - Vertical contributions of hydrocarbons and nitriles near Titan's north pole. *Icarus, 89*, 152-167.

Coustenis, A., Gendron, E., Lai, O., Veran, J.-P., Woillez, J., Combes, M., Vapillon, L., Fusco, T., Mugnier, L. & Rannou, P. (2001). Images of Titan at 1.3 and 1.6 μm with Adaptive Optics at the CFHT. *Icarus, 154*(2), 501-515.

Coustenis, A., Hirtzig, M., Bampasidis, G., Solomonidou, A., Bratsolis, E., Kyriakopoulos, K., Moussas, X. & Preka-Papadema, P. (2011). *Exploring the satellites of the outer planets with in situ elements.* Paper presented at the 2nd International Conference on Space Technology (ICST), Athens, Greece, 15-17 Sept., DOI:10.1109/ICSpT.2011.6064652.

Coustenis, A., Hirtzig, M., Gendron, E., Drossart, P., Lai, O., Combes, M. & Negrao, A. (2005). Maps of Titan's surface from 1 to 2.5 μm. *Icarus, 177*(1), 89-105.

Coustenis, A., Jennings, D. E., Jolly, A., Bénilan, Y., Nixon, C. A., Vinatier, S., Gautier, D., Bjoraker, G. L., Romani, P. N., Carlson, R. C. & Flasar, F. M. (2008). Detection of C_2HD and the D/H ratio on Titan. *Icarus, 197*, 539-548.

Coustenis, A., Jennings, D. E., Nixon, C. A., Achterberg, R. K., Lavvas, P., Vinatier, S., Teanby, N., Bjoraker, G. L., Carlson, R. C., Bampasidis, G., Flasar, F. & Romani, P. N. (2010b). Titan trace gaseous composition from CIRS at the end of the Cassini-Huygens prime mission. *Icarus, 207*, 461-476.

Coustenis, A., Lellouch, E., Maillard, J. P. & McKay, C. P. (1995). Titan's surface: composition and variability from the near-infrared albedo. *Icarus, 118*, 87-104.

Coustenis, A., Lellouch, E., Sicardy, B. & Roe, H. (2009b). Earth-Based perspective and Pre-Cassini-Huygens Knowledge of Titan. In R. H. Brown, J.-P. Lebreton & J. H. Waite (Eds.), *Titan from Cassini-Huygens* (pp. 535): Spinger.

Coustenis, A., Lunine, J., Lebreton, J.-P., Matson, D., Erd, C., Reh, K., Beauchamp, P., Lorenz, R., Waite, H., Sotin, C., Gurvits, L. & Hirtzig, M. (2009c). Earth-Based Support for the Titan Saturn System Mission. *Earth Moon and Planets, 105*, 135-142.

Coustenis, A., Moussas, X. & Bampasidis, G. (2009d). *Future Titan Saturn System Outreach.* Paper presented at the European Planetary Science Congress, 14-18 September, Potsdam, Germany.

Coustenis, A., Raulin, F., Bampasidis, G. & Solomonidou, A. (2012). Life in the Saturnian Neighborhood. In P. J. Seckbach (Ed.), *Cellular Origin, Life in Extreme Habitats and Astrobiology*: Springer.

Coustenis, A., Salama, A., Lellouch, E., Encrenaz, T., Bjoraker, G. L., Samuelson, R. E., de Graauw, T., Feuchtgruber, H. & Kessler, M. F. (1998). Evidence for water vapor in Titan's atmosphere from ISO/SWS data. *Astronomy and Astrophysics, 336*, L85-L89.

Coustenis, A., Salama, A., Schulz, B., Ott, S., Lellouch, E., Encrenaz, T. H., Gautier, D. & Feuchtgruber, H. (2003). Titan's atmosphere from ISO mid-infrared spectroscopy. *Icarus, 161*, 383-403.

Coustenis, A. & Taylor, F. W. (2008). Titan: exploring an Earthlike World. *Series on atmospheric, oceanic and planetary physics, vol 4. World Scientific, Singapore.*

Coustenis, A., Tokano, T., Burger, M., Cassidy, T., Lopes, R., Lorenz, R., Retherford, K. & Schubert, G. (2010c). Atmospheric/Exospheric Characteristics of Icy Satellites. *Space Science Reviews, 153*(1), 155-184.

Craddock, R. A. & Howard, A. D. (2002). The case for rainfall on a warm, wet early Mars. *Journal of Geophysical Research (Planets), 107*, 5111.

Cravens, T. E., Robertson, I. P., Ledvina, S. A., Mitchell, D., Krimigis, S. M. & Waite, J. H. (2008). Energetic ion precipitation at Titan. *Geophysical Research Letters, 35*, 03103.

Crespin, A., Lebonnois, S., Vinatier, S., Bézard, B., Coustenis, A., Teanby, N. A., Achterberg, R. K., Rannou, P. & Hourdin, F. (2008). Diagnostics of Titan's stratospheric dynamics using Cassini/CIRS data and the 2-dimensional IPSL circulation model. *Icarus, 197*, 556-571.

Cui, J., Yelle, R. V., Vuitton, V., Waite Jr, J. H., Kasprzak, W. T., Gell, D. A., Niemann, H. B., Muller-Wodarg, I. C. F., Borggren, N., Fletcher, G. G., Patrick, E. L., Raaen, E. & Magee, B. A. (2009). Analysis of Titan's neutral upper atmosphere from Cassini Ion Neutral Mass Spectrometer measurements. *Icarus, 200*(2), 581-615.

Dainty, A. M., Toksoz, M. N., Anderson, K. R., Pines, P. J., Nakamura, Y. & Latham, G. (1974). Seismic Scattering and Shallow Structure of the Moon in Oceanus Procellarum. *Moon, 9*, 11-29.

Dalton, J. B. (2010). Spectroscopy of Icy Moon Surface Materials. *Space Science Reviews, 153*, 219-247.

Dalton, J. B., Cruikshank, D. P., Stephan, K., McCord, T. B., Coustenis, A., Carlson, R. W. & Coradini, A. (2010). Chemical Composition of Icy Satellite Surfaces. *Space Science Reviews, 153*, 113-154.

Dandouras, I., Garnier, P., Mitchell, D. G., Roelof, E. C., Brandt, P. C., Krupp, N. & Krimigis, S. M. (2009). Titan's exosphere and its interaction with Saturn's magnetosphere. *Philosophical Transactions of the Royal Society A: Mathematical, Physical and Engineering Sciences, 367*(1889), 743-752.

Dandouras, J. & Amsif, A. (1999). Production and imaging of energetic neutral atoms from Titan's exosphere: a 3-D model. *Planetary and Space Science, 47*, 1355-1369.

Dang-Nhu, M., Blanquet, G., Walrand, J. & Raulin, F. (1989). Spectral intensities in the ν4-band of benzene at 15 μm. *Journal of Molecular Spectroscopy, 134*, 237-239.

Danielson, R. E., Caldwell, J. J. & Larach, D. R. (1973). An Inversion in the Atmosphere of Titan. *Icarus, 20*, 437-443.

Davies, W. M. (1899). The geographical cycle. *Geographical Journal, 14*, 481-504.

Davies, W. M. (2009). Groupwork as a form of assessment: common problems and recommended solutions. *Higher Education, 58*(4), 563-584.

Dayton, D., Gonglewski, J., Restaino, S., Martin, J., Phillips, J., Hartman, M., Kervin, P., Snodgress, J., Browne, S., Heimann, N., Shilko, M. L., Pohle, R., Carrion, B., Smith, C. & Thiel, D. (2002). Demonstration of new technology MEMS and liquid crystal adaptive optics on bright astronomical objects and satellites. *Optics Express, 10*, 1508.

de Graauw, T., Helmich, F. P., Phillips, T. G., Stutzki, J., Caux, E., Whyborn, N. D., Dieleman, P., Roelfsema, P. R., Aarts, H., Assendorp, R., Bachiller, R., Baechtold, W., Barcia, A., Beintema, D. A., Belitsky, V., Benz, A. O., Bieber, R., Boogert, A., Borys, C., Bumble, B., Cais, P., Caris, M., Cerulli-Irelli, P., Chattopadhyay, G., Cherednichenko, S., Ciechanowicz, M., Coeur-Joly, O., Comito, C., Cros, A., de Jonge, A., de Lange, G., Delforges, B., Delorme, Y., den Boggende, T., Desbat, J. M., Diez-Gonzalez, C., di Giorgio, A. M., Dubbeldam, L., Edwards, K., Eggens, M., Erickson, N., Evers, J., Fich, M., Finn, T., Franke, B., Gaier, T., Gal, C., Gao, J. R., Gallego, J. D., Gauffre, S., Gill, J. J., Glenz, S., Golstein, H., Goulooze, H., Gunsing, T., Gusten, R., Hartogh, P., Hatch, W. A., Higgins, R., Honingh, E. C., Huisman, R., Jackson, B. D., Jacobs, H., Jacobs, K., Jarchow, C., Javadi, H., Jellema, W., Justen, M., Karpov, A., Kasemann, C., Kawamura, J., Keizer, G., Kester, D., Klapwijk, T. M., Klein, T., Kollberg, E., Kooi, J., Kooiman, P. P., Kopf, B., Krause, M., Krieg, J. M., Kramer, C., Kruizenga, B., Kuhn, T., Laauwen, W., Lai, R., Larsson, B., Leduc, H. G., Leinz, C., Lin, R. H., Liseau, R., Liu, G. S., Loose, A., Lopez-Fernandez, I., Lord, S., Luinge, W., Marston, A., Martin-Pintado, J., Maestrini, A., Maiwald, F. W., McCoey, C., Mehdi, I., Megej, A., Melchior, M., Meinsma, L., Merkel, H., Michalska, M., Monstein, C., Moratschke, D., Morris, P., Muller, H., Murphy, J. A., Naber, A., Natale, E., Nowosielski, W., Nuzzolo, F., Olberg, M., Olbrich, M., Orfei, R., Orleanski, P., Ossenkopf, V., Peacock, T., Pearson, J. C., Peron, I., Phillip-May, S., Piazzo, L., Planesas, P., Rataj, M., Ravera, L., Risacher, C., Salez, M., Samoska, L. A., Saraceno, P., Schieder, R., Schlecht, E., Schloder, F., Schmulling, F., Schultz, M., Schuster, K., Siebertz, O., Smit, H., Szczerba, R., Shipman, R., Steinmetz, E., Stern, J. A., Stokroos, M., Teipen, R., Teyssier, D., Tils, T., Trappe, N., van Baaren, C., van Leeuwen, B. J., van de Stadt, H., Visser, H., Wildeman, K. J., Wafelbakker, C. K., Ward, J. S., Wesselius, P., Wild, W., Wulff, S., Wunsch, H. J., Tielens, X., Zaal, P., Zirath, H., Zmuidzinas, J. & Zwart, F. (2010). The Herschel-Heterodyne Instrument for the Far-Infrared (HIFI). *Astronomy and Astrophysics, 518*(L6).

de Kok, R., Irwin, P. G. J., Teanby, N. A., Lellouch, E., Bezard, B., Vinatier, S., Nixon, C. A., Fletcher, L., Howett, C., Calcutt, S. B., Bowles, N. E., Flasar, F. M. & Taylor, F. W. (2007a). Oxygen compounds in Titan's stratosphere as observed by Cassini CIRS. *Icarus, 186*, 354-363.

de Kok, R., Irwin, P. G. J., Teanby, N. A., Nixon, C. A., Jennings, D. E., Fletcher, L., Howett, C., Calcutt, S. B., Bowles, N. E., Flasar, F. M. & Taylor, F. W. (2007b). Characteristics of Titan's stratospheric aerosols and condensate clouds from Cassini CIRS far-infrared spectra. *Icarus, 191*, 223-235.

De La Haye, V., Waite, J. H., Johnson, R. E., Yelle, R. V., Cravens, T. E., Luhmann, J. G., Kasprzak, W. T., Gell, D. A., Magee, B., Leblanc, F., Michael, M., Jurac, S. & Robertson, I. P. (2007). Cassini Ion and Neutral Mass Spectrometer data in Titan's upper atmosphere and exosphere: Observation of a suprathermal corona. *Journal of Geophysical Research (Space Physics), 112*, 07309.

de Vanssay, E., Gazeau, M. C., Guillemin, J. C. & Raulin, F. (1995). Experimental simulation of Titan's organic chemistry at low temperature. *Planetary and Space Science, 43*, 25-31.

Delitsky, M. L. & McKay, C. P. (2010). The photochemical products of benzene in Titan's upper atmosphere. *Icarus, 207*, 477-484.

Dermott, S. F. & Sagan, C. (1995). Tidal effects of disconnected hydrocarbon seas on Titan. *Nature, 374*, 238-240.

Des Marais, D. J., Harwit, M. O., Jucks, K. W., Kasting, J. F., Lin, D. N. C., Lunine, J. I., Schneider, J., Seager, S., Traub, W. A. & Woolf, N. J. (2002). Remote Sensing of Planetary Properties and Biosignatures on Extrasolar Terrestrial Planets. *Astrobiology, 2*, 153-181.

DeWitt, H. L., Trainer, M. G., Pavlov, A. A., Hasenkopf, C. A., Aiken, A. C., Jimenez, J. L., McKay, C. P., Toon, O. B. & Tolbert, M. A. (2009). Reduction in Haze Formation Rate on Prebiotic Earth in the Presence of Hydrogen. *Astrobiology, 9*, 447-453.

DiSessa, A. A. (1981). Unlearning Aristotelian physics: a study of knowledge-based learning. *Cognitive Science, 6*(1), 37-75.

Doornkamp, J. C. & King, C. A. M. (1971). *Numerical analysis in geomorphology: an introduction* (Vol. 372): Edward Arnold.

Dougherty, M. K., Kellock, S., Southwood, D. J., Balogh, A., Smith, E. J., Tsurutani, B. T., Gerlach, B., Glassmeier, K. H., Gleim, F., Russell, C. T., Erdos, G., Neubauer, F. M. & Cowley, S. W. H. (2004). The Cassini Magnetic Field Investigation. *Space Science Reviews, 114*, 331-383.

Dougherty, M. K., Khurana, K. K., Neubauer, F. M., Russell, C. T., Saur, J., Leisner, J. S. & Burton, M. E. (2006). Identification of a Dynamic Atmosphere at Enceladus with the Cassini Magnetometer. *Science, 311*, 1406-1409.

Efthimiou, C. J. & Llewellyn, R. A. (2006). Avatars of Hollywood in physical science. *Physics Teacher, 44*, 28-32.

Ehlmann, B. L., Mustard, J. F., Murchie, S. L., Bibring, J.-P., Meunier, A., Fraeman, A. A. & Langevin, Y. (2011). Subsurface water and clay mineral formation during the early history of Mars. *Nature, 479*, 53-60.

EJSM. (2009). *NASA/ESA Final Report.*

Elachi, C., Allison, M. D., Borgarelli, L., Encrenaz, P., Im, E., Janssen, M. A., Johnson, W. T. K., Kirk, R. L., Lorenz, R. D., Lunine, J. I., Muhleman, D. O., Ostro, S. J., Picardi, G., Posa, F., Rapley, C. G., Roth, L. E., Seu, R., Soderblom, L. A., Vetrella, S., Wall, S. D., Wood, C. A. & Zebker, H. A. (2004). Radar: The Cassini Titan Radar Mapper. *Space Science Reviews, 115*, 71-110.

Elachi, C., Wall, S., Allison, M., Anderson, Y., Boehmer, R., Callahan, P., Encrenaz, P., Flamini, E., Franceschetti, G., Gim, Y., Hamilton, G., Hensley, S., Janssen, M., Johnson, W., Kelleher, K., Kirk, R., Lopes, R., Lorenz, R., Lunine, J., Muhleman, D., Ostro, S., Paganelli, F., Picardi, G., Posa, F., Roth, L., Seu, R., Shaffer, S., Soderblom, L., Stiles, B., Stofan, E., Vetrella, S., West, R., Wood, C., Wye, L. & Zebker, H. (2005). Cassini Radar Views the Surface of Titan. *Science, 308*, 970-974.

Elachi, C., Wall, S., Janssen, M., Stofan, E., Lopes, R., Kirk, R., Lorenz, R., Lunine, J., Paganelli, F., Soderblom, L., Wood, C., Wye, L., Zebker, H., Anderson, Y., Ostro, S., Allison, M., Boehmer, R., Callahan, P., Encrenaz, P., Flamini, E., Francescetti, G., Gim, Y., Hamilton, G., Hensley, S., Johnson, W., Kelleher, K., Muhleman, D., Picardi, G., Posa, F., Roth, L., Seu, R., Shaffer, S., Stiles, B., Vetrella, S. & West, R. (2006). Titan Radar Mapper observations from Cassini's T3 fly-by. *Nature, 441*(7094), 709-713.

Elias, B. (2008). Match the Emitter to the Task. *Photonics Spectra, 42*(10).

Ellis, R. (2003). *Task-Based Language Learning and Teaching*: Oxford University Press.

Enya, K., Kataza, H. & Bierden, P. (2009). A Micro Electrical Mechanical Systems (MEMS)-based Cryogenic Deformable Mirror. *Publications of the Astronomical Society of the Pacific, 121*(877), 260-265.

Esposito, L. W., Barth, C. A., Colwell, J. E., Lawrence, G. M., McClintock, W. E., Stewart, A. I. F., Keller, H. U., Korth, A., Lauche, H., Festou, M. C., Lane, A. L., Hansen, C. J., Maki, J. N., West, R. A., Jahn, H., Reulke, R., Warlich, K., Shemansky, D. E. & Yung, Y. L. (2004). The Cassini Ultraviolet Imaging Spectrograph Investigation. *Space Science Reviews, 115*, 299-361.

Eviatar, A. & Podolak, M. (1983). Titan's gas and plasma torus. *Journal of Geophysical Research, 88*, 833-840.

Fanale, F. P., Li, Y. H., De Carlo, E., Farley, C., Sharma, S. K., Horton, K. & Granahan, J. C. (2001). An experimental estimate of Europa's "ocean" composition-independent of Galileo orbital remote sensing. *Journal of Geophysical Research, 106*, 14595-14600.

Fegley, B. (1995). Properties and Composition of the Terrestrial Oceans and of the Atmospheres of the Earth and Other Planets. In T. Ahrens (Ed.), *Global Earth Physics A Handbook of Physical Constants* (pp. 320-345). Washington DC: Am. Geophys. Pub.

Figueredo, P. H. & Greeley, R. (2004). Resurfacing history of Europa from pole-to-pole geologimapping. *Icarus, 167*, 287-312.

Flasar, F. M. (1983). Oceans on Titan? *Science, 221*, 55-57.

Flasar, F. M., Achterberg, R. K., Conrath, B. J., Gierasch, P. J., Kunde, V. G., Nixon, C. A., Bjoraker, G. L., Jennings, D. E., Romani, P. N., Simon-Miller, A. A., Bezard, B., Coustenis, A., Irwin, P. G. J., Teanby, N. A., Brasunas, J., Pearl, J. C., Segura, M. E., Carlson, R. C., Mamoutkine, A., Schinder, P. J., Barucci, A., Courtin, R., Fouchet, T., Gautier, D., Lellouch, E., Marten, A., Prange, R., Vinatier, S., Strobel, D. F., Calcutt, S. B., Read, P. L., Taylor, F. W., Bowles, N., Samuelson, R. E., Orton, G. S., Spilker, L. J., Owen, T. C., Spencer, J. R., Showalter, M. R., Ferrari, C., Abbas, M. M., Raulin, F., Edgington, S., Ade, P. & Wishnow, E. H. (2005). Titan's Atmospheric Temperatures, Winds, and Composition. *Science, 308*(5724), 975-978.

Flasar, F. M. & Conrath, B. J. (1990). Titan's stratospheric temperatures - A case for dynamical inertia? *Icarus, 85*, 346-354.

Flasar, F. M., Kunde, V. G., Abbas, M. M., Achterberg, R. K., Ade, P., Barucci, A., Bezard, B., Bjoraker, G. L., Brasunas, J. C., Calcutt, S., Carlson, R., Cesarsky, C. J., Conrath, B. J., Coradini, A., Courtin, R., Coustenis, A., Edberg, S., Edgington, S., Ferrari, C., Fouchet, T., Gautier, D., Gierasch, P. J., Grossman, K., Irwin, P., Jennings, D. E., Lellouch, E., Mamoutkine, A. A., Marten, A., Meyer, J. P., Nixon, C. A., Orton, G. S., Owen, T. C., Pearl, J. C., Prange, R., Raulin, F., Read, P. L., Romani, P. N., Samuelson, R. E., Segura, M. E., Showalter, M. R., Simon-Miller, A. A., Smith, M. D., Spencer, J. R., Spilker, L. J. & Taylor,

F. W. (2004). Exploring The Saturn System In The Thermal Infrared: The Composite Infrared Spectrometer. *Space Science Reviews, 115*, 169-297.

Flasar, F. M., Samuelson, R. E. & Conrath, B. J. (1981). Titan's atmosphere: temperature and dynamics. *Nature, 292*(5825), 693-698.

Flaud, J. M., Kwabia Tchana, F., Lafferty, W. J. & Nixon, C. A. (2010). High resolution analysis of the ν_{26} and $2\nu_9$-ν_9 bands of propane: modelling of Titan's infrared spectrum at 13.4 μm. *Molecular Physics, 108*, 699-704.

Foote, M. C., Jones, E. W. & Caillat, T. (1998). Uncooled thermopile infrared detector linear arrays with detectivity greater than 109 cmHz1/2/W. *IEEE Transactions on Electron Devices, 45*(9), 1896-1902.

Forget, F. & Pierrehumbert, R. T. (1997). Warming Early Mars with Carbon Dioxide Clouds That Scatter Infrared Radiation. *Science, 278*(5341), 1273-1276.

Fortes, A. D. (2000). Exobiological Implications of a Possible Ammonia-Water Ocean inside Titan. *Icarus, 146*, 444-452.

Fortes, A. D. (2012). Titan's internal structure and the evolutionary consequences. *Planetary and Space Science, 60*, 10-17.

Fortes, A. D., Grindrod, P. M., Trickett, S. K. & Vočadlo, L. (2007). Ammonium sulfate on Titan: Possible origin and role in cryovolcanism. *Icarus, 188*, 139-153.

Foster, P. (1998). A Classroom Perspective on the Negotiation of Meaning. *Applied Linguistics, 19*, 1-23.

Frykholm, J. & Glasson, G. (2005). Connecting Science and Mathematics Instruction: Pedagogical Context Knowledge for Teachers. *School Science and Mathematics, 105*(3), 127-141.

Fulchignoni, M., Ferri, F., Angrilli, F., Ball, A. J., Bar-Nun, A., Barucci, M. A., Bettanini, C., Bianchini, G., Borucki, W., Colombatti, G., Coradini, M., Coustenis, A., Debei, S., Falkner, P., Fanti, G., Flamini, E., Gaborit, V., Grard, R., Hamelin, M., Harri, A. M., Hathi, B., Jernej, I., Leese, M. R., Lehto, A., Lion Stoppato, P. F., Lopez-Moreno, J. J., Makinen, T., McDonnell, J. A. M., McKay, C. P., Molina-Cuberos, G., Neubauer, F. M., Pirronello, V., Rodrigo, R., Saggin, B., Schwingenschuh, K., Seiff, A., Simoes, F., Svedhem, H., Tokano, T., Towner, M. C., Trautner, R., Withers, P. & Zarnecki, J. C. (2005). In situ measurements of the physical characteristics of Titan's environment. *Nature, 438*(7069), 785-791.

Fulchignoni, M., Ferri, F., Angrilli, F., Bar-Nun, A., Barucci, M. A., Bianchini, G., Borucki, W., Coradini, M., Coustenis, A., Falkner, P., Flamini, E., Grard, R., Hamelin, M., Harri, A. M., Leppelmeier, G. W., Lopez-Moreno, J. J., McDonnell, J. A. M., McKay, C. P., Neubauer, F. H., Pedersen, A., Picardi, G., Pirronello, V., Rodrigo, R., Schwingenschuh, K., Seiff, A., Svedhem, H., Vanzani, V. & Zarnecki, J. (2002). The Characterisation of Titan's Atmospheric Physical Properties by the Huygens Atmospheric Structure Instrument (Hasi). *Space Science Reviews, 104*(1), 395-431.

Furner, J. M. & Ramirez, M. (1999). Making Connections: Using GIS to Integrate Mathematics and Science. *TechTrends, 43*, 34-39.

Galand, M., Yelle, R., Cui, J., Wahlund, J.-E., Vuitton, V., Wellbrock, A. & Coates, A. (2010). Ionization sources in Titan's deep ionosphere. *Journal of Geophysical Research, 115*(A7).

Garcia, F., Hixsom, E. L., Huerta, C. I. & Orozco, H. (1999). Seismic Accelerometer. *Instrumentation and Measurement Technology Conference, IMTC/99, Proceedings of the 16th IEEE, 3*, 1342-1346.

Garnier, P., Dandouras, I., Toublanc, D., Brandt, P. C., Roelof, E. C., Mitchell, D. G., Krimigis, S. M., Krupp, N., Hamilton, D. C. & Waite, H. (2007). The exosphere of Titan and its interaction with the kronian magnetosphere: MIMI observations and modeling. *Planetary and Space Science, 55*, 165-173.

Garnier, P., Dandouras, I., Toublanc, D., Roelof, E. C., Brandt, P. C., Mitchell, D. G., Krimigis, S. M., Krupp, N., Hamilton, D. C. & Wahlund, J. E. (2010). Statistical analysis of the energetic ion and ENA data for the Titan environment. *Planetary and Space Science, 58*(14-15), 1811-1822.

Garnier, P., Wahlund, J. E., Rosenqvist, L., Modolo, R., Agren, K., Sergis, N., Canu, P., Andre, M., Gurnett, D. A., Kurth, W. S., Krimigis, S. M., Coates, A., Dougherty, M. & Waite, J. H. (2009). Titan's ionosphere in the magnetosheath: Cassini RPWS results during the T32 flyby. *Annales Geophysicae, 27*, 4257-4272.

Gazit, E., Yair, Y. & Chen, D. (2005). Emerging Conceptual Understanding of Complex Astronomical Phenomena by Using a Virtual Solar System. *Journal of Science Education and Technology, 14*(5), 459-470.

Geballe, T. R., Kim, S. J., Noll, K. S. & Griffith, C. A. (2003). High-Resolution 3 Micron Spectroscopy of Molecules in the Mesosphere and Troposphere of Titan. *The Astrophysical Journal Letters, 583*, L39-L42.

Gendron, E., Coustenis, A., Drossart, P., Combes, M., Hirtzig, M., Lacombe, F., Rouan, D., Collin, C., Pau, S., Lagrange, A. M., Mouillet, D., Rabou, P., Fusco, T. & Zins, G. (2004). VLT/NACO adaptive optics imaging of Titan. *Astronomy and Astrophysics, 417*, L21-L24.

Gibbard, S. G., Macintosh, B., Gavel, D., Max, C. E., de Pater, I., Ghez, A. M., Young, E. F. & McKay, C. P. (1999). Titan: High-Resolution Speckle Images from the Keck Telescope. *Icarus, 139*(2), 189-201.

Gibbard, S. G., Macintosh, B., Gavel, D., Max, C. E., de Pater, I., Roe, H. G., Ghez, A. M., Young, E. F. & McKay, C. P. (2004). Speckle imaging of Titan at 2 microns: surface albedo, haze optical depth, and tropospheric clouds 1996-1998. *Icarus, 169*, 429-439.

Gibbs, M. G. & Berendsen, M. (2006). Effectiveness of Amateur Astronomers as Informal Science Educators. *Astronomy Education Review, 5*(2), 114-126.

Gillett, F. C. (1975). Further observations of the 8-13 micron spectrum of Titan. *The Astrophysical Journal, 201*, L41-L43.

Gleyzer, A., Denisyuk, M., Rimmer, A. & Salingar, Y. (2004). A Fast Recursive GIS Algorithm for Computing Strahler Stream Order in Braided and Nonbraided Networks. *Journal of the American Water Resources Association, 40*, 937-946.

Gombosi, T. I., Armstrong, T. P., Arridge, C. S., Khurana, K. K., Krimigis, S. M., Krupp, N., Persoon, A. M. & Thomsen, M. F. (2009). Saturn's Magnetospheric Configuration, *Saturn from Cassini-Huygens*.

Goodman, J. W. (1976). Some fundamental properties of speckle. *Journal of the Optical Society of America (1917-1983), 66*, 1145-1150.

Grard, R., Hamelin, M., Lopez-Moreno, J. J., Schwingenschuh, K., Jernej, I., Molina-Cuberos, G. J., Simoes, F., Trautner, R., Falkner, P., Ferri, F., Fulchignoni, M., Rodrigo, R., Svedhem, H., Beghin, C., Berthelier, J. J., Brown, V. J. G., Chabassiere, M., Jeronimo, J. M., Lara, L. M. & Tokano, T. (2006). Electric properties and related physical characteristics of the atmosphere and surface of Titan. *Planetary and Space Science, 54*, 1124-1136.

Grasset, O. & Sotin, C. (1996). The Cooling Rate of a Liquid Shell in Titan's Interior. *Icarus, 123*, 101-112.

Grasset, O., Sotin, C. & Deschamps, F. (2000). On the internal structure and dynamics of Titan. *Planetary and Space Science, 48*, 617-636.

Greeley, R., Klemaszewski, J. E. & Wagner, R. (2000). Galileo views of the geology of Callisto. *Planetary and Space Science, 48*(9), 829-853.

Greenberg, R. (2010). Transport Rates of Radiolytic Substances into Europa's Ocean: Implications for the Potential Origin and Maintenance of Life. *Astrobiology, 10*, 275-283.

Griffith, C. A. (1993). Evidence for surface heterogeneity on Titan. *Nature, 364*, 511-513.

Griffith, C. A., Lora, J. M., Turner, J., Penteado, P. F., Brown, R. H., Tomasko, M. G., Doose, L. & See, C. (2012). Possible tropical lakes on Titan from observations of dark terrain. *Nature, 486*, 237-239.

Griffith, C. A., Owen, T. & Wagener, R. (1991). Titan's surface and trophosphere, investigated with groundbased, near-infrared observations. *Icarus, 93*, 362-378.

Grotzinger, J., P. & Knoll, A., H. (2003). Stromatolites in precambrian carbonates: Evolutionary Mileposts or Environmental Dipsticks? *Annual Review of Earth and Planetary Sciences, 27*(313-358).

Gurnett, D. A., Kurth, W. S., Kirchner, D. L., Hospodarsky, G. B., Averkamp, T. F., Zarka, P., Lecacheux, A., Manning, R., Roux, A., Canu, P., Cornilleau-Wehrlin, N., Galopeau, P., Meyer, A., Bostrom, R., Gustafsson, G., Wahlund, J. E., Γ…hlen, L., Rucker, H. O., Ladreiter, H. P., Macher, W., Woolliscroft, L. J. C., Alleyne, H., Kaiser, M. L., Desch, M. D., Farrell, W. M., Harvey, C. C., Louarn, P., Kellogg, P. J., Goetz, K. & Pedersen, A. (2004). The Cassini Radio and Plasma Wave Investigation. *Space Science Reviews, 114*, 395-463.

Gurwell, M. A. (2004). Submillimeter Observations of Titan: Global Measures of Stratospheric Temperature, CO, HCN, HC_3N, and the Isotopic Ratios $^{12}C/^{13}C$ and $^{14}N/^{15}N$. *The Astrophysical Journal Letters, 616*, L7-L10.

Gurwell, M. A. (2008). *Carbon, Nitrogen And Oxygen Isotopic Ratios In Titan's Stratosphere.* Paper presented at the DPS meeting #40, Bulletin of the American Astronomical Society.

Hadamard, J. (1923). *Lectures on Cauchy's Problem in Linear Partial Differential Equations.*: Dover Publications.

Hall, D. T., Feldman, P. D., McGrath, M. A. & Strobel, D. F. (1998). The Far-Ultraviolet Oxygen Airglow of Europa and Ganymede. *The Astrophysical Journal, 499*, 475.

Hall, D. T., Strobel, D. F., Feldman, P. D., McGrath, M. A. & Weaver, H. A. (1995). Detection of an oxygen atmosphere on Jupiter's moon Europa. *Nature, 373*, 677-679.

Hall, J. L., Lunine, J., Sotin, C., Reh, K., Vargas, A. & Couzin, P. (2011). *Titan Aerial Explorer (TAE): Exploring Titan By Balloon.* Paper presented at the nterplanetary Probe Workshop 8, Portsmouth, VA

Halloun, I. A. (1997). Schematic Concepts for Schematic Models of the Real World: The Newtonian Concept of Force. *Sci Ed, 82*, 239-263.

Halloun, I. A. & Hestenes, D. (1985). The initial knowledge state of college physics students. *Am. J. Phys., 53* (11), 1043-1048.

Hamelin, M., Beghin, C., Grard, R., Lopez-Moreno, J. J., Schwingenschuh, K., Simoes, F., Trautner, R., Berthelier, J. J., Brown, V. J. G., Chabassiere, M., Falkner, P., Ferri, F., Fulchignoni, M., Jernej, I., Jeronimo, J. M., Molina-Cuberos, G. J., Rodrigo, R. & Tokano, T. (2007). Electron conductivity and

density profiles derived from the mutual impedance probe measurements performed during the descent of Huygens through the atmosphere of Titan. *Planetary and Space Science, 55*, 1964-1977.

Hanel, R., Conrath, B., Flasar, F. M., Kunde, V., Maguire, W., Pearl, J. C., Pirraglia, J., Samuelson, R., Herath, L., Allison, M., Cruikshank, D. P., Gautier, D., Gierasch, P. J., Horn, L., Koppany, R. & Ponnamperuma, C. (1981). Infrared observations of the Saturnian system from Voyager 1. *Science, 212*, 192-200.

Hanel, R., Crosby, D., Herath, L., Vanous, D., Collins, D., Creswick, H., Harris, C. & Rhodes, M. (1980). Infrared spectrometer for Voyager. *Applied Optics, 19*, 1391-1400.

Hanel, R. A., Conrath, B. J., Jennings, D. E. & Samuelson, R. E. (2003). *Exploration of the Solar System by Infrared Remote Sensing* (2nd ed.): Cambridge University Press.

Hansen, C. J., Shemansky, D. E., Esposito, L. W., Stewart, A. I. F., Lewis, B. R., Colwell, J. E., Hendrix, A. R., West, R. A., Waite, J. H., Teolis, B. & Magee, B. A. (2011). The composition and structure of the Enceladus plume. *Geophysical Research Letters, 38*, 11202.

Hansen, P., C. (1992). Numerical tools for analysis and solution of Fredholm integral equations of the first kind. *Inverse Problems, 8*, 849-872.

Harri, A.-M., Makinen, T., Lehto, A., Kahanp, H. & Siili, T. (2006). Vertical pressure profile of Titan-observations of the PPI/HASI instrument. *Planetary and Space Science, 54*, 1117-1123.

Hart, M. H. (1979). Habitable zones about main sequence stars. *Icarus, 37*(1), 351-357.

Hartung, M., Herbst, T. M., Dumas, C. & Coustenis, A. (2006). Limits to the abundance of surface CO_2 ice on Titan. *Journal of Geophysical Research (Planets), 111*.

Hayes, A., Aharonson, O., Callahan, P., Elachi, C., Gim, Y., Kirk, R., Lewis, K., Lopes, R., Lorenz, R., Lunine, J., Mitchell, K., Mitri, G., Stofan, E. & Wall, S. (2008). Hydrocarbon lakes on Titan: Distribution and interaction with a porous regolith. *Geophysical Research Letters, 35*, E09204.

Hayes, A. G., Aharonson, O., Lunine, J. I., Kirk, R. L., Zebker, H. A., Wye, L. C., Lorenz, R. D., Turtle, E. P., Paillou, P., Mitri, G., Wall, S. D., Stofan, E. R., Mitchell, K. L. & Elachi, C. (2010). Transient Surface Liquid in Titan's Polar Regions from Cassini. *Icarus, 221, 655*.

Hayes, A. G., Aharonson, O., Lunine, J. I., Kirk, R. L., Zebker, H. A., Wye, L. C., Lorenz, R. D., Turtle, E. P., Paillou, P., Mitri, G., Wall, S. D., Stofan, E. R., Mitchell, K. L. & Elachi, C. (2011). Transient Surface Liquid in Titan's Polar Regions from Cassini. *Icarus, 211*, 655-671.

Heacox, D. (2002). *From Differentiating Instruction in the Regular Classroom: How to Reach and Teach All Learners, Grades 3-12*: Free Spirit Publishing Inc.

Heller, P., Keith, R. & Anderson, S. (1992). Teaching problem solving through cooperative grouping. Part 1: Group versus individual problem solving. *American Journal of Physics, 60*, 627-636.

Henry, C. A. (2002). An Introduction to the Design of the Cassini Spacecraft. *Space Science Reviews, 104*, 129-153.

Hidayat, T., Marten, A., Bezard, B., Gautier, D., Owen, T., Matthews, H. E. & Paubert, G. (1997). Millimeter and Submillimeter Heterodyne Observations of Titan: Retrieval of the Vertical Profile of HCN and the $^{12}C/^{13}C$ Ratio. *Icarus, 126*, 170-182.

Hidayat, T., Marten, A., Bezard, B., Gautier, D., Owen, T., Matthews, H. E. & Paubert, G. (1998). Millimeter and Submillimeter Heterodyne Observations of Titan: The Vertical Profile of Carbon Monoxide in Its Stratosphere. *Icarus, 133*(1), 109-133.

Hill, T. W., Thomsen, M. F., Tokar, R. L., Coates, A. J., Lewis, G. R., Young, D. T., Crary, F. J., Baragiola, R. A., Johnson, R. E., Dong, Y., Wilson, R. J., Jones, G. H., Wahlund, J. E., Mitchell, D. G. & Horanyi, M. (2012). Charged nanograins in the Enceladus plume. *Journal of Geophysical Research, 117*(A5), A05209.

Hirtzig, M., Coustenis, A., Gendron, E., Drossart, P., Hartung, M., Negrao, A., Rannou, P. & Combes, M. (2007). Titan: Atmospheric and surface features as observed with Nasmyth Adaptive Optics System Near-Infrared Imager and Spectrograph at the time of the Huygens mission. *J. Geophys. Res., 112*(E02S91).

Hirtzig, M., de Bergh, C., Courtin, R., Bezard, B., Coustenis, A., Lellouch, E., Rannou, P., Drossart, P., Campargue, A., Kassi, S., Wang, L., Boudon, V., Nikitin, A., Tyuterev, V. & Solomonidou, A. (2011). *Application of new methane linelists to Cassini and Earth-based data of Titan.* Paper presented at the EPSC-DPS Joint Meeting 2011, Nantes, France.

Hirtzig, M., Tokano, T., Rodriguez, S., le Mouelic, S. & Sotin, C. (2009). A review of Titan's atmospheric phenomena. *Astronomy and Astrophysics Review, 17*(2), 105-147.

Horton, R. E. (1945). Erosional development of streams and their drainage basins; Hydrophysical approach to quantitative morphology. *Geol. Soc. America Bull., 56*, 275-370.

Houghton, J. T. (1986). *The physics of atmospheres* (2nd ed.): Cambridge University Press.

Huang, S.-S. (1959). Occurrence of Life in the Universe. *American Scientist 47*, 397-402.

Hunten, D. M. (1977). *Titan's atmosphere and surface.* Paper presented at the IAU Colloq. 28, Planetary satellites, Tucson.

Hussmann, H., Choblet, G. l., Lainey, V. r., Matson, D. L., Sotin, C., Tobie, G. & van Hoolst, T. (2010). Implications of Rotation, Orbital States, Energy Sources, and Heat Transport for Internal Processes in Icy Satellites. *Space Science Reviews, 153*, 317-348.

Husson, N., Bonnet, B., Chedin, A., Scott, N. A., Chursin, A. A., Golovko, V. F. & Tyuterev, V. G. (1994). The GEISA data bank in 1993: a PC/AT compatible computers' new version. *Journal of Quantitative Spectroscopy and Radiative Transfer, 52*, 425-438.

Husson, N., Bonnet, B., Scott, N. A. & Chedin, A. (1992). Management and Study of Spectroscopic Information - The GEISA program. *Journal of Quantitative Spectroscopy and Radiative Transfer, 48*, 509-518.

Iess, L., Jacobson, R. A., Ducci, M., Stevenson, D. J., Lunine, J. I., Armstrong, J. W., Asmar, S. W., Racioppa, P., Rappaport, N. J. & Tortora, P. (2012). The Tides of Titan. *Science DOI: 10.1126/science.1219631, Published Online June 28 2012.*

Irwin, P. G. J., Teanby, N. A., de Kok, R., Fletcher, L. N., Howett, C. J. A., Tsang, C. C. C., Wilson, C. F., Calcutt, S. B., Nixon, C. A. & Parrish, P. D. (2008). The NEMESIS planetary atmosphere radiative transfer and retrieval tool. *Journal of Quantitative Spectroscopy and Radiative Transfer, 109*, 1136-1150.

Israel, G., Cabane, M., Brun, J. F., Niemann, H., Way, S., Riedler, W., Steller, M., Raulin, F. & Coscia, D. (2002). Huygens Probe Aerosol Collector Pyrolyser Experiment. *Space Science Reviews, 104*, 433-468.

Israel, G., Szopa, C., Raulin, F., Cabane, M., Niemann, H. B., Atreya, S. K., Bauer, S. J., Brun, J. F., Chassefiere, E., Coll, P., Cond, E., Coscia, D., Hauchecorne, A., Millian, P., Nguyen, M. J., Owen, T., Riedler, W., Samuelson, R. E., Siguier, J. M., Steller, M., Sternberg, R. & Vidal-Madjar, C. (2005). Complex organic matter in Titan's atmospheric aerosols from in situ pyrolysis and analysis. *Nature, 438*, 796-799.

Jacobsen, R. T., Stewart, R. B. & Jahangiri, M. (1986). Thermodynamic Properties of Nitrogen from the Freezing Line to 2000 K at Pressures to 1000 MPa. *Journal of Physical and Chemical Reference Data, 15*(2), 735-909.

Jacobson, R. A., Antreasian, P. G., Bordi, J. J., Criddle, K. E., Ionasescu, R., Jones, J. B., Mackenzie, R. A., Meek, M. C., Parcher, D., Pelletier, F. J., Owen, W. M., Roth, D. C., Roundhill, I. M. & Stauch, J. R. (2006). The Gravity Field of the Saturnian System from Satellite Observations and Spacecraft Tracking Data. *The Astronomical Journal, 132*, 2520-2526.

Jacquinet-Husson, N., Arie, E., Ballard, J., Barbe, A., Bjoraker, G., Bonnet, B., Brown, L. R., Camy-Peyret, C., Champion, J. P., Chedin, A., Chursin, A., Clerbaux, C., Duxbury, G., Flaud, J. M., Fourrie, N., Fayt, A., Graner, G., Gamache, R., Goldman, A., Golovko, V., Guelachvili, G., Hartmann, J. M., Hilico, J. C., Hillman, J., Lefevre, G., Lellouch, E., Mikhailenko, S. N., Naumenko, O. V., Nemtchinov, V., Newnham, D. A., Nikitin, A., Orphal, J., Perrin, A., Reuter, D. C., Rinsland, C. P., Rosenmann, L., Rothman, L. S., Scott, N. A., Selby, J., Sinitsa, L. N., Sirota, J. M., Smith, A. M., Smith, K. M., Tyuterev, V. G., Tipping, R. H., Urban, S., Varanasi, P. & Weber, M. (1999). The 1997 spectroscopic GEISA databank. *Journal of Quantitative Spectroscopy and Radiative Transfer, 62*, 205-254.

Jacquinet-Husson, N., Crepeau, L., Armante, R., Boutammine, C., Chedin, A., Scott, N. A., Crevoisier, C., Capelle, V., Boone, C., Poulet-Crovisier, N., Barbe, A., Campargue, A., Benner, D. C., Benilan, Y., Bezard, B., Boudon, V., Brown, L. R., Coudert, L. H., Coustenis, A., Dana, V., Devi, V. M., Fally, S., Fayt, A., Flaud, J. M., Goldman, A., Herman, M., Harris, G. J., Jacquemart, D., Jolly, A., Kleiner, I., Kleinbohl, A., Kwabia-Tchana, F., Lavrentieva, N., Lacome, N., Xu, L.-H., Lyulin, O. M., Mandin, J. Y., Maki, A., Mikhailenko, S., Miller, C. E., Mishina, T., Moazzen-Ahmadi, N., Muller, H. S. P., Nikitin, A., Orphal, J., Perevalov, V., Perrin, A., Petkie, D. T., Predoi-Cross, A., Rinsland, C. P., Remedios, J. J., Rotger, M., Smith, M. A. H., Sung, K., Tashkun, S., Tennyson, J., Toth, R. A., Vandaele, A. C. & Vander Auwera, J. (2011). The 2009 edition of the GEISA spectroscopic database. *Journal of Quantitative Spectroscopy and Radiative Transfer, 112*, 2395-2445.

Jacquinet-Husson, N., Scott, N. A., Chedin, A., Bonnet, B., Barbe, A., Tyuterev, V. G., Champion, J. P., Winnewisser, M., Brown, L. R., Gamache, R., Golovko, V. F. & Chursin, A. A. (1998). The GEISA system in 1996: towards an operational tool for the second generation vertical sounders radiance simulation. *Journal of Quantitative Spectroscopy and Radiative Transfer, 59*, 511-527.

Jacquinet-Husson, N., Scott, N. A., Chedin, A., Crepeau, L., Armante, R., Capelle, V., Orphal, J., Coustenis, A., Boonne, C., Poulet-Crovisier, N., Barbe, A., Birk, M., Brown, L. R., Camy-Peyret, C., Claveau, C., Chance, K., Christidis, N., Clerbaux, C., Coheur, P. F., Dana, V., Daumont, L., De Backer-Barilly, M. R., Di Lonardo, G., Flaud, J. M., Goldman, A., Hamdouni, A., Hess, M., Hurley, M. D., Jacquemart, D., Kleiner, I., Kopke, P., Mandin, J. Y., Massie, S., Mikhailenko, S., Nemtchinov, V., Nikitin, A., Newnham, D., Perrin, A., Perevalov, V. I., Pinnock, S., Regalia-Jarlot, L., Rinsland, C. P., Rublev, A., Schreier, F., Schult, L., Smith, K. M., Tashkun, S. A., Teffo, J. L., Toth, R. A., Tyuterev, V. G., Vander Auwera, J., Varanasi, P. & Wagner, G. (2008). The GEISA spectroscopic database: Current and future archive for Earth and planetary atmosphere studies. *Journal of Quantitative Spectroscopy and Radiative Transfer, 109*, 1043-1059.

Jacquinet-Husson, N., Scott, N. A., Chedin, A., Garceran, K., Armante, R., Chursin, A. A., Barbe, A., Birk, M., Brown, L. R., Camy-Peyret, C., Claveau, C., Clerbaux, C., Coheur, P. F., Dana, V., Daumont, L., Debacker-Barilly, M. R., Flaud, J. M., Goldman, A., Hamdouni, A., Hess, M., Jacquemart, D., Kupke, P., Mandin, J. Y., Massie, S., Mikhailenko, S., Nemtchinov, V., Nikitin, A., Newnham, D., Perrin, A., Perevalov, V. I., Regalia-Jarlot, L., Rublev, A., Schreier, F., Schult, I., Smith, K. M., Tashkun, S. A., Teffo, J. L., Toth, R. A., Tyuterev, V. G., Vander Auwera, J., Varanasi, P. & Wagner, G. (2005). The 2003 edition of the GEISA/IASI spectroscopic database. *Journal of Quantitative Spectroscopy and Radiative Transfer, 95*, 429-467.

Janson, S. W., Helvajian, H. & Breuer, K. (1999). MEMS, Microengineering and Aerospace Systems. *AIAA 99-3802*.

Jaumann, R., Brown, R. H., Stephan, K., Barnes, J. W., Soderblom, L. A., Sotin, C., Le Mouelic, S., Clark, R. N., Soderblom, J., Buratti, B. J., Wagner, R., McCord, T. B., Rodriguez, S., Baines, K. H., Cruikshank, D. P., Nicholson, P. D., Griffith, C. A., Langhans, M. & Lorenz, R. D. (2008). Fluvial erosion and post-erosional processes on Titan. *Icarus, 197*(2), 526-538.

Jeans, J. (1925). *The dynamical theory of gases* (4th ed.): republished by Dover Publisher 1954.

Jennings, D. E., Anderson, C. M., Samuelson, R. E., Flasar, F. M., Nixon, C. A., Bjoraker, G. L., Romani, P. N., Achterberg, R. K., Cottini, V., Hesman, B. E., Kunde, V. G., Carlson, R., de Kok, R., Coustenis, A., Vinatier, S., Bampasidis, G., Teanby, N. A. & Calcutt, S. B. (2012). Titan's far-infrared winter hazemakes its debut in the south. *Astrophysical Journal Letters, in press*.

Jennings, D. E., Flasar, F. M., Kunde, V. G., Samuelson, R. E., Pearl, J. C., Nixon, C. A., Carlson, R. C., Mamoutkine, A. A., Brasunas, J. C., Guandique, E., Achterberg, R. K., Bjoraker, G. L., Romani, P. N., Segura, M. E., Albright, S. A., Elliott, M. H., Tingley, J. S., Calcutt, S., Coustenis, A. & Courtin, R. (2009). Titan's Surface Brightness Temperatures. *Astrophysical Journal, 691*, L103-L105.

Jennings, D. E., Nixon, C. A., Jolly, A., Bézard, B., Coustenis, A., Vinatier, S., Irwin, P. G. J., Teanby, N. A., Romani, P. N., Achterberg, R. K. & Flasar, F. M. (2008). Isotopic Ratios in Titan's Atmosphere from Cassini CIRS Limb Sounding: HC3N in the North. *The Astrophysical Journal, 681*, L109-L111-L109-L111.

Jha, C. M., Bahl, G., Melamud, R., Chandorkar, S. A., Hopcroft, M. A., Kim, B., Agarwal, M., Salvia, J., Mehta, H. & Kenny, T. W. (2007). Cmos-Compatible Dual-Resonator MEMS Temperature Sensor with Milli-Degree Accuracy. *International Solid-State Sensors, Actuators and Microsystems Conference, Transducers*, 229-232.

Jolly, A., Benilan, Y., Cane, E., Fusina, L., Tamassia, F., Fayt, A., Robert, S. & Herman, M. (2008). Measured integrated band intensities and simulated line-by-line spectra for $^{12}C_2HD$ between 25 and 2.5 μm, and new global vibration-rotation parameters for the bending vibrations. *Journal of Quantitative Spectroscopy and Radiative Transfer, 109*(17-18), 2846-2856.

Jolly, A., Benilan, Y. & Fayt, A. (2007). New infrared integrated band intensities for HC_3N and extensive line list for the v5 and v6 bending modes. *Journal of Molecular Spectroscopy, 242*, 46-54.

Jolly, A., Fayt, A., Benilan, Y., Jacquemart, D., Nixon, C. A. & Jennings, D. E. (2010). The v8 Bending Mode of Diacetylene: From Laboratory Spectroscopy to the Detection of 13C Isotopologues in Titan's Atmosphere. *The Astrophysical Journal, 714*, 852-859.

Jones, G. H., Arridge, C. S., Coates, A. J., Lewis, G. R., Kanani, S., Wellbrock, A., Young, D. T., Crary, F. J., Tokar, R. L., Wilson, R. J., Hill, T. W., Johnson, R. E., Mitchell, D. G., Schmidt, J., Kempf, S., Beckmann, U., Russell, C. T., Jia, Y. D., Dougherty, M. K., Waite, J. H. & Magee, B. A. (2009). Fine jet structure of electrically charged grains in Enceladus' plume. *Geophysical Research Letters, 36*, 16204.

Kapitsa, A. P., Ridley, J. K., de Q. Robin, G., Siegert, M. J. & Zotikov, I. A. (1996). A large deep freshwater lake beneath the ice of central East Antarctica. *Nature, 381*, 684-686.

Karau, S. J. & Williams, K. D. (1993). Social loafing: A meta-analytic review and theoretical integration. *Journal of Personality and Social Psychology, 65*(4), 681-706.

Kargel, J. S. (2006). Enceladus: Cosmic Gymnast, Volatile Miniworld. *Science, 311*, 1389-1391.

Kargel, J. S., Kaye, J. Z., Head, J. W., Marion, G. M., Sassen, R., Crowley, J. K., Ballesteros, O. P., Grant, S. A. & Hogenboom, D. L. (2000). Europa's Crust and Ocean: Origin, Composition, and the Prospects for Life. *Icarus, 148*, 226-265.

Kasting, J. F. (1988). Runaway and moist greenhouse atmospheres and the evolution of earth and Venus. *Icarus, 74*, 472-494.

Kasting, J. F. & Howard, M. T. (2006). Atmospheric composition and climate on the early Earth. *Philosophical Transactions of the Royal Society B: Biological Sciences, 361*(1474), 1733-1742.

Kasting, J. F., Whitmire, D. P. & Reynolds, R. T. (1993). Habitable Zones around Main Sequence Stars. *Icarus, 101*(1), 108-128.

Keating, T., Barnett, M., Barab, S. A. & Hay, K. E. (2002). The Virtual Solar System Project: Developing Conceptual Understanding of Astronomical Concepts Through Building Three-Dimensional Computational Models. *Journal of Science Education and Technology, 11*(3), 261-275.

Kennett, J. P., Cannariato, K. G., Hendy, I. L., & Behl, R. J. (2003). *Methane hydrates in Quaternary climate change: the clathrate gun hypothesis*: American Geophysical Union.

Kerr, N. L. & Bruun, S. E. (1983). The dispensability of member effort and group motivation losses: Free-rider effects. *Journal of Educational Computing Research, 5*, 1-15.

Khare, B. N., Sagan, C., Arakawa, E. T., Suits, F., Callcott, T. A. & Williams, M. W. (1984). Optical constants of organic tholins produced in a simulated Titanian atmosphere - From soft X-ray to microwave frequencies. *Icarus, 60*, 127-137.

Khare, B. N., Sagan, C., Ogino, H., Nagy, B., Er, C., Schram, K. H. & Arakawa, E. T. (1986). Amino acids derived from Titan Tholins. *Icarus, 68*, 176-184.

Khurana, K. K., Kivelson, M. G., Stevenson, D. J., Schubert, G., Russell, C. T., Walker, R. J. & Polanskey, C. (1998). Induced magnetic fields as evidence for subsurface oceans in Europa and Callisto. *Nature, 395*(6704), 777-780.

Kim, S. J. & Caldwell, J. (1982). The abundance of CH3D in the atmosphere of Titan, derived from 8- to 14-micron thermal emission. *Icarus, 52*, 473-482.

Kim, S. J., Geballe, T. R., Noll, K. S. & Courtin, R. (2005). Clouds, haze, and CH_4, CH_3D, HCN, and C_2H_2 in the atmosphere of Titan probed via 3 μm spectroscopy. *Icarus, 173*, 522-532.

Kivelson, M. G., Khurana, K. K., Russell, C. T., Volwerk, M., Walker, R. J. & Zimmer, C. (2000). Galileo Magnetometer Measurements: A Stronger Case for a Subsurface Ocean at Europa. *Science, 289*, 1340-1343.

Kivelson, M. G., Khurana, K. K. & Volwerk, M. (2002). The Permanent and Inductive Magnetic Moments of Ganymede. *Icarus, 157*, 507-522.

Kliore, A. J., Anderson, J. D., Armstrong, J. W., Asmar, S. W., Hamilton, C. L., Rappaport, N. J., Wahlquist, H. D., Ambrosini, R., Flasar, F. M., French, R. G., Iess, L., Marouf, E. A. & Nagy, A. F. (2004). Cassini Radio Science. *Space Science Reviews, 115*, 1-70.

Knapmeyer, M., Akito, A., Bampasidis, G., Banerdt, W. B., Coustenis, A., Fouch, M. J., Garnero, E. J., Khavroshkin, O., Kobayashi, N., Moussas, X., Pike, W. T., Seidensticker, K. J., Solomonidou, A., Yu, H. & Zakharov, A. (2012). *Planetary Seismometers: An Overview*. Paper presented at the EGU 2012, Vienna, Austria.

Kostiuk, T., Fast, K., Livengood, T. A., Goldstein, J., Hewagama, T., Buhl, D., Espenak, F. & Ho Ro, K. (1997). Ethane abundance on Titan. *Planetary and Space Science, 45*, 931-939.

Kostiuk, T., Hewagama, T., Fast, K. E., Livengood, T. A., Annen, J., Buhl, D., Sonnabend, G., Schmolling, F., Delgado, J. D. & Achterberg, R. (2010). High spectral resolution infrared studies of Titan: Winds, temperature, and composition. *Planetary and Space Science, 58*, 1715-1723.

Kostiuk, T., Livengood, T. A., Hewagama, T., Sonnabend, G., Fast, K. E., Murakawa, K., Tokunaga, A. T., Annen, J., Buhl, D. & Schmolling, F. (2005). Titan's stratospheric zonal wind, temperature, and ethane abundance a year prior to Huygens insertion. *Geophysical Research Letters, 32*, 22205-22205.

Kostiuk, T., Livengood, T. A., Sonnabend, G., Fast, K. E., Hewagama, T., Murakawa, K., Tokunaga, A. T., Annen, J., Buhl, D., Schmolling, F., Luz, D. & Witasse, O. (2006). Stratospheric global winds on Titan at the time of Huygens descent. *Journal of Geophysical Research (Planets), 111*.

Krasnopolsky, V. A. (2009). A photochemical model of Titan's atmosphere and ionosphere. *Icarus, 201*(1), 226-256.

Kress, R. (1999). *Linear integral equations* (2nd ed.). New York: Springer-Verlag.

Krimigis, S. M., Mitchell, D. G., Hamilton, D. C., Krupp, N., Livi, S., Roelof, E. C., Dandouras, J., Armstrong, T. P., Mauk, B. H., Paranicas, C., Brandt, P. C., Bolton, S., Cheng, A. F., Choo, T., Gloeckler, G., Hayes, J., Hsieh, K. C., Ip, W. H., Jaskulek, S., Keath, E. P., Kirsch, E., Kusterer, M., Lagg, A., Lanzerotti, L. J., LaVallee, D., Manweiler, J., McEntire, R. W., Rasmuss, W., Saur, J., Turner, F. S., Williams, D. J. & Woch, J. (2005). Dynamics of Saturn's Magnetosphere from MIMI During Cassini's Orbital Insertion. *Science, 307*, 1270-1273.

Krimigis, S. M., Mitchell, D. G., Hamilton, D. C., Livi, S., Dandouras, J., Jaskulek, S., Armstrong, T. P., Boldt, J. D., Cheng, A. F., Gloeckler, G., Hayes, J. R., Hsieh, K. C., Ip, W. H., Keath, E. P., Kirsch, E., Krupp, N., Lanzerotti, L. J., Lundgren, R., Mauk, B. H., McEntire, R. W., Roelof, E. C., Schlemm, C. E., Tossman, B. E., Wilken, B. & Williams, D. J. (2004). Magnetosphere Imaging Instrument (MIMI) on the Cassini Mission to Saturn/Titan. *Space Science Reviews, 114*, 233-329.

Krishnamoorthy, R. & Bifano, T. (1995). MEMS arrays for deformable mirrors. *SPIE, 2641*(96-104).

Kuiper, G. P. (1944). Titan: a Satellite with an Atmosphere. *Astrophysical Journal, 100*, 378-383.

Kuiper, G. P. (1952). *The atmospheres of the earth and planets*. Chicago: University of Chicago Press.

Kulikov, Y. N., Lammer, H., Lichtenegger, H. I. M., Terada, N., Ribas, I., Kolb, C., Langmayr, D., Lundin, R., Guinan, E. F., Barabash, S. & Biernat, H. K. (2006). Atmospheric and water loss from early Venus. *Planetary and Space Science, 54*(13-14), 1425-1444.

Kunde, V. G., Ade, P. A., Barney, R. D., Bergman, D., Bonnal, J.-F., Borelli, R., Boyd, D., Brasunas, J. C., Brown, G., Calcutt, S. B., Carroll, F., Courtin, R., Cretolle, J., Crooke, J. A., Davis, M. A., Edberg, S., Fettig, R., Flasar, M., Glenar, D. A., Graham, S., Hagopian, J. G., Hakun, C. F., Hayes, P. A., Herath, L., Horn, L., Jennings, D. E., Karpati, G., Kellebenz, C., Lakew, B., Lindsay, J., Lohr, J., Lyons, J. J., Martineau, R. J., Martino, A. J., Matsumura, M., McCloskey, J., Melak, T., Michel, G., Morell, A., Mosier, C., Pack, L., Plants, M., Robinson, D., Rodriguez, L., Romani, P., Schaefer, W. J., Schmidt, S., Trujillo, C., Vellacott, T., Wagner, K. & Yun, D. (1996). Cassini infrared fourier spectroscopic investigation. *Proc. Soc. Photo-Opt. Instum. Eng., 2803*, 162-177.

Kunde, V. G., Aikin, A. C., Hanel, R. A., Jennings, D. E., Maguire, W. C. & Samuelson, R. E. (1981). C_4H_2, HC_3N and C_2N_2 in Titan's atmosphere. *Nature, 292*, 686-688.

Kuskov, O. L. & Kronrod, V. A. (2005). Internal structure of Europa and Callisto. *Icarus, 177*(2), 550-569.

Lacis, A. A. & Oinas, V. (1991). A description of the correlated-k distribution method for modelling nongray gaseous absorption, thermal emission, and multiple scattering in vertically inhomogeneous atmospheres. *Journal of Geophysical Research, 96*, 9027-9064.

Lammer, H., Bredehoft, J., Coustenis, A., Khodachenko, M., Kaltenegger, L., Grasset, O., Prieur, D., Raulin, F., Ehrenfreund, P., Yamauchi, M., Wahlund, J. E., Grießmeier, J. M., Stangl, G., Cockell, C., Kulikov, Y., Grenfell, J. & Rauer, H. (2009). What makes a planet habitable? *Astronomy and Astrophysics Review, 17*(2), 181-249.

Lange, C., Sohl, F., Coustenis, A., Jaumann, R., Karatekin, O., Schmitz, N., Solomonidou, A., Wagenbach, S., Rosta, R. & van Zoest, T. (2011). *Concept Study for a Titan Geophysical Network.* Paper presented at the EGU, Vienna, Austria.

Lavvas, P. P., Coustenis, A. & Vardavas, I. M. (2008a). Coupling photochemistry with haze formation in Titan's atmosphere, Part I: Model description. *Planetary and Space Science, 56*, 27-66.

Lavvas, P. P., Coustenis, A. & Vardavas, I. M. (2008b). Coupling photochemistry with haze formation in Titan's atmosphere, Part II: Results and validation with Cassini/Huygens data. *Planetary and Space Science, 56*, 67-99.

Le Mouelic, S., Paillou, P., Janssen, M. A., Barnes, J. W., Rodriguez, S., Sotin, C., Brown, R. H., Baines, K. H., Buratti, B. J., Clark, R. N., Crapeau, M., Encrenaz, P. J., Jaumann, R., Geudtner, D., Paganelli, F., Soderblom, L., Tobie, G. & Wall, S. (2008). Mapping and interpretation of Sinlap crater on Titan using Cassini VIMS and RADAR data. *Journal of Geophysical Research (Planets), 113*, 04003.

Leary, J., Strain, R., Lorenz, R. & Waite, J. H. (2008). Titan explorer flagship mission study, Public Report. *http://www.lpi.usra.edu/opag/Titan_Explorer_Public_Report.pdf.*

Lebreton, J.-P., Coustenis, A., Lunine, J., Raulin, F., Owen, T. & Strobel, D. (2009). Results from the Huygens probe on Titan. *Astronomy and Astrophysics Review, 17*, 149-179.

Lebreton, J.-P., Witasse, O., Sollazzo, C., Blancquaert, T., Couzin, P., Schipper, A.-M., Jones, J. B., Matson, D. L., Gurvits, L. I., Atkinson, D. H., Kazeminejad, B. & Perez-Ayucar, M. (2005). An overview of the descent and landing of the Huygens probe on Titan. *Nature, 438*, 758-764.

Lee, J. S., Jurkevich, L., Dewaele, P., Wambacq, P. & Oosterlinck, A. (1994). Speckle filtering of synthetic aperture radar images: A review. *Remote Sensing Reviews, 8*(4), 313-340.

Lellouch, E., Coustenis, A., Gautier, D., Raulin, F., Dubouloz, N. & Frere, C. (1989). Titan's atmosphere and hypothesized ocean: A reanalysis of the Voyager 1 radio-occultation and IRIS 7.7-μm data. *Icarus, 79*(2), 328-349.

Lellouch, E., Coustenis, A., Sebag, B., Cuby, J. G., Lopez-Valverde, M., Schmitt, B., Fouchet, T. & Crovisier, J. (2003). Titan's 5-μm window: observations with the Very Large Telescope. *Icarus, 162*, 125-142.

Lellouch, E., Hunten, D. M., Kockarts, G. & Coustenis, A. (1990). Titan's thermosphere profile. *Icarus, 83*, 308-324.

Lemmon, M. T., Karkoschka, E. & Tomasko, M. (1993). Titan's Rotation: Surface Feature Observed. *Icarus, 103*(2), 329-332.

Letourneur, B. & Coustenis, A. (1993). Titan's atmospheric structure from Voyager 2 infrared spectra. *Planetary and Space Science, 41*, 593-602.

Lewis, J. S. (1971). Satellites of the Outer Planets: Their Physical and Chemical Nature. *Icarus, 15*, 174.

Lewis, J. S. (2004). *Physics and chemistry of the solar system* (2nd ed.): Academic Press.

Lewis, J. S. & Prinn, R. G. (1973). Titan Revisited. *Comments on Astrophysics and Space Physics, 5*, 1.

Li, B., Zhang, G. Q., Yang, D. G., Fengze, H. & Yang, H. (2010). The effect of diaphragm on performance of MEMS pressure sensor packaging. *11th International Conference on Electronic Packaging Technology & High Density Packaging*, 601-606.

Likert, R. (1932). A Technique for the Measurement of Attitudes. *Archives of Psychology, 140*, 1-55.

Lin, L. & Yun, W. (1998). MEMS pressure sensors for aerospace applications. *IEEE Aerospace Conference Proceedings 1*, 421-429-436.

Lindal, G. F., Wood, G. E., Hotz, H. B., Sweetnam, D. N., Eshleman, V. R. & Tyler, G. L. (1983). The atmosphere of Titan: An analysis of the Voyager 1 radio occultation measurements. *Icarus, 53*(2), 348-363.

Linick, S., Boyles, C. & Woncick, P. (2006). *Cassini Distributed Instrument Operations – What We've Learned Since Saturn Orbit Insertion.* Paper presented at the AIAA 9th International Conference on Space Operations (SpaceOps), Rome, Italy, June 19-24

Linn, M. C., Clark, D. & Slotta, J. D. (2003). WISE design for knowledge integration. *Science Education, 87*(4), 517-538.

Livengood, T. A., Hewagama, T., Kostiuk, T., Fast, K. E. & Goldstein, J. J. (2002). NOTE: Improved Determination of Ethane (C_2H_6) Abundance in Titan's Stratosphere. *Icarus, 157*, 249-253.

Livengood, T. A., Kostiuk, T., Sonnabend, G., Annen, J. N., Fast, K. E., Tokunaga, A., Murakawa, K., Hewagama, T., Schmolling, F. & Schieder, R. (2006). High-resolution infrared spectroscopy of ethane in Titan's stratosphere in the Huygens epoch. *Journal of Geophysical Research (Planets), 111*.

Lopes, R. M. C., Mitchell, K. L., Stofan, E. R., Lunine, J. I., Lorenz, R., Paganelli, F., Kirk, R. L., Wood, C. A., Wall, S. D., Robshaw, L. E., Fortes, A. D., Neish, C. D., Radebaugh, J., Reffet, E., Ostro, S. J., Elachi, C., Allison, M. D., Anderson, Y., Boehmer, R., Boubin, G., Callahan, P., Encrenaz, P., Flamini, E., Francescetti, G., Gim, Y., Hamilton, G., Hensley, S., Janssen, M. A., Johnson, W. T. K., Kelleher, K., Muhleman, D. O., Ori, G., Orosei, R., Picardi, G., Posa, F., Roth, L. E., Seu, R., Shaffer, S., Soderblom, L. A., Stiles, B., Vetrella, S., West, R. D., Wye, L. & Zebker, H. A. (2007). Cryovolcanic features on Titan's surface as revealed by the Cassini Titan Radar Mapper. *Icarus, 186*, 395-412.

Lopes, R. M. C., Stofan, E. R., Peckyno, R., Radebaugh, J., Mitchell, K. L., Mitri, G., Wood, C. A., Kirk, R. L., Wall, S. D., Lunine, J. I., Hayes, A., Lorenz, R., Farr, T., Wye, L., Craig, J., Ollerenshaw, R. J., Janssen, M., Legall, A., Paganelli, F., West, R., Stiles, B., Callahan, P., Anderson, Y., Valora, P., Soderblom, L. & Cassini, R. T. (2010). Distribution and interplay of geologic processes on Titan from Cassini radar data. *Icarus, 205*, 540-558.

Lora, J. M., Goodman, P. J., Russell, J. L. & Lunine, J. I. (2011). Insolation in Titan's troposphere. *Icarus, 216*, 116-119.

Lorenz, R. (1997). Did Comas Sola discover Titan's atmosphere? *Astronomy and Geophysics, 38*, 16.

Lorenz, R., Hurford, T., Bills, B., Sohl, F., Roberts, J., Sotin, C. & Hussmann, H. (2009). White Paper for The Case for a Titan Geophysical Network Mission *Solar System Decadal Survey 2013-2023*.

Lorenz, R. D. (1993). The life, death and afterlife of a raindrop on Titan. *Planetary and Space Science, 41*, 647-655.

Lorenz, R. D., Lopes, R. M., Paganelli, F., Lunine, J. I., Kirk, R. L., Mitchell, K. L., Soderblom, L. A., Stofan, E. R., Ori, G., Myers, M., Miyamoto, H., Radebaugh, J., Stiles, B., Wall, S. D., Wood, C. A. & Team, t. C. R. (2008a). Fluvial channels on Titan : Initial Cassini radar observations. *Planetary and Space Science, 56*(8), 1132-1144.

Lorenz, R. D., Mitchell, K. L., Kirk, R. L., Hayes, A. G., Aharonson, O., Zebker, H. A., Paillou, P., Radebaugh, J., Lunine, J. I., Janssen, M. A., Wall, S. D., Lopes, R. M., Stiles, B., Ostro, S., Mitri, G. & Stofan, E. R. (2008b). Titan's inventory of organic surface materials. *Geophysical Research Letters, 35*, 02206.

Lorenz, R. D., Niemann, H. B., Harpold, D. N., Way, S. H. & Zarnecki, J. C. (2006a). Titan's damp ground: Constraints on Titan surface thermal properties from the temperature evolution of the Huygens GCMS inlet. *Meteoritics and Planetary Science, 41*, 1705-1714.

Lorenz, R. D., Stiles, B. W., Kirk, R. L., Allison, M. D., del Marmo, P. P., Iess, L., Lunine, J. I., Ostro, S. J. & Hensley, S. (2008c). Titan's Rotation Reveals an Internal Ocean and Changing Zonal Winds. *Science, 319*(5870), 1649-1651.

Lorenz, R. D., Turtle, E. P., Stiles, B., Le Gall, A., Hayes, A., Aharonson, O., Wood, C. A., Stofan, E. & Kirk, R. (2011). Hypsometry of Titan. *Icarus, 211*, 699-706.

Lorenz, R. D., Wall, S., Radebaugh, J., Boubin, G., Reffet, E., Janssen, M., Stofan, E., Lopes, R., Kirk, R., Elachi, C., Lunine, J., Mitchell, K., Paganelli, F., Soderblom, L., Wood, C., Wye, L., Zebker, H., Anderson, Y., Ostro, S., Allison, M., Boehmer, R., Callahan, P., Encrenaz, P., Ori, G. G., Francescetti, G., Gim, Y., Hamilton, G., Hensley, S., Johnson, W., Kelleher, K., Muhleman, D., Picardi, G., Posa, F., Roth, L., Seu, R., Shaffer, S., Stiles, B., Vetrella, S., Flamini, E. & West, R. (2006b). The Sand Seas of Titan: Cassini RADAR Observations of Longitudinal Dunes. *Science, 312*, 724-727.

Lucarini, V. (2005). *Kramers-Kronig Relations In Optical Materials Research*: Springer.

Lunine, J. I., Stevenson, D. J. & Yung, Y. L. (1983). Ethane ocean on Titan. *Science, 222*, 1229-1230.

Lutz, B. L., de Bergh, C. & Owen, T. (1983). Titan - Discovery of carbon monoxide in its atmosphere. *Science, 220*, 1374-1374.

Luz, D., Civeit, T., Courtin, R., Lebreton, J. P., Gautier, D., Rannou, P., Kaufer, A., Witasse, O., Lara, L. & Ferri, F. (2005). Characterization of zonal winds in the stratosphere of Titan with UVES. *Icarus, 179*, 497-510.

Maguire, W. C., Hanel, R. A., Jennings, D. E., Kunde, V. G. & Samuelson, R. E. (1981). C_3H_8 and C_3H_4 in Titan's atmosphere. *Nature, 292*, 683-686.

Marion, G. M., Fritsen, C. H., Eicken, H. & Payne, M. C. (2003). The Search for Life on Europa: Limiting Environmental Factors, Potential Habitats, and Earth Analogues. *Astrobiology, 3*, 785-811.

Marten, A., Hidayat, T., Biraud, Y. & Moreno, R. (2002). New Millimeter Heterodyne Observations of Titan: Vertical Distributions of Nitriles HCN, HC_3N, CH_3CN, and the Isotopic Ratio $^{15}N/^{14}N$ in Its Atmosphere. *Icarus, 158*, 532-544.

Martin, D. H. & Puplett, E. (1970). Polarised interferometric spectrometry for the millimetre and submillimetre spectrum. *Infrared Physics, 10*(2), 105-109.

Martineau, R. J., Hu, K., Manthripragada, S., Kotecki, C. A., Babu, S. R., Peters, F. A., Burgess, A. S., Mott, D. B., Krebs, D. J., Graham, S., Ewin, A. J., Miles, A., Bly, V. T., Nguyen, T. L., McCloskey, J. & Shu, P. K. (1996). *HgCdTe detector technology and performance for the Composite Infrared Spectrometer (CIRS)/Cassini mission. Cassini/Huygens: A mission to the Saturnian systems; Proceedings of the Meeting, Denver, CO; 5-6 Aug.* 178-186.

Marty, B., Guillot, T., Coustenis, A., Achilleos, N., Alibert, Y., Asmar, S., Atkinson, D., Atreya, S., Babasides, G., Baines, K., Balint, T., Banfield, D., Barber, S., Bézard, B., Bjoraker, G. L., Blanc, M., Bolton, S., Chanover, N., Charnoz, S., Chassefière, E., Colwell, J. E., Deangelis, E., Dougherty, M., Drossart, P., Flasar, F. M., Fouchet, T., Frampton, R., Franchi, I., Gautier, D., Gurvits, L., Hueso, R., Kazeminejad, B., Krimigis, T., Jambon, A., Jones, G., Langevin, Y., Leese, M., Lellouch, E., Lunine, J., Milillo, A., Mahaffy, P., Mauk, B., Morse, A., Moreira, M., Moussas, X., Murray, C., Mueller-Wodarg, I., Owen, T. C., Pogrebenko, S., Prangé, R., Read, P., Sanchez-Lavega, A., Sarda, P., Stam, D., Tinetti, G., Zarka, P. & Zarnecki, J. (2009a). Kronos: exploring the depths of Saturn with probes and remote sensing through an international mission. *Experimental Astronomy, 23*(3), 947-976.

Marty, B., Guillot, T., Coustenis, A., Achilleos, N., Alibert, Y., Asmar, S., Atkinson, D., Atreya, S., Babasides, G., Baines, K., Balint, T., Banfield, D., Barber, S., Bezard, B., Bjoraker, G. L., Blanc, M., Bolton, S., Chanover, N., Charnoz, S., Chassefiere, E., Colwell, J. E., Deangelis, E., Dougherty, M., Drossart, P., Flasar, F. M., Fouchet, T., Frampton, R., Franchi, I., Gautier, D., Gurvits, L., Hueso, R., Kazeminejad, B., Krimigis, T., Jambon, A., Jones, G., Langevin, Y., Leese, M., Lellouch, E., Lunine, J., Milillo, A., Mahaffy, P., Mauk, B., Morse, A., Moreira, M., Moussas, X., Murray, C., Mueller-Wodarg, I., Owen, T. C., Pogrebenko, S., Prange, R., Read, P., Sanchez-Lavega, A., Sarda, P., Stam, D., Tinetti, G., Zarka, P., Zarnecki, J., Schmidt, J. & Salo, H. (2009b). Erratum: Kronos: exploring the depths of Saturn with probes and remote sensing through an international mission. *Experimental Astronomy, 23*, 977-980.

Matson, D. L., Castillo-Rogez, J. C., Davies, A. G. & Johnson, T. V. (2012). Enceladus: A hypothesis for bringing both heat and chemicals to the surface. *Icarus, 221*(1), 53-62.

Matson, D. L., Castillo, J. C., Lunine, J. & Johnson, T. V. (2007). Enceladus' plume: Compositional evidence for a hot interior. *Icarus, 187*, 569-573.

Matson, D. L., Spilker, L. J. & Lebreton, J.-P. (2002). The Cassini/Huygens Mission to the Saturnian System. *Space Science Reviews, 104*, 1-58.

McCord, T. B., Hansen, G. B., Clark, R. N., Martin, P. D., Hibbitts, C. A., Fanale, F. P., Granahan, J. C., Segura, M., Matson, D. L., Johnson, T. V., Carlson, R. W., Smythe, W. D. & Danielson, G. E. (1998a). Non-water-ice constituents in the surface material of the icy Galilean satellites from the Galileo near-infrared mapping spectrometer investigation. *Journal of Geophysical Research, 103*(E4), 8603-8626.

McCord, T. B., Hansen, G. B., Fanale, F. P., Carlson, R. W., Matson, D. L., Johnson, T. V., Smythe, W. D., Crowley, J. K., Martin, P. D., Ocampo, A., Hibbitts, C. A. & Granahan, J. C. (1998b). Salts on Europa's Surface Detected by Galileo's Near Infrared Mapping Spectrometer. *Science, 280*(5367), 1242-1245.

McCord, T. B., Hansen, G. B. & Hibbitts, C. A. (2001). Hydrated Salt Minerals on Ganymede's Surface: Evidence of an Ocean Below. *Science, 292*, 1523-1525.

McEwen, A. S., Hansen, C. J., Delamere, W. A., Eliason, E. M., Herkenhoff, K. E., Keszthelyi, L., Gulick, V. C., Kirk, R. L., Mellon, M. T., Grant, J. A., Thomas, N., Weitz, C. M., Squyres, S. W., Bridges, N. T., Murchie, S. L., Seelos, F., Seelos, K., Okubo, C. H., Milazzo, M. P., Tornabene, L. L., Jaeger, W. L., Byrne, S., Russell, P. S., Griffes, J. L., Martinez-Alonso, S., Davatzes, A., Chuang, F. C., Thomson, B. J., Fishbaugh, K. E., Dundas, C. M., Kolb, K. J., Banks, M. E. & Wray, J. J. (2007). A Closer Look at Water-Related Geologic Activity on Mars. *Science, 317*(5845), 1706-1709.

McKay, C. P., Lorenz, R. D. & Lunine, J. I. (1999). Analytic Solutions for the Antigreenhouse Effect: Titan and the Early Earth. *Icarus, 137*, 56-61.

McKay, C. P., Porco Carolyn, C., Altheide, T., Davis, W. L. & Kral, T. A. (2008). The Possible Origin and Persistence of Life on Enceladus and Detection of Biomarkers in the Plume. *Astrobiology, 8*, 909-919.

McKay, C. P. & Smith, H. D. (2005). Possibilities for methanogenic life in liquid methane on the surface of Titan. *Icarus, 178*, 274-276.
McKinnon, W. (1998). *Geodynamics of Icy Satellites*: Dordrecht Kluwer Academic Publishers, Astrophysics and space science library (ASSL).
McKinnon, W. B. (1999). Convective instability in Europa's floating ice shell. *Geophysical Research Letters, 26*, 951-954.
McMurry, J. (2008). *Organic Chemistry* (7th ed.): Thomson Brooks/Cole.
Meier, R., Smith, B. A., Owen, T. C. & Terrile, R. J. (2000). The surface of Titan from NICMOS observations with the Hubble Space Telescope. *Icarus, 145*, 462-473.
Melosh, H. J. & Nimmo, F. (2011). *Long-Term Strength of Icy vs Silicate Planetary Bodies.* Paper presented at the 42nd Lunar and Planetary Science Conference, March 7–11, The Woodlands, Texas.
Menor-Salván, C., Ruiz-Bermejo, M., Osuna-Esteban, S., Muñoz-Caro, G. & Veintemillas-Verdaguer, S. (2008). Synthesis of Polycyclic Aromatic Hydrocarbons and Acetylene Polymers in Ice: A Prebiotic Scenario. *Chemistry & Biodiversity, 5*(12), 2729-2739.
Michael, M. & Johnson, R. E. (2005). Energy deposition of pickup ions and heating of Titan's atmosphere. *Planetary and Space Science, 53*, 1510-1514.
Michelson, A. A. (1881). On the Velocity of Light. *Nature, 24*, 460-461.
Miller, S. L. (1953). A Production of Amino Acids under Possible Primitive Earth Conditions. *Science, 117*, 528-529.
Miller, S. L. & Urey, H. C. (1959). Organic Compound Synthesis on the Primitive Earth. *Science, 130*, 245-251.
Mitri, G., Bland, M. T., Showman, A. P., Radebaugh, J., Stiles, B., Lopes, R. M. C., Lunine, J. I. & Pappalardo, R. T. (2010). Mountains on Titan: Modeling and observations. *Journal of Geophysical Research (Planets), 115*, 10002.
Mitri, G., Showman, A. P., Lunine, J. I. & Lopes, R. M. C. (2008). Resurfacing of Titan by ammonia-water cryomagma. *Icarus, 196*(1), 216-224.
Mitri, G., Showman, A. P., Lunine, J. I. & Lorenz, R. D. (2007). Hydrocarbon lakes on Titan. *Icarus, 186*, 385-394.
Moreno, R., Lellouch, E., Lara, L. M., Courtin, R., Bockelee-Morvan, D., Hartogh, P., Rengel, M., Biver, N., Banaszkiewicz, M. & Gonzalez, A. (2011). First detection of hydrogen isocyanide (HNC) in Titan's atmosphere. *Astronomy and Astrophysics, 536*(L12).
Moreno, R., Lellouch, E., Lara, L. M., Feuchtgruber, H., Rengel, M., Hartogh, P. & Courtin, R. (2012). The abundance, vertical distribution and origin of H_2O in Titan's atmosphere: Herschel observations and photochemical modelling. *Icarus*, 221,753-767.
Moriconi, M. L., Lunine, J. I., Adriani, A., D'Aversa, E., Negrao, A., Filacchione, G. & Coradini, A. (2010). Characterization of Titan's Ontario Lacus region from Cassini/VIMS observations. *Icarus, 210*(2), 823-831.
Moussas, X. & Bampasidis, G. (2009). *The Antikythera Mechanism as an educational device to teach modelling of the Solar System and the Universe.* Paper presented at the European Planetary Science Congress, 14-18 September, Potsdam, Germany.
Moussas, X., Bampasidis, G., Bitsakis, Y., Tassios, T., Anastasiou, M., Efstathiou, K., Fasoulopoulos, G., Kioleoglou, I., Edmunds, M., Zafeiropoulou, M., Roumeliotis, M., Malzbender, T., Ramsey, A., Kriaris, D., Spandagos, E., Giannopoulos, N., Porligi, A., Daniels, E., Wright, M. T., Sabry, R., El-Mikaty, H., Henriksson, G., Munktell, I.-M., Vafea, F., Koufos, S., Prassopoulos, D., Zafiropoulos, V., Karakonstantis, A., Aggeioplasti, K., Delidou, E., Papoulias, C., Papoulias, G., Haley, P., Mimouni, J., Valls-Gabaud, D., Biggs, M., Chochol, D., Szubiakowski, J., Plucinska, E., Jacyno, A., Kakouris, A., Palus, P., Jancuskova, D., Feriancikova, M., Czart, K., Xenakis, N., Gkini, M. E., Perpyraki, E., Tziannoudakis, L. & Antoniou, P. (2011a). The gears of the Antikythera Mechanism: an educational pathfinder to the solar system. *The Role of Astronomy in Society and Culture, Proceedings of the International Astronomical Union, IAU Symposium, 260*, E1.
Moussas, X., Bampasidis, G., Bitsakis, Y., Tassios, T., Anastasiou, M., Efstathiou, K., Fasoulopoulos, G., Kioleoglou, I., Edmunds, M., Zafeiropoulou, M., Roumeliotis, M., Malzbender, T., Ramsey, A., Kriaris, D., Spandagos, E., Giannopoulos, N., Porligi, A., Daniels, E., Wright, M. T., Sabry, R., El-Mikaty, H., Henriksson, G., Munktell, I.-M., Vafea, F., Koufos, S., Prassopoulos, D., Zafiropoulos, V., Karakonstantis, A., Aggeioplasti, K., Delidou, E., Papoulias, C., Papoulias, G., Haley, P., Mimouni, J., Valls-Gabaud, D., Biggs, M., Chochol, D., Szubiakowski, J., Plucinska, E., Jacyno, A., Kakouris, A., Palus, P., Jancuskova, D., Feriancikova, M., Czart, K., Xenakis, N., Gkini, M. E., Perpyraki, E., Tziannoudakis, L. & Antoniou, P. (2011b). *The gears of the Antikythera Mechanism: an educational pathfinder to the solar system.* Paper presented at the The Role of Astronomy in Society and Culture, IAU Symposium 2009, Paris, France.
Moussas, X. (2010a). The Antikythera Mechanism as an educational device, *European Planetary Science Congress (EPSC)*. Rome, Italy.

Moussas, X., Bampasidis, G., Coustenis, A. & Solomonidou, A. (2010b). *Outreach for Cassini Huyghens mission and future Saturn and Titan exploration: From the Antikythera Mechanism to the TSSM mission.* Paper presented at the EGU General Assembly, 2-7 May, Vienna, Austria.

Moussas, X., Coustenis, A., Solomonidou, A., Bampasidis, G., Bratsolis, E. & Stamogiorgos, S. (2012). *The oldest computer in today's education: The great attractor of children to science, the Antikythera Mechanism, as an educational instrument.* Paper presented at the EGU General Assembly, 22-27 April, Vienna, Austria.

Moussas, X., Dialynas, K., Babasides, G., Fasoulopoulos, G., Dimitropoulou, V., Prassopoulos, D., Kouphos, S., Spandagos, E. & Strikis, J. (2006). *Outreach of Astronomy with emphasis to the Solar System by the Space group in Greece.* Paper presented at the European Planetary Science Congress, 18 - 22 September, Berlin, Germany.

Muhleman, D. O., Grossman, A. W., Butler, B. J. & Slade, M. A. (1990). Radar reflectivity of Titan. *Science, 248*, 975-980.

Muller-Wodarg, I. C. F., Yelle, R. V., Cui, J. & Waite, J. H. (2008). Horizontal structures and dynamics of Titan's thermosphere. *Journal of Geophysical Research, 113*(E10), E10005.

Muyzer, G. & Stams, A. J. M. (2008). The ecology and biotechnology of sulphate-reducing bacteria. *Nature Reviews. Microbiology, 6*(6), 441-454.

Nagel, K., Breuer, D. & Spohn, T. (2004). A model for the interior structure, evolution, and differentiation of Callisto. *Icarus, 169*(2), 402-412.

Nakamura, R. & Ohtani, E. (2011). The high-pressure phase relation of the MgSO4-H2O system and its implication for the internal structure of Ganymede. *Icarus, 211*(1), 648-654.

Nakamura, Y., Latham, G. V. & Dorman, H. J. (1982). Apollo lunar seismic experiment - final summary. *Journal of Geophysical Research, 87*, 117-117.

Nam, S., Artikova, S., Chung, T., Garipov, G., Jeon, J. A., Jeong, S., Jin, J. Y., Khrenov, B. A., Kim, J. E., Kim, M., Kim, Y. K., Klimov, P., Lee, J., Lee, H. Y., Na, G. W., Oh, S. J., Panasyuk, M., Park, I. H., Park, J. H., Park, Y. S., Yoo, B. W. & Yoo, H. J. (2008). A telescope for observation from space of extreme lightnings in the upper atmosphere. *Nuclear Instruments and Methods in Physics Research Section A: Accelerators, Spectrometers, Detectors and Associated Equipment, 588*(1-2), 197-200.

Nathanson, H. C., Newell, W. E., Wickstrom, R. A. & Davis, J., J. R. (1967). The Resonant Gate Transistor. *IEEE Transactions on Electron Devices.*

Negrao, A., Coustenis, A., Lellouch, E., Maillard, J. P., Rannou, P., Schmitt, B., McKay, C. P. & Boudon, V. (2006). Titan's surface albedo variations over a Titan season from near-infrared CFHT/FTS spectra. *Planetary and Space Science, 54*, 1225-1246.

Negrao, A., Hirtzig, M., Coustenis, A., Gendron, E., Drossart, P., Rannou, P., Combes, M. & Boudon, V. (2007). The 2-μm spectroscopy of Huygens probe landing site on Titan with Very Large Telescope/Nasmyth Adaptive Optics System Near-Infrared Imager and Spectrograph. *Journal of Geophysical Research (Planets), 112.*

Neish, C. D., Lorenz, R. D., Kirk, R. L. & Wye, L. C. (2010). Radarclinometry of the sand seas of Africa's Namibia and Saturn's moon Titan. *Icarus, 208*, 385-394.

Nelson, R. M., Kamp, L. W., Lopes, R. M. C., Matson, D. L., Kirk, R. L., Hapke, B. W., Wall, S. D., Boryta, M. D., Leader, F. E., Smythe, W. D., Mitchell, K. L., Baines, K. H., Jaumann, R., Sotin, C., Clark, R. N., Cruikshank, D. P., Drossart, P., Lunine, J. I., Combes, M., Bellucci, G., Bibring, J.-P., Capaccioni, F., Cerroni, P., Coradini, A., Formisano, V., Filacchione, G., Langevin, Y., McCord, T. B., Mennella, V., Nicholson, P. D., Sicardy, B., Irwin, P. G. J. & Pearl, J. C. (2009a). Photometric changes on Saturn's Titan: Evidence for active cryovolcanism. *Geophysical Research Letters, 36*, 04202.

Nelson, R. M., Kamp, L. W., Matson, D. L., Irwin, P. G. J., Baines, K. H., Boryta, M. D., Leader, F. E., Jaumann, R., Smythe, W. D., Sotin, C., Clark, R. N., Cruikshank, D. P., Drossart, P., Pearl, J. C., Hapke, B. W., Lunine, J., Combes, M., Bellucci, G., Bibring, J. P., Capaccioni, F., Cerroni, P., Coradini, A., Formisano, V., Filacchione, G., Langevin, R. Y., McCord, T. B., Mennella, V., Nicholson, P. D. & Sicardy, B. (2009b). Saturn's Titan: Surface change, ammonia, and implications for atmospheric and tectonic activity. *Icarus, 199*, 429-441.

Ness, N. F., Acuna, M. H. & Behannon, K. W. (1982). The induced magnetosphere of Titan. *Journal of Geophysical Research, 87*, 1369-1381.

Neubauer, F. M., Backes, H., Dougherty, M. K., Wennmacher, A., Russell, C. T., Coates, A., Young, D., Achilleos, N., Andre, N., Arridge, C. S., Bertucci, C., Jones, G. H., Khurana, K. K., Knetter, T., Law, A., Lewis, G. R. & Saur, J. (2006). Titan's near magnetotail from magnetic field and electron plasma observations and modeling: Cassini flybys TA, TB, and T3. *Journal of Geophysical Research (Space Physics), 111*, 10220.

Nguyen, M. J., Raulin, F., Coll, P., Derenne, S., Szopa, C., Cernogora, G., Israël, G. & Bernard, J. M. (2007). Carbon isotopic enrichment in Titan's tholins? Implications for Titan's aerosols. *Planetary and Space Science, 55*, 2010-2014.

Niemann, H. B., Atreya, S. K., Bauer, S. J., Biemann, K., Block, B., Carignan, G. R., Donahue, T. M., Frost, R. L., Gautier, D., Haberman, J. A., Harpold, D., Hunten, D. M., Israel, G., Lunine, J. I., Mauersberger, K., Owen, T. C., Raulin, F., Richards, J. E. & Way, S. H. (2002). The Gas Chromatograph Mass Spectrometer for the Huygens Probe. *Space Science Reviews, 104*, 553-591.

Niemann, H. B., Atreya, S. K., Bauer, S. J., Carignan, G. R., Demick, J. E., Frost, R. L., Gautier, D., Haberman, J. A., Harpold, D. N., Hunten, D. M., Israel, G., Lunine, J. I., Kasprzak, W. T., Owen, T. C., Paulkovich, M., Raulin, F., Raaen, E. & Way, S. H. (2005). The abundances of constituents of Titan's atmosphere from the GCMS instrument on the Huygens probe. *Nature, 438*, 779-784.

Niemann, H. B., Atreya, S. K., Demick, J. E., Gautier, D., Haberman, J. A., Harpold, D. N., Kasprzak, W. T., Lunine, J. I., Owen, T. C. & Raulin, F. (2010). Composition of Titan's lower atmosphere and simple surface volatiles as measured by the Cassini-Huygens probe gas chromatograph mass spectrometer experiment. *Journal of Geophysical Research (Planets), 115*, E12006.

Nimmo, F., Spencer, J. R., Pappalardo, R. T. & Mullen, M. E. (2007). Shear heating as the origin of the plumes and heat flux on Enceladus. *Nature, 447*, 289-291.

Nixon, C. (1998). *Remote sounding of the atmosphere of Titan.* University of Oxford, PhD Thesis, Oxford.

Nixon, C. A., Achterberg, R. K. & Flasar, F. M. (2010). *Infrared limb sounding with Cassini CIRS: Optimal viewing strategy using horizon nodes.* Paper presented at the IEEE Aerospace Conference, Big Sky, MT, USA.

Nixon, C. A., Achterberg, R. K., Vinatier, S., Bezard, B., Coustenis, A., Irwin, P. G. J., Teanby, N. A., de Kok, R., Romani, P. N., Jennings, D. E., Bjoraker, G. L. & Flasar, F. M. (2008a). The $^{12}C/^{13}C$ isotopic ratio in Titan hydrocarbons from Cassini/CIRS infrared spectra. *Icarus, 195*, 778-791.

Nixon, C. A., Brasunas, J. C., Lakew, B., Fettig, R., Jennings, D. E., Carlson, R. C. & Kunde, V. G. (2004). *In-flight Far-Infrared Performance of the CIRS Instrument on Cassini.* Paper presented at the International Thermal Detectors Workshop (TDW2003), RECON No. 20040068207, p. 1-12 - 1-15

Nixon, C. A., Jennings, D. E., Bézard, B., Teanby, N. A., Achterberg, R. K., Coustenis, A., Vinatier, S., Irwin, P. G. J., Romani, P. N., Hewagama, T. & Flasar, F. M. (2008b). Isotopic Ratios in Titan's Atmosphere from Cassini CIRS Limb Sounding: CO_2 at Low and Midlatitudes. *Astrophysical Journal, 681*, L101-L103.

Nixon, C. A., Jennings, D. E., Flaud, J. M., Bezard, B., Teanby, N. A., Irwin, P. G. J., Ansty, T. M., Coustenis, A., Vinatier, S. & Flasar, F. M. (2009). Titan's prolific propane: The Cassini CIRS perspective. *Planetary and Space Science, 57*, 1573-1585.

Noll, K. S., Johnson, R. E., Lane, A. L., Domingue, D. L. & Weaver, H. A. (1996). Detection of Ozone on Ganymede. *Science, 273*, 341-343.

Orton, G. (1992). *Ground-based observations of Titan's thermal spectrum.* Paper presented at the ESA Symposium on Titan (SEE N92-32348 23-91).

Paillou, P., Mitchell, K., Wall, S., Ruffie, G., Wood, C. A., Lorenz, R., Stofan, E., Lunine, J., Lopes, R. & Encrenaz, P. (2008). Microwave dielectric constant of liquid hydrocarbons: Application to the depth estimation of Titan's lakes. *Geophys. Res. Lett., 35*(L05202).

Pappalardo, R. T., Head, J. W., Collins, G. C., Kirk, R. L., Neukum, G., Oberst, J., Giese, B., Greeley, R., Chapman, C. R., Helfenstein, P., Moore, J. M., McEwen, A., Tufts, B. R., Senske, D. A., Breneman, H. H. & Klaasen, K. (1998a). Grooved Terrain on Ganymede: First Results from Galileo High-Resolution Imaging. *Icarus, 135*, 276-302.

Pappalardo, R. T., Head, J. W., Greeley, R., Sullivan, R. J., Pilcher, C., Schubert, G., Moore, W. B., Carr, M. H., Moore, J. M., Belton, M. J. S. & Goldsby, D. L. (1998b). Geological evidence for solid-state convection in Europa's ice shell. *Nature, 391*, 365.

Park, J. H., Garipov, G. K., Jeon, J. A., Khrenov, B. A., Kim, J. E., Kim, M., Kim, Y. K., Lee, C. H., Lee, J., Na, G. W., Nam, S., Park, I. H. & Park, Y. S. (2008). Obscura telescope with a MEMS micromirror array for space observation of transient luminous phenomena or fast-moving objects. *Optics Express, 16*, 20249.

Parkinson, C. D., Liang, M. C., Hartman, H., Hansen, C. J., Tinetti, G., Meadows, V., Kirschvink, J. L. & Yung, Y. L. (2007). Enceladus: Cassini observations and implications for the search for life. *Astronomy and Astrophysics, 463*, 353-357.

Patel, V. M., Easley, G. R. & Chellappa, R. (2011). *Component-based restoration of speckled images.* Paper presented at the 18th IEEE International Conference on Image Processing (ICIP) UMIACS, Univ. of Maryland, College Park, MD, USA

Patterson, G. W., Collins, G. C., Head, J. W., Pappalardo, R. T., Prockter, L. M., Lucchitta, B. K. & Kay, J. P. (2010). Global geological mapping of Ganymede. *Icarus, 207*, 845-867.

Paubert, G., Gautier, D. & Courtin, R. (1984). The millimeter spectrum of Titan - Detectability of HCN, HC_3N, and CH_3CN and the CO abundance. *Icarus, 60*, 599-612.

Paubert, G., Marten, A., Rosolen, C., Gautier, D. & Courtin, R. (1987). *First radiodetection of HCN on Titan.* Paper presented at the Bulletin of the American Astronomical Society.

Pavlov, A. A., Hurtgen, M. T., Kasting, J. F. & Arthur, M. A. (2003). Methane-rich Proterozoic atmosphere? *Geology, 31*(1), 87-90.

Pavlov, A. A., Kasting, J. F., Brown, L. L., Rages, K. A. & Freedman, R. (2000). Greenhouse warming by CH_4 in the atmosphere of early Earth. *Journal of Geophysical Research, 105*, 11981-11990.

Perron, J. T. & de Pater, I. (2004). Dynamics of an ice continent on Titan. *Geophysical Research Letters, 31*.

Peters, K., E., Walters, C., C. & Moldowan, J. M. (2005). The Biomarker Guide, Volume 1: Biomarkers and Isotopes in the Environment and Human History. *Cambridge University Press*.

Pilbratt, G. L., Riedinger, J. R., Passvogel, T., Crone, G., Doyle, D., Gageur, U., Heras, A. M., Jewell, C., Metcalfe, L., Ott, S. & Schmidt, M. (2010). Herschel Space Observatory. An ESA facility for far-infrared and submillimetre astronomy. *Astronomy and Astrophysics, 518*(L1).

Pollack, J. B. (1973). Greenhouse Models of the Atmosphere of Titan. *Icarus, 19*, 43-43.

Porco, C. C., Baker, E., Barbara, J., Beurle, K., Brahic, A., Burns, J. A., Charnoz, S., Cooper, N., Dawson, D. D., Del Genio, A. D., Denk, T., Dones, L., Dyudina, U., Evans, M. W., Fussner, S., Giese, B., Grazier, K., Helfenstein, P., Ingersoll, A. P., Jacobson, R. A., Johnson, T. V., McEwen, A., Murray, C. D., Neukum, G., Owen, W. M., Perry, J., Roatsch, T., Spitale, J., Squyres, S., Thomas, P., Tiscareno, M., Turtle, E. P., Vasavada, A. R., Veverka, J., Wagner, R. & West, R. (2005). Imaging of Titan from the Cassini spacecraft. *Nature, 434*, 159-168.

Porco, C. C., Helfenstein, P., Thomas, P. C., Ingersoll, A. P., Wisdom, J., West, R., Neukum, G., Denk, T., Wagner, R., Roatsch, T., Kieffer, S., Turtle, E., McEwen, A., Johnson, T. V., Rathbun, J., Veverka, J., Wilson, D., Perry, J., Spitale, J., Brahic, A., Burns, J. A., Del Genio, A. D., Dones, L., Murray, C. D. & Squyres, S. (2006). Cassini Observes the Active South Pole of Enceladus. *Science, 311*, 1393-1401.

Porco, C. C., West, R. A., Squyres, S., McEwen, A., Thomas, P., Murray, C. D., Delgenio, A., Ingersoll, A. P., Johnson, T. V., Neukum, G., Veverka, J., Dones, L., Brahic, A., Burns, J. A., Haemmerle, V., Knowles, B., Dawson, D., Roatsch, T., Beurle, K. & Owen, W. (2004). Cassini Imaging Science: Instrument Characteristics And Anticipated Scientific Investigations At Saturn. *Space Science Reviews, 115*, 363-497.

Postberg, F., Kempf, S., Hillier, J. K., Srama, R., Green, S. F., McBride, N. & Grun, E. (2008). The E-ring in the vicinity of Enceladus. II. Probing the moon's interior - The composition of E-ring particles. *Icarus, 193*, 438-454.

Postberg, F., Kempf, S., Schmidt, J., Brilliantov, N., Beinsen, A., Abel, B., Buck, U. & Srama, R. (2009). Sodium salts in E-ring ice grains from an ocean below the surface of Enceladus. *Nature, 459*, 1098-1101.

Postberg, F., Schmidt, J., Hillier, J., Kempf, S. & Srama, R. (2011). A salt-water reservoir as the source of a compositionally stratified plume on Enceladus. *Nature, 474*(7353), 620-622.

Prockter, L. M., Head, J. W., Pappalardo, R. T., Senske, D. A., Neukum, G., Wagner, R., Wolf, U., Oberst, J. O., Giese, B., Moore, J. M., Chapman, C. R., Helfenstein, P., Greeley, R., Breneman, H. H. & Belton, M. J. S. (1998). Dark Terrain on Ganymede: Geological Mapping and Interpretation of Galileo Regio at High Resolution. *Icarus, 135*, 317-344.

Radebaugh, J. (2009). Planetary science: Titan's sticky dunes? *Nature Geoscience, 2*, 608-609.

Radebaugh, J., Lorenz, R. D., Kirk, R. L., Lunine, J. I., Stofan, E. R., Lopes, R. M. C., Wall, S. D. & the Cassini Radar, T. (2007). Mountains on Titan observed by Cassini Radar. *Icarus, 192*, 77-91.

Radebaugh, J., Lorenz, R. D., Lunine, J. I., Wall, S. D., Boubin, G., Reffet, E., Kirk, R. L., Lopes, R. M., Stofan, E. R., Soderblom, L., Allison, M., Janssen, M., Paillou, P., Callahan, P., Spencer, C. & The Cassini Radar, T. (2008). Dunes on Titan observed by Cassini Radar. *Icarus, 194*, 690-703.

Radebaugh, J., Lorenz, R. D., Wall, S. D., Kirk, R. L., Wood, C. A., Lunine, J. I., Stofan, E. R., Lopes, R. M. C., Valora, P., Farr, T. G., Hayes, A., Stiles, B., Mitri, G., Zebker, H., Janssen, M., Wye, L., Legall, A., Mitchell, K. L., Paganelli, F., West, R. D., Schaller, E. L. & Cassini, R. T. (2011). Regional geomorphology and history of Titan's Xanadu province. *Icarus, 211*, 672-685.

Rages, K. & Pollack, J. B. (1983). Vertical distribution of scattering hazes in Titan's upper atmosphere. *Icarus, 55*, 50-62.

Rainey, E. S. & Stevenson, D. J. (2003). Oceans in ice-rock bodies: conditions for the existence of subsurface liquid water. *AGU Fall Meeting Abstracts, 51*, 0447.

Ramirez, S. I., Coll, P., Buch, A., Brasse, C., Poch, O. & Raulin, F. (2010). The fate of aerosols on the surface of Titan. *Faraday Discussions, 147*, 419.

Ramirez, S. I., Coll, P., da Silva, A., Navarro-Gonzalez, R., Lafait, J. & Raulin, F. (2002). Complex Refractive Index of Titan's Aerosol Analogues in the 200-900 nm Domain. *Icarus, 156*, 515-529.

Rannou, P., Cours, T., Le Mouelic, S., Rodriguez, S., Sotin, C., Drossart, P. & Brown, R. (2010). Titan haze distribution and optical properties retrieved from recent observations. *Icarus, 208*, 850-867.

Rannou, P., Lebonnois, S., Hourdin, F. & Luz, D. (2005). Titan atmosphere database. *Advances in Space Research, 36*, 2194-2198.

Rappaport, N. J., Iess, L., Wahr, J., Lunine, J. I., Armstrong, J. W., Asmar, S. W., Tortora, P., di Benedetto, M. & Racioppa, P. (2008). Can Cassini detect a subsurface ocean in Titan from gravity measurements? *Icarus, 194*, 711-720.

Raulin, F. (2007). Question 2: Why an Astrobiological Study of Titan Will Help Us Understand the Origin of Life. *Origins of Life and Evolution of Biospheres, 37*(4), 345-349.

Raulin, F. (2008a). Astrobiology and habitability of Titan. *Space Science Reviews, 135*(1), 37-48.

Raulin, F. (2008b). Planetary science: Organic lakes on Titan. *Nature, 454*, 587-589.

Raulin, F., Coll, P. & Navarro-Gonzalez, R. (2005). Prebiotic Chemistry: Laboratory Experiments and Planetary Observation. In M. Gargaud & B. Barbier & H. Martin & J. Reisse (Eds.), *Lectures in Astrobiology, Volume 1* (pp. 449-449). Berlin/Heidelberg: Springer-Verlag.

Raulin, F., Frere, C., Do, L., Khlifi, M., Paillous, P. & de Vanssay, E. (1992). *Organic chemistry on Titan versus terrestrial prebiotic chemistry: Exobiological implications*.

Raulin, F., Gazeau, M. C. & Lebreton, J. P. (2008). Latest news from Titan. *Planetary and Space Science, 56*, 571-572.

Raulin, F. o. & Owen, T. (2002). Organic Chemistry and Exobiology on Titan. *Space Science Reviews, 104*, 377-394.

Rawlinson, N., Pozgay, S. & Fishwick, S. (2010). Seismic tomography: A window into deep Earth. *Physics of the Earth and Planetary Interiors, 178*(3-4), 101-135.

Richardson, J. D. (1998). Thermal plasma and neutral gas in Saturn's magnetosphere. *Reviews of Geophysics, 36*, 501-524.

Ritt, B., Sarrazin, J., Caprais, J.-C., Noel, P., Gauthier, O., Pierre, C., Henry, P. & Desbruyeres, D. (2010). First insights into the structure and environmental setting of cold-seep communities in the Marmara Sea. *Deep Sea Research Part I: Oceanographic Research Papers, 57*(9), 1120-1136.

Rodgers, C. D. (2000). *Inverse Methods for Atmospheric Sounding: Theory and Practice*: World Scientific.

Roe, H. G., de Pater, I., Gibbard, S. G., Macintosh, B. A., Max, C. E., Young, E. F., Brown, M. E. & Bouchez, A. H. (2004a). A new 1.6-micron map of Titan's surface. *Geophys. Res. Lett., 31*, 17-20.

Roe, H. G., de Pater, I. & McKay, C. P. (2004b). Seasonal variation of Titan's stratospheric ethylene (C_2H_4) observed. *Icarus, 169*, 440-461.

Roe, H. G., Greathouse, T. K., Richter, M. J. & Lacy, J. H. (2003). Propane on Titan. *The Astrophysical Journal Letters, 597*, L65-L68.

Roggemann, M. C., Bright, V. M., Welsh, B. M., Cowan, W. D. & Lee, M. (1999). Micro-electro-mechanical deformable mirrors for aberration control in optical systems. *Optical and Quantum Electronics, 31*(5), 451-468.

Romanowicz, B., Stakes, D., Dolenc, D., Neuhauser, D., McGill, P., Uhrhammer, R. & Ramirez, T. (2006). The Monterey Bay broadband ocean bottom seismic observatory. *Annals Of Geophysics, 49*(2/3).

Rotger, M., Boudon, V. & Vander Auwera, J. (2008). Line positions and intensities in the v12 band of ethylene near : An experimental and theoretical study. *Journal of Quantitative Spectroscopy and Radiative Transfer, 109*, 952-962.

Rothman, L. S., Gordon, I. E., Barbe, A., Benner, D. C., Bernath, P. F., Birk, M., Boudon, V., Brown, L. R., Campargue, A., Champion, J. P., Chance, K., Coudert, L. H., Dana, V., Devi, V. M., Fally, S., Flaud, J. M., Gamache, R. R., Goldman, A., Jacquemart, D., Kleiner, I., Lacome, N., Lafferty, W. J., Mandin, J. Y., Massie, S. T., Mikhailenko, S. N., Miller, C. E., Moazzen-Ahmadi, N., Naumenko, O. V., Nikitin, A. V., Orphal, J., Perevalov, V. I., Perrin, A., Predoi-Cross, A., Rinsland, C. P., Rotger, M., Simeckova, M., Smith, M. A. H., Sung, K., Tashkun, S. A., Tennyson, J., Toth, R. A., Vandaele, A. C. & Vander Auwera, J. (2009). The HITRAN 2008 molecular spectroscopic database. *Journal of Quantitative Spectroscopy and Radiative Transfer, 110*, 533-572.

Rothman, L. S., Jacquemart, D., Barbe, A., Chris Benner, D., Birk, M., Brown, L. R., Carleer, M. R., Chackerian, C., Chance, K., Coudert, L. H., Dana, V., Devi, V. M., Flaud, J. M., Gamache, R. R., Goldman, A., Hartmann, J. M., Jucks, K. W., Maki, A. G., Mandin, J. Y., Massie, S. T., Orphal, J., Perrin, A., Rinsland, C. P., Smith, M. A. H., Tennyson, J., Tolchenov, R. N., Toth, R. A., Vander Auwera, J., Varanasi, P. & Wagner, G. (2005). The HITRAN 2004 molecular spectroscopic database. *Journal of Quantitative Spectroscopy and Radiative Transfer, 96*, 139-204.

Rudolph, J., Ehhalt, D. H. & Khedim, A. (1984). Vertical profiles of acetylene in the troposphere and stratosphere. *Journal of Atmospheric Chemistry, 2*, 117-124.

Rymer, A. M., Smith, H. T., Wellbrock, A., Coates, A. J. & Young, D. T. (2009). Discrete classification and electron energy spectra of Titan's varied magnetospheric environment. *Geophysical Research Letters, 36*, 15109.

Sagan, C. (1973). The Greenhouse of Titan. *Icarus, 18*, 649-656.

Sagan, C. (1974). Organic chemistry in the atmosphere. *NASA Tecnhical Reports*(NASA-SP-340), 134-142.

Sagan, C. & Khare, B. N. (1971). Long-Wavelength Ultraviolet Photoproduction of Amino Acids on the Primitive Earth. *Science, 173*, 417-420.
Sagan, C. & Khare, B. N. (1979). Tholins - Organic chemistry of interstellar grains and gas. *Nature, 277*, 102-107.
Sagan, C., Khare, B. N. & Lewis, J. S. (1984). Organic matter in the Saturn system, *Saturn* (pp. 788-807).
Samuelson, R. E. (1983). Radiative equilibrium model of Titan's atmosphere. *Icarus, 53*, 364-387.
Samuelson, R. E., Hanel, R. A., Kunde, V. G. & Maguire, W. C. (1981). Mean molecular weight and hydrogen abundance of Titan's atmosphere. *Nature, 292*, 688-693.
Samuelson, R. E., Maguire, W. C., Hanel, R. A., Kunde, V. G., Jennings, D. E., Yung, Y. L. & Aikin, A. C. (1983). CO_2 on Titan. *Journal of Geophysical Research, 88*, 8709-8715.
Samuelson, R. E. & Mayo, L. A. (1991). Thermal infrared properties of Titan's stratospheric aerosol. *Icarus, 91*, 207-219.
Samuelson, R. E., Nath, N. R. & Borysow, A. (1997). Gaseous abundances and methane supersaturation in Titan's troposphere. *Planetary and Space Science, 45*, 959-980.
Schaefer, L. & Fegley, B. (2007). Outgassing of ordinary chondritic material and some of its implications for the chemistry of asteroids, planets, and satellites. *Icarus, 186*, 462-483.
Scheidegger, A. E. (1968). Horton's law of stream order number and a temperature-analog in river nets *Water Resources Research, 4*(1), 167-171.
Scheidegger, A. E. (2004). *Morphotectonics*. Berlin: Springer.
Schenk, P. M. & McKinnon, W. B. (1989). Fault offsets and lateral crustal movement on Europa - Evidence for a mobile ice shell. *Icarus, 79*, 75-100.
Schenk, P. M. & Pappalardo, R. T. (2004). Topographic variations in chaos on Europa: Implications for diapiric formation. *Geophysical Research Letters, 31*, 16703.
Schmidt, B. E., Blankenship, D. D., Patterson, G. W. & Schenk, P. M. (2011). Active formation of 'chaos terrain' over shallow subsurface water on Europa. *Nature, 479*(7374), 502-505.
Schmidt, J., Brilliantov, N., Spahn, F. & Kempf, S. (2008). Slow dust in Enceladus' plume from condensation and wall collisions in tiger stripe fractures. *Nature, 451*(7179), 685-688.
Schubert, G., Anderson, J. D., Travis, B. J. & Palguta, J. (2007). Enceladus: Present internal structure and differentiation by early and long-term radiogenic heating. *Icarus, 188*, 345-355.
Schubert, G., Hussmann, H., Lainey, V., Matson, D. L., McKinnon, W. B., Sohl, F., Sotin, C., Tobie, G., Turrini, D. & van Hoolst, T. (2010). Evolution of Icy Satellites. *Space Science Reviews, 153*, 447-484.
Scott, N. A. (1974). A direct method of computation of the transmission function of an inhomogeneous gaseous medium - I: Description of the method. *Journal of Quantitative Spectroscopy and Radiative Transfer, 14*, 691-704.
Scott, N. A. & Chedin, A. (1981). A fast line-by-line method for atmospheric absorption computations - The Automatized Atmospheric Absorption Atlas. *Journal of Applied Meteorology, 20*, 802-812.
Shafiq, M., Wahlund, J. E., Morooka, M. W., Kurth, W. S. & Farrell, W. M. (2011). Characteristics of the dust-plasma interaction near Enceladus' South Pole. *Planetary and Space Science, 59*, 17-25.
Shemansky, D. E., Stewart, A. I. F., West, R. A., Esposito, L. W., Hallett, J. T. & Liu, X. (2005). The Cassini UVIS Stellar Probe of the Titan Atmosphere. *Science, 308*(5724), 978-982.
Shreve, R. L. (1966). Statistical law of stream numbers. *Journal of Geology, 74*, 17-37.
Sicardy, B., Brahic, A., Ferrari, C., Gautier, D., Lecacheux, J., Lellouch, E., Roques, F., Arlot, J. E., Colas, F., Thuillot, W., Sevre, F., Vidal, J. L., Blanco, C., Cristaldi, S., Buil, C., Klotz, A. & Thouvenot, E. (1990). Probing Titan's atmosphere by stellar occultation. *Nature, 343*, 350-353.
Simoes, F., Grard, R., Hamelin, M., Lopez-Moreno, J. J., Schwingenschuh, K., Beghin, C., Berthelier, J. J., Besser, B., Brown, V. J. G., Chabassiere, M., Falkner, P., Ferri, F., Fulchignoni, M., Hofe, R., Jernej, I., Jeronimo, J. M., Molina-Cuberos, G. J., Rodrigo, R., Svedhem, H., Tokano, T. & Trautner, R. (2007). A new numerical model for the simulation of ELF wave propagation and the computation of eigenmodes in the atmosphere of Titan: Did Huygens observe any Schumann resonance? *Planetary and Space Science, 55*, 1978-1989.
Simon, S., Wennmacher, A., Neubauer, F. M., Bertucci, C. L., Kriegel, H., Saur, J., Russell, C. T. & Dougherty, M. K. (2010). Titan's highly dynamic magnetic environment: A systematic survey of Cassini magnetometer observations from flybys TA-T62. *Planetary and Space Science, 58*(10), 1230-1251.
Smith, B. A., Soderblom, L., Batson, R., Bridges, P., Inge, J. A. Y., Masursky, H., Shoemaker, E., Beebe, R., Boyce, J., Briggs, G., Bunker, A., Collins, S. A., Hansen, C. J., Johnson, T. V., Mitchell, J. L., Terrile, R. J., Cook, A. F., Cuzzi, J., Pollack, J. B., Danielson, G. E., Ingersoll, A. P., Davies, M. E., Hunt, G. E., Morrison, D., Owen, T., Sagan, C., Veverka, J., Strom, R. & Suomi, V. E. (1982). A New Look at the Saturn System: The Voyager 2 Images. *Science, 215*(4532), 504-537.
Smith, B. A., Soderblom, L., Beebe, R., Boyce, J., Briggs, G., Bunker, A., Collins, S. A., Hansen, C. J., Johnson, T. V., Mitchell, J. L., Terrile, R. J., Carr, M., Cook, A. F., Cuzzi, J., Pollack, J. B., Danielson, G. E.,

Ingersoll, A., Davies, M. E., Hunt, G. E., Masursky, H., Shoemaker, E., Morrison, D., Owen, T., Sagan, C., Veverka, J., Strom, R. & Suomi, V. E. (1981). Encounter with Saturn: Voyager 1 Imaging Science Results. *Science, 212*(4491), 163-191.

Smith, P. H., Lemmon, M. T., Lorenz, R. D., Sromovsky, L. A., Caldwell, J. J. & Allison, M. D. (1996). Titan's Surface, Revealed by HST Imaging. *Icarus, 119*(2), 336-349.

Snell, H. E., Moncet, J.-L., Anderson, G. P., Chetwynd, J. H., Miller, S. & Wang, J. G. (1995). *FASCODE for the environment (FASE).* Paper presented at the Proc. SPIE, 2471, pp. 88-95.

Soderblom, L. A., Brown, R. H., Soderblom, J. M., Barnes, J. W., Kirk, R. L., Sotin, C., Jaumann, R., MacKinnon, D. J., Mackowski, D. W., Baines, K. H., Buratti, B. J., Clark, R. N. & Nicholson, P. D. (2009). The geology of Hotei Regio, Titan: Correlation of Cassini VIMS and RADAR. *Icarus, 204*, 610-618.

Soderblom, L. A., Kirk, R. L., Lunine, J. I., Anderson, J. A., Baines, K. H., Barnes, J. W., Barrett, J. M., Brown, R. H., Buratti, B. J., Clark, R. N., Cruikshank, D. P., Elachi, C., Janssen, M. A., Jaumann, R., Karkoschka, E., Mouélic, S. L., Lopes, R. M., Lorenz, R. D., McCord, T. B., Nicholson, P. D., Radebaugh, J., Rizk, B., Sotin, C., Stofan, E. R., Sucharski, T. L., Tomasko, M. G. & Wall, S. D. (2007a). Correlations between Cassini VIMS spectra and RADAR SAR images: Implications for Titan's surface composition and the character of the Huygens Probe Landing Site. *Planetary and Space Science, 55*, 2025-2036.

Soderblom, L. A., Tomasko, M. G., Archinal, B. A., Becker, T. L., Bushroe, M. W., Cook, D. A., Doose, L. R., Galuszka, D. M., Hare, T. M., Howington-Kraus, E., Karkoschka, E., Kirk, R. L., Lunine, J. I., McFarlane, E. A., Redding, B. L., Bashar, R., Rosiek, M. R., See, C. & Smith, P. H. (2007b). Topography and geomorphology of the Huygens landing site on Titan. *Planetary and Space Science, 55*(13), 2015-2024.

Sohl, F., Choukroun, M., Kargel, J., Kimura, J., Pappalardo, R., Vance, S. & Zolotov, M. (2010). Subsurface Water Oceans on Icy Satellites: Chemical Composition and Exchange Processes. *Space Science Reviews, 153*, 485-510.

Solomonidou, A., Bampasidis, G., Hirtzig, M., Coustenis, A., Kyriakopoulos, K., St. Seymour, K., Bratsolis, E. & Moussas, X. (2012a). Morphotectonic features on Titan and their possible origin. *Planetary and Space Science,* in press, DOI: 10.1016/j.pss.2012.05.003

Solomonidou, A., Bampasidis, G., Kyriakopoulos, K., Bratsolis, E., Hirtzig, M., Coustenis, A. & Moussas, X. (2010). Imaging of potentially active geological regions on Saturn's moons Titan and Enceladus, using Cassini-Huygens data: With emphasis on cryovolcanism. *Hellenic Journal of Geosciences, 45*, 257-268.

Solomonidou, A., Coustenis, A., Bampasidis, G., Kyriakopoulos, K., Moussas, X., Bratsolis, E. & Hirtzig, M. (2011). Water Oceans of Europa and Other Moons: Implications For Life in Other Solar Systems. *Journal of Cosmology, 13*, 4191-4211.

Solomonidou, A., Moussas, X., Coustenis, A., Lebreton, J. P., Bampasidis, G., Kyriakopoulos, K., Kouloumvakos, A., Xystouris, G., Sigala, E. & Patsou, I. (2012b). *Cassini Scientist for a Day: an international contest in Greece.* Paper presented at the EGU General Assembly, 22-27 April, Vienna, Austria.

Sotin, C., Jaumann, R., Buratti, B. J., Brown, R. H., Clark, R. N., Soderblom, L. A., Baines, K. H., Bellucci, G., Bibring, J. P., Capaccioni, F., Cerroni, P., Combes, M., Coradini, A., Cruikshank, D. P., Drossart, P., Formisano, V., Langevin, Y., Matson, D. L., McCord, T. B., Nelson, R. M., Nicholson, P. D., Sicardy, B., Lemouelic, S., Rodriguez, S., Stephan, K. & Scholz, C. K. (2005). Release of volatiles from a possible cryovolcano from near-infrared imaging of Titan. *Nature, 435*, 786-789.

Spencer, J. R., Pearl, J. C., Segura, M., Flasar, F. M., Mamoutkine, A., Romani, P., Buratti, B. J., Hendrix, A. R., Spilker, L. J. & Lopes, R. M. C. (2006). Cassini Encounters Enceladus: Background and the Discovery of a South Polar Hot Spot. *Science, 311*, 1401-1405.

Spohn, T. & Schubert, G. (2003). Oceans in the icy Galilean satellites of Jupiter? *Icarus, 161*(2), 456-467.

Srama, R., Ahrens, T. J., Altobelli, N., Auer, S., Bradley, J. G., Burton, M., Dikarev, V. V., Economou, T., Fechtig, H., Gurlich, M., Grande, M., Graps, A., Grun, E., Havnes, O., Helfert, S., Horanyi, M., Igenbergs, E., Jessberger, E. K., Johnson, T. V., Kempf, S., Krivov, A. V., Kroger, H., Mocker-Ahlreep, A., Moragas-Klostermeyer, G., Lamy, P., Landgraf, M., Linkert, D., Linkert, G., Lura, F., McDonnell, J. A. M., Muhlmann, D., Morfill, G. E., Muller, M., Roy, M., Schafer, G., Schlotzhauer, G., Schwehm, G. H., Spahn, F., Stobig, M., Svestka, J., Tschernjawski, V., Tuzzolino, A. J., Wasch, R. & Zook, H. A. (2004). The Cassini Cosmic Dust Analyzer. *Space Science Reviews, 114*, 465-518.

Stamnes, K., Tsay, S., Wiscombe, W. & Jayaweera, K. (1998). Numerically stable algorithm for discrete-ordinate-method radiative transfer in multiple scattering and emitting layered media. *Applied Optics, 27*, 2502-2509.

Stark, B. & Bernstein, J. (1999). Reliability Overview. *in MEMS Reliability Assurance Guidelines for Space Applications (ed. B. Stark), JPL Publication 99-1.*

Stein, S. & Wysession, M. (2003). *An Introduction to Seismology, Earthquakes, and Earth Structure*: John Wiley & Sons.

Stephan, K., Jaumann, R., Karkoschka, E., Kirk, R. L., Barnes, J. W., Tomasko, M. G., Turtle, E. P., Corre, L. L., Langhans, M., Mouelic, S. L., Lorenz, R. D. & Perry, J. (2009). Mapping Products of Titan's Surface. In R. H. Brown & J.-P. Lebreton & J. H. Waite (Eds.), *Titan from Cassini-Huygens* (pp. 489-489): Springer.

Stevenson, D. J. (1992). *Interior of Titan.* Paper presented at the In ESA, Symposium on Titan (SEE N92-32348 23-91).

Stewart, J. B., Bifano, T. G., Bierden, P., Cornelissen, S., Cook, T. & Levine, B. M. (2006). Design and development of a 329-segment tip-tilt piston mirrorarray for space-based adaptive optics. *Proceedings of SPIE, 6113*, 181-189.

Stiles, B. W., Kirk, R. L., Lorenz, R. D., Hensley, S., Lee, E., Ostro, S. J., Allison, M. D., Callahan, P. S., Gim, Y., Iess, L., del Marmo, P. P., Hamilton, G., Johnson, W. T. K., West, R. D. & Cassini Radar Team, T. (2008). Determining Titan's Spin State From Cassini Radar Images. *The Astronomical Journal, 135*(5), 1669-1680.

Stiles, B. W., Kirk, R. L., Lorenz, R. D., Hensley, S., Lee, E., Ostro, S. J., Allison, M. D., Callahan, P. S., Gim, Y., Iess, L., Perci del Marmo, P., Hamilton, G., Johnson, W. T. K., West, R. D. & The Cassini, R. T. (2010). Erratum: "Determining Titan's Spin State from Cassini Radar Images" (2008, AJ, 135, 1669). *The Astronomical Journal, 139*, 311-311.

Stofan, E. R., Elachi, C., Lunine, J. I., Lorenz, R. D., Stiles, B., Mitchell, K. L., Ostro, S., Soderblom, L., Wood, C., Zebker, H., Wall, S., Janssen, M., Kirk, R., Lopes, R., Paganelli, F., Radebaugh, J., Wye, L., Anderson, Y., Allison, M., Boehmer, R., Callahan, P., Encrenaz, P., Flamini, E., Francescetti, G., Gim, Y., Hamilton, G., Hensley, S., Johnson, W. T. K., Kelleher, K., Muhleman, D., Paillou, P., Picardi, G., Posa, F., Roth, L., Seu, R., Shaffer, S., Vetrella, S. & West, R. (2007). The lakes of Titan. *Nature, 445*, 61-64.

Stofan, E. R., Lorenz, R. D., Lunine, J. I., Aharonson, O., Bierhaus, E., Clark, B., Griffith, C., Harri, A. M., Karkoschka, E., Kirk, R., Kantsiper, B., Mahaffy, P., Newman, C., Ravine, M., Trainer, M., Waite, H. & Zarnecki, J. (2010a). *Titan Mare Explorer (TiME): First In Situ Exploration of an Extraterrestrial Sea.* Paper presented at the Astrobiology Science Conference 2010: Evolution and Life: Surviving Catastrophes and Extremes on Earth and Beyond, League City, Texas.

Stofan, E. R., Lunine, J. I., Lopes, R., Paganelli, F., Lorenz, R. D., Wood, C. A., Kirk, R., Wall, S., Elachi, C., Soderblom, L. A., Ostro, S., Janssen, M., Radebaugh, J., Wye, L., Zebker, H., Anderson, Y., Allison, M., Boehmer, R., Callahan, P., Encrenaz, P., Flamini, E., Francescetti, G., Gim, Y., Hamilton, G., Hensley, S., Johnson, W. T. K., Kelleher, K., Muhleman, D., Picardi, G., Posa, F., Roth, L., Seu, R., Shaffer, S., Stiles, B., Vetrella, S. & West, R. (2006). Mapping of Titan: Results from the first Titan radar passes. *Icarus, 185*, 443-456.

Stofan, E. R., Lunine, J. I., Lorenz, R. D., Aharonson, O., Bierhaus, E., Clark, B., Griffith, C., Harri, A. M., Karkoschka, E., Kirk, R., Kantsiper, B., Mahaffy, P., Newman, C., Ravine, M., Trainer, M., Waite, H. & Zarnecki, J. (2010b). *Exploring the Seas of Titan: The Titan Mare Explorer (TiME) Mission.* Paper presented at the 41st Lunar and Planetary Science Conference, March 1-5, Woodlands, Texas.

Stoker, C. R., Boston, P. J., Mancinelli, R. L., Segal, W., Khare, B. N. & Sagan, C. (1990). Microbial metabolism of tholin. *Icarus, 85*, 241-256.

Strahler, A. N. (1952). Hypsometric (area-altitude) analysis of erosional topology. *Geological Society of America Bulletin, 63*(11), 1117.

Strobel, D. F. (1974). The Photochemistry of Hydrocarbons in the Atmosphere of Titan. *Icarus, 21*, 466-470.

Strobel, D. F. (2010). Molecular hydrogen in Titan's atmosphere: Implications of the measured tropospheric and thermospheric mole fractions. *Icarus, 208*(2), 878-886.

Strobel, D. F., Atreya, S. K., Bezard, B., Ferri, F., Flasar, F. M., Fulchignoni, M., Lellouch, E. & Muller-Wodarg, I. (2009). Atmospheric Structure and Composition. In B. R. (Ed.), *Titan from Cassini-Huygens* (pp. 235-257).

Strobel, D. F., Hall, D. T., Zhu, X. & Summers, M. E. (1993). Upper limit on Titan's atmospheric argon abundance. *Icarus, 103*, 333-336.

Strobel, D. F. & Shemansky, D. E. (1982). EUV emission from Titan's upper atmosphere - Voyager 1 encounter. *Journal of Geophysical Research, 87*, 1361-1368.

Strobel, D. F., Summers, M. E. & Zhu, X. (1992). Titan's upper atmosphere - Structure and ultraviolet emissions. *Icarus, 100*, 512-526.

Svedhem, H. k., Titov, D. V., Taylor, F. W. & Witasse, O. (2007). Venus as a more Earth-like planet. *Nature, 450*(7170), 629-632.

Swann, W. F. G. (1951). The teaching of physics. *Am. J. Phys., 19*, 182-187.

Swinyard, B., Nakagawa, T., Merken, P., Royer, P., Souverijns, T., Vandenbussche, B., Waelkens, C., Davis, P., Di Francesco, J., Halpern, M., Houde, M., Johnstone, D., Joncas, G., Naylor, D., Plume, R., Scott, D., Abergel, A., Bensammar, S., Braine, J., Buat, V., Burgarella, D., Cais, P., Dole, H., Duband, L., Elbaz, D., Gerin, M., Giard, M., Goicoechea, J., Joblin, C., Jones, A., Kneib, J. P., Lagache, G., Madden, S., Pons, R., Pajot, F., Rambaud, D., Ravera, L., Ristorcelli, I., Rodriguez, L., Vives, S., Zavagno, A., Geis, N., Krause,

O., Lutz, D., Poglitsch, A., Raab, W., Stegmaier, J., Sturm, E., Tuffs, R., Lee, H. M., Koo, B.-C., Im, M., Pak, S., Han, W., Park, J.-H., Nam, U.-W., Jin, H., Lee, D.-H., Yuk, I.-S., Lee, S., Aikawa, Y., Arimoto, N., Doi, Y., Enya, K., Fukagawa, M., Furusho, R., Hasegawa, S., Hayashi, M., Honda Kanagawa, M., Ida, S., Imanishi, Masatoshi, Inutsuka, S.-i., Izumiura, H., Kamaya, H., Kaneda, H., Kasuga, T., Kataza, H., Kawabata, K., Kawada, M., Kawakita, H., Kii, T., Koda, J., Kodama, T., Kokubo, E., Komatsu, Matsuhara, H., Matsumoto, T., Matsuura, S., Miyata, T., Miyata, M., Nagata, H., Nagata, T., Nakajima, T., Naoto, K., Nishi, R., Noda, A., Okamoto, A., Okamoto, Y. K., Omukai, K., Onaka, T., Ootsubo, T., Ouchi, M., Saito, H., Sato, Y., Sako, S., Sekiguchi, T., Shibai, H., Sugita, H., Sugitani, K., Susa, H., Pyo, T.-s., Tamura, M., Ueda, Y., Ueno, M., Wada, T., Watanabe, J. i., Yamada, T., Yamamura, I., Yoshida, N., Yoshimi, K., Yui, Y., Benedettini, M., Cerulli, R., Di Giorgio, A., Molinari, S., Orfei, R., Pezzuto, S., Piazzo, L., Saraceno, P., Spinoglio, L., de Graauw, T., de Korte, P., Helmich, F., Hoevers, H., Huisman, R., Shipman, R., van der Tak, F., van der Werf, P., Wild, W., Acosta-Pulido, J., Cernicharo, J., Herreros, J., Martin-Pintado, J., Najarro, F., Perez-Fourmon, I., Ramon Pardo, J., Gomez, F., Castro Rodriguez, N., Ade, P., Barlow, M., Clements, D., Ferlet, M., Fraser, H., Griffin, D., Griffin, M., Hargrave, P., Isaak, K., Ivison, R., Mansour, M., Laniesse, J., Mauskopf, P., Morozov, D., Oliver, S., Orlando, A., Page, M., Popescu, C., Serjeant, S., Sudiwala, R., Rigopoulou, D., Walker, I., White, G., Viti, S., Winter, B., Bock, J., Bradford, M., Harwit, M. & Holmes, W. (2009). The space infrared telescope for cosmology and astrophysics: SPICA A joint mission between JAXA and ESA. *Experimental Astronomy, 23*, 193-219.

Tanguy, L., Bezard, B., Marten, A., Gautier, D., Gerard, E., Paubert, G. & Lecacheux, A. (1990). Stratospheric profile of HCN on Titan from millimeter observations. *Icarus, 85*, 43-57.

Tarantola, A. (2005). *Inverse Problem Theory and Methods for Model Parameter Estimation*: Society for Industrial Mathematics.

Taylor, F. W. (2011). Comparative planetology, climatology and biology of Venus, Earth and Mars. *Planetary and Space Science, 59*(10), 889-899.

Teanby, N., Irwin, P., Nixon, C. & de Kok, R. (2012). Rapid Seasonal Change Observed at Titan's South Pole. *Nature*, In Press.

Teanby, N. A., Irwin, P. G. J., de Kok, R., Jolly, A., Bézard, B., Nixon, C. A. & Calcutt, S. B. (2009a). Titan's stratospheric C_2N_2, C_3H_4, and C_4H_2 abundances from Cassini/CIRS far-infrared spectra. *Icarus, 202*, 620-631.

Teanby, N. A., Irwin, P. G. J., de Kok, R. & Nixon, C. A. (2009b). Dynamical implications of seasonal and spatial variations in Titan's stratospheric composition. *Royal Society of London Philosophical Transactions Series A, 367*, 697-711.

Teanby, N. A., Irwin, P. G. J., de Kok, R. & Nixon, C. A. (2010). Seasonal Changes in Titan's Polar Trace Gas Abundance Observed by Cassini. *The Astrophysical Journal Letters, 724*, L84-L89.

Teanby, N. A., Irwin, P. G. J., de Kok, R., Nixon, C. A., Coustenis, A., Royer, E., Calcutt, S. B., Bowles, N. E., Fletcher, L., Howett, C. & Taylor, F. W. (2008). Global and temporal variations in hydrocarbons and nitriles in Titan's stratosphere for northern winter observed by Cassini/CIRS. *Icarus, 193*, 595-611.

Teanby, N. A., Irwin, P. G. J., de Kok, R., Vinatier, S., Bézard, B., Nixon, C. A., Flasar, F. M., Calcutt, S. B., Bowles, N. E., Fletcher, L., Howett, C. & Taylor, F. W. (2007). Vertical profiles of HCN, HC_3N, and C_2H_2 in Titan's atmosphere derived from Cassini/CIRS data. *Icarus, 186*, 364-384.

Thompson, W. R., Henry, T. J., Schwartz, J. M., Khare, B. N. & Sagan, C. (1991). Plasma discharge in N_2 + CH_4 at low pressures - Experimental results and applications to Titan. *Icarus, 90*, 57-73.

Tian, F., Stewart, A. I. F., Toon, O. B., Larsen, K. W. & Esposito, L. W. (2007). Monte Carlo simulations of the water vapor plumes on Enceladus. *Icarus, 188*, 154-161.

Tikhonov, A. N. & Arsenin, V. A. (1977). *Solution of Ill-posed Problems*. Washington: Winston & Sons.

Tobie, G., Čadek, O. & Sotin, C. (2008). Solid tidal friction above a liquid water reservoir as the origin of the south pole hotspot on Enceladus. *Icarus, 196*, 642-652.

Tobie, G., Giese, B., Hurford, T. A., Lopes, R. M., Nimmo, F., Postberg, F., Retherford, K. D., Schmidt, J., Spencer, J. R., Tokano, T. & Turtle, E. P. (2010). Surface, Subsurface and Atmosphere Exchanges on the Satellites of the Outer Solar System. *Space Science Reviews, 153*, 375-410.

Tobie, G., Grasset, O., Lunine, J. I., Mocquet, A. & Sotin, C. (2005). Titan's internal structure inferred from a coupled thermal-orbital model. *Icarus, 175*, 496-502.

Tobie, G., Lunine, J. I. & Sotin, C. (2006). Episodic outgassing as the origin of atmospheric methane on Titan. *Nature, 440*(7080), 61-64.

Tokano, T. (2009). Limnological Structure of Titan's Hydrocarbon Lakes and Its Astrobiological Implication. *Astrobiology, 9*, 147-164.

Tokar, R. L., Johnson, R. E., Thomsen, M. F., Wilson, R. J., Young, D. T., Crary, F. J., Coates, A. J., Jones, G. H. & Paty, C. S. (2009). Cassini detection of Enceladus' cold water-group plume ionosphere. *Geophysical Research Letters, 36*, 13203.

Tomasko, M. G., Archinal, B., Becker, T., Bézard, B., Bushroe, M., Combes, M., Cook, D., Coustenis, A., de Bergh, C., Dafoe, L. E., Doose, L., Douté, S., Eibl, A., Engel, S., Gliem, F., Grieger, B., Holso, K., Howington-Kraus, E., Karkoschka, E., Keller, H. U., Kirk, R., Kramm, R., Küppers, M., Lanagan, P., Lellouch, E., Lemmon, M., Lunine, J., McFarlane, E., Moores, J., Prout, G. M., Rizk, B., Rosiek, M., Rueffer, P., Schröder, S. E., Schmitt, B., See, C., Smith, P., Soderblom, L., Thomas, N. & West, R. (2005). Rain, winds and haze during the Huygens probe's descent to Titan's surface. *Nature, 438*(7069), 765 - 778.

Tomasko, M. G., Bezard, B., Doose, L., Engel, S., Karkoschka, E. & Vinatier, S. (2008a). Heat balance in Titan's atmosphere. *Planetary and Space Science, 56*, 648-659.

Tomasko, M. G., Buchhauser, D., Bushroe, M., Dafoe, L. E., Doose, L. R., Eibl, A., Fellows, C., Farlane, E. M., Prout, G. M., Pringle, M. J., Rizk, B., See, C., Smith, P. H. & Tsetsenekos, K. (2002). The Descent Imager/Spectral Radiometer (DISR) Experiment on the Huygens Entry Probe of Titan. *Space Science Reviews, 104*, 469-551.

Tomasko, M. G., Doose, L., Engel, S., Dafoe, L. E., West, R., Lemmon, M., Karkoschka, E. & See, C. (2008b). A model of Titan's aerosols based on measurements made inside the atmosphere. *Planetary and Space Science, 56*, 669-707.

Tomasko, M. G. & West, R. A. (2009). Aerosols in Titan's Atmosphere. In Brown R. et al. (Ed.), *Titan from Cassini-Huygens* (pp. 297).

Tosi, F., Orosei, R., Seu, R., Coradini, A., Lunine, J. I., Filacchione, G., Gavrishin, A. I., Capaccioni, F., Cerroni, P., Adriani, A., Moriconi, M. L., Negrao, A., Flamini, E., Brown, R. H., Wye, L. C., Janssen, M., West, R. D., Barnes, J. W., Wall, S. D., Clark, R. N., Cruikshank, D. P., McCord, T. B., Nicholson, P. D., Soderblom, J. M. & Cassini, V. a. R. T. (2010). Correlations between VIMS and RADAR data over the surface of Titan: Implications for Titan's surface properties. *Icarus, 208*, 366-384.

Toublanc, D., Parisot, J. P., Brillet, J., Gautier, D., Raulin, F. & McKay, C. P. (1995). Photochemical modeling of Titan's atmosphere. *Icarus, 113*, 2-26.

Trafton, L. (1974). Titan: Unidentified Strong Absorptions in the Photometric Infrared. *Icarus, 21*, 175-187.

Trafton, L. M. (1975). Near-infrared spectrophotometry of Titan. *Icarus, 24*, 443-453.

Trainer, M. G., Pavlov, A. A., DeWitt, H. L., Jimenez, J. L., McKay, C. P., Toon, O. B. & Tolbert, M. A. (2006). Organic haze on Titan and the early Earth. *Proceedings of the National Academy of Sciences, 103*(48), 18035-18042.

Trinks, H., Schröder, W. & Biebricher, C. (2005). Ice And The Origin Of Life. *Origins of Life and Evolution of Biospheres, 35*(5), 429-445.

TSSM (30 January 2009). *NASA/ESA Final Report.*

Turtle, E. P., Perry, J. E., Hayes, A. G., Lorenz, R. D., Barnes, J. W., McEwen, A. S., West, R. A., Del Genio, A. D., Barbara, J. M., Lunine, J. I., Schaller, E. L., Ray, T. L., Lopes, R. M. C. & Stofan, E. R. (2011). Rapid and Extensive Surface Changes Near Titan's Equator: Evidence of April Showers. *Science, 331*(6023), 1414-1417.

Turtle, E. P., Perry, J. E., McEwen, A. S., DelGenio, A. D., Barbara, J., West, R. A., Dawson, D. D. & Porco, C. C. (2009). Cassini imaging of Titan's high-latitude lakes, clouds, and south-polar surface changes. *Geophysical Research Letters, 36*, 02204.

Twomey, S. (2002). *Introduction to the Mathematics of Inversion in Remote Sensing*: Courier Dover Publications.

Tyler, G. L., Eshleman, V. R., Anderson, J. D., Levy, G. S., Lindal, G. F., Wood, G. E. & Croft, T. A. (1981). Radio science investigations of the Saturn system with Voyager 1 - Preliminary results. *Science, 212*, 201-206.

Tyler, R. H. (2008). Strong ocean tidal flow and heating on moons of the outer planets. *Nature, 456*, 770-772.

Tyson, R. (2011). *Principles of Adaptive Optics*: CRC Press.

Vander Auwera, J., Moazzen-Ahmadi, N. & Flaud, J. M. (2007). Toward an Accurate Database for the 12 μm Region of the Ethane Spectrum. *The Astrophysical Journal, 662*, 750-757.

Vervack, R. J., Sandel, B. R. & Strobel, D. F. (2004). New perspectives on Titan's upper atmosphere from a reanalysis of the Voyager 1 UVS solar occultations. *Icarus, 170*, 91-112.

Viereck, R. A. & Puga, L. C. (1999). The NOAA Mg II core-to-wing solar index: Construction of a 20-year time series of chromospheric variability from multiple satellites. *Journal of Geophysical Research, 104*, 9995-10006.

Vinatier, S. (2007). *Analyse des spectres infrarouges thermiques emis par l' atmosphere de Titan enregistres par l' instrument Cassini/CIRS.* PhD Thesis, Denis Diderot-Paris VII, Paris.

Vinatier, S., Bezard, B., Anderson, C. M., Coustenis, A. & Teanby, N. (2012a). Seasonal variations in Titan's stratosphere observed with Cassini/CIRS: temperature, trace molecular gas and aerosol mixing ratio profiles. Paper presented at the Titan Through Time; Unlocking Titan's Past, Present and Future, April 3th - 5th, NASA Goddard Space Flight Center.

Vinatier, S., Bezard, B., de Kok, R., Anderson, C. M., Samuelson, R. E., Nixon, C. A., Mamoutkine, A., Carlson, R. C., Jennings, D. E., Guandique, E. A., Bjoraker, G. L., Michael Flasar, F. & Kunde, V. G. (2010a). Analysis of Cassini/CIRS limb spectra of Titan acquired during the nominal mission II: Aerosol extinction profiles in the 600-1420 cm^{-1} spectral range. *Icarus, 210*, 852-866.

Vinatier, S., Bezard, B., Fouchet, T., Teanby, N. A., de Kok, R., Irwin, P. G. J., Conrath, B. J., Nixon, C. A., Romani, P. N., Flasar, F. M. & Coustenis, A. (2007a). Vertical abundance profiles of hydrocarbons in Titan's atmosphere at 15°S and 80°N retrieved from Cassini/CIRS spectra. *Icarus, 188*, 120-138.

Vinatier, S., Bezard, B. & Nixon, C. A. (2007b). The Titan $^{14}N/^{15}N$ and $^{12}C/^{13}C$ isotopic ratios in HCN from Cassini/CIRS. *Icarus, 191*, 712-721.

Vinatier, S., Bézard, B., Nixon, C. A., Mamoutkine, A., Carlson, R. C., Jennings, D. E., Guandique, E. A., Teanby, N. A., Bjoraker, G. L., Michael Flasar, F. & Kunde, V. G. (2010b). Analysis of Cassini/CIRS limb spectra of Titan acquired during the nominal mission. I. Hydrocarbons, nitriles and CO_2 vertical mixing ratio profiles. *Icarus, 205*, 559-570.

Vinatier, S., Rannou, P., Anderson, C. M., Bezard, B., de Kok, R. & Samuelson, R. E. (2012b). Optical constants of Titan's stratospheric aerosols in the 70-1500 cm^{-1} spectral range constrained by Cassini/CIRS observations. *Icarus, 219*, 5-12.

Vosniadou, S. (1991). Designing curricula for conceptual change restructuring: lessons from the study of knowledge acquisition in astronomy. *Journal of Curriculum Studies, 23*, 219–237.

Vuitton, V., Lavvas, P., Yelle, R. V., Galand, M., Wellbrock, A., Lewis, G. R., Coates, A. J. & Wahlund, J. E. (2009). Negative ion chemistry in Titan's upper atmosphere. *Planetary and Space Science, 57*(13), 1558-1572.

Vuitton, V., Yelle, R. V. & Cui, J. (2008). Formation and distribution of benzene on Titan. *Journal of Geophysical Research (Planets), 113*, 05007.

Vuitton, V., Yelle, R. V. & McEwan, M. J. (2007). Ion chemistry and N-containing molecules in Titan's upper atmosphere. *Icarus, 191*, 722-742.

Waite, J. H., Brockwell, T., Elliot, J., Reh, K., Spencer, J. & Outer Planets Satellites Decadal, S. (2010). Titan Lake Probe: The Ongoing NASA Decadal Study Preliminary Report. *EGU General Assembly, 2-7 May, Vienna, Austria, 12*, 14762.

Waite, J. H., Combi, M. R., Ip, W.-H., Cravens, T. E., McNutt, R. L., Kasprzak, W., Yelle, R., Luhmann, J., Niemann, H., Gell, D., Magee, B., Fletcher, G., Lunine, J. & Tseng, W.-L. (2006). Cassini Ion and Neutral Mass Spectrometer: Enceladus Plume Composition and Structure. *Science, 311*(5766), 1419-1422.

Waite, J. H., Lewis, W. S., Kasprzak, W. T., Anicich, V. G., Block, B. P., Cravens, T. E., Fletcher, G. G., Ip, W. H., Luhmann, J. G., McNutt, R. L., Niemann, H. B., Parejko, J. K., Richards, J. E., Thorpe, R. L., Walter, E. M. & Yelle, R. V. (2004). The Cassini Ion and Neutral Mass Spectrometer (INMS) Investigation. *Space Science Reviews, 114*, 113-231.

Waite, J. H., Lewis, W. S., Magee, B. A., Lunine, J. I., McKinnon, W. B., Glein, C. R., Mousis, O., Young, D. T., Brockwell, T., Westlake, J., Nguyen, M. J., Teolis, B. D., Niemann, H. B., McNutt, R. L., Perry, M. & Ip, W. H. (2009). Liquid water on Enceladus from observations of ammonia and ^{40}Ar in the plume. *Nature, 460*, 487-490.

Waite, J. H., Niemann, H., Yelle, R. V., Kasprzak, W. T., Cravens, T. E., Luhmann, J. G., McNutt, R. L., Ip, W.-H., Gell, D., De La Haye, V., Muller-Wordag, I., Magee, B., Borggren, N., Ledvina, S., Fletcher, G., Walter, E., Miller, R., Scherer, S., Thorpe, R., Xu, J., Block, B. & Arnett, K. (2005). Ion Neutral Mass Spectrometer Results from the First Flyby of Titan. *Science, 308*(5724), 982-986.

Waite, J. H., Young, D. T., Cravens, T. E., Coates, A. J., Crary, F. J., Magee, B. & Westlake, J. (2007). The Process of Tholin Formation in Titan's Upper Atmosphere. *Science, 316*(5826), 870-875.

Wallace, C. S., Prather, E. E. & Duncan, D. K. (2012). A Study of General Education Astronomy Students' Understandings of Cosmology. Part IV. Common Difficulties Students Experience with Cosmology. *Astronomy Education Review, 11*(1), 010104.

Wei, H. Y., Russell, C. T., Dougherty, M. K., Ma, Y. J., Hansen, K. C., McAndrews, H. J., Wellbrock, A., Coates, A. J., Thomsen, M. F. & Young, D. T. (2011). Unusually strong magnetic fields in Titan's ionosphere: T42 case study. *Advances in Space Research, 48*(2), 314-322.

West, R. A., Balloch, J., Dumont, P., Lavvas, P., Lorenz, R., Rannou, P., Ray, T. & Turtle, E. P. (2011). The evolution of Titan's detached haze layer near equinox in 2009. *Geophysical Research Letters, 38*, 06204.

Westlake, J. H., Bell, J. M., Waite, J. H., Johnson, R. E., Luhmann, J. G., Mandt, K. E., Magee, B. A. & Rymer, A. M. (2011). Titan's thermospheric response to various plasma environments. *Journal of Geophysical Research (Space Physics), 116*, 03318.

White, B. Y. (1983). Sources of Difficulty in Understanding Newtonian Dynamics. *Cognitive Science, 7*(1), 41-65.

Wilson, E. H. & Atreya, S. K. (2004). Current state of modeling the photochemistry of Titan's mutually dependent atmosphere and ionosphere. *Journal of Geophysical Research (Planets), 109*, 06002.

Witasse, O., Lebreton, J.-P., Bird, M. K., Dutta-Roy, R., Folkner, W. M., Preston, R. A., Asmar, S. W., Gurvits, L. I., Pogrebenko, S. V., Avruch, I. M., Campbell, R. M., Bignall, H. E., Garrett, M. A., van Langevelde, H. J., Parsley, S. M., Reynolds, C., Szomoru, A., Reynolds, J. E., Phillips, C. J., Sault, R. J., Tzioumis, A. K., Ghigo, F., Langston, G., Brisken, W., Romney, J. D., Mujunen, A., Ritakari, J., Tingay, S. J., Dodson, R. G., van't Klooster, C. G. M., Blancquaert, T., Coustenis, A., Gendron, E., Sicardy, B., Hirtzig, M., Luz, D., Negrao, A., Kostiuk, T., Livengood, T. A., Hartung, M., de Pater, I., Adamkovics, M., Lorenz, R. D., Roe, H., Schaller, E., Brown, M., Bouchez, A. H., Trujillo, C. A., Buratti, B. J., Caillault, L., Magin, T., Bourdon, A. & Laux, C. (2006). Overview of the coordinated ground-based observations of Titan during the Huygens mission. *Journal of Geophysical Research (Planets), 111*, E07S01.

Woldenberg, M. J. (1966). Horton's Laws Justified in Terms of Allometric Growth and Steady State in Open Systems. *Geological Society of America Bulletin, 77*(4), 431-434.

Wolf, D. A. & Neubauer, F. M. (1982). Titan's Highly Variable Plasma Environment. *Journal of Geophysical Research, 87*(A2), 881-885.

Wood, C. A., Lorenz, R., Kirk, R., Lopes, R., Mitchell, K., Stofan, E. & Cassini, R. T. (2010). Impact craters on Titan. *Icarus, 206*, 334-344.

Xin, J., Beilina, L. & Klibanov, M. V. (2010). Globally convergent numerical methods for coefficient inverse problems. *Computing in Science and Engineering, 12*(5), 64-76.

Yelle, R. V. (1991). Non-LTE models of Titan's upper atmosphere. *The Astrophysical Journal, 383*, 380-400.

Yelle, R. V., Strobell, D. F., Lellouch, E. & Gautier, D. (1997). *The Yelle Titan Atmosphere Engineering Models.* Paper presented at the Huygens: Science, Payload and Mission, ESA.

Young, D. T., Berthelier, J. J., Blanc, M., Burch, J. L., Coates, A. J., Goldstein, R., Grande, M., Hill, T. W., Johnson, R. E., Kelha, V., McComas, D. J., Sittler, E. C., Svenes, K. R., Szego, K., Tanskanen, P., Ahola, K., Anderson, D., Bakshi, S., Baragiola, R. A., Barraclough, B. L., Black, R. K., Bolton, S., Booker, T., Bowman, R., Casey, P., Crary, F. J., Delapp, D., Dirks, G., Eaker, N., Funsten, H., Furman, J. D., Gosling, J. T., Hannula, H., Holmlund, C., Huomo, H., Illiano, J. M., Jensen, P., Johnson, M. A., Linder, D. R., Luntama, T., Maurice, S., McCabe, K. P., Mursula, K., Narheim, B. T., Nordholt, J. E., Preece, A., Rudzki, J., Ruitberg, A., Smith, K., Szalai, S., Thomsen, M. F., Viherkanto, K., Vilppola, J., Vollmer, T., Wahl, T. E., Wuest, M., Ylikorpi, T. & Zinsmeyer, C. (2004). Cassini Plasma Spectrometer Investigation. *Space Science Reviews, 114*, 1-112.

Younglove, B. A. & Ely, J. F. (1987). Thermophysical Properties of Fluids. II. Methane, Ethane, Propane, Isobutane, and Normal Butane. *Journal of Physical and Chemical Reference Data, 16*(4), 577-798.

Yung, Y. L. (1987). An update of nitrile photochemistry on Titan. *Icarus, 72*(2), 468-472.

Yung, Y. L., Allen, M. & Pinto, J. P. (1984). Photochemistry of the atmosphere of Titan - Comparison between model and observations. *Astrophysical Journal Supplement Series, 55*, 465-506.

Zarnecki, J. C., Leese, M. R., Garry, J. R. C., Ghafoor, N. & Hathi, B. (2002). Huygens' Surface Science Package. *Space Science Reviews, 104*, 593-611.

Zarnecki, J. C., Leese, M. R., Hathi, B., Ball, A. J., Hagermann, A., Towner, M. C., Lorenz, R. D., McDonnell, J. A. M., Green, S. F., Patel, M. R., Ringrose, T. J., Rosenberg, P. D., Atkinson, K. R., Paton, M. D., Banaszkiewicz, M., Clark, B. C., Ferri, F., Fulchignoni, M., Ghafoor, N. A. L., Kargl, G., Svedhem, H., Delderfield, J., Grande, M., Parker, D. J., Challenor, P. G. & Geake, J. E. (2005). A soft solid surface on Titan as revealed by the Huygens Surface Science Package. *Nature, 438*(7069), 792-795.

Zebker, H. A., Stiles, B., Hensley, S., Lorenz, R., Kirk, R. L. & Lunine, J. (2009). Size and Shape of Saturn's Moon Titan. *Science, 324*, 921-921.

Zhou, Y. & Bifano, T. G. (2006). Characterization of contour shapes achievable with a MEMS deformable mirror. *Proceedings of SPIE, 6113*(123-130).

Zimmer, C., Khurana, K. K. & Kivelson, M. G. (2000). Subsurface Oceans on Europa and Callisto: Constraints from Galileo Magnetometer Observations. *Icarus, 147*, 329-347.